Transactions of the ASME®

Technical Editor,
G. K. SEROVY
Associate Technical Editors
Advanced Energy Systems
M. J. MORAN
Environmental Control
H. E. HESKETH
Fuels and Combustion Technologies
D. W. PACER
Gas Turbine
L. S. LANGSTON
Internal Combustion Engine
J. A. CATON
Nuclear Engineering
S. M. CHO
Power
R. W. PORTER

BOARD ON COMMUNICATIONS
Chairman and Vice-President
M. E. FRANKE

Members-at-Large
W. BEGELL
T. F. CONRY
T. DEAR
R. L. KASTOR
J. KITTO
R. MATES
W. MORGAN
E. M. PATTON
R. E. REDER
A. VAN DER SLUYS
F. M. WHITE
B. ZIELS

President, N. H. HURT, JR.
Executive Director,
D. L. BELDEN
Treasurer, ROBERT A. BENNETT

PUBLISHING STAFF
Mng. Dir., Publ.
CHARLES W. BEARDSLEY
Managing Editor,
CORNELIA MONAHAN
Sr. Production Editor,
VALERIE WINTERS
Production Assistant,
MARISOL ANDINO

Transactions of the ASME, Journal of Engineering for Gas Turbines and Power (ISSN 0742-4795) is published quarterly (Jan., Apr., July, Oct.) for $125.00 per year by The American Society of Mechanical Engineers, 345 East 47th Street, New York, NY 10017. Second class postage paid at New York, NY and additional mailing offices. POSTMASTER: Send address changes to Transactions of the ASME, Journal of Engineering for Gas Turbines and Power, c/o THE AMERICAN SOCIETY OF MECHANICAL ENGINEERS, 22 Law Drive, Box 2300, Fairfield, NJ 07007-2300.
CHANGES OF ADDRESS must be received at Society headquarters seven weeks before they are to be effective. Please send old label and new address.
PRICES: To members, $36.00, annually: to nonmembers, $125.00.
Add $15.00 for postage to countries outside the United States and Canada.
STATEMENT from By-Laws. The Society shall not be responsible for statements or opinions advanced in papers or . . . printed in its publications (B 7.1, para. 3), COPYRIGHT © 1992 by The American Society of Mechanical Engineers. Reprints from this publication may be made on condition that full credit be given the TRANSACTIONS OF THE ASME—JOURNAL OF ENGINEERING FOR GAS TURBINES AND POWER, and the author, and date of publication be stated.
INDEXED by Applied Mechanics Reviews and Engineering Information, Inc.
Canadian Goods & Services Tax Registration #126148048

Journal of Engineering for Gas Turbines and Power

Published Quarterly by The American Society of Mechanical Engineers
VOLUME 114 • NUMBER 2 • APRIL 1992

TECHNICAL PAPERS

161 **Performance Deterioration in Industrial Gas Turbines** (91-GT-228)
I. S. Diakunchak

169 **Marine Gas Turbine Evaluation and Research at the Admiralty Test House, RAE Pyestock** (91-GT-134)
C. J. Bruce and R. A. Cartwright

174 **Implanted Component Faults and Their Effects on Gas Turbine Engine Performance** (91-GT-41)
J. D. MacLeod, V. Taylor, and J. C. G. Laflamme

180 **Simulation of an Advanced Twin-Spool Industrial Gas Turbine** (91-GT-34)
Ping Zhu and H. I. H. Saravanamuttoo

187 **Real-Time Estimation of Gas Turbine Engine Damage Using a Control-Based Kalman Filter Algorithm** (91-GT-216)
L. J. Kerr, T. S. Nemec, and G. W. Gallops

196 **Analytical Condition Inspection and Extension of Time Between Overhaul of F3-30 Engine** (91-GT-277)
M. Nakao, M. Ikeyama, and S. Abe

201 **A Procedure for Automated Gas Turbine Blade Fault Identification Based on Spectral Pattern Analysis** (91-GT-259)
E. Loukis, K. Mathioudakis, and K. Papailiou

209 **Optimal Measurement and Health Index Selection for Gas Turbine Performance Status and Fault Diagnosis** (91-GT-294)
A. Stamatis, K. Mathioudakis, and K. Papailiou

217 **Optimizing Instrumentation When Measuring Jet Engine Blade Vibration** (91-GT-71)
J. H. Griffin

222 **Optimization of LM2500 Gas Generator and Power Turbine Trim-Balance Techniques** (91-GT-240)
B. D. Thompson

230 **An Approach for Evaluation of Gas Turbine Deposition** (91-GT-214)
R. A. Wenglarz

235 **An Investigation in the Variance in Particle Surface Interactions and Their Effects in Gas Turbines** (91-GT-380)
A. Hamed

242 **High-Temperature Erosion Resistance of Coatings for Gas Turbine** (91-GT-213)
W. Tabakoff, A. Hamed, M. Metwally, and M. Pasin

250 **Coating Effect on Particle Trajectories and Turbine Blade Erosion**
W. Tabakoff and M. Metwally

258 **Thermal Barrier Coating Life Prediction Model Development** (91-GT-40)
S. M. Meier, D. M. Nissley, K. D. Sheffler, and T. A. Cruse

264 **Thermal Strain-Tolerant Abradable Thermal Barrier Coatings** (91-GT-39)
T. E. Strangman

268 **Self-Induced Flow in a Stepped Rotating Tube** (91-GT-276)
S. Gilham, P. C. Ivey, and J. M. Owen

275 **Fracture Mechanics Approach to Creep Growth in Welded IN738LC Gas Turbine Blades** (91-GT-119)
W. P. Foo and R. Castillo

284 **High-Cycle Fatigue Design Evolution and Experience of Free-Standing Combustion Turbine Blades** (91-GT-13)
A. J. Scalzo

293 **Analysis of Cracked Gas Turbine Blades** (91-GT-16)
H. L. Bernstein and J. M. Allen

302 **NSTS Orbiter Auxiliary Power Unit Turbine Wheel Cracking Risk Assessment**
T. A. Cruse, R. C. McClung, and T. Y. Torng

309 **TMFSLAM—Design Analysis Tool for Coated Structures** (91-GT-141)
G. S. Bechtel, R. L. McKnight, and T. S. Cook

315 **HITCAN for Actively Cooled Hot-Composite Thermostructural Analysis** (91-GT-116)
C. C. Chamis, P. L. N. Murthy, S. N. Singhal, and J. J. Lackney

(Contents Continued on page 301)

Downloaded 03 Jun 2010 to 171.66.16.159. Redistribution subject to ASME license or copyright; see http://www.asme.org/terms/Terms_Use.cfm

321 The Utilization of Computer-Aided Drafting (CAD) in Quality Control of Gas Turbine Component Repairs (91-GT-138)
D. J. Baldwin

323 Blade Repair With Adaptive Vision Tracking (91-GT-208)
J. R. Anderson and M. J. Skinner

328 Development Testing of Epicyclic Gearing (91-GT-262)
D. E. Yates and G. J. Lack

334 A New Method for Calculating Burst Speed of Aeroengine Disks (91-GT-121)
Hong Qilin, Zheng Qizuan, Wang Ping, and Hou Guicang

338 Morphology of Globules and Cenospheres in Heavy Fuel Oil Burner Experiments
E. Y. Kwack, P. Shakkottai, P. F. Massier, and L. H. Back

346 The Transfer Number of Hydrocarbon Liquids (91-GT-98)
J. Odgers and D. Kretschmer

353 Temperature Effects on Fuel Thermal Stability (91-GT-97)
J. S. Chin, A. H. Lefebvre, and F. T.-Y. Sun

359 Two-Stage Slagging Combustor Design for a Coal-Fueled Industrial Gas Turbine (91-GT-212)
L. H. Cowell, R. T. LeCren, and C. E. Tenbrook

367 Separating Hydrogen From Coal Gasification Gases With Alumina Membranes (91-GT-132)
B. Z. Egan, D. E. Fain, G. E. Roettger, and D. E. White

371 Ceramic Candle Filter Performance at the Grimethorpe (UK) Pressurized Fluidized Bed Combustor (91-GT-381)
J. Stringer and A. J. Leitch

380 Prediction of Gas Turbine On- and Off-Design Performance When Firing Coal-Derived Syngas (91-GT-215)
M. S. Johnson

386 Calculation Approach Validation for Airblast Atomizers (91-GT-305)
N. K. Rizk and H. C. Mongia

395 Motion and Evaporation of Shear-Driven Liquid Films in Turbulent Gases (91-GT-207)
S. Wittig, J. Himmelsbach, B. Noll, H. J. Feld, and W. Samenfink

401 Development of an Innovative High-Temperature Gas Turbine Fuel Nozzle (91-GT-36)
G. D. Myers, J. P. Armstrong, C. D. White, S. Clouser, and R. J. Harvey

409 Measurements of the Entrainment Coefficient of Acoustically Pulsed Axisymmetric Free Air Jets (91-GT-235)
P. J. Vermeulen, P. Rainville, and V. Ramesh

416 CFD Analysis of Jet Mixing in Low NO_x Flametube Combustors (91-GT-217)
M. V. Talpallikar, C. E. Smith, M. C. Lai, and J. D. Holdeman

425 Evaluation of NO_x Mechanisms for Lean, Premixed Combustion (91-GT-257)
R. A. Corr, P. C. Malte, and N. M. Marinov

435 Isothermal Flow Fields in a Research Combustor for Lean Blowout Studies (91-GT-37)
G. J. Sturgess, S. P. Heneghan, M. D. Vangsness, D. R. Ballal, and A. L. Lesmerises

ANNOUNCEMENTS

195 Change of address form for subscribers

Inside back cover Information for authors

Downloaded 03 Jun 2010 to 171.66.16.159. Redistribution subject to ASME license or copyright; see http://www.asme.org/terms/Terms_Use.cfm

Performance Deterioration in Industrial Gas Turbines

I. S. Diakunchak
Gas and Steam Turbine Engineering,
Power Generation Technology Division,
Westinghouse Canada, Inc.,
Hamilton, Ontario, Canada

This paper describes the most important factors affecting the industrial gas turbine engine performance deterioration with service time and provides some approximate data on the prediction of the rate of deterioration. Recommendations are made on how to detect and monitor the performance deterioration. Preventative measures, which can be taken to avoid or retard the performance deterioration, are described in some detail.

Introduction

Why does performance degradation of gas turbine engines occur with operating time?

Even under normal engine operating conditions, with a good inlet filtration system, and using a clean fuel, the engine flow path components will become fouled, eroded, corroded, covered with rust scale, damaged, etc. (Upton, 1974; DeGreef et al., 1978; Bammert and Woelk, 1980; Bammert and Stobe, 1970; Haub and Hauhe, 1990). The result will be deterioration in engine performance, which will get progressively worse with increasing operating time.

Types of engine performance deterioration may be listed under the following main headings:

1 Performance deterioration recoverable with cleaning/washing.

2 Performance deterioration nonrecoverable with cleaning/washing.

3 Permanent performance deterioration, which is not recoverable after an overhaul and the refurbishment of all clearances, replacement of damaged parts, etc.

Recoverable Deterioration. Normal operation of an engine, even if it is equipped with a good filter, results in the accumulation of dirt, dust, pollen, etc., particles on the compressor airfoils and gas path surfaces, as well as blockage of the inlet filters (Thames et al., 1989; Saravanamuttoo and Lakshminarasimha, 1985). These particles, in addition to soot particles produced in the combustor, can also accumulate on the flow path surfaces of the turbine. Oil leaks into the compressor inlet or the presence of oily hydrocarbons or other sticky chemicals in the atmosphere exacerbate the situation. The oil or "oily" substances in the incoming air act as glue to fix the dirt particles to the compressor airfoil and shroud surfaces. In the back end of the compressor, where the temperatures are high enough, these "oils" bake on to the surfaces to produce a fairly thick coating. In the case of a compressor in a gas turbine installed in a paper mill, the paper fibers plus some "oily" substance present in the atmosphere resulted in a fairly thick, rough, baked-on coating on most of the compressor flow path surfaces. When crude oil is burned in the gas turbine engine, the hot end is subjected to additional harmful deposits, including salt deposits originating in the inlet air or from fuel additives.

The "fouling" of the flow path surfaces, described above, results in varying degrees of performance deterioration in the different components of the gas turbine engine, and hence in a decrease in the overall engine performance. Compressor fouling results in a reduction of inlet mass flow and compressor efficiency. Hot-end fouling results mostly in a reduction in the overall turbine efficiency and in a reduction in engine firing temperature.

The following methods are used in cleaning the flow path components of gas turbine engines, without the necessity of engine disassembly:

1 On-line dry cleaning of compressors with new catalyst, rice husks, pecan shells, or some other dry abrasive material.

2 On-line (at base load or part power) wash of compressor with water, water mixed with detergent, or some other suitable fluid, which is preferably nontoxic, nonflammable, and biodegradable.

3 Soak wash (with the engine not running) with a suitable fluid. This method is probably the most efficient for cleaning the compressor, and especially the hot-end components, which were coated with deposits as a result of running on crude oil fuel, without opening up the engine.

The use of appropriate filters will attenuate the rate of fouling, but will not eliminate it. Smooth airfoil surfaces, or those coated with coatings, which reduce surface roughness, will be less susceptible to fouling and will give better response to cleaning or washing.

Icing up of the filter, the inlet cylinder, the inlet guide vanes, and the front part of compressor can have a significant effect on engine performance and operation. The resulting performance deterioration may be even more severe and more sudden than that due to "normal" compressor fouling. The icing phenomenon is temporary, and, assuming it does not result in compressor damage, will not affect the rate of performance deterioration with time.

Nonrecoverable With Cleaning/Washing. Even with regular cleaning/washing, some surface deposits will remain and

Contributed by the International Gas Turbine Institute and presented at the 36th International Gas Turbine and Aeroengine Congress and Exposition, Orlando, Florida, June 3-6, 1991. Manuscript received at ASME Headquarters March 4, 1991. Paper No. 91-GT-228. Associate Editor: L. A. Riekert.

Copyright © 1992 by ASME
Downloaded 02 Jun 2010 to 171.66.16.112. Redistribution subject to ASME license or copyright; see http://www.asme.org/terms/Terms_Use.cfm

will detract from the performance of the affected component. Any flow path damage, surface erosion/corrosion, tip and seal clearance increase, cylinder distortion, etc., will not be affected by cleaning/washing and the resulting performance deterioration will remain and perhaps get worse with time.

Permanent Performance Deterioration. During an engine overhaul the flow path components are thoroughly cleaned, damaged parts are replaced or damaged areas "blended out," tip and seal clearances are restored to "as new" condition, any obvious leakage paths are sealed up, the pertinent airfoils recoated, etc. These actions ensure that the engine is restored as closely as possible to the "as new and clean" condition. After completion of a major overhaul, the engine performance would theoretically be expected to be as per the initial performance acceptance test. However, it is usually the case that the engine performance is not restored to the "as new" condition because of cylinder distortion (and hence eccentricity in clearances and increased leakage paths), increased surface roughness of flow path components (due to erosion or rust scale deposits on compressor disks and annulus surfaces), distortion in platforms causing loss of aerodynamic performance and increased leakage, airfoil untwist, etc. Fortunately, under normal circumstances the unrecoverable performance deterioration is small.

Factors Affecting Performance Deterioration

Contaminants. Air-borne contaminants are listed below:

1 Hard particles (causing erosion and fouling): dust, dirt, sand, rust, ash, carbon particles.

2 Soft particles (causing fouling): oil, unburned hydrocarbons, soot, air-borne industrial chemicals, fertilizers, herbicides, insecticides, pollen, plant spores, air-borne insects, air-borne salts.

About 80 percent of particulate contaminants are below 2 μm in diameter. If an evaporative cooler is used, then water-borne contaminants, such as dirt and salts, may be introduced. These may result in fouling and corrosion. Contaminants affecting the hot end include some of those listed above, plus fuel-borne contaminants, those produced as a result of the combustion process, contaminants in water or steam injected for NO_x control, and any particles, such as rust scale, etc., introduced through the cooling air system piping.

Fouling. Fouling is defined as degradation of flow capacity and efficiency caused by adherence of particular contaminants to the gas turbine engine airfoil and annulus surfaces. The result of fouling is build up of material, which changes the shape of the airfoil, changes the airfoil inlet angle, increases surface roughness, and reduces the airfoil throat opening. The end result is reduced component performance.

Fouling, which can normally be eliminated by cleaning, can occur in both the compressor and the turbine. Compressor fouling is more common and has the more serious effect on engine performance. Typically about 70 to 85 percent of all gas turbine engine performance loss accumulated during operation is attributable to compressor fouling. The contaminants that cause compressor fouling enter the compressor with the inlet air. Those that cause turbine fouling enter the turbine with the inlet air, cooling air, fuel, fuel additives, and water/steam used for NO_x control.

All compressors are susceptible to fouling. The degree of fouling, the rate of fouling, and the effect on performance depend on the following: compressor design, compressor airfoil loading, airfoil incidences, airfoil surface smoothness/coating, type and condition of the air-borne contaminants, the site environment, and the climatic conditions (high humidity increases the rate of fouling) (Seddigh and Saravanamuttoo, 1990). Compressor fouling not only reduces the inlet flow and compressor efficiency, but also reduces the compressor surge margin (Mezheritsky and Sudarev, 1990) and may result in compressor surge. Turbine fouling will depend on the ability of the contaminants to reach the turbine and to adhere to the gas path surfaces. Operation of a gas turbine engine on residual fuel oil, heavy oil, or crude oil will have a corrosive effect on the hot end gas path components. The corrosion plus deposits on the flow path surfaces will result in engine performance deterioration.

Types of Filters. The function of gas turbine inlet filters is to remove particles, such as dirt, dust, soot, etc., from the compressor inlet flow and prevent compressor fouling, erosion, and corrosion. The three main types of filters are listed below:

1 Inertial filter: This is the simplest and least expensive type of filter. It functions by centrifuging out particles from the inlet flow. The accumulated dirt is then removed (continuous 5 to 10 percent bleed). The velocity in the filter has to be fairly high to make it work. This filter is effective in removing particles above 20 μm diameter. Thus, this type of filter is good in preventing erosion due to the presence of large dust or dirt particles in the inlet air. But it is not very effective in removing particles less than 20 μm in diameter, and hence it is not very efficient in preventing compressor fouling. Compressor fouling is generally caused by particles with diameter of 5 μm or less. The pressure loss in the inertial filter is about 1 in. (25 mm) H_2O, and it does not increase with service.

2 Self-cleaning pulse filter: The system utilizes high-efficiency media filter cartridges, which are sequentially cleaned during normal turbine operation by pulses of pressurized air. The compressed air jets set up vibration waves in the cartridges and shake off the dirt, which collects on the bottom. The inlet air enters the cylindrical cartridges from the sides and then flows radially outward through a venturi. The "pulse" air blows radially downward into the cartridges. As the contaminants build up on the outside surfaces of the cartridges, the pressure drop across the cartridges will increase. When the pressure drop reaches a preset limit [usually 1 to 1.5 in. (25 to 37.5 mm) H_2O above the initial "operating" pressure drop of about 1 in. (25 mm) H_2O] the automatic "pulse" cleaning sequence is activated. The air "pulse" is controlled by a timer/sequencer, which operates air valves attached to a high-pressure air supply. This is a good filter to use when moisture is present in the air and where icing is likely to occur (the "pulse" knocks off the ice particles as they are formed). The efficiency of this filter can be quite high.

3 High-efficiency filter: This filter uses glass fiber filter pads, which must be replaced when the loss becomes excessive. The engine must be stopped for filter pad replacement. There are special filters available that prevent salt migration downstream. The pressure loss with clean filter pads is about 1 in. (25 mm) H_2O. This type of filter has the highest efficiency.

The choice of the most effective inlet filtration system depends on the site conditions, and may include a combination of the above filter types. It should be pointed out that the cost of even the most expensive inlet filtration system will be recovered as a result of improved engine performance.

Coatings. There are two main reasons for coating of compressor airfoils with a suitable coating, which results in reduced surface roughness on compressor airfoils. The first reason is improved performance and the second is corrosion protection.

On a new engine, due to reduced airfoil surface roughness, the coating of compressor airfoils will result in an improvement in compressor performance and hence in output power and heat rate. This is only a part of the performance benefit resulting from the coating. In environments that have dust particles, etc., rough blades will foul very quickly. The result is a serious loss of performance over a period of several days. By washing the compressor only some of the performance loss is regained. Over a long period of time, even with repeated

Downloaded 02 Jun 2010 to 171.66.16.112. Redistribution subject to ASME license or copyright; see http://www.asme.org/terms/Terms_Use.cfm

washing, the engine performance will have deteriorated by several percent. With coated blades the fouling rate is greatly reduced, the intervals between washes is increased (to at least double the interval with uncoated airfoils), the airfoils are easier to clean, and there is no significant reduction in the "clean" engine performance after many washes (i.e., there is no decrease in performance after a wash from one wash to the next). Thus over a long operating period the average performance with coated compressor airfoils may be 1 to 3 percent better than with uncoated airfoils.

Coating compressor airfoils with a coating such as Sermetel 5380 DP will result in reduced airfoil surface roughness, in increased protection from corrosion, and perhaps in some protection from erosion.

Cleaning. The objective of cleaning is to restore the gas turbine engine flow path surfaces as closely as possible to their initial new condition. In installations where fouling is considered to be a serious problem, the cleaning operation should be started soon after engine commissioning and continued at regular intervals. If initially the engine is allowed to get massively fouled, subsequent dry cleaning or even on-line washing may produce only limited results.

Compressor Cleaning. The following methods are employed to restore the compressor airfoil and annulus surfaces to the "clean" condition for an engine that is fully assembled:

1 Manual cleaning: Hand cleaning of the inlet duct, inlet guide vanes, and perhaps the first-stage compressor blades may be carried out by accessing these components from the inlet, when the engine is shut down. This hand cleaning can be quite effective, since the airfoil throat areas of the front stages have the most influence on the compressor inlet flow.

2 "Dry" cleaning: The compressor is cleaned on-line by injecting dry abrasive media, such as new catalyst, crushed pecan nut shells, etc. By the scouring action of the abrasive particles the deposits attached to the compressor surfaces are dislodged and blown downstream. There is a danger that the use of dry abrasive materials may result in erosion by airfoil surface coatings and blockage of turbine airfoil cooling holes. Dry abrasive cleaning is usually not recommended for coated compressor airfoils. Figure 1 shows the effect of progressive fouling on the mass flow of an industrial gas turbine, as well as the results of on-line dry cleaning and hand cleaning of the front components of the compressor.

3 Washing: Water or water mixed with detergents is injected into the compressor inlet when the engine is on-line. The water used in this operation must be clean and free from such impurities as sulfates, carbonates, and chlorides, which will be deposited as scale in the rear compressor stages where the air temperature is above the boiling point. The contaminants adhering to the compressor surfaces are "washed" away or dissolved and removed. Although sometimes the contaminants removed from the front stages may be deposited on the downstream stages, this is a very effective cleaning method. An even more effective method is to soak wash when the engine is shut down.

The selection of the most effective compressor cleaning method (whether dry cleaning or water/detergent washing or both) depends on the type and condition of the contamination. Dry cleaning is usually most efficient if the compressor is fouled by dry hard deposits. Contamination by oil or salt deposits is best taken care of by washing. Experimentation and good record keeping may be required to arrive at the optimum cleaning procedure.

Hot End Cleaning. Removal of deposits from the hot end components is more difficult to accomplish. This is done by injecting water through the existing atomizing air system when the engine is cold, with the rotor being rotated at about the ignition speed by the starting device. The injection is followed by shut down and a soak period. This cycle is repeated and finally followed by a spin to dry the engine (DeGreef et al., 1978). The effectiveness of the water washing depends primarily on the duration of the soaking.

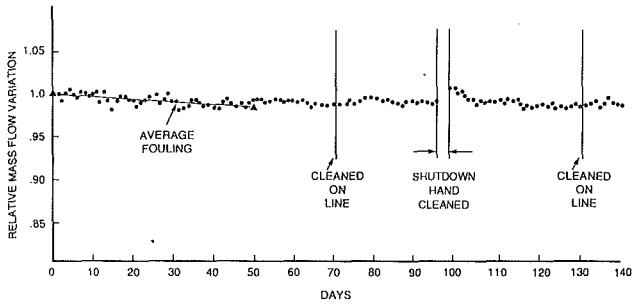


Fig. 1 Relative mass flow variation with time

Corrosion, Erosion, Damage. Corrosion is the loss of material from flow path components caused by the chemical reaction between these components and contaminants that enter the gas turbine with the inlet air, fuel, or injected water/steam. Salts, mineral acids, and reactive gases such as chlorine and sulfur oxides, in combination with water, can cause wet corrosion, especially of the compressor airfoils. Coating of compressor airfoils will protect them against wet corrosion and prevent the resulting performance deterioration. Elements such as sodium, vanadium, and lead, in metallic or compound form, can lead to high-temperature corrosion of turbine airfoils. The result is a loss in both the service life of turbine components and in engine performance. Even in gas turbines running on clean gas fuel there will be hot-end component surface oxidation, which will result in the formation of a rough scale and hence performance deterioration.

Erosion is the abrasive removal of material from the flow path components by hard particles suspended in the air or gas stream. Particles causing erosion are usually 20 μm or more in diameter. The erosion of airfoil surfaces results in increased surface roughness, changes in the inlet metal angle (hence change in airfoil incidence), change in airfoil profile, change in airfoil throat opening, and increase in blade tip and seal clearances. The results of the above changes are increased losses and therefore a decrease in performance. Occasionally erosion results in reduced airfoil trailing edge thicknesses. This may be beneficial to performance, but is unacceptable from mechanical integrity considerations.

Damage is often caused by large foreign objects striking the flow path components of the gas turbine engine. These objects enter the engine with the inlet air or are the result of pieces of the engine itself breaking off and being carried downstream. Pieces of ice breaking off from the inlet of the compressor, or large pieces of carbon breaking off from fuel nozzles, can also result in damage to internal components. The resulting damage can lead at worst to a catastrophic engine failure or at best to nonrecoverable (with cleaning) engine performance deterioration.

Engine Operation and Maintenance Practices. The manner in which the engine is operated will have an effect on the performance deterioration rate. The starting cycle results in the most severe hot end thermal gradients experienced during normal engine operation. At ignition the combustor exit temperature exceeds that during normal operation for a short time until the control system regulates the fuel and air flows to lower it. Therefore, the oxidation and corrosion experienced by the hot end components are most severe during this time and will add to the engine performance degradation. During the starting cycle the rotor assembly passes through its critical speeds. The resultant increase in vibration, if the rotor is not balanced perfectly, will cause blade tip and seal rubs. Also on

Downloaded 02 Jun 2010 to 171.66.16.112. Redistribution subject to ASME license or copyright; see http://www.asme.org/terms/Terms_Use.cfm

start-up, the transient differential expansion rates between the large mass stationary components and the lighter mass rotor assembly may result in blade tip and seal rubs. The increased clearances will result in increased leakage and hence in performance deterioration. Operation at peak rating will have similar results, as described above, with the exception of rubs due to running through criticals, and will cause performance deterioration. Frequent emergency trips from base load will also have a negative effect on engine performance. Therefore, an engine that is subjected to many starting and emergency trip cycles and/or is operated for considerable periods of time at peak rating will experience a more severe performance degradation than an engine that is operated at or below base load.

Maintenance practices of a gas turbine engine have a considerable impact on the rate of engine performance deterioration. The control system must be properly maintained to ensure correct fuel scheduling during starting and normal operation, in order to prevent excessive temperature gradients. The fuel system and the water/steam injection systems must be maintained properly to prevent contaminants from getting into the engine. Proper maintenance of the combustion system is required to ensure low circumferential and radial temperature gradients. It is very important that the engine be operated within the specified safe operating envelope. Regular inspection of the inlet filter system and regular compressor cleaning should be instituted. Following correct engine maintenance practices will result in reduced rate of performance deterioration.

Performance Deterioration

Inlet. Fouling of high-efficiency filters occurs progressively with time. The blockage of the filter pads results in increased inlet loss and hence in engine performance deterioration. This performance loss is recovered completely when new filter pads are installed. The performance deterioration for an industrial gas turbine engine with increasing inlet loss is shown in Fig. 2. For a 6 in. (150 mm) H_2O inlet loss increase, the engine output power decreases by about 2.6 percent and the heat rate increases by about 1 percent.

Compressor. Some information available from the open literature indicates that fouling causing a 5 percent reduction in inlet flow will also reduce the compressor efficiency by about 2.5 percent (Saravanamuttoo and Lakshminarasimha, 1985). The resulting decrease in engine power will be about 10 percent. Usually the fouling trend is assumed to have a linear characteristic with time. Experimental tests on the compressor of a small turboprop gas turbine engine indicated that the prime effect of fouling is on the inlet air flow rather than on compressor efficiency, and that the reduction in flow varies with operating speed (being higher at design speed).

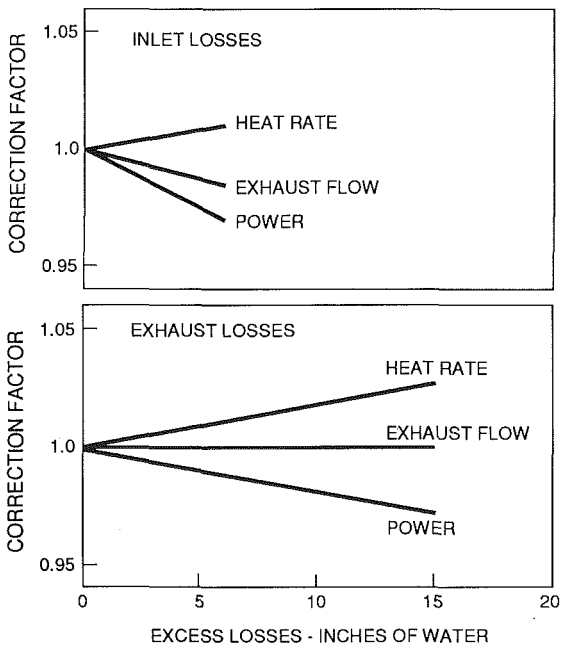


Fig. 2 Correction factor curves for inlet and exhaust duct losses

Site test data obtained on a large industrial gas turbine indicated that compressor fouling resulted in a 5 percent reduction in inlet mass flow and 1.8 percent reduction in compressor efficiency. This amount of fouling would reduce the engine output power by about 7 percent and increase the heat rate by about 2.5 percent.

Bleed valve leakage, flange and horizontal joint leakage, and improper positioning of the inlet guide vanes will have a deleterious effect on the compressor performance. The compressor control bleed valves have a tendency to bind in the open position or to leak during full-load operation. The latter is the more likely occurrence, which will get progressively worse with time and result in a performance penalty. The improper stagger of the inlet guide vanes will also result in a decrease in compressor performance.

The performance deterioration due to "nicks," tip and seal rubs, erosion, damage, etc., may be significant in some cases, but usually it is considerably less than that due to compressor fouling. It should be pointed out that compressor fouling and other compressor performance deterioration causes have no effect on engine firing temperature.

Hot End. Under "hot end" are included: combustion system, turbine, and exhaust diffuser. The combustion system is not likely to be the direct cause of performance deterioration with time. Irrespective of the fuel used (whether natural gas, distillate oil, or even crude oil) and even if the fuel nozzles are coated with carbon deposits, the combustion efficiency will not decrease. However, carbon deposits breaking off from the nozzles and soot produced as a result of incomplete fuel burning will result in performance deterioration. Also, changes in the combustor outlet pattern factor may result in a temporary or permanent deformation of downstream components, which in turn will result in performance deterioration. Hot end cylinder warping, which will increase with time, may result in flange and horizontal joint leakage, and hence in performance deterioration.

Fouling of the turbine airfoils and annulus, surface erosion, "nicks" and deformation, blade tip and seal land rubs, and increased leakage and cooling flows will result in performance deterioration. Experiments carried out on a multistage axial turbine showed that both reduction in airfoil profile thickness (as caused by erosion) and increase in airfoil profile thickness (resulting from surface deposits) result in a significant performance reduction (Bammert and Stobe, 1970). Any changes in the exhaust diffuser performance can be included in the overall turbine efficiency changes. A decrease of 1 percent in the overall turbine efficiency in an engine such as the CW251B12 will result in about 2.5 percent decrease in output power and a similar increase in heat rate. In addition, because of a decrease in the turbine temperature drop, the engine will be underfired by about 12°F (6.7°C) (note that the engine is controlled to a specified exhaust temperature). This will result in a further 1.2 percent decrease in output power and about 0.2 percent increase in heat rate. Thus the cumulative result of a 1 percent decrease in turbine efficiency with time is about 3.7 percent decrease in output power and about 2.7 percent increase in heat rate.

Gearbox, Generator, Auxiliaries, and Exhaust System. The components included under this heading will also suffer performance deterioration with time and as a result will

Downloaded 02 Jun 2010 to 171.66.16.112. Redistribution subject to ASME license or copyright; see http://www.asme.org/terms/Terms_Use.cfm

affect the overall engine performance. It is more difficult to detect the performance losses in these components or to predict their rate of increase with time. The exception is the exhaust system loss. The increase in exhaust loss can be measured and steps can be taken to remedy the situation if the loss becomes excessive. Figure 2 shows the effect of exhaust loss increase on the CW251B12 engine performance. It should be noted that an increase in exhaust loss will result in a reduction in the firing temperature and hence a further reduction in engine performance. Thus a 6 in. (150 mm) H_2O increase in exhaust loss will result in about a 4.2°F (2.3°C) decrease in the firing temperature. Hence the total engine performance deterioration will be a 1.4 percent decrease in power and a 1.1 percent increase in heat rate.

Overall Plant. The overall plant performance deterioration is the result of the combined effect of all of the performance shortfalls of the individual components described previously. Past experience with gas turbines has shown that after 3000 operating hours the output power loss can be as high as 20 percent under unfavorable conditions and as low as 2 percent under the most favorable conditions (Scheper et al., 1978). For instance, a 2 in. (50 mm) H_2O increase in inlet loss, a 5 percent decrease in inlet mass flow, a 1.8 percent decrease in compressor efficiency, and a 0.5 percent decrease in turbine efficiency, will result in a 10 percent decrease in output power and a 4.2 percent increase in heat rate.

The control system can also affect the perceived performance deterioration. If the control system is not properly adjusted, the engine may be operated below the desired base load setting. This will lead to decreased output power and higher heat rate.

Methods of Detection of Fouling/Performance Deterioration

Detection of the extent of compressor fouling or engine performance deterioration is necessary before the appropriate actions can be taken to restore the performance shortfall. A side benefit of monitoring the compressor fouling or engine performance is the early detection of potential engine mechanical problems, and their resolution before the occurrence of a catastrophic engine failure.

Economic considerations may enter into the determination of compressor cleaning frequency. On-line washing usually requires running the engine at part load, while soak washing necessitates shutting down the engine for a considerable period of time. In both cases there is a loss in power, and hence in revenue. Therefore, washing more frequently than required is a wasteful procedure. However, if compressor washing is delayed too long, the resulting performance deterioration will also cause a loss in revenue. Thus it is important to be able to detect compressor fouling and to institute an optimum compressor washing frequency. The optimum will depend on the particular situation at each installation. As a general recommendation, the compressor should be cleaned/washed when the estimated mass flow decrease reaches the 2 to 3 percent level.

Compressor Fouling. Compressor fouling, and hence engine performance deterioration, can be detected using the following methods:

1 Change in combustion shell pressure: The combustion shell pressure is one of the parameters used by the control system to maintain the engine at base load. Therefore, it is a readily available and accurate measurement. When the compressor is fouled the inlet mass flow is reduced, and as a result the engine matches at a lower pressure ratio. Therefore, the amount of compressor fouling can be deduced at any time by comparing the actual site combustor shell pressure to the expected pressure if the compressor were clean. One complication is that the combustor shell pressure varies with barometric

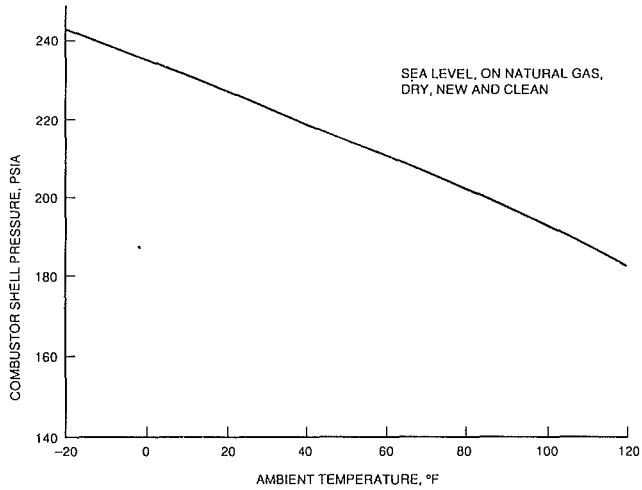


Fig. 3 Combustor shell pressure versus ambient temperature

pressure, inlet loss, compressor inlet temperature, and output power (assuming operation not at base load). If the assumption is made that the engine is operated at base load and that the inlet loss and barometric pressure variations are small, then the expected or "clean" combustor shell pressure variation with inlet temperature is a unique line (a typical curve is shown on Fig. 3 for an engine at sea level on natural gas fuel). To check for fouling at any time, the site measured combustor shell pressure can then be plotted on this curve. If the point is below the line, then the compressor is assumed to be fouled. Each percentage point that the actual pressure is below the line corresponds to a one percent reduction in inlet flow.

2 Measurement of inlet cylinder depression: Measurement of the inlet cylinder depression with the aid of a manometer gives an indication of inlet flow. The compressor inlet cylinder acts like an accelerating flow nozzle, since there is a continuous reduction in area from the inlet flange to the inlet guide vane inlet plane. Therefore, there will be a large difference in the static pressures measured at the inlet flange and the inlet guide vane inlet plane. As in a nozzle, the ratio of the static pressure difference measured at the two planes divided by the pressure at inlet is independent of the pressure loss upstream of the measurement plane for a given volume flow. A change in the inlet cylinder pressure ratio will result only from obstructions within the compressor itself, and hence can be used to detect compressor fouling.

Assuming that a proper inlet cylinder flow calibration curve is not available, a plot of the static pressure ratio versus the nondimensional compressor speed ($N/\sqrt{\theta}$, where θ is as defined on Fig. 4) is produced when the compressor is "new and clean." In order to get a large enough variation of inlet speed, the data may have to be recorded over a length of time, in which there is a significant ambient temperature variation. The inlet cylinder static pressure ratio obtained at any time in the future is then plotted on this graph. If the new points fall below the "clean" curve, then the compressor is fouled. The reduction in compressor inlet flow is proportional to the square root of the reduction in the inlet cylinder static pressure ratio.

3 Inlet scroll calibration curve: The compressor inlet scroll calibration curve is obtained during a shop test of the engine when accurate measurements are made of the inlet flow and the static pressures at the compressor inlet flange and just upstream of the inlet guide vanes. Figure 5 shows a typical inlet scroll calibration curve, which is the nondimensional inlet mass flow plotted versus the inlet cylinder static pressure ratio. Occasionally there is an inconsistency between shop and site inlet flow measurements, even when the compressor is "new and clean," i.e., there is a difference in the inlet flow, for the same $N/\sqrt{\theta}$, between shop and site. This may be explained by

Downloaded 02 Jun 2010 to 171.66.16.112. Redistribution subject to ASME license or copyright; see http://www.asme.org/terms/Terms_Use.cfm

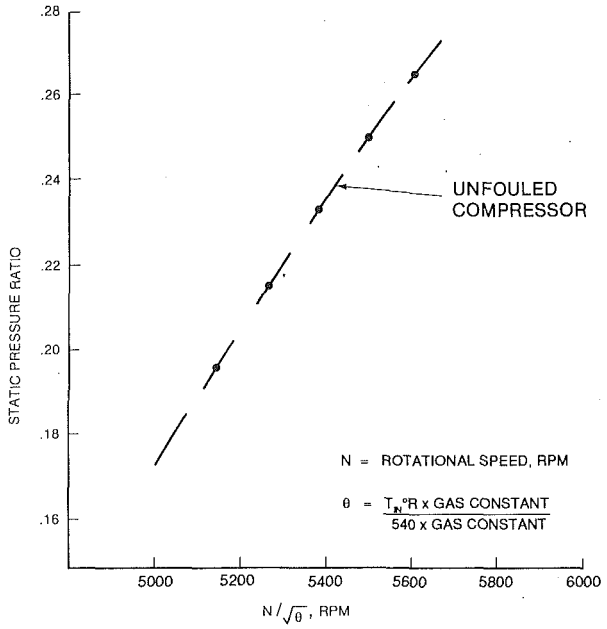


Fig. 4 Inlet cylinder static pressure ratio versus nondimensional speed

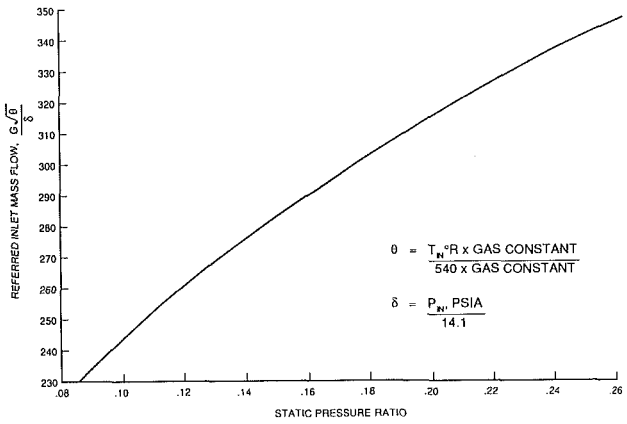


Fig. 5 Typical inlet scroll calibration curve

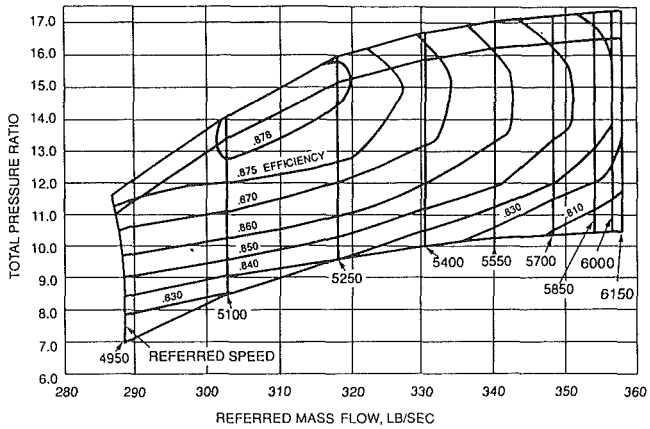


Fig. 6 Compressor map

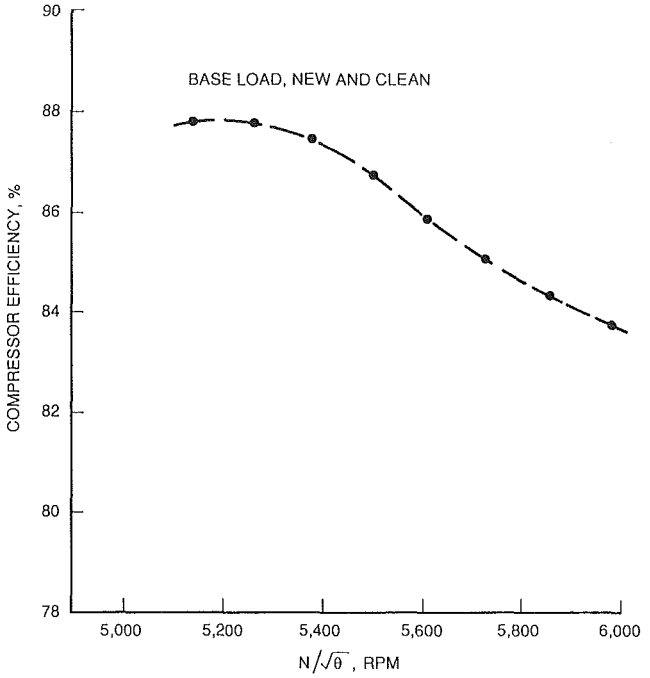


Fig. 7 Compressor efficiency versus referred speed

the differences in the inlet ducting, pressure tap, and pressure line installations between shop and site. To be on the safe side, a new "clean" curve should be obtained from the site data as follows: As soon as possible after engine commissioning, when the compressor is clean, data points should be obtained over a wide ambient temperature range. With the compressor pressure ratio and nondimensional speed determined from site data, we obtain the expected nondimensional inlet mass flow from the compressor map (see Fig. 6, derived from shop tests) at the different ambient temperature base load operating conditions. Then we plot the nondimensional inlet mass flow versus the site measured inlet cylinder pressure ratio. A smooth curve should be drawn through these points parallel to the original shop inlet scroll calibration curve. Then, as the engine operating hours increase, with the site measured inlet cylinder pressure ratio, the inlet mass flow is read from the calibration curve (preferably the one established at site). This mass flow is then compared to the "clean" compressor mass flow from Fig. 6 to determine the amount of compressor fouling that has occurred.

With the aid of the shop test derived compressor map it is also possible to determine the amount of compressor efficiency decrease that has taken place with operating time. A graph showing the base load compressor efficiency variation versus nondimensional speed can be used for this purpose (see Fig. 7). The compressor efficiency may be estimated approximately from the overall pressure ratio (combustion shell pressure divided by the ambient pressure, or preferably the compressor inlet pressure) and the compressor temperature rise from inlet to the combustor shell. The compressor efficiency estimated in this manner will be lower than the actual one because of the probable inclusion of inlet duct loss, inaccurate compressor exit pressure, and temperature pick-up across the combustor outlet transition ducts. However, as with the compressor inlet mass flow, efficiency data can be collected when the compressor is "new and clean" and can subsequently be used for comparison when compressor fouling has occurred.

Engine Performance. The extent of compressor fouling and the other deleterious effects that occur in an engine with increasing operating time can be determined by periodically monitoring the engine output power and comparing it to the expected value, or to the value when the engine was new and clean. This type of monitoring is more complicated than just detecting compressor fouling. The simplicity or complication may range from the measurement of just a few key performance parameters to a full-blown on-line health monitoring system. To detect the power shortfall some or most of the following parameters must be measured: output power, auxiliary power, power factor, speed, inlet temperature, relative humidity, bar-

Downloaded 02 Jun 2010 to 171.66.16.112. Redistribution subject to ASME license or copyright; see http://www.asme.org/terms/Terms_Use.cfm

ometric pressure, exhaust temperature, combustor shell pressure, inlet loss, exhaust loss, water/steam injection rate, and instrumentation bleed air, if any. With the above information and with the aid of the correction curves for the deviation of site conditions from the standard or guarantee power, the site output power is corrected to standard conditions and compared to the "clean" engine power. The amount of the power shortfall from the expected value will indicate the extent of compressor fouling or other problems causing performance deterioration.

A further complication could be introduced by measuring fuel flow, fuel temperature, fuel lower heating value, etc., so as to be able to determine the engine heat rate and compare it to the "clean" value. For this exercise similar correction curves, as described above, will have to be used.

Cost of Fouling/Performance Deterioration

There is a significant cost to the gas turbine engine operator associated with fouling and the resulting performance deterioration. To make an approximate estimate of the cost, the following assumptions are made:

1 Simple Cycle CW251B12 Econopac Engine, on natural gas fuel, no injection.
2 Net output power = 46,500 kW
Net heat rate = 10,550 Btu/kW·h.
The above are average yearly values.
3 Engine on base load operation for 8000 hours per year.
4 Cost of electricity is $0.04/kW·h.
5 Cost of natural gas fuel is $2/MBtu
6 Improper cleaning, maintenance, etc., will result in an average yearly decrease in power of 3 percent and increase in heat rate of 1 percent.

The resulting yearly power shortfall = $0.03 \times 46{,}500 \times 8000 = 11.2 \times 10^6$ kW·h. The cost of the power shortfall = $11.2 \times 10^6 \times 0.04 = \$446{,}400$. The resulting yearly excess fuel flow = $0.01 \times 10550 \times (1-0.03) \times 46{,}500 \times 8000 = 38.07 \times 10^9$ Btu. The cost of the excess fuel = $2 \times 38.07 \times 10^9/10^6 = \$76{,}140$. The total yearly cost of the assumed average performance deterioration is $522,500. Over the three-year operating period between major overhauls the total cost will be about 1.5 million dollars.

In the case of a combined cycle application there will be an additional cost due to reduced steam production in the waste heat boiler. Although compressor fouling results in an increase in exhaust temperature (at the same ambient temperature), the reduced exhaust flow has a greater negative effect. Thus the net effect is reduced steam production as a result of compressor fouling.

Prediction of Performance Deterioration With Time

There are several reasons why the prediction of performance deterioration with time is required. At the negotiation stage the prospective customer may request this information so as to be able to carry out a long-term economic benefit analysis on the engine. A user of the engine may wish to know what is a reasonable performance deterioration after a specified number of service hours and what constitutes excessive fouling or performance deterioration rate, which may require urgent remedial action. The vendor may be required to guarantee engine performance over a specified number of operating hours and will require a realistic prediction of the performance deterioration rate.

The exact degree of performance deterioration occurring with service time is impossible to predict accurately due to the large number of previously described variables. The amount of actual field test performance data that has been published on gas turbine engine performance deterioration with time is very limited. Some approximate published data (DeGreef et al., 1978) and some in-house test results are available.

At one installation site test data indicated that up to 8 percent power loss occurred over a two-week period. Most of this power shortfall could be recovered by cleaning the compressor with new catalyst. At another installation, after incorporation of coated compressor airfoils, the fouling rate was reduced considerably and on-line washing of the compressor recovered all of the power shortfall. At a third installation, after six months of continuous operation without compressor cleaning, the engine experienced a 4.3 percent loss in power. A series of on-line, at reduced load, water washes recovered all but 0.5 percent of the power shortfall. It should be pointed out that this engine had a good inlet filtration system and coated compressor stator airfoils.

In order even to make an attempt at the prediction of performance deterioration, some ground rules or assumptions must be made. In the prediction of the likely engine performance deterioration with time the following assumptions were made:

1 Types of fuel used: (*a*) natural gas, (*b*) distillate oil, and (*c*) heavy or crude oil.
2 Clean environment.
3 The engine will start its service life at time zero in the "new and clean" condition with zero performance shortfall.
4 Continuous base load operation for three years (24,000 hours or equivalent service hours) before a major overhaul. During the overhaul the engine is refurbished to almost "as new" condition, i.e., tip and seal clearances restored, damaged parts removed, "nicks" blended out, flow path surfaces cleaned, etc.
5 Good filtration system used, clean operating environment (no oil leaks, no corrosive chemicals, no sand), no major foreign object damage, coated compressor airfoils.
6 Proper operating and maintenance procedures.
7 Effective and regular cleaning/washing of the compressor over the operating period.

Based on the above assumptions, the previously described engine component performance deteriorations, and some actual field test data, the overall engine performance deterioration with time can be estimated very approximately. The assumed shape of the typical performance deterioration versus service hours curve is shown on Fig. 8. This curve shows results of frequent compressor cleaning and also the nonrecoverable, with cleaning, performance deterioration line. It should be pointed out that the nonrecoverable with cleaning performance deterioration will apply equally to power and heat rate. This can be explained by the fact that once the effect of compressor fouling (which has a more significant influence on air flow and hence power, than on compressor efficiency and heat rate) has been removed then the degradation of power and heat rate will be approximately similar.

In predicting performance deterioration with time the following scenario is assumed: that the engine has been manufactured correctly and does not have any hidden problems waiting to happen, is well maintained, is properly operated, does not experience overtemperaturing during starts, is not subjected to an excessive number of trips from full load, and is cleaned regularly (when the power loss reaches 2 to 3 percent) over the entire operating period. Although this scenario may be described as optimistic, it is not impossible to achieve in practice if all of the recommendations listed below are adhered to. In this case, after the three years of operation the permanent performance deterioration (after cleaning) is 1.25 percent on natural gas fuel, 1.75 percent on distillate oil fuel, and 3 percent on crude or residual oil fuel. Note that the performance deterioration percentages apply to both output power and heat rate, as was explained previously. After a major overhaul and complete refurbishing of the flow path parts, the permanent performance shortfall will be almost eliminated. The remaining unrecovered performance shortfall will be 0.25 percent for both natural gas and distillate oil fuels, and 0.5 percent for crude

Downloaded 02 Jun 2010 to 171.66.16.112. Redistribution subject to ASME license or copyright; see http://www.asme.org/terms/Terms_Use.cfm

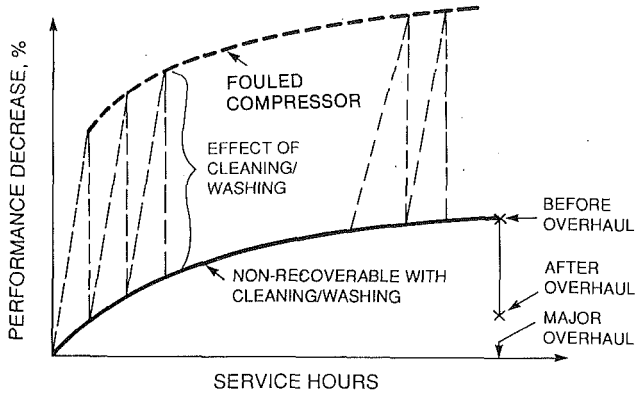


Fig. 8 Typical performance deterioration

or residual oil fuel. The residual performance decrement is higher for crude/residual oil fuel because of the more severe deleterious effect of these fuels on the hot end, compared to natural gas or distillate oil. Figure 9 shows the typical performance deterioration (nonrecoverable with frequent cleaning) with operating time for the three cases. After the overhaul the engine performance deterioration will experience a rate similar to when it was new, that is the shape of the curve will be the same as in the first 24,000 operating hours, but its starting point will be the residual performance decrement.

Recommendations

Based on the considerations described in this report, the following recommendations are made to obtain minimum engine performance deterioration rate and to achieve optimum engine performance over its entire service life:

1 To retard the rate of compressor fouling, the engine site installation should incorporate the optimum inlet filtration system for the particular site environmental conditions.

2 Smooth and/or coated compressor, and if possible turbine, airfoils should be used.

3 Clean fuels and injected steam/water should be used.

4 The official site performance acceptance test should be carried out immediately after engine commissioning and initial synchronization in order to obtain reliable "benchmark" engine performance and health monitoring type of information when the engine is in the new and clean condition.

5 Engine performance deterioration and compressor fouling should be monitored regularly and recorded.

6 Appropriate and regular compressor, and if necessary turbine, cleaning procedures should be used.

7 Good operating and maintenance procedures should be employed.

8 The control system should be carefully monitored and adjusted as required to eliminate possibility of overtemperaturing on starts, operation above base load firing temperature for prolonged periods, and spurious engine trips.

9 Any required remedial actions as regards engine performance or mechanical integrity should be executed promptly.

10 During a major overhaul the engine should be restored as closely as possible to its original new and clean condition.

Conclusions

1 The most important factors affecting industrial gas turbine engine performance deterioration with time were discussed.

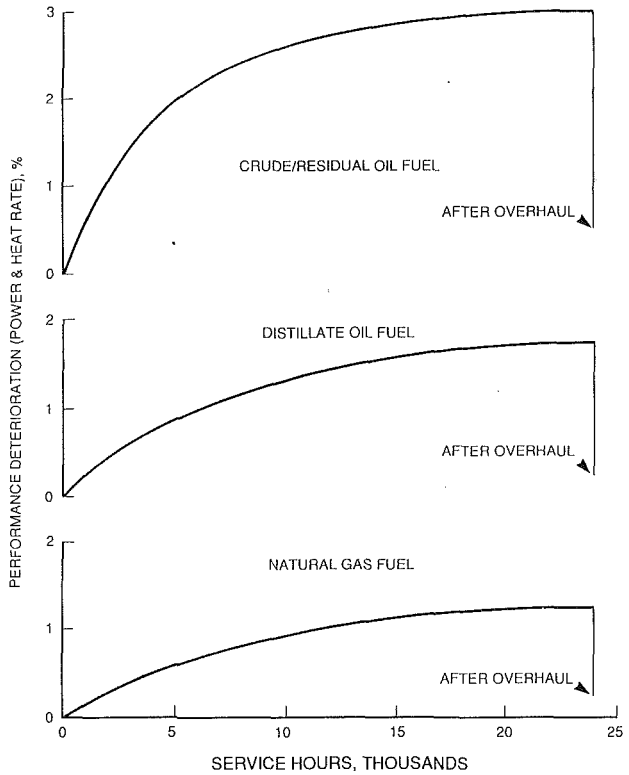


Fig. 9 Performance deterioration with service hours, nonrecoverable with proper cleaning

2 Methods of monitoring and preventing performance deterioration were outlined.

3 Estimates of the cost of performance deterioration were presented.

4 Approximate engine performance deterioration rates with operating time were proposed.

5 Recommendations were made on how to keep industrial gas turbine engine performance deterioration to a minimum.

References

Bammert, K., and Stobe, H., 1970, "Results of Experiments for Determining the Influence of Blade Profile Changes and Manufacturing Tolerances on Efficiency, the Enthalpy Drop, and the Mass Flow of Multi-Stage Axial Turbines," ASME Paper No. 70-WA/GT-4.

Bammert, K., and Woelk, G. U., 1980, "The Influence of the Blading Surface Roughness on the Aerodynamic Behavior and Characteristic of an Axial Compressor," ASME Journal of Engineering for Power, Vol. 102, No. 2.

DeGreef, J. L., Maes, P., and Johnson, K. W., 1978, "Operating Experience on Residual Fuel Oil With a W251 Combustion Turbine," ASME Paper No. 78-GT-104.

Haub, G. L., and Hauhe, W. E., 1990, "Field Evaluation of On-Line Compressor Cleaning in Heavy Duty Industrial Gas Turbines," ASME Paper No. 90-GT-107.

Mezheritsky, A. D., and Sudarev, A. V., 1990, "The Mechanism of Fouling and the Cleaning Technique in Application to Flow Parts of the Power Generation Plant Compressors," ASME Paper No. 90-GT-103.

Saravanamuttoo, H. I. H., and Lakshminarasimha, 1985, "A Preliminary Assessment of Compressor Fouling," ASME Paper No. 85-GT-153.

Scheper, G. W., et al., 1978, "Maintaining Gas Turbine Compressors for High Efficiency," *Power Engineering*, Vol. 82, Aug.

Seddigh, F., and Saravanamuttoo, H. I. H., 1991, "A Proposed Method for Assessing the Susceptibility of Axial Compressors to Fouling," ASME Journal of Engineering for Gas Turbines and Power, Vol. 113, pp. 595-601.

Thames, J. M., Stegmaier, J. W., and Ford, J. J., 1989, "On-Line Washing Practices and Benefits," ASME Paper No. 89-GT-91.

Upton, A. W. J., 1974, "Axial Flow Compressor and Turbine Blade Fouling: Some Causes, Effects, and Cleaning Methods," presented at the First Symposium on Gas Turbine Operations and Maintenance, National Research Council of Canada, Oct.

Downloaded 02 Jun 2010 to 171.66.16.112. Redistribution subject to ASME license or copyright; see http://www.asme.org/terms/Terms_Use.cfm

Marine Gas Turbine Evaluation and Research at the Admiralty Test House, RAE Pyestock[1]

C. J. Bruce
Head of Marine Engines Section.

R. A. Cartwright
Marine Engines Section.

Royal Aerospace Establishment,
Pyestock, Farnborough,
Hants, United Kingdom

The Admiralty Test House (ATH) at the Royal Aerospace Establishment Pyestock has provided test bed facilities for evaluation of marine gas turbines and ancillary equipments for Royal Naval use since 1952. While the ATH is presently undergoing an extensive refurbishment program in preparation for trials of the Rolls-Royce 20-MW Spey SM1C, research continues on a number of innovative gas turbine condition monitoring techniques. This paper presents a brief history of the Marine Gas Turbine Section and describes the facilities of the ATH following major refurbishment. The capabilities of the steady-state and transient data gathering facilities are outlined, together with the automated engine and test control systems, which provide cost-effective engine evaluation in both endurance and minor equipment trials.

Background

The National Gas Turbine Establishment (NGTE) at Pyestock was formed in 1946 following the nationalization and relocation of Frank Whittle's original company, Power Jets Ltd., to a site close to the Royal Aircraft Establishment at Farnborough, Hampshire.

While the development work and manufacturing for the new technology were placed in the hands of commercial aircraft engine companies, research and engine evaluation were continued at Pyestock, where expertise and test resources, beyond the scope of any single manufacturer, were concentrated as a national asset.

The potential benefits of gas turbines as a means of marine propulsion had been subject to investigation by the Admiralty in parallel to the advances in aero engine designs throughout the late 1940s. In 1948, plans were drawn up to incorporate a Marine Wing at the already expanding NGTE, where innovative designs of marine gas turbines could be more fully investigated before introduction into Royal Naval service.

The Admiralty Test House (ATH), Fig. 1, was commissioned in 1952 and since then has provided test bed facilities for evaluation of a wide variety of marine gas turbine propulsion and generation units together with ancillary equipments for Royal Naval use. In 1989, the ATH organization was combined with that of the Marine Diesels Section to form the Marine Engines Section of the Royal Aerospace Establishment (RAE) Propulsion Department.

Co-located with the Materials, Combustion, Turbomachinery and other specialist sections of the Propulsion Department, where much of Europe's gas turbine expertise is concentrated, the ATH is able to provide a unique independent service to both engine manufacturers and marine operators.



Fig. 1 The Admiralty Test House, RAE Pyestock

Development work by Rolls-Royce on the successful marinized versions of the Tyne and Olympus engine designs was closely associated with the ATH trials program during the 1960s and 1970s. More recently, the 13-MW Spey SM1A has undergone extensive evaluation and development work, accumulating over 5000 running hours on the test bed in a simulated marine environment. This engine is now entering service with the Royal Navy in Type 22 and 23 frigates and in other warship installations with the Japanese Defence Agency and the Royal Netherlands Navy.

This paper presents details of the ATH facility following recent refurbishment in advance of trials on the 20-MW Rolls-Royce SM1C marine gas turbine. Examples of recent work are cited to illustrate the capability of the ATH, where comprehensive data gathering and automated test control systems combine to provide cost-effective engine evaluation in both endurance and minor equipment trials.

[1] This paper represents the views of the authors and not the United Kingdom MInistry of Defence (MOD(N)).

Contributed by the International Gas Turbine Institute and presented at the 36th International Gas Turbine and Aeroengine Congress and Exposition, Orlando, Florida, June 3–6, 1991. Manuscript received at ASME Headquarters February 20, 1991. Paper No. 91-GT-134. Associate Editor: L. A. Riekert.

Copyright © 1992 by ASME
Downloaded 02 Jun 2010 to 171.66.16.112. Redistribution subject to ASME license or copyright; see http://www.asme.org/terms/Terms_Use.cfm

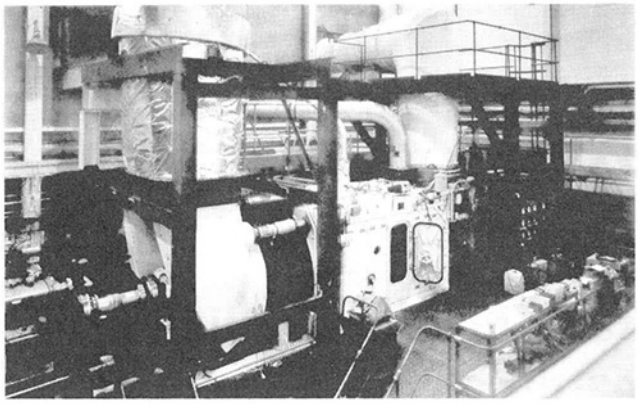


Fig. 2 The Spey marine gas turbine installation

Admiralty Test House Facilities

The ATH was primarily established for extended endurance running over several thousand hours under simulated marine environment conditions. The facilities are fully self-contained and require no external services other than electrical power. These have recently been refurbished and updated to meet the requirements of the SM1C and overcome some of the short-term expediency measures of the first Spey installation described by Kingsland (1986). The facilities comprise:

- A 22.25 m × 3.12 m reinforced concrete test bed.
- Three Heenan and Froude DA 790 hydraulic dynamometers capable of 14.92 MW each. Two of these may be run in tandem as on the present Spey bed (Fig. 2), with a capacity of up to 29.8 MW. These brakes have accumulated a total of some 20,000 hours use. Major overhaul of the brakes will allow continuation of use through the next series of trials. A number of studies into options for regenerative braking have been conducted but found that the capital expenditure involved could not be recovered in the relatively short (3000–5000 hours) period of time associated with a single engine trial.
- Inlet and exhaust ducting designed to allow free passage of the 20 ton and 1 ton overhead cranes.
- Recent work has involved the manufacture of new downtake sections to straighten the intake air flow and a new air meter more suitable for SM1C flow rates.
- Fuel, power turbine lube oil, and HP air storage and supply systems. Brake cooling water pumping and distribution systems, including an emergency header tank. All these systems have been subjected to major renovation and enhancement, following nearly 40 years of continuous use.
- Industrial grade air filters together with a salt ingestion system are used to clear inland pollutants from the intake air before the marine aerosol is created by the injection of measured levels of brine into the airstream. New equipment has been provided to maintain the salt/air weight ratios correct for the higher flow rates of the SM1C.
- A comprehensive data gathering and engine control system capable of recording of engine, plant, and environmental data under both steady-state and transient conditions.

In addition to those plant services currently in use on the Spey bed, facilities exist for a second test rig, using the third dynamometer, formerly occupied by the Tyne engine. A small wind tunnel is located on the second floor of the building, which has been used for authoritative investigations into marine aerosol conditions, intake filter packages, and debris ingestion trials. Details of this work were reported by Hobday and Havill (1988).

Engine Control System

Automatic control of the engine under test is achieved using an Intercole Systems Spectra minicomputer. Software is incorporated to allow endurance, performance assessment, and other trial schedules to be written and subsequently selected to drive the engine throughout each day's trials.

A typical endurance mission will consist of a specified number of hours at representative engine power levels with regular handling acceleration/decelerations and performance gathering schedules. Performance at steady state is assessed during the regular pre- and post-compressor wash performance map schedules, during which 86 items of data (pressures, temperatures, speeds, etc.) are captured at each of the 11 power settings ranging from idle to full power conditions. These data can be used for on-line monitoring of the engine or detailed analysis at a later occasion. More detail of this data system is given later in this paper.

Dynamometer Control System

The Heenan and Froude DA790 hydraulic dynamometers are controlled to simulate the torque/speed characteristics of typical Royal Naval marine installations. Recently updated to microprocessor control, the dynamometer control system allows automatic variation of brake power in response to engine speed changes. When in automatic engine control, the Spectra computer provides the power demand signal to predetermined power schedules.

Brake control system schedules may be written and selected to drive the brakes on a variety of different ship speed/torque curves. In this way, the engine under examination may be tested in any proposed marine installation without the financial penalties caused by any requirement for gearing and propeller systems. A recent trial was conducted where the specific fuel consumptions of the SM1C and SM1A were compared for all RN Spey installations, under both normal and "One shaft trailing" conditions.

Steady-State Data Gathering

The ATH Steady-State Data Gathering system (ATHSYS) uses the same Spectra computer for scan initiation, data logging, and analysis as the engine control system. The system scans at medium speed (3–4 seconds per scan) and captures onto a rolling buffer. When engine conditions have steadied, data are automatically transferred to storage on hard disk in the Spectra computer. Thermodynamic calculations are carried out on the raw data by the computer and the resulting corrected and performance data stored with the raw data. At the end of a performance map, the whole data set may be printed out for analysis.

Data from the rolling buffer or from hard disk may also be analyzed or plotted using the same data base. Over the length of an endurance trial, these data may be analyzed in the "power domain," in order to provide a picture of how the engine performs across its power range, or in the "time domain" for trend predictions. Time domain trending has long been pursued in attempts to characterize the falloff in performance as engine condition deteriorates. In-service and ATH test experience has shown that variations of only a few percent are likely to represent the difference between a new, healthy engine and one withdrawn from service after several thousand hours operation with significant component defects. Such small variations are undetectable due to the measurement uncertainties of in-service instrumentation. The main reasons for continuing a detailed assessment of steady-state data within the ATH are:

(*a*) Accumulation of steady-state data confirms that the instrumentation system is continuing to function correctly.

(*b*) The "time trends" may be used to confirm that the endurance trial is being conducted strictly in accordance with the schedules agreed between the manufacturers, the customer, and the test authority.

Downloaded 02 Jun 2010 to 171.66.16.112. Redistribution subject to ASME license or copyright; see http://www.asme.org/terms/Terms_Use.cfm

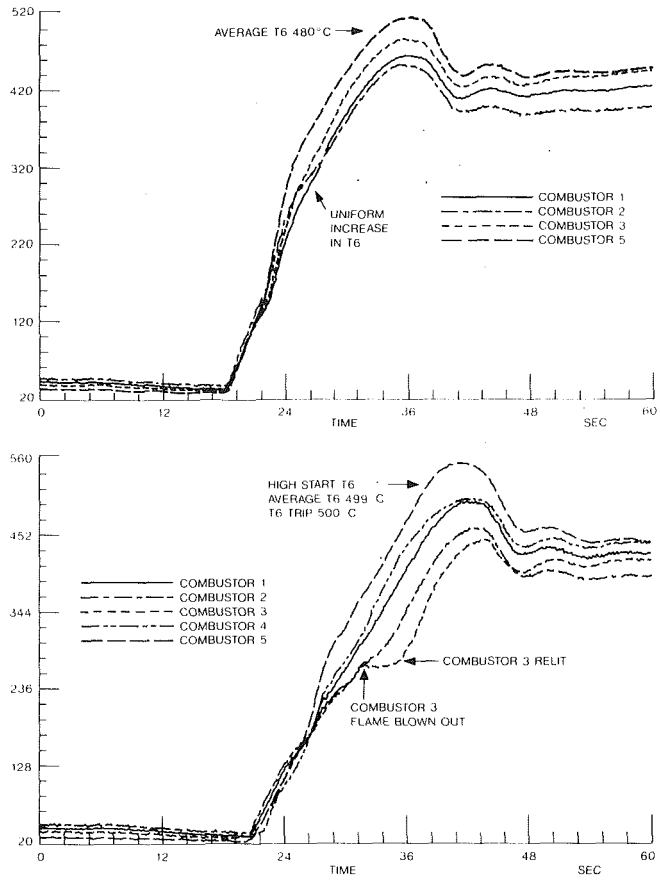


Fig. 3 VHS plots of power turbine entry temperatures during engine start sequence (showing comparison between a good and a poor start)

Transient Data Gathering System

There are many gas turbine characteristics that do not show up as steady-state phenomena. A more detailed understanding of the engine's performance and the first signs of deterioration are most often more clearly shown under transient conditions.

The Very High Speed Transient Data Gathering System (VHS) is used to scan selected parameters at rates exceeding 1 kHz. This system was also supplied by Intercole Systems and uses a Research Machines Nimbus AX20 286 desktop machine for scan initiation and data storage and processing.

Throughout an endurance trial, sample transients are conducted on a regular basis in order to demonstrate the earliest signs of engine degradation. One of the most useful transients used is that of the start sequence, which will show faults in any of the controls, fuel and air systems as well as engine component defects.

During a recent trial, analysis of this transient identified a number of minor faults as well as showing the effects of combustor degradation. Figure 3 shows the effect of corrosion in combustor number three, where the excessive level of primary air has caused the flame to blow out. Re-ignition occurs some 4–5 seconds later through the intercombustor duct but the excessive amount of unburned fuel released during this period causes the maximum power turbine entry temperature to rise to within one degree of the trip level. It must be stressed that once this engine was running, no effects of this defect could be observed on its steady-state or transient performance.

Engine Management Systems

The ATH facility is primarily intended for endurance running of engines over several thousands of hours. This is an expensive operation during which every opportunity is taken to mitigate the costs by research into engine management techniques. Such techniques include engine health and condition monitoring but collectively are targeted to more efficient and effective engine management. Such activities are run as research items within the Marine Engine Section with a view to providing first-hand indications as to their value for eventual RN use. During the recent SM1A trials, the following techniques have been under review:

Smoke Monitoring. On-line smoke density monitoring is conducted using the Sigrist Photometer. Traces from this machine clearly show the overall level and eventing that occurs as carbon is shed from the combustors. In addition, RAE Combustion Division conduct regular chemical and physical analyses of the uptake gas throughout any endurance trials, to monitor combustion efficiency and overall emission levels. These tests provide depth to the ATH on-line results and also tie in well with the frequent video endoscope and visual engine inspections.

Vibration Analysis. Vibration data are gathered from the compressors, turbines, and power turbine by the ATHSYS using the manufacturer's velocity transducers. These give results that are satisfactory for in-service watchkeeping purposes but have insufficient high-frequency response to be of any real value for condition monitoring.

Significant advances in the capabilities of the latest vibration analysis techniques have been seen in the commercial market place. The benefits of these to the marine environment are currently under review at the ATH and an innovative system produced by Stewart Hughes Ltd. (SHL) has recently been acquired. This system offers considerably greater potential for obtaining early warning of developing faults from the engine's vibration signatures than previously possible by analysis of simple velocity probe signals.

The SHL Vibration Data Analysis System uses a suite of ten accelerometers to collect vibration data from significant sites around the engine. Complex signal processing and pattern recognition techniques are then used to identify the signature of particular faults (bearing failures, gear faults, etc.). This system has demonstrated the capability to identify certain engine faults down to component level.

Electrostatic Debris Detection Systems. Electrostatic detection for debris in the gas path is conducted using the Ingested Debris and Engine Distress Monitoring Systems (IDMS and EDMS), also produced by SHL.

The IDMS detects the ingress of foreign objects into the intake. The effects of blade or seal rubs as well as the effects of other gas path degradation in the exhaust gas are shown by analysis of the EDMS data. Although these systems are far from being ready for installation at sea, they demonstrate two clear benefits in the ATH trials environment:

(*a*) Following any catastrophic damage to the compressor elements during the trial, FOD can either be identified as the cause or, more importantly, positively excluded from the list of contributory factors. Manufacturers are often very quick to attribute any such failures to "FOD" and blame the engine operator. This system will help to identify the true cause of any such unfortunate occurrence.

(*b*) Early warning of blade or seal rubs, which may go on to catastrophic failure, and other gas path degradation is provided by analysis of the EDMS signals.

A more detailed presentation of the results from the evaluation of these systems is the subject of another paper to be presented at this conference (Cartwright and Fisher, 1991).

Visual Inspection Techniques. Visual inspection of the gas path of an engine remains one of the most reliable methods of condition monitoring available to the engineer. However, until recently, the technique has been limited by the fact that conventional endoscopes are single user devices. This creates

Downloaded 02 Jun 2010 to 171.66.16.112. Redistribution subject to ASME license or copyright; see http://www.asme.org/terms/Terms_Use.cfm

difficulty with training in their effective use and causes problems when one operator observes a defect, then has to describe his findings verbally or pass the instrument to another engineer. All too often the cry of "The endoscope has moved!" is heard and all signs of the defect are lost.

In order to overcome this problem and to provide a more permanent record of the engine inspections, the ATH has pioneered the use of video endoscope techniques for assessment of test engines. During this work, a number of equipments were investigated before the Videoprobe 2000 system was selected for evaluation. In this system a monochrome charged couple device is located at the tip of a 6 mm flexible endoscope, which gives greatly improved picture definition when compared to fiber optic bundle units. Light from a 300 W source is strobed through three color filters and the returning signals recompiled to give a high-definition full-color picture of the subject. Inspections of the engine are recorded onto a conventional video cassette recorder at frequent intervals throughout any period of trials.

A further development of the video inspection technique is the use of an image processing system with which stills from the recorded inspection can be digitized and stored as "Pic" files on a Nimbus VX40 386 PC. The LazaReporter system, supplied by Thermoteknix systems Ltd, allows the digitized pictures to be processed (enhanced, compared, etc.) and printed on a laser printer, together with titles and other text. An example from the LazaReporter system is given at Fig. 4, where loss of a compressor blade tip can clearly be seen. These pictures may be used for reporting or may be faxed to a customer for immediate briefing of a defect or occurrence.

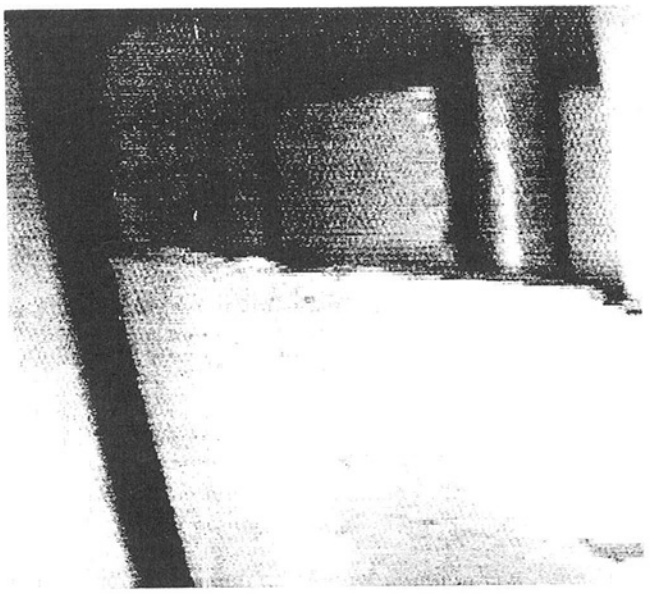


Fig. 4 LazaReporter digitized still for endoscope inspection; damage to compressor blade clearly visible

Lube Oil Monitoring. Monitoring of engine lubricating oil for ferrous contamination has been conducted using magnetic chip detectors (MCDs) for several years. This technique has proven value but suffers from the major disadvantage that removal of MCD plugs requires the engine to be shut down. On-line detection using nonintrusive sensors is an attractive alternative. Two such systems, the SENSYS Ferroscan and TEDECO QDM, are currently under investigation but there is limited confidence in the results gathered to date.

Performance Monitoring—MIDGTS. The Model for Inspection and Diagnosis of Gas Turbine Systems (MIDGTS) is a trending and diagnostic program, based on the principle that trends in steady-state data produced by a fault condition may, when examined as a set, represent one particular engine defect. The program was developed for the Canadian Navy by Gastops Ltd. A version of the software, supplied to the ATH for evaluation on the SM1A, is now the subject of investigation and development by both ATH staff and Gastops Ltd.

Performance Monitoring—System Identification. Work has recently been undertaken to exploit the potential of engine transient performance for condition and performance monitoring purposes. On-line recursive system identification techniques, originally intended for control system design, have been used to produce, and continually update, a series of transfer function models characterizing the engine's dynamic performance. By either tracking the variation in estimated model parameters, or by statistically monitoring the differences between engine parameters and model predictions, it is possible to quantify the effects of fault conditions on performance variations. Feature maps, Fig. 5, of these variations for given fault conditions can then be constructed, and with the use of pattern recognition techniques a fully automated fault classification and diagnostic facility can be produced. This work is in its early stages of development but shows considerable promise.

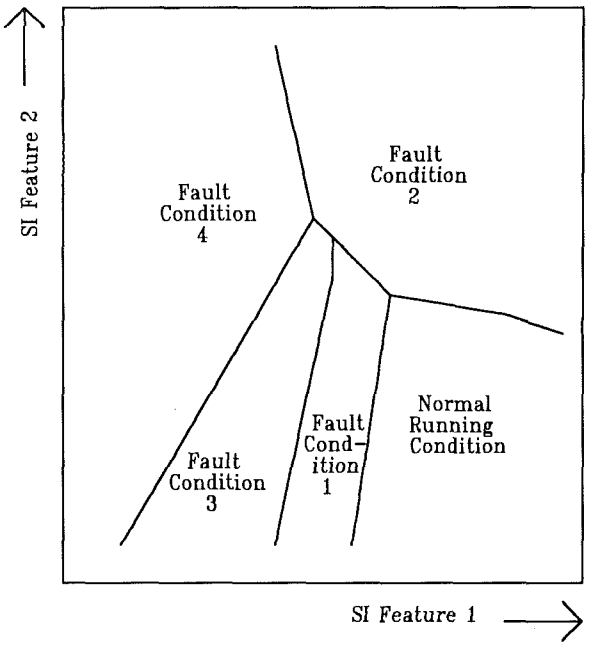


Fig. 5 System identification fault distribution

Engine Lifting—Low Cycle Fatigue Monitoring. The life expectancy of major engine rotating components has been determined to date by recording of the accumulated engine hours. A more accurate and cost-effective technique, under review at the ATH, relies upon automatic counting of the low cycle fatigue (LCF) damage accumulation, using the Smiths Industries engine life computer. A change to LCF count as the basis for engine overhaul management is expected to produce significant reductions in the through-life costs of maintaining the Royal Navy's fleet of marine gas turbines.

Utilization of Gas Turbines in RN Service—ELMD. Effective endurance testing of marine gas turbines requires detailed information to be available on precisely how the engines are utilized in the fleet, in terms of accumulation of time at different power levels. The Engine Load Monitoring Device (ELMD) is a simple instrument, designed and produced by RAE staff, which monitors engine low-pressure spool speed (N1) and "clocks up" cumulative engine running time spent in each of ten speed bands. Because of the consistent rela-

Downloaded 02 Jun 2010 to 171.66.16.112. Redistribution subject to ASME license or copyright; see http://www.asme.org/terms/Terms_Use.cfm

tionship between N1 and engine power, not available on other engine measured parameters, the ELMD will identify how the engine is utilized in each of ten corresponding power bands.

Initial results from the ELMDs in the fleet are beginning to identify precisely how Royal Naval frigates utilize their boost engines. Analysis of these data was instrumental in producing the most effective engine test profiles for the SM1C endurance trial currently in progress.

Conclusion—The Independent Test Authority

The Admiralty Test House has a long history as an independent test authority for the assessment of gas turbines for potential Royal Naval use. The facilities have recently been comprehensively renovated and upgraded in preparation for the SM1C trials currently in progress.

Advances in engine management techniques offer significant benefits in the way in which engine life cycles are managed. However, these techniques often rely upon the optimistic claims of the manufacturers and must be integrated into service only after independent evaluation under the rigorous conditions found in the marine environment.

Arguments exist as to the need for such facilities at a time when defense and ship procurement policies are under continued review. However, history has proven the value of testing, independent from the influences of the equipment manufacturers, as a means of highlighting those problems that would not have become evident until later in service. Rectification then becomes expensive both in terms of nugatory capital expenditure and in the operational restrictions imposed upon vessels undergoing repair.

References

Cartwright, R. A., and Fisher, C., 1991, "Marine Gas Turbine Condition Monitoring by Gas Path Electrostatic Detection Techniques," ASME Paper No. 91-GT-000.

Hobday, J. S., and Havill, J., 1988, "A New Approach to Evaluating the In-Service Performance of Marine Gas Turbine Air Filters," ASME JOURNAL OF ENGINEERING FOR GAS TURBINES AND POWER, Vol. 110, pp. 621–627.

Kingsland, J. M., 1984, "Test Installation for the SM1A Marine Spey at RAE Pyestock," ASME Paper No. 84-GT-248.

Downloaded 02 Jun 2010 to 171.66.16.112. Redistribution subject to ASME license or copyright; see http://www.asme.org/terms/Terms_Use.cfm

Implanted Component Faults and Their Effects on Gas Turbine Engine Performance

J. D. MacLeod
Research Officer,
National Research Council,
Ottawa, Ontario, K1A 0R6 Canada

V. Taylor
Staff Engineer,
Standard Aero Ltd.,
Winnipeg, Manitoba, R3H 1A1 Canada

J. C. G. Laflamme
Directorate of Transport and Helicopter
Engineering and Maintenance,
Department of National Defence,
Ottawa, Ontario, K1K 0K2 Canada

Under the sponsorship of the Canadian Department of National Defence, the Engine Laboratory of the National Research Council of Canada (NRCC) has established a program for the evaluation of component deterioration on gas turbine engine performance. The effect is aimed at investigating the effects of typical in-service faults on the performance characteristics of each individual engine component. The objective of the program is the development of a generalized fault library, which will be used with fault identification techniques in the field, to reduce unscheduled maintenance. To evaluate the effects of implanted faults on the performance of a single spool engine, such as an Allison T56 turboprop engine, a series of faulted parts were installed. For this paper the following faults were analyzed: (a) first-stage turbine nozzle erosion damage; (b) first-stage turbine rotor blade untwist; (c) compressor seal wear; (d) first and second-stage compressor blade tip clearance increase. This paper describes the project objectives, the experimental installation, and the results of the fault implantation on engine performance. Discussed are performance variations on both engine and component characteristics. As the performance changes were significant, a rigorous measurement uncertainty analysis is included.

Background

In recent years, the Canadian Department of National Defence has expressed serious concern over the rapidly escalating cost of operation and maintenance of aircraft gas turbine engines. The components of major concern were compressor and turbine blades and vanes. The increasing rate of rejection of these items during overhaul prompted a reassessment of the time between overhaul for certain engine types.

The blades and vanes of gas turbine engines are susceptible to deterioration as a result of erosion and wear. The deterioration, in the form of increased surface roughness, loss of material, and alteration of aerodynamic profile, manifests itself in terms of reduced stall margin, poorer fuel economy, and increased operating temperatures.

The Engine Laboratory of the National Research Council of Canada has actively supported the development of military aero-engine performance monitoring and fault isolation procedures. Current projects are aimed at correlating changes in gas turbine components and overall engine performance to physical degradation within the engine.

The Engine Laboratory was requested to develop a generic fault library for a single spool gas turbine engine, with possible expansion to accommodate a multispool configuration.

To develop the fault library, it was decided that a set of typical faults would be selected from a survey of 30 flight engines, during a normal overhaul cycle. The survey indicated that first-stage turbine nozzles were rejected 97 percent of the time, during overhaul, while the rejection rate for first-stage turbine blades was 74 percent. Compressor stator seals had a rejection rate of 100 percent, while first and second-stage compressor blades were rejected at a rate of 47 and 24 percent, respectively.

Previous experience with the Allison T56 engine, at the Engine Laboratory (MacLeod and Laflamme, 1988, 1989, 1990), provided a good basis from which to build a data base of high-quality empirical data from well-documented instrumentation.

Experimental Installation

To assess properly the effects of implanted faults on the performance of a gas turbine engine, a sophisticated test setup with specialized instrumentation was required. A description of the engine and instrumentation used for this assessment is included to illustrate the complexity of this project.

Engine Description. The test vehicle for this fault implantation study was an Allison T56-A7B single spool turboprop engine from a C-130 Hercules cargo aircraft. This engine was an excellent candidate for this study because it has no variable geometry or transient bleed valve operation that might affect the repeatability of the engine. The T56 engine has a 14-stage compressor, with bleed valves that are only open below the idle speed, a six-can combustor, and a four-stage turbine.

The single shaft is coupled to a reduction gearbox mounted forward of the compressor. For the NRCC tests, power was transmitted through the gearbox to a flywheel and a Froude

Contributed by the International Gas Turbine Institute and presented at the 36th International Gas Turbine and Aeroengine Congress and Exposition, Orlando, Florida, June 3-6, 1991. Manuscript received at ASME Headquarters February 6, 1991. Paper No. 91-GT-41. Associate Editor: L. A. Riekert.

Copyright © 1992 by ASME
Downloaded 02 Jun 2010 to 171.66.16.112. Redistribution subject to ASME license or copyright; see http://www.asme.org/terms/Terms_Use.cfm

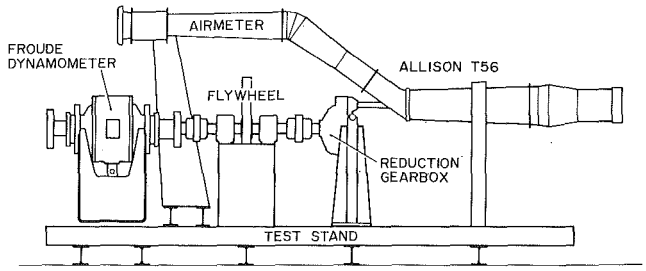


Fig. 1 Schematic of T56 turboprop engine on test stand

waterbrake dynamometer. A schematic diagram of the engine test configuration is shown in Fig. 1. The engine control is one of a constant speed design using a governor to maintain a constant rotor speed of 13820 rpm. Power is controlled by setting the turbine inlet temperature with the power lever angle.

Instrumentation. Instrumentation used on the T56 was divided into two categories; external and internal. The external instrumentation included a high Mach number (0.8) airmeter in front of the engine, compressor inlet pressure and temperature rakes, a tailpipe airmeter mounted after the turbine, variation sensors on the engine carcass, and turbine-type fuel flowmeters. The high-velocity airmeter facilitated accurate flow measurement because of the large local difference between the total and static pressure. A diffuser mounted behind the airmeter reduced the airspeed to normal engine inlet conditions. The internal instrumentation consisted of total temperature and pressure probes in every stage of the compressor, as well as compressor discharge and turbine inlet pressure and temperature rakes. With this degree of instrumentation, it was possible to monitor not only the condition of the overall engine, but also the performance of its major components, and the individual compressor stages.

The data were recorded using a NEFF 620 data acquisition system controlled by a DEC PDP 11/34 computer. Measurement uncertainty estimates were available for the complete instrumentation package. A complete methodology for fuel flow measurement has been documented (Grabe, 1988).

Test Sequence

To establish the effects of implanted faults on overall engine performance, it was first important to establish an effective test sequence to get as much information as possible for the fault library, without delaying or overlapping valuable testing periods. Engine and damaged component selections were made to minimize the required overhaul time, while attempting to test or simulate valid in-service faults.

The T56 engine chosen for the implanted fault testing had approximately 24,000 flight hours, 4200 hours since its last overhaul. This engine already contained a fault that was the result of service exposure. Testing of the engine was performed to establish the "as-received" condition of the engine. Performance signatures of the overall engine and its individual components were then quantified.

In the experimental program, the engine was run at a fixed aerodynamically corrected rotational speed to provide a common basis for comparison, i.e., the mechanical speed of the engine was adjusted using the dynamometer, as a function of the ambient temperature. The procedure used for each test run established a series of increasing power settings, for a given corrected rotor speed. At each power setting, the engine was allowed to stabilize for five minutes, then two sets of data were recorded. Typically, up to six power settings (12 data points) were recorded for each test. Several different corrected speeds, ranging from 13,000 to 14,500 rpm, were run to assess the effects of corrected speed on any performance changes.

After the initial testing was completed, the engine was sent to the overhaul contractor to be disassembled and the first set of faulted components removed. On return to NRCC, the engine was retested using the same procedures used in the initial tests, to establish the engine signature without faults. The engine was again sent to the overhaul contractor, to install a second set of faulted components.

First Fault Implantation. During the first disassembly process, the engine components were documented for dimensional changes beyond overhaul specifications. In this case, the first-stage turbine nozzle guide vanes were found to be eroded, as well as cracked, bowed, and corroded (McLarty, 1988). Since the engine had reached the scheduled overhaul time limit, the vanes may have accumulated more than one overhaul cycle of service exposure. All vane damage was service induced.

The inspection criterion for nozzle erosion is the vane effective flow area (EFA). To measure the amount of erosion, the six vane assemblies were tested in a Fleming AF36 airflow rig, calibrated against a master nozzle. Each nozzle was flow checked three times, with a calibration run before and after the complete flow measurement test. The accuracy of the airflow rig is ± 1.0 percent or better.

Results of the airflow rig testing indicated that the eroded nozzle vanes had an EFA approximately 6.0 percent (± 1.4 percent) larger than new replacement nozzle vanes. New nozzle guide vanes were then installed in the turbine during reassembly.

The compressor was completely disassembled, and all individual blades were removed. During removal, each blade was numbered, so that it could be returned to its original position upon reassembly. After disassembly, each piece underwent a petroleum solvent wash, followed by an inspection. The compressor stator front and rear airseals were removed and replaced because of service-induced wear/damage. Damage on these corrugated aluminum stator seals was indicated by worn radii, thinning (erosion), and occasional nicks and dents. Upon reassembly, rotor blades were replaced in the same numbered order, and their balance checked. The entire compressor was then mated with the combustor and turbine modules, and returned to NRCC for testing.

Second Fault Implantation. Excessive compressor blade tip wear is a typical service fault if the compressor rotor becomes unbalanced or misaligned because of severe front or rear compressor bearing damage. For the second round of fault implantation, it was decided to artificially grind the tips of the first and second stage compressor blades down to the minimum length normally seen in service. In this case, the shorter blades increased the tip clearance by 0.020 in. (0.5 mm), or 133 percent relative to the unground blades (Taylor, 1990). In an attempt to isolate damage to a certain portion of the compressor, the remaining 12 compressor stages were left in their original condition.

Another fault, which is regarded as typical of in-flight service, is first-stage turbine blade untwist. These blades untwist and stretch as a result of creep damage during sustained high temperature operation. Blade untwist is measured as the difference in height of two corners of the blade shroud edge, with the blade fixtured horizontally by the firtree, with the trailing edge up. The limit for blade untwist on the first-stage turbine is 0.015 in. (0.38 mm).

For the second fault implantation, a set of service-exposed turbine blades with an average untwist of 0.0248 in. (0.68 mm), a 140 percent increase, were installed during the rebuild process. Upon completion of the fault implantation processes, the entire engine was reassembled and sent to NRCC for testing.

Data Presentation

Data recorded during a test were stored in basic engineering

Downloaded 02 Jun 2010 to 171.66.16.112. Redistribution subject to ASME license or copyright; see http://www.asme.org/terms/Terms_Use.cfm

units so that observers could visually check the data quality as the test progressed. After a test was completed, the data were normalized, and used to calculate performance parameters such as pressure and temperature ratios, corrected air and fuel flow, etc. These parameters were then curve-fitted to quadratic equations, using a least-squares method. The independent variable for curve-fitting engine data was corrected turbine inlet temperature. Comparisons between various test runs were then made using the curvefitted values of each parameter. All data presented in this study were taken at 100 percent corrected rotor speed, or 13,820 rpm. For curve-fit comparisons, the reference value used for the corrected turbine inlet temperature was 2200 R (1220 K).

Effects of Ambient Conditions

The NRCC test cell has no provision for controlling the ambient inlet air temperature. The engine was therefore operated over a wide range of temperatures experienced over the Canadian seasons. All performance data were corrected to standard day reference conditions for comparison. Previous experience at NRCC (MacLeod, 1987; Jarvo and Muir, 1989) and other test facilities (Greco and Gordon, 1966) suggests that the normal standard day corrections do not ensure that the data will collapse to a single curve. Since temperature lapse rate data were not available for all of the parameters being considered in this study, test data presented here were all recorded at similar ambient temperature conditions.

The use of the long inlet duct on the T56 (Fig. 1) causes a significant pressure loss and distortion at the compressor face, which is similar to the aircraft nacelle installation. This pressure loss simulates an altitude of nearly 500 m and a ram pressure ratio (compressor inlet total pressure divided by the static pressure at the exhaust exit plane) of approximately 0.97. The effect of ram pressure ratio on output power was accounted for using the manufacturer's procedures (Detroit Diesel Allison, 1983).

Since humidity affects the thermodynamic properties of the engine cycle, limitations on the atmospheric conditions (75 percent relative humidity or less) were monitored to avoid condensation in the inlet air stream and minimize performance corrections (Grabe, 1989).

Test Results

For this study, 14 performance parameters were chosen to describe the condition of the engine for each power setting. The selection of appropriate parameters was made to analyze the performance of the overall engine and of its individual components, namely the compressor, combustor, and turbine. To assess the compressor behavior, isentropic efficiency, corrected airflow, corrected speed, and compressor pressure and temperature ratios were examined. For combustor performance, combustor pressure and temperature ratios were analyzed. Isentropic efficiency was chosen as a suitable parameter to describe the performance of the turbine.

Corrected fuel flow, corrected output power, and specific fuel consumption were selected to define overall engine behavior, as were engine temperature and pressure ratios. Corrected torque was added as a redundancy check on corrected output power.

Since the most significant faults were implanted in the turbine during this project, the strongest emphasis was in monitoring changes in the turbine performance and, in turn, the effects on overall engine performance. Combustor and compressor performance were included to see whether a change in turbine operation would have any affect on upstream components.

In addition, the performance changes of the individual compressor stages were analyzed by comparing the total pressure ratio across each stage.

Data Quality. For this study, the quality of the data for each test was determined by the back-to-back repeatability of each of the performance parameters. This was done by comparing the deviations of the individual data points from the curve-fitted quadratic equations derived from the data. A mean value of the deviation of the data from its curve was used to estimate the repeatability of each parameter within each test.

To establish the quality of the data recorded series of tests (within a fault implantation sequence), an analysis of the run-to-run repeatability was performed. This analysis consisted of comparing curve-fitted test data recorded under the same ambient conditions during the same test sequence. A mean deviation between the curve-fits of each of the performance parameters was then used to define the repeatability within each test sequence.

An estimate of the overall repeatability of each of the parameters was accomplished by combining the back-to-back and run-to-run repeatabilities. With these estimated repeatability values, a true comparison of the effects of the particular fault could be carried out.

Back-to-Back Repeatability. For each power setting during a test, two complete scans were recorded by the data acquisition system. To assess the back-to-back repeatability, the values of these recorded points were compared to the curve-fit generated points at a specified turbine inlet temperature. This procedure gave an indication of how close the repeated data points were to each other, and the "goodness" of the curve-fit to the actual data points. These deviations are shown in Table 1 for the baseline testing, and first and second fault implantation test series.

The corrected output power and specific fuel consumption reveal a noticeable scatter, as do the turbine efficiency and corrected torque. All other parameters indicate very small deviations from their respective curves.

The deviations in the corrected output power and specific fuel consumption are to be expected because each of these parameters were calculated from two or three measured quantities. The scatter in the turbine efficiency is also expected because it is calculated using an approximate value for the specific heat ratio within the turbine. In addition the turbine efficiency is an inverse parabolic function, which may not be conducive to a least-squares curve-fit.

Run-to-Run Repeatability. Within each series of tests, at least three complete runs were recorded for each corrected rotor speed condition. Having established the agreement of the test data with the generated curve-fits, the next step was to determine how well these curves collapsed within each test series. To evaluate the run-to-run repeatability of the data within each test series, the values of curve-fitted data were compared from at least two runs taken at similar ambient conditions. These deviations are shown in Table 2 for the baseline testing and the first and second fault implantation test series.

Close examination of the run-to-run repeatability results showed that most parameters were reasonably tight, with the exception of corrected output power and specific fuel consumption. Certain parameters, such as turbine efficiency and engine pressure ratio, had better run-to-run repeatability than back-to-back repeatability. In the case of turbine efficiency, this anomaly presumably results from difficulties in representing the uniquely shaped efficiency function with a quadratic equation.

Combined Repeatability. Before a comparison of the fault implantation data could be made, it was necessary to establish the overall or combined repeatability of the data from each test series. Since the same equipment, instrumentation suite, data system, and facility were used for each test, it was unlikely that the measurement bias errors would have changed. Thus

Downloaded 02 Jun 2010 to 171.66.16.112. Redistribution subject to ASME license or copyright; see http://www.asme.org/terms/Terms_Use.cfm

Table 1 Back-to-back repeatability

PARAMETER	DEVIATION (%)			EXPECTED RANDOM ERROR (%)
	BASE	FAULT1	FAULT2	
Compressor efficiency	±0.06	±0.07	±0.06	±0.03
Corrected airflow	±0.06	±0.08	±0.06	±0.10
Corrected fuel flow	±0.12	±0.05	±0.10	±0.12
Corrected output power	±0.16	±0.24	±0.38	±1.10
Specific fuel consumption	±0.35	±0.29	±0.29	±1.10
Corrected speed	±0.03	±0.02	±0.03	±0.01
Compressor pressure ratio	±0.05	±0.11	±0.09	±0.06
Compressor temperature ratio	±0.02	±0.03	±0.04	±0.00
Turbine efficiency	±0.20	±0.50	±0.23	±0.02
Combustor temperature ratio	±0.02	±0.03	±0.03	±0.00
Combustor pressure ratio	±0.05	±0.09	±0.03	±0.08
Engine temperature ratio	±0.18	±0.18	±0.07	±0.00
Engine pressure ratio	±0.22	±0.18	±0.14	±0.03
Corrected torque	±0.17	±0.27	±0.39	±1.10

Reference: Corrected speed = 13820 RPM
Corrected Turbine Inlet Temperature = 2200 °R (1220 K)

Table 2 Run-to-run repeatability

PARAMETER	DEVIATION (%)			EXPECTED RANDOM ERROR (%)
	BASE	FAULT1	FAULT2	
Compressor efficiency	±0.16	±0.12	±0.24	±0.03
Corrected airflow	±0.17	±0.12	±0.16	±0.10
Corrected fuel flow	±0.22	±0.05	±0.16	±0.12
Corrected output power	±0.45	±0.12	±0.39	±1.10
Specific fuel consumption	±0.54	±0.17	±0.36	±1.10
Corrected speed	±0.11	±0.14	±0.18	±0.01
Compressor pressure ratio	±0.05	±0.17	±0.07	±0.06
Compressor temperature ratio	±0.08	±0.11	±0.07	±0.00
Turbine efficiency	±0.16	±0.14	±0.05	±0.02
Combustor temperature ratio	±0.06	±0.01	±0.07	±0.00
Combustor pressure ratio	±0.05	±0.12	±0.02	±0.08
Engine temperature ratio	±0.14	±0.14	±0.07	±0.00
Engine pressure ratio	±0.07	±0.02	±0.08	±0.03
Corrected torque	±0.45	±0.14	±0.52	±1.10

Reference: Corrected speed = 13820 RPM
Corrected Turbine Inlet Temperature = 2200 °R (1220 K)

the population of observed measurements taken at the same environmental conditions for a given test series would be combined to form an overall datum with a defined data scatter.

If, when compared to the data taken under similar environmental conditions for the engine testing, there was a shift outside the scatter band established during the fault implantation study, then a performance shift, caused by the particular fault, would be deemed to have occurred.

A statistical approach using the methods described by Abernethy and Thompson (1973) was used to calculate bias and precision errors, and the measurement uncertainty for this experiment. These results are shown in Tables 1 and 2 as expected random error. This information was compared to a more basic method using the observed repeatabilities. To accomplish this, a worst case scenario was assumed. In other words, it was assumed that both the back-to-back and run-to-run repeatabilities were acting in the same direction within each test series, and opposing each other between each test series.

Therefore, the overall repeatability would be the sum of all run-to-run and back-to-back repeatabilities. Thus, the method chosen to define the overall repeatabilities always overestimates the more appropriate statistical value, such as the root-sum-square method. A list of the overall repeatabilities, during the first fault implantation series, for each of the parameters is given in Table 3.

In general, the quality of the test data for each test series appeared to be very good, with the possible exception of output power and specific fuel consumption. Overall, the test data recorded for the fault implantation study were considered to be of sufficiently good quality to be used for an accurate comparison.

Comparison of Fault Data. Having established the overall repeatabilities of the performance parameters selected for the

Table 3 Fault implantation effects

PARAMETER	OVERALL REPEATABILITY (%)	DEVIATION FAULT1 (%)	DEVIATION FAULT2 (%)	UNCERTAINTY (%)
Compressor efficiency	±0.41	-0.35	-0.17	±0.87
Corrected airflow	±0.43	+0.60	-4.02	±0.27
Corrected fuel flow	±0.44	+3.24	+6.95	±0.43
Corrected output power	±0.97	-0.31	+4.71	±1.42
Specific fuel consumption	±1.35	+3.55	+2.24	±1.52
Corrected speed	±0.30	-0.26	-0.13	±0.13
Compressor pressure ratio	±0.38	-0.88	-2.51	±0.25
Compressor temperature ratio	±0.24	-0.12	-0.94	±0.40
Turbine efficiency	±1.00	+0.84	-3.56	±0.90
Combustor temperature ratio	±0.12	+0.12	+0.95	±0.49
Combustor pressure ratio	±0.31	-0.20	+0.05	±0.35
Engine temperature ratio	±0.64	+0.06	+2.47	±0.40
Engine pressure ratio	±0.49	+0.32	-3.78	±0.12
Corrected torque	±1.03	-0.45	+5.79	±1.41

Reference: Corrected speed = 13820 RPM
Corrected Turbine Inlet Temperature = 2200 °R (1220 K)

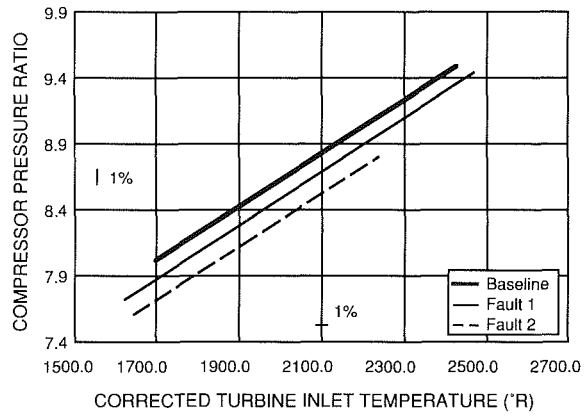


Fig. 2 Compressor pressure ratio versus corrected turbine inlet temperature

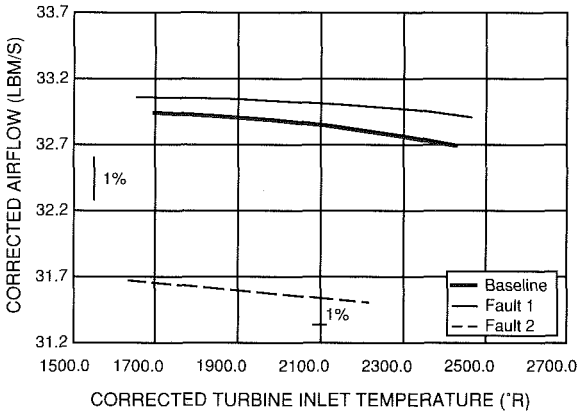


Fig. 3 Corrected airflow versus corrected turbine inlet temperature

performance evaluation, the comparison of the baseline and fault tests was carried out. The observed shifts in the various performance parameters are given in Table 3. Several of these shifts are shown graphically in Figs. 2–6.

First Fault Implantation Results. To assess the various effects of the first implanted faults, eroded first-stage turbine nozzles, and worn compressor seals, the engine and its individual components were considered separately. The effects on compressor performance were noticed in the compressor pressure ratio (Fig. 2), which showed a decrease of 0.88 percent from the baseline tests. This decrease was more than double the pessimistic repeatability of the measured parameter. The corrected airflow (Fig. 3) showed an increase of 0.60 percent, which was slightly higher than the repeatability. The compressor efficiency and compressor temperature ratio did not

Downloaded 02 Jun 2010 to 171.66.16.112. Redistribution subject to ASME license or copyright; see http://www.asme.org/terms/Terms_Use.cfm

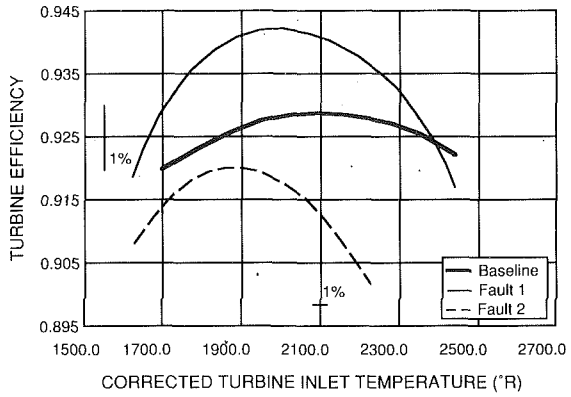


Fig. 4 Turbine efficiency versus corrected turbine inlet temperature

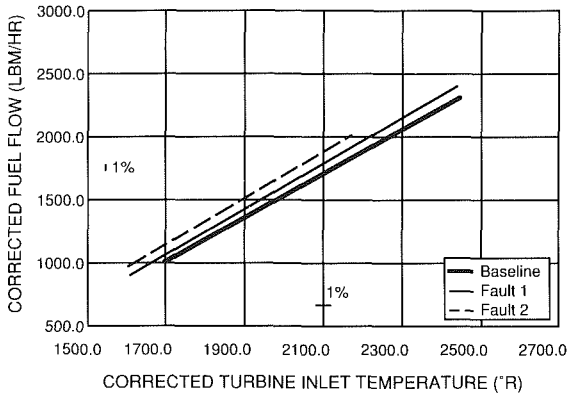


Fig. 5 Corrected fuel flow versus corrected turbine inlet temperature

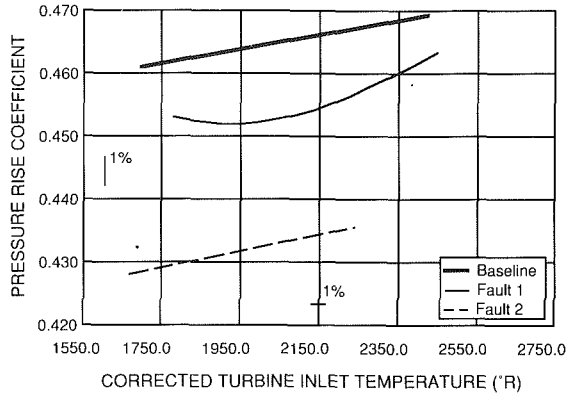


Fig. 6 First-stage compressor pressure rise coefficient versus corrected turbine inlet temperature

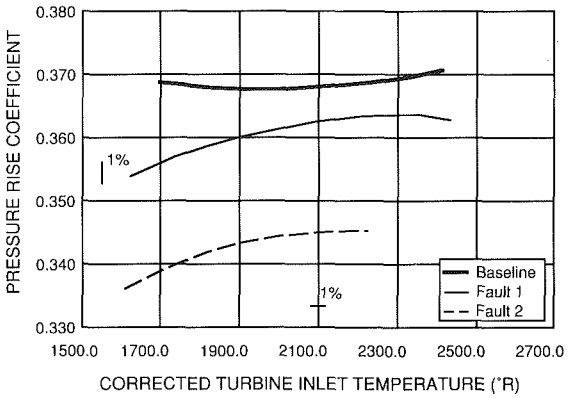


Fig. 7 Second-stage compressor pressure rise coefficient versus corrected turbine inlet temperature

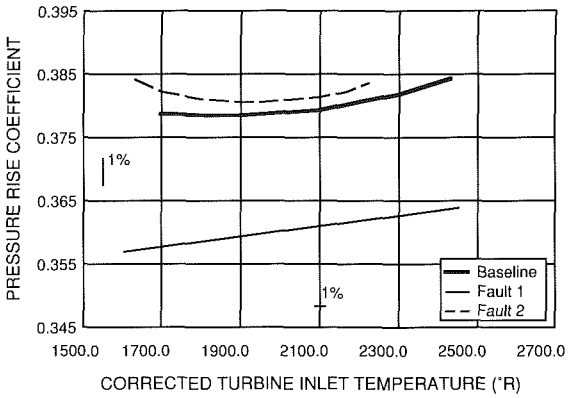


Fig. 8 Third-stage compressor pressure rise coefficient versus corrected turbine inlet temperature

indicate any significant shifts. The corrected speed for both tests was within 0.3 percent of the target value of 13,820 rpm.

The combustor pressure and temperature ratios did not indicate any significant changes. This was unexpected since previous experience (MacLeod and Laflamme, 1988, 1989) had indicated a strong relationship between the exit conditions of the compressor and the combustor pressure losses. The changes in turbine efficiency were less than the repeatability at the reference turbine inlet temperature. Through the mid-power range, however, there was a noticeable increase in the turbine efficiency (Fig. 4).

Concerning the overall engine performance, the corrected fuel flow increased by 3.24 percent, as shown in Fig. 5, which is far greater than the projected repeatability. Shifts in the corrected torque and corrected output power were within the overall repeatability band. Specific fuel consumption increased according to the increase in fuel flow. Changes in the engine temperature and pressure ratios were negligible.

The effects of the implanted faults on the individual compressor stages are shown in Figs. 6, 7, and 8.

In this analysis, the stage pressure rise coefficients were compared to isolate performance changes. To reduce space, only the first three compressor stage results are presented. The first fault implantation results (Figs. 6, 7, and 8) show a decrease in pressure rise in each of the three stages, ranging from 2 to 4 percent.

Second Fault Implantation Results. For the second set of implanted faults, the changes in performance were more dramatic. The compressor pressure ratio (Fig. 2) decreased by nearly 2.5 percent, while the corrected airflow (Fig. 3) decreased by approximately 4 percent, nearly an order of magnitude beyond their corresponding repeatabilities. Once again, the compressor efficiency and corrected speed were well within their overall repeatability limits. The compressor temperature ratio decreased by nearly 1.0 percent, which would explain why there was no significant change in the compressor efficiency.

The turbine efficiency (Fig. 4) decreased by more than 3.5 percent, while the combustor temperature ratio increased by nearly 1.0 percent. The combustor pressure ratio showed no noticeable changes.

Considering the overall engine performance, the corrected fuel flow (Fig. 5) increased by approximately 7 percent, while the output power increased by 4.7 percent. This resulted in a net increase in specific fuel consumption of 2.24 percent. The engine temperature ratio increased by approximately 2.5 percent, while the engine pressure ratio (Fig. 9) decreased by 3.78 percent.

The results of the intercompressor measurements were sig-

Downloaded 02 Jun 2010 to 171.66.16.112. Redistribution subject to ASME license or copyright; see http://www.asme.org/terms/Terms_Use.cfm

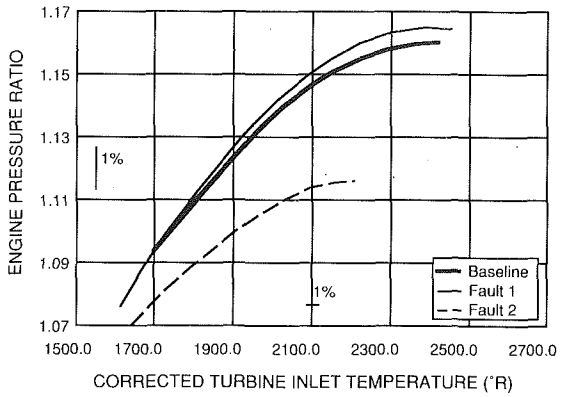


Fig. 9 Engine pressure ratio versus corrected turbine inlet temperature

nificant in that the pressure rise coefficient for the first (Fig. 6) and second stages (Fig. 7) had decreased by approximately 5 percent, whereas the third stage (Fig. 8) showed no apparent change in pressure rise.

Discussion of Fault Implantation Results. The results of the performance evaluation of the implanted faults were compared assuming the overall repeatability was the worst combination of all of the back-to-back and run-to-run repeatabilities. A comparison (Table 1) of the back-to-back repeatability to the expected random error shows very close agreement on most parameters, with the exception of torque. The run-to-run repeatability was shown (Table 2) to be slightly greater than the expected random error, indicating some portion of the bias error was included. On most parameters, the overall repeatability was found to be more pessimistic than the estimated uncertainties (Table 3) calculated using the methods described by Abernethy and Thompson (1973).

For this paper, no attempt was made to distinguish between performance changes directly attributable to the implanted fault and those changes that occurred as a result of cycle rematching.

The results of the first fault implantation indicated that the effects of the worn compressor seals were so minute that detection was unlikely. Initial compressor stator seal wear occurs during the first engine after seal replacement (seal break-in run). Changes in engine performance during the break-in period were well within the repeatabilities of the individual parameters.

The effects of the first-stage turbine nozzle erosion were easily detected. The decrease in compressor pressure ratio and slight increase in airflow were expected, since the turbine nozzle is choked, and an increase in effective flow area would produce less back pressure on the compressor. The increase in fuel flow is in keeping with the need to input more heat to obtain the same temperature conditions in the turbine inlet, for a lower combustor pressure. It is interesting that the turbine efficiency curve changes shape, such that the maximum efficiency occurs at the midpower setting, and drops off much more rapidly at high and low power than the healthy turbine.

The results of the second set of implanted faults indicated that the increased blade tip clearance on the first two compressor stages reduced the overall compressor pressure ratio, and that pressure losses were isolated only on the faulted stages, i.e., the third and subsequent compressor stages were unaffected. The increased blade tip clearance also produced a significant decrease in the corrected airflow, which confirms that the initial compressor stages determine the engine airflow. The results of previous experience with T56 engines (MacLeod and Laflamme, 1988, 1989) indicated a close relationship between the blade tip clearances and performance shifts in compressor pressure ratio and airflow.

The increase in turbine blade untwist appears to have significantly decreased the turbine efficiency, as well as modified the shape of efficiency curve. The drop-off in efficiency was greatest at the highest and lowest power setting. Since the compressor exit temperature was lower, more fuel was required to keep the turbine inlet temperature at the reference value. However, with the compressor requiring less power, because of the lower airflow, the higher fuel flow produced an increase in output power.

Conclusions

In setting up a project to quantify the effects of implanted faults on engine performance, there is some difficulty in defining the statistically measurable performance shift. The data presented here for the Allison T56 engine illustrate that while some parameters have reasonably large repeatabilities associated with them, others have quite small limits, which makes them ideal for measuring small but important changes in performance. In addition, even less repeatable parameters may prove useful when large shifts in performance are present, or for analyzing performance trends in various engine components.

The results of the fault implantation study to date have indicated that performance shifts from all but one of the four implanted faults were measurable. The eroded turbine nozzles affected the compressor pressure ratio and the fuel flow, while the turbine blade untwist affected the turbine efficiency. The increased compressor blade tip clearance affected the compressor pressure ratio, airflow, and fuel flow. The worn compressor stator seals did not affect the engine performance enough to be detected.

Recommendations

It is recommended that additional faults be implanted in the T56 engine to broaden the scope of the project and to increase the database of information for development of an operation fault library for use in field overhaul installations. Such faults could include compressor blades with reduced chord length or increased surface roughness, or turbine blades with leading edge damage.

References

Abernethy, R. B., and Thompson, J. W., 1973, "Handbook of Uncertainty in Gas Turbine Measurements," AEDC-TR-73-5.

Detroit Diesel Allison, 1983, "T56-A-14LFE Overhaul Manual, Vol. I," C-14-33-000/MP-001, Publication No. 17RC3.

Grabe, W., 1988, "Fuel Flow Measurement in Gas Turbine Testing," National Research Council of Canada, TR-ENG-001.

Grabe, W., 1989, "Humidity Effects on Gas Turbine Performance," National Research Council of Canada, TR-ENG-003.

Greco, L., and Gordon, S., 1966, "Allison T56-A-14 Engine—Official Sea Level Low and High Temperature, and Altitude Performance Tests," NAEC-AEL-1836.

Jarvo, J., and Muir, D. E., 1989, "Ambient Temperature Effects on Gas Turbine Performance," GasTOPS Report GTL-19-31.2-TR.1.

MacLeod, J. D., 1987, "Effect of Inlet Temperature Variation on Gas Turbine Engine Performance," National Research Council of Canada, LM-ENG-007.

MacLeod, J. D., and Laflamme, J. C. G., 1988, "The Effects of a Compressor Rebuild on Gas Turbine Engine Performance," AGARD CP-448-26.

MacLeod, J. D., and Laflamme, J. C. G., 1989, "The Effects of a Compressor Rebuild on Gas Turbine Engine Performance: Final Results," AGARD CP-461-3.

MacLeod, J. D., and Laflamme, J. C. G., 1990, "Compressor Coating Effects on Gas Turbine Engine Performance," National Research Council of Canada Report No. 31352.

McLarty, V., 1988, "NRC T56-A-7B Test Bed Engine: SAL Teardown, Inspection and Rebuild Data," Standard Aero Ltd. Report 0123.

Taylor, V., 1990, "NRC T56-A-7B Test Engine: Rebuild With 2nd Set of Fault Implantations," Standard Aero Ltd. Report 0664.

Downloaded 02 Jun 2010 to 171.66.16.112. Redistribution subject to ASME license or copyright; see http://www.asme.org/terms/Terms_Use.cfm

Ping Zhu[1]
Graduate Student.

H. I. H. Saravanamuttoo
Professor.
Fellow ASME

Department of Mechanical & Aerospace Engineering,
Carleton University,
Ottawa, Canada

Simulation of an Advanced Twin-Spool Industrial Gas Turbine

A full-range mathematical model of the LM-1600 gas turbine has been developed, for future use in EHM studies. No data were available from the manufacturer other than sales brochures giving some design and off-design performance. The model was developed using generalized component characteristics and shows excellent agreement with field data from a pipeline operator. A new method has been developed for doing the matching calculations, starting from the turbine (hot) end rather than from the compressor operating point. This method permits solution on a PC, and can be used for studying the full range of operating conditions and the development of fault matrices.

Introduction

When a new model of gas turbine is introduced, the user has no background of operational experience, and in-service faults or deterioration may be difficult to identify. Mathematical modeling of the engine's thermodynamic performance is a powerful tool, permitting the user to predict fault matrices, which can be used for fault identification. A major problem, however, is the lack of information required to construct such a model. This paper discusses the work required to create a model of the recently introduced General Electric LM-1600, which has been ordered by a number of major pipelines. This work represents a form of "reverse" engineering, using publicly available data. The first step required is to define the thermodynamic design point, specifying temperatures and pressures through the engine, knowing the overall specified performance. The next step is to estimate compressor and turbine characteristics to provide a model capable of operating over the entire running range. An alternative method, which does not need compressor characteristics, has also been developed, based on gas dynamic relationships between the three turbines. The predictions compare very favorably with results from the field. Once this stage has been reached it is possible to implant faults in the model and produce fault matrices. It will become increasingly important, for modern engines of modular construction, to be able to detect faults to the module level. The model developed can be run on a PC, which is compatible with installations on pipeline compressor stations.

Design Point Calculation

The initial step in developing the computational engine model is to re-establish the design point conditions from available data. Since this information will be incorporated into the off-design model, it is very important to ensure that an accurate design point is obtained.

As an advanced high-temperature gas turbine, the LM-1600 has cooled HP and LP turbine blades. The coolant is extracted from the middle stage and exit of the HP compressor. The simplified flow pattern is shown in Fig. 1. Variable geometry is required because of the high overall pressure ratio, and IGV, VSV, and VBV are all used. At the design point, the IGV and VSV are fully open and the VBV fully closed.

A design point mathematical model containing basic thermodynamic equations and compatibility equations is set up first, to solve the unknown design point parameters. The problem here is lack of information. Most design point parameters of the LM-1600 have not been published. The major sources of information are the manufacturer's sales brochure and *Gas Turbine World* (Farmer, 1988). The most reliable design point parameters specify engine overall performance. To solve the design point model, it is necessary to make empirical assumptions for two parameters, and the assumptions are validated by the following analysis.

It is known that if a mathematical model has two freely specified variables, the solution point is any point within a two-dimensional domain; all the other calculated parameters will have different values corresponding to every different solution point. In real gas turbine operation, every parameter has a valid range of value; out of the range, the parameter would be meaningless. To establish the validity of the assumed

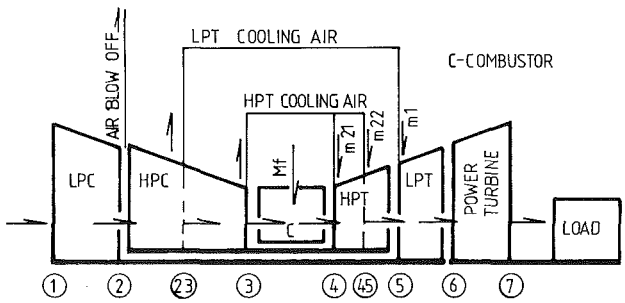


Fig. 1 Simplified flow pattern of the LM-1600

[1]Present address: Pratt & Whitney Canada.

Contributed by the International Gas Turbine Institute and presented at the 36th International Gas Turbine and Aeroengine Congress and Exposition, Orlando, Florida, June 3-6, 1991. Manuscript received at ASME Headquarters February 6, 1991. Paper No. 91-GT-34. Associate Editor: L. A. Riekert.

Copyright © 1992 by ASME
Downloaded 02 Jun 2010 to 171.66.16.112. Redistribution subject to ASME license or copyright; see http://www.asme.org/terms/Terms_Use.cfm

parameters, the model initially locates the solution point within a limited two-dimensional domain. Further, even in this domain, inaccurate assumptions could cause some other calculated parameters to be out of their value range. This later consideration would shrink the two-dimensional solution domain again.

For the LM-1600, if we assume compressor efficiency and HP turbine exit temperature, the validity analysis can be carried out by calculating the cooling air flow rates. Since all the cooling air flows must be positive, the possible solution domain indicated by this analysis is actually quite small. This means the assumed values are close to the correct ones.

It is important to choose the correct mathematical model and clearly define the flow pattern in the model design point calculation. An oversimplified flow pattern, which often ignores the cooling flow and fuel flow, would cause major errors for a high-temperature gas turbine. An overcomplicated pattern would increase the difficulty of model solving and programming, but would not necessarily increase the modeling accuracy.

The results of the design point calculation are listed in Table 1, which is an optional output of the engine model and provides basic information to the user.

Generalized Component Characteristics

The generalized compressor map can represent only the overall performance; incorporating the effects of variable geometry would require a more complex model using stage stacking methods.

The major impediment in developing a component-based gas turbine model is the lack of component characteristic maps. For most engines on the market, the full-scale component maps are normally proprietary to the manufacturers and are seldom published. Although some simplified methods, which will be discussed later, have been introduced to avoid this difficulty, some important performance information such as rotor speeds, compressor running line, surge margin, etc., would not be predictable without the maps.

The LM-1600 is the industrial version of the F404, a widely used military engine, with the three-stage fan of the aero-engine cropped to match the flow requirement of the HP compressor. The major components of the two engines are almost identical. No component characteristics are available. To overcome the problem, a generalized compressor map developed by Saravanamuttoo and Maclsaac (1983) has been used. The map is derived from several gas turbine compressors by relative scaling of the available maps. The resulting map has been found valid for low and midpressure ratio compressors up to PR 8:1. This is shown in Fig. 2. By slightly modifying the efficiency contours and scaling up the speed lines to meet the designed pressure ratio and nondimensional mass flow of the LM-1600, this generalized compressor map functions very well in the engine model.

A generalized speed-independent turbine characteristic curve is used to model the turbine performance. The curve can be

Table 1 Design point calculation

```
**********************************************************************
*                        GAS PROPERTIES                              *
**********************************************************************
          1     2    2-3    3     4    4-5    5     6     7
Pres.(Psia):  14.7  58.8 171.9 323.4 307.2   -    97.5  53.7  14.7
Temp.(K):     288.  447.  631.  768. 1483. 1443. 1155. 1014.  734.
**********************************************************************
*                     COMPONENT PERFORMANCE                          *
**********************************************************************
                    LPC       HPC       HPT       LPT       PT
Pressure Ratio:     4.000     5.500     3.150     1.818     3.651
Isentropic Eff:      .879      .874      .887      .880     1.000
Effective Area (Square inch):          33.145    94.091   147.413
Work Output(IG-Hp): 19000.:       SFC(lb/IGHp-hr):  .3430:
**********************************************************************
*                        GAS FLOW (lb/s)                             *
**********************************************************************
   Inlet air  Fuel flow  Cooling air  HT Nozzle  HT Rotor  LT N&R
      95.0      1.8103      9.0198      4.4874    2.2912    2.2411
Percentage to Inlet:        .09494      .04724    .02412    .02359
Calculation Constant:                 .292E-02  .149E-02  .317E-03
```

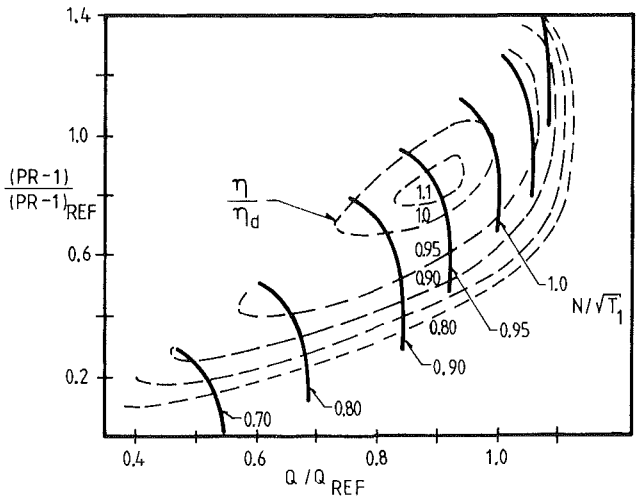


Fig. 2 Generalized compressor characteristic

expressed either by a polynomial or a modified nozzle equation. The method has been widely used and proven accurate. The significance of this turbine curve is not only its simplicity, but also that it reduces the location domain of the turbine working point from a two-dimensional area to a one-dimensional curve.

The comparisons of model-predicted results with field measurements are shown in Figs. 3 and 4. They indicate that provided a generalized map is the representation of a component in the same class, simulation of overall performance by a component-based engine model can be done fairly well. Absolute accuracy of the map, which implies the requirement of the real component characteristic map, is not possible; using the generalized map, further improvement of modeling accuracy by slightly modifying the map is quite simple.

The use of the compressor map allows the model to give a complete picture of engine operation to the user. The maps and the running lines can actually be shown on a screen or copied through a plotter. This will help inexperienced gas tur-

Nomenclature

C_p = specific heat
M = mass flow
P = total pressure
T = total temperature
γ = specific heat ratio
$\epsilon_a = (\gamma - 1)/\gamma_{air}$
$\epsilon_g = (\gamma - 1)/\gamma_{gas}$
η = efficiency

Subscripts

a = air
c = compressor
g = gas
h_p = high pressure
l_p = low pressure
m = mechanical
t = turbine

Abbreviations

EHM = Engine Health Monitoring
HP = High Pressure
IGV = Inlet Guide Vanes
ISO = International Standards Organization
LP = Low Pressure
OPR = Overall Pressure Ratio
PR = Pressure Ratio
TIT = Turbine Inlet Temperature
VBV = Variable Bleed Valve
VSV = Variable Stator Vanes

Downloaded 02 Jun 2010 to 171.66.16.112. Redistribution subject to ASME license or copyright; see http://www.asme.org/terms/Terms_Use.cfm

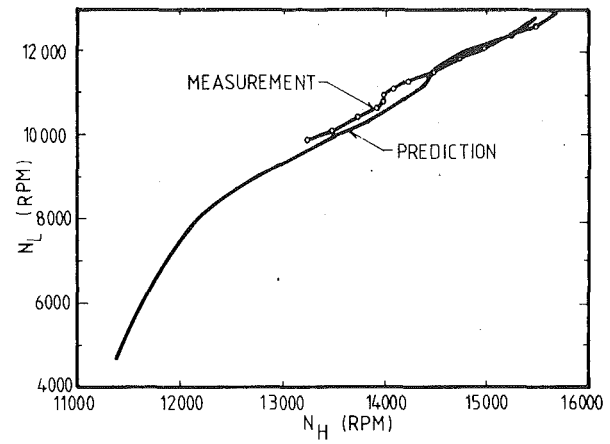


Fig. 3 Comparison between model prediction and field measurement (N_L versus N_H)

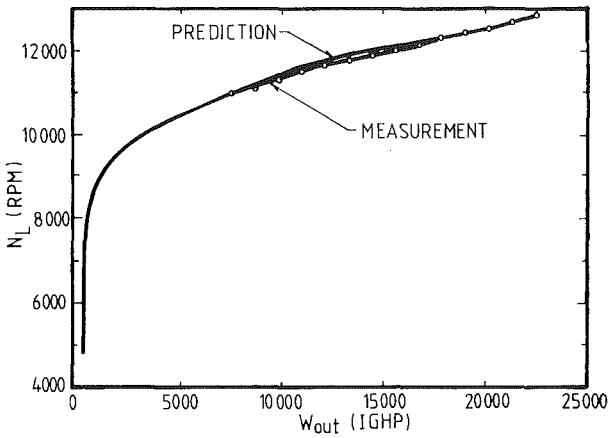


Fig. 4 Comparison between model prediction and field measurement (N_L versus W_{out})

bine operators to gain some knowledge by operating the model engine and comparing the results with those of the real one.

The LM-1600 has variable geometry components. The generalized compressor map can represent only the overall performance, so it incorporates the effects of the variable geometries.

Hot End Method

A steady-state gas turbine model is based on compatibility relations of flow and work. The model can be mathematically and/or graphically expressed. The solution process is often described as *component matching*.

The normal component matching procedure is introduced by Cohen et al. (1987). Because of the difficulty of obtaining the maps, some simplified methods have been developed. One of them is by Wittenberg (1976); in this method, a generalized turbine curve and estimated component efficiencies are used instead of real component maps. The calculation is restricted to thermodynamic relationships. For a twin-spool gas generator, choking of the LP turbine is assumed; hence the operating point of the HP turbine is fixed. Then the component matching is simplified to the solving of the LP-spool work compatibility relation, which is graphically expressed as a cross point of two curves for the LP compressor and the LP turbine. If compressor maps are available, Wittenberg's method can be applied with greater accuracy by correcting for the variation of efficiency.

Wittenberg's method can be further modified for computer application. When the generalized turbine model and estimated component efficiencies are used, a mathematical engine model, which consists of flow compatibility, work compatibility, and pressure equilibrium relations, can be expressed as a set of N equations with $N+1$ unknowns (this may also be true if the relationship between the efficiencies and component operating parameters are found from valid characteristic maps).

For a land-based twin-spool gas generator turbine with negligible cooling flow and fuel flow, N equals 10. Theoretically, if one of the unknowns is specified, the model can be uniquely solved. This mathematical uniqueness reflects the steady-state operation of gas turbines; i.e., corresponding to each steady-state operating point, there is a unique set of gas turbine parameters which are thermodynamically coupled. If one of the parameters varies independently, the others will follow and vary dependently. This causes the change of engine operating point. At every operating point, each parameter takes a unique value.

Since these N model equations are highly nonlinear and highly coupled, the key to solving the equation is to specify a suitable parameter to make the solution process simple. Analysis shows that most of the parameters are not suitable to be the specified one, since solving of a nonlinear equation set will be required. This is difficult numerically, and also takes more computing time and memory. Analysis also shows that the proper solution process should start from the engine *hot end*. If the power turbine pressure ratio is initially specified, the operating conditions of the power turbine, the LP turbine, and the HP turbine can easily be fixed by the generalized turbine characteristic and flow compatibility. Considering the thermodynamic relations and pressure equilibrium, the LP and HP-spool work compatibility equations can be simplified by the following steps:

1 The original equations can be written as:

Work compatibility between LP compressor and LP turbine:

$$M_a C_{pa}(T_2 - T_1) = \eta_m M_g C_{pg}(T_5 - T_6) \tag{1}$$

Work compatibility between HP compressor and HP turbine:

$$M_a C_{pa}(T_3 - T_2) = \eta_m M_g C_{pg}(T_4 - T_5) \tag{2}$$

2 Substituting the thermodynamic relationship between pressure ratio and total temperature into Eqs. (1) and (2), we can rewrite them as:

$$\frac{M_a C_{pa}\ T_1}{\eta_m M_g C_{pg} \eta_{lpc}}\left[\left(\frac{P_2}{P_1}\right)^{\epsilon_a} - 1\right] = \eta_{lpt} T_4$$

$$\left(1 - \eta_{hpt}\left[1 - \left(\frac{1}{P_4/P_5}\right)^{\epsilon_g}\right]\right)\left[1 - \left(\frac{1}{P_5/P_6}\right)^{\epsilon_g}\right]$$
$$\frac{M_a C_{pa}\ T_1}{\eta_m M_g C_{pg} \eta_{hpc}}\left(1 + \frac{1}{\eta_{lpc}}\left[\left(\frac{P_2}{P_1}\right)^{\epsilon_a} - 1\right]\right)$$
$$\left[\left(\frac{P_3}{P_2}\right)^{\epsilon_a} - 1\right] = \eta_{hpt} T_4\left[1 - \left(\frac{1}{P_4/P_5}\right)^{\epsilon_g}\right]$$

3 From the previous assumption and solved turbine pressure ratios, Eq. (1) now contains only two unknowns: P_2/P_1 and T_4, and can be simplified as:

$$\left[\left(\frac{P_2}{P_1}\right)^{\epsilon_a} - 1\right] = A\ T_4 \tag{1-1}$$

Equation (2) contains three unknowns: P_3/P_2, P_2/P_1, and T_4. To use the pressure equilibrium relation, we can write P_3/P_2 as a function of P_2/P_1 and presolved turbine pressure ratios. Again if we substitute Eq. (1-1) into (2), then (2) can be simplified as a second-order equation, which contains only one unknown:

$$B\ T_4^2 + C\ T_4 + D = 0 \tag{2-1}$$

Downloaded 02 Jun 2010 to 171.66.16.112. Redistribution subject to ASME license or copyright; see http://www.asme.org/terms/Terms_Use.cfm

where A, B, C, and D are coefficients derived from the known and the presolved turbine parameters.

One of the two roots of Eq. (2-1) would be the solution of T_4. The other root is negative and of no importance. Finding P_2/P_1 from Eq. (1-1) and fixing the conditions of the LP compressor and HP compressor by the solved variables and flow compatibilities is then quite straightforward.

The advantages of this hot end method are:

1 The whole process contains only simple calculations, which do not require any unnecessary computerized graphic work or matrix calculations that are needed in many currently used engine models. The process is very suitable for computation because the program is relatively short and the solution takes much less time than either graphic or matrix calculations. This method is especially useful when a portable PC model is required by the user in the field.

2 The physical meaning of the process, which is based on the concept of steady state operation, is clear.

3 Since all points along the power turbine characteristic line are possible operating points, the solved turbine working points would always be valid. The solved compressor working points would be along the running line if the efficiency is accurately assumed, or very close to the line if a compressor map is available for further accuracy correction. The correction is made by the work compatibility Eqs. (1-1) and (2-1). It does not need to go back to the beginning of the calculation, so convergence occurs very rapidly.

4 Though in most cases of interest, the LP turbines are choked, the assumption of LP turbine choking is not needed in the hot end method. This is still true even if the LP turbine is largely unchoked at very low output. The solution process is valid for the full range of engine operation.

5 Since the hot end method is not initiated from the compressor end, any variation of compressor running lines would not affect component matching. For a deteriorated engine or an engine with variable geometry, the running line moves as engine condition and/or inlet conditions change. In this type of engine model, using the hot end method would facilitate the programming, increase the modeling flexibility, and save memory space as well as computing time.

If an engine has a complicated flow pattern and fuel flow or bleed flows cannot be neglected, the number of unknowns in the mathematical engine model will increase. It is then necessary to include new modeling equations, which are related to the new unknowns, into the engine model. For example, if blow off through the VBV is required, a VBV model should be incorporated, adding another equation to the engine model; then the hot end method can still be applied.

The application of the hot end matching process can be enhanced by a numerical method of one-dimensional searching. It is known that all the important gas turbine operating parameters increase monotonically with power turbine pressure ratio. This means that any one of the parameters can be specified, and the one-dimensional searching subroutine will find the corresponding operating point by searching the related power turbine pressure ratio along the characteristic line. For the LM-1600 model, eleven parameters, as shown in Table 2, are provided to the user. Any one of them can be used as the engine model independent parameter. Since the generalized compressor map is built into the model, mechanical speeds of the rotors can also be selected as the independent parameter. Thus the model is similar to the real engine, making it easier to relate to field operation.

Model Results

1 Model Design and Output. The model can simulate the nominal engine and five deteriorated engine conditions, and can run at any inlet conditions. A window of design point calculation, Table 1, is left to the user for information and

Table 2 Selection of independent parameter

No.	Selectable Parameters
1	Work Output
2	Turbine Inlet Temperature
3	Gas Generator Exhaust Temperature
4	Power Turbine Exhaust Temperature
5	Inlet Mass Flow Rate
6	Fuel Flow Rate
7	LP Compressor Pressure Ratio
8	HP Compressor Pressure Ratio
9	Overall Pressure Ratio
10	Power Turbine Pressure Ratio
11	LP-spool Speed

Table 3 Modeling results (table output)

```
**********************************************************************
*                          GAS PROPERTIES                            *
**********************************************************************
St.  Pressure(Psia)  Temperature(K)  Mass Flow (lb/S)  N-D Mass Flow
1          14.7          288.0           94.70           109.33
2          58.8          447.8           94.70            34.08
2-3       171.7          632.0           92.47
3         323.0          770.2           85.72
4         306.9         1488.5           87.54            11.85
4-5                     1448.8
5          97.4         1159.3           94.29            33.73
6          53.6         1017.8           96.52            57.45
7          14.7          736.5
**********************************************************************
*                       COMPONENT PERFORMANCE                        *
**********************************************************************
                  LPC       HPC       HPT       LPT       PT
N--D Mass Flow:   109.33    34.08     11.85     33.73     57.45
Pressure Ratio:     4.00     5.49      3.15      1.82      3.65
Turbine Choke PR:                     2.02      2.03      1.85
Efficiency:         .8759     .8708
Work (GHP):       9244.1   18458.7   18458.1   9244.6
LP Spool Speed:  12365. Rpm;        HP Spool Speed:  15222. Rpm;
**********************************************************************
*                          COMPRESSOR DATA                           *
**********************************************************************
        P3(Stagnation)/P01     P3(Static)/P01     Mach No.(3)
              21.97                20.70             .2937

**********************************************************************
*                      COOLING and BLEED FLOW                        *
**********************************************************************
                  HPT Nozzle   HPT Rotor   LPT N&R          Bleed
Flow Rate (lb/s):     4.4682      2.2814     2.2332          .0000
Ratio to Inlet Flow:  .04718      .02409     .02358          .00000

**********************************************************************
*                    OVERALL ENGINE PERFORMANCE.                     *
**********************************************************************
Work Output:        19000.00 IGHp;                12312.19 SH-Kw;
Fuel Flow Rate:       1.816 lb/s,     6537. lb/hr;     2965. Kg/hr;
Fuel/Air Ratio:     .021182 ;      Thermal Efficiency:      .4020 ;
SFC:      .34404 lb/IGHp-hr ;      Heat Rate:      6330.34 BTU/IGHp-hr ;
```

possible modification in the future. According to his modeling purpose, the user can choose engine condition (nominal or deteriorated), and inlet conditions and then specify the independent modeling parameter to run the model; two types of output are available:

(a) Table output: shown in Table 3, provides thermodynamic gas parameters at each engine station, component performance, cooling flow, and bleed flow as well as overall engine performance at the user specified working condition. This is a detailed description of engine working status. Taking the parameters of interest from several operating points, the user can plot curves of parameter variation for further analysis.

(b) Graphic output: there are twelve possible graphic outputs. Two of them show the LP and HP compressor maps and the running lines. Others show the variation of important operating parameters. On all the graphics, the predicted baselines for the nominal engine at ISO standard inlet conditions

Downloaded 02 Jun 2010 to 171.66.16.112. Redistribution subject to ASME license or copyright; see http://www.asme.org/terms/Terms_Use.cfm

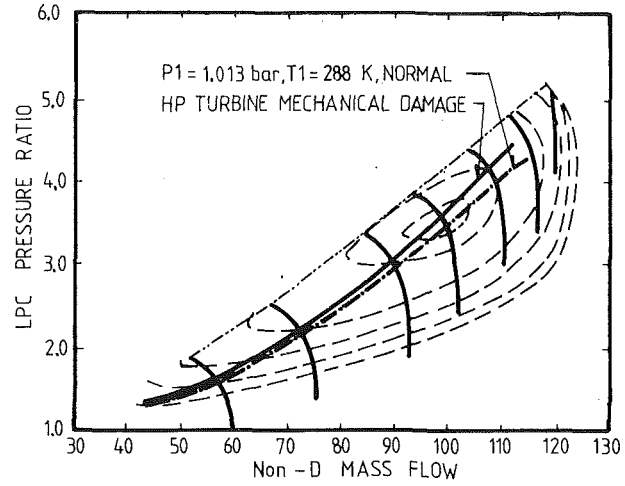


Fig. 5 Graphic output 1, LPC running line

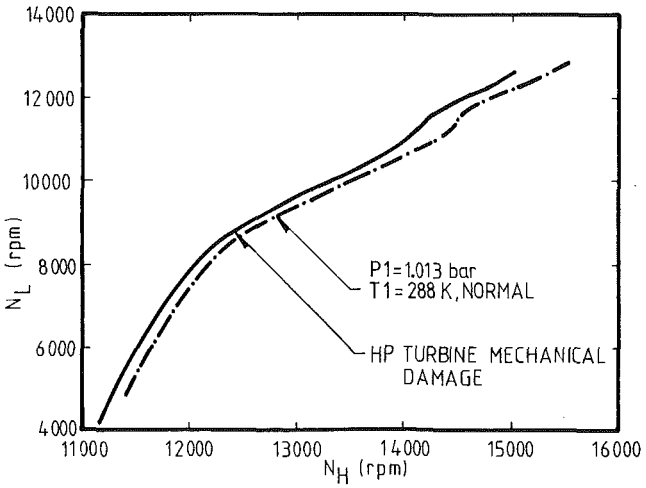


Fig. 6 Graphic output 3, LP-spool mechanical speed versus HP-spool mechanical speed

are plotted to compare with the operating lines at the specific running condition. The graphic output gives the user a visible concept of engine operation and deterioration. Two of the graphics are shown as examples, Figs. 5 and 6.

2 Engine Performance Simulation

(*a*) Nominal Engine Simulation: This is based on the original component maps and engine parameters obtained from the design point. No additional restrictions are added to the engine model.

(*b*) Deteriorated Engine Simulation: Williams (1981) has listed eight common deteriorated conditions in pipeline gas turbine application. Five of them are incorporated in the model as follows:

1 LP compressor mechanical damage: by 5 percent drop of LPC efficiency.

2 Compressor excessive leakage: by 3 percent overboard leakage flow at the HP compressor exit.

3 HP turbine mechanical damage: by 5 percent drop of HP turbine efficiency.

4 HP turbine erosion: by 2 percent increase of HP turbine flow area.

5 LP turbine erosion: by 2 percent increase of LP turbine flow area.

(*c*) Comparisons: Some deteriorated performance parameters, OPR, TIT, and HP-speed versus LP-speed, plotted with those of the nominal engine, are shown in Figs. 7, 8, and 9.

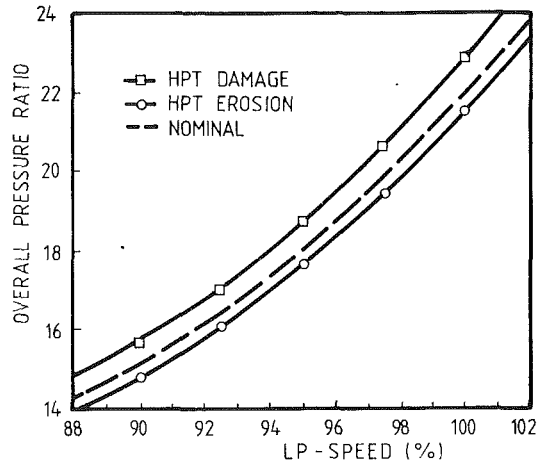


Fig. 7 OPR versus LP-speed

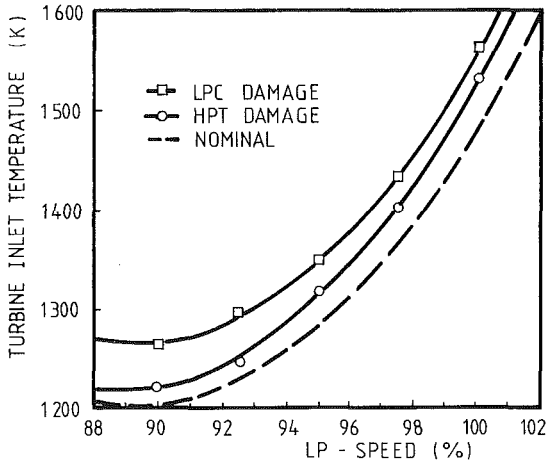


Fig. 8 TIT versus LP-speed

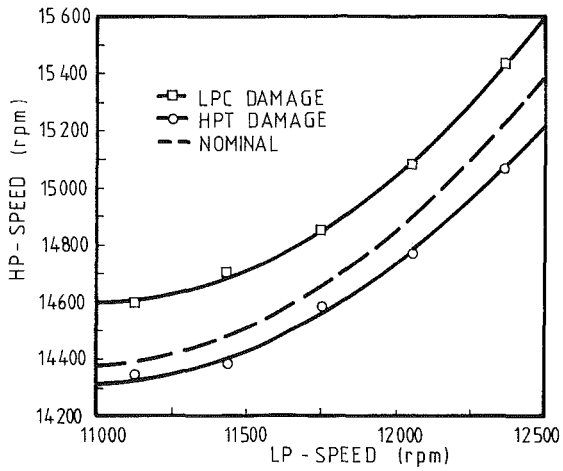


Fig. 9 HP-speed versus LP-speed

Detailed analysis and a fault matrix which will be discussed later, show that at a specified LP-speed:

1 Deteriorations (1), (3), and (5) will increase OPR and deteriorations (2) and (4) will decrease OPR.

2 All the deteriorations will result in higher TIT except deterioration (4).

3 Deteriorations (1), (2), and (5) will raise the HP-speed and deteriorations (3) and (4) will lower the speed.

4 Except for deterioration (2), most deteriorations will raise fuel flow and work output. The increase in work output is

Downloaded 02 Jun 2010 to 171.66.16.112. Redistribution subject to ASME license or copyright; see http://www.asme.org/terms/Terms_Use.cfm

Table 4 Fault matrix

DETERIORATED CONDITIONS	SPEED	OPR	TIT	M_a	M_f	sfc	WORK OUTPUT	HP SPEED	LP WORK	HP WORK
$0.95\eta_{lpc}$	HIGH	↑	↑	∪	↑	↑	↑	↑	↑	↑
	MID	↑	↑	∩	↑	↑	↑	↑	↑	↑
	LOW	↑	↑	∩	↑	↑	↑	↑	↑	↑
0.03 Bleed	HIGH	↓	↑	—	↑	↑	↓	↑	↓	↓
	MID	↓	↑	↑	↑	↑	↓	↑	↑	↓
	LOW	↓	↑	↑	↑	↑	↓	↑	↑	↑
$0.95\eta_{hpt}$	HIGH	↑	↑	↓	↑	↑	↑	↓	↑	↓
	MID	↑	↑	↓	↑	↑	↑	↓	↑	↓
	LOW	↑	↑	↓	↑	↑	↑	↓	↑	↓
$1.024\ A_{hpt}$	HIGH	↓	↓	∪	∪	—	↓	↓	∪	↓
	MID	↓	↓	∪	∩	∩	↑	↓	↑	↓
	LOW	↓	↓	∪	↑	↑	∩	↓	↑	↓
$1.02\ A_{lpt}$	HIGH	↑	↑	↑	↑	↑	↑	↑	↓	↑
	MID	↑	↑	↑	↑	∩	↑	↑	↓	↑
	LOW	↑	↑	↑	↑	∪	↑	↑	↓	↑

LP – SPEED = INDEPENDENT VARIABLE.

caused by the increase of fuel flow and hence TIT. If, however, the maximum allowable TIT is taken as the control parameter, this will result in reduced rotor speed and decreased work output.

Here the HP turbine erosion may appear to improve performance. If erosion causes the HP turbine flow area to increase, the work load of the HP-spool decreases and the load of the LP-spool increases. For fixed TIT or work output, the LP rotor has to run at a higher speed, which may not be permissible for mechanical reasons. For actual erosion, it would also be expected there would be some drop of the efficiency; so the erosion may be the combination of deteriorations (3) and (4) that more likely will depress the performance rather than improve it.

As examples of graphic output, Fig. 5 shows the LP compressor map and the comparison of running lines; Fig. 6 shows the relationship between the two rotor speeds. As HP turbine mechanical damage is specified in these maps, it appears that the deterioration will raise the LP compressor running line toward surge and lower the HP-speed for a specified LP-speed.

3 Development of Fault Matrix. A fault matrix is a common tool used for field diagnostic analysis. By evaluating the trends of parameter variation, the operator can roughly locate the engine problem for further investigation.

Since only a few faults might be found in service, the complete fault matrix cannot be developed by real engine operation. It has to be produced by a diagnostic model with simulated faults implanted. A fault matrix produced by the LM-1600 model is shown in Table 4. The LP-spool speed is taken as the independent variable in the matrix, where the LP-speed varies from 100 percent design speed to 95 percent and 90 percent. The sign of "↑" or "↓" indicates parameter increase or decrease compared with the nominal engine; "∩" or "∪" indicates slight increase or decrease; and "—" means almost no change. It can be seen that the magnitude of the independent parameters has some effect on the various trends; for this reason, a restricted operating range should be specified for use with the fault matrices.

The model has been verified against field results from a pipeline. Because of the short time the engine has been in service, no extensive information on faults is available; thus, the fault matrix presented is developed from the mathematical model and has still to be proven. If either the VSVs or IGVs are out of tolerance, considerable shift in the parameters will result if LP speed is used as the independent variable; the fault matrix may, therefore, be a useful tool for checking errors in the variable geometry settings. Alternatively, HP speed could be used as the independent variable, and another fault matrix developed.

The fault matrix is a useful tool, because the effect of specific deteriorations can be implanted; not all of these may occur in service, and some may only be experienced at very high running hours, so the mathematical model offers a significant predictive capability.

Conclusions

A mathematical model representing the performance of the LM-1600 has been generated, showing excellent agreement with field results. The model is flexible in use and can generate fault matrices, which can be used for diagnostic purposes, a feature that is particularly useful when little operating experience has been built up. The model has modest computing requirements and can be run on a PC compatible with those installed at pipeline compressor stations.

Acknowledgments

This work is based on the M.Eng. thesis written by Ping Zhu at Carleton University. The authors would like to express their thanks to the Natural Sciences and Engineering Research Council of Canada (NSERC) for financial support of the work.

References

Cohen, H., Rogers, G. F. C., and Saravanamuttoo, H. I. H., 1987, *Gas Turbine Theory*, 3rd ed., Longman Scientific and Technical.

Farmer, R., 1988, "GT-660 Turbine Powered by an LM-1600 Gas Generator is Rated at 18000 Hp," *Gas Turbine World*, Dec., pp. 10–21.

G. E. Company, Marine & Industrial Engines and Service Division, 1988, "Design, Performance and Operational Features of the LM-1600 Gas Generator," brochure.

Saravanamuttoo, H. I. H., and MacIsaac, B. D., 1983, "Thermodynamic Model for Pipeline Gas Turbine Diagnostics," JOURNAL OF ENGINEERING FOR POWER, Vol. 105, pp. 875–884.

Williams, L. J., 1981, "The Use of Mathematical Modeling in the Analysis of Gas Turbine Compressor Unit Test," ASME Paper No. 81-GT-217.

Wittenberg, H., 1976, "Prediction of Off-Design Performance of Turbojet and Turbofan Engine Based on Gasdynamic Relationships," Delft University of Technology, The Netherlands.

Downloaded 02 Jun 2010 to 171.66.16.112. Redistribution subject to ASME license or copyright; see http://www.asme.org/terms/Terms_Use.cfm

Table 4 Fault matrix

DETERIORATED CONDITIONS	SPEED	OPR	TIT	M_a	M_f	sfc	WORK OUTPUT	HP SPEED	LP WORK	HP WORK
$0.95\eta_{lpc}$	HIGH	↑	↑	∪	↑	↑	↑	↑	↑	↑
	MID	↑	↑	∩	↑	↑	↑	↑	↑	↑
	LOW	↑	↑	∩	↑	↑	↑	↑	↑	↑
0.03 Bleed	HIGH	↓	↑	—	↑	↑	↓	↑	↓	↓
	MID	↓	↑	↑	↑	↑	↓	↑	↑	↓
	LOW	↓	↑	↑	↑	↑	↓	↑	↑	↑
$0.95\eta_{hpt}$	HIGH	↑	↑	↓	↑	↑	↑	↓	↑	↓
	MID	↑	↑	↓	↑	↑	↑	↓	↑	↓
	LOW	↑	↑	↓	↑	↑	↑	↓	↑	↓
$1.024\ A_{hpt}$	HIGH	↓	↓	∪	∪	—	↓	↓	∪	↓
	MID	↓	↓	∪	∩	∩	↑	↓	↑	↓
	LOW	↓	↓	∪	↑	↑	∩	↓	↑	↓
$1.02\ A_{lpt}$	HIGH	↑	↑	↑	↑	↑	↑	↑	↓	↑
	MID	↑	↑	↑	↑	∩	↑	↑	↓	↑
	LOW	↑	↑	↑	↑	∪	↑	↑	↓	↑

LP – SPEED = INDEPENDENT VARIABLE.

caused by the increase of fuel flow and hence TIT. If, however, the maximum allowable TIT is taken as the control parameter, this will result in reduced rotor speed and decreased work output.

Here the HP turbine erosion may appear to improve performance. If erosion causes the HP turbine flow area to increase, the work load of the HP-spool decreases and the load of the LP-spool increases. For fixed TIT or work output, the LP rotor has to run at a higher speed, which may not be permissible for mechanical reasons. For actual erosion, it would also be expected there would be some drop of the efficiency; so the erosion may be the combination of deteriorations (3) and (4) that more likely will depress the performance rather than improve it.

As examples of graphic output, Fig. 5 shows the LP compressor map and the comparison of running lines; Fig. 6 shows the relationship between the two rotor speeds. As HP turbine mechanical damage is specified in these maps, it appears that the deterioration will raise the LP compressor running line toward surge and lower the HP-speed for a specified LP-speed.

3 Development of Fault Matrix. A fault matrix is a common tool used for field diagnostic analysis. By evaluating the trends of parameter variation, the operator can roughly locate the engine problem for further investigation.

Since only a few faults might be found in service, the complete fault matrix cannot be developed by real engine operation. It has to be produced by a diagnostic model with simulated faults implanted. A fault matrix produced by the LM-1600 model is shown in Table 4. The LP-spool speed is taken as the independent variable in the matrix, where the LP-speed varies from 100 percent design speed to 95 percent and 90 percent. The sign of "↑" or "↓" indicates parameter increase or decrease compared with the nominal engine; "∩" or "∪" indicates slight increase or decrease; and "—" means almost no change. It can be seen that the magnitude of the independent parameters has some effect on the various trends; for this reason, a restricted operating range should be specified for use with the fault matrices.

The model has been verified against field results from a pipeline. Because of the short time the engine has been in service, no extensive information on faults is available; thus, the fault matrix presented is developed from the mathematical model and has still to be proven. If either the VSVs or IGVs are out of tolerance, considerable shift in the parameters will result if LP speed is used as the independent variable; the fault matrix may, therefore, be a useful tool for checking errors in the variable geometry settings. Alternatively, HP speed could be used as the independent variable, and another fault matrix developed.

The fault matrix is a useful tool, because the effect of specific deteriorations can be implanted; not all of these may occur in service, and some may only be experienced at very high running hours, so the mathematical model offers a significant predictive capability.

Conclusions

A mathematical model representing the performance of the LM-1600 has been generated, showing excellent agreement with field results. The model is flexible in use and can generate fault matrices, which can be used for diagnostic purposes, a feature that is particularly useful when little operating experience has been built up. The model has modest computing requirements and can be run on a PC compatible with those installed at pipeline compressor stations.

Acknowledgments

This work is based on the M.Eng. thesis written by Ping Zhu at Carleton University. The authors would like to express their thanks to the Natural Sciences and Engineering Research Council of Canada (NSERC) for financial support of the work.

References

Cohen, H., Rogers, G. F. C., and Saravanamuttoo, H. I. H., 1987, *Gas Turbine Theory*, 3rd ed., Longman Scientific and Technical.

Farmer, R., 1988, "GT-660 Turbine Powered by an LM-1600 Gas Generator is Rated at 18000 Hp," *Gas Turbine World*, Dec., pp. 10–21.

G. E. Company, Marine & Industrial Engines and Service Division, 1988, "Design, Performance and Operational Features of the LM-1600 Gas Generator," brochure.

Saravanamuttoo, H. I. H., and MacIsaac, B. D., 1983, "Thermodynamic Model for Pipeline Gas Turbine Diagnostics," JOURNAL OF ENGINEERING FOR POWER, Vol. 105, pp. 875–884.

Williams, L. J., 1981, "The Use of Mathematical Modeling in the Analysis of Gas Turbine Compressor Unit Test," ASME Paper No. 81-GT-217.

Wittenberg, H., 1976, "Prediction of Off-Design Performance of Turbojet and Turbofan Engine Based on Gasdynamic Relationships," Delft University of Technology, The Netherlands.

DISCUSSION

A. Stamatis[2] and K. Mathioudakis[2]

This paper presents an interesting piece of work in the area of gas turbine performance simulation. We would like to pose

[2]Laboratory of Thermal Turbomachines, National Technical University of Athens, Athens, Greece.

Copyright © 1992 by ASME

Downloaded 02 Jun 2010 to 171.66.16.112. Redistribution subject to ASME license or copyright; see http://www.asme.org/terms/Terms_Use.cfm

some questions to the authors, because we think that some points are not sufficiently clear in the paper.

Our first question is related to the way that component maps have to be modified in order to match overall engine performance. Since the authors state that their model is useful for inexperienced operators, we wonder how such operators will be able to produce the required changes on map parameters, without risking being involved in a lengthy trial and error procedure. The authors do not seem to be aware of the existence of methods of automatically adapting the component maps to engine performances (Stamatis et al., 1990a).

A second question is related to the calculation method itself. It is not clear to us how the iterations are done. Since constants A, B, C, D contain the compressor efficiencies, their estimation will have to be effected at each iteration. It seems, therefore, that at each step it will be necessary to "go back to the beginning of the calculation," contrary to what the authors state. With respect to the comments of the authors about other iteration procedures, we would like to know what the authors mean by "difficult numerically." Do they imply long computer time, or problems of nonconvergence and instability? Although the authors discard solution procedures involving matrix methods, they do not state how their iteration procedure is effected, implying that it is a direct substitution one. For such a method, however, it is known that convergence problems may exist. In this respect we would like to mention the work of Wang Yonghong (1991), which has actually introduced the same idea as the one the authors employ in engine modeling, while it discusses comprehensively the numerical aspects of the problem.

We would also like to have information about the reduction in computer memory and running time achieved by the proposed method. Could the authors provide figures about memory requirements and speed of their model, as well as of models over which they claim improvement? Here we would like to comment that in our opinion the necessary speed of calculations is being provided by present-day computer capabilities. In this respect we think that sacrificing model accuracy by simplifying assumptions (as for example by assuming a single turbine characteristic at low pressure ratios or not correcting for compressor efficiency variation) should be avoided. Our experience is that very low running times (fractions of a minute) can be achieved when using full models in today's standard portable PCs.

A final point we would like to have the authors' comments on, is the usefulness of fault matrices. Although they were of great value when first introduced, in the early 1970's, we think their current usefulness is being overemphasized in the present paper. Such matrices give only qualitative information about faults and anyway cannot at all resolve situations with simultaneous presence of different component faults. On the other hand, quantitative methods capable of directly identifying component problems as to their kind and location have been introduced (Stamatis et al., 1990b). In any case the present-day needs (as identified, for example, by Doel, 1990) require information interpretable by expert systems, rather than relying on observations by the engine operator. The method of the present paper does not seem to reply to such needs.

References

Doel D., 1990, "The Role of Expert Systems in Commercial Gas Turbine Engine Monitoring," ASME Paper No. 90-GT-374.

Stamatis, A., Mathioudakis, K., and Papailiou, K. D., 1990, "Adaptive Simulation of Gas Turbine Performance," ASME JOURNAL OF ENGINEERING FOR GAS TURBINES AND POWER, Vol. 112, No. 2, pp. 168–175.

Stamatis, A., Mathioudakis, K., Smith, M., and Papailiou, K. D., 1990, "Gas Turbine Component Fault Identification by Means of Adaptive Performance Modeling," ASME Paper No. 90-GT-376.

Wang Yonghong, 1991, "A New Method of Predicting the Performance of Gas Turbine Engines," ASME JOURNAL OF ENGINEERING FOR GAS TURBINES AND POWER, Vol. 113, pp. 106–111.

Authors' Closure

The authors are grateful for the interest in their paper.

It was made clear in the paper that there was absolutely no information available to the authors on either compressor or turbine characteristics. The objective of the work was to produce a full-range thermodynamic model of the engine, which had recently entered service. Compressor characteristics were generated from generalized maps previously published, while single line characteristics based on nozzle data were used for turbines; there would certainly not have been any point in using variable speed turbine characteristics. It should also be noted that the gas generator turbines operate over restricted running ranges, and only the power turbine is subjected to operation over a wide range of speed and pressure ratio. When field test data became available the authors made adjustments to the characteristics to achieve good agreement; it was never intended that field operators would be involved in this process.

The Hot End Method introduced in the paper (HEM) permits all turbine working points to be established initially, and by using pressure equilibrium the work compatibilities can be reduced to a second-order equation with only one unknown. As this equation is solved, the compressor working points can be fixed on the maps; any errors in compressor efficiency can be corrected through iteration and update of the constants A, B, C, and D. This is a half-loop iteration and it is not necessary to go back to the beginning of the calculation. The computer program was computed in the winter of 1989 and the work of Wang Yonghong did not become known to the authors until after the publication of this paper. Both Wang's method and the HEM start from the turbine matching process, fixing the turbine operating points. Wang makes use of this to avoid the numerical instability of the full matrix and then solves a reduced matrix for work compatibility and the cold end; HEM solves the second-order equation directly and finds the rest of the unknowns from flow compatibilities of the cold end. HEM uses a simple one-dimensional search method based on the basic thermodynamic cycle. The authors feel that the simple mathematical model using basic concepts is preferable to a more complex numerical model.

The authors agree that the power of modern PCs makes computing speed a secondary issue; this particular model required about 1.5–2 min running time. They do not agree that using multiline turbine characteristics would improve accuracy, especially where no data are available.

There is no doubt that in the future expert systems will play a role. The key point, however, is where can the data be found to produce the required rules? It will certainly not be easy to generate these from actual field data; failures may arise where no previous information was available, so no rules would exist. Different engine types will exhibit different deterioration modes, but a large amount of operational data will eventually determine the more common causes of failure. The fault matrix is still valuable as a means of systematically predicting the effect of various faults that can be introduced; what is needed, however, is experimental work to define better the magnitudes of efficiency/flow deterioration in components and studies of this type are being initiated at Carleton University by Sjolander. Another potential source of information is test bed evaluation of engines returned for overhaul in "as-received" condition. A great deal of work still must be done to develop soundly based rules for use in expert systems.

Downloaded 02 Jun 2010 to 171.66.16.112. Redistribution subject to ASME license or copyright; see http://www.asme.org/terms/Terms_Use.cfm

some questions to the authors, because we think that some points are not sufficiently clear in the paper.

Our first question is related to the way that component maps have to be modified in order to match overall engine performance. Since the authors state that their model is useful for inexperienced operators, we wonder how such operators will be able to produce the required changes on map parameters, without risking being involved in a lengthy trial and error procedure. The authors do not seem to be aware of the existence of methods of automatically adapting the component maps to engine performances (Stamatis et al., 1990a).

A second question is related to the calculation method itself. It is not clear to us how the iterations are done. Since constants A, B, C, D contain the compressor efficiencies, their estimation will have to be effected at each iteration. It seems, therefore, that at each step it will be necessary to "go back to the beginning of the calculation," contrary to what the authors state. With respect to the comments of the authors about other iteration procedures, we would like to know what the authors mean by "difficult numerically." Do they imply long computer time, or problems of nonconvergence and instability? Although the authors discard solution procedures involving matrix methods, they do not state how their iteration procedure is effected, implying that it is a direct substitution one. For such a method, however, it is known that convergence problems may exist. In this respect we would like to mention the work of Wang Yonghong (1991), which has actually introduced the same idea as the one the authors employ in engine modeling, while it discusses comprehensively the numerical aspects of the problem.

We would also like to have information about the reduction in computer memory and running time achieved by the proposed method. Could the authors provide figures about memory requirements and speed of their model, as well as of models over which they claim improvement? Here we would like to comment that in our opinion the necessary speed of calculations is being provided by present-day computer capabilities. In this respect we think that sacrificing model accuracy by simplifying assumptions (as for example by assuming a single turbine characteristic at low pressure ratios or not correcting for compressor efficiency variation) should be avoided. Our experience is that very low running times (fractions of a minute) can be achieved when using full models in today's standard portable PCs.

A final point we would like to have the authors' comments on, is the usefulness of fault matrices. Although they were of great value when first introduced, in the early 1970's, we think their current usefulness is being overemphasized in the present paper. Such matrices give only qualitative information about faults and anyway cannot at all resolve situations with simultaneous presence of different component faults. On the other hand, quantitative methods capable of directly identifying component problems as to their kind and location have been introduced (Stamatis et al., 1990b). In any case the present-day needs (as identified, for example, by Doel, 1990) require information interpretable by expert systems, rather than relying on observations by the engine operator. The method of the present paper does not seem to reply to such needs.

References

Doel D., 1990, "The Role of Expert Systems in Commercial Gas Turbine Engine Monitoring," ASME Paper No. 90-GT-374.

Stamatis, A., Mathioudakis, K., and Papailiou, K. D., 1990, "Adaptive Simulation of Gas Turbine Performance," ASME JOURNAL OF ENGINEERING FOR GAS TURBINES AND POWER, Vol. 112, No. 2, pp. 168–175.

Stamatis, A., Mathioudakis, K., Smith, M., and Papailiou, K. D., 1990, "Gas Turbine Component Fault Identification by Means of Adaptive Performance Modeling," ASME Paper No. 90-GT-376.

Wang Yonghong, 1991, "A New Method of Predicting the Performance of Gas Turbine Engines," ASME JOURNAL OF ENGINEERING FOR GAS TURBINES AND POWER, Vol. 113, pp. 106–111.

Authors' Closure

The authors are grateful for the interest in their paper.

It was made clear in the paper that there was absolutely no information available to the authors on either compressor or turbine characteristics. The objective of the work was to produce a full-range thermodynamic model of the engine, which had recently entered service. Compressor characteristics were generated from generalized maps previously published, while single line characteristics based on nozzle data were used for turbines; there would certainly not have been any point in using variable speed turbine characteristics. It should also be noted that the gas generator turbines operate over restricted running ranges, and only the power turbine is subjected to operation over a wide range of speed and pressure ratio. When field test data became available the authors made adjustments to the characteristics to achieve good agreement; it was never intended that field operators would be involved in this process.

The Hot End Method introduced in the paper (HEM) permits all turbine working points to be established initially, and by using pressure equilibrium the work compatibilities can be reduced to a second-order equation with only one unknown. As this equation is solved, the compressor working points can be fixed on the maps; any errors in compressor efficiency can be corrected through iteration and update of the constants A, B, C, and D. This is a half-loop iteration and it is not necessary to go back to the beginning of the calculation. The computer program was computed in the winter of 1989 and the work of Wang Yonghong did not become known to the authors until after the publication of this paper. Both Wang's method and the HEM start from the turbine matching process, fixing the turbine operating points. Wang makes use of this to avoid the numerical instability of the full matrix and then solves a reduced matrix for work compatibility and the cold end; HEM solves the second-order equation directly and finds the rest of the unknowns from flow compatibilities of the cold end. HEM uses a simple one-dimensional search method based on the basic thermodynamic cycle. The authors feel that the simple mathematical model using basic concepts is preferable to a more complex numerical model.

The authors agree that the power of modern PCs makes computing speed a secondary issue; this particular model required about 1.5–2 min running time. They do not agree that using multiline turbine characteristics would improve accuracy, especially where no data are available.

There is no doubt that in the future expert systems will play a role. The key point, however, is where can the data be found to produce the required rules? It will certainly not be easy to generate these from actual field data; failures may arise where no previous information was available, so no rules would exist. Different engine types will exhibit different deterioration modes, but a large amount of operational data will eventually determine the more common causes of failure. The fault matrix is still valuable as a means of systematically predicting the effect of various faults that can be introduced; what is needed, however, is experimental work to define better the magnitudes of efficiency/flow deterioration in components and studies of this type are being initiated at Carleton University by Sjolander. Another potential source of information is test bed evaluation of engines returned for overhaul in "as-received" condition. A great deal of work still must be done to develop soundly based rules for use in expert systems.

Copyright © 1992 by ASME

Downloaded 02 Jun 2010 to 171.66.16.112. Redistribution subject to ASME license or copyright; see http://www.asme.org/terms/Terms_Use.cfm

L. J. Kerr

T. S. Nemec

G. W. Gallops

Pratt & Whitney,
United Technologies Corporation,
West Palm Beach, FL

Real-Time Estimation of Gas Turbine Engine Damage Using a Control-Based Kalman Filter Algorithm

A second-generation Kalman filter algorithm is described that has sufficient accuracy and response for real-time detection and estimation of gas turbine engine gas path damage caused by normal wear, mechanical failures, and ingestion of foreign objects. The algorithm was developed for in-flight operation of aircraft engines but also has application for marine and industrial gas turbines. The control measurement and microcomputer requirements are described. The performance and sensitivity to engine transients and measurement errors is evaluated. The algorithm is demonstrated with actual engine data of ice and bird ingestion tests.

I. Introduction

Luppold (1989) described a Kalman filter algorithm for identifying in-flight gas turbine engine performance variations for integrated aircraft control and diagnostic systems. In addition to providing engine performance estimates for in-flight optimization, the algorithm was capable of identifying off nominal engine component performance such as typically provided by condition monitoring expert systems (Urban, 1980; Smith et al., 1982; Lucas and Paas, 1988; Doel, 1990). The slow response of the algorithm, however, limited its usefulness for in-flight damage detection and accommodation.

This paper describes a second-generation implementation of the original concept with response sufficiently fast for in-flight damage detection and control accommodation. The second-generation algorithm also has reduced control microcomputer requirements for memory and processor speed. Section II describes the overall model concept and the specific implementation for this study. Section III illustrates the model performance with simulated and actual engine data examples. Section IV summarizes important conclusions of the study.

II. Observer Model

Concepts. The steady-state and transient aerothermodynamic performance of a gas turbine plant is normally simulated by an assembly of one-dimensional thermodynamic component modules, which are solved numerically subject to continuity, momentum and energy constraints. Component characteristics are tabulated in maps representing relationships between component pressure, temperature, flow capacity and efficiency. Generally, for real-time control applications, a simpler linear representation of the plant is formulated known as a state variable model (SVM), where the interrelation of the engine states, inputs and outputs is described with a set of linear differential equations. The linear relationships about a point are normally derived from an aerothermodynamic source model by perturbing the inputs and states at an equilibrium power condition.

By composing a set of these reference point models for a range of power conditions and defining one or more internal parameters for selection of the appropriate point, a piecewise linear SVM is formulated that has steady-state and dynamic accuracy comparable to the aerothermodynamic source model. This high accuracy and the small control microprocessor timing and memory requirements relative to the source model make the SVM attractive for real-time control algorithms. In addition, the state space representation of the SVM lends itself to classical linear control design concepts and modern software tools used in developing the Kalman filter described next.

The architecture of the piecewise linear SVM is illustrated in Fig. 1. The primary elements are the reference steady-state and dynamic model database and the linear calculations. The reference data are defined at a particular flight condition, and in order to extend the flight envelope capability, inputs to the model are transformed to this reference flight condition using standard gas turbine performance correction factors based on inlet pressure and temperature. The linear calculations are performed at the reference flight condition and then the model outputs are transformed back to the actual flight condition. Calculations such as aerothermodynamic nozzle relations, inlet recovery, thrust, etc., may be performed to produce auxiliary outputs.

Accurate representation of the steady-state reference data is a key factor in obtaining good model performance and, typically, requires that the steady-state data be functions of more than one selection parameter. Conversely, model performance is not sensitive to the accuracy of the dynamic ref-

Contributed by the International Gas Turbine Institute and presented at the 36th International Gas Turbine and Aeroengine Congress and Exposition, Orlando, Florida, June 3–6, 1991. Manuscript received at ASME Headquarters March 4, 1991. Paper No. 91-GT-216. Associate Editor: L. A. Riekert.

Copyright © 1992 by ASME
Downloaded 02 Jun 2010 to 171.66.16.112. Redistribution subject to ASME license or copyright; see http://www.asme.org/terms/Terms_Use.cfm

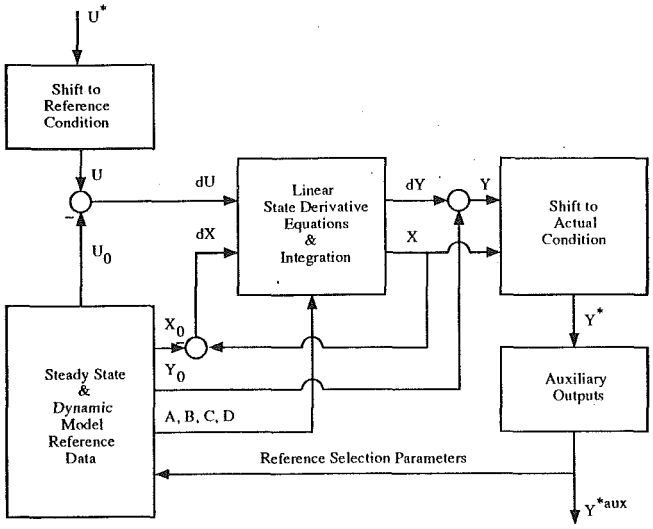


Fig. 1 Piecewise linear engine model

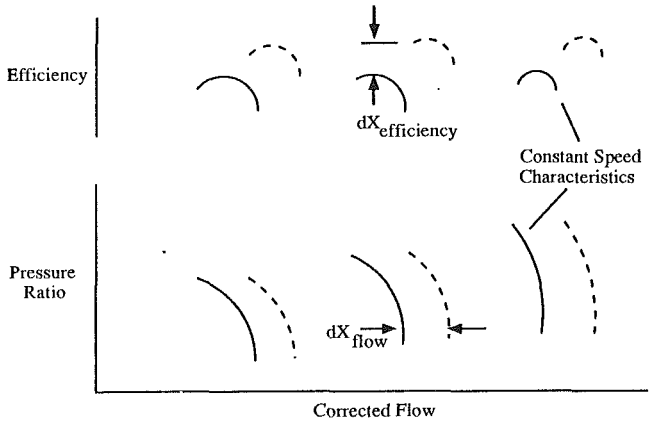


Fig. 2 Typical compressor characteristics

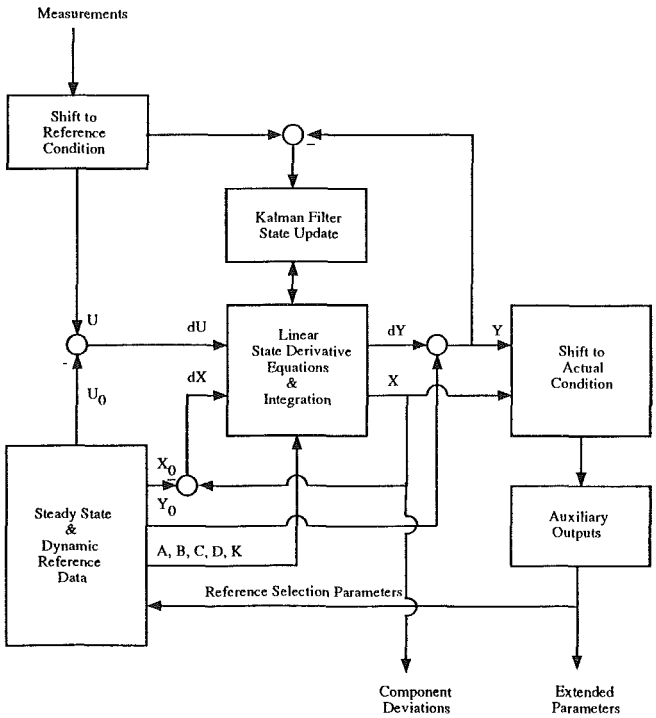


Fig. 3 Kalman filter observer model

erence data and univariate functions have proven to be adequate. For the application described in this paper, the accuracy of both the steady-state and dynamic reference data, as derived from the aerodynamic source model, is sufficient. However, the piecewise linear SVM is not dependent on source model accuracy since the approach allows the incorporation of actual engine test data.

Normally, an engine model, regardless of the type, represents one specific example of an engine configuration. To create a generalized model capable of representing the effects of normal fabrication tolerances, wear and damage requires that adjustments be made to the component representations and the component interfaces based on observation of the operating characteristics of the specific engine of interest.

Engine wear and damage may be represented in the aerothermodynamic source model as explicit deviations in the normal component characteristics. These component deviations are commonly formulated as offsets in component flow capacity and efficiency as shown in Fig. 2. In the piecewise linear SVM, the component deviations are represented simply as inputs. The linear relationships pertaining to the states and outputs are derived from the aerothermodynamic source model by perturbing the component deviations just as for the other inputs. In the Kalman filter design described next, the component deviations are transformed into states that are estimated by nulling differences between measurements and corresponding model outputs.

The Kalman filter is a recursive linear algorithm, which estimates system states (Gelb, 1974). The structure of the Kalman filter, shown in Fig. 3, is similar to the SVM, except that the filter uses feedback to null the differences between the measurements and the corresponding model outputs. The differences between the measurements and outputs are the residuals. The selection of the feedback gain matrix, K, is dependent upon the expected properties of the residuals. In order to compute the gain matrix K, a matrix Riccati equation must be solved. For turbine engine applications, the linearized system model is assumed time-invariant and the Kalman filter gain matrix converges to a unique steady-state value if the system is both observable and controllable. Thus the Kalman filter gain matrix is computed off-line using one of the several computer-aided control system design packages, which contains numerical algorithms for solving the algebraic Riccati equation.

The authors prefer that the resulting algorithm be called an observer model rather than Kalman filter because the overall

Nomenclature

A = matrix of state derivatives WRT states
B = matrix of state derivatives WRT inputs
C = matrix of output derivatives WRT states
D = matrix of output derivatives WRT inputs
K = Kalman filter gain matrix
SVM = state variable model
U = model input vector
WRT = with respect to
Y = model output vector
$\mathbf{Y}^{*aux}$ = auxiliary output vector

Subscript

0 = reference data

Superscript

* = actual flight condition

Downloaded 02 Jun 2010 to 171.66.16.112. Redistribution subject to ASME license or copyright; see http://www.asme.org/terms/Terms_Use.cfm

function is more encompassing than simply estimating the component deviations, which only secondarily affect the model outputs.

Study Configuration. The engine configuration used in the current study is the PW1128, a nonproduction technology demonstrator related to the F100 engine family. The source model for the reference data is the standard proprietary performance simulation for this engine configuration. The dynamic reference data were derived from the source model using software procedures conventionally used to obtain the Jacobian matrices for engine control design. For this study, a single set of reference data was adequate with inlet pressure and temperature at sea level static conditions.

As seen in Table 1, the inputs to the filter algorithm are typical control effectors: primary burner fuel flow, fan variable vanes, compressor variable vanes, along with available measured engine parameters: low rotor speed, high rotor speed, burner pressure, etc. Outputs include component deviation factors for fan and compressor airflow and fan and compressor efficiency. Extended outputs include flow, pressure and temperature at the major engine stations and net thrust. The steady-state reference data are bivariately interpolated as a function of low rotor speed along lines of mixing plane flow parameter. The dynamic reference data and the associated K matrix are selected univariately as a function of low rotor speed only.

For this application, the selected component deviations are fan efficiency and airflow and compressor efficiency and airflow. These four parameters are observable with the available engine sensor suite. Additional component deviations were not observable with the available measurements. The choice of these component deviation parameters is biased for damage estimation in the compression system. Turbine damage also will be included in the estimates indirectly making them composite compressor-turbine estimates.

The algorithm requirements for a current proprietary control microcomputer are estimated to be 13 ms per pass. An actual timing demonstration of the algorithm was performed in fixed point Ada language on a Motorola 68020 microprocessor with 20 MHz clock. Execution time per pass is 5 ms. Memory requirement in this implementation is less than 64 kbytes with 32 bit reference data. Microcomputer requirements are even smaller with 16 bit reference data, which is adequate with proper scaling.

Table 1 PW1128 Observer model parameters

Inputs	
Position Feedbacks	
WFP	Primary burner fuel flow
A80	Nozzle area
FVV	Fan variable vanes
CVV	Compressor Variable Vanes
Sensor Measurements	
NL	Low rotor speed
NH	High rotor speed
P00	Ambient pressure
P20	Inlet pressure
P40	Burner pressure
P65	Mixing plane pressure
T20	Inlet temperature
T45	Turbine interstage temperature
Outputs	
Component Deviations	
Fan flow factor	
Compressor flow factor	
Fan efficiency factor	
Compressor efficiency factor	
Extended Parameters	
W20	Fan airflow
W25	Compressor airflow
P25	Compressor inlet pressure
T25	Compressor inlet temperature
T30	Compressor exit temperature
T65	Mixing plane temperature
FNET	Net thrust

III. Evaluation

Luppold (1989) extensively demonstrated that the basic steady-state accuracy of the initial approach is typically better than 3–5 percent over the conventional tactical fighter flight envelope. Although steady-state accuracy was not a principal objective of the current study, a limited evaluation of the second generation observer model algorithm indicates that accuracy is similar.

The focus of this study is on factors related to the real-time operating environment such as the capability to track engine transients, sensitivity to measurement errors and rapid damage identification for control action. The following simulated and actual data evaluations were performed using a floating point FORTRAN language version of the observer model algorithm, operating at an update cycle time of 20 ms. The model reference data and the gain matrix, K, were derived directly from the aerothermodynamic source model or through conventional control design procedures. No attempt was made to match the reference data or gains on either an overall basis or for specific test cases.

Engine Transients. The requirement to track transients is the result of two factors. First, the rapid temperature and pressure changes that occur make both wear and damage more likely during these intervals than in steady-state operation. Second, real transient effects not represented in the source model must be correctly identified by the observer model to avoid misinterpretation as damage.

Figure 4 illustrates the behavior of the model on a simulated idle-to-rated power acceleration. The dynamics and accuracy of extended parameters shown are good. Emphasis is placed on the extended parameters here because they are only indirectly related to the parameters for which the filter nulls errors. The component deviation estimates (not shown) have small dynamic variations less than 2 percent, except for compressor efficiency, which exhibits a peak of +15 percent during the most rapid portion of the transient.

Measurement Errors. Measurement errors are a normal factor in the real-time operating environment. Sensor errors of modern controls are only a part of the problem. So-called position errors also are significant. These errors occur because the local value indicated by the measurement is not equivalent to the aerothermodynamic parameter represented in the source model. Some but not all of these latter errors may be removed by adjusting reference data. Luppold (1989) discusses approaches for estimation of the errors as biases, but most are not practical for real-time applications. Fortunately, the capability to accommodate large errors from failures is not required for modern redundant controls because sensor faults can be isolated and sensor values substituted.

For small errors, the observer model attempts to "explain" the sensor bias with erroneous component deviation estimates. The magnitudes of the errors are related to observability and the Kalman filter gain design. Biases that cannot be "explained" in terms of the component deviations result in quasi-steady unresolved residuals. Figure 5 illustrates the observer model behavior in response to individual sensor biases. In the ideal case (perfect model and high observability), the residual magnitude would be equal to the bias magnitude. The results show this configuration is less than ideal because of the low observability imposed by limiting to existing control sensors. Even so, the observer model demonstrates a remarkable insensitivity to bias for most parameters. The unresolved residual magnitude can even serve as a sensor fault indicator for the observer model. Fault isolation is not possible, however, with the current algorithm.

Downloaded 02 Jun 2010 to 171.66.16.112. Redistribution subject to ASME license or copyright; see http://www.asme.org/terms/Terms_Use.cfm

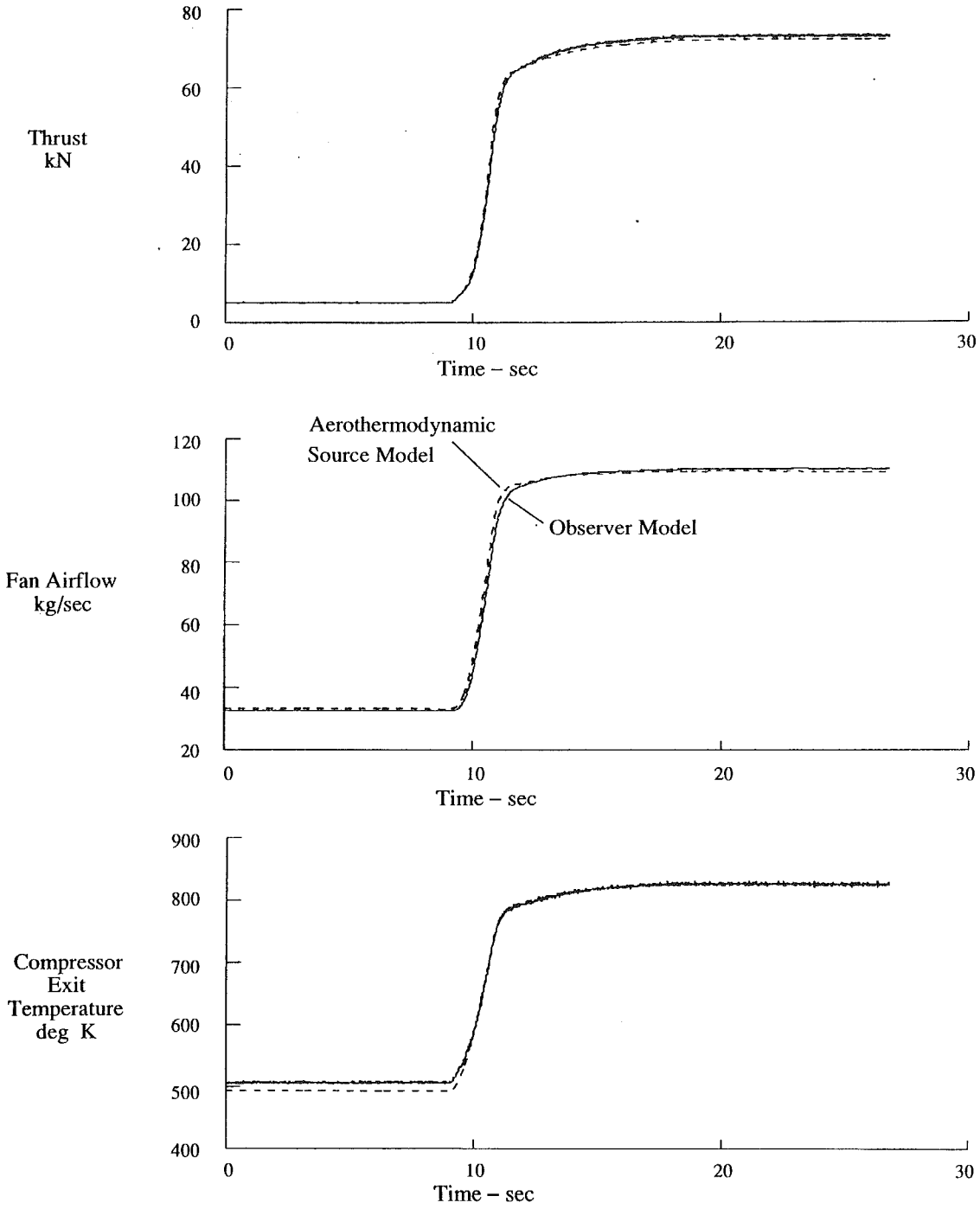


Fig. 4 Observer model outputs for throttle snap acceleration

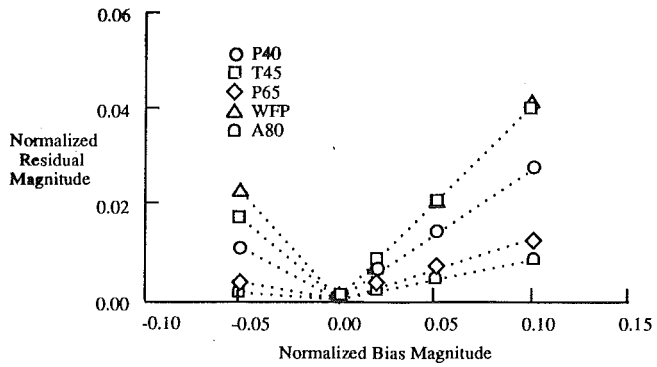


Fig. 5 Indications of measurement bias

Downloaded 02 Jun 2010 to 171.66.16.112. Redistribution subject to ASME license or copyright; see http://www.asme.org/terms/Terms_Use.cfm

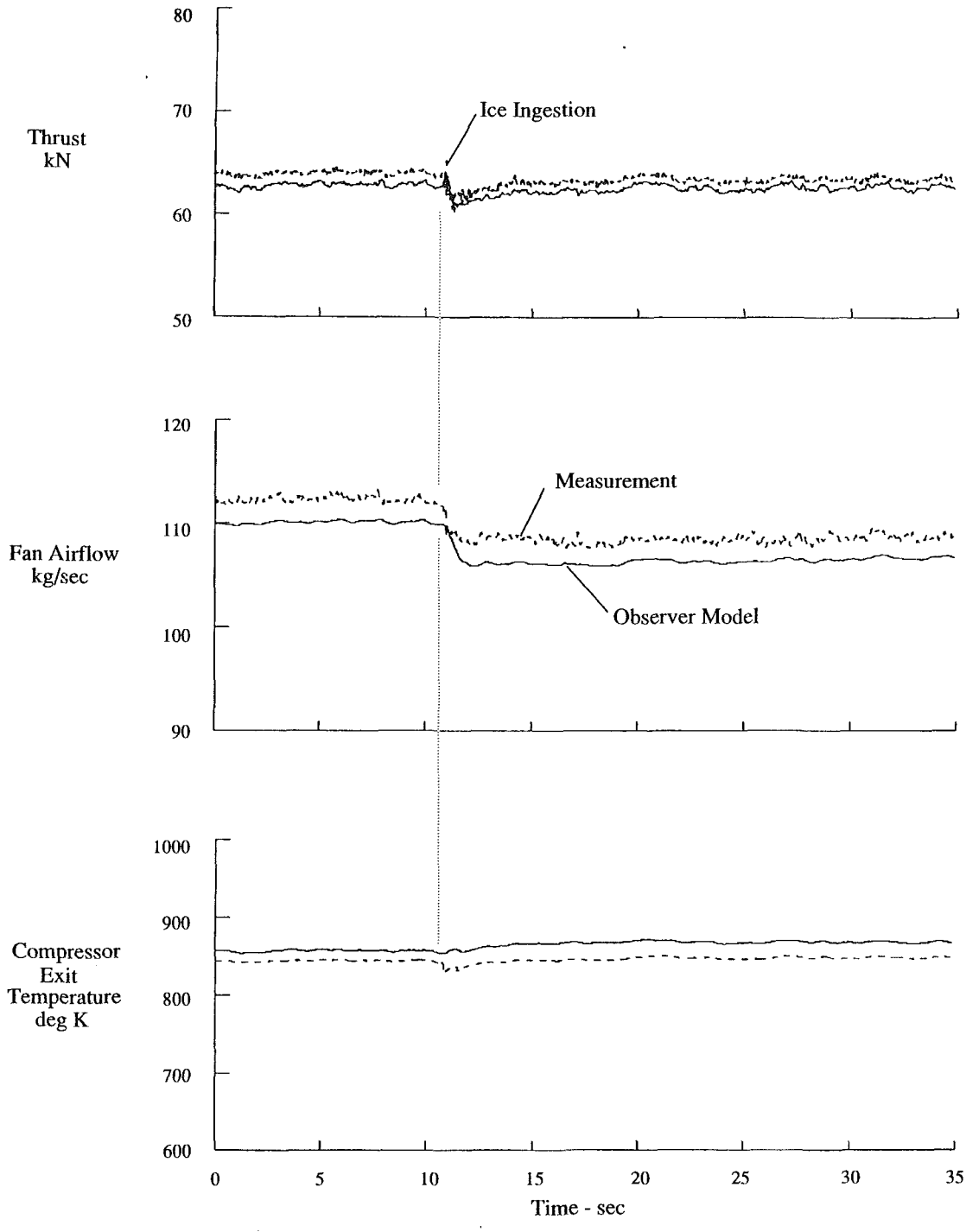


Fig. 6 Comparison with measurements—moderate foreign object damage

Downloaded 02 Jun 2010 to 171.66.16.112. Redistribution subject to ASME license or copyright; see http://www.asme.org/terms/Terms_Use.cfm

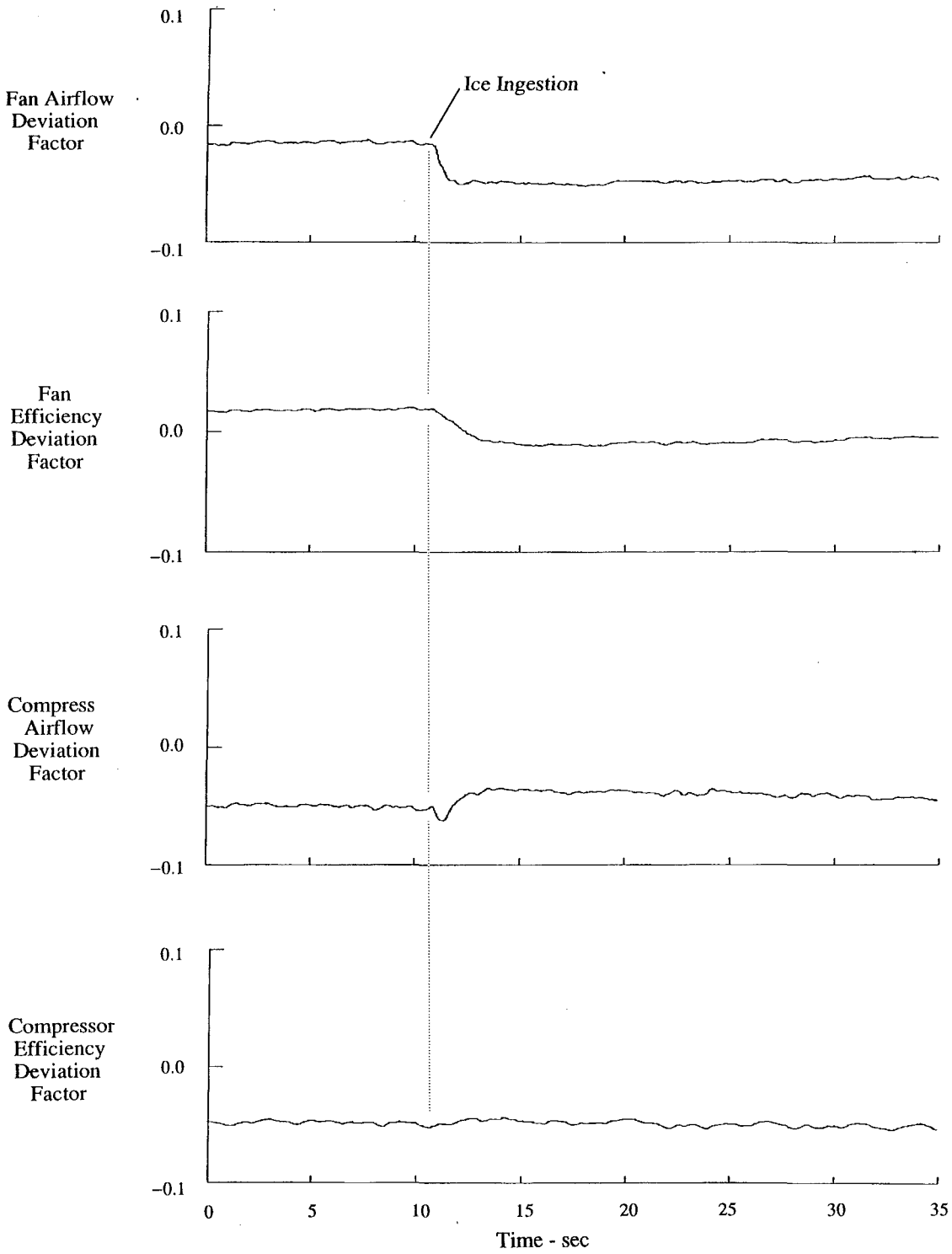


Fig. 7 Observer model estimates of moderate foreign object damage

Downloaded 02 Jun 2010 to 171.66.16.112. Redistribution subject to ASME license or copyright; see http://www.asme.org/terms/Terms_Use.cfm

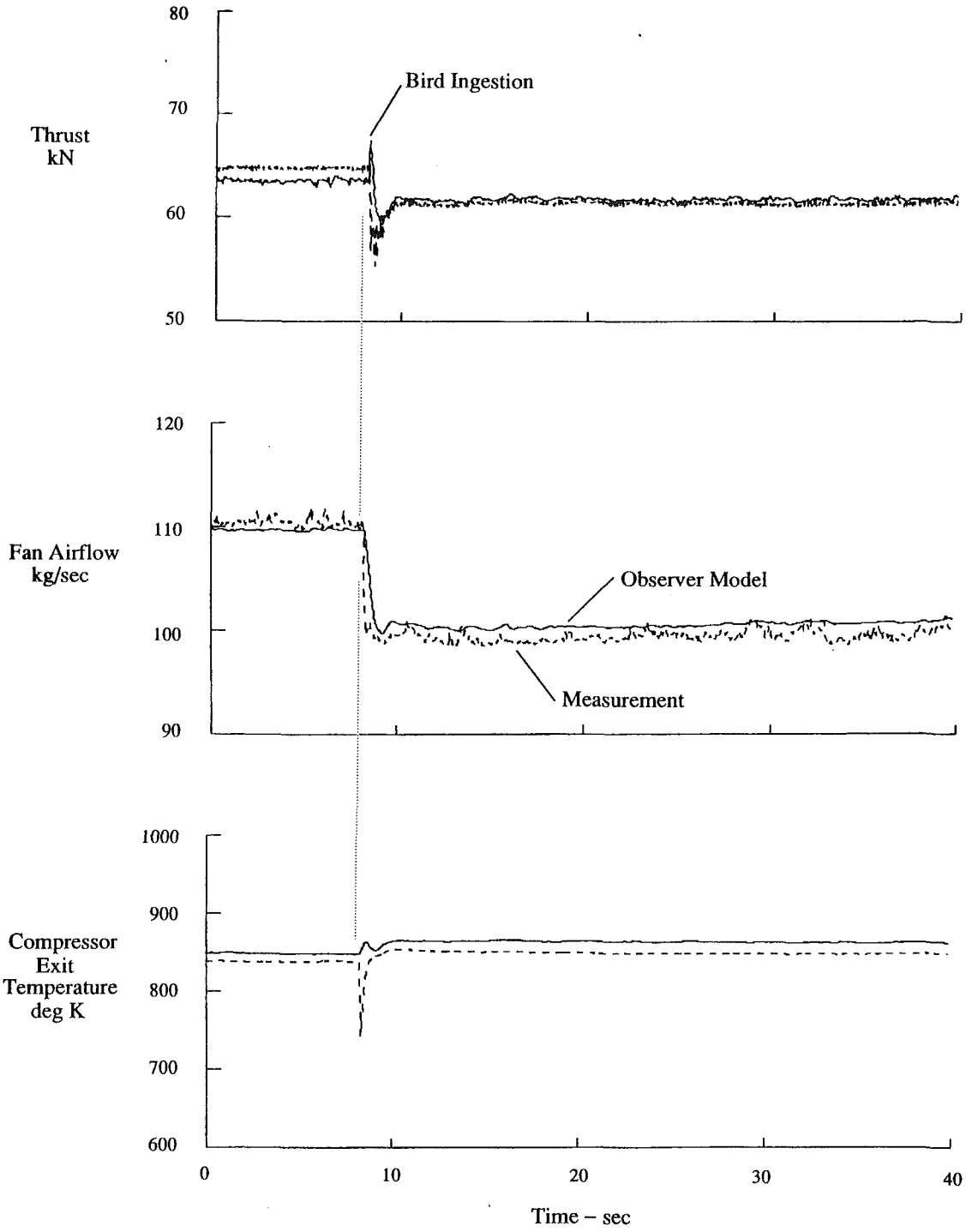


Fig. 8 Comparison with measurements—severe foreign object damage

Downloaded 02 Jun 2010 to 171.66.16.112. Redistribution subject to ASME license or copyright; see http://www.asme.org/terms/Terms_Use.cfm

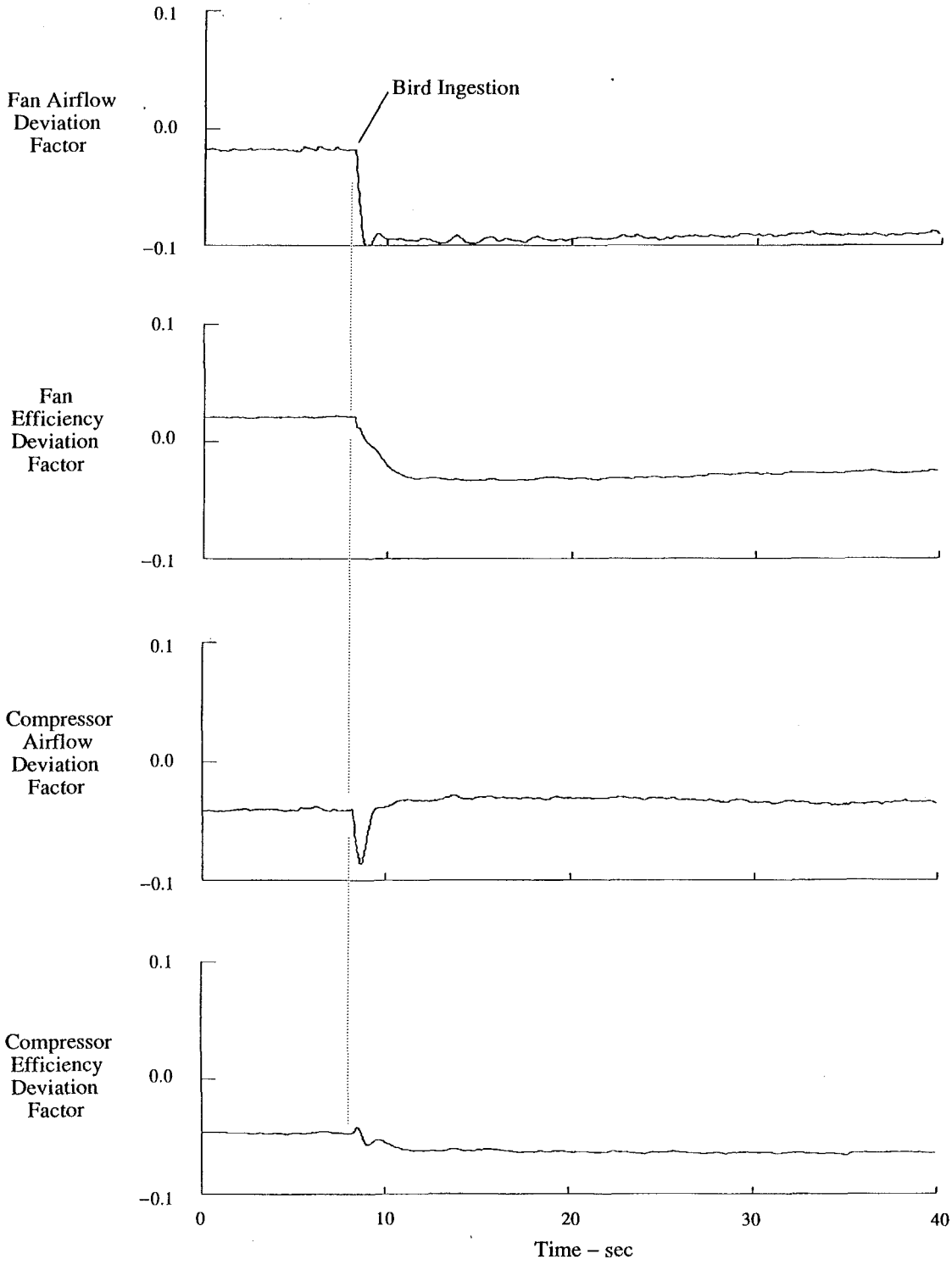


Fig. 9 Observer model estimates of severe foreign object damage

Downloaded 02 Jun 2010 to 171.66.16.112. Redistribution subject to ASME license or copyright; see http://www.asme.org/terms/Terms_Use.cfm

Damage Events. Luppold (1989) demonstrated that the initial approach could accurately identify component damage levels resulting from the ingestion of foreign objects. The time required to fully identify these presumably instantaneous events was on the order of 10 s, however. Practical real-time applications require that damage identification be comparable with engine control outer loop bandwidth or on the order of 1 s. The cases below repeat the events discussed by Luppold (1989).

Figures 6 and 7 illustrate the observer model results for a moderate damage event. The extended outputs show good agreement with corresponding measurements considering the measurements themselves are subject to approximately 2 percent uncertainty. The damage estimates indicate 3 percent fan efficiency and airflow loss and no compressor efficiency loss which are consistent with the mechanical indications for this event. The 2 percent indicated compressor airflow increase may be the result of alteration of the fan exit profile.

Figures 8 and 9 illustrate a severe damage event. Again, the extended outputs compare well with the measurements. The damage estimates indicate about 7 percent fan damage and 2 percent compressor damage. These are consistent with the mechanical indications. Except for fan efficiency, the damage estimates respond in less than 1 s.

IV. Conclusion

A second-generation Kalman filter algorithm for real-time gas turbine engine damage identification has been described. The algorithm has small control microcomputer requirements relative to current hardware capability. Data for the algorithm are created using a standard aerothermodynamic source model and conventional control design procedures and software tools. The accuracy and response of the algorithm are sufficient for in-flight damage detection and control accommodation.

Acknowledgment

The authors gratefully acknowledge R. H. Luppold, currently at Charles Stark Draper Laboratories, for his guidance in formulating the current observer model program structure and for developing the Kalman filter software design tools now in use at Pratt & Whitney. Mr. Luppold was affiliated with United Technologies Optical Systems while he participated in this work.

References

Doel, D. L., 1990, "The Role of Expert Systems in Commercial Gas Turbine Engine Monitoring," ASME Paper No. 90-GT-374.

Gelb, A., 1974, *Applied Optimal Estimation*, The M.I.T. Press, Cambridge, MA, pp. 102–144.

Lucas, H., and Paas, J. E., 1988, "Introduction and Application of the General Electric Turbine Engine Monitoring Software Within KLM Royal Dutch Airlines," ASME JOURNAL OF ENGINEERING FOR GAS TURBINES AND POWER, Vol. 110, pp. 23–27.

Luppold, R. H., Roman, J. R., Gallops, G. W., and Kerr, L. J., 1989 "Estimating In-Flight Engine Performance Variations Using Kalman Filter Concepts," AIAA Paper No. AIAA-89-2584.

Smith, C., Broadie, M., and DeHoff, R., 1982, "Turbine Engine Fault Isolation Program," Air Force Wright Aeronautical Laboratories Report AFWAL-TR-82-2058.

Urban, L. A., 1980, "Gas Path Analysis—A Tool for Engine Condition Monitoring," presented at the 33rd Annual International Air Safety Seminar, Flight Safety Foundation, Inc., Christchurch, New Zealand.

Downloaded 02 Jun 2010 to 171.66.16.112. Redistribution subject to ASME license or copyright; see http://www.asme.org/terms/Terms_Use.cfm

M. Nakao
Development Department,
Air Staff Office,
Japan Defense Agency,
9-7-45, Akasaka, Roppongi,
Minato-ku, Tokyo, Japan

M. Ikeyama
Engineering & Programs Department,
Aero-Engine Div.,
Aero-Engine & Space Operations,
Ishikawajima-Harima
Heavy Industries Co., Ltd.,
3-5-1, Mukodai-cho,
Tanashi-shi, Tokyo, Japan

S. Abe
Engineering & Programs Department,
Aero-Engine Div.,
Aero-Engine & Space Operations
Ishikawajima-Harima
Heavy Industries Co., Ltd.,
229, Tonogaya, Mizuho-cho,
Nishitama-gun, Tokyo, Japan

Analytical Condition Inspection and Extension of Time Between Overhaul of F3-30 Engine

F3-30 is the low-bypass-ratio turbofan engine developed to power the T-4 intermediate trainer for the Japan Air Self Defense Force (JASDF). The actual field service was started in Sept., 1988. The program to extend time between overhaul (TBO) of the F3-30 has been running. Analytical condition inspection (ACI) and accelerated mission testing (AMT) were conducted to confirm sufficient durability to extend TBO. Most deteriorations of parts and performance due to AMT were also found by ACI after field operation with approximately the same deterioration rate. On the other hand, some deteriorations were found by ACI only. These results show that ACI after field operation is also necessary to confirm the TBO extension, although AMT simulates the deterioration in field operations very well. The deteriorations that would be caused by the field operation during one extended-TBO were estimated with the results of ACI and AMT, and it was concluded that the F3-30 has sufficient durability for TBO extension to the next step.

Introduction

The F3-30 turbofan engine was developed by Technical Research and Development Institute (TRDI) of Japan Defense Agency (JDA) for the T-4 intermediate trainer aircraft.

Full-scale development of the F3-30 engine was started in 1980. Preliminary flight rating test (PFRT) and qualification test (QT) were completed in 1983 and 1986, respectively. These tests were conducted basically in accordance with MIL-E-5007D, and the details are described by Yamada et al. (1987).

The structure of the F3-30 is shown in the cross-sectional drawing of Fig. 1. The 16.38 kN (3680 lb)-thrust F3-30 is a two-shaft low-bypass turbofan engine with a two-stage fan driven by a two-stage low-pressure (LP) turbine. The high-pressure (HP) compressor has five axial stages driven by a single-stage turbine, which has air-cooled blades and vanes. The HP compressor has two stages of variable stator vanes.

With respect to engine performance, the F3-30 is designed to meet the requirement of an intermediate trainer flying at transonic speed with high maneuverability. Therefore, the F3-30 engine has good restart characteristics and sufficient surge margin. These properties have been demonstrated through the flight tests and actual operation. The principal engine parameters are listed in Table 1.

The F3-30 engine has satisfactory reliability. As of Nov. 1990, 159 production engines have been delivered to the JASDF, and the total flight time accumulated to 28,000 hours, including the flight test hours during its development. The accumulated unscheduled engine removal (UER) rate of the production engines is only 0.6 times per 1000 flight hours. At the initial service, HP turbine blades were failed by HCF. However, no problems have occurred since the application of dampers at the blade roots. The effect of the damper was confirmed by measurement of the blade vibration level with the optical method.

In the production stage of the F3-30 engine, the durability improvement is planned according to the component improvement program for the TBO extension, while the excellent reliability and maneuverability must be maintained or improved.

Concept to Extend TBO

TBO must be extended maintaining the engine reliability. Before TBO extension, the durability of all components of the engine is confirmed by the following tests and inspections:

1 ACI: special inspection of time-up engine operated in the field.
2 AMT: engine endurance test on the test cell.
3 Cyclic spin test for life limited parts: to confirm the LCF life of the rotating parts.

In addition to the above tests and inspection, another AMT is conducted. This AMT simulates the long time operation to find the parts to be improved for the future long TBO. This AMT is conducted using the engine with the components improved through the component improvement program to confirm the effectiveness of the design and process changes while

Contributed by the International Gas Turbine Institute and presented at the 36th International Gas Turbine and Aeroengine Congress and Exposition, Orlando, Florida, June 3-6, 1991. Manuscript received at ASME Headquarters March 4, 1991. Paper No. 91-GT-277. Associate Editor: L. A. Riekert.

Copyright © 1992 by ASME
Downloaded 02 Jun 2010 to 171.66.16.112. Redistribution subject to ASME license or copyright; see http://www.asme.org/terms/Terms_Use.cfm

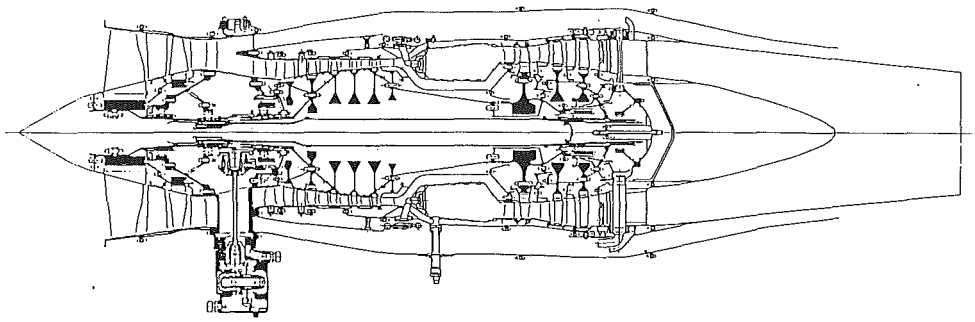


Fig. 1 Cross section of F3-30 turbofan engine

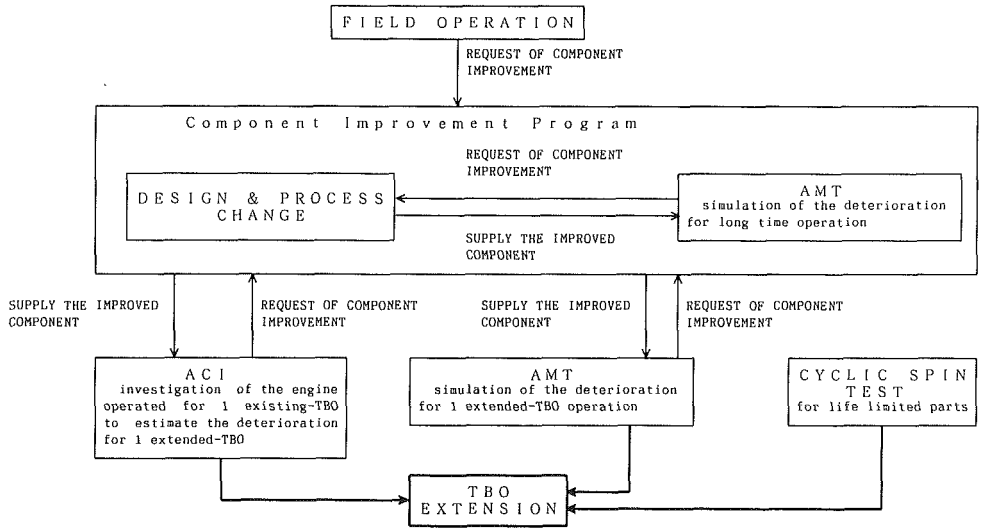


Fig. 2 Relationship among AMT, ACI, and TBO extension

Table 1 Engine parameters (SLTO)

Thrust	16.38 kN (3680 lb)
Weight	340 kg (750 lb)
Engine Inlet Dia.	560 mm(22 in)
Total Air Flow	34 kg/s (75 lb/s)
Bypass Ratio	0.9
Turbine Inlet Temperature	1050 °C (1922 °F)
HP Rotor Speed (Ng)	21,100 rpm
LP Rotor Speed (Nf)	15,300 rpm

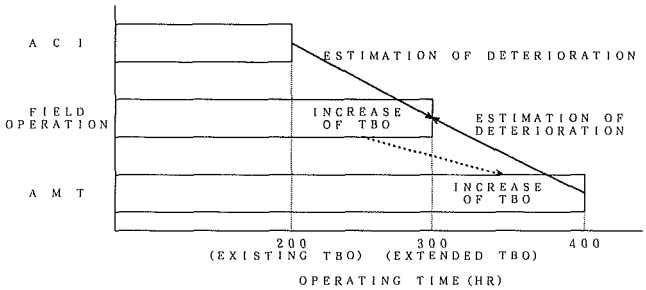


Fig. 3 Estimation of deterioration

the above ACI and AMT are conducted with the existing engine configuration. The component improvement program is planned with the information from ACI, AMT, and field experiences. The relationship among these tests and inspection is show in Fig. 2.

The deteriorations after the actual operation for the extended TBO are estimated with the results of ACI and AMT. ACI is conducted with the engine used for one existing TBO, while AMT is conducted for one extended TBO plus the increased hours of TBO by this extension (equivalent engine time). Therefore, the deteriorations after the operation for one extended TBO are interpolated from the results of ACI and AMT, as shown in Fig. 3.

TBO is extended after confirming that the durability of the F3-30 is sufficient for TBO extension, judging from the results of ACI and AMT.

Status of Investigation and Test

As described by Yanagihara and Tateno (1990), AMT preceding the actual service was conducted from 1986 to 1988 to simulate the operation for long TBO. The following deteriorations were found after the AMT, and counteractions were taken.

1 Wear at the bearing race of the lever, actuating compressor variable stator vanes, as shown in Fig. 4, was found. The contact area between the bearing and the race was increased to reduce the contact stress. The effects of this design change were also verified in this AMT.

2 Cracks at the airfoil and the shroud of HP turbine nozzle guide vane were found. The material of the HP turbine vane is to be changed from cobalt alloy to nickel directional solidification alloy to improve the heat fatigue property. Furthermore, the cooling design is to be improved to lower the metal temperature.

Downloaded 02 Jun 2010 to 171.66.16.112. Redistribution subject to ASME license or copyright; see http://www.asme.org/terms/Terms_Use.cfm

In addition to the above AMT preceding the actual service, ACI and AMT were conducted to confirm that the F3-30 has enough durability to extend TBO. The status of these ACI and AMT is shown in Fig. 5.

Procedure of ACI

The ACI was conducted as follows:

1 Dirty inspection of engine assembly at reception.

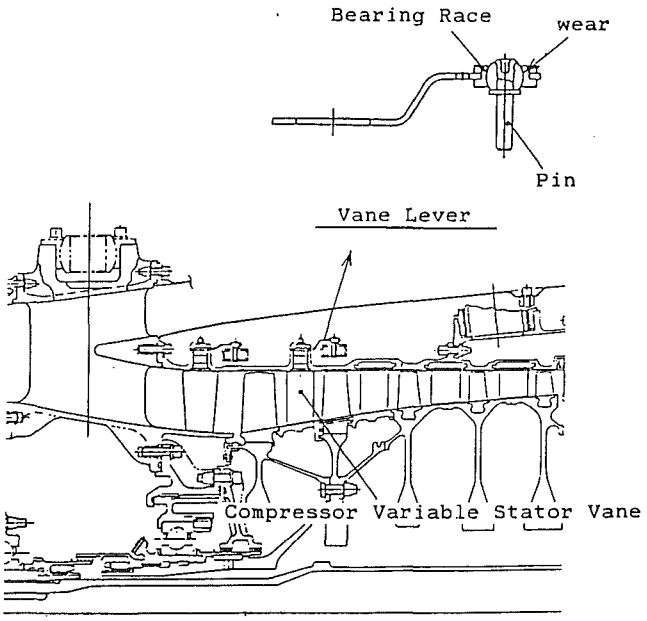


Fig. 4 Bearing race wear of the vane lever

2 Test run to compare the performance at shipping.

3 Clearance and loosing torque check during disassembly.

4 Dirty inspection for each part.

5 Fluorescent penetrant inspection, X-ray inspection, eddy current inspection, magnetic particle inspection, and visual inspection.

6 Dimensional check.

On the other hand, AMT is conducted according to the procedure described by Yanagihara and Tateno (1990).

Results of ACI

The ACI of the F3-30 was conducted for the first time. The deteriorations found by ACI were compared with the deteriorations caused by AMT.

The TBO before extension was 200 hours and the next step of TBO is 300 hours. Therefore, ACI was conducted with the engine operated for 200 hours. AMT was conducted for 400-

Table 2 Deterioration groups

		AMT	
		FOUND	NOT FOUND
ACI	FOUND	15 (GROUP 1)	5 (GROUP 2)
	NOT FOUND	1 (GROUP 3)	

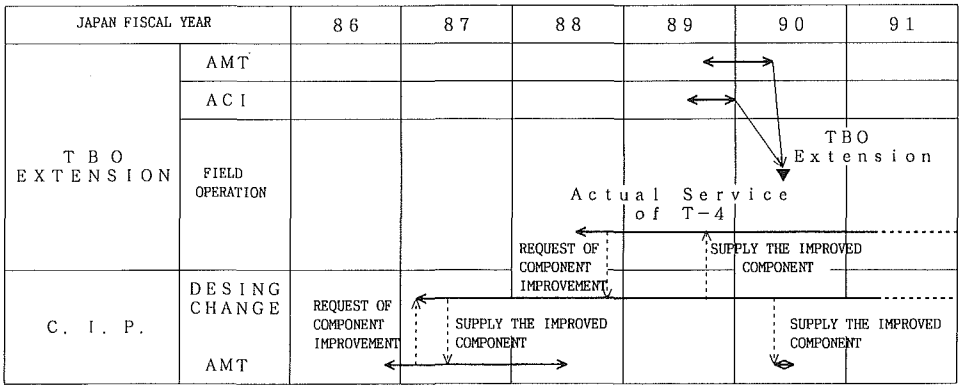


Fig. 5 ACI and AMT status

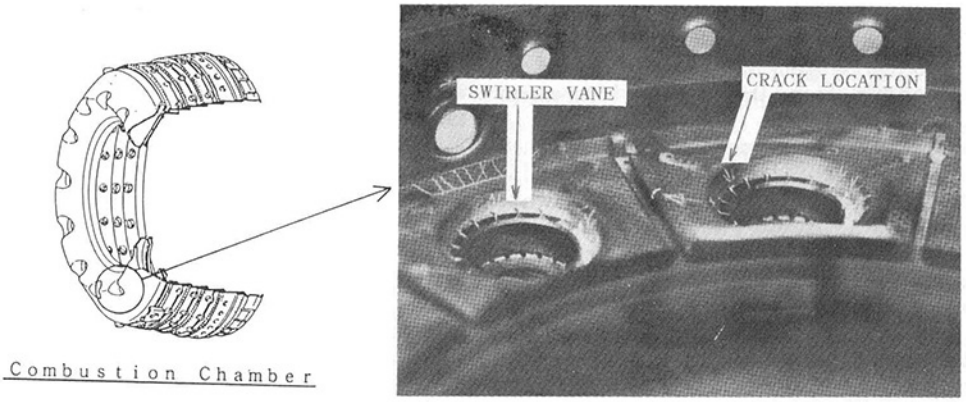


Fig. 6 Cracks of combustion chamber swirler vane

Downloaded 02 Jun 2010 to 171.66.16.112. Redistribution subject to ASME license or copyright; see http://www.asme.org/terms/Terms_Use.cfm

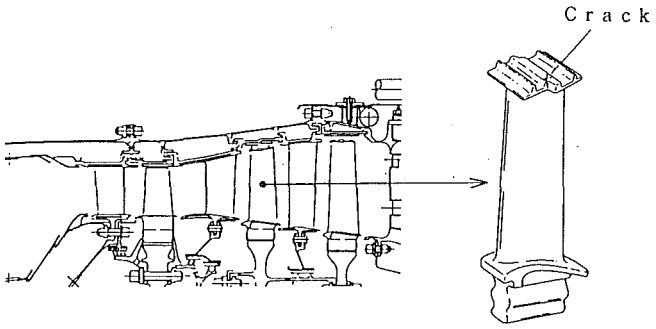


Fig. 7 LP turbine blade crack

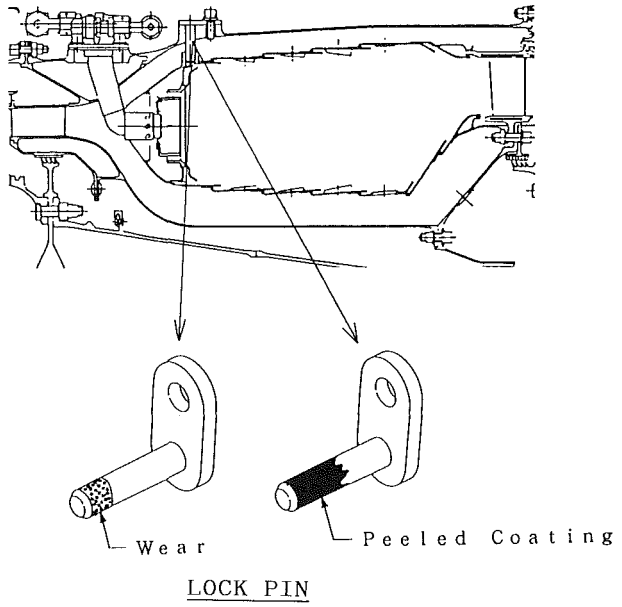


Fig. 8 Wear of combustion chamber lock pin

hour equivalent engine time, which is the sum of the extended TBO, 300 hours, and the increase of TBO, 100 hours, as shown in Fig. 3.

Parts Deteriorations. Sample engines for ACI had been operated for the first one TBO satisfactorily. AMT was also completed satisfactorily.

The deteriorations found by ACI and AMT were very light and did not affect the engine operation. They were grouped as follows.

Group 1: deteriorations found by both ACI and AMT.

Group 2: deteriorations found by ACI only.

Group 3: deteriorations found by AMT only.

AMT simulates the deteriorations caused by LCF, creep, hot corrosion, etc., and the group 1 and 3 deteriorations are considered to be caused by these factors. On the other hand, the group 2 deteriorations are considered to be caused by factors that are not simulated by AMT, for example, HCF at low rating and corrosive environment during field operation. The group 3 deteriorations, which are caused by AMT only, are considered to have occurred after long operation because the engine run time of AMT is longer than the usage of the sample engine for ACI.

The number of deteriorations of each group is shown in Table 2. Three quarters of all the deteriorations come under group 1. On the other hand, there are only 5 kinds of deterioration in group 2. These results show that AMT simulates the field operation very well, but not perfectly, and ACI is also necessary to confirm durability for the extension of TBO.

The typical deteriorations of each group are as follows:

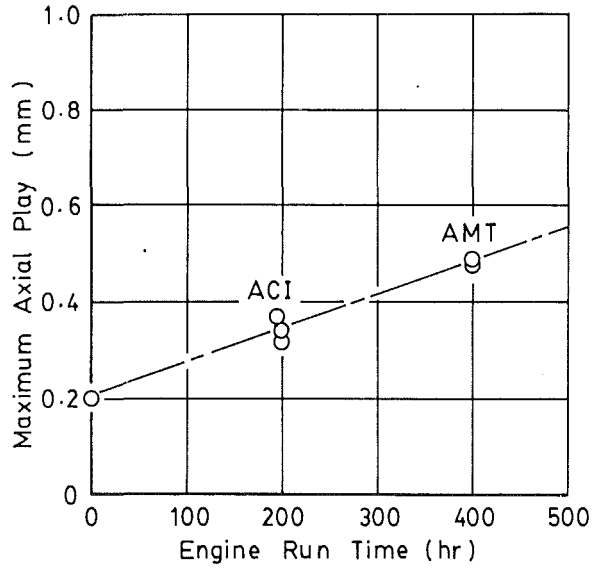


Fig. 9 Bearing axial play of lever

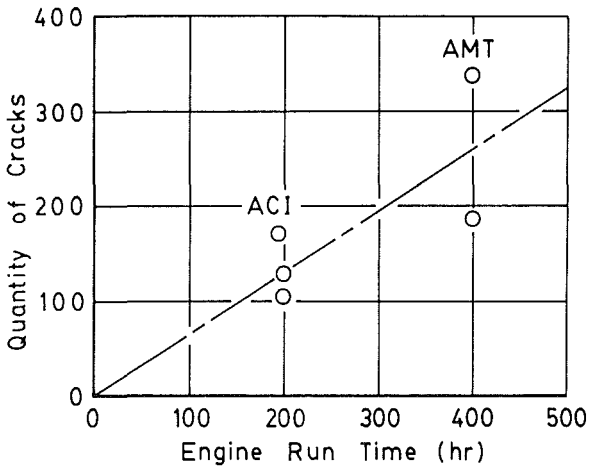


Fig. 10 Quantity of swirler vane crack

Group 1.

1 Wear at the bearing race of the lever, actuating compressor variable stator vanes, as shown in Fig. 4 (this deterioration was found at the former AMT and described by Yanagihara and Tateno, 1990).

2 Crack at the weld of the swirler vanes in the combustion liner, as shown in Fig. 6.

Group 2. Crack at the hardface weld on the abutment face of the outer shroud of first-stage LP turbine blade, as shown in Fig. 7.

Group 3. Wear and peeled coating of the combustion liner lock pin, as shown in Fig. 8.

The relations between the engine running hours and the group 1 deteriorations listed above are shown in Figs. 9 and 10. The measured axial play of the bearing portion of the lever, which correlates with the bearing race wear, is shown in Fig. 9. The quantity of cracks at the swirler vanes of combustion liner is shown in Fig. 10. The increasing rates of wear and the quantity of the cracks in AMT shows good agreement with those found by ACI. Therefore, these deteriorations found by ACI after field operation are interpolated with the deteriorations found by the inspection after AMT. This fact shows that AMT is the effective method to estimate the deterioration caused by the field operation quantitatively. The wear and the

Downloaded 02 Jun 2010 to 171.66.16.112. Redistribution subject to ASME license or copyright; see http://www.asme.org/terms/Terms_Use.cfm

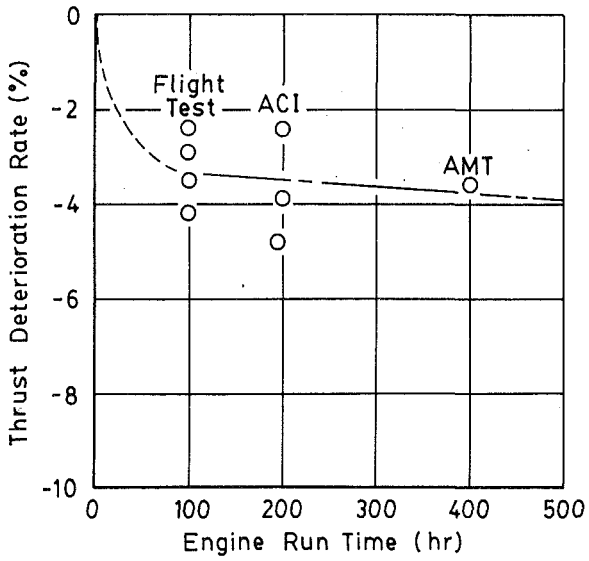


Fig. 11 Thrust deterioration

cracks are not considered to increase more than the deteriorations caused by this AMT during the extended TBO.

All of the other deteriorations, including group 2 and group 3 deteriorations, are also light and these deteriorations are not considered to increase more than the operating limitations during the extended TBO. Therefore, it is possible to extend TBO from 200 hours to 300 with hours respect to the parts deterioration.

However, the counteractions for the deteriorations found by ACI and caused by AMT are taken to improve the durability of components for the future longer TBO. For example, the counteractions against the above damages are as follows:

Group 1

1 Wear at the bearing race of the lever, actuating compressor variable stator vanes. Counteraction: described in former section.

2 Crack at the weld of the swirler vanes in the combustion liner. Counteraction: introduction of the precise cast swirler without weld.

Group 2. Crack at the first-stage LP turbine blade. Counteraction: improvement of the welding process.

Group 3. Wear at the lock pin for combustion liner. Counteraction: the combustion liner is to be improved totally for better durability. The wear of lock pin is to be monitored with the improved combustion liner.

The above design and process changes are being applied and investigated.

Performance Deterioration. Thrust was decreased by 5 percent after one TBO. However, considering the deterioration rate at the flight test and AMT, the thrust decreases rapidly during the first 100-hour operation and after that the rate of thrust decrease becomes smaller than before, as shown in Fig. 11.

SFC increased less than 2 percent after the field operation for one TBO and after AMT. Moreover, the absolute value of SFC was much less than the operation limit.

From the above results it was concluded that the extension of TBO would not cause any serious performance deterioration.

Extension of TBO. Judging from the results of ACI and AMT described above, TBO was extended from 200 hours to 300 hours in July 1990.

Conclusion

Method to extend the TBO of a turbofan engine was discussed. It was concluded that the analytical condition inspection (ACI) after field operation is necessary in addition to the accelerated mission test (AMT) to estimate the deteriorations during the extended TBO.

Judging from the results of ACI and AMT conducted in 1990, TBO of the F3-30 was extended, 300 hours, as the first step of the TBO extension program. Hereafter, TBO of the F3-30 is to be extended further, according to this method.

References

Yamada, H., Hamatani, H., and Ishizawa, K., 1987, "Development of the XF3-30 Turbofan Engine," ASME Paper No. 87-GT-26.

Yanagihara, H., and Tateno, A., 1990, "Accelerated Mission Tests and Reliability Improvement of F3-30 Engine," ASME Paper No. 90-GT-322.

Downloaded 02 Jun 2010 to 171.66.16.112. Redistribution subject to ASME license or copyright; see http://www.asme.org/terms/Terms_Use.cfm

A Procedure for Automated Gas Turbine Blade Fault Identification Based on Spectral Pattern Analysis

E. Loukis
Research Assistant.

K. Mathioudakis
Lecturer.

K. Papailiou
Professor.

Laboratory of Thermal Turbomachines,
National Technical University of Athens,
Athens, Greece

A method for diagnosing the existence and the kinds of faults in blades of a gas turbine compressor is presented in the present paper. The innovative feature of this method is that it performs the diagnosis automatically, that is, it gives a direct answer to whether a fault exists and what type of fault it is, without requiring the interpretation of results by a human expert. This is achieved by derivation of the values of discriminants calculated from spectral patterns of fast response measurement data. A decision about the corresponding engine status is then derived according to the values of the discriminants. In the paper, the procedure of examining the suitability of particular parameter discriminants and the constitution of a related knowledge base is described. The derivation of decisions by a computer, and on what engine condition a particular measurement data set corresponds, are then described.

1 Introduction

Development of effective gas turbine condition monitoring and fault diagnosis methods has been the target of considerable research in recent years. Whether the methods are of the gas path analysis type or based on dynamic data, such as vibrations, the aim is to take advantage of the capabilities of modern computers in order to provide a fast and reliable answer to what the condition of the engine is when measurements are available. The introduction of expert systems, in particular, has provided the possibility of integrating the data processing and decision making techniques into computerized procedures, which can provide information of direct use even to the inexperienced user.

The existence of mechanical faults can be revealed by vibration monitoring techniques, which cover a wide range of faults, as, for example, discussed by Lifson et al. (1990). On the other hand, the possibility of detecting even minor faults of individual blades has been demonstrated by Mathioudakis et al. (1991). Derivation of the decision about the existence of a fault is based on the calculation of some characteristic quantities and the user's judgment, according to the observed features and existing experience.

The methodology proposed in the present paper gives the possibility of extracting a decision about the existence of a fault by a digital computer, eliminating the need for interpretation of the results by specialized personnel. The extraction of such a decision is possible by application of pattern recognition methods. Such methods have been applied in various other domains, e.g., monitoring of bearing elements (e.g., Li and Wu, 1989), machine tools (Emel and Kannatey-Asihm, 1989), gearboxes (Barschdorff et al., 1987). Applications to turbomachinery faults related to dynamic data have first been proposed by Barschdorff (1986). The work presented there was based on features of time traces from casing accelerometers.

The work we present here is based on spectral features of measurements of various dynamic quantities, such as internal pressure, casing acceleration, and acoustic data. Its particular feature is that before applying the pattern recognition technique, the data are preprocessed in order to derive fault signatures. On the other hand, the test case analyzed consists of a commercial industrial gas turbine operating at different loads, representing thus a realistic industrial test case of application.

The way the method is organized allows its direct inclusion in an expert system. In particular, it replies to the need of obtaining computer tools for the diagnosis of specific engine problems, as identified by Doel (1990).

2 Experimental Data

The present investigation was based upon measurements on an industrial gas turbine into which different faults were introduced. The test engine was the Ruston Tornado, described by Carchedi and Wood (1982). The instrumentation layout and measurement conditions are described by Loukis et al. (1991). For completeness, we repeat here the instruments used and the examined faults.

During the experimental campaign four categories of measurement were performed simultaneously:

(*a*) Unsteady internal wall pressure, instruments PT1 to PT5. PT2 faces rotor 1, PT3 rotor 2, etc.

Contributed by the International Gas Turbine Institute and presented at the 36th International Gas Turbine and Aeroengine Congress and Exposition, Orlando, Florida, June 3–6, 1991. Manuscript received at ASME Headquarters March 4, 1991. Paper No. 91-GT-259. Associate Editor: L. A. Riekert.

Copyright © 1992 by ASME
Downloaded 02 Jun 2010 to 171.66.16.112. Redistribution subject to ASME license or copyright; see http://www.asme.org/terms/Terms_Use.cfm

(*b*) Casing vibration, with accelerometers mounted at the outside compressor casing (instruments ACC1 to ACC6).

(*c*) Shaft displacement at compressor bearings, with a Bently Nevada system.

(*d*) Sound pressure levels, with double-layer microphones.

Five experiments were performed testing the datum healthy engine and engines with the following four faults:

Fault 1. Rotor fouling: All stage 2 rotor blades were coated with textured paint in order to roughen blade surface and alter their contour, in order to simulate a fault of all the blades of a rotor.

Fault 2. Individual rotor blade fouling: Two blades of stage 1 rotor, separated by five intact blades, were coated by textured paint in order to simulate a slight individual rotor blade fault.

Fault 3. Individual rotor blade twisted: A single blade of stage 1 rotor was twisted in order to simulate a severe rotor blade fault.

Fault 4. Stator blade restaggering: two stage 1 stator blades were mistuned in order to simulate a stator fault.

All subsequent numbered references to faults in the following text will correspond to the above classification.

Tests were performed at four different engine loads: full load, half load, quarter load, and no load (termed operating point *A*, *B*, *C*, *D*, respectively, hereafter), with the intact engine as well as the faulty engines. This means that for each fault we obtain four data sets, one at each load.

3 Spectral Difference Pattern Analysis

In order to develop an automated fault identification method, it is necessary to derive some quantitative characteristics of measured signals, reflecting the presence of faults. The derivation of fault signatures in the form of spectral comparison indices has been demonstrated by Mathioudakis et al. (1991), for the case of unsteady pressure transducer measurements. This technique is used as a departing point for the methodology presented in this paper. Using this procedure, we examine not only fast response pressure measurements, but all the different dynamic measurements mentioned in the previous section.

A difference pattern (used as fault index) derived from the measured signal of an instrument is defined by the following expression:

$$p(f) = 20[\log_{10}(sp(f) - \log_{10}(sph(f))] \tag{1}$$

$p(f)$ is the fault index, which is thus a set of values in function of frequency, $sp(f)$ is the power spectrum of the signal of the measuring instrument from a faulty engine, $sph(f)$ is the same spectrum from a healthy engine. It is useful to remember that expression (1) was selected among several algebraic combinations of spectra of pressure measurements, by Mathioudakis et al. (1991), on the basis of two observations: This index showed high sensitivity to each examined fault and produced distinguishable forms for each fault.

The purpose of the fault index analysis we present now is: (*i*) to improve diagnostic capabilities by selecting only the most useful information contained in indices, (*ii*) to derive some scalar functions characteristic of the fault index, and (*iii*) to exploit these scalar functions for the development of a system for the classification of the fault.

3.1 Derivation of Reduced Fault Index Patterns. Inspection of the fault indices calculated for the different measuring instruments has shown that the presence of one of the examined faults results in the appearance of differentiations mainly at multiples of the shaft rotational frequency. For the case of pressure transducers, it was even found that patterns are formed that are distinguishable by visual inspection. It was therefore decided to filter out values of the indices at frequencies other than the shaft harmonics, since the most useful diagnostic information is contained at these harmonics.

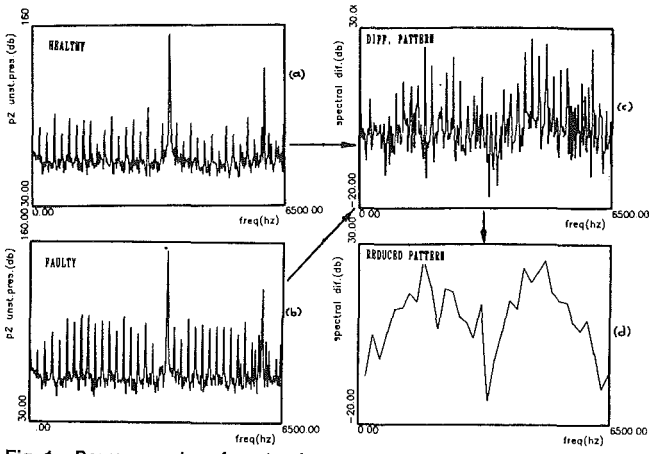


Fig. 1 Power spectra of unsteady pressure transducer 2 (PT2) with the corresponding fault index and the reduced pattern

This is done by a filter of unit gain at the rotational harmonics and zero at the other frequencies, defined by the following equation:

$$h(f) = \begin{cases} 1 \text{ if } f \text{ rotational harmonic} \\ 0 \text{ if } f \text{ not rotational harmonic} \end{cases} \tag{2}$$

The pattern that results from filtering the difference pattern with the above filter will be referred to as *reduced pattern* in the following, and mathematically is given by the following equation:

$$p_r(f) = p(f) \cdot h(f) \tag{3}$$

where

$p_r(f)$ = reduced different pattern at frequency f
$p(f)$ = difference pattern at frequency f
$h(f)$ = filter gain at frequency f

An example of the above procedure is given in Fig. 1. In Fig. 1(*a*) we can see the power spectrum of unsteady pressure transducer 2 in the frequency band 0–6500 Hz, for the healthy case, while Fig. 1(*b*) shows the corresponding power spectrum for Fault 4. The difference pattern and the reduced pattern are shown in Figs. 1(*c*) and 1(*d*), respectively.

It is now evident that a reduced pattern consists of a set of values $p_r(f)$, corresponding to frequencies f that are multiples of the shaft rotational frequency f_r. In the following discussion, we will refer to $p_r(f)$ as $p_r(i)$, where $p_r(i)$ is the reduced pattern at frequency ixf_r. If we consider an N-dimensional space with coordinates the N shaft harmonics in the considered frequency band, a reduced pattern corresponds to one point in this space (the point is defined by the values of the coordinates, which are the N values contained in $p_r(i)$).

Before introducing the discriminants derived from the reduced index patterns, we should mention the necessary features of reduced patterns that make them suitable for fault classification.

A first indication of the differentiation of the readings of a specific instrument by a fault is the amplitude of the corresponding reduced pattern (by "amplitude" we mean the range between the minimum and maximum values of the pattern). If the reduced pattern of a fault is of higher amplitude than that of another fault, this means that the transducer is more sensitive to the first fault than to the second.

On the other hand, in order to be suitable as fault signatures, the reduced patterns have to exhibit two basic features:

(*a*) Reduced patterns corresponding to one fault should be similar, when different experiments with this fault are considered.

(*b*) Reduced patterns of two different faults should be dissimilar in order to be distinguishable.

Downloaded 02 Jun 2010 to 171.66.16.112. Redistribution subject to ASME license or copyright; see http://www.asme.org/terms/Terms_Use.cfm

For the practical purpose of classifying patterns according to their corresponding faults, it is required that a higher degree of similarity exist between patterns of one fault, than exists between patterns of different faults.

In order to apply similarity criteria, which are objective (do not depend on the opinion of the experimenter) and quantitative (so that a computer can examine them), we introduce scalar similarity discriminants for the patterns, as explained in the following.

3.2 Reduced Pattern Discriminants. Two discriminant functions were selected, one of them expressing the quantitative similarity (influenced by both the shape and amplitude of compared patterns), the other expressing the shape similarity (influenced only by the shape of the compared patterns).

The first discriminant function is the usual Euclidean distance between reduced patterns, when they are viewed as points in an N-dimensional space. It expresses the quantitative similarity between patterns, both in shape and in actual values, and for the reduced patterns P_1 and P_2 is defined by the following equations:

$$d_E(P_1, P_2) = \frac{1}{N} \sum_{i=1}^{N} (P_1(i) - P_2(i))^2 \tag{5}$$

where $d_E(P_1, P_2)$ = Euclidean distance between the reduced patterns P_1 and P_2; $P_1(i)$, $P_2(i)$ = values of the reduced patterns P_1 and P_2 at the ith harmonic of shaft rotational frequency; N = number of rotational harmonics in the considered frequency band.

Small values of this quantity indicate that P_1 and P_2 are similar (identical if $dE(P_1, P_2) = 0$). It increases for decreasing quantitative similarity between P_1, P_2.

The second discriminant function is the normalized cross-correlation coefficient. It expresses the shape similarity between patterns and does not depend on the range of values of the patterns. For the reduced patterns P_1 and P_2, it is defined by the following equations:

$$dc(P_1, P_2) = \left| \frac{CC(P_1, P_2)}{AC(P_1) \cdot AC(P_2)} \right| \tag{5}$$

where

$$CC(P_1, P_2) = \frac{1}{N} \sum_{i=1}^{N} (P_1(i) - \underline{P_1})(P_2(i) - \underline{P_2})$$

and

$$AC(P_k) = \left[\frac{1}{N} \sum_{i=1}^{N} (P_k(i) - \underline{P_k})^2 \right]^{1/2}, \quad k = 1, 2$$

It takes values between 0 and 1 and increases for increasing similarity between the two patterns (for patterns of identical shape, it takes the value 1).

In order to use the two discriminants for fault classification, we must possess reference patterns for each fault. If we possess such reference patterns, then for any given signal we can produce the discriminants and depending on their values we decide which is the fault corresponding to the signal. In the following paragraph we discuss how available measurement data can be judged with respect to the possibility of defining fault reference patterns.

3.3 Criteria for Measurement Suitability. In order to examine whether particular measurement data are suitable for defining reference fault patterns that are discriminable through the above functions, we apply the following procedure:

(*i*) An averaged reduced pattern of a specific fault is calculated using all available reduced patterns of this fault, from different experiments and operating points:

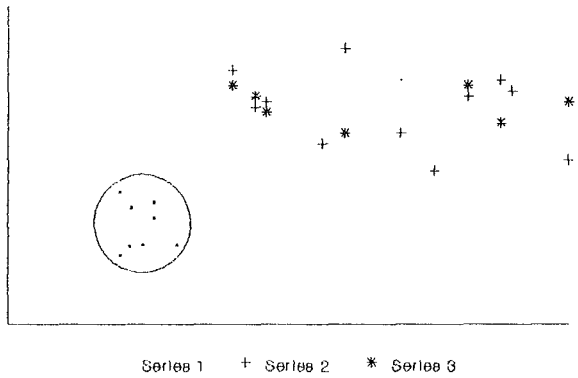


Fig. 2 The concept of a "well-defined pattern," visualized in a two-dimensional space

$$RP = \frac{1}{m} \sum_{j=1}^{m} P_j(i)$$

for m available experimental patterns. This is used as a reference pattern for the fault.

(*ii*) The discriminant values for all the reduced patterns (including both those coming from the examined fault and those coming from the other faults), with respect to this reference pattern are calculated.

(*iii*) Their values are inspected in order to examine if the reduced patterns of the fault are closer to the reference one, than to the reduced patterns of the other faults. This can be mathematically expressed by the following conditions:

For the Euclidean Distance (Discriminant 1):

$$\max_{k=1}^{LF} d_E(RP, P_k) < \min_{j=1}^{LA} d_E(RP, P_j)$$

For the Correlation Coefficient (Discriminant 2):

$$\min_{k=1}^{LF} d_c(RP, P_k) > \max_{j=1}^{LA} d_C(RP, P_j)$$

where RP = the average reduced pattern; P_k = the kth pattern from data from the same fault from LF experiments; P_j = the jth pattern from data from other faults, from LA experiments.

If one of these two conditions is fulfilled, the considered fault is characterized by an averaged reduced pattern, which can be distinguished from the other fault patterns. Such an average reduced pattern can be used as a signature of the fault and will be termed a *well-defined pattern* in the following.

If the reduced patterns are viewed as points in a multidimensional space, then the concept of a well-defined average reduced pattern can be expressed as the requirement of having all data points from the specific experiment within a supersphere and all the remaining points outside it. This can be visualized for a two-dimensional space, for example, as shown in Fig. 2. The points of patterns corresponding to the examined fault belong to a circle centered at average pattern, which represents the center of gravity of the points for a well-defined pattern. All the points of the other faults lie outside this circle.

In order to illustrate the application of the above procedure, it has been applied to the data from the experiments described in section 2. Conclusions as to the magnitudes and the repeatability properties of the four fault patterns are presented and discussed for all the instruments.

4 Measured Signal Features

For each fault and measuring instrument, the averaged reduced pattern is calculated from the data sets at the four operating points described in section 2.

Downloaded 02 Jun 2010 to 171.66.16.112. Redistribution subject to ASME license or copyright; see http://www.asme.org/terms/Terms_Use.cfm

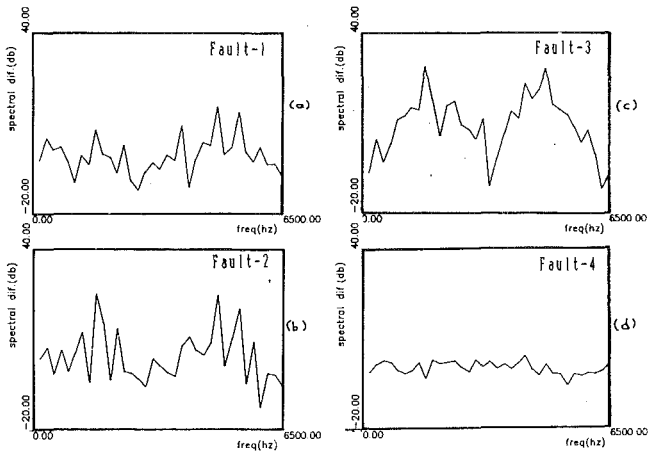


Fig. 3 Averaged patterns for each fault, derived from unsteady pressure transducer 2 (PT_2) measurements

4.1 Unsteady Pressure Transducers. The four average reduced patterns produced by the four faults on PT_2, facing the first stage rotor, are shown in Fig. 3. We remark that Faults 2 and 3 are characterized by high-magnitude patterns. The means that this transducer is highly sensitive to both blading faults of the rotor it faces. On the other hand Fault 1 is characterized by a lower magnitude patterns compared to Faults 2 and 3. So the transducer senses a fault of the rotor one stage downstream, but less intensively. Finally Fault 4 is characterized by a very low magnitude pattern, which means that the transducer is not sensitive to a stator fault of the same stage. This is probably due to the fact that Fault 4 is not rotating and its location although very near to the transducer axially is circumferentially 90 deg apart from it.

The values of the discriminants calculated for each reference pattern and all the available reduced patterns are shown in Fig. 4. In Fig. 4(*a*) we see the values of the Euclidean distance between the average patterns of Fault 1 on one hand and the four patterns of this fault, as well as the twelve other fault patterns, on the other. The first four patterns, corresponding to Fault 1 at operating points *A*, *B*, *C*, *D* are characterized by lower Euclidean distance values than all the other patterns. Therefore Fault 1 has a well-defined pattern on the signals of PT_2, using the Euclidean distance. We can see that the same happens with the other three faults as well.

In Fig. 4(*b*) the values of the normalized cross-correlation coefficient between the average pattern of Fault 1 on one hand and the four patterns of this fault and also the twelve other fault patterns on the other. We can remark that the first four patterns corresponding to Fault 1 at operating points *A*, *B*, *C*, *D* are characterized by higher normalized cross-correlation coefficient values than all the other patterns, corresponding to the other three faults. So Fault 1 has a well-defined pattern at PT_2 using the normalized cross-correlation coefficient. This is in agreement with what has been concluded using the Euclidean distance. In Fig. 4(*b*) we can remark that the same happens with faults 2 and 3 but not with Fault 4.

For Fault 4 using the normalized cross-correlation coefficient, the pattern of PT_2 is found to be not well defined, in disagreement with what has been found using the Euclidean distance. This can be explained taking into account that the patterns of Fault 4 are of low magnitude; therefore they are much more influenced by noise and field changes with the operating point than the other faults patterns. These factors change the shape significantly but the magnitude of the patterns does not change very much. This fact shows that examining the value of one discriminant only may not reveal all the available information.

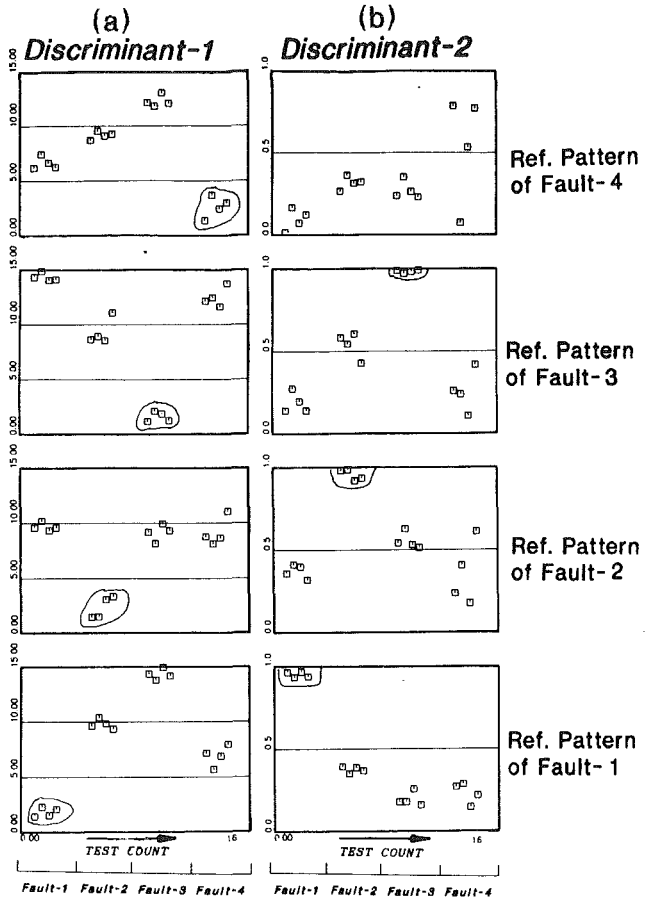


Fig. 4 Discriminant values for data from unsteady pressure transducer 2 (PT_2) measurements; all available data sets are compared to each fault reference pattern

Applying the same procedure on the data from transducer PT_5 gives the results of Fig. 5. We can remark that all faults have well-defined patterns both from the quantitative and the shape similarity point of view. However, the distances separating the clusters of points corresponding to the data of the various faults are reduced. The discriminability of faults is therefore reduced.

The procedure has been repeated for pressure transducers PT_3 and PT_4, leading to the confirmation of the conclusion that the difference patterns, although they are attenuated by traveling downstream some stages, still remain well defined.

From the above reduced pattern analysis, we come to the conclusion that a blading fault mainly influences the pressure transducer of the corresponding stage, and also influences pressure transducers several stages downstream to a lower degree.

4.2 Accelerometers. As a second step the accelerometers located on the external compressor casing surface were investigated. The average reduced patterns at ACC_4 are shown in Fig. 6. We remark that at ACC_4 Fault 4 is characterized by a high magnitude pattern, much higher than the same fault at PT_2. The other faults are characterized by lower magnitude patterns. Therefore this accelerometer is very sensitive to Fault 4, but shows also a lower sensitivity to the other three faults. This increased accelerometer sensitivity to Fault 4 is explained if we take into account that Fault 4 is one of stationary blading, which is mechanically connected to the compressor casing, where the accelerometers are located. Discriminant values for the data from ACC_4 are shown in Fig. 7. We remark that not only Fault 4, but the other faults as well have well-defined patterns both from quantitative and shape similarity point of

Downloaded 02 Jun 2010 to 171.66.16.112. Redistribution subject to ASME license or copyright; see http://www.asme.org/terms/Terms_Use.cfm

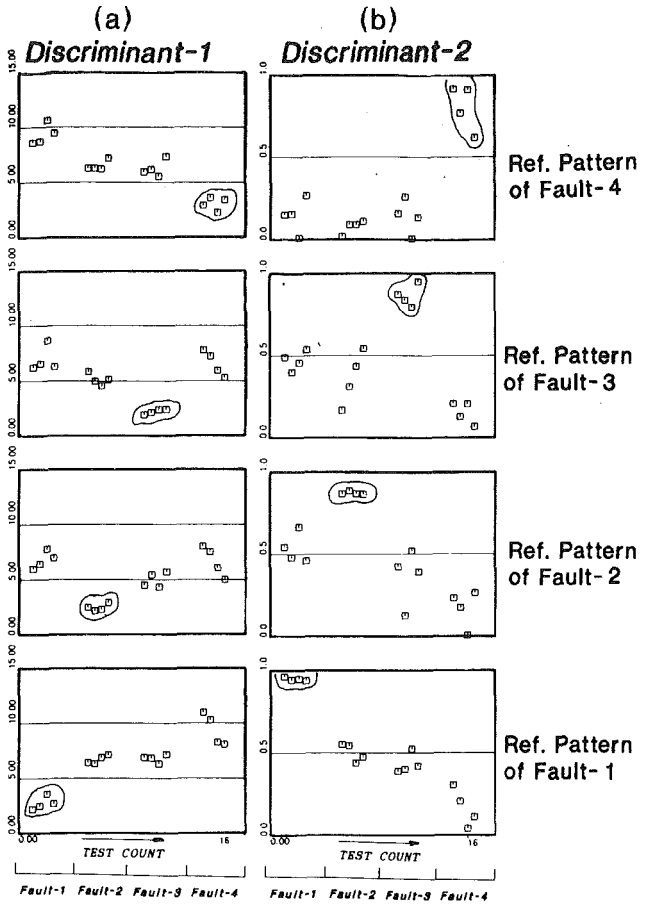


Fig. 5 Discriminant values for data from unsteady pressure transducer 5 (PT_5) measurements; all available data sets are compared to each fault reference pattern

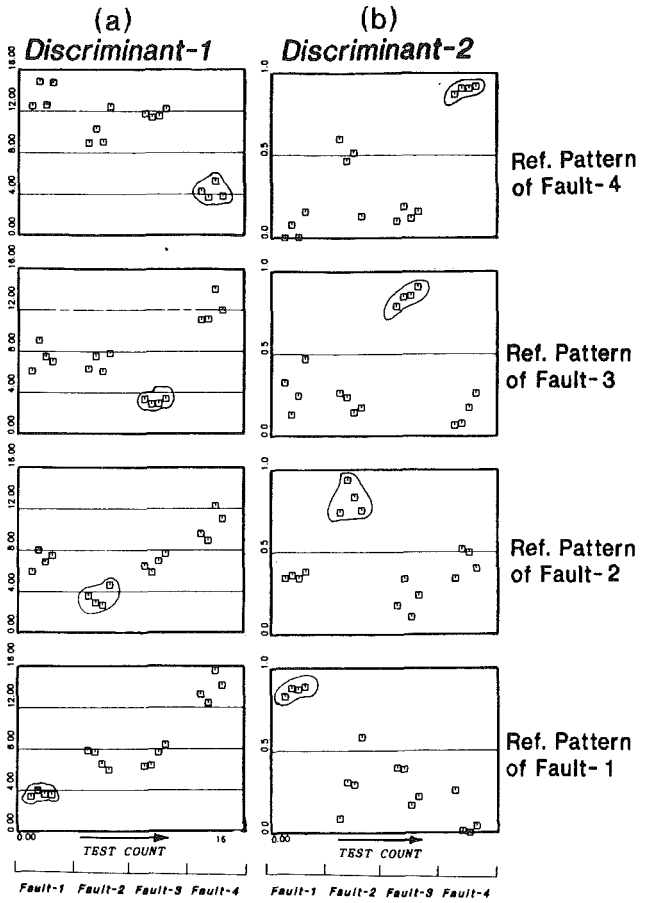


Fig. 7 Discriminant values for data from accelerometer 4 (ACC_4) measurements; all available data sets are compared to each fault reference pattern

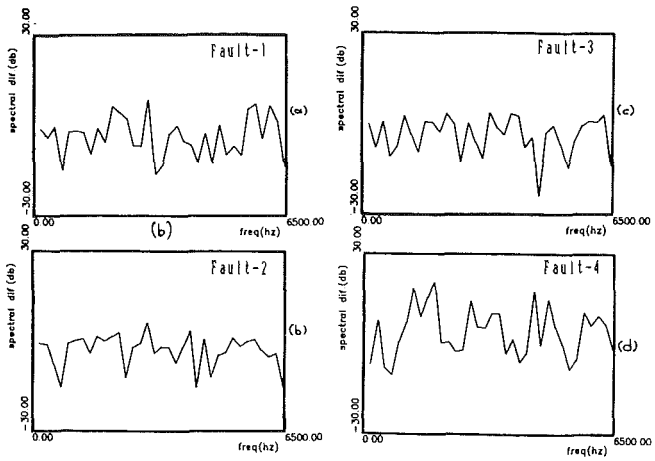


Fig. 6 Averaged patterns for each fault, derived from accelerometer 4 (ACC_4) measurements

view. Comparing to the results of Fig. 4, we can also remark that the separation of the clusters is not as clear as for PT_2.

The same procedure has been repeated for all the accelerometers. It was concluded that at all accelerometers Fault 4 has a high magnitude pattern, while Fault 3 has only at some of them high magnitude patterns, while in the others lower magnitude ones. Faults 1 and 2 have lower magnitude patterns at all the accelerometers. Also Faults 3 and 4 have at all the accelerometers well-defined patterns, Fault 1 only at some of them, and Fault 2 presents well-defined patterns in none of the accelerometers.

From the above reduced pattern analysis, we conclude that the accelerometers are all influenced by Faults 3 and 4 significantly. They are also influenced by the other two faults as well, but to a lower extent, depending on the axial and the circumferential position of the accelerometer.

4.3 Microphones. Discriminant values for the data from one of the microphones are shown in Fig. 8. We note that Faults 2, 3, 4 have well-defined patterns, but this does not happen with Fault 1. The conclusion, after repeating the same procedure for the second microphone as well, is that the microphones are influenced significantly by Faults 3 and 4, but also to a lower extent by Faults 1 and 2.

4.4 Bearing Proximity Probes. Discriminant values for the data from a bearing proximity probe are shown in Fig. 9. We remark that only Fault 4 has a well-defined pattern while the others do not. From examining the other bearing proximity probes as well, the conclusion that they show only some sensitivity to Fault 4, while to all the other faults they do not, is confirmed.

5 Automated Fault Diagnosis

Based on the reduced spectral patterns, and the results of the previous section, an automated fault diagnosis method has been developed. This method has as input the time trace of a specific instrument and as output the fault selection based on it. The classification algorithm used, is the minimum-distance

Downloaded 02 Jun 2010 to 171.66.16.112. Redistribution subject to ASME license or copyright; see http://www.asme.org/terms/Terms_Use.cfm

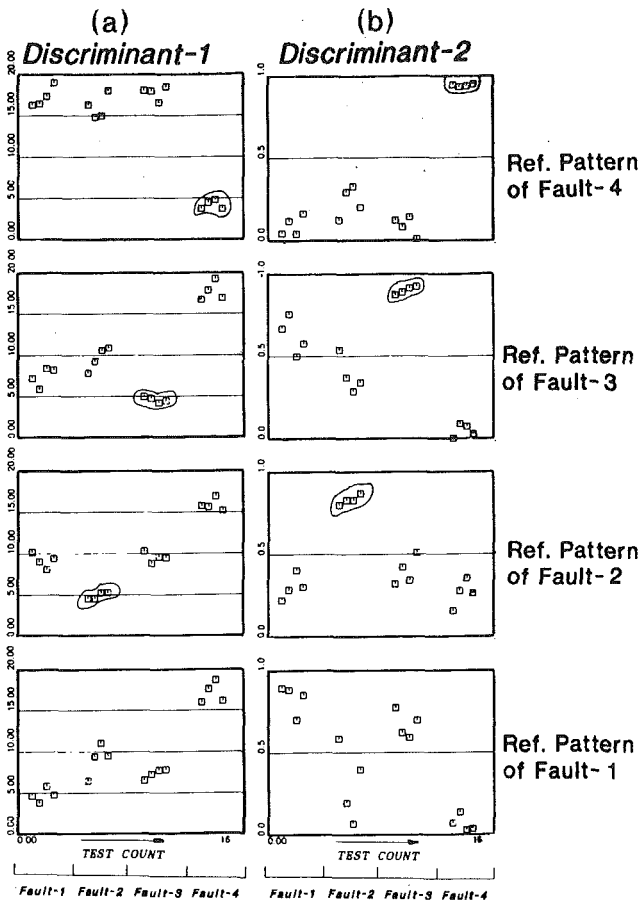


Fig. 8 Discriminant values for data from microphone measurements; all available data sets are compared to each fault reference pattern

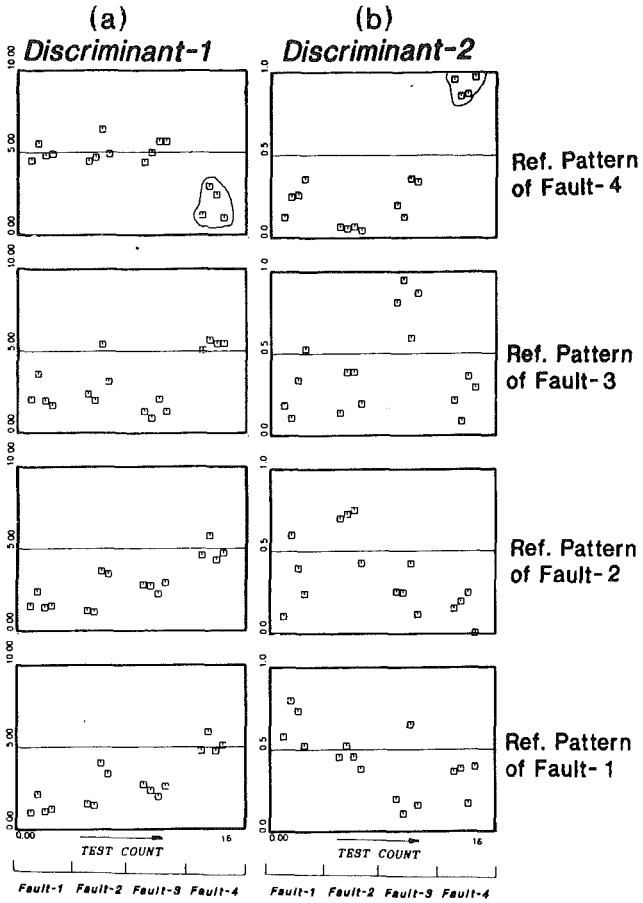


Fig. 9 Discriminant values for data from bearing proximity probe measurements; all available data sets are compared to each fault reference pattern

method (Sing-Tze, 1984), with number of classes equal to the number of faults.

For the input time trace, first the spectral density and then the reduced difference patterns are calculated. The distances of the calculated reduced pattern from the average reduced pattern of each fault are calculated, and the nearest of the faults is selected. This is given mathematically by the following expression:

For the Euclidean distance

$$I_{\text{fault}} = I \text{ for which } d_E\ (RP_I, P) \text{ is minimum}$$

For the correlation coefficient or

$$I_{\text{fault}} = I \text{ for which } d_c\ (RP_I, P) \text{ is maximum}$$

where P is the pattern under classification and RP_I reference fault patterns. The flow chart of the method is given in Fig. 10.

Typical results of its application are given for three instruments in Figs. 11–13, in order to demonstrate the principle of the method. Results for PT_2 signals are given in Fig. 11(a, b) for the Euclidean distance and the normalized cross-correlation coefficient respectively. In Fig. 11(a) we can see the results for the four patterns of Fault 1, corresponding to the operating points A, B, C, D. For each of them we can see the four Euclidean distance values from the four faults' averaged patterns. We remark that for all four patterns the first of the values, corresponding to the average pattern of the first fault, is the lowest. Therefore the above method leads to a correct selection for all four patterns using the Euclidean distance. In Fig. 11(b) we can see the same results as in 11(a), but using the normalized cross-correlation coefficient. Again we remark that for all four patterns the first of the values, corresponding

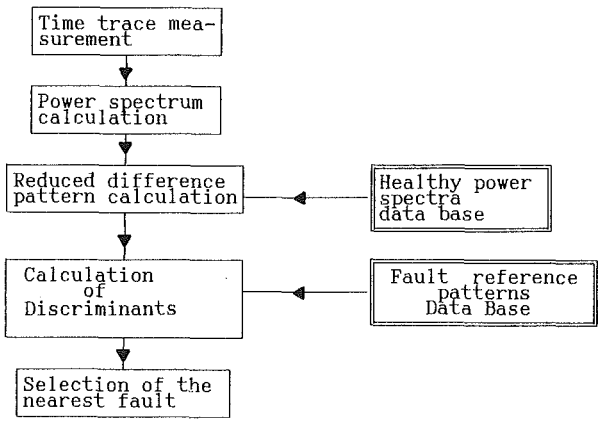


Fig. 10 Flow chart of the automated fault diagnosis method

to the average patterns of the first fault, is the highest. Therefore the above method leads to a correct selection, using the normalized cross-correlation coefficient as well.

Corresponding results for the ACC_4 are shown in Fig. 12, and for the microphone in Fig. 13. We note that for both instruments the above method leads to a correct selection, for the cases of the figures.

The above method has been applied to the experimental data, for all the instruments described in section 2. For each instrument the average reduced patterns of the four faults have been calculated and used as reference patterns. From the results for each instrument the four success rates (= percentage of the reduced patterns for which a correct selection has been done)

Downloaded 02 Jun 2010 to 171.66.16.112. Redistribution subject to ASME license or copyright; see http://www.asme.org/terms/Terms_Use.cfm

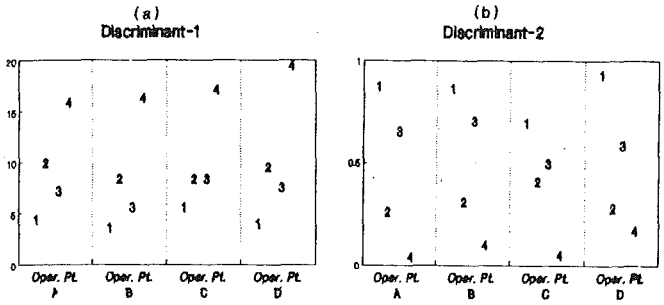


Fig. 11 Discriminant values for experimental data from PT_2, when Fault 1 is present, calculated with respect to the four reference fault patterns, for each operating point

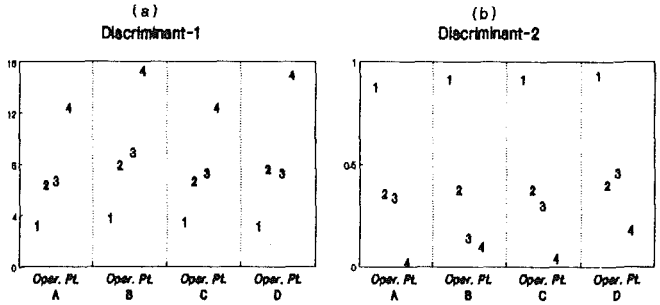


Fig. 12 Discriminant values for experimental data from ACC_4, when Fault 1 is present, calculated with respect to the four reference fault patterns, for each operating point

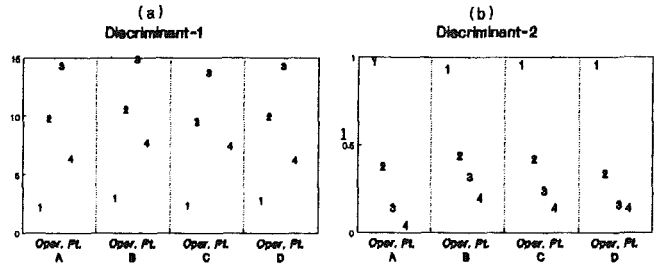


Fig. 13 Discriminant values for experimental data from microphone, when Fault 1 is present, calculated with respect to the four reference fault patterns, for each operating point

corresponding to the four faults were calculated. The table of success rates using the Euclidean distance is given in Fig. 14, and the one using the normalized cross-correlation coefficient in Fig. 15.

We can see that generally there are high success ratios for the unsteady pressure transducers, lower for the accelerometers and the microphone, while much lower for the bearing proximity probe, except for Fault 4. These differences are due to the fact that the unsteady pressure transducers are more directly influenced by the faults, while the accelerometers do not feel the fault influence directly but filtered by the compressor casing dynamics. The same happens with the microphone, which feels the fault influence filtered both by the compressor casing dynamics and the surrounding air. Finally, the bearing proximity probe feels the fault influence highly attenuated and filtered.

By comparing Figs. 14 and 15 we can see that the two discriminants do not show significant performance differences, the Euclidean distance seeming slightly better. It should be pointed out here that both these figures are based on the particular data sets we obtained. They should therefore be viewed as a measure of the effectiveness of establishing the present procedure and not as capability of the method to distinguish faults. Such a capability should only be tested if new data from independent experiments were added. This statement is also

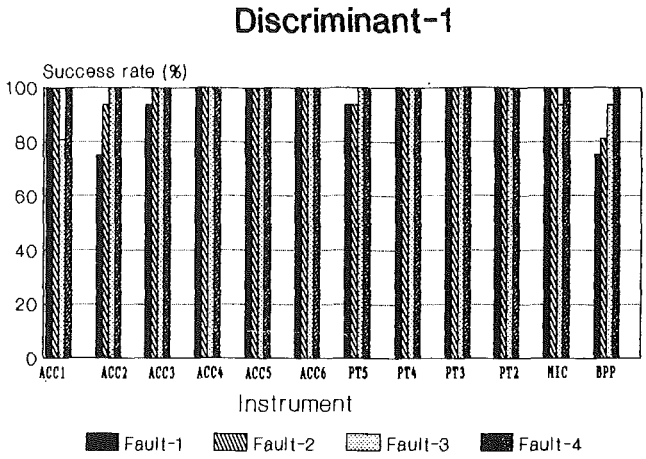


Fig. 14 Success rate in fault identification, when discriminant 1 is used

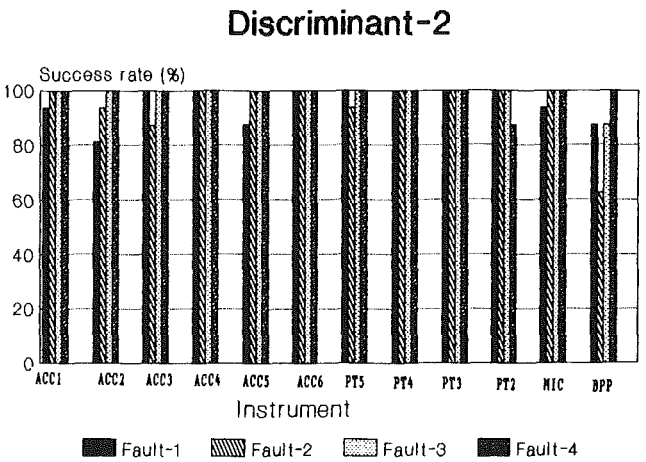


Fig. 15 Success rate in fault identification, when discriminant 2 is used

valid concerning the comparative capabilities of the various instruments.

6 Discussion

The technique presented in the previous sections has been developed on the basis of the data available from experiments in an industrial gas turbine with specific implanted faults. From this point of view part of the findings can be considered of general validity while others will be particular to the specific engine.

The signatures used as a reference for the fault classification came from the experiments. While they are valid for the particular engine, it is still to be investigated whether they can be used for other engines with the same success. In that respect, it would be very useful if signatures can be produced by computer simulation, in which case a variety of engines would be covered. The research group of the authors has started work in this direction, with some success so far (see Mathioudakis et al., 1991).

On the other hand, in order to extend the present technique to other fault cases, it is necessary to obtain their corresponding signatures. Once such signatures are available, the procedure to be applied is exactly the same. This means that extension to a wider range of faults can be achieved by simply extending the data base of reference fault signatures associated with the technique.

One aspect of the present methodology that might not be of general applicability is the derivation of the reference pat-

Downloaded 02 Jun 2010 to 171.66.16.112. Redistribution subject to ASME license or copyright; see http://www.asme.org/terms/Terms_Use.cfm

terns. The application of the filter, which extracts information on shaft rotational harmonics, was based on our observation that blade faults produce differentiation mainly at these harmonics. This means that faults that produce differentiation only of the broad band part of the spectrum or rotor subharmonics (as for example rotating stall) would not be covered. In that case the part of the technique covering the derivation of the patterns has to be modified, by modification of the applied filter Eq. (2). In the same respect, the spectral differences of Eq. (1) can also be replaced by another expression.

A question that arises when monitoring techniques have to be applied is which are the most suitable measurements for this purpose. Although an answer to this question does not emerge from what we have presented, we have tried to include comments on the physical significance of the results obtained. Understanding this significance is helpful in choosing appropriate instruments and measuring locations. An effort to produce a systematic method of investigating this problem is under way of development.

There are certain aspects of the method that can be improved. For example, the discriminant functions were introduced here on the basis of observations and intuitions. It would be possible to establish such functions from a requirement of optimal fulfillment of certain diagnostic criteria. On the other hand, the way that decisions are taken now is of the Yes–No type. It would be desirable to include fault statistics and derive decisions of faults and associated probabilities. Work is under way in these directions by the research group of the authors.

7 Conclusions

A technique for automated fault diagnosis from dynamic measurement data has been developed.

Fault patterns were established, by manipulation of signal power spectra. Criteria for examining the suitability of the patterns for fault identification were set. A procedure for examining the possibility to establish reference patterns for each fault and each kind of measurement was presented. Having established such patterns, a technique for deciding whether a measurement signal corresponds to a particular fault was developed.

The technique was developed on the basis of experimental data coming from various instruments on an industrial gas turbine with implanted blade faults. High rates of success were found on the basis of the available data.

The present technique is such that it can be extended to include a wider range of faults, as long as additional data are available. Finally, suggestions for improving its efficiency were discussed.

References

Barschdorff, D., and Korthauer, R., 1986, "Aspects of Failure Diagnosis on Rotating Parts of Turbomachines Using Computer Simulation and Pattern Recognition Methods," presented at the International Conference on Condition Monitoring, Brighton, United Kingdom, May 21–23, Paper H1.

Barschdorff, D., 1986, "Monitoring and Expert Systems for Automatic Failure Detection," presented at the Symposium Mantenimiento Predictivo y Control de Maquinas Rotativas, Universidad de Oviedo, Gijon, Spain, July 15.

Barschdorff, D., Neuman, H. E., and Nitsche, W., 1987, "Gearbox Failure Diagnostics," *VDI Berichte*, No. 644, pp. 241–248.

Carchedi, F., and Wood, G. R., 1982, "Design and Development of a 12:1 Pressure Ratio Compressor for the Ruston 6-MW Gas Turbine," ASME JOURNAL OF ENGINEERING FOR POWER, Vol. 104, pp. 823–831.

Doel, D., 1990, "The Role of Expert Systems in Commercial Gas Turbine Engine Monitoring," ASME Paper No. 90-GT-374.

Emel, E., and Kannatey-Asibu, E., Jr., 1988, "Tool Failure Monitoring in Turning by Pattern Recognition Analysis of AE Signals," ASME *Journal of Engineering for Industry*, Vol. 110, pp. 137–145.

Li, J. C., and Wu, S. M., 1989, "On-Line Detection of Localized Defects in Bearings by Pattern Recognition Analysis," ASME *Journal of Engineering for Industry*, Vol. 111, pp. 331–336.

Lifson, A., Smalley, A., Quentin, G., and Zanyk, J., 1990, "Assessing Diagnostic Techniques for Problem Identification in Advanced Industrial Gas Turbines," ASME Paper No. 90-GT-365.

Loukis, E., Wetta, P., Mathioudakis, K., Papathanasiou, A., and Papailiou, K., 1991, "Combination of Different Unsteady Quantity Measurements for Gas Turbine Blade Fault Diagnosis," ASME Paper No. 91-GT-201.

Mathioudakis, K., Papathanasiou, A., Loukis, E., Papailiou, K., 1991, "Fast Response Wall Pressure Measurement as a Means of Gas Turbine Blade Fault Identification," ASME JOURNAL OF ENGINEERING FOR GAS TURBINES AND POWER, Vol. 113, pp. 269–275.

Sing-Tze Bow, 1984, *Pattern Recognition*, Marcel Dekker Inc., New York–Basel.

Downloaded 02 Jun 2010 to 171.66.16.112. Redistribution subject to ASME license or copyright; see http://www.asme.org/terms/Terms_Use.cfm

Optimal Measurement and Health Index Selection for Gas Turbine Performance Status and Fault Diagnosis

A. Stamatis
Research Associate.

K. Mathioudakis
Lecturer.

K. Papailiou
Professor.

Laboratory of Thermal Turbomachines,
National Technical University of Athens,
Athens, Greece

In this paper, we present a method for defining the health estimation parameters and the measurements that must be used when a monitoring system for an engine is being set up. The particular engine layout, the available measuring instruments, and the accuracy by which data can be collected are the factors taken into account. The particular health condition estimation factors that have to be used are defined as a function of this information and the desired depth of fault identification. A fast selection procedure based on the method of singular value decomposition is presented. The uncertainty in the estimations is also derived, thus giving an additional element of information useful for decision making. The proposed method, together with adaptive performance modeling, provides a self-sufficient tool, which can be applied for setting up and subsequent exploitation of a health monitoring expert system. The advantage of the procedure is that it provides a frame of application, allowing quick implementation in a new engine of interest, other than the ones previously considered.

1 Introduction

The significant savings and the efficient production planning that can be achieved by implementation of condition monitoring techniques have led to a rapid growth of related systems in recent years. Techniques employing aerothermodynamic measurement data, in particular, have received considerable attention, since they provide information not only about the condition of components but also relevant to the current performance of an engine.

A variety of techniques has appeared in the open literature. With the exception of techniques based purely on observation of measured quantities (not very efficient in general), a common feature of the existing methods is the derivation of some characteristic parameters by appropriate processing of measurement data. The advantage of calculating parameters is that they exhibit a direct link to component condition. Such parameters can, for example, be the deviations in component performance parameter values, introduced by Urban (1972), the component modification factors of Stamatis et al. (1990a), or the fouling index of Seddigh and Saravanamuttoo (1991). Of course these parameters do not need to be related only to steady-state performance, as is the case of the above references, but can also be related to dynamic engine operation, as for example some of the "health indices" of Cue and Muir (1991) or the dynamic model parameters of Merrington et al. (1991).

When application of a technique is envisaged on an engine, the existence of certain restrictions is recognized. Considering an existing engine, one is found with a given set of available measurements. Addition of instrumentation can be difficult or even impossible. It is therefore important to have the possibility to adopt a convenient formulation of a method, so that an optimal use of the existing measurements is achieved. On the other hand, when a new engine is designed, or when an intervention to instrument an engine is performed, it is desirable to define an optimum combination of sensors to be installed. Finally, a problem commended by Doel (1990) can be the transposition of a technique that is already applied to one engine to another engine with a different component configuration.

The method proposed in the present paper intends to cover needs related to the abovementioned problems. The formulation is based on the assumption that a performance model is available for the engine under consideration, and that this model can be used for estimation of the "health indices" of a particular method. This assumption is fulfilled by the current situation in the field, since almost all of the advanced monitoring methods developed recently employ such a model in one way or another. The implementation of the proposed technique to the case of an industrial gas turbine is presented, in order to demonstrate its effectiveness and provide a concrete idea about its application.

In the following we present first some brief comments about the use of simulation codes in condition monitoring, then the mathematical formulation of the method, and finally its implementation, in conjunction to a condition monitoring technique developed in the past by the authors.

Contributed by the International Gas Turbine Institute and presented at the 36th International Gas Turbine and Aeroengine Congress and Exposition, Orlando, Florida, June 3-6, 1991. Manuscript received at ASME Headquarters March 4, 1991. Paper No. 91-GT-294. Associate Editor: L. A. Riekert.

Copyright © 1992 by ASME
Downloaded 02 Jun 2010 to 171.66.16.112. Redistribution subject to ASME license or copyright; see http://www.asme.org/terms/Terms_Use.cfm

2 Performance Simulation and Condition Monitoring

Understanding the impact of individual component condition and performance on overall engine performance can be achieved through the development of a simulation code on a computer. Such codes have been in existence for a number of years (e.g., Sellers and Daniel, 1975) and methods for improving their efficiency have been published even very recently (e.g., Yonghong, 1991; Sugiyama, 1990). The general principles on which the development of such codes is based are well known and can be found even in textbooks (e.g., Cohen et al., 1987). We give here a brief account of the methodology in order to show how the methods are used for monitoring purposes and therefore provide the background for our subsequent discussion.

An engine performance model is built by employing:

(*a*) component performance data: These data consist of component performance parameter values at points covering the full range of operating conditions of the engine (usually known as component performance map).

(*b*) principles of aerothermodynamics, in order to express the relationship between various parameters characterizing the state of the working fluid.

(*c*) compatibility conditions, usually named matching conditions, which ensure that the operation of each individual component is compatible with the remaining components of the engine.

More details about the procedure of formulating such models have been presented by Stamatis et al. (1990a).

The inclusion of component performance data in a simulation code gives the possibility to study the engine response to individual components alterations. If the performance is simulated for an engine in intact condition, the modified performance can be obtained by introducing the component data as they have been modified by the presence of a fault. This gives the possibility to study the effects of a fault under consideration on any performance variable or parameter of interest. The engine model can, in this way, provide us with the pattern of expected variation of measured quantities for every fault studied. Having such a model one can produce information on component faults, through appropriate "health indices." These health indices can be parameters related to individual component condition. They can be either component characteristic parameters (e.g., Stamatis et al., 1990b) or combinations of global performance parameters (Cue and Muir, 1991; Seddigh and Saravanamuntoo, 1991). Irrespective of what particular parameters are used as indices, the methods for fault detection rely on the following principle: The values of the indices are estimated and when they exceed certain values, this is assigned to particular component faults.

It must be mentioned that "adaptive" engine models greatly facilitate this kind of study. Such models have the possibility of automatic interaction with component data and the variations of parameters or measured variables can be examined in many different combinations. They thus have a wide range of input–output combinations, giving the possibility to study the cause or effect of any variation on a component or engine level.

It follows, by using a performance model in the manner described above, that the observed engine behavior can be simulated by means of the model and the particular set of health indices.

3 Implementation of ECM Methods and Choice of Related Health Indices

When the introduction of an engine condition monitoring (ECM) method is envisaged on a particular engine, the kind of method to be applied and the particular parameters to be employed, once the method has been selected, have to be chosen. Although the quantitative analysis facing the details of the second problem is the subject of the methodology of this paper, it is useful to follow some general guidelines in the original selection of method and indices.

The following requirements have to be fulfilled by the indices employed:

- They must ensure fault isolation on a component level. For this purpose it is useful if separate indices are assigned to each component or kind of component.
- They must be sensitive to measurement variations. Even small deviations in the measured quantities should reflect on the health indices, in order to be able to uncover faults or degradations of very small extent.
- They should have a physical significance. If the indices have a physical significance (e.g., efficiency deviation), the interpretation of signatures and correspondence to a fault is facilitated, since it becomes relevant to basic laws.

(It is desirable to isolate the effects of individual sensor measurements. This property is only desirable for logistic purposes, since it ensures minimum interdependence on sensor faults and inaccuracies.)

Application of these general guidelines may lead to a very large set of health indices in order to describe the engine condition fully. The final choice is, however, restricted from practical limitations in the amount of information that can be acquired experimentally. It is very costly to provide and install instrumentation on a new engine, while it is very difficult or even impossible on an engine in service.

The problems that may be faced in such a situation can be summarized as follows:

- When a given set of measured quantities is provided, what is the optimum set of health indices? The particular problem is to define the best possible parameters for a given measurement possibility. This is a problem faced usually by the engine user, who has very few or no possibilities of intervening and adding measurements on the engine.
- When the decision for instrumenting an engine has to be

Nomenclature

$\mathbf{f}$ = $(m \times 1)$ health index vector (diagnostic vector)
$\mathbf{F}$ = prediction algorithm (computational code)
J = Jacobian matrix, Eq. (18)
m = number of health indices
n = number of measured quantities
$PS4$ = compressor outlet pressure
$PS9$ = compressor turbine outlet pressure
SY = overall sensitivity measure for each parameter, Eq. (8)
$T4$ = compressor outlet temperature
$T9$ = compressor turbine outlet temperature
$T12$ = exhaust temperature
$\mathbf{u}$ = $(l \times 1)$ operating condition vector
$W1$ = inlet mass flow rate
WF = fuel flow rate
$\mathbf{Y}$ = $(n \times 1)$ dependent parameter vector (measurable)

Superscripts

(r) = reference quantity
T = transpose of a matrix

Downloaded 02 Jun 2010 to 171.66.16.112. Redistribution subject to ASME license or copyright; see http://www.asme.org/terms/Terms_Use.cfm

taken, both the manufacturer and the user are faced with the inverse problem:

(*a*) The user wants to know the optimum set of measuring instruments to be added in order to provide enough information for a required level of resolution.

(*b*) The manufacturer wants to decide which instruments will accompany the engine, in order to ensure a good capability of in-service monitoring.

The analysis presented in the following sections shows how these questions can be answered. One additional piece of information produced by this analysis is the study of the influence that different kinds of measurement errors have on the derivation of indices. In particular, when the measurements are accompanied by certain errors, it is possible to estimate how this error propagates into the final derived indices.

4 Mathematical Formulation of the Selection Problem Measurement and Index Selection

An engine performance model of the form previously described can be expressed as a mathematical relation linking the independent parameters of an engine to the dependent parameters, namely parameters whose values are derived when the engine operating point is set.

$$\mathbf{Y} = \mathbf{F}(\mathbf{u}) \tag{1}$$

Such a relation can be generalized to include the possibility of representing various "health conditions" of the engine. In this case the functional relation includes equations expressing component alternations in the presence of fault.

The form of the generalized nonlinear static performance model can be stated as

$$\mathbf{Y} = \mathbf{F}(\mathbf{f};\ \mathbf{u}) \tag{2}$$

For a given operating conditions vector $\mathbf{u}$, the relations of expression (2) can be written in the form

$$\mathbf{Y} = \mathbf{F}(\mathbf{f}) \tag{3}$$

The above expression can be used to perform the optimum selection analysis for the purposes mentioned previously. These purposes can now be formulated as the following problems.

4.1 The Problem of Measurement Selection (Problem I). Let $\mathbf{f}^{(r)}$ be the baseline diagnostic vector corresponding to a healthy engine (typically $\mathbf{f}^{(r)} = I$), and $\mathbf{f}^{(j)}$ the diagnostic vector resulting when the jth element of f deviates from the baseline value ($\mathbf{f}^{(r)}$) by a percentage amount h_j:

$$\mathbf{f}^{(j)} = \mathbf{f}^{(r)} + h_j \mathbf{e}^{(j)} \qquad (j = 1,\ldots,m)$$

$$e_k^{(j)} = 0 \quad V \quad k \neq j$$

$$e_j^{(j)} = 1 \tag{4}$$

h_j is a small constant ($0.001 \leq h_j \leq 0.01$). Then, from Eq. (3) we have

$$\mathbf{Y}^{(r)} = \mathbf{F}(\mathbf{f}^{(r)}) \tag{5}$$

$$\mathbf{Y}^{(j)} = \mathbf{F}(\mathbf{f}^{(j)}) = \mathbf{F}(\mathbf{f}^{(r)} + h_j e^{(j)}) \tag{6}$$

The sensitivity of each dependent parameter on each individual health index is evaluated as

$$\Delta Y_k^{(j)} = \{ Y_k^{(j)} - Y_k^{(r)} \} / Y_k^{(r)} \qquad k = 1,\ldots,n \tag{7}$$

We also define an overall sensitivity measure for each parameter with the norm

$$SY_k = \left[\frac{1}{m} \sum_{j=1}^{m} \{ \Delta Y_k^{(j)} \}^2 \right]^{1/2} \qquad k = 1,\ldots,n \tag{8}$$

So, the problem of selecting the appropriate measurements is expressed mathematically as follows: For a given set of health condition indices, we must select as measured parameters these parameters giving on the norm of Eq. (8) the m greater values.

4.2 The Problem of Index Selection (Problem II). Suppose the set of n measured variables is given for an already existing engine and has dimension $n < m$. Then the estimation of the full set of m health indices is impossible. In that case some rules and criteria have to be applied in order to choose the optimum solution taking into account the various factors involved in the problem.

(*a*) Rule I: The accuracy of the estimated subset must be maximum (minimum uncertainty). We split the vector $\mathbf{f}$ into the estimated portion $\mathbf{f}_v$ and the constant portion $\mathbf{f}_c$

$$\mathbf{f} = [\mathbf{f}_v\ \mathbf{f}_c]^T \tag{9}$$

Then from Eq. (3) we can write

$$\mathbf{f}_v = \mathbf{F}^{-1}(\mathbf{Y},\ \mathbf{f}_c) \tag{10}$$

where $\mathbf{F}^{-1}$ is the inverse of the prediction algorithm. Then we apply the procedure described by the following relations:

$$\mathbf{Y}^{(i)} = \mathbf{Y}^{(r)} + h_i e^{(i)} \tag{11}$$

$$\mathbf{f}_v^{(i)} = \mathbf{F}^{-1}(\mathbf{Y}^{(i)},\ \mathbf{f}_c) \tag{12}$$

$$\Delta \mathbf{f}_{v,k}^{(i)} = \{ \mathbf{f}_{v,k}^{(i)} - \mathbf{f}_{v,k}^{(r)} \} / \mathbf{f}_{v,k}^{(r)} \tag{13}$$

$$S\mathbf{f}_{v,k} = \left[\sum_{i=1}^{n} \left(\frac{1}{n} \{ \Delta \mathbf{f}_{v,k}^{(i)} \}^2 \right) \right]^{1/2} \tag{14}$$

The above procedure is the nonlinear counterpart of the approaches used for linear GPA (Urban, 1972). As in these approaches, in order to choose the most appropriate n indices among m candidates we have to repeat the procedure for all possible combinations and choose the set of indices giving the minimum values to the norm of relation (14), which stands as an average rms error of the estimation. Since a lengthy amount of processing may be involved in such a procedure, a fast alternative can be used in order to have a first selection of the proper indices. This alternative will be described in the next section.

(*b*) Rule II: Indices must be suitable for identification of faults according to fault frequency. As the various power plants are used in different environments and are subjected in different stressing effects, the faults frequently encountered may influence different components (e.g., different indices) for each case. For example, a military jet engine functioning in a sea environment is likely to exhibit compressor faults (fouling due to salt deposition). In the case of an industrial engine the most frequent faults are in the combustor and turbine section. So, some indices are more physically constant than others.

(*c*) Rule III: The error propagation due to nonestimated indices must be minimal. This criterion simply expresses the fact that even the physically constant indices may have a small variation (accounting for aging deterioration), which may have a dramatic result on the estimated indices accuracy. In that sense in order to prevail for "false alarms" the sensitivity of the estimated indices on the nonestimated indices variation has to be determined. The procedure takes advantage of calculations already done in problem I and rule I of problem II. That is, from Eq. (2) we have the measured vector $\mathbf{Y}^{(j)}$ variation considering $\mathbf{f}^{(j)}$ resulting from variation of some index belonging to f_c. Then we use relations (12)–(14) to predict how the algorithm interprets changes in the nonestimated indices in terms of the estimated parameters.

Application of each rule provides a classification of different index sets according to the degree they comply with them. Engineering judgment will still be necessary, when a set of optimum indices is derived from another set of rules.

4.3 A Procedure for Fast Selection of Indices. In order to encompass the problem of time-consuming, lengthy cal-

Downloaded 02 Jun 2010 to 171.66.16.112. Redistribution subject to ASME license or copyright; see http://www.asme.org/terms/Terms_Use.cfm

culations for the procedure described in rule (a) of problem II, an alternative procedure has been developed based on the singular value decomposition mathematical method (Press et al., 1986). This procedure has the advantage of being easily and quickly implementable. It produces thus a first selection of indices.

The steps of the procedure are the following:

(a) Dividing Eq. (3) by Eq. (5) and expanding in Taylor series we have:

$$\frac{\mathbf{Y}_i}{\mathbf{Y}_i^{(r)}} = 1 + \frac{1}{\mathbf{F}(\mathbf{f}^{(r)})} \left(\frac{\vartheta \mathbf{F}}{\vartheta \mathbf{f}}\right)_{\mathbf{f}=\mathbf{f}^{(r)}} (\mathbf{f} - \mathbf{f}^{(r)}) + \ldots \tag{15}$$

$$\frac{\mathbf{Y}_i - \mathbf{Y}_i^{(r)}}{\mathbf{Y}_i^{(r)}} = \left(\frac{\vartheta \ln \mathbf{F}}{\vartheta \mathbf{f}}\right)_{\mathbf{f}=\mathbf{f}^{(r)}} (\mathbf{f} - \mathbf{f}^{(r)}) + \ldots \tag{16}$$

$$\Delta \mathbf{Y} = \mathbf{J} \Delta \mathbf{f} \tag{17}$$

where the Jth Jacobian matrix

$$J = \left[\frac{\vartheta \ln(\mathbf{F}(\mathbf{f}))}{\vartheta \mathbf{f}}\right] \tag{18}$$

(b) The Jacobian matrix is decomposed (due to the relevant theorem of linear algebra) into the form

$$J = U\, W\, V^T \tag{19}$$

where

$U = (n \times m)$ column orthogonal matrix
$W = (m \times m)$ diagonal matrix
$V = (m \times m)$ orthogonal matrix
and $w_i \geq 0$, $i = 1, \ldots m$.

The following lemma is valid from linear algebra: "Linear combinations of elements of Δf that correspond to the directions of the greater singular values vectors are estimated with the greater accuracy."

As a consequence of the above lemma, health indices with the greater "contribution" (i.e., the maximum projections in the direction of the greater singular values vectors) are estimated with minimum uncertainty.

So a practical and fast selection is to pick up as constant indices, these $(m-n)$ indices that have the minimum projection in the direction of the n "greater" singular values vectors, or equivalently, the $(m-n)$ indices that have the maximum projections in the direction of the $(m-n)$ "lower" singular values vectors.

5 Application to an Industrial Gas Turbine

The Ruston's Tornado gas turbine, described by Wood (1981) and Charchedi and Wood (1982) was the engine used to implement the methodology and to investigate the various relevant technical aspects.

An adaptive simulation code of this engine, operating in single-shaft mode, has been developed by Stamatis et al. (1989). This code relates component health indices with engine measured quantities. Each health index is defined as the ratio of the value of a characteristic component parameter (e.g., efficiency) to the value of that parameter corresponding to the intact condition of the component, provided that the independent parameters that define the operating point for that component are kept unchanged.

For a given operating point of the Tornado defined by the values of the shaft speed and the external load, the values of eight health indices (two indices for each mass component, according to Stamatis et al., 1990a) must be supplied in order to calculate the expected values of the whole set of performance parameters. As a consequence of the above reasoning, eight independent measured quantities are necessary in order to use the code in the inverse mode and to estimate the indices characterizing the condition of the engine components.

Unfortunately, even in the best case (e.g., manufacturer's test rig instrumented engine), seven measurements are incorporated in the engine, namely: fuel flow rate, compressor diffuser exit pressure and temperature, exhaust gas temperature, pressure and temperature between gas generator and power turbine, and engine airflow.

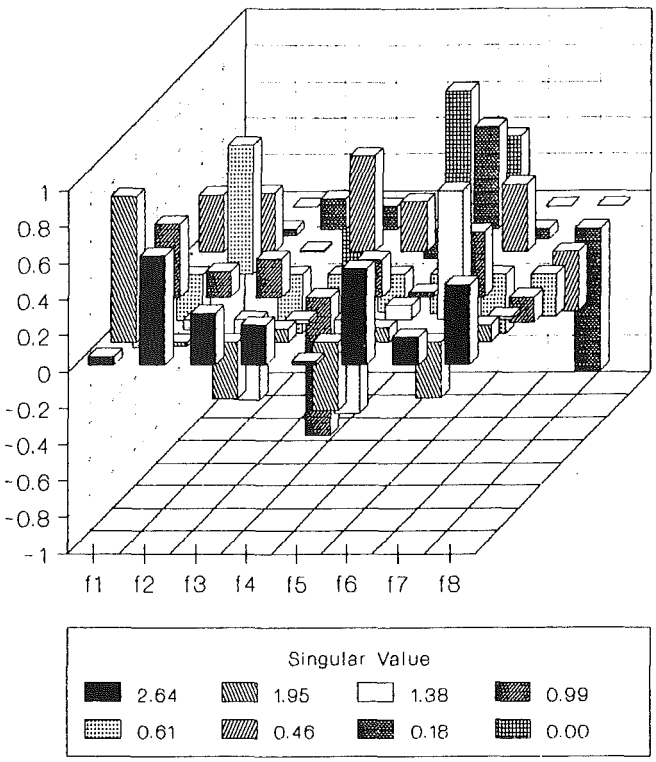


Fig. 1 Singular value decomposition of the model Jacobian matrix: projections of vectors corresponding to singular values of index axes

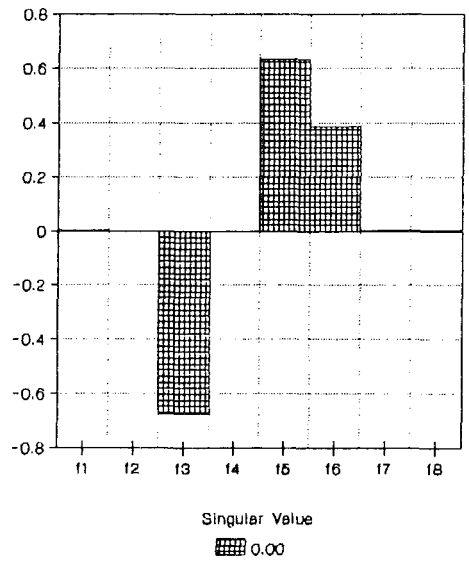


Fig. 2 Singular value decomposition: projections of the vector corresponding to minimal singular value on indices axes

The results presented in section 5.1 correspond to the case of the above measurement set, while those given in section 5.2 correspond to a reduced measurement set that is more realistic for production engines.

5.1 Case of the Extended Measurement Set. Following the general requirements described in section 3, the following health indices have been selected for characterizing engine condition: f_1, f_2, for compressor swallowing capacity and effi-

Downloaded 02 Jun 2010 to 171.66.16.112. Redistribution subject to ASME license or copyright; see http://www.asme.org/terms/Terms_Use.cfm

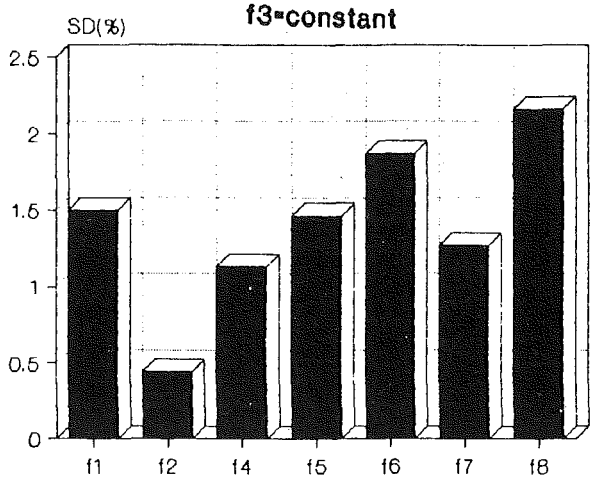


Fig. 3 Health index estimation uncertainty due to measurement noise

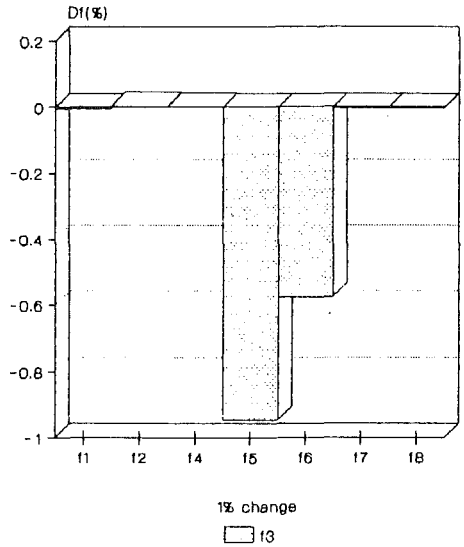


Fig. 4 Nonestimated index error propagation: effect of 1 percent error in nonestimated index f_3, on the estimated indices

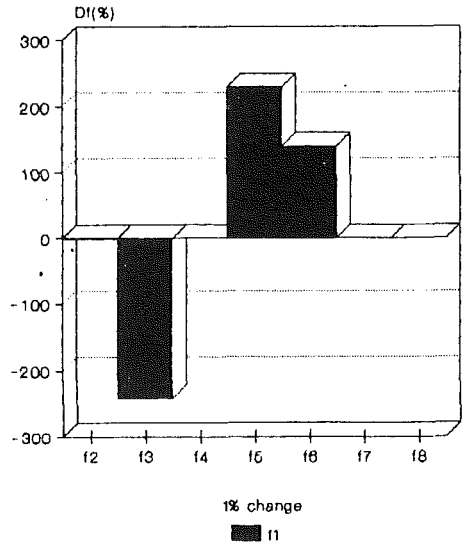


Fig. 5 Nonestimated index error propagation: effect of 1 percent error in nonestimated index f_1, on the estimated indices

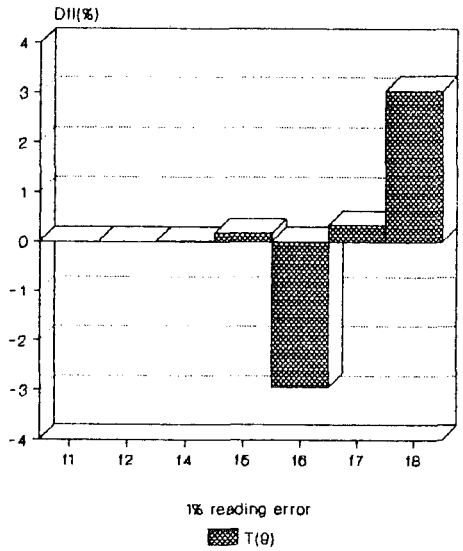


Fig. 6 Impact of bias error of the turbine interduct temperature sensor on estimated health indices

ciency, f_3, f_4 for burner pressure loss and efficiency, f_5, f_6 for core turbine mass flow capacity and efficiency, f_7, f_8 for power turbine mass flow capacity and efficiency. Since we have only seven measurements, we can estimate only seven factors, and therefore we must choose which one to neglect.

Calculations made by using the procedure described in section 4.2 show that the subset of seven estimated indices that is the most insensitive to measurement's nonrepeatability noise (Rule I) should be one in which one of the indices f_3, f_5, f_6 is kept constant.

The implementation of the singular value decomposition alternative is exhibited on Fig. 1. Each plane parallel to the page contains the projections of the singular vector corresponding to each singular value. In Fig. 2 the plane corresponding to minimum singular value (zero) is shown. The singular vector corresponding to the minimum singular value has the largest projections in the direction of indices f_3, f_5, f_6. So, the effective way to increase estimation accuracy is to keep one of these indices constant, a conclusion drawn from the full analysis as well.

In order to decide which of the above three indices should be kept constant, the rule of fault frequency (Rule II) was taken into account. Engine historical experience leads to the decision to keep index f_3 constant. Figure 3 demonstrates the resulting uncertainty of each index when f_3 is kept constant, assuming typical standard deviations for the accuracy of the measurements.

The next step was to examine the third rule, of the nonestimated index fault propagation. In Fig. 4 we see that a physical variation of this index will be interpreted from the model, as a combined modification of indices f_5, f_6, which may denote a change of the turbine condition (although the real problem is in the burner).

It is worth noting that this false interpretation is due to values that do not exceed the typical uncertainty limits, which were demonstrated in Fig. 3. In order to demonstrate what the situation would be if an index other than the ones suggested by the previous analysis is kept constant, we calculate the errors resulting from one percent deviation in f_1, if this index is kept constant. The results are shown in Fig. 5. We see that if f_1 is taken as the nonestimated index, instead of f_3, corresponding to a possible deterioration of the compressor, this would lead to dramatic estimation errors and consequently a high rate of false alarms.

During the calculations mentioned above, the sensor systematic error signature is derived. For example, Fig. 6 presents

Downloaded 02 Jun 2010 to 171.66.16.112. Redistribution subject to ASME license or copyright; see http://www.asme.org/terms/Terms_Use.cfm

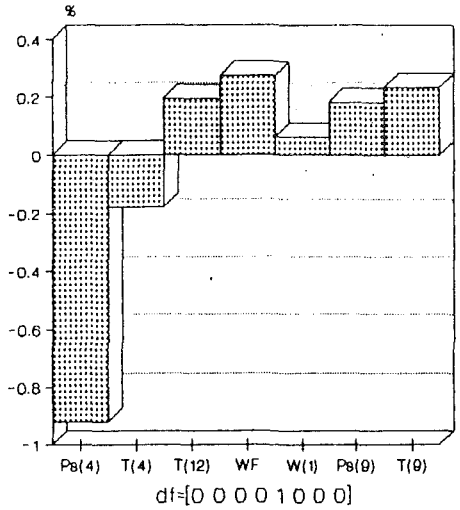


Fig. 7 Influence of 1 percent deviation of index f_5 on the measurement values

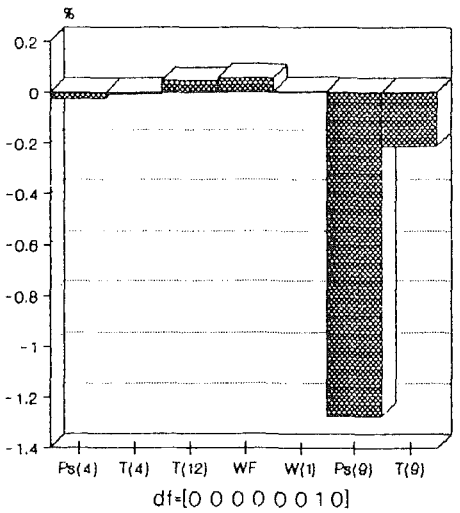


Fig. 8 Influence of 1 percent deviation of index f_7 on the measurement values

the impact of a small bias error of the turbine interduct temperature sensor on estimated health indices. It is seen that an opposite direction change of equal magnitude on indices f_6 and f_8 is expected.

5.2 Case of Reduced Measurement Sets. As the measurement set needed to diagnose faults in all components is not available in practice for production engines, an investigation has been undertaken to select reduced sets of measurements that would be sensitive to the most interesting indices, in the sense of inservice deterioration.

We assume that we obtain four measurements from the engine. In order to monitor the condition of the two main components, the compressor and the gas generator turbine, we need the indices f_1, f_2, f_5, f_6. In order to choose the appropriate measurements, we apply the analysis of section 4.1. An example of a result is shown in Fig. 7. This figure shows that if someone is interested in monitoring index f_5, one has to include in the measurement set the compressor exit pressure. The measurements chosen in this way are finally the compressor exit pressure (P_4) and temperature (T_4), the engine exit temperature (T_{12}), and the fuel flow (WF).

Another indicative calculation example is shown in Fig. 8. This figure shows that if one were interested in monitoring f_7, the measurement set should include the gas generator turbine

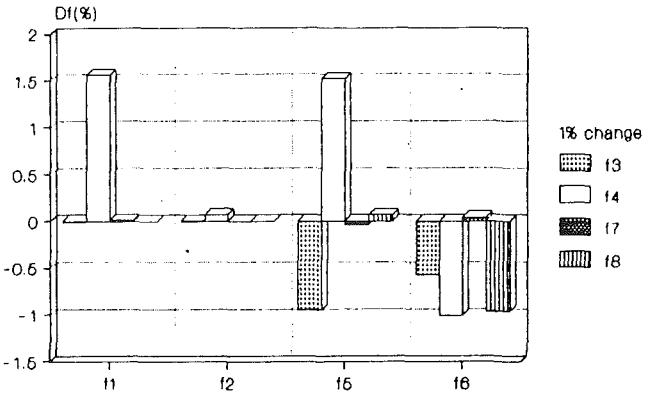


Fig. 9 Effect of nonestimated index variation on the estimation of compressor and gas generator turbine indices

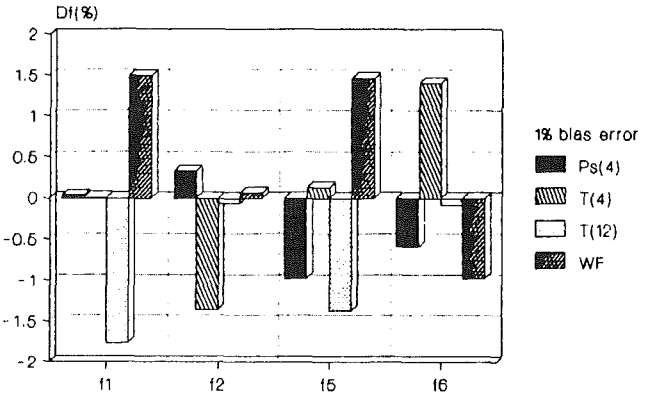


Fig. 10 Deviations of estimated indices due to measurement errors

exit pressure. Such a measurement is very difficult to perform in engines operating in the field.

In Fig. 9 the effects of small changes in the nonestimated indices on the estimated compressor and gas generator turbine indices are presented, while Fig. 10 presents systematic sensor error signatures for the estimated indices.

The above choice of measurements and indices was used in order to diagnose various experimentally simulated compressor faults described by Stamatis et al. (1990b). This study is done in order to examine the results, when the reduced factor set is used instead of the extended one. The results are shown in Fig. 11. The faults are manifested by the movement of the compressor indices in the f_1, f_2 plane. It must be pointed out that the same movement of points has been observed when the set of seven indices was considered, as presented in the above reference. Turbine health condition indices remain clustered around the point (1, 1), indicating that the turbine remains intact, confirming the known experimental condition of the engine, with faults implanted only in the compressor section.

Any other component fault or systematic sensor error has not occurred, because in that case, from Fig. 5 alteration of indices f_5, f_6 is expected.

6 Discussion of Application Aspects

We have shown how the application of the methodology presented above leads to the successful choice of a set of health indices. In the process of selection, the uncertainties in the estimation as well as the possibilities offered by choosing various other factors are also revealed.

A by-product of the procedure is the derivation of sensor fault signature. The health indices derived for a variation of the reading of each instrument constitute sensor fault signa-

Downloaded 02 Jun 2010 to 171.66.16.112. Redistribution subject to ASME license or copyright; see http://www.asme.org/terms/Terms_Use.cfm

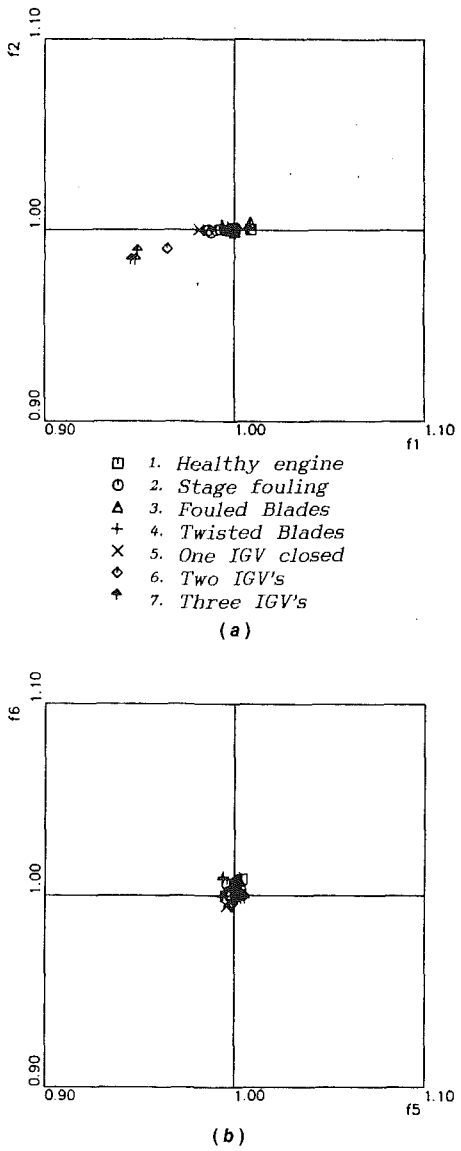


Fig. 11 Compressor fault points on diagnostic planes defined by the health indices axes of the (*a*) compressor, and (*b*) gas generator turbine

tures, since the derivation of the reading from the true value can be the effect of the sensor fault (see, for example, Fig. 6). A sensor fault of course can be of much larger value than the small derivation considered in Section 5.1, resulting in a different health index pattern for a nonlinear engine behavior. As a final comment, it can be mentioned that the derivation of sensor fault signatures is another aspect of application of the technique. Such signatures can be added to a fault library, already containing signatures of component faults, and can be potentially used together with appropriate expertise, to distinguish the kind of fault.

The application presented previously referred to fault detection by employing the adaptive performance modeling technique. Although this technique is mostly suitable for implementing the present methodology, any technique based on the derivation of health indices can be implemented. Concerning the problem of index selection, the formulation of Section 4.2 is general enough to be applied for any technique. The formulation of Section 4.1, concerning measurement selection, is less general in that it assumes that the employed performance model can incorporate health index variations and estimate their effect on measured variables. This will not be the case if the health indices are not directly linked to component performance parameter. It can, however, be stated that by the nature of the problem, it is generally possible to include such a dependence by adding some mathematical relations, in order to construct the prediction algorithm F (which directly relates measurements with the desired form of indices).

The importance of having the capability to perform the tasks the present technique can perform was recognized as soon as systematic methods for gas path analysis were introduced by Urban (1972). He provided analytical relations for estimating sensitivity of measurements (resulting from linearization of component parameter interrelations), for certain engine configurations and some tables providing a guide to selecting appropriate parameters. That technique, being based on analytical relations, would suffer from all the drawbacks an analytical engine modeling suffers with respect to computer models: need for simplifying assumptions, separate consideration of each new engine considered, reduced capability of incorporating secondary effects such as bleeds, auxiliary losses, etc. The present technique, on the other hand, being based on computerized performance models, is as much up to date as the performance model employed. Another important advantage of the present approach is that it is not restricted to linearized approaches, as the abovementioned procedure is, since it employs the full nonlinear engine model.

We have shown that for a given total set of health indices, we can select the most appropriate ones according to the amount of experimental information available. The particular indices employed had a significance for each individual component. It is possible, however, to consider new indices that are a combination of these. In this case the correspondence to a component may be lost, but the kind of grouping can, for example, correspond to a nature of a fault, such as geometric alternations of the gas path, increased clearances, faulty spray patterns, etc. In that case the procedure outline above has to be modified, but the problem will always be of the form of minimizing an objective function, or analyzing a Jacobian matrix.

Finally, it should be mentioned that the procedure presented here gives the possibility of adapting a monitoring technique to any new engine of interest. As long as a computer performance model is available for the new engine, the procedure can be applied, since it does not require any kind of a priori information about that engine. On the other hand, the procedure itself is implemented in computer programs. It provides thus a systematic, fast, and concrete way of deriving the necessary conclusions, as opposed to manual tuning of parameters, which might be considered as an alternative. The computational power required is not substantial. The applications presented here were conducted on a personal computer. The method constitutes therefore a powerful tool for extending the application of a successful monitoring method on new engines.

7 Conclusions

A method for selecting measurements and parameters for setting up a gas turbine status estimation method has been presented. General rules for selecting health indices have first been presented. A mathematical formulation of the two problems—of measurement selection and index selection—has been presented and the corresponding criteria were set. For the case of index selection, a fast procedure for index selection based on singular value decomposition has been presented.

The applicability of the proposed method was demonstrated on an industrial gas turbine. Health indices were selected for two cases, one with an extended measurement data set available and one with fewer measurements. In both cases the selected indices were able to identify faults implanted in the engine compressor.

It was shown that during application of the method, the

Downloaded 02 Jun 2010 to 171.66.16.112. Redistribution subject to ASME license or copyright; see http://www.asme.org/terms/Terms_Use.cfm

estimation of uncertainties in the calculated health indices is achieved. At the same time signatures of sensor faults are produced.

Finally, the applicability of the method with respect to different cases of monitoring methods and engines has been discussed.

References

Carchedi, F., and Wood, G. R.., 1982, "Design and Development of a 12:1 Pressure Ratio Compressor for the Ruston 6-MW Gas Turbine," ASME JOURNAL OF ENGINEERING FOR POWER, Vol. 104, pp. 823–831.

Cohen, H., Rogers, G. F. C., and Saravanamuttoo, H. I. H., 1987, *Gas Turbine Theory*, 3rd ed., Longman Group, United Kingdom.

Cue, R. W., and Muir, D. E., 1991, "Engine Performance Monitoring and Troubleshooting Techniques for the CF-18 Aircraft," ASME JOURNAL OF ENGINEERING FOR GAS TURBINES AND POWER, Vol. 113, pp. 11–19.

Doel, D., 1990, "The Role of Expert Systems in Commercial Gas Turbine Engine Monitoring," ASME Paper No. 90-GT-374.

Merrington, G., Kwon, O. K., Goodwin, G., and Carlsson, B., 1991, "Fault Detection and Diagnosis in Gas Turbines," ASME JOURNAL FOR GAS TURBINES AND POWER, Vol. 113, pp. 276–282.

Press, W. H., Flannery, B. P., Teukolsky, S. A., and Vetterling, W., 1986, *Numerical Recipes*, Cambridge University Press, United Kingdom.

Seddigh, F., and Saravanamuttoo, H. I. H., 1991, "A Proposed Method for Assessing the Susceptibility of Axial Compressors to Fouling," ASME JOURNAL OF ENGINEERING FOR GAS TURBINES AND POWER, Vol. 113, pp. 595–601.

Sellers, J., and Daniele, C., 1975, "DYNGEN—A Program for Calculating Steady-State and Transient Performance of Turbojet and Turbofan Engines," NASA TN D-7901, Apr.

Stamatis, A., Mathioudakis, K., Berios, G., and Papailiou, K., 1989, "Jet Engine Fault Detection With Differential Gas Path Analysis at Discrete Operating Points," presented at the 9th ISABE, Athens, Greece, Sept.

Stamatis, A., Mathioudakis, K., and Papailiou, K. D., 1990a, "Adaptive Simulation of Gas Turbine Performance," ASME JOURNAL OF ENGINEERING FOR GAS TURBINES AND POWER, Vol. 112, No. 2, pp. 168–175.

Stamatis, A., Mathioudakis, K., Smith, M., and Papailiou, K. D., 1990b, "Gas Turbine Component Fault Identification by Means of Adaptive Performance Modeling," ASME Paper No. 90-GT-376.

Sugiyama, N., 1990, "Generalized High Speed Simulation of Gas Turbine Engines," ASME Paper No. 90-GT-270.

Urban, L. A., 1969, "Gas Turbine Engine Parameter Interrelationships," HS VAL, Windsor Locks GK.

Urban, L. A., 1972, "Gas Path Analysis Applied Turbine Engine Condition Monitoring," AIAA Paper No. 72-1082.

Wood, G. R., 1981, "The Ruston Tornado. A 6 MW Gas Turbine for Industrial Application," ASME Paper No. 81-GT-171.

Yonghong, W., 1991, "A New Method of Predicting the Performance of Gas Turbine Engines," ASME JOURNAL OF ENGINEERING FOR GAS TURBINES AND POWER, Vol. 113, pp. 106–111.

Downloaded 02 Jun 2010 to 171.66.16.112. Redistribution subject to ASME license or copyright; see http://www.asme.org/terms/Terms_Use.cfm

Optimizing Instrumentation When Measuring Jet Engine Blade Vibration

J. H. Griffin
Department of Mechanical Engineering,
Carnegie Mellon University,
Pittsburgh, PA 15213

An analytical model of bladed disk vibration is used to calculate the statistical variations in blade amplitudes that can occur in mistuned turbomachinery blading. The results provide a basis for evaluating alternative strategies for instrumenting the stage. This approach is illustrated by applying it to an unshrouded fan stage. It is found for this stage that the best strategy is to instrument blades that have frequencies near the tuned system frequency. A procedure is proposed for establishing how gages should be allocated from stage to stage throughout the engine.

1 Introduction

During jet engine tests the blades are often instrumented with strain gages in order to measure vibration.[1] The vibratory stress levels are monitored in order to prevent blades from failing because of high cycle fatigue. In addition, the vibratory strain data may be used to assess the likely durability of the engine when it is in production. This paper discusses an approach that can be used to determine how many gages should be used on each stage and on which blades they should be placed in order to optimally achieve these objectives.

Data from gages on rotating components must be transferred to monitoring and recording equipment either by telemetry or by slip rings. In either case, the number of strain gages that can be used during an engine test to monitor vibratory stress is limited by the number of channels that are available to transfer the data. Blade vibration can be difficult to assess when the number of gages is limited because the vibratory stresses can vary widely from blade to blade due to "blade mistuning" effects. Mistuning refers to small variations in the dynamic properties of the engine blading that cause the blades to vibrate at slightly different frequencies and which, because of complex system dynamics, can lead to large variations in resonant stresses from blade to blade. Recently, analytical models of mistuning have been developed that can be used to compute the statistical information that characterizes the blades' response (e.g., Griffin, 1988). This information is useful when deciding how best to instrument the stage.

Research on mistuned stages initially focused on trying to understand the vibratory response of individual bladed disks and why such large variations in amplitudes between blades could occur for blades that were nominally identical. Some examples of early papers written on this subject are the papers by Armstrong and Stevenson (1960), Whitehead (1966), and Ewins (1969, 1970). In general, it was found that in mistuned stages individual blades behave in an almost unpredictable fashion. Huang (1982) suggested viewing the problem as one in which the structural properties are treated as statistical variables. Griffin and Hoosac (1984) used Monte Carlo-type simulations of the vibratory response of a large number of bladed disks in order to examine the system's statistical properties. One of the advantages of the Monte Carlo approach is that the blades' responses can be readily correlated with their properties.[2] It is for this reason that a Monte Carlo approach is used here since it then becomes relatively easy to study the effectiveness of various strategies for selecting which blades should be instrumented. For other purposes analytical methods of calculating the statistics either can be computationally more efficient (Sinha and Chen, 1989) or can provide better physical insights (Pierre, 1990) than using simulations.

The statistical approach as developed in the cited research is based on the concept that large groups of blades will always contain some blades that have small vibratory stresses, some that have large stresses, and many with stresses that lie between the extremes. This phenomenon gives rise to the concept of a *statistical distribution of peak amplitudes*, which gives the probability that the maximum amplitude of a blade will be less than a specified value. The distribution of peak amplitudes is essentially the same for any large group of blades. Thus, while the response of an individual blade is inherently unpredictable, the statistical properties of the system are stable and can be used to predict durability.

The statistical information about blade amplitudes together with the fatigue properties of the blade material can be used to set a vibratory *stress limit* for the stage, which should not be exceeded during a test if high cycle fatigue is to be avoided. It can also provide a *stress ratio* that relates the mean value

[1] Some test facilities use optical methods for measuring the amplitude of vibration of the blade tips. When this method is employed the vibration of all of the blades on the stage can be measured and it is not necessary to use the optimization methods described in this paper.

Contributed by the International Gas Turbine Institute and presented at the 36th International Gas Turbine and Aeroengine Congress and Exposition, Orlando, Florida, June 3-6, 1991. Manuscript received at ASME Headquarters February 12, 1991. Paper No. 91-GT-71. Associate Editor: L. A. Riekert.

[2] Another advantage of the Monte Carlo approach is that it is like performing a large number of experiments and, consequently, automatically accommodates the possibility of mode localization or any other physical mechanism that might instigate amplitude scatter.

Copyright © 1992 by ASME
Downloaded 02 Jun 2010 to 171.66.16.112. Redistribution subject to ASME license or copyright; see http://www.asme.org/terms/Terms_Use.cfm

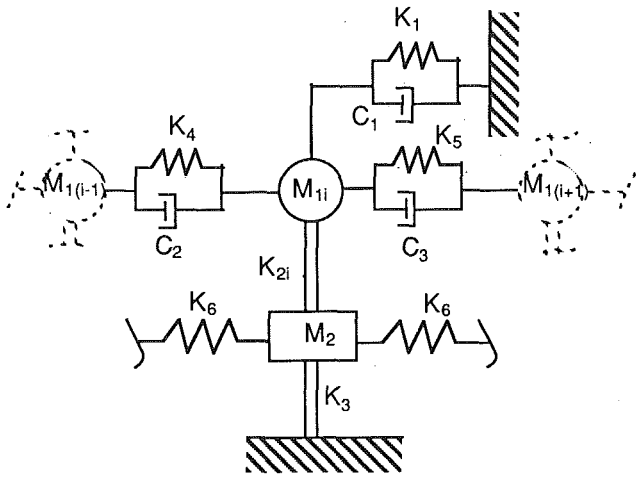


Fig. 1 Lumped parameter system

of the vibratory stress that is measured to the worst stress that is likely to occur in a fleet of nominally identical engines and thus predict fleet durability. In essence, the stress limit and the stress ratio are calculated by determining their nominal (expected) values and their scatter (standard deviation). In general, the nominal values and scatter in these quantities depend on how many blades are instrumented and how those blades are selected. In this paper we will examine how an analytical model of mistuning can be used to select the strategy that minimizes scatter, to determine the number of blades that need to be instrumented in order to achieve a consistent measurement error from stage to stage, and to calculate the stress limit and stress ratio for a given strategy and number of instrumented blades.

The work is reported as follows. First an analytical model for predicting mistuning will be described together with the procedures for performing the Monte Carlo simulations. Next, several instrumentation strategies will be proposed and criteria will be given for assessing their merits. As an example, the strategies will be evaluated and an optimum approach established for an unshrouded fan stage. The main conclusions are summarized in the last section.

2 Mistuning Model

2.1 Simplified Structural Model. Because Monte Carlo simulations are computationally intensive, the analytical model of the bladed disk should be as simple as possible and still adequately represent mistuning. The simplified model used in this study was also used by Griffin (1988). The model is briefly reviewed here for completeness. A representative segment of the model is depicted in Fig. 1. The lumped system of masses, springs, and dashpots corresponds to one blade and its associated wedge of the disk. The parallel lines are beamlike spring elements, which have zero extensional flexibility and transverse stiffnesses as noted. In the simplified model the upper mass, M_{1i}, and spring, K_{2i}, represent the ith blade, the lower mass, M_2, and stiffnesses K_3 and K_6, represent the disk, and the remaining spring and damping elements represent aerodynamic forces. A complete rationale of how the values of the parameters were selected is given in the earlier paper. Detailed information about the mode shapes of vibration, the geometry, etc., is available in an Air Force final report (Griffin, 1987). The primary idea is that nominal values of the parameters are chosen so that the vibratory response of the nominal, simplified model matches that of the perfectly tuned bladed disk. Then, in the Monte Carlo simulations, the individual blade parameters, M_{1i} and K_{2i}, are perturbed in order to cause blade frequency variations, which are consistent with those observed in practice.

In developing a mathematical model of the bladed disk, it is necessary to characterize the structural properties of the stage in terms of its natural frequencies and mode shapes, the damping in the system, and the phase and magnitude of the generalized force acting on the stage. Except for the magnitude of the generalized force, all of these factors can either be calculated analytically or estimated from previous experience. The underlying vibration theory that is used to predict peak amplitudes is linear. Consequently, the magnitude of excitation acts as a multiplicative factor, which scales all of the amplitudes. This has two implications. The first is that the relative scatter in the peak amplitudes can be calculated before any tests of the stage are conducted and, as a result, this information can be used in order to optimize placement of the gages. The second implication is that a scaling factor for the distribution needs to be established during the engine tests. Once the scaling factor is known, the analytical model can be used to predict the overall statistics for the stage.

In order to calculate the vibratory response of the system, the equations of motion are written for the simplified model system and for a specified engine order excitation,[3] n_E

$$M_{1i}\ddot{x}_{1i}+(C_1+C_2+C_3)\dot{x}_{1i}-C_2\dot{x}_{1(i-1)}-C_3\dot{x}_{1(i+1)}+(K_1+K_{2i}+K_4+K_5)x_{1i}-K_4x_{1(i-1)}-K_5x_{1(i+1)}=f_0\cos(\omega t-i\psi) \quad (1)$$

and

$$M_2\ddot{x}_{2i}+(K_{2i}+K_3+2K_6)x_{2i}-K_6(x_{2(i-1)}+x_{2(i+1)})-K_{2i}x_{1i}=0 \quad (2)$$

where $i=1, 2, \ldots, N$ and N is the number of blades on the disk. The x's denote the displacement of the mass with the corresponding subscript. The excitation is characterized by an unknown magnitude, f_0 (which for purposes of the simulations is set equal to unity), a frequency ω equal to $2\pi n_E$ multiplied by the speed of the engine in revolutions per second, and the phase angle ψ, which is equal to $2\pi n_E/N$.

For a given rpm (revolutions per minute) of the engine the frequency of excitation ω is fixed and the equations of motion, Eqs. (1) and (2), are solved in the usual manner. The displacements are assumed to be sinusoidal, i.e., the motion of each mass is represented as the sum of sin ωt and cos ωt terms with unknown coefficients. This representation is then substituted into the equations of motion and the coefficients of the linearly independent terms equated. This process results in four algebraic equations for each blade, disk segment. For N blades there are $4N$ simultaneous, linear, algebraic equations in $4N$ unknown coefficients, which are then solved over a range of frequencies in order to determine the peak amplitudes of each blade on the disk.

2.2 Monte Carlo Simulation. The Monte Carlo simulation of the stage's structural response occurs in the following manner. First, a bladed disk is constructed in which the blades are selected randomly, i.e., the blades' properties vary statistically in a manner that gives rise to variations in blade frequencies that are consistent with those measured in the laboratory.[4] Once the structural properties of the bladed disk assembly are determined, the vibratory response is then cal-

[3] It is assumed that the excitation acting on the blade has a period corresponding to one revolution of the stage. Consequently, it can be represented in terms of a Fourier series. The "engine order" denotes which Fourier component of the excitation is under consideration.

[4] The frequencies of 26 blades were measured in the laboratory and were found to be approximately normally distributed with a standard deviation of approximately 0.6 percent of the mean frequency for the first three modes. It was assumed for purposes of the simulation that this ratio would be maintained under engine operating conditions. Since the blades have higher nominal frequencies under rotating conditions, the frequency standard deviations used in the mistuning analyses were scaled up accordingly.

Downloaded 02 Jun 2010 to 171.66.16.112. Redistribution subject to ASME license or copyright; see http://www.asme.org/terms/Terms_Use.cfm

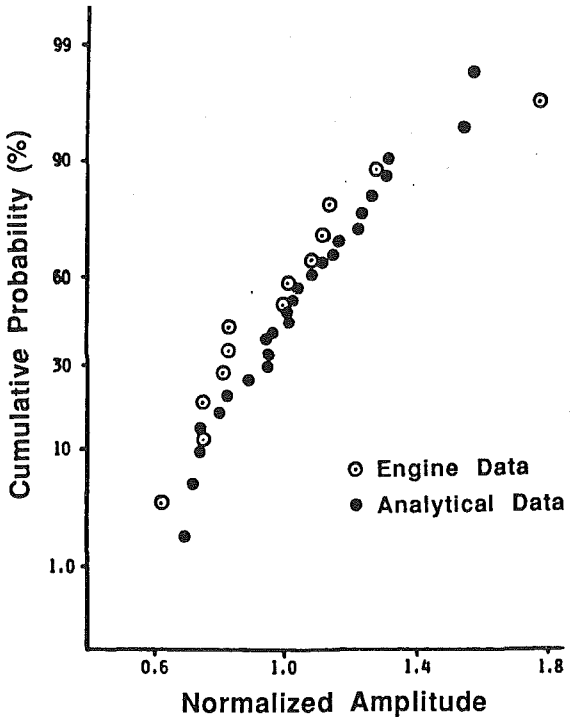


Fig. 2 Comparison of engine and analytical data

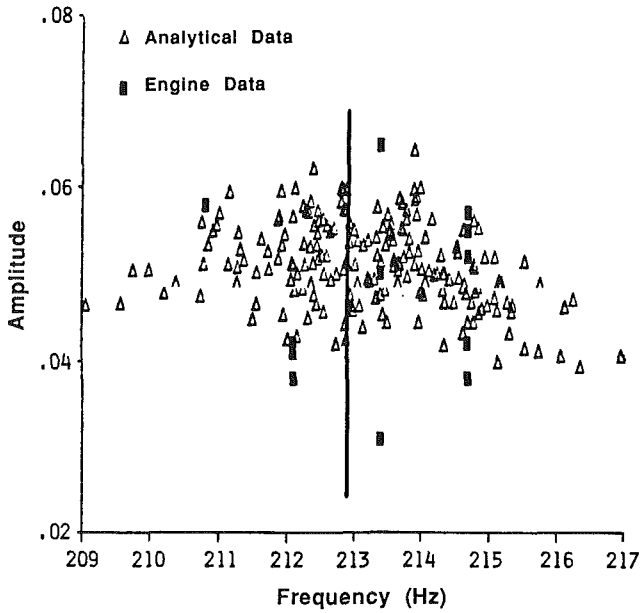


Fig. 3 Peak amplitude correlated with blade frequency

culated for a particular engine order excitation over a range of frequencies in order to determine each blade's peak response. This process is repeated for a number of disks in order to compile a large data base from which the statistical properties can be extracted. From the data base the statistical distribution of peak amplitudes can be constructed or, if desired, the peak amplitudes can be correlated with blade properties.

2.3 Simulation of a Fan Stage. Griffin (1988) simulated the vibratory response of an unshrouded fan stage and the results were compared with engine test data. It was found that the mistuning model did a good job of predicting the scatter in the vibratory response for both the first and second blade modes (refer to Fig. 2 for a comparison of predicted and measured blade amplitude distributions for the first mode). In this paper, the data base generated by Monte-Carlo simulation

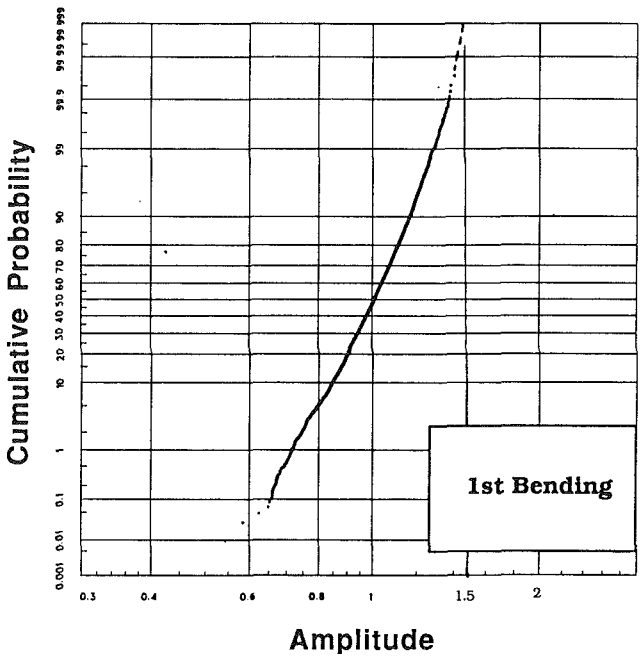


Fig. 4 Peak amplitude distribution function

for the first mode will be utilized to assess alternative instrumentation strategies. The bench test frequencies of the blades, which are essentially the same as "blade alone" frequencies, will be used as criteria in order to decide which blades should be instrumented. In a study of a turbine disk by Griffin and Hoosac (1984) it was found that the highest responding blades tend to have individual blade frequencies close to the tuned bladed disk frequency (the frequency that the bladed disk would have if the blades were perfectly tuned). This was also found to be the case for the fan disk, as is indicated by the analytical and engine data of Fig. 3.[5] Note that the highest responding blades tend to have blade alone frequencies near the solid vertical line used to indicate the tuned bladed disk frequency.

3 Instrumentation Study

3.1 Instrumentation Strategies and Criteria. As discussed in the last section, there is a correlation between a blade's frequency and its probability of having a large amplitude. This suggests that we measure each blade's frequency in a standard fixture prior to the engine test and decide which blades should be instrumented based on their measured frequency. Four strategies are proposed for selecting which blades will be instrumented. They are:

1 Instrument the blades randomly.
2 Instrument the lowest frequency blades.
3 Instrument the highest frequency blades.
4 Instrument the blades with frequencies nearest the tuned system frequency.

In order to assess how well each strategy works we have to identify the objectives of the measurements. We have identified two: The first is to prevent the stage from failing during the test. What we need to know in this case is the peak amplitude of the highest responding blade on the disk. If we only instrument a subset of the blades, then we need to know how the worst stress that we measure compares with the highest

[5]The results from the analytical model exhibit less scatter because they do not include the effect of strain gage measurement errors. This error was not included in order to exhibit better the correlation between the maximum amplitude and the blade frequency. The analytical simulation assumes that the phase of the excitation is consistent with a second engine order excitation. The engine strain gage data were filtered in a consistent manner so that their frequency content is two times the engine rpm.

Downloaded 02 Jun 2010 to 171.66.16.112. Redistribution subject to ASME license or copyright; see http://www.asme.org/terms/Terms_Use.cfm

stress for the stage. Let this stress ratio be defined as R, i.e., the ratio of the peak amplitude of the highest responding blade instrumented to that of the highest responding blade on the disk. Then R may be characterized in terms of its mean value, R_m, and its standard deviation, σ_R.

The second objective is to predict fleet durability. As previously discussed, this requires that we determine a scaling factor for the peak amplitude distribution. Here we characterized the scaling factor in terms of the mean value of the distribution. The peak amplitude distribution for the lowest frequency mode of the fan stage was calculated for a 200 disk sample and is depicted in Fig. 4. The ratio of the mean amplitude of the population to the highest amplitude on the 200 disks is approximately 0.65. If we instrument a subset of the blades, then we need to know how the mean value of the peak stresses for this subset compares with the mean value for the entire distribution. Let this amplitude ratio be defined as A^*, i.e., the ratio of the mean peak amplitude measured to that of the distribution. Again this quantity may be characterized in terms of its mean value A^*_m, and its standard deviation, σ_A.

The standard deviations, σ_A and σ_R, depend on the characteristics of the stage, the number of blades instrumented, N_b, and the strategy that is used in selecting which blades to instrument. The best strategy will be the one that reduces σ_A and σ_R as much as possible for a fixed N_b. This optimization process will be demonstrated in the following section.

3.2 Results for a Fan Stage. Four quantities are assessed for an unshrouded fan stage as functions of the number of instrumented blades: R, σ_R, A^*, and σ_A. These quantities are estimated by using a 50-disk simulation in which N_b blades are instrumented preferentially by their blade alone frequencies. For example, when N_b equals two, two blades on each disk are chosen according to the strategy being implemented and R and A^* are determined for each disk. Then from the 50 samples the mean and standard deviation of R and A^* are calculated.

R_m is plotted as a function of N_b in Fig. 5. For example, the results of Fig. 5 indicate that if the four highest frequency blades on the wheel are instrumented (strategy 3) then, on average, the highest measured vibratory stress will be about 85 percent of the highest vibratory stress on the stage. Note that the observed trends are consistent with the data of Fig. 3. That is, you tend to sample more of the high responding blades and R_m is higher if you preferentially instrument the blades with frequencies closest to the tuned system frequency (strategy 4). If you instrument the high-frequency blades you will not tend to sample the high responding blades and R_m is lowest. Lastly, by instrumenting more blades you increase the likelihood of measuring the highest responding blade ($R_m \rightarrow 1$ as $N_b \rightarrow 26$, the number of blades on the disk).

The standard deviation in R/R_m is plotted in Fig. 6. This information indicates, for example, that if the four highest frequency blades are instrumented then the standard deviation in R, σ_R, will be approximately 8.8 percent of R_m. Since R_m is equal to 0.85, $\sigma_R \approx 0.075$. Consequently, the minimum value of R might be approximated as $R_m - 3\sigma_R \approx 0.63$. This conservative estimate of R could be used to give a safety factor ($1/R = 1.6$) that relates the highest vibratory stress that is measured to the highest vibratory stress on any blade in the disk. From the figure, it is clear that the strategy that gives the lowest standard deviation in R is strategy 4, instrument the blades with frequencies closest to the natural frequency of the tuned system. Consequently, this strategy is most likely to measure the highest vibration on the disk and would require the smallest safety factor—approximately 1.3 in this example.

Analogously, the mean value of A^*, A^*_m is depicted in Fig. 7. A^* is the ratio of the average peak amplitude measured to the average peak amplitude of the entire population. For example, if the four highest frequency blades are instrumented then their mean value would have to be divided by 0.92 in order to estimate the expected value of the mean amplitude of

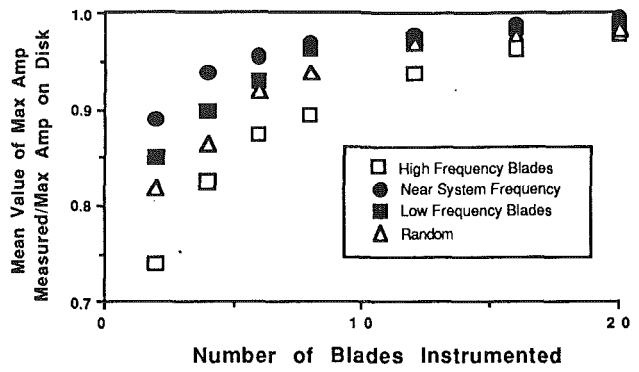


Fig. 5 R_m as a function of N_b

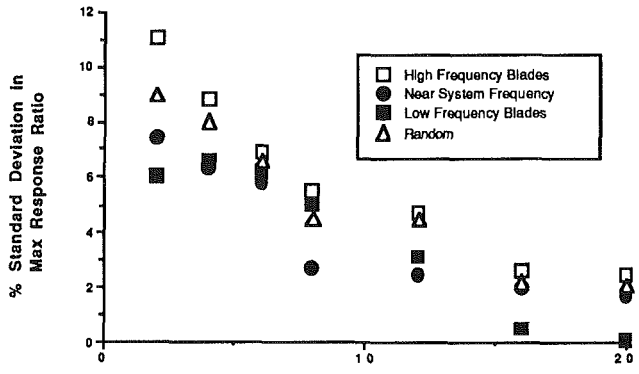


Fig. 6 Standard deviation in R

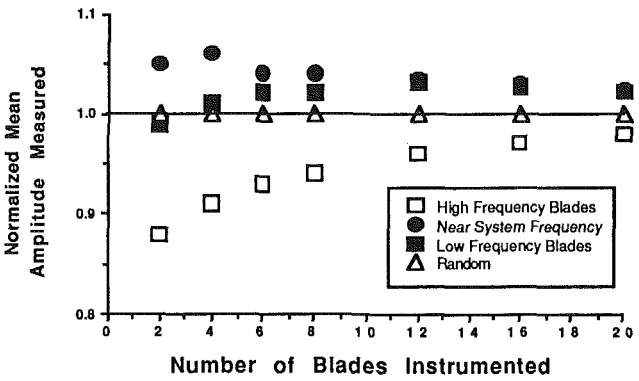


Fig. 7 Mean amplitude ratio

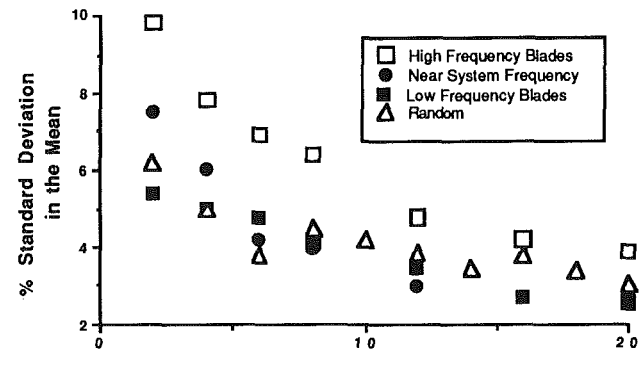


Fig. 8 Standard deviation in mean amplitude ratio

Downloaded 02 Jun 2010 to 171.66.16.112. Redistribution subject to ASME license or copyright; see http://www.asme.org/terms/Terms_Use.cfm

the entire population. From the figure we can observe that if we instrument the blades randomly, we have an unbiased sample and A_m^* equals one and that this result is independent of the number of blades instrumented. If one of the other instrumentation strategies is used, then the measurements are biased and we might have a disproportionate number of low responding blades (strategy 3) or of high responding blades (strategy 4).

The standard deviation in A^*/A_m^* is shown in Fig. 8. If we use the same example of instrumenting the four highest frequency blades, then we observe that σ_A/A_m^* is 7.8 percent. Since A_m^* is 0.92, σ_A is approximately 0.072. A conservative estimate of A^* might be $A_m^* - 3\sigma_A \approx 0.70$. The results of Fig. 8 indicate that the scatter is about the same if either strategies 1, 2, or 4 are used but is significantly higher if the high-frequency blades are preferentially instrumented. As a result, it is clear for the stage under consideration that strategy 3, instrumenting the high-frequency blades, may be eliminated as a viable alternative.

It is apparent that for this fan stage the primary consideration in deciding on an instrumentation strategy will be based on how the strategy affects the standard deviation in R. The value of reducing σ_R is that we reduce the probability of making a "type I error." In this context a type I error occurs when we stop a perfectly safe engine test because we mistakenly think that the vibratory stress is so high that it will cause blade failure. Since strategy 4 results in the lowest value of σ_R for a given value of N_b, it is this approach that should be followed in instrumenting the blades for this fan stage.

Lastly, it is necessary to decide how many blades should be instrumented. In making this decision a number of factors must be taken into account: the total number of gages available for all stages, the gage survival rate, the number of stages, and the curves for σ_R as a function of N_b for each important engine order of excitation on each stage. One approach would be that the gages should be distributed so that σ_R is the same for all stages.[6] Practically, this means that a rationale has been developed that will allocate more gages to stages that are likely to exhibit large amplitude variations and fewer gages to those in which the blades are predicted to respond more uniformly.

4 Conclusions

An approach has been demonstrated for determining the number and identity of the blades that should be instrumented when measuring blade vibration in turbomachinery. The primary ideas that were utilized are:

1 For many stages there is a correlation between a blades's "blade alone" frequency and its peak amplitude that can be established through Monte Carlo simulation. Consequently, various strategies can be proposed for instrumenting the stage that take into account the frequencies of the blades.

2 The optimum strategy for deciding which blades to instrument on a stage is the one that results in the smallest standard deviation in the quantities of interest and, hence, provides the best estimate of their actual values. This reduces the changes of deciding that the vibratory stresses are too large when, in factor, they are not.

3 The number of gages that should be allocated for each stage should be such that measurement errors are consistent from stage to stage. Thus, stages that are predicted to have larger amounts of scatter will have more gages than those in which the blades are predicted to behave more uniformly.

Currently, there is a significant amount of research activity that seeks to develop methods for predicting the excitation forces that act on the stage. When the technology for making these predictions matures then the amplitude of the force, f_0, in Eq. (1) will be known and we will be able to estimate completely the statistical distributions before the engine tests are conducted. From an instrumentation point of view, this would mean that the approach summarized above as point 3 could be modified to take into account the magnitude of the response so that those stages that are predicted to have the highest vibratory stresses would be allocated more gages.

[6]Gage failure rate, perhaps as a function of stage temperature and the centrifugal acceleration acting on the gage, could be taken into account so that the expected number of gages after failures would result in a constant value of σ_R.

Acknowledgments

The author wishes to thank Mr. Thomas M. Hoosac, Mr. Carl E. Meece, Jr., and Dr. Yehia M. Elaini of Pratt and Whitney Aircraft for their support and advice in pursuing this research. In particular this work would not have been possible without the aid of Mr. Hoosac, project manager for Pratt and Whitney. This work was supported by the Aero Propulsion Laboratory, Wright-Patterson Air Force Base, Contract No. F33615-84-C-2454, under the direction of Mr. William A. Stange.

References

Armstrong, E. K., and Stevenson, R. E., 1960, "Some Practical Aspects of Compressor Blade Vibration," *Journal of the Royal Aeronautical Society*, Vol. 64, No. 591, pp. 117–130.

Ewins, D. J., 1969, "The Effects of Detuning Upon the Forced Vibrations of Bladed Disks," *Journal of Sound Vibration*, Vol. 9, pp. 65–79.

Ewins, D. J., 1970, "A Study of Resonance Coincidence in Bladed Disks," *Journal of Mechanical Engineering Science*, Vol. 12, No. 5.

Griffin, J. H., and Hoosac, T. M., 1984, "Model Development and Statistical Investigation of Turbine Blade Mistuning," ASME *Journal of Vibration, Acoustics, Stress, and Reliability in Design*, Vol. 106, pp. 204–210.

Griffin, J. H., 1987, "An Improved Method of Measuring Blade Vibration and Predicting Engine Durability," Final Report to the Aero Propulsion Laboratory, Wright-Patterson Air Force Base, OH, Apr. Report No. AFWAL-TR-86-2118.

Griffin, J. H., 1988, "On Predicting the Resonant Response of Bladed Disk Assemblies," ASME JOURNAL OF ENGINEERING FOR GAS TURBINES AND POWER, Vol. 110, pp. 45–50.

Huang, Wen-he, 1982, "Vibration of Some Structures With Periodic Random Structures," *AIAA Journal*, Vol. 20, No. 7.

Pierre, C., 1990, "Weak and Strong Vibration Localization in Disordered Structures: A Statistical Investigation," *Journal of Sound and Vibration*, Vol. 139, pp. 111–132.

Sinha, A., and Chen, S., 1989, "A Higher Order Technique to Compute the Statistics of Forced Response of a Mistuned Bladed Disk Assembly," *Journal of Sound and Vibration*, Vol. 130, pp. 207–221.

Whitehead, D. S., 1966, "Effect of Mistuning on the Vibrations of Turbomachine Blades Induced by Wakes," *Journal of Mechanical Science*, Vol. 8, No. 1, pp. 15–21.

Downloaded 02 Jun 2010 to 171.66.16.112. Redistribution subject to ASME license or copyright; see http://www.asme.org/terms/Terms_Use.cfm

Optimization of LM2500 Gas Generator and Power Turbine Trim-Balance Techniques

B. D. Thompson
Mechanical Engineer,
Naval Sea Systems Command,
Washington, DC
Assoc. Mem. ASME

A procedure has been developed by the U.S. Navy to trim-balance, in-place, the gas generator and power turbine rotor of the LM2500 Marine Gas Turbine Engine. This paper presents the theoretical background and the techniques necessary to optimize the procedure to balance the gas generator rotor. Additionally, a method was developed to trim balance LM2500 power turbines. To expand the implementation of both gas generator and power turbine trim-balancing, a capability has to be developed to minimize the effort required (trial weight runs, etc.). The objective was to be able to perform consistently what are called "First-Shot" trim balances. First-Shot trim balances require only one weight placement to bring the engine vibration levels to within the specified goals (less than 0.002 of an in. maximum amplitude) and that being the final trim weight. It was realized that the Least-Squares Influence-Coefficient Method, even with a good set of averaged influence coefficients, can lead to a number of trial weight experiments before the final trim weights can be placed. The method used to maximize the possibility of obtaining a First-Shot trim balance was to use modal information to tailor the influence coefficient sets to correct the most predominant and correctable imbalance problem. Since the influence coefficients were tailored, it became necessary to be able to identify, in the initial vibration survey, the type of response a particular LM2500 has. Using modal information obtained from a LM2500 rotor dynamics model and from the early trim-balance efforts, it was possible to identify the modal response of a given LM2500 and optimize the trim balance of that engine. With these improved techniques a 70 percent success rate for First-Shot trim balance has been achieved and the success rate of the trim balance procedure, as a whole, has been near 100 percent.

Introduction

One of the leading causes of LM2500 marine gas turbine engine removals over the past decade, from US Navy ships, has been excessive engine self-generated vibration. This was usually due to residual unbalance in the gas generator rotor. Thompson et al. (1989) showed that trim-balancing the gas generator rotor could effectively reduce this vibration. This work also discussed the cost savings that could result from the trim-balance effort. These savings came mainly from eliminating the need to remove the LM2500 gas generator for a depot repair and from the reduced maintenance the balanced engine requires. Other beneficial consequences of vibration reduction are increased availability, reliability and reduced structure-borne noise.

This paper presents the improvements to the technique of trim-balancing LM2500 gas generators that have been made since the first paper. Additionally, a technique for trim-balancing LM2500 power turbines and the detailed vibration analysis of LM2500 gas turbine system response necessary to perform cost-effective trim balances is presented. Also presented is the theoretical background used to develop the computer program the US Navy uses to trim balance LM2500 gas generators and power turbines.

Background

Procedures for in-place balancing rotors that operate above one or more "critical" speeds at which residual imbalance excites resonant vibrations in the rotor, or in the structure supporting the rotor, have been around for more than two decades. Goodman's (1963) work on the least-squares method identified an important new procedure at a time when computers were first being introduced. Later work by Lund and Tonneson (1971) reduced the method to a workable software tool, which was later evaluated by Tessarzik et al. (1972), Tessarzik and Badgley (1974) and others.

The LM2500 marine gas turbine engine is fundamentally an aircraft derivative engine based very closely on the TF39 and CF6-6 designs. One of the important aspects of aircraft engines is relatively lightweight construction, which leads to mechanical designs where minimizing the weight is the primary consideration. Typically, in such designs, it is common to use

Contributed by the International Gas Turbine Institute and presented at the 36th International Gas Turbine and Aeroengine Congress and Exposition, Orlando, Florida, June 3–6, 1991. Manuscript received at ASME Headquarters March 4, 1991. Paper No. 91-GT-240. Associate Editor: L. A. Riekert.

Copyright © 1992 by ASME
Downloaded 02 Jun 2010 to 171.66.16.112. Redistribution subject to ASME license or copyright; see http://www.asme.org/terms/Terms_Use.cfm

roller or ball bearings, minimize the number of rotor support bearings, lightweight rotors and casings, and use squeeze film damper bearing technology to improve system vibration response. Therefore, the vibration response of the LM2500 gas turbine is not a response based on the mass-elastic characteristics of the rotors and their bearing supports. It also includes the mass-elastic properties of the gas turbine structure and mounts. The result is that this type of system can have several rotor-structure "critical speeds" in the gas turbine operating range.

It would seem then that use of the least-squares influence-coefficient method to trim balance the LM2500 gas generator or power turbine rotor would be a straightforward application of these techniques. The least-squares influence-coefficient technique as proposed by Goodman (1963) and developed by Lund and Tonneson (1971) assumes that the system being balanced behaves in a linear manner. This means that the engine influence coefficients are invariant and the engine vibration response is repeatable. In the case of the LM2500, and probably other aircraft derivative engines as well, nonlinear vibration response is introduced by hysteresis in the lightweight rotor system, as well as, by thermal effects and the squeeze film damper bearing(s). Therefore, some difficulty could be encountered by the uneducated application of the least-squares influence-coefficient method.

LM2500 Trim-Balance Considerations

The requirements for trim-balancing US Navy LM2500 gas turbines are as follows:

1 Procedure should be usable by personnel that do not have a detailed understanding of the least-squares influence-coefficient theory and specialized knowledge of LM2500 rotor dynamics;

2 Equipment used has to be portable and "off the shelf hardware";

3 Effort required to trim-balance an LM2500 has to be a minimum;

4 Vibration reduction has to be significant from as high as 0.005+ in. (5 mils), on the standard shipboard; instrumentation, to less than 0.002 in. (2 mils) and preferably lower;

5 Because of access, on installed engines, the only balance planes available are the 3rd and the 9th stages in the high pressure compressor.

Development of Trim-Balance Technique

A common method of trim-balancing high-speed flexible or semi-flexible rotor systems is to use a form of the Influence-Coefficient Method with a least-squares solution for systems that are typically overspecified. This method for determining correction weights was developed initially by Goodman (1963) and is presented here in a form used by the U.S. Navy to trim balance the LM2500 Marine Gas Turbines.

An influence coefficient is defined as the change in unbalance in a rotor due to the insertion of a known weight over the change in vibration response due to this weight.

$$\alpha_i = \frac{\delta W}{\delta Z_i} \tag{1}$$

Knowing the influence coefficients for a rotor system, one can calculate the trim correction weights for the case where the number of vibration measurement equals the number of balance planes ($n = m$). In a mathematical sense, this will bring the residual vibrations to zero.

$$[Z]_n = [I]_{n,m} * [W]_m \tag{2}$$

In a typical flexible rotor system, the matrix, represented by $[I]$, is not square; there are usually many more vibration measurements (n) than balance correction planes (m). Therefore, $n > m$ and the system, in mathematical terms, is overspecified.

$$0 \neq [Z_R]_n = [I]_{n,m} * [W]_m - [Z]_n \tag{3}$$

Since the system is overspecified, the residual vibrations can never be brought to zero. A method is then required to minimize the residual vibrations; one common way to do this is the least-squares method, which finds the correction weights that will minimize the sum of the squares of the residual vibrations. The least-squares technique for calculating trim correction weights can be written as

$$[\bar{I}]^T_{n,m} * [I]_{n,m} * [W]_m = -[\bar{I}]^T_{n,m} * [Z]_n \tag{4}$$

Therefore, for $n > m$, we have

$$[W]_m = -([\bar{I}]^T_{n,m} * [I]_{n,m})^{-1} * [\bar{I}]^T_{n,m} * [Z]_n \tag{5}$$

This formulation will calculate the correction weight(s) that will minimize the sum of the squares of the residual vibration.

One of the shortcomings of the least-squares technique for calculating a set of trim weights is that there is no explicit control over the size of individual residual vibrations, only that the sum squared of the residual vibrations has been minimized. One technique for obtaining some control over the size of the residuals is to weigh certain speed points higher than others in the least-squares solution. This can be accomplished by the following formulations

$$\epsilon_{ij} = \frac{|X_i|_{j-1}}{(\text{rms})_{j-1}} * \epsilon_{i,j-1} \text{ for } i = 1 \rightarrow n \tag{6}$$

$$(\text{rms})_j = \sqrt{\sum_{i=1}^{n} \frac{|X_i|_j^2}{n}} \tag{7}$$

where $e(i, j)$ make up the diagonal elements of matrix $[E]$, with the nondiagonal elements being zero. Therefore

$$[W]_m = -([\bar{I}]^T_{n,m} * [E]_j * [I]_{n,m})^{-1} * [\bar{I}]_{n,m} * [E]_j * [Z]_n \tag{8}$$

This is an iterative scheme, where Eq. (6) is used to increase the importance of certain speed points over others based on

Nomenclature

α_i = influence coefficient of the ith speed point
δW = change in rotor imbalance
δZ = change in vibration response of the ith speed point
$[Z]$ = vibration-response column matrix
$[I]$ = influence coefficient matrix
$[W]$ = correction weights column matrix
$[Z_R]$ = residual vibration-response column matrix
$[I]_T$ = conjugate transpose of the influence-coefficient matrix
X_i = vibration-amplitude response of the ith speed point
rms = root mean square of vibration amplitude
ϵ_{ij} = weighing factor for individual speed point
$[E]$ = weighing matrix
S_i = weighted-sensitivity factor for ith speed point
S_W = sum of the individual weighted sensitivities
W_L = single speed, single sensor, single plane correction weight
W_{ave} = sensitivity-weighted vector average correction weight
n = number of vibration measurements
m = number of balance planes

Downloaded 02 Jun 2010 to 171.66.16.112. Redistribution subject to ASME license or copyright; see http://www.asme.org/terms/Terms_Use.cfm

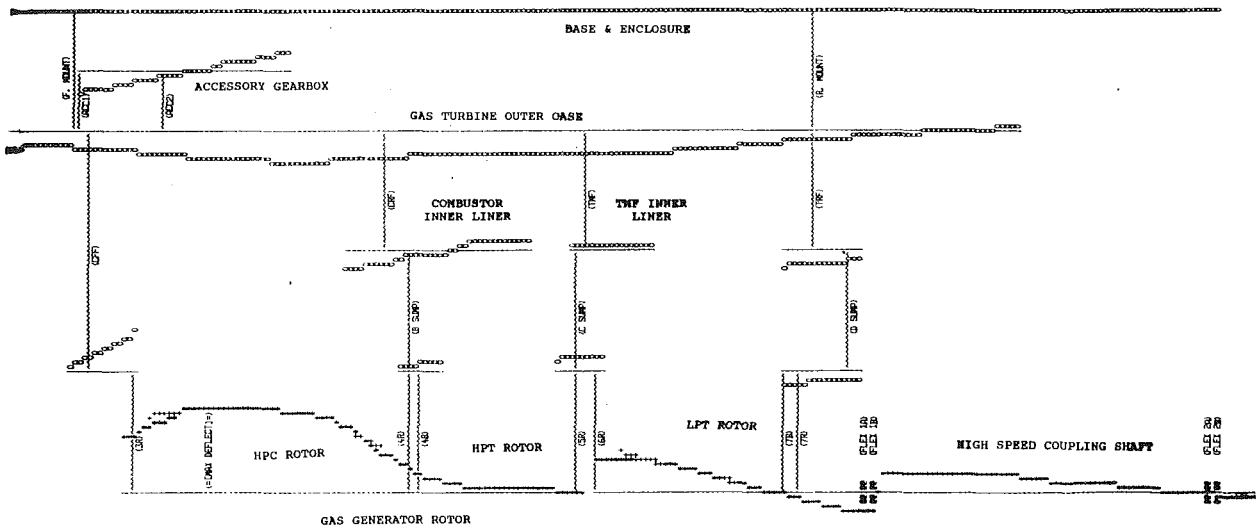


Fig. 1 LM2500 high pressure compressor rotor mode

the predicted residual vibration from the initial least-squares solution. A weighted least-squares solution is then calculated, Eq. (8), with a new set of predicted residuals. Equation (6) is then used to weigh these new residuals and another least-squares solution is made. In general, the iterations converge when the reduction of the maximum residual vibration becomes less than a predetermined limit

$$||X_i|_j - |X_i|_{j-1}|_{\max} < \text{Prescribed limit} \tag{9}$$

thereby reducing the maximum residual vibration. Generally, although not always, this iteration scheme converges.

Modifications to Least-Squares Method. In order to determine the effectiveness of the weighted least-squares iterative approach, Eq. (9), in minimizing the maximum residual vibration, several factors are calculated. These factors determine the direction the calculations are proceeding and the relationship between the "optimized" solution and the least-squares solution. One of these factors is the "Optimization Effectiveness" and is defined as follows:

$$\eta_{\text{opt}} = \frac{(\Sigma \text{ Squared residuals})_{\text{Least squares}}}{(\Sigma \text{ Squared residuals})_{\text{Weighted iteration}}} \tag{10}$$

Obviously, if the sum squared of the residuals for a weighted iteration gets larger than the sum squared of the residuals for the baseline, the solution is diverging and further computations are unnecessary. It has been found that a well-behaved optimized solution will exhibit a n (opt) of no smaller than 0.8. This means that the weighted iterations, in trying to minimize the maximum residual vibration, allowed the sum squared of the residuals to rise no more than 1.25 times the least-squares solution. Another tool used to determine the effectiveness of the optimized solution is to look at how the individual residual vibration estimates for each speed-point-sensor location are changing through the weighing process. This is done by the following factor

$$\eta_{\text{ratio}} = \frac{(X_{\text{Weighted Iteration } j})_i}{(X_{\text{Least squares}})_i} \tag{11}$$

If the weighted iterations are allowing vibration levels for most speed-point-sensor locations to increase for small reductions in vibration at one for two speeds or sensor locations, then this cannot be considered a well-behaved problem.

Results, calculated from Eq. (10) that are much less than 0.8 and/or large numbers calculated from Eq. (11) at important speed points, suggest that using the weighted iteration optimizing scheme, Eq. (8), is not the best solution. In these cases, using the least-squares solution or one of the weighted iterations off of it can give better results.

Application to the LM2500 Marine Gas Turbine

LM2500 Gas Generator Trim-Balancing. Trim-balancing aircraft derivative gas turbines, in particular the LM2500, required that some modifications be made to the influence-coefficient least-squares technique. It was learned early on in the process that there was no one solution for trim-balancing a given LM2500. For a typical LM2500 trim balance, there can be several solutions, some of which appear to be equally as good or bad. The possible solutions could be, for example, a weighted least-squares iteration scheme in which the maximum residual vibration is minimized, Eqs. (8) and (9); the unmodified least-squares solution, Eq. (5); or a weighted iteration off of the least-squares solution. A solution also could be just a vector average of all the single-sensor, single-plane corrections. Choosing the best solution requires more knowledge of the engine response behavior than is immediately available in the vibration data. The objective then was to create the tools necessary to effectively trim balance LM2500s, while at the same time minimizing the effort required.

To accomplish this goal a good understanding of the modal response of the LM2500 is required. This involved calculating system critical speeds and the associated mode shapes. To help determine the primary modes of LM2500 vibration a rotordynamic model that could produce mode shapes at the engine's critical speeds was created (Thompson and Badgley, 1988). A good set of generic LM2500 influence coefficients also was required for each balance plane (HPC stages 3 and 9) in the gas generator. Obtaining these coefficients would require a number of trial weight experiments. A trial weight experiment involved taking a baseline vibration survey of the engine (both amplitude and phase); then installing a weight in one of the balance planes. Finally, a trial weight vibration survey is done at exactly the same speed points where the baseline survey was performed. From the two vibration runs and the trial weight size and location, one can perform the vector calculation to determine the influence coefficient set through the engine running range, Eq. (1).

Once a stable set of influence coefficients had been acquired (in the LM2500's case 4 to 5 engines worth), a correlation needed to be developed between the influence coefficients and the engine's primary modes of vibration. A review of the analytically calculated vibration modes and the initial sets of influence coefficients showed that the primary vibration re-

Downloaded 02 Jun 2010 to 171.66.16.112. Redistribution subject to ASME license or copyright; see http://www.asme.org/terms/Terms_Use.cfm

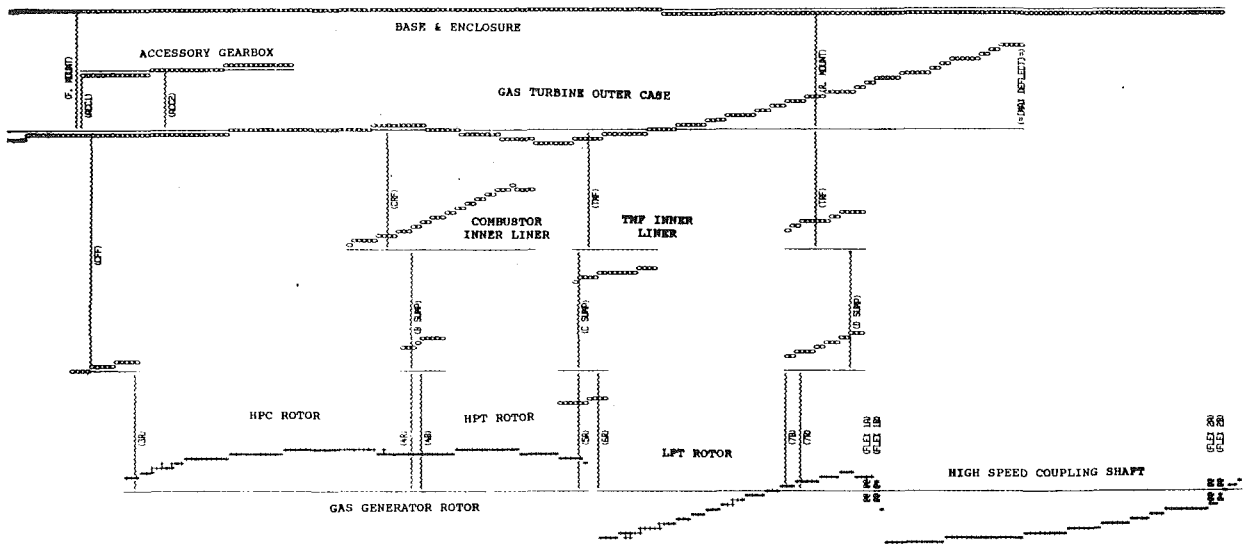


Fig. 2 LM2500 gas generator structural mode

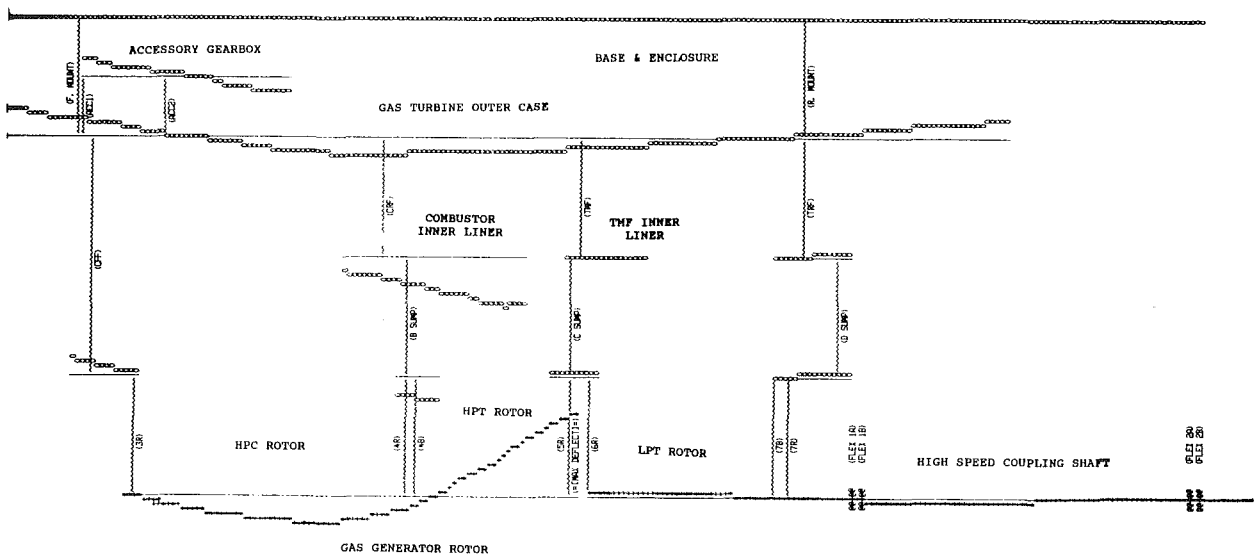


Fig. 3 LM2500 high pressure turbine rotor mode

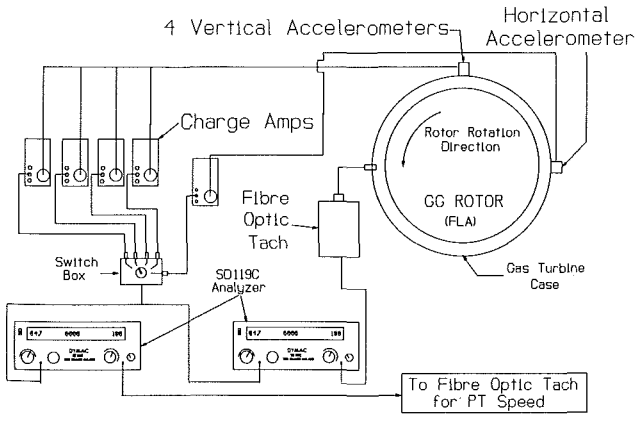


Fig. 4 LM2500 trim balance and vibration monitoring setup

sponse from 3 out of 4 modes, that are important in the gas generator running range, can be corrected by application of trim weights in a single plane. To optimize the trim balance of the LM2500 gas generator it became necessary to identify from a baseline vibration survey the predominant modes in a particular engine. Further correlations between the analytically calculated mode shapes and the initial sets of influence coefficients showed that the compressor bending mode, Fig. 1, the gas generator system mode, Fig. 2, and the compressor system mode could be corrected in a single balance plane in the compressor. The HPT mode, Fig. 3, cannot be corrected in a single plane in the compressor.

Figure 4 shows a typical LM2500 vibration survey equipment setup. Normally, this would consist of 4 or 5 engine case mounted accelerometers, SD-119 trim-balance analyzers (or equivalent), a set of 4 or 5 charge amplifiers, cabling and an optical sensor(s) to provide both engine speed and phase information. Figure 5 shows the general LM2500 configuration and the location of major components. An example of a typical LM2500 baseline vibration survey response is shown in Fig. 6. Figure 6 shows that TMF vibration is highest at 7000 rpm, due to the GG system mode, and CRF vibration is highest at 8250 rpm, due to the compressor modes. Correlating 2-D mode shapes and empirical data, it is clear that the same unbalance was causing both responses. Therefore, influence coefficients for the TMF sensor location at 7000 rpm and the CRF sensor location at 8250 rpm would have to reflect this. It also was found that the GG system mode does not exist if the primary unbalanced response is from the HPT mode. This is because the relationship between the stiffness of the 5R squeeze film

Downloaded 02 Jun 2010 to 171.66.16.112. Redistribution subject to ASME license or copyright; see http://www.asme.org/terms/Terms_Use.cfm

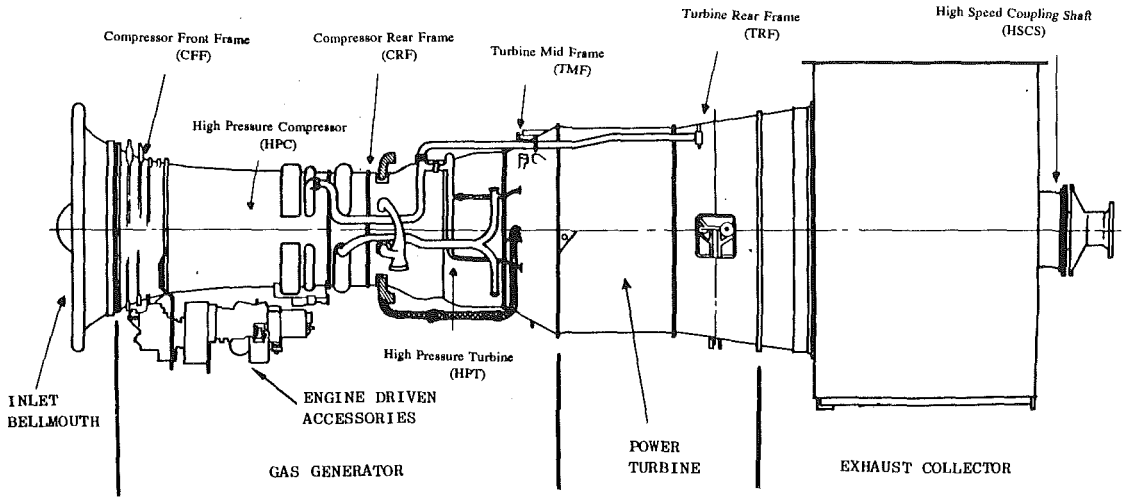


Fig. 5 LM2500 gas turbine configuration

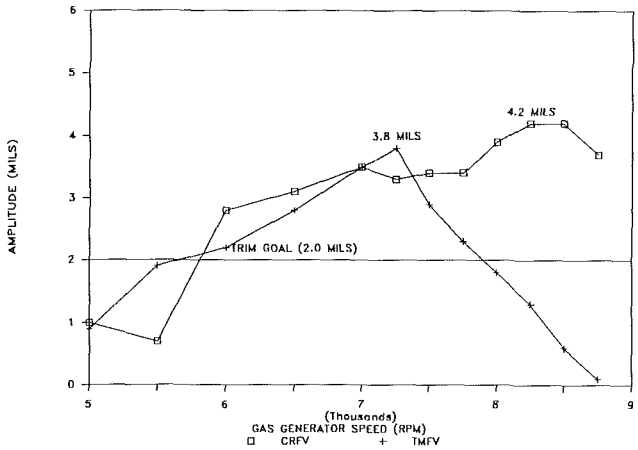


Fig. 6 Typical LM2500 vibration survey

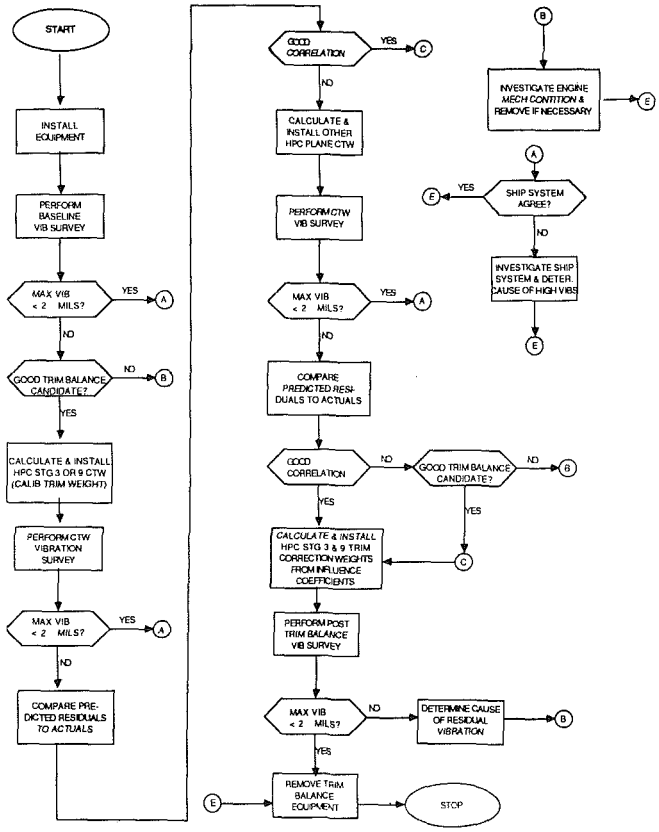


Fig. 7 Flow chart for LM2500 trim balance

damper bearing and the other stiffnesses in the system is different. There are other correlations such as this between sensor locations and speed ranges. These correlations defined a pattern of how the influence coefficients would change through the gas generator speed range for each sensor location and balance plane. These patterns were developed into sets of generic influence coefficients, with one set for each sensor location and balance plane. As empirical data were obtained they were selectively added to these sets.

Calibration Trim Weight Calculation (Gas Generators). The application of trim-balancing on LM2500 gas generators follows the outline defined in Fig. 7. Following the baseline vibration survey, which typically includes speed points from 5000 rpm to 9000 rpm, the size and location of a Calibration Trim Weight (CTW) is calculated and then installed in the engine. The objective of this trim weight is to minimize the vibration response of the engine and to gather engine specific influence coefficients, if further balancing is required. To calculate a CTW a series of guidelines are used as tools in this process. These include the correlations between vibration modes previously defined and phase correlations between sensor locations. Figure 8(*a*) shows the phase angle of the vibration for sensor locations CFFV and CRFV for compressor bending (unbalance) response. Figure 8(*b*) shows the phase angle of the vibration at the same sensors, but for a response in which the HPT mode is important.

To maximize the effectiveness of the Calibration Trim Weight a series of tools are used to determine if the vibration response can be corrected in a single plane on a particular engine. These tools were designed to be used along with the optimization effectiveness and optimization ratio factors, Eq. (10) and (11). Among these tools is a weighted sensitivity factor that is defined as follows:

$$S_i = X_i^* \frac{100}{\alpha_{i,m}} \text{ for } i = 1 \rightarrow n \tag{12}$$

$$S_w = \sum_{i=1}^{n} S_i \tag{13}$$

Downloaded 02 Jun 2010 to 171.66.16.112. Redistribution subject to ASME license or copyright; see http://www.asme.org/terms/Terms_Use.cfm

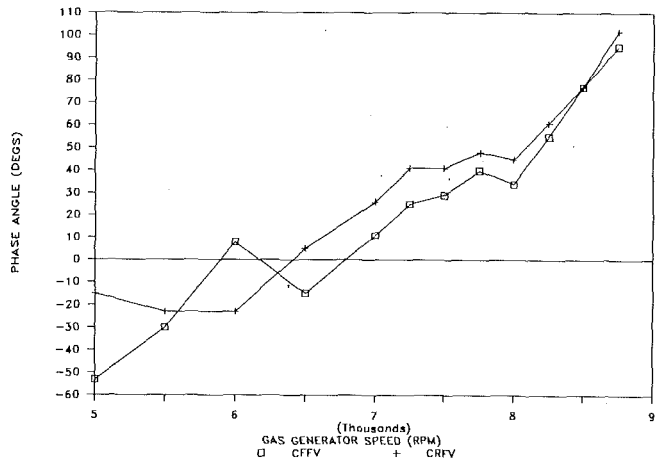


Fig. 8(*a*) Phase response between CFFV and CRFV sensors for HPC unbalance response

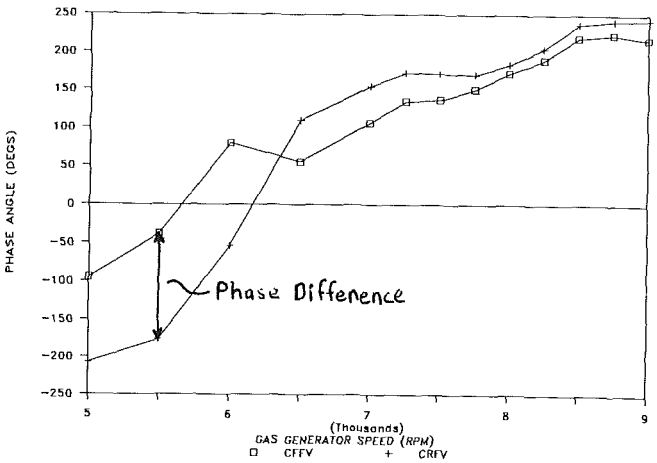


Fig. 8(*b*) Phase response between CFFV and CRFV sensors for HPT unbalance response

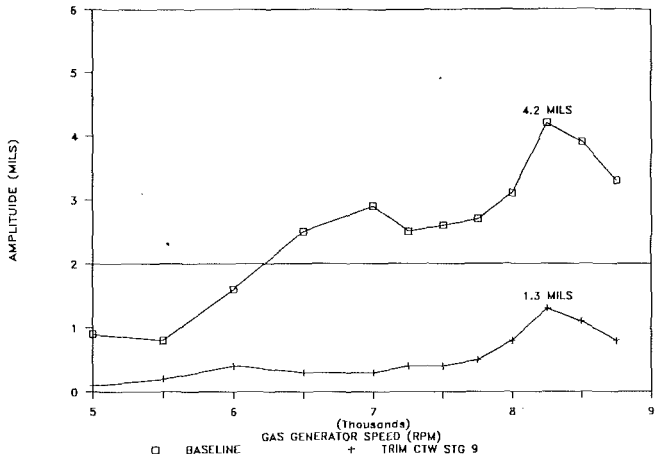


Fig. 9 First-shot trim-balance baseline and CTW HPC Stage 9

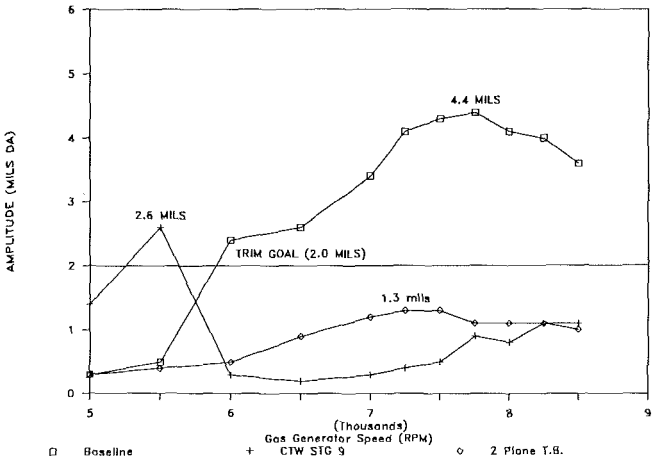


Fig. 10 Two-plane trim-balance baseline—CTW HPC Stage 9 and Two Plane Trim

Equation (12) defines the most important sensor locations—speed points on a particular engine, based on the particular influence coefficient and amplitude. Equation (13) is the summation of all these weighted sensitivity factors for each sensor location and speed point. A single-speed, single-sensor, single-plane trim weight can be calculated for each speed and sensor location as follows:

$$W_i = Z_i^* \alpha_{i,m} \text{ for } i = 1 \rightarrow n \tag{14}$$

A sensitivity-weighted vector average can then be calculated as follows:

$$W_{\text{ave}} = \sum_{i=1}^{n} \frac{S_i^* W_i}{S_w} \tag{15}$$

This trim weight calculation will typically give the single plane correction weight required to correct the primary response without any adjustment for modal characteristics. Its primary purpose is to be used as a comparison to the trim weights defined by Eq. (8). A set of predicted residuals based on the weight defined by Eq. (15) can be used to determine if there are any speed-sensor location regions that would be adversely affected by application of this single plane trim weight to correct the primary response.

In the typical application of these techniques to the trim balance of a LM2500 gas generator, it has been found that if the trim weight produced by Eq.(15) approximates the trim weight produced by Eq. (8) then the engine can be successfully balanced in a single plane. If this result is seen when calculating the Calibration Trim Weight (CTW) then the probability is very high that the engine can be trim balanced (to a level lower than the target) by the first shot weight. This has a significant impact in the level of effort required to trim balance LM2500 marine gas turbines.

Trim-Balance Direction After Calibration Trim Weight. Calculation of a Calibration Trim Weight (CTW) for the first-shot attempt to trim balance an LM2500 is a well-defined procedure as just discussed. If the first-shot trim weight is successful in reducing the peak vibration level below the target then, obviously, the procedure has been completed. If, on the other hand, the target goals have not been reached, then the procedure becomes one of analysis to determine the best possible direction to take. This analysis includes determining the cause of the unacceptable vibration due to the installation of the CTW. The possible directions include:

1 Install a CTW in the other balance plane.

2 Perform a two-plane balance solution using engine specific influence coefficients for one plane and generic influence coefficients for the other plane.

3 Calculate single-plane solution for the same plane the CTW was installed, using the engine specific influence coefficients.

The procedure for continuing the trim balance is less deterministic than for calculating the initial Calibration Trim Weight. Using options 1 and 3, one can use the same tools used to calculate the initial CTW.

Ultimately, for certain engines, it has been found that an

Downloaded 02 Jun 2010 to 171.66.16.112. Redistribution subject to ASME license or copyright; see http://www.asme.org/terms/Terms_Use.cfm

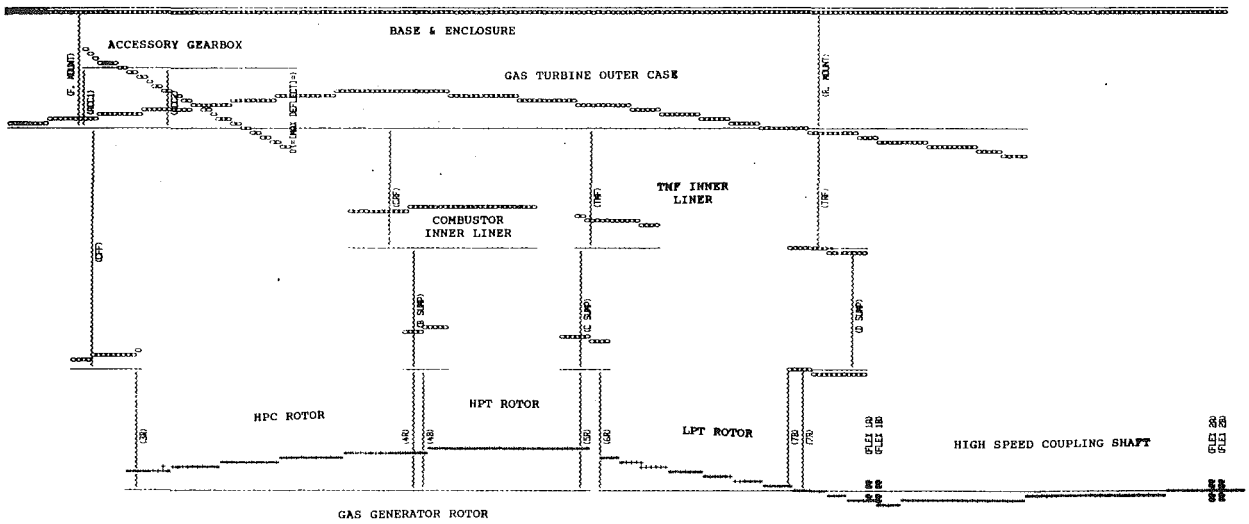


Fig. 11 LM2500 gas turbine structural mode (26 Hz)

acceptable vibration level cannot be obtained unless engine specific influence coefficients from both available balance planes are used to calculate a two-plane trim balance. In these cases, the primary vibration response is the result of unbalance exciting both the HPT mode as well as the compressor mode. Fortunately, the number of these engines, where this level of effort is required, is small and accounts for only 5–10 percent of the engines trim-balanced.

Results of Gas Generator Trim Balances. Figure 9 shows the effective application of a calibration trim weight to a LM2500 gas generator. Note that the trim-balance goals have been met with just one weight addition. This is the most cost-effective trim balance possible. Figure 10 shows the results of a two-plane trim balance where engine specific influence coefficients were used to calculate both balance weights. This type of correction was necessary because this engine showed vibration response from both the HPT unbalance mode and the HPC unbalance mode. This is the most difficult type of LM2500 trim balance to do because the HPT unbalance mode has an inherently nonlinear response.

Trim-Balancing LM2500 Power Turbines. The same trim-balancing techniques and tools that were applied to the gas generator also can be applied to trim-balancing the power turbine. The power turbine rotor/drive train system consists of the power turbine itself the High Speed Coupling Shaft (HSCS) and the reduction gear's input pinion shaft.

Power turbine rotor system response can be broken down into two parts. Unbalance response that excites the first gas turbine structural bending mode is a system mode that is a function of engine mount stiffness and overall gas turbine bending stiffness. Figure 11 shows this system mode, which nominally occurs at a frequency of 26 Hz. Typically, power turbine unbalance will excite this mode. Additionally, it is known that other nonsynchronous sources of vibration also will excite this mode. This includes combustor rumble and exhaust gas turbulence. The other part of the power turbine frequency vibration is what is known as the drive shaft mode. This mode typically occurs between 3000 and 3400 rpm, in the vertical direction. It is a function of the lateral stiffness of the flex couplings (in the HSCS), the effective engine mount lateral stiffnesses, and the stiffness of the first lateral support bearing on the input pinion shaft. Typically, the first lateral support bearing to the input pinion shaft is a plain journal bearing that only reacts the weight of the shaft it supports. This means that it may be lightly loaded; thereby have a low lateral stiffness with the resulting possibilities of high lateral vibration.

Another aspect of power turbine frequency vibration is that its response is highly dependent on the engine mount stiffness. The design of the LM2500 gas turbine installation, in the U.S. Navy, results in asymmetric mount stiffness properties between the vertical direction and the horizontal direction. This means that those modes, which are a function of mount stiffness, will occur at different speeds between the lateral directions. An example of this is the drive shaft mode, which nominally occurs at 3200 rpm in the vertical direction but occurs nominally at 2400 rpm in the horizontal direction. In the 2-D sense, for power turbine frequency vibration, the orbit of the engine is very elliptical.

The U.S. Navy's approach to power turbine trim-balancing is to reduce the unbalance driven response at 26 Hz. The 26 Hz mode is very sensitive to power turbine unbalance; sensitivities have been measured in the range of 50 g-in./mil. This means that modest buildup of dirt on power turbine blades or the addition of clips to the blades to correct interlock wear can add substantially to this response. To trim balance a power turbine, a power turbine frequency baseline vibration survey is performed, first. The speed range for this survey is typically from 1400 rpm to 3600 rpm. Initially, single engine operation is used until the engine torque limit is reached. Then another engine is brought on line to push the speed higher. Depending on ship class, four engines may have to be brought on line to get to a power turbine speed of 3600. To get accurate measurements of vibration amplitude and phase, it is required that normal engine torque loading be applied. It has been found that running the power turbine at low torque loads or unloaded through the speed range can give misleading results. The primary reason is that effective engine mount stiffness is a function of engine torque.

Good sets of generic influence coefficients have been developed for correction weights in the 6th stage of the power turbine. Figures 12(*a*) and 12(*b*) show the angle and the magnitude part of these coefficients for the CRF sensor location. It should be noted that the angle changes very rapidly through the 26 Hz mode and, as noted before, the sensitivity is very high. This is a typical response of a lightly damped structural resonance. Therefore, using the speeds near 26 Hz or 1560 rpm in the initial trim balance calculations is difficult. A small change in speed can result in a large change in angle and sensitivity. This causes problems because each individual engine has its first structural mode at a slightly different speed: again the effect of variations in engine mount stiffness. As a result, the speed points in the neighborhood of 1560 rpm are not used in the calculation of the CTW. The application of

Downloaded 02 Jun 2010 to 171.66.16.112. Redistribution subject to ASME license or copyright; see http://www.asme.org/terms/Terms_Use.cfm

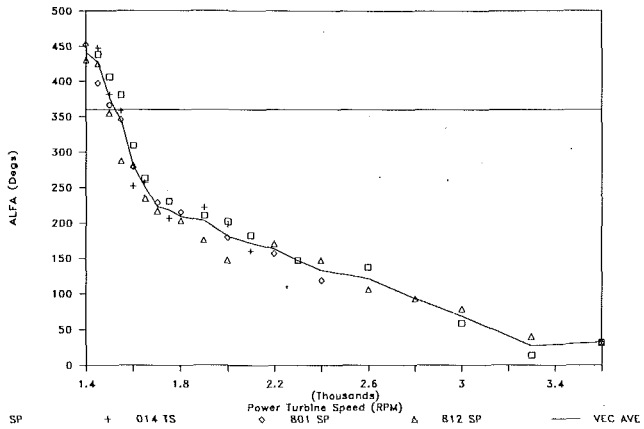


Fig. 12(*a*) Angle part of influence coefficient (ALFA) for LPT Stage 6

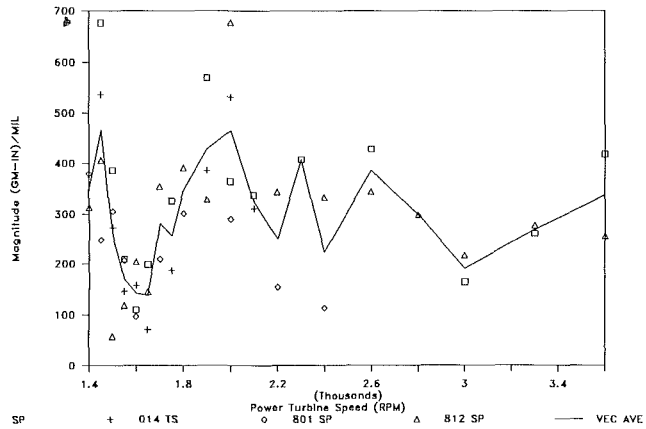


Fig. 12(*b*) Magnitude part of influence coefficient for LPT Stage 6

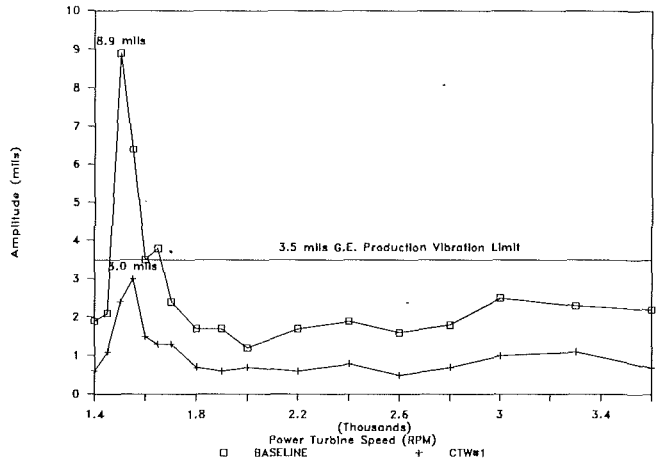


Fig. 13 Power turbine trim balance with no drive shaft mode response

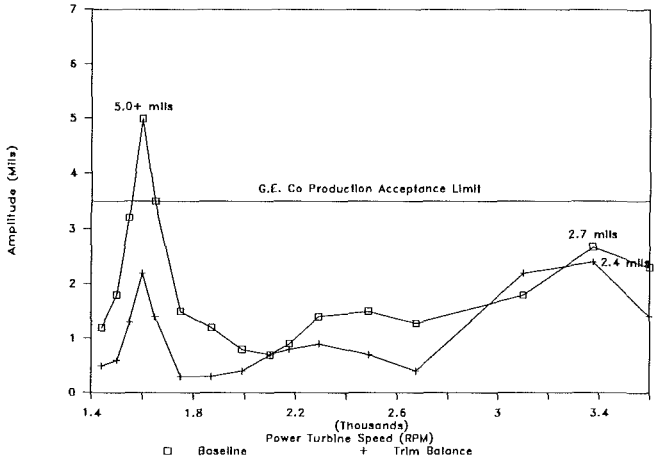


Fig. 14 Power turbine trim balance with drive shaft mode response

the CTW typically results in a large reduction of 26 Hz vibration response but it is usually not optimum. Optimum means the maximum reduction in vibration, without pushing up the vibration of other modes (other speeds). This approach to power turbine trim-balancing is structured in such a way that the CTW is on the light side of the optimum. After the installation of the weights, the CTW vibration survey is performed; from this, the specific influence coefficients for this power turbine can be calculated. Using the specific influence coefficients, the optimum trim-balance weight can be calculated. Because the CTW is kept on the light side of optimum, installation of the final correction weights entails installing additional clips to the CTW set.

Results of Power Turbine Trim-Balancing. Figure 13 shows the result of a power turbine trim balance where the only mode of importance was the 26 Hz mode. Note that the vibration reduction caused by the CTW was substantial but not optimum. Figure 14 shows the result of a power turbine trim balance where both the 26 Hz mode and the drive shaft mode are important. Note that there was substantial reduction in the 26 Hz mode but almost no reduction in the drive shaft mode.

Conclusions

The U.S. Navy, in particular NAVSEA, has developed the technology to effectively and economically trim balance LM2500 gas generators and power turbines. This technology is based on the Influence-Coefficient Least-Squares Method of trim-balancing over specified systems. Additions to this method involve incorporating the modal characteristics of the LM2500 gas turbine into the procedure. Also a method of accommodating the nonlinearities of the LM2500 has been incorporated. The method presented and the computer program developed to support it have been successfully used by U.S. Navy engineers and engineering technicians to trim balance over 50 LM2500 gas generators and power turbines.

References

Goodman, T. P., 1963, "A Least-Squares Method for Computing Balance Corrections," ASME Paper No. 63-WA-295.

Lund, J. W., and Tonneson, J., 1971, "Analysis and Experiments on Multi-Plane Balancing of a Flexible Rotor," presented at the ASME Third Vibrations Conference, Toronto, Canada.

Tessarzik, J. M., Badgley, R. H., and Anderson, W. J., 1974, "Flexible Rotor Balancing by the Exact Point-Speed Influence Coefficient Method," ASME *Journal of Engineering for Industry*, Vol. 94, No. 1, pp. 148–158.

Tessazik, J. M, and Badgley, R. H., 1974, "Experimental Evaluation of the Exact Point-Speed and Least-Squares Procedures for Flexible Rotor Balancing by the Influence Coefficient Method," ASME *Journal of Engineering for Industry*, Vol. 96, No. 2, pp. 633–643.

Thompson, B. D., and Badgley, R. H., 1988, "Application of an Advanced Rotordynamics Model to the Complete Structure of a Marine Gas Turbine Engine," ASME JOURNAL OF ENGINEERING FOR GAS TURBINES AND POWER, Vol. 110, No. 4, pp. 578–584.

Thompson, B. D., Badgley, R. H., and Raczkowski, R., 1989, "Methods and Procedures for Trim-Balancing the LM2500 Marine Gas Turbine in the Test Cell and Aboard Ship," ASME Paper No. 89-GT-318.

Downloaded 02 Jun 2010 to 171.66.16.112. Redistribution subject to ASME license or copyright; see http://www.asme.org/terms/Terms_Use.cfm

An Approach for Evaluation of Gas Turbine Deposition

R. A. Wenglarz
Allison Division of General Motors,
Indianapolis, IN 46206

An approach for estimating deposition in gas turbines is described. This approach extrapolates deposition data from lower cost experiments than turbine engine or cascade tests. The purpose is a method to screen candidate fuels and turbine protection methods so that only the most promising need be evaluated in turbine tests. The deposition approach is applied to estimate deposition maintenance intervals for a tested fuel, evaluate benefits of hot gas cleanup, and provide fuel screening criteria.

Introduction

In the past, combustion turbines have been among the most tolerant heat engines for ingestion of limited quantities of fuel and air-borne contaminants. For example, tolerable levels of flowpath deposition, erosion and corrosion (DEC) resulting in acceptable commercial maintenance intervals have been achieved for turbomachines operating with residual and crude oils and effluent from blast furnaces and catalytic crackers (Wenglarz, 1987a).

New applications are currently being explored for which turbines will operate with fuel-borne contaminants. Some of these applications (e.g., wood fuels, PFBC, direct coal-fired turbines) might require service with higher contaminant levels than for past commercial experience. Furthermore, turbine designs have been changing over the years to result in rising expander flowpath gas and surface temperatures and increasing gas velocities relative to vane and blade surfaces. Consequently, the severities of the turbine flowpath DEC environments are increasing.

The higher ash levels and increased complexity and variability of fuel ash chemistry for advanced fuels in addition to more severe flowpath environments for many future turbine systems will require much more testing than for past turbines to identify turbine protection approaches and achieve acceptable flowpath lifetimes. As to be discussed, costs would be very high to conduct these tests primarily using engine and cascade runs that have been utilized in the past to develop turbine capabilities to operate with alternate fuels.

Consequently, a supplemental and lower cost test and data extrapolation approach to evaluate turbine flowpath degradation has been developing in recent years (Wenglarz and Cohn, 1983; Wenglarz, 1987b). While turbine engine tests and sometimes cascade tests will always be needed for final verifications, the simplified approach can be used for screening to significantly reduce the number of these expensive tests. The cost and schedule for evaluating alternate fuels and turbine protection approaches can thereby be decreased. The following discusses in detail recent advances in the simplified approach and its application to evaluate deposition in an industrial turbine.

Contributed by the International Gas Turbine Institute and presented at the 36th International Gas Turbine and Aeroengine Congress and Exposition, Orlando, Florida, June 3-6, 1991. Manuscript received at ASME Headquarters March 4, 1991. Paper No. 91-GT-214. Associate Editor: L. A. Riekert.

Overview of Turbine Deposition Evaluation Approach

The degradation of turbine flowpaths due to fuel or air contaminants can be separated into two processes:

- Delivery of ash and contaminant material to turbine surfaces
- Interaction of delivered material with those surfaces

Interaction with surfaces includes sticking and buildup (deposition), impact removal (erosion) and chemical attack (corrosion). Turbine deposition, erosion, and corrosion (DEC) can be assessed by using and combining evaluations based on each of the two processes of delivery and surface interaction of foreign material in turbines. The discussion which follows describes such assessments for turbine deposition. Erosion and corrosion assessments are briefly described in an earlier paper (Wenglarz, 1987b).

Delivery of material to turbine airfoil surfaces can be calculated using multiphase flow models developed in recent years (Wenglarz, 1987b). These evaluations yield rates of delivery and arrival conditions (e.g., impact velocities and angles) versus particle characteristics (gas stream concentrations, size distributions, etc.). Relatively low cost experiments (compared to cascade or engine tests) are conducted using the fuel of concern with controlled particle impact rates and conditions on simple geometry specimens.

The mass fraction of delivered material that adheres to the surfaces (sticking fraction) and other data are measured for the specimens exposed to the same gas and surface temperatures as the turbine airfoil passage of concern. A simplified test facility, which has been used to obtain such deposition (and corrosion) data for two turbine rows, is illustrated in Fig. 1.

Information including measured sticking fraction versus impact conditions and calculated impact rates and conditions for the airfoil are then combined to estimate deposition in the airfoil row. This turbine deposition evaluation approach is described in detail in the Appendix. The following gives applications of the approach.

Applications of Approach

The following evaluations using the simplified test/data extrapolation approach will be described:

(*i*) Estimates of the deposit removal maintenance interval for a tested coal-water fuel

Copyright © 1992 by ASME
Downloaded 02 Jun 2010 to 171.66.16.112. Redistribution subject to ASME license or copyright; see http://www.asme.org/terms/Terms_Use.cfm

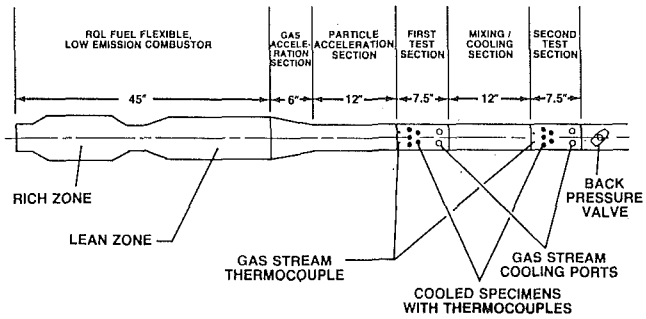


Fig. 1 Simplified deposition, erosion, corrosion test facility

(*ii*) Projection of particle cleanup system effects on fuel ash sticking fractions necessary for a specified turbine maintenance interval to remove deposits

(*iii*) Fuel screening criteria for deposition that is applicable to a wide range of fuels for a specified turbine

Maintenance Interval for a Tested Fuel. The facility described earlier was used to test coal-water fuels with coal ash levels cleaned to the vicinity of 1 percent. No hot gas cleanup system was used to remove particulate from the fuel combustion products before entering the deposition test sections. Details of physical (Wenglarz and Fox, 1990a) and chemical (Wenglarz and Fox, 1990b) aspects of deposition and corrosion from these fuels are described elsewhere. Figure 2 indicates a histogram of the mass distribution of products of combustion particulate captured with an isokinetic particle probe for a combustion test, which achieved over 99 percent combustion efficiency. Data from deposition tests conducted with a fuel formulated from the same coal feedstock indicated a fuel ash sticking fraction of 0.06 for the gas and surface temperatures of the first stator of a 5000 hp industrial turbine. Deposit density for specimen upstream surfaces was measured to be 1.9 g/om^3. Since deposit thicknesses were more than an order of magnitude less on downstream specimen surfaces than on the upstream surfaces, inertial impaction deposition was seen to dominate over other mechanisms of particle delivery (turbulent diffusion, Brownian diffusion, etc.). This indicated that the data extrapolation approach described here applies to the tested coal-water fuels (see conditions of applicability in Appendix).

Application of the deposition data extrapolation approach to the turbine first stator passages, which conditions were represented in the test, resulted in an estimated turbine deposit removal maintenance interval of less than one hour for the tested fuels. In many cases, a practical turbine deposit removal maintenance interval using on-line nutshelling might be no less than daily (24 h). This interval is much longer than that estimated for the fuels tested without a hot gas cleanup system to remove particulate.

Cleanup System Effects. Hot gas cleanup increases the allowable ash sticking fraction for a specified maintenance interval due to reduction of the amount of ash material that would enter a turbine and be delivered to the turbine airfoil surfaces. The following evaluates whether use of inertial separators [only proven hot gas cleanup devices up to 1100°C (2000°F)] might remove sufficient particulate to result in a one day deposition maintenance interval for the coal-water fuels which tests were described in the last section.

A simple factoring of the sticking fraction and maintenance interval by the reduced gas stream particle concentrations entering the turbine often does not adequately represent the benefits of hot gas cleanup. This is because most cleanup systems remove a higher percentage of larger particles than smaller particles. Since a greater fraction of larger particles than smaller particles is delivered to turbine surfaces, the benefits of most

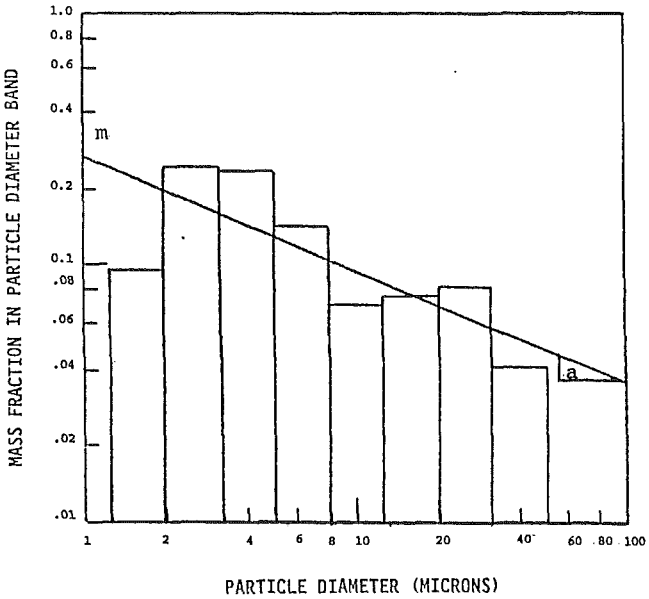


Fig. 2 Measured POC distribution from 1 percent ash CWF

cleanup devices are more than proportional to the reduction in particulate levels entering the turbine.

Performance characteristics of a particulate cleanup device are often described using its grade efficiency curve. This curve gives the fraction of particulate removed by the device versus particle diameter. The grade efficiency curve for inertial separators can usually be adequately represented by an exponential function. Expressed in terms of physical performance parameters, this function can be written:

$$\text{grade efficiency} = 1 - \exp[-1.609(D^2 - D_0^2)/(D_{80}^2 - D_0^2)] \quad \text{for } D \geq D_0$$

$$= 0 \quad \text{for } D < D_0$$

where D_{80} is the particle diameter for which the grade efficiency is 0.8 (80 percent capture) and D_0 is the particle diameter for which the grade efficiency is zero (no capture).

Particle loadings and size distributions entering the 5000 hp turbine for cyclones located between the combustor and turbine were estimated for the coal-water fuel, which tests were described in the last section. These evaluations considered that a full-scale combustor operated with this fuel would produce a similar size distribution curve to that measured (Fig. 2) in the subscale combustor tests of the fuel. The cyclone grade efficiencies (expressed in terms of D_0 and D_{80}) were applied to the POC distribution in Fig. 2. The resulting loadings and distributions, together with Eq. (A-1) in the appendix, were used to project the fuel ash sticking fractions required to achieve a one day deposit removal maintenance interval. Deposition maintenance was assumed necessary in this and following evaluations at a 10 percent loss in turbine power.

Figure 3 gives the results of these evaluations for an expected bounding range of performance parameters, D_0 and D_{80}, corresponding to cyclones sized to clean the combustor flow of the 5000 hp turbine. The upper range of cyclone performance somewhat exceeds that (D_0 = 1.7 microns, D_{80} = 7 microns) for high efficiency Stairmand cyclones tested at the Grimethorpe coal-fired PFBC plant (Wheeldon and Burnard, 1987) which are about the size required for the 5000 hp turbine.

Figure 3 shows that cyclones can increase by a factor up to 4, the sticking fraction needed to achieve a one day deposition maintenance interval for the fuel tested. However, Fig. 3 also shows that the needed sticking fraction for the fuel ash is still much less than the measured value (0.06) indicated in the last

Downloaded 02 Jun 2010 to 171.66.16.112. Redistribution subject to ASME license or copyright; see http://www.asme.org/terms/Terms_Use.cfm

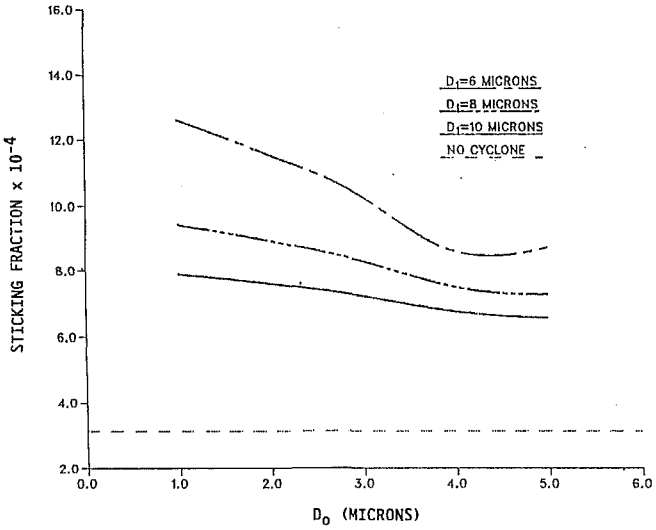


Fig. 3 Sticking fraction for one day deposition maintenance interval versus cyclone performance

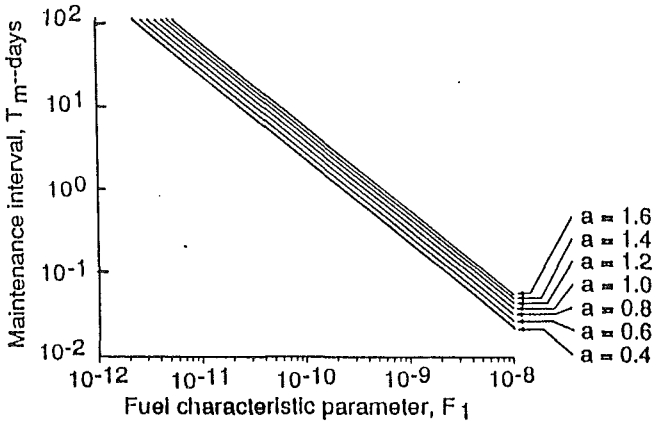


Fig. 4 Fuel screening curves for deposition in 5000 hp turbine

section. Consequently, the simplified deposition test and data extrapolation method indicate that the 1 percent ash coal-water fuels tested will not likely provide the desired one day maintenance interval even for cyclone cleanup of the combustor effluent. This evaluation of cyclone effects was obtained without the significant additional cost of fabrication, installation, and running tests with these devices.

A sensitivity analysis of the maintenance interval relations (see Appendix) has been used to identify the most promising approaches to control turbine deposition from coal-water fuels. Simplified deposition, erosion, and corrosion tests have shown that some of these deposition control approaches could substantially reduce deposition compared to that for the early test fuels which were described in the last section. Other deposition control approaches yet to be evaluated in the simplified tests are expected to significantly further reduce deposition.

Fuel Screening Criteria. Prospects for acceptable deposit removal maintenance intervals were just described using simplified tests of a particular coal-water fuel. The data extrapolation approach will now be generalized to identify deposition screening criteria for the same turbine and other fuels evaluated in a simplified test facility.

The straight line in the log-log plot in Fig. 2 can be used to approximate the product of combustion (POC) mass distribution described by the histogram. In general, this and most POC distributions (other than those passing filters) can (for fuel screening purposes) be adequately represented by such a straight line. This is because relatively large percentage errors for small particle fractions often have a small effect on deposition due to the low particle delivery rates (and contribution to deposition) for small diameters. Also, relatively large percentage errors for the large diameter end of the distribution often have a small effect on deposition because of the low concentrations of large particles.

The straight line in Fig. 2 can be represented by the two parameters, a (slope of line) and m (intercept at a particle diameter of one micron). However, since the sum of the mass fraction contributions for all particle diameters is equal to 1, m and a are not independent. Consequently, m can be expressed in terms of a so that the turbine maintenance interval T_m can be written:

$$T_m = \frac{F_2\ (\text{turbine},\ a)}{F_1\ (\text{fuel, cleanup})}$$

where

$$F_1 = \mathrm{Srf}(1-e)/\rho_d$$

$$F_2 = d_{\max}\Big/\left(\rho \sum_{1}^{n} m_i V_i\right)$$

and the terms in F_1 and F_2 are defined in the Appendix.

The function F_1 primarily involves parameters representing fuel characteristics (e.g., sticking fraction S and deposit density ρ_d) as measured in simplified deposition tests in addition to an inertial separator overall particle removal efficiency e. The function F_2 primarily reflects flowpath deposition characteristics, such as throat dimension and deposition velocities V_i, determined from particle delivery analyses for the stator passage.

The deposition maintenance interval T_m can be plotted for various values of a as a function of fuel characteristic parameter F_1. Such a plot (shown in Fig. 4) provides a fuel (and cleanup system) screening criteria for the specified turbine, using properties for a fuel measured in a simplified DEC test. The fuel is arbitrary within the class that primarily produces impaction deposition as it is for most alternate fuels tested to date (e.g., resid oils, coal-derived liquids, and coal-water fuels). In many cases, the effects of inertial separators can be adequately estimated without actually utilizing separators in the simplified DEC test. As was demonstrated in the last section, predicted or measured grade efficiencies (particle removal efficiencies versus particle diameter) can be applied to the measured POC distributions from the test to obtain predicted size distributions (e.g., value of a) entering the turbine and the overall removal efficiency e.

Past test experience with alternate fuels has shown that, for an unknown fuel, there can be the four orders of magnitude uncertainly in turbine deposition maintenance interval that is shown in Fig. 4. Consequently, application of the screening approach just described could be used to eliminate from consideration the worst fuels and reduce the number of fuels, cleanup systems, etc., that need to be evaluated in expensive engine or cascade tests.

Discussion

An approach has been described which extrapolates deposition data from simplified deposition, erosion, and corrosion test facilities to estimate maintenance intervals in gas turbines. The equipment costs for such simplified facilities are significantly lower than up to $500,000 for cascade facilities and $1,000,000 for moderate size (5000 hp) turbine facilities. Operation costs also can be significantly lower for the simplified facilities than several thousand dollars per hour for cascade tests and the order of $10,000 per hour for engine runs. Op-

Downloaded 02 Jun 2010 to 171.66.16.112. Redistribution subject to ASME license or copyright; see http://www.asme.org/terms/Terms_Use.cfm

eration costs are particularly important because the development of a new ash bearing fuel for turbines can require extensive testing. For example, over 7300 hr of engine runs were conducted in an early coal-fired turbine project in Australia (Cohn, 1985). Even more testing might be expected for modern turbines, which have up to 240 m/s (800 fps) higher gas velocities, 390°C (700°F) higher gas temperatures, and 280°C (500°F) higher surface temperatures.

No laboratory physical or chemical analyses of new fuels are known that can be used to estimate turbine deposition rates or even whether or not significant deposition will occur. For example, deposition rates for the coal water fuels mentioned earlier were determined to be very high in simplified deposition tests, even at a reduced gas temperature of a turbine first rotor. This temperature was over 190°C (350°F) below the coal ash initial deformation temperature as measured with the standard ASTM procedure developed for coal boiler plant fuels.

The turbine deposition evaluation approach discussed here is at a relatively early stage of development and would not be expected to provide as accurate deposition evaluations as cascade or engine tests. However, deposition predictions with bounding uncertainties, a factor of four or higher, can provide valuable information for screening fuels or turbine protection approaches. A relatively inexpensive test approach would be useful if it shows whether the turbine maintenance interval in hours is in the 0.1–0.4, 1–4, 10–40, 100–400, or 1000–4000 range. Such extremes in projected maintenance intervals have been indicated from tests of coal derived liquids (Mulik et al., 1985) and coal water fuels (Wenglarz and Fox, 1990a).

The deposition evaluation of the coal water fuel, previously described, projected a deposit removal maintenance interval of less than 1 h compared to minimum objective of 24 h. Should the prediction uncertainty be up to a factor of 5, the fuel would still be judged unacceptable, even for the use of cyclone separators. Although the same conclusion could have been obtained with more precise data from cascade or engine tests using cyclone separators, the cost would have been much higher.

An earlier version of a simplified deposition test data extrapolation approach has been shown to produce estimated deposition maintenance intervals for residual oils in the range of turbine field experience for such fuels (Wenglarz and Cohn, 1983). The approach described here improves prediction accuracy over the earlier version. Current plans are to compare predicted deposition using this improved approach with that measured from runs of a test turbine engine. Refinements also are being pursued for application to turbine operation with hot gas filters.

Acknowledgments

This work and its description were supported by the Allison Division of General Motors and the U.S. Department of Energy (DOE), Morgantown Energy Technology Center from the Advanced Coal-Fueled Turbine Systems Program. The DOE project manager for this program is Paul Micheli and the Allison project manager is Colin Wilkes.

References

Cohn, A., 1985, "Workshop Proceedings: Direct Coal-Fired Combustion Turbines," EPRI Report AP-3939-SR, Apr.

Mulik, P. R., Wenglarz, R. A., et al., 1985, "Coal-Derived Liquid Fuel Performance Under Gas Turbine Conditions," *Energy Progress*, Vol. 5, No. 3, Sept., pp. 136–142.

Wenglarz, R. A., and Cohn, A., 1983, "Turbine Deposition Evaluations Using Simplified Tests," ASME Paper No. 83-GT-115.

Wenglarz, R. A., 1987a, "Direct Coal-Fueled Combustion Turbines," ASME Paper No. 87-GT-269.

Wenglarz, R. A., 1987b, "Turbine Deposition, Erosion, and Corrosion Evaluations Using a Simplified Test Approach," ASME Paper No. 87-GT-214.

Wenglarz, R. A., and Fox, R. G., Jr., 1990a, "Physical Aspects of Deposition From Coal-Water Fuels Under Gas Turbine Conditions," ASME JOURNAL OF ENGINEERING FOR GAS TURBINES AND POWER, Vol. 112, pp. 9–14.

Wenglarz, R. A., and Fox, R. G., Jr., 1990b, "Chemical Aspects of Deposition/Corrosion From Coal-Water Fuels Under Gas Turbine Conditions," ASME JOURNAL OF ENGINEERING FOR GAS TURBINES AND POWER, Vol. 112, pp. 1–8.

Wheeldon, J. M., and Burnard, G. K., 1987, "Performance of Cyclones in the Off-Gas Path of a Pressurized Fluidized Bed Combustor," *Filtration and Separation*, May/June, pp. 178–187.

APPENDIX

Turbine Deposition Projection Method

Maximum Allowable Deposit Thickness. Figure A-1 represents airfoil cross sections in the first stage of a turbine. The concave pressure surfaces and convex suction surfaces on the airfoils are indicated along with the throat location of the minimum flow area through the passages. Deposition at the first stator vane airfoil locations bounding the throats is most significant because it reduces the total mass flow through the turbine and overall power loss. Airfoil aerodynamic performance also is degraded most by deposit buildup on trailing-edge regions.

The effect of throat reduction and decreases of aerodynamic performance on the overall power loss due to deposition for a specific turbine can be determined by using the same aerodynamics computer code used to design the vanes. Once a maximum allowable turbine power loss is specified (such as 10 percent), the maximum allowable combined deposit thickness on the pressure and suction throat surfaces is determined. Dividing the maximum allowable combined deposit thickness by the combined pressure surface and suction surface thickness buildup rates at the throat yields the deposit removal maintenance interval needed to restrict the turbine power loss to the prescribed maximum allowable value.

Deposit Buildup. The delivery rate of particles to the suction surface throat region is much less than the delivery rates to the pressure surface throat region except for small particle

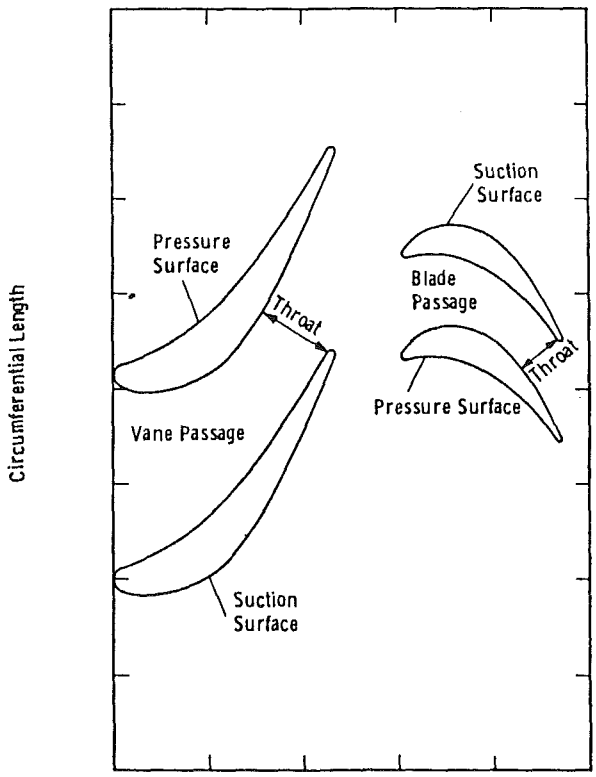


Fig. A-1 Turbine first-stage airfoils

Downloaded 02 Jun 2010 to 171.66.16.112. Redistribution subject to ASME license or copyright; see http://www.asme.org/terms/Terms_Use.cfm

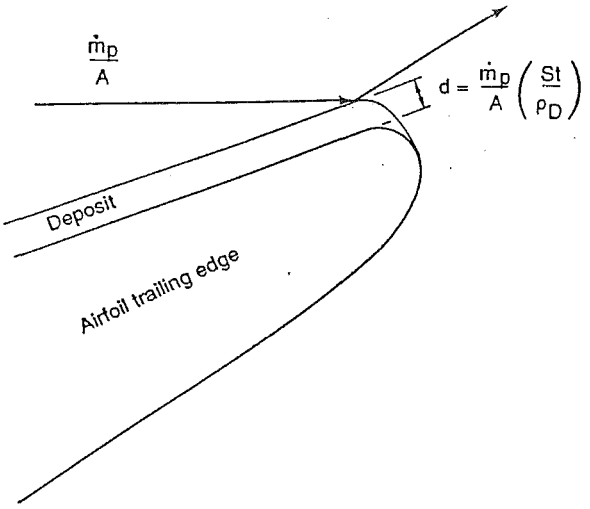


Fig. A-2 Deposition at pressure surface throat boundary

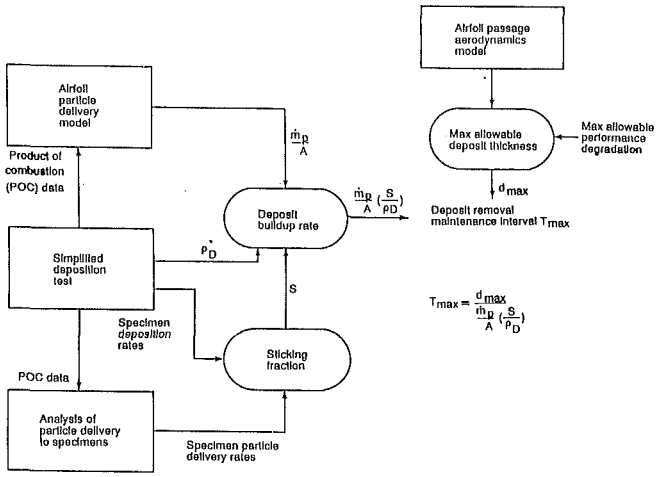


Fig. A-3 Procedure for deposition evaluations using simplified tests

distributions passing filters. Hot gas filters are being evaluated for turbine applications but have not yet been developed. Consequently, in many cases, suction surface deposition can be neglected compared to deposition on the pressure surfaces. Figure A-2 illustrates deposit buildup at the pressure surface throat surface. Particulates arrive at mass delivery rates per unit area of $\dot{m}_p/A$. The overall sticking fraction is S for the arriving particles that contribute to buildup of the deposit with density ρ_d. The deposit thickness d at time t is given by the product of mass delivery rate, sticking fraction, and time divided by the deposit density. Setting the deposit thickness to the maximum allowable throat blockage $d_{\max}$ (obtained as described previously) for the specified allowable turbine power loss and solving the resulting equation for the turbine maintenance interval T_m gives

$$T_m = \frac{d_{\max}}{\frac{\dot{m}_p}{A}\frac{S}{\rho_d}} \tag{A-1}$$

Simplified Test Facility. The following describes how the terms in the previous equation are obtained through simplified and relatively low cost deposition, erosion, and corrosion (DEC) tests to yield turbine maintenance interval estimates. Figure 1 shows a simplified DEC test facility developed in the past at Allison Division of General Motors. A subscale combustor is operated with the fuel of concern. The combustion stream is accelerated to turbine inlet flow velocities prior to entering the first test section. Several cooled, wedge-shaped specimens are exposed in the test section at gas and surface temperatures of the first stator vanes of the turbine of concern. The specimens are constructed with the alloys and coatings of the turbine represented and candidate alternate materials for improved DEC performance. Air is injected at the exit of the first test section to adjust the inlet temperature entering the second test section to the value of a downstream turbine row. The materials and surface temperatures of specimens used in the second test section are the same as those in the represented turbine row.

Turbine Deposition Estimates. Figure A-3 illustrates how data from simplified tests are used for turbine maintenance interval estimates. Specimen weight gain rates due to deposition, deposit density, ρ_d, and products of combustion (POC) data are obtained from the simplified tests. The POC data can be obtained using an isokinetic probe to capture combustion product particulate. The particle size distribution (which can be measured with a Coulter Counter) and ash density are used in a multiphase flow analyses for the specimens to determine the mass arrival rates of material carried to the specimen surfaces. The sticking fraction S is computed as the ratio of deposit mass buildup rates to ash mass arrived rates on the specimens.

The POC data from the simplified test or POC data from a turbine scale combustor operated with the same fuel is used to estimate the POC mass characteristics entering a turbine operated with the same test fuel. These POC characteristics can be modified to represent the effect of hot gas cleanup prior to the turbine. Particle delivery analyses are then used to compute the mass delivery rates for each particle size band to the first stator throat boundaries of the turbine being evaluated. The summation of these delivery rates over all the size bands of the POC distribution yields the total mass delivery rate $(\dot{m}_p/A)$.

$$\frac{\dot{m}_p}{A} = \rho r f (1-e) \sum_{1}^{n} m_i V_i \tag{A-2}$$

where

ρ = gas density entering the passage
r = fuel to air mass ratio
f = ash to fuel mass fraction
e = particle removal fraction for cleanup system
n = number of particle size bands in a histogram representing the particle size distribution
m_i = mass fraction of particles in band i of the histogram
V_i = deposition velocity for the median particle diameter of band i

The deposition velocities V_i, $i = 1$ to n are determined for the turbine passage using multiphase flow analyses.

The foregoing procedure gives all the quantities in Eq. (A-1) needed to compute the turbine deposit removal maintenance interval.

Downloaded 02 Jun 2010 to 171.66.16.112. Redistribution subject to ASME license or copyright; see http://www.asme.org/terms/Terms_Use.cfm

An Investigation in the Variance in Particle Surface Interactions and Their Effects in Gas Turbines

A. Hamed
Department of Aerospace Engineering and Engineering Mechanics, University of Cincinnati, Cincinnati, OH 45221

This work presents the results of a study conducted to investigate particle surface interaction characteristics and their effects on the particle dynamics and blade erosion in axial flow gas turbines. The particle restitution velocities measured experimentally using Laser Doppler Velocimetry in a special tunnel are analyzed using statistical methods. The resulting distribution functions of the rebounding particle velocities after surface impacts are introduced in the particle trajectory simulations through the turbine blade passages, using a methodology that combines particle dynamics computations in a probabilistic model. The presented results for the simulated ash particle dynamics demonstrate the effect of the experimentally measured variance in the particle restitution characteristics on the particle surface impacts, and the associated blade erosion in an axial flow turbine.

Introduction

The flow in gas turbines is frequently laden with solid particles in many applications. Sand, dust or volcanic ash can be ingested into the engine from their surroundings or particles also can be by-products of combustion in many advanced fuels. Because of their higher inertia, the particles tend not to follow the flow streamlines in the blade passages, and to impact the blade surface and the inner and outer annulus (Hamed et al., 1988). The erosion and increased roughness of the impacted surfaces lead to a loss in aerodynamic performance (Tabakoff, 1984). In particular, the pitting and cutting of the blade leading and trailing edges and the increased tip clearance have detrimental effects on the performance (Tabakoff et al., 1990), and the blade life in case of severe erosion damage. Experience with coal-burning gas turbines have shown that even the small ash particles of diameters between one and 30 microns, can be very damaging to the exposed turbine components. It is often very difficult to remove these particles from the gas stream with conventional separation techniques without excessive penalties in performance.

The prediction of blade erosion in multistage turbomachines presents a very difficult problem. The blade-erosion pattern is generally complex as it depends on many factors such as the blade row location, blade geometry, particle characteristics, blade material, and flow conditions (Hamed et al., 1988; Tabakoff, 1984). The erosion of metals by solid particle laden flow have been investigated experimentally under different values of flow parameters that affect the erosion rate (Hamed et al., 1988; Tabakoff et al., 1980). The results of these investigations indicate that the erosion rate is affected by the impacting velocity, impingement angle, the metal and gas temperatures and by the particle and target materials. The experimental erosion data can be used to predict blade erosion if the particle impact locations, as well as their impacting velocities and impingement angles relative to the blade surfaces, are known.

The first particle dynamics simulations conducted by Hussein and Tabakoff (1973) demonstrated the effects of particle size, material density and initial velocity on their trajectories. More recently, Hamed (1989) modeled the secondary flow effects which were found to be significant on the simulated trajectories of ash particles and the associated blade erosion for smaller particles. In all these simulations, the equations governing the particle motion are integrated numerically in the flow field and their rebounding velocities after surface impacts are determined from empirical correlations that represent the experimentally measured rebound velocities (Tabakoff et al., 1974; Kotwall and Tabakoff, 1985).

At present, gas particle flow analysis procedures are deterministic in nature. They are based on the supposition that the particle trajectory in the flow field is uniquely determined by the particle's physical characteristics and its initial conditions. However, many of the parameters affecting the particle dynamics including the particle rebound characteristics and the particle-size exhibit variance, whose probability distribution functions can be determined experimentally. In these deterministic simulations, a unique value for the rebound velocity and angle is associated with each particle surface impact, based on empirical correlations of the mean value of the experimentally measured particle restitution parameters. Experimental results indicate that the rebound characteristics for a given particle target material combination (Tabakoff, 1989) exhibits variance at a fixed text condition. The exhibited variance in the experimentally measured particle rebound characteristics, therefore, is not represented in the simulations. Besides causing erosion, the particle surface impacts affect subsequent particle trajectories and their distribution in the flow field (Hamed, 1988).

Contributed by the International Gas Turbine Institute and presented at the 36th International Gas Turbine and Aeroengine Congress and Exposition, Orlando, Florida, June 3-6, 1991. Manuscript received at ASME Headquarters March 11, 1991. Paper No. 91-GT-380. Associate Editor: L. A. Riekert.

Copyright © 1992 by ASME
Downloaded 02 Jun 2010 to 171.66.16.112. Redistribution subject to ASME license or copyright; see http://www.asme.org/terms/Terms_Use.cfm

The purpose of this work is to develop a better understanding of the interactions between particulate flows and solid surfaces. Theoretical and experimental studies are combined to determine the probabilistic nature of these interactions and their influence in coal-burning gas turbines. The experimental work was conducted in an especially designed particulate flow wind tunnel in which the velocity, temperature, particle concentration and target orientation can be changed systematically. The particle impact and rebound velocities are measured using a nonintrusive LDV (Laser Doppler Velocimeter) system. The probability density distribution functions for the measured particle restitution parameters are determined through a statistical analysis of the rebound data. A numerical procedure is developed that combines the particle dynamics computations in a probabilistic model to simulate the experimentally observed variance in the particle restitution characteristics. The results of the computations demonstrate the influence of these surface interactions on the particle trajectories. Results also are presented for the associated distribution functions of the blade surface impact parameters, frequency, and blade surface erosion, and their sensitivity to the experimentally determined variance in the particle rebound characteristics.

Experimental Investigation of Particle Surface Interactions

The experimental investigation was conducted to measure the particle rebound characteristics after surface impacts. A target sample of the blade material is placed in the particulate flow wind tunnel equipped with a glass window for particle velocity measurements. The tunnel is designed to perform the particle surface interaction tests under varying impact velocities and impingement angles (Tabakoff and Wakeman, 1979). The particle incoming and rebound velocities are measured very close to the impacted target surface using laser-Doppler velocimetry (Tabakoff et al., 1987).

The experimental setup consists of the tunnel, with its particle feeder, the LDV and optics, and the data acquisition system (Tabakoff, 1989). Referring to Fig. 1, the tunnel functions as follows: The particles from the feeder A, are introduced into a secondary air source and carried up to the particle injector C, where it mixes with the main air supply B. The particles are then accelerated by the high-velocity air in a constant-area duct D, and impact the specimen in the test section E. The particles are then separated from the air by a cyclone separator G, and collected in the container H. The test air is further filtered through a commercial 5-μm filter F. The test section is designed so that the particle-laden air is channeled over the specimen and the aerodynamics of the fluid, surrounding the blade sample, are preserved. This section contains several interchangeable inserts so that the flow properties can be determined using conventional instrumentation.

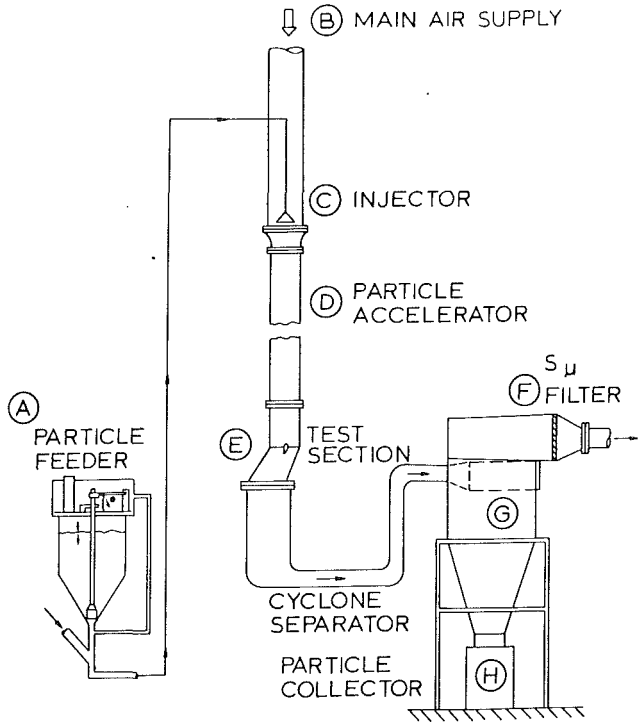


Fig. 1 Particulate flow tunnel used in the experimental investigation of particle surface interactions

Particle Restitution Measurements. A laser-Doppler velocimetry system was used to determine the magnitude and direction of the particles rebounding velocities. A five Watt argon-ion Spectra Physics, model 164-09 laser tube is used as the light source. The optical components of the laser-Doppler velocimeter are arranged in the backward scatter mode to measure three simultaneous velocity components of a single particle. The scattered light from the particles in the measuring volume is collected in the off-axis backward scatter mode, and used to measure three simultaneous velocity components of the particles. Frequency shifters are used on all the three beams to remove the ambiguity in the particle velocity direction and reduce fringe bias errors. The analog data from the photomultipliers in the receiving optics, mixed with the signals from frequency shifters, are transferred to three separate signal processors.

The data acquisition system consists of three signal processors, an external circuit and a personal computer with the associated hardware and software. While the data acquisition is software driven, the data timing is controlled by an external circuit, both of which were developed for the system. The LDV

Nomenclature

A = particle cross-sectional area
C_D = particle drag coefficient
D_p = particle diameter
m = particle mass
r = radial coordinate
R_V = particle velocity restitution ratio
R_β = particle directional restitution ratio
Re = Reynolds number
s = sensitivity
t = time
V = particle relative velocity to the gas
V_1 = particle relative impact velocity
w = gas velocity
z = axial coordinate
β_1 = particle relative impingement angle
γ = particle blade impact frequency, number of impacts/cm^2/g particles
ϵ = target material erosion parameter, mg/gm
ϵ_b = blade surface specific mass erosion parameter, mg/cm^2/g particles
θ = angular coordinate
μ = gas coefficient of dynamic viscosity
ρ = gas density
ω = rotor speed, rad/s

Subscripts

g = gas
N = normal to the surface
p = particle
r = component in radial direction
T = tangential to the surface
z = component in axial direction
θ = component in circumferential direction

Downloaded 02 Jun 2010 to 171.66.16.112. Redistribution subject to ASME license or copyright; see http://www.asme.org/terms/Terms_Use.cfm

Table 1 Summary of the experimentally measured restitution parameters and their variance for Rene 41

Impact Angle		10	15	30	45	60	75
Velocity Restitution Ratio *RV*	Mean	0.921	0.852	0.784	0.624	0.561	0.333
	St. Dev./ Mean	0.142	0.081	0.111	0.136	0.182	0.312
Directional restitution Parameter *RB*	Mean	0.861	0.799	0.709	0.716	0.62	0.431
	St. Dev./ Mean	0.626	0.491	0.190	0.479	0.382	0.427

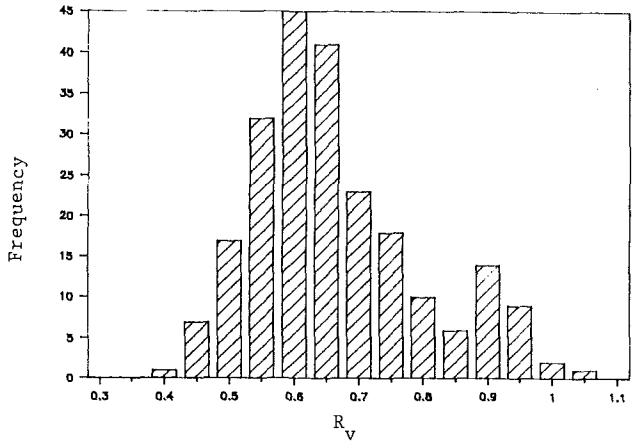


Fig. 2(*a*) LDV measurement of particle velocity restitution ratio at 15 deg impingement angle

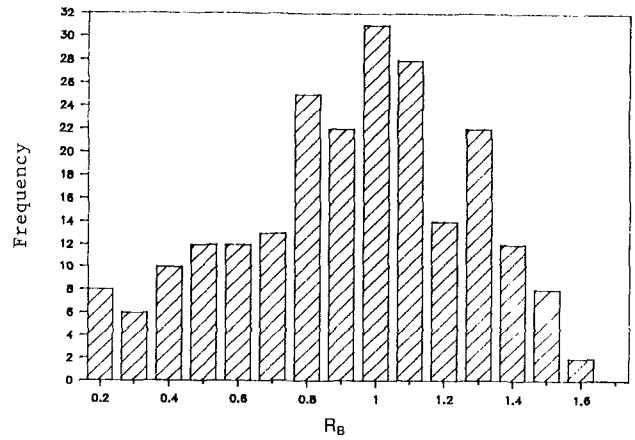


Fig. 2(*b*) LDV measurement of particle directional restitution ratio at 15 deg impingement angle

signals from the photomultipliers are processed in three TSI 1990 counter type signal processors, and the processed data are collected by an IBM PC/AT compatible computer for further processing. A Metrabyte model CTM-05 countertimer interface and three model PIO12, 24-bit parallel digital Input/Output (I/O) interfaces are used to transfer the data to the computer. The control of the data transfer and the synchronization of data coming from three different channels are performed by the external circuit.

Experimental results are presented for the particle restitution characteristics of fly-ash particles impacting Rene 41 target samples. The LDV measurements of the rebound velocities were obtained at different impact angles (β_1 = 10, 15, 30, 45, 60, 75). The incoming particle velocity, V_1, measured at the center of the test section was 98 m/s (320 fps). The magnitude and direction of the particle rebound velocities (V_2, β_2) were determined from the synchronized laser measurements. Figures 2(*a*, *b*) present the experimentally measured particle restitution characteristics $R_V = V_2/V_1$ and $R_\beta = \beta_2/\beta_1$ at 15 deg impact

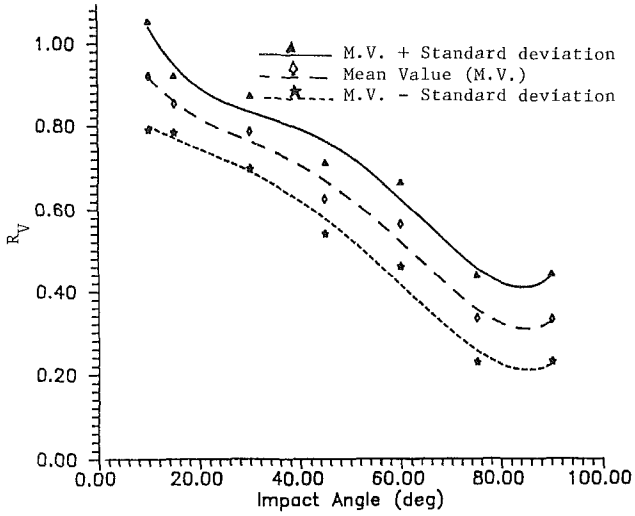


Fig. 3(*a*) Variation of particle velocity restitution ratio and standard deviation with impact angle

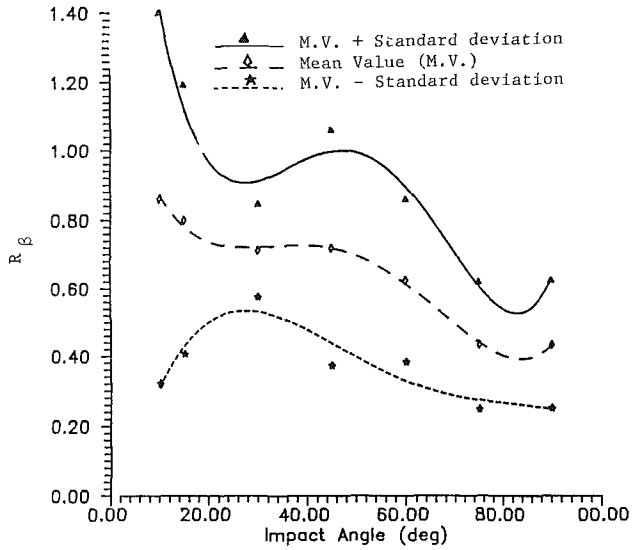


Fig. 3(*b*) Variation of particle directional restitution ratio and standard deviation with impact angle

angle. The histograms reflect the variance in the rebounding particle characteristics due to the different geometric configurations and relative orientation of the particles at impact. A statistical analysis of the particle restitution characteristics was conducted to determine the mean value and standard deviation at the tested impact angles. The results are presented in Figs. 3(*a*, *b*) and Table 1. According to Fig. 3, the variance in the restitution angle is generally greater than that in the restitution velocities. The least-square curve fits of the mean value of the experimentally determined restitution parameters, plus and minus the standard deviation, also are shown in Figs. 3(*a*, *b*).

Erosion Measurements. The erosion tests are conducted in

Downloaded 02 Jun 2010 to 171.66.16.112. Redistribution subject to ASME license or copyright; see http://www.asme.org/terms/Terms_Use.cfm

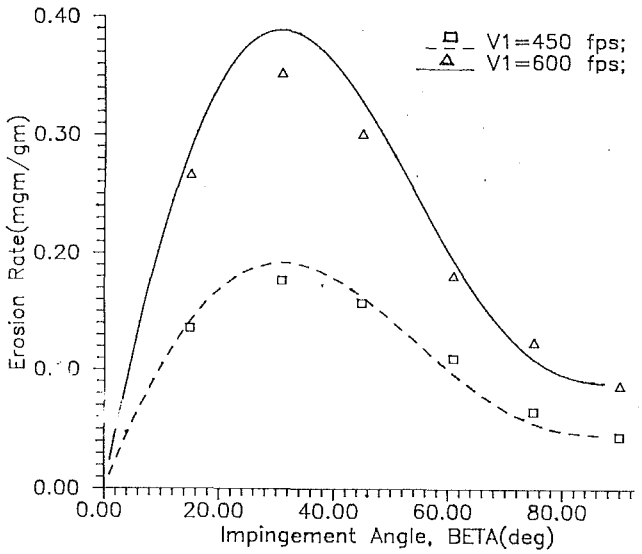


Fig. 4 Erosion rate for Rene 41

the same tunnel, shown schematically in Fig. 1. A target sample of the blade material is placed in an especially designed holder such that only its top surface is subjected to the particle impacts, while the other surface is protected by the holder that also protects the sample leading edge. The erosion tests are conducted at the specified velocity and temperature, which can be controlled by changing the flow conditions in the tunnel and the impingement angle, which is controlled by changing the orientation of the sample holder. The erosion rate is determined from the difference between the sample weights before and after the erosion test, and the monitored mass of particles impacting the target surface. According to experimental results, the erosion rate is dependent upon the particles' impact velocity, impingement angle, and the restitution parameters for a given particle target material combination, Eq. (3).

The erosion characteristics of Rene 41, were determined experimentally at six different impact angles (β_1 = 15, 30, 45, 60, 75, 90) and two impacting velocities of 450 and 600 fps. The experimental erosion results are shown in Fig. 4, together with curves representing the empirical correlations determined, using regression analysis and the particle restitution characteristics. The experimental data from the erosion tests were used to obtain the following empirical equation for the erosion mass parameter, ϵ, which is defined as the ratio of the eroded mass of target material to the mass of impinging particles.

$$\epsilon = K_1 V_1^{N_1} \cos^2\beta_1(1-R_T^2) + K_2 V_1^{N_2}\sin^2\beta_1(1-R_N)^2 \quad (1)$$

R_T and R_N are the tangential and normal restitution coefficients. The values of K_1, K_2, N_1 and N_2 were determined using regression analysis. For Rene 41 erosion by fly-ash particles

$$K_1 = 1.702\times 10^{-7}, \quad N_1 = 2.47 \quad (2)$$

$$K_2 = 2.940\times 10^{-8}, \quad N_2 = 2.33 \quad (3)$$

The erosion rate is expressed in mg per gram of particles and the particle impact velocity V_1 is expressed in fps.

Particle Dynamics

Under particulate flow conditions in turbomachines, the effect of the forces, due to gravity and interparticle interactions, are negligible compared to those due to aerodynamic and centrifugal forces (Hamed et al., 1988). In addition, the force of interaction between the two phases is dominated by the drag due to the difference in velocity between the solid particles and the flow field. The general form of the equations of motion of particles immersed in a fluid are written in a rotating fame of reference, using cylindrical polar coordinates. The three components of the equations of motion are given by

$$\frac{\delta^2 r}{\delta t^2} - r\left(\frac{\delta\theta}{\delta t}\right)^2 - 2r\,\omega\,\frac{\delta\theta}{\delta t} - r\,\omega^2 = \frac{1}{2}\frac{\rho V^2 A C_D}{m}\frac{V_r}{|\overline{V}|} \quad (4)$$

$$r\frac{\delta^2\theta}{\delta t^2} + 2\frac{\delta r}{\delta t}\frac{\delta\theta}{\delta t} + 2\omega\frac{\delta r}{\delta t} = \frac{1}{2}\frac{\rho V^2 A C_D}{m}\frac{V_\theta}{|\overline{V}|} \quad (5)$$

$$\frac{\delta^2 z}{\delta t^2} = \frac{1}{2}\frac{\rho V^2 A C_D}{m}\frac{V_z}{|\overline{V}|} \quad (6)$$

In the foregoing equations, ω is the angular velocity of the rotor about the z-axis.

The first term on the right-hand side of Eqs. (4)–(6) represents the drag force on the particles, which is dependent on the relative velocity of the gas with respect to the particles, $\overline{V}$. The three components of this relative velocity vector are

$$V_r = w_r - \frac{\delta r}{\delta t}, \quad (7)$$

$$V_\theta = w_u - \frac{r\delta\theta}{\delta t}, \quad (8)$$

$$V_z = w_z - \frac{r\partial\theta}{\delta\tau}, \quad (9)$$

where w_r, w_u and w_z are the radial, tangential and axial components of the gas velocity relative to the rotor, and $\delta r/\delta t$, $r\delta\theta/\delta t$, and $\delta z/\delta t$ are the radial, tangential and axial velocity components of the particle velocity in the rotating reference frame.

Equations (4)–(9) also are used in the stator by setting ω equal to zero and replacing the relative gas velocity w_g by the absolute gas velocity.

The drag coefficient of a spherical particle is well known from the experimental measurements over a wide range of Reynolds numbers. The value of C_D was determined using the following relations

$$C_D = 4.5 + \frac{24}{\mathrm{Re}} \qquad \mathrm{Re} < 1.0 \quad (10)$$

$$C_D = 28.5 - 24.0(\log \mathrm{Re}) + 9.0682(\log \mathrm{Re})^2 - 1.7713(\log \mathrm{Re})^3 + 0.1718(\log \mathrm{Re})^4 - 0.0065(\log \mathrm{Re})^5 \qquad 1.0 < \mathrm{Re} < 3000 \quad (11)$$

$$C_D = 0.4 \qquad 3000 < \mathrm{Re} < 2.5\times 10^{-5} \quad (12)$$

The Reynolds number is expressed as

$$\mathrm{Re} = \frac{\rho|\overline{V}|D_p}{\mu} \quad (13)$$

where ρ_g represents the gas density, D_p the particle diameter, and C_D the particle drag coefficient.

Flow-Field Simulation. The flow field is assumed to be unaffected by the particles under the prevailing conditions in the turbine. The flow, in each blade row passage, is determined from a quasi-three-dimensional solution procedure based on the meridional and blade-to-blade codes (Katsanis, 1977, 1965), respectively. The flow field, obtained from the juxtaposition of a number of blade-to-blade solutions from hub-to-tip, reflects the axial, radial and circumferential variation in the flow, due to blade configuration and hub and tip contours. The computations are performed by integrating the particle equations of motions in cylindrical polar coordinates in a frame of reference fixed in each blade row. Only the circumferential components of the particle velocity and location at exit from a blade row are adjusted for relative rotation to represent the inlet particle conditions to the following blade row.

Particle Trajectory Simulations. The particle trajectory simulations consist of the numerical integration of the equa-

Downloaded 02 Jun 2010 to 171.66.16.112. Redistribution subject to ASME license or copyright; see http://www.asme.org/terms/Terms_Use.cfm

tions of motion of the particles, in the three-dimensional turbomachinery flow field. A fourth-order Runge–Kutta scheme and a fixed time step are used to advance the solution of the particle trajectory equations in the three-dimensional flow field of a blade row passage. If it is determined that the particle crossed any of the blade passage boundaries, the time step is reduced iteratively to bring the particle trajectory to the impacted surface. The local unit normal vector to the surface at the computed impact location is used, together with the computed particle velocity components at impact to determine the impact velocity and impingement angle relative to the surface. The magnitude and direction of the rebounding particle velocity relative to the impacted surface are determined from correlations of the experimentally measured particle restitution characteristics. The computational results from the particle trajectory code simulations are processed for all the particle surface impact locations and the magnitude and direction of the impact velocities relative to the surface. These data are used as an input for surface erosion simulation code, which is based on the use of the empirical correlations of the experimentally measured target erosion (Eqs. (1)–(3)).

Probabilistic Modeling. The deterministic particle trajectory computations are combined in a probabilistic structure to simulate the variance in the particle rebounding characteristics as determined in the experimental study. The solution to the multiple integral representing the joint probability density function requires that the deterministic simulation relating the response function and the random variables (Negpal et al., 1988) or the diverse (Moore et al., 1989) be performed a large number of times. Numerous techniques have been developed to reduce the computation time, through decreasing the number of required simulations. In the first- and second-order reliability methods, this is accomplished by transforming the integral into an approximately equal integral that can be evaluated more efficiently (Madsen et al., 1986). Usually, the transformation maps the probability distribution for each random variable into a standard normal distribution. The mathematical optimization for the limit state function in the transformed space is then performed to determine the region for the main contribution to the integral.

The probabilistic analysis in the present study is based on the Fast Probability Integration (FPI) method of Wu and Wirsching (1987), which is an extension of the First-Order Reliability Method. The algorithm establishes quadratic polynomial approximations to the limit state at the most-probable point, then transforms the quadratic form into a linear one. Burnsick (1985) compared the results of the applications of Monte Carlo simulation, the method of moments and the fast probability integration methods to sample problems with a small number of random variables. His results indicate that the FPI method has high accuracy with respect to the Monte Carlo simulation for less computational effort. Dias and Nagtegal (1985) demonstrated the convergence properties of the FPI method for small changes about the deterministic solution at the expansion point.

Results and Discussion

The results of the probabilistic three-dimensional particle trajectory simulations and the corresponding blade erosion predictions are presented for the first stage of a two-stage turbine. The turbine blade configuration and operating conditions were described by Roelke et al. (1966). The simulations were conducted at the flow conditions corresponding to 7.071 lb/s mass flow rate at 1893 rpm for 15 μm fly-ash particles. Figure 5 presents the distribution of the predicted mean values of the stator and rotor pressure surface erosion and impact frequency. The corresponding blade suction surface erosion was very small compared to the pressure surface and, therefore,

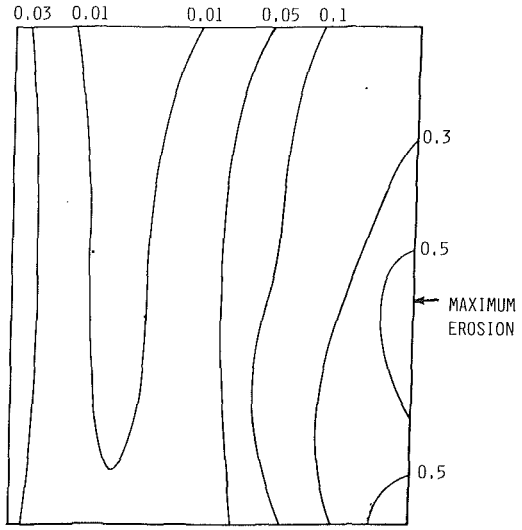


Fig. 5(*a*) Stator blade pressure surface erosion distribution (median in $mg/cm^2/gm \times 10^3$)

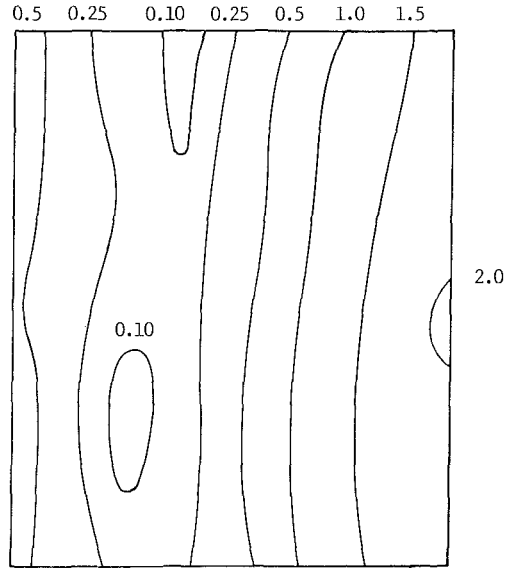


Fig. 5(*b*) Stator blade pressure surface impact frequency (median in $Imp/cm^2/gm \times 10^{-6}$)

they were not included in the results. Figure 6 presents the distribution of the predicted mean value and standard deviation of the rotor blade pressure surface erosion. Tables 2 and 3 summarize the results of the probabilistic simulations for the particle impact frequency and blade erosion for the overall pressure surface erosion, as well as the locations corresponding to maximum erosion. The tables list the predicted mean value and standard deviation of the impact frequency and erosion. The tables also give the sensitivity, S_{RV} and $S_{R\beta}$, of these parameters to the variance in the velocity restitution coefficient (R_V) and directional restitution parameter (R_β). According to these results, the relative variance in the erosion and impact frequency is greater in the rotor than the stator. This is a consequence of the fact that the effects of the variance in the restitution characteristics can be realized only after the first impact. Table 2 shows that the stator blade pressure surface erosion is more sensitive to the variance in the velocity restitution ratio R_V than the directional restitution parameter R_β. On the other hand, the rotor blade pressure surface erosion is equally sensitive to the variance in both R_V and R_β. The results of the probabilistic analysis in Table 3 indicate that the rotor impact frequency is more sensitive to the variance in the di-

Downloaded 02 Jun 2010 to 171.66.16.112. Redistribution subject to ASME license or copyright; see http://www.asme.org/terms/Terms_Use.cfm

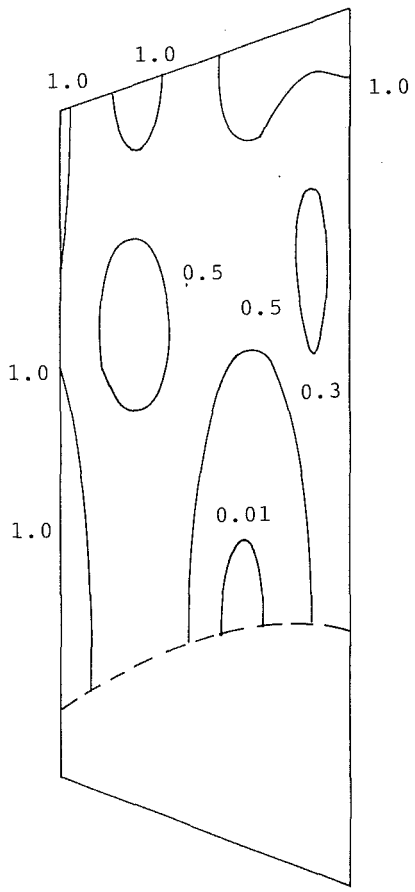


Fig. 6(*a*) Distribution of predicted mean values of blade pressure surface erosion, mg/cm²/gm × 10^3

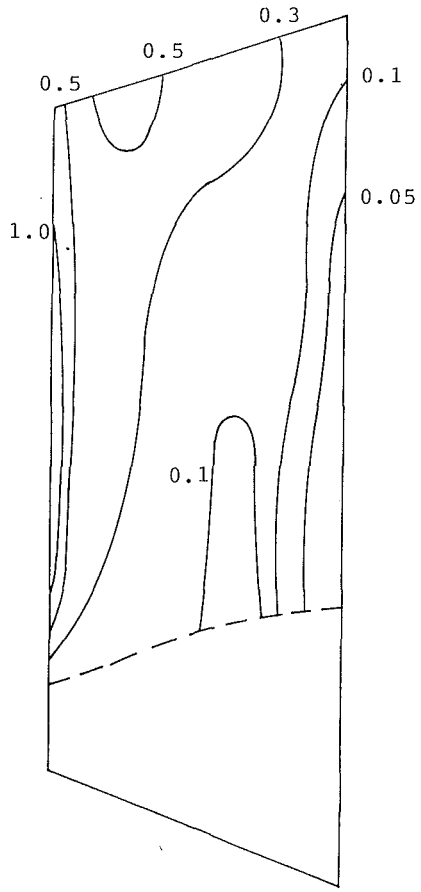


Fig. 6(*b*) Distribution of predicted standard deviation in rotor pressure surface erosion, mg/cm²/gm × 10^4

Table 2 Variance and sensitivity for the impact and erosion parameters for the stator pressure surface at maximum erosion

	(*a*) At Maximum Erosion Location		(*b*) Overall Blade	
	Erosion (mg/cm²/gm)	Impact Frequency (Imp/cm²/gm)	Erosion (mg/cm²/gm)	Impact Frequency (Imp/cm²/gm)
Mean Value	0.85×10^{-3}	0.252×10^{7}	0.734×10^{-4}	0.493×10^{6}
St. Dev./MV	0.045	0.151	0.006	0.076
S_{R_V}	0.919	0.394	1.0	0.628
S_{R_β}	0.394	0.919	0	0.778

Table 3 Variance and sensitivity for the impact and erosion parameters for the rotor pressure surface at maximum erosion

	(*a*) At Maximum Erosion Location		(*b*) Overall Blade	
	Erosion (mg/cm²/gm)	Impact Frequency (Imp/cm²/gm)	Erosion (mg/cm²/gm)	Impact Frequency (Imp/cm²/gm)
Mean Value	0.1242×10^{-2}	0.31×10^{7}	0.179×10^{-5}	0.2306×10^{7}
St. Dev./MV	0.255	0.231	0.132	0.2007
S_{R_V}	0.789	0.419	0.703	0.179
S_{R_β}	0.615	0.908	0.711	0.984

rectional restitution ratio. This is a consequence of the repeated rotor blade pressure surface impacts associated with the smaller rebound angles than the mean values.

The rotor blade erosion data and the corresponding impact data of Table 3 also are presented in Figs. 7 and 8 in the form of cumulative distribution functions. These figures combine the rotor blade erosion and impact frequency results for the overall blade and the maximum blade erosion location. One can clearly observe larger variance in both blade erosion and impact frequency at the maximum erosion location compared to the variance in the overall blade erosion.

A comparison of A: the erosion determined from the particle trajectory simulations using the mean values of the restitution parameters, and B: the predicted mean values of erosion and impact frequency using the fast probability integral method with the measured variance in the particle restitution ratios gives the following:

	Stator Erosion		Rotor Erosion	
	Maximum mg/cm²/g	Overall mg/cm²/g	Maximum mg/cm²/g	Overall mg/cm²/g
A	0.89×10^{-3}	0.85×10^{-3}	0.17×10^{-2}	0.2034×10^{-3}
B	0.132×10^{-3}	0.129×10^{-3}	0.1242×10^{-2}	0.18×10^{-3}

Downloaded 02 Jun 2010 to 171.66.16.112. Redistribution subject to ASME license or copyright; see http://www.asme.org/terms/Terms_Use.cfm

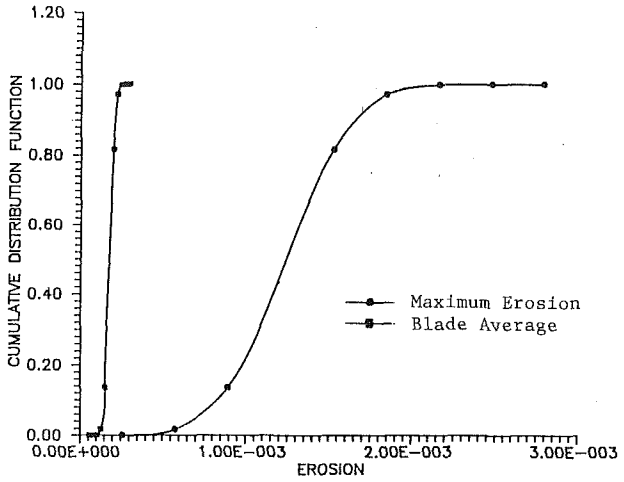


Fig. 7 Cumulative distribution function of rotor blade erosion, mg/cm²/gm

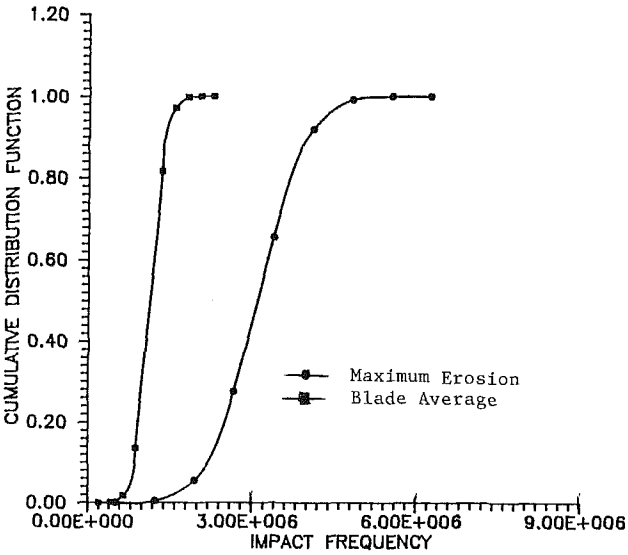


Fig. 8 Cumulative distribution function of rotor impact frequency Imp/cm²/gm

According to the results in this table, one can conclude that the simulations based on the mean value of the measured particle restitution ratios are conservative in terms of overpredicting the erosion mean value, both at the location of maximum erosion as well as for the overall blade erosion. The cumulative distribution erosion curves (Fig. 7) indicate that the probability is 92 percent and that the maximum rotor pressure surface erosion is less than 0.17×10^{-2}, the prediction using the mean values of the restitution ratios (prediction *A*). On the other hand, the probability is 82 percent that the overall rotor pressure surface erosion is less than 0.2034×10^{-3} (prediction *A*).

Conclusions

Experimental methods and numerical simulations are combined to characterize the variance in the particle rebound conditions after surface interactions and to model their influence on the particle trajectories in a turbine stage. The results of the experimental measurements using laser-Doppler velocimetry provide probability density functions for the particle restitution ratios. The particle dynamics simulations are conducted in a probabilistic structure, using fast probability integration methods, to predict the associated variance in the predicted turbine blade surface erosion. The results of the probabilistic study provide the sensitivity of the blade erosion parameters to the variance in the particle restitution ratios, and the degree of confidence in the deterministic predictions using their mean values.

Acknowledgments

This work was sponsored by NSF Grant CTS-9012309 and Department of Energy Subcontract, Martin Marietta 19X89628C.

References

Burnsick, O. H., 1985, "Probabilistic Structural Analysis for Space Propulsion System Components," *Advances in Aerospace Structural Analysis*, AD-09 *Proceedings of Symposium on Probabilistic Design and Analysis*, WAM ASME, Miami, FL.

Dias, J. B., and Nagtegal, J. C., 1985, "Efficient Algorithms for Use in Probabilistic Finite Element Analysis," ibid.

Hamed, A., Tabakoff, W., and Wenglarz, R., 1988, "Particulate Flow and Blade Erosion," von Karman Institute for Fluid Dynamics Lecture Series, 1988-08, May.

Hamed, A., 1988, "Effect of Particle Characteristics on Trajectories and Blade Impact Patterns," ASME *Journal of Fluids Engineering*, Vol. 110, pp. 33-37.

Hamed, A., 1989, "Influence of Secondary Flow on Turbine Erosion," ASME *Journal of Turbomachinery*, Vol. 111, pp. 310-314.

Hussein, M., and Tabakoff, W., 1973, "Dynamic Behavior of Solid Particles Suspended by Polluted Flow in Turbine Stage," *J. of Aircraft*, Vol. 10, No. 7, pp. 334-340.

Katsanis, T., 1965, "Fortran Program for Calculating Transonic Velocities on a Blade-to-Blade Stream Surface of a Turbomachine," NASA TND-2809.

Katsanis, T., and McNally, W. D., 1977, "Revised Fortran Program for Calculating Velocities and Streamlines on the Hub-Tip Mid Channel Stream Surface of an Axial, Radial, or Mixed Flow Turbomachine or Annular Duct, Vols. 1 and 2," NASA TND-8430 and NASA TND-8431.

Kotwal, R., and Tabakoff, W., 1981, "A New Approach for Erosion Prediction Due to Fly Ash," ASME JOURNAL OF ENGINEERING FOR POWER, Vol. 102, pp. 265-270.

Madsen, H. O., Krenk, S., and Lind, N. C., 1986, *Methods of Structural Safety*, Prentice Hall, Englewood Cliffs, NJ.

Moore, N., and Ebbeler, C., 1989, "A Methodology for Probabilistic Prediction of Structural Failures of Launch Vehicle Propulsion Systems," *Proc. AIAA/ASME/ASCE/AHS/ASC, 31st Structures, Structural-Dynamics and Materials Conference*, Chatsworth, CA, pp. 30-45.

Nagpal, V. K., Rubinstein, R., and Chamis, C. C., 1988, "Probabilistic Structural Analysis to Quantify Uncertainties Associated With Turbopump Blades," NASA TM 100278.

Roelke, R. J., Stabe, R. G., and Evans, D. G., 1966, "Cold-Air Performance Evaluation of Scale Model Oxidizer Pump-Drive Turbine for the M-1 Hydrogen-Oxygen Rocket Engine—II. Overall Two-Stage Performance," NASA TND-3368.

Tabakoff, W., Grant, G., and Ball, R., 1974, "An Experimental Investigation of Certain Aerodynamic Effects on Erosion," AIAA Paper No. 74-639.

Tabakoff, W., and Wakeman, T., 1979, "Test Facility for Material Erosion at High Temperature," *Erosion, Prevention and Applications*, ASTM STP 664, American Society for Testing & Materials, pp. 123-135.

Tabakoff, W., Hamed, A., and Ramachandran, J., 1980, "Study of Material Erosion in High Temperature Coal Gas Streams," ASME JOURNAL OF ENGINEERING FOR POWER, Vol. 102, pp. 148-152.

Tabakoff, W., 1984, "Review—Turbomachinery Performance Deterioration Exposed to Solid Particulates Environment," ASME *Journal of Fluids Engineering*, Vol. 106, pp. 125-134.

Tabakoff, W., and Hamed, A., 1986, "The Dynamics of Suspended Solid Particles in a Two-Stage Gas Turbine," ASME *Journal of Turbomachinery*, Vol. 108, pp. 298-302.

Tabakoff, W., Malak, M. F., and Hamed, A., 1987, "Laser Measurements of Solid-Particle Rebound Parameters Impacting on 2024 Aluminum and 6A1-4V Titanium Alloys," *AIAA Journal*, Vol. 25, No. 5, pp. 721-726.

Tabakoff, W., 1989, "Measurements of Particles Rebound Characteristics on Materials Used in Gas Turbines," AIAA Paper No. 89-1693.

Tabakoff, W., Lakshminarasimha, A. N., and Pasin, M., 1990, "Simulation of Compressor Performance Deterioration Due to Erosion," ASME *Journal Turbomachinery*, Vol. 112, pp. 78-83.

Wu, Y. T., and Wirsching, P. H., 1987, "A New Algorithm for Structural Reliability Estimation," ASCE *Journal of Engineering Mechanics*, Vol. 113, No. 9, pp. 1319-1336.

Downloaded 02 Jun 2010 to 171.66.16.112. Redistribution subject to ASME license or copyright; see http://www.asme.org/terms/Terms_Use.cfm

High-Temperature Erosion Resistance of Coatings for Gas Turbine

W. Tabakoff

A. Hamed

M. Metwally

M. Pasin

Department of Aerospace Engineering and Engineering Mechanics, University of Cincinnati, Cincinnati, OH 45221

An experimental investigation was conducted to study the ash particle rebound characteristics and the associated erosion behavior of superalloys and aluminide coatings subjected to gas-particle flows at elevated temperature. A three-component LDV system was used to measure the restitution parameters of 15 micron mean diameter coal-ash particles impacting some widely used superalloys and coatings at different angles. The presented results show the variation of the particle restitution ratios with the impingement angle for the coated and uncoated superalloys. The erosion behaviors of INCO-738, MAR 246 and X40 superalloys and protective coatings C, N, RT22 and RT22B also have been investigated experimentally at high temperature using a specially designed erosion tunnel. The erosion results show the effect of velocity, temperature and the impact angle on the erosion rate (weight loss per unit weight of particles). Based on the experimental results of the particle mass effect on both weight losses and erosion rates, the coating lives have been estimated for different particle concentrations.

Introduction

The major problem confronting developers of coal-burning boilers, fluidized beds and turbines is the serious erosion of the system components by the suspension of fly ash in the hot combustion gases. A permanent loss of performance is associated with the surface erosion, which is caused by particle surface impacts. The performance loss depends upon the location and the condition of the deteriorated surfaces. These are critical to the aerodynamic performance of turbine blades which are particularly sensitive to the blade leading, the trailing-edge configuration and the condition of the blade suction surface. Computer codes are used to model the particle dynamics in turbomachinery flow fields through the various blade rows, and to determine the particle impact conditions with the various surfaces, which affect their erosion. The codes, however, require empirical equations for particle restitution characteristics (Tabakoff et al., 1986; Tabakoff and Hamed, 1987) to represent the effect of particle surface interaction on the particle trajectories and the resulting surface erosion.

Nickel and cobalt base superalloy blades and vanes are widely used in the hot section of gas turbines. Protective coatings have been used, to enhance superalloy resistance to hot erosion-corrosion. The most widely used coatings are those based on the NiAl (on nickel base superalloys) and CoAl (on cobalt base superalloys) formed by interaction of superalloy surfaces with aluminum. To improve the resistance to hot erosion-corrosion, aluminide coatings are modified to contain elements such as chromium, platinum, rhodium, and silicon. The objective of this research work is to investigate the basic erosion processes and fluid mechanics associated with the material degradation in the components of various coal conversion and utilization systems. This is accomplished through a study of the rebound characteristics of particles impinging various surfaces and through the measurement of erosion rates of materials and coatings exposed to high temperature gas particle flows. The overall goal is to develop a quantitative model, which will facilitate the prediction of erosion in systems operating in particulated environments.

Experimental Setup

The experimental setup consists of the following: (*a*) the erosion wind tunnel; (*b*) the LDV system; (*c*) the data acquisition system.

(a) Erosion Wind Tunnel. The high-temperature erosion test facility was designed to provide erosion and rebound data in the range of operating temperatures experienced in compressors and turbines. In addition to the high temperatures, the facility properly simulates all the erosion parameters which were determined to be important from aerodynamics point of view. These parameters include particle velocity, angle of impact, particle size, particle concentration, and sample size. Close attention was given to the aerodynamic effects to insure that important parameters, such as the angle of impact, are not masked or altered.

A schematic of the erosion test facility is shown in Fig. 1. It consists of the following components: particle feeder (A), main air supply pipe (B), combustor (C), particle preheater (D), particle injector (E), acceleration tunnel (F), test section (G), and exhaust tank (H).

Contributed by the International Gas Turbine Institute and presented at the 36th International Gas Turbine and Aeroengine Congress and Exposition, Orlando, Florida, June 3-6, 1991. Manuscript received at ASME Headquarters March 4, 1991. Paper No. 91-GT-213. Associate Editor: L. A. Riekert.

Copyright © 1992 by ASME

Downloaded 02 Jun 2010 to 171.66.16.112. Redistribution subject to ASME license or copyright; see http://www.asme.org/terms/Terms_Use.cfm

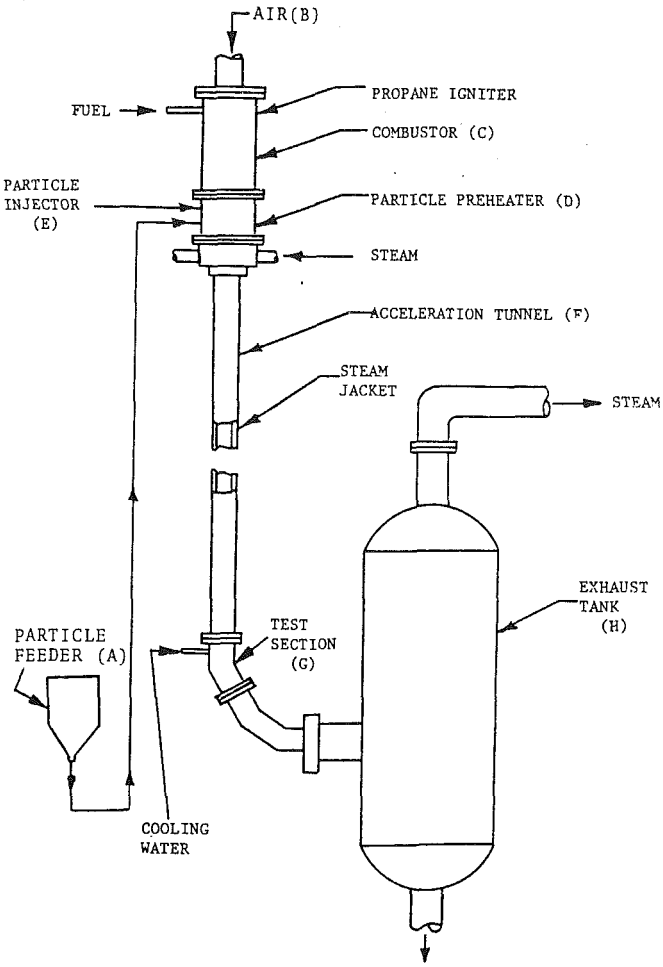


Fig. 1 Schematic of erosion test facility

The equipment functions as follows: A measured amount of abrasive grit of a given mixture of constituents is placed into the particle feeder (A). The particles are fed into a secondary air source and blown up to the particle preheater (D), and then to the injector (E), where they mix with the main air supply (B), which is heated by the combustor (C). The particles are then accelerated by the high-velocity air in a constant-area steam-cooled duct (F) and impact the specimen in the test section (G). The particulate flow is then mixed with the coolant and dumped in the exhaust tank. Figure 1 shows that the tunnel geometry is uninterrupted from the acceleration tunnel into the test section. In this manner, the particle-laden flow is channeled over the specimen and the aerodynamics of the fluid passing over the sample are preserved.

A detailed description of the wind tunnel and the particle feeder is given by Tabakoff and Wakeman (1979).

(b) LDV System. The LDV system used in the measurements of the particle restitution characteristics is described in detail by Tabakoff et al. (1986) and Tabakoff and Hamed (1987). It consists of the laser tube, the optics, the frequency shifters and the photomultipliers. The light source is a five Watt Argon-ion Spectra Physics, model 164-09 laser tube. The laser beam leaving the tube is separated in the dispersion prism into components with different wavelengths. Three beams with the highest intensities are used to measure the three velocity components. The beams with green (0.5145 μm) and blue (0.488 μm) colors are sent through an optical train in the axial direction. The third beam with purple color (0.4765 μm) passes through a second optical train whose transmitting optics are inclined at 30 deg from the axial direction. Each beam is polarized through a polarization rotator and split into two equal intensity components in the beam splitter. After passing through the focusing lenses, the two beams of each color cross and produce a set of fringes. Six beams cross at one common measuring volume producing three sets of fringes, one for each color. The orientation of the perpendicular bisectors of the three sets of fringes gives the coordinate system for the three-dimensional velocity measurements. The dimensions of the fringe pattern in the measurement volume are a function of the LDV optics. TSI model 9189 beam expanders were used to increase the spatial resolution, improve the single-to-noise ratio, and reduce the measurement volume diameter 3.75 times. The focal length of the transmitting lenses is 480 mm and the crossing angle for the 1.5-mm-dia beams is 9.82 deg. Two separate beam collimaters, one on the blue-green optical train and the other on the purple optical train, were installed before the beam splitters for precise control of the probe volume characteristics. In particular, it was possible to insure that the focused beams intersected at their beam waists to avoid frequency broadening effects and maximize signal quality. The scattered light from the particles in the measuring volume is collected in the off-axis backward scatter mode. Frequency shifters were used on all the three beams to sense the flow direction and reduce fringe bias errors. The analog data from the photomultipliers in the receiving optics, mixed with the signals from frequency shifters, are transferred to three separate signal processors.

(c) Data Acquisition System. The data acquisition system consists of three signal processors, an external circuit and a personal computer with the associated hardware and software. While the data acquisition is software-driven, the data timing is controlled by an external circuit. The LDV signals coming from the photomultipliers are processed in the three TSI 1990 counter-type signal processors. The processed data are collected by an IBM PC/AT compatible computer for further calculations and data storage. The control of the data transfer and the synchronization of data coming from three different channels are performed by the external circuit.

The logic for the data acquisition system is as follows: The frequency of the internal oscillator clock in the CTM-05 countertimer is specified initially through the interactive software. This clock generates a square wave at the selected frequency and the period of the wave determines the coincidence window for the data coming from the processors connected to the three LDV channels. During the data collection, the external circuit is activated in order to detect the arrival of data ready signals. Whenever the external circuit receives a data ready pulse, it sends a data inhibit signal to the associated processor, preventing it from acquiring new data. When all the three data ready signals arrive within the specified coincidence limit, the circuit holds the data at the output buffers of the processors, and instructs the computer to transfer them into a file through the digital input port. The external circuit is then reset through the digital output port of CTM-05, the processors are reactivated and the procedure is repeated until a specified number of samples is collected.

Test Conditions and Tested Materials

It is well known that particle velocity, particle impingement angle, particle characteristics and material sample temperature strongly influence the erosion rate. These parameters were varied in the present test program for the different tested materials listed in Tables 1 and 2. The properties of the superalloys can be found in *Aerospace Structural Metals Handbook* (1963) and *Alloy Digest* (1969). The particle velocity was controlled by varying the tunnel airflow. The particle impingement angle was set by rotating the sample relative to the flow-stream direction. The sample temperature was varied by heating the flow stream which heats the sample to the desired temperature.

Downloaded 02 Jun 2010 to 171.66.16.112. Redistribution subject to ASME license or copyright; see http://www.asme.org/terms/Terms_Use.cfm

Table 1 Tested superalloys

Superalloy	Chemical composition
INCO IN-738	16 Cr, 8.5 Co, 3.4 Al, 3.4 Ti, 2.6 W, 1.75 Mo, 1.75 Ta, 0.9 Cb, balance Ni
MAR-M246	10 Co, 10 W, 9 Cr, 5.5 Al, 2.4 Mo, 1.5 Ta, 1.5 Ti, balance Ni
X40	25 Cr, 10 Ni, 7.5 W, balance Co

Table 2 Tested coatings

Coating	Treatment	Substrate	Thickness (mils)	Heat treatment
C	Aluminized	X40*	3	—
N	Aluminized	M246**	3	—
RT22	Platinum Aluminized	M246	5	yes
RT22B	Rhodium/Platinum Aluminized	M246	3	yes

*X40: Cobalt-based X40 superalloy
**M246: Nickel-based MAR-M246 superalloy

Table 3 Chemical analysis of fly ash

Chemical	Percentage
Silicon dioxide (SiO_2)	48.08
Iron oxide (Fe_2O_3)	20.05
Aluminide oxide (Al_2O_3)	21.16
Magnesium oxide (MgO)	0.93
Sulphur trioxide (SO_3)	1.20
Moisture content	0.13
Loss of ignition	0.73
Available alkalis as Na_2O	0.64
Undetermined	7.08

The experimental measurements were obtained for fly-ash particles with impact velocities ranging between 600 and 1200 fps (366 m/s) at temperatures ranging from ambient to 1500°F (815.5°C). Table 3 lists fly-ash particle chemical composition. Flat rectangular specimens were used in the tests. The specimens for the erosion test were 1 in. (0.0254 m) long, 0.25 in. (0.00635 m) thick, and 0.5 in. (0.0127 m) wide, while the rebound test specimens were 0.25 in. (0.00635 m) wide. The maximum specimen blockage was on the order of 10 percent. Test data were accumulated by setting the particle impingement angle at 15, 30, 45, 60, and 90 deg for each of the different test temperatures and particle velocities.

Restitution Test Results

The rebound dynamics of particles can be described in a statistical sense only. This becomes obvious when one examines the number of geometric situations that might occur at impact. After an incubation period, the target material will become pitted with craters and, in fact, after a slightly longer period, a regular ripple pattern will form on the eroded surfaces. Thus the local impact angle between the small particles and the eroded surface may deviate considerably from the geometric average. The individual impact angle and velocity of a particle also depend on its size. Furthermore, the particles themselves are irregular in shape, some with sharp corners. As the particle approaches the specimen, the orientation of the particle is, for the most part, random. Thus some particles will impact on a flat surface and do very little work on the target material. Others will impact with a corner oriented in a manner similar to that of a cutting tool and will remove material from the surface.

The restitution coefficient or restitution ratio is a measure of the kinetic energy loss upon impact of two objects. Since the erosion is dependent on the erodent particle kinetic energy loss upon impacting the target, the restitution ratio will give a good indication of the type of the particle-material interaction. An erosive impact occurs when the contaminant particle is much harder than the target material. Therefore, the restitution ratio will be a measure of the distortion of the target material rather than distortion of the erosive particle.

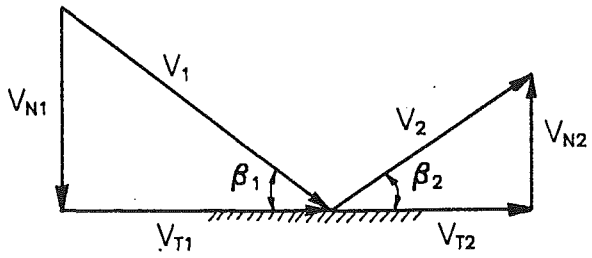


Fig. 2 Rebound velocity and angle notation

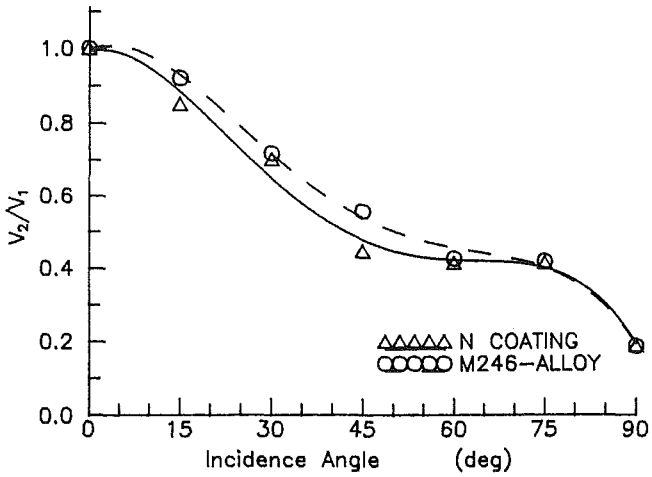


Fig. 3 Total velocity restitution ratio versus incidence angle β_1 for M246 alloy and N-coating, V_1 = 320 fps, fly ash

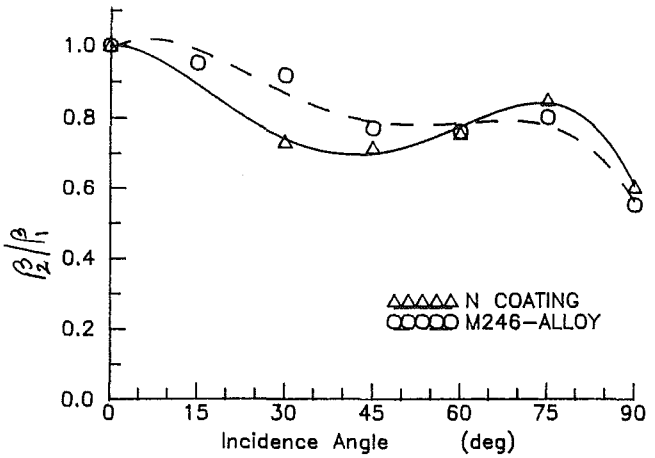


Fig. 4 Directional coefficient (β_2/β_1) versus incidence angle β_1 for M246 alloy and N-coating, V_1 = 320 fps, fly ash

Grant and Tabakoff (1975) were the first to investigate thoroughly the rebound characteristics of high-speed eroding particles. The study was carried out on annealed 2024 aluminum alloy. The data were described using histograms to illustrate their statistical distribution. It was concluded that the restitution ratio V_2/V_1, which is directly related to the kinetic energy loss during an impact, does not give sufficient information in regard to erosion. With this in mind, the restitution ratio was broken down into a normal velocity restitution ratio V_{N2}/V_{N1} (the normal component of the particle velocity after impact divided by the normal component of the particle velocity before impact), and a tangential velocity restitution ratio V_{T2}/V_{T1} (the tangential component of the particle velocity after impact divided by the tangential component of the particle velocity before impact) as shown in Fig. 2. The previous measurements at various incidence angles and flow velocities indicate that

Downloaded 02 Jun 2010 to 171.66.16.112. Redistribution subject to ASME license or copyright; see http://www.asme.org/terms/Terms_Use.cfm

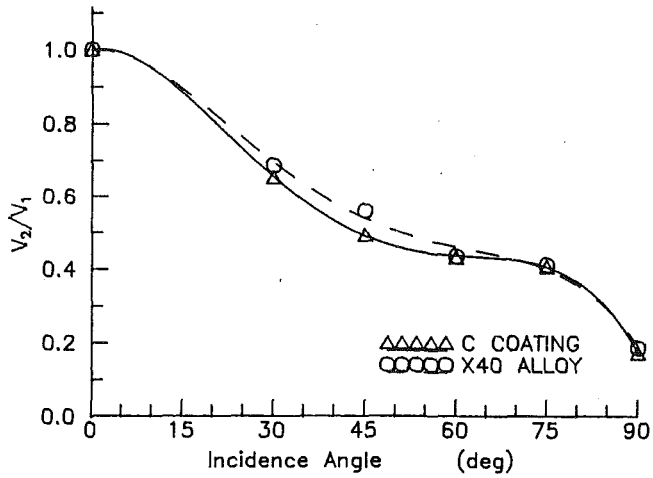


Fig. 5 Total velocity restitution ratio versus incidence angle β_1 for X40 alloy and C-coating, V_1 = 320 fps, fly ash

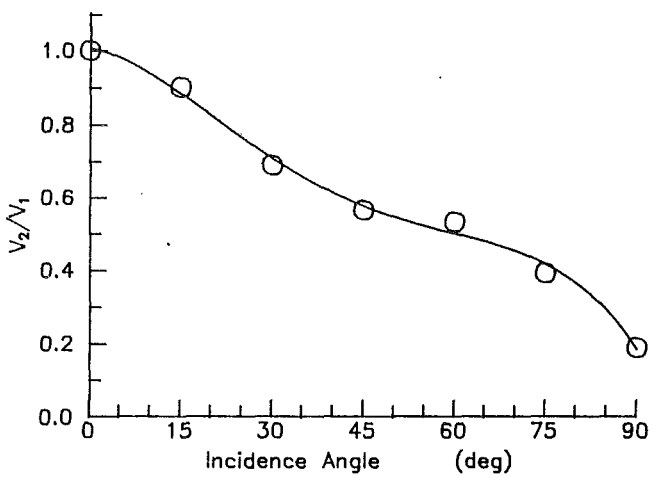


Fig. 7 Total velocity restitution ratio versus incidence angle β_1 for INCO-738, V_1 = 320 fps, fly ash

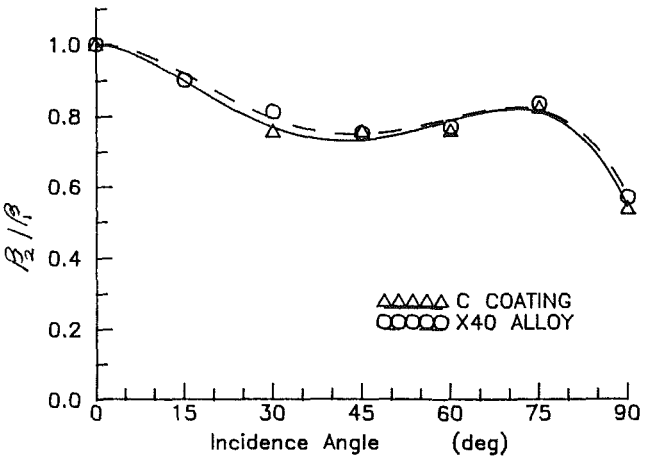


Fig. 6 Directional coefficient (β_2/β_1) versus incidence angle β_1 for X40 alloy and C-coating, V_1 = 320 fps, fly ash

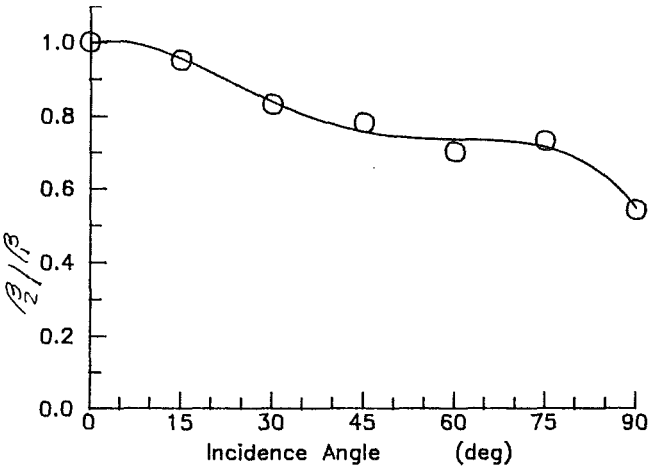


Fig. 8 Directional coefficient (β_2/β_1) versus incidence angle β_1 for INCO-738, V_1 = 320 fps, fly ash

these ratios are mainly dependent upon the impingement angle for a given particle material combination (Grant and Tabakoff, 1975).

In this investigation, the fly-ash particle rebound conditions are measured using laser doppler velocimetry for particle laden flow over some of the sample materials listed in Tables 1 and 2. The experimental results are presented in the form of total velocity (V_2/V_1) and the directional (β_2/β_1) restitution ratios. The fly-ash particle-size distribution covers a wide range of particle diameters. Tabakoff et al. (1983) demonstrated that the individual impact angle and impact velocity of a particle depend on its size. The average of the measured impact velocities and angles have been used in restitution parameter calculations. The average of the particle impact velocities for the present investigation was 320 fps (97.6 m/s) in all the particle restitution experiments.

Figures 3 and 4 present the results for M246 alloy with and without "*N*" coating, while Figs. 5 and 6 present similar results for X40 alloy with and without "*C*" coating. The restitution ratios of INCO-738 alloy are shown in Figs. 7 and 8. These figures present the measured variation of the restitution ratios with the impact angle up to 90 deg range. The restitution ratios were assumed unity at 0 deg angle. The curves in Figs. 3–8 represent the mean values of the experimentally measured restitution parameter at each impact angle. To facilitate the use of these experimental data in particle trajectory and erosion computations, empirical equations were obtained using a least-square polynomial curve fitting of the mean values of the restitution parameters. The solid and broken lines in Figs. 3–8 represent the polynomial curve fitting and may be expressed by the following equations:

For M-246 Alloy

$$\frac{V_{T2}}{V_{T1}} = e_T = 1.00 - 0.00832249\beta_1 - 8.09523 * 10^{-5}\beta_1^2 + 1.78601 * 10^{-6}\beta_1^3$$

$$\frac{V_{N2}}{V_{N1}} = e_N = 1.00 + 0.00809841\beta_1 - 0.0012261 1\beta_1^2 + 2.30864 * 10^{-5}\beta_1^3 - 1.2922 * 10^{-7}\beta_1^4$$

$$\frac{V_2}{V_1} = e_V = 1.00 + 0.00601123\beta_1 - 0.000957896\beta_1^2 + 1.77426 \times 10^{-5}\beta_1^3 - 9.94 \times 10^{-8}\beta_1^4$$

$$\frac{\beta_2}{\beta_1} = e_\beta = 1.00 + 0.00872424\beta_1 - 0.000834276\beta_1^2 + 1.63771 \times 10^{-5}\beta_1^3 - 9.75683 * 10^{-8}\beta_1^4$$

Downloaded 02 Jun 2010 to 171.66.16.112. Redistribution subject to ASME license or copyright; see http://www.asme.org/terms/Terms_Use.cfm

X-40 Alloy

$$\frac{V_{T2}}{V_{T1}} = e_T = 1.00 - 0.0110425\beta_1 + 2.38155 * 10^{-5}\beta_1^2 + 9.38784 * 10^{-7}\beta_1^3$$

$$\frac{V_{N2}}{V_{N1}} = e_N = 1.00 - 0.00393812\beta_1 - 0.0007443\beta_1^2 + 1.66937 * 10^{-5}\beta_1^3 - 1.01213 * 10^{-7}\beta_1^4$$

$$\frac{V_2}{V_1} = e_V = 1.00 + 0.000951\beta_1 - 0.00725\beta_1^2 + 1.43015 \times 10^{-5}\beta_1^3 - 8.34 * 10^{-8}\beta_1^4$$

$$\frac{\beta_2}{\beta_1} = e_\beta = 1.00 + 0.001295\beta_1 - 0.000645\beta_1^2 + 1.55053 \times 10^{-5}\beta_1^3 - 1.008 * 10^{-7}\beta_1^4$$

"N" Coating

$$\frac{V_{T2}}{V_{T1}} = e_T = 1.00 - 0.0124107\beta_1 + 2.97165 * 10^{-5}\beta_1^2 + 9.35159 * 10^{-7}\beta_1^3$$

$$\frac{V_{N2}}{V_{N1}} = e_N = 1.00 + 0.00275521\beta_1 - 0.0012869\beta_1^2 + 2.72264 * 10^{-5}\beta_1^3 - 1.604 * 10^{-7}\beta_1^4$$

$$\frac{V_2}{V_1} = e_V = 1.00 + 0.0037812\beta_1 - 0.000977626\beta_1^2 + 1.94275 \times 10^{-5}\beta_1^3 - 1.12 * 10^{-7}\beta_1^4$$

$$\frac{\beta_2}{\beta_1} = e_\beta = 1.00 - 0.000159243\beta_1 - 0.000723929\beta_1^2 + 1.81865 * 10^{-5}\beta_1^3 - 1.185 * 10^{-7}\beta_1^4$$

"C" Coating

$$\frac{V_{T2}}{V_{T1}} = e_T = 1.00 - 0.014949\beta_1 + 0.00011676\beta_1^2 + 3.27 * 10^{-7}\beta_1^3$$

$$\frac{V_{N2}}{V_{N1}} = e_N = 1.00 - 0.0096558\beta_1 - 0.0006071 * \beta_1^2 + 1.61091 * 10^{-5}\beta_1^3 - 1.048881^{-7}\beta_1^4$$

$$\frac{V_2}{V_1} = e_V = 1.00 + 0.0024071\beta_1 - 0.000934\beta_1^2 + 1.89526 \times 10^{-5}\beta_1^3 - 1.11169 \times 10^{-7}\beta_1^4$$

$$\frac{\beta_2}{\beta_1} = e_\beta = 1.00 - 0.001127\beta_1 - 0.0005889\beta_1^2 + 1.53245 \times 10^{-5}\beta_1^3 - 1.03 \times 10^{-7}\beta_1^4$$

INCO IN-738

$$\frac{V_{T2}}{V_{T1}} = e_T = 1.00 - 0.00677\beta_1 - 0.00033\beta_1^2 + 9.713 * 10^{-6}\beta_1^3 - 5.881 * 10^{-8}\beta_1^4$$

$$\frac{V_{N2}}{V_{N1}} = e_N = 1.00 + 0.00529\beta_1 - 0.00111\beta_1^2 + 2.16 * 10^{-5}\beta_1^3 - 1.224 * 10^{-7}\beta_1^4$$

$$\frac{V_2}{V_1} = e_V = 1.00 - 0.00299\beta_1 - 0.00049\beta_1^2 + 1.05 * 10^{-5}\beta_1^3 - 6.502 * 10^{-8}\beta_1^4$$

$$\frac{\beta_1}{\beta_1} = e_\beta = 1.00 + 0.00321\beta_1 - 0.00057\beta_1^2 + 1.162 * 10^{-5}\beta_1^3 - 6.958 * 10^{-8}\beta_1^4$$

where V_1 and V_2 represent the particle impact and rebound velocities while β_1 and β_2 are the impingement and rebound angles, measured from the impact surface in degrees.

Erosion Test Results

The erosion tests were conducted to obtain two types of erosion data, namely, the erosion rates and the cumulative erosion mass loss for the superalloys and coatings listed in Tables 1 and 2. The erosion rate is defined as the ratio between the change in the sample mass and the mass of the impacting particles. The erosion rate tests were carried out in one cycle using 100 gm of particles impacting the sample surface. The cumulative erosion mass loss tests on the other hand were conducted in multiple cycles. In each cycle, the specimen was impacted by a preweighed increment of particle mass. After each particle mass increment had impacted the sample, its surface was cleaned, the specimen was weighed, and the change in specimen weight was recorded. The erosion rate for each successive particle increment was determined from the relation:

$$\text{erosion rate} = \frac{\text{change in mass of sample}}{\text{mass of impacting particles}}.$$

The cumulative mass erosion tests were conducted only at the impact angles corresponding to maximum erosion. The obtained results are published by Tabakoff et al. (1990).

Erosion Test Results for Superalloys. *INCO IN-738 Alloy.* INCO IN-738 is a nickel-based alloy. The variation of the erosion rate of this alloy with impingement angles is shown in Fig. 9 for different impact velocities [600 fps (183 m/s)–1000 fps (305 m/s)] and temperature of 900°F (482°C). This figure indicates the ductile behavior of INCO-738 superalloy, with maximum erosion rate at 30 deg impingement angle for the three velocities.

X40 Superalloy. The variation of the erosion rate of cobalt-based X40 superalloy with the impingement angle is shown in Fig. 10 for various particle velocities (600, 800, and 1000 fps (183, 244, and 366 m/s)) and temperatures of 900°F (482°C). This figure indicates the ductile erosion behavior of X40 alloy, with maximum erosion at 45 deg particle impact angle.

The practical operating conditions of this alloy are 1500°F (815.5°C) and 1200 fps (366 m/s). Therefore, the X40 alloy also was tested at these conditions and the results are shown in Fig. 11. The maximum erosion rate at these conditions was 3.7 mg/g at 45 deg impingement angle.

MAR-M246 Superalloy. The erosion behavior of nickel-based MAR-M246 superalloy is shown in Fig. 12. The figure presents the erosion rate variation with the impingement angle

Downloaded 02 Jun 2010 to 171.66.16.112. Redistribution subject to ASME license or copyright; see http://www.asme.org/terms/Terms_Use.cfm

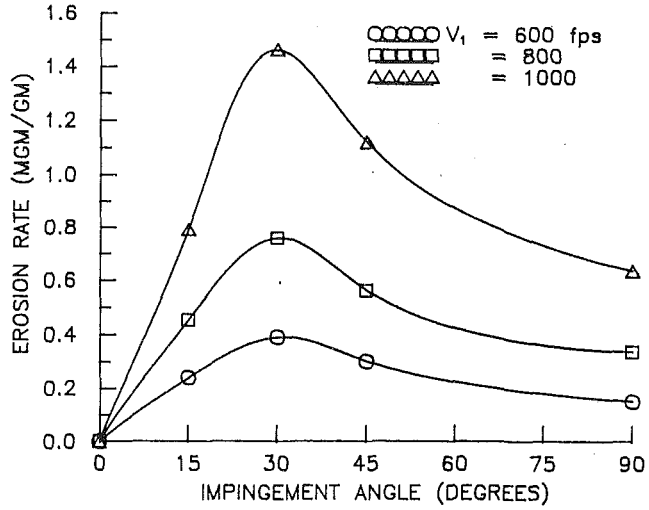


Fig. 9 INCO 738 erosion rate for different velocities, T = 900°F, fly ash

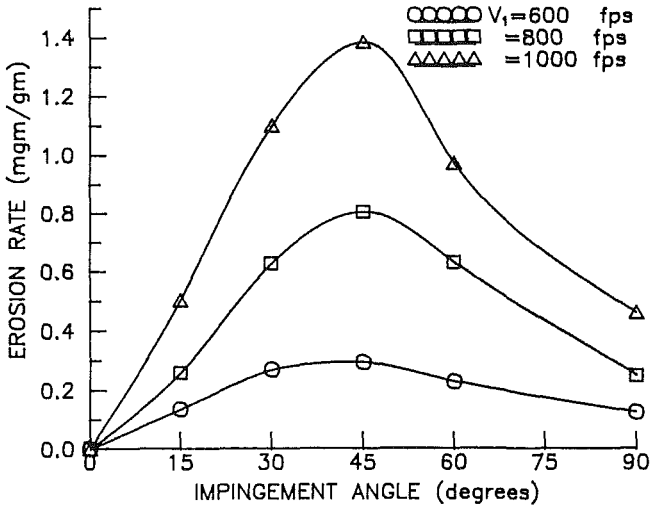


Fig. 10 X40 alloy erosion rate for different velocities, T = 900°F, fly ash

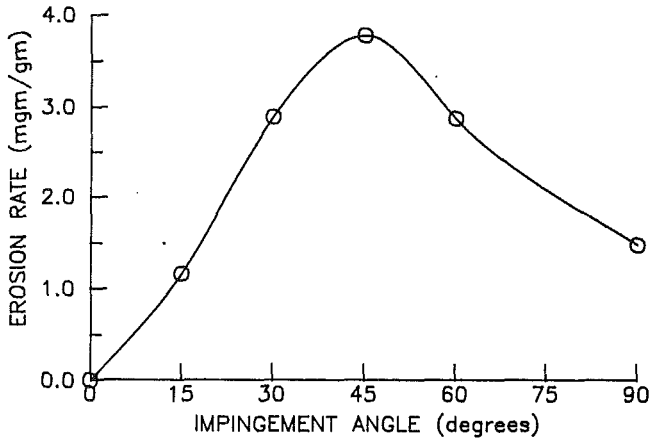


Fig. 11 X40 alloy erosion rate at T = 1500°F, V_1 = 1200 fps, fly ash

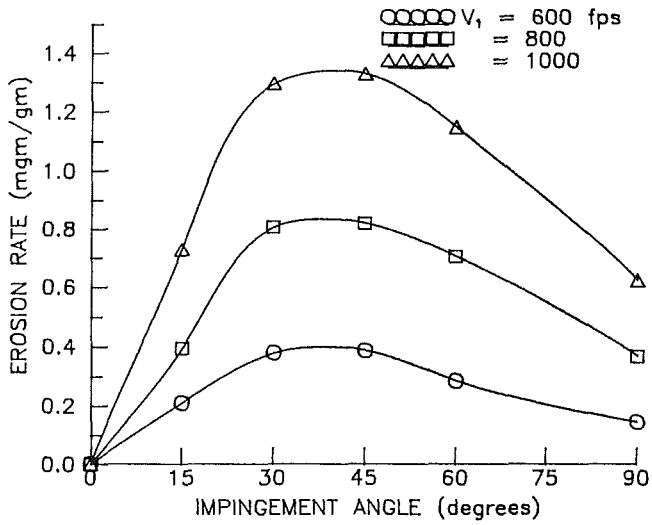


Fig. 12 M246 alloy erosion rate for different velocities, T = 900°F, fly ash

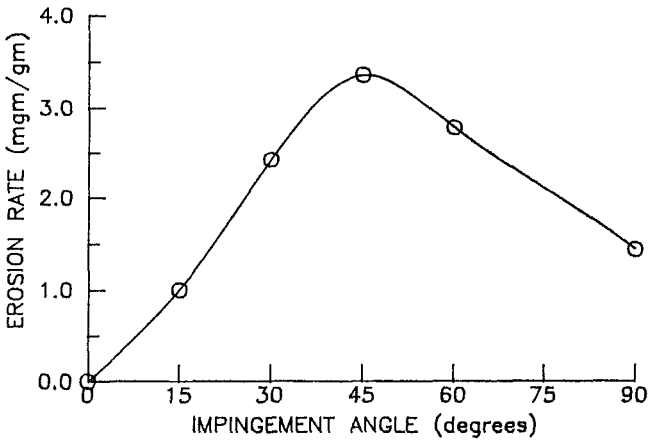


Fig. 13 M246 alloy erosion rate at T = 1500°F, V_1 = 1200 fps, fly ash

for different velocities [600, 800, and 1,000 fps (183, 244, and 366 m/s)] and temperatures of 900°F (482°C). It is clear that at these conditions MAR-M246 exhibits a ductile erosion pattern with maximum erosion rate at 30–45 deg.

Figure 13 shows the erosion rate versus the impingement angle for the M246 material operating at temperature of 1500°F (815.5°C) and impact velocity of 1200 fps (366 m/s). The maximum erosion rate at these conditions is 3.3 mg/g at 45 deg impact angle.

Erosion Test Results for Coatings. *"C"-Coating.* The "C"-coating is a cobalt-based aluminide that was applied to the cobalt-based X40 superalloy. The "C"-coating erosion characteristics are shown in Fig. 14. The erosion-rate variation with the impingement angle shows a ductile erosion pattern with maximum erosion at 60 deg impingement angle for the coated sample, at 1500°F (815.5°C) and 1200 fps (366 m/s). The erosion-rate results of Fig. 14 indicate that this coating provides a significant erosion protection, compared to the substrate X40 shown in Fig. 11.

"N"-Coatings. The "N"-coating is a nickel-base aluminide that was applied to nickel-base M246 superalloy. The erosion rate variation with the impingement angle for N-coating is shown in Fig. 15 for temperature of 1500°F (815.5°C) and impact velocity of 1200 fps (366 m/s). Inspection of this figure reveals that this material exhibits a ductile erosion pattern, with maximum erosion at 45 deg.

RT22 Coating. This coating is a platinum aluminide that was applied to nickel-based MAR-M246 superalloy. Figure 16 shows that the erosion rate curve follows the familiar form of ductile erosion with a peak at 30 deg. Comparing Figs. 16 and 15, one can conclude that the platinum content in the aluminide

Downloaded 02 Jun 2010 to 171.66.16.112. Redistribution subject to ASME license or copyright; see http://www.asme.org/terms/Terms_Use.cfm

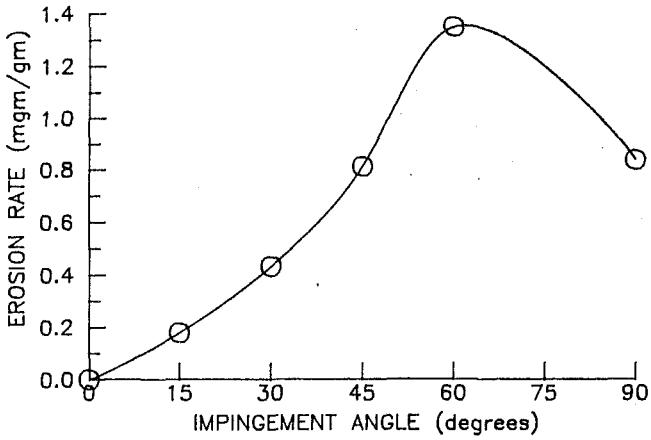


Fig. 14 C-coating erosion rate at T = 1500°F, U_p = 1200 fps, e fly ash

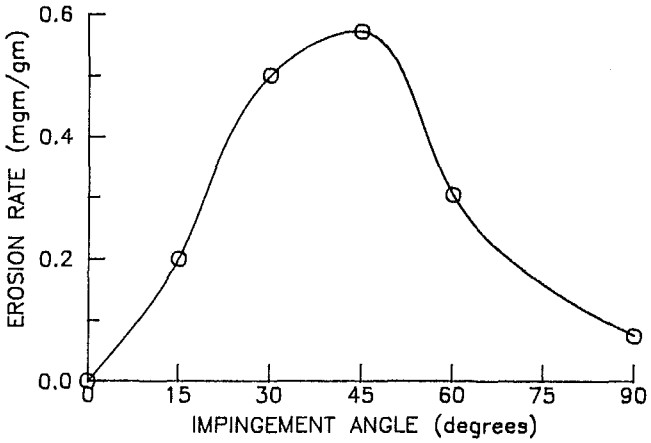


Fig. 15 N-coating erosion rate at T = 1500°F, V_1 = 1200 fps, fly ash

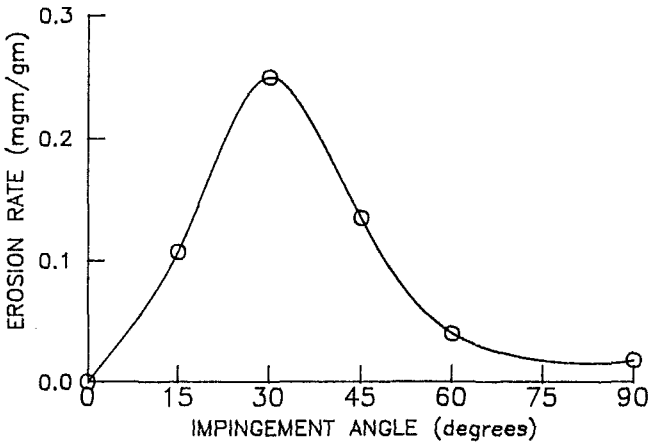


Fig. 16 RT22-coating erosion rate at T = 1500°F, V_1 = 1200 fps, fly ash

coating enhances the erosion resistance. The erosion rate is reduced to less than one-half the erosion rate of the "N" aluminide coating. In addition, the angle at which maximum erosion occurs decreases to 30 deg.

RT22B Coating. This coating is rhodium platinum aluminide that was applied to MAR-M246 superalloy. The effect of the impingement angle on the erosion rate is shown in Fig. 17, which indicates a maximum erosion rate at 30 deg impingement angle for the same conditions as Fig. 16. Comparing Figs. 17 and 16, one can see the erosion pattern of RT22B and

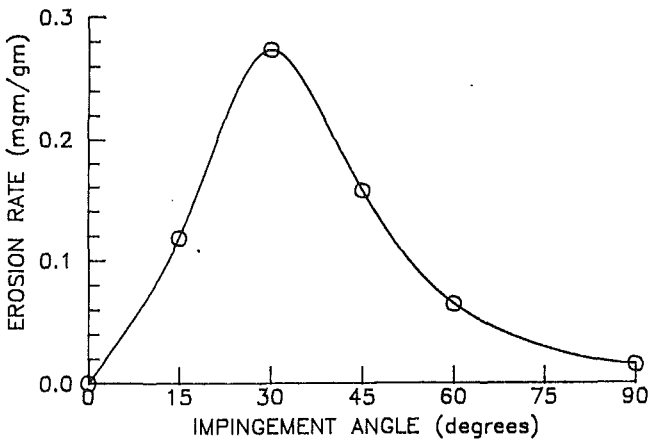


Fig. 17 RT22B-coating erosion rate at T = 1500°F, V_1 = 1200 fps, fly ash

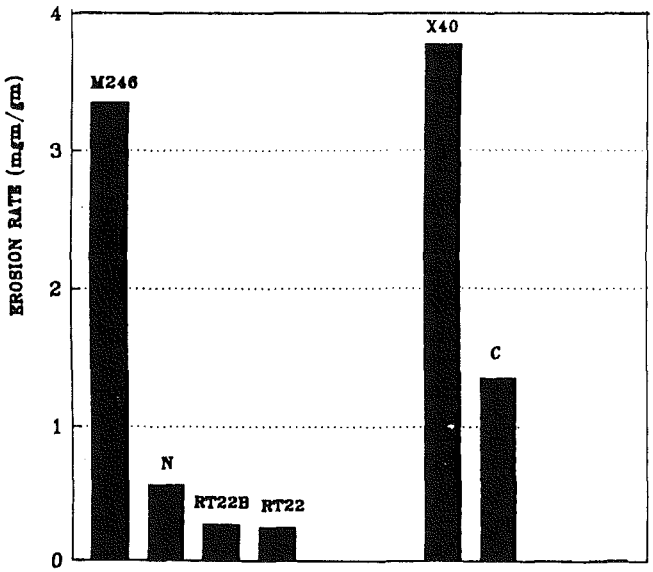


Fig. 18 Comparison of maximum erosion rate of coatings and superalloys (T = 1500°F, V_1 = 1200 fps, fly ash)

RT22 coatings are similar with only small differences in the erosion rates. From this comparison, it can be concluded that the rhodium in the coating may decrease the material erosion resistance.

Comparison of Maximum Erosion Rates. Figure 18 presents the maximum erosion rates (at 1500°F (815.5°C), 1200 fps (366 m/s)) of the superalloys and coatings investigated. The results in this figure indicate that protective coatings enhance greatly the superalloy resistance to hot erosion. The aluminide-coated-sample erosion rates ("C" and "N" coatings) are less than one-third the erosion rate of the base materials (M246 and X40). The platinum-aluminide coating (RT22) offers the best performance with more than ten times reduction in the erosion rate compared to the base material (M246). Comparing the maximum erosion rate of aluminide coatings ("N" and "C"), and platinum-aluminide coating (RT22) indicates that platinum content enhances the erosion resistance of the aluminide coatings. The RT22 coating has the minimum erosion rate, less than one-half the erosion rate of "N" coating and one order of magnitude less than the erosion rate of the base material (M246).

Coating Life Estimate

Cumulative test results indicate the particle dose effect on

Downloaded 02 Jun 2010 to 171.66.16.112. Redistribution subject to ASME license or copyright; see http://www.asme.org/terms/Terms_Use.cfm

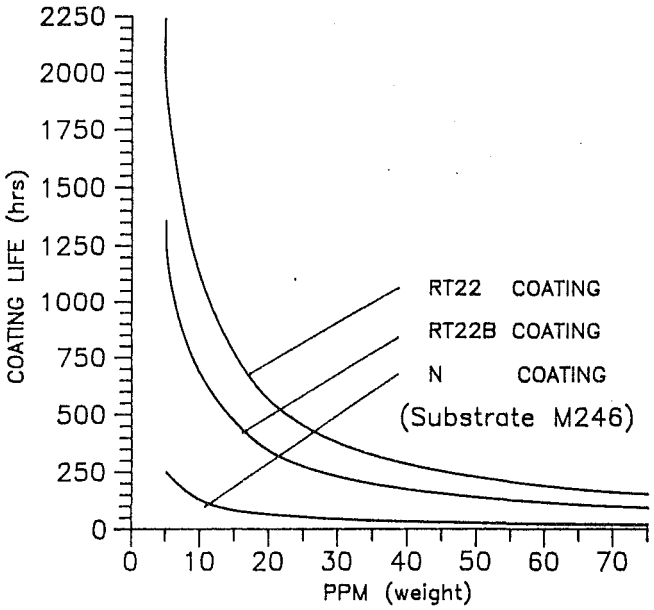


Fig. 19 Coating life variation with particle concentration at maximum erosion angle, T = 1500°F, U = 1200 fps, fly ash

both weight loss and erosion rate. Although the concentration of the particles in the test tunnel, PPM (based on weight), is kept low enough to avoid particle interactions, it is still much higher than in practical applications. Therefore, the actual coating life in terms of time is much longer than determined in the erosion wind tunnel. However, the relationship between the coating life and the mass of impacting particles as determined in the erosion tunnel will hold true in practical applications. Using these data, we have calculated the coating lives of nickel-based coatings and cobalt-based coatings for different particle concentrations. The computations were performed for the maximum erosion rates at 1500°F (815.5°C) temperature and 1200 fps (366 m/s). Figure 19 presents the estimated coating life versus particle concentration (ppm). It is clear from this figure that the coating life is strongly dependent on the particle concentration (ppm), and decreases rapidly as the particle concentration increases. According to this study, the RT22 coating has the longest life, Fig. 19. This is attributed to the fact that it has the best erosion-resistance, Fig. 18, and thicker coating.

Conclusions

From the experimental investigation conducted to study the ash particle rebound characteristics, it was found that the V_2/V_1 and β_2/β_1 parameters did not change significantly between coatings "C" and "N" in regard to the superalloys M246, X40 and INCO738. The erosion rate for all materials investigated increased with the increase of the particle velocities and temperatures. The impingement angle corresponding to maximum erosion was not affected by increased velocities and temperatures. Comparison of maximum erosion rates at 1500°F (815.5°C) and 1200 fps (366 m/s) of the superalloys investigated showed that the aluminide-coated samples "C" and "N" are less than one-third the erosion rate of the base materials (M246 and X40). The platinum-aluminide coating (RT22) offers the best erosion protection and longest life prediction for given particle concentration.

Acknowledgment

The authors acknowledge financial support from U.S. Department of Energy under Subcontract No. 19X-89628C, Oak Ridge National Laboratory, TN. We are grateful for this support and acknowledge our useful discussions with Drs. R. Judkins, P. Carlson, and E. Hoffman. Special thanks to Dr. Richard Wenglarz from Allison Company for the preparation of the tested coatings "C" and "N".

References

Aerospace Structural Metals Handbook, 1963, Syracuse University Press.

Alloy Digest, 1969, Engineering Alloy Digest Inc., Upper Montclair, NJ.

Grant, G., and Tabakoff, W., 1975, "Erosion Prediction in Turbomachinery Resulting from Environmental Solid Particles," *Journal of Aircraft*, Vol. 12, No. 5, pp. 471–478.

Tabakoff, W., and Wakeman, T., 1979, "Test Facility for Material Erosion at High Temperature," ASTM Special Publication 664, pp. 123–135.

Tabakoff, W., Hamed, A., and Beacher, B., 1983, "Investigation of Gas Particle Flow in an Erosion Wind Tunnel," *Wear*, Vol. 86, pp. 73–88.

Tabakoff, W., Hamed, A., and Eroglu, H., 1986, "Study of Particle Rebound Characteristics and Material Erosion at High Temperature," Final Technical Report, ORNL/Sub/84-89628/01, Fossil Energy Materials Program, U.S. Department of Energy.

Tabakoff, W., and Hamed, A., 1987, "Laser Measurements of Solid Particles Rebound Parameters Impacting on 2024 Aluminum and 6A1-4V Titanium Alloys," *AIAA Journal of Aeronautics and Astronautics*, Vol. 25, pp. 721–726.

Tabakoff, W., Hamed, A., Metwally, A., Yeuan, J., and Pasin, M., 1990, "Study of Particle Rebound Characteristics and Material Erosion at High Temperature," Technical Report ORNL/Sub/84-89628/03, Fossil Energy Material Program, U.S. Department of Energy.

Downloaded 02 Jun 2010 to 171.66.16.112. Redistribution subject to ASME license or copyright; see http://www.asme.org/terms/Terms_Use.cfm

Coating Effect on Particle Trajectories and Turbine Blade Erosion

W. Tabakoff

M. Metwally

Department of Aerospace Engineering
and Engineering Mechanics,
University of Cincinnati,
Cincinnati, OH 45221

Gas turbine engines operating in dusty environments are exposed to erosion and performance deterioration. In order to improve the erosion resistance, nickel and cobalt superalloy blades and vanes are widely used in the hot section of gas turbines. Protective coatings have been used to enhance superalloy resistance to hot erosion. An investigation has been conducted to study coal ash particle dynamics and resulting blade erosion for both uncoated and coated blades of a two-stage axial flow gas turbine. A quasi-three-dimensional flow solution is obtained for each blade row for accurate computation of particle trajectories. The change in particle momentum due to collision with the turbine blades and casings is modeled using restitution parameters derived from three-component laser-Doppler velocimeter measurements. The erosion models for both blade superalloy and coatings are derived based on the erosion data obtained by testing the blade superalloy and coatings in a high-temperature erosion wind tunnel. The results show both the three-dimensional particle trajectories and the resulting blade impact locations for both uncoated and coated blade surfaces. In addition are shown the distribution of the erosion rate, impact frequency, impact velocity, and impact angle for the superalloy and the coating. The results indicate significant effects of the coating, especially on blade erosion and material deterioration.

Introduction

Gas turbines operating with working fluids containing solid particles are subjected to corrosion and erosion. A permanent loss of turbomachinery performance results from the change in the blade shape and the increased blade surface roughness as reported by Tabakoff (1984) for axial flow compressors. Experience with coal-burning gas turbines has shown that even the small ash particles of mean diameters from 1 to about 30 μm can be very damaging to the exposed turbine components. It is very difficult to remove these particles from the gas stream with conventional separation techniques. In order to minimize the adverse effects of particle erosion, nickel and cobalt base superalloy blades and vanes are widely used in the hot section of gas turbines. Protective coatings have been used to enhance superalloy resistance to hot erosion-corrosion. The most widely used coatings are those based on the NiAl (on nickel base superalloys) and CoAl (on cobalt base superalloys) formed by interaction of superalloy surfaces with aluminum. To improve resistance to hot erosion-corrosion, aluminide coatings are modified to contain elements such as chromium, platinum, rhodium, and silicon. A knowledge of the particle trajectory path, including the probable impact locations and the particle impact characteristics, is required for accurate prediction of blade erosion. An analytical tool was developed by the authors to provide such knowledge of the particle behavior through the three-dimensional blade passages of axial flow turbomachinery.

Turbomachinery blade erosion has been the subject of many analytical and experimental investigations by the authors (Hamed and Fowler, 1983; Hamed et al., 1986; Tabakoff and Hamed, 1977; Tabakoff et al., 1980; Tabakoff, 1987, 1988). Although it is well known that protective coatings are widely used in the hot section of gas turbines, all particle dynamics and blade erosion studies have been conducted for uncoated ferrous alloys. In this paper, the computation of the three-dimensional particle trajectories, and the resulting blade erosion, are conducted in a two-stage axial flow turbine, for uncoated and coated nickel base superalloy. The results are presented for MAR-M246 nickel base superalloy and platinum aluminide (RT22) coating as erosion rate, impact frequency, impact velocity, and impingement angle contours on the blade pressure surfaces. The distribution of these erosion parameters over the blade surfaces provides valuable information, which can be used in taking specific measures to alleviate the blade erosion problem. The computed results of the particle trajectories and blade erosion parameters have been conducted for 15 μm weight average fly ash particles.

Contributed by the International Gas Turbine Institute and presented at the 5th International Symposium and Exposition on Gas Turbines in Cogeneration, Repowering, and Peak-Load Power Generation, Budapest, Hungary, September 3–5, 1991. Manuscript received by the International Gas Turbine Institute March 1991. Associate Editor: L. A. Riekert.

Analysis

The equations governing the particle motion in the turbomachinery flow field written in cylindrical polar coordinates

Copyright © 1992 by ASME
Downloaded 02 Jun 2010 to 171.66.16.112. Redistribution subject to ASME license or copyright; see http://www.asme.org/terms/Terms_Use.cfm

relative to a frame of reference fixed with respect to the rotating blade are:

$$\frac{d^2r_p}{d\tau^2} = F_r + r_p\left(\frac{d\theta_p}{d\tau} + \omega\right)^2 \quad (1)$$

$$r_p\frac{d^2\theta_p}{d\tau^2} = F_\theta - 2\frac{dr_p}{d\tau}\left(\frac{d\theta_p}{d\tau} + \omega\right) \quad (2)$$

$$\frac{d^2z_p}{d\tau^2} = F_z \quad (3)$$

where r_p, θ_p, and z_p define the particle location in cylindrical polar coordinates, and ω is the blade angular velocity. The centrifugal force and Coriolis acceleration are represented by the last term on the right-hand side of Eqs. (1) and (2). The first term on the right-hand side of Eqs. (1)-(3) represents the force of interaction between the two phases, per unit mass of particles. This force is dependent on the relative velocity between the particles and the gas flow, as well as the particle size and shape. Under the particulate flow conditions in turbomachines, the effects of the forces due to gravity and to interparticle interactions are negligible, compared to those due to the aerodynamic and centrifugal forces. The force of interaction between the two phases is dominated by the drag due to the difference in velocity between the solid particles and the gas flow. The force of interaction per unit mass of solid particles is given by

$$\bar{F} = \frac{3}{4}\frac{\rho}{\rho_p}\frac{C_D}{d}\left[\left(V_r - \frac{dr_p}{d\tau}\right)^2 + \left(V_\theta - \frac{d\theta_p}{d\tau}\right)^2 + \left(V_z - \frac{dz_p}{d\tau}\right)^2\right]^{1/2}(\bar{V} - \bar{V}_p) \quad (4)$$

where V_r, V_θ, and V_z represent the relative gas velocities in the radial, circumferential and axial directions, respectively, and ρ and ρ_p are the gas and solid particle material densities, d the particle diameter, and C_D the particle drag coefficient. This coefficient is dependent on the Reynolds number, which is based on the relative velocity between the particle and the gas. Empirical relations, as those presented by Tabakoff and Hamed (1986), are used to fit the drag curve over a wide range of Reynolds numbers.

Particle Trajectories. The particle trajectory calculations consist of the numerical integration of the Eqs. (1)-(3) in the flow field, up to the point of blade, hub, or tip impact. The magnitude and direction of particle rebounding velocity after these impacts are dependent on the impacting conditions and the particle and surface materials.

The particle rebounding conditions are determined from empirical correlations of the restitution parameters. These correlations are based on the experimental measurements of the particle impact and rebound velocities near the metal surface. The LDV measurements are obtained for particle-laden flows over metal samples set at various angles relative to the flow in a special tunnel described by Tabakoff et al. (1980) and Tabakoff and Hamed (1982). The restitution ratios were found to be mainly dependent upon the impingement angle (Tabakoff and Malek, 1985; Tabakoff et al., 1985a), for a given particle–material combination.

Empirical correlations were used in the present study to determine the magnitude and direction of the particle rebounding velocity after the surface impacts. The following empirical correlations were obtained by Tabakoff et al. (1990a, 1990b) for the restitution parameters in terms of the impingement angle for fly ash particles impacting targets of the material under investigation.

For the MAR-M246 Alloy

$$\frac{V_2}{V_1} = 1.00 + 0.00601123\,\beta_1 - 0.000957986\,\beta_1^2 + 1.77426\times10^{-5}\beta_1^3 - 9.94\times10^{-8}\beta_1^4 \quad (5)$$

$$\frac{\beta_2}{\beta_1} = 1.00 + 0.00872424\,\beta_1 - 0.000834276\,\beta_1^2 + 1.63771\times10^{-5}\beta_1^3 - 9.75683\times10^{-8}\beta_1^4 \quad (6)$$

For the Platinum Aluminide Coating (RT22)

$$\frac{V_2}{V_1} = 1.0 - 0.01386\,\beta_1 + 2.4201\times10^{-4}\beta_1^2 - 2.0988\times10^{-6}\beta_1^3 \quad (7)$$

$$\frac{\beta_2}{\beta_1} = 1.0 - 0.0175\,\beta_1 + 4.1312\times10^{-4}\beta_1^2 - 2.9876\times10^{-6}\beta_1^3 \quad (8)$$

where V_1 and β_1 represent the particle impact velocity and impingement angle, while V_2 and β_2 are the particle rebounding velocity and angle.

In the case of rotor blade impacts, the velocities and angles of impact and rebound are considered relative to the rotating blade. The particle trajectory after each blade impact and the particle distribution through the blade are influenced by the rebound correlations and the local turbine blade geometry as reported by Hussein and Tabakoff (1973). The blade airfoil, hub, and casing geometry must therefore be accurately represented in the trajectory analysis as it strongly influences the predicted particle dynamics. In particular, since a large number of particles impact the blunt leading edges of the turbine blades before entering the blade passage, the blading leading edge geometry has a strong influence on the rest of the trajectory calculations. In order to represent the radial variation in the blade shape on the particle trajectory, the blade surface coordinates are specified at a number of sections between the hub and tip.

Turbine Blade Passage Flow Fields. The large flow turning angles generally encountered in turbine blading produce large pitchwise as well as radial and axial flow field variations. The computed three-dimensional flow field data, on a representative grid in the blade-to-blade passage, are used to interpolate for the flow properties at each time step during the numerical integration of the particle equations of motion.

In the present study, the flow field in a blade passage is synthesized from a number of blade-to-blade stream surface solutions using the Katsanis (1965) code. The pitchwise and streamwise variations in the flow properties are reflected in each flow field solution on a blade-to-blade stream surface. The influence of the hub and tip contours and the hub-to-tip variation in the blade shapes, on the other hand, are represented in the stream surface shapes and stream filament thickness, as determined from a midchannel hub-to-tip stream surface solution by Katsanis and McNally (1977).

Blade Erosion. Sample coupons from the blade material are tested in the erosion tunnel to provide experimental measurements of the material erosion characteristics. The target erosion is dependent upon the particle impact velocity, impingement angle, and flow and target temperatures for a given particle target material combination, as shown by Tabakoff and Hamed (1977). Experimental measurements reported by Tabakoff et al. (1990a) for fly ash particles impacting samples of the materials under investigation were used to obtain the following equations. The erosion mass parameter, ϵ, is defined as the ratio of the eroded mass of target material to the mass of impinging particles.

Downloaded 02 Jun 2010 to 171.66.16.112. Redistribution subject to ASME license or copyright; see http://www.asme.org/terms/Terms_Use.cfm

$$\epsilon = C_1\left(\frac{V_1}{100}\right)^{N1}\sin^{N2}\beta_1\cos^{N3}\beta_1[1-e_T^2] + C_2\left(\frac{V_1}{100}\right)^{N4}\sin^2\beta_1[1-e_N^2] \quad (9)$$

where V_1 and β_1 are impact velocity and impact angle, respectively. The constants C_1 and C_2 and the exponents $N1$, $N2$, $N3$, and $N4$ have the following values:

	MAR-M246 alloy	Platinum aluminide coating (RT22)
$C1$	0.044678	0.00224
$C2$	0.9866×10^{-3}	0.1944×10^{-4}
$N1$	2.32	2.72
$N2$	1.15	0.65
$N3$	2.15	4.75
$N4$	2.94	2.75

e_T and e_N are the tangential and normal restitution ratios calculated by the following relations:

For MAR-M246 Alloy

$$e_T=\frac{V_{T2}}{V_{T1}}=1.00-0.00832249\,\beta_1-8.09523\times10^{-5}\beta_1^2+1.78601\times10^{-6}\beta_1^3 \quad (10)$$

$$e_N=\frac{V_{N2}}{V_{N1}}=1.00+0.00809841\,\beta_1-0.00122611\,\beta_1^2+2.30864\times10^{-5}\beta_1^3-1.2922\times10^{-7}\beta_1^4 \quad (11)$$

For Platinum Aluminide Coating (RT22)

$$e_T=\frac{V_{T2}}{V_{T1}}=1.0+8.164\times10^{-4}\beta_1-5.981\times10^{-4}\beta_1^2+1.2835\times10^{-5}\beta_1^3-7.2016\times10^{-8}\beta_1^4 \quad (12)$$

$$e_N=\frac{V_{N2}}{V_{N1}}=1.0-0.025\,\beta_1+4.9815\times10^{-4}\beta_1^2-3.5967\times10^{-6}\beta_1^3 \quad (13)$$

The computation of blade erosion combines the model for the mass erosion parameter (Eq. (9)) with the results of the particle trajectory calculations. The latter provide the impact velocities and impingement angles for a large number of particle trajectories.

Calculation Procedure

Two separate computer codes are used, one for calculating particle trajectories in the blade passages and another for predicting the blade erosion. The output of the particle trajectory code consists of three files. The first file provides the input for particle trajectory plots. The second particle trajectory output file contains all particle exit conditions from a given blade row, and is used as input to provide the initial conditions for the particle trajectories in the following blade row. These data are first adapted to a new frame of reference, which is fixed in each blade row. The particle axial and radial location is not affected by the relative motion between successive blade rows. The circumferential variation in the particle distribution at the exit of a given blade row is evened out at the entry to the following blade row due to the relative motion between successive blade rows. This effect is simulated in the computations by redistributing the particles randomly in the circumferential direction, in the new frame of reference, which is fixed relative to the subsequent blade row. The third file contains all computed particle impact data, including the impact locations, the impact velocity and impingement angle relative to the solid surfaces, for use in the code for blade surface erosion predictions.

The code for blade surface erosion computations uses as input the particle impact data, and the various coefficients of the empirical equation for blade material erosion. The output from this program includes the blade erosion distribution, as well as the distribution of the impact velocity, impingement angles, and the frequency of particle blade surface impacts.

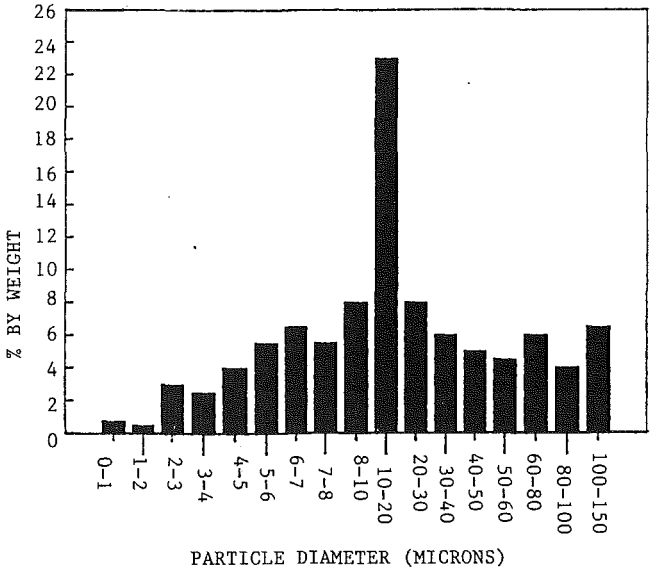


Fig. 1 Fly ash particle size distribution

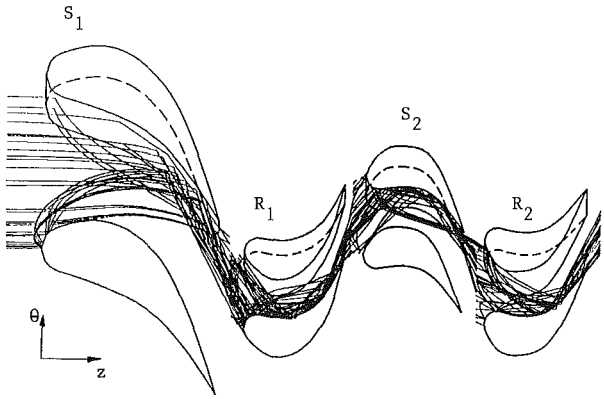


Fig. 2(*a*) Projection of particle trajectories in θ-z plane for RT22 coating

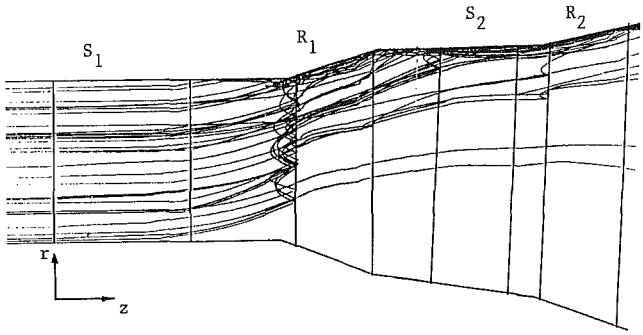


Fig. 2(*b*) Projection of particle trajectories in r-z plane for RT22 coating

Results and Discussion

The particle trajectory and blade erosion analysis were carried out for both MAR-M246 alloy and RT22 (platinum aluminide) coating through a two-stage axial flow turbine, which was described by Roelke et al. (1966). The blade erosion results presented were obtained from the trajectories corresponding

Downloaded 02 Jun 2010 to 171.66.16.112. Redistribution subject to ASME license or copyright; see http://www.asme.org/terms/Terms_Use.cfm

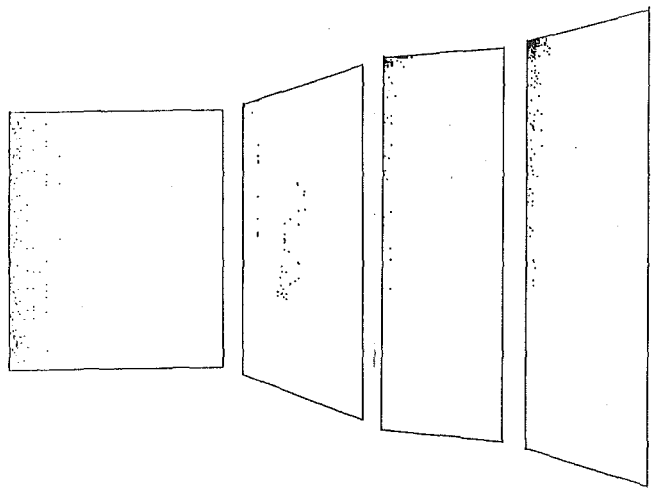


Fig. 3 Particle impact location on the blade suction surfaces for RT22 coating

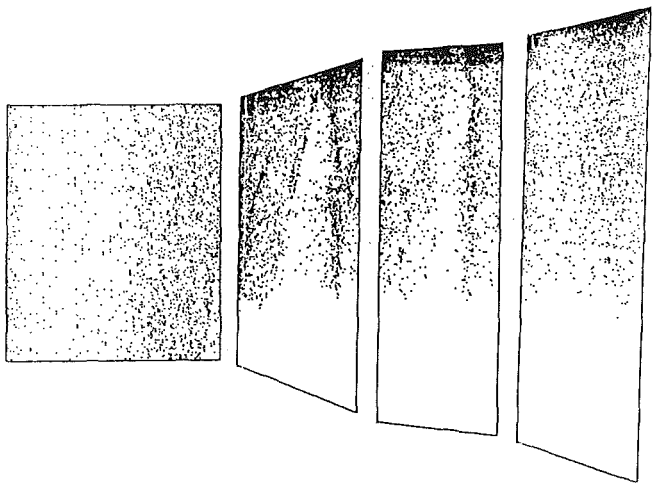


Fig. 4 Particle impact location on the blade pressure surfaces for RT22 coating

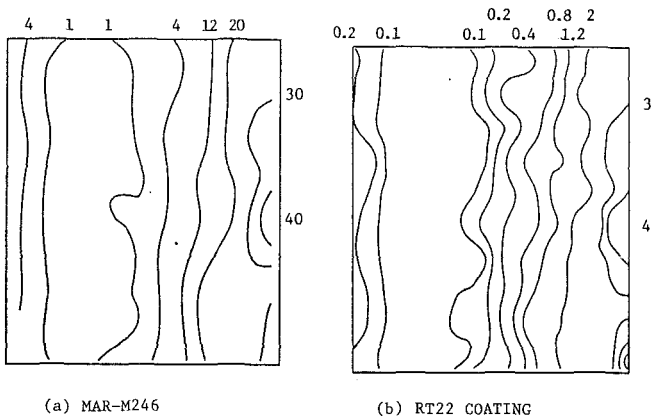


Fig. 5 First-stator pressure surface erosion rate × 10^5 (mg/g/cm^2)

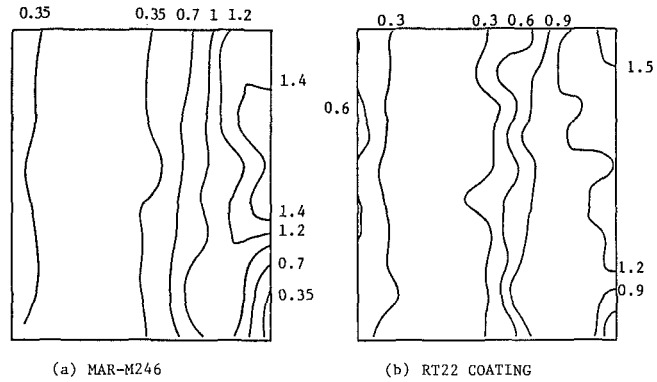


Fig. 6 First stator pressure surface impact frequency × 10^{-6} (g^{-1} cm^{-2})

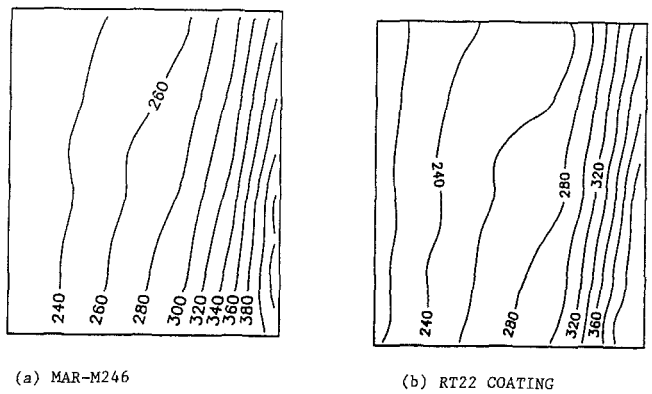


Fig. 7 First stator pressure surface impact velocity (m/s)

to 75,000 ingested particles or 22×10^{-5} g of ash in the gas turbine for standard inlet air equivalent conditions at 1893 rpm and 3.21 kg/s weight flow. The results are presented for the particle trajectories and the resulting blade erosion, for the fly ash particles whose size distribution is shown in Fig. 1. The presented results are obtained for uniform particles, of 15 μm weight average mean particle diameter.

At the gas turbine inlet, the particles were assumed to have no velocity lag relative to the gas. Their spatial locations were randomly distributed, according to the mass flow, using statistical methods. The results presented here show typical particle trajectories and the associated blade erosion pattern. The results are also presented for particle blade impact data that influence erosion, which include the distribution of impact frequency, impact velocity, and impingement angle over the blade pressure surfaces.

Particle Trajectories. The computed three-dimensional particle trajectories for coated and uncoated blades show no significant differences. Therefore, the particle trajectories are presented for the coated blade only. Figure 2(*a*) shows samples of particle trajectories in the different blade rows as viewed from the tip in the z-θ plane. An examination of Fig. 2(*a*) reveals that all the particles impact the blade pressure surface at least once but not the blade suction surface. Figure 2(*a*) shows that, while only about one third of the particles impact the blade leading edge of the first nozzle, almost all the particles impact the blade leading edge of subsequent blade rows. This is due to the fact that the direction of the particle motion relative to the blades at inlet is generally very different from the inlet flow angles in all the blade rows, except in the first nozzle. After the blade leading edge impacts, these particles lose most of their initial axial momentum with some rebounding such that their axial velocities are in the upstream direction. The influence of the flow field on the trajectories of these particles can be observed to be more significant after the blade leading edge impact. The flow field influence is manifested in the particles re-acquiring axial velocities, while their circumferential velocities are reduced under the influence of the aerodynamic forces of interaction. All the particles that initially impact the leading edge, on either pressure or suction side, again impact the blade pressure surface closer to the trailing edge.

Figure 2(*b*) shows the projection of the particle trajectories

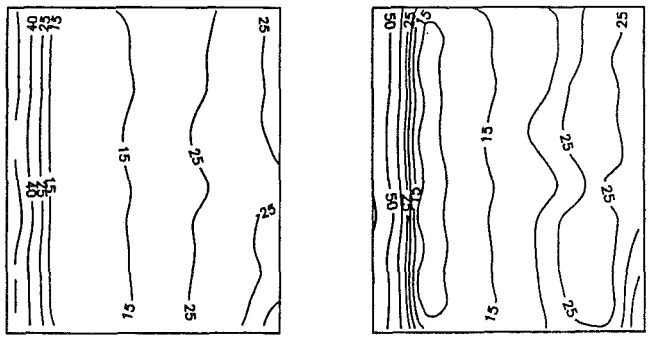
Downloaded 02 Jun 2010 to 171.66.16.112. Redistribution subject to ASME license or copyright; see http://www.asme.org/terms/Terms_Use.cfm

in the meridional (z–r) plane throughout the turbine. The particle impacts with the blade blunt leading edges can be clearly seen in this figure as they are characterized by subsequent upstream particle motion. One can observe in Fig. 2(b) the strong influence of the impact with the blades on the particle radial motion. The particle blade impacts impart circumferential rebounding particle velocities, causing particle centrifugation away from the hub. This centrifugal effect is found to be significant only after the first rotor blade impact.

Particle Impact Locations. Because of the large similarity of the predicted particle impact locations for coated and uncoated blade, only the results of coated blades are presented. The particle-blade impact location are shown in Figs. 3 and 4 over the blade suction and pressure surfaces, respectively. Comparing the two figures, one can see the blade pressure surfaces are subject to much more impacts than the suction surfaces. The very few suction surface impacts are seen to be mostly restricted to the zone near the leading edge (Fig. 3), while the rest of the blade suction surface is not subject to any particle impacts. Figure 4 shows that in the first nozzle, the blade pressure surface impacts increase toward the trailing edge with no radial variation in the impact pattern. The particle-blade impact pattern, however, is seen to change strongly in the radial direction in subsequent blade rows. The absence of particle-blade impacts towards the hub can be seen in Fig. 4 to start in the first rotor. The portion of the blade surface with no particle impacts continues to grow in subsequent blade rows. The trajectories of Fig. 2(b) show that the particle centrifugation after rotor blade impacts, and the blade flaring at the hub, combine to produce this effect.

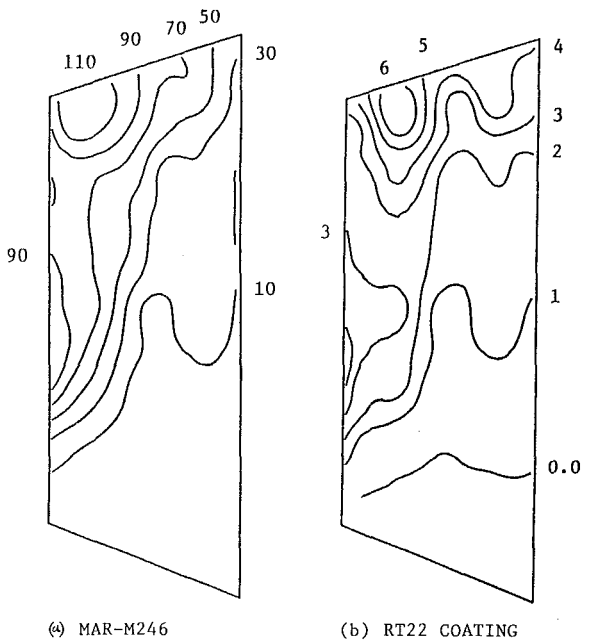
Blade Erosion. The blade erosion prediction is based on the particle computed impact data as determined from the particle trajectory calculations, and erosion model (9). The results of blade erosion rate computations, as well as the parameters that contribute to the erosion, namely, the frequency of particle blade impacts, the particle impact velocity, and particle impact angle, are presented for both uncoated and coated blade rows. The blade mass erosion rate is defined as the blade mass removal per unit area of the blade surface per unit mass of ingested particles in (mg m^{-2} g^{-1}). The blade surface impact frequency is defined as the number of particle impacts per unit area of blade surface per unit mass of ingested particles (m^{-2} g^{-1}). The erosion results will only be presented for the blade pressure surfaces, since the blade suction surface erosion was found to be insignificant because of the small number of particle impacts.

Figures 5–20 present the blade erosion results for the uncoated and coated pressure surfaces of a two-stage turbine. The first stator erosion rate and related parameters are shown in Figs. 5–8 for both coated and uncoated blades. The results indicate that although the coating has very slight effect on the erosion pattern, it has a strong influence on the values of the erosion rates. For both coated and uncoated blades, Fig. 5 shows a low erosion zone near the middle of the first stator pressure surface, which can be attributed to the low impact frequencies in this area (Fig. 6). The erosion rate increases toward the blade trailing edge (Fig. 5) due to increase of impact velocity (Fig. 7) and impact frequency (Fig. 6) and the favorable values of the impact angles near the trailing edge (Fig. 8). Comparing the values of maximum erosion at the midspan of the trailing edge (Fig. 5) reveals that the coated blade maximum erosion is one order of magnitude less than that of uncoated blade. With simple calculations, it can be shown that coated blade life will be one order of magnitude longer than that of the uncoated blades.



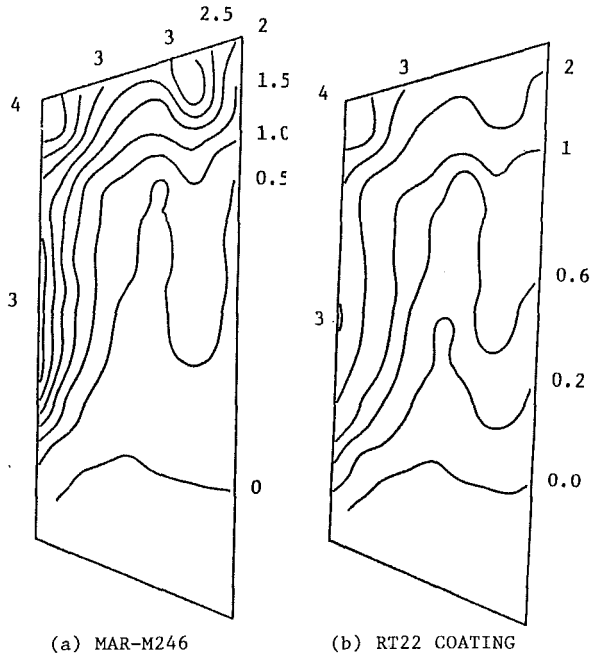
(a) MAR-M246 (b) RT22 COATING

Fig. 8 First stator pressure surface impact angle (deg)



(a) MAR-M246 (b) RT22 COATING

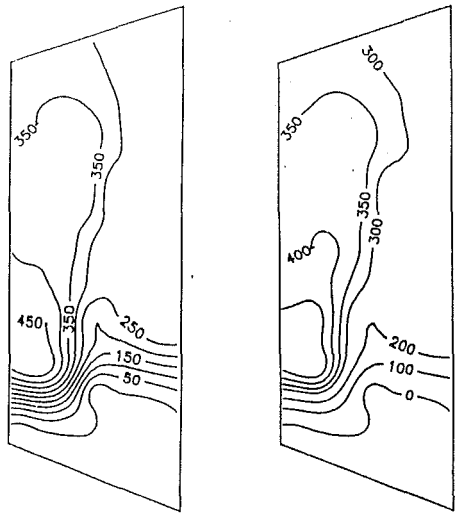
Fig. 9 First rotor pressure surface erosion rate × 10^5 (mg/g/cm^2)



(a) MAR-M246 (b) RT22 COATING

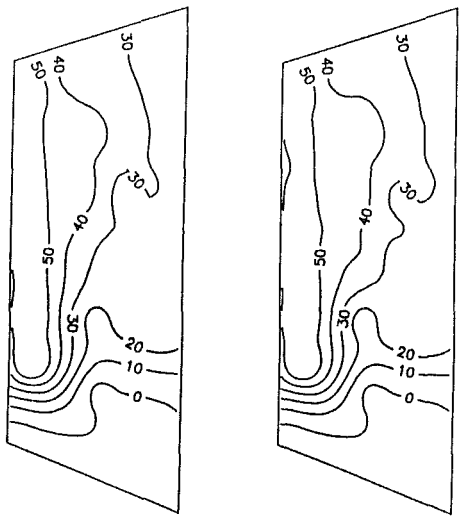
Fig. 10 First rotor pressure surface impact frequency × 10^{-6} (g^{-1} cm^{-2})

Downloaded 02 Jun 2010 to 171.66.16.112. Redistribution subject to ASME license or copyright; see http://www.asme.org/terms/Terms_Use.cfm



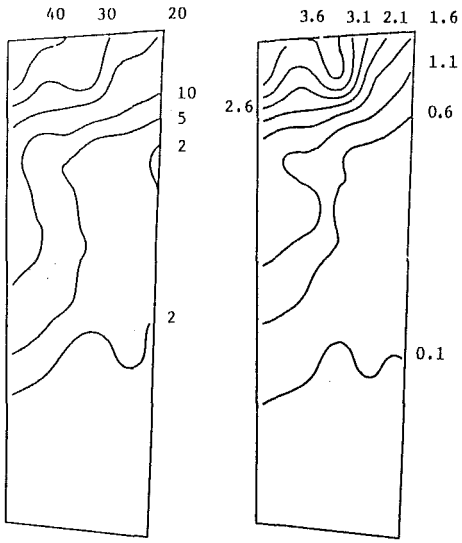
(a) MAR-M246 (b) RT22 COATING

Fig. 11 First rotor pressure surface impact velocity (m/s)



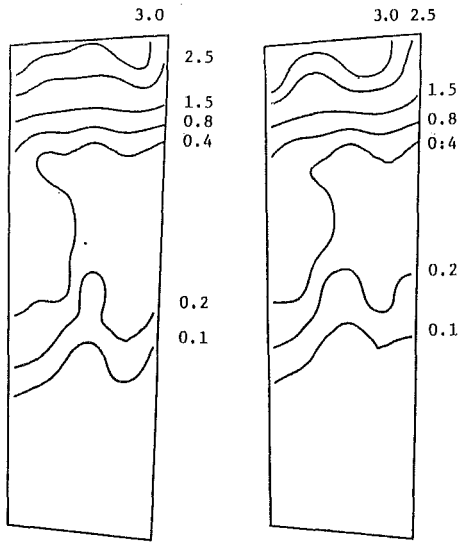
(a) MAR-M246 (b) RT22-COATING

Fig. 12 First rotor pressure surface impact angle (deg)



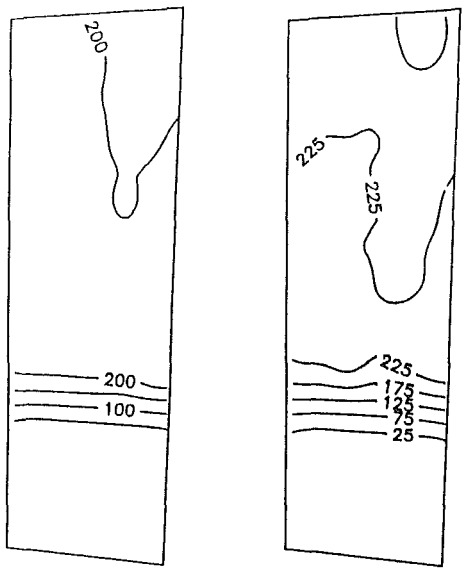
(a) MAR-M246 (b) RT22 COATING

Fig. 13 Second stator pressure surface erosion rate × 10^5 (mg/g/cm^2)



(a) MAR-M246 (b) RT22 COATING

Fig. 14 Second stator pressure surface impact frequency × 10^{-6} (g^{-1} cm^{-2})

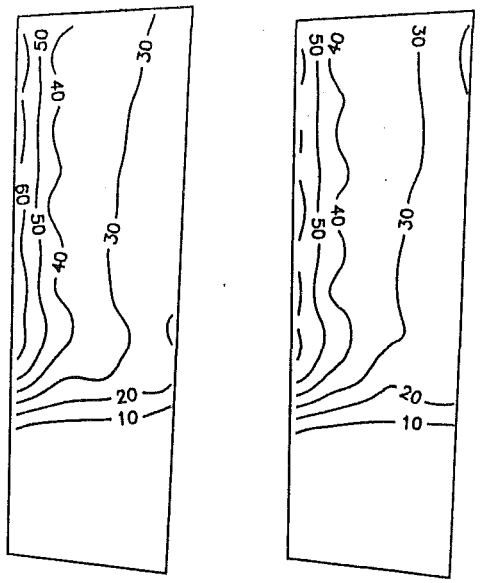


(a) MAR-M246 (b) RT22 COATING

Fig. 15 Second stator pressure surface impact velocity (m/s)

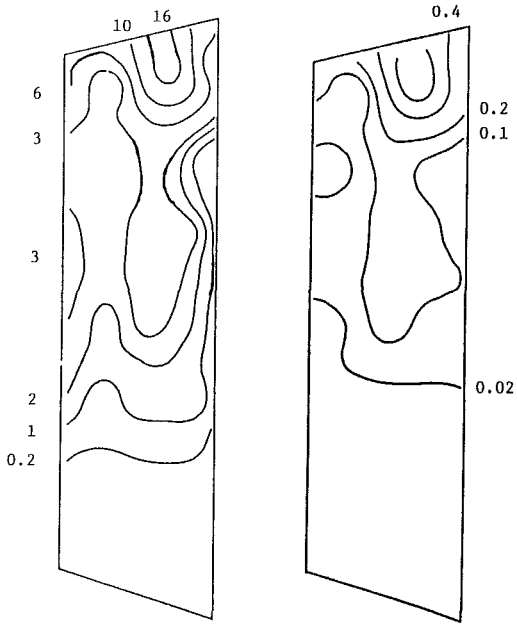
The first rotor blade erosion related parameters over the pressure surface are shown in Figs. 9–12 for coated and uncoated blades. Figure 9 shows that no erosion is predicted near the hub over a region extending from one seventh the blade span at the leading edge to one fifth the span at the trailing edge. This is caused by the particle radial migration under the effect of the centrifugal force. Beyond the no-erosion region, the blade erosion increases radially toward the blade tip and increases axially from the blade trailing edge to the blade leading edge due to increase of both the impact frequency (Fig. 10) and impact velocity (Fig. 11) in these directions. Figure 9 shows that the maximum erosion is at the tip leading edge corner for both coated and uncoated blades. The strong effect of coating on the blade erosion can be clearly seen by comparing the values of maximum erosion for both cases. The results show that the coated blade erosion is twenty time less than that of uncoated blade. This remarkable reduction of the

Downloaded 02 Jun 2010 to 171.66.16.112. Redistribution subject to ASME license or copyright; see http://www.asme.org/terms/Terms_Use.cfm



(a) MAR-M246 (b) RT22 COATING

Fig. 16 Second stator pressure surface impact angle (deg)

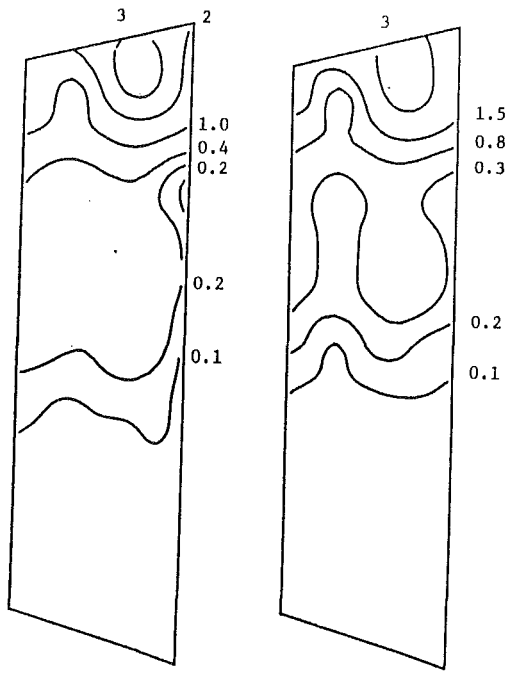


(a) MAR-M246 (b) RT22 COATING

Fig. 17 Second rotor pressure surface erosion rate × 10^5 (mg/g/cm^2)

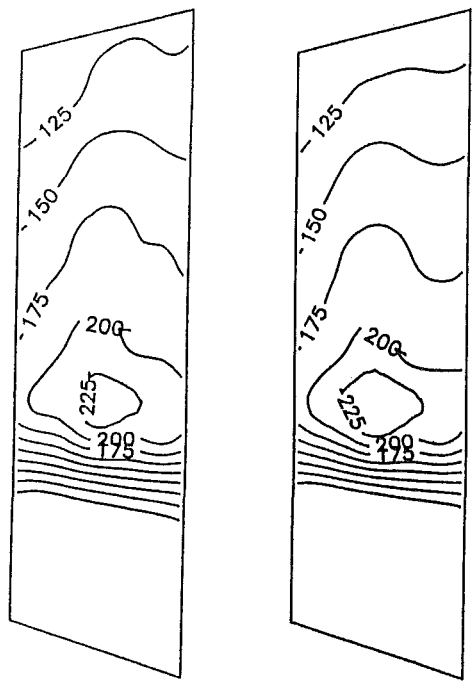
coated blade erosion results in much longer blade life and high turbine performance for very long time.

The results of the blade erosion analysis for the second stator pressure surface are presented in Figs. 13–16 for coated and uncoated blades. The maximum predicted blade erosions are at the tip leading edge corners for both cases, as shown in Fig. 13. The results indicate that the coating has a very slight effect on the impact frequency, impact velocity, and impact angle. However, the blade coating has a very strong influence on the blade erosion. The uncoated blade maximum erosion is one order of magnitude higher than the coated blade erosion. The results show an increase of blade erosion, impact frequency, and impact velocity toward the blade tip (Figs. 13–15), while the impact angle increases toward the blade leading edge with little variation in the radial directions (Fig. 16).



(a) MAR-M246 (b) RT22 COATING

Fig. 18 Second rotor pressure surface impact frequency × 10^{-6} (g^{-1} cm^{-2})

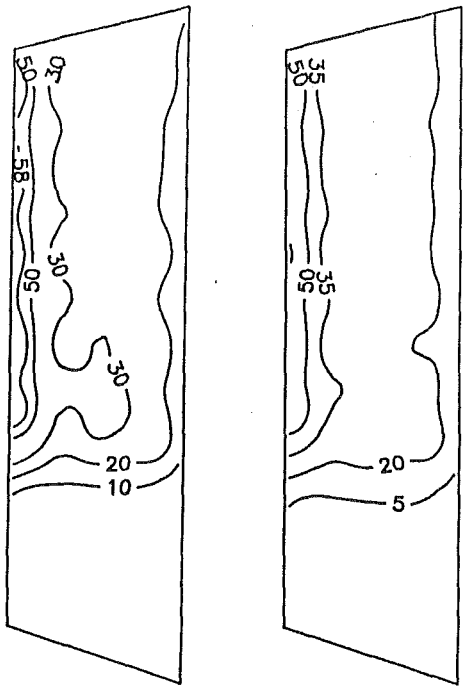


(a) MAR-M246 (b) RT22 COATING

Fig. 19 Second rotor pressure surface impact velocity (m/s)

The results for the second rotor blade pressure surface are shown in Figs. 17–20. The highest erosion rates are close to the blade tip section with maximum erosion at the tip trailing edge for coated and uncoated blades as shown in Fig. 17. Comparing Figs. 17(*a*) and 17(*b*), one can see that the maximum erosion of the coated blade is 25 times less than that of the uncoated blade. Figures 18(*a*) and 18(*b*) show that the impact frequency increases toward the tip with maximum value at tip trailing edge corner. The impact velocity is maximum at

Downloaded 02 Jun 2010 to 171.66.16.112. Redistribution subject to ASME license or copyright; see http://www.asme.org/terms/Terms_Use.cfm



(a) MAR-M246 (b) RT22 COATING

Fig. 20 Second rotor pressure surface impact angle (deg)

one third of the blade span and decreases toward blade hub and tip.

Conclusions

The presented results provide a detailed description of particle trajectories and blade surface erosion pattern through a two-stage gas turbine engine for both coated and uncoated blades. The results of particle trajectory computations show no significant variation in the computed three-dimensional trajectories for coated and uncoated blades, which indicates the insignificant effect of coating on the particle dynamics through the turbine blade rows. The blade surface erosion results show that the first rotor represents the most critical blade row erosion. The location of the blade row influences not only the magnitude of the blade erosion, but also the erosion pattern and the location of maximum blade erosion. In the first stator blade, the maximum erosion is at the trailing edge near the middle of the blade span. The rest of the blade rows in the turbine suffer the maximum erosion at the outmost radial locations and the erosion pattern is quite similar to the impact frequency distribution over the blade surfaces. Although the coating has a very slight influence on the erosion patterns, it has a very strong effect on the erosion levels. The maximum erosion rates for the coated blade rows are, at least, one order of magnitude less than the uncoated ones. Since the blade life increases as the erosion rate decreases, the coated blade life will be one order of magnitude longer.

Acknowledgments

This research work was partially supported by the U.S. Department of Energy, Contract No. 19X-89628C, Oak Ridge National Laboratory, Oak Ridge, TN.

References

Hamed, A., 1981, "Particle Dynamics of Inlet Flow Fields With Swirling Vanes," Paper No. AIAA 81-0001.

Hamed, A., and Fowler, S., 1983, "Erosion Pattern of Twisted Blades by Particle Laden Flows," ASME JOURNAL OF ENGINEERING FOR POWER, Vol. 105, pp. 839–843.

Hamed, A., 1984, "Solid Particle Dynamic Behavior Through Twisted Blade Rows," ASME *Journal of Fluids Engineering*, Vol. 106, pp. 251–256.

Hamed, A., Tabakoff, W., and Mansour, M., 1986, "Turbine Erosion Exposed to Particulate Flow," ASME Paper No. 86-GT-258.

Hussein, M. F., and Tabakoff, W., 1973, "Dynamic Behavior of Solid Particles Suspended by Polluted Flow in a Turbine Stage," *Journal of Aircraft*, Vol. 10, pp. 434–440.

Katsanis, T., 1965, "Fortran Program for Calculating Transonic Velocities on a Blade-to-Blade Stream Surface of a Turbomachine," NASA TND-2809.

Katsanis, T., and McNally, W. D., 1977, "Revised Fortran Program for Calculating Velocities and Streamlines in the Hub-Tip Mid Channel Stream Surface of an Axial, Radial, or Mixed Flow Turbomachine or Annular Duct, Vols. 1 and 2," NASA TND-8430 and NASA TND-8431.

Roelke, R. J., Stabe, R. G., and Evans, D. G., 1966, "Cold-Air Performance Evaluation of Scale Model Oxidizer Pump-Drive Turbine for the M-1 Hydrogen-Oxygen Rocket Engine-II. Overall Two-Stage Performance," NASA TND-3368.

Tabakoff, W., and Hamed, A., 1977, "Aerodynamic Effects on Erosion in Turbomachinery," JSME and ASME Paper No. 70, presented at the 1977 Joint Gas Turbine Congress, Tokyo, Japan, May.

Tabakoff, W., Hamed, A., and Ramachandran, J., 1980, "Study of Metals Erosion on High Temperature Coal Gas Streams," ASME JOURNAL OF ENGINEERING FOR POWER, Vol. 102, pp. 148–152.

Tabakoff, W., and Hamed, A., 1982, "Investigation of Gas Particle Flow in Erosion Wind Tunnel," presented at the 7th Annual Conference on Materials for Coal Conversion and Utilization, National Bureau of Standards, Gaithersburg, MD, Nov.

Tabakoff, W., 1983, "A Study of the Surface Deterioration Due to Erosion," ASME JOURNAL OF ENGINEERING FOR POWER, Vol. 105, pp. 47–52.

Tabakoff, W., 1984, "Review—Turbomachinery Performance Deterioration Exposed to Solid Particles Environments," ASME *Journal of Fluids Engineering*, Vol. 106, pp. 106–125.

Tabakoff, W., and Malak, M. F., 1985, "Laser Measurements of Fly Ash Rebound Parameters for Use in Trajectory Calculations," ASME Paper No. 85-GT-161.

Tabakoff, W., Malak, M. F., and Hamed, A., 1985, "Laser Measurements of Solid Particles Rebound Parameters Impacting on 2024 Aluminum and 6Al-4V Titanium Alloys," Paper No. AIAA-85-1570.

Tabakoff, W., and Hamed, A., 1986, "The Dynamics of Suspended Solid Particles in a Two-Stage Gas Turbine," ASME *Journal of Turbomachinery*, Vol. 108, pp. 298–302.

Tabakoff, W., 1987, "Compressor Erosion and Performance Deterioration," ASME *Journal of Fluid Engineering*, Vol. 109, pp. 298–306.

Tabakoff, W., 1988, "Turbomachinery Alloys Affects by Solid Particles," ASME Paper No. 88-GT-295.

Tabakoff, W., Hamed, A., Metwally, M., Yeuan, J., and Pasin, M., 1990a, "Study of Particle Rebound Characteristics and Material Erosion at High Temperature," Final Technical Report, Fossil Energy Materials Program, U.S. Department of Energy, ORNL/Sub/84-89628/03, Oct.

Tabakoff, W., Hamed, A., Metwally, M., Yeuan, J., and Pasin, M., 1990b, "Study of Particle Rebound Characteristics and Material Erosion at High Temperature," Progress Technical Report, Fossil Energy Materials Program, U.S. Department of Energy, ORNL/Sub/84-89628/04, Nov.

Downloaded 02 Jun 2010 to 171.66.16.112. Redistribution subject to ASME license or copyright; see http://www.asme.org/terms/Terms_Use.cfm

S. M. Meier

D. M. Nissley

K. D. Sheffler

United Technologies,
Pratt & Whitney,
East Hartford, CT 06108

T. A. Cruse

Mechanical Engineering Department,
Vanderbilt University,
Nashville, TN 37235

Thermal Barrier Coating Life Prediction Model Development

A thermal barrier coated (TBC) turbine component design system, including an accurate TBC life prediction model, is needed to realize the full potential of available TBC engine performance and/or durability benefits. The objective of this work, which was sponsored in part by NASA under the Hot Section Technology (HOST) Program (Contract NAS3-23944), was to generate a life prediction model for electron beam–physical vapor deposited (EB–PVD) zirconia TBC. Specific results include EB–PVD zirconia mechanical and physical properties, coating adherence strength measurements, interfacial oxide growth characteristics, quantitative cyclic thermal spallation life data, and a spallation life model.

Introduction

In this study a thermal barrier coating is a thin, about 0.01 in. (0.254 mm), layer of ceramic applied to the gas path surface of cooled turbine components such as airfoils and vane platforms. This insulative ceramic layer reduces the temperature of the underlying metal structure relative to the gas path temperature. This relative temperature reduction can provide significant benefits (Duvall and Ruckle, 1982; Sheffler and Gupta, 1988) in the form of either component durability extension or system performance improvement (obtained through increased gas path temperature or reduced cooling), depending on the degree of risk the designer is willing to assume in the event of spallation loss of the insulative ceramic layer. This risk can be substantially reduced if the ceramic coating spallation life can be reliably predicted. Thus, full achievement of TBC performance benefits depends on development of an accurate TBC life prediction model.

Earlier work has shown that the spallation life of a first-generation plasma-deposited zirconia TBC is related to the severity of cyclic thermal loading. This work led to development of a life prediction model, which correlated spallation life with exposure time, temperature, and number of thermal cycles (DeMasi et al., 1989). The objective of the present work is to extend the life modeling effort to include a more durable ceramic (Meier et al., 1990) produced by the method of electron beam–physical vapor deposition (EB–PVD) (Strangman, 1982). This process generates a highly columnar ceramic microstructure, which possesses superior strain tolerance and cyclic thermal spallation life, as compared to earlier coating systems (Fig. 1). Spallation of EB–PVD ceramic occurs by cracking at the thermally grown oxide (TGO) layer (predominantly alumina)–metal interface. This TGO grows between the metal and EB–PVD ceramic layers during prolonged thermal exposure (Fig. 2).

Specific activities involved in development of the EB–PVD life prediction model included measurement of EB–PVD ceramic physical and mechanical properties and adherence strength, measurement of TGO growth kinetics, generation of quantitative cyclic thermal spallation life data, and development of a spallation life prediction model. The results for EB–PVD TBC are presented and compared with selected results obtained for plasma-deposited TBC in the following sections.

EB–PVD Physical Properties

Thermal expansion and thermal conductivity were measured to support heat transfer and thermal stress analyses required for life prediction modeling. These tests were performed at Holometrix Inc. of Cambridge, MA, under subcontract. Thermal expansion was measured both parallel and perpendicular to the EB–PVD ceramic columns using a comparative technique with coated and uncoated substrates. Thermal conductivity was measured only in the direction parallel to the ceramic columns. Tests were conducted on virgin (as-deposited) ceramic and also on ceramic that had been thermally exposed for 50 hours at 2100°F (1149°C) to simulate the effects of sintering or phase changes that might occur in an engine environment.

Thermal expansion results are shown in Fig. 3. Included for reference are results obtained on plasma-deposited ceramic (DeMasi et al., 1989). Within the range of experimental error (1 percent for perpendicular, 10 percent for parallel measurements), these results show no significant difference between the expansion properties of the plasma and EB–PVD deposited ceramic. Also, no directional or exposure sensitivity was observed in the EB–PVD ceramic.

Thermal conductivity was measured by the steady-state com-

Contributed by the International Gas Turbine Institute and presented at the 36th International Gas Turbine and Aeroengine Congress and Exposition, Orlando, Florida, June 3–6, 1991. Manuscript received at ASME Headquarters February 6, 1991. Paper No. 91-GT-40. Associate Editor: L. A. Riekert.

Copyright © 1992 by ASME
Downloaded 02 Jun 2010 to 171.66.16.112. Redistribution subject to ASME license or copyright; see http://www.asme.org/terms/Terms_Use.cfm

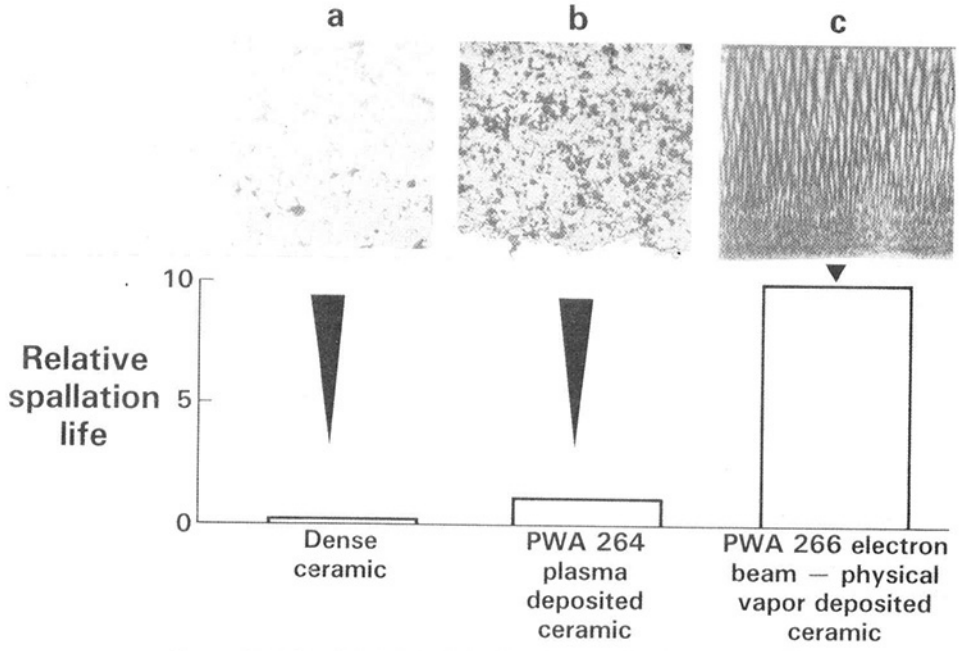


Fig. 1 Ceramic microstructure modification provides increases in life

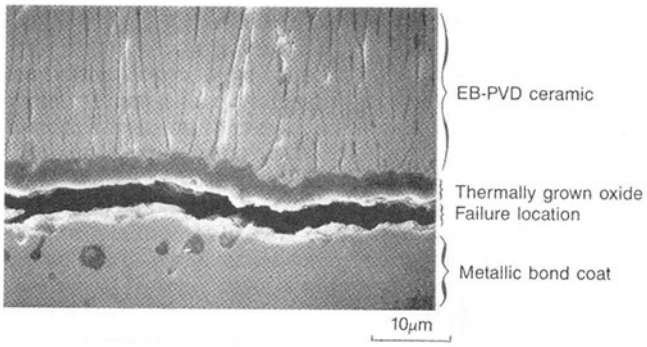


Fig. 2 Ceramic spallation failure observed on laboratory and engine test components: Note separation at TGO-metal interface

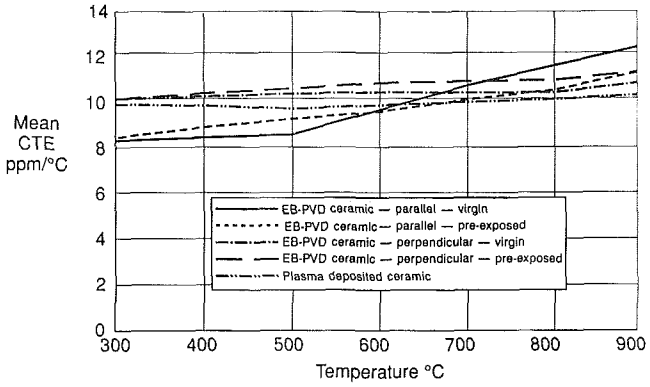


Fig. 3 Thermal expansion of 7 percent yttria partially stabilized zirconia coatings

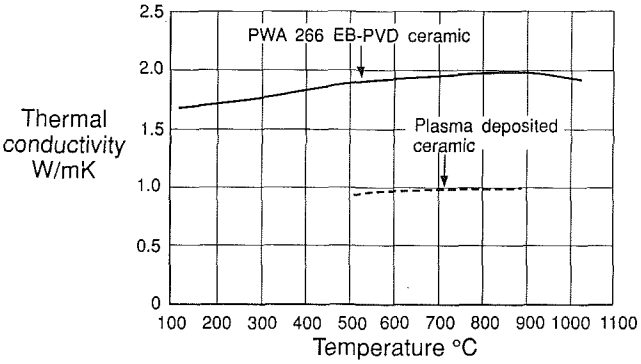


Fig. 4 Thermal conductivity of 7 percent yttria partially stabilized zirconia coatings

parative method according to ASTM standard E1225-87. Results are shown in Fig. 4. Previously obtained results for the plasma system are shown for purposes of comparison. In this case there is a significant difference between the conductivities of the two structures, which is attributed to the anisotropy of the EB-PVD ceramic as compared to the isotropic plasma structure (compare Figs. 1*b* and 1*c*). Nevertheless, very significant metal temperature reduction (Meier et al., 1990) and durability benefits (Fig. 1) have been shown in engine testing of EB-PVD ceramic-coated airfoils.

Ceramic Mechanical Behavior

The objectives of this effort were to obtain EB-PVD zirconia mechanical property data and to create a ceramic constitutive model for use in analysis of EB-PVD ceramic cyclic stress and strain. Tension and compression testing of the zirconia ceramic was conducted with the uniaxial stress applied parallel to the plane of the coating (perpendicular to the EB-PVD ceramic columns). Properties were not measured directly on free-standing ceramic but were calculated by comparative tension and compression testing of thin-walled single crystal superalloy tubes with and without EB-PVD zirconia coating deposited on the external diameter. Ceramic thickness was on the order of 0.08 in. (2.03 mm). Metal wall thickness was 0.022 to 0.045 in. (0.56 to 1.14 mm) for compression and 0.005 in. (0.13 mm) for tensile specimens. An extensometer was used to obtain load versus strain data for each test. Monotonic tension and compression tests were conducted over a temperature range from room temperature to 2200°F (1204°C). Sustained load compressive creep tests were conducted at 1400°F (760°C), 1600°F (871°C), and 1800°F (982°C). Mechanical testing and data analysis were conducted at Southwest Research Institute, San Antonio, TX (Cruse et al., 1990).

As illustrated in Figs. 5 and 6, the bimaterial ceramic/substrate composite response is generally bilinear in compression

Downloaded 02 Jun 2010 to 171.66.16.112. Redistribution subject to ASME license or copyright; see http://www.asme.org/terms/Terms_Use.cfm

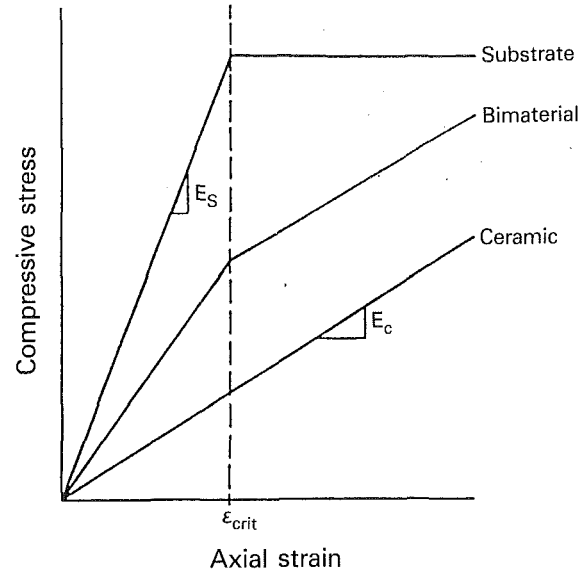


Fig. 5 Schematic compression test response

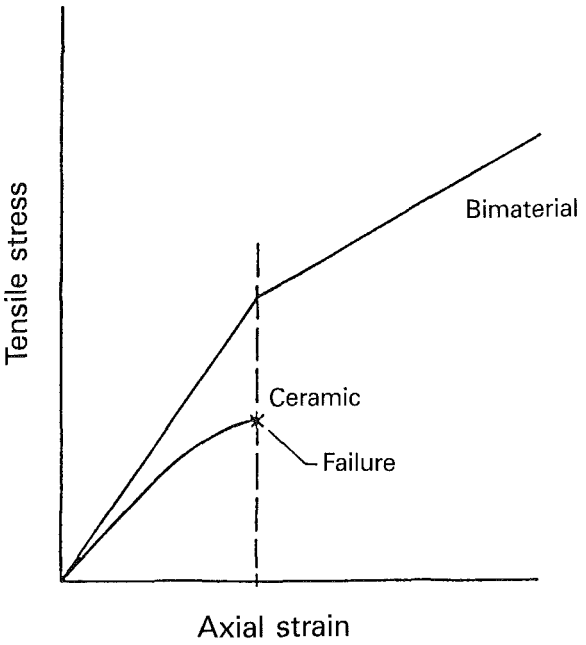


Fig. 6 Schematic tension test response

and tension. In compression, the onset of bilinear behavior occurs when the substrate becomes plastic, as shown schematically in Fig. 5. However, in tension, the bilinear response is attributed to cracking and debonding of the ceramic, after which the load is carried by the substrate (Fig. 6). This bimaterial behavior forms the basis for calculation of ceramic properties from the uncoated and ceramic-coated specimen responses. When the substrate is perfectly plastic or the ceramic debonds, static equilibrium is sufficient to determine the loads in both components. When both materials are linearly elastic, however, the system is statically indeterminate, and it becomes necessary to apply compatibility conditions to solve for the individual loads in the ceramic and substrate. The ceramic response for the elastic regime was deduced by using the thick-walled cylinder solution (Timoshenko and Goodier, 1970; Boresi and Sidebottom, 1985) and applying Hooke's law.

Deduced tensile and compressive moduli are shown in Fig. 7. While the compression results seem reasonably consistent, considerably more scatter is seen in the tensile modulus data. Within the limits of this scatter, modulus values appear to be consistent in both tests.

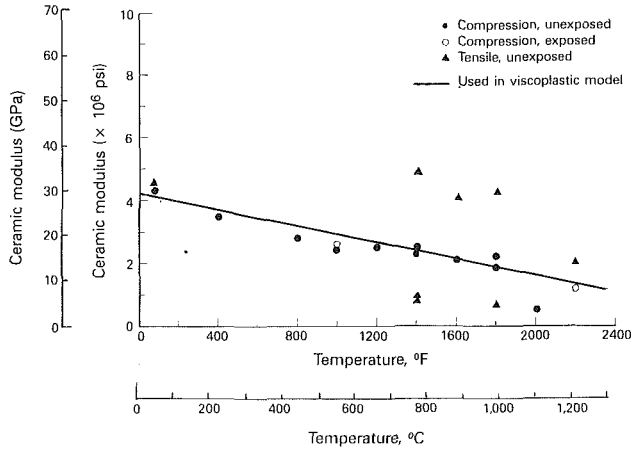


Fig. 7 Influence of temperature on ceramic modulus calculated from results of metallic and coated metallic specimen tests

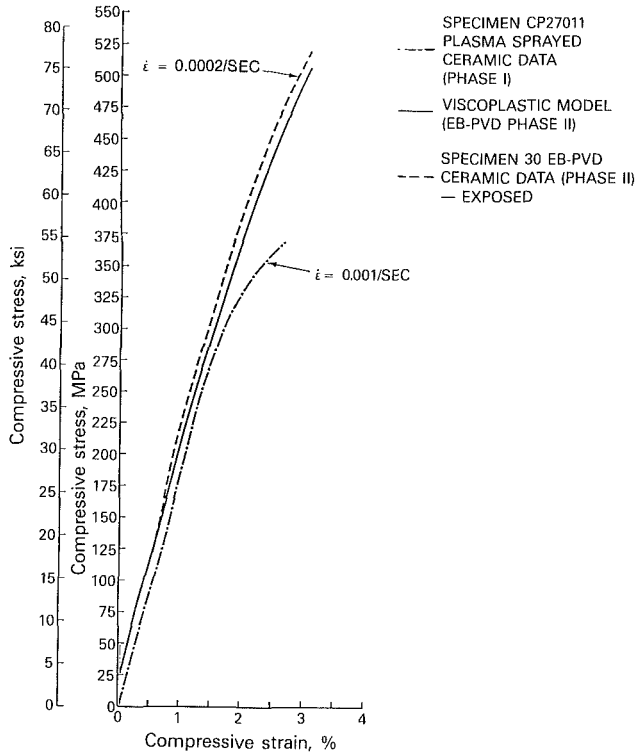


Fig. 8 Comparison of calculated EB-PVD compressive stress-strain behavior with experimentally measured results for EB-PVD and plasma ceramic at 1000°F (538°C)

The ceramic response in compression is judged to be linearly elastic up to about 1 percent strain at room temperature, increasing to about 3 percent at 1800°F (982°C). Above this temperature, the linear strain limit drops off to about 2 percent. Specific results exhibit considerable scatter, and engineering judgment is required to achieve consistent data interpretations. The ceramic remained adherent past yielding of the substrate and up to the point of gross buckling of the substrate.

Compression test results of EB-PVD ceramic are compared to plasma-sprayed ceramic in Fig. 8. As shown, the EB-PVD elastic limit strength is about 45–50 ksi (310–345 MPa) at 1000°F (538°C). Note that the EB-PVD ceramic exhibits higher strength than the plasma-sprayed ceramic at 1/5 the strain rate. On an equal strain rate basis, the plasma-sprayed ceramic would exhibit roughly 10 times more inelastic deformation than the EB-PVD ceramic.

Downloaded 02 Jun 2010 to 171.66.16.112. Redistribution subject to ASME license or copyright; see http://www.asme.org/terms/Terms_Use.cfm

Unlike the expectation prior to test, the EB-PVD ceramic does have *some* apparent in-plane tensile strength. In general, the specimen tensile behavior was seen to be elastic, up to a ceramic fracture strain. At that point the ceramic ceased to have axial (in-plane) load-carrying capability but did act to reinforce the substrate, a very striking phenomenon but of little design importance. After correcting for residual stresses due to fabrication, all EB-PVD ceramic tensile strengths and elastic limits are less than approximately 1.0 ksi (6.9 MPa).

The tensile testing program included planned unloadings at various strain levels to evaluate whether the EB-PVD ceramic fractures would close, causing a restiffening of the bimaterial specimen. The conclusion of these tests is affirmative, in that when the strain is reduced to the range of the apparent ceramic fracture strain, the specimens exhibited higher stiffness, consistent with the stiffness prior to ceramic fracture during the first loading. It was thereby concluded that the mechanism of EB-PVD ceramic tensile fracture is consistent with reducing the stiffness to zero above a critical strain level, but requires a bilinear model to account for closure effects as strain is reduced below the critical value.

The EB-PVD ceramic constitutive model development effort concentrated on modeling "first-order" ceramic behavior. Elastic modulus was assumed to be a linear function of temperature (see Fig. 7) and the Poisson ratio was taken to be 0.25. EB-PVD ceramic column separation and accumulated cracking at low tensile stress levels was modeled by assuming that the columns open freely as the ceramic stress transitions into tension. Upon reverse (i.e., compressive-going) loading, the columns close at the same strain level, which opened the columns during the tensile-going portion of the cycle. The compressive ceramic behavior was modeled by using Walker's isotropic viscoplastic formulation (Walker, 1981). Constitutive model correlation capability is presented in Fig. 8. In general, the model duplicates the observed EB-PVD ceramic compressive monotonic behavior quite well. The tensile and compressive EB-PVD constitutive formulations have been generalized to three dimensions and incorporated into computer software. The software is compatible with the MARC™ general purpose and LAYER (Nissley, 1990) finite element programs.

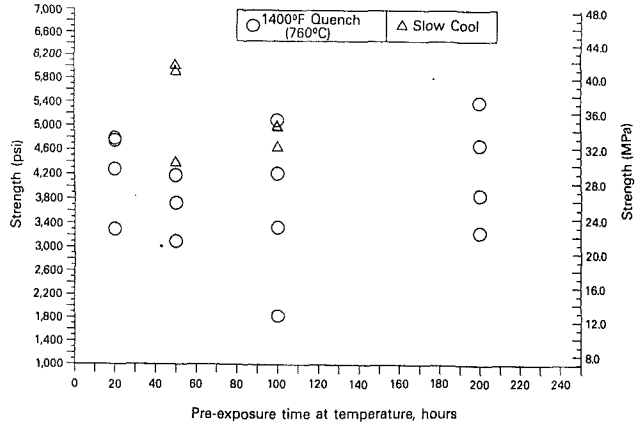


Fig. 9 Adherence strength of EB-PVD ceramic as a function of exposure time at 2100°F (1149°C). Note that coating fails at the thermally grown oxide/metal interface in this test which duplicates the engine failure mode. Strength of virgin coating is greater than the low strength of adhesive used in test

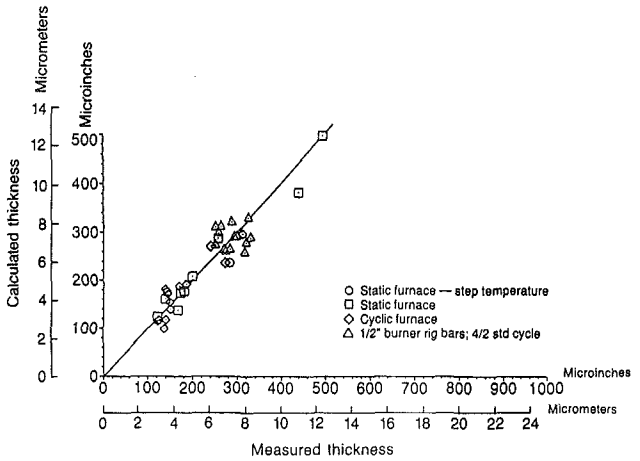


Fig. 10 Calculated versus measured thermally grown oxide thickness

Out-of-Plane Strength

Interfacial strength tests were conducted on virgin EB-PVD coatings and on coatings that were thermally exposed for times and temperatures ranging from 20 to 500 h and from 1900 to 2100°F (1038 to 1149°C). Specimens were fabricated by EB-PVD ceramic coating one end of a flat, ground 1/4 in. (6.35 mm) diameter nickel superalloy pin. A similarly ground aluminum pin was then adhesively bonded to the coated face to form a cylindrical tensile test specimen, which was pulled to failure.

Results are summarized in Fig. 9. Several attempts to test virgin ceramic all resulted in failure of the epoxy adhesive, indicating an out-of-plane coating strength greater than the 6000 psi (41.4 MPa) strength of the adhesive. As shown in Fig. 9, strengths of exposed specimens were all below this level, with essentially no dependence of strength on exposure time. All out-of-plane test specimen failures occurred at the TGO-metal interface (see Fig. 2), which accurately simulated the failure mode seen in engine and rig testing.

Oxidation Model

Based on the demonstrated influence of oxidation on the plasma-deposited TBC spallation life (Miller and Lowell, 1982; DeMasi et al., 1989) and on the EB-PVD failure location (Fig. 2), a bond coat oxidation model was developed as part of the EB-PVD life modeling effort. Oxide thickness data for the EB-PVD oxidation model were obtained from both furnace and burner rig tested specimens. Furnace testing involved both static and cyclic exposures for various times, cycles, and temperatures ranging from 1900 to 2100°F (1038 to 1149°C), and up to 1800 hours. Burner rig testing involved cyclic exposure of virgin and furnace pre-exposed specimens in a jet-fueled burner. The burner rig cycle involved a 4-min immersion in the jet-fueled flame, followed by a 2-min forced air cool. Destructive oxide thickness measurements were obtained using scanning electron microscopy of metallographic sections.

Considerable care was required to retain ceramic and oxide layers on furnace exposure specimens during cool-down after removal from the furnace. Whereas the EB-PVD ceramic has exceptional resistance to cyclic thermal spallation, its tolerance to static exposure is limited for the specimen geometry used in this program. Spallation occurs during cool-down from furnace exposures as short as 40 h. In contrast, this same coating system survives up to 1000 cumulative hours of hot time in cyclic exposure at comparable temperatures. The sensitivity to static exposure seems to be related to the interface stresses that arise at the specimen free edges. Previous work with the plasma ceramic system indicated that it also would spall during cool-down from static furnace exposure, but only after exposure times of the same magnitude as those accumulated prior to failure in cyclic testing at the same temperature. In both cases (plasma and EB-PVD ceramic), spallation during cool-down from furnace exposure could be prevented by very slow cooling.

The following oxide thickness model was obtained:

Downloaded 02 Jun 2010 to 171.66.16.112. Redistribution subject to ASME license or copyright; see http://www.asme.org/terms/Terms_Use.cfm

$$\delta = \{\exp[Q(1/T_o - 1/T)]t\}^n \quad (1)$$

where:

δ = oxide thickness (μm)
$Q = \Delta H/R = 27777.4$
ΔH = apparent activation energy
R = universal gas constant
T_o = temperature constant = 2423.7 K
$n = 0.332$
T = temperature (K)
t = time (s)

Best-fit values of the constants Q, T_o, and n were obtained by nonlinear regression analysis. This model provides a good fit of the data, as shown in Fig. 10, where calculated oxide thickness is plotted versus observed thickness.

Life Prediction Design Data Generation Test Method

TBC life modeling involved correlation of ceramic spallation life measured in an instrumented burner rig with TGO growth characteristics and thermomechanically induced TGO strain levels. It involves exposure of an instrumented, TBC-coated superalloy bar in a jet fueled burner rig. Specimen temperature was controlled by modulation of the fuel-air ratio. To simulate engine cyclic transients, the specimen was periodically cycled out of the flame into an air-cooling jet. Thermal stress levels developed in the burner rig specimen were controlled by manipulation of thermal exposure parameters such as temperature, cycle rate, hot and cold cycle times, transient heating rate, and specimen internal cooling air flow rate. As shown in Fig. 2, this test faithfully duplicates the engine spallation failure mode.

Burner rig test parameters were varied to generate design data over a wide range of simulated mission cycles. These tests were grouped in three generic cycle types: the "strain emphasis" cycle, where many rapid thermal cycles were imposed, the "oxide emphasis" cycle, where significant hold time was imposed at the cycle maximum temperature, and the "mixed mode" cycle, which combined elements of the strain and oxide cycles.

Life Prediction Modeling

Past experience with plasma-sprayed TBC (DeMasi et al., 1989) indicated that inelastic deformation of the ceramic was a critical life parameter. However, nonlinear analysis of the EB-PVD ceramic behavior during burner rig specimen thermal cycling indicates that the EB-PVD ceramic remains elastic. For that reason and because spallation failure of the EB-PVD TBC system is caused by cracking at the TGO-metal interface (Fig. 2), life modeling efforts have used TGO elastic strains instead of EB-PVD ceramic strains.

The TGO mechanical strain was taken to be due to the thermal growth mismatch between the TGO and the substrate, resulting in TGO elastic strain (or stress). The coefficient of thermal expansion (CTE) for the TGO, not measured in this program, was assumed to be linearly dependent on temperature based on CTE values obtained for aluminum oxide from literature (ASM International, 1989). The free elongation of the TGO at temperature was taken to be:

$$\delta L/L = \int_{Tsf}^{T} \alpha(T)dT = \alpha_0(T - T_{sf}) + 1/2\alpha_1[(T - T_o)^2 - (T_{sf} - T_o)^2] \quad (2)$$

where

T = metal/EB-PVD ceramic interface temperature
T_{sf} = strain (or stress)-free temperature for the oxide (taken to be the maximum metal/EB-PVD ceramic interface temperature + 98°C (200°F))

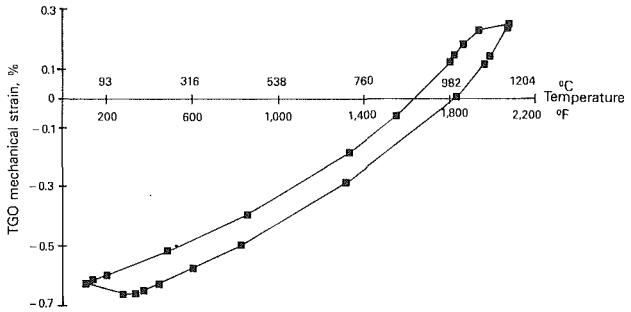


Fig. 11 Representative TGO mechanical strain history calculated for the burner rig specimen geometry and strain emphasis cycle

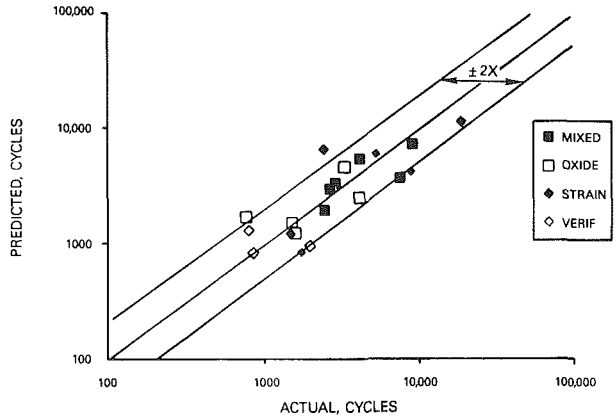


Fig. 12 Correlation results for the fatigue model

$\delta L/L$ = free thermal elongation of the TGO
$\alpha_0 = 0.36 \times 10^{-5}$ in./in./°F (0.65×10^{-5} mm/mm/°C)
$\alpha_1 = 0.91 \times 10^{-9}$ in./in./°F (1.64×10^{-9} mm/mm°C)

The mechanical strain in the TGO was then calculated for a particular cycle by subtracting the results from Eq. (2) from the substrate total strain.

$$\epsilon(T) = \epsilon_{ss}(T) - (\delta L(T)/L) \quad (3)$$

where:

ϵ = mechanical strain in the TGO
ϵ_{ss} = substrate total strain

The substrate cyclic total strain was obtained from an elastic three-dimensional analysis for each of the EB-PVD ceramic coated burner rig specimens. A representative TGO mechanical strain cyclic history is presented in Fig. 11.

Several cyclic damage models for the TGO were evaluated by applying them to the life data. Each damage model was taken to be a power law relation, consistent with elementary fatigue models and with the damage model developed for plasma-sprayed TBC (DeMasi et al., 1989). The general form of the power law life model is

$$N = A\Delta\epsilon^b \quad (4)$$

where N is the cyclic life, A is an empirical normalizing constant, and b is the empirical power law coefficient. The strain range ($\Delta\epsilon$) in Eq. (4) was assumed to be the maximum TGO tensile mechanical strain, obtained from Eq. (3). The parameter A was found in the earlier study (DeMasi et al., 1989) to depend on the amount of oxide growth, although the specific rationale for the dependence was not determined.

The fatigue life model is given as

$$N = [(\Delta\epsilon_{ff}/\Delta\epsilon)(1 - \delta/\delta_c)^c + (\delta/\delta_c)^c]^b \quad (5)$$

where:

δ_c = critical oxide thickness which causes EB-PVD ceramic spallation without cycling = 0.00055 in. (0.0140 mm)

Downloaded 02 Jun 2010 to 171.66.16.112. Redistribution subject to ASME license or copyright; see http://www.asme.org/terms/Terms_Use.cfm

$b = 7.64$
$\Delta\epsilon_{ff}$ = constant = 0.016 mm/mm (in/in)
$c = 1.0$
δ = oxide thickness at a particular cycle number

Since static furnace failures did not occur, we simply take δ_c strain to be an empirical factor.

The fact that the same life model formulation works for both plasma-sprayed and EB-PVD TBC systems suggests that the failure mechanisms are the same for both systems. The current study suggests that the maximum TGO tensile mechanical strain (or stress) is controlling for both types of TBC systems.

Calculated versus actual lives are presented in Fig. 12. The baseline data set consisting of oxide, strain, and mixed-mode cycles was well-correlated by the fatigue model. Calculated lives of the baseline data set with two exceptions were within a factor of ± 2 of the actual lives. The model was successfully exercised by predicting the lives of three verification tests within the $\pm 2\times$ life scatter band.

Summary

In this NASA-sponsored program, a life model for an EB-PVD TBC system was developed to support component designs. Life data useful for model development were obtained by exposing instrumented, EB-PVD ceramic-coated cylindrical specimens in a jet fueled burner rig. Monotonic compression and tensile mechanical tests and physical property tests were conducted to obtain the EB-PVD ceramic behavior required for burner rig specimen analysis. As part of that effort, a nonlinear constitutive model was developed for the EB-PVD ceramic. Spallation failure of the EB-PVD TBC system consistently occurred at the TGO-metal interface. Calculated out-of-plane stresses were a small fraction of that required statically to fail the TGO. Thus, EB-PVD TBC spallation was attributed to the interfacial cracking caused by in-plane TGO strains. Since TGO mechanical properties were not measured in this program, calculation of the burner rig specimen TGO in-plane strains was performed by using alumina properties. A life model based on maximum in-plane TGO tensile mechanical strain and TGO thickness correlated the burner rig specimen EB-PVD ceramic spallation lives within a factor of about $\pm 2\times$. Life model predictive capability was confirmed by applying the model to three verification tests. Prediction of the verification tests was within the scatter band of the correlated data set.

Acknowledgments

The authors would like to thank NASA for their support of "TBC Life Prediction Model Development" under contract No. NAS3-23944 and especially Dr. Robert A. Miller, NASA program manager. In addition, the authors would like to extend their sincere appreciation to those who have aided in the processing, testing, characterization, and modeling of the EB-PVD ceramic coating system and corresponding life model. In particular, the following people have truly made substantial program contributions: Donald Broadhurst, Claude Clavette, Glenn Cottnoir, Charles Giggins, Dinesh Gupta, Jack Lally, Ernest Littlefield, Jeanine Marcin, Joseph McIlrath, Jr., Richard Mullin, Andrew Nagy, Carl Popelar, Leo Riendeau, Raymond Skurzewski, Nicholas Ulion, and Merritt Wight.

References

ASM International, 1989, *ASM Engineered Materials Reference Book*.

Boresi, A. P., and Sidebottom, O. M., 1985, *Advanced Mechanics of Materials*, 4th ed., Wiley, New York, pp. 492–500.

Cruse, T. A., Nagy, A., and Popelar, C. F., 1990, "Mechanical Testing of Advanced Coating System: Vol. I," Final Report, SwRI Project No. 06-1778-001, Cooperative Agreement No. NCC 3-89, Southwest Research Institute, San Antonio, TX, June.

DeMasi, J. T., Ortiz, M., and Sheffler, K. D., 1989, "Thermal Barrier Coating Life Prediction Model Development," Phase I Final Report, Contract NAS3-23944, NASA CR-182230.

Duvall, D. S., and Ruckle, D. L., 1982, "Ceramic Thermal Barrier Coatings for Turbine Engine Components," ASME Paper No. 82-GT-332.

Meier, S. M., Nissley, D. M., and Sheffler, K. D., 1990, "Status of Ceramic Thermal Barrier Coatings—Gas Turbine Applications and Life Prediction Methods," *Proceedings of the 1990 Coatings for Advanced Heat Engines Workshop*, CONF-9008151, Castine, ME.

Miller, R. A., and Lowell, C. E., 1982, "Failure Mechanisms of Thermal Barrier Coatings Exposed to Elevated Temperature," *Thin Solid Films*, Vol. 99, p. 265.

Nissley, D. M., 1990, "Layer User and Programmer Manual," NASA CR-187038, Nov.

Sheffler, K. D., and Gupta, D. K., 1988, "Current Status and Future Trends in Turbine Application of Thermal Barrier Coatings," ASME JOURNAL OF ENGINEERING FOR GAS TURBINES AND POWER, Vol. 110, pp. 605–609.

Strangman, T. E., 1982, U.S. Patent No. 4,321,311, "Columnar Grain Ceramic Thermal Barrier Coatings," March.

Timoshenko, S. P., and Goodier, J. N., 1970, *Theory of Elasticity*, 3rd ed., McGraw-Hill, New York, pp. 69–71.

Walker, K. P., 1981, "Research and Development Program for Nonlinear Structural Modeling With Advanced Time-Temperature Dependent Constitutive Relationships," NASA CR-165533, Nov.

Downloaded 02 Jun 2010 to 171.66.16.112. Redistribution subject to ASME license or copyright; see http://www.asme.org/terms/Terms_Use.cfm

Thermal Strain-Tolerant Abradable Thermal Barrier Coatings

T. E. Strangman
Garrett Auxiliary Power Division,
Allied-Signal Aerospace Company,
Phoenix, AZ 85020

Thermal barrier coatings (TBCs) are applied to hot gas path surfaces to reduce metal temperatures and thermal stresses for improved turbine component durability. Improvements in engine performance are achieved when TBCs enable reductions in cooling air usage and turbine blade tip-shroud clearances. This paper describes the development of thick TBCs with superior strain tolerance. A pattern of grooves or slant steps incorporated into the surface to be coated enables the development of shadow gaps in the ceramic layer during plasma spray deposition. These gaps segment the TBC, permitting ceramic-metal thermal expansion mismatch and thermal strains to be accommodated by free expansion.

Introduction

Thermal Barrier coatings (TBCs) are used on high-temperature combustor, liner, and turbine gas path surfaces to reduce metal temperatures and minimize component distortion and cracking for improved component durability.

TBCs can also significantly improve engine performance by minimizing air-cooling and leakage losses. For example, in order to avoid damage to turbine blade tips, clearances are set to avoid rubs with the turbine shroud. Although a large clearance avoids damage to blade tips, it permits a significant amount of high-pressure gas to leak past the tips of turbine blades without doing any work. This can reduce turbine efficiency by a few percent. Abradable TBCs applied to the turbine shroud can be used to minimize blade tip-shroud clearance. They are particularly attractive when they also enable reductions in the air-cooling requirement.

In most cases, thin TBCs are applied to metallic (nickel- and cobalt-base superalloys) combustors and liners. These coatings are generally applied by plasma spraying and typically have two layers; i.e., an inner oxidation-resistant bond coating layer (e.g., 125 μm NiCrAlY) and an insulative stabilized zirconia outer layer (e.g., 250 μm 8 percent Y_2O_3–92 percent ZrO_2).

The plasma-sprayed microstructure must be controlled in order to avoid spalling of the insulative zirconia layer during service. Compressive residual stresses, which contribute to buckling and spalling of the zirconia layer, are minimized by cooling the superalloy component during plasma spraying. A rough bond coating–zirconia interface is required to achieve good mechanical bonding. In addition, combinations of subcritical microporosity and microcracks are present in the coating to minimize thermal and ceramic—metal thermal expansion mismatch stresses within the ceramic layer.

When the ability to air-cool engine components (i.e., shrouds, combustors, liners) is limited by either cold-wall heat transfer coefficients or the temperature of available cooling air, thicker (750 to 1500 μm) zirconia layers can be used to achieve metal temperature design goals.

However, without additional modification to the TBC system, increasing zirconia thickness can result in stresses near the ceramic-metal interface that are sufficient for spalling to occur during thermal cycling. Several approaches have been evaluated, with varying degrees of success, to achieve satisfactory adhesion of thick zirconia coatings; viable approaches include the following:

(*a*) Grading the ceramic-metal interface
(*b*) Compliant bond coating
(*c*) Increasing zirconia layer porosity
(*d*) Segmenting the zirconia coating

Thick TBC systems that incorporate these strain-accommodating modifications have been successfully demonstrated in engines, and in some cases have achieved production status. However, as discussed in the following paragraphs, the engine designer may be required to accept compromises with respect to maximum shroud metal temperature capability (which affects cooling air requirements and engine performance) or cost.

Graded TBCs. Grading the TBC system from the (Ni, Co)CrAlY bond coating to the stabilized zirconia layer by incorporating one or more intermediate layers into the coating system has been used by several investigators (Bill et al., 1978; Biehler, 1987; Shiembob, 1978, 1982; Yonushonis et al., 1987) to minimize ceramic–metal thermal expansion mismatch stresses in thick TBCs. Graded TBCs have the advantage that they can be economically manufactured in one plasma-spraying operation. Also, as-deposited graded coatings typically have improved adhesion, relative to two-layered systems. Graded TBCs have been successfully used on both turbine shrouds and pistons in diesel engines.

Unfortunately, graded TBCs have one significant disadvantage. Zirconia is almost transparent to oxygen diffusion. Consequently, the metallic powder dispersed in the zirconia is exposed to an oxidizing environment. The metallic surface area exposed to oxidation is several orders of magnitude greater than that of the bond coating of a conventional two-layered coating. Volumetric expansion of the oxidized metallic par-

Contributed by the International Gas Turbine Institute and presented at the 36th International Gas Turbine and Aeroengine Congress and Exposition, Orlando, Florida, June 3-6, 1991. Manuscript received at ASME Headquarters February 6, 1991. Paper No. 91-GT-39. Associate Editor: L. A. Riekert.

Copyright © 1992 by ASME
Downloaded 02 Jun 2010 to 171.66.16.112. Redistribution subject to ASME license or copyright; see http://www.asme.org/terms/Terms_Use.cfm

ticles in the graded layer creates large compressive stresses, which can buckle the graded layer and spall the insulative zirconia layer. In some instances, compressive stresses within the oxidized graded layers have been sufficient to distort the metallic substrate (Ruckle and Duvall, 1982).

In order to achieve environmental lives that are comparable with two-layered TBCs, the cermet (NiCrAlY + zirconia) layer(s) of a graded TBC system must be cooled to a lower temperature—up to 200°C lower—than the bond coating temperature of components with two-layered TBCs. This condition is typically not a problem for oil-cooled piston engines, where the choice of alloy typically dictates cooler temperatures anyway. However, increased use of cooling air for turbine shrouds with graded TBCs reduces the engine performance benefit, relative to shrouds coated with a two-layered TBC system. Also, since oxidation of the graded layer can produce significant stresses, the superalloy shroud may need to be more robust (heavier) in order to avoid distortion in service.

Compliant Layer TBCs. Inserting a compliant metallic layer between the substrate and the zirconia is another effective method of reducing the ceramic-metal thermal expansion mismatch and thermal stresses to acceptable levels. Feltmetal™ pads (Erickson and Panzera, 1978; Tolokan et al., 1983; Stepka and Ludwig, 1980) and spongy plasma sprayed metallic layers (Bill and Wisander, 1983) have been used to achieve this objective on turbine shrouds. Also, since TBCs with compliant layers do not transmit significant stress to the metallic substrate, the stiffness (weight) of the superalloy shroud can be reduced, relative to shrouds with graded TBCs.

TBCs with compliant Feltmetal™ pads are also limited by oxidation, but not to the extent of graded TBCs. Metals wires used in the felt are produced from oxidation resistant alloys and are significantly coarser in cross section than the metallic powder used in graded TBCs. Also, there is sufficient void space to accommodate the volumetric expansion of oxidation products without causing significant stress. In order to meet oxidation life goals with compliant layer TBCs, the metallic bond coating (e.g., NiCrAlY) applied on top of the strain isolator pad must be cooled to about the same temperature as the bond coating of a two-layered TBC system.

The thermal conductivity of a metallic strain isolator pad is intermediate between that of zirconia and a superalloy. Therefore, TBCs with strain isolator pads can significantly reduce cooling air requirements of metallic structures. However, since oxidation life considerations require a lower substrate temperature for a component protected with a strain isolated TBC, slightly more cooling air is required, relative to a component insulated with a comparable thickness two-layer TBC.

Alternatively, increasing ceramic layer porosity can potentially improve abradability while reducing the effective elastic modulus of the ceramic layer (and associated ceramic–metal thermal expansion mismatch stresses). Clingman et al. (1981) produced high-porosity TBCs by cospraying hollow alumina–silica microspheres with zirconia. This concept was extended by Holtman et al. (1984) with the design of a highly compliant TBC system for diesel engine application, which incorporated both a strain isolator pad and an increased porosity zirconia coating layer.

A major disadvantage of TBCs using compliant Feltmetal™ layers is cost. Forming and braze-bonding of the strain isolator pad can add significant material and labor cost to the overall cost of the component.

One compliant layer approach that has been developed to avoid the cost of Feltmetal™ is to produce a spongy plasma-sprayed bond coating by co-spraying polyester powder with (Ni, Co)CrAlY powder (Bill and Wisander, 1983). The polyester phase is burned out at a low temperature prior to deposition of the zirconia layer. While this type of compliant layer has obvious cost advantages, it has a finer distribution

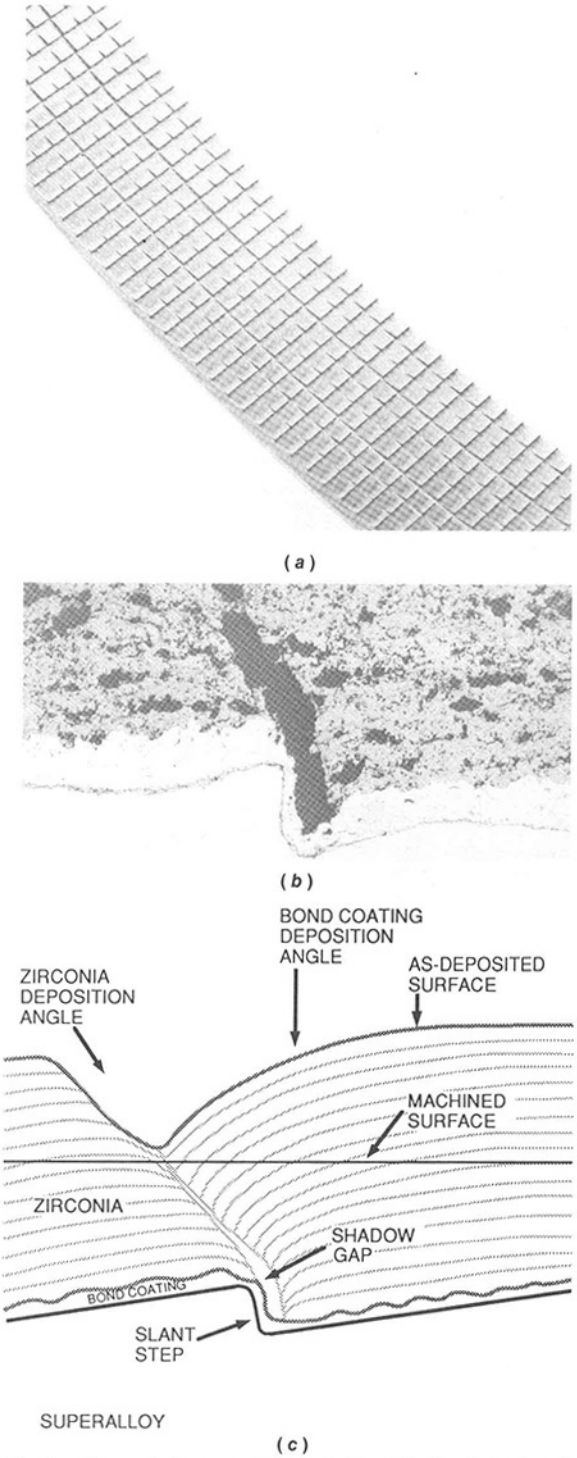


Fig. 1 A pattern of steps or grooves in the metallic shroud surfaces (A) enables plasma spray deposition of thick segmented (strain-tolerant) zirconia thermal barrier layer (B and C)

of the metallic phase, which will be more prone to oxidation damage than the coarser wire used in the felt metal.

Segmented TBCs. Segmentation of the zirconia layer in a two-layer TBC system is another viable method to relieve ceramic-metal thermal expansion mismatch stresses. It has been demonstrated (Anderson and Sheffler, 1983) that plasma spray parameters can be selected to segment zirconia coatings during deposition. Adjusting plasma spray parameters to segment zirconia coatings has inherent economical advantages; i.e., it does not add additional layers or process steps.

However, plasma spray parameters that promote segmentation have also tended to produce a higher density micro-

Downloaded 02 Jun 2010 to 171.66.16.112. Redistribution subject to ASME license or copyright; see http://www.asme.org/terms/Terms_Use.cfm

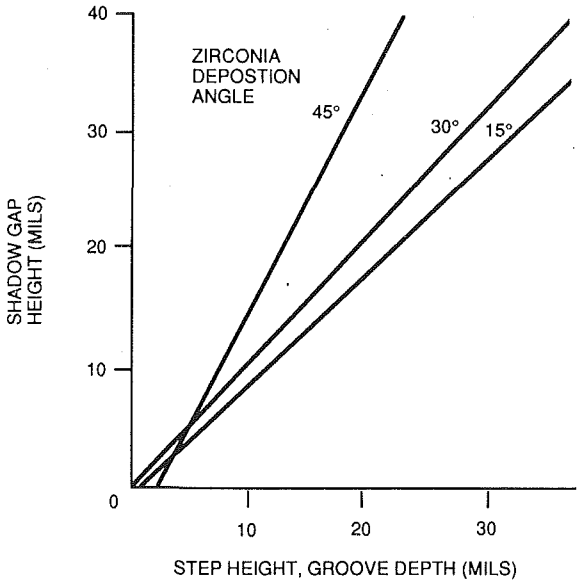


Fig. 2 Segmentation of TBC during plasma spraying is dependent upon step height (groove depth) and zirconia deposition angle

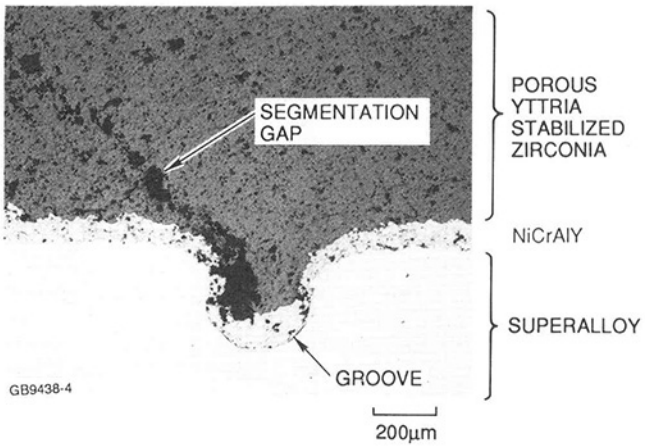


Fig. 3 Strain-tolerant segmented TBC system is deposited with sufficient porosity for flow thermal conductivity

structure. It is anticipated that higher density segmented TBCs will have higher thermal conductivity and possibly reduced abradability. Thick dense zirconia coatings will have less insulating value, relative to a comparable thickness zirconia coating with conventional levels of porosity and microcracking. Tight plasma spray process controls are also required to avoid nucleating cracks in the plane of the coating, which could eventually lead to spalling.

Stress relieving segmentation cracks in zirconia coatings can be created as demonstrated (Bill and Wiander, 1981) during a post-coating laser glazing operation. Subsequent studies by the author verified that laser glazing can segment zirconia coatings. Unfortunately, the laser glazing parameters used in the study densified the zirconia coating and nucleated in-plane cracks. Laser glazing is also unattractive from a processing cost standpoint; i.e., it requires additional equipment and labor.

Strain-Tolerant Abradable TBC Development

While the above approaches to achieving thick, strain-tolerant TBCs have enjoyed success, there is a continuing need to reduce cost, improve TBC temperature capability, and maximize engine performance. The following paragraphs describe the recent development of a substrate geometry segmented TBC system, which has achieved these objectives.

As previously noted, segmentation of the zirconia layer can effectively eliminate long-range ceramic–metal thermal expansion mismatch and thermal stresses within the zirconia layer. It has been recently demonstrated, as illustrated in Fig. 1, that small steps or grooves in the superalloy substrate can create shadow gaps that segment the TBC coating during plasma spray deposition (Strangman, 1988, 1990). Expensive post-coating processes, such as laser glazing, are not required to achieve segmentation.

The processing "trick" required to produce segmenting gaps with the coating is to plasma spray the zirconia layer at an angle (e.g., 45 deg) from the surface normal. Angled deposition permits the substrate grooves or steps to create shadow gaps, which propagate up into the zirconia layer during deposition. As the zirconia layer becomes thicker, the segmentation gaps eventually bridge and the zirconia becomes continuous. As indicated in Fig. 2, the height of segmentation is dependent upon both the depth of the steps or grooves and the spray angle. For a step height (groove depth) of 0.5 mm (20 mils) and a spray angle of 45 deg, the zirconia can be segmented to a thickness of about 1 mm (40 mils).

The coating system that Garrett is using in production is illustrated in Fig. 3. It is composed of an air plasma sprayed Ni–31 Cr–11Al–0.5Y bond coating and an air plasma sprayed 8 percent yttria stabilized zirconia top coat. This is the same materials system that Garrett uses for thinner TBCs applied to combustors and liners. With the exception of the 45-deg angle specified for the zirconia coating, plasma spray parameters are the same as used for deposition of conventional thickness TBCs.

Using substrate geometry to segment the zirconia layer and conventional TBC plasma spray deposition parameters permits the zirconia layer to be deposited with a low thermal conductivity microstructure (Fig. 3). Angled deposition slightly increases microporosity in the zirconia layer, which is beneficial from thermal conductivity and abradability standpoints.

Inspection of Figs. 1 and 3 shows that bond coating uniformity is achieved on the flat surface of the substrate, but not in near-vertical faces of the steps and grooves. However, since the TBC significantly reduces both metal temperatures and thermal gradients in the superalloy, a thin bond coating on the groove surface is not viewed as a problem for current applications; i.e., the metal temperature within a groove is only slightly higher than the temperature of the uncoated backface of the shrouds. The shadow gap within the groove or step face also provides a means of accommodating oxidation products without creating significant stress. It should also be noted that thin bond coatings and imperfections (including discontinuities) on step and groove surfaces that are near-normal to the plane of the TBC have not led to TBC spalling during several thousand thermal cycles in an engine environment.

For future applications requiring greater high-temperature oxidation resistance, bond coating uniformity can be improved by changing the plasma spray deposition angle to coat the faces of slant-steps better or by using tapered grooves.

Cost of substrate geometry segmented TBCs is also significantly lower, compared with other insulative shroud coatings that Garrett has evaluated (e.g., ceramic filled honeycomb and TBCs with a compliant Feltmetal interlayer). Simple geometry patterns of grooves can be easily machined into the surface to be coated. Investment cast turbine shrouds offer opportunities for even greater savings; the pattern of slant-steps and/or grooves can be incorporated into the wax pattern tooling.

Abradability. The abradability of this segmented zirconia shroud is comparable to that of other plasma-sprayed zirconia and ceramic-filled honeycomb shrouds that Garrett has evaluated. Laboratory and engine tests have demonstrated that abrasive blade tips are required to cut into the shrouds and minimize blade tip wear.

Downloaded 02 Jun 2010 to 171.66.16.112. Redistribution subject to ASME license or copyright; see http://www.asme.org/terms/Terms_Use.cfm

Development of abrasive turbine blade tip coatings to cut the zirconia shroud coating is continuing. Thus far the best results have been achieved with thin blade tip coatings that contain coarse abrasive grit (e.g., 150-μm-dia BN particles) in an oxidation-resistant metallic matrix. For example, laboratory abradability tests were conducted at a shroud temperature of 700°C and blade tip speed of 425 m/s. The rotor had six abrasive tipped blades, which successfully cut into the zirconia coating and achieved a shroud/blade tip wear ratio greater than ten. The plasma-sprayed zirconia coating was also cut by abrasive blade tips at shroud temperatures in the 900 and 1000°C range, but with significantly increased blade tip wear.

Engine Experience. Substrate geometry segmented TBCs have been demonstrated on both axial and radial turbine shrouds. In a Garrett turbofan engine test, abrasive coated blade tips cut into the plasma-sprayed zirconia shroud coating to a depth of 250 μm.

Production usage of thick segmented TBCs was initiated on a radial turbine shroud in 1988. Field experience with this thick segmented TBC has been good after several thousand hours of service in a Garrett auxiliary power unit. High time shrouds now have in excess of 3000 hours (cycles) of service without spalling or erosion.

Summary

Incorporation of a slant step and/or groove pattern into the substrate permits zirconia coatings to be segmented by shadow gaps formed during plasma spray deposition. The resulting two-layered TBC system has excellent strain tolerance, good oxidation resistance, low thermal conductivity, good abradability when rubbed with abrasive blade tips, and low process cost.

References

Anderson, N. P., and Sheffler, K. D., 1983, "Development of Strain Tolerant Thermal Barrier Coating Systems," NASA Report CR-168251.

Biehler, D. I., 1987, "Thick Thermal Barrier Coatings for Diesel Engine Components," in: *Proceedings of the 1987 Coatings for Advanced Heat Engines Workshop* (Dept. of Energy publication CONF-870762), Castine, ME, pp. III-19 to III-27.

Bill, R. C., Shiembob, L. T., and Stewart, O. L., 1978, "Development of Sprayed Ceramic Seal Systems for Turbine Gas Path Sealing," NASA Report TM-79022.

Bill, R. C., and Wisander, D. W., 1981, "Laser Surface Fusion of Plasma Sprayed Ceramic Turbine Seals," U.S. Patent Application 6-242795, filed Mar. 11.

Bill, R. C., and Wisander, D. W., 1983, "Fully Plasma-Sprayed Compliant Backed Ceramic Turbine Seal," U.S. Patent Application 6-500045, filed June 1.

Clingman, D. L., Schechter, B., Cross, K. R., and Cavanagh, J. R., 1981, "Abradable Dual-Density Ceramic Turbine Seal System," NASA Report CR-165309.

Erickson, A. R., and Panzera, C., 1978, "Abradable Seal Material and Composition Thereof," U.S. Patent 4,094,673, June 13.

Holtman, R. L., Layne, J. L., and Schechter, B., 1984, "An Investigation of Enhanced Capability Thermal Barrier Coating Systems for Diesel Engine Components," NASA Report CR-174820.

Ruckle, D. L., and Duvall, D. S., 1982, "Ceramic Thermal Barrier Coatings for Turbine Engine Components," ASME Paper No. 82-GT-322.

Shiembob, L. T., 1978, "Development of a Plasma Sprayed Ceramic Gas Path Seal for High Pressure Turbine Application," NASA Report CR-135387.

Shiembob, L. T., 1982, "JT9D Ceramic Outer Air Seal System Refinement Program—Phase 2," NASA Report CR-167962.

Stepka, F. S., and Ludwig, L. P., 1980, "Composite Wall Concept for High Temperature Turbine Shrouds: Heat Transfer Analysis," NASA Report TM-81539.

Strangman, T. E., 1988, "Abradable Strain-Tolerant Ceramic Coated Turbine Shroud," U.S. Patent 4,764,089, Aug. 16.

Strangman, T. E., 1990, "Method of Making an Abradable Strain-Tolerant Ceramic Coated Turbine Shroud," U.S. Patent 4,914,794, Apr. 10.

Tolokan, R. P., Brady, J. B., and Jarrabet, G. P., 1983, "Strain Isolated Ceramic Coatings," ASME Paper No. 83-GT-223.

Yonushonis, T. M., Roehling, D. P., Hoag, K. L., Novak, R. C., Matarese, A. P., and Huston, R. P., 1987, "Thick Thermal Barrier Coatings for Diesel Engine Components," *Proceedings of the 1987 Coatings for Advanced Heat Engines Workshop*, Dept. of Energy publication CONF-870762, Castine, ME, pp. III-11 to III-17.

Downloaded 02 Jun 2010 to 171.66.16.112. Redistribution subject to ASME license or copyright; see http://www.asme.org/terms/Terms_Use.cfm

S. Gilham
W. S. Atkins Engineering Sciences Ltd.,
Surrey, KT18 5BW, United Kingdom

P. C. Ivey
School of Mechanical Engineering,
Cranfield Institute of Technology,
Cranfield, Beds, MK43 0AL,
United Kingdom

J. M. Owen
School of Mechanical Engineering,
University of Bath,
Bath, BA2 7AY, United Kingdom

Self-Induced Flow in a Stepped Rotating Tube

Self-induced flow occurs when a tube, open at one end and sealed at the other, is rotated about its central axis: Fluid flows along the axis from the open end toward the sealed end and returns in a layer adjacent to the inner surface of the tube. This mechanism, which can occur under isothermal or nonisothermal conditions, is believed to be responsible for the so-called "hot-poker effect" that was observed during anti-icing tests on the nose bullet of an aeroengine. This paper describes a combined theoretical and experimental study of self-induced flow. It is shown that, for the length-to-diameter (L/D) ratios and rotational Reynolds numbers associated with the anti-icing tubes of aeroengines, the laminar flow near the sealed end of the tube is similar to that of the so-called free disk. Swirl in the air outside the open end reduces the self-induced flow, but flow can reach the sealed end of a stepped tube that has either a sudden contraction or a sudden enlargement.

1 Introduction

The performance of a jet engine can be adversely affected by the formation of ice in the air intakes. Large pieces of ice may be centrifuged off the central portion of the rotating nose bullet and ingested by the compressor, with resulting damage to the blades.

Ice-protection systems for rotating nose bullets often involve the use of hot air. As shown in Fig. 1, hot air can be passed from the turbine end of the engine, along the hollow compressor shaft, and through an anti-icing tube attached to the nose bullet; after impinging on the inner surface of the bullet, the air is exhausted through vents into the engine intake. Unfortunately, this hot air is entrained by the compressor, causing a loss of performance and a reduction in the operating surge margin.

During tests on the anti-icing system of a Rolls-Royce engine, it was decided to solve the problem of hot-air ingestion by blocking the outlet vents. Surprisingly, despite the fact that there was no longer a superposed flow of hot air along the tube, the anti-icing was still effective. The "hot-poker effect," as this anti-icing mechanism was graphically termed, was attributed to a thermosyphon phenomenon, which created convection from the open to the sealed end of the compressor shaft, and a patent was taken out by Rolls-Royce (1979).

While this chance discovery was effective for one engine, there was no guarantee that it would work in engines with a different shaft geometry. Research workers at the University of Sussex were invited to investigate the phenomenon so as to provide guidelines for the engine designers, and Owen and Pincombe (1981), using flow visualization, observed an effect that had never been reported in the scientific literature: It became known as "self-induced flow in a rotating tube." If a tube, open at one end and sealed at the other, is rotated about its central axis, fluid will flow from the open end along the axis toward the sealed end and will return to the open end in an annular layer on the inner wall of the tube.

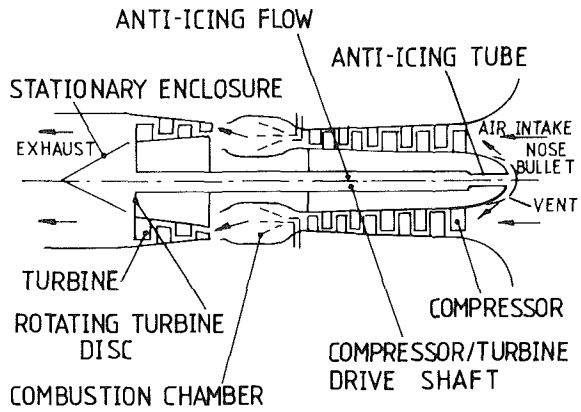


Fig. 1 Schematic diagram of a jet engine showing anti-icing system for nose bullet

A simplified representation is shown in Fig. 2: The "short-tube" case is where the self-induced flow reaches the sealed end; the "long-tube" case is where the recirculating flow never penetrates the entire length of the tube. The "short-tube" case is associated with high rotational speeds and/or low values of length-to-diameter ratio, such as those occurring in aeroengines, and it was therefore believed to be the cause of the "hot-poker effect" mentioned above. It should be emphasized, however, that self-induced flow occurs inside isothermal as well as differentially heated rotating tubes; it is not, therefore, caused by a thermo-syphon effect.

Subsequent research was conducted by Ivey (1988) and Gilham (1990), and a combined theoretical and experimental study of the isothermal self-induced flow in a constant-diameter tube of length L and radius a, rotating with an angular speed Ω in a quiescent environment, is described by Gilham et al. (1991). The authors showed that numerical solutions of the Navier–Stokes equations (based on the multigrid elliptic solver of

Contributed by the International Gas Turbine Institute and presented at the 36th International Gas Turbine and Aeroengine Congress and Exposition, Orlando, Florida, June 3–6, 1991. Manuscript received at ASME Headquarters March 4, 1991. Paper No. 91-GT-276. Associate Editor: L. A. Riekert.

Copyright © 1992 by ASME
Downloaded 02 Jun 2010 to 171.66.16.112. Redistribution subject to ASME license or copyright; see http://www.asme.org/terms/Terms_Use.cfm

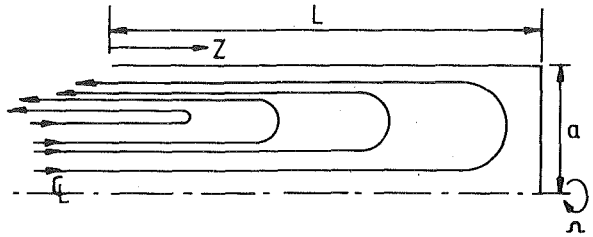


Fig. 2(*a*) Short-tube case

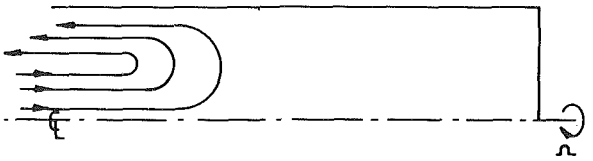


Fig. 2(*b*) Long-tube case

Fig. 2 Simplified diagram showing self-induced flow in a rotating tube

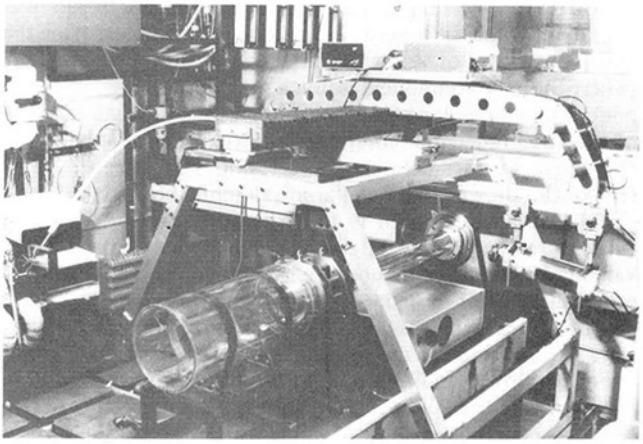


Fig. 3 Rotating-tube rig used for the optical measurements (stationary enclosure is at left-hand end of glass tube; laser transmitting optics are to left of tube; receiving optics to right)

Vaughan et al., 1989) were in mainly good agreement with experimental results obtained using flow visualization and laser-Doppler anemometry. In general, the flow depends on the Ekman number, E, (which is the inverse of the rotational Reynolds number Re_ϕ), and the length-to-radius ratio, G. However, for $G \geq 20$, the flow throughout most of the tube depends on the modified Ekman number, $E^* = GE$. The short-tube case occurs for $E^* < 0.2$, and the flow reaching the sealed end forms a free-disk-type boundary layer (see Owen and Rogers, 1989) on the end wall.

In an aeroengine, the hollow compressor shaft is usually stepped in diameter and opens into the wheel-space of the low-pressure turbine, as shown in Fig. 1. The conditions are, therefore, different from those studied by Gilham et al., and it is the object of this paper to consider the effects of stepped tubes, and of inlet conditions, on the self-induced flow. The heat transfer problem will be discussed elsewhere.

The experimental apparatus is described in Section 2. Self-induced flow in a constant-diameter tube is discussed in Section 3, and the effects of shaft geometry and inlet conditions are considered in Section 4.

2 Experimental Apparatus

2.1 Rotating-Tube Rig. Figure 3 shows the rotating-tube rig used for the optical measurements. A horizontal glass tube (with one end enclosed by a stationary casing that was open to the atmosphere and the other end sealed by a perspex disk) was supported on either two (as in Fig. 3) or three ball-bearing assemblies, which themselves were attached to a baseplate. The tube was rotated at speeds up to 6000 rpm by an electric motor and belt drive, and the rotational speed was measured to an accuracy of 1 percent by an electronic tachometer.

Glass tubes of diameter up to 75 mm and length up to 1.5 m could be inserted into the bearing assemblies. With three-bearing assemblies, stepped tubes could be made by inserting a large-diameter tube between the first and second bearings and a small tube between the second and third bearings. For the "reducing-diameter case," the large-diameter tube was left open to the atmosphere and the small-diameter tube was sealed; for the "increasing-diameter case," the small-diameter tube was left open and the large-diameter tube was sealed.

In some of the tests with a constant-diameter tube, a "rotor–stator system" was fitted into the stationary enclosure at the open end of the tube. This system comprised a disk of 190 mm diameter attached to the end of the rotating tube and a stator of 146 mm diameter located at axial distances between 36 mm and 219 mm from the rotating disk.

2.2 Optical Instrumentation. Velocity measurements inside the tube were obtained be laser-Dopler anemometry (LDA) operating in the forward-scatter real-fringe model. Silicone oil particles of approximately 2 μm diameter were used to "seed" the air inside the stationary enclosure at the open end of the tube. A 15 mW Spectra-Physics He–Ne laser was used as the light source, and a Malvern Instruments beam-splitter and frequency-shift unit were employed in the transmitting optics. The beam separation at transmission was 20 mm and the focal length of the transmitting lens was 150 mm, which resulted in a probe volume approximately 110 μm diameter and 1.7 mm length with a fringe spacing of 4.75 μm. The receiving optics included an F1.8 lens of 50 mm focal length, a 50 μm pinhole and an EMI photomultiplier, and the resulting signal (with Doppler frequencies mainly in the range 30–100 kHz) was processed by a Cambridge Consultants tracking filter used in the frequency counting mode. In this mode of operation the instrument was accurate to ± 0.1 percent.

Uncertainty in the measured velocity was caused by radial and angular misalignment of the probe volume, refraction in the glass tube, velocity biasing due to the size of the probe volume, and round-off errors in the measured frequencies. Of

Nomenclature

a = internal radius of tube
b = outer radius of disk in rotor–stator system
c_w = $Q/\nu a$ = nondimensional flow rate
D = internal diameter of tube
E = Re_ϕ^{-1} = Ekman number
E^* = GE = modified Ekman number
G = L/a = length-to-radius ratio
L = length of tube
p = pressure
Q = volumetric flow rate
Re_ϕ = $\Omega a^2/\nu$ = rotational Reynolds number
r = radius
s = axial distance between rotor and stator
t = time
V_r = radial component of velocity
V_z = axial component of velocity
V_ϕ = tangential component of velocity
z = axial distance from open end
ζ = $(L-z)(\Omega/\nu)^{0.5}$ = nondimensional axial distance from sealed end
ν = kinematic viscosity
ρ = density
Ω = angular velocity

Subscripts

1 = open-ended section of stepped tube
2 = sealed section of stepped tube

Downloaded 02 Jun 2010 to 171.66.16.112. Redistribution subject to ASME license or copyright; see http://www.asme.org/terms/Terms_Use.cfm

these, the uncertainty caused by angular misalignment was considered to be the largest. For example, when measuring the axial component of velocity near the outer radius of the tube (where the axial component is much smaller than the tangential one), a small angular misalignment can cause a small fraction of the large tangential component of velocity to be added to the signal. Further details of uncertainties are given by Ivey (1988) who showed that angular misalignment of only 0.25 deg could give large errors in V_z near the outer part of the tube.

Measurements of the tangential component of velocity were validated by sealing the tube to ensure solid body rotation; no such validation of the axial component was possible. However, despite all the problems, most of the results presented below were in good agreement with the computed velocities.

For the flow visualization, a 4 W Spectra Physics argon-ion laser, a cylindrical lens, and a biconvex lens were used to produce a collimated sheet of light, which entered the tube at the open end. The light sheet was parallel to, and coincident with, the axis of the tube and, to reduce flare, the width of the light sheet was slightly less than the diameter of the tube. A Concept smoke generator, which could be pulsed, released clouds of oil particles (approximately 0.25 μm diameter) into the air surrounding the open end of the tube. Photographs were obtained with a Canon A1 camera, operating in the "aperture-preferred mode" at F1.4, using ISO 400 black and white film.

Further details of the experimental apparatus are given by Ivey (1988).

3. Self-Induced Flow in a Constant-Diameter Rotating Tube

3.1 Simple Explanation of Self-Induced Flow. Consider the case of a sealed air-filled tube rotating about its central axis. For incompressible flow, solid-body rotation occurs such that $V_\phi = \Omega r$, and the radial pressure gradient is given by

$$\frac{dp}{dr} = \rho\frac{V_\phi^2}{r} = \rho\Omega^2 r \tag{1}$$

If $p = p_0$ at $r = 0$, it follows that

$$p = p_0 + \frac{1}{2}\rho\Omega^2 r^2 \tag{2}$$

The pressure is therefore highest at the tube wall, where $r = a$, and lowest at the center; this radial pressure distribution is balanced by reactive forces on the ends at $z = 0$ and $z = L$.

Consider now the case where the solid end at $z = 0$ is removed so that the tube is open to the atmosphere. The radial pressure distribution inside the tube cannot be balanced at the open end: High-pressure air near the outer part of the tube will flow into the atmosphere to be replaced by an axial inflow along the center of the tube. For low rotational speeds, the self-induced recirculating flow will be confined to a region near the open end (the "long-tube case"); for high speeds, the flow will reach the sealed end (the "short-tube case"). Self-induced flow does not depend on buoyancy; it is not, therefore, a thermosyphon effect. (Heat transfer measurements were conducted by Ivey (1988), and solutions of the energy equation were obtained by Gilham (1990), which suggested that buoyancy effects are unlikely to affect the flow significantly.)

3.2 Numerical Method. For steady, incompressible, axisymmetric laminar flow, the Navier–Stokes and continuity equations can be written in a stationary cylindrical-polar coordinate system (see Schlichting, 1979) as

$$V_r\frac{\partial V_r}{\partial r} + V_z\frac{\partial V_r}{\partial z} - \frac{V_\phi^2}{r} = -\frac{1}{\rho}\frac{\partial p}{\partial r} + \nu\left[\frac{\partial^2 V_r}{\partial r^2} + \frac{1}{r}\frac{\partial V_r}{\partial r} - \frac{V_r}{r^2} + \frac{\partial^2 V_r}{\partial z^2}\right] \tag{3}$$

$$V_r\frac{\partial V_\phi}{\partial r} + V_z\frac{\partial V_\phi}{\partial z} - \frac{V_r V_\phi}{r} = \nu\left[\frac{\partial^2 V_\phi}{\partial r^2} + \frac{1}{r}\frac{\partial V_\phi}{\partial r} - \frac{V_\phi}{r^2} + \frac{\partial^2 V_\phi}{\partial z^2}\right] \tag{4}$$

$$V_r\frac{\partial V_z}{\partial r} + V_z\frac{\partial V_z}{\partial z} = -\frac{1}{\rho}\frac{\partial p}{\partial z} + \nu\left[\frac{\partial^2 V_z}{\partial r^2} + \frac{1}{r}\frac{\partial V_z}{\partial r} + \frac{\partial^2 V_z}{\partial z^2}\right] \tag{5}$$

$$\frac{1}{r}\frac{\partial}{\partial r}(rV_r) + \frac{\partial V_z}{\partial z} = 0 \tag{6}$$

For the boundary conditions, no slip conditions were used for the cylindrical wall ($r = a$) and the end wall ($z = L$) of the tube, and a symmetry axis was assumed at $r = 0$. The open end of the tube presented difficulties as the conditions at the plane of the open end are unknown. Gilham (1990) overcame this problem by assuming that there was a large, annular disk of inner radius a and outer radius b attached to the open end of the tube. (As discussed in Section 4.2, velocity measurements near the sealed end of the tube suggested that a disk at the open end has only a small effect.) Gilham further assumed that the boundary conditions used by von Kármán (1921) for an infinite disk rotating in a quiescent environment (the so-called free disk) were applicable to the finite disk. Thus all the fluid was assumed to flow axially (with $V_r = V_\phi = 0$) into the system upstream of the disk and to flow radially out of the system via the boundary layer on the disk at $r = b$ with

$$\frac{\partial}{\partial r}\left[\frac{V_r}{r}\right] = \frac{\partial}{\partial r}\left[\frac{V_\phi}{r}\right] = \frac{\partial V_z}{\partial r} = 0 \tag{7}$$

The Navier-Stokes equations were converted to finite-difference equations, which were then solved by a nonlinear multigrid algorithm incorporating the SIMPLEC pressure-correction scheme of van Doormaal and Raithby (1984). The number of finite-difference nodes used, and the computational time taken, depended on the values of L/D and Re_ϕ. For example, for $L/D = 5$, $\mathrm{Re}_\phi = 500$, and with a total of 14,625 nodes in the solution domain, the computing time on a VAX 8530 was 672 minutes; for a single-grid computation, the time was 3578 minutes!

Further details of the boundary conditions and numerical solutions are given by Gilham (1990) and Gilham et al. (1991).

3.3 Flow Visualization. Photographs of flow visualization near the sealed end ($0.62 \le z/L \le 1.0$) of a rotating tube, taken by Ivey (1988), are shown in Fig. 4. The glass tube was 73 mm in diameter and 1050 mm in length ($L/D = 14.4$), and the rotational speed was 175 rpm ($\mathrm{Re}_\phi = 1600$). Smoke, made from micron-sized oil particles, was introduced near the open end, and "slit-illumination" was created by a 4 W argon-ion laser. The photographs were taken with a Canon A1 camera, using the "aperture-preferred mode," at five frames per second and a shutter speed of 1/15 second. The time $t = 0$ refers to the time when smoke was first seen to have entered the tube, and subsequent times refer to this datum.

Figure 4(a) shows that the smoke-front in the core is approaching the sealed end of the tube, which it reached at $t \approx 3.6$ seconds. (Careful inspection is needed to distinguish between the white smoke and the "flare" from solid surfaces, particularly at the sealed end.) In Fig. 4(c), the smoke has moved radially outward on the sealed end and has begun to return, in the annular layer, toward the open end. The returning smoke can be seen more clearly in Figs. 4(d) and 4(e).

3.4 Velocity Profiles. The radial variations of the nondimensional axial and tangential components of velocity near the open end ($z/L = 0.129$) and sealed end ($z/L = 0.984$) of a rotating tube with $\mathrm{Re}_\phi = 1600$ and $L/D = 21.3$ are shown in Fig. 5. It should be noted that the nondimensional velocity components $V_z/(\Omega\nu)^{0.5}$ and $V_\phi/\Omega r$ correspond to those used in the free-disk solutions referred to above. The experimental data were obtained by Ivey (1988), using laser-Doppler anemometry (LDA), and the numerical solution by Gilham (1990),

Downloaded 02 Jun 2010 to 171.66.16.112. Redistribution subject to ASME license or copyright; see http://www.asme.org/terms/Terms_Use.cfm

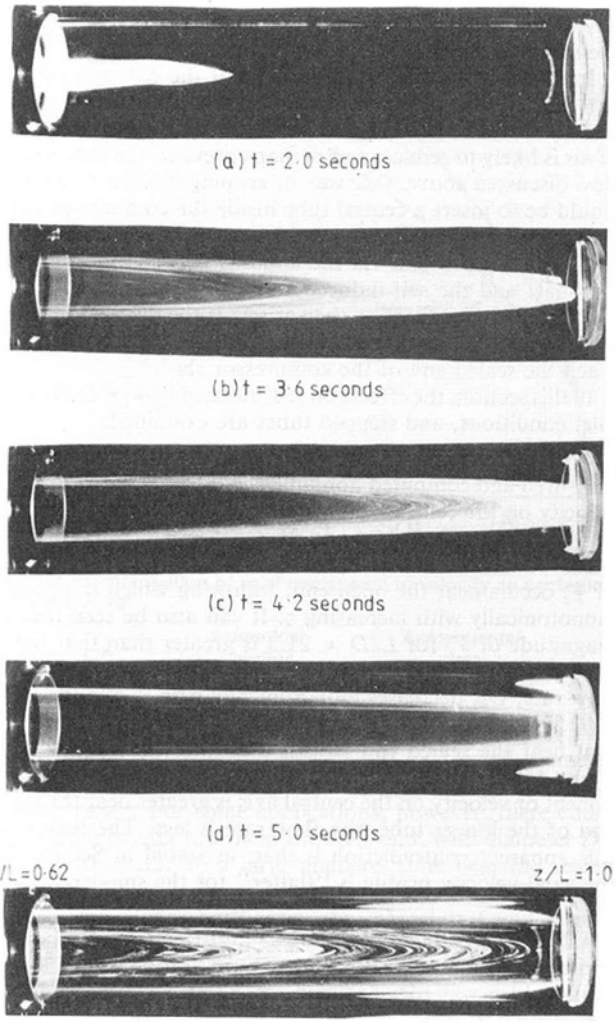


Fig. 4 Flow visualization near sealed end of tube (L/D = 14.4, Re_ϕ = 1600)

using the Navier–Stokes multigrid elliptic solver.

Referring to Fig. 5(*a*), it can be seen that the central core extends to $r/a \approx 0.6$, which is the point where $V_z = 0$. In the annular layer $0.6 < r/a < 1$, the tangential component is sheared almost linearly; in the core, for $r/a < 0.6$, $V_\phi/\Omega r > 0$. (If fluid enters the tube from a quiescent environment, then the presence of swirl in the core near the inlet suggests that there is transfer of angular momentum from the fluid leaving the tube to that entering. This momentum transfer can significantly affect the amount of flow that enters the tube, as is discussed below.)

Figure 5(*b*) shows the velocity profiles near the sealed end of the tube. (The error bars shown in this figure are the estimated experimental uncertainties calculated by Ivey.) The magnitude of the tangential component of velocity, in both the core and the annular layer, has increased, and the axial component of velocity has decreased, compared with that at the open end; the radial extent of the core has also been reduced to $r/a \approx 0.575$. The (mainly) good agreement between the measured and computed velocities at the open and sealed ends gives confidence in both the measurements and numerical solutions; it also confirms that the flow is indeed laminar.

Figure 6 shows the velocity profiles near the sealed end for Re_ϕ = 9300 and L/D = 14.4, and it can be seen that the fluid is drawn progressively into a "free-disk-type" boundary layer on the rotating end wall. The computations illustrate how the shape of the axial component of velocity changes progressively from $\zeta = 280$ to $\zeta = 1.4$, where $\zeta = (L-z)(\Omega/\nu)^{0.5}$ is the nondimensional distance from the sealed end. The value ζ =

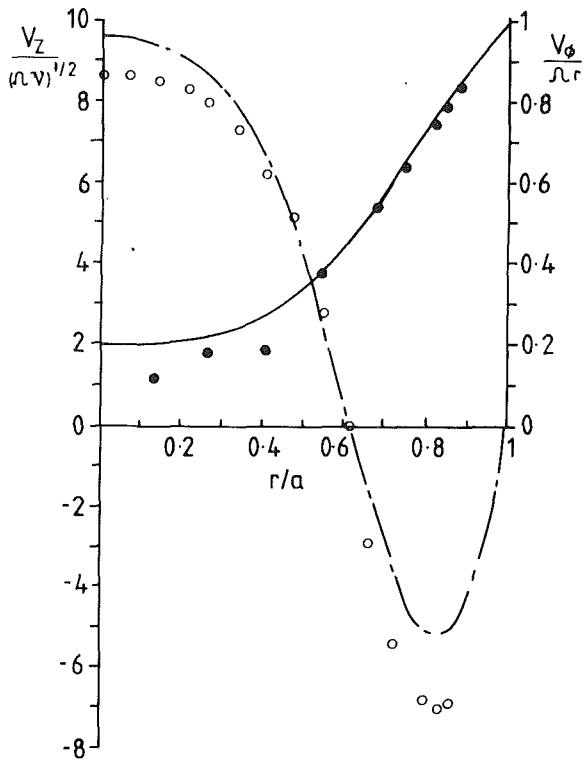


Fig. 5(*a*) Near open end: z/L = 0.129

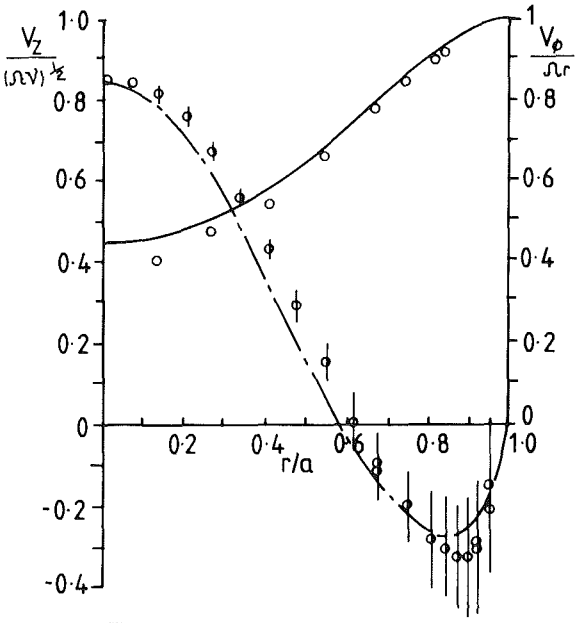


Fig. 5(*b*) Near sealed end: z/L = 0.984

Fig. 5 Radial profiles of axial and tangential components of velocity: $Re_\phi = 1.6 \times 10^3$, L/D = 21.3

Component of velocity	Numerical solution	Experimental data
Axial	—·—	○
Tangential	——	●
Error bar		|

5.5 corresponds to the approximate thickness of the boundary layer on a free disk where $V_\phi/\Omega r = 0$ and $V_z/(\Omega\nu)^{0.5} = 0.8845$ (see Owen and Rogers, 1989). Thus, the experimental data and numerical solutions illustrate the transition from self-induced flow in the tube to free-disk-type flow near the sealed end.

The general effect of increasing Re_ϕ, or decreasing G, is to reduce the swirl in the core, to flatten the axial velocity profile, and to reduce the thickness of the wall layers. As shown by

Downloaded 02 Jun 2010 to 171.66.16.112. Redistribution subject to ASME license or copyright; see http://www.asme.org/terms/Terms_Use.cfm

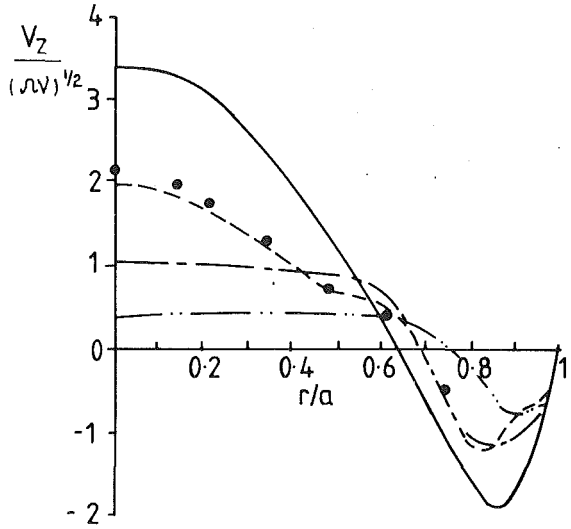


Fig. 6(*a*) Axial component of velocity

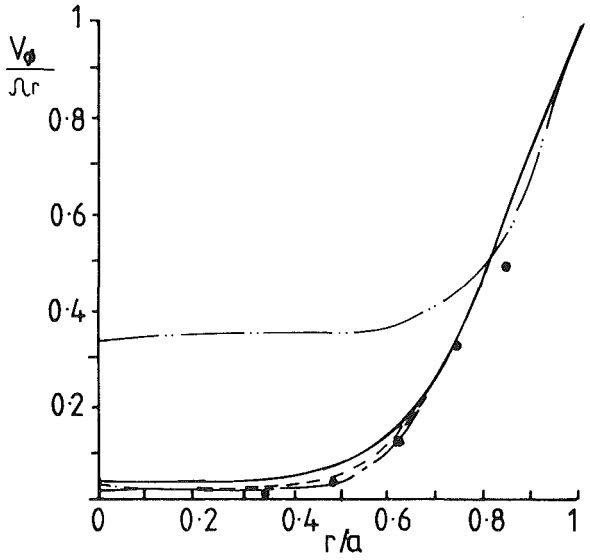


Fig. 6(*b*) Tangential component of velocity

Fig. 6 Radial profiles of the axial and tangential components of velocity near the sealed end: $Re_\phi = 9.3 \times 10^3$, $L/D = 14.4$

		Numerical Solution	Experimental Data
z/L	ζ		
0.9000	280	———	
0.9840	44	- - - - - -	•
0.9880	5.5	——·——	
0.9995	1.4	——··——	

Gilham et al. (1990), the flow rate along the tube increases as Re_ϕ is increased. However, owing to the flattening of the axial velocity profile, the magnitude of the axial component of velocity on the centerline, at a fixed axial location, can actually decrease as Re_ϕ increases or as L/D decreases.

The above observations should apply to the short-tube cases that are expected to occur inside the compressor shaft of an aeroengine. It would appear that the flow (and therefore the heat transfer) that occurs at the sealed end of the shaft should be similar to that of the laminar free disk.

4 Effects of Shaft Geometry and Inlet Conditions

In an aeroengine, the compressor shaft is usually stepped from a large diameter near the open (turbine) end to a small diameter near the sealed (nose bullet) end. The open end of the hollow shaft is surrounded by an enclosure in which the low-pressure turbine disk forms one of the surfaces; swirl of the air in the enclosure is likely to have a significant effect on the self-induced flow inside the compressor shaft.

In some engines, holes in the wall of the compressor shaft are used to transport cooling air from the compressor to the turbine via the open end of the shaft. This superposed flow of air is likely to reduce, and perhaps prevent, the self-induced flow discussed above. One way of keeping the two flows apart would be to insert a central tube inside the compressor shaft; the superposed cooling air would travel from the holes in the shaft to the open end via the annulus between the tube and the shaft and the self-induced flow would flow through the central tube. The question then arises: If the diameter near the inlet were to be restricted, would the self-induced flow still reach the sealed end of the compressor shaft?

In this section, the effects on self-induced flow of L/D ratios, inlet conditions, and stepped tubes are examined.

4.1 Effect of L/D Ratio. The axial distribution of the measured and computed nondimensional axial components of velocity on the central axis ($r=0$) is shown in Fig. 7 for $Re_\phi = 9300$ and $L/D = 14.4$ and 21.3.

For both L/D ratios, it can be seen that the maximum value of V_z occurs near the open end, following which it decreases monotonically with increasing z. It can also be seen that the magnitude of V_z for $L/D = 21.3$ is greater than that for $L/D = 14.4$. For both L/D ratios, the computed nondimensional flow rate, C_w, decreases monotonically with increasing z; for $L/D = 21.3$, the flow rate near the open end is greater, and that near the sealed end is less, than that for $L/D = 14.4$. Thus, despite the fact that, as shown in Fig. 7, the axial component of velocity on the central axis is greater near the sealed end of the longer tube, the flow rate is less. The reason for this apparent contradiction is that, as stated in Section 3.4, the axial velocity profile is "flatter" for the smaller value of L/D.

4.2 Effect of Inlet Conditions. For $L/D = 21.3$, the open end of the tube was surrounded by a stationary enclosure, inside which was the shrouded rotor-stator system shown in Fig. 8(*a*). The inside diameter of the tube was 73 mm and the outside of the rotating and stationary disks were 190 mm and 146 mm, respectively. The axial distance, s, between the two disks could be varied, and tests were conducted with $s/b = 0.38$ and 2.3, where b is the radius of the rotating disk (rotor). Tests were also conducted in which either the stationary disk (stator) or both disks were removed.

The variation with Re_ϕ of $V_z/(\Omega\nu)^{0.5}$, measured on the centerline at $z/L = 0.984$, is shown in Fig. 8(*b*); the "datum case" refers to measurements made without the rotor or the stator. It can be seen that the rotor by itself, or the rotor-stator system with $s/b = 2.3$, has little effect on the velocity. However, with $s/b = 0.38$, the rotor-stator system significantly reduces the velocity near the sealed end of the tube. Additional tests with a shrouded rotor-stator system, in which a cylindrical shroud was attached to the stationary disk, revealed an even greater reduction of the velocity near the sealed end.

The reduction of flow caused by the rotor-stator system was attributed to the rotation created in the core of fluid between the rotating and stationary disks. The angular speed of this rotating core is approximately 40 percent of that of the rotating disk (see Owen and Rogers, 1989), and any increase in the swirl of the fluid entering the rotating tube will cause a decrease in the strength of the self-induced flow. For application in an aeroengine, the inlet of the hollow compressor shaft should be protected, if possible, from the conditions near the open end, and a patent for a device to do this has been applied for by Rolls-Royce (1988).

4.3 Effect of Stepped Tubes. As stated above, the hollow compressor shaft in an aeroengine is usually stepped from a

Downloaded 02 Jun 2010 to 171.66.16.112. Redistribution subject to ASME license or copyright; see http://www.asme.org/terms/Terms_Use.cfm

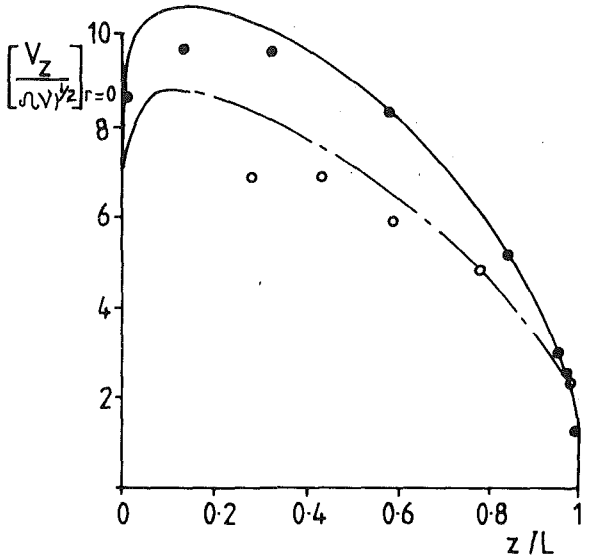


Fig. 7 Axial distribution of axial component of velocity on centerline: $Re_\phi = 9.3 \times 10^3$

L/D	Numerical solution	Experimental data
14.4	—·—	○
21.3	———	●

large diameter (D_1) near the open end to a small diameter (D_2) near the sealed end; this will be called the "reducing-diameter case." For some applications, however, there could be a small-diameter tube near the open end, with diameter D_1, which is connected to a large-diameter tube near the sealed end, with diameter D_2; this will be called the "increasing-diameter case." For both cases, the subscripts 1 and 2 refer to the tubes near the open and sealed ends, respectively.

4.3.1 Reducing-Diameter Case ($D_2 < D_1$). As shown in Fig. 9(*a*), a tube of length L_1 and diameter D_1 was connected, with a step change, to one length L_2 and diameter D_2 ($D_2 < D_1$). The large-diameter end of the resulting stepped tube was left open, and the small-diameter end was sealed. Tests were conducted with $L_1 = 745$ mm and $D_1 = 73$ mm ($L_1/D_1 = 10.2$) and with values of L_2 and D_2 to give $L_2/D_2 = 14.8$ for $D_2/D_1 = 0.8$, and $L_2/D_2 = 21.3$ for $D_2/D_1 = 0.5$.

The variation with $Re_{\phi,2}$ of $V_z/(\Omega\nu)^{0.5}$, measured on the central axis at $(Z_2/L_2) = 0.984$, is shown in Fig. 9(*b*). The results for the stepped tubes are close to those for equivalent constant-diameter tubes (where $L/D = L_2/D_2$). It would appear, therefore, that for $0.5 \le D_2/D_1 \le 0.8$ the flow near the sealed end of the small diameter tube is virtually the same as that for the equivalent constant-diameter tube. The open-ended large-diameter tube does not appear to affect significantly the flow in the small-diameter sealed tube. However, as $D_2/D_1 \to 1$, the flow near the sealed end must approach that for a constant-diameter tube where $L/D = (L_1 + L_2)/D_2 > L_2/D_2$. Tests have not been conducted to find the "critical value" of D_2/D_1 above which the effect of the large-diameter tube becomes significant, nor have tests been carried out to determine the effect of the shape of the transition between the small-diameter and large-diameter tubes.

4.3.2 Increasing-Diameter Case ($D_2 > D_1$). Tests were conducted for a tube with $L_1 = 663$ mm and $D_1 = 59$ mm ($L_1/D_1 = 11.2$) inserted inside a tube of length $L = L_1 + L_2 = 1560$ mm and diameter $D = D_2 = 74$ mm to give $L_2/D_2 = 12.5$ and $D_2/D_1 = 1.25$. One end of the small-diameter tube was open to the atmosphere and one end of the large-diameter tube was sealed (see Fig. 10*a*). LDA measurements of the axial component of velocity on the central axis were conducted near the sealed end at $z/(L_1 + L_2) = 0.981$. For comparison, measurements were also made near the sealed end of the larger tube with the smaller one removed ($L/D = 21.1$).

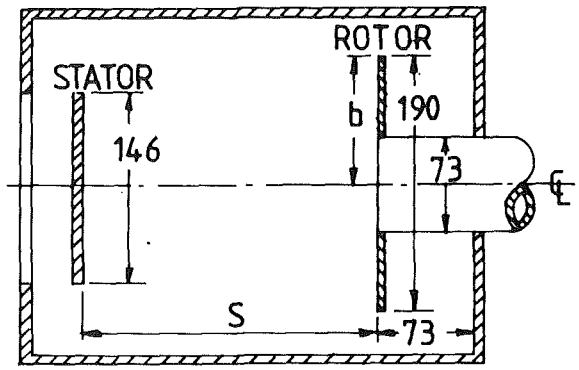


Fig. 8(*a*) Rotor-stator system at open end (dimensions in mm)

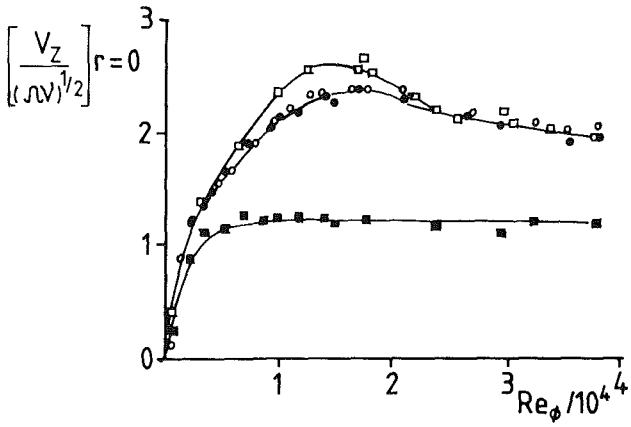


Fig. 8(*b*) Axial component of velocity near sealed end

Fig. 8 Effect of a rotor-stator system on the measured variation, with Re_ϕ, of the centerline axial component of velocity: $z/L = 0.984$, $L/D = 21.3$

Enclosure	Experimental data
Datum	□
Datum and rotor	○
Rotor-stator: s/b = 0.38	■
Rotor-stator: s/b = 2.3	●

Figure 10(*b*) shows the variation of the nondimensional axial component of velocity with $Re_{\phi,2}$. While the reduced-diameter inlet does cause a reduction in the axial component of velocity near the sealed end, the attenuation is relatively small for $Re_{\phi,2} \ge 3 \times 10^4$. It would appear, therefore, that such a restriction at the inlet of the hollow compressor shaft in an aeroengine need not prevent a significant amount of the self-induced flow from reaching the sealed end.

Conclusions

Self-induced flow is not caused by a thermosyphon effect; it can occur under isothermal conditions in a rotating tube open at one end and sealed at the other. It is created by the radial pressure gradients within the tube; high-pressure air near the tube wall flows in an annular layer toward the open end; continuity is satisfied by a central core of fluid, which flows axially from the open end toward the sealed end.

The "short-tube" case, which is relevant to aeroengines, is where the flow reaches the sealed end; the "long-tube" case, which occurs at low rotational speeds, is where the recirculating self-induced flow is confined to a region near the open end. Only the former case is considered here.

Flow visualization, LDA measurements, and numerical solutions of the laminar Navier–Stokes equations have been used to study the flow in a constant-diameter tube. The nondimensional axial velocity ($V_z/(\Omega\nu)^{0.5}$) in the core reaches a maximum value (> 1) near the open end and is reduced toward the

Downloaded 02 Jun 2010 to 171.66.16.112. Redistribution subject to ASME license or copyright; see http://www.asme.org/terms/Terms_Use.cfm

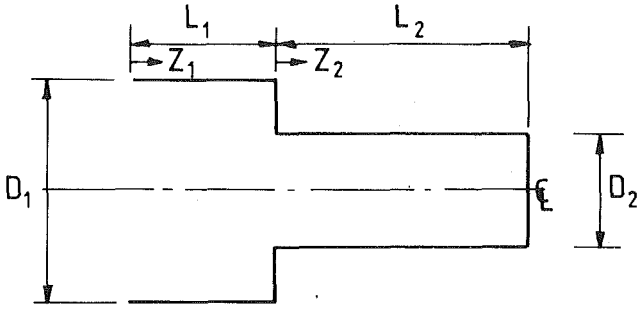


Fig. 9(*a*) Reducing-diameter case

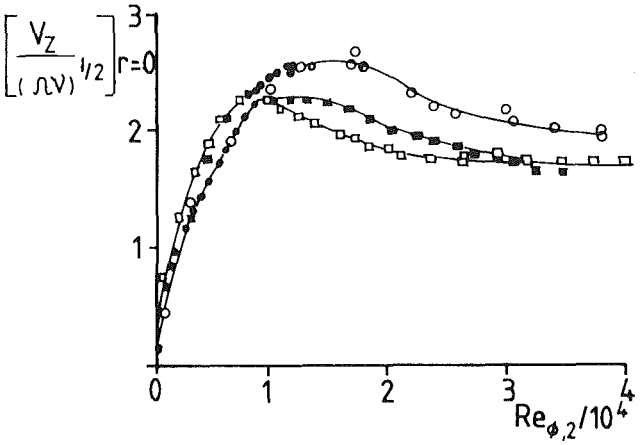


Fig. 9(*b*) Axial component of velocity near sealed end

Fig. 9 Effect of reducing-diameter tube on the measured variation, with $Re_{\phi,2}$ of the centerline axial component of velocity: $z_2/L_2 = 0.984$

L_2/D_2	D_2/D_1	Experimental data
14.4	0.8	■
21.3	0.5	●

Open symbols refer to equivalent constant-diameter tube ($L/D = L_2/D_2$)

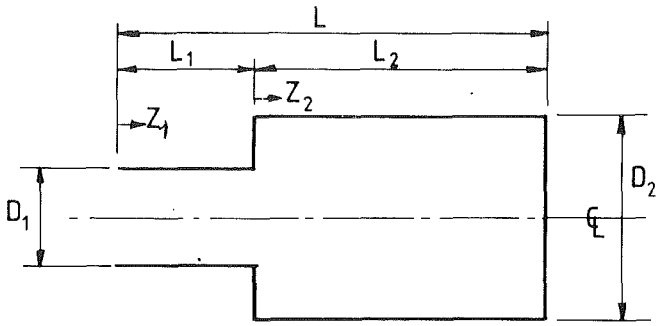


Fig. 10(*a*) Increasing-diameter case

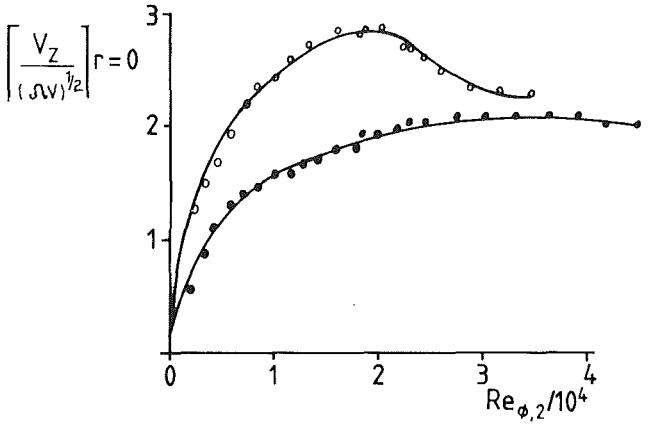


Fig. 10(*b*) Axial component of velocity near sealed end

Fig. 10 Effect of increasing-diameter tube on the measured variation, with $Re_{\phi,2}$ of the centerline axial component of velocity: $z/L_1 = 0.981$

Increasing-diameter tube	Experimental data
($D_2/D_1 = 1.25$, $L_1/D_1 = 11.2$, $L_2/D_2 = 12.5$)	●
Constant-diameter tube ($L/D = 21.1$)	○

free-disk value at the sealed end; and the flow rate within the tube decreases monotonically with distance from the open end. For the ranges of Re_ϕ and L/D studied, the nondimensional flow rate near the sealed end increases with increasing Re_ϕ and with decreasing L/D. In a gas turbine, the low-pressure turbine disk can create swirl in the air near the open end of the compressor shaft, and this swirl will reduce the strength of the self-induced flow along the hollow shaft.

For a stepped tube comprising an open-ended large-diameter tube attached to a small-diameter tube sealed at one end, the flow near the sealed end is controlled by the L/D ratio and by the Reynolds number of the small-diameter tube. For a stepped tube comprising an open-ended small-diameter tube attached to a large-diameter tube sealed at one end, although the flow near the sealed end is less than that of a large-diameter tube of the same overall length, a significant amount of flow can still reach the sealed end.

Acknowledgments

This work was conducted while we were in the School of Engineering and Applied Sciences at the University of Sussex, and we wish to thank Rolls-Royce plc for supporting this project. We also wish to thank Dr. J. R. Pincombe, for his advice, and Mr. O. Eartink, who obtained the LDA measurements shown in Fig. 10.

References

Gilham, S., 1990, "Theoretical Study of Self-Induced Flow in a Rotating Tube," D. Phil. thesis, University of Sussex, United Kingdom.

Gilham, S., Ivey, P. C., Owen, J. M., and Pincombe, J. R., 1991, "Self-Induced Flow in a Rotating Tube," *J. Fluid Mech.*, Vol. 230, pp. 505-524.

Ivey, P. C., 1988, "Self-Induced Flow in a Rotating Tube," D. Phil. thesis, University of Sussex, United Kingdom.

Kármán, Th. von, 1921, "Über Laminare and turbulente Reibung," *Z. angew. Math. Mech.*, Vol. 1, pp. 233-252.

Owen, J. M., and Pincombe, J. R., 1981, "Rotationally Induced Flow and Heat Transfer in Circular Tubes," Report No. 81/TFMRC/32, School of Engineering and Applied Sciences, University of Sussex, United Kingdom.

Owen, J. M., and Rogers, R. H., 1989, *Flow and Heat Transfer in Rotating-Disc Systems. Vol. 1: Rotor-Stator Systems*, Research Studies Press, Taunton, United Kingdom.

Rolls-Royce Ltd., 1979, "Nose Bullet Anti-icing for Gas Turbine Engines," United Kingdom Patent No. GB 2,046,843B.

Rolls-Royce plc, 1988, "Gas Turbine Engine Anti-icing System," United Kingdom Patent Application GB 2,217,393A.

Schlichting, H., 1979, *Boundary-Layer Theory*, McGraw-Hill, New York.

Van Doormaal, J. P., and Raithby, G. D., 1984, "Enhancements of the SIMPLE Method for Predicting Incompressible Fluid Flows," *Numerical Heat Transfer*, Vol. 7, pp. 147-163.

Vaughan, C. M., Gilham, S., and Chew, J. W., 1989, "Numerical Solutions of Rotating Disc Flows Using a Non-linear Multigrid Algorithm," *Proc. 6th Int. Conference on Numerical Methods in Laminar and Turbulent Flow*, Vol. 6, pp. 63-73, Pineridge Press, United Kingdom.

Downloaded 02 Jun 2010 to 171.66.16.112. Redistribution subject to ASME license or copyright; see http://www.asme.org/terms/Terms_Use.cfm

Fracture Mechanics Approach to Creep Growth in Welded IN738LC Gas Turbine Blades

W. P. Foo
Senior Engineer,
Development Project Engineering.

R. Castillo
Senior Metallurgist,
Materials Engineering.

Gas & Steam Turbine
Engineering Department,
Power Generation Technology Division,
Westinghouse Canada Inc.,
Hamilton, Ontario, Canada

Microcracks caused by hot cracking or strain age cracking mechanisms are very likely to be discovered in the weld repair zone of precision-cast IN738LC gas turbine blades. The possibility of crack propagation under the operating conditions of the gas turbine thereby becomes a crucial issue for gas turbine designers. The creep crack growth rate in air of the hipped and fully heat-treated IN738LC was measured at the service temperature experienced by the first-stage turbine blade tip. The corresponding growth behavior was also studied. The creep crack growth rate, da/dt, versus crack tip stress intensity factor, K_I, a relation that exhibits the typical primary, secondary, and tertiary behavior, supports the applicability of K_I as an appropriate correlating parameter for the creep crack growth of this Ni-based superalloy under the loading conditions used in this study. Microstructural examination illustrated that the creep crack growth of IN738LC principally takes place by the nucleation, growth, coalescence, and link-up of grain boundary microvoids and microcracks. An excellent approximation of the stress intensity factor under service loading conditions in the vicinity of the crack tip was obtained by using the Westinghouse WECAN finite element analysis. It is shown that the crack tip stress intensity factor under normal loading conditions will not be able to drive the transverse through-the-wall-thickness blade tip crack in this study.

1.0 Introduction

The performance of a gas turbine dictates the efficiency of a power plant to a large extent. Since efficiency has a strong economic implication, to improve or even just to maintain the performance of the gas turbine is highly imperative.

Many factors affect the performance of a gas turbine; leakage can be considered as one of the most crucial factors, especially leakage of the expanding hot gas through the clearance between the tips of the turbine blades and the turbine casing. It is therefore the ultimate desire of gas turbine designers and in the interest of gas turbine users to maintain a blade tip clearance as tight as practically possible.

Unfortunately, due to the differential thermal expansion of the horizontally split gas turbine casing and the thermal and mechanical expansion of the rotating rotor during transient and steady-state operations, rubbing between the turbine blades and the inner circumferential surface of the casing is unavoidable. The repetitive tip rubs in start-up and shut-down cycles plus the occasional damage due to foreign object impact erode away the tips of the turbine blades, and consequently, enlarge the clearance. This results in a deterioration of the engine performance.

To restore the performance of the gas turbine engine, the designed blade tip clearance has to be re-established. The most cost-effective way to achieve this is to salvage each turbine blade by weld repair instead of replacing it. In fact, the use of weld-repaired turbine blades has become a common practice throughout the industry, resulting in a dramatic reduction in overall operating cost.

Nevertheless, welding on a turbine blade manufactured from Ni-based superalloy is not an easy task. The problem of cracking during and after the welding process using compatible strength filler metal is well known. Even after welding with a more ductile filler metal, hot cracking or strain age cracking is still very likely to be found in the heat-affected zone under current welding technology. The possibility of crack propagation in a gas turbine blade operating in an elevated temperature environment under sustained centrifugal loadings becomes a very significant issue.

Recognition that failure of high-temperature components can occur by propagation of a single crack, which can nucleate from pre-existing flaws, weld defects, or regions of stress concentration, has led to a significant increase in crack growth studies during the past few years [1]. Creep crack growth is the process in which a single macroscopic crack advances under a sustained load at elevated temperatures well within the creep regime ($T > 0.5T_m$).

Analogous to the fatigue crack growth curves, the creep crack growth rates, da/dt, of Ni-based superalloys, when plotted as a function of the stress intensity factor K_I, often exhibit a three-stage behavior. Stage I corresponds to an initial transient where da/dt varies rapidly with the loading parameter.

Contributed by the International Gas Turbine Institute and presented at the 36th International Gas Turbine and Aeroengine Congress and Exposition, Orlando, Florida, June 3-6, 1991. Manuscript received at ASME Headquarters February 20, 1991. Paper No. 91-GT-119. Associate Editor: L. A. Riekert.

Copyright © 1992 by ASME
Downloaded 02 Jun 2010 to 171.66.16.112. Redistribution subject to ASME license or copyright; see http://www.asme.org/terms/Terms_Use.cfm

The extent of this stage relative to the other stages depends to a large extent upon the initial value of the stress intensity factor. Stage II is characterized by a power law dependency of the creep crack growth rate, da/dt, upon the stress intensity factor given by:

$$da/dt = BK_I^n \quad (1)$$

Finally, da/dt accelerates very rapidly in Stage III, which corresponds to the onset of highly unstable fast fracture, which only occupies a very small fraction of the entire life.

The characteristics of creep crack growth have been found to be dependent on both the macro- and microstructures of the material, operating conditions such as temperature and mechanical loads, environment, and physical geometry. For creep in superalloys, two major parameters have been used to correlate creep crack growth data. They are the stress intensity factor K_I and the path-independent integral C^* [5, 6]. According to the extensive theoretical work done by Riedel and Rice [7], K_I can be used to correlate the creep crack growth data if the crack grows while the material is relatively brittle and behaves in a predominantly elastic manner except in a creep zone confined to a small volume in the vicinity of the crack tip. On the other hand, the C^* concept only applies if crack propagation is accompanied by extensive creep deformation of the entire specimen. Under short-time test conditions, K_I is definitely a more appropriate parameter, while C^* is more suitable in longer time conditions.

IN738LC, being a high-strength creep-resistant Ni-based superalloy, possesses limited ductility, even at elevated temperatures. Hot cracks or strain age cracks resulting from the weld repair process also exhibit little plastic deformation and will propagate very much like brittle, intergranular cracks [8]. These two facts point to the validity of applying K_I as the correlation parameter for the creep crack growth data on the IN738LC considered in this study.

The creep crack propagation mechanism is a complex phenomenon. Not only will the fracture toughness of the material come into the picture, but the metallurgical changes of the microstructure during creep will also play an important role. Safe operation of turbine blades within the interval of overhaul inspections without failure affects the reliability of the gas turbine engine. Thus, the dormant behavior of the weld heat-affected zone cracks on these blades has to be ensured. The present study was undertaken to analyze the possibility of creep crack growth in a weld-repaired gas turbine blade.

A finite element code was utilized to evaluate the stress field in the vicinity of the crack tip. Creep crack growth tests were designed and performed to study the relations of the creep crack propagation rates of IN738LC with various mechanical loadings at the operating temperature of the turbine blades in air. The results of the test data, combined with the analytically determined crack tip stress intensity factor of the heat-affected zone crack at the turbine blade tip, make the prediction of crack propagation feasible.

2.0 Experimental Procedure

IN738LC, a Ni-based superalloy, was obtained in the form of precision cast turbine blades. The chemical composition of the test material IN738LC is illustrated in Table 1. In order to obtain the most relevant mechanical and metallurgical properties of the superalloy used in service, all the test specimens were directly machined from a fully hipped and heat-treated turbine blade.

The as-cast turbine blade was put through a hot isostatic pressing (HIP) cycle to close and heal any internal microporosity and microflaw. After the hot isostatic cycle, a standard heat treatment was given to the alloy: partial solutioning at 1120°C for 2 hours in vacuum followed by an air-cool; aging at 845°C for the 24 hours under a protective atmosphere followed by an air-cool.

Figure 1 shows the IN738LC microstructure of a sample taken from a fully hipped and heat-treated turbine blade. The microstructure contains a bimodal γ' distribution within the γ' matrix. The γ' distribution consisted of secondary γ' spheroids of approximately 200 nm diameter and primary γ' cuboids of approximately 1000 nm average side length.

The dominant carbide in IN738LC after the standard HIP and heat-treatment cycles is MC. It occurs as blocky primary particles at the grain boundaries and in the grain interiors (see Fig. 1). Secondary $M_{23}C_6$ takes the form of fine discrete particles precipitated primarily at grain boundaries.

2.1 Creep Crack Growth Tests. Owing to the existence of the series of internal cooling air holes that were cast in the turbine blade and its complex geometry, 11 single edge-notched specimens were machined to the form and dimensions shown in Fig. 2.

The initial starter notch had a root radius of approximately 0.003 in., which was located at the center of the gage length. This sharp notch produced a stress concentration effect for the subsequent precracking operation.

The K_I calibration expression for the single edge notched specimen is given by Brown and Strawley [11]:

$$K_I = \sigma\sqrt{\{a[1.99 - 0.41(a/w) + 18.7(a/w)^2 - 38.48(a/w)^3 + 53.85(a/w)^4]\}} \quad (2)$$

Ten specimens were fatigued precracked at room temperature using an INSTRON high cycle fatigue (HCF) machine. The ΔK used in the precracking was 40 $MNm^{-3/2}$.

The creep crack growth behavior of IN738LC was studied in air at 816°C. The fatigue-precracked specimens were each loaded in a creep cell and heated up to this temperature by

Nomenclature

T_m = melting temperature
σ = effective applied stress
σ_y = centrifugal stress
R = universal gas constant
T = temperature
Q_c = activation energy for volume self-diffusion
a = crack length
Δa = change in crack length
w = specimen width
da/dt = creep crack growth rate
K_I = mode I stress intensity factor
ΔK = range of stress intensity factor = $K_{max} - K_{min}$
K_{max} = maximum stress intensity factor
C^* = path-independent integral
K_{min} = minimum stress intensity factor
B = material constant
n = creep exponent
u = shear modulus
P = applied load
P_m = modified Larson-Miller parameter
b = magnitude of Burgers' vector
B' = non-temperature-dependent constant
R_c = resistance across the crack
σ_{ij}^* = nodal point stress
σ_y^* = nodal point centrifugal stress
K_I^* = nodal point stress intensity factor
r = distance from crack tip
θ = angle between the nodal point and the horizontal x axis in reference to the crack tip

Downloaded 02 Jun 2010 to 171.66.16.112. Redistribution subject to ASME license or copyright; see http://www.asme.org/terms/Terms_Use.cfm

Table 1 Nominal composition of cast IN738LC

ELEMENT	C	Mo	Cr	Ni	W	Fe	Co	Al	Ti	Nb	Ta	Zr	B
AMOUNT (wt.%)	0.09	1.6	16.03	Balance	2.5	0.14	8.3	3.4	3.39	0.74	1.70	0.03	0.01

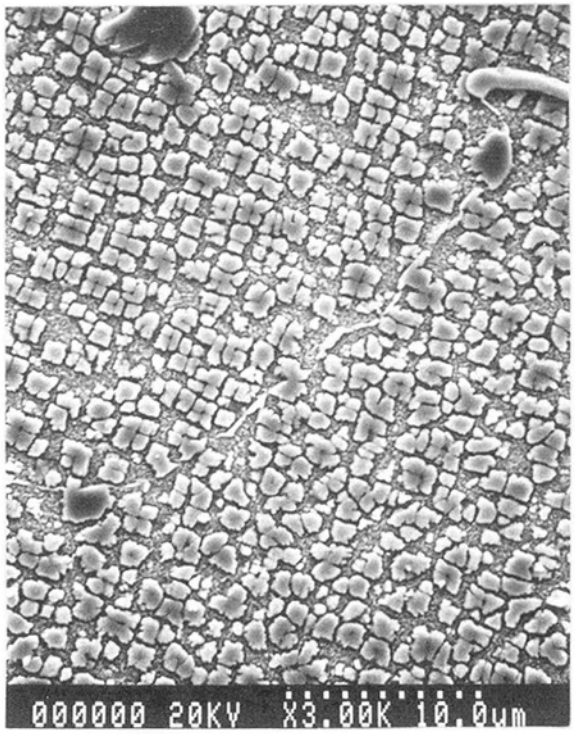


Fig. 1 SEM micrograph of IN738LC in the fully hipped and heat-treated condition

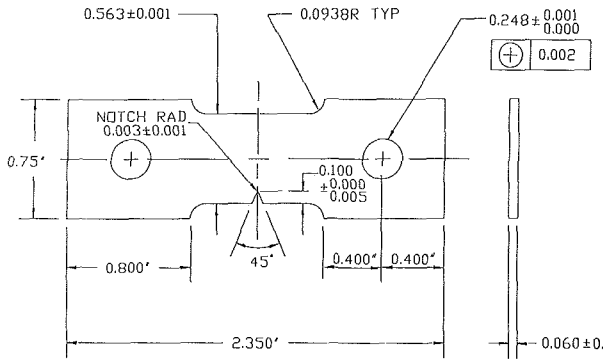


Fig. 2 Geometry of the single edge notched CCGR test specimen (all dimensions are in inches)

three built-in circumferential heating element bands. The temperature of each specimen at the vicinity of the crack during the test was measured by using a thermocouple attached to the grip. The temperature was controlled to ±2°C throughout every test.

Crack lengths were monitored throughout the duration of each test using a modified d-c potential drop technique. In this method, instead of measuring the potential across the crack, the resistance across the crack was measured. A constant current of 10.00±0.02 A was passed through two Ni-Cr wires spot welded to the specimen. A millivoltmeter was bridged across the specimen by using two platinum wires spot welded to the specimen. The Ni-Cr wires and the platinum wires were all insulated with ceramic shells to minimize oxidation at the high-temperature environment.

To ensure the success of applying the modified d-c potential drop method to the creep crack growth tests, a resistance versus

Table 2 Creep crack growth data of IN738LC

K_I, MNm$^{-3/2}$	Δ Rc, mΩ	Δ a, m	Δ T, sec.	da/dt, m/sec
45	0.070	2.532×10^{-4}	1.546×10^{6}	1.638×10^{-10}
50	0.168	6.078×10^{-4}	6.804×10^{4}	8.933×10^{-9}
55	0.629	2.276×10^{-3}	6.360×10^{4}	3.579×10^{-8}
60	0.403	1.458×10^{-3}	7.242×10^{3}	2.013×10^{-7}
65	0.509	1.841×10^{-3}	4.610×10^{3}	3.994×10^{-7}
70	0.692	2.503×10^{-3}	1.800×10^{3}	1.391×10^{-6}
75	0.526	1.903×10^{-3}	1.280×10^{3}	1.487×10^{-6}
80	0.475	1.718×10^{-3}	4.100×10^{2}	4.191×10^{-6}
85	0.509	1.841×10^{-3}	2.000×10^{2}	9.207×10^{-6}
90	0.506	1.831×10^{-3}	7.800×10^{1}	2.347×10^{-5}

crack length calibration curve has to be determined. One of the specimens was used for the calibration. A crack of known length was machined into the calibration specimen at the location of the notch. The specimen was then spot welded with the Ni-Cr wires and platinum wires and the measuring circuit connected. It was then heated up to the test temperature in the creep cell and the resistance across the crack measured. This was repeated with different machined crack lengths and a calibration curve was plotted using the data recorded. This calibration curve was used throughout the creep crack growth tests to monitor the value of the crack length.

2.2 Experimental Results. The values of the resistance, crack length, time duration, and creep crack growth rate at various K_I loads are tabulated in Table 2. Figure 3 shows the creep crack growth rates of IN738LC as a function of the crack tip stress intensity factors at 816°C.

All creep crack growth data corresponding to values of K_I between 50 MNm$^{-3/2}$ and 85 MNm$^{-3/2}$ fall in a linear relationship in the log-log plot; this established Stage II of this curve. Tests conducted with K_I values of 125 MNm$^{-3/2}$, 100 MNm$^{-3/2}$, and 92.5 MNm$^{-3/2}$ all showed instantaneous unstable fast fracture in which the corresponding crack growth rates could not be recorded. The fact that the creep crack growth rate at $K_I = 90$ MNm$^{-3/2}$ deviates from the linear relationship indicates that the transition from Stage II to the tertiary Stage III lies between $K_I = 85$ MNm$^{-3/2}$ and 90 MNm$^{-3/2}$.

The creep crack growth data corresponding to lower K_I values were especially difficult to obtain in this material. A test that was run with a K_I of 45 MNm$^{-3/2}$ took 1.546×10^6 seconds, to show an increase in crack length of 0.00997 in. The incubation period for this *da/dt* point was found to be extremely long. It occupied over 80 percent of the total time tested before substantial crack growth was observed.

This point also falls off the linear curve, indicating the probable onset of the threshold regime. The threshold K_I for nonpropagating creep crack was never found in this experiment due to the much longer time duration required to complete the corresponding test(s).

Downloaded 02 Jun 2010 to 171.66.16.112. Redistribution subject to ASME license or copyright; see http://www.asme.org/terms/Terms_Use.cfm

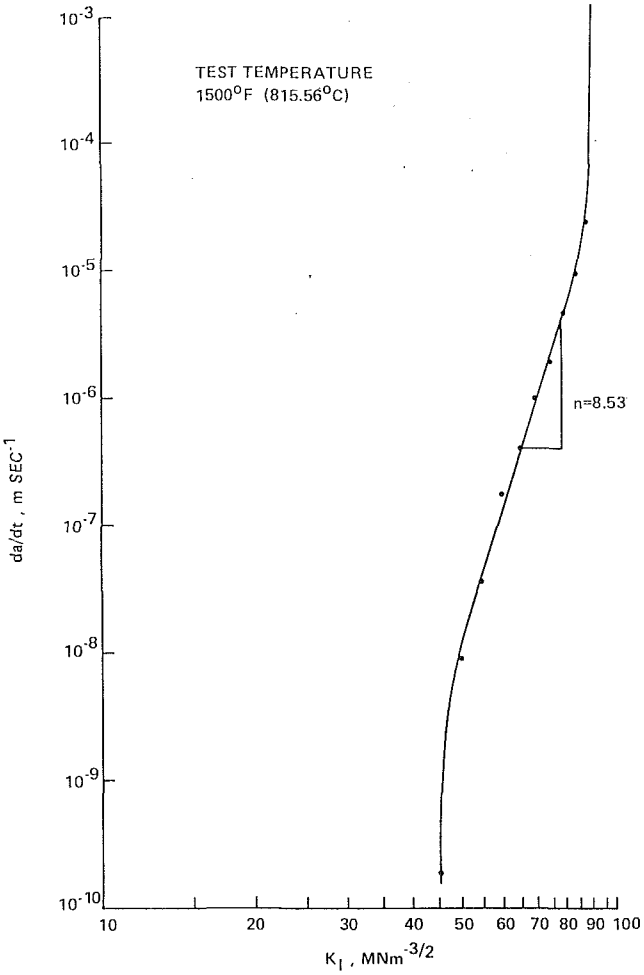


Fig. 3 Creep crack growth rates versus stress intensity factors of IN738LC at 816°C

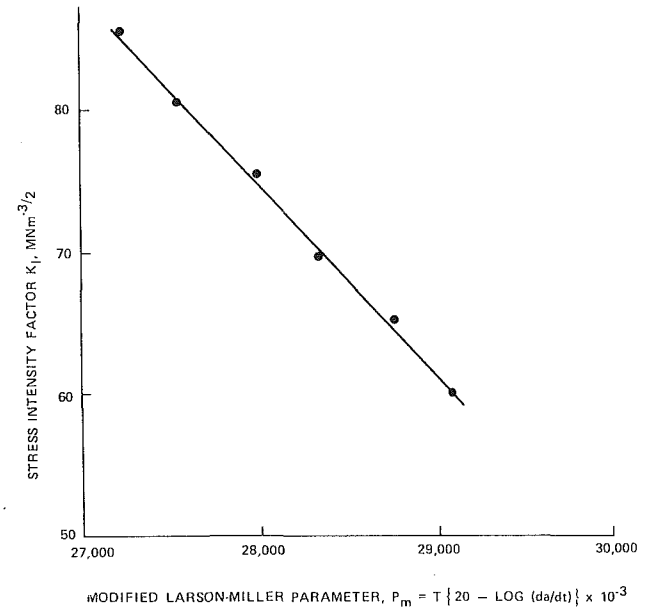


Fig. 4 Modified Larson-Miller Parametric representation of the creep crack growth data in IN738LC

The fact that the creep crack growth rates are temperature dependent suggests that for a given environment, a single engineering parameter that includes temperature exists to correlate the creep crack growth data over a wide temperature

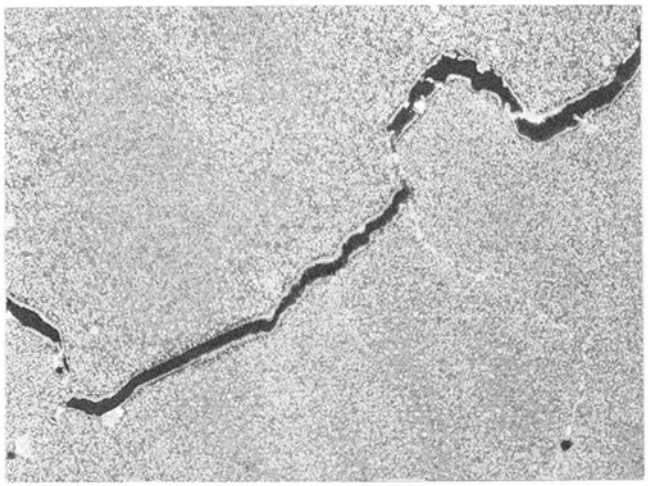


Fig. 5 Intergranular nature of creep crack growth in IN738LC (200 ×)

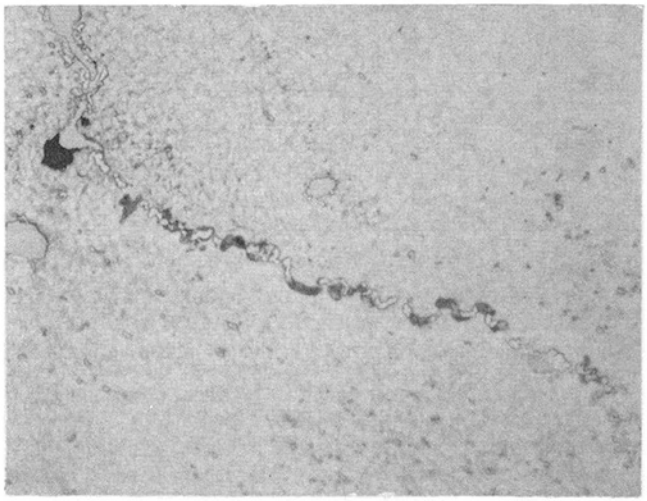


Fig. 6 Microvoid nucleation and coalescence in grain boundaries (1000 ×)

range. The Larson–Miller parameter [12], which is widely used for correlating stress rupture data of superalloys over a range of temperature, was modified by Bain and Pelloux [13] as below:

$$P_m = T\,\{20\text{-}\log(da/dt)\} \times 10^{-3} \tag{3}$$

where T = temperature in K.

The above relationship gives a parametric representation of the creep crack growth data. Results of this plot using the current experimental data are shown in Fig. 4.

Metallographic examination of the specimen loaded with $K_I = 45$ MNm$^{-3/2}$ shows that creep cracking in IN738LC was predominantly intergranular. Figure 5 illustrates this characteristic. As can be seen in Fig. 6, microvoids and microcracks were nucleated and coalesced in the grain boundaries ahead of the crack tip and in the vicinity of MC carbides in the γ matrix. Figure 7 shows the microvoid-coalesced grain boundaries in the vicinity of the growing crack tip. Figure 8 is a composite fractograph taken from the fracture surface of the specimen loaded with a $K_I = 55$ MNm$^{-3/2}$. From this fractograph, the fracture surfaces of the HCF precrack, the transition transgranular mode, and the predominant intergranular mode of the creep crack and the final overload mode are observed. Coarsening of both the primary cuboidal γ' and the secondary spheroidal γ' can be observed in Fig. 9(*a*). It is noted in the micrographs that the primary cuboids coarsened at the expense of the secondary spheroids. This coarsening behavior can be compared to the unexposed or uncrept IN738LC microstructure shown in Fig. 9(*b*).

Downloaded 02 Jun 2010 to 171.66.16.112. Redistribution subject to ASME license or copyright; see http://www.asme.org/terms/Terms_Use.cfm

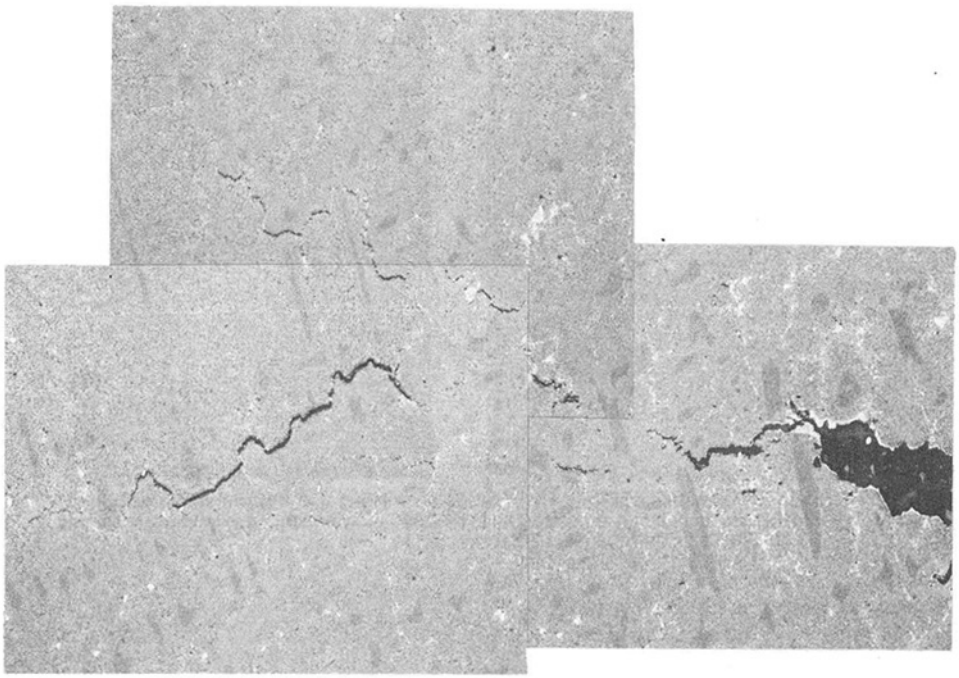


Fig. 7 The nucleation, coalescence, and link-up of microvoids and microcracks at the grain boundaries and MC carbides in the vicinity of the creep crack tip (50 ×)

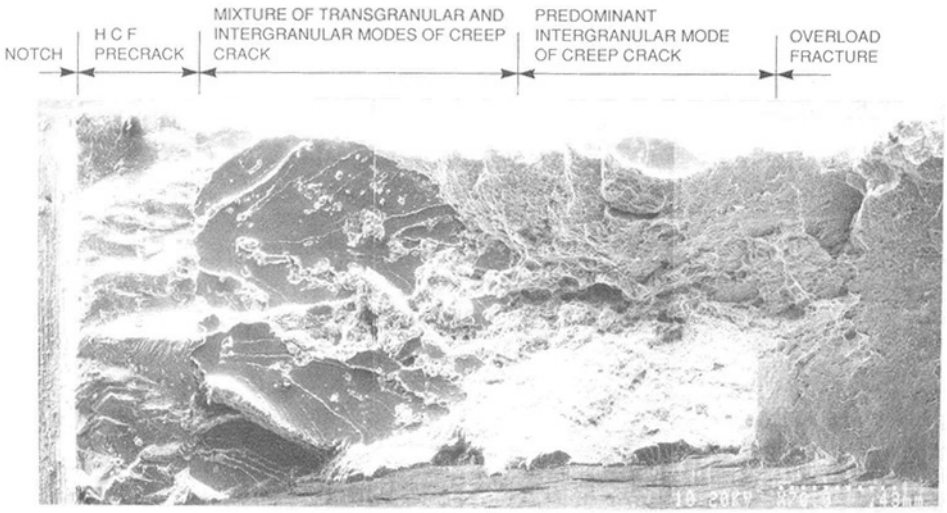


Fig. 8 SEM fractograph showing the fracture surface appearance of (SEN) specimen tested at K_s = 55 $MNm^{-3/2}$

3.0 Finite Element Analysis

In order to predict the possibility of crack propagation under loading conditions, a knowledge of the corresponding crack tip stress intensity factor is essential. A rigorous determination of the crack tip stress intensity factor requires an exact solution formulated for the cracked structure. However, in most real cases, exact solutions are impractical to obtain. Therefore, a relatively straightforward numerical method using finite element code can be used to obtain the approximate crack tip stress intensity factor.

The finite element code used in this stress analysis is the WECAN finite element code, a general purpose program developed by the Westinghouse Electric Research and Development Center. The finite element models were constructed using the Westinghouse interactive graphic code FIGURES II.

3.1 Basic Engineering Assumptions. The permissible weld repair zone of a turbine blade is confined to the blade tip due to the simplicity in its stress state and its relatively low magnitude of stresses. Since the principal loading in this portion of the turbine blade is a direct centrifugal load, the most probable crack that may propagate under loading is a transverse of chordwise crack. This is a Mode I phenomenon. Given the assumption that the entire tip region is weld repaired, the weld heat-affected zone will be oriented in a chordwise direction relative to the airfoil. If a crack is formed by either the hot cracking or the strain age cracking mechanism, it will most probably be a transverse crack.

Since the thickness of the tip cavity wall is only 0.060 in., the weld-induced crack in this analysis was assumed to be a through-the-wall thickness transverse crack and its length taken to be 0.080 in. This assumption allowed a more simple two-dimensional element construction for the finite element model.

A plane strain criterion was assumed for this stress analysis. This is valid because of the blade tip geometry and because

Downloaded 02 Jun 2010 to 171.66.16.112. Redistribution subject to ASME license or copyright; see http://www.asme.org/terms/Terms_Use.cfm

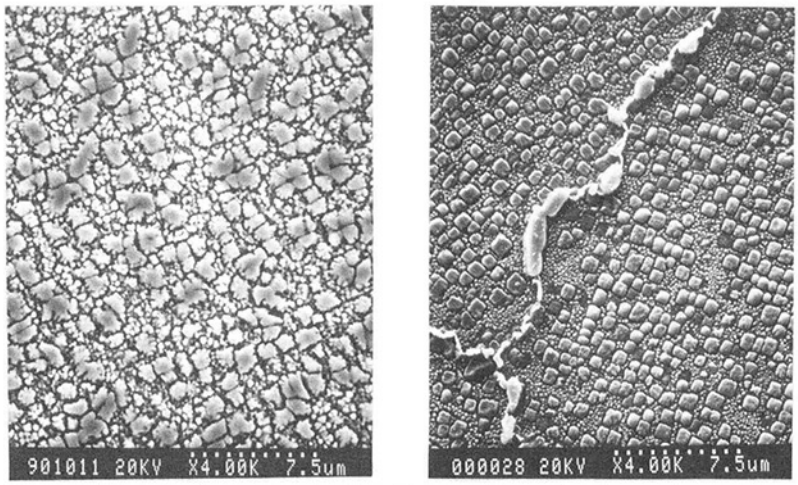


Fig. 9 SEM photomicrographs showing: (*a*) coarsening and agglomeration of primary cuboidal γ' and secondary spheroidal γ' in IN738LC after prolonged exposure at elevated temperature, and (*b*) unexposed microstructure

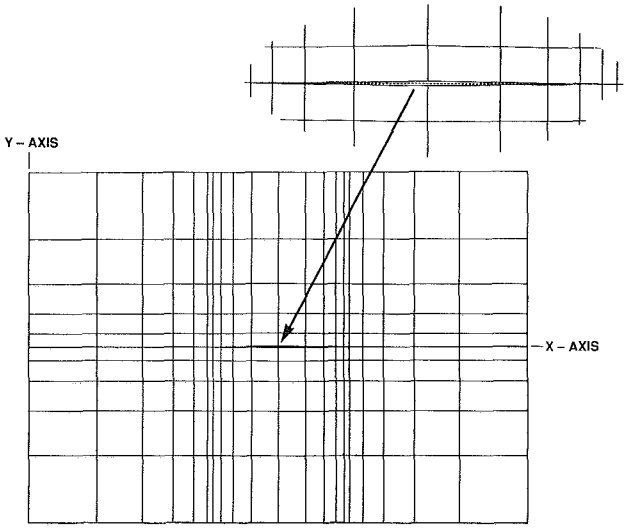


Fig. 10 Central-cracked model

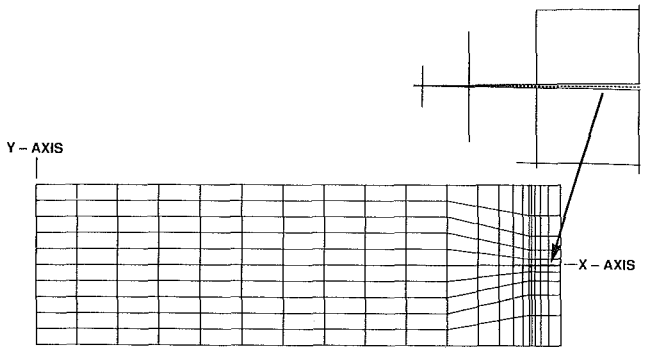


Fig. 11 Edge-cracked model

IN738LC is a low-ductility material, which exhibits little deformation during crack propagation.

Due to the assumed size of the crack as compared to that of the blade, the effect of airfoil curvature was negligible and therefore not considered. By the same token, only the surrounding material in the vicinity of the crack was deemed relevant to this analysis, not the whole blade.

3.2 The Finite Element Models. A two-dimensional WECAN isotropic element was chosen to construct the finite element models. It is an elastic quadrilateral element that possesses eight nodes, four at the corners and four at mid-sides. This arrangement allows the displacement on each side of an element to move in a quadratic pattern. Two finite element models were constructed to improve the level of confidence of the results. One model was a rectangular plate containing a centrally located 0.080-in.-long transverse crack (Fig. 10) and the other, a rectangular plate containing a 0.040-in.-long edge crack (Fig. 11). In each case, the elements were biased in order to achieve a more precise network of elements surrounding the crack tip. Progressively larger elements were used at the far end away from the crack tip to minimize the size of the matrix formulation. Thus, a better approximation of the stress field in the vicinity of the crack tip could be obtained.

The top of each model did not extend all the way up to the airfoil tip so that fewer elements could be used to construct the model. This effect was compensated for by applying the appropriate boundary conditions.

3.3 Load and Boundary Conditions. Gas bending load on this portion of the blade airfoil is negligible and therefore was not considered in the analysis. The only practical mechanical loading that was applied to both models under operating conditions was the direct centrifugal load. This centrifugal load was modeled to be a load distributed uniformly along the top sides of all the elements at the top of the models. Since the models only occupied a very small portion of the airfoil, no thermal gradient was taken into account. Both models were assumed to operate at a uniform temperature of 816°C, which was obtained from the tips of the same turbine blades in an engine test using pyrometry and thermal paint.

In the central-crack model, all the nodes along each vertical side of the plate were constrained to have zero movement in the chordwise x direction. The edge crack model was constructed based on the results of the central-crack model. Knowing the symmetric distribution of the centrifugal stress σ_y from the results of the central-crack model, the second model was constructed by cutting the central-crack model in half through the middle of the crack with a normal plane. All the nodes on this face were then constrained to have zero displacement in the x direction. More elements were also added to the bulk of the solid end of the model opposite to the half crack. The nodes on this end vertical face were all set free in the x direction to allow for free expansion in this direction. This was possible because the elements at this end were far enough from the crack tip and thus should not affect the stress field in the vicinity of the crack tip. All the nodes in each vertical side and the base of each model were constrained to the corresponding

Downloaded 02 Jun 2010 to 171.66.16.112. Redistribution subject to ASME license or copyright; see http://www.asme.org/terms/Terms_Use.cfm

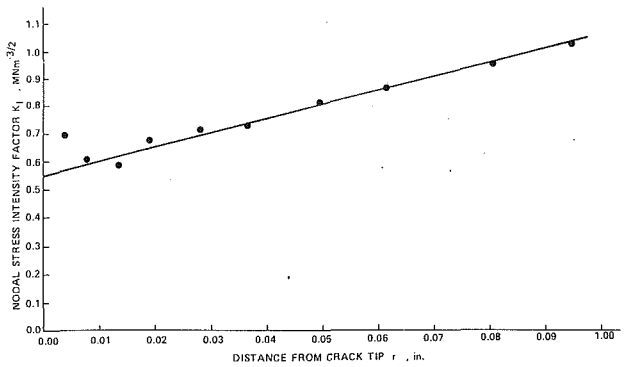


Fig. 12 K_I^* versus r curve: central-cracked model

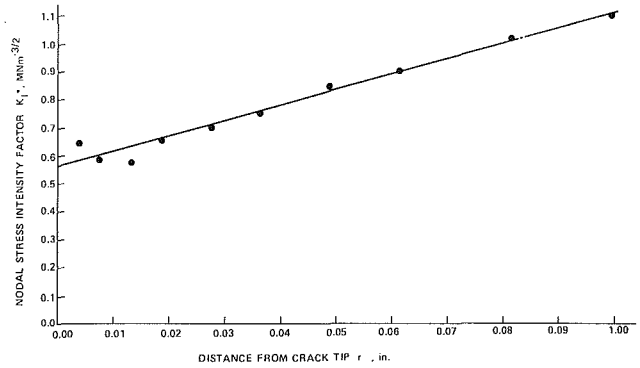


Fig. 13 K_I^* versus r curve: edge-cracked model

y direction displacements due to the centrifugal and thermal effect on the whole blade.

3.4 Analysis Results. The output of the finite element analysis does not directly yield a stress intensity factor at the crack tip. To calculate this value, a stress method [9] was utilized. The stresses were correlated to the plane strain crack tip stress equation, which is given by:

$$\sigma_{ij} = \{K_I/(2\pi r)^{1/2}\} f_{ij}(\theta) \tag{4}$$

where

$$f_{xx}(\theta) = \cos(\theta/2)\{1 - \sin(\theta/2)\sin(3\theta/2)\}$$
$$f_{yy}(\theta) = \cos(\theta/2)\{1 + \sin(\theta/2)\sin(3\theta/2)\}$$
$$f_{xy}(\theta) = f_{yx}(\theta) = \sin(\theta/2)\cos(\theta/2)\cos(3\theta/2)$$

Nodal point stresses σ_{ij}^* in the crack tip vicinity were substituted into the above equation and values of each nodal K_I^* can be computed as:

$$K_I^* = \{(2\pi r)^{1/2}/f_{ij}(\theta)\}\sigma_{ij}^*(r, \theta) \tag{5}$$

Since this is a Mode I phenomenon, good estimates of K_I by this stress method corresponding to the nodal centrifugal stresses σ_y^* can be obtained on the $\theta = 0$ deg plane [9]. Thus, $\sigma_{ij}^*(r, \theta) = \sigma_y^*(r, \theta)$ in this analysis. The K_I^* values were then plotted as a function of the corresponding r for $\theta = 0$ deg (see Figs. 12 and 13). The stress intensity factor at the crack tip was then obtained by extrapolating the K_I^* curve to cut the K_I^* axis at $r = 0$. The intercept of the curve and the axis is the appropriate value of K_I at the crack tip. This was found to be 0.545 MNm$^{-3/2}$ using the central-cracked model and 0.563 MNm$^{-3/2}$ using the modified edge-cracked model. There is only a 3 percent deviation. It has been noted that the finite element method is unable to represent the exact stress singularity conditions at the crack tip; therefore, the values obtained are approximate values. Yet, the K_I solutions were compatible with the results calculated using the following general equations [10] for uniform remote stress field:

$$K_I = \sigma\sqrt{(\alpha\ a)} \text{ for central located crack} \tag{6}$$

and

$$K_I = 1.1\ \sigma\sqrt{(\pi\ a)} \text{ for edge crack} \tag{7}$$

They yield values of 0.461 MNm$^{-3/2}$ and 0.508 MNm$^{-3/2}$, respectively. This indicates that the finite element solutions are good estimations.

4.0 Discussion

The major outcome of the creep crack growth tests is shown in Fig. 3, which plots da/dt as a function of K_I or IN738LC. The trend in the creep crack growth behavior of this superalloy illustrates the typical three-stage phenomenon, which is in agreement with the literature data.

The excellent conformance of the limited data from this experiment to the standard da/dt versus K_I curve indicates that the application of the linear elastic fracture mechanics (LEFM) parameter K_I to correlate the creep crack growth data in this material under the conditions of this study is practical. It further substantiates the fact that IN738LC, being a high creep strength superalloy, behaves in a brittle manner and possesses only small-scale creep deformation confined to the vicinity of the crack tip at the temperature used in this study. Moreover, the transition time concept of Riedel and Rice [7], which postulates the short-time validity of K_I and long-time validity of C^* in correlating the creep crack growth data, is provided to be applicable under the conditions of this experiment. Figure 14 illustrates a curve of the calculated transition time, t_a, versus K_I for IN738LC. The test durations for the various K_I loadings are also plotted in the same figure. The fact that the vast majority of test durations in this experiment are substantially lower than the transition times supports K_I to be an appropriate parameter to correlate creep crack growth data for IN738LC.

However, it is obvious that the test duration time for 45 MNm$^{-3/2}$ lies just below the transition time curve. Therefore it can be argued that all other creep crack growth data in the neighborhood of this possible "threshold" regime may start to lose their validity if they are correlated using K_I. This will be especially significant for data below 45 MNm$^{-3/2}$, which will definitely require a much longer testing time.

At the tertiary Stage III, the onset of unstable fast fracture evidently lies between K_I of 90 MNm$^{-3/2}$ and 92.5 MNm$^{-3/2}$. This critical stress intensity factor at the crack tip is the generally known K_{IC} value of IN738LC at 816°C. It indicates an increase from the K_{IC} of 74 MNm$^{-3/2}$ of this superalloy measured at approximately 704°C and reported in the literature [14]. This increase in the critical fracture toughness value with an increase in temperature may be attributed to the relative improvement in ductility of this alloy going from 704°C to 816°C. The size effect and the deviation in geometries of the different specimens used in each case may also contribute to the difference.

A power law dependency of da/dt with K_I characterizes Stage II of the curve. This power law can be represented by Eq. (1):

$$da/dt = BK_I^n$$

Assuming dislocation creep is the relevant process for creep crack growth, B will have the form of:

$$B = B'(ub/RT)\exp(-Q_C/RT) \tag{8}$$

where $\exp(-Q_c/RT)$ = Arrhenius term.

If grain boundary cavity growth ahead of the crack by the creep deformation of the surrounding material is a rate-determining factor, then combining Eqs. (1) and (8), the crack propagation rate da/dt will be of the form:

$$da/dt = B'(ub/RT)K_I^n\exp(-Q_c/RT) \tag{9}$$

which conforms to Norton's law [15].

From the curve in Fig. 3, n is found to be 8.53 at 816°C.

Downloaded 02 Jun 2010 to 171.66.16.112. Redistribution subject to ASME license or copyright; see http://www.asme.org/terms/Terms_Use.cfm

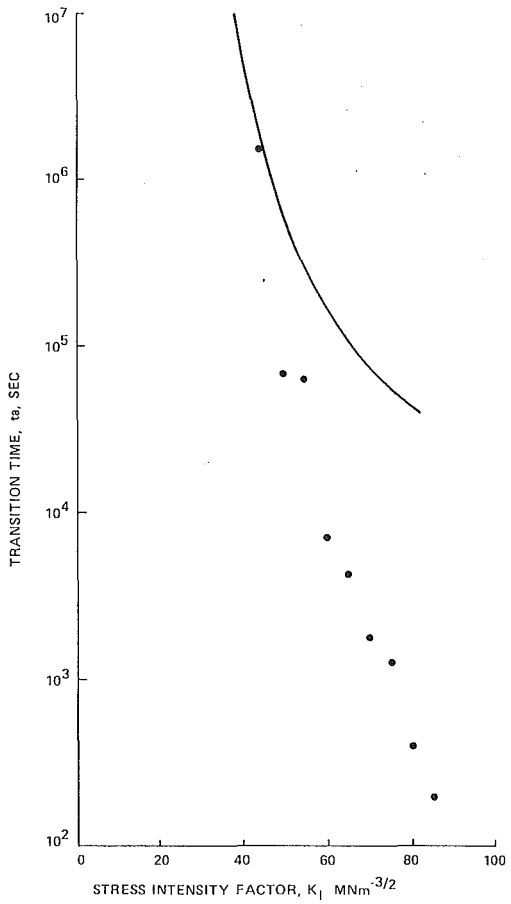


Fig. 14 Transition time curve

This value agrees in general with the steady-state creep stress exponent for IN738LC at 850°C found by Stevens and Flewitt to lie between 6.1 and 9.6 depending on the stress range [16].

Metallographic investigation further demonstrates the creep crack growth behavior of IN738LC. Figures 5, 6, and 7 show the intergranular nature of the creep crack. It propagated principally through the nucleation, growth, coalescence, and link-up of grain boundary microvoids and microcracks. The size and number of grain boundary cavities observed in these micrographs are extensive. The $M_{23}C_6$ carbide films that are seen along the grain boundaries probably contributed to the formation of these microvoids and microcracks.

An extensive quantity of microvoids are seen in the vicinity of the block MC carbides in the γ matrix ahead of the crack tip (Fig. 6). The fact that the MC carbides are extremely hard particles suggests that these microvoids were probably formed by the shearing action between the MC carbides during creep deformation at the front of the running crack. These microvoids at the MC carbides, by growing to substantial sizes, may link the growing crack tip and the coalesced microcracks and microvoids in the grain boundaries.

The composite fractograph indicates that this particular HCF precrack ended in the interior of two grains with a vertical dividing grain boundary located approximately in the middle of the specimen width normal to the crack front (Fig. 8). In order for the entire crack front to propagate under loads, the major portion of the crack front propagated transgranularly to meet the microvoid-coalesced grain boundaries to initiate the predominant intergranular mode of the creep crack. The remainder of the crack front followed the grain boundary normal to the crack front and traveled intergranularly. After a major section of intergranular crack propagation, the specimen failed in overload fracture. This suggests that creep crack growth of a pre-existing crack may go through a transition transgranular mode until the crack tip links up with the microvoid-coalesced grain boundaries to enter its predominant intergranular propagating mode. As previously mentioned, the microvoids nucleated between the MC carbides may be the interlinking mediums in this growing process.

The crack branching phenomenon of creep crack growth behavior in most Ni-based superalloys as reported in the literature [17] is not observed in this investigation. Although several grain boundary microcracks are seen in front of the crack tip (Fig. 7), there is no evidence of crack branching.

As the results demonstrated, the modified d-c potential drop method used to provide the continuous measurement and monitoring of the through-thickness crack length during the experiment was found to be both effective and accurate.

The data from this experiment were also used to establish a relationship between the modified Larson–Miller parameter and the crack tip stress intensity factor, as shown in Fig. 4. This plot indicates that this Larson–Miller parametric method may be used to both extrapolate and interpolate creep crack growth rate data to temperatures other than those tested. This finding widens the horizon of the creep crack growth testing by suggesting that no testing at other temperatures corresponding to similar loadings may be needed to obtain required information at those temperatures. However, it is important to note that this correlation can only be achieved for a particular load history in which K_I can be applied to correlate the creep crack growth data. Extrapolation to other loading conditions may not be applicable.

By comparing the K_I value at the crack tip of the heat-affected zone crack with the da/dt versus K_I curve of IN738LC in Fig. 3, it can be concluded that the 0.080 in. crack in this study is not likely to grow under normal operating conditions.

However, the effect of environment was not studied in this investigation. It is well known that the operating environment inside the hot gas path of a gas turbine is extremely hostile. The compound most commonly found is Na_2SO_4, which formed in the combustion chambers of the gas turbine by the reaction of Na-containing salts such as NaCl, which may be present in the air or fuel with SO_2/SO_3 created by combustion of the sulfur-bearing fuel. In conventional operating environments, the conversion of NaCl to Na_2SO_4 occurs according to the following reaction:

$$NaCl + SO_2 + 1/2(O_2) + H_2O \rightarrow Na_2SO_4 + 2HCl \qquad (10)$$

The Na_2SO_4 deposit is molten at the elevated temperature on the metal surfaces of the first-stage vanes and rotor blades. This modifies the oxidation conditions at the metal surfaces resulting in accelerated corrosion because of the formation of sulfides at the interface between the metal and the oxide layer. Corrosion then penetrates along the grain boundaries into the metal, and also causes blistering of the protective oxide layer.

Under creep load, the stress field will promote the corrosion attack on the grain boundaries leading to severe degradation of the creep properties of IN738LC. This creep corrosion interaction phenomenon is a complex issue, which should be dealt with in further research studies.

Furthermore, it is also important to point out that the applicability of K_I or C^* to IN738LC and other types of superalloys depends principally on the mechanical behavior of each superalloy at the test temperature as well as its susceptibility to the environment [18]. Therefore, the validity of the correlation of creep crack growth data using K_I has to be re-evaluated if environmental effects are to be incorporated.

5.0 Conclusions

The rotating blades, under normal operating conditions, with predominantly direct centrifugal stress distribution and thermal loadings, do not possess a high enough driving force

Downloaded 02 Jun 2010 to 171.66.16.112. Redistribution subject to ASME license or copyright; see http://www.asme.org/terms/Terms_Use.cfm

for a pre-existing transverse crack 0.80 in. long, induced by welding, to propagate.

The creep crack growth characteristics of fully hipped and heat-treated IN738LC follows the typical trend of a creep crack growth curve with sustained loading exhibiting primary Stage I, secondary Stage II, and tertiary Stage III behavior.

It was found that creep crack growth data of this Ni-based superalloy can be applied in extrapolating and interpolating to other temperatures using a modified Larson-Miller parameter.

Successful instantaneous crack length output throughout this experiment has shown that the modified d-c potential drop method is applicable to creep crack growth measurement and monitoring in IN738LC under the loading conditions described above.

Microstructural examination demonstrated that the creep crack growth mechanisms occurs by nucleation, growth, coalescence, and final link-up of grain boundary microvoids and microcracks, particularly at the late stage toward fracture.

The correlation of creep crack growth data using the LEFM stress intensity factor K_I for the small-scale yielding alloy IN738LC is applicable.

Excellent results from the finite element analysis demonstrated that this analytical tool is able to be utilized to perform analysis of the stress field at the crack tip of a high creep strength, low ductility alloy like IN738LC.

References

1 Sadananda, K., and Shahinian, P., *Eng. Frac. Mech.*, Vol. 15, 1981, pp. 327-342.

2 Guo, J., Ranucci, D., Picco, E, and Strocchi, P. M., "An Investigation on the Creep and Fracture Behaviour of Cast Ni-Base Superalloy IN738LC," *Metallurgical Transactions A*, Vol. 14A, 1983.

3 Tipler, H. P., "Metallographic Aspects of Creep Fracture in a Ni-Cr Base Alloy," presented at the 5th International Conference on Fracture.

4 Dyson, B. F., and Mclean, M., "Particle-Coarsening, σ_0 and Tertiary Creep," *Acta Metall.*, Vol. 31, 1983.

5 Irwin, G. P., "Structural Mechanics," 1st Symposium on Naval Structural Mechanics, Pergamon, Oxford, United Kingdom, 1960.

6 Landes, J. D., and Begley, J. A,. ASTM STP 590, 1976.

7 Riedel, H., and Rice, J. R., "Tensile Cracks in Creep Solids," ASTM SPT 700, 1980.

8 Thambiraj, R., Wallace, W., and Goldak, J. A., "PWHT Cracking in Superalloys," *International Metals Reviews*, Vol. 28, No. 1, 1983.

9 Chan, S. K., Tuba, I. S., and Wilson, W. K., "On the F.E.M. in Linear Fracture Mechanics," *Engineering Fracture Mechanics*, Vol. 2, 1970.

10 Hertzberg, R. W., *Deformation and Fracture Mechanics of Engineering Materials*, 2nd ed., Wiley, New York, 1983.

11 Brown, W. F., Jr., and Strawley, J. E., "Plane Strain Crack Toughness Testing of High Strength Metallic Materials," ASTM SPT 410, 1966.

12 Koul, A. K., Castillo, R., and Willett, K. P., "Creep Life Prediction in Ni-based Superalloys," *Materials Science and Engineering*, 1984.

13 Bain, K. R., and Pelloux, R. M., "Effect of Environment on Creep Crack Growth in PM/HIP René-95," *Metallurgical Transactions A*, Vol. 15A, 1984.

14 Holdsworth, S. R., "The Significance of Defects in Ni-Base Superalloys," *Superalloys*, 1980.

15 Lupinc, V., "Creep Strengthening Mechanisms," *Proceedings of High Temperature Alloys for Gas Turbines Conference*, Belgium, 1982.

16 Stevens, R. A., and Flewitt, P. E. J., "The Dependence of Creep Rate on Microstructure in a γ' Strengthened Superalloy," *Acta Metallurgica*, Vol. 29, 1981.

17 Scarlin, R. B., "Effects of Loading Frequency and Environment on Higher Temperature Fatigue Crack Growth in Ni-Base Alloys," *Fracture*, Vol. 2, Waterloo, Canada, 1977.

18 Sadananda, K., and Shahinian, P., "Cavities and Cracks in Creep and Fatigue," *Applied Science*, London, 1981.

Downloaded 02 Jun 2010 to 171.66.16.112. Redistribution subject to ASME license or copyright; see http://www.asme.org/terms/Terms_Use.cfm

High-Cycle Fatigue Design Evolution and Experience of Free-Standing Combustion Turbine Blades

A. J. Scalzo
Technical Director, Combustion Turbines,
Westinghouse Electric Corporation,
Orlando, FL 32826-2399

Combustion turbine blade design criteria can generally be classified as either temperature or fatigue related. Since less is usually known about the factors influencing the fatigue phenomenon, it is considered the more challenging. In addition, as analytical and experimental techniques became more sophisticated and more accurate, the natural tendency was to replace archaic "guidelines" or "rules" with less conservative approaches that at times led to the discovery of new high-cycle fatigue "thresholds." This paper presents the evolution of the combustion turbine blade high cycle fatigue design criteria for free-standing blades. It also presents the analysis and corrective actions taken to resolve several unique combustion turbine blade fatigue problems, all encountered over a 35-year period while the author has been employed at Westinghouse Electric Corporation. Included are high-cycle fatigue problems due to cooling air leakage, seal pin friction, and combustion temperature maldistribution, as well as flow-induced nonsynchronous vibration.

Introduction

The evolution of high-cycle fatigue combustion turbine blading design criteria has not been as dramatic as some other fields of engineering. Although many advancements have occurred in technologies such as aerodynamics, computers, experimental techniques, and metallurgy, many of the basic considerations for determining the mechanical design of a free-standing combustion turbine blade have essentially remained the same over the last 25 years. One notable exception is the aeroelastic criteria that have been upgraded in recent years.

A subject as broad as combustion turbine blading obviously is beyond the scope of a technical paper; hence the subject matter will be confined to the author's experience over a 35-year period. The period spans from the early 1950s to the present, and includes experiences as a design engineer, manager of mechanical design, and engine design and development manager, all while employed at the Westinghouse Electric Corp. To confine the scope further, in order to satisfy technical publication constraints, this paper will be limited to high-cycle fatigue considerations of free-standing blades. Subjects such as low-cycle fatigue, creep, creep/fatigue interaction, erosion/corrosion, shrouded blades, as well as corrosion-assisted fatigue will not be discussed. In addition to the evolution of high-cycle fatigue design criteria for free-standing blades, four unique and challenging high-cycle fatigue experiences will be discussed. Included is the first and only other than first mode failure of a free-standing blade encountered by the author; second, resonance caused by intermittent seal pin friction; third, a fatigue problem related to combustion system temperature maldistribution; and fourth, flow-induced nonsynchronous fatigue problems.

Contributed by the International Gas Turbine Institute and presented at the 36th International Gas Turbine and Aeroengine Congress and Exposition, Orlando, Florida, June 3-6, 1991. Manuscript received at ASME Headquarters January 29, 1991. Paper No. 91-GT-13. Associate Editor: L. A. Riekert.

Evolution of Turbine Blade Design Criteria

In 1953, when the author joined Westinghouse, the combustion turbine industry was in the early stages of development. Design rules for high-cycle fatigue considerations were initially very conservative, and were based on steam turbine and some early jet engine experiences. Prior to 1950, jet engine turbine blade design rules had been even more conservative than the steam turbine requirements. For example, the design criteria for establishing the blade chord or size of a jet engine turbine blade were based on a gas bending stress (raised by the appropriate stress concentration factor) of only 10 percent of the endurance limit of the material. This resulted in only a 3 KSI allowable gas bending stress for a 30 KSI endurance limit, which affected blade size and engine weight. Therefore, the jet engine turbine blade design criteria were changed to reflect some steam turbine experience and also jet engine blade material characteristics. Since the combustion turbine criteria evolved from both the steam turbine and jet engine technologies, a brief review of both will establish the starting point for the combustion turbine blade high-cycle fatigue design criteria in effect during the early 1950s.

Steam Turbine Design Criteria. Steam turbine free-standing blade design criteria in effect during the early 1950s for full annulus flow are completely described by Trumpler and Owens (1953). Blades were defined as either tuned or untuned.

Copyright © 1992 by ASME
Downloaded 02 Jun 2010 to 171.66.16.112. Redistribution subject to ASME license or copyright; see http://www.asme.org/terms/Terms_Use.cfm

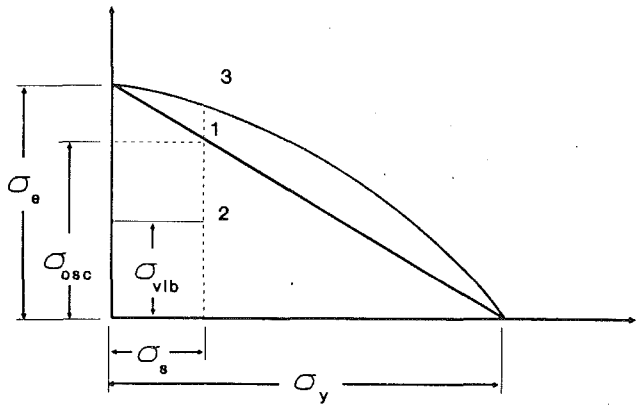


Fig. 1 Stress range diagram

Tuned blades were designed to avoid resonance with engine order (*EO*) frequencies (multiples of running speed) at synchronous speed for the primary modes of vibration. Untuned blades were designed based on an experience "strength" factor. To develop the needed data base, many successes and failures over at 12-year period were carefully analyzed to define stresses and blade natural frequencies precisely. The method used to correlate this data base included material data, centrifugal blade stress, blade bending stress, stress concentration factor, blade fundamental natural frequency, and an assumed shape of the allowable stress range diagram.

A stress range diagram is a plot of the vibratory stress to fail as a function of steady stress. A straight line was assumed based on material test data as shown in Fig. 1. The ordinate intercept is the endurance limit of the material while the abscissa intercept is the material 0.2 percent yield strength, both taken at he blades's operating temperature. Steady stress, σ_s, in the blade is taken as the sum of the centrifugal stress, σ_{cf}, and the steam bending stress, σ_b. From Fig. 1, the vibratory stress to fail, σ_{osc}, for a given steady stress, σ_s, is defined by point 1. In order to complete the picture, a value for blade vibratory stress, σ_{vib}, is required to establish point 2. Since the fundamental design objective is for the blade to provide torque, it follows that when the source of the excitation is from within the flow field, flow vector summations will result in primarily a first mode stimulus. Thus when this flow field contains EO frequencies that coincide with the blade's fundamental frequency, resonance will result. Based on this rationale, the blade vibratory stress can be considered to be directly proportional to the blade steam/gas bending stress raised by an appropriate stress concentration factor as follows:

$$\sigma_{vib} = AK\sigma_b \tag{1}$$

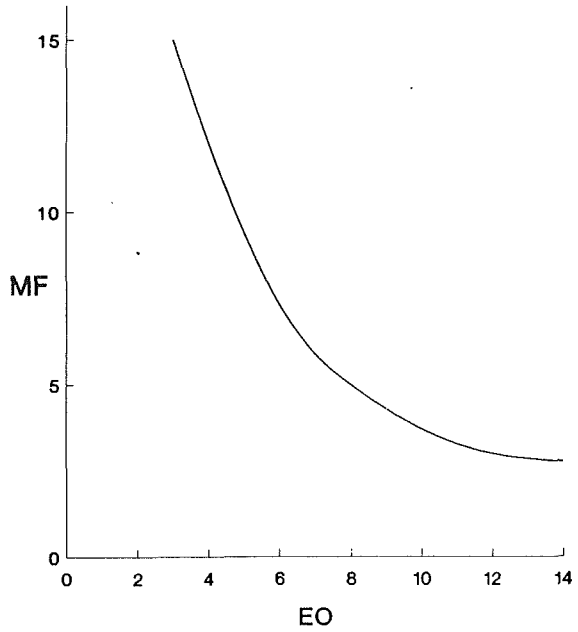


Fig. 2 Steam blading magnification factor

When the blade vibratory stress level reaches point 1, the level of stress is referred to as σ_{osc}, and the proportionality constant (A) will be referred to as the magnification factor (MF).

Therefore,

$$MF_{st} = \frac{\sigma_{osc}}{K\sigma_b} \tag{2}$$

From Fig. 1, the straight line function yields:

$$MF_{st} = \frac{\sigma_s}{K\sigma_b}(1 - \sigma_s/\sigma_y) \tag{3}$$

Calculating magnification factors for past blade design, and plotting them as a function of the blade's fundamental mode frequency expressed as *EO* frequencies, resulted in Fig. 2 from Trumpler and Owens (1953). This experience curve was used to size the blades to avoid high-cycle fatigue failures. Using the straight line assumption for the stress range diagram and the required MF curve, the blade allowable bending stress could be defined from which the blade chord or size could be selected to prevent high-cycle fatigue failures.

Jet Engine Design Criteria. The jet engine turbine blade high-cycle fatigue design criteria in place during the early 1950s were changed from the 10 percent rule to reflect steam turbine

Nomenclature

KSI = lb/in^2 × 10^{-3}
h = platform thickness, in.
w = platform width, in.
μ = friction coefficient
R, N = normal load, lb
MF = magnification factor
σ = stress, lb/in^2
EO = engine order
A = proportionality constant
K = stress concentration
$\Delta\phi$ = width of rectangular pulse
π = 3.1416
F = amplitude of rectangular pulse
a, b = Euler coefficients
c = amplitude of forcing function
H = harmonic coefficient
λ = reduced frequency parameter
C = blade chord, ft
V = exit velocity of air relative to blade, ft/sec
f = natural frequency, cps
ΔL = periodic load factor
δ = damping logarithmic decrement
θ = pin surface angle
ϕ = location of pulse, deg

Subscripts

s = steady
b = bending
cf = centrifugal force
osc = vibratory failure
vib = vibratory
st = straight line
el = elliptical
e = endurance limit
y = 0.2 percent yield
r = ratio
k = rectangular pulse identification
n = harmonic of forcing function
t = torsion
f = flexure

Downloaded 02 Jun 2010 to 171.66.16.112. Redistribution subject to ASME license or copyright; see http://www.asme.org/terms/Terms_Use.cfm

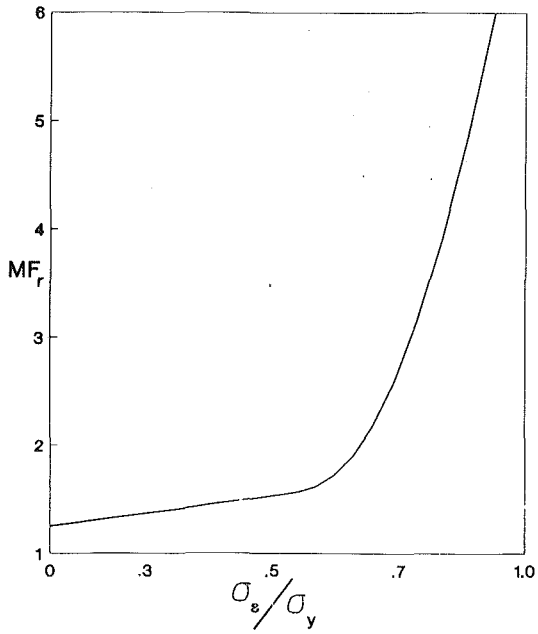


Fig. 3 Magnification factor ratio, elliptical to straight line

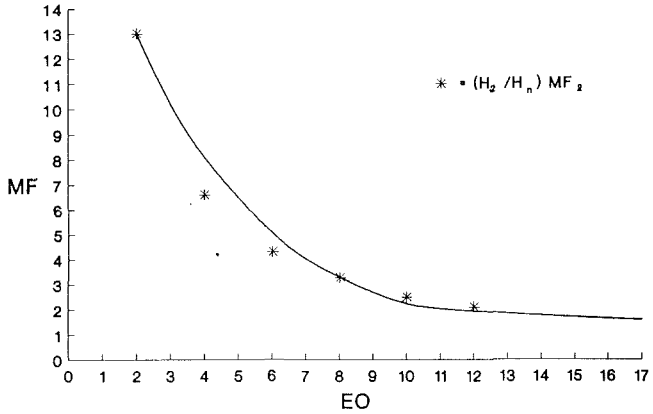


Fig. 4 Combustion turbine magnification factor with normalized harmonics of the second *EO* forcing function

blade experiences. Since the operational mode was variable speed, a modified version of the *MF* approach initiated by the steam turbine designers was selected. Instead of varying the allowable magnification factor as a function of *EO*, a fixed value of 2.5 was selected for higher frequency front end blading, and a value of 3.0 was selected for lower frequency rear stages. These values were based on jet engine experiences, both domestic and foreign. In addition, a review of material data indicated that the shape of the stress range diagram was material dependent. Available material test data supported a linear assumption for aluminum, and elliptical shaped stress range diagram for steel blades. An elliptical diagram is shown superimposed on the linear diagram in Fig. 1. Using the elliptical function, the magnification factor defined by point 3 becomes:

$$MF_{el} = \frac{\sigma_e}{K\sigma_b}\left[1-(\sigma_s/\sigma_y)^2\right]^{1/2} \tag{4}$$

A technique called "leaning" was introduced to improve vibratory strength by reducing the steady stress in the blade. This was accomplished by displacing the blade mass from the radial line to introduce centrifugal bending moments to offset the gas bending moment.

Combustion Turbine Design Criteria. Regardless of whether the turbine fluid is steam or gas, the vibratory stress in a blade is the result of the level of excitation present in the flow stream and the ability of the blade and root system to absorb the input energy. A system's ability to absorb input energy is dependent on the sum of fluid, material, and mechanical damping. It can be safely argued that a combustion turbine excitation is more complex, since discontinuities present in the flow path reflect airflow discontinuities from the compressor (including inlet effects) that are further distorted by the combustion system, as well as by turbine elements before and after the blade row in question. Furthermore, combustion turbine blades undergo the deleterious load effects of ambient temperature, evaporative coolers, steam/water injection for NO_X control, peak firing temperature, and back pressures due to use of heat recovery steam generators (HRSG). In spite of these many differences, the initial approach was patterned after the steam turbine approach because many of the materials and root system designs were taken from the steam turbine designs. In addition, a comparison between the elliptical versus the straight line stress range assumption indicated a large error in the value of *MF* was possible. To quantify this difference, the ratio of the elliptical (Eq. (4)) to the straight line (Eq. (3)) yields:

$$MF_r = \left[\frac{1+\sigma_s/\sigma_y}{1-\sigma_s/\sigma_y}\right]^{1/2} \tag{5}$$

This function, plotted in Fig. 3, indicates that when the stress ratio is low, the *MF* error is negligible; but for a typical factor of 0.5, the error is 1.732, which is significant. This concern and an ever-increasing wealth of material data provided strong support in the mid 1950s to change from an elliptical to a linear assumption for the stress range diagram shape.

The steam and jet engine design criteria in place during the early 1950s established the starting point for the combustion turbine blade high-cycle fatigue criteria. Based upon these experiences, the minimum allowable *MF* curve was defined as shown by the curve in Fig. 4. Reflecting early combustion turbine experience, only the first bending mode was detuned. The rationale for the first mode concern was discussed earlier; however, to emphasize the point further, the source of the excitation is assumed to the present in the turbine flow stream. (This point is emphasized since a violation of this assumption is identified in the first example to be discussed later in the paper.) In spite of the aforementioned differences between the steam and combustion turbines, this design criterion prevented simple first mode failures. The most difficult task during these early years was the determination of the blade's natural frequency because of the limitations of both analytical and experimental techniques, especially in simulating the effects of root fixity. In addition, turbines in utility service were expected to operate over a speed range of ±1.5 Hertz or ±90 rpm for for a 60 Hertz turbine, which further exacerbated the detuning problem. Prevention of simple first mode failures was due to two basic facts: First, aerodynamic loadings were light; and second, the magnification factor approach was conservative.

In the mid-1960's, the combustion turbine blade design criteria were re-evaluated as part of a new engine design program. Competitive pressures for improved efficiencies, at reduced cost, precipitated a review of past experience similar to the steam effort in the early 1950's. Putting all past data on the same basis, including the straight line stress range diagram, resulted in the data display in Fig. 5. This information tended to support a required *MF* independent of *EO*, which was similar to the earlier jet engine selection of 2.5 and 3.0. Based upon this historical data base, the minimum *MF* was selected to be 3.0 as calculated using the straight line stress range diagram. It is significant to note that the original criteria were based upon operation in resonance while the new criteria assumed detuning of the first mode. "Leaning" was also introduced, which increased *MF*. Blade fundamental mode resonant frequencies were also required to be tuned away from all *EO*

Downloaded 02 Jun 2010 to 171.66.16.112. Redistribution subject to ASME license or copyright; see http://www.asme.org/terms/Terms_Use.cfm

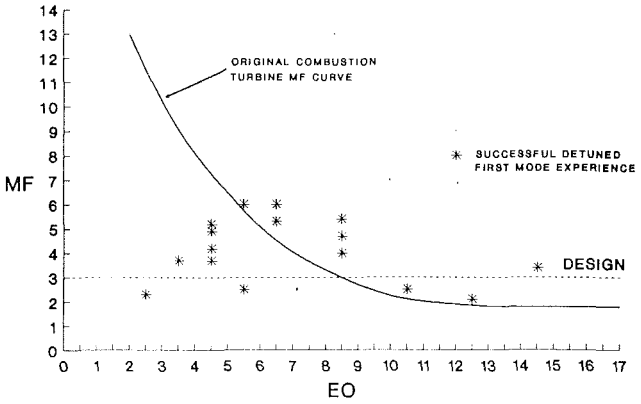


Fig. 5 Combustion turbine first mode detuning experience related to magnification factor

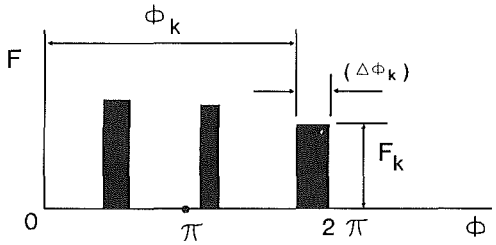


Fig. 6 Forcing function represented as an array of rectangular pulses

frequencies below the eighth, and tuned away from identifiable structural sources of *EO* excitation, such as the number of stationary vanes, number of vane segments, number of combustor baskets, etc. The rationale for the fundamental mode concern was supported in the preceding sections, while the concern for the eighth or lower *EO* resonant frequencies is supported by past experience such as Fig. 4, and also by a concern for the second *EO* syndrome.

The second *EO* syndrome is based upon the recognition that a combustion turbine is constructed using a horizontal joint that may lead to casing ovalization. In addition, seal leakages tend to be maximized at the horizontal joint (this will be discussed further in the example section), which was further exacerbated by the use of 180-deg turbine stationary segments in earlier turbine designs. Furthermore, there is an increase in blade damping cycles for higher *EO* frequencies, provided the source is due to low *EO* frequencies such as from the horizontal joint. All these factors resulted in a concern for low even *EO* frequencies.

Partington (1957) represented the exciting force in terms of a Fourier series made up of rectangular pulses as shown in Fig. 6. This facilitated the use of a digital computer since any forcing function could be reduced to a series of rectangular pulses. Also, the pulse width, $\Delta\phi_k$, was used to determine the value of the Euler coefficients as:

$$a_n = -\frac{1}{n\pi}\Sigma_1^k P_k[\cos n\phi_k \cos n(\Delta\phi_k) - \sin n\phi_k \sin n(\Delta\phi_k) - \cos n\phi_k] \quad (6)$$

and,

$$b_n = \frac{1}{n\pi}\Sigma_1^k P_k[\sin n\phi_k \cos n(\Delta\phi_k) + \cos n\phi_k \sin n(\Delta\phi_k) - \sin n\phi_k] \quad (7)$$

It follows that the Fourier coefficient, the magnitude of the nth harmonic becomes:

$$c_n = [a_n^2 + b_n^2]^{1/2} \quad (8)$$

A further simplification results when pulses are equal and the pulse width is small enough so that the sine can be assumed equal to $(\Delta\phi_k)$ and the cosine becomes equal to 1.0. This reduces the Fourier Coefficient to:

$$c_n = \frac{\Delta\phi}{\pi}[(\Sigma_1^k \sin n\phi_k)^2 + (\Sigma_1^k \cos n\phi_k)^2]^{1/2} \quad (9)$$

Furthermore, the radical can be assumed to be the harmonic coefficient, H_n, such that:

$$H_n = [(\Sigma_1^k \sin n\phi_k)^2 + (\Sigma_1^k \cos n\phi_k)^2]^{1/2} \quad (10)$$

This term can be used to make comparisons when the data base is consistent from the standpoint of pulse width and magnitude. For example, if we assume that the excitation force function is two equal and opposite forces, H_n will equal 2. Similarly, if we assume that the forcing function is ten equally spaced forces of equal magnitude, then H_n will equal 10. However, if we determine the fifth harmonic of the two equal distributed forces of the same magnitude, H_n will equal only 2, which is only 20 percent of a pure tenth harmonic forcing function. Normalizing the harmonics of a second harmonic forcing function results in the even harmonic points superimposed in Fig. 4.

The result in Fig. 4 is quite interesting in that the normalized second harmonic function plot using the second harmonic as the anchor point crosses above the magnification factor of 3.0 for the eighth harmonic. Actually the normalized value is 13/4 or 3.25. Only the trend of the points is valid, but it does demonstrate the benefit of high harmonics when the excitation source is due to a low harmonic coefficient such as 2.0. In addition, it gives credence to the experience curve shape since many older turbines had the potential for the second *EO* syndrome. However, since the turbines designed after the mid-1960s were designed with blade rings, supported by radial keys, to permit improved control for transient response and the elimination of casing distortion, the constant magnification factor of 3.0 was justified for the low harmonics, and was conservative for the higher harmonics.

In addition to the first mode detuning and magnification factor requirements, a third requirement was added, reflecting information from the jet engine field on self-excited vibration or flutter. Since weight is a premium with the jet engine designs, they encountered a new "threshold" as they made attempts to reduce weight. The early work was the result of compressor failures encountered in the late 1950s and early 1960s. Armstrong and Stevenson (1960) developed some guidelines to prevent flutter or aeroelastic failures. They presented two basic parameters to prevent aeroelastic failures, i.e., torsional and flexural, as:

Torsional frequency parameter,

$$\lambda_t = \frac{2\pi fC}{v} = 1.6 \quad (11)$$

Flexural frequency parameter,

$$\lambda_f = \frac{2\pi fC}{v} = .30 \quad (12)$$

These requirements were added to the combustion turbine fatigue design criteria in the mid-1960s to prevent aeroelastic failures in the compressor and turbine for all new designs. No problems related to this phenomenon had been encountered prior to this period, but the change to a less conservative criterion to select blade chords justified the addition of this consideration.

Unique High-Cycle Fatigue Experiences

Cooling Air Leakage Effects on Failure Mode. In the late 1950s, an unusual series of combustion turbine last row high-cycle fatigue incidents occurred. Fortunately, the cracked blades were discovered during normal inspections. One outstanding

Downloaded 02 Jun 2010 to 171.66.16.112. Redistribution subject to ASME license or copyright; see http://www.asme.org/terms/Terms_Use.cfm

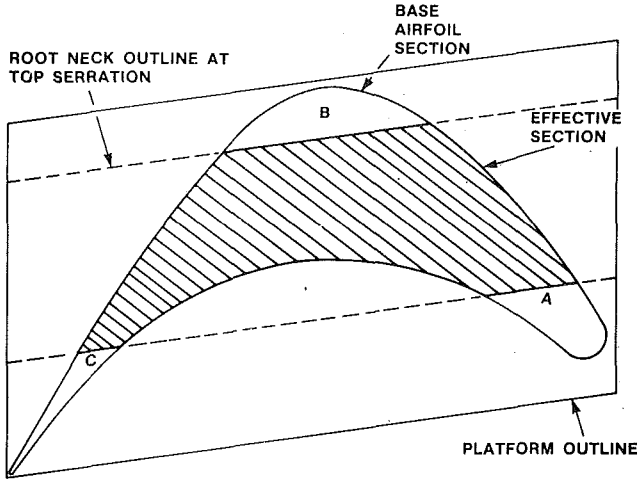


Fig. 7 Blade transfer area, airfoil to root neck

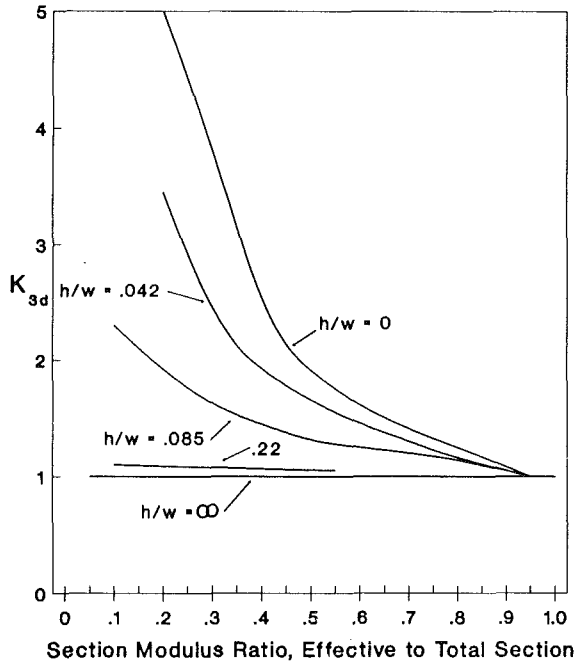


Fig. 8 Three-dimensional factor of bending stress concentration from photoelastic tests

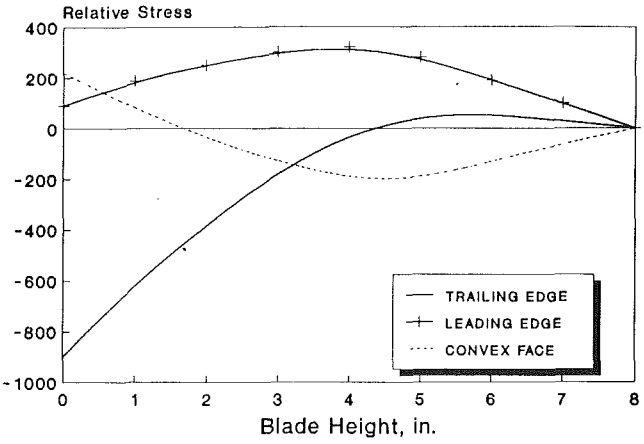


Fig. 9 Relative vibratory stress in the axial or stiff mode

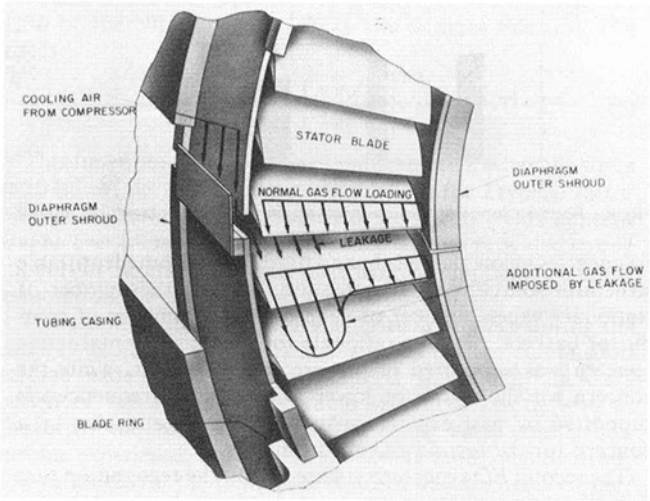


Fig. 10 Visualization of additional gas flow imposed on blades by horizontal joint leakage

characteristic of these incidents was the location of the high-cycle fatigue crack, which was at the trailing edge concave side under the blade platform. All previous blade incidents had resulted in crack initiations on the convex side or the leading edge of the blade, well inside the blade platform ends. Sampson (1953) performed fundamental three-dimensional photoelastic studies at the Westinghouse Corporate R&D Center and established the effects of transferring a centrifugal load from an airfoil shape to the rectangular shape of a root attachment. Three locations of high stress concentration were identified, as shown in Fig. 7, as A, B, and C. Past experience and analytical results for the fundamental mode were associated with location A or B, and no prior history supported location C. The levels of centrifugal peak stress at the three locations are very similar and can be represented by the curves in Fig. 8, where the ratio of the three to the two-dimensional stress concentration is related to the ratio of the effective base section to the neck section moment of inertia (with the ratio of platform thickness to width ratio (h/w) as a matrix parameter). Blade designs in the next engine design period (1960s) incorporated root "necks"or extensions to eliminate this three-dimensional effect.

Since the first mode was eliminated as a cause of failure because of the origin of the fatigue cracking, the next highest mode (the axial or stiff mode) was investigated. A plot of the relative second mode bending stress, as shown in Fig. 9, clearly identifies that this mode has a maximum stress at the trailing edge concave side that would support cracking at this location. Full-scale fatigue tests performed in the laboratory, using shaker and drive rods, confirmed the fatigue crack origin for the stiff mode. Furthermore, a review of frequency calculations and tests confirmed that this mode could be in resonance at running speed, since it was a variable speed machine designed by the requirements in Fig. 4. However, the design criteria were based on experiences with the fundamental mode, not the second or stiff bending mode. Determining the source of the excitation centered on external sources since internal sources were expected to excite the fundamental mode.

The *EO* frequency for the suspect mode was equal to 10 or 12, depending on the operating speed. Since this frequency range supported the second *EO* syndrome, as discussed earlier, the horizontal joint area became suspect. An investigation of the seal design revealed a high potential for excessive leakage of high pressure cooling air, as shown in Fig. 10. Improving the seal design completely eleminated this problem. The major benefit of this study is that when the source of the excitation is external to the flow path, modes other than the fundamental can become highly responsive. Also, the effects of the three-dimensional stress concentration on the location of crack ini-

Downloaded 02 Jun 2010 to 171.66.16.112. Redistribution subject to ASME license or copyright; see http://www.asme.org/terms/Terms_Use.cfm

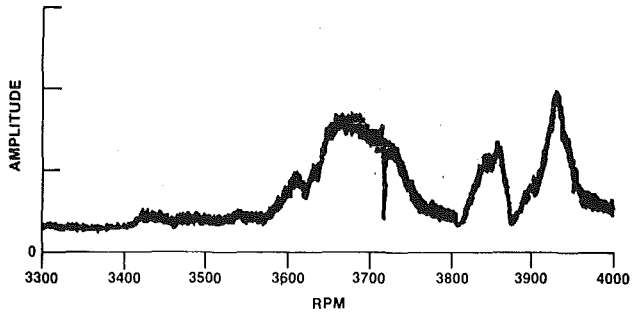


Fig. 11 Typical telemetry strain gage signal showing seal pin effects

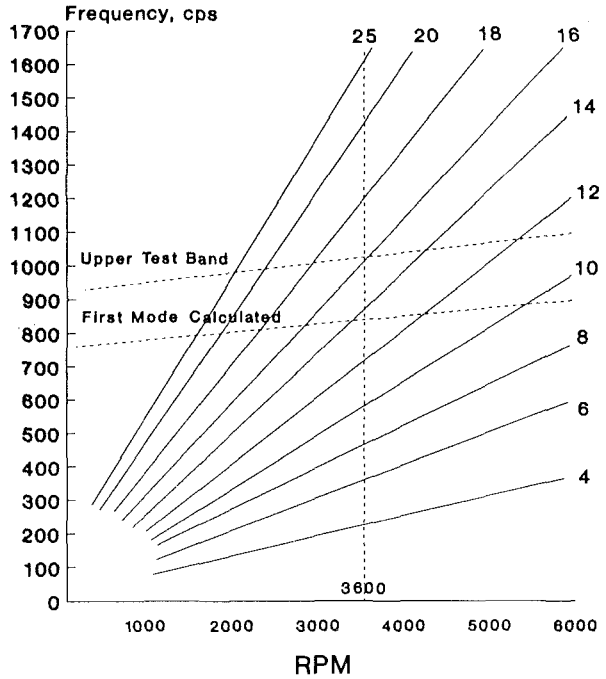


Fig. 12 *Calculated and telemetry strain gage test band frequencies of first mode*

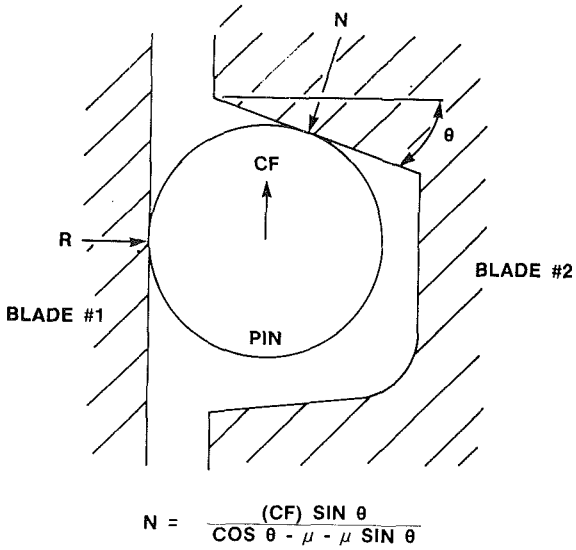


Fig. 13 Blade seal pin system, looking with flow

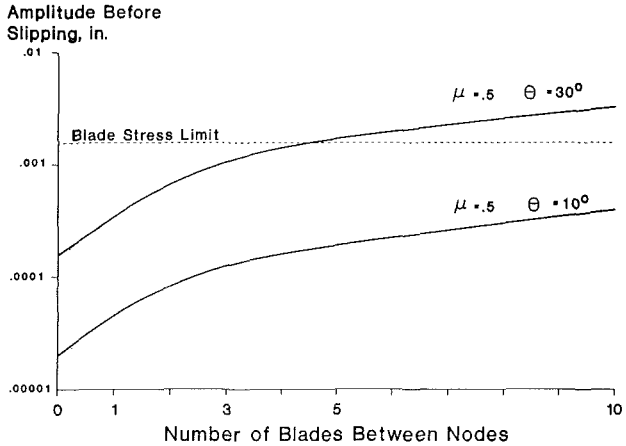


Fig. 14 Vibration amplitude/stress as related to blades between nodes and pin angle

tiation emphasized the need for "neck extensions" for future designs. In addition, the potential for second harmonic vibration effects also supported the need for improved cylinders and stationary vane designs. All of these improvements were incorporated in the new turbine designs of the 1960s.

Seal Pin Effects on Failure Mode. A high-cycle fatigue failure of a row 1 turbine blade was experienced early in 1970. The location of the fatigue crack initiation coincided with the fundamental mode, i.e., on the convex side. Initiation at the base of the airfoil, instead of under the platform, was supported by an additional stress riser due to foreign object damage prior to failure, and by the incorporation of the "extended neck, thick platform" approach implemented on all designs after 1965. All evidence pointed to a simple first mode failure; however, the first mode was detuned from first mode resonance with *EO* frequencies of all engine structures such as the 16 combustor baskets and the frequency was confirmed by a rotating strain gage test. Since the blade was above the eighth *EO* the design criteria did not require it to be tuned away from all higher *EO* frequencies. Obviously, one conclusion would have been that the eighth *EO* criterion was flawed and the problem was a simple first mode resonance. From Fig. 12, this would imply resonance at probably an *EO* of 12 or 14.

The investigation proceeded on four fronts: First, the customer was requested to avoid part-load operation that could result in a 16th *EO* resonance that coincided with the number of combustor baskets; second, a blade modification to reduce blade frequency, in view of the 16th *EO* concern, was initiated; third, the blade frequency was investigated using conventional shaker methods and holographic techniques at the Westinghouse Corporate R&D Center; fourth, the rotating strain gage magnetic tapes were reviewed using sophisticated filtering and plotting equipment, which was not available during the rotating test.

The review of the magnetic tapes revealed startling results as shown in Fig. 11. A multiplicity of first mode resonance points was found, resulting in the array of frequencies with the band width as shown in Fig. 12. In contrast with this, shaker tests and the holographic investigation revealed only a single well-defined fundamental mode frequency that verified the blade frequency calculations. Obviously, a coupling mechanism was present in the blade system that provided cross talk between blades in order for this to result in a multiplicity of resonance conditions that raised the frequency to coincide with the 16 *EO* forcing function resulting from the number of combustor baskets. After an extensive review, the seal pin system shown in Fig. 13 was selected as the most logical source of the blade coupling mechanism. The reaction at N is always larger than at R; therefore, assuming friction coefficients equal, the pin will slip at R first and point "N" becomes the instantaneous center for plane motion. High-temperature friction studies indicated that a coefficient of 0.5 or higher can be realized. Assuming a μ of 0.5 results in a force ratio of 4.5 and an R

Downloaded 02 Jun 2010 to 171.66.16.112. Redistribution subject to ASME license or copyright; see http://www.asme.org/terms/Terms_Use.cfm

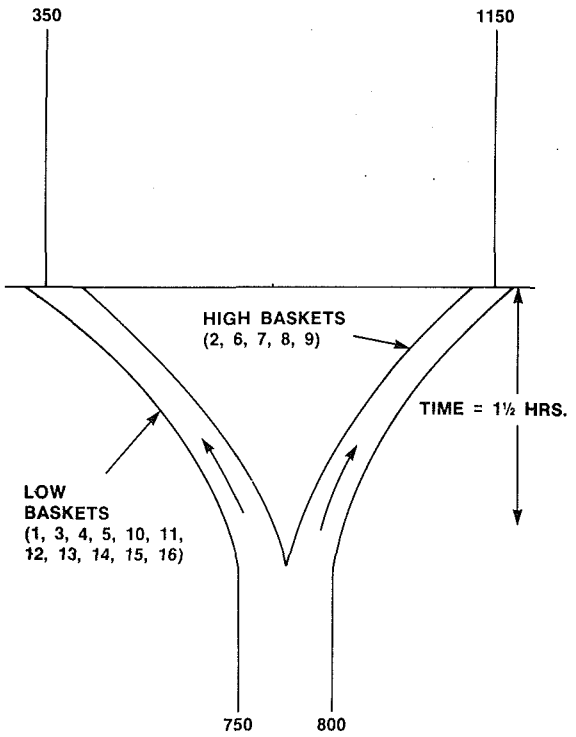


Fig. 15 Exhaust blade path temperature readings prior to blade failure

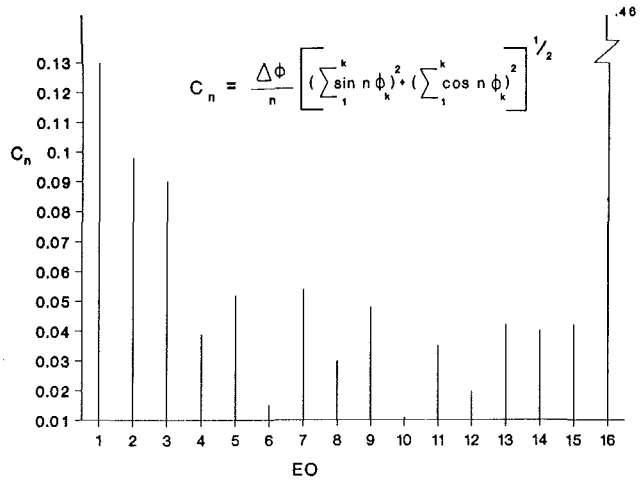


Fig. 16 Fourier coefficients for clogged fuel nozzles

force of 1350 pounds since the centrifugal force of the pin is 300 pounds.

Having defined the pin mechanics, the basic question of how this affected blade frequency remained to be answered. Assuming that the elastic connection between blades was tangential compression of pin and blade platform, yielded a frequency spectrum comparable to the strain gage test band shown in Fig. 12. The solution was simply to reduce the contact surface angle to reduce the friction force, thus eliminating the potential for resonance and also reducing the stress in the blade before slippage occurs. A change from 30 to 10 deg resulted in an order of magnitude reduction to a value below the blade stress limit as shown in Fig. 14.

Combustion System Effects on Failure Mode. First mode resonance with *EO* frequencies below the eighth is not permitted by the design criteria that have been in place for over 35 years. However, when the exciting force is very severe, even detuned blades may experience significant vibratory stresses.

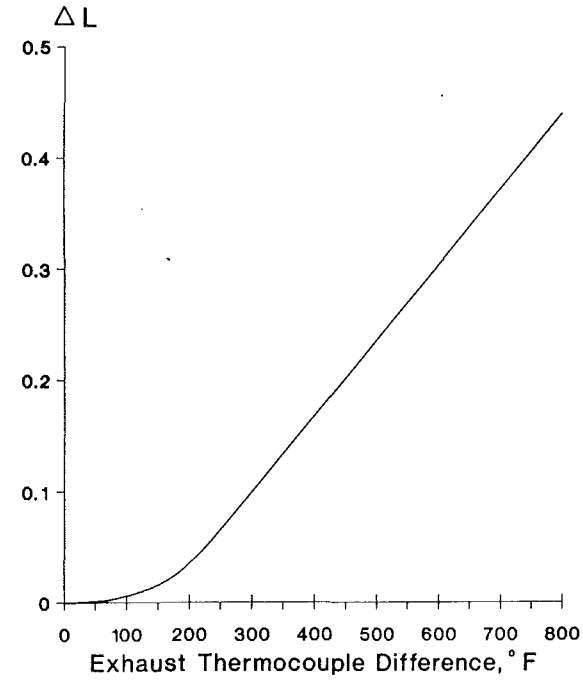


Fig. 17 Periodic blade load factor as a function of exhaust thermocouple difference

Also, margin from resonance can be reduced by the effects of allowable speed variation, manufacturing tolerances, part-load operation, and root fixity. In this incident, the subject blade was detuned above the third *EO* and had been in operation for over five years in over six turbines with no signs of distress. (Since the incident, the six turbines continued to use the original blade and have accumulated over 100,000 hours of operation on each unit.) However, after only 1640 hours on a similar unit, a high-cycle fatigue failure was experienced.

A review of operating data indicated that a severe excursion in blade path thermocouple readings had taken place prior to the failure as shown in Fig. 15. These thermocouples, used for the first time, were intended to monitor the health of the combustors. Since there was no prior operating experience, no control limit was selected; hence, no immediate action was taken other than scheduling a shutdown to clean nozzles.

It was concluded that the severe temperature maldistribution was the source of blade excitation. Since the pulse width was not insignificant, the computer program based on Eqs. (6), (7), and (8), were utilized to determine the Fourier coefficient, A trapezoidal shape was assumed for the pulse with the center being 50 percent of the width. Fourier coefficients are shown in Fig. 16 with the third *EO* value being 0.09. A parametric study of 16 equally spaced pulses indicated that the potential for higher Fourier coefficients was possible. For instance, three high pulses arranged selectively in the 16 array produce a Fourier coefficient of 0.26, and when nine of 16 are arranged selectively, a value of 0.45 is obtained. These high potentials will be utilized in later sections to define an allowable blade path temperature spread.

The vibratory stress developed in the blade was approximated using the response analysis of a uniform cantilever beam. Therefore, it can be shown that the vibratory stress can then be defined by:

$$\sigma_{\text{vib}} = \left(\frac{0.895\pi}{\delta}\right) c_n(\Delta L)\sigma_b K \tag{13}$$

Since the turbine exhaust temperature pattern is periodic with a clogged nozzle system, it follows that the aerodynamic loading will also be periodic. Results, shown in Fig. 17, indicate that the load fraction for 800°F is 0.44, and for 400°F it is

Downloaded 02 Jun 2010 to 171.66.16.112. Redistribution subject to ASME license or copyright; see http://www.asme.org/terms/Terms_Use.cfm

0.12. Assuming a log decrement of 0.5 percent for Inconel X material, 4800 psi for σ_b, 0.12 for a periodic load factor, 1.25 for K, and 0.09 for c_n, the blade vibratory stress calculates to be about 37 KSI. Using material test data, this vibratory stress would cause fatigue crack initiation in about 10^6 cycles at a steady stress of 35 KSI. If the blade was vibrating for 1.5 hours at a frequency of 200 Hz, the blade would experience 1.08 $\times$ 10^6 cycles, which agrees well with the preceding approximate analysis.

In order to prevent future incidents of turbine blade fatigue resulting from combustion system temperature maldistribution, a maximum allowable blade path temperature spread had to be defined. Assuming a material endurance of 27.5 KSI and a worst case scenario for the 16 array third harmonic Fourier coefficient of 0.45 as previously discussed, the maximum allowable periodic load fraction calculates to be 0.0175 using Eq. (13). As seen in Fig. 17, this equates to a blade path temperature spread allowable of 150°F. Since this allowable is a function of gas bending stress, it follows that the value must be determined for each turbine. The current procedure in force for the subject blade is to alarm at a spread of 100°F and unload at 150°F with an immediate trip set at 200°F. Since incorporating limits on blade path temperature spread, no recurrence of blade fatigue related to combustion system temperature maldistribution has been experienced.

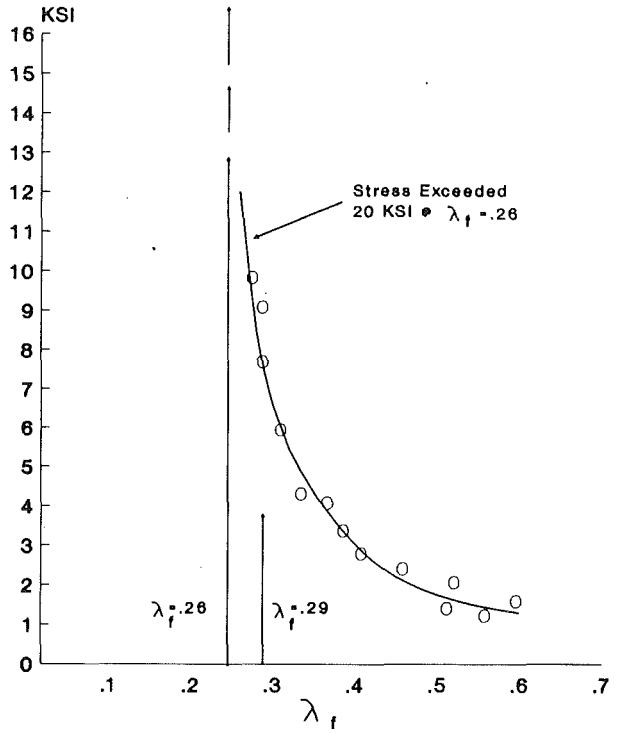


Fig. 18 Telemetry strain gage data of first mode vibratory stress

Flow-Induced Nonsynchronous Vibration. No problems related to flow-induced nonsynchronous vibration were experienced in combustion turbines for over a 30-year period from the early 1950s. However, in the early 1980s, three incidents were confirmed to be caused by this phenomenon. In all three cases, the blades were designed to satisfy the criteria established in the mid-1960s; i.e., first bending mode detuned when below the eighth *EO*, detuning of known structural *EO* frequencies required, *MF* over 3.00, as well as frequency parameters of over 1.6 for torsion and over 0.30 for first flexure. High-load buffeting, rather than stalled flutter, was confirmed to be the root cause for all three blade problems. In all three cases, operating changes such as mass flow and/or load limits were completely successful as temporary solutions, while final solutions were to raise the fundamental frequency while maintaining detuning against *EO* frequencies. All three incidents will be discussed as well as the successful corrective actions and a selected method of correlating design parameters via a useful parameter for future designs.

The first aeroelastic experience was encountered on the last row of a four stage turbine. Scalzo et al. (1986) completely describe the analyses and solution, while Gabriel and Donato (1986) describe the telemetry strain gage field program that confirmed the buffeting phenomenon and verified the new blade. (Additional data will be presented here that provide a suitable basis for correlation with the other incidents.) Although the design criteria were based on a flexural reduced frequency of 0.30, the effect of operating at low ambients was not part of the design process. In addition, the later addition of steam injection for power augmentation as well as operation at peak firing temperature further exacerbated the problem. The total effect of these added factors reduced the frequency parameter to the failure point. Results from the telemetry rotating strain gage test are shown in Fig. 18. At a reduced frequency value of 0.26, the buffeting stress in the first bending mode increased very rapidly and exceeded 20 KSI. A value of 0.292 was selected as a temporary safe limit until the blades were replaced with a new design. This value was maintained by use of the inlet guide vanes to limit mass flow. Replacement blades were designed by increasing first mode frequency to 198 Hz, resulting in a minimum λ_f of 0.35 under the most severe operating conditions.

The second incident occurred on the last row of a three-stage turbine as reported by O'Neil (1989). There are many similarities with the row 4 problem in addition to being designed to the same criteria. These are: Many blades contained high-cycle fatigue cracks and both had the first bending mode detuned below the third *EO*. In the row 3 last row blade, fatigue cracks were found during a normal inspection. Again, the scenario of high flow at low ambients was involved together with the effects of an evaporative cooler. Combining all these factors, the flexural frequency parameter was reduced from 0.36 to 0.31 at the time of the incident. The time of the incident was deduced by reviewing the recent operating history of the unit and revealed operation at a low of 50°F. To maintain a λ_f of 0.36, a load limit of 40.5 MW was imposed until the blades were replaced with higher frequency blades. The replacement blades were detuned above the third *EO* at 304 Hz and the λ_f was increased to 0.42 under the most severe operating conditions.

The third incident of nonsynchronous vibration was experienced with row 3 of a four-stage turbine. As with the first two blades, failure was related to operation at high loads. However, in this case, the reduced frequency was at a high level of 0.46 and reduced to 0.44 at time of failure by the effects of ambient, water injection for NO_X control, and operation at peak firing temperature. Restricting load to 12 percent above normal base maintained a λ_f of 0.48, and prevented further incidents until a replacement blade was available. A replacement blade was designed with the first mode increased to 333 Hz, resulting in a λ_f of 0.55 under the most severe operating conditions.

The three experiences with flow-induced nonsynchronous vibration clearly indicate that a simple constant value for frequency parameter is not adequate for turbine blades subjected to high load buffeting. Correlating blades on the basis of flow turning angle, for the upper 10 percent of the airfoil, was selected as the governing parameter together with the flexural frequency parameter. Results, shown in Fig. 19, present the three failures as a function of flow turning in the top 10 percent of the blade. Also, a proposed design curve is shown related to the three redesigned blades.

Downloaded 02 Jun 2010 to 171.66.16.112. Redistribution subject to ASME license or copyright; see http://www.asme.org/terms/Terms_Use.cfm

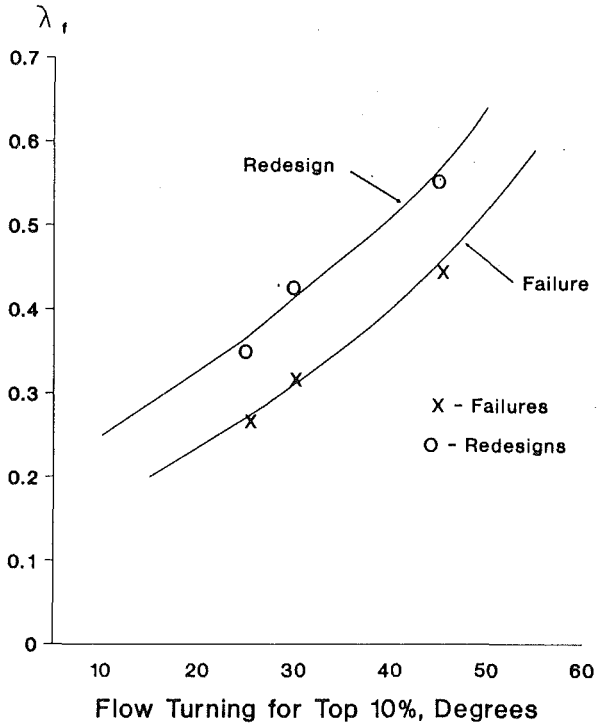


Fig. 19 Flexural frequency parameter related to flow turning

Summary and Conclusions

Advances in technology are usually made when new phenomena are encountered that require modifications to the design criteria in order to prevent recurrences. This usually occurs when a design extends beyond past experiences but is within constraints of existing criteria. It should also be emphasized that despite the high level of sophistication available in current computer codes, such as response analyses, experimental data are still required to estimate absolute values of vibratory stress. The fundamental concept of *MF* is sound since experience and analyses have definitely established that the first bending mode, upon which *MF* is based, is the most responsive mode, provided that the source of the excitation is contained within the flow stream. Originally, the concept of allowable magnification factor was developed from experience based on operation in resonance for variable speed turbines. This concept has evolved to be used for detuned blades and essentially provides sufficient strength to permit startup and shutdown capability. Therefore, the value of 3.0 has been verified to adequately provide this capability. Also, the normalized second *EO* syndrome trend approximates the original combustion turbine *MF* curve and lends credence to the curve, paticularly since the old structural designs tended to produce second *EO* forcing functions. Current designs use inner cylinders or blade rings, together with segmented stationary blading that tends to eliminate this concern and gives further support for the constant *MF* criteria.

The detuning criteria for first modes below the eighth *EO* as well as detuning principle modes from structural *EO* frequencies have stood the test of time. In over 35 years of combustion turbine experience, the only failure that was not due to the first mode resulted from an external excitation source; i.e., high-pressure leakage at the horizontal joint. In addition, in spite of the broad spectrum of excitation frequencies present in a combustion system, the only mode that has been excited is the fundamental bending mode. Response analyses have also confirmed that the first bending mode is an order of magnitude more responsive than higher modes.

Reviewing the aeroelastic or flow-induced nonsynchronous experiences indicates that the basic solution in all cases is simply to "make the blade stronger." Therefore, the 10 percent rule together with the detuning of the fundamental bending mode would have prevented all three problems but resulted in noncompetitive designs and still may not prevent future failures. Therefore, a more direct approach to flow-induced nonsynchronous vibration is required to provide design optimization with no loss in reliability. Clearly, a constant value of frequency parameter has been shown to be inadequate; therefore, designing as a function of flow turning improves the design criteria. Future computer codes (Aoki et al., 1991), correlated with dynamic cascade data (Kovats, 1979), together with engine operating experience will be used to provide future improvements in the design criteria to prevent flow-induced nonsynchronous blade failures.

Acknowledgments

Advances in technology in any organization are a summation of inputs from many participants over many years. In recognition of this, the author would like to acknowledge the dedicated support of the following engineering colleagues: James M. Allen, Richard J. Antos, William H. Dickson, Frank K. Gabriel, Lee D. McLaurin, Albert J. Partington, and Fred Sosa.

References

Aoki, S., Sato, T., Scalzo, A., Kovats, Z., and Namba, M., 1991, "Flutter Prevention of a Long Free-Standing Blade of a Large Industrial Gas Turbine," presented at the ASME Turbo Expo—Land, Sea, and Air, Orlando, FL.

Armstrong, A., and Stevenson, R. E., 1960, "Some Practical Aspects of Compressor Blade Vibration," *Journal of the Royal Aeronautical Society*, Vol. 64, No. 591, pp. 117–130.

Gabriel, F. K., and Donato, V., 1986, "Telemetry Measurement of Combustion Turbine Blade Vibration in a High Temperature Environment," ASME Paper No. 86-GT-207.

Kovats, Z., 1979, "Dynamic Cascade Facility and Methods for Investigating Flow-Excited Vibration and Aerodynamic Damping of Model Law Pressure Blade Groups," ASME Paper No. 79-WA/GT-6.

O'Neil, S. T., 1989, "Operating Experience With a 42.5 MW Gas Turbine Used in a Cogeneration Plant at a Paper Mill in the U.S.," ASME Paper No. 89-GT-197.

Partington, A. J., 1957, "Harmonic Analysis of Strut Excitation," Westinghouse Electric Corporation Internal Report, Orlando, FL.

Sampson, R. C., 1953, "Design Data From Photoelastic Tests of Turbine Blade Roots," Westinghouse Research Development Center Report, Orlando, FL.

Scalzo, A. J., Allen, J. M., and Antos, R. J., 1986, "Analysis and Solution of a Nonsynchronous Vibration Problem in the Last Row Turbine Blade of a Large Industrial Combustion Turbine," ASME JOURNAL OF ENGINEERING FOR GAS TURBINES AND POWER, Vol. 108, pp. 591–598.

Trumpler, W. E., Jr., and Owens, H. M., 1953, "Turbine-Blade Vibration and Strength," ASME Paper NO53-A-98.

Downloaded 02 Jun 2010 to 171.66.16.112. Redistribution subject to ASME license or copyright; see http://www.asme.org/terms/Terms_Use.cfm

Analysis of Cracked Gas Turbine Blades

H. L. Bernstein
Southwest Research Institute,
Materials and Mechanics Department,
San Antonio, TX 78228

J. M. Allen
Electric Power Research Institute,
Combustion Turbines Program,
Palo Alto, CA 94303

Results from an analysis of cracked first-stage blades (or buckets) from two General Electric MS7001E industrial/electric utility gas turbines are presented. Numerous cracks were observed along the leading-edge and midchord regions of the pressure and suction surfaces. In one unit cracks were found after 874 start-stop cycles, which included 218 trips from load and 11,000 service hours. Buckets in the sister engine were examined after 1800 cycles, which included 218 trips from load and 24,000 service hours. In both cases, cracks initiated in the platinum aluminide coating and propagated into the IN-738LC base metal. For the 11,000-hour bucket, 20-mil (0.5-mm) deep cracks were observed, and for the 24,000-hour bucket, the leading edge cracks had grown to the leading edge cooling hole, a distance of 0.2 in. (5 mm). The number of cycles to crack initiation was in good agreement with thermal mechanical fatigue (TMF) predictions from the REMLIF computer program, which is part of the Electric Power Research Institute's (EPRI) Life Management System. The cracking was greatly accelerated by the large number of trips experienced. The extensive crack propagation that occurred is thought to have been strongly assisted by oxygen and sulfur penetration along the grain boundaries. The coating on the leading edge degraded from the original platinum-aluminide plus beta phases to a gamma prime phase after 24,000 hours of service, but it was still protective except where it was cracked. Where the coating was cracked, environmental attack of the interdiffusion zone and base metal occurred, resulting in spallation of the coating and preferential grain boundary attack. Operating and maintenance considerations for optimizing bucket life in demanding cyclic duty environments are also discussed.

Introduction

Gas turbines used for electric utility peak load power generation are subjected to frequent startups and shutdowns. Starting and stopping subjects turbine blades (or buckets) to thermal stress cycling, which can cause thermal mechanical fatigue (TMF). The number of start-stop cycles required to initiate fatigue cracking depends on the severity of the cycling and the fatigue properties of the material, which in turn depends on the details of the TMF cycle and service exposure.

The most demanding cyclic duty with regard to turbine bucket TMF life is high service factor peak load generation, sometimes called intermediate operation. This is a common mode of operation in utility combined-cycle plants. In these circumstances, turbines are not only subjected to frequent starting and stopping, perhaps 300 times per year, but also to a large number of hours, on the order of 3000 hours per year. In contrast, a simple cycle peaking unit typically will have fewer starts and will operate for less than 1000 hours per year. Thus, in utility combined-cycle units, the buckets are subject to greater time-dependent effects on cyclic life than they are in simple cycle peaking turbines.

In this paper, a metallurgical analysis of extensively cracked first-stage turbine buckets from two dual-fueled (natural gas and distillate oil) General Electric MS7001E (Frame 7E) units in combined cycle peaking service is presented. Thermal mechanical fatigue (TMF) crack initiation life predictions are also presented and the results compared with the field data. The propagation of these cracks into the bucket substrate material, and the possible role of environment (oxygen and sulfur) in assisting this crack growth are qualitatively assessed.

An operation and maintenance (O&M) strategy for optimizing TMF life of buckets operating in this kind of environment is also suggested.

Background

Two General Electric MS7001E gas turbines operating in intermediate load duty at the same generating site have been specially monitored since 1984 under the Electric Power Research Institute's (EPRI) Life Management System (LMS) Project [1]. The turbine control parameters of exhaust temperature and compressor discharge pressure were automatically recorded every minute, as was compressor discharge temperature. The number of startups/shutdowns and type (normal start, fast start, normal shutdown, trip from load, etc.) were also monitored. The purpose of recording these data was to input the detailed operating history to a computer program called REMLIF [1] for computing the amount of bucket creep and TMF life that has been consumed based on actual engine operation, and to compare and calibrate these predictions with inspection results. (In addition to the first-stage buckets, the REMLIF program computes the life of the first-stage nozzle.)

Contributed by the International Gas Turbine Institute and presented at the 36th International Gas Turbine and Aeroengine Congress and Exposition, Orlando, Florida, June 3-6, 1991. Manuscript received at ASME Headquarters January 25, 1991. Paper No. 91-GT-16. Associate Editor: L. A. Riekert.

Copyright © 1992 by ASME
Downloaded 02 Jun 2010 to 171.66.16.112. Redistribution subject to ASME license or copyright; see http://www.asme.org/terms/Terms_Use.cfm

The first-stage buckets were replaced during a recent overhaul of one of these units after 1800 start/stop cycles and 24,000 hours of operation. Of the 1800 shutdowns experienced, 218 were tripouts from load. As stated above, the unit has dual-fuel capability, and was operated on both natural gas, the primary fuel, and on distillate oil during winter months when natural gas was in short supply. Steam injection was used for NO_x control. The buckets were scrapped because of extensive cracking that initiated in the protective coating and which propagated well into the bucket base metal. One of the retired buckets was nondestructively and destructively evaluated to determine the extent and nature of the cracking.

A bucket from a sister engine was removed after 874 start–stop cycles and 11,000 hours of operation. Of the 874 shutdowns, 217 of them were trips from load. Portions of this bucket were made available for examination. The results of the examination of these two buckets are the primary focus of this paper.

The bucket material was IN-738LC with a nominal chemical composition (in wt %) of 16 Cr, 8.5 Co, 2.6 W, 1.7 Mo, 3.4 Ti, 3.4 Al, 0.9 Cb, 0.10 C, 0.01 B, 1.7 Ta, 0.10 Zr, and balance Ni. The buckets were coated with a platinum aluminide (Pt–Al) pack diffusion coating. The final heat treatment of the buckets is in two steps: (1) solution treatment at 2050°F (1120°C) in vacuum for two hours, and (2) an aging treatment of 1550°F (845°C) in vacuum for 24 hours.

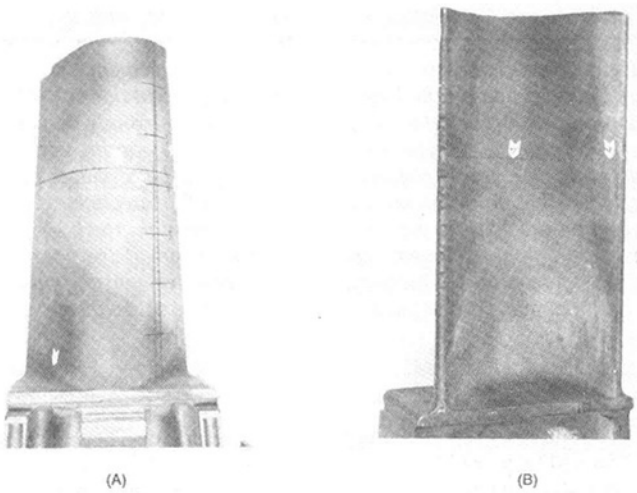


Fig. 1 24,000-hour bucket as received and marked for sectioning: (A) suction side, (B) pressure side; marks are in 1-in. (25 mm) increments; arrows are specimen locations

Metallurgical Analysis

A 24,000-hour bucket was obtained before any cleaning was performed. Portions of an uncleaned 11,000-hour bucket from the sister engine also were available. The majority of this airfoil was missing except for the leading edge, the top 25 percent, and the bottom 10 percent joining the platform.

The 24,000-hour bucket was sectioned at a distance of 4.2 in. (107 mm) from the platform, which is 60 percent of the bucket height and in the middle of the hottest area of the bucket as indicated by the oxidation patterns. A section of the 11,000-hour bucket was taken at 5.4 in. (137 mm) from the platform because of the lack of other bucket material. This section is at 78 percent of the bucket height and is in a region of less oxidation attack because of a lower temperature. (The operating temperature of a bucket is graded from cooler at the platform to maximum temperature at about 60 percent height to cooler at the tip.) These sections are shown in Fig. 1, on the as-received 24,000-hour bucket, which is marked for specimen removal.

In addition to the above sections, sections were made at 0.2 in. (5.0 mm) above the platform on the suction side between the third and fourth cooling holes from the trailing edge, as shown by the lower marker in Fig. 1. This section was made in order to obtain a condition of the coating as close to the original coating as possible. This is an area of low temperature, an area unlikely to be affected by foreign object damage, and an area less likely to have significant deposits that could cause hot corrosion.

Prior to sectioning the specimens, the surface was coated with an electroless nickel plating. The metallurgical sections were examined in a light, optical microscope and a scanning electron microscope. Specimens were examined unetched, etched with Kallings #2, and etched with a lactic acid etch (50 percent lactic acid, 30 percent nitric acid, 2 percent HF, 18 percent distilled water).

The metallurgical condition of the base metal was a normal, cast, dendritic structure. Gross coarsening of the gamma prime particles, indicative of overheating, was not observed. Consequently, this study focused on the fatigue cracking and coating degradation.

Macroscopic Examination. Overview photographs of the subject first-stage bucket from the unit with 24,000 hours operation are shown in Figs. 1(*a*) and 1(*b*). Multiple TMF cracks from approximately 25 to 80 percent of the leading edge (as measured from the platform) can be seen in Fig. 1(*b*). Figure 2(*a*) shows how these cracks have opened up due to corrosion and erosion. Some of these cracks propagated all the way to

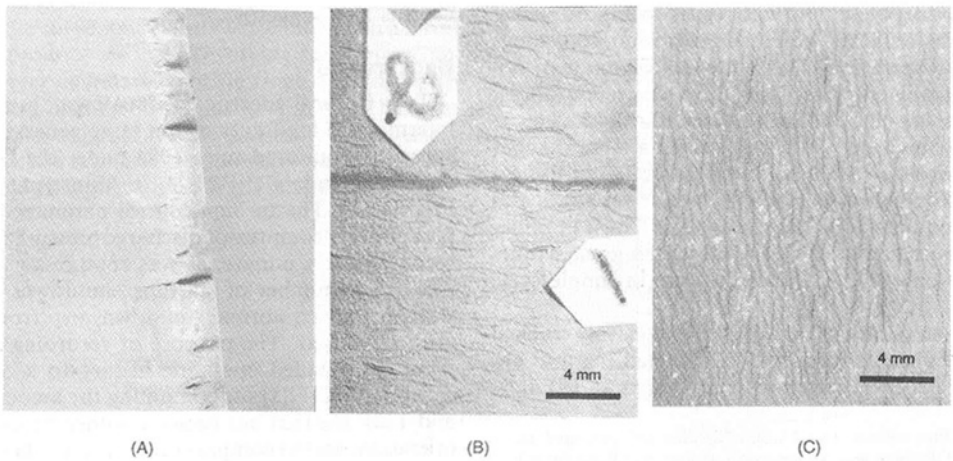


Fig. 2 24,000-hour bucket: (A) leading edge, (B) suction side, (C) pressure side

Downloaded 02 Jun 2010 to 171.66.16.112. Redistribution subject to ASME license or copyright; see http://www.asme.org/terms/Terms_Use.cfm

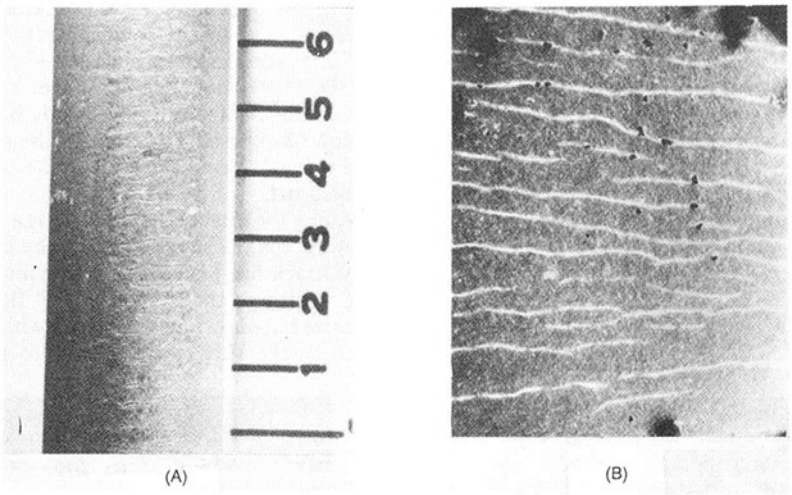


Fig. 3 11,000-hour bucket: (A) leading edge (scale in tenths of an inch), (B) suction side—replica

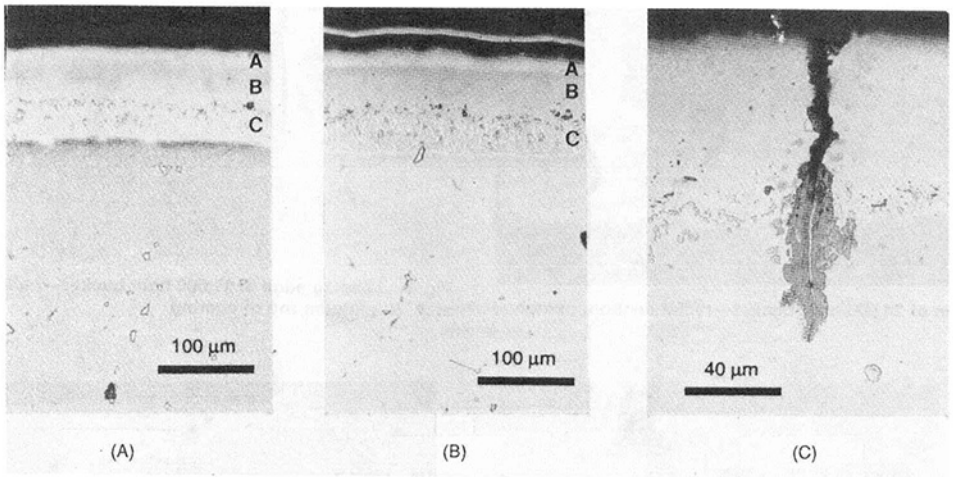


Fig. 4 Coating near platform: (A) 24,000-hour bucket, lactic acid, (B) 11,000-hour bucket, lactic acid, (C) 24,000-hour bucket with coating crack, unetched; A is the platinum-aluminide layer; B is the nickel-aluminide, or β layer; and C is the interdiffusion zone

the leading edge cooling hole, a distance of about 0.2 in. (5.0 mm).

Extensive cracking also occurred on the suction and pressure surfaces of the airfoil, as shown in Figs. 2(b) and 2(c). These cracks run predominantly in the transverse direction on the suction side, Fig. 2(b), and predominantly in the radial direction on the pressure side, Fig. 2(c). They also penetrate the blade coating and extend into the base metal by as much as 20 mils (0.5 mm).

The 11,000-hour bucket exhibited multiple coating cracks along the leading edge, as shown in Fig. 3(a). These cracks extended into the base metal by as much as 20 mils (0.5 mm). The suction surface also had multiple coating cracks as shown in Fig. 3(b).

Microscopic Examination. *Suction Side Near Platform and Trailing Edge.* A metallographic section was taken on the suction side of the airfoil toward the trailing edge and the platform. This section provided a sample of the coating as close to the original coating condition as possible. The condition of the 11,000-hour coating is shown in Fig. 4(a) and of the 24,000-hour coating in Fig. 4(b). Both coatings have a conventional, three-zone platinum-aluminide microstructure consisting of an outer $PtAl_2$ zone; a middle NiAl, or β, zone; and the inner, or interdiffusion, zone.

Both the 11,000 and 24,000-hour coatings exhibited radial cracking, as shown in Fig. 4(c) for the 24,000-hour bucket. These cracks were attacked by the environment and were beginning to penetrate into the base metal.

Leading Edge. The 24,000-hour bucket exhibited extensive leading edge cracking, with cracks having penetrated through to the leading edge cooling hole, as shown in Fig. 5. This crack propagated in an intergranular manner, as shown in Figs. 5 and 6(a). The crack initiation features have been removed by the loss of material in the wedge area.

The coating on the leading edge, Fig. 6(b), was substantially degraded to a single γ' phase. In some places the coating was entirely missing, as shown in Fig. 5. Where the coating was missing, Fig. 6(c), a scale formed containing oxides primarily of nickel and aluminum, but also of Ti, Cr, Co, etc. Internal attack of the base metal by oxygen and nitrogen occurred beneath the oxide scale.

The chemical compositions of the high-temperature attack in the crack, Fig. 6(d), were determined by Energy Dispersive Spectroscopy (EDS). Oxides, nitrides, and sulfides were found in the corrosion product and base metal in the crack propagation region. Internal sulfides rich in titanium were found in the base metal near the crack faces, as shown in Fig. 6(d).

The 11,000-hour bucket exhibited extensive leading edge

Downloaded 02 Jun 2010 to 171.66.16.112. Redistribution subject to ASME license or copyright; see http://www.asme.org/terms/Terms_Use.cfm

cracking, with cracks having penetrated 20 mils (0.5 mm) into the base metal. A crack beginning to penetrate into the base metal along a grain boundary is shown in Fig. 7.

The coating has broken into a two-phase structure. The dark phase is the NiAl, β phase with platinum in solid solution. The light phase is gamma prime with platinum in solid solution.

Where the coating has been cracked, high-temperature attack has occurred. This attack is greater in the interdiffusion zone, which is not as resistant to attack as the coating or the base metal.

Suction Side. Extensive suction side cracking of the 24,000-hour bucket occurred as shown in Fig. 8(*a*), which has a straight crack of about 20 mils (0.5 mm) into the base metal. The crack faces and the base metal ahead of the crack tip have been attacked by the environment.

The coating is a two-phase, $\beta + \gamma'$ structure, similar to that of the 11,000-hour leading edge. More severe attack of the interdiffusion zone has occurred. It can be seen that the corrosion has caused a portion of the coating to be lifted up on one side of the crack, and on the other side the coating has spalled off.

Along the intact coating there is a nonuniform attack of the coating. On the suction side of the leading and trailing edges, this attack has penetrated to the interdiffusion zone.

Cracking of the suction side of the 11,000-hour bucket has occurred as shown in Fig. 8(*b*), which has a 7.5-mil (0.2-mm) deep crack. This crack appears to follow a grain boundary,

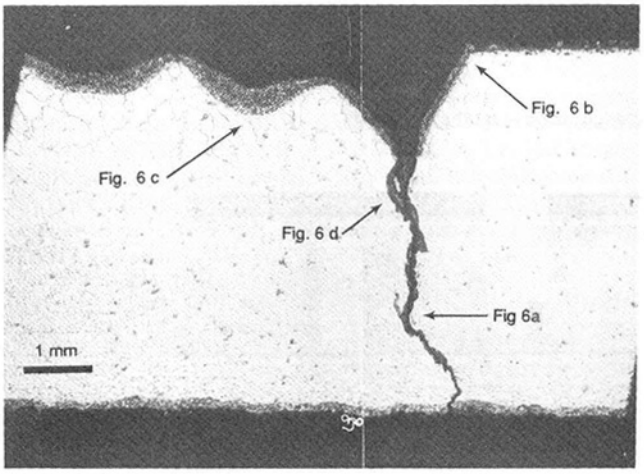


Fig. 5 Leading edge of 24,000-hour bucket—radial section, unetched

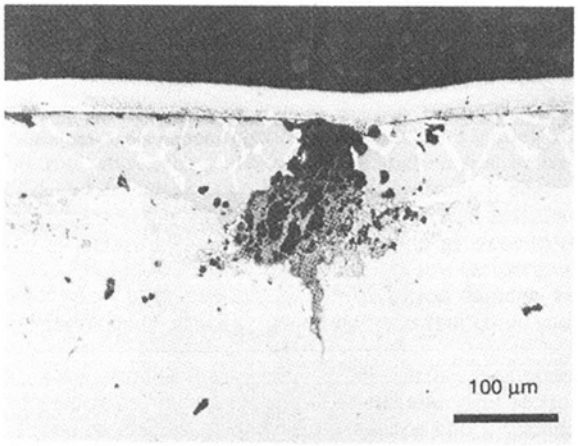


Fig. 7 Leading edge of 11,000-hour bucket—radial section, lactic acid etch, Ni plate on top of coating

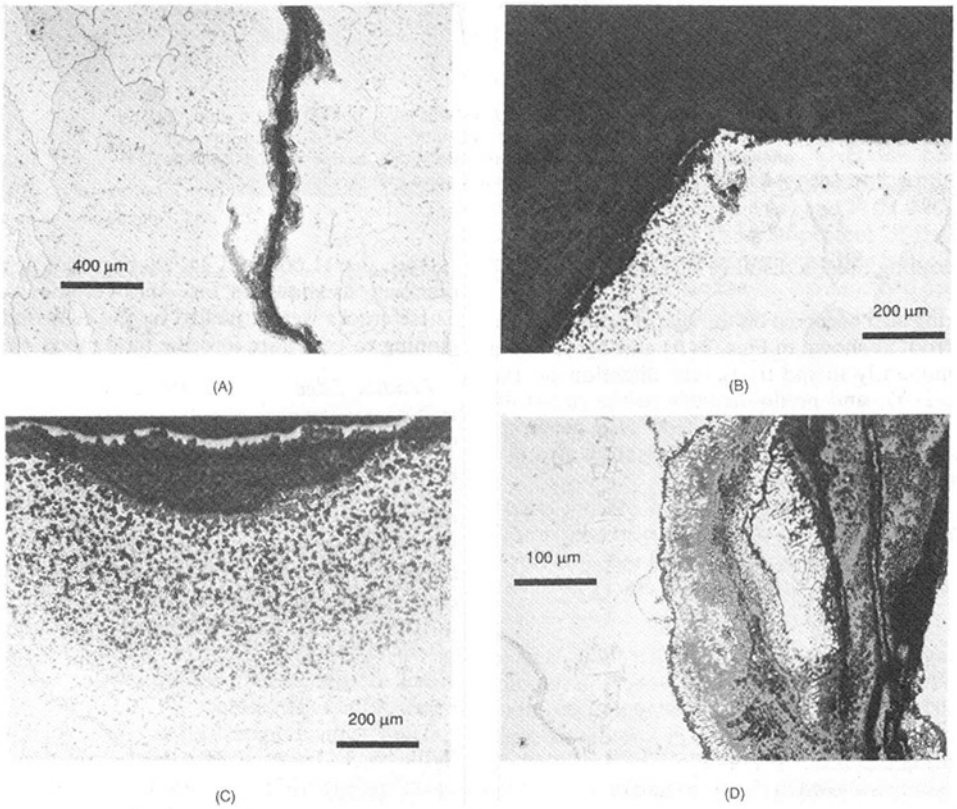


Fig. 6 Detailed views of leading edge crack in 24,000-hour bucket: (A) intergranular branch crack, (B) coating, (C) environmental attack at area of missing coating, (D) environmental attack in crack; (A), (B), (D) are Kallings #2, (C) is unetched

Downloaded 02 Jun 2010 to 171.66.16.112. Redistribution subject to ASME license or copyright; see http://www.asme.org/terms/Terms_Use.cfm

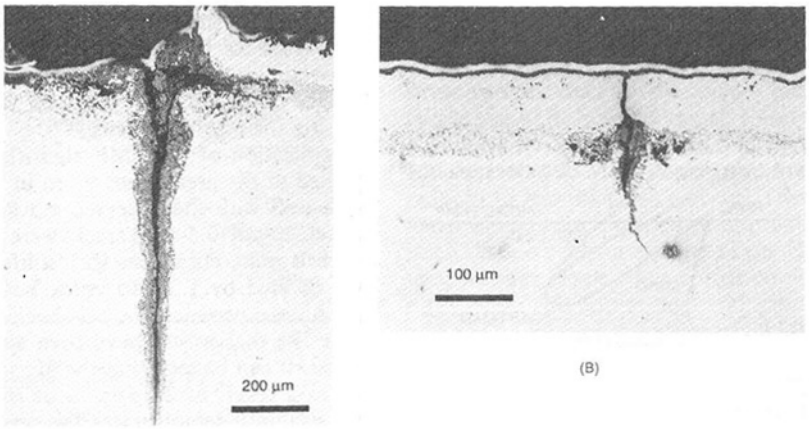


Fig. 8 Suction side cracks—radial sections: (A) 24,000-hour bucket, unetched, (B) 11,000-hour bucket, lactic acid etch, Ni-plate on top of coating

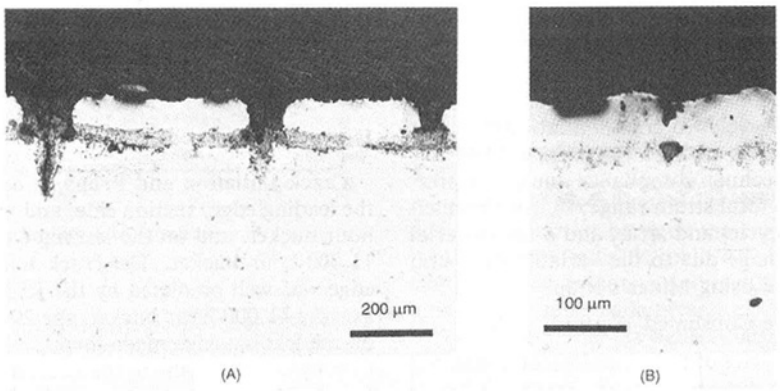


Fig. 9 Pressure side coating—transverse sections, lactic acid etch: (A) 24,000-hour bucket, (B) 11,000-hour bucket

which has been attacked environmentally ahead of the crack tip.

The coating of the 11,000-hour bucket is a single phase, (Ni, Pt) Al, or β. This phase forms during high-temperature operation when the $PtAl_2$ in the platinum-aluminide outer layer dissolves, and the outer and middle layers combine to form a single layer.

Pressure Side. The condition of the pressure side is similar to that of the suction side, except that the cracks are in the radial direction instead of the transverse direction. There is a biaxial stress state in the midchord region of the suction and pressure sides. The maximum principal stress during shutdown is in the radial direction on the suction side and in the chordwise direction on the pressure side. The maximum principal stress is thought to determine tensile cracking of brittle materials such as coatings [2]. These differences in direction of stress account for the different cracking patterns.

Extensive radial cracking occurred on the pressure side of the 24,000-hour bucket, as shown in Fig. 9(a), in which the cracks are straight and 20 mils (0.5 mm) deep.

The different stages in the development of a fatigue crack can be seen in Fig. 9(a). First, the coating cracks and is attacked by the environment. Second, the interdiffusion zone is attacked by the environment, and some base metal attack occurs. Third, a fatigue crack begins to form in the base metal, in the area that has been attacked. Fourth, the fatigue crack grows into the base metal, and the environment attacks the metal along and ahead of the crack.

The coating is in a two-phase, $\beta + \gamma'$ condition, similar to that of the suction side. Where the coating is cracked, extensive attack of the interdiffusion zone has occurred. This attack has caused spallation of some of the coating.

Similar to the suction side, the pressure side has areas where a nonuniform attack of the coating has occurred. This attack has penetrated to the interdiffusion zone on the pressure side in areas near the leading and trailing edges, and has almost reached this zone in Fig. 9(a).

The coating on the pressure side of the 11,000-hour bucket is in a single-phase, β, condition, as shown in Fig. 9(b), similar to that of the suction side of this bucket. Pressure side cracks were not found in the section examined, but base metal attack due to breaching of the coating was observed. (The breached coating was located above or below the plane examined.) Pressure side cracks may have been present in midheight sections of the airfoil.

Fatigue Analysis

The EPRI life management computer program REMLIF was used to calculate the life of the buckets. The REMLIF program is a Fortran PC code containing TMF algorithms and creep algorithms, which were developed by General Electric, to calculate life consumption based on actual engine operation [1]. The TMF algorithm relates the strain-temperature response from transient/steady-state heat conduction and generalized plane strain finite element stress analyses of the mean height airfoil section to TMF life as determined from laboratory specimens [3]. The strain-temperature response of the leading edge,

Downloaded 02 Jun 2010 to 171.66.16.112. Redistribution subject to ASME license or copyright; see http://www.asme.org/terms/Terms_Use.cfm

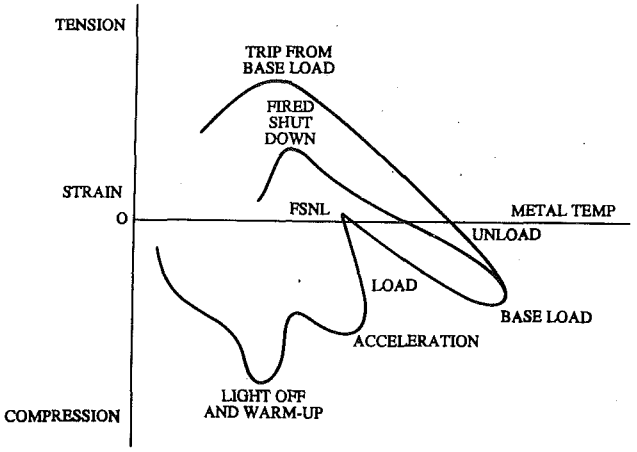


Fig. 10 Typical startup and shutdown strain-temperature profile of Frame 7E bucket leading edge (after [3])

the most responsive part of the bucket, is shown in Fig. 10 for various operating events. The TMF data were correlated and least-squares curve fitted by the equation:

$$N_f = A\,(\Delta\epsilon_t)^{\alpha}(\sigma_{\max})^{\beta} \qquad (1)$$

where: N_f is the number of cycles to crack initiation (number of cycles to a detectable drop in load range in a TMF test caused by an increase in specimen compliance due to the presence of a crack); $\Delta\epsilon_t$ is the total strain range; $\sigma_{\max}$ is the maximum tensile stress in the cycle; and A, α, and β are material constants. Cumulative damage due to the variable start-stop cycles incurred is computed using Miner's Rule:

$$\text{Percent Fatigue Life Consumed} = 100\,\Sigma\, n_i/N_i \qquad (2)$$

where: n_i is the number of cycles of type i, and N_i is the number of cycles to crack initiation for cycle type i.

A significant parameter governing cycles to failure in the TMF tests was found to be the maximum tensile stress [3]. This stress also has been found to be important to predict the isothermal, low-cycle fatigue life of other high-strength, low-ductility, nickel-base superalloys [4, 5]. This parameter is important because significant changes in mean stress occur when the specimen is held at peak tensile or compressive stress for as little as one minute [6]. This shift in mean stress must be accounted for in order to predict accurately the fatigue life. The maximum tensile stress is one method to account for the shift in mean stress. It should be noted that the maximum tensile stress is related to the strain range, since increasing the strain range increases the maximum tensile stress. The maximum tensile stress is also very important in determining coating cracking [2] and crack propagation after environmental attack has occurred.

As shown in Fig. 10, the maximum tensile stress, or strain, occurs on shutdown of the machine at temperatures well below 1000°F (537°C) and is much higher when the turbine is tripped out from full load than it is when the machine is shut down normally. During steady-state operation, the surface of the leading edge of the bucket is in compression due to thermal stress from the internal air cooling. The surface compressive stresses relax significantly during service because of the high surface versus bulk temperature of the bucket, thereby increasing the maximum tensile stress during shutdown.

Table 1 TMF life predictions, bucket leading edge

Operating History	Life Consumed	Life Consumed if No Trips
11,000 hours 874 starts 217 trips	129%	60%
24,000 hours 1,800 starts 218 trips	191%	123%

Application of the TMF algorithm to the subject buckets resulted in the predictions listed in Table 1.[1] The predictions agree well with the observed cracking. For the 11,000-hour bucket, 20-mil (0.5-mm) cracks were found on the leading edge, which is quite consistent with a life prediction of 677 cycles (874 divided by 1.29) to crack initiation for the pattern of operation experienced by this bucket. Also shown in Table 1 is the life that would have been consumed had no trips occurred. It can be seen that the life was reduced by a factor of two as a result of 25 percent of the shutdowns being trips. This example demonstrates the severe consequences of trips on hot part life and the importance of reducing their occurrence to a minimum.

The 24,000-hour bucket experienced over twice as many startups and hours of operation and was much more severely cracked and degraded, as described earlier. Based on the operating pattern of this unit, crack initiation was calculated (Table 1) to have occurred after 942 starts (1800 divided by 1.91); hence about half of the operating time was spent propagating the bucket cracks.

Discussion

Crack Initiation and Propagation. Cracking occurred on the leading edge, suction side, and pressure side of the 24,000-hour bucket, and on the leading edge and suction side of the 11,000-hour bucket. The crack initiation life of the leading edge was well predicted by the REMLIF computer program. For the 11,000-hour bucket, the 20-mil (0.5-mm) deep cracks on the leading edge made them unsuitable for refurbishment. Cracks were forming on the suction side of this bucket as well. For the 24,000-hour bucket, the leading edge cracks propagated all the way to the leading edge cooling hole, a distance of approximately 0.2 in. (5.0 mm), and followed heavily oxidized and corroded grain boundaries. The pressure and suction side cracks penetrated to a depth of 20 mils (0.50 mm). In addition, both buckets had cracks beginning to form on the airfoil suction side as low as 0.2 in. (5.0 mm) above the platform.

Crack initiation occurred by the following sequence: (1) coating cracking and attack of the cracked coating by the environment; (2) attack of the interdiffusion zone and base metal by the environment; and (3) crack initiation of the base metal. From the metallurgical evidence, the environment appears to be very significant to crack initiation because the environmental attack preceded the crack initiation. Both transgranular and intergranular crack initiation occurred. The intergranular crack initiation and propagation that were observed are further evidence of environmental attack ahead of the crack tip, which embrittles the grain boundaries and changes the fatigue fracture mode from transgranular to intergranular [7]. (Since the bucket surface is in compression during steady-state operation, creep cracking is not expected.)

Several investigators have studied the effect of environment on the fatigue behavior of nickel base superalloys. McMahon and Coffin [8, 9] have described a process of crack initiation and propagation for U-500 and U-700 that is strongly assisted by oxidation of the grain boundaries. It has been shown by

[1] It should be noted that all trips were considered to be trips from base load. Trips from part load, hot starts, and load cycling were not considered. These factors, as well as others, such as ambient temperature, all influence the fatigue life, but are very difficult to determine from operational records. Years of operator log sheets must be carefully reviewed to obtain the data and, frequently, these data may never have been recorded. The results of this paper show that good predictions can be obtained by considering the major cyclic events of startup, normal shutdown, and trip from full load.

Downloaded 02 Jun 2010 to 171.66.16.112. Redistribution subject to ASME license or copyright; see http://www.asme.org/terms/Terms_Use.cfm

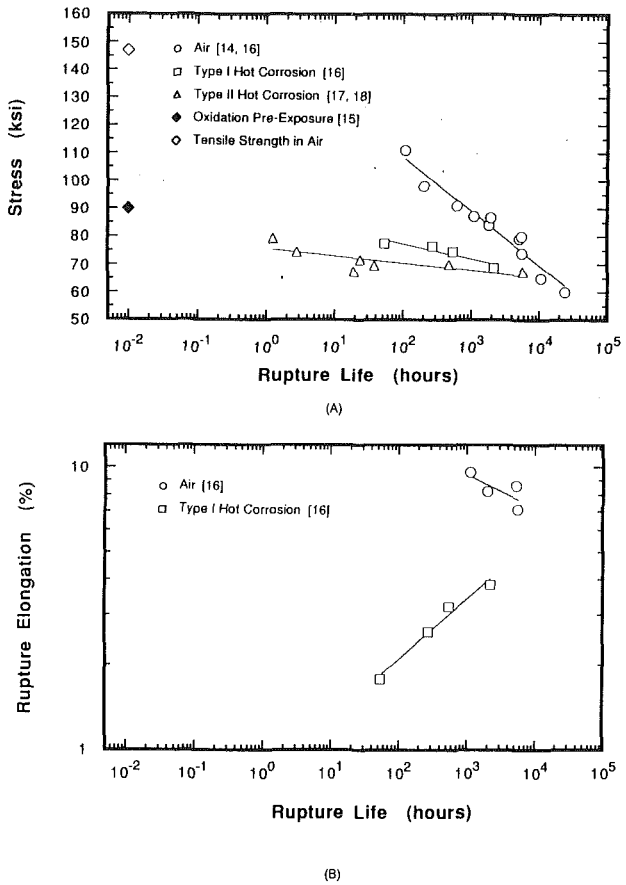


Fig. 11 Effect of environment on stress rupture of IN-738 at 1292-1300°F (700-704°C): (A) rupture life, (B) rupture elongation; the test conditions are described more fully in the text

Whitlow et al. [7] that a hot corrosion environment drastically reduces the low-cycle fatigue (LCF) life of uncoated U-720 and of Pt-Al coated U-720 when tensile stresses are sufficiently high to crack the coating. Antolovitch et al. [10] have shown that the LCF life of René 80 is similarly reduced when pre-exposed in air at high temperatures. Floreen and Kane [11] have shown that the fatigue crack growth rate of IN-718 is greatly increased in air compared to helium, and that sulfur further accelerates the crack growth rate compared to air. Ericsson [12], Cook and Skelton [13], and Grünling et al. [14], have reviewed the effect of environment upon the mechanical properties of materials.

It has been established in high-stress accelerated tests [15-18], that oxidation and hot corrosion can dramatically reduce the low-temperature tensile strength, ductility, and stress rupture life of IN-738. These data are meaningful relative to TMF cracking because it is the high tensile stresses that occur on shutdown at low temperatures, Fig. 10, that are primarily responsible for the accelerated failure of service embrittled buckets.

Woodford [15] pre-exposed IN-738LC specimens for 200 hours in air at 1832°F (1000°C) and then stress rupture tested them at various stress-temperature conditions. At 90 ksi (620 MPa) and 1292°F (700°C), failure occurred in 0.01 hours, a 3000 order of magnitude reduction in rupture life. Huber and Rosselet [16] exposed IN-738LC test specimens to 1562°F (850°C) gas from a burner rig burning light distillate oil containing 0.5 percent sulfur, 15 ppm sodium, and 5 ppm vanadium before stress rupture testing at 1292°F (700°C). The results are shown in Figs. 11(*a*) and 11(*b*). It can be seen that above about 410 MPa (60 ksi), the effect on life and ductility strongly increases with stress. Whitlow et al. [17, 18] obtained similar stress rupture results for IN-738 tested in a 60/40 mole fraction $Na_2SO_4/MgSO_4$ melt containing 1 wt. percent NaCl at 1300°F (704°C). The results from all three studies are summarized in Fig. 11. Based on extrapolation of the hot corrosion, stress rupture data to the approximate time to failure in a tensile test (0.01 hour), it appears that the tensile strength also has been reduced from about 145 ksi (1,000 MPa) to the 80-100 ksi (550-690 MPa) range, and that the ductility has been reduced to less than one percent. These data suggest that the material can be embrittled to approximately the same extent in all three corrosion regimes (Type II hot corrosion at lower temperatures, Type I hot corrosion at intermediate temperatures, and oxidation at high temperatures). This is consistent with the findings of Woodford et al. [19], on oxygen and sulfur embrittlement of pure nickel (Ni-270), where it was found that grain boundary sulfur penetration is faster and much less temperature dependent than oxygen penetration.

The practical significance of these data is that greatly accelerated environmentally assisted cracking can be expected when coating fracture occurs in buckets operating in aggressive environments because the tensile stresses that occur during full load emergency shutdowns (or trips) are on the order of the aforementioned fracture strength of embrittled IN-738, while during a normal shutdown, Fig. 10, they are high enough to cause accelerated cyclic crack growth along the embrittled grain boundaries.

Coating Condition. The degradation of a platinum-aluminide coating occurs by the consumption of aluminum from the coating to form aluminum oxide on the surface. The aluminum oxide actually protects the coating and base metal by acting as a barrier between the coating and the environment. As the aluminum oxide spalls off due to thermal cycling, erosion, etc., the coating supplies additional aluminum to form a new aluminum oxide layer.

As the aluminum (as well as platinum) content of the coating is reduced, the phases of the coating microstructure change to accommodate the lower aluminum levels. These phase changes are as follows: (1) The $PtAl_2$ particles in the outermost layer dissolve in the NiAl to form a single-phase (Ni, Pt)Al or β phase; (2) the β phase breaks up into a two-phase structure of γ' (Ni, $Pt)_3Al$, and β; (3) there is insufficient aluminum to maintain the β phase, and a single γ' phase is left; (4) the single γ' phase breaks up into a γ phase, Ni + solid solution elements, and γ'; (5) the γ phase is left; and (6) the coating is completely consumed. This process has been described by Levine [20] for an aluminide coating.

In practice, the coating is protective if it is a single phase, β. The coating begins to lose its protection when the two-phase, $\beta + \gamma'$ structure is present. When there is no longer any β phase, the coating is no longer protective and should be replaced. In practice, the coating should be replaced prior to reaching the single-phase γ' structure. The coating degrades most by oxidation on the hottest section of the bucket, which may be the leading edge, depending on the bucket design. Even though the majority of the coating is still protective, the coating should be replaced when the coating at the hottest section is no longer protective, because it may not be possible to refurbish the buckets once base metal attack occurs.

The coating of the 11,000-bucket was a two-phase, $\beta+\gamma'$ structure at the leading edge and a single-phase, β structure on the pressure and suction sides. The coating was protective on the sections that were examined, which were not at the hottest location on the bucket. However, cracking of the coating required the bucket to be recoated for continued use.

The coating of the 24,000-hour bucket was a single-phase γ' structure at the leading edge. On the pressure and suction surfaces the coating was a two-phase, $\beta + \gamma'$ structure. The coating was missing where attack of the interdiffusion zone caused the coating to spall off. There were a number of areas where the environmental attack had almost penetrated the

Downloaded 02 Jun 2010 to 171.66.16.112. Redistribution subject to ASME license or copyright; see http://www.asme.org/terms/Terms_Use.cfm

coating. The coating on this bucket needed replacing due to the single-phase, γ' condition on the leading edge, as well as the extensive cracking and attack of the coating.

The cracking of the coating aggravated the degradation of the coating because it exposed the interdiffusion zone and base metal to environmental attack. Where the interdiffusion zone was attacked, the coating was sometimes spalled.

Operating and Maintenance Considerations

In view of the high cost of replacement buckets, the benefits of optimizing the life of these parts is substantial. A life management program can help achieve this goal.

Life management entails continuous monitoring of operating parameters and periodic input of this information into a life management computer program, such as the REMLIF code described earlier. This provides the operator with a quantitative assessment of life consumption and also allows him to see what the rate of life consumption has been versus what it could be if corrective action is undertaken. For example, early elimination of the full-load trips in the case histories presented in this paper might have increased the life by 50 to 100 percent.

In order to extend the life of these parts to the greatest extent possible, it is critical that maintenance be scheduled and performed before the buckets are fatigue damaged beyond repair, as they were in the examples discussed herein. This can be done with the aid of predictions from the REMLIF computer program and periodic inspections of the leading edge of the buckets. It is necessary that the buckets be refurbished before environmental attack of the substrate occurs because it may not be possible to recondition buckets after this attack has occurred. After the coating is stripped and the bucket inspected for cracks, buckets free of surface indications can then be recoated and reheat treated to restore the buckets to essentially "like new" condition. It may be possible to repeat this process, thereby greatly extending the life at a fraction of the cost of new buckets.

Because coating life can control the life of buckets in higher firing temperature engines, and in view of the fact that new and improved coatings are continually being offered, it is important that a replacement coating be selected that is capable of protecting the base metal from both the environmental attack and the fatigue cycling that the bucket is subjected to. This dual requirement is particularly demanding since improvements to the fatigue durability decrease the resistance to environmental attack, and increases in environmental resistance decrease the fatigue capability. It is doubtful that any coating could have resisted the fatigue cycling of the current example and maintained adequate protection from environmental attack. A more ductile coating than the aluminide type may improve the coating fatigue performance, but with potentially less environmental resistance.

Summary

Cracked first-stage buckets from a General Electric MS7001E gas turbine burning natural gas and #2 fuel oil were analyzed. Numerous cracks were found along the leading edge and midchord regions of the suction surface after 874 start-stop cycles, which included 217 trips from load and 11,000 service hours. The leading edge cracks were 20 mils (0.5 mm) deep. Buckets from a sister engine were examined after 1800 start-stop cycles, which included 218 trips from load and 24,000 service hours. These buckets had much more extensive cracking, including leading edge cracks to the leading edge cooling hole, a distance of about 0.2 in. (5.0 mm), and suction side cracks 20 mils (0.5 mm) deep.

A thermal mechanical fatigue analysis was performed using the REMLIF computer program from the EPRI Life Management System. This program predicted that 129 percent of the life of the 11,000 buckets had been expended, and 191 percent of the life of the 24,000-hour buckets were expended. These predictions are consistent with the observed amount of cracking.

The primary cause of the extensive amount of cracking was the large percentage of trips that occurred. These trips can consume many times the fatigue life of a normal shutdown. The crack growth was accelerated by grain boundary attack by oxygen and sulfur, which were found in the crack faces.

The degradation of the platinum-aluminide coating was examined. On the leading edge, the coating had degraded to a two-phase structure at the leading edge after 11,000 hours, and a single phase, γ', after 24,000 hours. On the suction and pressure surfaces, the coating was still a single-phase, β structure after 11,000 hours, but a two-phase, $\beta + \gamma'$ structure after 24,000 hours. The coating begins to lose protection when the two-phase structure forms.

The coating was extensively cracked at almost all locations examined. Where the coating was cracked, environmental attack of the coating, interdiffusion zone, and base metal occurred. The attack of the interdiffusion zone resulted in the coating lifting and spalling off. In addition to the cracking, there were areas of the coating where the high-temperature attack had almost penetrated the coating.

Based on this study, the process of crack initiation appears to be: (1) coating cracking; (2) environmental attack of the coating, interdiffusion zone and base metal; and (3) crack initiation in the base metal at the area that was attacked by the environment. Crack propagation appears to be assisted strongly by the environment, with environmental attack ahead of the crack tip, and in some cases, propagation along grain boundaries that have been attacked by oxygen and sulfur.

Acknowledgments

The authors would like to thank the Electric Power Research Institute for funding this work under RP's 2421-2,3 and RP3064-1, and to the General Electric Company who provided the TMF algorithms. The authors would also like to thank Mr. Harold Saldana, Mr. James Malik, and Ms. Loretta Mesa of Southwest Research Institute who did the metallography, wrote the REMLIF computer program, and typed the manuscript, respectively. Mr. Chester Sims, Dr. Donald Boone, and Dr. Gerald Leverant are thanked for their consultation during this study. Last, but not least, we wish to thank the utility who provided the buckets and their operational information, without which this study would not have been possible.

References

1 Bernstein, H. L., "Life Management System for General Electric Frame 7E Gas Turbine," R. Viswanathan and J. M. Allen, eds., *Proceedings of EPRI/ASM Conference on Life Assessment and Repair Technology for Combustion Turbine Hot Section Components*, Phoenix, AZ, Apr. 1990.

2 Linask, I., and Dierberger, J., "A Fracture Mechanics Approach to Turbine Airfoil Design," ASME Paper No. 75-GT-79, 1975.

3 Russell, E. S., "Practical Life Prediction Methods for Thermal-Mechanical Fatigue of Gas Turbine Buckets," *Proceedings of the Conference on Life Prediction for High-Temperature Gas Turbine Materials*, V. Weiss and W. T. Bakker, eds., EPRI Report AP-4477, Palo Alto, CA, 1986, pp. 3-1 to 3-39.

4 Bernstein, H. L., "An Evaluation of Four Creep-Fatigue Models for a Nickel-Base Superalloy," in: *Low-Cycle Fatigue and Life Prediction*, ASTM STP 770, C. Amzallag, B. N. Leis, and P. Rabbe, eds., American Society for Testing and Materials, 1982, pp. 105–134.

5 Bernstein, H. L., "A Stress-Strain-Time Model (SST) for High-Temperature, Low-Cycle Fatigue," *Methods for Predicting Material Life in Fatigue*, W. J. Ostergren and J. R. Whitehead, eds., ASME, #G00166, New York, 1979, pp. 89–100.

6 Bernstein, H. L., "The Stress Behavior of Three Advanced Nickel-Base Superalloys During High-Temperature, Low-Cycle Fatigue," AFWAL-TR-80-4075, Wright-Patterson Air Force Base, OH, June 1980.

7 Whitlow, G. A., Johnson, R. L., Pridemore, W. H., and Allen, J. M., "Intermediate Temperature, Low Cycle Fatigue Behavior of Coated and Uncoated Nickel Base Superalloys in Air and Corrosive Sulfate Environments," ASME *Journal of Engineering Materials and Technology*, Vol. 106, 1984, pp. 43–49.

Downloaded 02 Jun 2010 to 171.66.16.112. Redistribution subject to ASME license or copyright; see http://www.asme.org/terms/Terms_Use.cfm

8 McMahon, C. J., and Coffin, L. F., Jr., "Mechanisms of Damage and Fracture in High-Temperature, Low-Cycle Fatigue of a Cast Nickel-Based Superalloy," *Metallurgical Transactions*, Vol. 1, Dec. 1970, p. 3443.

9 McMahon, C. J., Jr., "On the Mechanism of Premature In-Service Failure of Nickel-Base Superalloy Gas Turbine Blades," *Materials Science and Engineering*, Vol. 13, 1974, pp. 295–297.

10 Antolovich, S. D., Domas, P., and Strudel, J., "Low Cycle Fatigue of René 80 as Affected by Prior Exposure," *Metallurgical Transactions A*, Vol. 10A, Dec. 1979, p. 1859.

11 Floreen, S., and Kane, R. H., "Effects of Environment on High-Temperature Fatigue Crack Growth in a Superalloy," *Metallurgical Transactions A*, Vol. 10A, Nov. 1979, p. 1745.

12 Ericsson, T., "Review of Oxidation Effects on Cyclic Life at Elevated Temperature," *Canadian Metallurgical Quarterly*, Vol. 18, 1979, pp. 177–195.

13 Cook, R. H., and Skelton, R. P., "Environment-Dependence of the Mechanical Properties of Metals at High Temperature," *International Metallurgical Reviews*, Vol. 19, 1974, p. 199.

14 Grünling, H. W., Keienburg, K. H., and Schweitzer, K. K., "The Interaction of High Temperature Corrosion and Mechanical Properties of Alloys," in: *High Temperature Alloys for Gas Turbines 1982*, R. Brunestad, D. Coutsouradis, T. B. Gibbons, V. Lindblom, D. B. Meadowcraft, and R. Stickler, eds., D. Reidel, London, 1982, pp. 507–543.

15 Woodford, D. A., "Environmental Damage of a Cast Nickel Base Superalloy," *Metallurgical Transactions*, 12A, 1981, pp. 299–308.

16 Huber, P., and Rosselet, A., "Influence of Hot Corrosion on the Creep Rupture Behavior of Nickelbase Alloys," in: *Environmental Degradation of High Temperature Materials*, Series 3, 13, 2, The Institution of Metallurgists, London, 1980, pp. 2/35–2/39.

17 Whitlow, G. A., Beck, C. G., Viswanathan, R., and Crombie, E. A., "The Effects of a Liquid Sulfate/Chloride Environment on Superalloy Stress Rupture Properties at 1300°F (704°C)," *Metallurgical Transactions*, Vol. 15A, 1984, pp. 23–28.

18 Courtesy of Westinghouse Electric Corp., unpublished data, 1984.

19 Woodford, D. A., "Gas Phase Embrittlement of Superalloys-Implications for Life Assessment," *Proceedings of EPRI/ASM Conference on Life Assessment and Repair Technology for Combustion Turbine Hot Section Components*, R. Viswanathan and J. M. Allen, eds., Phoenix, AZ, Apr. 1990.

20 Levine, S. R., NASA TMX-2370, 1971.

Downloaded 02 Jun 2010 to 171.66.16.112. Redistribution subject to ASME license or copyright; see http://www.asme.org/terms/Terms_Use.cfm

T. A. Cruse
Vanderbilt University,
Nashville, TN 37235

R. C. McClung

T. Y. Torng

Southwest Research Institute,
San Antonio, TX 78228

NSTS Orbiter Auxiliary Power Unit Turbine Wheel Cracking Risk Assessment

Introduction

The National Space Transportation System (NSTS) Orbiter has three hydrazine-powered auxiliary power units (APU). These APUs provide power during both ascent and descent phases of the mission for gimballing the Space Shuttle Main Engines (SSME), and for deflecting the flight control surfaces. Each APU drives a hydraulic power source for these control requirements.

The APU derives its power from a single-wheel, double-pass turbine. High-pressure ammonia, derived from catalytic reaction of the hydrazine fuel, passes through the supersonic cascade twice: once from a high-pressure nozzle five blade passages wide (first stage), and a second time from a twenty-blade, low-pressure nozzle on the back face of the turbine wheel (second stage). The power turbine disk is shown in Fig. 1. The airflow passage is symmetric about the turbine wheel midplane, as shown in Fig. 2. The pressure is supplied to the turbine in a series of high-frequency pressure pulses resulting from valve operation on the hydrazine fuel source. The frequency of pulsing actually controls the power generated by the APU.

The typical mission duty cycle for each APU consists of a hot gas start (HGS), normal power level use during ascent, shutdown, re-start and normal power operation for descent, and final shutdown. In the event an APU is shut down during ascent or descent, the remaining two APUs are commanded to a high power condition resulting in a wheel speed increase of 10 to 13 percent over the nominal speed. The amount of time spent at the high-speed condition is denoted by HST. Additionally, the launch requirements include starting one APU for test purposes prior to launch.

Cracking of turbine wheel blades was recognized as a problem from the early days of the Orbiter program. The problem and its potential severity came to the forefront, however, in the fall of 1987. During routine overhaul of an APU, a broken turbine blade was discovered on the first-stage side of the test turbine wheel. The total run time on this wheel was 4.2 hours including time on the vehicle, the APU having flown in position 3 of Atlantis on missions 51-J and 61-B. The blade fracture was localized and resulted in the liberation of a very small fragment, which caused no secondary damage and posed no threat to the safety of the vehicle. However, the incident raised significant concerns for establishing the probability of a more serious fracture in future space launch operations.

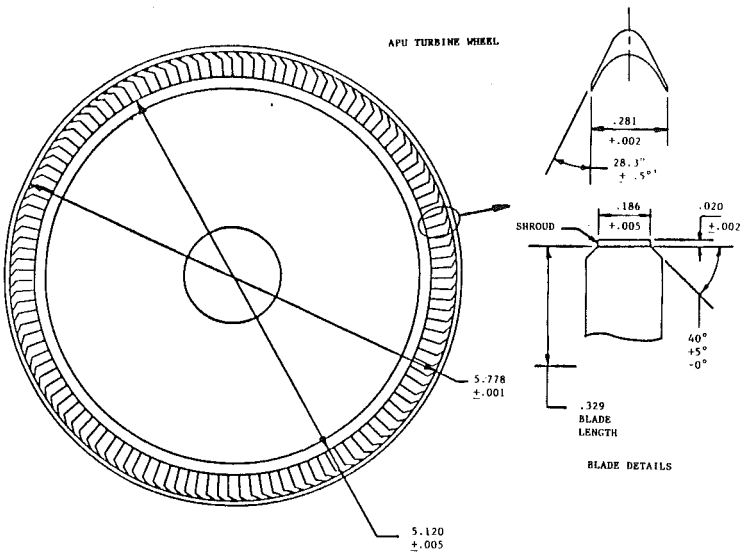
The concern for flight safety led to a detailed risk assessment associated with the continued use of turbine wheels, with this known cracking problem. While test data strongly suggested that the turbine blade cracking would not result in the loss of a full turbine airfoil, the probability of such an event had to be estimated. The steps in this study included a determination of the causes of cracking, a determination of the 0.999/95 percent reliability-based life of cracked turbine blade wheels subject to continued use, and finally, the estimation of fleet-wide probability of blade liberation, if the wheels were used beyond the 0.999/95 percent reliability-based life. The determination of the 0.999/95 percent reliability life was based on a Weibull probability interpretation of high-time testing of cracked turbine wheels. The fleet-wide reliability study was undertaken to relieve the potentially substantial cost of turbine wheel inspections that might result from limiting the allowable risk to 0.001 ($=1.0-0.999$).

The study was successful in all respects. A reasonable source of the cracking was confirmed, based on related technical experience in the steam turbine industry. The useful flight limit on APU turbine wheels, in order to maintain the 0.999/95 percent reliability, was defined, based on selected, high-time operation of turbine wheels with large blade cracks. No blade crack grew to a critical size during extended testing of the wheels. Finally, the fleet-wide investigation showed that the small numbers of turbine wheels in service with a cracking potential posed no significant risk of fracture up to the point of part replacement. A new turbine wheel airfoil design that eliminates the current cracking problem was developed by the Sundstrand Corporation engineering team. This has been substantiated by extensive testing of new wheels at cycle levels substantially beyond those for which the current wheels cracked; no cracks were detected in the new wheels.

Contributed by the International Gas Turbine Institute for publication in the JOURNAL OF ENGINEERING FOR GAS TURBINES AND POWER. Manuscript received by the International Gas Turbine Institute August 1991. Associate Editor: L. S. Langston.

Copyright © 1992 by ASME
Downloaded 02 Jun 2010 to 171.66.16.112. Redistribution subject to ASME license or copyright; see http://www.asme.org/terms/Terms_Use.cfm

APU TURBINE WHEEL BLADE CRACKING SUMMARIZED



- o SIGNIFICANT APU TEST EXPERIENCE HAS BEEN ACCUMULATED
- o NO BLADE HAS BEEN LIBERATED IN CURRENT DESIGN
- o SRB WHEEL CRACKS FIRST NOTED
- o SRB/ORBITER DESIGNS QUITE SIMILAR
- o ALL APU'S NOW HAVE DEMONSTRATED BLADE CRACKING POTENTIAL
- o BLADE CRACKS DO NOT THREATEN THE TURBINE WHEEL BODY
- o APU'S CONTINUE RUNNING OR HAVE LOW SPEED SHUTDOWN WITH EXTENSIVE BLADE CRACKING
- o INVENTORY REQUIRES CONSIDERATION OF OPERATIONS WITH CRACKED BLADES

Fig. 1 Detailed view of the APU turbine wheel

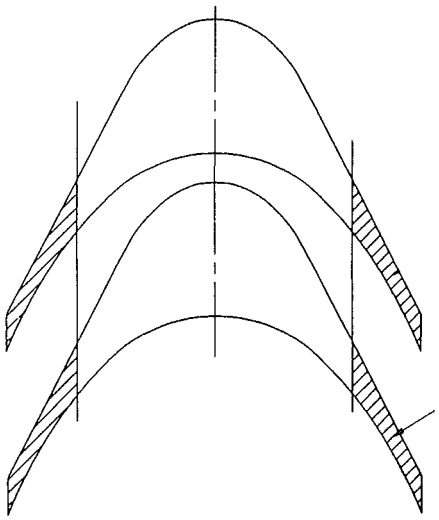
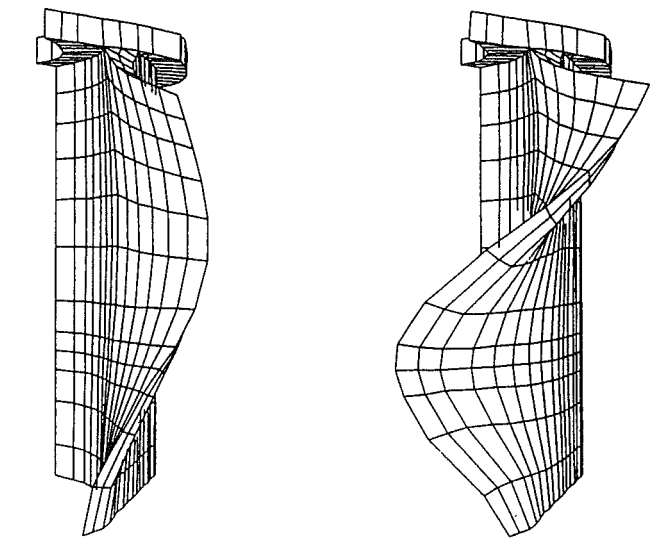


Fig. 2 Supersonic passage for APU turbine wheel



First Mode
(similar to second)

Third Mode

Fig. 3 First three mode shapes

Fundamental Cause of Cracking

The first step in establishing component reliability was to identify the probable source of stress in the blades that leads to cracking. Early fractographic inspections of cracked blades suggested that crack initiation and growth were associated with high cycle fatigue (HCF) and low applied ΔK values. Multiple fracture origins were detected and some striations and arrest marks were observed.

A likely source of HCF in rotating machinery is resonance vibration due to periodic airfoil excitation. The pressure load that occurs once per wheel revolution has a higher order frequency decomposition due to the nature of partial-admission turbines. The resonance condition will be discussed in more detail in a subsequent section. Low damping in integral turbine wheels, such as the one used in the APU, can support high resonance stresses.

The fractographic observations were the motivation for modal analysis and stress analysis of the blade. These investigations, conducted by both Sundstrand (the APU manufacturer) and SwRI, found three vibration modes of potential significance. Mode shapes of the first and third airfoil bending modes are depicted in Fig. 3. The first and second mode have the same modal shape but are distinguished by whether the opposite halves of the blade move in symmetry or antisymmetry, relative to each other. The first two modes were found to have natural frequencies around 55 and 60 kHz. The third mode was predicted to resonate at about 85 kHz. The locations

Downloaded 02 Jun 2010 to 171.66.16.112. Redistribution subject to ASME license or copyright; see http://www.asme.org/terms/Terms_Use.cfm

of maximum stress for these different modes were found to correspond to the actual locations of crack initiation. Three distinct cracking locations were indicated: one at the tip, one in the fillet region along the leading edge of the root (designated as the fillet location), and one near the root but slightly farther out along the leading edge (designated as the outboard location). These positions corresponded closely to the locations of maximum strain associated with the first three vibration modes. A very high percentage of blades was found with tip cracks, while a lower percentage were found with cracks in the two leading edge locations: fillet and outboard locations. Identification of the blade natural frequencies and Fourier decomposition of the periodic pressure pulse permitted construction of a Campbell-type, resonance diagram, as shown in Fig. 4.

The pressure pulse for the partial-admission nozzle is idealized as a square wave with duration 21.6 deg, corresponding to the width of the first stage opening, and total period 360 deg. The horizontal lines on the Campbell plot represent the natural frequencies, and the $(m+0.5)/T$ diagonal lines indicate the frequency at which maximum energy is available for a given harmonic of the periodic pulse at a given rotational speed. The nN diagonal lines simply denote integer multiples of the running speed. Intersections of the horizontal and $(m+0.5)/T$ diagonal lines identify potential resonances. While no resonances are indicated precisely at running speeds, several intersections occur near the running range and would be crossed during start-up and other speed changes. High cycle fatigue due to resonant vibration is consistent with these analyses.

Historical Experience in the Turbine Industry

The hypothesis of resonance fatigue is consistent with historical experience in the steam turbine industry [1, 2]. In particular, Westinghouse experienced a major problem with blade cracking in partial admission steam turbines during the 1930s and 40s. The problem first emerged when new turbine designs required higher pressures, temperatures, and (especially) rotational speeds, and it motivated a major research effort stretching over six years. While the blade dimensions, pressures, temperatures, and speeds were all quite different from the current APU design, the critical nondimensional ratio of blade natural frequency to wheel speed was roughly the same.

Westinghouse hypothesized that resonant vibration was to blame. They analyzed the problem by assuming that two conditions should be satisfied for worst-case vibration. First, there should be some integer number n cycles of blade vibration per revolution, $f=nN$, where f is the blade natural frequency and N is the rotational speed of the wheel, and there should be some half integer number of cycles in the loaded part of the revolution, $f=(m+0.5)/T$, where T is the duration of the pressure pulse; see Fig. 5. This is precisely the same as the Campbell diagram construction, if we identify worst-case conditions as the coincidence of a $(m+0.5)/T$ diagonal line with a nN line (note that only every tenth nN line is shown for clarity, so there is always a nN line very near a $(m+0.5)/T$ line).

Westinghouse further evaluated these assumptions and computations by conducting a major experimental study, placing small mirrors on the ends of selected blades in a full-scale test rig and making optical measurements of actual blade motion in loaded service. They confirmed resonant vibration as the source of large blade stresses, but they also found that the simple square wave pulse shape was not exactly correct; see Fig. 6. The data indicated that additional forces were associated with a blade entering and exiting the gas zone. Prior to the entrance, the blade is idle and experiences no gas stress. At the entrance, the blade is first struck on its back as gas fills the zone between it and the blade ahead. Since there is no gas pressure on the concave side of the blade, there is a net negative force. When the blade is in the center of the gas zone, it

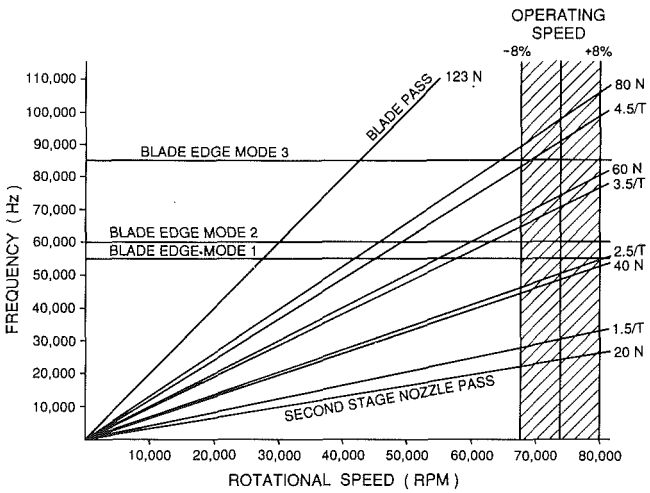


Fig. 4 Campbell diagram for partial admission turbine

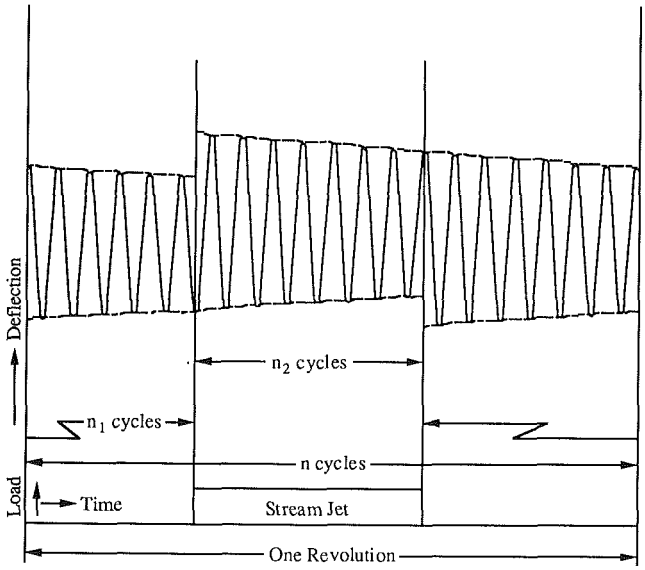


Fig. 5 Half-integer forcing harmonic

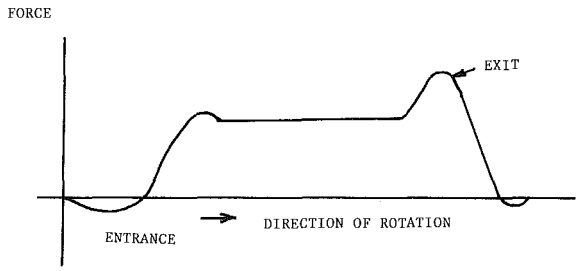


Fig. 6 Nonrectangular blade loading pulse

experiences a steady positive force. But when the blade exits the gas zone, it is first suddenly relieved of negative pressure as the space between it and the blade ahead empties of gas. This produces a sharp positive force on the blade, the so-called exit peak. The maximum blade resonance occurs, then, when these additional impulses occur in the proper relationship to the blade natural frequencies. A comprehensive analysis of these phenomena is quite complex [3].

Crack Growth Characteristics

Crack growth in the turbine blades is characterized by two

Downloaded 02 Jun 2010 to 171.66.16.112. Redistribution subject to ASME license or copyright; see http://www.asme.org/terms/Terms_Use.cfm

phases. In the first, the cracks are of a size comparable to the (duplex) microstructure of the René-41, nickel-base superalloy. These short cracks are generally surface cracks with initiation sites located near, but not on the edge of the blade. The short cracks were seen to have highly variable crack growth rates, consistent with high frequency (vibratory) load response. At a surface length of about 0.060 in., the cracks begin to be through-thickness cracks, best characterized by their length from the edge of the airfoil. Long cracks (on the order of 0.090 in.) were judged to be readily and reliably detected by fluoropenetrant examination; and were found to grow in a slow manner with growth rate scatter consistent with low-cycle data scatter in the nickel-base material class.

The development of long through-cracks brings about a major change in the resonant response of the blade. Finite element modal analysis of blades with simulated cracks showed that small cracks have little effect on the natural frequencies, but long cracks have a large effect, causing the natural frequencies to decrease substantially. A blade with a 0.050 in. tip crack and a 0.030 in. fillet root crack saw a decrease in the lowest two natural frequencies of less than 4 percent and a decrease in the third natural frequency of less than 11 percent. But the introduction of a single outboard root crack of length 0.100 in. to a previously uncracked blade caused a complete change in the nature of the modal response. The first symmetric mode disappeared and the remaining two lowest natural frequencies dropped by 30 percent. The fundamental nature of blade displacement was also changed from a bending mode to a flapping mode.

The natural frequency changes are associated with a general decrease in the crack growth rate for cracks longer than about 0.060 in. It is probable that the development of long cracks cause a detuning of the blade as natural frequencies change, thereby reducing the crack driving force (even though the physical crack length is increasing). The change in crack mode (not the same as vibration mode) from a Mode I or opening mode configuration to a Mode III or tearing mode configuration may also contribute to the observed decrease in crack growth rate.

Crack growth data were obtained from several tests of APUs in Sundstrand test cells. Repeated mappings of crack sizes were obtained over a range of APU operations, including multiple starts and exposures to high-speed operation. Crack size data used to characterize long cracks were restricted to data pairs with an average crack length greater than 0.065 in. and a minimum crack length greater than 0.050 in. These limits were chosen in order to eliminate data that might be heavily influenced by the short-to-long crack size transition. Careful examination and comparison of the data from several different wheels and APU tests led to the conclusion that both hot gas starts (HGS) and high-speed run time caused crack growth in the various tests. Correlation of crack size with both HGS and HST was therefore used for the risk assessment.

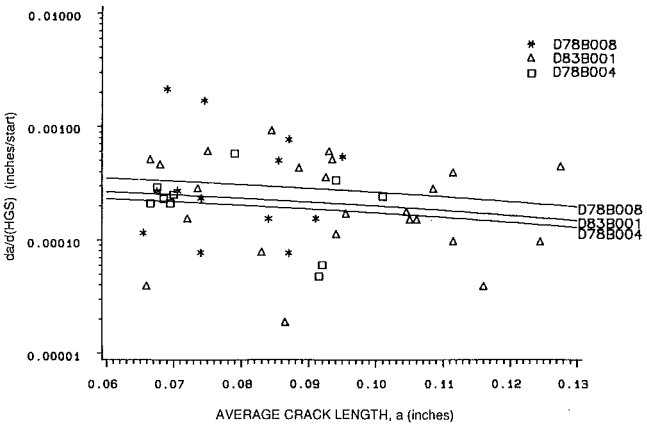


Fig. 7 Crack growth rate data fitting

The crack growth rate data for three turbine wheels are shown in Fig. 7. Note that *da/dHGS* is shown on a logarithmic scale, while the average crack length is presented on a linear scale, due to the narrow range of data considered. The lines on this figure were generated by a linear regression of the different data sets. The characteristic slope of the data was determined from a regression of all three data sets combined. This slope was then imposed on the regression of each individual data set as the best means of comparing the different data sets. Many studies of fatigue crack growth in the literature have shown that the slope of the data (e.g., the exponent in a Paris Law representation) is relatively constant for a given material system and load regime, reflecting the fundamental mechanism of crack advance. The intercept of the data (e.g., the coefficient in a Paris model representation), on the other hand, can exhibit considerable variation and is related to scatter in material properties.

Reliability Analysis

The standard reliability requirement for flight conditions is for the component to retain a reliability of 0.999 with 95 percent confidence. Ordinarily, probabilistic fracture mechanics would be used to predict the number of load cycles the component could experience while retaining the desired reliability and confidence. Unfortunately, the turbine wheel cracking problem is not well suited to analytical simulation of failure potential, owing to the high cycle fatigue cracking caused by blade resonance. The stress levels, crack tip stress intensity factor, and numbers of actual stress-reversal cycles cannot be quantified for this very complex problem. However, a maximum crack size of about 0.125 in. could be estimated for the fillet crack, given the level of high-speed centrifugal stress on the blade.

On the other hand, NASA and Sundstrand were able to develop significant test experience on turbine wheels with large cracks in each cracking location. Continued operation of these wheels, with loading conditions duplicating those that are experienced in flight, was demonstrated. The high-time test experience is used to estimate a lower bound on the number of hot gas starts (or high speed run time) that could result in a turbine blade fracture. The Weibull–Bayesian approach to reliability estimation for mechanical systems [4, 5] is used to project the number of HGS/HST that correspond to the target reliability of 0.001, based on the high-time test data.

The demonstrated safe life for the turbine wheel with cracked blades was the amount of high-speed test time and hot gas starts for a wheel containing at least one crack in either of the two fillet locations, with a length greater than 0.090 in. This minimum size was taken because such a size assured that the highly uncertain HCF response of the blade was no longer dominant in the crack growth rates, and because such a crack length could be reliably detected during bench examination of the turbine wheels. The confidence level was based on testing the wheels with a number of actual cracks greater than or equal to this length threshold; this testing by Sundstrand did not result in any actual loss of a turbine airfoil.

Selection of a Weibull Shape Parameter

The high test time on a turbine wheel is used to estimate a lower bound on the characteristic life parameter of the Weibull distribution, based on the actual number of blade cracks. The actual testing did not provide sufficient data to characterize the Weibull shape parameter for the life distribution—a typical state of affairs in a failure investigation. However, extensive crack growth testing in nickel-base alloys has demonstrated that the scatter in fracture mechanics lives, based on material considerations only, is conservatively represented by the value

Downloaded 02 Jun 2010 to 171.66.16.112. Redistribution subject to ASME license or copyright; see http://www.asme.org/terms/Terms_Use.cfm

$\beta = 6.683$. This value is derived from crack growth data for long cracks in a nickel-base turbine disk alloy with a sample size of 141 [6]. This value was based on a two-parameter Weibull fit to the data, which implies that minimum failure times can approach zero as the probability of failure approaches zero. In reality, the crack growth life data used here approach a distinctly nonzero minimum life at low probabilities of failure, typical of a three-parameter Weibull distribution. The two-parameter Weibull distribution used is therefore conservative at high levels of reliability. Reference [7] indicates that the current approach to the fracture mechanics life is substantially conservative, relative to other René-41 data. Based on the number of high-time turbine wheels with large cracks, the reliability requirement of 0.999/95 percent confidence resulted, effectively, in a life factor of a little more than four between the demonstrated life and the certifiable life of flight hardware.

Another reliability issue is the effect of multiple APU builds and operations on the shape parameter of the Weibull model. It has been assumed in this study, since the testing involved three APUs and multiple builds of each APU, that build scatter is implicit in the test time value used to estimate the population characteristic life. The issue of operational differences from one APU to another, for the same nominal mission, was not specifically addressed except by reference to the fact that the turbine wheel speeds and temperatures for turbine cycles are expected to fall in a narrow range. The risk of crack propagation was therefore judged to be dominated by the material issue, at the risk level of 0.001.

A degree of confirmation of $\beta = 6.683$ was obtained by comparison to the long crack growth rate data base for the APU turbine blades. As shown in Fig. 7, the scatter in crack growth rates within a single wheel was quite great. The wheel-to-wheel scatter, as characterized by the different regression lines, was quite small. It is this wheel-to-wheel scatter that β is commissioned to represent, since the demonstrated experience of 123 blades on a single wheel (or 17 long cracks on a single wheel) implicitly integrates the crack growth scatter within a single wheel.

Fleet Assessment

The current auxiliary power unit (APU) flight limits on hot gas starts (HGS) and high-speed time (HST) are set by a requirement to retain a minimum component level reliability of 0.999 with 95 percent confidence between turbine wheel inspections. The flight limits have been established based on high-time testing of selected turbine wheels containing crack sizes greater than the inspection limit of 0.090, without blade separation. The use of these flight limits is expected to result in the need to remove selected APUs from the Orbiter, for turbine wheel inspections.

The retained-reliability limits are conservative, due to the small population of flight wheels. The cost of inspection of the turbine wheels is quite high due to the need to force-pull APUs from the Orbiter. The number of replacement APUs is quite limited. For these reasons, the use of a probabilistic failure assessment for the total APU "fleet" may provide relief from these costs and inspection burdens, while not incurring significant potential for turbine wheel blade separation. The findings on the fleet risk assessment for the APU turbine wheels indicate that the current flight limits can be increased, and that mandatory inspection pulls of the APUs are not needed. These conclusions are based on predictions that significantly less than one blade failure is expected prior to retirement of the current configuration turbine wheels.

Average component reliability for a population of components subject to the same usage does not account for fleet size effects on the expected number of separations, expected fleet usage on a specific component basis, or the risk-reduction impact of inspection programs, with retirement of cracked components. For small populations of components, the average component-reliability may impose conservative limits on part usage. Fleet assessment of the expected number of turbine blade separations in a fleet inspection program is a viable alternative to the use of the retained-reliability limits, and provides a more realistic simulation of the probable fleet experience during an inspection program.

A fleet risk assessment for the Orbiter fleet was made by a Monte Carlo simulation of the probability of a single blade separation, taking account of the likely flight manifest for the period of time until the current configuration blades are retired. Of the three current flight vehicles, one is flying with the new configuration wheels, and therefore incurs no risk of blade separation. Vehicles Columbia and Atlantis have APUs with the old configuration turbine wheel. The Monte Carlo simulation considers the probable exposures of the individual APUs to hot gas starts and high-speed operation for each simulated launch. Continued use of the APUs beyond the current flight limits will result in an increase in risk, per APU, beyond the current risk of 0.001. The Monte Carlo simulation is used to predict the total risk of a single blade separation, for both vehicles and the associated APUs. The assessment, of course, changes as the flight manifest changes.

Risk Simulation Code

The Monte Carlo computer code simulates the potential for blade fracture due to continued use of current-configuration turbine wheels use with inspections set at user-defined working inspection limits (WIL). The WIL levels may be equal to or higher than the current flight limits. No APU is force-pulled until exceeding a defined WIL parameter, after a full mission has been flown. Each simulation corresponds to one statistical sample of the probable outcome of the planned use of the turbine wheels according to the flight mission plan. The mission plan is user defined in terms of the numbers of planned flights for an APU, such as the plan given in Fig. 8.

Each flight has an uncertain number of hot gas starts for each APU and a probability of requiring high-speed operations. Twenty options for the flight simulation are considered, as indicated in Fig. 8. The options are based on past experience such as the frequency of pad aborts, the frequency of APU malfunction, and the expected (upper limit) minutes of HST, should this condition occur. Pad check-out for APUs is considered, with the code selecting the APU with the lowest, current level of risk for use as the check-out APU. One rare, double fault, event is considered: the abort-once around (AOA) event after one APU has malfunctioned such that both APUs are operating at high speed. This event would result in as much as 108 minutes of HST.

The increment of risk for each flight is calculated as the risk for the turbine wheel after the simulated flight in terms of the simulated number of HGSs and amount of HST (if any), minus the risk prior to the flight. This increment in risk is the hazard rate for a mission. Risk is computed from the user-defined Weibull distributions for each kind of exposure (HGS, HST). Since crack growth due to either exposure (HGS, HST) is additive, the level of risk for an exposure to HST is totally dependent on the level of risk already achieved for the number of HGSs. The code assesses the increment of risk for HGS exposure first, and then increases the risk for HST (if any). The code evaluates a risk increment for the HST damage mode in terms of an equivalent amount of HGS risk, and this HST risk is added to the HGS risk increment incurred by the flight.

For each flight, the code simulates whether or not a blade separation has occurred due to the simulated number of HGSs and minutes of HST. The probability of blade separation for each APU in each flight considers each of these operational

Downloaded 02 Jun 2010 to 171.66.16.112. Redistribution subject to ASME license or copyright; see http://www.asme.org/terms/Terms_Use.cfm

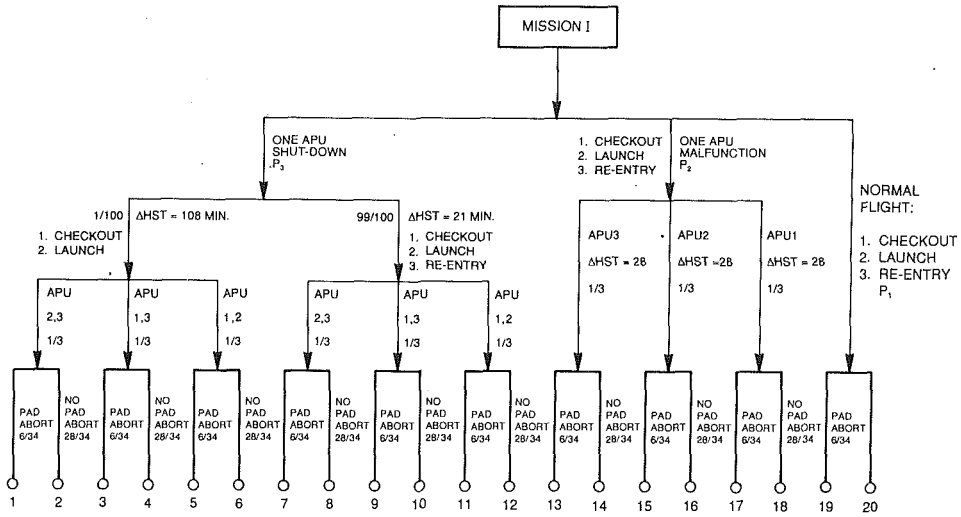


Fig. 8 Possible mission scenarios for Orbiter launches

conditions separately. At the current level of incremental flight risk, the code randomly selects a number from zero to one. The value of the number is then compared to the risk increment; if the number is smaller than the risk increment, then a blade separation has occurred; otherwise, no blade separation has occurred. The number of blade (wheel) separations is added over the fleet for each simulation. After a certain number of fleet mission simulations, the number of separations is divided by the number of simulations. The result is the fleet risk. In general, no blade separations will occur (corresponding to high component reliability). However, the random simulation process will cause separations at an average rate given by the component reliability model, based on the simulated flight exposures for each APU. The more simulations used, the higher will be the confidence in the final flight risk.

After each flight, the current levels of the HGS and HST values are compared to the user-defined working inspection limits (WIL). If the numbers exceed the limits, then the APU is pulled and replaced by the next available APU on the spares list. The pulled APU is inspected for cracks or separations. If a blade has failed or a crack greater than the 0.090 limit exists, then the wheel is scrapped. The number of scrapped wheels is counted. The probability of a scrapped wheel is computed by dividing that number of events by the number of simulations. The number of required inspections after each fleet is also stored and used to predict the likely inspection requirements.

Assessment of the presence or absence of long cracks (>0.090 in.) is based directly on existing wheel inspection records, and does not involve simulation or calculation of initiation/propagation rates. The inspection results identify, for each wheel, the total number of HGS accumulated at each inspection and the longest crack detected. For example, 17 wheels were shown to have endured at least ten hot gas starts without developing 0.090 in. cracks. On the other hand, seven wheels had developed one or more 0.090 in. cracks after 11 or more HGS, and no wheels were shown to survive more than 35 HGS without developing at least one 0.090 in. crack. At any given number of hot gas starts, the data base includes a certain quantity of wheels that have been shown to be free of long cracks and another quantity of wheels that have been shown to have developed such cracks (or to have developed such cracks at a lower number of hot gas starts). For the present simulation, the probability of a wheel having a 0.090 in. crack at any total number of HGS (this number was not reset after inspection) was calculated from the simple ratio involving the two quantities. A least-squares polynomial function was generated to describe the probability levels between the two extremes of 0 percent long cracks (10 HGS) and 100 percent long cracks (36 HGS).

Two confidence intervals are used in the analysis. The first concerns convergence of the Monte Carlo simulation results. The simulated risk from Monte Carlo is a best estimate; a confidence interval for the simulation indicates a range of risk that contains the actual risk, with the specified confidence. The simulation of the fleet risk for a complete Mission Plan scenario is repeated a number of times, to assure adequate convergence of the estimated number of blade separations that may be expected. The second confidence interval is to estimate an upper bound to the actual risk, with a specified confidence, recognizing that the fleet risk assessment parameters are not exact. Two variables dominate our uncertainty in the fleet risk assessment.

The first variable is the uncertainty in actual turbine wheel fatigue crack growth rate for the specific wheels in a given Orbiter. The approach used in the fleet risk assessment simulations has been to take the 95 percent lower bound on the characteristic material strength for the simulation, as defined in [1]. Thus the quoted fleet risk assessment levels conservatively include the lower bound on material strength. The second variable affecting the confidence interval is the uncertainty of the actual distribution of APU HGS parameters (including the effect of HST in the effective number of hot gas starts). For the purpose of the current simulations, the uncertainty in mean expected number of HGS/flight ($\mu = 2.57$) is treated by taking a 95 percent upper bound on HGSs as the new simulated mean value.

As a result of the fleet assessment, no force-pulling of APUs for turbine wheel inspection was required, in order to have better than 95 percent confidence that no blade separation would occur prior to the planned retirement of the original-design turbine wheels. It was found that the overall, expected number of failure events was much less than one. However, the simulations also showed that at least one of the APU turbine wheels would substantially exceed the required 0.001 level of part risk. Thus, the final application of flight limits, or their waiver, becomes a management issue, not a risk issue.

Summary

The turbine wheel cracking problem investigation showed the power and utility of systematic probabilistic risk assessment to a flight certification and safety resolution requirement. The use of probabilistic considerations allows for management of risk and logistics issues in a rational manner. However, real

Downloaded 02 Jun 2010 to 171.66.16.112. Redistribution subject to ASME license or copyright; see http://www.asme.org/terms/Terms_Use.cfm

crack initiation and propagation problems often do not lend themselves to purely analytical studies. The application of Weibull-Bayesian methods is a powerful way for establishing lower bounds to component risk, when the failure mode and scatter characteristics can be defined or estimated. Engineering judgment and statistical insight need to be applied in order to avoid undue conservatism in the result, thereby minimizing the cost impact of setting operational limits.

The high-cycle fatigue (vibration) problem is generally not suited to probabilistic modeling, such as done herein, because of the extremely high degree of scatter intrinsic to such problems. However, in this case, the cracks seem to trend toward crack arrest in a low cycle fatigue mode, due to a detuning of the resonance model. Such fortuitous conditions are not to be expected in the usual cases of high cycle fatigue.

Acknowledgments

The authors gratefully recognize the team effort that went into this important reliability study. Notable contributors from the staff of engineers at Sundstrand were Mr. Robert Guirl, Mr. Alistair Caldwell, and Mr. Paul Grout. Rockwell engineers were responsible as prime contractors of the Orbiter for both technical and direct financial support of some of this work, notably through Mr. Tibor Farkas. The principal sponsor of the work was NASA, represented by Mr. Walter Scott, APU subsystem manager. Weibull analysis of the cracking data for the turbine wheels was supported by Dr. Robert Mason and Ms. Janet Buckingham, both of Southwest Research Institute.

References

1 Hague, F. T., "Superposed Turbine Blade Research," *Mechanical Engineering*, Vol. 61, 1940, pp. 275–277.

2 Kroon, R. P., "Turbine-Blade Vibration Due to Partial Admission," ASME *Journal of Applied Mechanics*, Vol. 62, 1940, pp. A-161–A-165.

3 Pigott, R., "Turbine Blade Vibration Due to Partial Admission," *Int. J. Mechanical Sciences*, Vol. 22, 1980, pp. 247–264.

4 Abernathy, R. B., et al., *Weibull Analysis Handbook*, AFWAL-TR-83-2079, Air Force Wright Aeronautical Laboratories, 1983.

5 Nelson, W., "Weibull Analysis of Reliability Data With Few or No Failures," *Journal of Quality Technology*, Vol. 17, No. 3, 1985, pp. 140–146.

6 Besuner, P. M., "Probabilistic Fracture Mechanics," in: *Probabilistic Fracture Mechanics and Reliability*, Martinus Nijhoff, 1987, pp. 387–436.

7 Forman, R. G., "A Fracture Mechanics Study of the Turbine Wheel in the Space Shuttle Auxiliary Power Unit," *Theoretical and Applied Fracture Mechanics*, Vol. 3, 1985, pp. 71–84.

APPENDIX

Monte Carlo Simulation Details

The simulation begins by selecting a three-APU mission, which may be one of the three flight conditions. Each flight condition has an assigned probability based on actual experience to date, including a normal flight (P_1), an APU controller error, resulting in an inadvertant high-speed operation during launch with a specified duration (P_2), and an APU controller error (P_3) resulting in a single APU shut-down resulting in the other two APUs operating in the high-speed mode. Additionally, each mission must consider a random simulation of a pad abort after APU start, and the need for one APU to be started for on-pad check-out. The code selects the APU with the lowest current risk for the pad check-out, since this decision is an operationally controlled decision.

The risk level for each APU is estimated by using two major factors, which serve as index variables. These two variables are hot gas starts (HGS) and high-speed time (HST). The risk calculation considered uses the 95 percent confidence, lower-bound Weibull distribution of turbine wheel reliability, for both HGS and HST. Both Weibull distributions are constructed by Weibayes analysis and defined by shape parameter (β) and characteristic value (η).

The correlation between the risks (or crack growth) for HGS and HST is not known. To be conservative, the total computed risk will directly combine (add) the risk for each of these two types of failure. Therefore, the total fleet risk for the APU considered is the cumulative risk of original HGS plus the added risk for the high-speed time, starting at the level of risk that has been developed by the preceding HGS values. The risk of certain amounts of HST can be equated to the risk of some matching number of hot gas starts.

If a simulated failure occurs in the simulation, then that turbine wheel is not simulated again. Each wheel failure only counts once. The procedures for calculating the increment of risk due to the increments of HGS and HST for each wheel:

- Define initial risk state
- Determine the mission flight conditions for each APU
- Increment the risk for each APU, according to its flight parameters
- Select a value (U_i) from a uniform distribution
- Compare the individual APU risk value (R_i) to U_i
  - If $R_i \leq U_i$, then there is no failure;
  - If $R_i > U_i$, then a failure is predicted.
- Update the HGS, HST indices for each APU

After each mission, the current level of HGS and HST parameters is compared to the user-defined limit. If the number exceeds the limit, then turbine wheel inspection is required. The inspection findings are based on empirical data of crack size versus HGS and HST parameters. Based on these data, the probability of long crack (PLC) is constructed; if the crack is greater than 0.090 in. then the turbine wheel is counted as being withdrawn from service. The details of the inspection simulation include the following items:

- If the wheel has a predicted failure, the wheel is scrapped
- If the wheel is not failed, the crack length is simulated
  - Select the probability of a long crack (P_{lc})
  - Select a value from the uniform distribution (U_i)
  - Scrap the wheel if $P_{lc} > U_i$
- Inspect each wheel; replace scrapped wheels

The results of each mission are accumulated until an inspection is required. The data from the inspection findings are then used to accumulate the failure and scrappage statistics. The missions are incremented until the APU is pulled for turbine wheel replacement, or for turbine wheel inspection. Success is when an APU is able to fly the planned manifest of missions from its current state to its retirement state, without turbine wheel fracture, and without the need for an in-service inspection. If the risk is too high, then the inspection interval can be decreased by the user, until the risk of turbine wheel fracture is reduced to an acceptable level.

The code simulates each Orbiter, in terms of its installed APUs. The total risk is the total number of failures simulated for all vehicles, divided by the total number of simulations. Therefore, the total risk is averaged across the number of vehicles. The code will, however, show which vehicle and which APU is dominating the total, fleet risk. It is to be emphasized, however, that the actual risk in each APU simulation is only a 50 percent confidence result, or best estimate given the input data.

Downloaded 02 Jun 2010 to 171.66.16.112. Redistribution subject to ASME license or copyright; see http://www.asme.org/terms/Terms_Use.cfm

TMFSLAM—Design Analysis Tool for Coated Structures

G. S. Bechtel

R. L. McKnight

T. S. Cook

General Electric Aircraft Engines,
Cincinnati, OH 45215

Hot flowpath components in aircraft gas turbine engines are subject to a severe operating environment. The large thermal gradients can produce high thermal strains that, when combined with mechanical loads and a deleterious environment, can lead to premature failure. To combat this possibility, designers spend considerable time determining the stress and strain fields in these components as the parts undergo typical operating histories. These field quantities can then be used to determine failure parameters and determine life limiting locations. The field determinations can be difficult and, in combination with numerous potential failure mechanisms, the structural assurance process can take a considerable time to complete. To shorten this process, a personal computer (PC) based preliminary design system has been developed. This system, called Thermo-mechanical Fatigue—Structural Life Assessment Method (TMFSLAM), permits the user to rapidly evaluate the interactive effects of duty cycle, geometry, and materials on component life. The quantitative results determined by TMFSLAM will be available to make decisions on design changes, material substitution, etc.

Introduction

While the procedures and models developed in this investigation can be applied to any coated structure, the study has concentrated on hot section blades. These components are difficult to analyze for a number of reasons. Their geometry is complex with numerous curved surfaces, sharp corners, and cooling holes. Many blades are made of anisotropic materials and often have multiple coatings. The gas temperatures and heating rates are high enough to produce significant nonlinear material behavior. Finally, the manufacturing history can play an important role in determining the local response at some critical location.

The importance of accounting for the nonlinear material behavior can be seen by examining the cycle undergone by the blade. The cycle can be very complex, e.g., Fig. 1, with the high temperature producing significant nonlinear behavior in the structure. It is vitally important that this nonlinear deformation in both the coating(s) and the substrate be characterized. This was demonstrated in previous studies on coated blades by McKnight et al. (1982), Hillery et al. (1987), Swanson et al. (1987), and Heine et al. (1989). In the work of Hillery et al. (1987), coated specimens underwent pure thermal cycles (21–871–21°C) with a hold at maximum temperature. Analysis of the experiments showed that thermal expansion of the substrate caused creep of the coating, which caused cracking when the specimen was cooled. When a mechanical strain component is added to the thermal cycle, the magnitude and the phasing of the strain and temperature are important. For an out-of-phase cycle, where the maximum strain occurs at the minimum temperature, the low ductility coating can crack at the minimum temperature. The in-phase cycle, where the maximum strain and temperature occur together, can produce tensile creep of the coating; the accumulated creep can lead to a ductile failure mode.

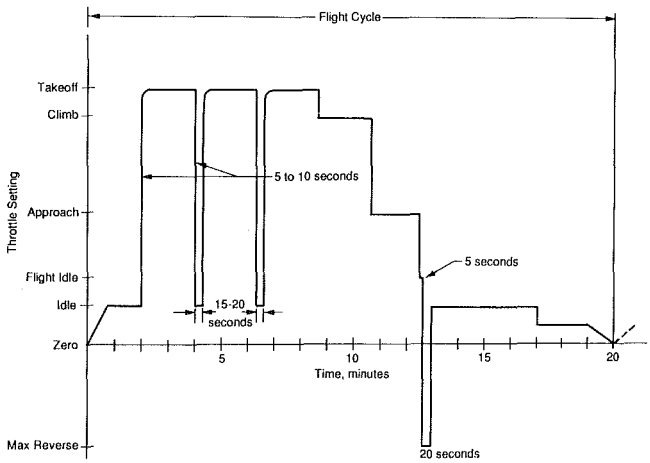


Fig. 1 Test cycle definition

In these initial studies, large three-dimensional finite element models were frequently employed. These models were time-consuming to build and quite expensive to run, although advances in computation technology have brought the costs down. Easier to use, simpler and faster tools were needed to do preliminary design and trade-off studies. One such effort was described by McKnight et al. (1991) as it applied the Hot Section Technology thrust sponsored by NASA. The current code, TMFSLAM, is an outgrowth of that work and is aimed at coated airfoils.

Analysis System Description

A major objective of the analysis system was to automate

Contributed by the International Gas Turbine Institute and presented at the 36th International Gas Turbine and Aeroengine Congress and Exposition, Orlando, Florida, June 3–6, 1991. Manuscript received at ASME Headquarters February 20, 1991. Paper No. 91-GT-141. Associate Editor: L. A. Riekert.

Copyright © 1992 by ASME
Downloaded 02 Jun 2010 to 171.66.16.112. Redistribution subject to ASME license or copyright; see http://www.asme.org/terms/Terms_Use.cfm

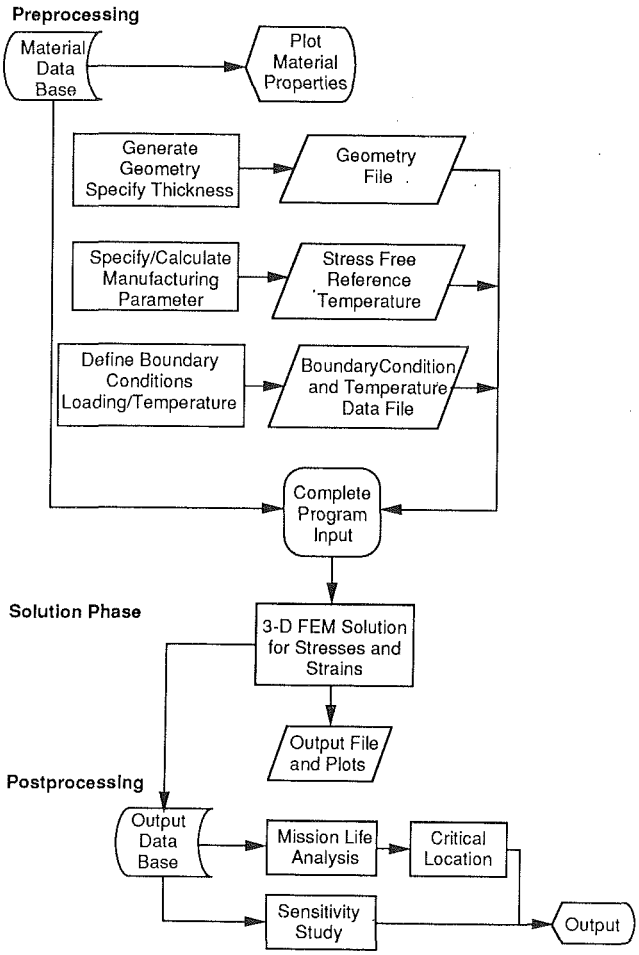


Fig. 2 TMFSLAM analysis system flow chart

the structural analysis as much as possible while leaving the user the option to vary inputs critical to the design process. Before discussing some specific features of the system, the overall scheme will be presented. Figure 2 gives the flow chart for the system and indicates the breakdown in preprocessing, solution and postprocessing phases.

The preprocessing routines are used to automate and check the input to the solution phase computer models. One such routine is used to generate a geometry file in a recipe-like manner, using a minimum number of key parameters, such as coating thicknesses, etc. Another routine is used to calculate various parameters associated with the manufacturing process, such as the stress-free reference temperature. Yet another routine is used to facilitate the designation of boundary conditions, and to assign a temperature distribution to the model. The combined output of these preprocessing routines was used as the input to the solution phase nonlinear finite element program.

The finite element models developed for the solution phase of this system are based on two different levels of analysis. The first level consists of relatively simple models that are built using the various preprocessing routines. All problem parameters, such as coating thicknesses, material properties, temperatures, etc., are easily input or modified. In this way, the effects of several key problem factors can be investigated in a fast and efficient manner.

The second level of analysis involves more complex user supplied geometries and boundary conditions. This allows the user to investigate the effects of more complicated geometries on coating systems. This includes the ability to model cooling holes, edges, and other stress concentrations.

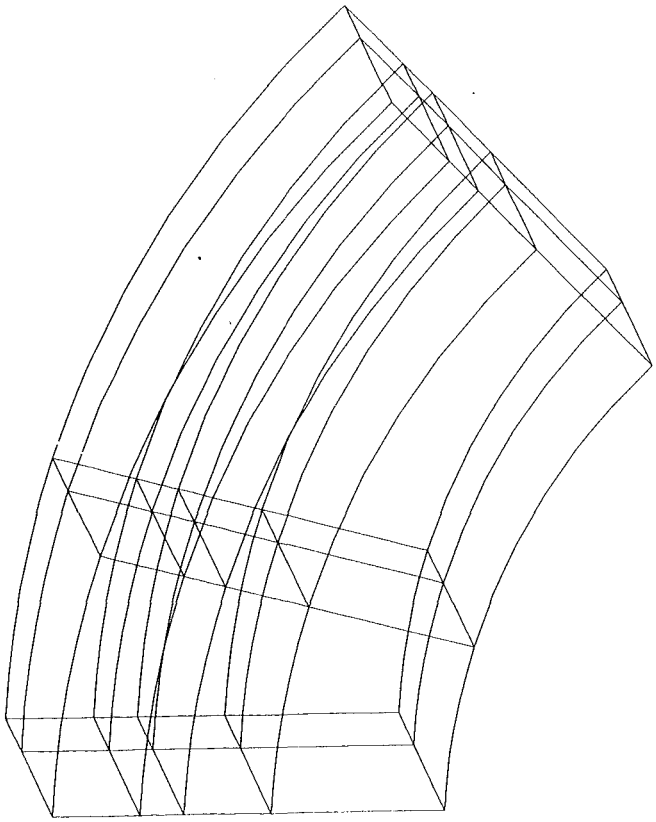


Fig. 3 One-eighth symmetry cylindrical tube finite element model

The 3D nonlinear finite element code used for both levels of analysis is a specially modified version of an existing 3D code already in use at GEAE. The program has been modified so that it can be run on the IBM PC-AT. Other modifications and enhancements include gauss point inelasticity calculations, and a number of new output options. The program is capable of simulating manufacturing processes such as high temperature coating application. Stress and strain output is written to both a printed output file, and to a special postprocessing file.

After the solution phase is complete, several postprocessing options are available. These options include determining critical locations, and making life predictions. It also is possible to accumulate the output of several analyses for parametric sensitivity studies.

Graphical display of both the input and the output further increases the usefulness of the programs.

Model Geometry

As just noted, the code can be operated with either the built-in "recipe" geometries, or with a user supplied geometry in the usual finite element method approach. In either case, the code uses 20 noded curved side isoparametric brick elements to model any curved sections. Multiple materials may be run to model the substrate, bond and top coat. However, because the system is PC based, the model is limited to 24 elements. This seemingly small number of bricks is capable of modeling quite complex geometries. With this limitation and because local geometry, coating strains, and duty cycle studies are of primary interest, five model geometry "recipes" have been included in the preprocessing routines. These geometries are a flat plate, a hollow cylinder, and three plate and hole geometries. A typical tube model is shown in Fig. 3, and a typical plate with hole model is shown in Fig. 4. These models provide the user with the ability to evaluate the strains in both the substrate and the coating for various duty cycles, etc. More-

Downloaded 02 Jun 2010 to 171.66.16.112. Redistribution subject to ASME license or copyright; see http://www.asme.org/terms/Terms_Use.cfm

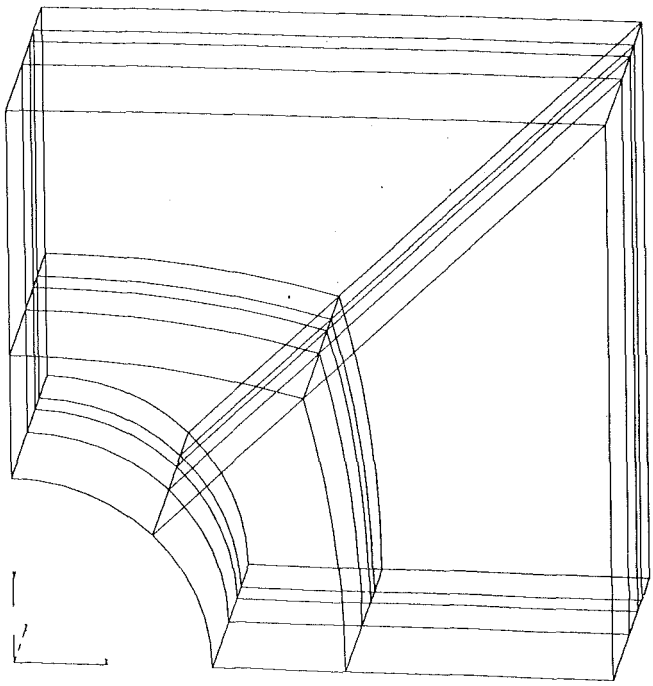


Fig. 4 One-quarter symmetry plate with hole finite element model

over, since these are well-tested geometries, the user can employ them with confidence that troublesome problems have been removed. For example, because the coating is always thin compared to the substrate, certain geometries can produce elements with very high aspect ratios. The built-in geometries contain constraints to prevent large differences in aspect ratios among the elements and any resulting numerical problems.

Finite Element Module

The key component in TMFSLAM is a finite element code especially adapted to the PC for the solution phase. This module is derived from the in-house code, CYANIDE, used for cyclic inelastic analysis. This code is based on the classical incremental plasticity theory, which utilizes the Prandtl-Reuss flow rule, the Von Mises yield criteria, and the kinematic hardening rule in the strain space as the constitutive model. Besseling's subvolume method (Besseling, 1953) is used within this constitutive framework. In the subvolume method, a strain-hardening material is considered as a composition of several subvolumes, each of which is an elastic-ideally plastic material. The subvolumes have identical elastic constants but different yield stresses. In the loading process beyond the elastic limit, the first subvolume is subjected to plastic deformation and other subvolumes may yield in sequence, depending on the severity of loading. It is noted that the yield surfaces in Besseling's model contact at a point with common tangency if the loading is proportional, but they can intersect each other in nonproportional loading (Cook et al., 1988).

The numerical scheme of the plasticity analysis used is the pseudo-force method in which the right-hand-side force vector is revised in the plasticity iterations. The equilibrium relation can be written as

$$[K]\{d\} = \{F\} + \{F_p\} \tag{1}$$

where

K is the elastic stiffness
d is the displacement
F is the applied force
F_p is the plastic force

The plastic force vector is updated in every iteration, but since the method does not require modification of the stiffness matrix in the plastic iterations, it is consequently very economical. However, if the temperature changes between loading steps, then the stiffness must be recomputed.

When the structure undergoes time-dependent deformation, the approach is essentially the same. A solution is done for each time step using an iterative technique to predict incremental creep strain components and revise the right side of the basic structural stiffness matrix equation by adding a plastic force vector to account for the creep effects

$$[K]\{d\} = \{F\} + \{F_{cp}\} \tag{2}$$

in a manner similar to that used in the Besseling technique for time-independent plasticity.

Material Data

The program requires a full complement of physical property, constitutive, and creep data in order to determine the behavior for a specified cycle. The literature was surveyed and data collected for several coatings as well as one isotropic and one anisotropic blade material. These data are incomplete, particularly for the anisotropic alloy and the coatings. Mechanical property data for free-standing coatings are difficult to obtain, with the result that data like creep properties are sketchy. Since the finite element code requires temperature interpolation of these properties, the available data have been censored to avoid inconsistencies. For other materials, real or hypothetical, property data input to the code must be complete enough to allow reasonable estimates of plastic and time-dependent behavior. Despite this, the existing data on coatings provide a framework for material development studies in which strength, stiffness, creep strength, etc., can be varied and the payoffs determined.

The stress and strain fields determined by TMFSLAM are intended to be used in a life prediction model. However, there is very little high temperature fatigue data available for coated materials. Studies on TMF of hot section materials have indicated that the hysteretic energy can be used to predict TMF life (Cook et al., 1988; Heine et al., 1989). TMFSLAM therefore calculates the inelastic work done in the cycle and supplies the result for each material. If experimental data are available, then the values could be used to predict life. In the event such data do not exist, and they likely would not in preliminary studies, it could still be used as a basis of comparison. It would be expected that the larger the inelastic work, the more damaging the cycle; thus those factors that cause this increase should be generally avoided.

Manufacturing History and Stress-Free Reference Temperature

Since most coatings are applied at high temperature, the thermal coefficient mismatch will produce a residual stress state in the system at the start of the duty cycle. The relatively low strength of the coatings makes it imperative that this starting point be known.

The concept of the stress-free reference temperature (Hillery et al., 1987) provides a simple method of incorporating the effects of processing history. The stress-free reference temperature for each material in a model is calculated so that the thermal growth of two different materials matches up at a "stress-free" temperature. Thus the stress-free reference temperature is a function of the analysis reference temperature, the thermal expansion coefficients of the different materials, and the stress-free temperature.

The stress-free temperature may be determined according to the coating process. Consider a simple process in which the base metal is heated up to some temperature, the molten coating material is applied to the base metal, and then they are cooled to room temperature. In this case, the stress-free temperature is the temperature of the base metal at which the

Downloaded 02 Jun 2010 to 171.66.16.112. Redistribution subject to ASME license or copyright; see http://www.asme.org/terms/Terms_Use.cfm

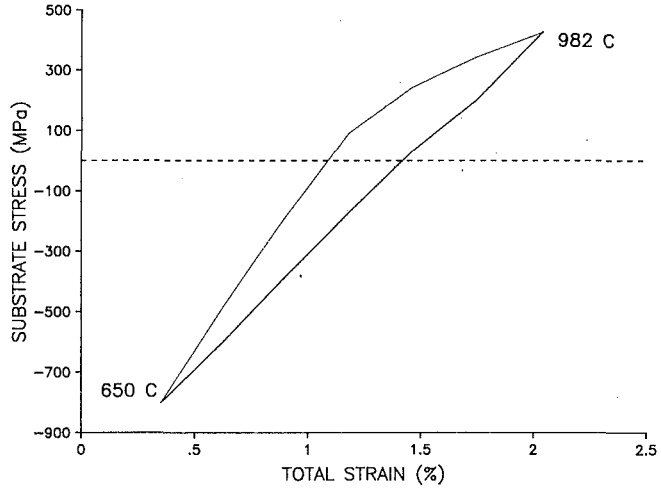


Fig. 5(*a*) Stress-strain response of René 80 during in-phase TMF cycle

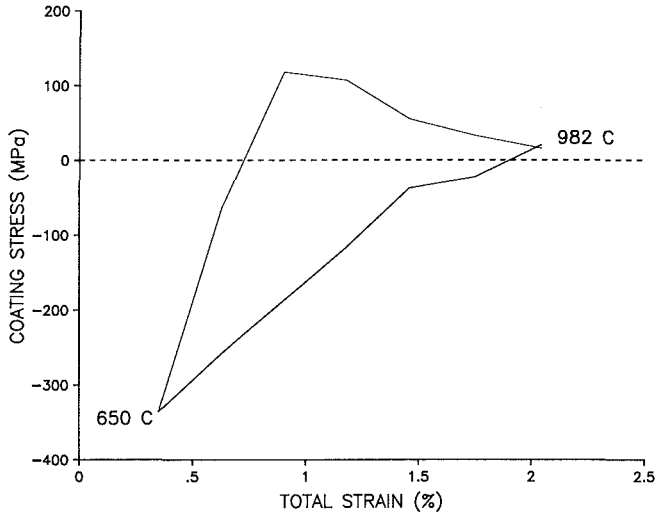


Fig. 5(*b*) Stress-strain response of aluminide coating during in-phase TMF cycle

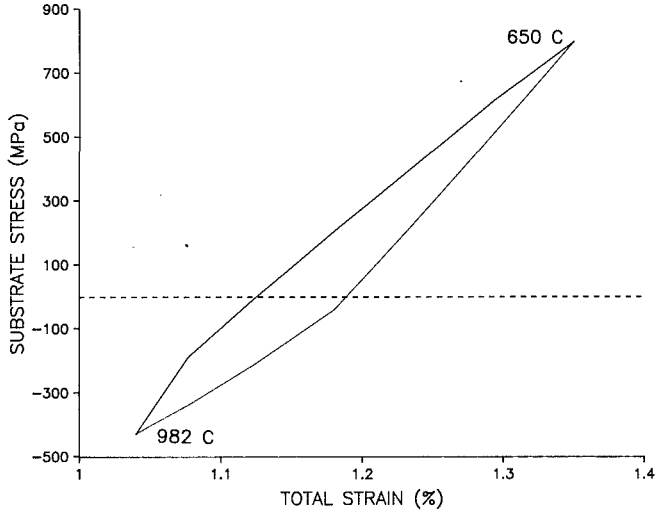


Fig. 6(*a*) Stress-strain response of René 80 during out-of-phase TMF cycle

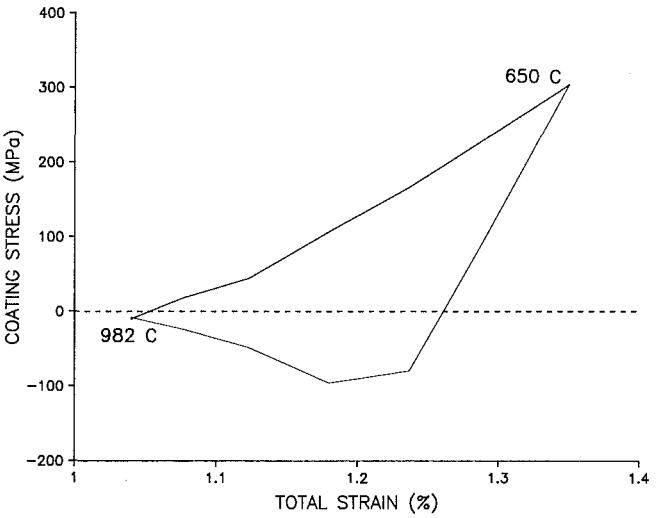


Fig. 6(*b*) Stress-strain response of aluminide coating during out-of-phase TMF cycle

coating material is applied. If the coating process ends with an annealing process that removes the residual stresses totally, then the stress-free temperature will be the annealing temperature.

Application of TMFSLAM

As an example of how this tool can be used, two simple TMF cycles were evaluated using the simple coated plate geometry model. The blade materials examined were a substrate of René 80 with an aluminide coating; the appropriate material data are contained within the code. The model was subjected to a thermal cycle of 650–982°C, and a mechanical strain of ±0.5 percent. Both an in-phase cycle, maximum strain at maximum temperature, and an out-of-phase cycle, maximum strain at minimum temperature, were run. The resulting stress-total strain cycles are shown in Figs. 5 and 6 for both the substrate and the coating. The hysteresis loop for the substrate is typical of a TMF test (Cook et al., 1988), and reflects primarily the effect of temperature on the modulus. The coating behavior is more complex and is the result of both the modulus and strength change with temperature. At high temperature, the coating is very weak and flows readily to accommodate the imposed strain. Note that for the in-phase cycle, during unloading, the material yields in compression until the increased stiffness of the coating material causes the coating to behave elastically. The coating loops are consistent with the failure pattern often seen in these materials. For the out-of-phase cycle, the high strain at the low temperature can exceed the limited ductility there and lead to premature cracking. For the in-phase cycle, the large tensile going plastic strain is primarily reversed elastically, leading to coating failure by either surface rippling or spallation.

A more complex cycle was derived from the flight envelop cycle of Fig. 1 and termed the squealer tip cycle. Using the same two materials, the biaxial strain and temperature cycle given in Table 1 is applied. Figures 7 and 8 give the Von Mises effective stress in the two materials under the constitutive assumptions of elastic, elastic-plastic, and elastic-plastic-creep. (Since the application is multiaxial, the effective stress was chosen to illustrate the results.) The figures demonstrate the large effect that the inclusion of inelastic effects have on the effective stress. The high temperature at the start of the cycle produces creep in the substrate but the lower temperatures render the rest of the cycle creep-free. In the coating, however, the low strength at high temperature allows the coating to flow under stress and results in virtually no creep during this cycle.

A hold time at maximum temperature was added to the initial loading in the squealer tip cycle (load step 4 in Table 1). The additional deformation during the hold lowers the effective stress compared to the baseline cycle as shown in Fig. 9. How-

Downloaded 02 Jun 2010 to 171.66.16.112. Redistribution subject to ASME license or copyright; see http://www.asme.org/terms/Terms_Use.cfm

Table 1 Blade squealer tip cycle

Load Case	Time Step (hours)	Temperature (°C)	Total Mechanical Strains ε-xx (%)	ε-yy (%)	ε-xy (%)
1	0	343	0.000	0.000	0.000
2	0.002	1038	-0.285	0.101	0.000
3	0.002	982	-0.255	0.089	0.000
4	0.0125	1093	-0.293	0.106	0.000
5	0.060	1071	-0.280	0.101	0.000
6	0.060	343	0.025	-0.008	0.000
7	0.060	704	-0.060	0.020	0.000
8	0.060	343	0.000	0.000	0.000

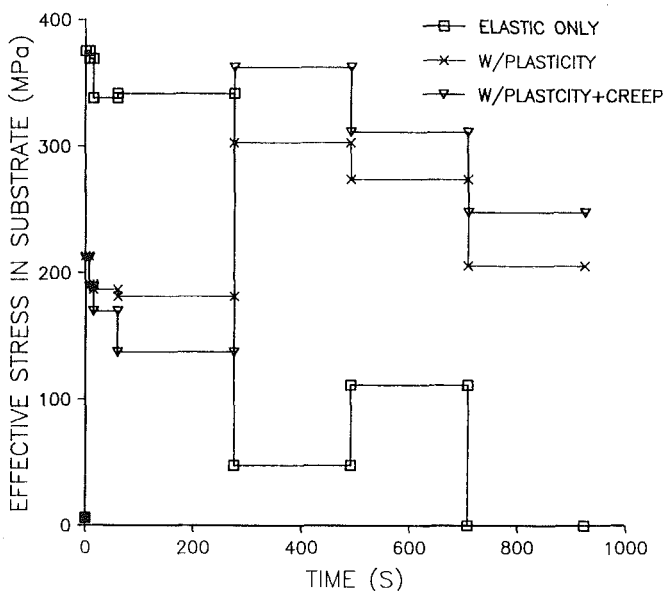


Fig. 7 Effect of constitutive model on stress in René 80 during squealer tip cycle

ever, when the load is reversed, the effective stress in the hold-time cycle is higher.

TMFSLAM provides a fast and easy approach to determining the effect of constitutive properties and cycle shape on stresses in the components. In addition, the importance of other parameters, such as coating application temperature, coating thickness, and cooling hole diameter, can be quickly evaluated. Coating application temperature was found to have a major impact on the thermal mismatch strains and therefore the inelastic work done during the initial cycles. The effect of hole diameter is well known, but when redistribution due to creep and plasticity is included, it is possible to obtain a detailed picture of the deformation fields at these critical locations. The designer is then able to make judgments about the trade-offs in high temperature properties and their impact on TMF life.

One aspect of coating life prediction that the recipe models cannot handle is coating edge effects. In the analysis of thermal barrier coating (Hillery et al., 1987), coating thickness was found to be an important factor in coating life; thicker coatings produced higher stresses at the edge of the coating substrate interface. When coating thickness was varied in one of the simple plate models, no effect was noted. In order to model the thickness interface, the interface and edge would have to be modeled with specific geometry created by the user the input into TMFSLAM. This points out that the careful user will examine key parameters using different model geometries. Important effects can be overlooked if an inappropriate geometry is selected to evaluate the variable.

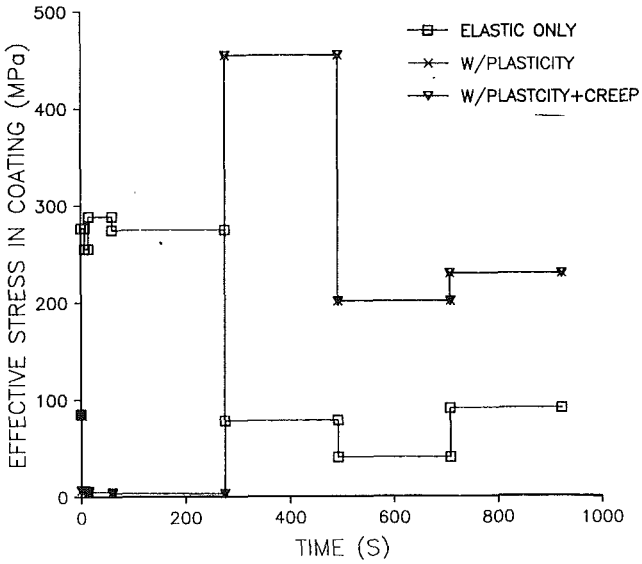


Fig. 8 Effect of constitutive model on stress in aluminide coating during squealer tip cycle

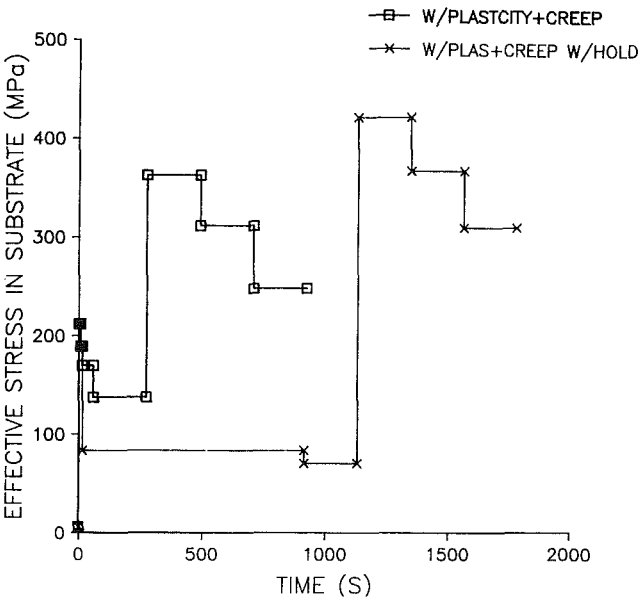


Fig. 9 Effect of constitutive model on stress in René 80 during squealer tip cycle with hold time

Summary

TMFSLAM is an example of the codes being developed to improve productivity and reduce development time. These efforts in "concurrent" engineering provide the designers with tools to quickly evaluate and optimize the interactive effects of duty cycle, mechanical parameters, manufacturing processes, and material variables. By allowing the user to evaluate these interactions in simple as well as complex geometries on a PC, significant reductions in engineering and development time can be achieved. However, like all tools, TMFSLAM must be used carefully and the results subjected to critical judgment. As explained, certain variables will be more important in some geometries than others. The benefits of speed and productivity are available to the user but the results must be evaluated critically.

Acknowledgment

This work was conducted under Contract N62269-88-C-0208,

Downloaded 02 Jun 2010 to 171.66.16.112. Redistribution subject to ASME license or copyright; see http://www.asme.org/terms/Terms_Use.cfm

for the Naval Air Development Center. The authors gratefully acknowledge this support.

References

Besseling, J. F., 1953, "A Theory of Plastic Flow for Anisotropic Hardening in Plastic Deformation of an Initially Isotropic Material," Report S. 410, National Aeronautical Research Institute, Amsterdam.

Cook, T. S., Kim, K. S., and McKnight, R. L., 1988, "Thermal Mechanical Fatigue of Cast René 80," Low Cycle Fatigue, ASTM STP 942, H. D. Solomon, G. R. Halford, L. R. Kaisand, and B. N. Leis, eds., *American Society for Testing and Materials*, Philadelphia, PA, pp. 692–708.

Heine, J. E., Warren, J. R., and Cowles, B. A., 1989, "Thermal Mechanical Fatigue of Coated Blade Materials," WRDC-TR-89-4027.

Hillery, R. V., Pilsner, B. H., McKnight, R. L., Cook, T. S., and Hartle, M. S., 1987, "Thermal Barrier Coating Life Prediction Model Development," NASA CR-180807.

McKnight, R. L., Laflen, J. H., and Spamer, G. T., 1982, "Turbine Blade Tip Durability Analysis," NASA CR-165268.

McKnight, R. L., Cook, T. S., Bechtel, G. S., and Huang, H. T., 1991, "Application of HOST Technology to the SSME HPFTP Blade," ASME JOURNAL OF ENGINEERING FOR GAS TURBINES AND POWER, Vol. 113, pp. 140–144.

Swanson, G. A., Linask, I., Nissley, D. M., Norris, P. P., Meyer, T. G., and Walker, K. P., 1987, "Life Prediction and Constitutive Models for Engine Hot Section Anisotropic Materials," NASA CR-179594.

Downloaded 02 Jun 2010 to 171.66.16.112. Redistribution subject to ASME license or copyright; see http://www.asme.org/terms/Terms_Use.cfm

HITCAN for Actively Cooled Hot-Composite Thermostructural Analysis

C. C. Chamis

P. L. N. Murthy

NASA Lewis Research Center,
Cleveland, OH 44135

S. N. Singhal

J. J. Lackney

Sverdrup Technology, Inc.,
Cleveland, OH 44142

A computer code, HITCAN (High Temperature Composite Analyzer) has been developed to analyze/design hot metal matrix composite structures. HITCAN is a general purpose code for predicting the global structural and local stress-strain response of multilayered (arbitrarily oriented) metal matrix structures both at the constituent (fiber, matrix, and interphase) and the structure level and including the fabrication process effects. The thermomechanical properties of the constituents are considered to be nonlinearly dependent on several parameters, including temperature, stress, and stress rate. The computational procedure employs an incremental iterative nonlinear approach utilizing a multifactor-interaction material behavior model, i.e., the material properties are expressed in terms of a product of several factors that affect the properties. HITCAN structural analysis capabilities (static, load stepping—a multistep static analysis with material properties updated at each step, modal, and buckling) for cooled hot structures are demonstrated through a specific example problem.

Introduction

High-temperature metal matrix composites (HT-MMCs) have shown potential as structural materials for 21st century propulsion systems. The thermomechanical properties of HT-MMCs vary nonlinearly with respect to such parameters as temperature, stress, and stress rate. This nonlinear material behavior may alter the structural response significantly. Since experimental investigations are usually high in cost, computational models that include nonlinear material behavior simulating the real-life response of components made from HT-MMC materials are required.

The need for developing analysis models at all levels of composite construction (i.e., fiber/matrix/interphase, ply, laminate) for multilayered fibrous composites was recognized almost two decades ago. Based on this need, multilevel analysis computer codes have since been developed to simulate multilayered fibrous composite behavior computationally. Research related to various aspects of HT-MMC materials and structures has been conducted at the Lewis Research Center of the National Aeronautics and Space Administration (NASA) for several years. Building upon parts of this research effort, a high-temperature composite analyzer code HITCAN has been developed [1].

The objective of this paper is to summarize HITCAN's capabilities with a specific illustrative example, which demonstrates its application versatility and suitability for the thermostructural analysis of actively cooled hot structures.

Contributed by the International Gas Turbine Institute and presented at the 36th International Gas Turbine and Aeroengine Congress and Exposition, Orlando, Florida, June 3-6, 1991. Manuscript received at ASME Headquarters February 20, 1991. Paper No. 91-GT-116. Associate Editor: L. A. Riekert.

HITCAN Capabilities/Description

HITCAN capabilities include prediction of global structural and local stress-strain response of multilayered high-temperature metal matrix composite structures. It can also be used for modal and buckling analyses. Each layer of the composite can be of different material and can be arbitrarily oriented.

The current version of the code can handle a large number of layers. HITCAN is primarily designed for metal matrix composites. However, it can be readily adapted for other composites as well.

In general, the analysis capabilities of HITCAN are primarily governed by those of its constituent module codes, MHOST [2], METCAN [3], and a dedicated mesh generator adapted from COBSTRAN [4].

MHOST is capable of handling standard two- and three-dimensional, beam, and shell finite elements, many types of boundary conditions, most types of loadings (e.g., concentrated, distributed, pressure, temperature, static, transient, cyclic, and impact), anisotropic composite materials, elastic and inelastic analyses, eigenvalue extraction for buckling and modal analyses. These capabilities have been demonstrated for various types of structures (such as beam, plate, ring, curved panel, and built-up structures; i.e., structures made of a combination of several different types of geometries). METCAN is capable of modeling thermomechanical properties as multifactor-interaction functions of temperatures, stress, stress rate, etc. METCAN treats material nonlinearly at the constituent level. COBSTRAN is capable of modeling both linear and curved geometries using cubic spline interpolators in rectilinear coordinates.

A special feature of HITCAN is its dedicated database for available fiber/matrix/interphase constituents of current in-

Copyright © 1992 by ASME
Downloaded 02 Jun 2010 to 171.66.16.112. Redistribution subject to ASME license or copyright; see http://www.asme.org/terms/Terms_Use.cfm

Table 1 HITCAN capabilities for composite materials

Type of Analysis \ Type of Structure	Beam	Plate	Ring	Curved Panel	Built-up Structure
Static	*tested*	*tested*	*tested*	*tested*	*tested*
Buckling[(a)]	*tested*	*tested*	*tested*	*tested*	*tested*
Load Stepping	*tested*	*tested*	*tested*	*tested*	*tested*
Modal[(b)]	*tested*	*tested*	*tested*	*tested*	*tested*
Time-domain	-	-	-	-	-
Loading					
Mechanical	*tested*	*tested*	*tested*	*tested*	*tested*
Thermal	*tested*	*tested*	*tested*	*tested*	*tested*
Cyclic	-	-	-	-	-
Impact	-	-	-	-	-
Constitutive Models					
P = Constant	*tested*	*tested*	*tested*	*tested*	*tested*
P = f(T) (temp. dep.)	*tested*	*tested*	*tested*	*tested*	*tested*
P = f(σ) (stress dep.)	*tested*	*tested*	*tested*	*tested*	*tested*
P = f($\dot{\sigma}$) (stress rate dep.)	*tested*	*tested*	*tested*	*tested*	*tested*
P = f(t) (creep)	-	-	-	-	-
P = f(T,σ, $\dot{\sigma}$) (combination)	*tested*	*tested*	*tested*	*tested*	*tested*
P = f(T,σ, $\dot{\sigma}$, t)	-	-	-	-	-
Fiber Degradation	*tested*	*tested*	*tested*	*tested*	*tested*
Fabrication Stresses	*tested*	*tested*	*tested*	*tested*	*tested*
Ply Orientations[(c)]					
Arbitrary	*tested*	*tested*	*tested*	*tested*	*tested*

(a) Tested 1 buckling mode

(b) Tested 4 vibration modes

(c) Tested 3 ply orientations:
Unsymmetric: (0/+45/90)
Symmetric: $(0/45)_s$
Balanced: $(0/90)_s$

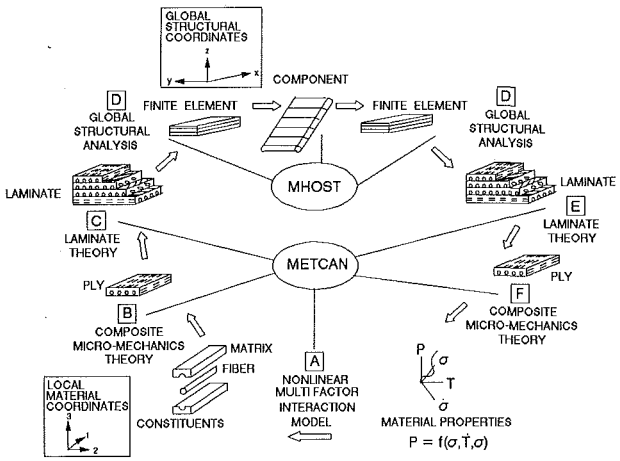


Fig. 1 HITCAN: an integrated approach for high-temperature composite structural analysis

Table 2 Constituent material properties at unstressed reference temperature (70°F)

SiC Fiber		Ti-15-3-3-3 Matrix	
ρ_f	0.11 lb/in^3	ρ_m	0.172 lb/in^3
E_f	62 Mpsi	E_m	12.3 Mpsi
ν_f	0.3 in/in	ν_m	0.32 in/in
G_f	23.8 Mpsi	G_m	4.7 Mpsi
α_f	1.8x10^{-6} in/in-°F	α_m	4.5x10^{-6} in/in-°F
T_{Mf}	4870 °F	T_{Mm}	1800 °F
S_{f11T}	500 ksi	S_{mT}	130 ksi
S_{f11C}	650 ksi	S_{mC}	130 ksi
S_{f22T}	500 ksi	S_{mS}	91 ksi
S_{f22C}	650 ksi		
S_{f12s}	300 ksi		
D_f	5.6 mils		

Conversion Factors for SI units:

1 lb/in^3 = 0.2714 MN/m^3
1 psi = 6.895x10^3 N/m^2
1 mil = 0.0254x10^{-3} m
°F = 1.8 °C + 32

Notation:

D: Fiber Diameter
E: Elastic Modulus
G: Shear Modulus
S: Strength
T: Temperature
ρ: Density
ν: Poisson's Ratio
α: Coefficient of Thermal Expansion

Subscripts:

C: Compression
f: Fiber
M: Melting
m: Matrix
s: Shear
T: Tension
11: Direction 11 along the fiber direction
22: Direction 22 transverse to the fiber
12: Direction 12 (shear)

Table 3 Exponents used for multifactor-interactive material behavior models (material: SiC/Ti 15-3-3-3)

Material Properties	Factors Affecting Material Properties					
	Temperature		Stress		Stress Rate	
	Matrix	Fiber	Matrix	Fiber	Matrix	Fiber
Moduli	0.5	0.25	0.5	0.25	0.5	0.25
Poisson's Ratios	0.5	0.25	0.5	0.25	0.5	0.25
Strengths	0.5	0.25	0.0	0.0	0.5	0.25
Thermal Expansion Coefficients	0.5	0.25	0.0	0.0	0.5	0.25

terest to hot structures applications. The user needs to specify only a code name of the constituents input. HITCAN automatically searches, selects, and updates the appropriate properties from its database. A list of materials and their properties for the materials coded in the HITCAN database can be found in [3]. The database includes graphite, boron, silicon carbide, and tungsten fibers, and aluminum, titanium, copper, magnesium, and beryllium matrix materials.

The current version of HITCAN includes most (but not all) features of MHOST and METCAN. Work is continuing on including more features into HITCAN. Table 1 lists HITCAN features. The features that have been demonstrated through example problems [1] are marked "tested" in italic letters in Table 1. Although the enhancement of the code continues, in its current form, it is applicable to a wide variety of composite thermostructural analysis problems.

The source code HITCAN consists of about 10,000 FOR-

Downloaded 02 Jun 2010 to 171.66.16.112. Redistribution subject to ASME license or copyright; see http://www.asme.org/terms/Terms_Use.cfm

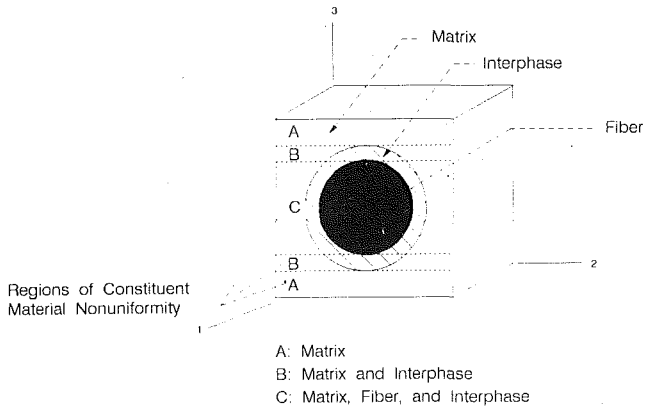


Fig. 2 Schematics for regions of constituent material nonuniformity

TRAN statements. The accompanying codes METCAN and MHOST are comprised of about 7000 and 50,000 statements, respectively. Complete documentation of HITCAN including theoretical developments, user's manual, and demonstration manual are expected to be available in the near future. Figure 1 shows the approach used by HITCAN for analyzing composite structures. The left part of Fig. 1 depicts the determination of laminate properties based on known constituent properties. The top part depicts the finite element analysis, which provides the structural response at the laminate level. The right part shows the decomposition of the structural response at the constituent level. Finally, the bottom left part shows the updating of constituent material properties. This is accomplished by using: (1) the multifactor-interaction equation in METCAN, (2) input parameters from Table 2 and 3, and (3) calculated constituent stresses in selected regions as shown in Fig. 2.

HITCAN accomplishes the approach shown in Fig. 1 by calling upon: (1) the model (mesh) generator, (2) the finite element code MHOST, and (3) the multilevel material behavior code METCAN. HITCAN manages the flow of information between MHOST and METCAN. It also serves the function of transforming the input-output between MHOST and METCAN to the desired form. The flow-chart in Fig. 3 shows the major computational procedure steps, in the order in which they are executed by the code. A brief description of the approach follows.

Step 1. Finite Element Model Generation. HITCAN generates a finite element model of the structure, based on coordinates of a few representative points. This is accomplished by interpolators coded in HITCAN. The temperature and pressure loadings are also input only at the representative points, to be interpolated for the rest of the model automatically by the code. Notice that the finite elements are at the laminate level but the material properties input in step 1 are at the constituent materials level.

Step 2. Constituent Material Property Generation. Based on reference constituent material properties available at the end of Step 1, METCAN generates constituent material properties including an interactive dependence on parameters such as temperature, stress, and stress rate before the next load step (see multifactor-interaction equations in [3]). This step is illustrated through the item A, marked in boxed letter in Fig. 1.

Step 3. Laminate Material Property Generation. The material properties available at the end of Step 2 need to be converted to those at the laminate level before conducting the finite element analysis. METCAN accomplishes Step 3 by using

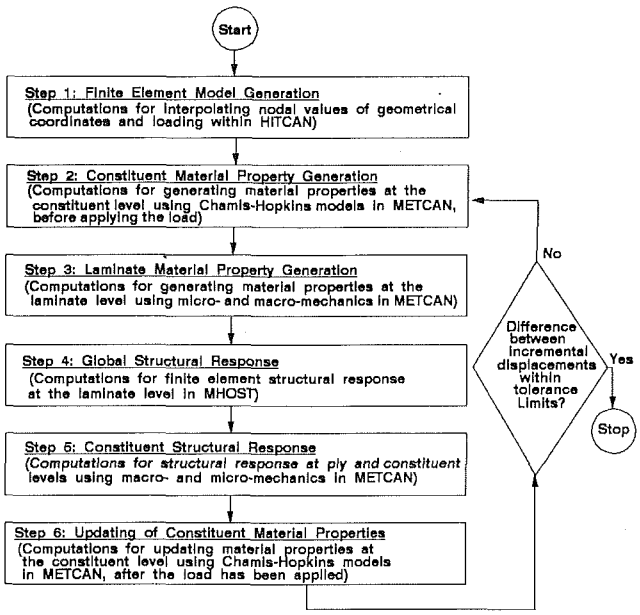


Fig. 3 Flow chart for HITCAN computational procedure

micro- and macromechanics theories. This step is illustrated through items B and C, marked in boxed letters in Fig. 1.

Step 4. Global Structural Response. All information necessary for the global finite element structural analysis becomes available at the end of Step 3. MHOST accomplishes Step 4 by calculating the structural response at the laminate level. This step is illustrated by the item D, marked in boxed letter in Fig. 1.

Step 5. Constituent Structural Response. Based on laminate structural response calculated in Step 4, METCAN calculates the ply and constituent level structural response using macro- and micromechanics theories, shown by items E and F, marked in boxed letters in Fig. 1.

Step 6. Updating of Constituent Material Properties. Since the constituent material properties depend on calculated constituent stress response, which, in turn, depends on constituent material properties, an iterative scheme is used to obtain both the structural response and material properties which are compatible with each other. For a specific load step, the ply level response (strains) and structure level response (strains at nodes) are compared at the end of each iteration with the response at the end of the previous iteration. Notice that the ply level response is in the local materials coordinate system, whereas the structure level response is in the global structural coordinate system. Figure 1 shows both of these coordinate systems. If the difference in the response for two consecutive iterations is within a predetermined tolerance level, it is assumed that the solution has reached a satisfactory level of convergence. This step is illustrated through a diamond-shaped block in Fig. 3.

Additional Capabilities. Additional features such as fiber degradation and fabrication-induced stresses have been incorporated in the computational procedure. Fiber degradation is accounted for by decreasing the diameter of the fiber based on a user-specified fraction of the original fiber diameter. This creates an interphase, of a specified thickness, between the fiber and matrix. The stresses during fabrication are calculated by defining the cool down process from the consolidation temperature to reference temperature as a specified load history added prior to the application of actual loads.

Downloaded 02 Jun 2010 to 171.66.16.112. Redistribution subject to ASME license or copyright; see http://www.asme.org/terms/Terms_Use.cfm

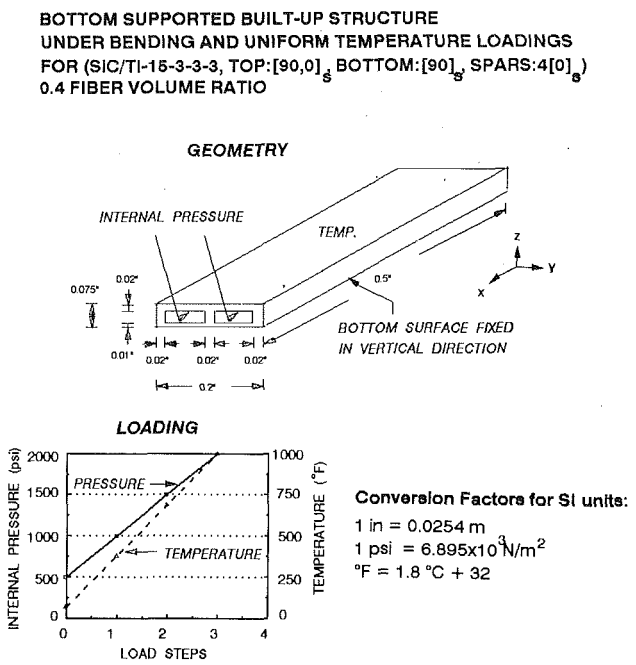


Fig. 4 Geometry and loading for built-up structure

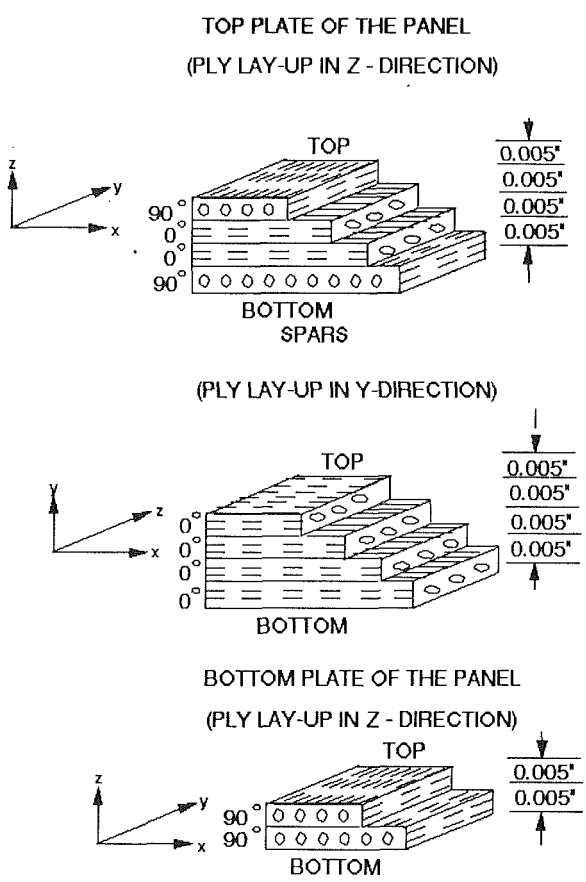


Fig. 5 Ply lay-ups for the built-up structure; conversion factors for SI units: 1 in. = 0.0254 m

HITCAN Demonstration

HITCAN capabilities have been demonstrated through illustrative examples for five types of structures [1]. Four of these represent basic geometries that are the building blocks of most structures of practical interest. They are beam, plate, ring, and curved panel. The fifth one is a built-up structure. Several types of analyses, marked "tested" in italics in Table 1, were conducted for each type of structure. The analyses tested include static, buckling, modal, and nonlinear load stepping. The load stepping analysis consists of multistep static analysis with material properties updated at each step. All analyses were based on multilevel interactive material behavior. The sensitivity of structural response to various parameters was determined by repeating the load stepping analysis for various forms of multifactor-interaction constitutive models, for various ply orientations, and for various additional features including fiber degradation and fabrication-induced stresses. Reference [1] includes results for all these cases. The results for buckling, load stepping, and sensitivities analysis for the built-up structure are summarized herein. These results include all the responses required to assess the adequacy of a design, in general.

The geometry and loading conditions for the built-up structure are shown in Fig. 4. The built-up structure is made of two horizontal plates at top and bottom, joined by three vertical spars. The material chosen is SiC/Ti 15-3-3-3 (where SiC stands for silicon carbide fiber and Ti 15-3-3-3 for an alloy of titanium with 15 percent vanadium, 3 percent aluminum, 3 percent chromium, and 3 percent tin). This material was chosen because it is being considered as a viable candidate for some of the high temperature applications associated with the National Aerospace Plane (NASP). The material properties of SiC fiber and Ti 15-3-3-3 matrix, in the unstressed reference state, are given in Table 2. In all cases, the reference temperature was 70°F both for material properties and thermal loading, the fiber volume ratio was 0.4, the laminate consisted of four-ply layer top surface, two-layer bottom surface, and four-layer spars. The finite element was a four-node isoparametric shell element with six degrees of freedom per node, and the exponents used for the multifactor-interaction constitutive material behavior model are given in Table 3. The ply orientations were chosen to be a $(90/0)_s$ top surface, $(90)_s$ bottom surface, and 4(0) spars. The first ply is at the top surface and the last ply is at the bottom surface. The ply orientation of 0 deg means fibers oriented in the x direction. Other, i.e., nonzero, orientations represent fibers oriented at the specified angle of rotation with respect to x axis toward the y axis. The ply orientations for the top and bottom plates and spars are shown in Fig. 5.

The buckling results are shown in Fig. 6 for the three different load conditions (mechanical load, mechanical load with 10 percent fiber diameter degradation, and combined thermal and mechanical loads). The results demonstrate the HITCAN capability for this type of thermostructural analysis. They indicate that temperature degrades the buckling resistance of this built-up structure by almost 10 percent.

The results for the load stepping analysis are summarized in Fig. 7 where two natural frequencies, the displacement at a select point and the stresses in a specific ply as well as in the constituents (regions, A, B, and C are depicted in Fig. 2) are shown. A wealth of information is in this figure: (1) The two frequencies are relatively close together and degrade with degrading material properties, (2) the displacement increases slightly nonlinearly with linearly increasing load, (3) the stresses in the constituent remain mainly nonlinear except for the interphase where failure (transverse stress) is indicated beyond load step 1.

The collective results in Fig. 7 demonstrate the versatility and detail depth that the HITCAN capabilities provide for the thermal/structural analysis of aerospace structures. Although results are not shown here for actively cooled hot structures,

Downloaded 02 Jun 2010 to 171.66.16.112. Redistribution subject to ASME license or copyright; see http://www.asme.org/terms/Terms_Use.cfm

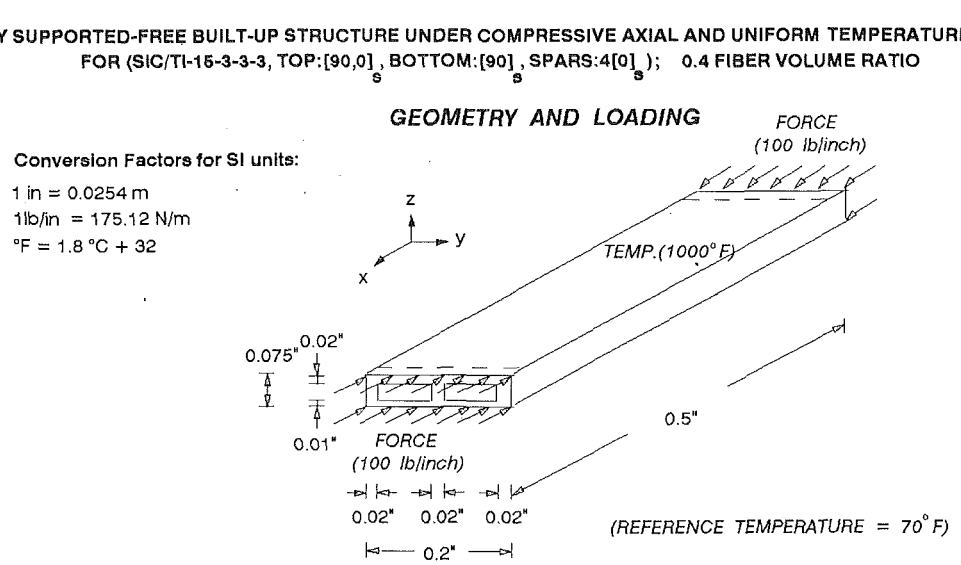


Fig. 6 Buckling analysis for built-up structure under thermomechanical loading

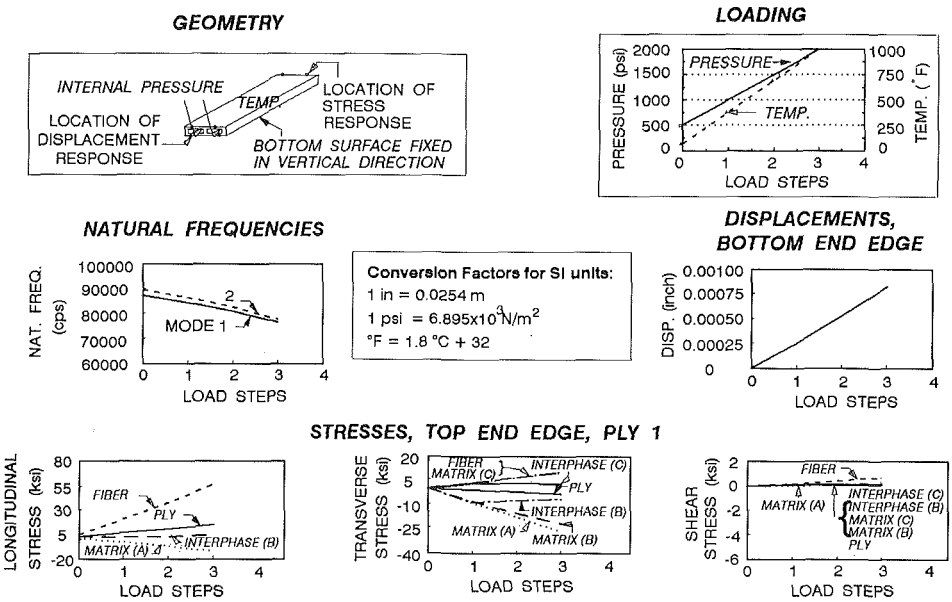


Fig. 7 Base case results for built-up structure

it is apparent that they can be handled once the coolant pressure and temperature profiles are known.

The effects of fiber degradation, fabrication-induced stresses, and material behavior (sensitivity analysis) on displacement and ply stresses at load step 3 are summarized in Fig. 8. The fabrication-induced stresses and temperature have generally the most effect on ply stresses and displacements for the specific built-up structure. The temperature and applied load stress effects are graphically illustrated in Fig. 9. As can be seen, the temperature effect dominates for the sample problem shown here.

Conclusions

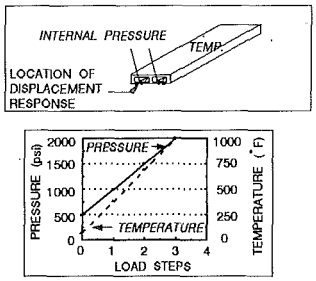
The capabilities of a high-temperature composite analyzer code, HITCAN, have been demonstrated. HITCAN was developed for performing most of the typical structural analysis tasks for designing with multilayered metal matrix composites. It employs multifactor-interaction constitutive material behavior models. It includes additional features such as fiber degradation and fabrication-induced stresses. Because of the multilevel analysis approach, HITCAN has the utility for studying the influence of individual constituent in-situ behavior on global structural response. Several features of HITCAN

Downloaded 02 Jun 2010 to 171.66.16.112. Redistribution subject to ASME license or copyright; see http://www.asme.org/terms/Terms_Use.cfm

BOTTOM SUPPORTED BUILT-UP STRUCTURE UNDER BENDING AND UNIFORM TEMPERATURE LOADINGS
FOR (SIC/TI-15-3-3-3, TOP:$[90,0]_s$, BOTTOM:$[90]_s$, SPARS:$4[0]_s$); 0.4 FIBER VOLUME RATIO

RESPONSE: AT LOAD STEP 3

GEOMETRY AND LOADING



CONSTITUTIVE RELATIONSHIPS

(NONLINEAR MULTI-FACTOR INTERACTION MODEL)

RELATIONSHIP	DISP. [BOTTOM END EDGE] (inch)	STRESSES, PLY 1 [TOP END EDGE] (ksi)		
		LONGITUDINAL	TRANSVERSE	SHEAR
$P \simeq$ CONSTANT	0.000710	15.2	-2.6	0.1
$P = f(T)$ TEMP. DEPENDENCE	0.000828	16.4	-3.6	1.0
$P = f(\sigma)$ STRESS DEPENDENCE	0.000707	14.3	-2.4	0.1
$P = f(\dot{\sigma})$ STRESS RATE DEPENDENCE	0.000710	15.2	-2.6	0.1
$P = f(T, \sigma, \dot{\sigma})$ COMBINATION	0.000823	15.2	-3.3	0.1

NOTATION:
P = MATERIAL PROPERTY *T = TEMPERATURE*
σ = STRESS *σ̇ = STRESS RATE*

FABRICATION-INDUCED STRESSES

FABRICATION-INDUCED STRESSES	DISP. [BOTTOM END EDGE] (inch)	STRESSES, PLY 1 [TOP END EDGE] (ksi)		
		LONGITUDINAL	TRANSVERSE	SHEAR
NO	0.000823	15.2	-3.3	0.1
YES	0.000420	12.2	0.5	0.02

FIBER DEGRADATION

DEGRADATION	DISP. [BOTTOM END EDGE] (inch)	STRESSES, PLY 1 [TOP END EDGE] (ksi)		
		LONGITUDINAL	TRANSVERSE	SHEAR
NO	0.000823	15.2	-3.3	0.1
YES	0.000886	14.4	-2.6	0.1

Fig. 8 Sensitivity analysis for built-up structure; conversion factors for SI units: 1 in. = 0.0254 m; 1 psi = 6.895 × 10^3 N/m^2; °F = 1.8°C + 32

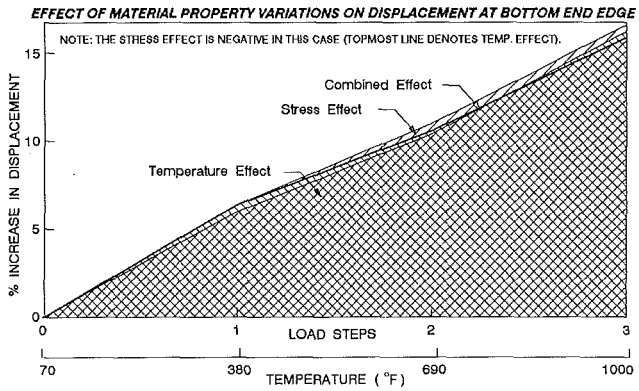


Fig. 9 Sensitivity to constitutive models for built-up structure

have been demonstrated through a specific example problem. These features make HITCAN a powerful tool for analyzing/designing metal matrix composites for actively cooled hot aeropropulsion structures.

References

1 Singhal, S. N., Lackney, J. J., Chamis, C. C., and Murthy, P. L. N., "Demonstration Capabilities of High Temperature Composites Analyzer Code HITCAN," NASA TM 102560, 1990.

2 Nakazawa, S., "The MHOST Finite Element Program: 3-D Inelastic Analysis Methods for Hot Section Components. Vol. II—User's Manual," NASA CR-182235, 1989.

3 Murthy, P. L. N., and Hopkins, D. A., "Metal Matrix Composites Analyzer: METCAN User's Guide," NASA Report (in draft form), 1988.

4 Aiello, R. A., and Chamis, C. C., "Composite Blade Structural Analyzer (COBSTRAN) Theoretical/Programmer's Manual," NASA TM-101958, 1989.

Downloaded 02 Jun 2010 to 171.66.16.112. Redistribution subject to ASME license or copyright; see http://www.asme.org/terms/Terms_Use.cfm

The Utilization of Computer-Aided Drafting (CAD) in Quality Control of Gas Turbine Component Repairs

D. J. Baldwin
Engineering Technician,
Hickham Industries, Inc.,
Turbine Component Repair
& Service Division,
LaPorte, TX 77571

In order to maintain a proper standard of excellence in any company, a quality control program must be implemented. This program must be designed to ensure that adequate quality is being provided to the customer. A thorough inspection department is of utmost importance in establishing a proper quality control system where every step of the repair process is monitored and recorded. All documentation produced should be of the highest quality standards possible, which can be obtained through the use of Computer-Aided Drafting (CAD). It is the intent of this paper to demonstrate how CAD can be utilized throughout the quality control process in order to provide clear, accurate, and concise information for the customers as well as the company.

Introduction

Recently there has been an increase in customer concerns regarding quality control programs in the gas turbine component repair industry. This is largely due to an increase in customer knowledge of the components and the repair processes necessary to qualify a part. Customers are becoming more actively involved not only in the step-by-step repair planning process, but also in the documentation of each part's life span. They are keeping record of all components and their histories from the time of purchase to the time they are deemed "scrap." This better enables them to determine the life expectancy of individual components and to coordinate their repair outages accordingly. Thus, the importance of clear, concise, and accurate documentation cannot be overemphasized.

Document Specifications

It is the main objective of a quality control program to ensure the quality of the part being repaired. This is monitored closely by the inspection department, which has certified inspectors who are trained in nondestructive testing procedures and the required specifications needed to qualify each individual component. All testing results should be recorded on forms produced specifically for each component and the particular testing procedure being performed. These forms should have a pictorial representation of the part along with any tables needed to record data in an organized manner that could be easily interpreted by anyone involved in the repair process (i.e., production staff, customer, engineers, sales representatives).

For example (Fig. 1), an inspection form of a General Electric frame 3, first-stage nozzle assembly, has a drawing of the component where the inspectors record all indications found during nondestructive evaluation testing (such as cracks, pits, foreign object damage, etc.). This information helps the production staff to determine the condition of the part and the repairs needed. It also renders useful information to the sales

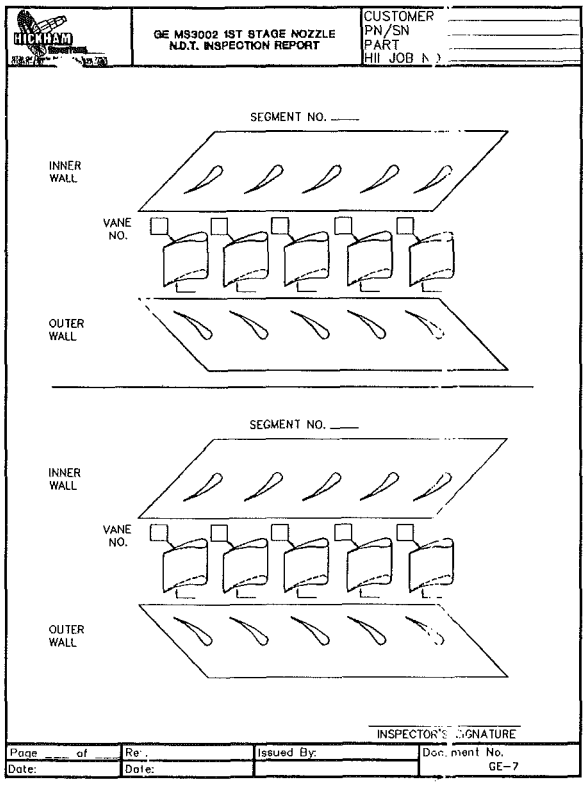


Fig. 1 GE/F3 first-stage nozzle assembly

Contributed by the International Gas Turbine Institute and presented at the 36th International Gas Turbine and Aeroengine Congress and Exposition, Orlando, Florida, June 3-6, 1991. Manuscript received at ASME Headquarters February 20, 1991. Paper No. 91-GT-138. Associate Editor: L. A. Riekert.

Copyright © 1992 by ASME
Downloaded 02 Jun 2010 to 171.66.16.112. Redistribution subject to ASME license or copyright; see http://www.asme.org/terms/Terms_Use.cfm

department, which enables them to provide more accurate bids to the customer.

At the top of the document is the part identification information, which identifies each specific part by manufacturer, model, and serial number. This is beneficial to the customer as well as the repair facility in tracking the part and its history of repairs.

Information Processing System

In order to produce all the documentation needed to qualify each individual component that is repaired in the facility, a practical information processing system needs to be implemented. Computer-Aided Drafting (CAD) can provide the most effective means of achieving this. It is a system that produces drawings in a quick, accurate, and concise manner by utilizing the variety of functions that are in the program. CAD systems have the capabilities of drawing virtually anything that can be produced on a drafting board but in a shorter time span and with better line and text quality for increased legibility. Revisions are also made simpler in CAD because once a drawing has been completed, it is stored and can be retrieved at any time to make all necessary changes. Once these alterations have been made, the revised drawing can be stored under a different name so that both versions of the drawing will be in memory for use at any time. This application is utilized most when all repairs have been made to the component and documentation is being compiled for the customer. The CAD operator can retrieve the original drawing of a part, input all data collected by the inspection department for the test procedure that was performed, and store that drawing under another name (e.g., number assigned to that particular job). It can then be plotted, printed, and compiled with all other documentation for that job, and sent to the customer. The end result is a professional accumulation of documentation that outlines the processes that were performed to ensure the quality of the component repaired.

Conclusion

With the need for more documentation throughout the repair process, it is imperative that an expedient and efficient means of information processing be implemented. This can be achieved through the use of Computer-Aided Drafting (CAD), whereby drawings are produced on the computer rather than manually.

Computer-Aided Drafting provides an effective means of producing quantities of information in the least amount of time and expense. It has numerous advantages over manual drafting, such as speed, accuracy, neatness, legibility, revisions, cost, repetition, and variety of functions. It is by far the most effective means of coping with the ever-rising increase in documentation needed throughout the quality control process.

Acknowledgments

The author wishes to thank Colin Walker, Aurelio Salazar, Wayne Greaves, and John Hall for their continuous encouragement and support.

References

Bertoline, G., 1985, *Fundamentals of CAD*, Delmar Publishers Inc., Albany, NY.

Blauth, R., and Machover, C., 1980, *The CAD/CAM Handbook*, Computervision Corporation, Bedford, MA.

Lamit, L. G., and Paige, V., 1987, *Computer-Aided Design and Drafting*, Merrill Publishing Company, Columbus, OH.

Downloaded 02 Jun 2010 to 171.66.16.112. Redistribution subject to ASME license or copyright; see http://www.asme.org/terms/Terms_Use.cfm

J. R. Anderson

M. J. Skinner

Ferranti Sciaky, Inc.,
Chicago, IL 60638

Blade Repair With Adaptive Vision Tracking

The paper discusses the repair welding of compressor and other blades contained in gas turbine engines. The specific topics of discussion are the application requirements, the general metallurgical considerations, the synchronized pulsation arc welding process, the adaptive vision system employed and the computer-controlled welding system. Reference to an actual installation of this technology will be included.

Introduction

Aviation has grown rapidly since December, 1903, when Orville Wright became the first man to fly a heavier-than-air craft for 12 s, covering 120 ft. Civil and military aircraft sales in 1988 rose to approximately 61 billion dollars. In 1989, the major United States civil airlines spent an estimated 7 billion dollars for maintenance [1].

The engines that are employed in aircraft have changed equally as fast to accommodate requirements such as faster speeds, heavier loads, larger aircraft and better fuel economy. As a result, gas turbine engines have become unique, complex machines. In manufacturing and maintenance, they require leading-edge technology in more disciplines than any other widely available product.

A gas turbine engine requires close clearance tolerances between components and abutting surfaces to maintain proper airflow, performance and fuel economy. During normal use of the engine, parts expand and contract at different rates causing slight interference in some cases and airflow between them in others. The end result is wear on knife edges and other surfaces contained in various blades, vanes and rotary seals. After a predetermined service time period, the worn components are either replaced or repaired. The repaired edges are built up with weld deposits to return them to the proper size and/or to improve their wear-resistant characteristics.

To repair and manufacture the engine components, a need exists in the industry for computer-controlled systems that produce consistent high-quality weldments. Examples of these components are high and low pressure turbine blades, compressor blades, nozzle guide vanes and rotary seals that can be seen in Fig. 1.

The edge thicknesses that must be built up range from 0.010 to 0.100 of an inch. In many cases, the edge thicknesses are not consistent between common parts. As a result, vision systems that not only track the part but also adapt the welding parameters are often required.

The components are typically manufactured with high-temperature alloy materials. Even though many of them are considered non-weldable or at best difficult to weld, a low heat input welding process has proven to be effective. The process also must be applied in a consistent and repeatable manner.

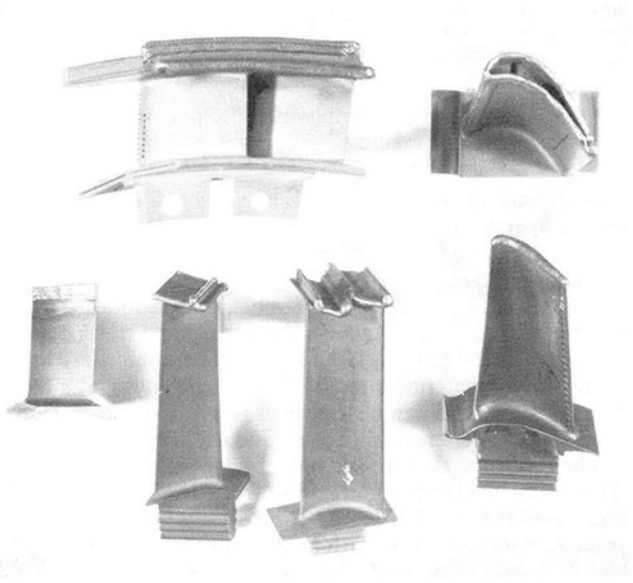


Fig. 1

The advanced welding and vision tracking technology required to build up these edges will be discussed in this article. Although the technology is employed in many components in an engine, for example purposes, the article will place emphasis on compressor blades.

Application/Metallurgical Considerations

The purpose of automating the process is to perform a consistent multipass weld buildup on blade or vane tips that meet metallurgical and profile requirements. Blades and vanes are typically manufactured with high-temperature materials that are primarily designed for resistance to creep and oxidation. The materials are highly alloyed with nickel, molybdenum, chromium, cobalt, aluminum, titanium and tungsten and are prone to cracking.

Cracking is typically experienced in the heat-affected zone (HAZ) during welding or after postweld heat-treat operations. These heat treatments are designed to relieve stresses and enhance mechanical properties. The HAZ cracking that occurs

Contributed by the International Gas Turbine Institute and presented at the 36th International Gas Turbine and Aeroengine Congress and Exposition, Orlando, Florida, June 3-6, 1991. Manuscript received at ASME Headquarters March 4, 1991. Paper No. 91-GT-208. Associate Editor: L. A. Riekert.

Copyright © 1992 by ASME
Downloaded 02 Jun 2010 to 171.66.16.112. Redistribution subject to ASME license or copyright; see http://www.asme.org/terms/Terms_Use.cfm

during welding is the result of phase transformations that occur along the grain boundaries. Along the fusion line, melting of the grain boundaries can occur. Thermal strains can act on the liquid portion of the boundaries and pull them apart. Brittle structures also may form during solidification. This may lead to cracking as residual stresses increase [2].

Other metallurgical defects that can be formed during the welding of high-temperature materials are lack of fusion, oxide formation, tungsten inclusions and porosity. These problems are generally a result of poor welding practice or lack of repeatability.

Automation provides the necessary control over the welding process that is required to eliminate the majority of the welding defects. The cracking or excessive grain growth that can occur during welding can be eliminated or kept at a minimum. These inherent problems can be reduced to within acceptable limits by monitoring and controlling the heat input and filler wire. This will insure that the optimum microstructure is formed in the HAZ.

Regardless of welding parameters, microcracking and grain growth are likely to occur. However, components used in a gas turbine engine often can contain some acceptable limit of internal imperfections. A limited amount of microcracking, grain growth or porosity that has been judged not to be detrimental to the performance of the part can be acceptable. The actual requirements in the repair specifications vary; they depend on the following criteria:

- Material type
- Section of the engine in which the part is used
- Engine manufacture

Blade and vane tips suffer wear, creep and erosion during service operation, and often experience intergranular cracking at the tip. In some cases, tip preparation is required to remove the damaged areas. On several stages of the compressor blades and vanes, it is necessary to premachine the squealer tip to remove the rounded corners on the leading and trailing edges. Due to the airfoil geometry, the edge thickness and chord length change when material is removed from the end of the blade. The thickness also can change as a result of the airflow and other wear experienced during engine use, Fig. 2.

The tip of the compressor blade ranges in design thickness from .010–.100 from leading to trailing edge. On other blades and vanes the thickness range can be greater. It is critical to produce a uniform weld with an adequate bead width to meet profile requirements and allow for multiple weld passes. The required number of passes often depends on the amount of material removed during tip preparation.

To insure that a uniform weld is produced, the welding parameters must be tailored to match the edge thickness. A thin edge can be melted away when using welding parameters designed for a thicker section. Conversely, incomplete fusion can occur when welding a thick edge with parameters designed for a thinner edge. It is necessary to consider also the effect of welding parameters on the metallurgical characteristics of the blade.

The leading and trailing edges are the most difficult area to build up due to the thin tip thickness. In these regions, it becomes necessary to provide adequate buildup over the edges and prevent undercutting. The variation in cord length previously mentioned can cause the start and stop location to be customized for each part. The end of the weld path must end at the proper location on the blade tip. If it moves beyond the end of the tip, for example, the edge will be melted away causing insufficient buildup. The start routine also must begin at the proper location.

The optimum bead profile provides a uniform multipass weld buildup, which is slightly thicker and longer than the tip of the blade. A major cost savings objective is to minimize the

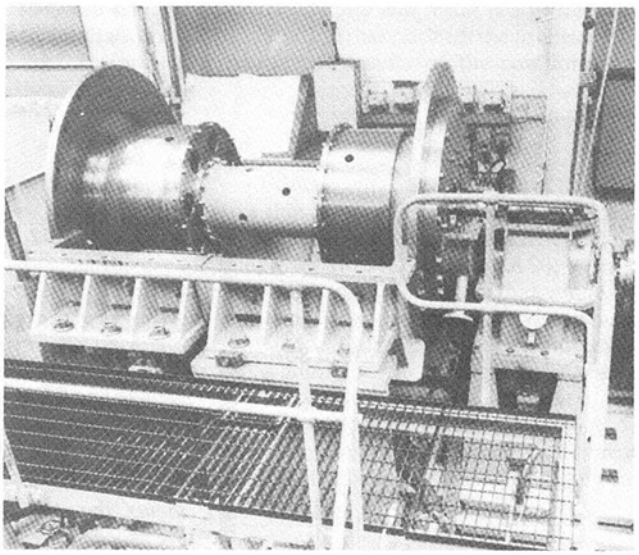


Fig. 2

postweld machining time. The buildup also must provide an adequate amount of material for final machining of the part width height and chord length.

Welding Process

The systems use the microplasma arc-welding process with computer-synchronized pulsation of the current and wire feed rate. In the plasma process, the arc is focused through a nozzle orifice. As a result, the plasma arc is constricted and forms a cylindrical column, in contrast to a GTAW (TIG) arc that is a conical shape.

Three primary benefits are realized by employing the microplasma arc-welding process. The first is that higher current densities and higher energy concentration are provided by a constricted arc than by a GTAW arc with the same parameters. This translates into a more productive use of the arc temperature, a thinner weld puddle and less heat generated in the surrounding area of the workpiece. Another benefit is that a plasma arc is directionally stable. This allows weld buildups to be made in tight locations with the torch position being less critical. Since wire is added during the build-up process, the arc gap or length is critical to provide proper clearance. At lower current values and applicable voltages, the length of a GTAW arc is small, while longer arc lengths can be used with a columnar plasma arc.

Proper inert gas coverage is critical to produce quality weld build-up deposits. This is especially true when employing the microplasma process. A special torch is required that includes a gas diffusion lens to insure adequate coverage. In most cases, a secondary auxiliary shield gas that surrounds the torch and includes a diffusion lens also is necessary.

The arc-welding process is implemented with computer synchronized pulsation of the current and the filler wire. The technique was developed to reduce the resultant heat input and allow filler material to be consistently added to thin edge surfaces. In the weld build-up technique, the direct current is pulsed in a square wave form. This allows a lower average power to be used, thus contributing to reducing heat input.

Also in the overlay process, the filler wire is pulsed in a square wave form. The current and wire feed pulse rates are synchronized so that when the current is at the programmed high value, the wire feed speed is also at the respective high positive value. This allows the wire to be present in the arc at the correct instant in time. The pulsation insures that a droplet of filler material is formed and transferred to the workpiece during the high current pulse.

Downloaded 02 Jun 2010 to 171.66.16.112. Redistribution subject to ASME license or copyright; see http://www.asme.org/terms/Terms_Use.cfm

In comparison, if the weld buildup is made using the conventional pulsed arc-welding process with a constant wire feed rate, the wire also is present in the arc during the low current pulse. Since the low current value is not of sufficient amplitude to completely melt the wire, the end of the wire becomes preheated. As a result, a ball can be formed that is not transferred to the workpiece edge. During the high current pulse, an overly large droplet is then transferred. The droplet must be of proper size with sufficient surface tension to remain on the thin edge of the workpiece, and begin to solidify before the next high pulse. When an overly large droplet is transferred, the surface tension is inadequate and an uneven weld buildup is created.

The precise synchronized pulsation is made possible by generating direct command signals from the computer control. The current pulsation can be programmed by entering the high and low amplitude values along with the respective high and low pulse duration times. The high and low wire feed rates are then entered and the control synchronizes the correct wire feed pulse duration times. To compensate for various materials and their melting characteristics, a wire feed pulse start and stop delay also can be programmed. This feature alters the high wire feed pulse duration time to a longer or shorter value than that of the respective high current pulse. The programming option allows the filler wire to be present in the arc longer for some materials or shorter for those with lower melting points.

The combination of the process characteristics, the pulsation of both the current and wire feed parameters, and the accurate process control by the computer system, allows a smooth and consistent weld buildup to be produced with minimum heat input.

Welding System

Due to the metallurgical characteristics and the physical design of the pieceparts, it is critical that the welding operation be completed as was initially developed and proven to yield acceptable results. To successfully execute the application, the welding system must accurately and repeatably produce the welding process parameters along with the axis motions and positions. This insures that the entire welding operation is consistently repeated. It also enables the torch position, weld travel path and process parameters to be accurately reproduced.

The hardware and software of the welding facility also must be designed to allow a vision tracking system to become an integral part of the package. In an integrated package, the vision boards handle processing of the images, while the system control determines the axes and weld parameter offsets. The communications between the boards also are handled on the single computer backplane in the most efficient and expedient manner. In contrast, if the vision system is separate from the welding facility control, the division of software tasks is more difficult and the communications must be handled through an external link such as a RS232 or equivalent.

The welding facility used for the application is a fully integrated system consisting of precision welding components, multiple axes torch and piecepart manipulators, and a single industrial computer control.

The torch manipulator includes an 'X' (right/left), a 'Z' (up/down) and a 'C' (torch rotation) axes, while the piecepart manipulator consists of a 'Y' (in/out) axis that supports a two-axis weld positioner. Each machine tool precision axis is a separate device driven by a servomotor assembly that is commanded by the computer system. The linear axes use ball screws with preloaded nuts and precision dovetail trackways with appropriately sized ball bushings. The rotary axes are direct gear driven. Each of the axes includes an optical incremental encoder to supply position feedback to the computer control system.

The linear axes of the welding facility are accurate to within



Fig. 3

± 0.002 of an inch and are repeatable to ± 0.0005 of an inch. All of the axis velocities are maintained to within one percent of the programmed value.

The welding facility takes full advantage of a computer control system that was designed specifically for advanced arc welding application and has the largest installed base of the same. The computer system provides precise, coordinated control of the machine axes. Equally as important, the same system provides the required programmable control and monitoring of all the essential process parameters.

The system allows the user to choose from three programming formats. A simple graphics format is provided for single axis welds with minimal process changes. A blocks menu format is used to program coordinated axes and numerous process changes. Another format uses NC language and common welding terminology. This flexible format allows the use of higher level software systems such as curve fitting.

In either, the blocks menu or NC format, axes can be programmed in incremental or absolute positions or in a velocity mode. The welding parameters can be related to time or position of the axes. The axis position and welding parameter values can be directly included in the part program or located in separate tables. If the table method is used, the part program refers to either Axes Position Table (APT) or Electrical Axes Table (EPT) points.

The computer control employs an international VME bus architecture with dual 68000 class processors to provide the

Downloaded 02 Jun 2010 to 171.66.16.112. Redistribution subject to ASME license or copyright; see http://www.asme.org/terms/Terms_Use.cfm

processing power and calculation time required. The control system uses a standard Eurocard 19-in. card cage with a multiple slot VME back plane. The rack includes the processor cards, memory board, analog and discrete I/O, encoder cards, and communication ports. Each control also includes an industrial PC/AT compatible computer with color monitor as a user interface. A hand-held pendant also is incorporated that provides a message center and manual operation features.

In addition to the mechanical system and the control, a critical part of the welding facility is the precision welding components. The welding power supply is a solid-state device that uses Metal Oxide Silicon Field Effect Transistor (MOSFET) technology. The repeatable unit provides less than one percent current ripple and has a pulsation rise of less than one ms when pulsing over the full 200 ampere range.

The wire feed assembly is a multiple roller device that allows pulsation to be completely programmable through the computer control. The assembly also includes a special guide arrangement with precision slides and micrometer adjustments in three axes, along with an angular alignment. The machine tool precision welding facility provides the process, axes and machine control that are required to accurately and repeatably produce high quality weld deposits.

Vision System Overview

With automated welding equipment, the travel path is generally programmed by directing the torch tip from point to point and collecting the required points along the blade or vane. The process parameters required for each of these points are then assigned to meet the edge thickness requirements for that particular part. This is a critical operation since the proper parameters and torch-to-part orientation are essential to consistently produce a quality weld. Without the aid of a feedback system capable of measuring the edge thickness along the part and defining the new weld path, the programming to accommodate part-to-part variations can be so tedious that automation is no longer feasible.

In manual welding, a skilled welder controls the welding torch, while simultaneously introducing filler wire and adjusting the weld current. To compensate for the changes in edge thickness and travel path, the welder observes both the weld pool and the position of the torch and makes adjustments accordingly.

An analysis of the application requirements justified the need to integrate a vision tracking system. For the vision system to be effective for automated blade and vane repair, the following advanced features are required. The system has to detect the start and end points and produce a final weld path, which tracks the blade within ± 0.002 in. of the centerline of the blade or vane edge. The system also must be able to measure the edge thickness at programmed locations along the blade. The edge thickness information should then be used to assign the proper parameters along the blade or vane.

There are a number of vision-based tracking systems on the market that have been integrated with W2000 control for various applications. For compressor blade application, a structured light system was chosen based on its reliability, cost and the ability to accurately track and measure blade contours. Other vision systems can be integrated that are faster but more expensive.

The vision sensor is built with a transmitter and receiver module. The transmitter section consists of a laser diode and problem-oriented focusing lens. The receiver section consists of an antiblooming CCD component with a high resolution picture element. The sensor transmits a laser beam of approximately .400 in length. The CCD camera acts as receiver and detects the laser light reflection on the blade [3].

The mounting of the sensor is a significant issue to maintain the laser line perpendicular to the blade. If this is not done consistently, errors in edge thickness and location will result. The solution is to mount the sensor to the rotatory weld head, which allows the laser line to rotate into the proper position. The sensor should be located approximately 2.75 in. from the workpiece, which allows for adequate clearance for the plasma torch during joint tracking and welding.

The vision sensor and process board are integral parts of the VME based W2000 controller. The vision system scans the blade at each of the predetermined points set up by the user. It then digitizes the video analog signal and verifies the first and last pixel. This pixel information defines the edges of the blade. The vision processor then sends this information in an eight byte communication packet to the Interface Control Processor (ICP) of the W2000. The ICP then passes this packet to the Graphic User Interface (GUI).

The GUI, with the use of patented Ferranti Sciaky Inc. (FSI) vision module software and the vision scan information, calculates and defines the necessary information. The general procedure involves scanning each predetermined point until the first valid edge is detected. This is the arc start point. The system then scans across the remainder of the blade, measuring the edge thickness and defining the proper torch offsets. This process continues until two consecutive invalid edges are detected (determines arc stop point). A Vision Adaption Table (VAT) automatically provides the weld parameters for each of the measured edges along the blade. This parameter information is then stored in the Electrical axes Parameter Table (EPT). The torch offset information (including the proper start and stop points) and the EPT weld parameters are used during the welding operation.

Vision System Setup

The vision system requires that predetermined locations be defined before performing the scan pass. The axis position table (APT) is used to establish the point by point coordinates of any given axes. These point coordinates are absolute and are derived from a zero set position. The points can be defined by manually imputing them through the terminal, by offline programming or with a vision utility program. They are actually camera points that will later be converted to torch points by the FSI vision software. The user must define the blade application requirements before creating the vision scan program.

The user must define the APT beginning maximum point (BEG MAX). This determines the last possible APT point to be accepted as the starting edge (Arc Start Point). The APT end minimum point (END MIN) also must be defined. This determines the first possible APT point to be accepted as the end of the blade (Arc Stop Point).

The number of points required and the distance between each of these points are dependent on the blade application. The first step is to determine the maximum variation of chord length among the blades. The next step is to observe the average size of the weld pool that is created when the initial arc is struck. The number of points required can now be approximated by dividing the maximum chord length variation by the average size of the initial weld pool. For the blade and vane applications, the distance between these points is normally 0.010–0.015. Please refer to Fig. 4, and note that between BEG MAX 12 and the END MIN 27 the distance between the APT points is greater. The distance between these points is determined by the number of points required to track the remainder of the blade contour and provide adequate edge thickness information.

With blade application requirements defined, the user can now teach the machine the vision pass APT points. The user creates a vision scan program to position to all these points in numeric order. A vision utility program can be used to expedite this process. The camera must be positioned to the start of the

Downloaded 02 Jun 2010 to 171.66.16.112. Redistribution subject to ASME license or copyright; see http://www.asme.org/terms/Terms_Use.cfm

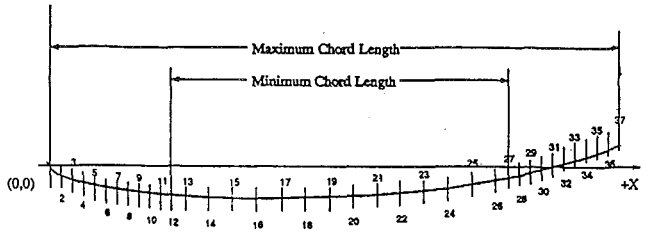


Fig. 4

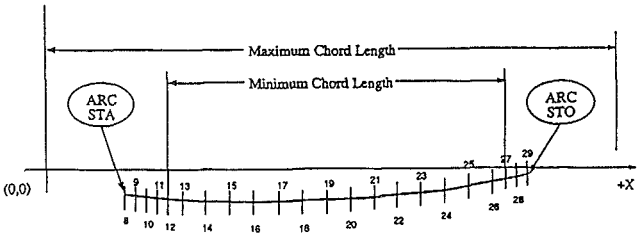


Fig. 5

blade. A teach program is run such that the camera maintains the image of the blade during the teach pass. The machine-vision system proceeds to digitize the blade edge and calculate the required APT points at user-defined intervals. These points are automatically stored as a disk file on the GUI and read into a companion utility program. This program allows the user to perform curve-fitting techniques. The techniques will help define the points needed up to the APT BEG MAX and the points after the APT END MIN. The program then calculates the tangent angles required for each point to insure that the vision line is maintained perpendicular to the blade.

Vision System Software Function

The following functions are performed by the vision scanner and FSI software after the vision pass program is executed:

The initial function is to define the first valid edge. The vision system scanner will begin at APT point one, if an edge is not detected by the vision system at this point, an error code message (Invalid edge) is sent to the FSI vision software. This point will be ignored and the scanner will move to the next APT point. This process continues until one of the following situations occurs. In the first case, the scanner detects a valid edge, and the APT point is stored as the Arc Start Point. Please refer to Fig. 5 where point 8 was detected and stored as the arc start. If a valid edge is not detected at or before the APT BEG MAX point, a message is generated, "Fatal Error—Invalid Edge detected before expected beginning point." This will abort the scanning process.

The next function performed by the software involves multiple tasks. For each camera APT point defined as a valid edge, an information packet is sent to the FSI software. The FSI software will use this information to redefine the camera APT point as the torch location. The vision to camera offset and the camera rotation angle are taken into account for this calculation. The FSI software also will use the vision information to calculate the edge thickness for that APT point. A vision adaption table (VAT) is used to automatically assign the corresponding parameters for the measured edge thickness, Fig. 3. If an edge thickness falls between the VAT table thickness increments, the software interpolates the parameters for that thickness. The user creates the VAT table parameters during blade development. The weld parameters obtained from the VAT table are stored in an electrical axes parameter table. These parameters are then used during the weld operation with the appropriate torch APT points, Fig. 4.

The final function is to define the last valid edge. After the vision system scanner has gone beyond the END MIN, the scanner continues until two consecutive Invalid Edges are detected. The last valid edge is recorded as the APT Arc Stop Point. Point 29 was detected and stored as the arc stop in Fig. 5.

With the vision weld pass completed, the redefined APT points (including the proper start and stop points) along with the parameters for thickness variation are utilized to produce the first weld pass. The torch path information is carried over and used with the remaining build-up passes. A weld program is executed for each subsequent weld pass. Within these programs, the user can preprogram percentage overrides for each of the weld parameters listed on the VAT table.

Conclusion

The application discussed in this article represents an example of how implementing the correct technology can solve complex welding challenges. The system and example blade application are in production at a major European jet engine overhaul facility.

The application requirements were met by employing a fully integrated package. An arc-welding process that was adapted specifically for the application was used. A machine tool precision welding system was utilized to provide the accuracy, repeatability and computer control required. To accommodate the piecepart inconsistencies that could not be eliminated by tooling, a vision tracking system was needed. Finally, the package required a computer system that could precisely control all of the technology and adapt the welding program based on information received from the vision system. The combination of these technologies made the application a success. One or more alone would not have been sufficient.

Acknowledgments

The authors wish to thank P. Wollenhaupt, Vision System Support, and J. Kaszynski, Metallurgy Support.

References

1 *World Aviation Directory*, McGraw-Hill Publication, Winter, Dec. 1990.
2 Liburdi, J., Lowden, P., and Pilcher, C., *Automated Welding of Turbine Blades*, June 1989.
3 Packer, S., Pietrzak, K., Skinner, M., and Dunne, K., *Preweld Joint Tracking System for Weld Path Teaching*, Nov. 1989.

Downloaded 02 Jun 2010 to 171.66.16.112. Redistribution subject to ASME license or copyright; see http://www.asme.org/terms/Terms_Use.cfm

Development Testing of Epicyclic Gearing

D. E. Yates

G. J. Lack

NEI Allen Ltd.—Allen Gears,
Worcestershire, United Kingdom

The increasing use of epicyclics for high-powered marine and industrial applications has resulted in world-wide interest in this type of gearing. The coaxial input and output, reduced losses, small size, and low weight are some of the advantages. The use of a full-size development test rig using the power circulation method has been fundamental to the evolution of double helical, flexible annulus epicyclics, and has led to a detailed understanding of their operating principles. This understanding has been essential for the analytical modeling and the development of innovative design concepts. The paper outlines some of the work that has been carried out in the test rig at NEI Allen Ltd.—Allen Gears. The method of measuring the dynamic load sharing is discussed and some of the results that have led to improvements in the design and manufacturing methods are given. Test rig work continues currently with the development of low-noise gears and vibration isolation.

Introduction

The evolution of high-power epicyclic gears for marine, naval, and industrial applications is well known and has been reported widely (Allen and Jones, 1952; Jones, 1967; Yates, 1976).

The use of two simple design features, the balancing of the tooth loads on the sun and internal gear ring and the use of three or more planet wheels, enables the size and weight of epicyclic gears to be reduced significantly compared with parallel shaft gears with comparable tooth loading.

The coaxial input and output, the lack of high-speed bearings with the consequent reduction in losses, and the use of much smaller components that are easier to manufacture, handle, and measure, are some of the other features that make epicyclics attractive for many applications.

The development of surface-hardened gears with their high load capacity has been complementary to the development of epicyclic gears. The conformal profile of the internal gear mesh allows a through hardened material to be used for the internal gear, while the full advantage of the higher load capacity of the surface-hardened sun and planet wheels is taken at the sun mesh.

Spur gears were used in the early epicyclic designs since the absence of axial thrust from the tooth forces resulted in uniform and symmetric loading on the planet bearings. The generation of high tooth contact noise and vibration with these gears soon led to the adoption of double helical teeth for all high speed applications. The double helical gears with their larger effective face width and lower stresses resulted in a reduction in gear diameter for a given power and speed.

Since those early days, this type of gearing has evolved into the compact, lightweight, reliable unit of today. The success of this development may be judged in Fig. 1, which shows the cumulative power of epicyclic gears supplied by the authors' company. The total power of nearly 22,000 MW includes 13,000 MW of gears for marine propulsion, which range from the small 2600 kW units of the early naval fast patrol boats to the 25,000 kW steam turbine main propulsion gears of VLCCs and fast container vessels.

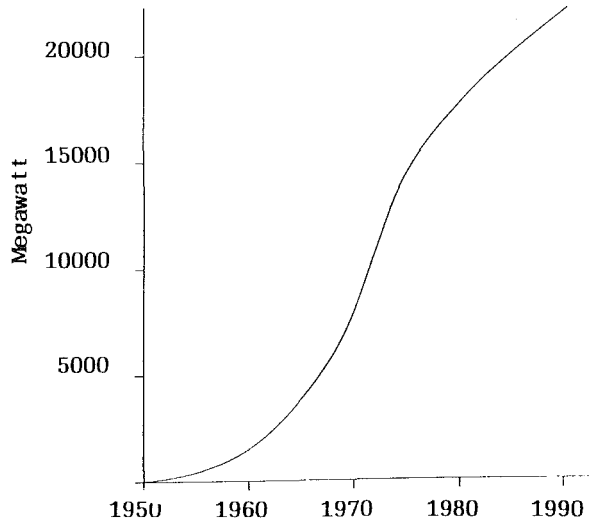


Fig. 1 Cumulative power of epicyclic gears supplied by NEI Allen Ltd.—Allen Gears

Development Testing

Testing has played an important part in the successful development of this type of gearing and has been used to confirm the performance under working conditions.

It has been necessary to develop a thorough understanding of the operating principles of these gears in order to manufacture straight from the drawing board.

Contributed by the International Gas Turbine Institute and presented at the 36th International Gas Turbine and Aeroengine Congress and Exposition, Orlando, Florida, June 3–6, 1991. Manuscript received at ASME Headquarters March 4, 1991. Paper No. 91-GT-262. Associate Editor: L. A. Riekert.

Copyright © 1992 by ASME
Downloaded 02 Jun 2010 to 171.66.16.112. Redistribution subject to ASME license or copyright; see http://www.asme.org/terms/Terms_Use.cfm

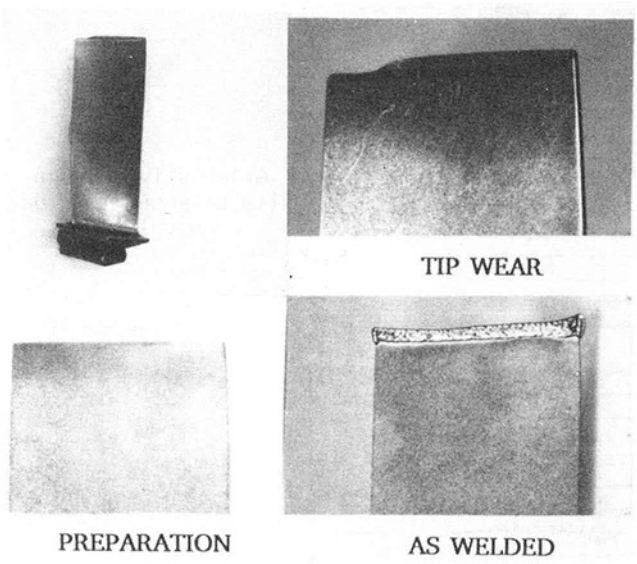


Fig. 2 Back-to-back test rig

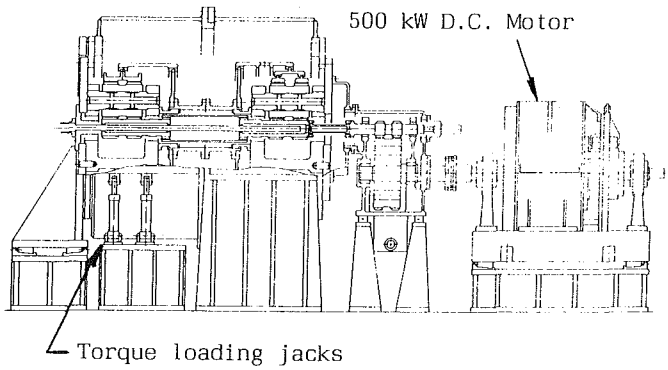


Fig. 3 Sectional arrangement of back-to-back development test rig

More than 15 years ago, a permanent test rig was established at the authors' company for carrying out development work on full size gears. A detailed description of the rig and some of the instrumentation has already been published (Cole et al., 1976; Warin, 1978).

The rig employs the back-to-back or power circulation principle to load two gears with the same speed ratio and directions of rotation. It is equally suitable for testing planetary or star gears transmitting up to 20 MW, at a sunwheel speed of 6000 rpm.

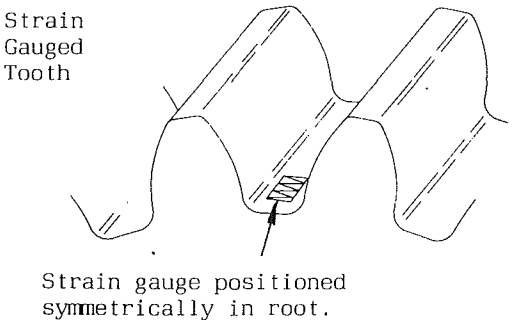
The construction of the rig is illustrated in Fig. 2 and the sectional arrangement drawing (Fig. 3) shows two star gears under test.

The circulated torque is applied by rotation of the torque reaction member of one gear relative to the other. Since the reactions from the two gears are coaxial, this can be achieved by using stationary hydraulic jacks, thus enabling the load to be varied while the gears are rotating.

In the particular build shown in Fig. 3, the test star gears are part of the development of an improved construction for the internal gears.

Measurement of Load Distribution

One of the essential parts of the development work has been the measurement of the dynamic load distribution between the individual gears and along their helices. The measurements have been carried out on both the sunwheel and the internal gears by means of arrays of strain gages positioned in the gear tooth roots.



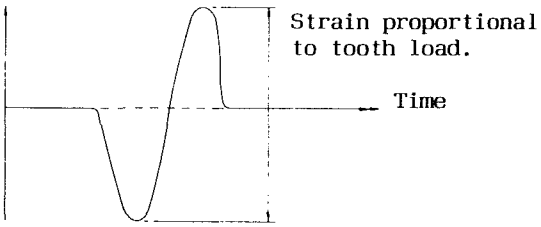


Fig. 4 Typical strain record as the gaged tooth passed through a mesh

Each gage was located normal to the axis of the tooth and positioned symmetrically in the root to enable it to be equally suitable for either direction of load. The gage readings were used as strain comparators and therefore were not required to measure the maximum strain or its absolute value. Furthermore, because the dynamic strain was being measured, it was unnecessary to temperature compensate the gages.

The strain gage positioned symmetrically in the root measures tensile and compressive stress as the tooth passed through the mesh with another gear. A typical record would be similar to that shown in Fig. 4.

In order to compensate for positional errors and other gage variations, it was necessary to calibrate each gage. The development of the static calibration method and the justification for the symmetrically placed gages is given in the appendix.

The load distribution associated with each component is obtained by relating the strains to the individual gear rotations. In order to obtain a clear distribution, it was necessary to carry out the test on a gear with a large cycle of engagement and to analyze the signals over at least 50 strain cycles.

The cycle of engagement is the number of revolutions required to rotate all the components to their starting position.

Transmission of the Strain Signals

The sunwheel strain signals were transmitted from the gear by means of multichannel slip ring units. Those from the rotating internal gear in the star configuration were transmitted by means of a multichannel telemetry system, and those from the stationary annulus in the planetary configuration by direct connection.

Full descriptions of the instrumentation and its development are given by Cole et al. (1976) and Warin (1978).

In order to minimize the number of slip ring channels connected to the sunwheel, the gages at any one axial position were connected in series, but phased so that the stress cycles occurred sequentially.

In the case illustrated in Fig. 5, the epicyclic had five planets and three gages at each axial position. The figure shows how the gages at one axial position were located and the strain signals sequenced.

All the tooth root strain readings were recorded photographically from a multichannel oscilloscope. A typical record of six sunwheel gage channels is shown in Fig. 6, which gives the uncalibrated strain signals from three different axial positions of each helix. The high and low-speed timing markers are also

Downloaded 02 Jun 2010 to 171.66.16.112. Redistribution subject to ASME license or copyright; see http://www.asme.org/terms/Terms_Use.cfm

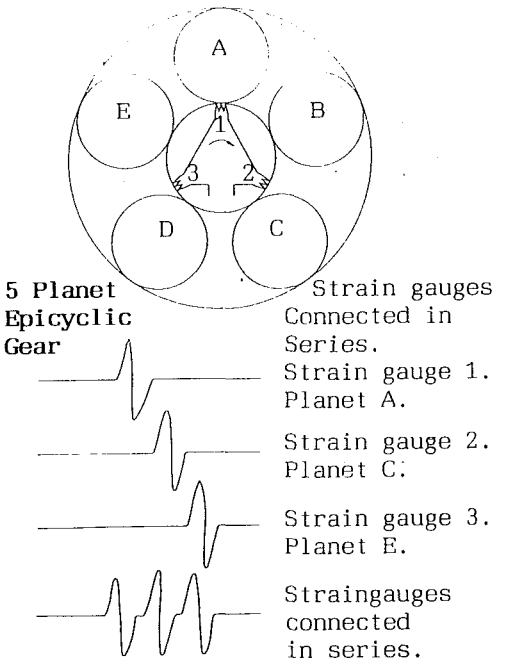


Fig. 5 Sequencing of strain gages on the sunwheel of a five-planet gear

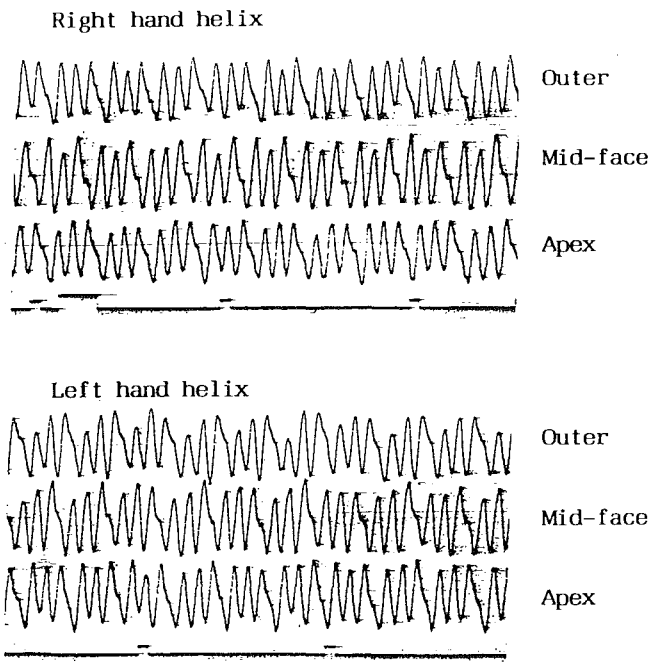


Fig. 6 A typical record of six sunwheel gage channels

recorded and enable the individual meshing teeth to be identified.

A digitizer was employed to record the individual peak-to-peak strains and feed the data into a computer for calibration, sorting, and averaging.

Load Distribution Across the Internal Gear Helix

The Stoeckicht double helical epicyclic gear employed a separate internal gear ring for each helix in order to permit assembly. The two helices were connected by a sleeve with helical coupling teeth of the same hand as the running teeth. This permitted a balance of axial and radial forces between the running and coupling teeth, but the radial displacement of the axial tooth forces resulted in a couple on the gear ring with a consequent toroidal deformation and maldistribution of load across the helix.

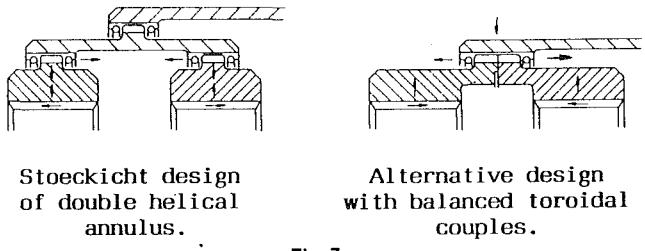


Fig. 7

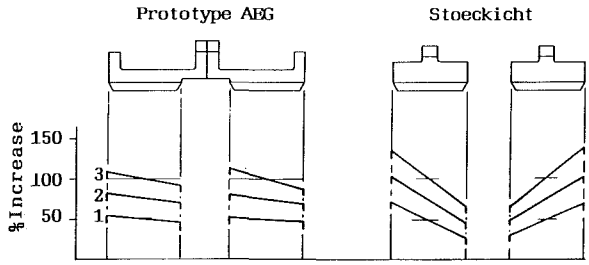


Fig. 8 Measured load distribution across annulus face width at (1) 50 percent full torque, (2) 75 percent (3) 100 percent

This had been predicted analytically and was confirmed by service experience where harder marking at the opposite ends of both helices of this type of gear had been noted.

An alternative patented arrangement was designed by Allen Gears, in which the axial forces generated at the running teeth were balanced by the reaction forces at the end faces of the spur coupling teeth and the toroidal couple was balanced by the tooth separating forces acting on each internal gear ring.

Figure 7 shows a comparison between the original Stoeckicht and the improved design.

Tests to measure the face load distribution of the two designs were carried out simultaneously using the techniques outlined in this paper.

Strain gages were positioned at two axial points on each annulus helix of both gears.

The details of the gears are shown in Table 1; the resultant load distributions are shown in Table 2 and Fig. 8.

The load distributions of the Stoeckicht design are clearly dependent on the transmitted torque and amounted to an average face load distribution factor of 1.47 at full load. The distribution factors for the alternative design are much less load dependent and amount to 1.13, at the same load.

Load Sharing

While the load sharing between a three-planet epicyclic is kinematically balanced if one of the elements is allowed to float, the full potential of epicyclic gears cannot be realized without good load sharing when more than three planets are used.

The load sharing depends on the sum of all the errors determining the planet mesh positions and the flexibility in the system to accommodate them. Several methods of achieving the flexibility have been employed. The authors' company uses a flexible annulus designed to deflect under the action of the tooth separating forces.

Datum tests were carried out to prove the dynamic load sharing of the flexible annulus system of a five planet gear manufactured to the conventional tolerances using strain gage arrays on the sunwheel and internal gears. Table 1 gives the tooth particulars of the gears. The tests were then repeated with a special planet spindle in one position, which gave a planet tangential displacement of 127 μm and is equivalent to a single flank tooth error of 250 μm.

Downloaded 02 Jun 2010 to 171.66.16.112. Redistribution subject to ASME license or copyright; see http://www.asme.org/terms/Terms_Use.cfm

Table 1

TEST GEAR			
GEAR TYPE	DOUBLE HELICAL-STAR OR PLANETARY		
	SUN	PLANET	ANNULUS
NUMBER OF TEETH	32	28	88
NORMAL D.P.		4	
PRESSURE ANGLE (deg)		22.5	
HELIX ANGLE (deg)		30	
REF. CIRCLE DIA (mm)	234.6	205.3	645.2
FACE WIDTH (mm)		2x98.4	
NUMBER OF PLANETS		5	
BASIC RATIO		2.75	

STOECKICHT GEAR			
GEAR TYPE	DOUBLE HELICAL-STAR OR PLANETARY		
	SUN	PLANET	ANNULUS
NUMBER OF TEETH	44	37	121
NORMAL D.P.		5	
PRESSURE ANGLE (deg)		22.5	
HELIX ANGLE (deg)		30	
REF. CIRCLE DIA (mm)	258.1	217.0	709.8
FACE WIDTH (mm)		2x113.3	
NUMBER OF PLANETS		5	
BASIC RATIO		2.75	

Table 2 Load distribution

Load at end of teeth expressed as % of mean load at full torque.

	PROTOTYPE AEG				STOECKICHT			
TORQUE	R.H. HELIX		L.H. HELIX		R.H. HELIX		L.H. HELIX	
	OUTER	APEX	OUTER	APEX	OUTER	APEX	OUTER	APEX
50%	56	44	52	48	78	22	26	74
75%	84	66	79	71	110	40	40	110
100%	113	87	112	88	141	59	53	147

Table 3 Variation in load between star wheels measured by sun and annulus tooth root gages

Effect of 127μ spindle position error on Star 'B'

TORQUE	ROTATION	STRAIN GAUGES	TEST	%VARIATION OF LOAD BETWEEN STARS A	B	C	D	E
AHEAD	AHEAD	SUN	DATUM	1.6	0.5	-1.4	-0.8	0.0
			ERROR	8.4	-10.7	6.1	-0.7	-3.2
			DIFFERENCE	6.8	-11.2	7.5	0.1	-3.2
		ANNULUS	DATUM	-0.5	-1.6	-2.0	3.6	0.3
			ERROR	10.3	-13.5	8.2	-0.3	-4.8
			DIFFERENCE	10.8	-11.9	10.2	-3.9	-5.1
AHEAD	ASTERN	SUN	DATUM	0.8	0.7	-1.7	-0.8	1.0
			ERROR	6.7	-10.5	8.9	-2.7	-2.5
			DIFFERENCE	5.9	-11.2	10.6	-1.9	-3.5
		ANNULUS	DATUM	0.6	-1.4	-2.1	3.3	-0.5
			ERROR	10.9	-15.5	9.4	-1.3	-3.3
			DIFFERENCE	10.3	-14.1	11.5	-4.6	-2.8
ASTERN	ASTERN	SUN	DATUM	0.4	0.6	-0.9	-2.0	1.9
			ERROR	-7.1	10.8	-10.4	0.8	5.8
			DIFFERENCE	-7.5	10.2	-9.5	2.8	3.9
		ANNULUS	DATUM	0.1	0.7	-1.1	-2.0	2.3
			ERROR	-10.7	14.1	-12.8	3.5	6.0
			DIFFERENCE	-10.8	13.4	-11.7	5.5	3.7
ASTERN	AHEAD	SUN	DATUM	0.8	1.7	-0.7	-3.0	1.2
			ERROR	-9.1	10.9	-7.4	-0.1	5.6
			DIFFERENCE	-9.9	9.2	-6.7	2.9	4.4
		ANNULUS	DATUM	-0.2	0.5	-0.5	-1.9	2.0
			ERROR	-12.0	15.2	-12.3	1.4	7.5
			DIFFERENCE	-11.8	14.7	-11.8	3.3	5.5
THEORETICAL				-11.2	13.8	-11.2	4.3	4.3

The tests were run with both directions of torque and rotation and the results are shown in Table 3. The marine notation of ahead and astern has been used to specify the directions of load and rotation. The gage arrays on both the internal gear and sunwheel provided two independent measurements of the load distribution.

The calculated distribution, based on classical thin ring bending theory and a gear tooth stiffness of 14 N/(mm•μm), is also shown and compares closely with the measurements.

Table 4 Measurement of load distribution caused by Carrier elastic deflection

	% INCREASE OF LOAD			
	SUNWHEEL		ANNULUS	
	L.H.	R.H.	L.H.	R.H.
PLANETARY	12	-7	27	28
STAR	37	30	36	23
CARRIER TWIST	24.5	11.5	31.5	25.5
AVERAGE CARRIER TWIST	23			

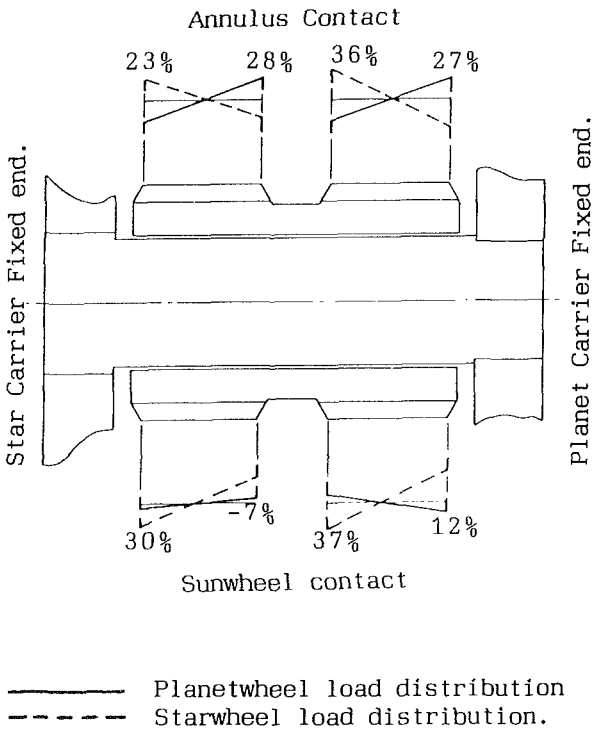


Fig. 9 Measurement of load distribution caused by Carrier twist

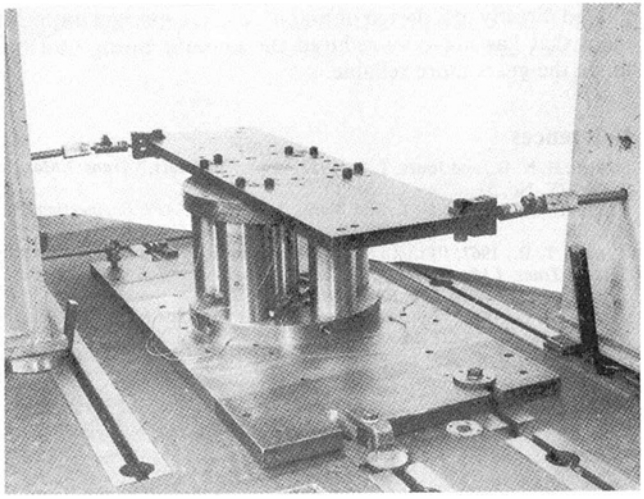


Fig. 10 Experimental determination of Carrier twist of bolted carrier

Carrier Twist

The planet carrier supports both ends of each planet spindle and transmits the load to the output end.

Any twist of the carrier results in a tilt of the planet spindles and a maldistribution of load between the planets and the sunwheel or internal gear. Thus the torsional stiffness of the

Downloaded 02 Jun 2010 to 171.66.16.112. Redistribution subject to ASME license or copyright; see http://www.asme.org/terms/Terms_Use.cfm

carrier can be critical in the design of a gear and may require correction or preset of the spindles to ensure that the load distribution at full load is uniform at the expense of the load maldistribution at part load.

As stated earlier, the test rig is suitable for planetary and star gears. One pair of test gears was designed so that they could be employed for either gear type. The technical particulars of the gears are as given in Table 1.

Tests were carried out using the strain-gaged gear in both modes such that the direction of the applied torque and the contacting tooth flanks were identical but the torque reactions were taken at opposite ends of the carrier. The observed differences in load distribution between the two configurations are the result of the changed direction of the carrier twist. The results are given in Table 4 and are shown graphically in Fig. 9.

The measurement of carrier rigidity was used to confirm and refine the theoretical analysis and led to the development of a new construction of carrier for large low ratio gears where the conventional construction with press fit planet spindles would have been torsionally weak. The new design incorporates spindles that are bolted into the carrier to increase the torsional stiffness.

Figure 10 shows some of the development testing to determine the optimum bolting arrangement. The design was thoroughly tested both using the development test rig and in service. This arrangement is now in use for low ratio application.

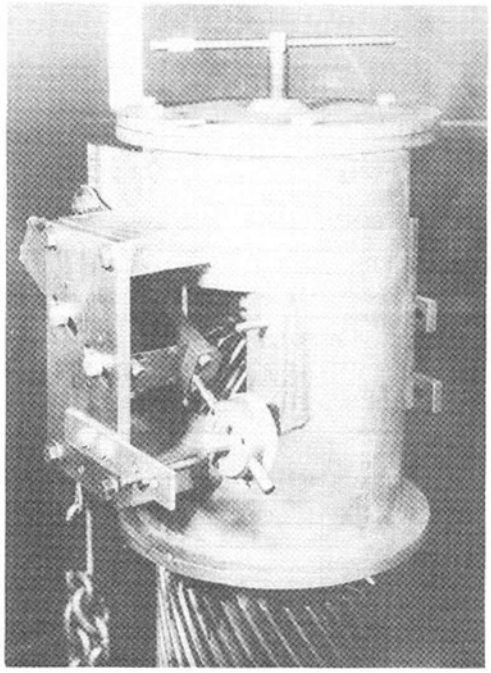


Fig. A1 Test rig for static calibration of sunwheel strain gages

Concluding Remarks

The test rig has been essential to the continuous development of epicyclic gears where innovations have been thoroughly tested before being used in service.

Development testing has been used in conjunction with the analytical approach to understand the operation of gears under service conditions and formulate general design principles.

The assessment of deliberate manufacturing errors has confirmed the load sensitivity to the errors and has enabled the optimum tolerances to be adopted in the manufacturing processes.

Each of the development investigations given in this paper has led directly to a design or manufacturing method improvement that has not only reduced the manufacturing cost but made the gears more reliable.

References

Allen, H. N. G., and Jones, T. P., 1952, "Epicyclic Gears," *Trans. I.Mar.E.*, Vol. LXIV, No. 5.

Cole, G. F. T., Lack, G. J., and Warin, J. W., 1976, *APE Engineering*, No. 23.

Jones, T. P., 1967, "Fifteen Years' Development of High Power Epicyclic Gears," *Trans. I.Mar.E.*, Vol. 79, No. 8.

Warin, J. W., 1978, *APE Engineering*, No. 27.

Yates, D. E., 1976, "Epicyclic Gearing for Gas Turbine Main Propulsion," ASME Paper No. 76-GT-24.

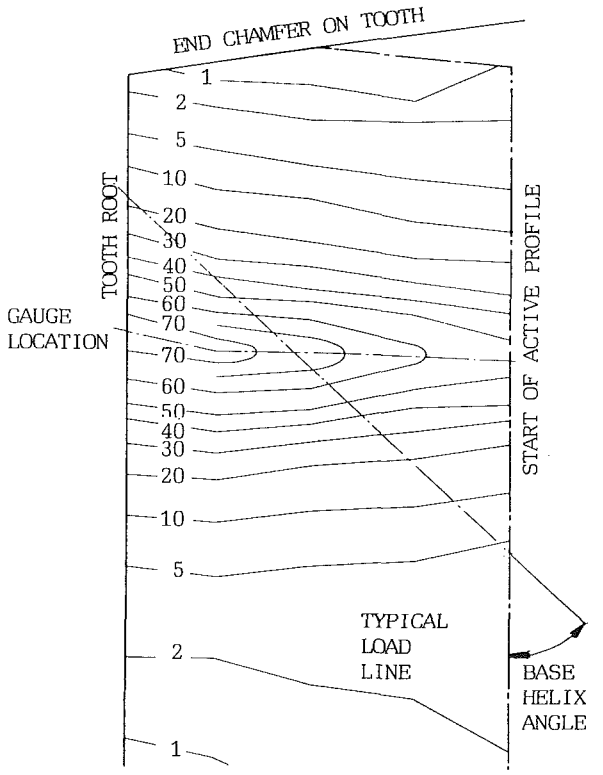


Fig. A2 Map of compressive microstrain plotted in the base tangent plane

APPENDIX

The Measurement of Tooth Load by Means of Tooth Root Strain Gages and the Calibration of the Gears

A static loading rig was constructed that enabled a point load to be applied normal to the tooth surface at any position on any tooth of one of the sunwheels from the test rig, and is shown in Fig. A1. The load was applied by means of a dead weight acting through a low friction pivot system and the point of application was accurately measured. A strain gage was positioned symmetrically in one tooth root and was connected to a strain indicator.

A complete set of gage readings covering different axial and radial positions of the load within the contact zone of the gage tooth was obtained. A map of the strain readings plotted on the base tangent plane of the tooth is shown in Fig. A2 and a typical line of contact inclined at the base helix angle is also indicated. When the gear is rotated, the lines of contact sweep across this zone, causing the gage to be subjected to a cycle

Downloaded 02 Jun 2010 to 171.66.16.112. Redistribution subject to ASME license or copyright; see http://www.asme.org/terms/Terms_Use.cfm

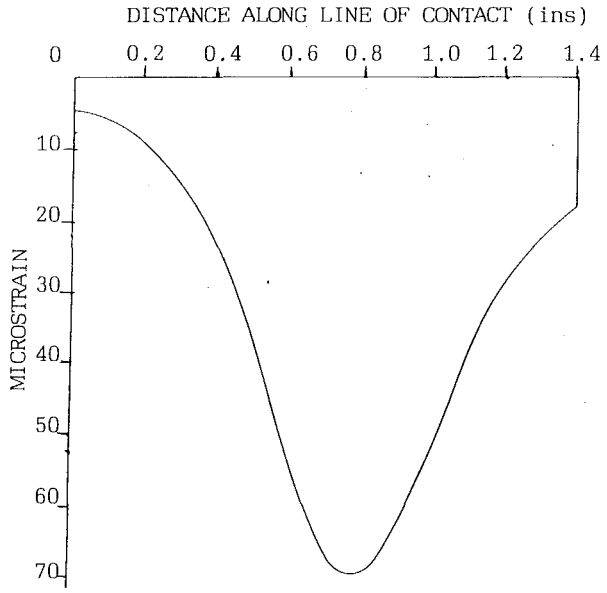
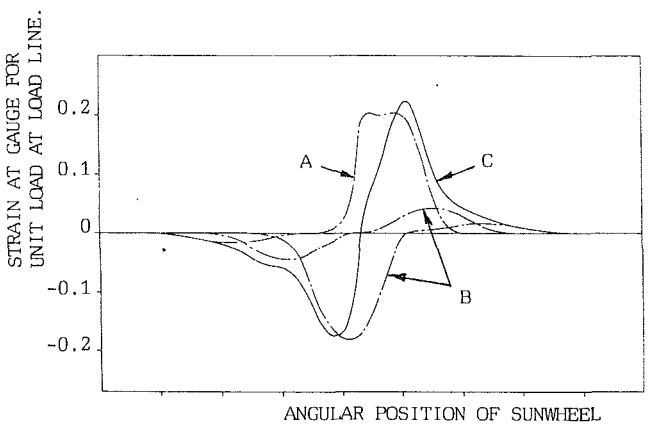


Fig. A3 Variation of strain along the typical line of contact



A. Strain from loaded tooth space.
B. Strain from adjacent tooth spaces.
C. Sum of strain from gauged and adjacent tooth spaces.

Fig. A4 Strain as sunwheel is rotated

of compressive and tensile stress as the load transverses the gaged and adjacent teeth. The strain measured at the gage position for a uniformly distributed load along the line of contact will be given by the integral of the strains along the line of contact. Figure A3 shows the strain plotted along the line of contact given in Fig. A2, from which the integral has been obtained to give the total strain at the gage point.

Figure A4 shows the strain at the gage point resulting from a uniformly distributed load on the gaged and adjacent teeth as the gear is rotated through the mesh. The total strain at the gage point is the sum of the strains from the individual teeth and is illustrated by the full line on the figure.

The total peak-to-peak strain is proportional to the applied load and therefore can be used as a calibration of the gage, although the technique in deriving it is somewhat lengthy.

Further tests using a roller and dead weight to apply the load to the gaged and adjacent teeth are illustrated in Fig. A5. This gave a very close approximation to the peak-to-peak strain

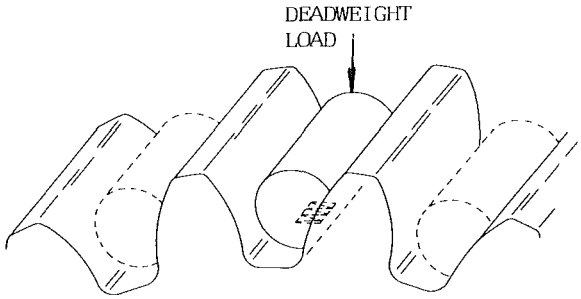


Fig. A5 Diagram showing method of obtaining approximate calibration of strain gages

determined from the method given above. The tensile part of the strain cycle was obtained from the gaged tooth space reading and the compressive part for the two directions of loading was obtained from the two adjacent tooth space readings.

Downloaded 02 Jun 2010 to 171.66.16.112. Redistribution subject to ASME license or copyright; see http://www.asme.org/terms/Terms_Use.cfm

Hong Qilin

Zheng Qixuan

Wang Ping

Hou Guicang

Jet Propulsion Dept.,
Beijing University of Aeronautics
and Astronautics,
Beijing, 100083,
People's Republic of China

A New Method for Calculating Burst Speed of Aeroengine Disks

An approximate analytical large deformation method, based on the Nadai deformation theory, for calculating the burst speed of aeroengine disks, is presented in this paper. The basic equations are developed and the calculation procedures are illustrated. The burst speeds are calculated for some tested disks, and the calculation results are compared with the test results; the differences between two results are shown to be less than 8 percent. This shows that the new method is both simple and convenient. Therefore, it could be employed in the development of aeroengine disks.

1 Introduction

Rotating disks are critical components in an aeroengine. Failure prevention is an important design criterion for aeroengine disks. The disks can overspeed and burst due to malfunction of the control system, shaft decoupling, or afterburner failure. The necessity of avoiding burst is met by providing an overspeed margin to avoid catastrophic failure of engine. Therefore, exact prediction of disk burst speed is one of the current research topics. When the maximum rotor speed approaches the disk burst speed, the plastic strain is well into the strain-hardening range. Therefore, the concepts that belong in both nonlinear material and nonlinear geometry behavior are employed, but it is inconvenient to solve the double nonlinear problems. In this paper, an approximate analytical method based on the Nadai deformation theory considering large deformation and strain-hardening material is employed to calculate the disk burst speed in plane stress state.

2 Basic Equations

This method is based on the Nadai (1931) deformation theory, and assumes that a disk will burst when the octahedral shear strain γ of the material reaches its ultimate value γ_b. It supposes that the disk is operated in simple loading condition, i.e., the directions and the ratios of principal strain are constant, and the elastic deformation is neglected in the total strain.

2.1 Basic Equations for Constant Thickness Disk (Wu, 1951). The equilibrium equation in polar coordinates is obtained from the equilibrium of forces in the radial direction of a small element

$$r\frac{d\sigma_r}{dr}+r\sigma_r\frac{d\epsilon_z}{dr}=(\sigma_\theta-\sigma_r)e^{(\epsilon_r-\epsilon_\theta)}-\rho\omega^2r^2e^{(-\epsilon_z)} \tag{1}$$

The compatibility equation for large strains can be expressed as

$$r\frac{d\epsilon_\theta}{dr}=e^{(\epsilon_r-\epsilon_\theta)}-1 \tag{2}$$

The plane plastic stress yield surface based on the deformation theory is an ellipse, whose major axis and minor axis are equal to 3τ and $\sqrt{3}\tau$, respectively, where τ is octahedral shear stress.

Introducing the parameter α, the equation of the yield surface may be transformed into a more useful form. We obtain

$$\left.\begin{aligned}\frac{(\sigma_\theta+\sigma_r)}{\sqrt{2}}&=3\tau\sin\alpha\\ \frac{(\sigma_\theta-\sigma_r)}{\sqrt{2}}&=\sqrt{3\tau}\cos\alpha\end{aligned}\right\} \tag{3}$$

Rewriting the principal stresses as functions of τ and α, we have

$$\left.\begin{aligned}\sigma_r&=\sqrt{6\tau}\sin\left(\alpha-\frac{\pi}{6}\right)\\ \sigma_\theta&=\sqrt{6\tau}\sin\left(\alpha+\frac{\pi}{6}\right)\end{aligned}\right\} \tag{4}$$

where τ is a function of γ, and varies with r and load. In these equations, the parameter α is closely related to the ratio of principal stresses, inasmuch as

$$\frac{\sigma_r}{\sigma_\theta}=\frac{\sin\left(\alpha-\frac{\pi}{6}\right)}{\sin\left(\alpha+\frac{\pi}{6}\right)} \tag{5}$$

and σ_r/σ_θ varies almost linearly with α for the range of α encountered in the present problem (Fig. 1).

The principal strains can be expressed as functions of α and γ as follows:

$$\left.\begin{aligned}\epsilon_r&=\frac{\gamma}{\sqrt{2}}\sin\left(\alpha-\frac{\pi}{3}\right)+\alpha_tT\\ \epsilon_\theta&=\frac{\gamma}{\sqrt{2}}\sin\left(\alpha+\frac{\pi}{3}\right)+\alpha_tT\end{aligned}\right\} \tag{6}$$

Contributed by the International Gas Turbine Institute and presented at the 36th International Gas Turbine and Aeroengine Congress and Exposition, Orlando, Florida, June 3–6, 1991. Manuscript received at ASME Headquarters February 20, 1990. Paper No. 91-GT-121. Associate Editor: L. A. Riekert.

Copyright © 1992 by ASME
Downloaded 02 Jun 2010 to 171.66.16.112. Redistribution subject to ASME license or copyright; see http://www.asme.org/terms/Terms_Use.cfm

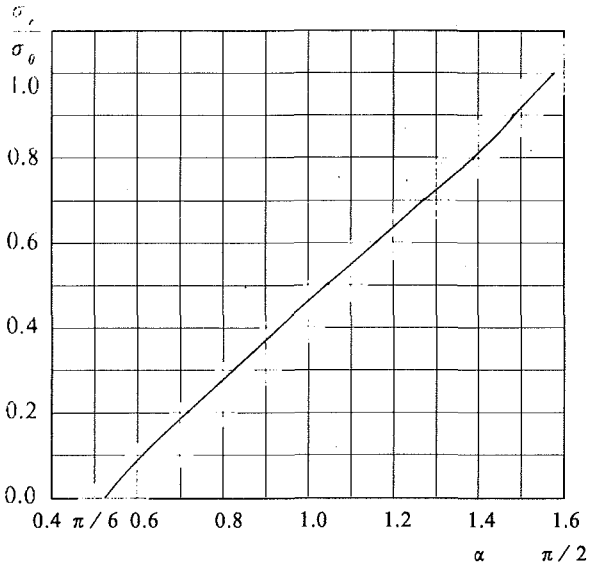


Fig. 1 Variation of σ_r/σ_θ versus α

where α_t represents the linear expansion coefficient of material and T is temperature difference.

Substituting Eqs. (4) and (6) into Eqs. (1) and (2), we have

$$\left.\begin{aligned} Ar\left(\frac{d\alpha}{dr}\right)+Br\left(\frac{d\gamma}{dr}\right)&=C\\ Dr\left(\frac{d\alpha}{dr}\right)+Er\left(\frac{d\gamma}{dr}\right)&=F\end{aligned}\right\} \tag{7}$$

where

$$\left.\begin{aligned} A&=2\sin\left(\alpha+\frac{\pi}{3}\right)-2\sin\left(\alpha-\frac{\pi}{6}\right)\frac{\gamma\cos\alpha}{\sqrt{2}}\\ B&=2\sin\left(\alpha-\frac{\pi}{6}\right)\left(\frac{1}{\tau}\frac{d\tau}{d\gamma}-\frac{\sin\alpha}{\sqrt{2}}\right)\\ C&=2\cos\alpha e^{(-\gamma\sqrt{3/2}\cos\alpha)}-\sqrt{\frac{2}{3}}\frac{1}{\tau}\rho\omega^2r^2e^{(\frac{\gamma}{\sqrt{2}}\sin\alpha+2\alpha_tT)}\\ &\quad+4r\sin\left(\alpha-\frac{\pi}{6}\right)\frac{d(\alpha_tT)}{dr}\\ D&=2\gamma\sin\left(\alpha-\frac{\pi}{6}\right)\\ E&=-2\sin\left(\alpha+\frac{\pi}{3}\right)\\ F&=2\sqrt{2}\left(1+r\frac{d(\alpha_tT)}{dr}-e^{-\gamma\sqrt{3/2}\cos\alpha}\right)\end{aligned}\right\} \tag{8}$$

Therefore the parameters α and γ can be solved in terms of

$$\left.\begin{aligned} r\frac{d\alpha}{dr}&=\frac{CE-FB}{AE-DB}\\ r\frac{d\gamma}{dr}&=\frac{FA-CD}{AE-DB}\end{aligned}\right\} \tag{9}$$

2.2 Simplification for Variable Thickness Disk. A series of constant thickness rings can be used to represent a variable thickness disk (Nie, 1964). The parameters at the outer radius of the ring for No. j are assumed to be α_j, γ_j, and the parameters at the interior radius for No. $(j+1)$ are assumed to be α'_{j+1}, γ'_{j+1}. According to the equilibrium of active forces at interface of adjacent two rings, we obtain using Eq. (4)

$$\tau'_{j+1}=\tau_jM\frac{\sin\left(\alpha_j-\frac{\pi}{6}\right)}{\sin\left(\alpha'_{j+1}-\frac{\pi}{6}\right)} \tag{10}$$

where $M=\dfrac{h_j}{h_{j+1}}$. h_j and h_{j+1} represent the ring thickness of No. j and No. $(j+1)$, respectively.

It is obvious from Eq. (6) that the following equation is obtained in terms of the compatibility for radial displacement at the interface of two rings, i.e.,

$$\gamma'_{j+1}=\gamma_j\frac{\sin\left(\alpha_j+\frac{\pi}{3}\right)}{\sin\left(\alpha'_{j+1}+\frac{\pi}{3}\right)} \tag{11}$$

Therefore the parameters α'_{j+1} and γ'_{j+1} can be obtained in terms of α_j, γ_j by using $\tau\sim\gamma$ relation. The quantity τ is a known function of γ, which is experimentally determined from simple tensile specimen tests.

2.3 Boundary Conditions. Suppose r_k is the outer radius of the disk, and σ_{rk} is the radial stress at the outer radius of disk. Then for a disk without a central hole, $r/r_k = 0$, $\sigma_r = \sigma_\theta$, $\alpha_0 = \pi/2$, and for a disk with a central hole, $r/r_k = r_0/r_k$, $\sigma_r = 0$, $\alpha_0 = \pi/6$, we have

$$\sigma_{rk}(\omega)=\frac{[W(r_k+u_k+l)+m(r_k+u_k+\Delta)]\omega^2}{2\pi(r_k+u_k)h_k} \tag{12}$$

where W and m represent the total mass of the turbine blades and the tower protrusions between adjacent blade roots in a disk; l is the distance from the center of gravity of the blade to the rim, and Δ is the distance from center of gravity of the tower protrusion to the rim. u_k and h_k represent the radial displacement and thickness at the rim of disk, respectively. They can be obtained as follows:

Nomenclature

A, B, C, D, E, F = coefficients of nonlinear differential equations
h_0 = initial thickness of disk
$\mathbf{n}$ = rotation speed of disk
n_p = burst speed of disk
r = radial coordinate of disk
α = parameter involving ratio of principal stresses
γ = octahedral shear strain
ϵ_r = logarithmic strain
ϵ_θ = logarithmic angular strain
ϵ_z = logarithmic axial strain
θ = angular coordinate of disk
σ_r = radial stress
σ_θ = angular stress
τ = octahedral shear stress
ω = angular velocity of disk

Downloaded 02 Jun 2010 to 171.66.16.112. Redistribution subject to ASME license or copyright; see http://www.asme.org/terms/Terms_Use.cfm

$$u_k = r_k\left[e^{\gamma k}\frac{\sin(\alpha_k+\pi/3)}{\sqrt{2}} + (\alpha_t T)r_k - 1\right] \tag{13}$$

$$h_k = h_0 e\left[-\gamma_k\frac{\sin\alpha_k}{\sqrt{2}} - 2(\alpha_t T)r_k\right] \tag{14}$$

3 Calculation Procedures

The disk burst speed can be calculated by the following steps, when the geometry, material, and operating environment of disk are known:

1 The disk burst angular speed is estimated from the average stress method and considered as the initial value ω_k.

2 The disk may be divided into a number of constant-thickness rings. α_0 can be determined on the basis of the boundary conditions. Suppose $\alpha_1' = \alpha_0 \cdot \gamma_1' = \gamma_b$, then the calculation may be carried out from the interior to the exterior of the disk.

3 The coefficients of the nonlinear differential equations A, B, C, D, E, F can be calculated using α_1' and γ_1', then α_1 and γ_1 may be calculated by using Eqs. (9).

4 α_2' and γ_2' can be calculated using Eqs. (10) and (11). Iterating on steps (3) and (4), α_k, γ_k, and σ_{rk} at the outer radius of disk may be determined.

5 It is obvious that u_k and h_k can be calculated by substituting α_k and γ_k into Eqs. (13) and (14), then ω_{k+1} can be calculated by using Eq. (12). If $|\omega_{k+1} - \omega_k| \le \delta$ (δ is a given engineering tolerance), the iteration can be stopped, i.e., ω_{k+1} is the disk burst angular speed ω_p. If not, ω_{k+1} can be substituted for ω_k, and steps (2)–(5) are iterated again.

Table 1 Variation of α versus n

n \ r	40.00	48.775	57.55	66.325	74.66	75.00
8376	0.5236	0.6776	0.7951	0.8840	0.9414	0.9541
9511	0.5236	0.6732	0.7893	0.8812	0.9401	0.9532
9796	0.5236	0.6703	0.7586	0.8765	0.9353	0.9484
10084	0.5236	0.6642	0.7762	0.8656	0.9239	0.9369
10168	0.5236	0.6601	0.7700	0.8583	0.9162	0.9271
10100	0.5236	0.6486	0.7519	0.8365	0.8929	0.9055
$\Delta\alpha$	0.0000	0.0029	0.0432	0.0477	0.0485	0.0486

4 Verifying of the Simple Loading Condition

As Wu (1951) noted, the external loading of the disks increases with ω^2 and the principal stress directions are invariable. If the ratio of the principal stresses in any point of the disk is invariable with increasing rotational speed **n**, the deformation theory of plasticity applies. The ratio of the principal stresses (σ_r/σ_θ) is dependent on α. If the variation of α with n is very small, the simple loading condition is coincident and the calculation is correct. As an example, the variation of α versus n for a variable thickness disk with temperature distribution and external loading is listed in Table 1. It shows that the variation of α with rotational speed **n** is very small and the simple loading condition is basically coincident.

5 The Comparison Between Calculation Results and Test Results

The disk burst speed resulting from the application of the average stress method, the analytic method using the small deformation theory, and the analytic method using the large deformation theory can be compared. The calculation results are compared with test results, which are listed in Table 2.

Table 2 Comparison between calculation results and test results of the disk burst speed

No. of disk	Sample charcteristics	test values of disk burst speed (r.p.m.)	Calculating values of disk burst speed n_p and relative errors Δ%					
			Average Stress Method		Analytic Method using small deformation theory		Analytic Method using large deformation theory	
			n_p	Δ%	n_p	Δ%	n_p	Δ%
1	Plexiglass;constant thickness; R.T.	9552	12050	−26.15	9460	0.96	9449	1.08
2	Carbon steel; Constant thickness; R.T.	11278	10720	4.95	10694	5.18	10849	3.80
3	Carbon steel; Variable thickness; R.T.	11850	11356	4.17	11243	5.12	11426	3.58
4	Carbon steel; Variable thickness with eccentric hub; R.T.	11430	11356	0.65	11243	1.64	11426	0.035
5	Carbon steel; Constant thickness; high temperature	9750	9070	6.88	8725	10.51	8525	12.56
6	GH33A Varialbe thickness with eccentric hub; 421 ° −580℃	14500	16301	12.40			15685	8.00

Downloaded 02 Jun 2010 to 171.66.16.112. Redistribution subject to ASME license or copyright; see http://www.asme.org/terms/Terms_Use.cfm

The relative errors of the three methods have been obtained. There are six test disks in Table 2; the sixth disk is a real disk, and others are model disks.

6 Conclusions

By comparing the calculation results with test results for the disk burst speed, the following conclusions are obtained:

1 The average stress method is applicable to disks made of malleable material. This method is both simple and convenient; therefore, the calculation results can be employed as the initial value of the disk burst speed in the primary design.

2 The analytic method using the small deformation theory is not applicable unless the disk is made of relatively low-ductility material.

3 The analytic method using the large deformation theory is recommended for calculation of the burst speed of various disks. The tolerances are less than 8 percent. This method can be employed in the detailed design of the disks.

4 Because the power of the heater used in the high-temperature burst test of the disk is too small, it leads to a sudden temperature drop in the high-speed disk. Therefore the test value of the disk burst speed in high-temperature conditions is larger and so is the error (see No. 5 in Table 2). If the heater in the test rig is improved, the test value of the burst speed may be closed to the calculation results of the analytic method using large deformation theory (see No. 6 in Table 2).

References

Nadai, A., 1931, *Plasticity*, McGraw-Hill, New York.

Nie Jingxu, 1964, "The Analysis of Elastoplastic Stresses for Variable Thickness Disk in Temperature Distribution and the Calculation of Its Ultimate Rotation Speed," BH-B68, BIAA.

Wu, M. H. L., 1951, "General Plastic Behavior and Approximate Solutions of Rotating Disk in Strain-Hardening Range," NACA TN 2367.

Downloaded 02 Jun 2010 to 171.66.16.112. Redistribution subject to ASME license or copyright; see http://www.asme.org/terms/Terms_Use.cfm

E. Y. Kwack
Member of Technical Staff.
Assoc. Mem. ASME

P. Shakkottai
Member of Technical Staff.

P. F. Massier
Member of Technical Staff.

L. H. Back
Group Supervisor.
Fellow ASME

Jet Propulsion Laboratory,
California Institute of Technology,
Pasadena, CA 91109

Morphology of Globules and Cenospheres in Heavy Fuel Oil Burner Experiments

Number 6 fuel oil was heated, sprayed, and burned in an enclosure using a small commercial oil burner. Samples of residues that emerged from the flame were collected at various locations outside the flame and observed by a scanning electron microscope. Porous cenospheres, larger globules (of size 80 μm to 200 μm) that resemble soap bubbles formed from the very viscous liquid residue, and unburned oil drops were the types of particle collected. Qualitative relationships of the morphology of these particles to the temperature history to which they were subjected were made.

Introduction

Combustion of a heavy oil, such as No. 6, produces as residue a large number of carbonaceous solid particles, which range in size between about one and a few hundred microns. In general, these spheroidal particles are known as cenospheres. It is well known that these residues are formed during the liquid-phase thermal decomposition process. Since cenospheres are microporous, the burning rate of the larger ones is limited by the diffusion of O_2 to the outer surface and into the pores, so that cenospheres burn much more slowly than the original liquid droplets (Goldstein and Siegmund, 1976). On the other hand, the burning rate of the smaller cenospheres might be controlled by chemistry, just as for other small carbonaceous porous particles (Laurendeau, 1978; Smoot and Smith, 1979; Smith, 1982). Therefore, in oil-fired furnaces and boilers, cenospheres may not burn completely and thereby may contribute to operational problems, such as fouling and corrosion of heat transfer surfaces, as well as to air pollution. The incomplete combustion of cenospheres also affects the combustion efficiency since their total mass may not be a negligible fraction of the fuel that is burned, particularly for some of the viscous heavy oils that reach the market more frequently.

Previous investigations have been conducted to reduce cenosphere emissions by controlling operational conditions or by adding water to the fuel (Jacques et al., 1977; Dryer, 1977). Whereas adding water does not prevent the formation of cenospheres, or reduce the mass of coke formed, emulsification distributes the coke into larger numbers of smaller cenospheres and increases their burnout rate. It may also be practical to enhance the combustion of cenospheres by better combustor design (Gavalas et al., 1985).

A number of experimental and analytical studies have been aimed at understanding the detailed processes of the formation of cenospheres (Michael and El-Wakil, 1967; Jacques et al., 1977; Shyu et al., 1972; Jordan et al., 1977; Marrone et al., 1984; Dryer, 1986) and at understanding the combustion of cenospheres (Gavalas et al., 1985; Loewenberg et al., 1987; Northrop, 1988). Experiments with a single drop suspended from a filament and with monosize free-fall drops have produced some information on formation. For example, the experimental studies with a single drop suspended from a filament (Michael and El-Wakil, 1967; Shyu et al., 1972; Jacques et al., 1977; Jordan et al., 1977) provided the histories of temperature, mass, and diameter for burning droplets even though these properties may have been altered by heat transfer associated with the presence of a suspending filament. Ratios of diameter and mass of cenospheres to those of the original fuel drops were measured for well-controlled combustion conditions in free-fall experiments (Marrone et al., 1984; Dryer, 1986). The work of Marrone et al. (1984) showed that cenospheres were formed (i.e., coke formation occurred) during the latter stages of burning when about 10 percent of the mass of the original droplet remained. Variation of droplet size or dilution of the heavy oil by non-coking No. 2 fuel oil did not affect the amount of coke produced per unit of heavy fuel burned.

In most of these experimental studies, microphotography was used to observe the detailed burning processes of fuel drops as well as to measure changes in size. Microphotography may be good enough to measure the size of fuel drops, but its depth of field is too narrow to provide clear observation of the detailed structure of fuel drops. In other studies by Clayton and Back (1989), the detailed structure of cenospheres has been

Contributed by the Fuels and Combustion Technologies Division for publication in the JOURNAL OF ENGINEERING FOR GAS TURBINES AND POWER. Manuscript received by the Fuels and Combustion Technologies Division July 1989. Associate Editor: D. W. Pacer.

Copyright © 1992 by ASME
Downloaded 02 Jun 2010 to 171.66.16.112. Redistribution subject to ASME license or copyright; see http://www.asme.org/terms/Terms_Use.cfm

shown in pictures taken by a scanning electron microscope (SEM). Samples used in these SEM pictures were collected downstream of the boiler tubes of residual-oil-fired steam power plants so that most of them were mature cenospheres or partially burned cenospheres. Also, quenching probes have been used to collect cenospheres for measuring the total amount produced (Marrone et al., 1984). However, quenching probes are not useful for morphological studies.

In this investigation, the results of a more heuristic approach are presented. This approach does not provide data on thermal histories of various sizes of droplets along the multitude of paths in the burning process of fuel sprays, because it is not possible to isolate and follow the myriad of individual droplet trajectories. Rather, if the particles were intercepted and captured, it may be possible to learn more about the various stages of droplet heating and burning. The observations presented herein were obtained by simply placing a collection surface in the settling path of the combustion product residue to acquire data on the particles. Information on cenospheres and globules (later defined), as well as heated oil drops, is reported based on SEM observations.

Experiments

The formation of particulates has been observed during the combustion of No. 6 fuel oil in a commercial burner installed in our spray combustion facility. The burner was designed to burn No. 2 fuel oil (Ray Burner JPEO, $2.85–17.1 \times 10^{-3}$ m^3/h (0.75–4.5 GPH), 41–185 kW (140,000–630,000 Btu/hr)). Because of its high viscosity at room temperature [about 500 times that of No. 2 oil (Hazard, 1966)], the No. 6 oil was first preheated to 63°C to allow pumping and then to a higher temperature to achieve satisfactory atomization. The spray was conical, having an included angle of 80 deg. The nozzle was placed on the bottom of a combustion chamber (122 cm × 122 cm × 122 cm) and the No. 6 oil injected vertically upward. A detailed schematic diagram of the experimental setup and preheating system is shown in Fig. 1. Ignition occurred if the injection temperature was higher than 138°C, but the flame was very small and only a portion of the fuel burned. The flame became larger and more stable as the injection temperature was increased. At an injection temperature of 193°C, a 30-cm-long flame was observed. In our facility, the residence time was shorter and temperatures were lower compared to large industrial furnaces, and therefore it was expected that unburned and partially burned fuel drops would be produced, which was found to be the case. In addition, a large number of cenospheres were also produced. The fuel nozzle pressure was 1.0 MPa (130 psig) at this temperature. Even so, unburned agglomerations of drops occasionally spilled from the flame, allowing acquisition of data on heated oil drops as well.

For warm-up purposes, the whole system was allowed to run for about 20 min after ignition. Samples of particulates

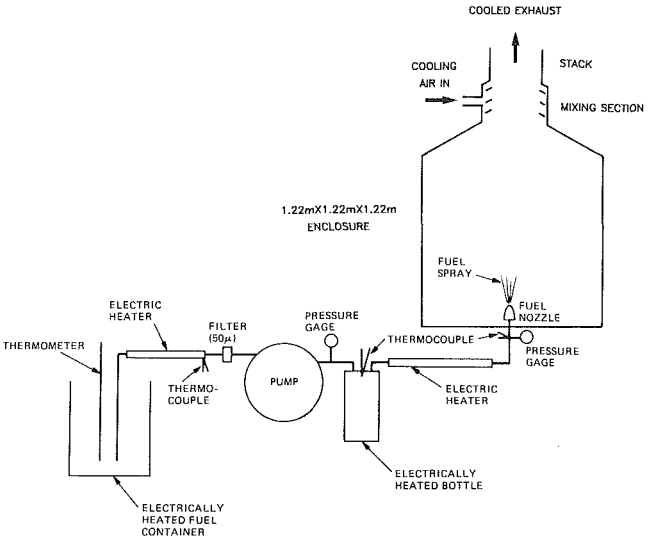


Fig. 1 Experimental setup

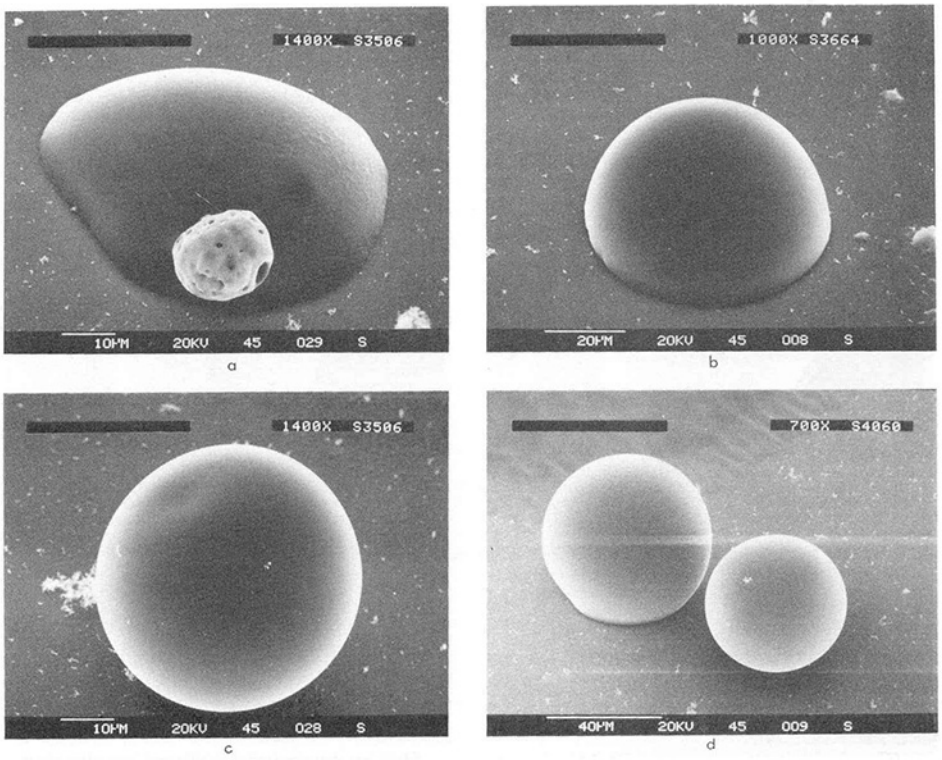


Fig. 2 Fuel drops at early burning stages

Downloaded 02 Jun 2010 to 171.66.16.112. Redistribution subject to ASME license or copyright; see http://www.asme.org/terms/Terms_Use.cfm

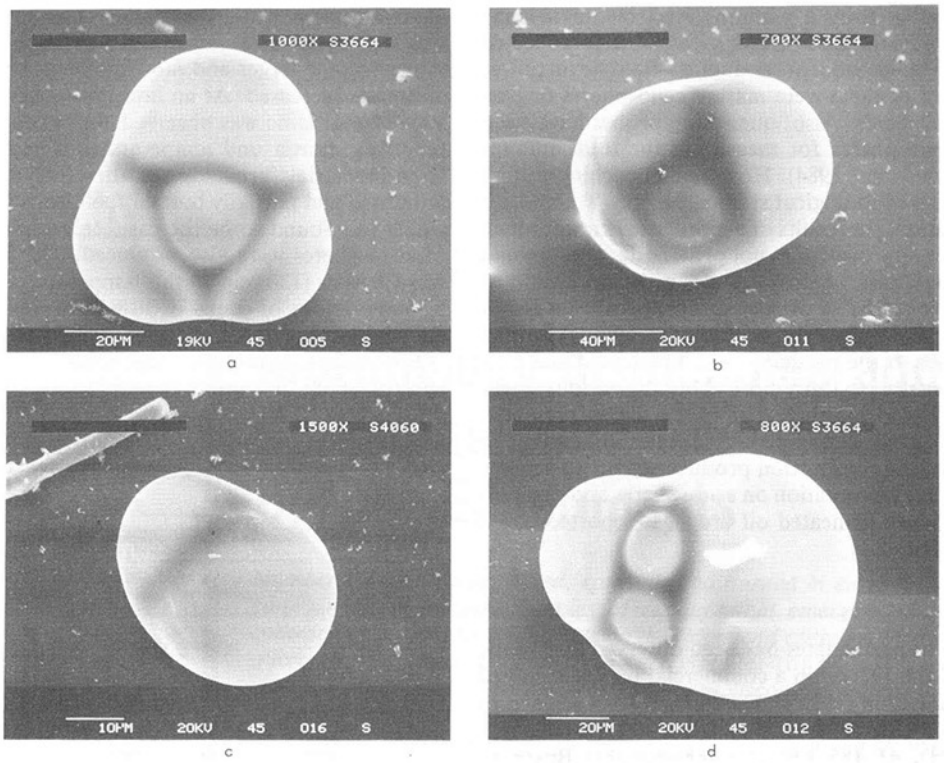


Fig. 3 Swollen fuel drops

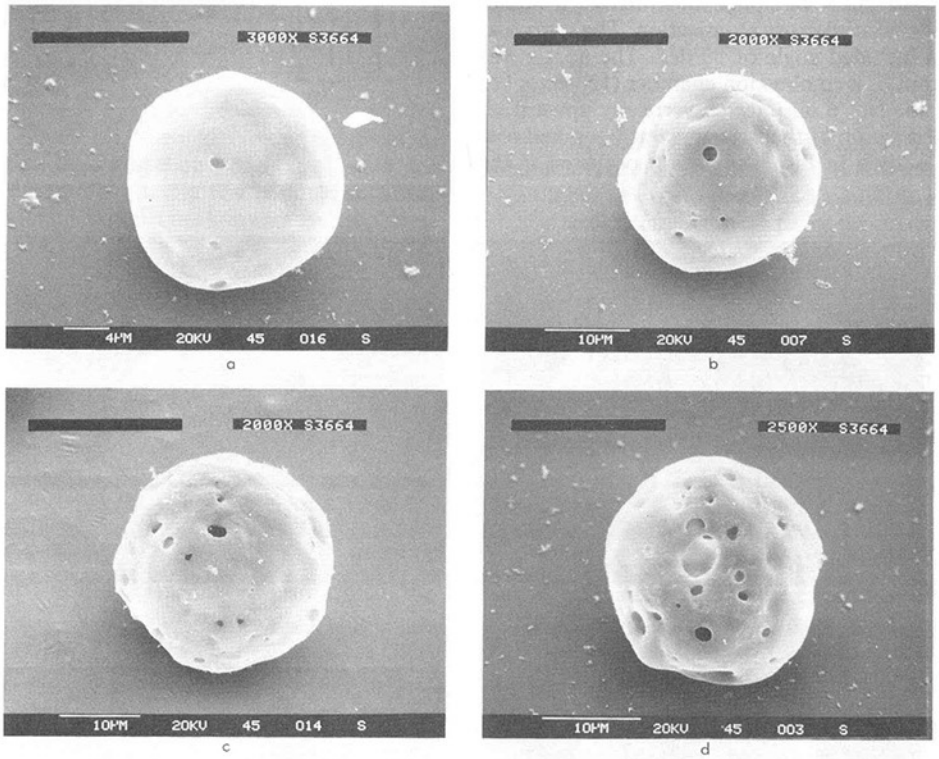


Fig. 4 Fuel drops with blowholes

that emerged from the flame were then collected on glass slides (3.8 cm × 7.6 cm). The glass slides were placed slightly higher than the flame tip and about 20 cm to the side of the flame. Sampling was carried out for 1–4 min. Some of the particles collected on the glass slides were then magnified with a scanning electron microscope (Cambridge Stereoscan 250 Mk 2) and photographed. Charging was prevented by coating the particles on the slides with a thin (about 100 Å) layer of gold–palladium alloy, which is the usual practice.

Results and Discussion

The various particles found on the glass slides were divided into several groups depending on their shape and structure

Downloaded 02 Jun 2010 to 171.66.16.112. Redistribution subject to ASME license or copyright; see http://www.asme.org/terms/Terms_Use.cfm

(i.e., burning stage): irregular-shaped oil drops, ellipsoidal oil drops, spherical oil drops, globules, immature cenospheres, and mature cenospheres whose detailed structures are shown in Figs. 2–7, 9, and 10. A length scale and magnification are given at the lower left and the upper right-hand corners of these figures, respectively.

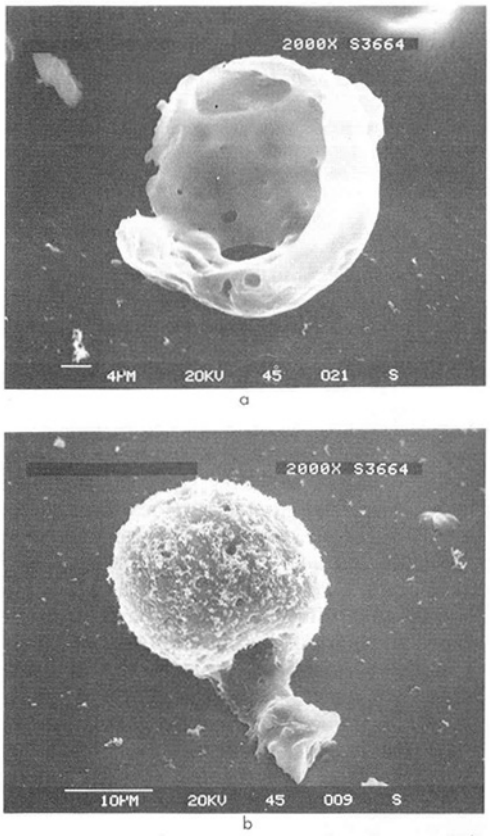


Fig. 5 Ruptured fuel drops showing inside structure and stickiness

Figure 2 shows fuel drops at an early burning stage. Some of them are spherical (Figs. 2*c* and 2*d*), while others are comparatively flattened (Figs. 2*a* and 2*b*). The settling velocity of the fuel drops should have been low (order of 10 cm/s), since the fuel drops were very small, about 50 μm. If some of the fuel drops had not burned enough, they would not have been very viscous or have enough surface tension to maintain a spherical shape on impact with a glass slide, even though the settling velocity was low. The size of most spherical fuel drops was between 40 and 60 μm, with the average about 47 μm. The small particle with holes in Fig. 2(*a*) is a cenosphere that came to rest on the ellipsoidal fuel drop.

The bulging shapes of the fuel drops seen in Fig. 3 are the result of evaporation inside the drops, which causes swelling. In Fig. 3(*a*), evaporation has caused the drop to swell into a multilobed volume. Figures 3(*b*) and 3(*c*) show volumes that are irregular. In Fig. 3(*d*), again there are lobes, two big ones and a number of small ones along a ring where the bigger lobes meet. It is not possible to see any internal partitions between the lobes. The hot fuel vapor that causes expansion will recondense after cooling and must be present inside. Also, after cooling, atmospheric pressure will try to collapse this bulging shape and the thickness of the skin must be thick enough to withstand this.

As the pressure inside the drop increases by evaporation of the volatile components inside the drop, fuel vapor will eventually escape through weak portions of the surface, rupturing the viscous shell and leaving blow holes (Fig. 4). The ejection of fuel vapor will continue to create more holes at the surface until all the volatile components in the drop have burned and a tarry coke particle is formed. These particles, which have been referred to as immature cenospheres, are not believed to contain a large amount of solid carbon since the major thermal cracking has not occurred yet (Marrone et al., 1984). Therefore, they are soluble in an organic solvent such as trichloroethylene, but they still have considerable strength. The ejection of the volatile components may not be intense enough

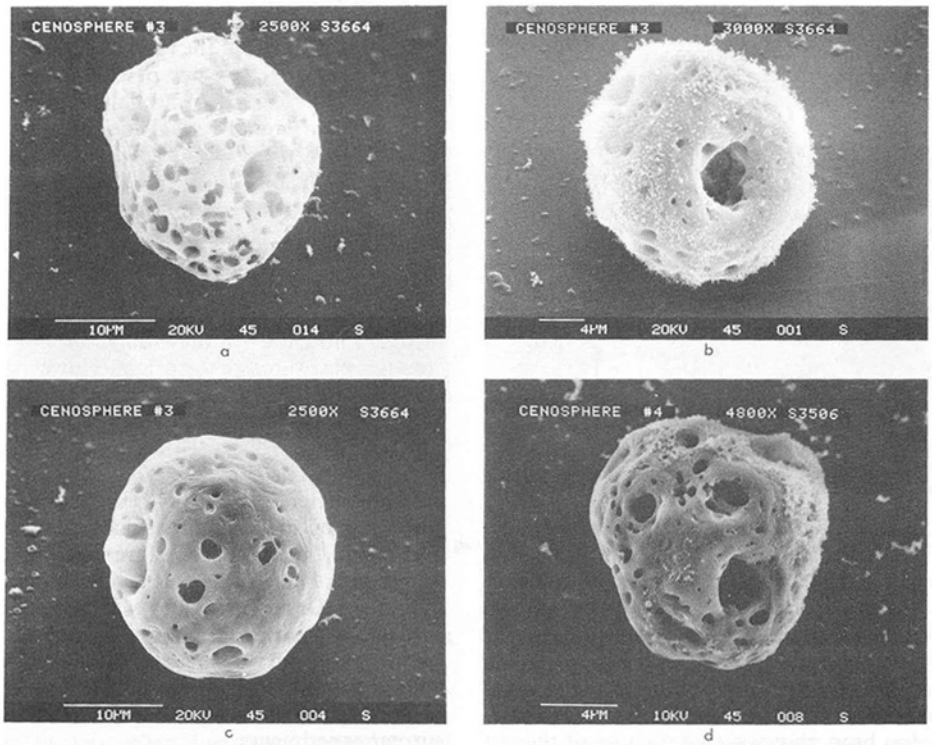
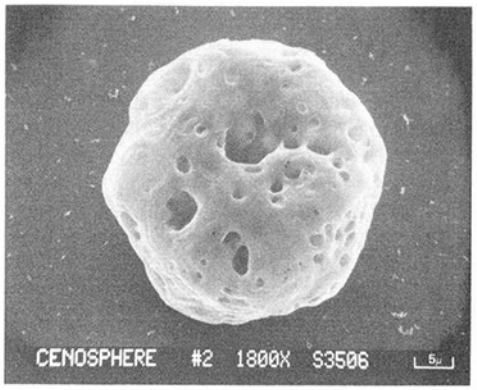
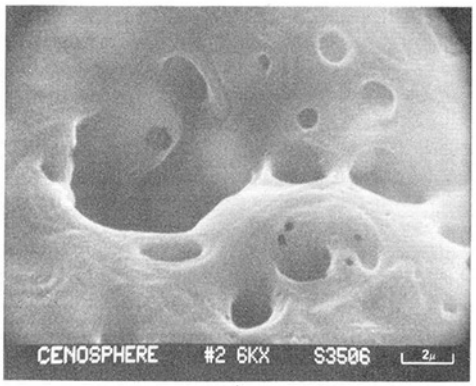


Fig. 6 Cenospheres

Downloaded 02 Jun 2010 to 171.66.16.112. Redistribution subject to ASME license or copyright; see http://www.asme.org/terms/Terms_Use.cfm



a



b

Fig. 7 Cenospheres with holes in blowholes

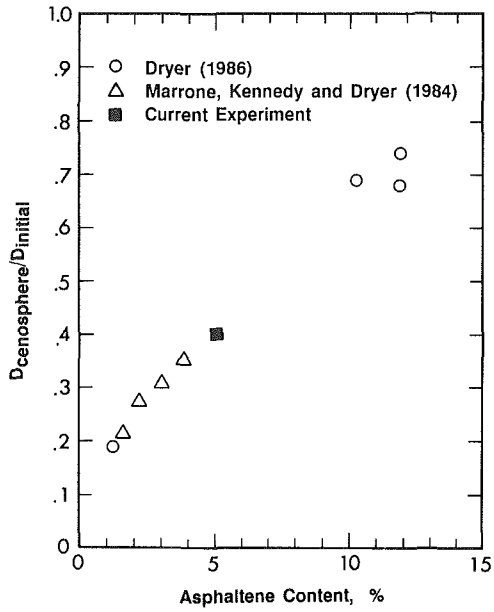


Fig. 8 $D_{cenosphere}/D_{initial}$ versus asphaltene content

always to shatter the droplet. However, sometimes the vapor pressure built up inside the drop may be so high that it may break the drop into several pieces (Fig. 5*a*). As the volatile components burn, the entire drop may become very viscous or tarry so that nothing flows out even though the bottom surface of the drop breaks open (Fig. 5*b*).

After all the volatile components have burned, thermal decomposition occurs to leave carbonaceous residues, i.e., cenospheres (Fig. 6). It has been observed that the rate of thermal decomposition is insignificant early in combustion and reaches

Table 1 Physical properties and constituents of No. 6 oil used in the experiments*

Property/Constituent	Quantity
Specific gravity at 15.6°C	0.9779
API gravity at 15.6°C	13.2
Ash content, wt percent	0.06
Fuel asphaltene, wt percent	
ASTM D3279	4.96
Richfield	8.53
Speight	7.42
Residue asphaltene above 508°C, wt percent	
ASTM D3279	11.84
Richfield	20.60
Speight	18.10
Elemental, wt percent	
Carbon	85.85
Hydrogen	11.27
Nitrogen	0.72
Sulfur	1.71
Flash point	96.7°C

*More detailed information is reported elsewhere (Massier et al., 1988)

a maximum later when the drop temperature reaches 800–900 K (Michael and El-Wakil, 1967; Marrone et al., 1984). Since thermal decomposition of heavy, residual fuel components evolves large amounts of gaseous hydrocarbons, such as methane and ethane, these gaseous hydrocarbons are released through the tarry surface, which accounts for the blowholes in the cenospheres. Cenospheres have many blowholes of various sizes indicating different degrees of disruptive ejections of fuel vapor and gaseous hydrocarbons from the interior of the particles. The largest blowhole in Fig. 6 is about 20 percent of the cenosphere. Clayton and Back (1989), who investigated the physical and chemical characteristics of cenospheres collected from industrial burners, found that the size of the blowholes could be as large as 50 percent of the diameters of the cenospheres, with a typical cenosphere containing only about 18 percent solid material on a volumetric basis. Many blowholes contained several smaller holes along their sides (Figs. 6*d* and 7). The size of the cenospheres collected on the glass slides varied from 1 to 40 μm. However, most of them are in the range of 15 to 25 μm and the average is about 20 μm.

The relationship for the ratio of diameter of the cenospheres to that of initial diameter of fuel drops was evaluated and reported as a function of asphaltene content by Dryer (1986) using four different residual fuel oils. The results are shown in Fig. 8 as open circles. Asphaltene content can be determined by various methods. In Fig. 8 all the results were plotted versus asphaltene content determined by the ASTM D3279 method. Marrone et al. (1984) measured the same ratio using mixtures of a fuel oil with 3.7 percent by weight of asphaltene and No. 2 fuel oil to get a range of values of asphaltene content. These are shown as open triangles in Fig. 8. Between 5 and 10 percent there are no data. All these data lie on a straight line, which does not pass through the origin. However, the size of a cenosphere relative to the initial drop size is still largely determined by its asphaltene content. If we assume that the sizes of spherical fuel drops collected on slides (Fig. 2) represent typical initial drops, the ratio of the diameter of a cenosphere to this initial diameter is about 0.4. For the present experiments the No. 6 fuel oil used had an asphaltene content of 4.96 percent by weight. Other properties are listed in Table 1. Our result is plotted in Fig. 8 as a single solid square that agrees well with other data. Dryer (1986) and Marrone et al. (1984) also measured the ratios of the mass of cenospheres to that of initial fuel drops, which also increase with increasing asphaltene content. From this relationship, as much as 5 percent of the mass of the original fuel droplets may be left as cenospheres in the current experiments.

The particles shown in Fig. 9 are larger than cenospheres

Downloaded 02 Jun 2010 to 171.66.16.112. Redistribution subject to ASME license or copyright; see http://www.asme.org/terms/Terms_Use.cfm

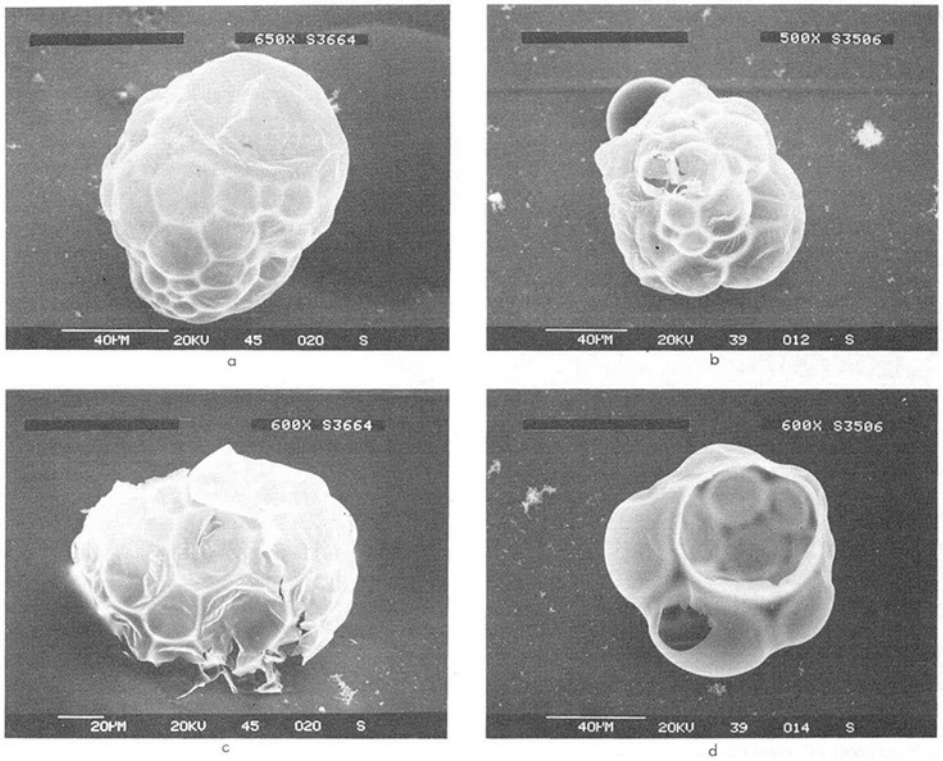


Fig. 9 Globules

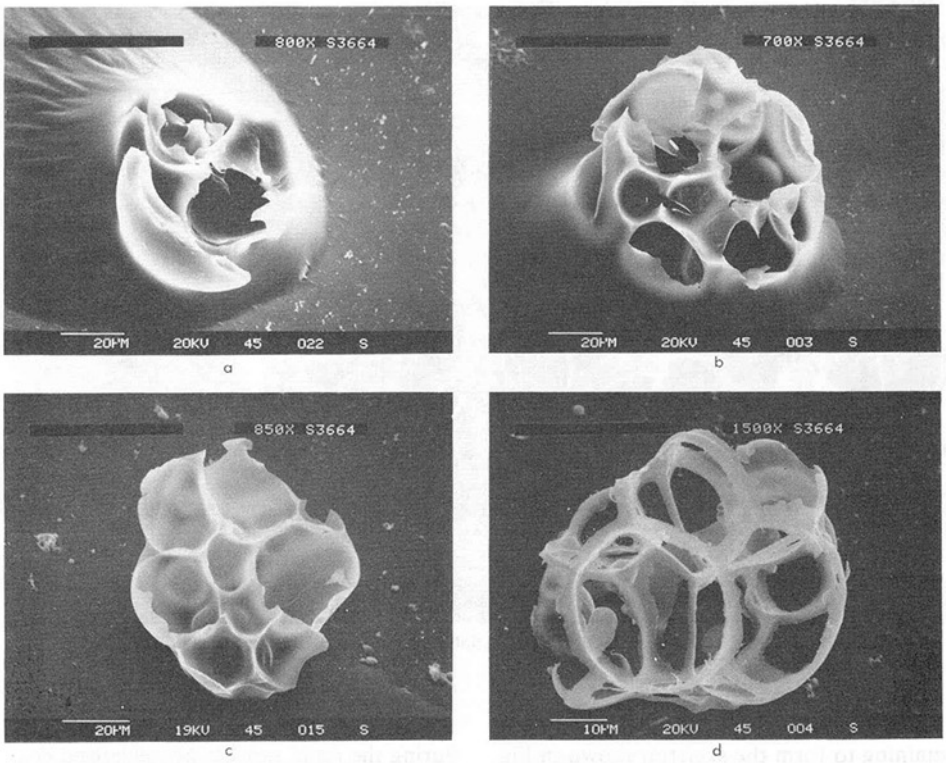


Fig. 10 Broken and partially burned globules

and have no blowholes at the surface. We will refer to this type of particle as a globule. They appear to contain many small bubbles. Figure 10 clearly reveals that the globules are hollow and contain many bubbles. These globules may be formed in the following way: When fuel vapor is ejected, fuel vapor blows out the viscous liquid fuel at the surface as bubbles, then the bubbles generated from the same blowhole or other adjacent blowholes stick together, forming larger hollow globules. If this is true, bubbles may contain small amounts of volatile fuel components. Globules may burn more easily than cenospheres because they have very thin membranes. Among the various particles on the glass slides, a globule was

Downloaded 02 Jun 2010 to 171.66.16.112. Redistribution subject to ASME license or copyright; see http://www.asme.org/terms/Terms_Use.cfm

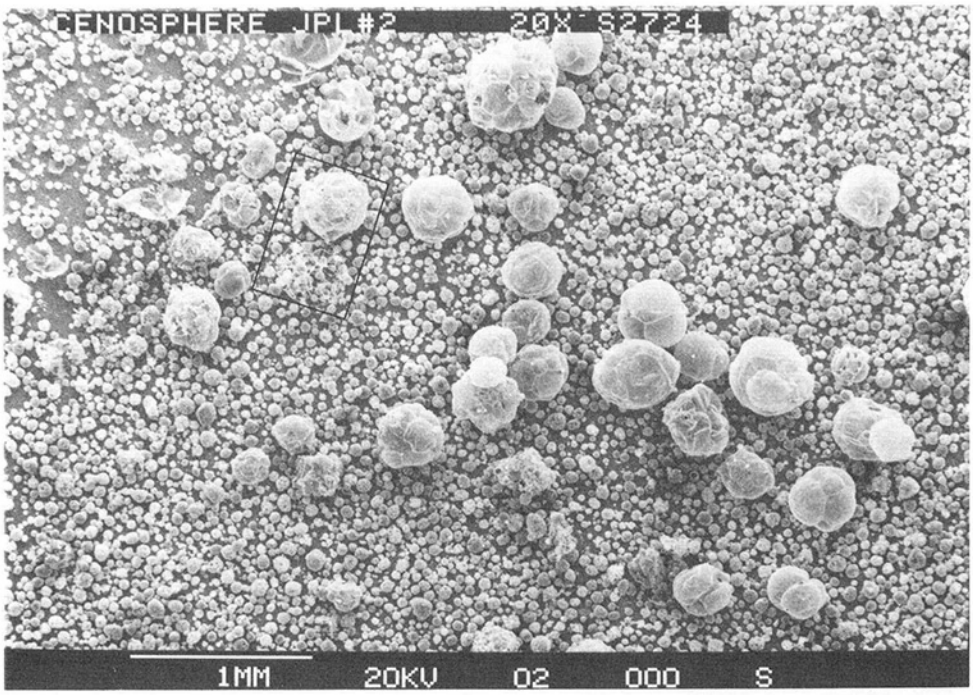


Fig. 11 Cenospheres and globules from an industrial burner

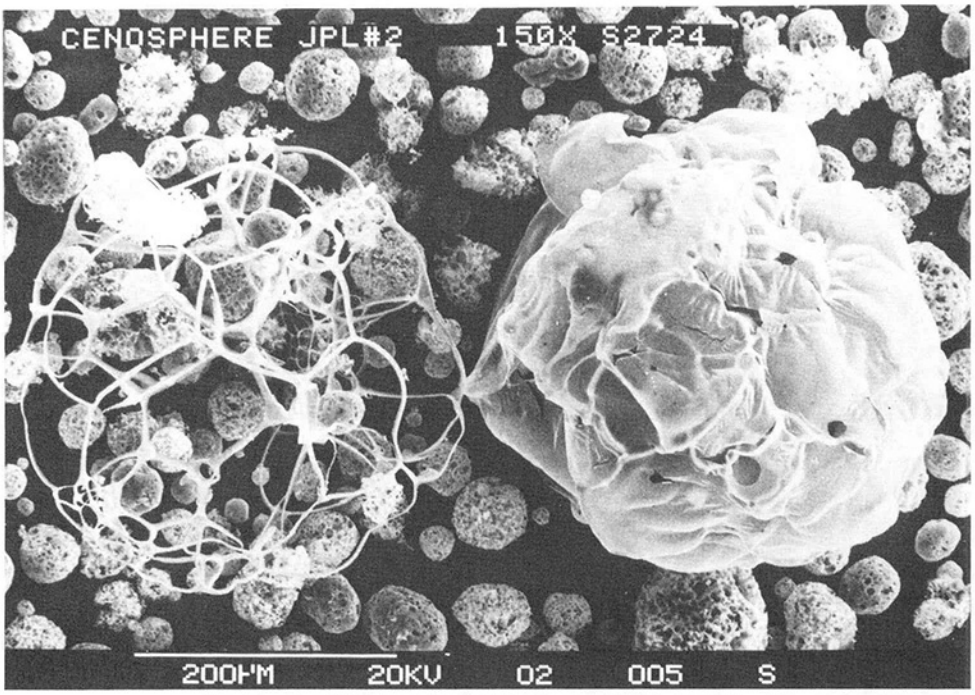


Fig. 12 Magnification of a partially burned globule from Fig. 11

found that may have burned partially with only the edges of the membranes remaining to form the skeleton shown in Fig. 10(*d*). The globules ranged in size from 80 to 200 μm.

Similar globules found in samples collected from an industrial burner (Clayton and Back, 1989) are shown in Fig. 11. These were not shown and not discussed in the Clayton and Back reference. Some of them are much larger than those on the glass slides shown herein. The largest one is about 600 μm. Figure 12 shows under high magnification the boxed area in Fig. 11. The globule on the left side of Fig. 12 is partially burned, and has a skeletal structure similar to the one in Fig. 10(*d*) from the current experiment.

Globules have been also observed by Street et al. (1969) during the rapid heating of pulverized coal.

Summary and Concluding Remarks

The burning of No. 6 fuel oil was observed in a spray combustion facility with a small commercially available burner with a 30-cm-long flame. Particles that emerged from the flame, and which were collected on glass slides, were exposed to a variety of thermal or burning environments. SEM pictures of these particles revealed the detailed morphological changes of droplets during combustion. The various particles included

Downloaded 02 Jun 2010 to 171.66.16.112. Redistribution subject to ASME license or copyright; see http://www.asme.org/terms/Terms_Use.cfm

irregular-shaped oil drops, spherical oil drops, globules, immature cenospheres, and mature cenospheres. The size of a typical, spherical oil drop was between 40 and 60 μm, and most of the cenospheres ranged in size from 15 to 25 μm. Globules that are formed during ejection of volatile fuel components through surfaces of droplets were found to have many small bubbles and ranged in size from 80 to 200 μm. Partially burned globules had only edges of the bubble membranes left in the form of a skeleton structure.

The size of the cenospheres was about 0.4 of that of the initial oil droplets. The asphaltene content of No. 6 fuel oil used in the current experiments was measured to be 4.96 wt percent. The remaining mass of cenospheres was estimated based on the asphaltene content from other experimental results, and was about 5 percent, which is not negligible. A method to enhance the combustion of cenospheres is required to reduce air pollution and operational problems such as fouling and corrosion, and to increase combustion efficiency.

Increase of combustion efficiency may be minimal by burning globules, since they contain only a small mass. However, they survive during combustion in industrial burners (Fig. 11), even though they have only thin membranes. Because they have very low density, they can be carried away easily by wind and may contribute to air pollution if not contained at the burning source.

Much larger industrial burners produce particles of the same type, although some are much larger than what we observed in the small burner. This shows that for some purposes, a rough simulation serves quite well in offering physical insight into the mechanisms that play a role in the production of cenospheres.

Acknowledgments

The authors wish to express their appreciation to Messrs. D. C. Schneider and J. J. Godley for their contributions in fabrication and assembly of the test setup, and in the conduct of the experiments. They also express their appreciation to Dr. J. Bellan and R. M. Clayton for valuable comments on the manuscript.

The research described in this paper was performed by the Jet Propulsion Laboratory, California Institute of Technology, and was supported by the U. S. Department of Energy, Office of Energy Utilization Research, Energy Conversion and Utilization Technologies Program, Mr. Marvin Gunn, Jr., Program Manager, through an interagency agreement with the National Aeronautics and Space Administration.

References

Clayton, R. M., and Back, L. H., 1989, "Physical and Chemical Characteristics of Cenospheres From the Combustion of Heavy Fuel Oil," ASME JOURNAL OF ENGINEERING FOR GAS TURBINES AND POWER, Vol. 111, pp. 679–684.

Dryer, F. L., 1977, "Water Addition to Practical Combustion Systems: Concepts and Applications," *Sixteenth International Symposium on Combustion*, pp. 279–295.

Dryer, F. L., 1986, "Review of Relationships Between Fuel Oil Properties and Particulate Remissions," presented at EPRI Heavy Fuels Workshop, Philadelphia, PA, Oct.

Gavalas, G. R., Loewenberg, M., Bellan, J., and Clayton, R. M., 1985, "Structure and Oxidation of Carbonaceous Cenospheres," Paper No. 30d, Annual AIChE Meeting, Chicago, IL, Nov. 10–15.

Goldstein, H. L., and Siegmund, C. W., 1976, "Influence of Heavy Fuel Composition and Boiler Combustion Conditions on Particulate Emissions," *Environmental Science and Technology*, Vol. 10, pp. 1109–1114.

Hazard, H. R., 1966, "Gas Turbine Fuels," in: *Gas Turbine Engineering Handbook*, J. W. Sawyer, ed., Chap. 9, Gas Turbine Publications, Stamford, CT, pp. 172–182.

Jacques, M. T., Jordan, J. B., Williams, A., and Hadley-Coates, L., 1977, "The Combustion of Water-in-Oil Emulsions and the Influence of Asphaltene Content," *Sixteenth International Symposium on Combustion*, pp. 307–319.

Jordan, J. B., Kimber, G. M., and Williams, A., 1977, "Ignition of Droplets of Liquid Fuels Solvent Extracted From Coal," *Fuel*, Vol. 56, pp. 417–421.

Laurendeau, N. M., 1978, "Heterogeneous Kinetics of Coal Char Gasification and Combustion," *Prog. Energy Combust. Sci.*, Vol. 4, pp. 221–270.

Loewenberg, M., Bellan, J., and Gavalas, G. R., 1987, "A Simplified Description of Char Combustion," *Chemical Engineering Communications*, Vol. 58, pp. 89–103.

Marrone, N. J., Kennedy, I. M., and Dryer, F. L., 1984, "Coke Formation in the Combustion of Isolated Heavy Oil Droplets," *Combustion Science and Technology*, Vol. 36, pp. 149–170.

Massier, P. F., Bellan, J., Kwack, E. Y., Shakkottai, P., Harstad, K., Gavalas, G. R., and Loewenberg, M., 1988, "Spray Combustion Modeling and Evaluation: Annual Report 1987," JPL D-4857.

Michael, M. I., and El-Wakil, M. M., 1967, "On the Self Ignition of Hydrocarbon Mixtures," *Eleventh International Symposium on Combustion*, pp. 1027–1035.

Northrop, P. S., 1988, "A Fundamental Study of Char Combustion: Changes in Particle Morphology During Oxidation," Ph.D. Thesis, California Institute of Technology, Pasadena, CA.

Shyu, R. R., Chen, C. S., Goudie, G. O., and El-Wakil, M. M., 1972, "Multicomponent Heavy Fuel Drop Histories in a High-Temperature Flow Field," *Fuel*, Vol. 51, pp. 135–145.

Smith, I. W., 1982, "The Combustion Rates of Coal Chars: A Review," *Nineteenth International Symposium on Combustion*, pp. 1045–1065.

Smoot, L. D., and Smith, P. J., 1979, "Modeling Pulverized-Coal Reaction Processes," in: *Pulverized-Coal Combustion and Gasification*, L. D. Smoot and D. T. Pratt, eds., Plenum Press, New York, Chap. 12.

Street, P. J., Weight, R. P., and Lightman, P., 1969, "Further Investigations of Structural Changes Occurring in Pulverized Coal Particles During Rapid Heating," *Fuel*, Vol. 48, pp. 343–365.

Downloaded 02 Jun 2010 to 171.66.16.112. Redistribution subject to ASME license or copyright; see http://www.asme.org/terms/Terms_Use.cfm

The Transfer Number of Hydrocarbon Liquids

J. Odgers

D. Kretschmer

Department of Mechanical Engineering,
Laval University, Quebec City,
Quebec, Canada, G1K 7P4

The transfer number (B) assumes considerable importance in the evaporation and diffusion of fuels prior to their combustion. Quite often the transfer number is assumed to be a constant for a given fuel. These notes examine the feasibility of this assumption. New correlations have been derived for the specific heats of the liquid fuels and their latent heats, over a wide range of temperatures and pressures, as also the effects of pressure upon the boiling characteristics. New prediction techniques are also proposed for critical temperatures and pressures. Taking note of the above correlations, it becomes possible to assess the values of B for a wide range of combustor operating conditions for any given fuel. The significance of these variations upon the probable combustion behavior of the fuels is then commented upon. The results show that the assumption of a constant value for B could lead to a significant misinterpretation of combustion behavior due to operating conditions and/or the use of different fuels.

1 Introduction

Over the past several years a great deal of data have become available pertinent to the role of different fuels as they affect the combustion behavior within gas turbine combustors. As more and more data became available, it has become possible to derive correlations containing a wider range of variables. It would seem that the transfer number of any given fuel could play a significant role in the evaporation and combustion behavior of alternative fuels. However, the fuel property data necessary for the complete evaluation of this transfer number are generally not available, and therefore, there has been a tendency to use this function as though it was a constant based upon an approximate value such as that cited by Spalding [1]

$$B_s = \frac{1575 - 0.5T_{av}}{T_{av} - 118.5} \tag{1}$$

In order to facilitate the comparison of this value with others as calculated below, it will be treated as though it was a reference, or standard, value and will be represented as B_s. In point of fact the function is much more accurately represented by

$$B = \frac{\dfrac{m_{og} \times q_n}{o/f} + c_g(T_g - T_B)}{h_{fg} + c_l(T_B - T_f)} \tag{2}$$

All of the right-hand side terms of Eq. (2), other than those referring to the air, are fuel dependent and must be evaluated at the operating conditions and with the appropriate fuel. This work will concern itself with the estimation of the value of the liquid transfer number {B in Eq. (2)}.

The terms other than specific heat and latent heat {c_l and h_{fg} in Eq. (2)} are generally known or easily derived, although T_B will require assessment at pressures other than atmospheric. As a first step toward the assessment of the transfer number, it will be necessary to obtain values of the various terms.

Other workers have attempted to make the calculation of B more accessible. For example, Chin and Lefebvre [2] considered the effects of various fuel properties upon both transfer number and the evaporation constant for five different fuels. The present work, by considering 47 different fuels, widens the scope and, in addition, derives new correlations for those terms that are generally difficult to obtain (namely c_l, h_{fg}, T_c, p_c, and T_B).

2 Specific Heat

Not a great many determinations relevant to the specific heat of hydrocarbon fuels have been published. The values used for the present study have been taken from [3-5]. Most other sources observed appeared to be taken from one or the other of (or were listed as a source by) the above publications. Compounds studied comprised paraffins, olefins, naphthenes, and aromatics.

The accuracy of the values is not cited in the references used. The ASTM handbook also fails to cite an accuracy due to the lack of "a sufficient number of volunteers...for determining the precision of the method" [6]. However, a good idea of the accuracy of the experimental technique may be obtained from a fairly recent publication on the determination of the specific heats of crude fractions [7], which suggests an accuracy of about 10 percent when comparing the experimental values for the heat capacity of n-pentane with samples published previously [8].

2.1 Existing Correlations. Various formulae have been proposed to assess the specific heat of hydrocarbon fuels. Barnett and Hibbard [9] propose

Contributed by the International Gas Turbine Institute and presented at the 36th International Gas Turbine and Aeroengine Congress and Exposition, Orlando, Florida, June 3-6, 1991. Manuscript received at ASME Headquarters February 19, 1991. Paper No. 91-GT-98. Associate Editor: L. A. Riekert.

Copyright © 1992 by ASME
Downloaded 02 Jun 2010 to 171.66.16.112. Redistribution subject to ASME license or copyright; see http://www.asme.org/terms/Terms_Use.cfm

$$c_l = \frac{758 + 3.3T}{\rho_{288}} \quad (\text{kJ/kg·K}) \tag{3}$$

Cragoe [10] gives

$$c_l = \frac{1}{\sqrt{d}}(0.403 + 0.00081\Theta) \quad (\text{cal/(g°C)}) \tag{4}$$

Watson and Nelson [11] give

$$c_l = 4186[0.7072 - 0.3178d + (0.00147 - 0.00055d)\Theta] \times (0.055K + 0.35) \quad (\text{J/(kg·K)}) \tag{5}$$

Fallon and Watson [12] suggest

$$c_l = [0.355 + 0.00128\,°\text{API} + (0.503 + 0.00117\,°\text{API}) \times 10^{-3}\Theta] \times (0.05K + 0.41) \quad (\text{cal/(g°C)}) \tag{6}$$

Davis [13] uses

$$c_l = \frac{(2.10 - d)(\Theta + 384.4)}{1127.8} \quad (\text{cal/(g°C)}) \tag{7}$$

A comparison of the values predicted by Eqs. (3)–(7) and the experimental ones is given in Figs. 1 and 2, and the corresponding statistical data may be found in Table 1. The data suggest that the correlation proposed by Fallon and Watson is the most satisfactory and, in addition, it demands only values for the density and boiling points (T_{av}), both of which are easily obtained. No matter which equation is used, all of them yield some predicted values well in excess of the anticipated 10 percent experimental scatter.

Figure 3(*a–e*) plots the experimental values for each individual correlation and identifies the compound classes. The line on each curve represents the equality line between experimental and predicted results. Once again the Fallow and Watson correlation is the most satisfactory. All the figures demonstrate the separation of the various classes of compounds. They also indicate that the cyclic compounds exhibit the most scatter. Tentatively this may be due to the increased bond strain for the lower molecular weight compounds.

Because of these observations, it was decided to examine the data in more detail and to consider the derivation of a new correlation.

2.2 A New Correlation. It is probable that one or more of the correlations given above could be modified to yield a separate correlation for each class of compound identified. This would be satisfactory if only pure substances were to be considered as fuels, or even if accurately known mixtures were to be used. However, for a correlation to have general application for commercial hydrocarbon fuels as well as pure compounds, it would not be possible (in at least 95 percent of cases) to specify accurately the fuel composition. As a part of the

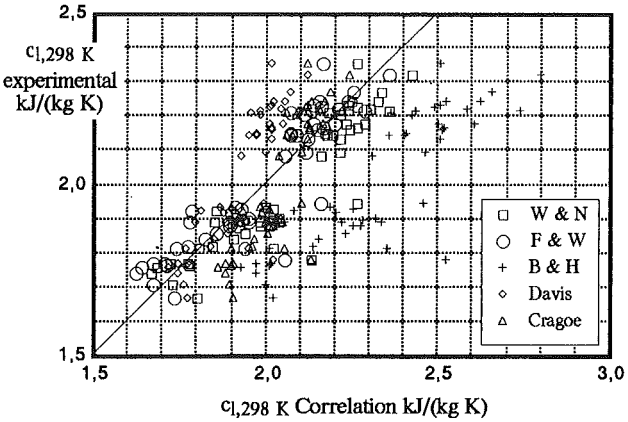


Fig. 1 Specific heat correlations

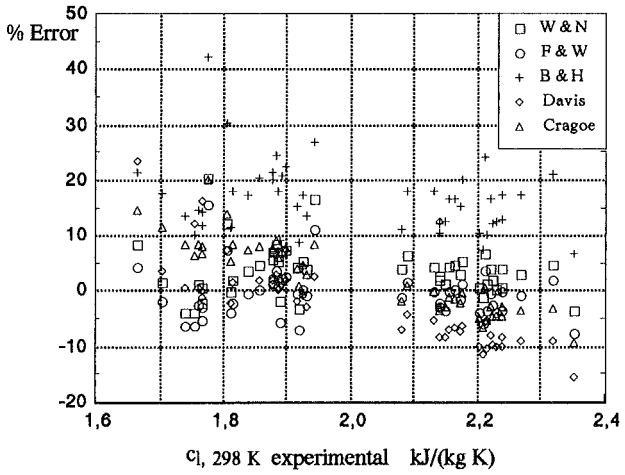


Fig. 2 Specific heat: correlation errors

Table 1 Statistical data pertinent to Figs. 1 and 2

Authors	n	Mean error, percent	Standard development, percent	Error range, percent
Cragoe	47	2.65	6.43	+20.06 to −6.51
Barnett and Hibbard	47	16.48	6.40	+42.23 to +6.73
Davis	47	−3.22	5.75	+13.88 to −14.72
Fallon and Watson	47	−0.68	4.41	+15.61 to −7.75
Watson and Nelson	47	3.56	4.68	+20.13 to −3.87

Nomenclature

°API = liquid density $= 141{,}500/\rho_{288} - 131.5$
a = const
B = any transfer number
B_s = transfer number of fuel calculated using Eq. (1)
b = const
c_l = specific heat of liquid, J/(kg K)
c_g = specific heat of gas (vapor), J/(kg K)
d = relative density at 288 K
f/a = fuel/air ratio, by mass
h = mass fraction of hydrogen in fuel
h_{fg} = latent heat of fuel at boiling point, J/kg
K = UOP characterization factor $= 1{,}22 \times 10^3 (T_{av})^3 \rho_{288}$
L = latent heat of vaporization; units other than SI
M = molar mass, kg/mol
m_{og} = mass fraction of oxygen in gas (air)
n = number of data points
o/f = oxygen/fuel ratio by mass
p = any pressure, Pa
p_c = critical pressure, Pa
p_o = reference pressure, Pa
q_n = calorific value of fuel, J/kg
T = any temperature, K
T_{av} = ASTM average boiling point, K
T_B = fuel boiling point (average), K
T_c = critical temperature, K
T_g = temperature of gas, K
T_l = temperature of liquid, K
T_r = reduced temperature $= T/T_c$
T_{st} = stoichiometric flame temperature, K
Θ = any temperature, °C or °F
λ = thermal conductivity, W/(mK)
ν_T = viscosity, kinematic at T, m^2/s
ρ_T = liquid density at T, kg/m^3

Downloaded 02 Jun 2010 to 171.66.16.112. Redistribution subject to ASME license or copyright; see http://www.asme.org/terms/Terms_Use.cfm

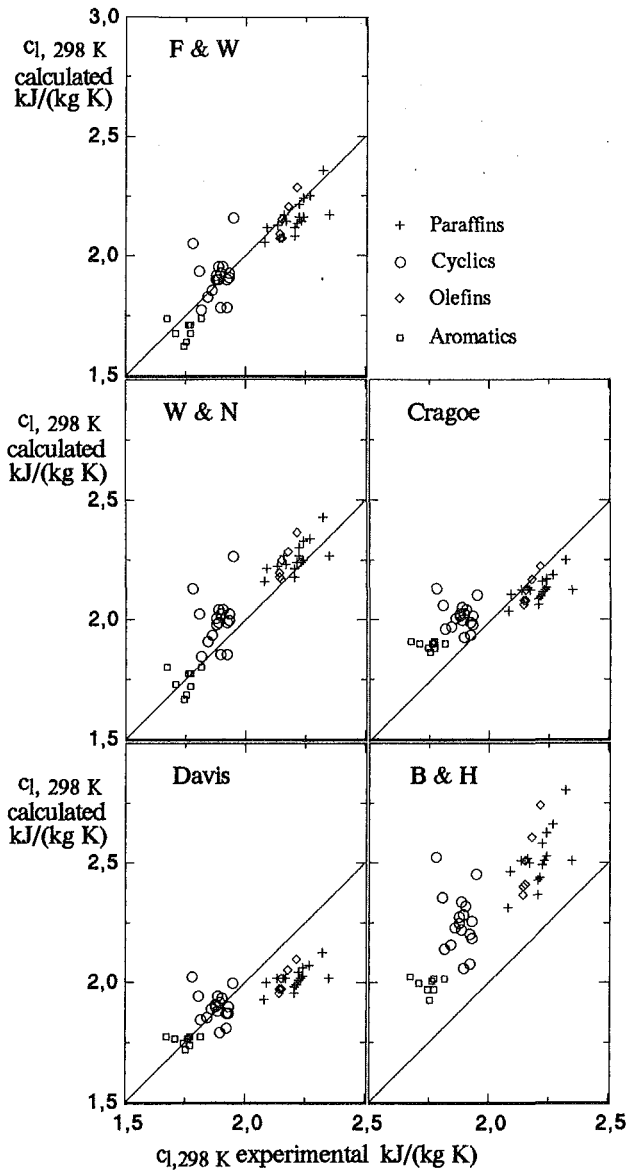


Fig. 3 Specific heats: effects of composition

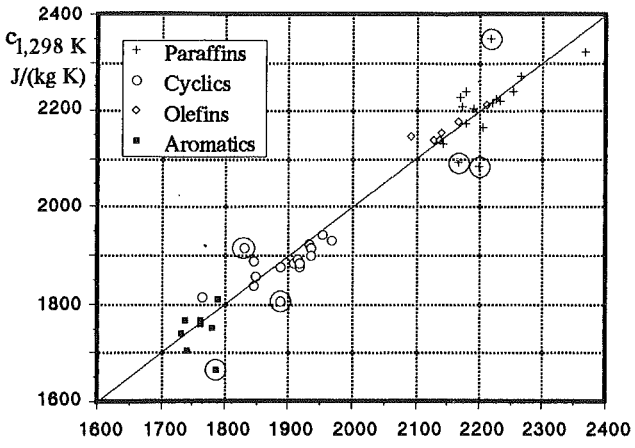
overall plan for the program on alternative fuels, an attempt has been made to calculate fuel properties using only three measurements (density, ASTM distillation, and viscosity). To date, satisfactory correlations have been obtained for density variation with temperature [14], flash point [15], molar mass [14], and calorific value [16]. The derived equation for the specific heat of liquid fuels is given below:

$$c_l = 1973 \times \left\{ 3925 \times \frac{\nu_{298}^{0.039} \times T_{av}^{0.341}}{\rho_{288}^{1.47}} \right\}^{S_h} - 42.1 \quad \text{(J/(kg K))} \qquad (8)$$

The resulting correlation is shown in Fig. 4. It is considered to be a very satisfactory correlation except that it requires knowledge of the hydrogen saturation S_h. This latter has been correlated with other properties [15], but with limited accuracy. Accordingly, a simpler correlation was sought, and the result is given in Eq. (9) and Fig. 5.

$$c_l = 1340 \times \left(0.0142 \times \frac{T_{av}^2}{\rho_{288}} \right)^{\left\{ \frac{8.028 \times 10^7}{T_{av} \rho_{288}^2} \right\}} + 30 \qquad (9)$$

The accuracy is considered to be very satisfactory. In Figs. 4 and 5, the "part data" refers to the values given for the correlation with the (apparently) inaccurate data removed from consideration (circled points).

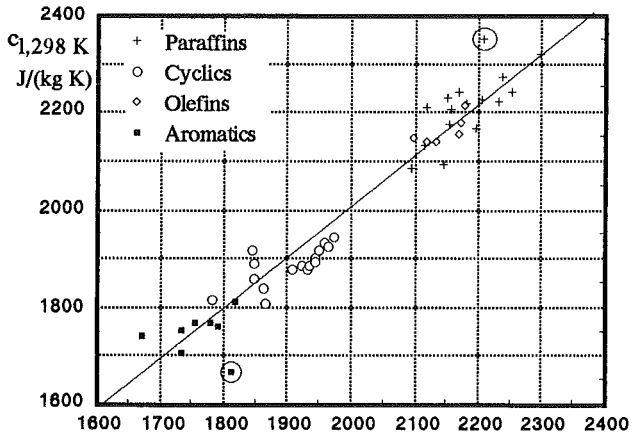


$$1973 \times \left(3925 \times \frac{\nu^{0,039}\, T_{av}^{0,341}}{\rho_{288}^{1,47}} \right)^{S_h} - 42,1 \text{ J/(kgK)}$$

y = -22,034 + 1,0090 x R^2 = 0,944 All Data
Mean absolute Error 1,6 % Maximum Error 7,1 %
Minimum error -5,6 % Standard deviation 2,3 %

y = -0,0561 + 0,9999 x R^2 = 0,978 Part Data
Mean absolute error 1,0 % Maximum error 2,1 %
Minimum error -3,3 % Standard deviation 1,4 %

Fig. 4 Specific heats: Eq. (8)



$$1340 \times \left(0,0142 \times \frac{T_{av}^2}{\rho} \right)^{\left\{ \frac{8,028 \times 10^7}{T_{av}\, \rho_{288}^2} \right\}} + 30 \text{ J/(kgK)}$$

y = -157,41 + 1,0793 x R^2 = 0,941 All Data
Mean absolute Error 1,9 % Maximum Error 8,7 %
Minimum error -6,1 % Standard deviation 2,5 %

y = -78,832 + 1,0402 x R^2 = 0,955 Part Data
Mean absolute error 1,7 % Maximum error 3,2 %
Minimum error -1,7 % Standard deviation 2,0 %

Fig. 5 Specific heats: Eq. (9)

2.3 Effects of Fuel Temperature on the Specific Heat. Figure 6 illustrates the variation with temperature of the specific heats of several organic liquids. Generally the specific heat increases as the liquid temperature is increased, although there appear to be some exceptions, probably due to the differences in experimental values as determined by the different sources.

Downloaded 02 Jun 2010 to 171.66.16.112. Redistribution subject to ASME license or copyright; see http://www.asme.org/terms/Terms_Use.cfm

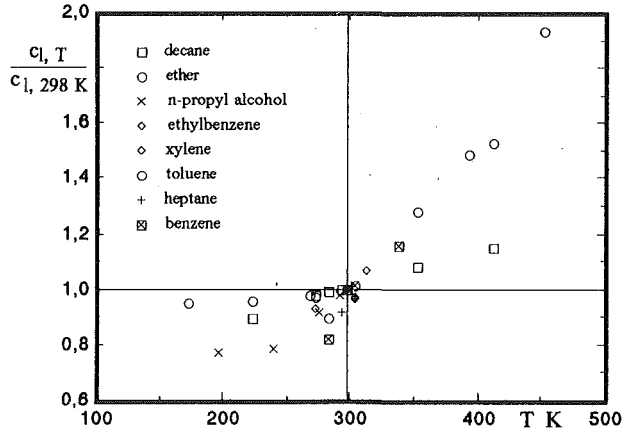


Fig. 6 Specific heats: variation with temperature

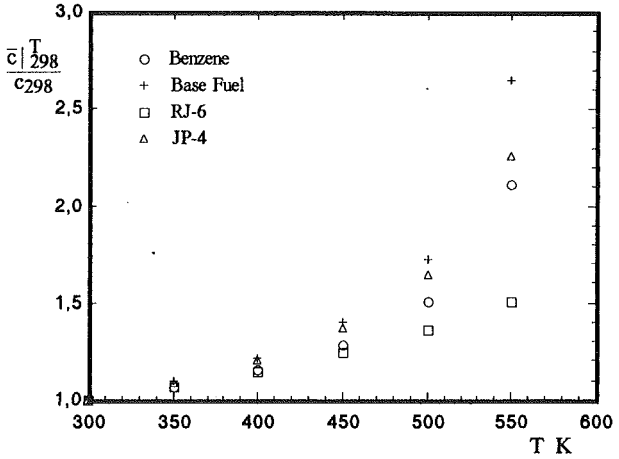


Fig. 7 Mean specific heats

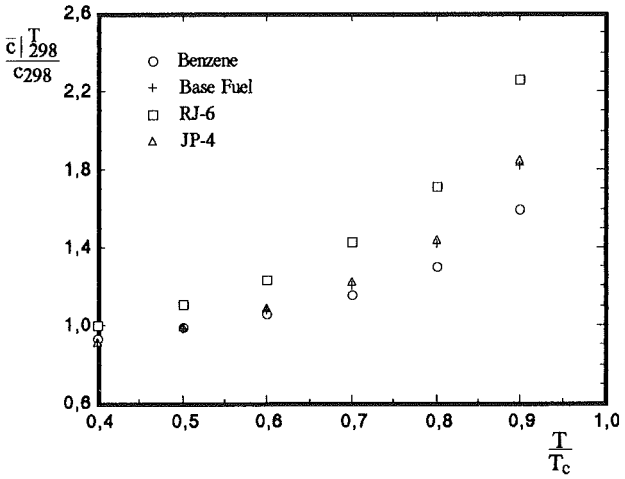


Fig. 8 Mean specific heats

A review of the available information on the changes of the liquid specific heats with temperature suggests that

$$\frac{c_{l,T}}{c_{l,298}} = \frac{a}{T_c - T} + b \tag{10}$$

The equations available that give the variation with temperature have all been derived for use over a very limited temperature range, and the variation is assumed to be linear. The best of these equations are those due of Watson et al. (Eqs. (5) and (6)). Assuming the average slope of the above equations to be correct at 298 K, we find for the terms of Eq. (10)

$$a = 4.55 \times 10^{-6} T_{av}^{2.97}$$

$$b = 1 - \frac{a}{T_c - 298}$$

$$\rightarrow \frac{c_{l,T}}{c_{l,298}} = 4.55 \times 10^{-6} T_{av}^{2.97} \left[\frac{1}{T_c - T} - \frac{1}{T_c - 298} \right] + 1 \tag{11}$$

However, it is the mean specific heat that is required

$$\bar{c}_l \Big|_{T_0}^{T} = \frac{1}{T - T_0} \times \int_{T_0}^{T} c_{l,T}\, dT \tag{12}$$

Using Eq. (11) and integrating,

$$\frac{\bar{c}_l \Big|_{T_0}^{T}}{c_{l,298}} = 1 + 4.55 \times 10^{-6} T_{av}^{2.97} \times \left[\frac{1}{T - T_o} \times \ln \frac{T_c - T_o}{T_c - T} - \frac{1}{T_c - 298} \right] \tag{13}$$

The mean specific heats, as yielded by Eq. (13), are given as functions of T and T_c in Figs. 7 and 8 using four different fuels as example. The fuel labeled "Base Fuel" is a paraffinic mixture of pure compounds used in our labs as a standard fuel for comparison purposes. The other three fuels were chosen as representing the extremes in fuel properties of all the fuels used in the present work.

It must be appreciated that the new equations derived above are only tentative and are based upon fragmentary data. Therefore, none of the above equations may be regarded as being of a very high order of accuracy. However, they do represent an improvement over the previous linear equations, which only had a very limited application. Additionally, the lack of accuracy may be compensated to some degree by the fact that in describing evaporation/diffusion phenomena, the correlating function of B is often used in the form $f(\ln(1+B))$.

3 Latent Heats of Evaporation

Even less information (than for the specific heat data) is available for the prediction of latent heats of evaporation.

Cragoe [17] gives

$$L = 1/d \times (110.9 - 0.09\Theta) \tag{14}$$

Here L is in Btu/lb, d = specific gravity at 60°/60°F and Θ; is in °F.

The accuracy of the above correlation is said to be ±10 percent and it appertains solely to atmospheric pressure. Another equation [18] relates the latent heat to the reduced temperature:

$$\frac{h_{fg,1}}{h_{fg,2}} = \left(\frac{1 - T_{r,1}}{1 - T_{r,2}} \right)^{0.38} \tag{15}$$

Some general considerations lead to the conclusion that any simple correlation should take into account both the boiling point and the molar mass. Since this latter can be expressed as a function of boiling point and liquid density, it may be that a relatively simple correlation could ensue, having sufficient accuracy for the present purpose.

Two simple correlations have been derived

$$h_{fg} = 3.361 \times 10^4 + 77.33 \frac{T_{av}}{M} \quad \text{(J/kg)} \tag{16}$$

$$h_{fg} = 2.084 \times 10^4 + 80.06 \frac{T_{av}}{M_{\text{predicted}}} \quad \text{(J/kg)} \tag{17}$$

In the second equation the predicted molar mass uses the expression derived in [19]

Downloaded 02 Jun 2010 to 171.66.16.112. Redistribution subject to ASME license or copyright; see http://www.asme.org/terms/Terms_Use.cfm

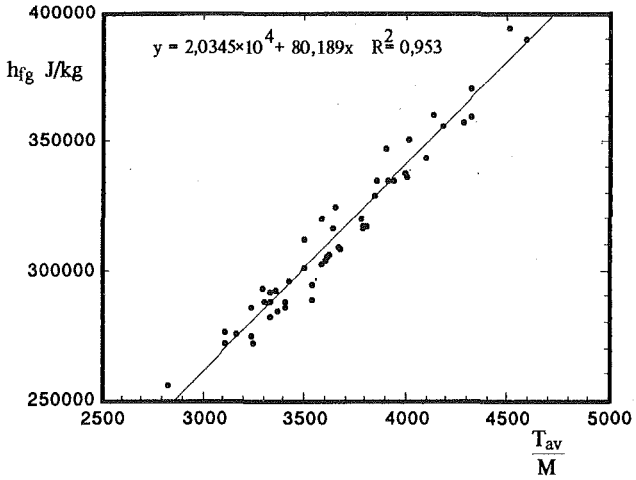


Fig. 9 Latent heats at T_{av}

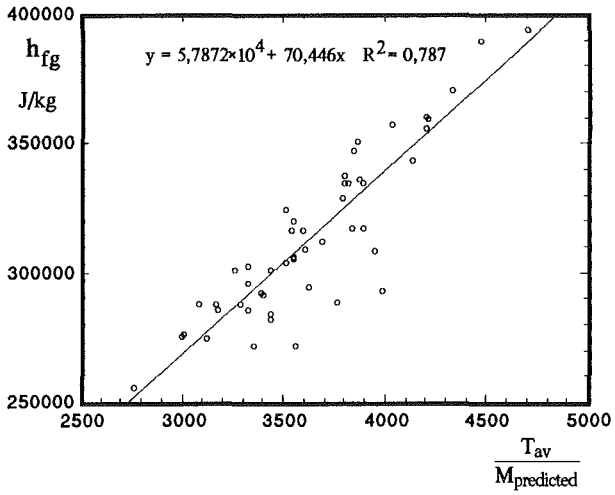


Fig. 10 Latent heats at T_{av}

$$M_{predicted} = 6.31 \times 10^{-5} \left[\frac{T_{av}}{\rho^{0.4}} \right]^{2.247} \tag{18}$$

The results of the two correlations are given in Figs. 9 and 10. It is obvious that the use of the actual molar masses gives a somewhat better correlation than the predicted ones, but in the case of commercial fuels where the molar mass will be unknown, the use of Eqs. (17) and (18) should prove to be reasonably satisfactory.

Obviously a change of pressure will bring about a change in the boiling point. One way to assess this change would be to produce a Cox chart where the vapor pressure of the fuel is plotted against a function of the temperature [20].

$$\ln p_v = a - \frac{b}{T - 59.6} \tag{19}$$

If two different vapor pressures are known, the constants in Eq. (19) may be calculated, as also the effects of pressure upon boiling point. Since T_{av} corresponds to the normal boiling point of a pure fuel, it remains to obtain another value. The Cox lines are said to apply to the critical point and, therefore, if the critical temperature and pressure can be calculated, the variation of boiling point with pressure may be obtained. Bearing in mind the initial "restriction" that all fuel properties should be expressed as functions of the data obtained from three test measurements (density, ASTM distillation, and a single viscosity) an attempt has been made to correlate the critical properties in terms of these measurements. The resulting correlations are illustrated in Figs. 11 and 12 and the corresponding equations are given below:

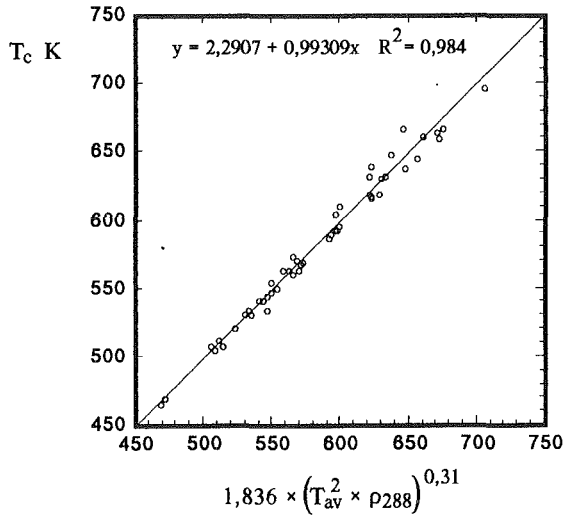


Fig. 11 Correlation for critical temperature

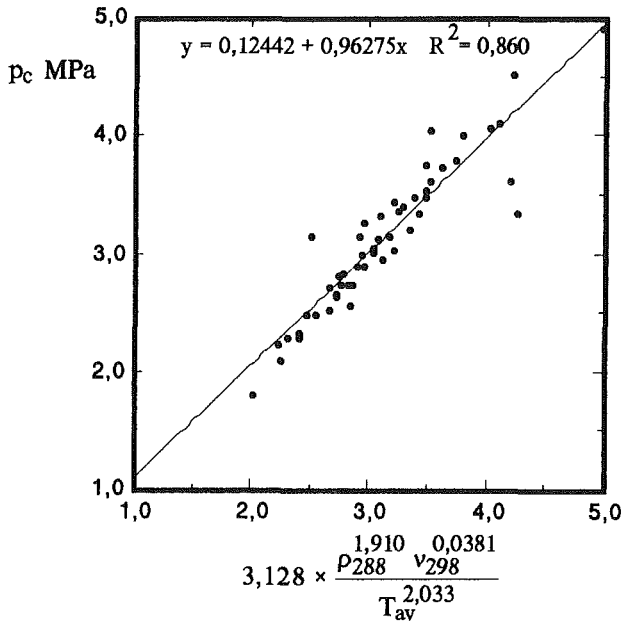


Fig. 12 Correlation for critical pressure

$$T_c = 1.836[T_{av}^2 \times \rho_{288}]^{0.31} \tag{20}$$

$$p_c = 3.128 \times 10^6 \times \frac{\rho_{288}^{1.910} \nu_{298}^{0.0381}}{T_{av}^{2.033}} \tag{21}$$

Using Eqs. (20) and (21), and substituting into the Cox equation (Eq. (18)), it now becomes possible to predict pressure effects upon the boiling point and latent heat, and these may be obtained from

$$\ln p_c = a + \frac{b}{T_c - 59.6} \text{ and } \ln p_0 = a + \frac{b}{T_{av} - 59.6} \tag{22}$$

$$b = \ln \frac{p_0}{p_c} \times \frac{(T_c - 59.6)(T_{av} - 59.6)}{T_c - T_{av}} \tag{23}$$

$$a = \ln p_0 - \ln \frac{p_0}{p_c} \times \frac{T_c - 59.6}{T_c - T_{av}} \tag{24}$$

$$\rightarrow T_B = 59.6 + \frac{b}{\ln p - a} \tag{25}$$

Downloaded 02 Jun 2010 to 171.66.16.112. Redistribution subject to ASME license or copyright; see http://www.asme.org/terms/Terms_Use.cfm

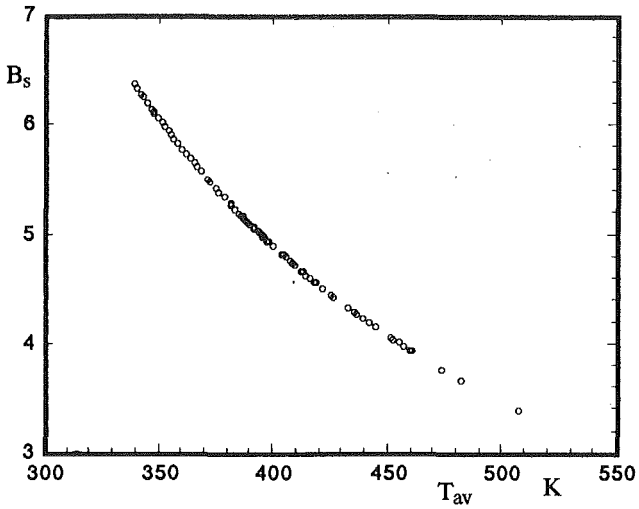


Fig. 13 Transfer number according to Spalding: Eq. (1)

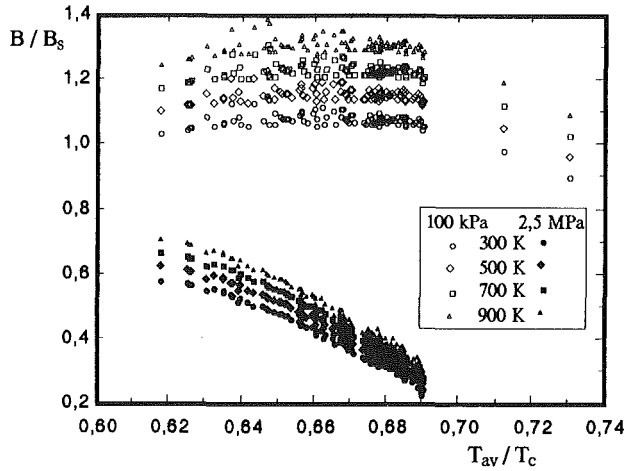


Fig. 14 Transfer number using variable specific heat

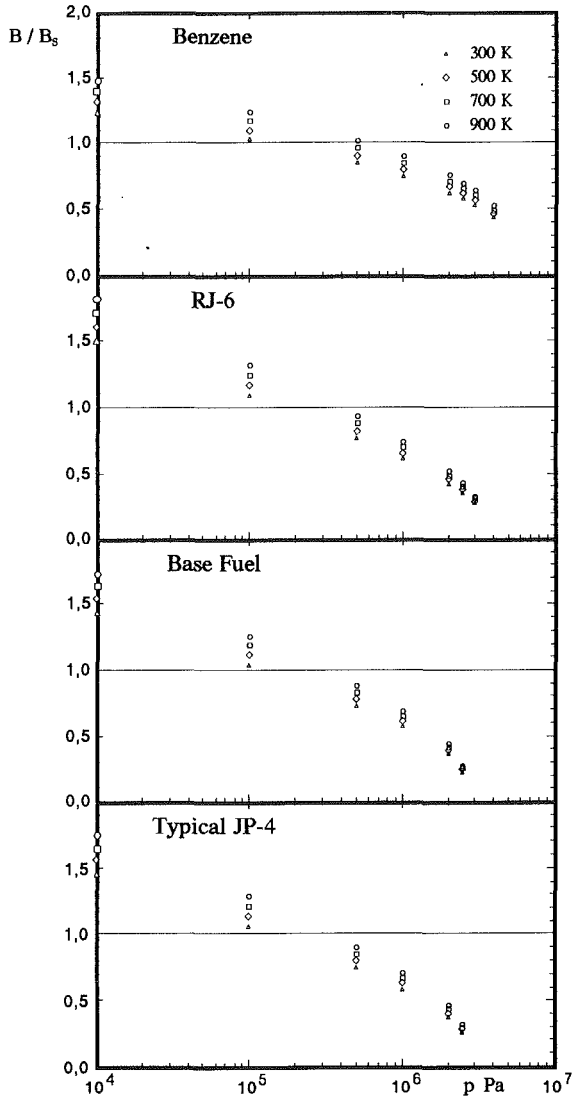


Fig. 15 Transfer number using variable specific heat

$$T_B = 59.6 + \frac{\ln \frac{p_0}{p_c} \times (T_c - 59.6)(T_{av} - 59.6)}{\ln \frac{p}{p_0} \times (T_c - T_{av}) + \ln \frac{p_0}{p_c} \times (T_c - 59.6)} \quad (26)$$

At this stage all of the factors governing the value of the transfer number are now available for a wide range of temperatures and pressures, and it becomes possible to evaluate B for the conditions generally appertaining to the operation of gas turbine combustors.

4 Calculation of Transfer Number and Its Significance

As mentioned previously, the "standard" transfer number (B_s) will be used as a comparator with values calculated from Eq. (2) using Eqs. (7)–(26) to substitute for fuel and/or operating conditions. B_s as a function of T_{av} is given in Fig. 13.

For all of the fuels, the ratio B/B_s was calculated for a range of air inlet temperatures (300, 500, 700, and 900 K) at two pressures, 100 kPa and 2.5 MPa (Fig. 14). The diagram clearly illustrates that there are very significant changes in the true value of B at the various conditions compared with B_s.

To demonstrate this more fully, four fuels have been selected and the ratio B/B_s has been calculated for a range of inlet temperatures and pressures typical of those to be found as operating conditions for gas turbine combustors. Typical results of these calculations are given in Fig. 15. (Only four fuels are shown as example). Benzene and RJ-6 were selected since they represent the extreme variations of the fuels examined, the base fuel was chosen because of its application as a standard, and the JP-4 was selected as being a typical gas turbine fuel. All the fuels show a very considerable variation of B as the conditions of inlet temperature and pressure are varied. The maximum variation of B/B_s is about a factor of six for any one fuel (about two if constant specific heat is used). The degree of confidence for these predictions is quite good except, possibly, at conditions near to criticality.

The most general application of the transfer number within combustion is to define the evaporative constant, β [21]:

$$\beta = 8 \left[\frac{\lambda}{c_p} \right]_{g,T_{st}} \times \frac{\ln (1+B)}{\rho_f} \quad (27)$$

Based upon the variations of B, the indications are that errors of about a maximum of ≈ 60 percent could occur in the estimation of β. It is therefore recommended that the true value of B be calculated for any correlation function involving β.

In all cases the variation of B is much smaller when a constant specific heat is assumed. In a sense, the two cases may be taken as expressing the "extremes" in the change of B, based upon the two different assumptions. Even though there are acknowledged weaknesses in the form of the temperature corrections employed (Section 2.2), it seems very clear that the

Downloaded 02 Jun 2010 to 171.66.16.112. Redistribution subject to ASME license or copyright; see http://www.asme.org/terms/Terms_Use.cfm

effects of temperature changes upon specific heat are such that some correction should be made. The magnitude of the variations obtained by the use of Eqs. (10)–(13) compares quite favorably with those of some other organic substances (not hydrocarbons) such as the freons and diethyl ether and suggest that their use will improve the accuracy of predicting the value of B compared with the assumption of a constant specific heat.

5 Conclusions

A series of equations has been developed for the estimation of the transfer number B. The variables examined cover a wide range of fuel and gas conditions equivalent to a gas turbine operating at inlet conditions of 300 to 900 K and from 10 kPa to 2.5 MPa pressure.

In order to make the assessment of B, it was necessary, for each fuel, to obtain values for (*a*) the liquid specific heat, (*b*) the latent heat of vaporization, (*c*) the critical temperature, and (*d*) the critical pressure. Only limited published data appear to be available for these properties, even for pure substances. Even fewer data are available for real fuels. Satisfactory prediction techniques have been developed to predict the above properties based solely upon the experimental measurements of a liquid density, the liquid viscosity at a single temperature, and the ASTM distillation.

The variations in the transfer number have been found to be quite significant, and it is recommended that for any combustion correlation purpose, the value of the transfer number used should be that calculated as directed in these notes.

References

1 Spalding, D. B., "The Calculation of Mass Transfer Rates in Absorption, Vaporization, Condensation and Combustion Processes," *Proc. Mech. Eng.*, Vol. 168, No. 19, 1954, pp. 545–570.

2 Chin, J. S., and Lefebvre, A. H., "Steady-State Evaporation Characteristics of Hydrocarbon Fuel Drops," *AIAA J.*, Vol. 21, No. 10, 1983, pp. 1437–1443.

3 ASTM Data Series Publication DS4A, *Physical Constants of Hydrocarbons C_1 to C_{10}*, prepared by ASTM Committee D-2, 1971.

4 Perry, J. H., ed., Chemical Engineer's Handbook, 3rd ed., McGraw-Hill, New York, 1951.

5 Spiers, E. M., ed., *Technical Data on Fuel*, 6th ed., British National Committee World Power Conference, London, 1962.

6 Annual Book of ASTM Standards, *Specific Heat of Liquids and Solids*, Test Method No. ASTM D-2766-83, 1984.

7 Lee, M. C., Ratcliffe, A. E., Maddox, R. D., Parham, W. F., and Maddox, R. N., "Heat Capacity Determined for Crude Fractions," *Hydrocarbon Processing*, 1978, pp. 187–189.

8 Reid, R. C., Prausnitz, J. M., and Sherwood, T. K., *The Properties of Gases and Liquids*, McGraw-Hill, New York, 3rd ed., 1977.

9 Barnett, J. C., and Hibbard, R. R., "Properties of Aircraft Fuels," NACA TN 3276, 1956.

10 Cragoe, C. S., *Thermal Properties of Petroleum Products*, Miscellaneous Publication of the US Bureau of Standards, No. 97, 1929.

11 Watson, K. M., and Nelson, E. F., *Ind. Eng. Chem.*, Vol. 25, 1933, p. 880.

12 Fallon, J., and Watson, K. M., presented before Petroleum Div. Am. Chem. Soc., Pittsburgh meeting, Sept. 1943 (see also Hougen and Watson, *Chemical Process Principles*, Wiley, New York, 1950, p. 335).

13 Davis, D. S., "Specific Heats of Mixed Liquid Petroleums," *Brit. Chem. Engrg.*, Sept. 1958, p. 506, citing Fortsch, A. R., and Whitman, W. G., "Specific Heats of Oils," *Ind. Eng. Chem.*, Vol. 18, 1926, pp. 795–800.

14 Odgers, J., and Vachon, M., *The Density of Liquid Hydrocarbons—Effects of Temperature*, Dept. of Mech. Engrg., Laval University Combustion Laboratories Report No. jo 180, Feb. 1988.

15 Kretschmer, D., and Odgers, J., "Correlation of Properties for a Wide Range of Liquid Fuels," *Workshop on Alternative Fuels for Transportation: Canadian Research Needs*, National Research Council of Canada, Ottawa, May 9–10, 1988.

16 Kretschmer, D., and Odgers, J., *The Prediction of the Calorific Values for Hydrocarbons*, Dept. of Mech. Engrg., Laval University Combustion Laboratories Report No. jo 164, Nov. 1986.

17 Cragoe, C. S., *Thermal Properties of Petroleum Products*, Miscellaneous Publication No. 97, U.S. Bureau of Standards 1929:4 cited in Technical Data on Fuels, Spiers, H. M., ed., 6th ed., The British National Committee World Power Conference, London, 1962.

18 Watson, K. M., *Ind. Eng. Chem.*, Vol. 23, 1931, p. 360; also Vol. 398, 1943.

19 Odgers, J., *The Prediction of the Molar Masses of Hydrocarbons*, Dept. of Mech. Engrg., Laval University Combustion Laboratories Report No. jo 108, Aug. 1982.

20 Odgers, J., Kretschmer, D., and Poirier, D., *On the Vapour Pressure of Hydrocarbons*, Dept. of Mech. Engrg., Laval University Combustion Laboratories Report No. jo 143, Jan. 1985.

21 Lefebvre, A. H., "Fuel Effects on Gas Turbine Combustion—Ignition, Stability, and Combustion Efficiency," ASME JOURNAL OF ENGINEERING FOR GAS TURBINES AND POWER, Vol. 107, 1985, pp. 24–37.

Downloaded 02 Jun 2010 to 171.66.16.112. Redistribution subject to ASME license or copyright; see http://www.asme.org/terms/Terms_Use.cfm

J. S. Chin
Visiting Professor.

A. H. Lefebvre
Reilly Professor of Combustion Engineering.

Thermal Science and Propulsion Center,
Purdue University,
West Lafayette, IN 47907

F. T.-Y. Sun
Gas Turbine Fuel Systems Division,
Parker Hannifin Corp.,
Cleveland, OH 44112

Temperature Effects on Fuel Thermal Stability

The thermal stability characteristics of four kerosine-type fuels are examined using a heated-tube apparatus that allows independent control of fuel pressure, fuel temperature, tube-wall temperature, and fuel flow rate. It is a closed loop system, and fuel flows through the heated tube for periods ranging from 6 to 22 h. The deposition rates of carbon on the tube walls are measured by weighing the tube before and after each test. The results obtained show that tube-wall and fuel temperatures both have a marked influence on deposition rates, the impact of fuel temperature being stronger than that of wall temperature. It is also found that deposition rates increase continuously with increases in tube-wall temperature. This finding contradicts the results of previous studies, which had led to the conclusion that deposition rates increase with increase in wall temperature up to a certain value, beyond which any further increase in wall temperature causes the deposition rate to decline.

Introduction

Thermal instability is the term used to describe the chemical degradation of hydrocarbon fuels due to the high temperatures encountered in an aircraft's fuel system prior to combustion. The main effect of this increase in fuel temperature is to stimulate oxidation reactions that lead to the formation of insoluble material, which has several adverse effects on engine performance. These include fouling of heat exchanger surfaces, which lowers the efficiency of heat transfer, and deposits in fuel nozzles, which tend to block small passages and distort the fuel spray.

Several laboratory techniques are available for characterizing the thermal oxidative tendencies of fuels. The current international requirement is that a fuel should perform acceptably in the Jet Fuel Thermal Oxidation Tester (JFTOT). This tester, and its forerunner the ASTM-CRC Fuel Coker, both pass the test fuel over a heated tube and then through a filter that traps any degradation products formed during the test. The fuel is rated partly by the extent of filter plugging, as indicated by the pressure drop across it, and also by the visual appearance of the deposition on the heated tube. The drawback to these test methods is that although some fuels are inherently easy to evaluate, since they exhibit a sharp threshold of temperature at which they start to form deposits, other fuels, and especially those having good thermal stability properties, are more difficult to evaluate, and it may be necessary to conduct a series of tests on one fuel at several different temperatures to determine the threshold or "breakpoint" temperature at which the fuel starts to form visible preheater deposits or to plug the filter. They are essentially pass-or-fail types of tests, which are quite inadequate for scientific research. In any case, engineers are basically interested in deposit thickness, as thickness is the major criterion in heat transfer and in the mechanical blockage of small tubes and passages, and thickness is not necessarily related to deposit color.

Research on fuel thermal stability has been actively pursued by the major fuel companies. The Esso Heat Transfer Unit was developed for the FAA Supersonic Transport Program as a research tool for relating fuel properties with heat exchanger degradation. The Shell Single-Tube Heat Transfer Rig was built originally to investigate how turbine fuels would perform in the fuel system of the Concorde, but was used later in a broader role to study aircraft fuel performance in general. Other nonspecification fuel testers that have shed useful light on fuel thermal degradation phenomena include the NASA Single Tube Heat Exchanger and the UTRC Fuel Deposit Test Apparatus. Fuller descriptions of these and other techniques used for studying the causes and effects of fuel thermal instability are contained in publications by Bachman (1985), Kendall and Mills (1985), Mills and Kendall (1986), Vranos and Marteney (1980), Szetala (1976), Roback et al. (1983), TeVelde et al. (1983), Szetala et al. (1985), Giovanetti and Szetala (1986), Baker et al. (1983), Cohen (1980), and Marteney and Spadaccini (1986).

None of the techniques now being used for the assessment of fuel thermal stability are entirely free from defects. Nevertheless, despite their shortcomings, these techniques have yielded useful information on the various mechanisms involved in the fuel degradation process, and also on the manner and extent to which thermal oxidation stability is influenced by the physical and chemical properties of the fuel. Thus it is now known that for conventional fuels the degradation process normally stems from oxidation of the fuel by dissolved oxygen in the fuel. This is the primary mechanism in initiating deposit formation. Oxidation products subsequently react with minor fuel constituents and with each other to generate the insoluble materials that deposit on fuel system surfaces. The process is accelerated by the presence in the fuel of heterocompounds containing nitrogen, sulfur, oxygen, and trace metals. Copper in particular has been found to be very detrimental to thermal

Contributed by the International Gas Turbine Institute and presented at the 36th International Gas Turbine and Aeroengine Congress and Exposition, Orlando, Florida, June 3-6, 1991. Manuscript received at ASME Headquarters February 19, 1991. Paper No. 91-GT-97. Associate Editor: L. A. Riekert.

Copyright © 1992 by ASME
Downloaded 02 Jun 2010 to 171.66.16.112. Redistribution subject to ASME license or copyright; see http://www.asme.org/terms/Terms_Use.cfm

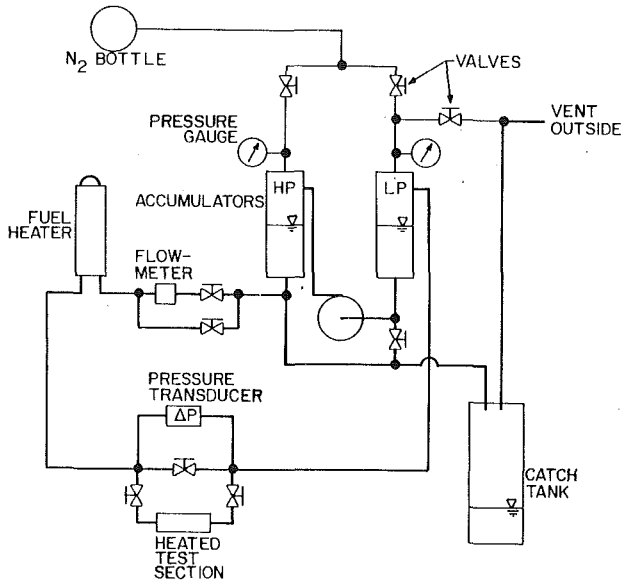


Fig. 1 Schematic diagram of fuel thermal stability rig

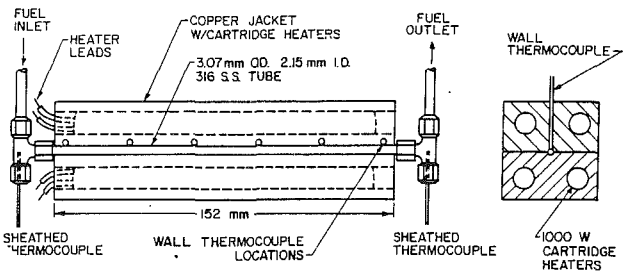


Fig. 2 Details of test section

stability. At fuel temperatures higher than around 700 K, fuel pyrolysis starts to influence deposition rates and, with further increases in fuel temperature, the reaction mechanism gradually changes from oxidation-controlled to pyrolysis-controlled, which causes the rate of deposition to decline. Thus, in discussing the influence of temperature on deposit formation, it is important to bear in mind that it is the fuel temperature that determines which reaction mechanism is dominant—oxidation or pyrolysis—not the tube-wall temperature.

The primary role played by temperature in the processes of fuel thermal degradation and deposit formation has been known for some time. A NASA workshop held in 1978 identified wall temperature as the most important parameter affecting deposition rates, fuel temperature being the second most important parameter. Subsequent research has generally confirmed this finding; for example, the results obtained by Giovanetti and Szetela (1986) for Jet A fuel showed that "carbon deposit rates were a strong function of tube wall temperature." In view of the prime importance of temperature to fuel thermal degradation and deposit formation, it is somewhat surprising to find in the literature that in most experimental studies the only temperature recorded is either fuel temperature or wall temperature, but not both. In some reported studies on the influence of temperature on thermal stability, it is not clear whether the temperature under consideration is that of the fuel or the wall. Thus it is easy to understand the considerable scatter that tends to characterize reported experimental data on the effect of temperature on deposit formation rates.

In the present research an attempt is made to study the separate effects of fuel and wall temperatures on deposition rates. This goal is achieved by continuously controlling and regulating the heat inputs to both the fuel and the tube wall to maintain constant fuel and wall temperatures throughout the duration of each test. The test method employed and the results obtained are described below.

Thermal Stability Rig

The main features of the fuel thermal stability rig are shown in Fig. 1. It is a closed-loop system, designed to recirculate fuel over wide ranges of temperature, flow rate, and pressure. The major components are the pump, accumulators to contain the test fuel, a fuel heater, a heated test section, a flow meter, and another meter for monitoring the pressure drop across the section. In operation, the test fuel flows from a 5-liter high-pressure accumulator through the flow meter and fuel heater into the test section from whence it flows into the low-pressure accumulator. The function of the pump is to transfer fuel from the low-pressure accumulator to the high-pressure accumulator. The pressures in both accumulators can be set to any desired values, up to a maximum of 4.1 MPa (600 psi), by using nitrogen gas from a high-pressure container.

The key component of the test section is a thin-walled stainless steel tube whose principal dimensions are: length, 152 mm; outer diameter, 3.07 mm; and inner diameter, 2.15 mm. This tube is clamped between two copper segments, as illustrated in Fig. 2. The semicircular grooves cut into the two copper segments form a cylindrical passage when the segments are placed together. The diameter of this passage is designed to be very slightly smaller than the outer diameter of the stainless steel tube to ensure good thermal contact between the tube and the copper segments when the latter are clamped together. A number of thermocouples are threaded through one of the copper segments in such a manner that in operation the thermocouple beads are pressed tightly against the stainless-steel tube. These thermocouples are used to measure tube-wall temperatures at inlet and outlet and at four equispaced stations in between. Fuel temperatures are measured only at the tube inlet and outlet.

The stainless steel tube is heated by using between one and four 1000-W electrical rod heaters, which are inserted into holes drilled into the copper segments, as shown in Fig. 2. This arrangement ensures that the tube is heated uniformly around its circumference and, in fact, calculations show that this circumferential uniformity is maintained even when only one electrical heater is operational.

For any given fuel, the fuel pressure and flow rate are set at suitable values and the heaters for the fuel and test section are both switched on. During the fuel heatup period, which is usually less than ten minutes, the flowing fuel bypasses the test section. When the fuel and tube-wall temperatures have both attained the desired values, the bypass valves are operated to divert the hot fuel through the test section. This is a most useful feature because it allows the start of the test to be clearly defined. Another useful feature of the present test rig is the feedback between the fuel and tube-wall thermocouples and the fuel and test section heaters, respectively, which allows both fuel and tube-wall temperatures to be maintained at preset values within 1°C throughout the entire duration of the test. This flexibility allows tests to be carried out on the influence of fuel temperature on deposition rates while maintaining a constant wall temperature. Alternatively, fuel temperature can be kept constant to permit the separate effect of variations in wall temperature on deposition rates to be studied.

Deposition rates are determined by weighing the tube before and after each test. The fuel supply connections at both ends of the tube are sealed using graphite ferrules. These ferrules are broken off after each test to reduce weight and thereby increase the ratio of the deposit mass to the tube mass. The weight of the tube is around 4000 mg. The deposits usually weigh between 2 and 20 mg depending on the fuel composition

Downloaded 02 Jun 2010 to 171.66.16.112. Redistribution subject to ASME license or copyright; see http://www.asme.org/terms/Terms_Use.cfm

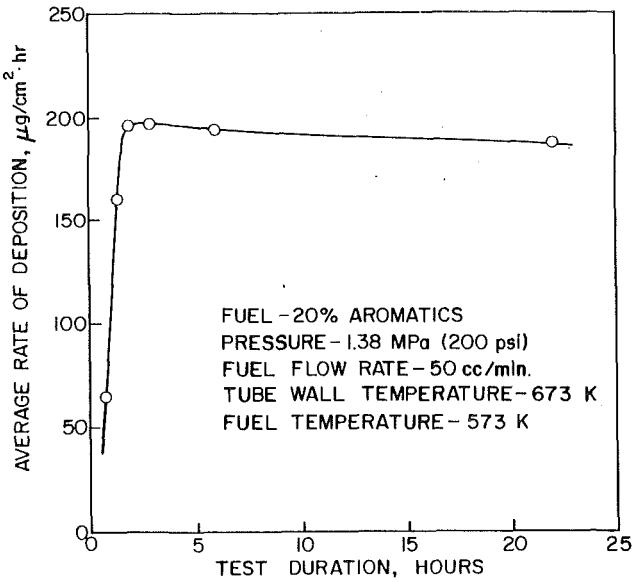


Fig. 3 Influence of test duration on deposition

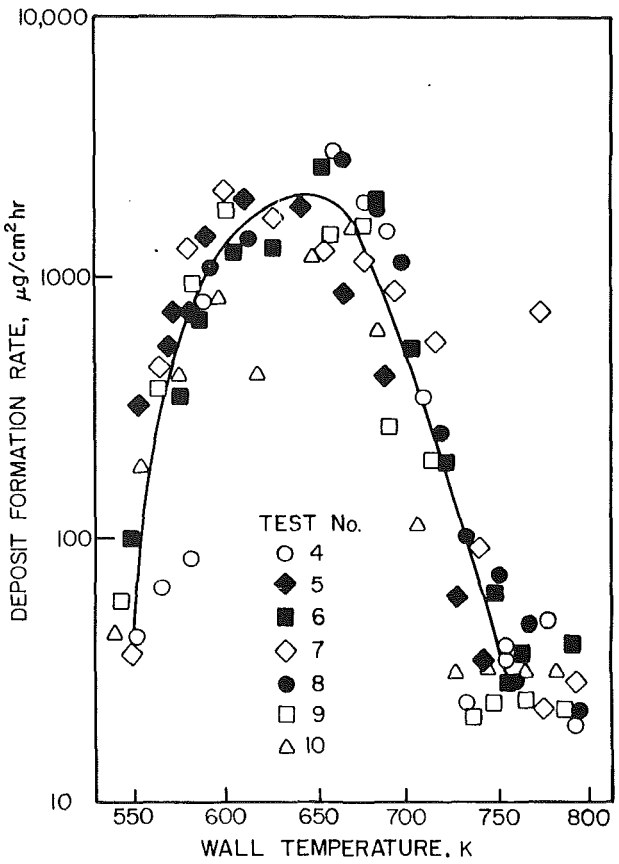


Fig. 4 Influence of tube-wall temperature on deposition rate (TeVelde and Glickstein, 1983)

and test conditions. As the balance employed has an accuracy of within 0.1 mg, the weighing procedure is considered capable of giving satisfactory results.

Tube treatment, both before and after each test, was found to affect the results obtained. After some experimentation the following procedure was established. Before weighing the tube prior to test it is exposed to the flame of a welding torch. As the tubes are manufactured by an extrusion process, flame heating is used to remove any remaining oil or grease. The tube is then dried using heated nitrogen gas. After the test the fuel is drained from the test section, which is allowed to cool down to normal room temperature. The tube is then removed from the test section and allowed to dry naturally for twelve hours before being weighed. This procedure is found to give consistent and repeatable results.

Results

Some of the results obtained using a light heating oil as the test fuel are shown in Fig. 3. This figure shows the average rate of deposition in $\mu g/cm^2 \cdot h$ plotted against the test duration in hours. The data presented in Fig. 3 were obtained by removing the tube for weighing several times during the total test duration of 22 hours. The same fuel was used throughout the test. The purpose of Fig. 3 is to illustrate how the rate of deposition increases initially and then remains fairly constant. It should be noted that the deposition rates shown in Fig. 3 are "average" values, not instantaneous values. For example, the graph shows that during the first six hours the average rate of deposition was 195 $\mu g/cm^2 \cdot h$. Thus the total deposition at the end of six hours was $6 \times 195 = 1170\ \mu g/cm^2$.

Figure 3 is typical of the results obtained at other test conditions and with other fuels. It illustrates that after the first few hours the rate of deposition settles down at a fairly uniform value, which suggests that most of the useful information to be gleaned from a test run can be extracted after five or six hours and there is little to be gained by protracting the test any further. Based on the knowledge and experience gained in a whole series of preliminary tests, it was decided to standardize on a test duration of six hours. This time period has no special significance, except that it allows a complete test to be performed within a normal working day.

Effect of Tube-Wall Temperature

The influence of wall temperature on deposition rates has been examined by several workers. TeVelde and Glickstein (1983) used a heated tube apparatus to evaluate the thermal stability characteristics of four liquid hydrocarbon fuels: a low aromatic JP5, a blend of 80 percent JP 5 and 20 percent cracked gas oil, a blend of 50 percent JP 5 and 50 percent No. 2 heating oil, and a shale-derived JP 5. Deposit formation rates were obtained for tube-wall temperatures ranging from 480 to 800 K. The deposition characteristics of all four fuels were found to be very sensitive to wall temperature, with peak formation rates occurring at surface temperatures around 650 K, as illustrated in Fig. 4. Examination of these data led TeVelde and Glickstein to the conclusion that the effect of tube wall temperature on deposit temperature was "similar for all four fuels, that is, formation rates increased rapidly with increasing surface temperature up to approximately 700 to 750°F (644 to 672 K) and then decreased with further increases in surface temperature." This conclusion appears to have considerable practical significance because it suggests that an effective method of reducing deposition rates would be by increasing the tube-wall temperature, provided the initial wall temperature is in excess of around 650 K. Other workers have reached similar conclusions, but the present work indicates that this conclusion is erroneous and is the result of an inherent defect in the method used to measure deposition rates. With this method the test fuel is arranged to flow through a resistance-heated stainless steel tube. During any given test the local wall temperature does not remaining constant but changes dramatically with time, as shown in Fig. 5 from TeVelde and Glickstein (1983). Moreover, the local wall temperature must always be a function of the local deposit thickness, because where the deposit is thicker, the wall temperature must be higher to maintain the same heat flux through the tube wall. Thus, at the entry section to the tube, deposition rates are low

Downloaded 02 Jun 2010 to 171.66.16.112. Redistribution subject to ASME license or copyright; see http://www.asme.org/terms/Terms_Use.cfm

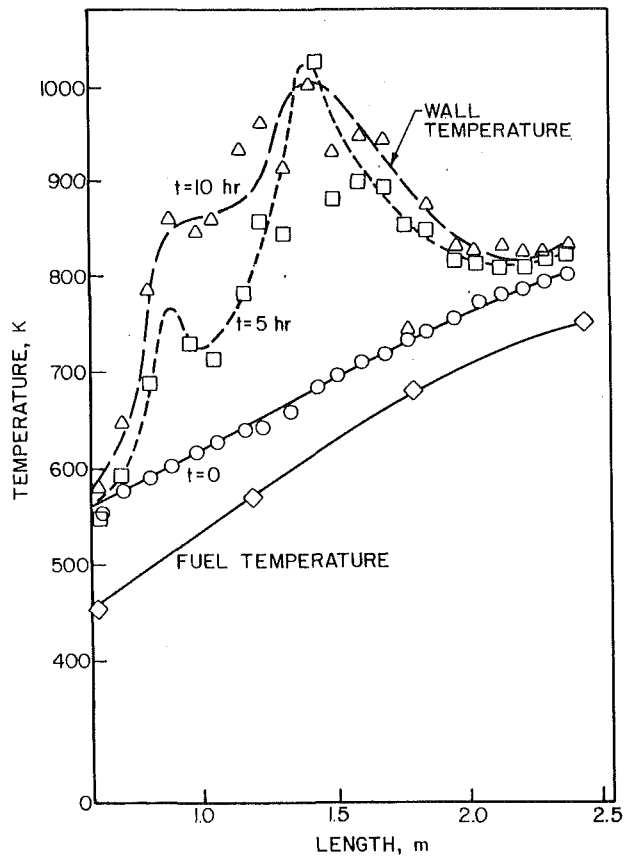


Fig. 5 Distribution of fuel and wall temperatures along tube length (TeVelde and Glickstein, 1983)

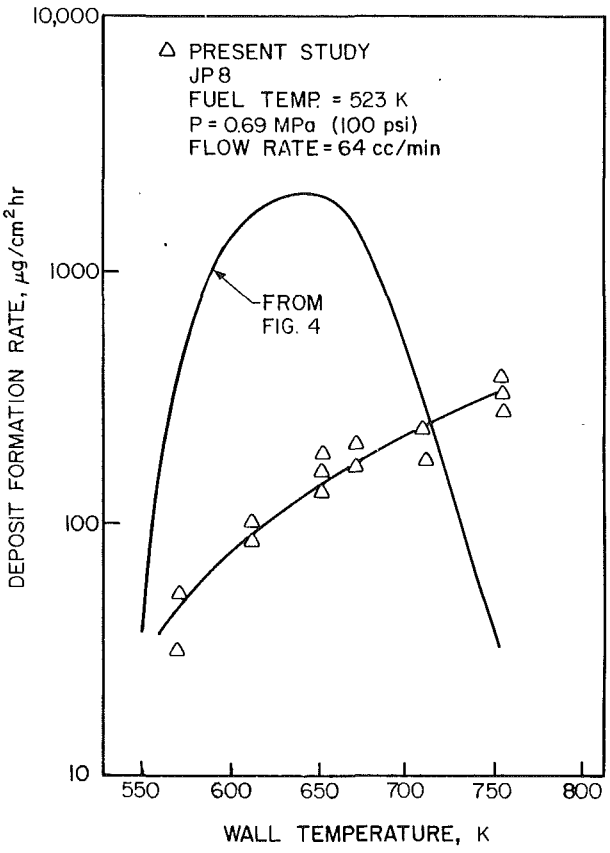


Fig. 6 Comparison of data from Fig. 4 with results of present study

because the fuel temperature is low. This, in turn, leads to a low wall temperature, as shown in Fig. 4.

As the fuel flows along the tube its temperature rises and, consequently, so also does the rate of deposition. This increase in deposit thickness leads to an increase in local wall temperature, as illustrated in Fig. 5. This figure shows that, at a point about halfway along the tube, the local wall temperature, whose initial value was around 650 K, has risen to around 1000 K after five hours operation. At this tube location, the combination of high fuel and high wall temperatures produces the high deposition rates shown in Fig. 4 for an initial wall temperature of 650 K. Fuel temperature continues to rise toward the downstream end of the tube, but this does not produce a high deposition rate because the mechanism of formation changes from auto-oxidation to pyrolysis. In fact, the rate of deposition actually declines in this range of high fuel temperatures. This causes a reduction in deposit thickness and hence a lowering of wall temperature during the test duration, as shown in Fig. 5. The combination of a lower wall temperature and the change in reaction mechanisms from auto-oxidation to pyrolysis causes the deposition rate to decline, despite the higher initial wall temperature, as shown in Fig. 4.

Thus, curves of the type shown in Fig. 4, which are intended to demonstrate the effect of tube-wall temperature on deposition rates, are really showing the combined effects of simultaneous variations in both wall and fuel temperatures. Of these, fuel temperature is the most important, and, in reality, the shape of the curve shown in Fig. 4 more aptly describes the effect on deposition rates of variations in fuel temperature than variations in wall temperature. In fact, for this particular apparatus, after several hours of operation the local wall temperature at any point along the tube length is much more indicative of the local deposit thickness than the local rate of deposition.

The results presented in Figs. 4 and 5, along with other data in the literature obtained using the resistance-heated tube method, all suffer from the drawback that they were acquired using an apparatus in which fuel and wall temperatures both increase appreciably along the length of the test tube. Moreover, the local wall temperature changes continuously and markedly during the test period. Under these conditions it is clearly difficult, if not impossible, to differentiate between the effects of wall temperature and fuel temperature on deposition rates.

The apparatus employed in the present research is free from these defects. The fuel temperature at entry to the test tube is governed by a preheater and is accurately controlled to within $\pm 0.5°C$. The temperature rise experienced by the fuel as it flows through the tube is always quite small and seldom exceeds 10°C. The tube-wall temperature is always maintained at a constant value throughout its entire length. By exercising separate control over fuel and wall temperatures, the effects on deposition rates of variations in these two parameters can be clearly distinguished.

Some of the results obtained with this apparatus on the effect of wall temperature on deposition rates are shown in Fig. 6. They illustrate the effect of wall temperature on deposition rates for a JP 8 fuel at a constant temperature of 523 K. The data are consistent with all other data obtained with this apparatus in showing a continuous increase in deposition rate with increase in wall temperature for a constant fuel temperature. Also shown in Fig. 6, for comparison, is a line drawn to represent the data points plotted in Fig. 4.

The results for JP 8 fuel shown in Fig. 6 are considered to represent the true effect of wall temperature on deposition rates. Provided the fuel temperature is maintained constant, an increase in wall temperature will always increase the rate of deposition. The observed differences between the two sets of data in Fig. 6 may be explained as follows. At low wall

Downloaded 02 Jun 2010 to 171.66.16.112. Redistribution subject to ASME license or copyright; see http://www.asme.org/terms/Terms_Use.cfm

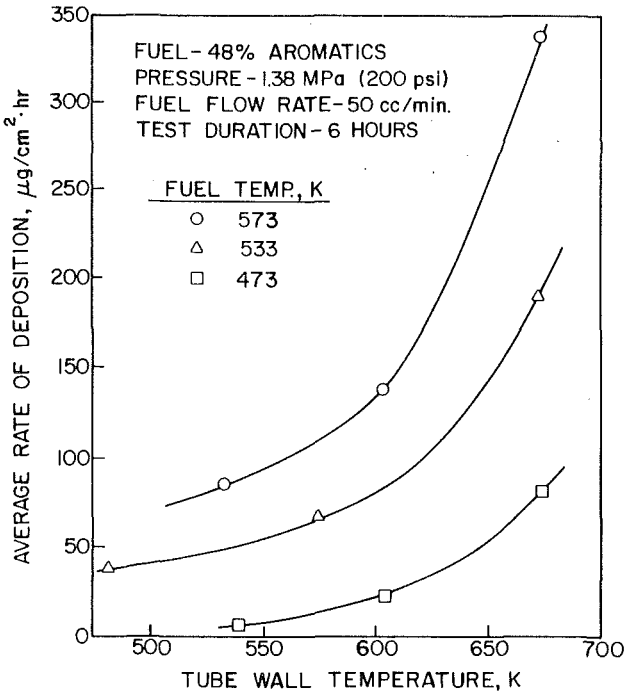


Fig. 7 Influence of tube-wall temperature on deposition rate

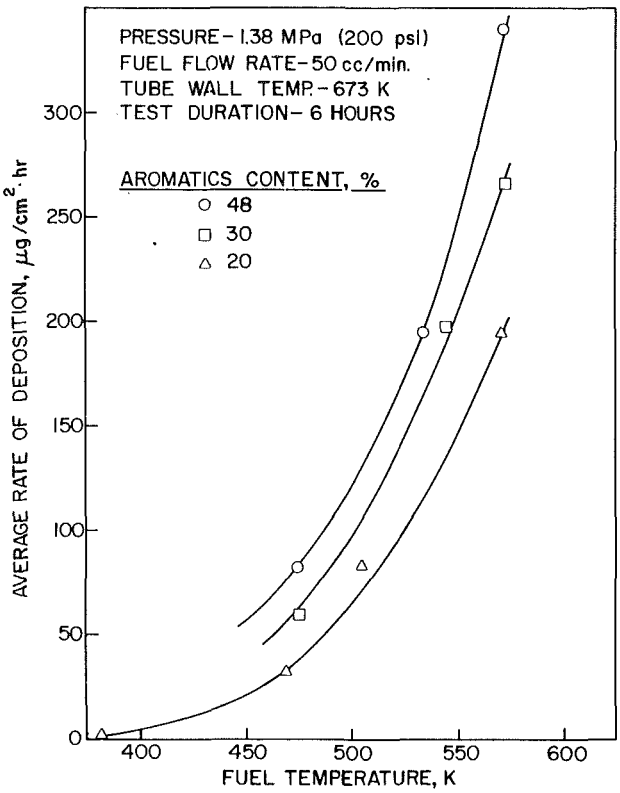


Fig. 8 Influence of fuel temperature on deposition rate

temperatures, fuel temperatures are also low, and both curves are characterized by low deposition rates. At higher temperatures, around 650 K, the UTRC data exhibit much higher deposition rates. This is attributed to (*a*) a much higher *actual* wall temperature of around 1000 K (see Fig. 5) as opposed to the *initial* wall temperature of 650 K, and (*b*) a much higher fuel temperature of 600 K in comparison with the JP 8 fuel temperature, which remained sensibly constant at 523 K. At the highest levels of wall temperature shown in Fig. 6, the rates of deposition for JP 8 are appreciably higher than for the UTRC fuels. This is attributed to the latter's higher temperatures (755 K versus 523 K), which cause deposit formation to occur by the pyrolysis mechanism as opposed to the more productive auto-oxidation mechanism for the lower temperature, JP 8 fuel. Thus, as noted earlier, the JP 8 data represent the true effect of wall temperature on deposit rates. In contrast, the UTRC data reflect the combined effects of variations in both wall and fuel temperatures, plus the added complication of a change in the mechanisms of deposit formation from auto-oxidation to pyrolysis at the higher levels of fuel temperature.

The effect of wall temperature on deposition rates is further illustrated by the results obtained using a kerosine-type fuel containing 48 percent aromatics, as shown in Fig. 7. These results clearly demonstrate the marked influence of wall temperature on rates of deposition and also show that this influence becomes more pronounced when an increase in wall temperature is accompanied by an increase in fuel temperature. This highlights the need for separate control of fuel temperature in experimental studies on the effect of wall temperature on deposition rates.

Effect of Fuel Temperature

Fuel temperature has a pronounced effect on thermal stability, as illustrated in Fig. 8. The results shown in this figure generally confirm the findings of all previous studies on the influence of fuel temperature on thermal stability. They show, for all three fuels, that deposition rates are relatively low for fuel temperatures below around 400 K, but rise steeply with increases in fuel temperature above around 500 K.

As mentioned earlier, one of the main assets of the apparatus used in this test program is that it allows separate and independent control of both tube-wall and fuel temperatures. This enables the relative importance of these two parameters to be determined. From inspection of Figs. 7 and 8 it is clear that, over the ranges of fuel and wall temperatures investigated, both of these parameters strongly affect thermal stability. However, these figures also show that the influence of fuel temperature is more pronounced than that of wall temperature. The observed apparent dominance of fuel temperature over wall temperature may be due in some measure to the fact that the thermal degradation reactions are influenced by fuel temperature throughout the whole test period, whereas wall temperatures can affect these reactions only during the much shorter residence time of the fuel in the test section.

Another explanation for the observed strong influence of fuel temperature is that deposition rates are governed primarily by the temperature of the fuel in the relatively slow-moving boundary layer near the tube wall. This temperature is dictated mainly by the bulk temperature of the fuel, which emphasizes the paramount importance of fuel temperature to deposition rates, as illustrated in Fig. 8. It is also strongly affected, albeit to a lesser extent, by the adjacent wall temperature which serves to raise or lower the fuel temperature in the boundary layer depending on whether the wall temperature is higher or lower than the fuel temperature.

Concluding Remarks

Thermal stability characteristics of four kerosine-type fuels have been investigated using a heated-tube apparatus, which permits independent control of fuel temperature, wall temperature, pressure, and flow velocity. The results obtained demonstrate the applicability of the apparatus for studying fuel thermal stability and deposition rates over a broad range of test conditions. The measurements indicate that consistent and repeatable results can be obtained to within ± 10 percent.

The results obtained to date shed useful light on the important role played by temperature in fuel thermal stability. They show that tube-wall and fuel temperatures both have a

Downloaded 02 Jun 2010 to 171.66.16.112. Redistribution subject to ASME license or copyright; see http://www.asme.org/terms/Terms_Use.cfm

marked influence on deposition rates, the impact of fuel temperature being stronger than that of wall temperature. They also show that deposition rates increase continuously with increase in wall temperature and do not decline at wall temperatures above around 650 K as the results of previous studies would appear to suggest.

Comparisons of the results obtained with light-distillate fuels of different aromatics content indicates that deposition rates are enhanced by an increase in aromatic content, the effect becoming less pronounced for fuels of higher aromatic content.

Acknowledgments

The authors are pleased to acknowledge the contribution made by Dr. David T. Walker, now at the University of Michigan, Ann Arbor, to the design and construction of the apparatus used in the experiments. They also wish to express their gratitude for the financial support received from the Parker Hannifin Corporation of Cleveland, Ohio.

References

Bachman, K. C., 1985, "Heat Transfer Unit Evaluates Performance of Jet Fuels for Supersonic Aircraft," SAE Paper No. 6750803.

Baker, C. E., Bittker, D. A. Cohen, S. M., and Seng, G. T., 1983, "Research on Aviation Fuel Instability," AGARD Conference Proceedings No. 353, *Combustion Problems in Turbine Engines*, pp. 2/1-2/10.

Cohen, S. M., 1980, "Fuels Research—Fuel Thermal Stability Overview," *Aircraft Research and Technology for Future Fuels*, NASA CP-2146, pp. 161-168.

Giovanetti, A. J., and Szetela, E. J., 1986, "Long Term Deposit Formation in Aviation Turbine Fuel at Elevated Temperatures," *AIAA J. Propul. Power*, Vol. 2, No. 5, pp. 450-456.

Kendall, D. R., and Mills, J. S., 1985, "The Influence of JFTOT Operating Parameters on the Assessment of Fuel Thermal Stability," SAE Paper No. 851871.

Marteney, P. J., and Spadaccini, L. J., 1986, "Thermal Decomposition of Aircraft Fuels," ASME JOURNAL OF ENGINEERING FOR GAS TURBINES AND POWER, Vol. 108, pp; 648-653.

Mills, J. S., and Kendall, D. R., 1986, "The Quantification Improvement of the Thermal Stability of Aviation Turbine Fuel," ASME JOURNAL OF ENGINEERING FOR GAS TURBINES AND POWER, Vol. 108, pp. 381-386.

Roback, R., Szetela, E. J., and Spadaccini, L. J., 1983, "Deposit Formation in Hydrocarbon Fuels," ASME JOURNAL OF ENGINEERING FOR GAS TURBINES AND POWER, Vol. 105, pp. 55-65.

Szetela, E. J., 1976, "Deposits From Heated Gas Turbine Fuels," ASME Paper No. 76-GT-9.

Szetela, E. J., Giovanetti, A. J., and Cohen, S., 1985, "Fuel Deposit Characteristics at Low Velocity," ASME Paper No. 85-1GT-130.

TeVelde, J. A., and Glickstein, M. R., 1983, "Heat Transfer and Stability of Alternative Aircraft Fuels," Vol. 1, Report AD A137404.

TeVelde, J. A., and Spadaccini, L. J., Szetela, E. J., and Glickstein, M. R., 1983, "Alternative Fuel Deposit Formation," AGARD Conference Proceedings No. 353, *Combustion Problems in Turbine Engines*, pp. 3/1-3/10.

Vranos, A., and Marteney, P. T., 1980, "Experimental Study of Turbine Fuel Thermal Stability in an Aircraft Fuel System Simulator," *Aircraft Research and Technology for Future Fuels*, NASA CP 2146, pp. 169-176.

Downloaded 02 Jun 2010 to 171.66.16.112. Redistribution subject to ASME license or copyright; see http://www.asme.org/terms/Terms_Use.cfm

marked influence on deposition rates, the impact of fuel temperature being stronger than that of wall temperature. They also show that deposition rates increase continuously with increase in wall temperature and do not decline at wall temperatures above around 650 K as the results of previous studies would appear to suggest.

Comparisons of the results obtained with light-distillate fuels of different aromatics content indicates that deposition rates are enhanced by an increase in aromatic content, the effect becoming less pronounced for fuels of higher aromatic content.

Acknowledgments

The authors are pleased to acknowledge the contribution made by Dr. David T. Walker, now at the University of Michigan, Ann Arbor, to the design and construction of the apparatus used in the experiments. They also wish to express their gratitude for the financial support received from the Parker Hannifin Corporation of Cleveland, Ohio.

References

Bachman, K. C., 1985, "Heat Transfer Unit Evaluates Performance of Jet Fuels for Supersonic Aircraft," SAE Paper No. 6750803.

Baker, C. E., Bittker, D. A. Cohen, S. M., and Seng, G. T., 1983, "Research on Aviation Fuel Instability," AGARD Conference Proceedings No. 353, *Combustion Problems in Turbine Engines*, pp. 2/1-2/10.

Cohen, S. M., 1980, "Fuels Research—Fuel Thermal Stability Overview," *Aircraft Research and Technology for Future Fuels*, NASA CP-2146, pp. 161-168.

Giovanetti, A. J., and Szetela, E. J., 1986, "Long Term Deposit Formation in Aviation Turbine Fuel at Elevated Temperatures," *AIAA J. Propul. Power*, Vol. 2, No. 5, pp. 450-456.

Kendall, D. R., and Mills, J. S., 1985, "The Influence of JFTOT Operating Parameters on the Assessment of Fuel Thermal Stability," SAE Paper No. 851871.

Marteney, P. J., and Spadaccini, L. J., 1986, "Thermal Decomposition of Aircraft Fuels," ASME JOURNAL OF ENGINEERING FOR GAS TURBINES AND POWER, Vol. 108, pp; 648-653.

Mills, J. S., and Kendall, D. R., 1986, "The Quantification Improvement of the Thermal Stability of Aviation Turbine Fuel," ASME JOURNAL OF ENGINEERING FOR GAS TURBINES AND POWER, Vol. 108, pp. 381-386.

Roback, R., Szetela, E. J., and Spadaccini, L. J., 1983, "Deposit Formation in Hydrocarbon Fuels," ASME JOURNAL OF ENGINEERING FOR GAS TURBINES AND POWER, Vol. 105, pp. 55-65.

Szetela, E. J., 1976, "Deposits From Heated Gas Turbine Fuels," ASME Paper No. 76-GT-9.

Szetela, E. J., Giovanetti, A. J., and Cohen, S., 1985, "Fuel Deposit Characteristics at Low Velocity," ASME Paper No. 85-1GT-130.

TeVelde, J. A., and Glickstein, M. R., 1983, "Heat Transfer and Stability of Alternative Aircraft Fuels," Vol. 1, Report AD A137404.

TeVelde, J. A., and Spadaccini, L. J., Szetela, E. J., and Glickstein, M. R., 1983, "Alternative Fuel Deposit Formation," AGARD Conference Proceedings No. 353, *Combustion Problems in Turbine Engines*, pp. 3/1-3/10.

Vranos, A., and Marteney, P. T., 1980, "Experimental Study of Turbine Fuel Thermal Stability in an Aircraft Fuel System Simulator," *Aircraft Research and Technology for Future Fuels*, NASA CP 2146, pp. 169-176.

DISCUSSION

L. J. Spadaccini[1]

The authors have incorrectly stated the results of the UTRC experiments. Their inference that "an effective method of reducing deposition rates would be by increasing the tube-wall temperature" is totally erroneous. Reference to the UTRC publications will verify that the trend of deposit formation rate versus temperature shown in Fig. 4 (i.e., the leveling off and subsequent decrease in deposit formation at temperatures above 600 K) was attributed to depletion of dissolved oxygen in the fuel and transition from auto-oxidation to pyrolysis. This hypothesis is substantiated by data acquired at the exit of the heated tube (where the temperatures were highest) that show little increase in wall temperature (due to deposition) with increasing test time (see Fig. 5). The decreasing deposit formation rate at higher temperatures was first observed at Exxon and reported by Taylor (1974). What was observed by UTRC was an upper temperature boundary for their experiment and, for that reason, the UTRC data correlations of deposit thickness versus time were limited to temperatures below 600 K.

Fuel preconditioning is of critical importance to fuel deposit formation. Preheating and recirculation can result in depletion of active species (e.g., oxygen, nitrogen, sulfur, and metals) from the fuel, spurious formation of deposit outside the test section in the preheater and hot transfer lines, and inadvertent lowering of the measured deposition rate in the test section. Although none of the test methods now in use completely simulate fuel heating in an aircraft system, in the UTRC apparatus all the thermal decomposition reactions occur within the test section where deposit rates are measured. In this regard, it is similar to the procedure adopted by the ASTM for evaluating the thermal oxidation stability of turbine fuels (JFTOT procedure).

[1]United Technologies Research Center, East Hartford, CT 06108.

References

Taylor, W. F., 1974, "Deposit Formation From Deoxygenated Hydrocarbons—I. General Features," *Ind. Eng. Chem., Prod. Res. Develop.*, Vol. 13, No. 2, pp. 133-138.

Authors' Closure

In the UTRC publication referenced as Marteney and Spadaccini (1986) in our paper, it was reported that "the fuel deposition data acquired can be utilized to predict the deposit buildup." Nowhere does it state that the deposition data plotted in Fig. 4 of this paper are valid only for wall temperatures below 600 K.

We agree with Dr. Spadaccini that "fuel conditioning is of critical importance to deposit formation" and that "preheating can result in depletion of active species." This highlights one of the main deficiencies of the UTRC apparatus. This apparatus features a test section that is essentially a heated tube, 2.5 m long. Thus the fuel that produces deposit toward the end of the test section has been subjected to considerable preheating during its passage through the long heated tube with consequent depletion of active species.

In regard to fuel circulation, we agree that it is unsuitable for basic studies on the deposition process and we much prefer a single-pass system for this type of research. However, the recirculation method does serve a useful purpose because it simulates more closely the actual aircraft situation in which the fuel may be heated and recirculated back into the fuel tank several times before it finally flows through the fuel nozzle into the combustion chamber.

We agree with Dr. Spadaccini that none of the test methods now in use (including ours) completely simulates fuel heating in an aircraft system. Nevertheless, we feel that our test technique, which has not remained static but is being continually refined and improved with experience, provides the most realistic simulation of an aircraft system that is available at this time.

Copyright © 1992 by ASME

Downloaded 02 Jun 2010 to 171.66.16.112. Redistribution subject to ASME license or copyright; see http://www.asme.org/terms/Terms_Use.cfm

Two-Stage Slagging Combustor Design for a Coal-Fueled Industrial Gas Turbine

L. H. Cowell

R. T. LeCren

C. E. Tenbrook

Solar Turbines Incorporated,
San Diego, CA 92138

A full-size combustor for a coal-fueled industrial gas turbine engine has been designed and fabricated. The design is based on extensive work completed through one-tenth scale combustion tests. Testing of the combustion hardware will be completed with a high pressure air supply in a combustion test facility before the components are integrated with the gas turbine engine. The combustor is a two-staged, rich-lean design. Fuel and air are introduced in the primary combustion zone where the combustion process is initiated. The primary zone operates in a slagging mode inertially removing coal ash from the gas stream. Four injectors designed for coal-water mixture (CWM) atomization are used to introduce the fuel and primary air. In the secondary combustion zone, additional air is injected to complete the combustion process at fuel lean conditions. The secondary zone also serves to reduce the gas temperatures exiting the combustor. Between the primary and secondary zones is a Particulate Rejection Impact Separator (PRIS). In this device much of the coal ash that passes from the primary zone is inertially separated from the gas stream. The two-staged combustor along with the PRIS have been designated as the combustor island. All of the combustor island components are refractory-lined to minimize heat loss. Fabrication of the combustor has been completed. The PRIS is still under construction. The combustor hardware is being installed at the Caterpillar Technical Center for high pressure test evaluation. The design, test installation, and test plan of the full-size combustor island are discussed.

Introduction

Solar Turbines Incorporated is currently sponsored by the U. S. Department of Energy Morgantown Energy Technology Center (DOE/METC) to develop a coal-fueled version of its 3.8 MW Centaur Type H gas turbine for industrial cogeneration applications. This six-year program culminates in a 100-h run of a coal-fueled gas turbine engine. The need to use indigenous fuels for power generation and cogeneration has been recognized by both goverment and industry. Mixtures of pulverized coal and water (CWM) have the potential of being burned directly in gas turbines using injection and fuel handling methods similar to those used for heavy petroleum fuels.

The development of the combustion system for the coal-fueled industrial gas turbine has been on-going for over five years. The main design tools used in this development are subscale combustor testing and flow visualization modeling. This paper describes the full-size combustor island components, the design parameters used in the scaleup, and the test plan to evaluate the performance of these components.

Performance Goals

The two-staged combustor is designed to efficiently utilize coal water mixture with a broad fuel specification in an environmentally sensitive manner. The combustion process is initiated in the primary zone. This zone is also the first location of coal ash removal from the gas stream. The second location for ash removal is accomplished in the PRIS. The combustion process is completed in the secondary combustion zone. A block diagram of the combustion system incorporated with the engine is included in Fig. 1. Performance of the combustion system is characterized by the operating parameters of combustor stability, carbon conversion, and emissions of particulate, oxides of nitrogen, carbon monoxide, and sulfur dioxide. Ash is removed in the primary combustion zone and PRIS in the form of molten slag. All components of the combustion system are refractory-lined to limit heat loss. A summary of the design point operating parameters is included in Table 1.

The primary zone and PRIS operate under reducing conditions at an equivalence ratio of 1.38 as seen in Table 1. The design point equivalence ratio has been determined through subscale rig testing. The equivalence ratio is set to insure that the gas temperatures in the primary zone and PRIS remain below 1895 K and emissions of NO_x and CO from the secondary combustion zone are acceptably low. The gas temperature at the outlet of the secondary zone is 1311 K at design point. This value is sufficiently high to accommodate a 30 K temperature drop through the system so that the turbine inlet temperature will be 1283 K.

Contributed by the International Gas Turbine Institute and presented at the 36th International Gas Turbine and Aerospace Congress and Exposition. Orlando, Florida, June 3-6, 1991. Manuscript received at ASME Headquarters March 4, 1991. Paper No. 91-GT-212. Associate Editor: L. A. Riekert.

Copyright © 1992 by ASME
Downloaded 02 Jun 2010 to 171.66.16.112. Redistribution subject to ASME license or copyright; see http://www.asme.org/terms/Terms_Use.cfm

Table 1 Operating parameters and performance goals of combustion island components

Design Point Operating Conditions	Primary Zone	PRIS	Secondary Zone
Equivalence Ratio	1.38	1.38	0.43
Temperature (K)	1895	1895	1311
Pressure (bars)	9.57	9.46	9.43
	Performance Ranking		
Parameter	Outstanding	Satisfactory	Unsatisfactory
Combustion Island Emissions (Dry Basis)			
NO_x (ppmv @ 15% O_2)	<125	125-175	>175
CO (ppmv @ 15% O_2)	<50	50-125	>250
SO_2 (ppmv @ 15% O_2)	<75	75-150	>150
Particulate (ppmm)	<120	120-270	>270
Carbon Conversion (%)	>98	95-98	<95
Turndown (ΔT_{max}) (ΔT_{min})	>3	2-3	<2
Slag Removal (%)			
Primary Zone	>70	60-70	<60
PRIS	>70	50-70	<50
Combustion Island	>88	75-87	<75

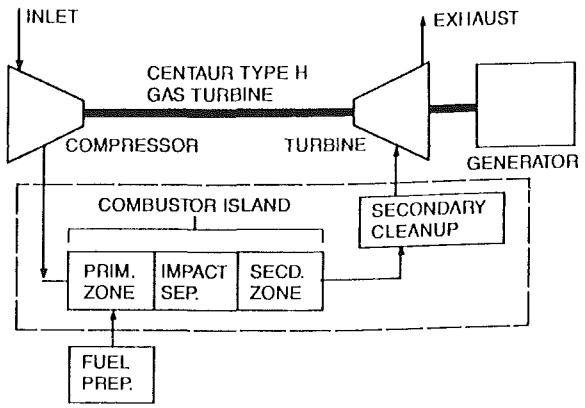


Fig. 1 Coal-fueled gas turbine

Performance ranking is detailed for the components of the combustion island in Table 1. These criteria include emissions control, combustion efficiency, combustion stability, and coal slag removal. The combustion island has capabilities for controlling emissions of NO_x and CO through staged combustion. SO_2 emissions are controlled through injection of calcia-based sorbents into the secondary zone. Combustion efficiency is determined through emissions measurements of CO, unburned hydrocarbons, and unburned carbon.

Combustion stability is evaluated in terms of turndown ratio and by tracking outlet temperature and pressure fluctuations. The turndown ratio is defined as the maximum temperature rise in the combustor island divided by the minimum temperature rise. The maximum temperature rise is obtained at the upper equivalence ratio for steady combustion in the primary zone and the lower temperature rise is at the lean limit of combustion. The combustor island when operating in a stable mode exhibits a constant outlet temperature and pressure. As the system becomes less stable, outlet temperature and combustor pressure can fluctuate over large intervals.

Coal ash removal by the slagging primary zone and the PRIS is indicated in Table 1 as slag removal efficiency. Slag removal efficiency is the percentage ash removed from the gas stream as computed from the coal ash input and ash emitted with the exhaust gases. The ash emitted with the secondary combustor exhaust is determined from batch particulate samples. The total ash collection in the combustion island is the combined slag removal from both the primary zone and PRIS. The primary zone slag capture is determined in a post-test batch weight difference measurement of the slag pit components.

The performance ranking goals indicated in Table 1 are based on the NSPS, subscale component testing, and a system study of the coal-fueled gas turbine. Since NSPS regulations for coal-fueled gas turbines are not written, standards set for coal-fueled boilers and conventionally fueled gas turbines were examined and the most stringent regulations were incorporated into the performance goals. Subscale combustor test results were used to determine if the performance ranking of the full-size components were possible. Subscale rig testing has shown that the combustor island surpasses all the "Outstanding" rankings listed in Table 1. Such performance is expected to be demonstrated in the full-sized unit. Solar also has completed a marketing and economic system assessment of the coal-fueled turbine. In this study, initial performance ranking goals were formulated to guarantee long Coal-Fueled Centaur engine life while addressing environmental issues associated with coal combustion that could have a negative impact in the market place.

Design Description

Through extensive subscale development, the design of the full-scale components should demonstrate superior performance with very little additional development. Table 2 compares test results taken with the subscale combustor and PRIS to the Outstanding performance rankings shown in Table 1. The design of the full-scale combustor and PRIS are described and contrasted to the subscale hardware in the following sections. The subscale combustor is one-tenth the full size on the basis of heat generation.

Primary Zone Combustor. The primary zone is operated fuel-rich at gas temperatures as high as 1895 K. The role of the primary zone is to initialize the combustion process and separate out over 60 percent of the coal ash from the gas stream. The key combustion processes that are completed in the primary zone include CWM atomization, water evaporation, ignition, devolatilization, and a majority of the char burnout. Rich combustion suppresses formation of NO_x by controlling reaction temperatures and limiting available oxygen. Species

Downloaded 02 Jun 2010 to 171.66.16.112. Redistribution subject to ASME license or copyright; see http://www.asme.org/terms/Terms_Use.cfm

Table 2 Performance ranking of full-scale combustor island compared to test results from subscale components

	Outstanding Ranking	Subscale Test Results
Combustion Island Emissions (Dry Basis)		
NO_x (ppmv @ 15% O_2)	<125	29
CO (ppmv @ 15% O_2)	<50	10
SO_2 (ppmv @ 15% O_2)	<75	49
Particulate (ppmm)	<120	41
Carbon Conversion (%)	>98	99+
Turndown Ratio $\frac{(\Delta T_{max})}{(\Delta T_{min})}$	>3	3
Slag Removal (%)		
Primary Zone	>70	61
PRIS	>70	95
Combustion Island	>88	98

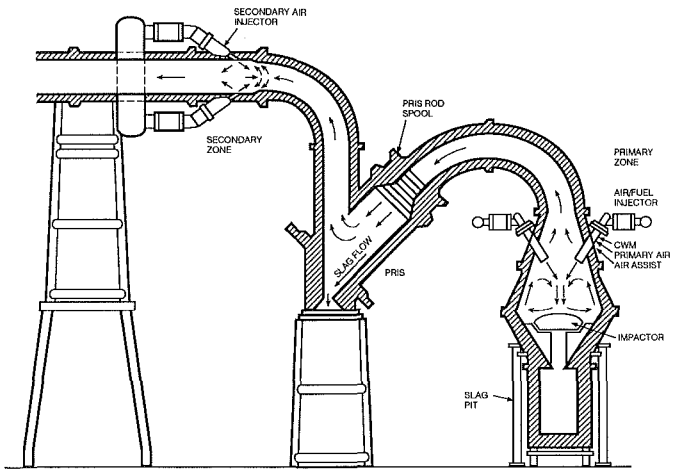


Fig. 2 Full-size combustor island

exiting the primary combustor include unburned fuel in the form of CO, hydrocarbons, and to a lesser degree char. Coal ash is inertially separated from the gas stream as liquid slag on the impactor and lower primary zone walls.

Description. A schematic of the full-scale combustor that will be tested is shown in Fig. 2. The primary zone consists of four CWM-air injectors, an inertial impact separator, and a slag tap. The four injectors are angled inward on the combustor centerline spraying downward toward the impactor. The injectors protrude into the combustion volume to improve aerodynamic stability. The air-fuel jets from each of the injectors merge at the combustor centerline to create one central jet. This CWM-air jet flows straight down along the centerline and strikes the center of the impactor. Inertial forces are high enough at the impactor to separate most of the coal ash from the gas stream. At the center of the impactor the jet is turned at a right angle and fans out radially along the surface of the impactor toward the primary zone wall. As the gas stream impacts the primary zone wall, the flow is again turned at a right angle so that it flows upward adjacent to the primary zone wall. From here, the gas stream flows past the injectors and out the primary zone creating a "plug" type flow in the upper duct. This pattern of downward flow at the combustor centerline and upward flow at the wall sets up a toroidal recirculation zone. A portion of the gas stream flowing upward along the wall is entrained into the recirculation zone. Larger

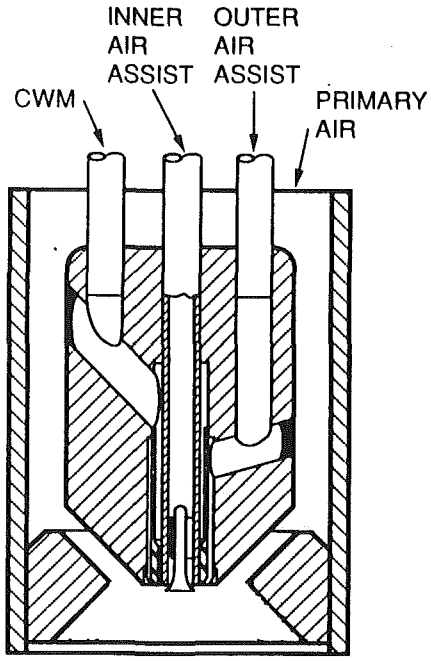


Fig. 3 CWM fuel injector for full-size combustor

particles of char and ash are more easily entrained due to gravitational forces than are smaller particles. The action increases residence time for char burnout and provides additional opportunities for ash separation. Based on this aerodynamic flow pattern and an assumed temperature distribution, the residence time in the primary combustor is estimated to be 180 msec. In the subscale combustor the residence time is estimated to be 150 msec.

The primary zone has a conical geometry to retard slag flow up the primary zone walls and increase the intensity of the recirculation zone. Slag separated on the impactor drains toward the outer edge and drips into the slag tap area below. The slag flow is funneled to a 4-in. slag tap hole. At this location, all the slag drips through the slag tap hole into the batch-type slag pit. The batch slag pit is filled during the test and emptied after the combustor has been shut down. Development and testing of a subscale on-line slag removal system has been completed. The design features a heated slag tap, water quench bath, and lock hopper. Full-size designs of this equipment are not complete, but testing of this hardware will be completed before the combustor island is integrated with the gas turbine.

Four CWM injectors use high velocity air assist flow to achieve the required level of fuel atomization. These injectors, shown in Fig. 3, introduce CWM into an annular passage surrounded on both sides by passages for air assist flow. The amount of air assist flow admitted on either side of the fuel passage is regulated by the effective area of both air assist passages at the injector tip. Both the inner and outer air assist ports are angled toward each other to provide maximum air/fuel relative velocities which at design point are in excess of 250 m/s. The high shear forces generated by these relative velocities provide fine CWM atomization. Design point operation yields sprays with mean CWM drop sizes estimated to be between 25–50 microns. These estimates are based on subscale injector spray measurements and still and high speed photography of the full-size injectors. Atomization studies used in the scaleup of the CWM injector are discussed in detail in the next section. Primary air is metered through the outermost annular passage. The passage is angled inward to force rapid mixing of the CWM spray and primary air. The angled primary air passages also create a fuel/air jet of relatively slight (20 deg) cone angle.

Downloaded 02 Jun 2010 to 171.66.16.112. Redistribution subject to ASME license or copyright; see http://www.asme.org/terms/Terms_Use.cfm

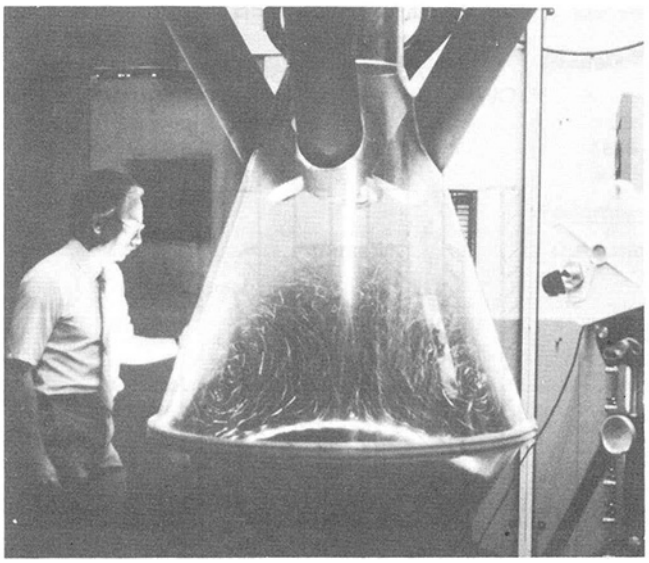


Fig. 4 Flow visualization model of full-scale combustor

Test Results. The full-scale design is based on test results using flow visualization of scaled and full-scale models, combustion tests of subscale hardware, and atomization studies of scaled and full-scale injectors. These results have been documented in detail elsewhere (Cowell et al., 1989; Roberts, 1988; LeCren, 1987) and are summarized briefly here.

Flow visualization has been completed with plexiglass models of the primary zone geometry using helium-filled soap bubbles to trace the aerodynamic streamlines. A picture of the full-size model is shown in Fig. 4. Subscale models of the primary zone have been built featuring both cylindrical and conical geometries. The location and number of injectors also have been modeled for subscale flow visualization purposes (Cowell and LeCren, 1989). Full-scale flow visualization models have been evaluated of a single injector design and a four injector design. With the four injector concept, the distance the injectors protrude into the combustion volume was varied from flush to one injector diameter in from the wall. The models were filmed and photographed.

Information gathered from the flow visualization models includes primary zone aerodynamic stability and intensity as a function of the variables just listed. As described earlier, the primary zone is designed to establish a strong central jet and intense recirculation zone. The flow visualization model of the full-size primary zone design demonstrated such behavior. As changes to the primary zone were incorporated into the flow visualization model, the flow became less stable. For example, as the distance the injectors protrude into the combustion volume was decreased from one diameter to flush with the wall, the central jet became weaker and less steady. At the least stable design, the impact location of the central jet on the impactor would precess around the top of the impactor generating a "lazy" unsteady recirculation zone. Based on these observations, the full-size injector protrudes into the combustion volume 0.75 injector diameters. The difference in aerodynamic stability of a flow visualization model of the primary zone featuring a single centerline mounted injector compared to results obtained with the four injector design were less apparent.

Subscale combustion test results taken with a primary zone of similar geometry to the full-size design are included in Table 2. The emissions are taken at the outlet of the secondary combustor. The results indicate that the subscale design meets or surpasses the "Outstanding Performance" ranking for all the parameters except primary zone slag capture. The primary combustion zone design has an influence on most of the performance parameters listed in Table 2. Of these parameters, this design has the largest influence on the formation of NO_x. With available oxygen and nitrogen, the reaction kinetics are favorable for generation of significant concentrations of NO_x at temperatures in excess of 1925 K. The primary zone operating under fuel rich conditions limits both available oxygen and flame temperature. Subscale testing has proven that the NO_x emissions from the system respond most sharply to changes in primary zone equivalence ratio. As indicated in Table 2, at design point equivalence ratio, the combustion island suppresses NO_x emissions substantially below goal. Subscale testing has been completed with changes to the primary zone volume and at varying combustor pressure with little influence on NO_x emissions. In a fuel lean combustion system, both of these variables have been shown to have a significant influence on NO_x emissions, but because of the lower concentration of available oxygen rich combustion zones are, in general, more tolerant of changes to pressure and volume on NO_x generation.

Carbon conversion to CO and CO_2 is accomplished in the primary zone. In general, subscale testing has indicated that CWM atomization is the single most important factor in determining the carbon conversion performance of the combustor island. Other factors that influence carbon conversion in the primary zone include the injector to impactor distance and the total available residence time in the primary zone. Carbon monoxide is produced in the primary zone by design since the process is fuel rich. Control of sulfur emissions are not addressed by the primary zone design.

Improving the primary zone slag capture has been a major focus of subscale testing. Design changes to the primary zone have included the number of CWM injectors, the shape, injector location and penetration, and varying injector to impactor distance. The subscale combustor has been operated at different test conditions including combustor loading, equivalence ratio, and pressure drop ratio. All of these design changes and operating variables have a strong influence on emissions and slag capture. The maximum slag capture in subscale testing with a common fuel stock was 70 percent. The slag capture dropped off considerably with a single injector, short injector to impactor distances, and decreased pressure drop ratio. The subscale test results are the most important information used in scaling the primary zone to full scale.

Injector development has been completed using subscale and full-scale injector designs. Injectors are designed with two major considerations: produce a spray of finely atomized CWM and provide rapid primary air and fuel mixing in the form of a narrow angled spray. The design used in the full-size combustor is shown in Fig. 3. The full-size injector hardware has been operated with CWM spraying at atmospheric pressure. The spray is evaluated by making drop size measurements and examining the spray through high speed still and motion photography. Injectors based on this design have been scaled, manufactured, and evaluated with design point CWM flow rates of 273, 682, and 2727 kg/h. The full-scale combustor uses four injectors each with a design flow rate of 682 kg/h. Drop-size measurements have been made with a line of sight laser diffraction drop-sizing system of sprays generated with the subscale injector capable of flowing 273 kg/h of CWM. In this injector, the Sauter Mean Diameter (SMD) drop size of the spray varied from 9–41 microns. Subscale combustion tests indicate that a significant rise in carbon conversion is realized as drop sizes are decreased. In these tests with identical combustor hardware burning similar blends of CWMs the carbon conversion was found to improve from 97–99 percent as the SMD drop size was reduced from 120–30 microns. Drop-size measurements of larger flow capacity injectors were not possible due to high spray densities. Sprays also are characterized through high speed motion and still photography. This technique is used to assess the spray symmetry and uniformity. Illustrated in Fig. 5 is a photograph of

Downloaded 02 Jun 2010 to 171.66.16.112. Redistribution subject to ASME license or copyright; see http://www.asme.org/terms/Terms_Use.cfm

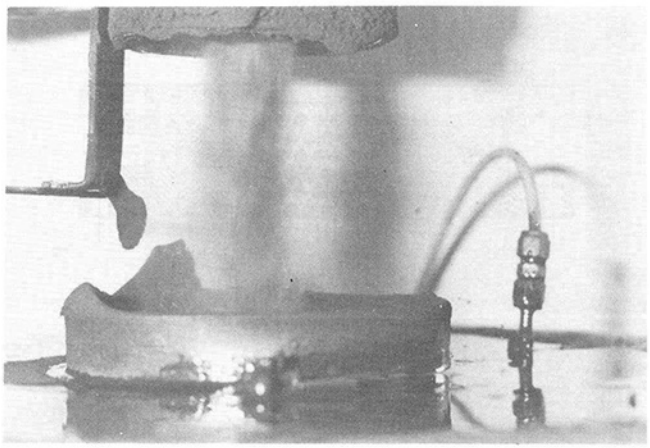


Fig. 5 1500 PPH injector No. 1 spraying CWM at 1000 PPH

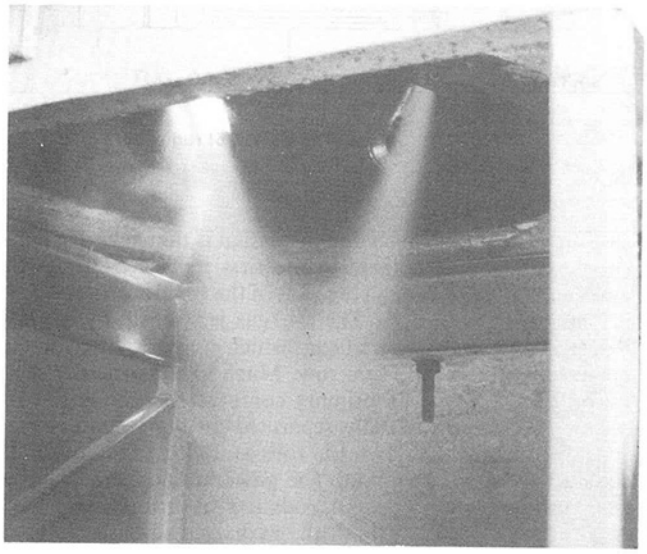


Fig. 6 Intersection of sprays from full-scale combustor hardware

the 682 kg/h injector spraying at 455 kg/h into atmosphere taken at an exposure of 35 μs. The spray is seen to be uniform with a cone angle of 20 deg. High speed motion photography with an exposure of 100 μs of the 682 kg/h injector shows the spray to be both steady and symmetrical with time. The four 682 kg/h injectors were installed in the full-scale injector casing. The injectors were operated with water to inspect the interaction of the four air/water jets. A photograph of this test is included in Fig. 6. The picture indicates that all four jets intersect and create a well-defined central jet. The full-scale injectors performed well in both atomization studies and spray evaluations and are anticipated to provide superior combustion.

Scale-Up Procedure. The full-size primary zone geometry is ten times larger by volume. The conical shape has improved the performance of the subscale combustor and so this has been incorporated into the full-scale design. Flow visualization of the conical geometry has demonstrated superior aerodynamic stability. The conical shape also permits situating the injectors at only a 20 percent larger distance from the impactor than in the subscale. Again, flow visualization has indicated that this distance is acceptable to maintain a high level of aerodynamic stability. The velocity of the central jet is the same in both the subscale and full-size designs over most of the length since the combustor pressure drop ratio will remain at 4 percent. The carbon conversion should be slightly enhanced in the full-size unit since the residence time is increased.

Slag capture is a function of the impact velocity of the central jet and the extent the ash is exposed through carbon combustion. The velocity of the central jet has remained constant in the scaleup but the distance the jet travels from the injectors has increased, which will result in a slightly decreased impact velocity. The increased injector to impactor distance will result in more complete coal combustion exposing more of the coal ash for separation at the impactor. Decreased impact velocity and greater ash exposure oppose each other in their influence on primary zone slag capture. The actual change in the operating parameters in the scaleup is small enough so that no significant difference in slag capture should be realized. Subscale testing of primary zones of varying length has confirmed that above a critical value the influence of primary zone length on slag capture is slight.

The full-size injector design is scaled so that the CWM and air assist velocities exiting the injector tip are constant. In injector designs, a key scaling parameter is the fuel-to-air relative velocity. In scaling the CWM injector, this parameter has remained constant at a relative velocity of 250 m/s. The atomization performance of the scaled injector has been verified on the flow bench as discussed earlier. The primary air is metered through an annular gap in the injector. Scaling this gap is completed to limit the primary airflow rate to the required value with a 4 percent pressure drop across the injector. The amount of primary air admitted into the combustion zone is set to achieve the desired heat input. For the Coal-Fueled Centaur, the heat input will be 13.9 MJ/s. Based on that heat input, the required fuel and air input is determined to achieve an equivalence ratio of 1.38. The equivalence ratio has been set and optimized to minimize NO_x formation and regulate PRIS inlet temperatures as discussed earlier.

Secondary Zone Combustor. The secondary zone is operated fuel lean with a design point outlet temperature of 1311 K. The secondary zone serves three major functions, including combustion of the unburned fuels from the primary combustion zone, dilution of the primary zone exhaust gases to meet turbine inlet temperature requirements, and the location for sorbent injection to control SO_2 emissions.

Description. The full-scale secondary zone is a volumetrically scaled design based on the subscale combustor. Combustion products from the primary zone and PRIS are introduced into the secondary zone through a 30-cm-dia inlet as illustrated in Fig. 2. The combustion products of the primary zone include unburned fuels in the form of CO, unburned hydrocarbons, and unburned carbon. Secondary air is injected into the secondary zone volume through six angled nozzles at 37 deg from the combustor centerline toward the incoming primary combustor exhaust. The secondary air jets intersect and impact the exhaust gases from the primary zone setting up a toroidal recirculation zone similar to that in the primary combustion zone. With rapid mixing and strong recirculation, the unburned fuels from the primary zone are rapidly consumed. Excess secondary air is injected to dilute the exhaust temperature down to the desired 1311 K. The gases exit the secondary zone through a 46 cm duct. Based on the assumed aerodynamic flow pattern the residence time in the secondary combustor is estimated to be 20–25 ms.

Test Results. Development of the secondary combustion zone has been completed exclusively through subscale combustor tests. The results in Table 2 include the contribution from the secondary combustor. As illustrated in Table 2, the subscale secondary combustor has exhibited "Outstanding Performance," suppressing NO_x formation while fully combusting CO and unburned hydrocarbons. The data indicate that the toroidal recirculation/mixing along with the lean stoichiometry are highly effective at regulating the secondary zone temperatures in the window where NO_x generation is low and

Downloaded 02 Jun 2010 to 171.66.16.112. Redistribution subject to ASME license or copyright; see http://www.asme.org/terms/Terms_Use.cfm

CO conversion to CO_2 is sufficiently high. The low emissions are also an indication of rapid and uniform mixing. This is because a nonuniform mixture leads to local "hot-spots" in the reaction volume where high NO_x concentrations are generated. Since NO_x emission levels are low the occurrences of hot-spots must be infrequent and therefore, the mixture must be well mixed. The secondary combustion zone has only a small influence on carbon conversion. While char will be further oxidized as it mixes with the secondary air, the temperature of the mixture is relatively low and the available residence time is too short to fully consume char entering the secondary zone.

As a dilution zone the secondary combustor has demonstrated broad flexibility in controlling the gas outlet temperature. The outlet temperature is set by the primary/secondary airflow split. The flow split is regulated by the effective flow areas of the primary and secondary air nozzles. Tests have been completed in the subscale combustor demonstrating outlet temperatures of 1144-1367 K for a preset flow split.

Testing has been completed in the subscale combustion island to determine the effectiveness of calcia-sorbent injection into the secondary combustor for SO_2 emission reductions. This test plan does not include provisions to complete similar tests at full scale because the sulfur capture exhibited by these sorbents is not a function of scale. Results from the subscale tests have been documented in Cowell et al. (1992). From these tests it has been concluded that calcia-sorbents can be highly effective at lowering SO_2 emissions. This is the control strategy that will be used on the Coal-Fueled Centaur.

Scale-Up Procedure. The full-size secondary zone is scaled by ten times the volume of the subscale combustor. The length/diameter of the full-size zone is the same as in the subscale at 1.4. The six secondary air injector nozzles have the same inlet velocity at both scales, but due to the higher mass flow rates the full-size nozzles have ten times the jet momentum flux. This parameter is used to determine the jet penetration into a combustor volume. With a tenfold increase the jet penetration into the full-size secondary zone will be significantly higher than in the subscale combustor. The increased jet penetration will lead to improved mixing of the incoming air and primary exhaust gases. Excellent mixing will insure low NO_x formations and uniform gas temperature dilution. The amount of secondary air admitted into the combustion zone is metered with the secondary air nozzles to control the outlet temperature. The nozzle effective area is matched with the area of the primary air injector to set the flow split. The air supply for both the primary and secondary zones comes from a single source. The split is determined by the effective flow areas of the primary and secondary air injector nozzles. The flow split is the ratio of primary air to secondary air. For the full-size combustor an initial setting of 2.8 has been selected based on subscale test results. This parameter will be further optimized during combustor testing.

Particulate Rejection Impact Separator (PRIS). The PRIS is a post-primary combustor clean-up system used to remove the majority of coal ash in the form of molten slag that escapes from the primary zone in the gas stream. The PRIS is a vessel positioned between the primary and secondary combustion zones. The test plan allows for testing to be completed at first without the PRIS in-line so that the combustor operation can be defined and evaluated. The PRIS would then be added for further testing of the combustion island. The full-scale PRIS has been developed through subscale testing and flow visualization of both subscale and full-scale models.

Description. The full-size PRIS design is shown in Fig. 2 and the rod insert spool is expanded in Fig. 7. The design consists of seven rows of 3.175 cm solid ceramic rods with 1.905 cm gaps between the rods. The rows of rods are staggered. The inlet duct is 40.6 cm and the outlet expands to 53.3 cm. The principle behind the design is that ash/slag laden gases enter the PRIS through the first row of rods. As the gases and ash pass through the gaps of the first row, the velocity is increased to 71.6 m/s. The ash/gas jets set up by the first row strike the second row of rods which are positioned directly behind the gaps of the first row. Much like the inertial separation completed in the primary combustion zone at the impactor, the ash is inertially separated on the second row of rods. The slag flows down the rods and along the bottom of the duct as a molten liquid. The gases are accelerated up to 71 m/s through the next row of rods and the process is repeated. As the duct expands at the fifth, sixth, and seventh rows, the velocity is decreased to reduce the occurrence of slag entrainment off the rods back into the gas stream. The velocity at the last row of rods is 42.7 m/s.

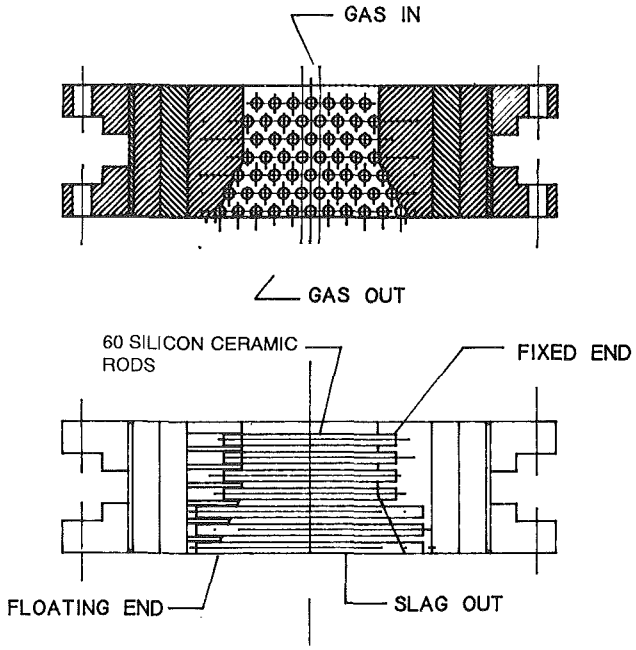


Fig. 7 Full-scale PRIS design of rod spool

The duct diameter opens to a constant 53.3 cm downstream of last row of rods to further reduce gas velocities. At this reduced gas velocity, drops of slag that are stripped off the final row will settle on the walls rather than remain entrained in the gas stream. Slag settling on the walls flows along the bottom of the duct toward the PRIS slag tap. The PRIS centerline is angled 45 deg from horizontal to promote slag flow toward the slag tap. The gases exhaust through a 30.5 cm duct located above the slag tap.

Test Results. PRIS designs have been evaluated through flow visualization and hot combustion tests. A full-size PRIS flow visualization model has been built and operated to evaluate the performance before the test hardware is fabricated. Results included in Table 2 were obtained from the subscale PRIS in-line of the combustion island.

Flow visualization models of the full-scale and subscale PRIS are pictured in Figs. 8 and 9. In these models, tests were conducted using helium-filled soap bubbles to trace the streamlines and atomized honey to simulate molten slag entering the PRIS. Flow visualization at the subscale level included evaluation of several alternative designs of impact separators. Results of the flow visualization are an important reason the rod-type PRIS design was selected.

Flow visualization of the full-scale PRIS design has been completed with both helium-filled soap bubbles and atomized honey. Tracing the streamlines of the PRIS flow patterns with

Downloaded 02 Jun 2010 to 171.66.16.112. Redistribution subject to ASME license or copyright; see http://www.asme.org/terms/Terms_Use.cfm

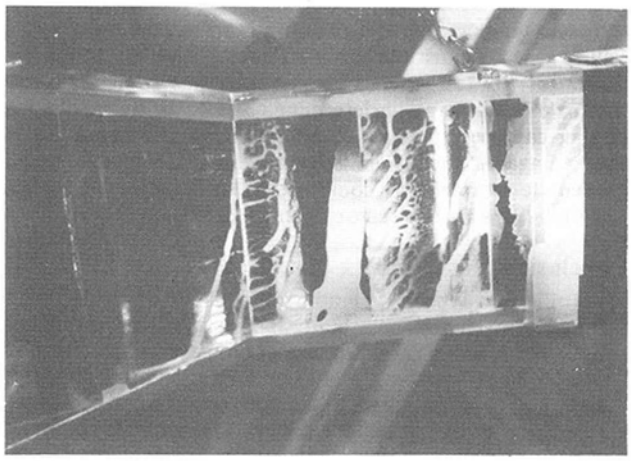


Fig. 8 Subscale flow visualization with honey injection of rod types PRIS

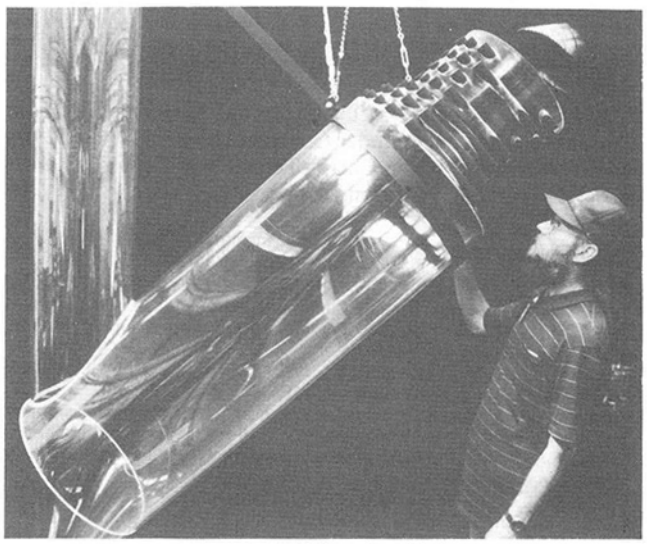


Fig. 9 Full-scale PRIS flow visualization model

bubbles indicates strongly turbulent flow around the rods settling to a plug-type flow in the volume past the rods. The flow turns sharply upward into the exhaust duct. Flow separation at the inner corner of this duct has been observed and changes to the design have been incorporated to prevent this separation. The initial pressure drop across the PRIS model has been measured to be 1.5 percent. With the change to the exhaust duct and by opening the diameter of the rod section the pressure loss was reduced to a more desirable 1.0 percent. The velocity profile along the length of the duct downstream of the rods appears to be flat over the entire distance. It is important to maintain gas flow along the bottom of this volume to prevent slag freezing. A uniform flow of high temperature gas insures adequate heat transfer to the slag flowing along the bottom of the duct to prevent slag freezing.

Injecting honey into the flow visualization model is completed to evaluate PRIS effectiveness at removing particulate from the gas stream and indicate slag flow patterns. Using honey as a slag simulant is a cost-effective means of assessing the performance of the PRIS with a high viscosity, non-Newtonian fluid. The viscosity of honey does match slag viscosities at temperatures found in the PRIS. The PRIS capture efficiency is generated by performing a mass balance of the honey injected into the PRIS compared to the honey collected below the slag tap. Test results have consistently indicated collection efficiencies above 98 percent. The honey flow along the bottom of the duct is steady without any "damming" at the slag tap.

PRIS tests have been completed with CWM combustion in the subscale combustion island. The subscale PRIS is of similar design to the full scale. Test results are shown in Table 2. The subscale PRIS performed well above the "Outstanding Performance" ranking removing 95 percent of the incoming coal ash/slag. Downstream of the PRIS in the secondary combustor zone the refractory was free of ash/slag buildup which was not the case when the combustor was tested without the PRIS. The PRIS rods were made of silicon carbide tubes and showed excessive erosion/corrosion. A parametric study of different potential ceramic materials will be completed before the full-scale rod material is selected.

Scale-Up Procedure. The full-size PRIS is scaled from the subscale design by matching gas velocities through the rods. The rod diameters and gaps between the rods are equal for both scales. The full-size PRIS is scaled by increasing the number of rods and sizing the duct diameter to provide the same gas velocities as calculated in the subscale design. By scaling at constant velocity, the full-scale PRIS should be equally effective at ash separation as the subscale design. This claim also has been supported with the flow visualization models. Models of the subscale PRIS captured 99 percent of the injected honey compared to 95 percent ash capture measured in the subscale PRIS operating under combustion conditions. The full-size model has demonstrated a capture of 98 percent honey. If like the subscale results the performance is slightly worse in actual combustion testing then the full-size PRIS should still operate at a collection efficiency above 90 percent. Material life of the PRIS rods remains a critical issue.

Test Facility

Testing of the combustor island will be completed independently of the engine at the Caterpillar Technical Center in Peoria, IL. The combustor island will include the primary combustor, PRIS, and secondary combustor installed together as illustrated in Fig. 10. A photograph of the full-size primary and secondary combustors is included as Fig. 11.

The facility is capable of providing 14.1 kg/s of total air flow at supply temperatures of 600 K. The combustor will be operated at 7.0 bars rather than the Centaur operating pressure of 9.5 bars due to air supply limitations. The Centaur-Type H uses 18.1 kg/s of total airflow. The combustor hardware will be instrumented for temperature, pressure, and emission measurements using standard techniques and commercially available equipment.

The combustor's operation and performance will be evaluated in a series of seven combustion tests. In these tests the combustor island will be operated on diesel fuel for a 4–6 h warm-up period. Refractory wall temperatures measured 2.5 cm from the inner surface of the primary combustor are monitored. When these temperatures reach 1367 K, the combustor is switched from diesel to CWM. Upon switching to CWM, all diesel fuel flow is terminated. The combustor island is operated burning CWM for 4–6 h at steady conditions. These conditions are a pressure of 7 bars, primary zone equivalence ratio of 1.38, air inlet temperature of 600 K, and a combustor pressure drop ratio of 4 percent. To protect the rods the inlet temperature to the PRIS is monitored and not allowed to exceed 1925 K. This temperature is controlled by increasing or decreasing the primary zone equivalence ratio. If a major adjustment to the equivalence ratio is necessary, the primary to secondary airflow split will be changed between tests so that the outlet temperature of the combustor can be maintained at 1310 K. At the conclusion of the CWM test, the combustor is switched over to diesel fuel again for a cool-down of 2 h.

During operation on CWM, data will be taken at approx-

Downloaded 02 Jun 2010 to 171.66.16.112. Redistribution subject to ASME license or copyright; see http://www.asme.org/terms/Terms_Use.cfm

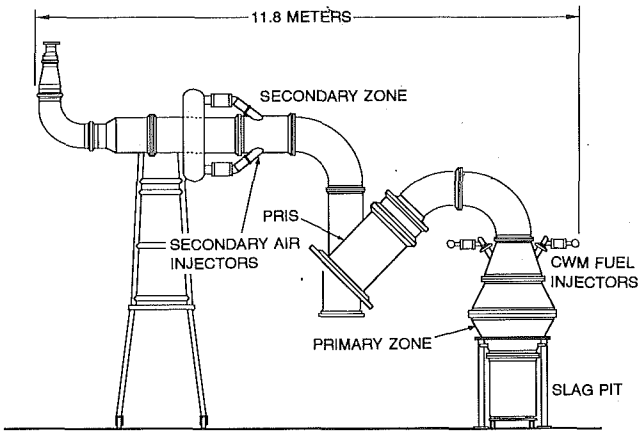


Fig. 10 Combustor island installed at test site

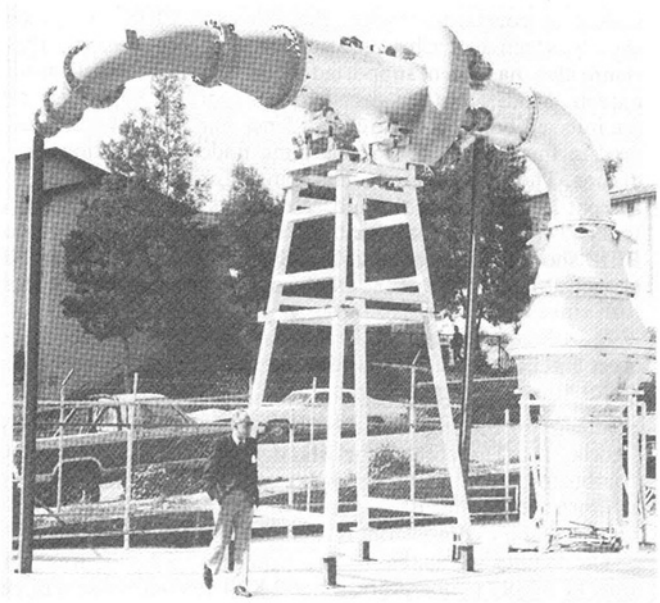


Fig. 11 Full-size combustor

imately 20-min intervals. Along with the operational data, a complete temperature and pressure map will be recorded, as well as gaseous emissions and particulate samples. At the conclusion of the test after the combustor has cooled, the slag capture efficiency will be determined by measuring the quantity of slag captured in the slag pits. This measurement can be checked against the ash emission rate as determined from the particulate sample. The combustor also is inspected for slag accumulations and refractory damage.

Conclusions

A full-size combustor island for a coal-fueled industrial gas turbine has been designed, built, and installed for testing. The combustor consists of a primary combustor, Particulate Rejection Impact Separator, and secondary combustor. The combustor has been designed based on results obtained with a subscale combustor of similar design. The subscale combustor has been operated over a range of conditions with a variety of CWM fuels with good results. The subscale combustor has demonstrated carbon conversion efficiencies greater than 99 percent, pollutant emissions below goals, and a broad range of operation. The combustor island will be tested in the near future.

Acknowledgments

The work described in this paper was performed by Solar Turbines Incorporated under Contract DE-AC21-86MC23166 from DOE-Morgantown Energy Technology Center, with Mr. Donald Geiling as Program Manager.

References

Cowell, L. H., Hansen, A. M., LeCren, R. T., and Stephenson, M. D., 1989, "Coal-Fueled Two-Stage Slagging Combustor Island and Cleanup System for Gas Turbine Application," *Proceedings Sixth Annual International Pittsburgh Coal Conference*, pp. 1040–1049.

Cowell, L. H., and LeCren, R. T., 1989, "Development of a Coal-Fueled Gas Turbine Slagging Combustor," ASME Paper No. 89-GT-115.

Cowell, L. H., Wen, C. S., and LeCren, R. T., 1992, "Experimental Evaluation of Sorbents for Sulfur Control in a Coal-Fueled Gas Turbine Slagging Combustor," ASME JOURNAL OF ENGINEERING FOR GAS TURBINES AND POWER, Vol. 114, pp. 152–158.

LeCren, R. T., and White, D. J., 1987, "The Burning of a Coal-Water Slurry Fuel in a Two-Stage Slagging Combustor," ASME Paper No. 87-GT-270.

Roberts, P. B., LeCren, R. T., Cowell, L. H., Hasen, A. M., and Noble, M., 1988, "Coal-Fueled Gas Turbine Combustor Island Development," ASME Paper No. 88-GT-89.

Downloaded 02 Jun 2010 to 171.66.16.112. Redistribution subject to ASME license or copyright; see http://www.asme.org/terms/Terms_Use.cfm

Separating Hydrogen From Coal Gasification Gases With Alumina Membranes

B. Z. Egan
Chemical Technology Division,
Oak Ridge National Laboratory,
Oak Ridge, TN 37831

D. E. Fain

G. E. Roettger

D. E. White

Technical Division,
Oak Ridge K-25 Site,
Oak Ridge, TN 37831

Synthesis gas produced in coal gasification processes contains hydrogen, along with carbon monoxide, carbon dioxide, hydrogen sulfide, water, nitrogen, and other gases, depending on the particular gasification process. Development of membrane technology to separate the hydrogen from the raw gas at the high operating temperatures and pressures near exit gas conditions would improve the efficiency of the process. Tubular porous alumina membranes with mean pore radii ranging from about 9–22 Å have been fabricated and characterized. Based on the results of hydrostatic tests, the burst strength of the membranes ranged from 800–1600 psig, with a mean value of about 1300 psig. These membranes were evaluated for separating hydrogen and other gases. Tests of membrane permeabilities were made with helium, nitrogen, and carbon dioxide. Measurements were made at room temperature in the pressure range of 15–589 psi. In general, the relative gas permeabilities correlated qualitatively with a Knudsen flow mechanism; however, other gas transport mechanisms such as surface adsorption also may be involved. Efforts are under way to fabricate membranes having still smaller pores. At smaller pore sizes, higher separation factors are expected from molecular sieving effects.

Introduction

Synthesis gas produced in coal gasification processes may contain hydrogen, carbon monoxide, nitrogen, water, carbon dioxide, hydrogen sulfide, and other gases, depending on the particular gasification process. The hydrogen and carbon monoxide in the synthesis gas have significant value. Hydrogen is an important raw material that has numerous uses in the chemical and fuel industries. If membrane technology could be developed to separate these gases under gasifier exit gas conditions, it would significantly improve process efficiency and economics and simultaneously provide for the recovery of valuable gases. Inorganic membranes could potentially be used for this purpose.

The purpose of this ongoing research and development program is to develop, fabricate, and test inorganic membrane systems for the separation and recovery of coal gasification gases, particularly hydrogen. Major aspects of the program include (*a*) identification and selection of candidate membrane materials; (*b*) fabrication and physical characterization of candidate membranes using specialized techniques available at the Oak Ridge K-25 Site; and (*c*) evaluation of the separations capability of the fabricated membranes in terms of permeabilities and fluxes of gases.

Until recently, inorganic membranes have been used primarily for microfiltration and ultrafiltration. While polymeric membranes have been used on a commercial scale to separate various gases, such as hydrogen and ammonia, oxygen and nitrogen, and carbon dioxide and methane, there has been no large-scale application of porous inorganic membrane separations to gases except for uranium enrichment. Polymeric membranes have limited stability and are susceptible to abrasion and chemical attack. Consequently, they cannot be used in separation processes at high temperatures and pressures. Porous metal, glass, and ceramic membranes are stable to much higher temperatures than polymeric membranes; the limitation is usually set by the seals and module materials rather than the membrane itself.

Several porous inorganic materials that could be used as membranes are commercially available (Egan, 1989), but the minimum pore diameter for each is in the range of 30–40 Å (3–4 nm). While some gas separations can be achieved with these materials, it is generally accepted that smaller pore diameters or other membrane modifications will be needed for efficient gas separations.

Commercially, at present, the bulk removal of acid gases from raw process gas such as synthesis gas is carried out by using solvent scrubbing processes such as methyldiethanolamine (MDEA), Selexol,™ and Rectisol.™ Most of these solvent scrubbing processes operate at temperatures below 200°F. Figure 1(*A*) is a simplified block flow diagram of a typical entrained-bed coal gasification-combined cycle (IGCC) process. Present technology requires cooling the product gases from 1500°F to 100°F to permit removal of carbon dioxide, hydrogen sulfide, and other contaminant gases. The cleaned fuel gas (carbon monoxide-hydrogen) must then be reheated to 500–600°F for downstream combustion in a gas turbine to generate power. The efficiency of the process could be increased sub-

Contributed by the International Gas Turbine Institute and presented at the 36th International Gas Turbine and Aeroengine Congress and Exposition, Orlando, Florida, June 3–6, 1991. Manuscript received at ASME Headquarters February 20, 1991. Paper No. 91-GT-132. Associate Editor: L. A. Riekert.

Copyright © 1992 by ASME
Downloaded 02 Jun 2010 to 171.66.16.112. Redistribution subject to ASME license or copyright; see http://www.asme.org/terms/Terms_Use.cfm

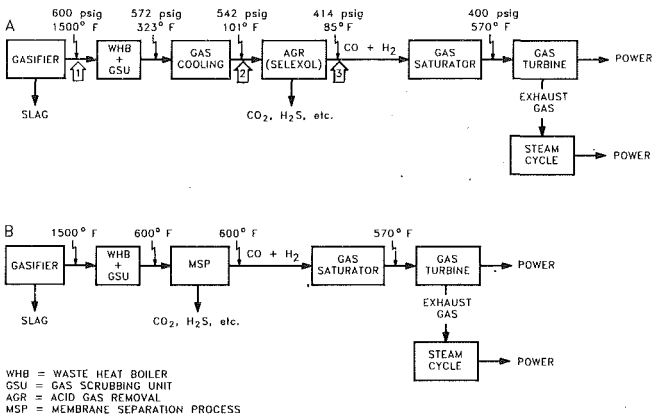


Fig. 1(*A*) Schematic of a typical entrained-bed IGCC process; (*B*) schematic of a conceptual IGCC process using a membrane gas separation system

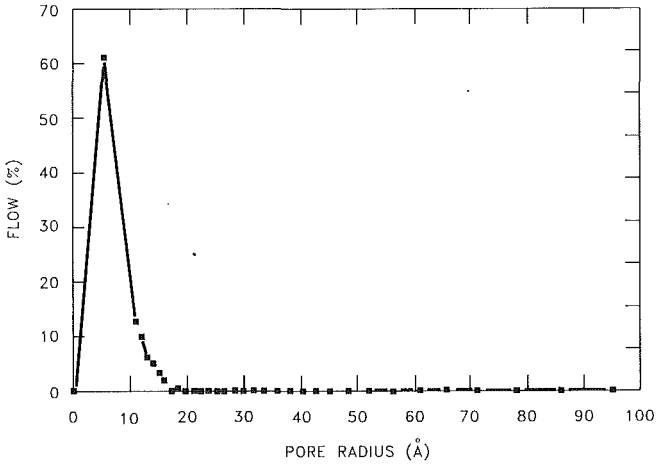


Fig. 2 Pore-size distribution of a fabricated alumina membrane

stantially if the contaminant gases could be separated at the higher downstream operating temperature. The proposed membrane separation process (Egan et al., 1988) would be developed to operate at conditions closer to the exit gas conditions than presently known processes. A block flow diagram for a conceptual membrane gas separation system for this application is shown in Fig. 1(*B*). Briefly stated, the gas cooling and the gas cleanup system would be replaced by a membrane separation system operating at high temperature.

The performance targets for the membrane separation process were determined, based on the coal gasification process operating temperatures and pressures and gas flux requirements. Potential membrane materials were selected, based on thermal and chemical stability, availability and cost of raw materials, and effects on gas transport mechanisms. The technical approach was to develop and fabricate membranes with small pores [less than 20 Å (2 nm)] and narrow pore-size distributions. For safety reasons, helium was used to simulate the behavior of hydrogen. Eventually, the best membranes will be tested with a coal gasification mixture containing hydrogen.

Results and Discussion

Selection of Membrane Materials. Metallic membranes have been used in a few cases for separating hydrogen from other gases, but most applications have been directed toward separating hydrogen, deuterium, and tritium isotopes. One application is the removal of tritium from radioactive effluent from nuclear fuel reprocessing plants; another is separation of the hydrogen isotopes produced in a fusion reactor. The most common metallic membrane is palladium, which is usually alloyed with silver to improve the physical and mechanical properties of the membrane.

The separation of several gases with porous glass membranes has been demonstrated. Some of the gases that have been separated using porous glass membranes include hydrogen, helium, argon, nitrogen, oxygen, carbon dioxide, carbon monoxide, and light hydrocarbons. Disadvantages of porous glass include limited thermal properties and relatively low gas permeabilities.

The most frequently used materials for metallic oxide membranes are alumina and silica. Some membranes contain mixtures of these, along with other oxides such as zirconia or titania. Alumina also is used frequently as the support for other membrane materials. Membranes with pore sizes ranging from a few angstroms to nearly a micrometer have been prepared. The permeation behavior of several gases has been studied using alumina or alumina-containing membranes. These gases include hydrogen, nitrogen, helium, argon, oxygen, carbon dioxide, sulfur dioxide, hydrogen sulfide, water, alcohols, and light hydrocarbons. Alumina membranes with a variety of pore sizes and configurations are available commercially.

Alumina was selected as the best membrane material for our initial studies for separating coal gasification gases because it has relatively low chemical reactivity, good thermal properties, and is readily adapatable to fabrication methods. A variety of low-cost alumina starting materials are readily available.

Membrane Fabrication and Characterization. Over 100 tubular membranes, each having a diameter of about 0.9 cm and a wall thickness less than 1 mm, have been fabricated. Preparation of such membranes involves the use of classified technology, which cannot be discussed in this paper.

The pore-size distributions of several experimental alumina membranes were measured using a dynamic pore-size measurement technique (Fain and Roettger, 1990) that uses a binary gas mixture containing about 8 percent carbon tetrachloride in nitrogen. The pressure is increased until the condensable carbon tetrachloride fills the pores of the membrane and there is no flow of nitrogen. As the pressure is decreased by measured amounts, a range of pore sizes is opened and the corresponding flow of nitrogen is measured. The pore size and flow rate are corrected for adsorption of the carbon tetrachloride on the surface of the porous material. Then the corrected flow rate is plotted against the corrected pore radius to give a cumulative pore-size distribution. An example of the pore-size distribution of an experimental membrane is shown in Fig. 2. The mean pore radius of the membranes has been reduced to less than 10 Å (1 nm), with essentially no pores with a radius larger than 20 Å (2 nm).

Membrane Test System. A test apparatus for measuring the gas permeabilities of membranes at high temperatures (up to 500°C) and pressures (up to 4 MPa) was designed and constructed (Egan et al., 1990). A flow diagram of the apparatus is shown in Fig. 3. Gases are supplied from cylinders through high-pressure regulators and an associated manifold. Pressures are regulated by pressure control valves, and gas flows are measured with differential-pressure transmitters. The gases are preheated in a tubular furnace, which also houses the membrane enclosed in an outer tube. Temperatures are measured with thermocouples. Exit gases are cooled with heat exchangers, if necessary, and analyzed by gas chromatography. Shutoff valves are operated by air-controlled actuators, which are supplied through solenoid-operated valves. The recorder/controllers, thermocouple readouts, and valve switches are installed in a separate instrument cabinet. For safety reasons, the system is enclosed in a free-standing fume hood.

Gas Permeability Measurements (Egan et al., 1990). Several alumina membranes having pore radii ranging from about

Downloaded 02 Jun 2010 to 171.66.16.112. Redistribution subject to ASME license or copyright; see http://www.asme.org/terms/Terms_Use.cfm

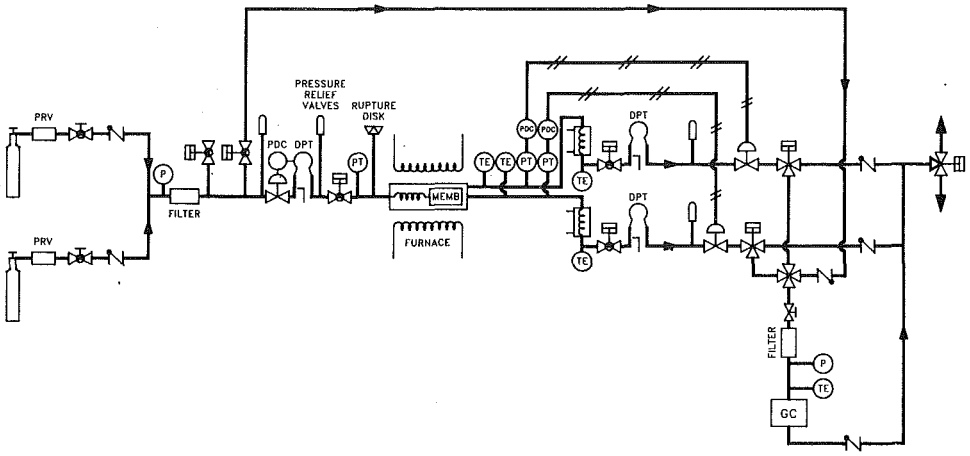


Fig. 3 Test apparatus for gas permeability measurements

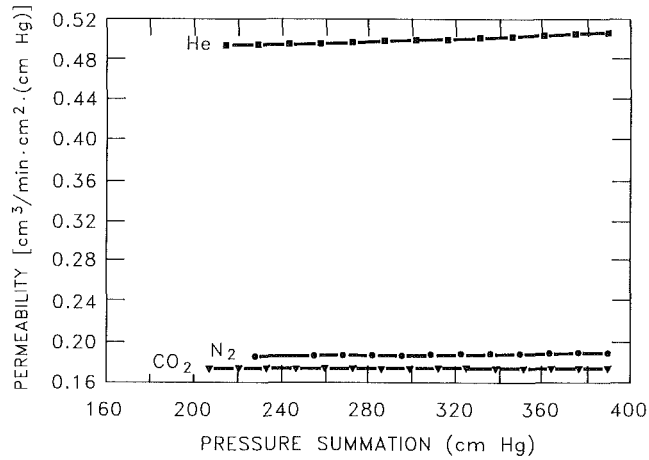


Fig. 4 Gas permeabilities of an alumina membrane (mean pore radius, 18Å)

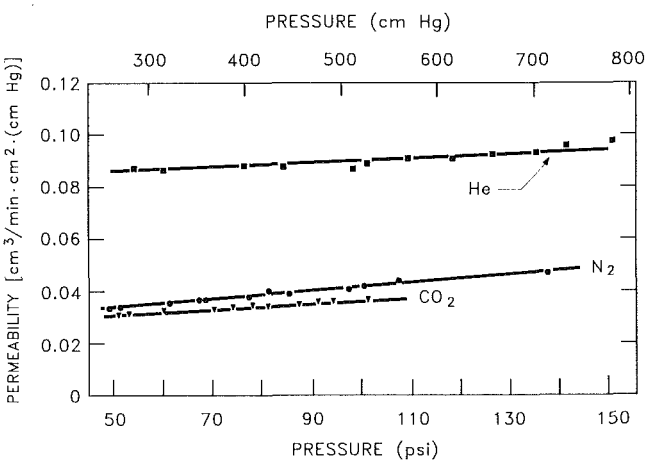


Fig. 5 Gas permeabilities of a fabricated alumina membrane at intermediate pressures (temperature = 20°C)

7–18 Å (0.7–1.8 nm) were fabricated and their permeabilities were measured at room temperature in different pressure ranges using helium, nitrogen, and carbon dioxide. Typical results for one of the membranes are shown in Fig. 4, in which the permeability versus pressure summation is plotted. The pressure summation values are the sums of the feed and permeate pressure. The permeabilities of the gases did not vary appreciably with pressure for the gases in the pressure range shown. Permeability measurements also were made at higher pressures using the test apparatus described in Fig. 3. These measurements were made at room temperature (20°C) in the feed-gas pressure range of 50–150 psi (0.34 to 1.02 MPa), Fig. 5. Nitrogen and helium permeabilities of another membrane sample were measured up to a feed gas pressure of 589 psi (4.06 MPa), Fig. 6.

The data for the low-pressure measurements are summarized in Fig. 7, in which the calculated separation factors (ratio of pure gas permeabilities) for helium/nitrogen and helium/carbon dioxide are plotted versus the average pore size for seven different alumina membranes. Also shown in Fig. 7 are the calculated ideal separation factors, assuming a Knudsen gas transport mechanism. Knudsen or free-molecule diffusion occurs when the pore is much smaller than the mean free path of the gas molecules, and the gas flux can be described by the expression:

$$G = \frac{8r(P_1 - P_2)}{3L(2\pi MRT)^{1/2}}$$

where

G = molecular flow
r = pore radius
P_1 = partial pressure of gas on the feed side
P_2 = partial pressure of gas on the permeate side
L = pore length
M = molecular weight
R = gas constant
T = absolute temperature

For Knudsen flow, the separation factor for binary gas mixtures can be estimated from the square root of the ratio of the molecular weights. The smaller molecules with a higher velocity move through the pores faster. These are ideal separation factors. Actual separation factors also depend on the molar composition (mol fraction) of the gases in the feed and permeate.

In general, the relative gas permeabilities of the fabricated membranes correlate qualitatively with a Knudsen flow mechanism; however, other gas transport mechanisms also may play a role when a pressure gradient is applied across the membrane (Hwang and Kammermeyer, 1966a, 1966b; Uhlhorn et al., 1989). When the mean free path of the gas molecules is much smaller than the mean pore radius of the porous membrane, laminar flow occurs. Surface diffusion occurs when the gas molecules are adsorbed on the surface of the membrane and move along the surface.The increase in permeability with increasing pressure, particularly in Figs. 5 and 6, may be partly due to these effects. The enhanced permeability of carbon dioxide, probably due to surface adsorption or other membrane interaction, reduces the helium/carbon dioxide separation factor.

Downloaded 02 Jun 2010 to 171.66.16.112. Redistribution subject to ASME license or copyright; see http://www.asme.org/terms/Terms_Use.cfm

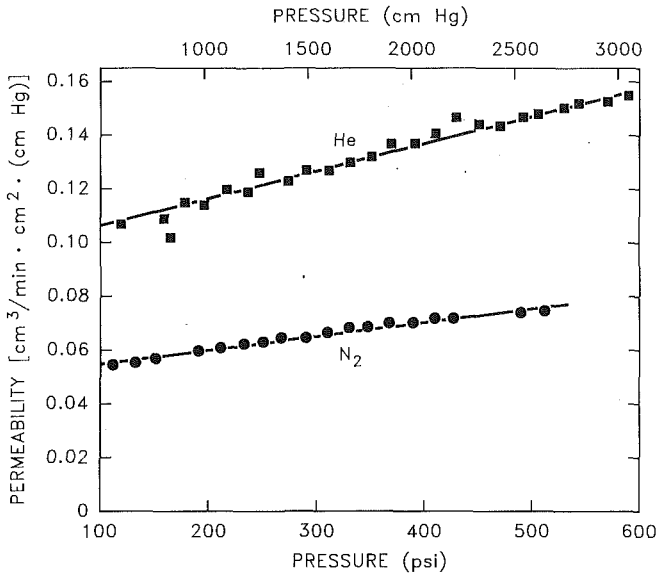


Fig. 6 Helium and nitrogen permeabilities of a fabricated alumina membrane at high pressure (temperature = 20°C)

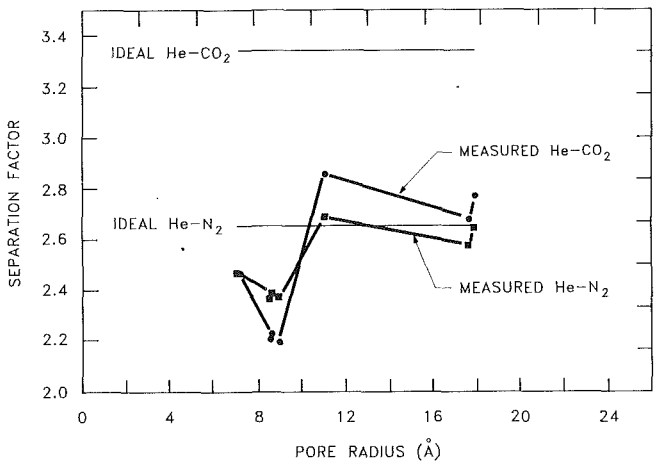


Fig. 7 Calculated separation factors from measured pure gas permeabilities for helium/carbon dioxide and helium/nitrogen for a series of alumina membranes with different pore sizes

Surface diffusion becomes more important as the pore size decreases. Consequently, the calculated helium/nitrogen and helium/carbon dioxide separation factors decrease somewhat as the membrane pore size decreases, Fig. 7. It is projected that as membranes are developed which have pore sizes comparable to the size of gas molecules, some molecular screening can occur (Fain and Rottger, 1990). Larger separation factors should then be achievable. Pore sizes of the fabricated membranes are not yet sufficiently small to show this behavior in Fig. 7. In practice, there will be a distribution of pore sizes, and the gas permeabilities can best be described by a combination of transport mechanisms.

Efforts are being made to produce membranes with mean pore radii below 5 Å. Other, related work is directed toward developing more effective alumina-metal seals so that gas permeability measurements can be made at higher temperatures.

Acknowledgments

Excellent technical assistance was provided by Dale Adcock and Betty Evans. The manuscript was prepared by Janet Brown. This research was sponsored by the U.S. Department of Energy, Morgantown Energy Technology Center, and the AR&TD Fossil Energy Materials Program, under contract DE-AC05-84OR21400 with Martin Marietta Energy Systems, Inc.

Portions of this paper were presented at the Tenth Annual Gasification and Gas Stream Cleanup Systems Contractors Review meeting, which was held in Morgantown, WV, on Aug. 28–30, 1990.

References

Egan, B. Z., 1989, "Using Inorganic Membranes to Separate Gases: R&D Status Review," ORNL/TM-11345, Oak Ridge National Laboratory, Oak Ridge, TN.

Egan, B. Z., Fain, D. E., Kidd, G. J., and Singh, S. P. N., 1988, "Gas Separations Using Inorganic Membranes," *Proceedings of the Eighth Annual Gasification and Gas Stream Cleanup Systems Contractors Review Meeting*, V. P. Kothari and J. R. Longanbach, eds., Morgantown Energy Technology Center, Morgantown, WV, Vol. II, pp. 519–524.

Egan, B. Z., Fain, D. E., Roettger, G. E., Singh, S. P. N., and White, D. E., 1990, "Gas Separations Using Inorganic Membranes," presented at the Tenth Annual Gasification and Gas Stream Cleanup Systems Contractors Review Meeting, Morgantown, WV, Aug. 28–30.

Fain, D. E., and Roettger, G. E., 1990, "Development of Ceramic Membranes for Gas Separation," *Proceedings of the Fourth Annual Conference on Fossil Energy Materials*, ORNL/FMP-90/1, R. R. Judkins and D. N. Braski, compilers, Oak Ridge National Laboratory, Oak Ridge, TN, pp. 183–194.

Fain, D. E., Kidd, G. J., Jr., Roettger, G. E., and White, D. E., 1990, "Development of Ceramic Membranes for Gas Separation—FY 1989 Development Activities," K/QT-352, Oak Ridge Gaseous Diffusion Plant, Oak Ridge, TN.

Hwang, S.-T., and Kammermeyer, K., 1966a, "Surface Diffusion in Microporous Media," *Canadian Journal of Chemical Engineering*, Vol. 44, pp. 82–89.

Hwang, S.-T., and Kammermeyer, K., 1966b, "Surface Diffusion of Deuterium and Light Hydrocarbons in Microporous Glass," *Separation Science*, Vol. 1, pp. 629–639.

Uhlhorn, R. J. R., Huis In't Veld, M. H. B. J., Keizer, K., and Burggraaf, A. J., 1989, "High Permselectivities of Microporous Silica-Modified γ-Alumina Membranes," *Journal of Materials Science Letters*, Vol. 8, pp. 1135–1138.

Downloaded 02 Jun 2010 to 171.66.16.112. Redistribution subject to ASME license or copyright; see http://www.asme.org/terms/Terms_Use.cfm

Ceramic Candle Filter Performance at the Grimethorpe (UK) Pressurized Fluidized Bed Combustor

J. Stringer
Electric Power Research Institute,
Palo Alto, CA 94304

A. J. Leitch
Electric Power Research Institute,
Cowdenbeath Office,
Cowdenbeath, United Kingdom

A pilot hot-gas particulate removal system, based on positive porous ceramic filters, has been tested on the Grimethorpe Pressurized Fluidized Bed Combustor facility. The filters are in the form of closed-ended tubes, 1.5 m long: These are generally called "candles." The dust accumulates on the outside of the candles, and is periodically removed by a pulse of air into the candle interior, which then flows outward through the candle wall in the reverse direction to the normal flow of the combustion gas. The EPRI system contained a maximum of 130 candles, which is approximately equivalent to the requirement for 7 MW(e) capacity, depending on the filter-operating parameters. The filter unit operated for a total of 860 h under PFBC conditions, of which 790 h were at defined process conditions, typically 850°C and 10 bar. The amount of gas flowing through each filter element was varied, and the time between cleaning pulses also was varied. The pressure drop through each filter element rose as the dust accumulated on the outer wall, and recovered after the cleaning pulse. However, the post-cleaning pressure drop does not recover to the original clean candle value, but increases with time. It is believed that a steady-state value is attained, but the exposure in the Grimethorpe test series was insufficient to establish this unequivocally. During the test, five candles failed. This appears to have been due to mechanical shock, as a result of candles lifting because of excessive pressure differentials across their support plate, and dropping back. The failures are not believed to be intrinsic to the technology. However, in addition a reduction in the strength of the candles with time of exposure was observed. This might also attain a steady-state value, but this too could not be established on the basis of the tests reported in this paper. This is clearly a matter of importance, and further work will be required to determine the suitability of the clay-bonded silicon carbide medium used in these tests for this application. A number of deficiencies in the design of the unit emerged with the operating experience, and suggestions have been made for improvements. However, it is clear that further work on design optimization is required. The pulse-cleaning air usage in the tests was greater than would be economically acceptable in a practical system. Further work needs to be done to optimize the cleaning cycle. Overall, the test was very successful, and, when operating properly, the filters removed essentially all of the dust in the gas exiting from the combustor. Apart from the issues with the candle strength and the pulse-cleaning air usage, the other problems were not believed to be of major importance in the further development of the technology. This paper will summarize the test results, emphasizing the problems of candle durability and the pulse-cleaning system.

Introduction

The principal features of a pressurized fluidized bed combustion (PFBC) system operating in the combined cycle mode are sketched in Fig. 1. Coal is combusted in a fluidized bed at a pressure of the order of 10–15 bar (1–1.5 MPa). The combustion gas exits the combustor and is expanded through a gas turbine. The turbine drives the system air compressor, and also an electric generator. The bed also contains a heat exchanger, which forms part of a steam circuit; the steam turbine also generates electricity.

The advantages of fluidized combustion are well known. The fluidized bed results in excellent gas/solids contact, so that efficient combustion can be attained at lower temperatures

Contributed by the International Gas Turbine Institute and presented at the 36th International Gas Turbine and Aeroengine Congress and Exposition, Orlando, Florida, June 3–6, 1991. Manuscript received at ASME Headquarters March 11, 1991. Paper No. 91-GT-381. Associate Editor: L. A. Riekert.

Copyright © 1992 by ASME
Downloaded 02 Jun 2010 to 171.66.16.112. Redistribution subject to ASME license or copyright; see http://www.asme.org/terms/Terms_Use.cfm

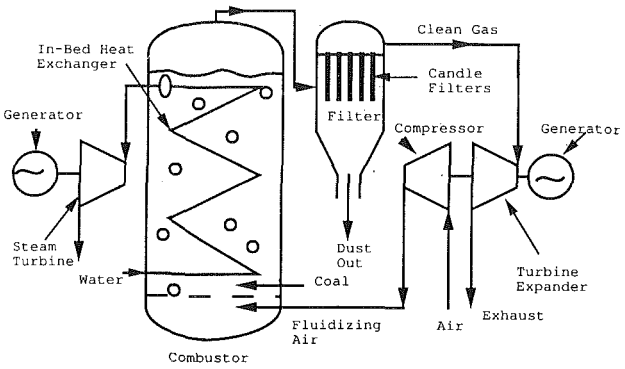


Fig. 1 General features of a pressurized fluidized bed combustion combined cycle power plant

than those in other combustion systems. In addition, the sulfur contained in the coal can be captured within the bed by a suitable acceptor, such as limestone, $CaCO_3$, or dolomite, $MgCO_3 \cdot CaCO_3$, forming $CaSO_4$. Sulfur capture efficiencies in excess of 90 percent are readily obtained. The optimum bed temperature is determined by a number of factors, including the combustion efficiency, the sulfur capture efficiency, and the need to avoid agglomeration within the bed: This combination of factors generally leads to a value in the range 1123 K (850°C; 1562°F) to 1173 K (900°C; 1652°F). From the point of view of the gas turbine expander, this is a low temperature, and advanced cycles are currently under investigation, which involve further heating the combustion gas before it enters the turbine.

The bed itself consists principally of coal ash and spent acceptor. Typically, there is less than 2 percent uncombusted coal or char in the bed at any time. The mean bed particle size is of the order of 800 μm, and the superficial velocity of the fluidizing air is typically 0.5–0.8 m/s. This last was originally much higher: Values as high as 3.7 m/s were suggested. The benefit of a higher superficial velocity is that it is this that principally determines the power that can be generated per unit cross-sectional area of the pressure vessel. However, the need to control erosion of the in-bed heat exchanger tubes has resulted in a reduction of the superficial velocity, and also some reductions in the mean bed particle size, although the exact values that are used in the successful practical systems are currently not reported.

The bed is relatively deep: The actual depth depends on several factors, most notably the in-bed gas residence time, and the overall height of the in-bed heat exchanger tube bundle. Typical values are 2–3.5 m.

The off-gas from the combustor contains a high concentration of particles, typically 20,000 ppmw (parts per million by weight). It is essential that the majority of these particles are removed before the gas enters the turbine expander. The exact particle loading that can be accepted by the turbine depends on the details of the turbine design: The robust expanders used to recover energy from the off-gas of catalytic regenerators can accept much higher particle loadings without unacceptable erosion damage than aircraft-derivative engines. Nevertheless, guidelines of the kind proposed by Stringer and Drenker (1981) are generally used: certainly less than 0.1 ppm of particles greater than 20 μm; not more than 1 ppm over 10 μm; and not more than 10 ppm in the range 4–10 μm. Particles less than 4 μm were regarded as not particularly damaging, but this conclusion may need to be re-examined. In addition to the erosion problem, deposition may be an issue: This has been examined in detail by Alvin and Wenglarz (1983).

These particle loadings can be achieved by two high-efficiency cyclones in series, but only just; and it has to be assumed that the cyclones are operating properly. With the particle size distribution in the off-gas, the large-particle limits previously given result in a total particle loading in the gas leaving the cyclones of approximately 100–200 ppm. This can easily lead to excessive fouling, although this does not appear to have been a problem in practice to date. It also is necessary to reduce the particle loading in the system off-gas for environmental reasons: In the U.S., this corresponds to approximately 28 ppm. If cyclones are used to protect the turbine, it will be necessary to have a further clean-up system at the back end.

For these two reasons, EPRI has been interested in the development of a hot-gas particle removal system, which will not only provide a positive protection for the turbine, but also will reduce the particle loading below the environmental limits, obviating the need for a further back-end system. The two approaches that seemed most promising were ceramic fabric bags and rigid porous ceramic filters, and testing of both these concepts has been in progress for several years. A further benefit is that the pressure drop across the cleaning system is reduced: Typically, the pressure drop across a high-efficiency cyclone train to attain the limits just given will be in the range 50–150 kPa, whereas the pressure drop over a rigid porous ceramic filter assembly, for example, is usually less than 25 kPa.

The EPRI hot-gas filter pilot plant installed at the Grimethorpe PFBC facility represented a major scale up, to close to commercial size, and was intended primarily to provide information that could lead to the design of a full-scale unit.

Design and Construction of the Filter

EPRI's prime contractor for this project was National Smokeless Fuels, a division of British Coal, acting as an agent for British Coal and the Central Electricity Generating Board. The overall design specifications for the filter were written by staff of the Grimethorpe PFBC Establishment in collaboration with EPRI staff. Westinghouse was selected as the contractor, and produced the detailed design. The unit was constructed by Foster-Wheeler Power Products. The initial plan had been to test both rigid ceramic elements and ceramic filter bags, and the filter vessel was designed to make this possible. In the event, only the rigid elements were tested.

The rigid element that had been tested in earlier EPRI work was the closed-ended cylindrical tube form: This is generally referred to as a candle. After an evaluation of the candles available from different manufacturers, it was decided to use Schumacher Diaschumalith candles, and staff from Schumacher GmbH gave valuable assistance in the design of the candle-mounting system and in the later evaluation of the candle performance. The cylindrical elements were 1.5 m long with an external diameter of 60 mm and a wall thickness of 15 mm. They consisted of an inner support made from silicon carbide granules with a thin outer layer composed of fine alumina fibers and silicon carbide grains. A clay binder was used as the bonding agent in each case. Tests carried out at British Coal's Coal Research Establishment and funded by British Coal and the CEGB, indicated that filter elements of this type had superior permeability to those used in earlier trials (Reed, 1986).

Details of the design and construction of the filter are presented elsewhere (Birkby et al., 1987; Reed et al., 1989), and only brief details will be presented here. Figure 2 shows a schematic of the filter vessel, which was 8.8 m high and 2.6 m in diameter. The pressure shell was refractory-lined, followed by layers of fiber blanket insulation protected by an internal stainless steel liner. The filter elements were supported in a circular plate, referred to as the tube sheet; the sheet can hold a maximum of 130 candles. The combustor off-gas enters below the sheet, and flows through the filter elements from the outside to the inside; the dust is retained on the outer surface of the element and the clean gas exits the unit above

Downloaded 02 Jun 2010 to 171.66.16.112. Redistribution subject to ASME license or copyright; see http://www.asme.org/terms/Terms_Use.cfm

Table 1 Summary of PFBC operating parameters during filter operation

Test series	Fuel feed	Sorbent feed	Combustor pressure bar	Combustor temperature °C
A2.1	UK Dry	UK Dry	8.1–10.6	850
A2.2	US Dry	US Dry	8.0–9.3	900
	US Wet	US Dry	7.3–10.6	800–900
	US Wet	US Wet	8.8–9.3	900
A2.3	UK Dry	UK Dry	10.3	900
	UK Wet	UK Dry	10.6	900

Table 2 Summary of filter operating hours at condition for the range of face velocities investigated

Face velocity (m/s)	A2.1 (hrs)	A2.2 (hrs)	A2.3 (hrs)	Total (A2.1 + A2.2 + A2.3) (hrs)
0.01	0	0	43.8	43.8
0.03	277	88.8	86.5	452.3
0.04	28	0	12.8	40.8
0.06	0	195.3	34.9	230.2
0.07	0	22.8	0	22.8
Total	305	306.9	178	789.9

the tube sheet. The elements are cleaned by a reverse pulse of air from a pressure vessel outside the filter vessel, which is directed axially down the inside of the elements. The dislodged dust cake then falls down the vessel, and is removed at the bottom using a screw cooler and a pressure seal lock hopper system.

The support structure for the tube sheet is required also to act as a pressure seal between the upper and lower compartments of the vessel, and also must accommodate the differential thermal expansions taking place during heat-up and cool-down. The single element bellows configuration, which appears in Fig. 2 as a deep V embedded in the wall refractory was originally sketched as a shallow structure, and the combustor gas inlet was toward the upper part of the candles. During the detailed design phase, it became clear that the support arrangement had to be much deeper, and this resulted in the gas inlet being toward the bottom of the candles. This may have had an adverse effect on the filter performance.

Initially, it had been planned to exhaust the full particle loading of the off-gas through the filter but, for operational reasons, it was decided to use a primary cyclone prior to the filter. This had a higher efficiency than expected, removing 80–95 percent of the coarser particles, reducing the particulates loading to around 900–3500 ppm by weight. This had two adverse effects on the experiment: The screw cooler was oversized, and it was feared that it would therefore run at too low a temperature and suffer corrosion damage due to condensation; and the filter dust cake would contain too few larger particles and therefore clean less effectively. The first problem did not occur; it is not possible to tell whether the second was a factor.

Details of the PFBC operating parameters during filter operation are given in Table 1. The UK feedstocks were Kiveton Park coal (1.6 percent S, 0.22 percent Cl) and Middleton limestone, while the US coal was Glenn Brooke (2.4 percent S, 0.09 percent Cl) with Plum Run dolomite sorbent. Both wet and dry fuel feed modes were used. The filter was exposed to PFBC off-gas at high temperature and pressure for over 860 h of which 790 h were at defined process conditions.

Data were collected for filter face velocities in the range 0.01–0.07 m/s. Table 2 shows the times at the different face velocities. Although the maximum face velocity of 0.07 m/s was attained for only a brief period, operation at 0.06 m/s was sustained for 230 h, which is an encouraging achievement.

The pulse cleaning cycle time for the filter elements was varied over the range 3 to 12 min, with the majority of the

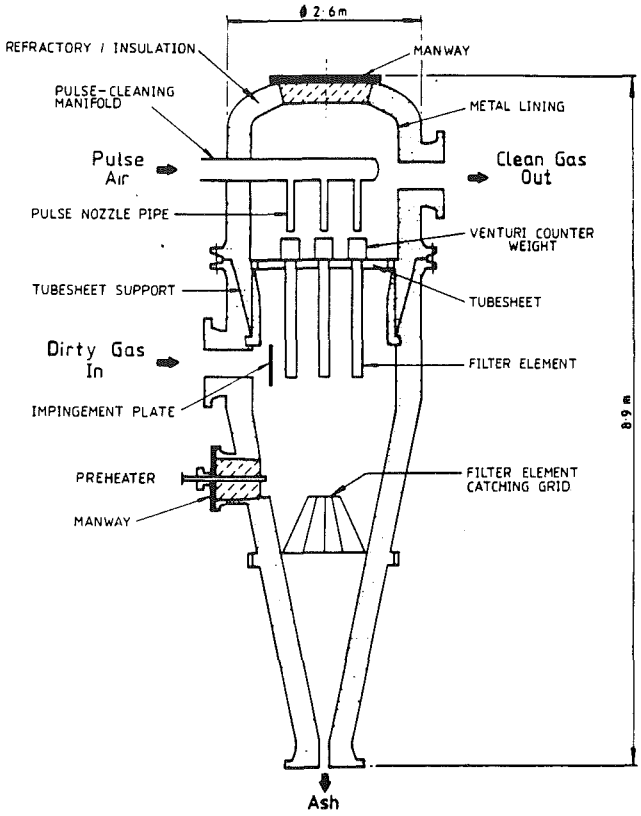


Fig. 2 Schematic diagram of the EPRI hot gas filter at Grimethorpe

test work being carried out on a 3-min cycle. This was undoubtedly more frequent than would have been necessary, but the aim was to attain a steady-state behavior of the candles ("condition" them) in as short a time as possible. At one point, a solenoid valve failure depleted the reservoir, and cleaning could not be resumed for several minutes. On the basis of this single observation, it did appear that the cleaning interval could be extended by at least a factor of five.

The overall project statistics for filter-element exposure to PFBC off-gas at high temperature and pressure comprise a cumulative total of over 72,000 filter-element-hours of active exposure and the achievement of over 1.3 million filter-element pulses.

Throughout the first test series, although 130 filter elements were exposed to PFBC off-gas, only 104 elements (by way of 8 manifolds) were actively filtering. The remaining 26 elements were rendered inactive. During the second test series, the number of active elements was eventually reduced to 72 (still by way of 8 manifolds), in order to achieve higher face velocities. For the third test series, a matrix of 80 elements was used, but this time all 10 manifolds were active, i.e., 8 filter elements per manifold.

A discussion of the overall performance of the complete system, and recommendations for modifications have recently been presented by Stringer et al. (1991). In this paper the factors affecting the performance of the candle elements will be reviewed in more detail. These were: (*a*) the candle mounting system; (*b*) the pulse cleaning system; and (*c*) the candles themselves. In the following text, these items will be discussed separately.

Candle-Mounting System

Figure 3 shows the candle-mounting arrangement.[1] The candles had a spherical section top, and there was a matching

[1]The sealing system is a modified Schumacher design for which international patent applications are pending.

Downloaded 02 Jun 2010 to 171.66.16.112. Redistribution subject to ASME license or copyright; see http://www.asme.org/terms/Terms_Use.cfm

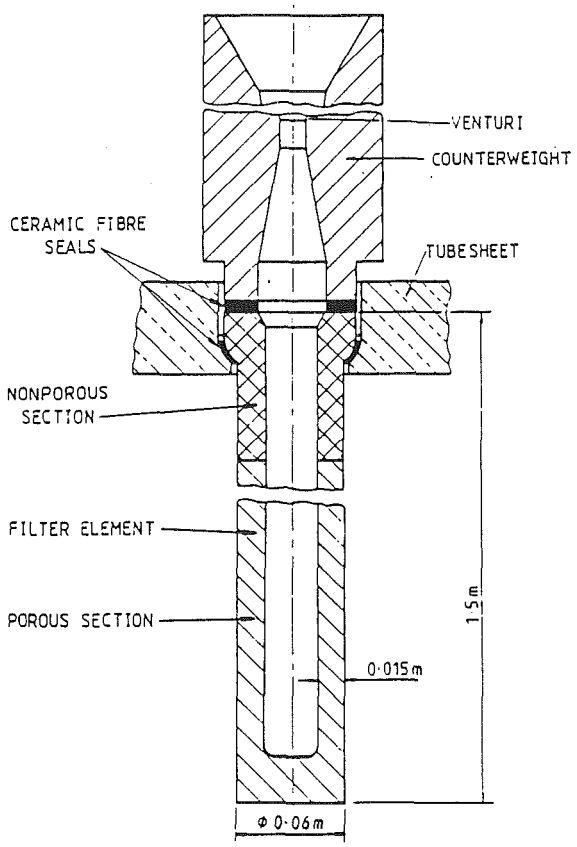


Fig. 3 Filter element support and sealing arrangement

cavity in the tube sheet. In any metal/ceramic structure, the interface between the metal and the ceramic is a problem, and should be as compliant as possible. This was achieved by the use of ceramic fiber washers or seals. The candle was held down by a weight, and again there was a fiber washer between the weight and the candle. The cleaning-pulse air flowed down an axial hole in the hold-down weight, and this was machined to form a venturi, with the objective of entraining clean hot gas with the air. Various alternative more positive hold-down designs were evaluated, but all had serious drawbacks. The maximum allowable pressure difference between the two sides of the tube sheet was then determined by that required to lift the candles out of their seats.

Calculations showed that candle and venturi weight would lift at 38 kPa, although subsequent cold testing at atmospheric pressure on freshly installed candles resulted in lifting at approximately 45 kPa. The limiting pressure drop that could be accepted in operation was set at 32 kPa.

In the event, a few candles did lift out of their seats during service. In addition to the pressure drop resulting from the combined resistance to flow of the candles and the venturis, which varies slowly, it turned out that there were additional transient pressure fluctuations associated with the cleaning process: Normal plant instrumentation would not detect these. When a candle and/or its weight lifted, the fiber washers blew out. The assembly then dropped, with direct metal-to-ceramic-to-metal contact. Schumacher was able to show in laboratory tests that this would be sufficient to cause failure of the elements, and five candle failures occurred for this reason, one late in Test Series A2.1 and four in Test Series A2.3. As a result, it is clear that the hold-down system requires redesign for commercial application. Maintainability of the system also is important, and it is clearly going to be difficult to replace candles from above the tube plate. It would be highly desirable to develop a mounting system that allows the elements to be replaced from beneath the plate.

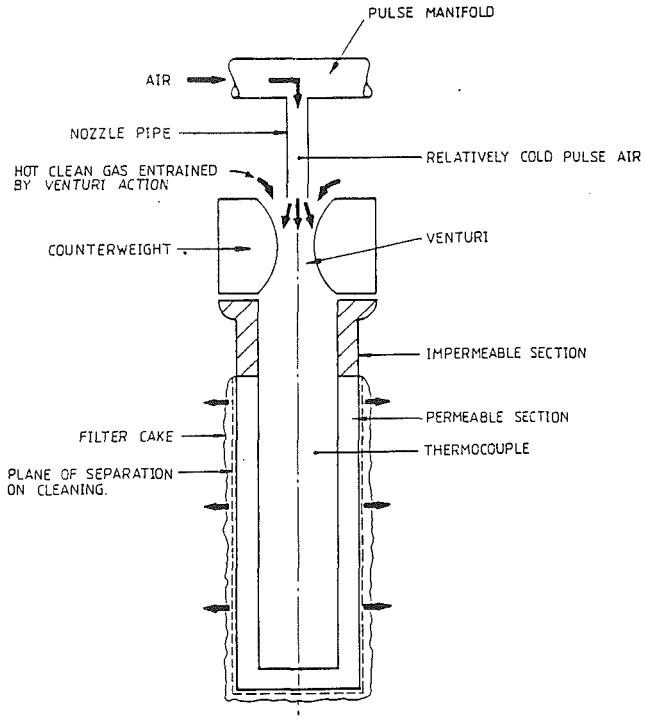


Fig. 4 Cleaning-pulse mode

Pulse-Cleaning System

As previously indicated, the removal of the dust cake from the candles was accomplished by the use of a reverse pulse of air. The process is illustrated schematically in Fig. 4. An external reservoir was charged by three auxiliary compressors. The pulse was initiated by opening a solenoid valve. The pressure pulse then entered a manifold, and was distributed to a number of candles through tubes welded to the manifold. In the original design, there were 10 manifolds, with 13 candles to each manifold. The manifolds were offset, to achieve maintainability of the filter: Each element could be lifted out and replaced from above the tube sheet without cutting the manifold. The blow-back tubes came out of the manifold from the side, and bent downward to enter the corresponding candle support weight venturi. In practice, the reaction force on pulsing deformed the blow-back tubes, and eventually caused failure of a number of them. In part, this was a materials problem: The blow-back tubes were of Type 310 stainless steel, which is prone to form sigma phase, which embrittles it; replacement with Incoloy 800H tubes resulted in improved performance. However, to combat the problem more effectively, the manifolds were repositioned directly above the candles, and the blow-back tubes exited the manifold from the bottom and went directly into the venturis. This means that candles could only be replaced by cutting out the manifold.

Before the filter system was commissioned, doubt was expressed about the likely effectiveness of the pulse pipework layout originally installed on the filter unit. The cause for concern was the presence of substantial lengths of pipework between the main air accumulator and the pulse solenoid valves, and also between the solenoid valves and the filter vessel. In addition, a large number of bends were present in the pipework, together with a substantial number of valves and stepped reducer pieces. The concern was that this would result in an attenuation of the pulse, reducing the rate of increase of pressure as the pulse entered the candle.

It can be argued that the cleaning efficiency will be markedly dependent on this initial rate of pressure increase, although that point has still to be established. This will be discussed later.

Downloaded 02 Jun 2010 to 171.66.16.112. Redistribution subject to ASME license or copyright; see http://www.asme.org/terms/Terms_Use.cfm

The potential problem was addressed, after Test Series A2.1, by redesigning the pipework. In addition, two new secondary air reservoirs were positioned on top of the filter vessel. The solenoid valves were located immediately downstream of the secondary reservoirs, as close as possible to the filter vessel, to insure that pulse attenuation would be minimized and that rapid pressure recovery would be achieved following pulsing. This revised system was used throughout the remainder of the test program.

Pulse Valves. The pulse valves were 2 in. (50 mm) electropneumatic globe-type (Model No. 31871-639) manufactured by the Aktomatic Valve Co. Inc., intended for operation with a differential pressure (DP) in the range 20–55 bar across the valve.

Initially, a differential pressure cell was installed across solenoid valve E as a diagnostic aid to pulse characterization and performance. Manifold E was chosen as this contained instrumented filter elements.

During cold commissioning of the pulse cleaning system, the threaded internal couplings came loose in four of the valves. The situation was resolved by modifying the valve internal couplings, effectively disconnecting the piston from the solenoid plunger. In addition, experience showed that the valves tended to malfunction for differential pressures of less than 20 bar (corresponding to the lower limit specified by the manufacturer). The response of the valves was disappointingly slow, and in order to ensure that sufficient time was available for the valves to open fully, a set point of 500 ms (valve open time) was used. This gave an actual opening time of around 1 s, due to the slow mechanical response of the valves. This has two implications: First, the pulse pressure increase rate is attenuated, with the potential consequence of reducing the cleaning effectiveness; and the cleaning-air use will be significantly greater than it needs to be. This is important, because the high-pressure cleaning air represents an efficiency penalty for the overall system.

Following the foregoing modification, it was possible to operate the pulse valves successfully, most of the time, by keeping the DP above 20 bar and the valve opening time set point at 500 ms.

During the three test series, one or more solenoid valves jammed open on occasion. As a result of such an incident, rapid depressurization of the air accumulator occurred through the faulty valve, leading to undesirable shock cooling of the ceramic filter elements in the corresponding manifold(s). A further consequence was that there was insufficient air available to sustain the operation of the pulse-cleaning system.

In general, inspections of valves that had jammed revealed nothing to indicate the cause of the malfunction. The aforementioned incidents, albeit isolated events, nevertheless cast doubt on the suitability of these Aktomatic valves for this duty, for which very high reliability is essential.

In addition to the issue of solenoid valve reliability, the total number of candles that can be cleaned on a single manifold with a single solenoid valve needs to be addressed. In the Grimethorpe rig, ten valves were required for an equivalent of 7 MW(e). If this were scaled up to a 350 MW(e) plant using the same filter conditions, it is apparent that some 500 large solenoid valves would be required, and would have to operate with a very high degree of reliability.

Air use in the cleaning was excessive, and the power used by the compressors represents an unacceptable loss. It is believed that the air consumed can be reduced significantly, perhaps by an order of magnitude, by doing some or all of the following:

- Decreasing pulse-cleaning frequency (i.e., increasing pulse-cleaning cycle time).
- Using faster acting pulse valves to give shorter duration pulses.
- Using pulse valves that operate reliably with a lower differential pressure across them (i.e., pulse air reservoir pressure can be reduced).
- Having more filter elements per manifold (this needs to be demonstrated).

Ceramic Filter Elements

The principle on which these filter elements operate is that the actual filtration is done by the filter cake itself: The ceramic element serves to support the cake. The problem with this approach is that if the dust penetrates into the porous ceramic itself the candle will blind irreversibly. The tendency to do this can be reduced by decreasing the pore size, but a consequence is that the pressure drop across the filter body becomes very high. The Diaschumalith design overcomes this by using a thin outer layer of very fine porosity, over the main body of the filter, which has a relatively coarse porosity. In practice, there was very little penetration of dust into the body of the candle. The tendency for irreversible dust impregnation can be further reduced by the cleaning step itself.

The mode of cleaning a rigid porous ceramic filter is quite different from that used for a bag filter. In the latter case, the pulse accelerates the fabric of the bag outward, dislodging the dust cake; but in the former case, the filter itself does not deform. The dislodging of the cake is done by the air passing out through the filter wall. There are two ways in which this can happen: In the first, the air is regarded as flowing relatively slowly through the pores, building up a pressure difference across the relatively impervious cake until its tensile strength is exceeded. In the second, a shock wave is thought to propagate through the porous medium, dislodging the cake. Which of these two processes actually occurs has important implications for the design of the system. The discussion of the cleaning system presented in the previous section makes it clear that the original opinion behind this project was that the second of these mechanisms was correct, in that every effort was made in the redesign of the blow-back piping to maximize the rate of pressure rise in the body of the candle at the start of the cleaning pulse.

The pressure drop across a fresh filter element is not completely recovered on pulsing: This is to be expected, in part because of the irreversible impregnation and, in part, because of the formation of the steady-state residual filter cake layer on the surface. It is hoped that the second of these terms is the major one.

The performance of the filter as a whole is best described in terms of a parameter called the permeance, **p**, where

$$\mathbf{p} = V\mu_T/\Delta P\mu_{20}$$

where V is the face velocity, which is the volumetric flow of gas through the filter divided by the surface area of the filter, ΔP is the pressure drop across the filter, and μ_T and μ_{20} are the viscosities of the gas at the operating temperature T and at 20°C, respectively. For air, the ratio of the viscosities between 850°C and 20°C is approximately 2.4.

Filter Performance. Overall, the filter performance was very good provided no candle failures were present. Unfortunately, the dust measurement system downstream of the filter did not operate successfully during Test Series A2.1, but the indications were that the particle loading downstream was significantly below 10 ppm. Later, the dust measurement equipment was improved, but chemical analysis of captured dust showed that the samples were contaminated by oxide from the stainless steel lining on the clean side of the filter. The measured dust loadings were still very low. It is common to report the efficiency of filtration systems, but this is not the best way to describe the performance of a filter system such as this. The performance should be reported as a downstream dust-loading and particle-size distribution. The results from these tests, al-

Downloaded 02 Jun 2010 to 171.66.16.112. Redistribution subject to ASME license or copyright; see http://www.asme.org/terms/Terms_Use.cfm

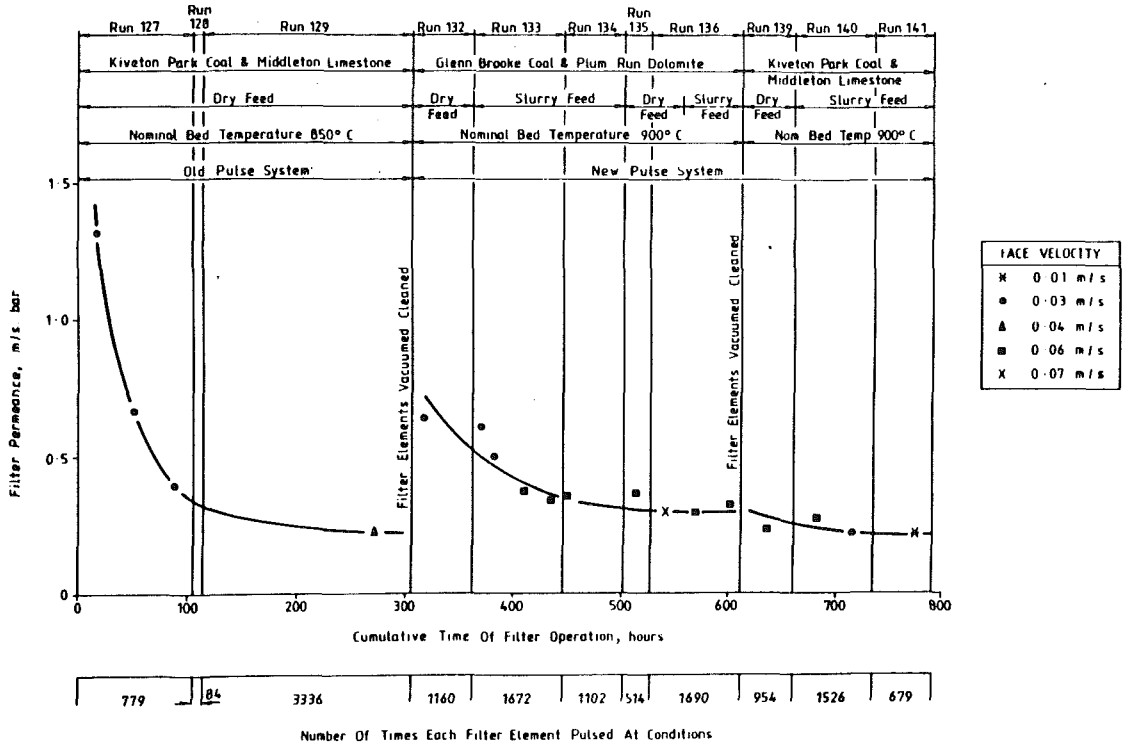


Fig. 5 Filter permeances (at temperature) for Test Series A2.1, A2.2 and A2.3

though incomplete, nevertheless make it quite clear that the effectiveness of the filtration, or the ability of a properly operating filter to attain the stated targets of cleanliness, is not an issue.

Figure 5 shows the change in permeance through the three test periods. The rapid drop at the beginning is because the candles were unused; the permeance falls because of the buildup of the dust cake and the impregnation of the surface layer by fine dust particles. At the end of the test, the remanent surface dust layer was removed by light brushing and vacuuming, resulting in the partial regeneration of the permeance at the beginning of the second period. The brushing and vacuuming were repeated at the end of the second test period, again leading to a partial, but much lesser, regeneration of the permeance. It is apparent that the permeance is increasingly dominated by the irreversible changes in the surface layer of the candle, and that the rate of change in this is diminishing. It is not clear that a steady-state permeance is attained in any of the tests, but the rate of decrease becomes small at the end of each test period. The permeance seems unaffected by the coal or acceptor, by the face velocity, or by the change from a dry to a wet feed.

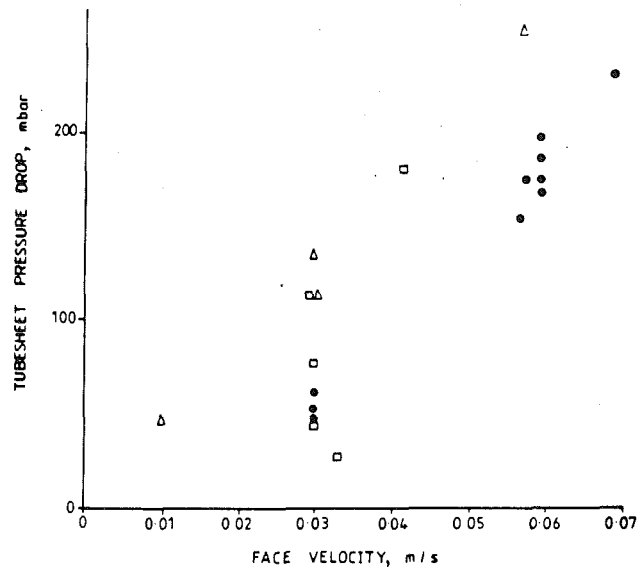
It should be noted that the difference in the terminal permeance seems to be little affected by the change in the blow-back system. It had been hoped that the changes in the arrangement of the piping should have resulted in a significant improvement of cleaning, as measured by the recovery of the pressure drop across the filter following a pulse. In fact, there appeared to be little change. The behavior of the two pulse systems has been subsequently analyzed quantitatively by Pitt (1991) and Pitt and Leitch (1991), who pointed out that the beneficial effect of the shortened distance between the reservoir and the vessel was outweighed by the reduction in pipe diameter. These analyses identified the main sources of the pressure drop as being the flow dividing junctions of the nozzle pipes with the manifold inside the filter vessel, and the valves in the external pipework, in particular those at reduced diameters. The reconstruction of the blow-back system did not address these locations.

In the cleaning operation, the desirable situation is that the cake does not dislodge from the actual surface of the filter. The fracture of the cake occurs within the cake itself, leaving a thin layer of dust remaining on the candle. This is the best way of operating the system because the filter/dust cake interface is then essentially stable, and further impregnation of the filter by dust will not occur. If the cleaning process is too severe, the filter surface is repeatedly exposed, and some further impregnation may occur on every cycle. This is called overcleaning. It is possible that, in this experiment, there may have been some tendency to overclean, not as a result of excess severity of the cleaning pulse, but because of cleaning more frequently than was necessary. The appearance of the dust cake on some of the filters after test suggested this, in that there were a number of areas on the surface where there appeared to be little or no remnant cake, resulting in a speckled appearance. Immediately after the modifications to the blow-back system, the appearance of the cleaned candles seemed to improve, but later the speckled appearance reappeared.

While the permeance is the best measure of the actual performance of the candles, the pressure drop across the filter is also a matter of concern, at least with the gravity hold-down system. The pressure drop is composed of two terms: the pressure drop across the candle and filter cake, and the pressure drop across the venturi weight. Figure 6 shows the total pressure drop as a function of face velocity: Approximately 25 percent of this is due to the venturis.

The scatter in the data is due to the variations in operating conditions: It is apparent that the pressure drop was higher in Test Series A2.3. This followed the failure of four candles, and it is believed that the dust, which consequently entered the upper (nominally clean) side of the vessel, was then blown *down* into the interior of the candles by entrainment in the cleaning-pulse jets. The inner surfaces of the intact candles were observed to be contaminated with dust at the end of the test, and some of this had impregnated the pores of the ceramic; some of the candles were as much as 50 percent filled with dust. The single high point for Test Series 2.1 at a face velocity of 0.042 m/s was for the last few hours of the test series, and

Downloaded 02 Jun 2010 to 171.66.16.112. Redistribution subject to ASME license or copyright; see http://www.asme.org/terms/Terms_Use.cfm



TEST SERIES	COAL	SORBENT
□ A2 1	KIVETON PARK	MIDDLETON LIMESTONE
• A2 2	GLENN BROOKE	PLUM RUN DOLOMITE
Δ A2 3	KIVETON PARK	MIDDLETON LIMESTONE

Fig. 6 Overall tubesheet pressure drop as a function of the face velocity

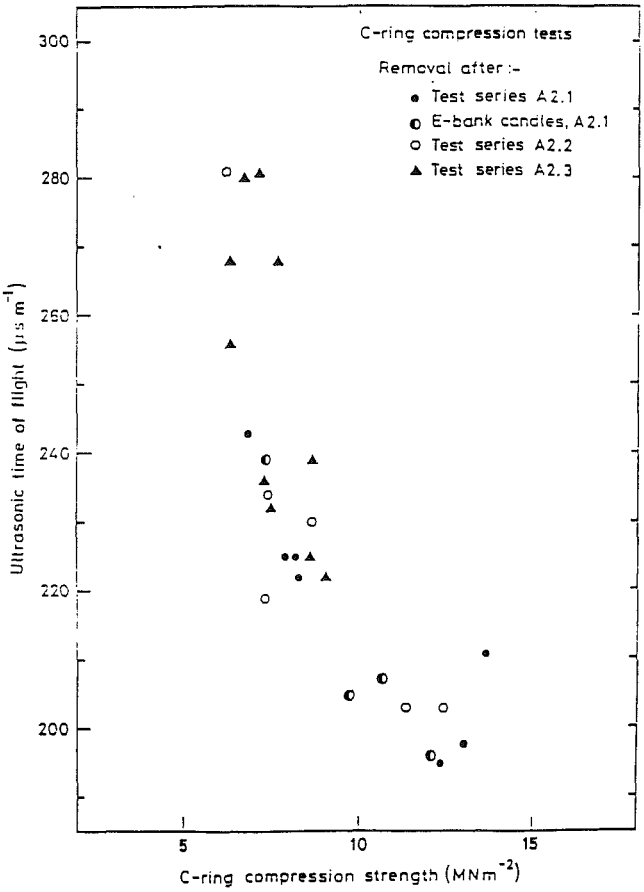


Fig. 7 Correlation between the time-of-flight of a sonic pulse and the *C*-ring compression strength for all the filter elements tested

it is probable that the candle failure observed at the end of the series had already occurred, leading to similar, albeit lesser, contamination.

Candle Failures and Weakening. Following the failure of one ceramic filter element during Test Series A2.1, a substantial materials investigation (Coal Products Ltd., 1991) was initiated. This work was extended to include the four subsequent failures that occurred during Test Series A2.3. During these tests, it became apparent that there was also a general weakening of the candles in service, although the catastrophic failures had nothing to do with this weakening. The study thus attempted to attack both issues. As is apparent from the prior discussion, the candle breaks proved to be due to mechanical lifting and dropping of the candle and venturi assembly. The loss of strength problem proved to be considerably more difficult. The elements investigated by both nondestructive and destructive techniques were new elements, used active elements, and used inactive elements, and were carried out by the following organizations: British Coal CRE, National Physical Laboratory, Ceram Research, Harwell, Schumacher GmbH and Dundee University. The ceramic fiber gaskets, used to seal the elements in the tube sheet and also to form a seal between the filter elements and the venturi weights, also were investigated as part of this work.

Test Results. Preliminary results of these investigations into the materials aspects of the ceramic filter elements were presented at an EPRI Technology Transfer workshop in 1988 (EPRI 1988) and, more recently, at the First International Conference on Ceramics in Energy Applications (Morrell et al., 1990). Full details are given in a summary report prepared for EPRI by British Coal (Coal Products Ltd., 1991).

The surface layer of the ceramic elements performed satisfactorily throughout the period of filter operation, and no signs of deterioration were detected.

Under normal filter operation, the filter elements and ceramic fiber sealing gaskets performed satisfactorily. However, insufficient operating hours at high-temperature, high-pressure conditions were achieved to enable service lifetime predictions to be made for the ceramic filter elements for commercial applications.

The weakening was general throughout the length of the filter elements, although the strength of the near-bore material was generally lower then that of the outer material. It was not, however, possible to determine the relative contributions of exposure hours and the number of pulse cleaning cycles.

Two test procedures proved to be of significant interest. These were mechanical tests of rings cut from the candles, and measurements of the sonic velocity along the length of the candles. This last was determined by measuring the length of time it took a sonic pulse to travel from a generator to a detector: It is called a time-of-flight test. The highly porous candle material consists of grains joined at necks, which are relatively small in diameter and widely spaced. Sound thus has to travel a tortuous path, and the apparent velocity will be strongly dependent on thinning and breakage of the necks. The propagation velocity will be relatively insensitive to cracks parallel to the axis, and it will take place preferentially in the relatively denser outside region of the candle. The mechanical testing of rings cut from ceramic tubes is a well-known technique; one approach which is useful for the current problem is to cut a small sector out, so that the cross section resembles the letter *C*: This is called the *C*-ring test. The load can then be applied in two ways: The ring can be compressed (attempting to close the *C*) or dilated (opening the *C*). These are called the *C*-ring compression and the *C*-ring tension tests, respectively. However, the failure of the *C*-ring is always in tension: In the compressive test the ring fails in tension at the outer surface of the tube, whereas in the tension test the initial tensile failure is at the inner surface. A good correlation was observed between the *C*-ring compression strength and the ultrasonic

Downloaded 02 Jun 2010 to 171.66.16.112. Redistribution subject to ASME license or copyright; see http://www.asme.org/terms/Terms_Use.cfm

time-of-flight for the ceramic elements under investigation, as shown in Fig. 7. No such strong correlation was obtained for the near-bore material, i.e., *C*-ring tension versus time-of-flight. This is perhaps not surprising, since, as previously indicated, the time-of-flight measurements probably give most information about changes in the ceramic near to the dense outer surface.

Microstructural examination of the ceramic material revealed that no marked damaged had resulted from exposure at HTHP conditions. Microcracks were, however, observed at the binder/grit interfaces. It was considered possible that the thermal cycling, due to the pulse cleaning, could have helped propagate the microcracks, contributing to the general weakening of the elements by thermal fatigue. The thermal cycling also was thought to have been sufficiently severe to cause thermal shock damage, and some larger cracks, parallel to the axis of the candles, were observed at the inner surfaces. However, this factor was not believed to have caused the in-service failures.

The pulse-cleaning air was relatively cool, and small-diameter unshielded thermocouples in some candles showed a transient temperature drop associated with the pulse. The maximum temperature drop measured was approximately 250°C, reached 1s after the initiation of the pulse (modified pulse-cleaning system). After 4 or 5s, the temperature was back close to the steady-state value. In the normal way, this would not be regarded as a very severe thermal shock for silicon carbide, even clay-bonded material. The relatively low temperature differential implies that there was significant entrainment of hot clean gas by the venturi. A complicating factor is that the cool gas is forced into the hot porous medium and, as a consequence, the effective thermal shock on the interparticle necks, which are of the less-thermal shock-resistant glassy phase, may be very high. Conversely, the gas will heat up very rapidly as it passes through the pores, and it is difficult to see how there could be any significant shock of the outer part of the candle: The weakening of the outer layers of the candle as indicated by the time-of-flight and the *C*-ring compression tests are difficult to rationalize as due to thermal shock induced by the pulse air. The longitudinal cracks on the inner bore could perhaps be caused by thermal effects: Cooling the inner bore will place the surface in tension, and ceramics are well known to be weak in tension. Cooling through 200°C would induce a strain of the order of 0.01 percent, which should be well below the fracture strain for silicon carbide.

Careful analysis failed to show any evidence of alkali metal attack at the outer surface. There may have been some small reaction with calcium sulfate, but overall there was little sign of any chemical attack. In siliceous refractories, the transformation of quartz to cristobalite can be damaging, but searches for cristobalite failed to show any difference between the used and unused candles. Another major concern is the effect of water vapor. Silicon carbide is sensitive to degradation by steam oxidation, and Semler (1991) has shown that material from the Diaschumalith candles is rapidly degraded by steam exposure at temperatures rather higher than those experienced in the PFBC, but there is considerable uncertainty as to the extrapolation of this result to lower temperatures. Further studies under more realistic conditions are now in progress.

It is important to point out that the good correlation between the acoustic time-of-flight measurements and the *C*-ring compression strength probably arises because they both measure principally the properties of the outer material of the candles. It does not necessarily imply that the actual failure of a candle would be initiated in the outer layers. No candle has yet failed as a result of this progressive weakening process, and thus no information is available on the failure mode. Any testing procedure must eventually be qualified by comparison with in-service performance, and it may eventually turn out that the damage to the inner bore, which could be thermal shock-related, is the more serious damage, although it is not well characterized by the *C*-ring tests. While it is a recommendation that the time-of-flight measurement method should be used as a convenient nondestructive quality-control method, which also may provide nondestructive information on the change in candle properties during exposure, caution needs to be exercised in relation to its ultimate relevance to candle failure prediction.

Summary and Recommendations

Overall, the performance of the EPRI hot-gas filter at Grimethorpe was very encouraging. During the periods when the system was operating properly, the filtration was very effective, with particle loadings almost certainly well below 10 ppm, and perhaps below 1 ppm. The pressure drop was low, and certainly very significantly less than cyclone trains. While the energy penalty represented by the pulse air was certainly too high, there were good reasons to believe that this could be reduced in practice by at least an order of magnitude. The dust cooling and removal system worked very well.

The pulse clean-up system is still far from optimization. More candles have to be cleaned from a single valve, and a more reliable valve with improved opening and closing characteristics is necessary. Improved design of the external and internal pulse-air piping is necessary, and it will help greatly if this is done, using the analytical procedures that have been developed.

The mounting system used for the candles is clearly unsatisfactory. It allowed candles to lift, resulting in their fracture: Even if they had not broken, the loss of the sealing fiber gaskets would have degraded the filter performance. The replacement of failed candle assemblies is difficult. Having a gravity hold-down system limits the permissible pressure difference across the plate, which relates not only to the normal running conditions, but also to transients that may be experienced during system upsets.

The progressive weakening of the candles is a matter of concern. While the mechanisms responsible for this have not been fully identified, it has been suggested that the type of bond material, proportion of bond material and the SiC grit size should be varied to help produce an element with improved physical properties to withstand the conditions experienced in the PFBC. Schumacher began development along these lines at an early stage.

The ultrasonic time-of-flight technique is recommended as a useful nondestructive, easy-to-use method of monitoring the performance of the ceramic filter elements throughout their service life. Of particular interest would be the development of an in situ method of carrying out these measurements.

Continuing studies on improved porous filter materials and filter assembly designs are clearly necessary. This test has made it clear how important it is to fully instrument any future tests, and to analyze as completely as possible the design and the experimental data.

References

Alvin, M. A., and Wenglarz, R. A., 1983, "An Assessment of Corrosion/Deposition Potential for PFBC Power Plant Turbines," *Proceedings, 7th International Conference on Fluidized Bed Combustion*, DOE/METC/83-48, U.S. Department of Energy, Washington, DC, pp. 957–967.

Birkby, C., Wheeldon, J. M., Tassicker, O. J., and Reed, G. P., 1987, "Process Design and Proposed Test Programme for a Filter Unit Operating in the Off-Gas Path of a Pressurised Fluidised Bed Combustor," *Proceedings, 1987 International Conference on Fluidized Bed Combustion*, J. P. Mustonen, ed., ASME, New York, pp. 993–999.

Coal Products Ltd., 1991, "An Investigation of the Behaviour of the Schumacher Filter Elements in the Hot-Gas Filter on the Grimethorpe PFBC," Report PFBC/COOP/TR9 under Research Project No. RP1336-08, Electric Power Research Institute, Palo Alto, CA.

Electric Power Research Institute, 1988, *EPRI Technology Transfer Workshop on the Grimethorpe PFBC Gas Filter Project*, EPRI, Palo Alto, CA.

Downloaded 02 Jun 2010 to 171.66.16.112. Redistribution subject to ASME license or copyright; see http://www.asme.org/terms/Terms_Use.cfm

Morrell, R., Butterfield, D. M., Clinton, D. J., Barratt, P. G., Oakey, J. E., Reed, G. P., Durst, M., and Burnard, G. K., 1990, "The Mechanical Performance of Ceramic Dust Filter Elements in the Tertiary Dust Capture Filter of the Grimethorpe Fluidised Bed Combustor (PFBC)," *Proceedings, 1st International Conference on Ceramics in Energy Applications*, Sheffield, United Kingdom, (in press).

Pitt, R. U., 1991, Final Report on Research Project RP 1336-07, Electric Power Research Institute, Palo Alto, CA (in press).

Pitt, R. U., and Leitch, A. J., 1991, "A Simple Method to Predict the Operation of Flue Gas Filter Pulse-Cleaning Systems," *Proceedings, 11th International Conference on Fluidized Bed Combustion*, American Society of Mechanical Engineers, New York, N.Y. (in press).

Reed, G. P., 1986, "Filtration of Hot Compressed Gases From Pressurised Fluid Bed Combustion of Coal," *Proceedings, 4th World Filtration Congress*, Ostend, Belgium, pp. 5.1–5.10.

Reed, G. P., Burnard, G. K., Tassicker, O. J., and Leitch, A. J., 1987, "A Large Ceramic Candle Filter Module on a Pressurized Fluidized Bed Combustor—Description and Preliminary Data," *Transactions of the BMFT and VGB International Conference on Advanced Coal and Power Plant Technology and Hot Gas Cleaning*, Dusseldorf, FRG, Paper V24.

Semler, C., 1991, "Evaluation and Testing of SiC Tube Filter Elements," Report on Research Project RP 1336-12, Electric Power Research Institute, Palo Alto, CA.

Stringer, J., and Drenker, S., 1981, "Turbine Erosion Problems and Hot-Gas Cleanup Requirements for PFB Combustion Systems," *Proceedings, American Power Conference*, Vol. 43, pp. 943–949.

Stringer, J., Leitch, A. J., and Clark, R. K., 1992, "The EPRI Hot-Gas Filter Pilot Plant at Grimethorpe: What Worked, What Broke, and Where Do We Go Now?" *Proceedings, 11th International Conference on Fluidized Bed Combustion*, ASME, New York, in press.

Downloaded 02 Jun 2010 to 171.66.16.112. Redistribution subject to ASME license or copyright; see http://www.asme.org/terms/Terms_Use.cfm

Prediction of Gas Turbine On- and Off-Design Performance When Firing Coal-Derived Syngas

M. S. Johnson
Mechanical Engineering Department,
California Polytechnic State University,
San Luis Obispo, CA 93407

This paper describes a procedure used to model the performance of gas turbines designed to fire natural gas (or distillate oil) when fired on medium-Btu fuel, such as coal-derived syngas. Results from such performance studies can be used in the design or analysis of Gasification Combined Cycle (GCC) power plants. The primary difficulty when firing syngas in a gas turbine designed for natural gas is the tendency to drive the compressor toward surge. If the gas turbine has sufficient surge margin and mechanical durability, Gas Turbine Evaluation code (GATE) simulations indicate that net output power can be increased on the order of 15 percent when firing syngas due to the advantageous increase in the ratio of the expander-to-compressor mass flow rates. Three classes of single-spool utility gas turbines are investigated spanning firing temperatures from 1985°F–2500°F (1358 K–1644 K). Performance simulations at a variety of part-load and ambient temperature conditions are described; the resulting performance curves are useful in GCC power plant studies.

Gas Turbine Modeling Requirements

The work described in this report was part of a larger study of Gasification Combined Cycle (GCC) power-plant performance (Johnson, 1989). The central objective of this study was to investigate the on- and off-design performance of these plants employing various gas turbines of interest to the electric utility industry. These gas turbines are large, single spool, constant speed machines characterized by two design point parameters: firing temperature and compressor pressure ratio. These parameters are measures of the "technology level" of a gas turbine; as blade material and cooling technologies improve, higher firing temperatures can be specified. As the firing temperature increases, the pressure ratio yielding peak combined-cycle efficiency also increases (Allen and Triassi, 1988).

There is very little information available in the open literature on the off-design performance of these gas turbines. This is especially true for gas turbines firing coal-derived syngas. The seemingly simple task of predicting the maximum capacity performance characteristics of a gas turbine designed for natural gas or distillate oil when firing syngas is actually an off-design performance problem. The solution to this problem requires all of the same modeling capabilities and information as the more common problems of predicting part-load performance or maximum gas turbine capacity as a function of ambient temperature. The problem of syngas firing is further complicated by the range of strategies available to gas turbine manufacturers for using this fuel. These strategies will be discussed later in this report.

Contributed by the International Gas Turbine Institute and presented at the 36th International Gas Turbine and Aeroengine Congress and Exposition, Orlando, Florida, June 3-6, 1991. Manuscript received at ASME Headquarters March 4, 1991. Paper No. 91-GT-215. Associate Editor: L. A. Riekert.

The result is that the prediction of the *on-design* performance of a GCC plant is a problem in *off-design* gas turbine performance. The following section describes the starting point for gas turbine off-design performance prediction and demonstrates the importance of understanding gas turbine compressor performance when solving these problems.

Some Gas Turbine Fundamentals

The solution to the off-design performance of single spool, constant speed gas turbines begins with the fact that the mass flow at the expander inlet is choked. The mass flow relation for choked flow of an ideal gas is shown below in Eq. (1).

$$\dot{m} = P_t A^* \sqrt{\frac{\mathrm{MW}}{T_t}} \sqrt{\frac{\gamma}{R_u}\left(\frac{2}{\gamma+1}\right)^{\frac{\gamma+1}{\gamma-1}}} \tag{1}$$

This expression is arranged in a somewhat nontraditional form to emphasize the important terms. The term under the large right-hand radical does not change much as a function of γ and to a first approximation it can be considered constant. The molecular weight is isolated in the center term because of its importance when the gas composition changes, as when the products of combustion change between natural gas and syngas firing.

Natural gas has a heating value of about 21,518 Btu/lbm (50,050 kJ/kg) while Texaco syngas with 28.2 mass percent water vapor has a heating value about one-sixth of that, around 3534 Btu/lbm (8220 kJ/kg). To reach the same firing temperature for the same compressor mass flow, a higher syngas flow rate is needed and *the mass flow rate into the expander*

Copyright © 1992 by ASME
Downloaded 02 Jun 2010 to 171.66.16.112. Redistribution subject to ASME license or copyright; see http://www.asme.org/terms/Terms_Use.cfm

must increase. Looking at Eq. (1), one sees that either the total pressure or the critical area must increase to accommodate this increased mass flow. (T_t is constant in this example since the firing temperature was assumed constant for both natural gas and syngas firing; the molecular weight does increase in this case—about 2 percent for Texaco syngas with 28 mass percent moisture content—but not nearly enough to make up for all of the increased mass flow.) A hardware modification to increase the critical area may be neither feasible nor desirable, since the gas turbine may need to switch between natural gas and syngas at various times during its service life. Thus, if the expander inlet gas molecular weight and total temperature remain unchanged from the natural gas design point, *the compressor pressure ratio must increase and/or the compressor mass-flow rate must decrease when firing syngas*. (Later in this report, compressor flow control using variable inlet guide vanes will be discussed. By partially closing these vanes, compressor airflow is reduced and syngas can be fired without increasing the pressure ratio over that of the natural gas design point. For the current discussion, the compressor airflow is assumed constant.)

Operating at an increased pressure ratio presents several complications. Increased thermal loads on the expander airfoils cannot be ignored. Also, since the mass flow through the expander has increased relative to the compressor flow, more power is transferred to the generator, and the torque on the shaft may be unacceptably high (Allen and Triassi, 1988). And in terms of compressor performance, operating at an increased pressure ratio may be impossible. As the pressure ratio increases, the compressor operating point moves toward *surge*. Surge is a complex, transient flow reversal that can cause severe damage to the compressor airfoils; to fire syngas by way of increasing the compressor pressure ratio, a gas turbine must have sufficient compressor *surge margin* to avoid this damaging condition.

If one assumes that the surge margin is adequate and that the expander and the shaft can handle the increased loads, one needs a compressor map to determine the off-design performance of the gas turbine when firing syngas. (This is the reason behind the earlier statement that the "simple" case of firing syngas is itself an off-design problem.) Actual compressor maps for modern gas turbine compressors are not available in the open literature. This is because compressors are very expensive to design, manufacture, and test, and the resulting information is critical to the competitive position of a gas turbine manufacturer. For this study, a one-dimensional, stage-by-stage axial compressor performance model was developed to generate the necessary compressor maps on a consistent basis. This model is described in detail in Johnson (1989). The compressors used here are all based on an advanced compressor designed by the Allison Gas Turbine Division of General Motors under a contract from the Electric Power Research Institute (Bettner and Sehra, 1986).

Gas Turbine Simulation With the GATE Code

The tool used for gas turbine performance prediction was the GATE (or GAs Turbine Evaluation) code, a computer program originally developed for EPRI by Mark Waters and Associates (Waters, 1983) for analyzing a wide variety of gas turbine cycles. Simple cycles and combined cycles can be investigated using GATE as well as cycles employing reheat, regeneration, intercooling, or steam injection. One of the most important features of GATE is a built-in means of estimating turbine cooling flow based on the user-specified cooling technology (for example, convection or film cooling) and the desired turbine airfoil metal temperature.

GATE has since been improved and is currently being developed and supported by EPRI and ENTER Software and is further described in Erbes et al. (1989). The version of GATE used in this study has the following additional features of special importance for the simulation of syngas firing:

1 The fuel stream can be a mixture of components such as methane, hydrogen, carbon monoxide, carbon dioxide, water vapor, nitrogen, and argon. These components are needed to simulate syngas.
2 On- and off-design performance prediction based on the choked mass flow relation shown in Eq. (1) is possible.
3 User-supplied compressor maps can be used.

The procedure used here for creating a GATE gas turbine model begins with "designing" a machine that matches a few important external characteristics of the natural gas firing case. These characteristics are typically exhaust flow rate, exhaust temperature, heat rate, and power output. This information is usually available from the gas turbine manufacturer. Other parameters often can be found in the open literature to augment this information. Pressure ratio, firing temperature, and number of turbine stages are examples of information that can be obtained to improve GATE model building. After the user supplies a compressor map, parameters such as turbine-stage efficiencies, turbine-cooling technology, and combustor pressure drop can be adjusted to match the external characteristics previously listed. The result is a gas turbine model calibrated against natural gas design point characteristics. Off-design calculations are made by running GATE in the off-design mode and changing input values for ambient temperature, firing temperature, fuel composition, etc. GATE reads the compressor map data when calculating the off-design pressure ratio and compressor isentropic efficiency. For off-design calculations, the isentropic efficiency of each turbine stage is assumed constant. This is a valid assumption for a wide range of turbine corrected speeds and pressure ratios (Cohen et al., 1987). Because of the favorable pressure ratio in the expander, flow separations are less likely and the turbine blading can operate over a wide range of incidence angles without much increase in total pressure loss.

To make performance predictions with guide vanes partially closed, a new compressor map was entered into GATE for each new guide vane setting. Maps for guide vane settings closed 5, 10, 15, 20, and 25 deg (as well as wide open) were generated using the compressor model. Gas turbine performance prediction at some other guide vane setting (say, 30 deg) would require new compressor simulation runs to generate the new map.

Models constructed in this manner will not be identical to the industrial machines from which they are derived, hence the designations "Gas Turbine A, Gas Turbine B, etc.," in Table 1. In fact, the "future technology" machine modeled

Nomenclature

A = flow area
$\dot{m}$ = mass flow rate
MW = molecular weight
N = shaft speed (rpm)
P = pressure
R_u = universal gas constant
T = temperature
γ = ratio of specific heats

Subscripts

t = total condition or property

Superscripts

* = critical value

Downloaded 02 Jun 2010 to 171.66.16.112. Redistribution subject to ASME license or copyright; see http://www.asme.org/terms/Terms_Use.cfm

Table 1 Natural gas design point gas turbine characteristics

Gas turbine	Output power (MW)	Exhaust temp. (°F)	Exhaust flow (lbm/s)	Heat rate (Btu/kWh)	Firing temp. (°F)	Pressure ratio
A	83.5	986	653.0	10485	1985	11.6:1
B	150.0	1081	987.5	9880	2300	14.0:1
C	173.2	1196	938.0	9732	2500	14.5:1

for this study, Gas Turbine C, has never been built; it is a projected "growth" version of Gas Turbine B. These models should, however, be representative of the class of real gas turbines with the same firing temperature and pressure ratio.

Strategies for Conversion From Natural Gas Firing to Syngas Firing

Five strategies for allowing a machine designed for natural gas to operate on syngas are described in this section. The reader should note that any or all these strategies can be applied in combination as long as the mass flow relation of Eq. (1) is satisfied.

Strategy 1: Inlet Guide Vanes "Wide Open." A single strategy for firing syngas in a gas turbine designed for natural gas was previously described to illustrate the nature of the problem. This strategy (increasing the compressor pressure ratio), while perhaps the simplest to describe, is the most aggressive technologically. This is because of the reduction in compressor surge margin, the increased torque on the shaft, and the increased thermal loads on the turbine airfoils mentioned previously. One can show (Johnson, 1989) that turbine airfoil heat transfer coefficients can increase from 5 percent (laminar) to 9 percent (turbulent) for an 11 percent increase in pressure ratio (or mass flow). This pressure ratio increase is characteristic of the GATE predictions made for the current study.

The rewards for this increased technical risk are increased output power and reduced heat rate (relative to the natural gas firing case). The ratio of expander mass flow to compressor mass flow is larger for this case than for the natural gas design point, and more gross electrical energy is produced by the gas turbine for a similar amount of fuel chemical energy. The medium-Btu syngas in an GCC plant is available at high pressure, and its compression costs (primarily air and oxygen compression in the air separation plant) are not charged against the gas turbine cycle but against the GCC plant as a whole.

Pressure ratio increase is one of the syngas firing strategies investigated in this report, with the single modification of a 35°F (19 K) firing temperature reduction to help maintain the natural gas design life of the turbine airfoils by compensating for the increased heat transfer coefficients. [This reduction is approximately 1 percent of the *absolute* expander inlet temperature and thus does not have a large effect on the choked flow relation of Eq. (1).] This was a rule-of-thumb temperature reduction suggested by General Electric engineers.

Strategy 2: Inlet Guide Vanes Partially Closed. The other strategy examined here was the use of variable inlet guide vanes (VIGVs). These stator vanes at the inlet to the compressor can be closed slightly to reduce the mass flow through the compressor. The approach used in this study was to rotate the guide vanes closed 15 deg; this led to an expander mass flow rate approximately equal to that of the natural gas case. The advantage to this strategy is that the turbine airfoil thermal loads are about the same as on natural gas. Output power increases a few percent over the natural gas case again because of a favorable ratio of expander mass flow to compressor mass flow, but this power increase is not as great as for the guide-vanes wide-open strategy outlined. The problem of reduced surge margin may still be present when guide vanes are closed. The required pressure ratio will be reduced as the guide vanes are closed, but the compressor also will suffer surge at a lower pressure. This is illustrated later in this paper.

Strategy 3: Expander Inlet Nozzle Redesign. Another intuitive strategy is a redesign of the expander inlet nozzle to increase the critical area, A^*, while leaving the pressure ratio constant. This may be practical for cases where the thermal and mechanical stresses on the turbine airfoils are so large that these components must be redesigned anyway, or for the situation where the manufacturer wants maximum output power on syngas but does not have enough compressor surge margin to achieve it. This strategy was not investigated in this study. The effects of this approach on the *balance* of the GCC plant should fall somewhere between the two strategies just mentioned; the gas turbine output power will be higher than for the previous strategies, while the exhaust flow rate will be similar to that of strategy 1. The pressure ratio and exhaust temperature will be similar to those of strategy 2.

Strategy 4: Expander Inlet Temperature Reduction. Increased expander mass flow also can be accommodated by decreasing the turbine firing temperature relative to the natural gas firing value. This is undesirable because of the significant penalties to output power and thermal efficiency. Because the square root of the absolute total temperature appears in Eq. (1), a 10 percent increase in mass flow would require a 17 percent decrease in absolute firing temperature. The loss in thermal efficiency due to this large reduction in firing temperature makes this strategy impractical by itself. However, if a gas turbine has very little compressor surge margin, some reduction in firing temperature may be useful when combined with other approaches, especially if the hardware modifications of strategy 3 are to be avoided.

Strategy 5: Gas Turbine Compressor Bleed for Air Separation Plant. This fifth strategy also was not investigated in the current study. This strategy can only be used if the GCC air separation plant is located on-site with the gas turbine units. Air can then be bled from the gas turbine compressor to supply the air separation plant. The waste nitrogen from the air separation plant is recompressed for return to the gas turbine combustor. For each kilogram of saturated syngas fired in the gas turbine, 1.54 kg of air is bled from the compressor exit, yet only 1.17 kg of waste nitrogen is returned to the gas turbine combustor (Kiersz et al., 1987). This effectively displaces 37 percent of the fuel mass flow, reducing, but not eliminating, the need for increased compressor pressure ratio and/or guide vane closure. This does allow for gas turbine operation with a larger surge margin relative to strategies 1 and 2.

Kiersz, et al. (1987) also report a plant heat rate reduction of 2 percent and a capital cost reduction of 2–3 percent for the same base case plant used in this study. This is due primarily to the elimination of electric-drive compressors in the air separation plant. The drawbacks to this scheme are increased plant complexity and integration. A 160 MW prototype plant using the PRENFLO coal gasification system and two Kraftwerk Union V64 gas turbines is likely to be commissioned in Germany in 1992 (Buskies and Gwodz, 1988).

Natural Gas Firing Design Point

The natural gas design point characteristics of the gas turbines simulated for this study are shown in Table 1. In the following sections, the development of each model is described. All of these models assume a 59°F (288 K) ambient temperature, 14.7 psia (101 kPa) ambient pressure, and 60 percent relative humidity. The discussion of each model is presented in the chronological order of development.

Gas Turbine B. The GATE model of Gas Turbine B (GTB) was derived from information on the General Electric MS7001F

Downloaded 02 Jun 2010 to 171.66.16.112. Redistribution subject to ASME license or copyright; see http://www.asme.org/terms/Terms_Use.cfm

and is intended to be representative of advanced technology gas turbines in this pressure ratio (14:1) and firing temperature (2300°F/1533 K) class. Another machine in this class is the Kraftwerk Union V84.3. The main external characteristics (exhaust flow rate, exhaust temperature, heat rate, and power output) used to anchor this model were found in Allen and Triassi (1988). Further information on pressure ratio, firing temperature, geometry, number of turbine stages, turbine cooling, etc., was found in Brandt (1987). The GATE results for the natural gas reference point are shown in Table 1.

Gas Turbine A. Gas Turbine A (GTA) is an approximation of a machine in the size and technology class of the General Electrical model MS7001E or Kraftwerk Union V84.2. The model compressor pressure ratio is 11.6:1 and the firing temperature is 1985°F (1358 K). The four important external characteristics used for model development, exhaust flow rate, exhaust temperature, heat rate, and power output, were taken from Allen and Triassi data for the MS7001E.

Much of the geometry of the GTB model was reused here, scaled downward by the mass flow. This was considered appropriate since the General Electric MS7001F is a machine "grown" from experience with the MS7001E. The development of the MS7001F and its relationship to the MS7001E is discussed by Brandt (1987).

The compressor model for GTA also was based on that of GTB. The last two stages of the GTB compressor were removed in the model to achieve a reference pressure ratio of 11.6:1. Cooling technology and turbine efficiency were adjusted (downward) relative to GTB to match the external characteristics just listed. The natural gas results are shown in Table 1.

Gas Turbine C. Gas turbine C did not have an actual "design point" in the sense of the other models. Only one operation point for GTC was needed for the planned overall GCC system study and it was obtained by growing GTB to a natural gas firing temperature of 2500°F (1644 K). The primary assumption is that GTC has the same basic frame as GTB but with improved materials and cooling technology in the turbine to allow cooling flow rates, on a percent basis, to remain unchanged at this elevated firing temperature.

Two GATE runs were made for GTC: natural gas and syngas firing with guide vanes wide open. The resulting natural gas compressor pressure ratio was up to 14.5 from 14.0 for GTB. This increase in pressure ratio was due to the increased fuel flow necessary to reach the elevated firing temperature. Also, as seen in Eq. (1), the increased firing temperature (increased T_t) will force an additional increase in pressure ratio to assure satisfaction of the choked flow relation.

The syngas firing characteristics of all three of these machines are further compared in the following section.

Maximum Capacity Syngas Firing

Syngas firing reference characteristics are shown in Table 2. The assumed ambient conditions were 59°F (288 K), 14.4 psia (99.3 kPa) and 60 percent relative humidity. These conditions are consistent with the site conditions for the base GCC plant used in previous GCC system studies. The gas turbine exit pressure drop was increased to 10 in. of water (2.5 kPa) to account for the pressure drop in the heat recovery steam generator.

Gas Turbine B has two entries in Table 2. The first (1) is for the "guide-vanes wide-open" syngas firing strategy and the second (2) is for the "guide-vanes partially-closed" strategy.

Off-Design Performance—Gas Turbine B

GATE simulation runs were made for Gas Turbine B to determine maximum capacity as a function of ambient temperature and to predict the performance characteristics at part-load down to about 20 percent power. These runs were made for both syngas and natural gas firing. Off-design runs were made only for Gas Turbine B as GCC plants using GTB were the only ones for which off-design runs were to be made. The following off-design performance curves, appropriately normalized, can be used to make *simple* estimates for the off-design performance of GTA and GTC.

Table 2 Syngas reference point gas turbine characteristics; number in parentheses in column one designates the syngas firing strategy

Gas turbine	Output power (MW)	Exhaust temp. (°F)	Exhaust flow (lbm/s)	Heat rate (Btu/kWh)	Firing temp. (°F)	Pressure ratio
A(1)	93.6	970	693.8	9522	1950	12.6:1
B(1)	174.5	1073	1014.0	8950	2265	15.6:1
B(2)	162.8	1114	929.2	9096	2300	14.3:1
C(1)	204.2	1192	1027.0	8855	2465	16.3:1

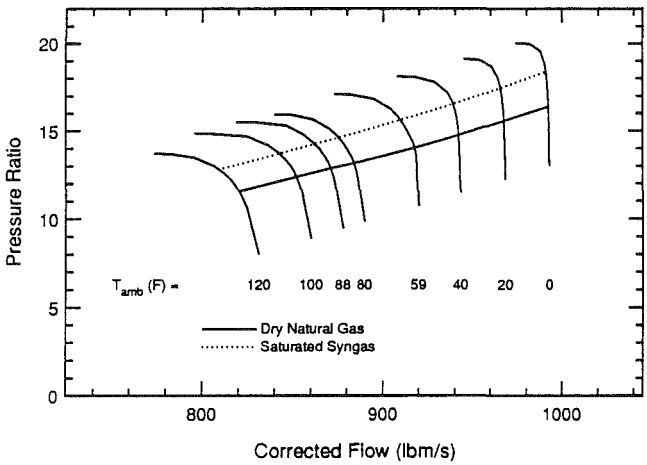


Fig. 1 Compressor operating lines for Gas Turbine B

Maximum Capacity Versus Ambient Temperature. Figure 1 shows a plot of the natural gas and syngas gas turbine operating lines on a compressor map for GTB. The pressure ratio for the syngas case (guide vanes wide open) is about 11 percent greater than that for the natural gas case for all ambient temperatures. The corrected speed lines are labeled with the ambient temperatures in Fig. 1 since these utility gas turbines all have a constant physical speed of 3600 rpm. The corresponding range in corrected speeds is about 95–105 percent.

Figures 2–5 show electrical power, exhaust temperature, exhaust flow, and heat rate, respectively, as functions of the ambient temperature. Curves for GTB firing both natural gas and syngas are presented. The trends for both cases are similar for all four plots; the "deltas" between the natural gas and syngas operation are perhaps the most useful results from these plots since they are relatively constant for all ambient temperatures.

Part-Load Operation. Part-load performance information for Gas Turbine B was needed for the proposed part-load GCC plant simulations. GATE runs were made to estimate part-load performance for both syngas firing strategies. Runs also were made for GTB firing natural gas for comparison purposes. All the part-power runs assumed an ambient temperature of 59°F, an ambient pressure of 14.4 psia, and a gas turbine back pressure of 10 in. of water (288 K, 99.3 kPa and 2.5 kPa).

The approach to part-load operation was to control the compressor airflow to maximize the turbine exhaust temper-

Downloaded 02 Jun 2010 to 171.66.16.112. Redistribution subject to ASME license or copyright; see http://www.asme.org/terms/Terms_Use.cfm

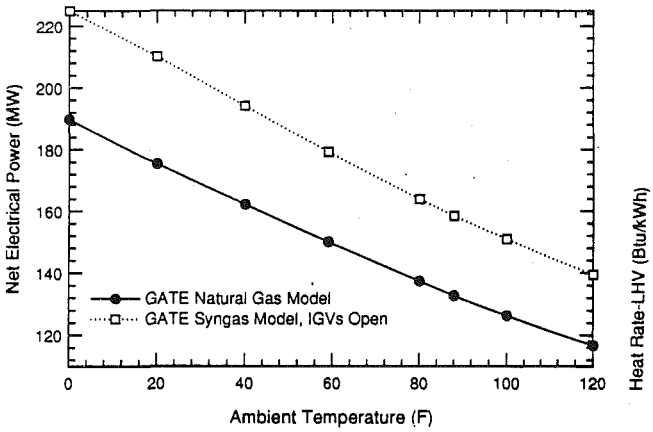


Fig. 2 Maximum capacity net electric power versus ambient temperature for Gas Turbine B

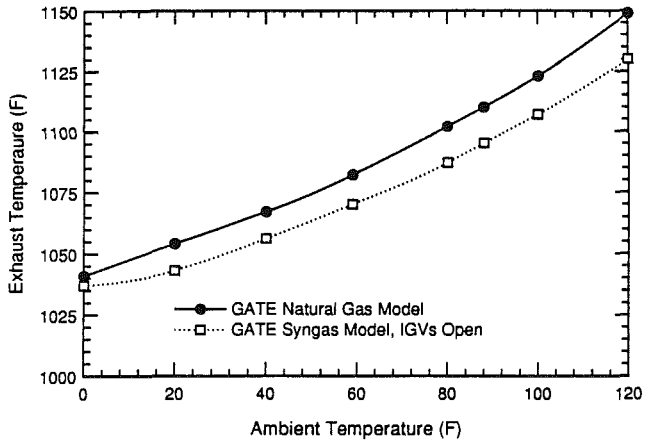


Fig. 3 Maximum capacity exhaust temperature versus ambient temperature for Gas Turbine B

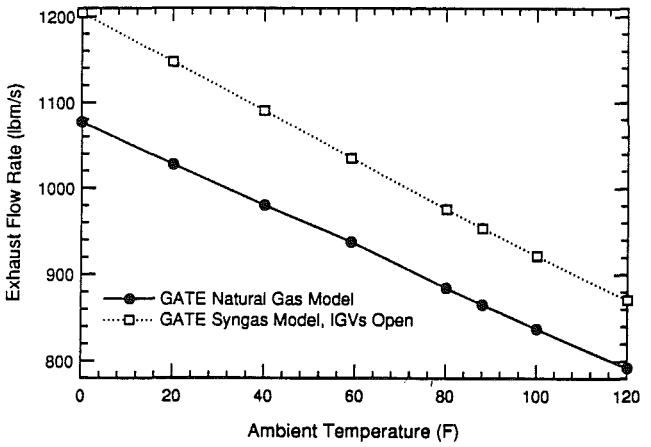


Fig. 4 Maximum capacity exhaust flow rate versus ambient temperature for Gas Turbine B

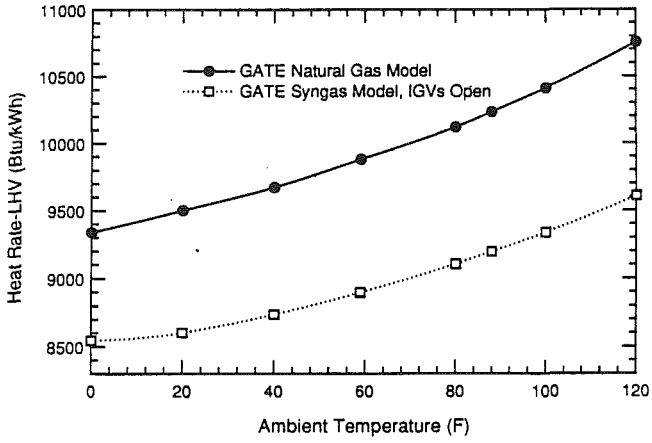


Fig. 5 Maximum capacity heat rate versus ambient temperature for Gas Turbine B

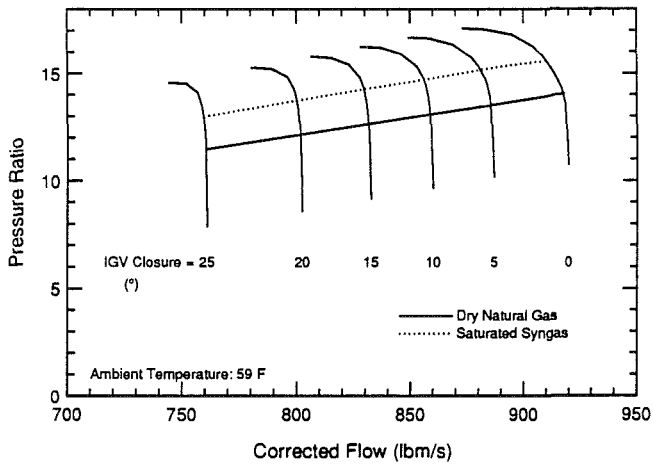


Fig. 6 Compressor operating lines for Gas Turbine B as IGVs are closed, ambient temperature: 59 F

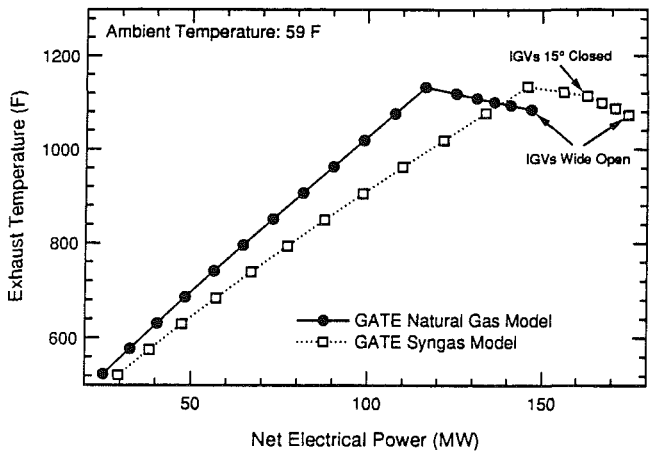


Fig. 7 Exhaust temperature versus power level for Gas Turbine B; ambient temperature 59°F

ature as the load was reduced. This is the technique used by General Electric when optimum heat recovery from the gas turbine exhaust is desired (Allen and Triassi, 1988; Rowen and Van Housen, 1983). It is accomplished by closing the inlet guide vanes to reduce the power output while maintaining the design point firing temperature. For GTB, guide vanes can be used to reduce the compressor airflow and engine output power to about 80 percent of the design value. This corresponds to guide vanes rotated closed 25 deg. After that, further power reductions are made by reducing the turbine firing temperature.

A compressor map with lines of constant IGV setting for GTB at an ambient temperature of 59°F is shown in Fig. 6. The natural gas and syngas part-power operating lines have been plotted on this map. These operating lines correspond to the first 20 percent of gas turbine power turndown as the IGVs are closed. The compressor pressure ratio when firing syngas is again about 11 percent higher than the natural gas value. Upon comparing Figs. 1 and 6, one sees that both syngas firing

Downloaded 02 Jun 2010 to 171.66.16.112. Redistribution subject to ASME license or copyright; see http://www.asme.org/terms/Terms_Use.cfm

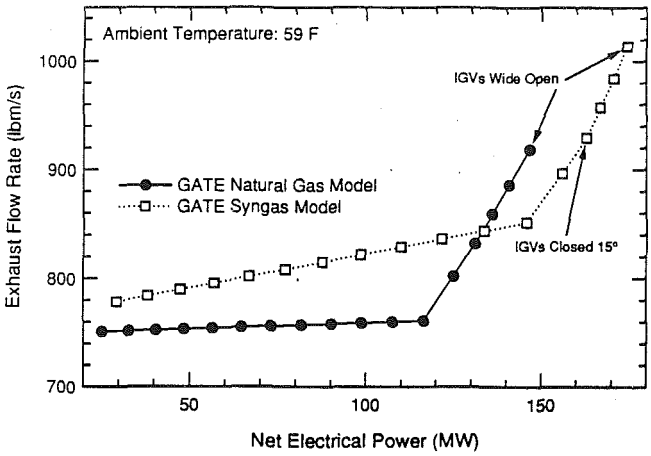


Fig. 8 Exhaust flow rate versus power level for Gas Turbine B; ambient temperature: 59°F

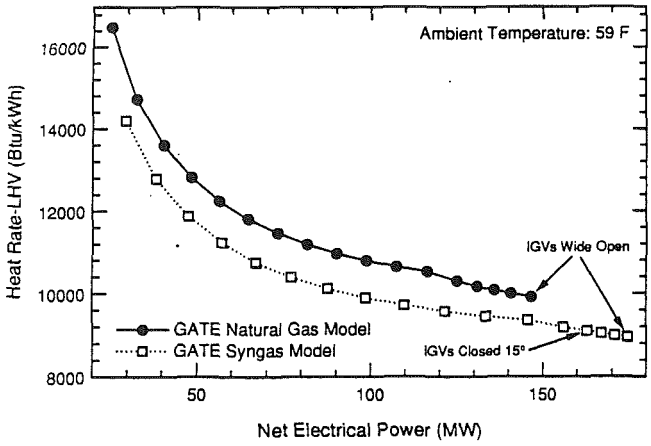


Fig. 9 Heat rate versus power level for Gas Turbine B, ambient temperature: 59°F

strategies 1 and 2 result in the similar reductions in compressor surge margin.

For the syngas-firing simulations, the firing temperature was increased linearly with IGV angle from 2265°F (1514 K) for guide-vanes wide-open to 2300°F (1533 K for guide-vanes closed 15 deg and then maintained at 2300°F for the remainder of the IGV range. This provided the 35°F (19 K) firing temperature reduction at maximum power for the syngas strategy 1 and made the GATE part-load simulation runs for strategy 2 a subset of the runs for strategy 1. However, while IGVs closed 15 deg represents the maximum power point for strategy 2, it is only a part-power condition (93 percent power) for strategy 1. This is illustrated in the part-load performance curves for GTB, discussed next.

Figures 7-9 show exhaust temperature, exhaust flow rate, and heat rate as a function of electrical power output for Gas Turbine B. Note that the arrow labeled "IGVs Closed 15°" identifies the maximum power point for syngas firing strategy 2. The slight kink at this point in the exhaust temperature plot is due to the 35°F temperature change previously discussed.

Conclusions

This paper has described the development and results of a procedure for predicting the performance of gas turbines designed to fire natural gas when fired on coal-derived syngas. Simulations indicate that net output power can be increased on the order of 15 percent when firing syngas if the gas turbine has sufficient durability and surge margin. Three classes of single-spool machines were simulated, covering "current," "advanced," and "future" technology utility gas turbines. Performance simulations at a variety of part-load and ambient temperature conditions are described. The resulting curves relating output power, heat rate, exhaust temperature, and exhaust flow rate are suitable for GCC power plant design, analysis, or simulation.

Acknowledgments

This work was completed under the sponsorship of the Electric Power Research Institute while the author was a graduate student at Stanford University. The helpful guidance of EPRI contract manager Dr. Michael J. Gluckman and graduate advisor Professor Robert H. Eustis is gratefully acknowledged. Dr. Rodney Gay and Dr. Michael Erbes of ENTER Software and Mr. Art Cohn of EPRI were helpful consultants on the use of the GATE program.

References

Allen, R. P., and Triassi, R. P., "GE Gas Turbine Performance Characteristics," GER-3567, General Electric Company, Schenectady, NY.

Bettner, J. L., and Sehra, A. K., 1986, *High-Efficiency Axial Compressor*, EPRI Report AP-4943, prepared by Allison Gas Turbine Division, General Motors Corporation.

Brandt, D. E., 1987, "Heavy-Duty Turbopower: The MS7001F," *Mechanical Engineering*, Vol. 109, No. 7, July, pp. 28–36.

Buskies, U. H., and Gwodz, J. C., 1988, "Concepts of PRENFLO-Based IGCC Power Plants," *Proceedings: Seventh Annual EPRI Contractors' Conference on Coal Gasification*, EPRI Report AP-6007-SR.

Cohen, H., et al., 1987, *Gas Turbine Theory*, 3rd ed., Longman Scientific and Technical, Essex, United Kingdom.

Erbes, M. R., et al., 1989, "GATE: A Simulation Code for Analysis of Gas-Turbine Power Plants," ASME Paper No. 89-GT-39.

Johnson, M. S., 1989, "The Effects of Gas Turbine Characteristics on Integrated Gasification Combined-Cycle Power Plant Performance," Ph.D. Thesis, Mechanical Engineering Department, Stanford University, CA.

Kiersz, D. F., et al., 1987, *Advanced Air Separation for Coal Gasification-Combined-Cycle Power Plants*, ERPI Report AP-5340, prepared by Union Carbide Corporation.

Rowen, W. I., and Van Housen, R. L., 1983, "Gas Turbine Airflow Control for Optimum Heat Recovery," ASME JOURNAL OF ENGINEERING FOR POWER, Vol. 105, pp. 72–79.

Waters, M., 1983, *Gas Turbine Evaluation (GATE) Computer Program—Thermodynamic Cycles, Methods, and Sample Cases*, EPRI Report AP-2871-CCM, prepared by Mark Waters and Associates.

Downloaded 02 Jun 2010 to 171.66.16.112. Redistribution subject to ASME license or copyright; see http://www.asme.org/terms/Terms_Use.cfm

Calculation Approach Validation for Airblast Atomizers

N. K. Rizk

H. C. Mongia

Allison Gas Turbine Division,
General Motors Corporation,
Indianapolis, IN 46206

In order to formulate a common approach that could provide the spray parameters of airblast atomizers, various processes of liquid preparation, breakup, and secondary atomization have been included in a semi-analytical calculation procedure. The air velocity components in the atomizer flow field are provided by mathematical expressions, and the spray droplets are considered to form at ligament breakup through a disturbance wave growth concept. The validation of the developed approach included the application to six atomizers that significantly varied in concept, design, and size. They represented both prefilming and plain-jet types, and the data utilized in the present effort were obtained with six different liquids. Satisfactory agreement between the measurements and the predictions has been achieved under wide ranges of air/fuel ratio and air pressure drop for various test liquids. The results of this investigation indicate the potential of using such an approach in the early phases of airblast atomizer design, and may be followed by more detailed calculations using analytical tools.

I Introduction

Although most fuel injectors operate on a fairly similar concept of providing high relative velocity between the fuel and the surrounding air, the injector performance may vary significantly from one design to another. It is realized that the method by which the liquid is prepared for atomization within the injector has a major impact on the spray characteristics (Rizk and Lefebvre, 1983). In recent years, the effort has been made to enhance the atomizer design that is currently required to operate on a wide range of conditions and with unconventional types of fuel. In gas turbine combustors, optimum fuel injector/dome swirler combination is sought to achieve satisfactory ignition and lean blowout characteristics, in addition to reduced levels of exhaust emissions.

To guide the design and development of the combustor, it is essential to acquire sufficient details of the atomizer performance. The calculation of the evaporation and mixing of the spray in the combustor primary zone involves such parameters as spray mean diameter, range of drop sizes in spray, and drop trajectory. The recent advances of the diagnostic techniques have made it possible to measure these parameters with a reasonable degree of accuracy. To render these data useful to the combustor components designer, expressions have been derived to describe the spray characteristics in terms of operating parameters, fuel properties, and atomizer dimensions (Lefebvre, 1989; Jasuja, 1979; Simmons, 1979).

In most of these equations, the aerodynamic and the fuel viscosity effects are assumed to play two different roles in the atomization of liquids and represented by two separate terms in the expression. Each equation is valid for certain type of atomizer, and its accuracy to follow the data of other concepts may not be adequate. Simmons (1979) gives an expression based on the aspect of momentum exchange between air and fuel, which was found to correlate the data of pressure and airblast atomizers. A range of empirical constants is offered in this investigation to fit the data of each type. The striking feature of all these equations is the wide variation of the dependency of the spray quality on various operating and geometric parameters according to the atomizer design.

Several drop size distribution functions have been recommended to estimate the volume fraction of the spray contained within each size group. These functions require the knowledge of some parameters related to the mean diameter and the spread of sizes in the spray, as described by Mugele and Evans (1951). An approach to evaluate the whole distribution from the knowledge of the mass mean diameter (MMD), or the Sauter mean diameter (SMD), is offered by Simmons (1977). A root-normal probability plot is used for this purpose, assuming a direct relationship between the two mean diameters.

The main advantage offered using these empirical approaches is the fact that a global picture of the whole spray is readily provided through simple calculations. Their applications could be easily extended to include alternative types of fuel, and a wide range of operation. On the other hand, analytical models have demonstrated the capability to provide the details of the atomizer flow field. They require either the estimation of the initial conditions at the exit of the atomizer, or the use of measured data profile at a certain distance from the atomizer as initial values (Mostafa and Mongia, 1987; Sturgess et al., 1984; Reitz and Bracco, 1982). A recently developed model has included the numerical simulation of the air flow through and exiting from the atomizer passages, and addressed the various atomization and droplet dispersion processes (Rizk and Mongia, 1989a).

Although the analytical tools may provide a valuable as-

Contributed by the International Gas Turbine Institute and presented at the 36th International Gas Turbine and Aeroengine Congress and Exposition, Orlando, Florida, June 3–6, 1991. Manuscript received at ASME Headquarters March 4, 1991. Paper No. 91-GT-305. Associate Editor: L. A. Riekert.

Copyright © 1992 by ASME
Downloaded 02 Jun 2010 to 171.66.16.112. Redistribution subject to ASME license or copyright; see http://www.asme.org/terms/Terms_Use.cfm

sistance for the optimization of the atomizer design, a semi-analytical approach is still needed in the preliminary phases of the design. By this means, relatively simple calculations can be performed to define the main features of the atomizer while using the same general approach for various atomization concepts. The success of such an approach relies on the consideration of the appropriate fundamental processes of spray formation.

An approach based on a semi-analytical concept has been developed to evaluate the characteristics of the sprays produced by airblast atomizers (Rizk and Mongia, 1989b, 1990a, 1990b). The approach considers the fuel preparation within the atomizer, ligament formation and breakup, and secondary atomization. It utilizes empirical expressions to evaluate the air velocity profiles downstream of the atomizer.

The present paper involves an investigation of the impact of the details of both the so-called prefilming and plain-jet airblast atomizers on the spray parameters using the developed approach. The paper covers the calculation procedure and the validation effort with a total of six atomizers that varied significantly in concept. Several liquids were employed in the testing of these atomizers to investigate the capabilities of the approach to simulate the influence of liquid properties on the atomization process.

II Airblast Atomizer Configurations

Six different atomizers were used in the present investigation. Their basic design features and key dimensions are illustrated in Fig. 1. The atomizers selected in this investigation are used in different gas turbine combustor applications and cover both prefilming and plain-jet concepts.

Atomizer A incorporates the so-called short prefilming device to prepare the fuel for atomization. The fuel is injected through six tangential ports into a swirl chamber to form a sheet that is immediately exposed to air on both sides. The outer air flows through a swirler, while the inner air passes through a number of tangential slots to the central passage. The atomizer is designed for use in small gas turbine engines.

Atomizers B and C are of identical design but they vary significantly in size. The atomizer B exit diameter is more than double that of atomizer C. They represent a different prefilming concept than the one used in atomizer A. In this long prefilmer type, the liquid enters the nozzle through the central fitting and flows radially outward through the air swirler vanes to the cylindrical shroud. It discharges tangentially along the shroud where the air is intended to promote even prefilming of the two opposed liquid jets between each two adjacent vanes. A co-rotating swirling air encloses the liquid film to enhance fuel breakup.

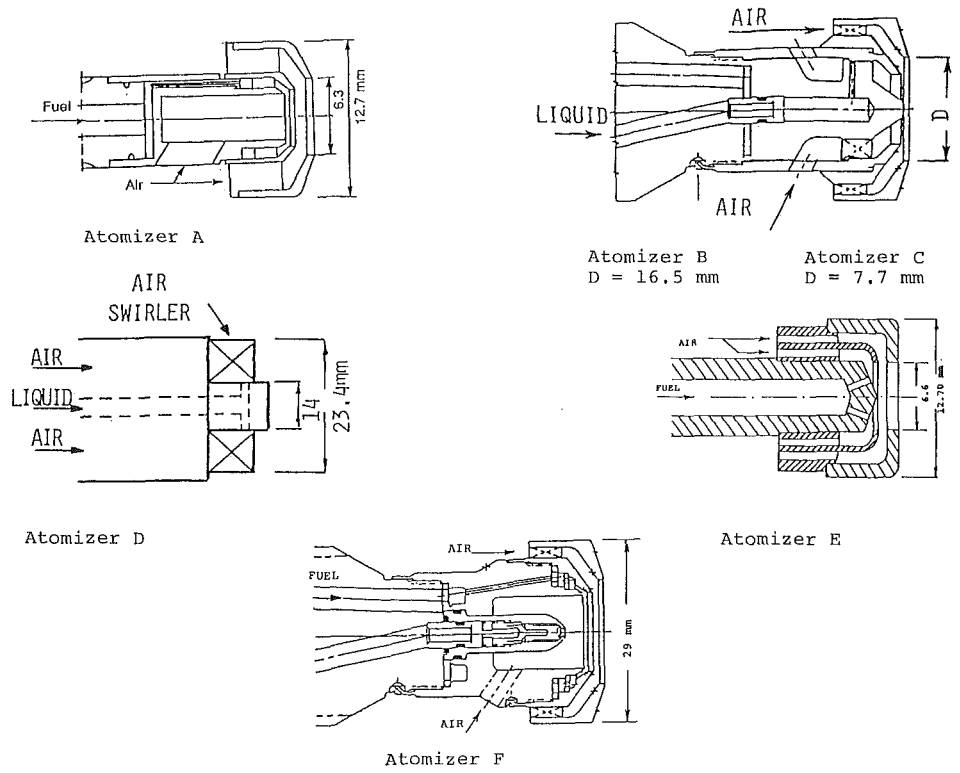


Fig. 1 Airblast atomizers used in the study

Nomenclature

C_D = drag coefficient
d = atomizer exit diameter, m
d_m = mean size distribution parameter, μm
f = total growth of wave
FAR = fuel/air ratio
K = atomizer correlating parameter
K_u = axial velocity distribution parameter
n = wave number
q = range distribution parameter
r = radial distance
Re = Reynolds number
S = swirl number
SMD = Sauter mean diameter, μm
T = film thickness, m
t = time
U = air velocity, m/s
V_i = droplet velocity, m/s
x = axial distance, m
μ = viscosity, kg/ms
ρ = density, kg/m^3
σ = surface tension, N/m

Downloaded 02 Jun 2010 to 171.66.16.112. Redistribution subject to ASME license or copyright; see http://www.asme.org/terms/Terms_Use.cfm

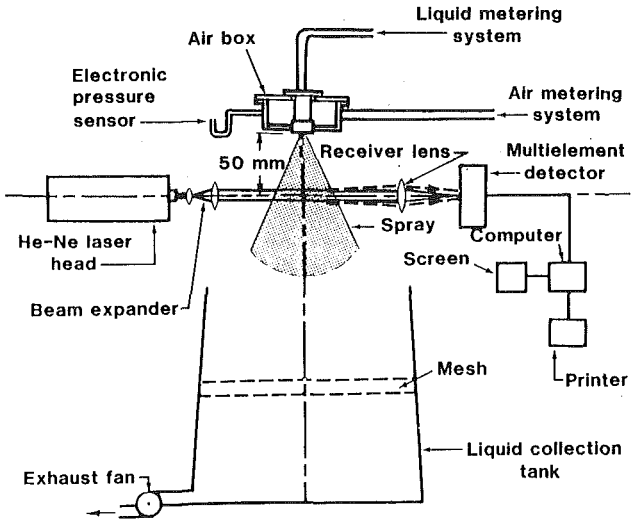


Fig. 2 Schematic diagram of test rig

Atomizers D and E are examples of airblast atomization concept where the liquid is injected in the form of jets into the atomizing air. In atomizer D, the liquid flows through a number of radially drilled holes, from which it emerges in the form of discrete jets that undergo in-flight disintegration by a crossflow swirling air. In atomizer E, the liquid is injected through five equally spaced holes located on the perimeter of a circle on the nozzle face. Atomizing air flows through two concentric swirlers that enclose the main body of the nozzle to impact the liquid jets at a much shallower angle than atomizer D.

Atomizer F represents a hybrid airblast type that is used in a current production combustor. It incorporates a pressure swirl pilot and a short prefilming secondary circuit. The prefilming device uses a liquid swirl chamber to produce a rotating body of liquid that forms a surface in contact with the inner airstream. A corotating swirling air encloses the film as it leaves the atomizer lip to enhance liquid breakup. Only the secondary circuit was used during the testing of this atomizer.

III Experimental

A schematic diagram of the test rig is illustrated in Fig. 2. The liquid nozzles, mounted in the end of an air plenum, sprayed downward into a tank. A blower exhausted the vapor from the tank, and the static pressure inside the plenum was measured with an electrical capacitance gage. Liquid flow through the nozzle was measured with a positive displacement pump. A Malvern instrument was used to obtain model-free drop size distribution. The Sauter mean diameter (SMD) was determined by numerically integrating the measured volume distributions that were taken at a 0.05-m downstream distance from the atomizer.

Six different liquids were employed in the testing of the atomizers. Table 1 lists the properties of these liquids that are relevant to atomization at standard atmospheric pressure and a temperature of 298 K at which all the testing were performed. The wide variation of the properties offers the opportunity to investigate the impact of each property on spray quality for various atomizer concepts. It also evaluates the capability of the developed approach to account for the liquid properties through different atomization processes.

IV Empirical Data Analysis

The influence of the atomization concept utilized in the fuel injector on the spray characteristics is best illustrated in terms

Table 1 Test liquids and their properties

Liquid	Density kg/m^3	Viscosity kg/ms	Surface tension N/m
Water	1000	0.00100	0.0620
Water/alcohol	997	0.00094	0.0510
Kerosine	784	0.0013	0.0277
JP-5	806	0.0016	0.0249
Gas Oil	830	0.0028	0.0300
MIL-C-7024	770	0.00092	0.0250

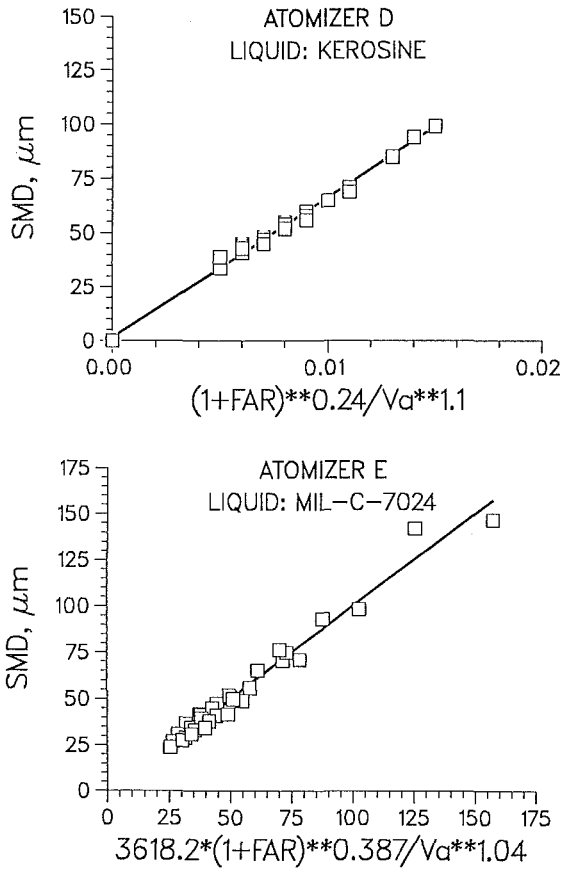


Fig. 3 Correlation of airblast atomizer data

of correlating parameters. The purpose of such effort is to determine whether a common correlation does exist for various atomizers. It is equally important to evaluate the response of each type to changes in the key operating parameters. A comparison between the data analysis of an atomizer and the reported correlations in the literature would help in selecting the appropriate empirical expression for a certain design.

In general, the spray quality of the atomizer is governed mainly by both the air pressure drop, as represented by the air velocity, and the air/liquid ratio level used in the atomizer. A correlating parameter K that is based on these two variables is plotted in Fig. 3 against the measured SMD for two atomizers used in this investigation. It is given by:

$$K = \frac{(1+\mathrm{FAR})^a}{Va^b} \tag{1}$$

This form of correlation is based on the analysis of the performance of various types of airblast atomizer as reviewed by Lefebvre (1989), Jasuja (1979), Simmons (1979), and Rizk (1977).

The figure shows that the data are well correlated by the parameter K for each atomizer. It is however found that the

Downloaded 02 Jun 2010 to 171.66.16.112. Redistribution subject to ASME license or copyright; see http://www.asme.org/terms/Terms_Use.cfm

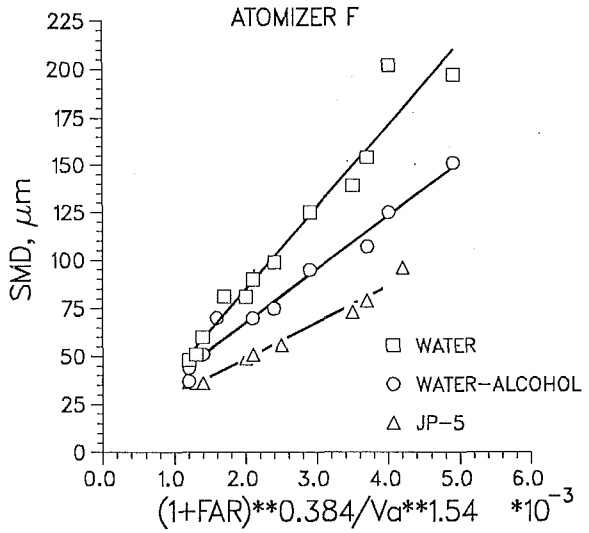


Fig. 4 Influence of liquid type on correlating parameter

exponents a and b in the above equation take different values for each type of atomizer. In fact, the correlation may even vary within a single group of atomizers according to the fuel injection configuration used in the design. For instance, in the two plain-jet atomizers D and E where the fuel is injected through multitude of fine holes in two different manners, the correlating parameter in each case is quite different. Moreover, comparing these correlations with the one obtained for the simplest form of plain-jet airblast type reported by Lorenzetto and Lefebvre (1977) reveals a major discrepancy in the dependency of the SMD on various parameters. The same conclusion may be drawn for other types of airblast atomizers.

The influence of the liquid properties on the spray SMD is illustrated in Fig. 4 for atomizer F. For the same value of the parameter K, the largest SMD is obtained for water spray. On the other hand, the JP-5 data demonstrate the lowest values of SMD among the three liquids. This is due to the differences in the physical properties between the three liquids. The adverse effect of the higher surface tension of the water has more than offset the ease of atomization caused by its lower viscosity.

The data given in this analysis confirm the previous finding that each type of airblast atomizer requires a separate correlation to describe its performance. This data analysis stresses the fact that a common calculation method may be realized if the various atomization processes are properly addressed in the approach. In the following sections, the proposed calculation concept and its validation with the experimental data are presented.

V Calculation Procedure of Spray Characteristics

In airblast atomization, sufficient details of the airflow field downstream of the atomizer are needed to evaluate various spray processes. Prior to the exposure to the high-velocity air, the liquid fuel is attenuated into fine jets or sheet. Due to the relative motion with respect to air, the liquid jet or sheet undergoes a breakup to form ligaments, which in turn disintegrate into drops (Rizk, 1977). If reasonably high relative velocity exists between the air and the drops, in-flight breakup of the drops may proceed.

In the present approach, the air velocity profile calculation utilizes the concept of velocity components decay along the nozzle axis (Beer and Chigier, 1972), and the detailed measurement of the flow field of large number of swirlers reported by Kilik (1976). The peak axial velocity U_m at a distance x is given in terms of peak velocity at the nozzle exit U_{mo} by:

$$U_m/U_{mo} = 3.93\ S^{0.8}\left(\frac{d}{x+a}\right)^c \tag{2}$$

where c is equal to $1.52\ S^{0.64}$, S is the swirl number defined in terms of angular momentum and axial thrust (Beer and Chigier, 1972), d is the orifice diameter, and a is the distance from the nozzle exit to the apparent origin of the flow and equal to $2.3d$.

The maximum tangential velocity W_m is similarly given in terms of peak value at nozzle W_{mo} by:

$$W_m/W_{mo} = \frac{8.34}{S^{0.186}}\left(\frac{d}{x+a}\right)^{2.5} \tag{3}$$

The axial velocity U at any radius r is calculated from the following equation:

$$U/U_m = \left(\frac{r}{r_o}\right)^2 \exp - k_u\left(\left(\frac{r}{x+a}\right)^3 - \left(\frac{r_o}{x+a}\right)^3\right) + A \tag{4}$$

and A is given by:

$$A = \left(0.65 - 2S\left(\frac{r_o}{x+a}\right) - \left(\frac{r}{x+a}\right)\right)\left(1 - \frac{r}{r_o}\right) \tag{5}$$

where r_o defines radial locations of maximum axial velocity, and k_u is a distribution parameter related to axial distance, defined as:

$$k_u = 0.667\left(\frac{x+a}{r_o}\right)^3 \tag{6}$$

Radial distribution of the swirl component is obtained from the assumption that the inner region of the profile conforms to a solid body rotation, and the outer region is a free vortex type motion. The size of the solid body core is experimentally determined (Beer and Chigier, 1972). The velocity profiles calculated by the above equations were used to determine various parameters of spray formation for the six atomizers under investigation at all operating conditions reported in the next section.

Comparison between the measurements obtained for atomizers A and F and the calculations is shown in Fig. 5. The details of the measurements for the two atomizers are given by McDonell and Samuelsen (1988) and Zimmerman (1985). Considering the relatively simple approach used to calculate the velocity profiles, fairly satisfactory agreement between the data and the calculations is achieved.

The calculation of the thickness (T) of the liquid film that is formed under the effect of air flow on the atomizer prefilmer is based on the evaluation of the interfacial friction factor between air and film (Rizk and Lefebvre, 1980). It is given by:

$$T^2(1 + 300\ T/d_h) = 16.1\ \mu_L\ W_L\ \mathrm{Re}^{0.25}/\rho_L\rho_a d_o U_a^2 \tag{7}$$

W_L is liquid flow rate, d_o is prefilmer diameter, d_h is hydraulic diameter of air passage, U_a is air velocity and Re is Reynolds number of airflow. In short prefilming devices, the actual film leaving the nozzle is determined by the fuel swirler and atomizer lip geometry. In plain-jet type, the liquid breakup is strongly influenced by the initial dimension of the jet.

The wave instability concept is adopted in the present approach to describe the liquid stream disintegration where the balance of forces caused by gas pressure, liquid viscosity, inertia and surface tension controls the breakup mechanism (Dombrowski and Jones, 1963). The governing equation is given by:

$$\left(\frac{\partial f}{\partial t}\right)^2 + \frac{\mu_L}{\rho_L} n^2\left(\frac{\partial f}{\partial t}\right) - \frac{2(\rho_a n U_r^2 - \sigma n^2)}{\rho_L T} = 0 \tag{8}$$

where U_r is relative velocity, f is total growth of wave, t is time, σ is surface tension, and n is the wave number of the disturbance imposed on the liquid stream. It is given by:

$$n = \frac{F^2 \rho_a U_r^2}{2\sigma} \tag{9}$$

and F is the ratio of wave growth of liquid to that of the inviscid liquid. Its maximum value is given by:

Downloaded 02 Jun 2010 to 171.66.16.112. Redistribution subject to ASME license or copyright; see http://www.asme.org/terms/Terms_Use.cfm

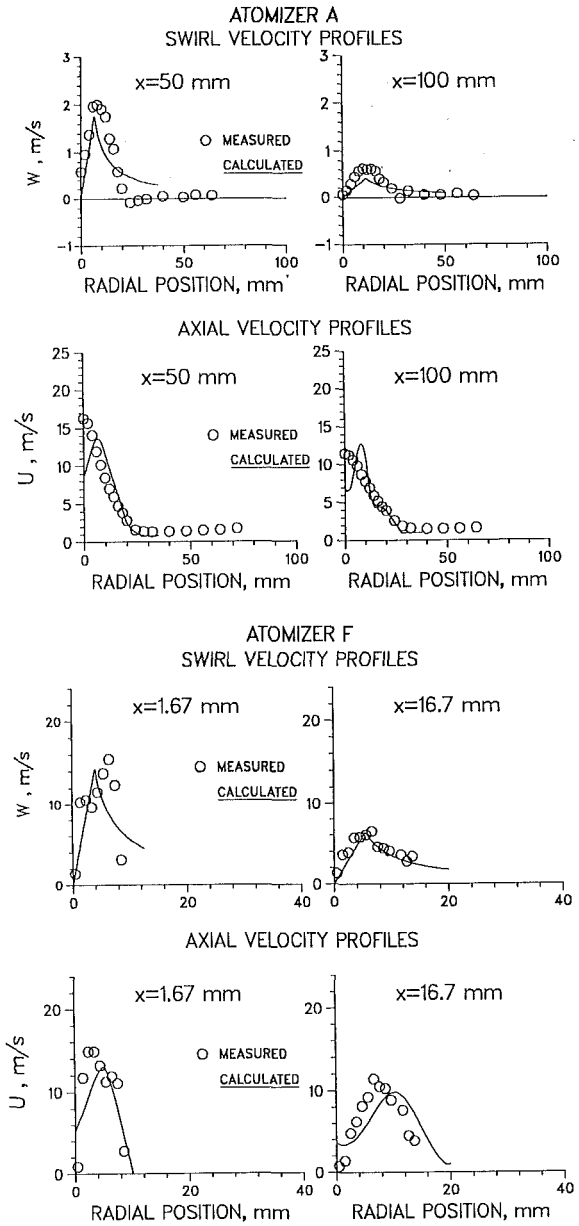


Fig. 5 Comparison between calculated and measured air velocity

$$1 - F^2 - VF^3 = 0 \tag{10}$$

where

$$V = \frac{\mu_L \rho_a U_r^2}{2} \left(\frac{T}{2\rho_L \sigma^3} \right)^{0.5} \tag{11}$$

Solving these equations yields the time taken for breakup that is needed to calculate an average ligament length. Although there are no available data on measured ligament length at airblast atomizer exit, the photographs shown by Rizk (1977) indicate that ligament breakup within a range agrees with the values calculated by the above equations. An average initial drop size D_i at ligament breakup is estimated from the conservation of mass of the disintegrated part corresponding to a full wave length as follows:

$$D_i = \frac{(3\pi d_{av}^2)^{1/3}}{n} \tag{12}$$

where d_{av} is average ligament diameter.

The drop formed at breakup is allowed to deform under the effect of relative velocity according to the Weber number level experienced by the drop. The deformed drops may undergo secondary breakup that is modeled using the stripping breakup mechanism (Jenkins and Booker, 1965). This is governed by a critical Reynolds number based on relative velocity U_r and instantaneous drop radius R. The rate of size variation is given by:

$$\frac{dR}{dt} = -A \left(\frac{\rho_a}{\rho_L} \right)^{0.33} \left(\frac{\mu_L \rho_a}{\mu_a \rho_L} \right)^{0.167} \left(\frac{\mu_L U_r}{\rho_L R} \right)^{0.5} \tag{13}$$

A is a constant of the order of unity. Because the above equation was derived for liquids of relatively low viscosity, the validation of this equation for high viscous liquids still needs to be performed.

Droplet trajectories are evaluated using the equation of motion of the droplet as given in the ith direction by:

$$\frac{dV_i}{dt} = \frac{3}{4} \frac{\rho_a}{\rho_L d} C_D (U_i - V_i) |U_i - V_i| \tag{14}$$

where V_i is droplet velocity, d is instantaneous drop size, and the drag coefficient C_D is calculated from the standard drag curve of solid spheres (Mostafa and Mongia, 1987). The above equations are used to evaluate the drop diameter of the spray, which is assumed to contain a single drop size (SMD), at various axial planes downstream of the ligament breakup location. The value of SMD is needed to compare performance of fuel injectors, and as an essential input to combustor performance correlations and analytical models. In addition to the calculation of the SMD, the present approach can also provide the spread in drop sizes in sprays.

To simulate realistic sprays that contain droplets of various sizes, a modified Rosin–Rammler distribution function is employed in the approach (Rizk and Lefebvre, 1985). The modified form is found to match the data more closely, under wide operating parameters, than the original distribution function, especially at the upper end of the drop size range (Lefebvre, 1989; Rizk and Lefebvre, 1985; Custer and Rizk, 1988). From the knowledge of the final SMD, the fractional volume V of the spray containing droplets smaller than a diameter d is calculated using the following equations:

$$V = 1 - \exp - \left(\frac{\ln d}{\ln d_m} \right)^q \tag{15}$$

where d_m represents a mean drop size, and q is related to the range of drop sizes present in the spray. They are given by Custer and Rizk (1988) as follows:

$$d_m = (0.91 \text{ SMD})^{1.18} \tag{16}$$

and

$$q = d_m / (0.126\, d_m + 1.2) \tag{17}$$

The size distribution of the relatively large drops formed at ligament breakup is then assumed, and various drop sizes are tracked through the flow field considering the secondary atomization effects described earlier. The procedure is repeated until the assumed distribution at ligament breakup yields drop sizes that agree, within prescribed limits, with the calculated distribution at completion of atomization, given by Eqs. (15)–(17). The details of the variation of drop sizes in this critical region near the atomizer provide useful tool to the drop evaporation calculation in locations where the measurements are usually difficult.

VI Calculation Approach Validation

The validating effort involved the application of the semi-analytical approach to the six atomizers under consideration. As described earlier, the atomizers selected for this investigation include airblast types of short and long prefilmer, as well as plain-jet devices. In this section, the predictions of the developed approach are compared with the experimental data.

Downloaded 02 Jun 2010 to 171.66.16.112. Redistribution subject to ASME license or copyright; see http://www.asme.org/terms/Terms_Use.cfm

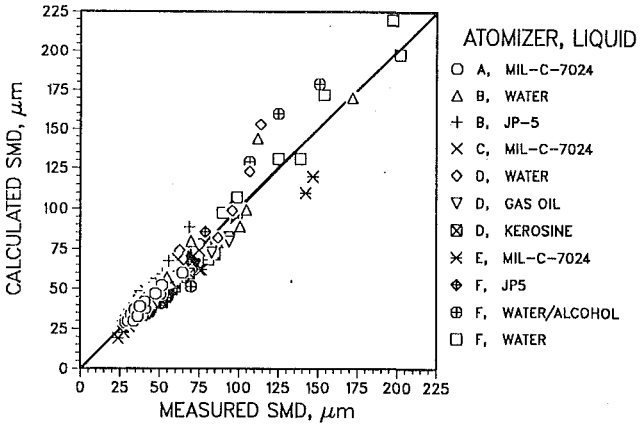


Fig. 6 Overall comparison between measurements and calculations of SMD

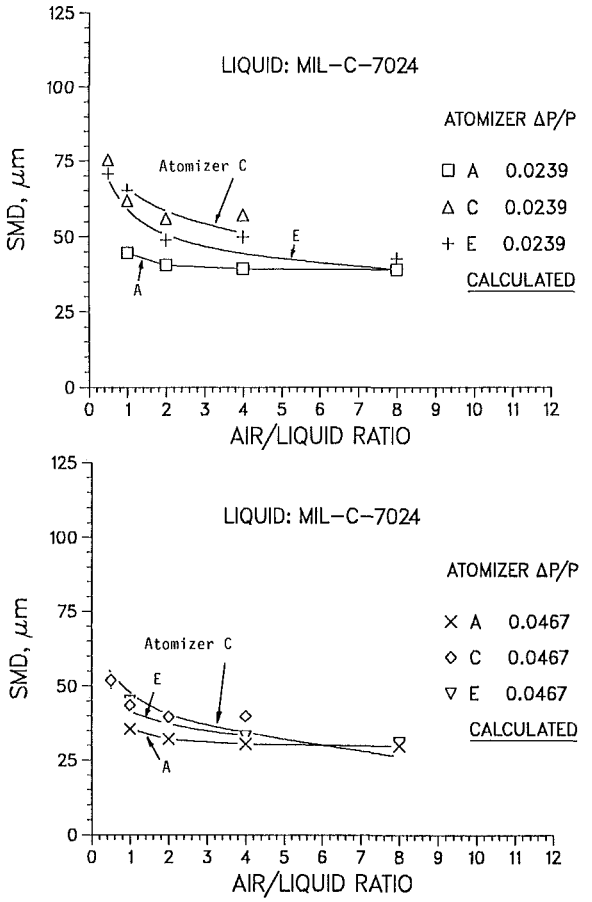


Fig. 7 Performance predictions of atomizers A, C, and E

This is to demonstrate the capability of the approach to detect such effects as atomizer configuration, operating parameters, and liquid type on spray characteristics.

Figure 6 shows an overall comparison between the SMD calculations and the data for all the cases studied in this investigation. It is seen that most of the points fall within a narrow band around the perfect correlation line, especially in the lower range of SMD. The higher range of SMD shows less satisfactory agreement between the measurements and predictions. Under these conditions of low air velocity and/or high liquid/air ratio the atomization process is inefficient, leading to the formation of large drop sizes, and variations in the measurements that are more difficult to predict.

In Fig. 7, the performance of atomizers A, C, and E at two

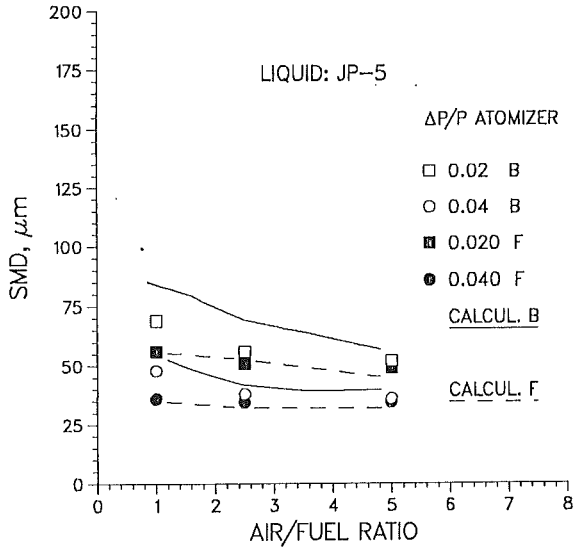


Fig. 8 Performance of prefilming airblast atomizers

different levels of air pressure differential is illustrated. The three atomizers, which are fairly similar in size were candidates for a small gas turbine application. It is obvious that the different atomization concepts used in the three designs have a significant impact on the behavior of the atomizer. The solid curves shown in this figure represent the predictions, which are in good agreement with the measured data.

The comparison between atomizers A and C shows the generally superior performance exhibited by the prefilming airblast atomizer over the plain-jet type. The performance of atomizer C, which is a long prefilmer, is less satisfactory than atomizer A, especially at low air pressure drop. The difference in performance between the two prefilming atomizers that belong to the same atomization concept is due to the differences in the design of the filming device and the method by which the air and film interact at the lip of the atomizer. In the atomizer C tested, the highest air velocity through the inner passage occurred at the holes leading to this passage. The air velocity employed to spread the liquid onto the prefilmer is consequently lower, leading to less efficient filming process. This explains the superiority of the plain-jet atomizer E over atomizer C in some instants.

Similar conclusions may be drawn from Fig. 8 where a comparison between two larger prefilming atomizers, B and F, is shown. Both the data and the predictions illustrate that under the same operating conditions atomizer F produces sprays of better quality than those of atomizer B.

Figure 9 includes the data obtained for atomizer B using water and JP-5 fuel. The figure shows the typical reduction in SMD with the increase in the air/fuel ratio and/or the air pressure drop. It is also noticed that no significant improvement in atomization may be gained by raising the air/fuel ratio over a value of about 5.0. The larger values of SMD for the water sprays are due to the differences of the physical properties between the two liquids. Once again the predictions of the SMD closely follow the measured data as illustrated in the figure.

The performance of the plain-jet airblast atomizer D is given in Fig. 10 for kerosine sprays obtained at air pressure drop range between 1.81 and 9.54 percent. The predictions of the present semi-analytical approach are also plotted in the figure. In light of the results given in this figure and those presented earlier, it is observed that the developed approach successfully detects the various effects of air/fuel ratio, air velocity, and fuel type on atomization. Thus, for virtually the same general calculation procedure the performance of significantly different atomizer concepts is predicted with reasonable accuracy.

Downloaded 02 Jun 2010 to 171.66.16.112. Redistribution subject to ASME license or copyright; see http://www.asme.org/terms/Terms_Use.cfm

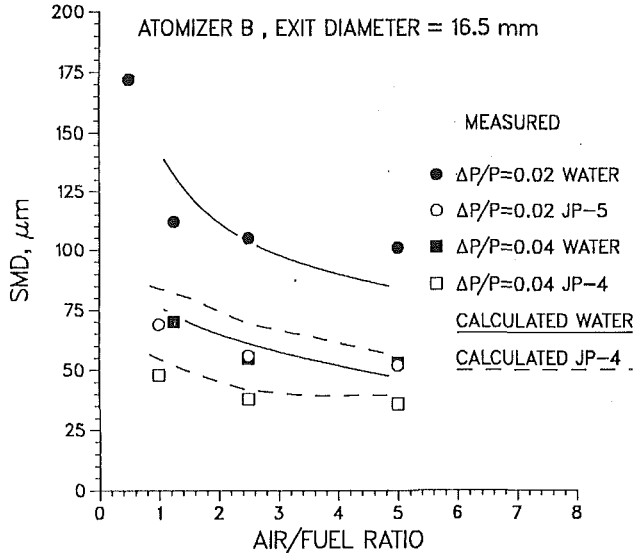


Fig. 9 Effect of liquid properties on performance of atomizer B

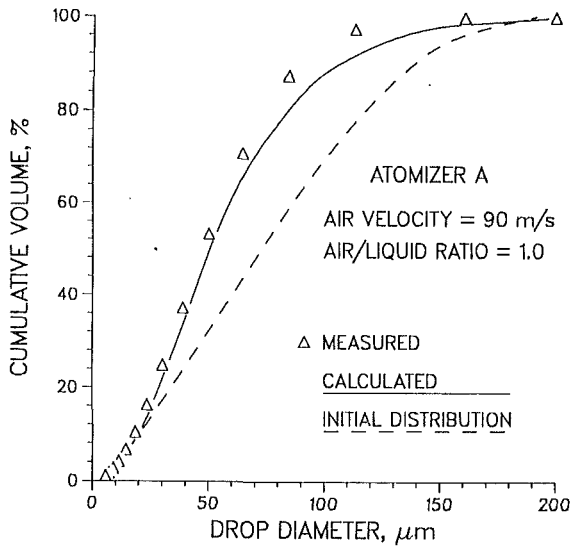


Fig. 11 Drop size distribution of spray produced by airblast atomizer

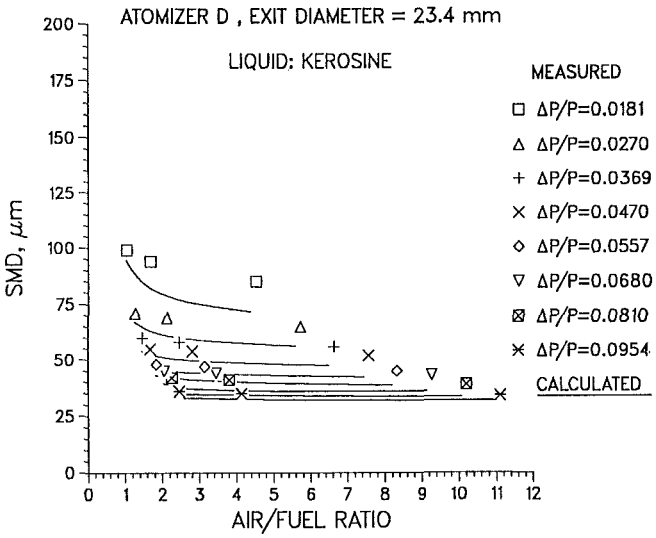


Fig. 10 Plain-jet airblast atomizer performance

The present approach also provides the details of the drop-size distribution in the spray. This information is needed to support the calculation of almost all combustor performance parameters through the evaluation of the evaporation history of various drop sizes in the spray. It is realized that the actual sprays demonstrate a wide radial variation in drop size, where large drops exist near the outer envelope of spray, and the fine drops fill the spray core (Rizk and Mongia, 1989a; McDonell and Samuelsen, 1988). The drop-size measurement using the Malvern, however, gives an in-line overall drop-size distribution across the spray. The measurement therefore gives more weight to smaller drops to some degree. The relatively simple approach followed in the present investigation provides an overall distribution consistent with the method of measurement. Rizk and Mongia (1989a) address the approach used to evaluate the local drop-size distribution in the spray that was measured by two-component phase Doppler interferometry.

Figure 11 shows the predictions of the initial distribution of drop sizes formed at ligament breakup close to the exit of atomizer A, as well as the distribution at the completion of the atomization process. The figure illustrates the reduction in drop sizes due to the relative velocity action of the air as the droplets travel downstream of the atomizer. The measured drop-size distribution at 0.05 m downstream distance is also plotted in the figure. Because the drops travel at different velocities, some variation in average drop size at different axial locations may occur until the relative velocity between the drops is diminished in the far region of the atomizer. In airblast atomization, however, all the drops accelerate rapidly to follow the air velocity profile within a short distance from the atomizer. The results given in Fig. 11 illustrate the effects of the secondary breakup on the drop-size distribution in the near region of the atomizer.

Examples of the calculations, selected to demonstrate the effects of liquid type and liquid/air ratio on drop-size distribution, are shown in Fig. 12. The figure indicates that the whole distribution is shifted toward smaller sizes as the liquid surface tension is reduced. The beneficial effect of an increase in the air/liquid ratio on the drop size distribution is also evident in the figure. It is obvious that at low air/liquid ratio fairly large drops will exist in the spray and may adversely affect its evaporation rate. Good agreement between the data and the calculations is shown in the figure.

The trajectories of the droplets in the flow field are also evaluated by the calculation procedure to give an indication of the radial spread of the droplets downstream of the nozzle. The momentum exchange between the various drop sizes and the surrounding air causes the drops to follow different paths. The large drops tend to penetrate the airflow streamlines to reach larger radii than the smaller ones.

Figure 13 shows an example of the calculation for atomizer F of the spray that is made up of five drop size groups of equal volume fractions. The drop sizes quoted in the figure are the values at the end of atomization process. It is realized that in actual sprays more spread in droplet trajectory occurs due to the fact that the droplets formed at ligament breakup follow several directions. The fine droplets also tend to follow the turbulent nature of the flow field to spread more towards the centerline. This explains the presence of liquid in the center of the supposedly hollow cone spray.

Although all the tests performed in the present investigation were performed at atmospheric conditions, the gas turbine atomizer is required to operate at elevated pressure and temperature environment most of the time. Testing of the atomizer is, therefore, required to be performed at these more realistic conditions. Atmospheric tests are still needed to compare the performance of atomizers proposed for certain applications due to their simplicity. On the other hand, the calculation approach adopted here accounts for the elevated conditions through their effects on filming, ligament breakup, and sec-

Downloaded 02 Jun 2010 to 171.66.16.112. Redistribution subject to ASME license or copyright; see http://www.asme.org/terms/Terms_Use.cfm

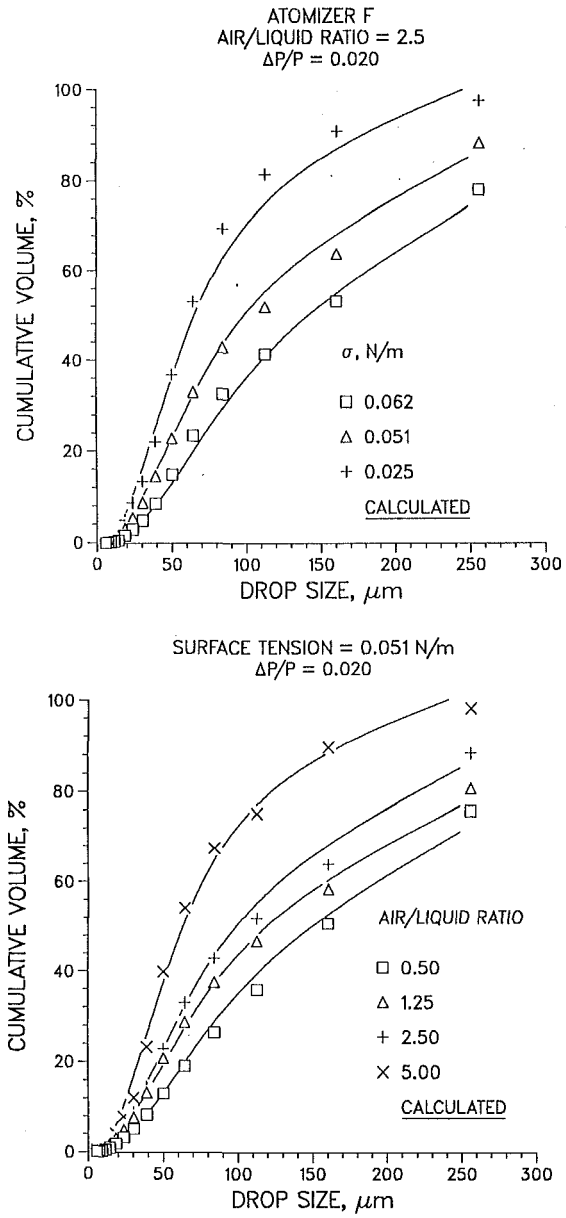


Fig. 12 Influence of liquid type and operating conditions on drop-size distribution

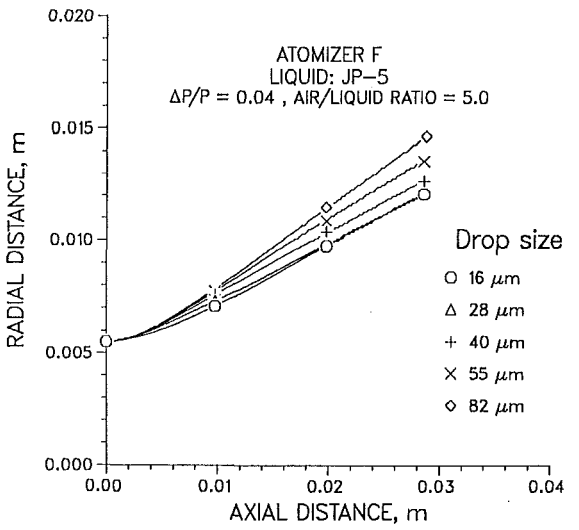


Fig. 13 Drop trajectories in spray

ondary atomization, in addition to the drop trajectory calculation.

In order to achieve improved predictions of the details of the spray, the dynamics of the two-phase flow should be utilized in a multidimensional flow domain. However, the relatively simple approach used here would be useful in preliminary phases of the design of the fuel injector, in addition to providing data to combustor performance calculations.

VII Conclusions

A means to estimate the spray characteristics of liquid atomizers has been always sought to guide the development of the combustor components. Over the years, expressions based on experimental data have been derived to describe various spray parameters. Although each expression can closely match the data of a certain design, the data analysis of the present investigation indicates that even within the same atomizer type, the spray quality depends on the method by which the liquid is injected into the air.

A calculation procedure based on semi-analytical principles has been formulated and validated against the experimental data obtained for six atomizers. It considers various liquid preparation and breakup processes, and utilizes empirical expressions to determine the air velocity components in the atomizer flow field.

The trends of variation of the mean drop size and drop-size distribution with air/liquid ratio and air pressure differential were successfully predicted by the current approach. It has been shown that, by this relatively simple procedure, the impact of the details of the atomizer on its performance is readily sensed.

The results of this investigation also indicate that by considering the effects of the physical properties of the liquid through the appropriate atomization processes, the calculation approach can be satisfactorily applied to various common liquids. The agreement between the calculation and the data of six liquids that significantly varied in properties was quite encouraging.

The variation of the drop-size distribution due to in-flight breakup as the spray proceeds downstream of the atomizer is also evaluated by the developed approach. Utilizing these data can certainly enhance the calculation of the evaporation history of the spray.

It is recognized that in later stages of the atomizer design process, more detailed calculations are needed. They should consider the influence of the carrier phase turbulence on the dispersion of the spray and offer better representation of initial conditions at ligament breakup.

References

Beer, J. M., and Chigier, N. A., 1972, *Combustion Aerodynamics*, Halsted Press Division, Wiley, New York.

Custer, J. R., and Rizk, N. K., 1988, "Effect of Design Concept and Liquid Properties on Fuel Injector Performance," *Journal of Propulsion and Power*, Vol. 4, No. 4, pp. 378–384.

Dombrowski, N., and Jones, W. R., 1963, "The Aerodynamic Instability and Disintegration of Viscous Liquid Sheets," *Chem. Eng. Science*, Vol. 18, pp. 203–214.

Jasuja, A. K., 1979, "Atomization of Crude and Residual Fuel Oils," ASME JOURNAL OF ENGINEERING FOR POWER, Vol. 101, pp. 250–258.

Jenkins, D. C., and Booker, J. D., 1965, "The Time Required for High Speed Air-streams to Disintegrate Water Drops," Ministry of Aviation, Aeronautical Research Council C. P., No. 827.

Kilik, E., 1976, "The Influence of Swirler Design Parameters on the Aerodynamics of the Downstream Recirculation Region," Ph.D. thesis, School of Mechanical Engineering, Cranfield Institute of Technology, United Kingdom.

Lefebvre, A.H., 1989, *Atomization and Spray*, Hemisphere Publishing Corporation, Washington, DC.

Lorenzetto, G. E., and Lefebvre, A. H., 1977, "Measurements of Drop Size on a Plain Jet Airblast Atomizer," *AIAA J.*, Vol. 15, No. 7, pp. 1006–1010.

McDonell, V. G., and Samuelsen, G. S., 1988, "Evolution of the Two-Phase

Downloaded 02 Jun 2010 to 171.66.16.112. Redistribution subject to ASME license or copyright; see http://www.asme.org/terms/Terms_Use.cfm

Flow in the Near Field of an Air-Blast Atomizer Under Reacting and Non-reacting Conditions," presented at the Fourth Int. Symp. on Applications of Laser Anemometry to Fluid Mechanics, Lisbon, Portugal.

Mostafa, A. A., and Mongia, H. C., 1987, "On the Modeling of Turbulent Evaporating Sprays: Eulerian Versus Lagrangian Approach," *International Journal of Heat and Mass Transfer*, Vol. 30, No. 12, pp. 2583–2593.

Mugele, R. A., and Evans, H. D., 1951, "Droplet Size Distribution in Sprays," *Indust. Eng. Chem.*, Vol. 43, pp. 1317–1324.

Reitz, R. D., and Bracco, F. V., 1982, "Mechanism of Atomization of a Liquid Jet," *Phys. Fluids*, Vol. 25, No. 10, pp. 1730–1742.

Rizk, N. K., 1977, "Studies on Liquid Sheet Disintegration in Airblast Atomizers," Ph.D. Thesis, Cranfield Institute of Technology, United Kingdom.

Rizk, N. K., and Lefebvre, A. H., 1980, "Influence of Liquid Film Thickness on Airblast Atomization," ASME JOURNAL OF ENGINEERING FOR POWER, Vol. 102, pp. 706–710.

Rizk, N. K., and Lefebvre, A. H., 1983, "Influence of Atomizer Design Features on Mean Drop Size," *AIAA Journal*, Vol. 21, No. 8, pp. 1139–1142.

Rizk, N. K., and Lefebvre, A. H., 1985, "Drop-Size Distribution Characteristics of Spill-Return Atomizers," *J. Propulsion and Power*, Vol. 1, No. 1, pp. 16–22.

Rizk, N. K., and Mongia, H. C., 1989a, "A Model for Airblast Atomization," accepted for publication in *J. Propulsion and Power*, AIAA Paper No. 89-2321.

Rizk, N. K., and Mongia, H. C., 1989b, "Semi-analytical Fuel Injector Performance Correlation Approach," AIAA Paper No. 89-2902.

Rizk, N. K., and Mongia, H. C., 1990a, "A Semi-analytical Approach Validation for Airblast Atomizers," Paper No. AIAA-90-0361.

Rizk, N. K., and Mongia, H. C., 1990b, "Further Validation of a Semi-analytical Approach for Fuel Injectors of Different Concepts," AIAA Paper No. 90-2190.

Simmons, H. C., 1977, "The Correlation of Drop-Size Distribution in Fuel Nozzle Sprays," ASME JOURNAL OF ENGINEERING FOR POWER, Vol. 99, No. 3, pp. 309–319.

Simmons, H. C., 1979, "The Prediction of Sauter Mean Diameter for Gas Turbine Fuel Nozzle of Different Types," ASME Paper No. 79-WA/GT-5.

Sturgess, S. A., Syed, S. A., and McManus, K. R., 1984, "Calculation of a Hollow-Cone Spray in a Uniform Air Stream," *Journal of Propulsion and Power*, Vol. 1, No. 5, pp. 360–368.

Zimmerman, D. R., 1985, "LDA Measurements of the Airflow From a 427 Fuel Nozzle," Technical Data Report EDR 12248, Allison Gas Turbine Division, GM Corp., Indianapolis, IN.

Downloaded 02 Jun 2010 to 171.66.16.112. Redistribution subject to ASME license or copyright; see http://www.asme.org/terms/Terms_Use.cfm

Motion and Evaporation of Shear-Driven Liquid Films in Turbulent Gases

S. Wittig
Mem. ASME.

J. Himmelsbach

B. Noll

H. J. Feld

W. Samenfink

Lehrstuhl und Institut
für Thermische Strömungsmaschinen,
Universität Karlsruhe (T.H.),
Karlsruhe, Germany

Detailed measurements of wavy liquid films driven by the shear stress of turbulent air flow are obtained for different air temperatures, air velocities, and flow rates of the liquid. The experimental conditions are chosen from characteristic data of liquid film flow in prefilming airblast atomizers and film vaporization employing combustors. For the measurement of the local film thickness and film velocity a new optical instrument—based on the light absorption of the liquid—has been developed, which can be used at high temperatures with evaporation. The measured data of the gas phase and the liquid film are compared with the results of a numerical code using a laminar as well as a turbulent model for the film flow and a standard numerical finite volume code for the gas phase. The results utilizing the two models for the liquid film show that the film exhibits laminar rather than turbulent characteristics under a wide range of flow conditions. This is of considerable interest when heat is transferred across the film by heating or cooling of the wall. With this information the optical instrument can also be used to determine the local shear stress of the gas phase at the phase interface. Using time-averaged values for the thickness, the velocity, and the roughness of the film, the code leads to relatively accurate predictions of the interaction of the liquid film with the gas phase.

Introduction

Knowledge of the parameters influencing the heat and mass transfer of wavy liquid films driven by the shear of a turbulent air flow is of dominant interest in various practical engineering applications. In extending our earlier experimental and computational studies of prefilming airblast atomizers (Aigner and Wittig, 1985, 1988; Sattelmayer and Wittig, 1986, 1989; Sattelmayer, 1985; Aigner, 1986) experimental and numerical tools for the study of two-phase flows with wavy liquid films have been developed. At the Institute for Thermal Turbomachinery at the University of Karlsruhe these tools are also used for the evaluation of film vaporization in combustors and the flow in intake pipes of internal combustion engines.

Several publications (Lefebvre, 1980; Wittig et al., 1984; Sattelmayer and Wittig, 1989) show that in prefilming airblast atomizers (Fig. 1) the wavy liquid films are influencing the velocity of the gas phase and thereby the spray characteristics. In order to predict the spray characteristics of airblast atomizers at various flow rates of the liquid and at different running conditions of the engine, the pressure drop caused by the liquid film must be taken into account.

Most of the previous investigations on prefilming airblast atomizers have been done at low temperatures. For the application of the correlations derived from these data for the prediction of the spray characteristics at the high-temperature and high-pressure conditions of gas turbines, the flow conditions of the gas at the atomizing edge must be known as well as the fuel temperatures, because the fuel properties vary strongly with temperature. With this information the boundary conditions for a calculation of the motion and evaporation of the spray in combustors (Wittig et al., 1988) are available.

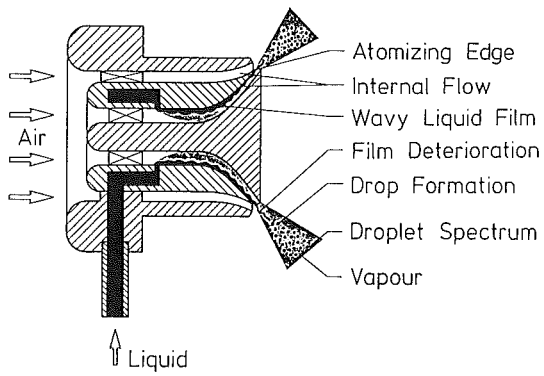


Fig. 1 Prefilming airblast atomizer (Sattelmayer and Wittig, 1989)

At high temperatures the two-phase flow inside the nozzle is characterized by a coupled heat and mass transfer at the liquid/gas interface (Fig. 2). Depending on the flow rates and temperatures of the gas and the liquid, different velocity profiles of the gas phase and of the liquid film are found. In addition, the temperature profiles of the gas and the liquid change locally, as well as the concentration profiles of the vapour. For different kinds of airblast atomizers the film can be heated only by the gas phase, or both by the gas phase and

Contributed by the International Gas Turbine Institute and presented at the 36th International Gas Turbine and Aeroengine Congress and Exposition, Orlando, Florida, June 3–6, 1991. Manuscript received at ASME Headquarters February 19, 1991. Paper No. 91-GT-207. Associate Editor: L. A. Riekert.

Copyright © 1992 by ASME
Downloaded 02 Jun 2010 to 171.66.16.112. Redistribution subject to ASME license or copyright; see http://www.asme.org/terms/Terms_Use.cfm

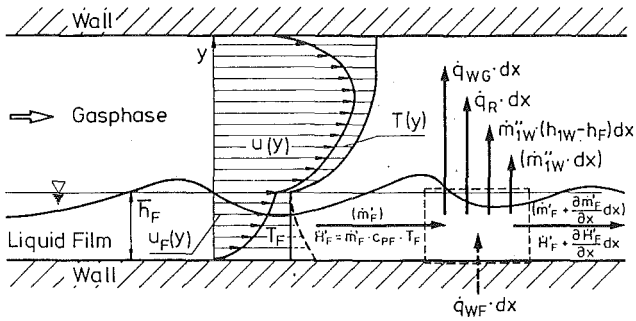


Fig. 2 Internal flow of a prefilming airblast atomizer

by the prefilming plate on which the film is flowing. Further problems appear in the correct description of the coupling conditions for the momentum, the heat and the mass transfer at the phase interface.

The aim of the present study is to extend our earlier studies (Aigner and Wittig, 1985, 1988; Sattelmayer and Wittig, 1986, 1989) to develop a numerical procedure for the prediction of all these influences for practical engine design. Therefore, a variety of simplifications were necessary. Their effects have been evaluated by detailed experimental verification.

Calculational Procedure

The turbulent gas flow over the wavy liquid film and the film flow itself are intrinsically unstable (Sattelmayer, 1985; Sattelmayer and Wittig, 1989). Therefore, an exact solution of the governing equations for momentum, heat, and mass transfer in the liquid and the gas phase is not applicable for practical use. Although encouraging studies on special problems of this complex two-phase flow are available (e.g., Jurman and McCready, 1989; Sheintuch and Dukler, 1989; Kuzan and Hanratty, 1989), these models cannot be applied for this investigation, because of the coupled heat and mass transfer and because of the unstable film waves.

However, as earlier studies have pointed out, reasonable results can be obtained using time-averaged calculational procedures (Whalley, 1987; Sattelmayer, 1985; Sattelmayer and Wittig, 1989). The dominant parameter for these calculations is the shear stress at the interface of the gas and the liquid. Assuming constant shear stress at the interface and in the film and neglecting gravity effects, two fundamental equations for the time-averaged film velocity profile were employed: A turbulent profile developed by Wurz (1971)

$$u_F^+ = \frac{1}{2\kappa'^2 y_F^+} - \frac{1}{\kappa'}\sqrt{1+\left(\frac{1}{2\kappa' y_F^+}\right)^2} + \frac{1}{\kappa'}\ln\left(2\kappa' y_F^+\left(1+\sqrt{1+\left(\frac{1}{2\kappa' y_F^+}\right)^2}\right)\right) \quad (1)$$

and a laminar profile

$$u_F^+ = y_F^+ \quad (2)$$

with

$$u_F^+ = \frac{u_F}{u_{\tau F}} = u_F\sqrt{\frac{\rho_F}{\tau_F}}$$

$$y_F^+ = \frac{y_F u_{\tau F}}{\nu_F}.$$

These two equations represent the two physical extremes for the time-averaged film velocities at a given shear stress. Because of the fundamental interest of this approach only the calculational results of these two profiles are presented. The results of a third equation with a three-layer approach (Whalley, 1987), which gave results between the above two profiles are omitted. For a water film of a given shear stress of 80 N/m^2 and a volumetric liquid flow of $\dot{V}_F/B = 1$ cm^2/s, the resulting velocity profiles are compared in Fig. 3.

The turbulent profile results in a higher thickness of the film and a lower surface velocity. However, in practical use the differences in film thickness will be less than in Fig. 3 because the shear stress is increasing with the film thickness, leading to an increasing film velocity. Following the approach of Cohen and Hanratty (1968) and Sattelmayer and Wittig (1989) for the coupling between the liquid film and the gas phase, an equivalent sand grain roughness approach is used:

$$k_s = \psi_\tau \cdot 2 \cdot \bar{h}_F$$

$$\psi_\tau = 0.735 + 0.009255 \cdot \tau_W \quad (3)$$

Measuring the boundary layer of the turbulent air over various liquid films and measuring the film thickness, Sattelmayer (1985) found this correlation of ψ_τ to give the best results when using the sand grain approach to get the velocity profile of the gas with the logarithmic law of the wall.

In this approach we take our numerical code TEFAC2D for

Nomenclature

C = constant in logarithmic law
c_p = specific heat, J/kg K
h_{so} = gap height without film, m
h_{cal} = calibration film thickness, m
$(h_{1W}-h_F)$ = latent heat evaporation, J/kg
H'_F = enthalpy flux of liquid per unit breadth, W/m
$\bar{h}_F$ = time-averaged film thickness, m
I = light intensity, W/m^2
k_s = equivalent sand grain roughness, m
k' = absorption coefficient of liquid, 1/m
$\dot{m}$ = mass flux, kg/s
n = index of refraction
p = pressure, N/m^2
$\dot{q}$ = heat flux per unit area, W/m^2
T = temperature, K
u = gas velocity, m/s
u_F = film velocity, m/s
u_τ = shear stress velocity, m/s
u_F^+ = nondimensional film velocity
$\dot{V}_F/B$ = liquid volume flux per unit breadth, m^2/s
x = coordinate, m
y = coordinate, m
y^+ = nondimensional wall distance
κ' = von Karman constant
ν = kinematic viscosity, m^2/s
ρ = density, kg/m^3
τ = shear stress, N/m^2
ψ_τ = efficiency factor of film roughness
$'$ = per unit breadth
$''$ = per unit area

Subscripts

F = film, liquid
cal = calibration
G = gas
o = reference
R = radiation
so = gas height without film
WG = heat conduction and convection between film and gas
W = wall
WF = heat conduction between prefilming plate and film
1 = steam, measuring plane 1

Downloaded 02 Jun 2010 to 171.66.16.112. Redistribution subject to ASME license or copyright; see http://www.asme.org/terms/Terms_Use.cfm

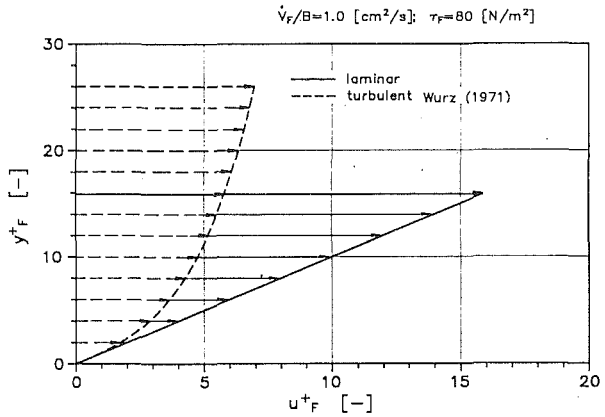


Fig. 3 Comparison of a laminar and a turbulent film velocity profile

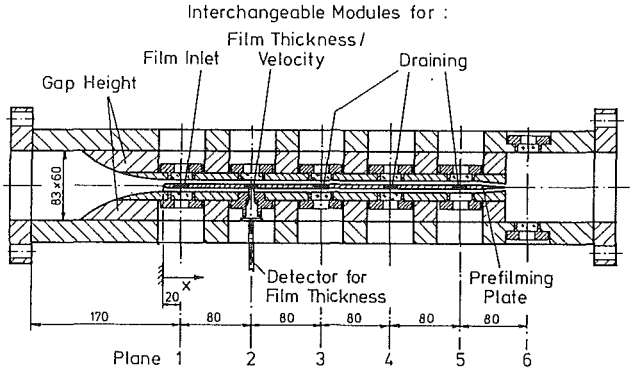


Fig. 4 Test section for evaporating liquid films

turbulent elliptic flows with a standard k–ϵ–turbulence model to calculate the turbulent gas flow in the gap. However, for this application a parabolic code could be used as well. The numerical methods of these codes are described in several publications (Patankar, *1980*; Noll, *1986*; Bauer, *1989*). A detailed description of the numerical method employed for the calculation of the two-phase flow with evaporating wavy liquid films will be published soon. However, the present paper is concerned with the evaluation of the calculational procedure by a comparison with the measurements.

Experimental Setup

For the evaluation of the theoretical procedure, measurements of the internal two-phase flows were accomplished. Figure 4 gives a detailed view of the test section, which has a primary cross section of 83×60 mm^2, converging to a cross section of 13×60 mm^2. With the prefilming plate for the liquid film along the centerline of the channel, two gaps of 4 mm height are formed.

The liquid film is flowing onto the prefilming plate through two rows of holes with a diameter of 0.5 mm and a lateral spacing of 0.8 mm at each side of the plate. These holes are supplied with liquid by holes of 2.5 mm diameter inside the prefilming plate. If conditions with heat transfer from the wetted wall to liquid film are chosen, the liquid is only supplied to one side of the plate. Under these conditions the prefilming plate is heated by the flow in the second gap without film. Otherwise the film is supplied to both sides of the prefilming plate, in order to provide adiabatic conditions on the wetted wall.

The shear at the interface of the gas and the liquid is driving the liquid film to the atomization edge, where the film is disintegrating into single droplets. Because of the fundamental nature of this investigation the length of the test section is much longer than in practical airblast atomizers. Thus the two-phase flow can be examined at fully developed flow conditions. For the analysis of the liquid film, there are five locations with windows for the optical film thickness and film velocity measurements. These windows can be exchanged by covers containing probes with pitot tubes and thermocouples for the gas phase. The starting positions of the film can be varied as well as the draining positions and the positions of the optical instrument for the liquid film by exchanging the single modules of the prefilming plate. To remove inconstancies between the modules and to improve the wetting of the surface, the prefilming plate was roughened by a sand-blast unit over a range of 50 mm breadth. Thus side wall effects are reduced as well as discontinuities.

Although the test section is designed for air temperatures of 973 K and pressures of 10 bar, the first investigation is only concerned with ambient pressures and with temperatures up to 573 K.

Measurement Techniques and Diagnostics

In the test section, the properties of both the gas and the liquid phase have to be determined. The velocities and the temperatures of the gas phase were measured using pitot-tubes of 0.6 mm outside diameter with integrated thermocouples of 0.25 mm diameter. Because of the specific design conditions, the measuring positions of the velocity and temperature profiles were 10 mm ahead of the measuring positions of film thickness and velocity shown in Fig. 4. The y positions of the profiles measured were corrected by the method of McMillan (1957) (cited by Sattelmayer, 1985). The temperatures of the prefilming plate were determined with thermocouples of 0.25 mm diameter, which were soldered into the surface before roughening the surface with the sand-blast unit.

For the study of the film flow, an optical instrument based on the light absorption in the liquid was used. As originally shown by Sill (1982), Sattelmayer (1985), and Sattelmayer et al. (1987), with this instrument the local film thickness can be determined quite well. In comparison with other methods using the variation of the conductivity or the capacitance with film thickness, this instrument has a very high local resolution because the light can be focused to 80 μm and less. Thus this instrument can determine the structure of wavy films with very short wavelengths as they appear at high gas velocities. In our later work this technique could be improved to determine in addition the surface velocity of the film. Figure 5 shows the experimental setup of the film thickness and film velocity measuring technique.

The beam of a laser is split into two measuring beams I_{F1} and I_{F2}, a reference beam I_o to determine the laser light intensity, and a calibration beam I_{cal} to determine the absorption coefficient with a film of defined thickness. The measuring beams pass the liquid film through a scattering window, which reduces interferences and influences of different angles of light coupling into the fiber of the detector. Measuring the film thickness, the intensities I_o and I_{cal} are used in addition to one measuring intensity. With I_o and I_{cal} the absorption coefficient can be determined:

$$k' = -\frac{1}{h_{cal}} \ln \frac{I_{cal}}{I_o} \tag{4}$$

resulting in the following equation for film thickness:

$$h_F = -\frac{1}{k'} \ln \frac{I}{I_o}. \tag{5}$$

If the instrument is used to determine the surface velocity of the film, only the measuring intensities I_{F1} and I_{F2} are of importance. The two beams are focused on the film with a distance of 5 mm. Pulsed coloring of the liquid is producing two correlating signals, which can be transformed into film velocities by statistical methods. Methylene blue or color from the food industry were used to color the liquid. Because of the high absorption coefficient of these colors, only a negligible

Downloaded 02 Jun 2010 to 171.66.16.112. Redistribution subject to ASME license or copyright; see http://www.asme.org/terms/Terms_Use.cfm

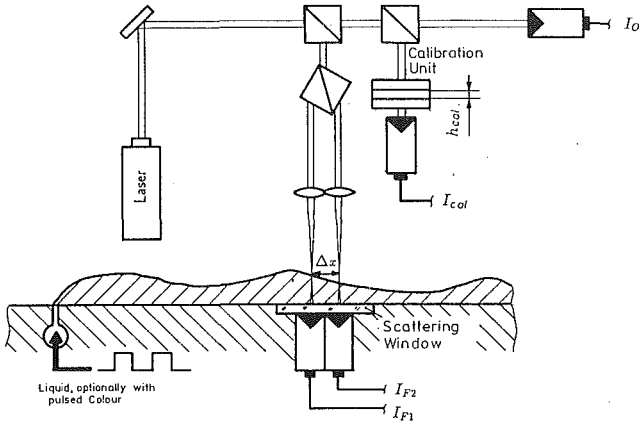


Fig. 5 Optical film thickness and film velocity measuring technique

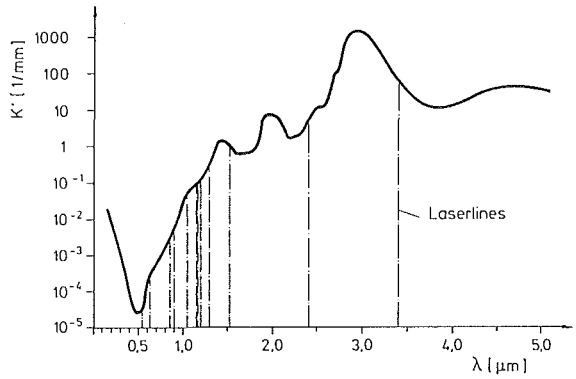


Fig. 6 Spectral absorption of liquid water (Hale and Querry, 1973)

mass flux of color was needed, which did not influence the film flow.

Sill (1982) and Sattelmayer (1985) used this setup to measure the film thickness under cold conditions with negligible evaporation. Thus they could adapt the measuring range of the film thickness by coloring the liquid in order to get the matching absorption coefficient. Of course, at high temperatures with evaporation the coloring of the liquid cannot be used, because the concentration of the color is changing under these conditions. Figure 6 shows that this problem can be solved by using an infrared light source.

Using infrared light, the absorption in the film is high enough to determine the thickness without coloring the liquid. In the new instrument two superposed He-Ne laser wavelengths are used, with the 1523 nm line for measuring the film thickness and the 633 nm line to adjust the optics. Since the index of refraction of liquid water is almost identical for both laser wavelengths ($n_{633nm} = 1.33$; $n_{1523nm} = 1.32$), the red laser beam can be used to measure the light losses by reflection from the wavy surface of the film. Additionally the light losses by scattering from droplets in the gap and losses by the coupling of the light into the fibers of the detector can be estimated.

Figure 7 shows the optical film thickness measuring instrument for evaporating and condensing liquids. This instrument consists of a sending, a focusing, and a receiving system. In the sending optics the red and the infrared beam are superposed with the aid of a beam splitter and then enlarged to get a better focus at the film. The beams are chopped with a rotating mirror. This provides a reference signal to determine the laser light intensity. The enlarged measuring beam is focused on the film and then coupled into a second glass fiber.

In the receiving system the reference and measuring intensities are combined again and then split into the red and infrared wavelength with the help of a interference filter. An Si detector is used for the red and a Ge detector for the infrared light. The signals of the detectors as well as the positions of

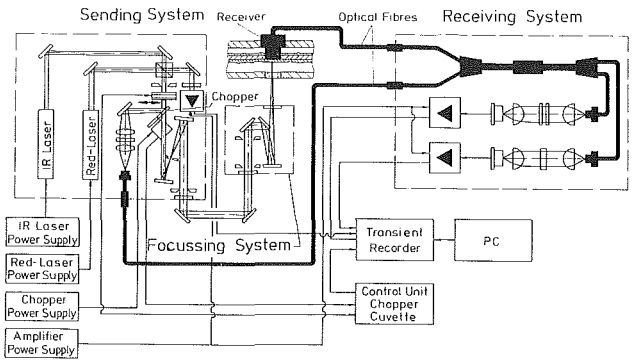


Fig. 7 Optical film thickness measuring instrument for evaporating and condensing liquid films

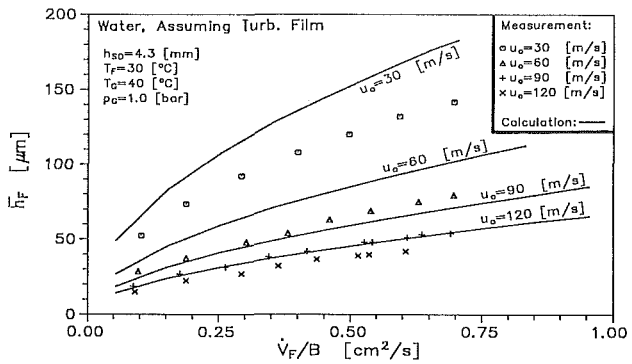


Fig. 8 Film thickness at fully developed flow (assuming a turbulent film)

the chopper, are received by a transient recorder. These signals are sent to a personal computer, which determines the film thickness.

Using only one detector to measure the red and the infrared light intensities and chopping the beams, this instrument is independent from drifts in the sensitivity of the detectors and the laser intensity. Additionally a third detector in the sending system measures the ripple of the infrared laser, because the available infrared lasers often show considerable ripple with high frequencies.

Results

For first tests of the new technique to determine the surface velocities of the film, the test section described by Sattelmayer (1985) was used at cold air conditions. A gap height of 4.3 mm was examined, in order to provide fully developed flow at the measuring position of the film velocity and thickness. Figure 8 gives a comparison of the measured (see also Sattelmayer, 1985) and the calculated film thickness if turbulent film flow is assumed.

The assumption of a turbulent film leads to a correct trend for the calculated film thickness. Nevertheless the calculated values are too high for all gas velocities and liquid flow rates. Assuming a laminar profile for the film velocity, the measured and calculated data fit much better (Fig. 9); however, at high flow rates of the liquid the calculation shows increasing differences, indicating that the film might not be fully laminar in this region.

The measured velocities at the film surface in Fig. 10 emphasize the assumption that the film is almost laminar. There is a good agreement of the numerical and experimental results for the assumption of the laminar profiles.

At high liquid flow rates the measured film velocities suddenly are much higher than the calculated values. In this flow regime the waves of the film are breaking and droplets are torn off the film. Under these conditions the film surface velocity cannot be determined, because these disturbances are

Downloaded 02 Jun 2010 to 171.66.16.112. Redistribution subject to ASME license or copyright; see http://www.asme.org/terms/Terms_Use.cfm

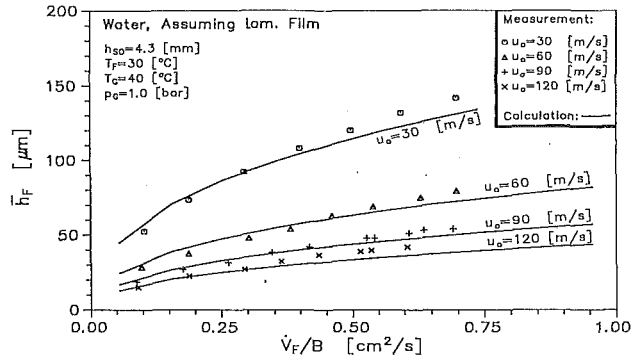


Fig. 9 Film thickness at fully developed flow (assuming a laminar film)

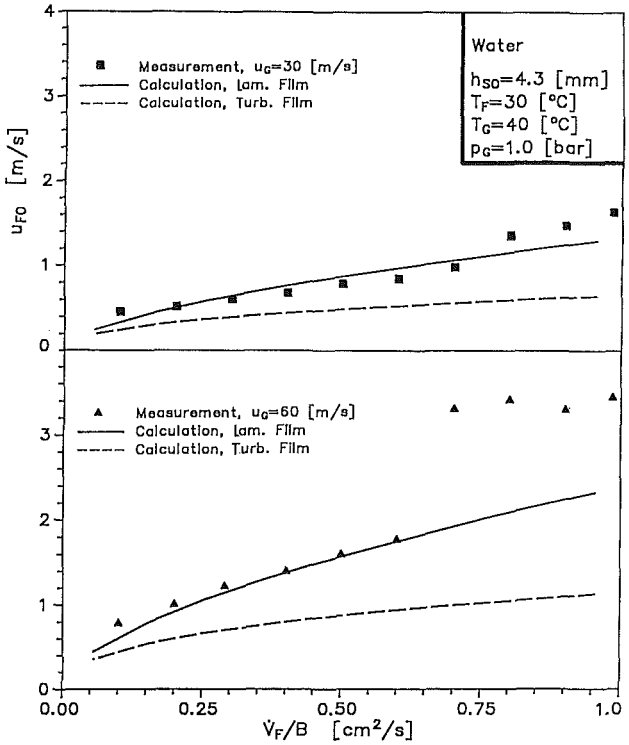


Fig. 10 Film surface velocities at fully developed flow

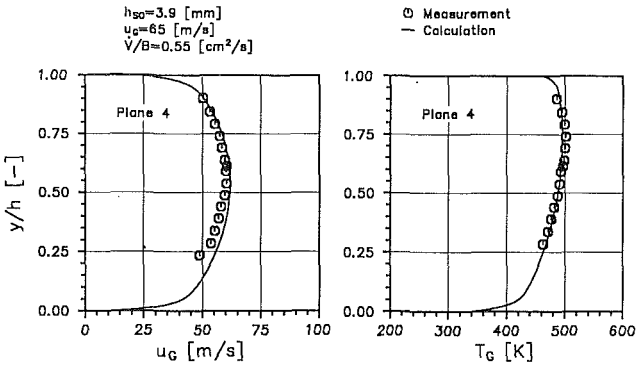


Fig. 11 Measured and calculated gas velocities and temperatures

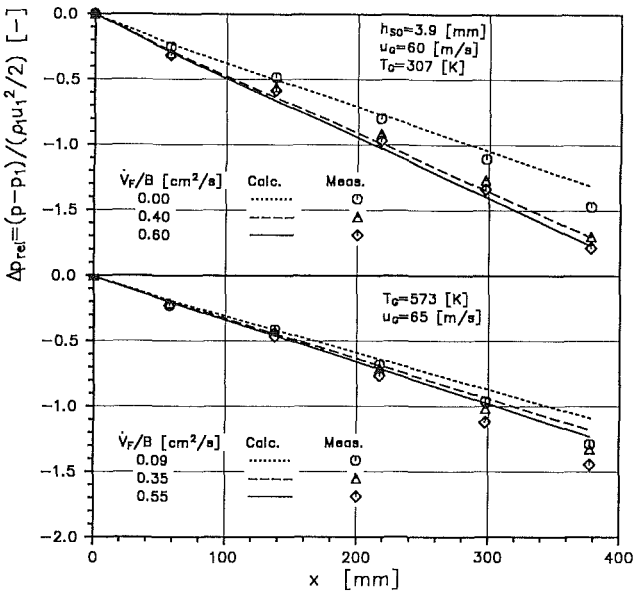


Fig. 12 Pressure drop in the gap for inlet gas temperatures of 307 K and 573 K

moving at a higher velocity than the film. However, the position where the measured velocities are rising very quickly can be used as a criterion to define the stability range of the film flow.

All these studies at gas velocities from 30 to 120 m/s indicate that the liquid film flow inside an airblast nozzle can be considered to be approximately laminar, if the liquid flow rate is not outside the range of stability. The waviness of the film does not induce significant turbulence into the film. This is of considerable interest if the heat transfer to the film has to be considered.

Based on these results, measurements were performed at elevated temperatures to test the applicability of the numerical code for the description of two-phase flows. For these experiments the new test section shown in Fig. 4 was used. In order to provide adiabatic conditions for the film, the prefilming plate was wetted on both sides. Characteristic results from measuring plane 4 are shown in Fig. 11. They illustrate that the velocity and temperature profiles in the gap can be calculated quite well. As the test section was not insulated during these studies, the temperature of the top wall was about 453 K. This was used in the numerical predictions as a boundary condition at the top wall. The coordinate of the grid point adjacent to the wall was optimized to be within $20 \leq y^+ \leq 40$.

The results for the pressure drops between measuring point 1, which is positioned at $x=0$ where the gap is starting to be parallel, and the other measuring points in the gap are shown in Fig. 12. Several flow rates of the liquid and two different gas temperatures are examined. While the pressure drop at low temperatures and evaporation rates can be predicted quite well, the differences between the numerical and the experimental results increase at elevated temperatures. Nevertheless the influence of the film flow rate on the pressure drop can be predicted at both gas temperatures.

A very significant test for the predicted interaction of the gas phase and the evaporating wavy liquid film can be obtained by comparing the measured and calculated thickness and velocity of the film. To determine the primary light intensity I_o for the film thickness measurements at elevated temperatures, an offset volume flux of the film flow of 0.09 cm^2/s was necessary for cooling the glass of the detector in the prefilming plate. As Figs. 13 and 14 with the data in plane 4 show, the differences between the measured and calculated film thicknesses and film velocities are acceptable. At high flow rates of liquid the measured velocities show the same characteristics as at cold conditions (Fig. 10): The film flow is not in the range of stability at this high flow rates. At low flow rates the experimental and numerical results for the film thicknesses and velocities agree quite well. Further investigations will have to examine if the increasing differences at elevated flow rates are an effect of the numerical code for the turbulent gas phase and the liquid film, or if the structure of the film is changing significantly at higher temperatures, so that the correlations

Downloaded 02 Jun 2010 to 171.66.16.112. Redistribution subject to ASME license or copyright; see http://www.asme.org/terms/Terms_Use.cfm

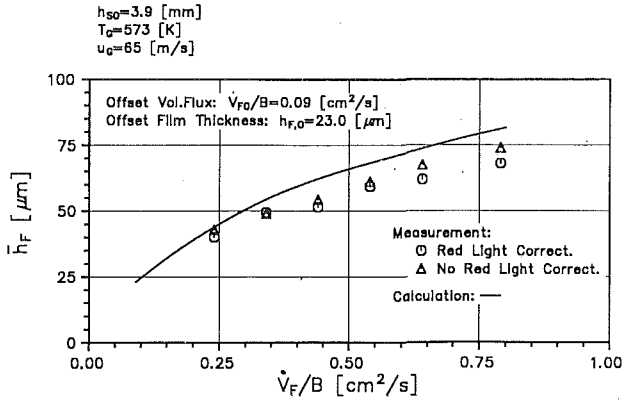


Fig. 13 Experimental and numerical results of the film thickness in plane 4

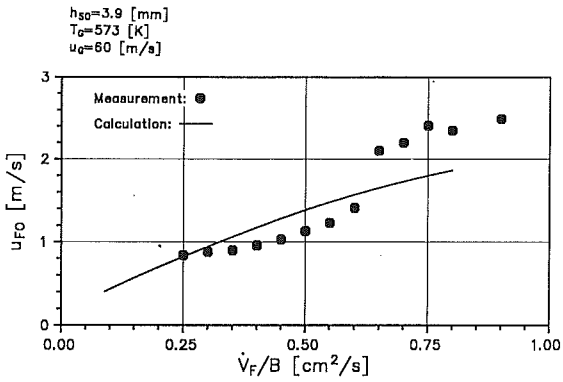


Fig. 14 Experimental and numerical results of the film surface velocity in plane 4

of ψ_τ would have to be modified. Before this can be done, a series of film thickness measurements at various gas temperatures and velocities and with various liquids will be necessary. In spite of the minor differences we feel that the numerical code can be used in practical applications.

Conclusions

The behavior of wavy liquid films can be described with acceptable accuracy by employing time-averaged velocity profiles of the film. Comparing measured time-averaged film thicknesses and film surface velocities with numerical results of a laminar and a turbulent velocity profile for the film, the film flow was found to be almost laminar within the range of stability of the film. The turbulent air and the waviness of the film do not induce significant turbulence into the film. Using a standard numerical code for the turbulent gas phase and a laminar profile for the film velocity, the interaction of the film and the gas phase can be estimated at cold conditions as well as at high-temperature conditions. The developed optical film thickness and film velocity measuring instrument is a very useful tool to examine the effects at the interface between the gas and the liquid.

Acknowledgments

The present study was supported by a grant from the SFB 167 (high-intensity combustors) of the Deutsche Forschungsgemeinschaft.

References

Aigner, M., and Wittig, S., 1985, "Performance and Optimization of an Airblast Nozzle: Drop Size Distribution and Volumetric Air Flow," *Proceedings of the International Conference on Liquid Atomization and Spray Systems*, London, United Kingdom, pp. IIC/3, 1–8.

Aigner, M., 1986, "Charakterisierung der bestimmenden Einflußgrößen bei der Luftgestützten Zerstäubung: Physikalische Grundlagen und meßtechnische Erfassung," Dissertation, Universität Karlsruhe, Institut für Thermische Strömungsmaschinen, Germany.

Aigner, M., and Wittig, S., 1988, "Swirl and Counterswirl Effects in Prefilming Airblast Atomizers," ASME JOURNAL OF ENGINEERING FOR GAS TURBINES AND POWER, Vol. 110, pp. 105–110.

Bauer, H.-J., 1989, "Überprüfung numerischer Ansätze zur Beschreibung turbulenter elliptischer Strömungen in komplexen Geometrien mit Hilfe konturangepaßter Koordinaten," Dissertation, Universität Karlsruhe, Institut für Thermische Strömungsmaschinen, Germany.

Cebeci, T., and Bradshaw, P., 1977, *Momentum Transfer in Boundary Layers*, Hemisphere Publishing Co., Washington, DC.

Cohen, L. S, and Hanratty, Th. J., 1968, "Effect of Waves at a Gas-Liquid Interface on a Turbulent Air Flow," *J. Fluid Mech.*, Vol. 31, pp. 467–479.

Hale, G. M., and Querry, M. R., 1973, "Optical Constants of Water in the 200 nm to 200 μm Wavelength Region," *Applied Optics*, Vol. 12, No. 3.

Jurman, L. A., and McCready, M. J., 1989, "Study of Waves on Thin Liquid Films Sheared by Turbulent Gas Flows," *Phys. Fluids*, Vol. A1(3), pp. 522–536.

Lefebvre, A. H., 1980, "Airblast Atomization," *Prog. Energy Combust. Science*, Vol. 6, pp. 233–261.

Ligrani, P. M., 1989, "Structure of Turbulent Boundary Layers," *Enclyclopedia of Fluid Mechanics*, Vol. 8, Golf Publishing Company, Houston, TX (ISBN 0-87201-542-4), pp. 111–189.

Noll, B., 1986, "Numerische Berrechnung brennkammertypischer Ein- und Zweiphasenströmungen," Dissertation, Universität Karlsruhe, Institut für Thermische Strömungsmaschinen, Germany.

Patankar, S. V., 1980, *Numerical Heat Transfer and Fluid Flow*, Hemisphere Publishing Corp., Washington, DC.

Renz, U., 1971, "Verdunstung mit und ohne Zerfallsreaktionen der Flüssigkeit," Dissertation, Universität Stuttgart, Institut für Thermodynamik der Luft- und Raumfahrt, Germany.

Rüd, K., 1985, "Transitionale Grenzschichten unter dem Einfluß hoher Freistromturbulenz, intensiver Wandkühlung und starken Druckgradienten in Heißgasströmungen," Dissertation, Universität Karlsruhe, Institut für Thermische Strömungsmaschinen, Germany.

Sattelmayer, Th., 1985, "Zum Einfluß der ausgebildeten, turbulenten Luft-Flüssigkeitsfilm-Strömung auf den Filmzerfall und die Tropfenbildung am Austritt von Spalten geringer Höhe," Dissertation, Universität Karlsruhe, Institut für Thermische Strömungsmaschinen, Germany.

Sattelmayer, Th., and Wittig, S., 1986, "Internal Flow Effects in Prefilming Airblast Atomizers: Mechanisms of Atomization and Droplet Spectra," ASME JOURNAL OF ENGINEERING FOR GAS TURBINES AND POWER, Vol. 108, pp. 465–472.

Sattelmayer, Th, Sill, K. H., and Wittig, S., 1987, "Optisches Meßgerät zur Bestimmung der Eigenschaften welliger Flüssigkeitsfilme," *Technisches Messen tm*, Vol. 54, No. 4, pp. 155–160.

Sattelmayer, Th., and Wittig, S., 1989, "Performance Characteristics of Prefilming Airblast Atomizers in Comparison With Other Airblast Nozzles," *Encyclopedia of Fluid Mechanics*, Vol. 8, Golf Publishing Company, Houston, TX (ISBN 0-87201-542-4), pp. 1091–1141.

Schultz, K.-J., 1976, "Theoretische und experimentelle Untersuchung einer turbulenten ebenen Zweistoffgrenzschicht längs eines verdunstenden Flüssigkeitsfilms," Dissertation, Universität Kaiserslautern, Germany.

Sheintuch, M., and Dukler, A. E., 1989, "Phase Plane and Bifurcation Analysis of Thin Wavy Films Under Shear," *AIChE Journal*, Vol. 35, No. 2, pp. 177–186.

Sill, K. H., 1982, "Wärme- und Stoffübergang in turbulenten Strömungsgrenzschichten längs verdunstender welliger Wasserfilme," Dissertation, Universität Karlsruhe, Institut für Thermische Strömungsmaschinen, Germany.

Spalding, D. B., 1977, *Genmix—A General Computer Program for Two-Dimensional Parabolic Phenomena*, Pergamon Press, Oxford, United Kingdom.

Spalding, D. B., and Patankar, S. V., 1967, *Heat and Mass Transfer in Boundary Layers*, Morgan-Grampian, London, United Kingdom.

Whalley, P. B., 1987, *Boiling, Condensation and Gas-Liquid Flow*, Clarendon Press, Oxford, United Kingdom.

Wittig, S., Leuckel, W., Sakbani, K., Aigner, M., Horvay, M., and Sattelmayer, Th., 1984, "Experimentelle und theoretische Untersuchung der Strömung und Tropfenbildungsmechanismen in Zerstäubungsdüsen für Gasturbinenbrennkammern," *Forschungsvereinigung Verbren nungskraftmaschinen (FVV)*, Abschlußbericht, Vol. 347.

Wittig, S., Klausmann, W., Noll, B., and Himmelsbach, J., 1988, "Evaporation of Fuel Droplets in Turbulent Combustor Flow," ASME Paper No. 88-GT-107.

Wurz, D., 1971, "Experimentelle Untersuchung des Strömungsverhaltens dünner Wasserfilme und deren Rückwirkung auf einen gleichgerichteten Luftstrom mäßiger bis hoher Unterschallgeschwindigkeit," Dissertation, Universität Karlsruhe, Institut für Thermische Strömungsmaschinen, Germany.

Downloaded 02 Jun 2010 to 171.66.16.112. Redistribution subject to ASME license or copyright; see http://www.asme.org/terms/Terms_Use.cfm

G. D. Myers
Senior Engineer,
Combustion, Aero/Thermo
Component Design.

J. P. Armstrong
Senior Engineer,
Mechanical Component Design.

C. D. White
Senior Engineer,
Advanced Technology Project.

Garrett Engine Division,
Allied-Signal Aerospace,
Phoenix, AZ 85010

S. Clouser
Naval Air Propulsion Center,
Trenton, NJ 08628

R. J. Harvey
Senior Design Engineer,
Delavan, Inc.,
West Des Moines, IA 50265

Development of an Innovative High-Temperature Gas Turbine Fuel Nozzle

The objective of the innovative high-temperature fuel nozzle program was to design, fabricate, and test propulsion engine fuel nozzles capable of performance despite extreme fuel and air inlet temperatures. Although a variety of both passive and active methods for reducing fuel wetted-surface temperatures were studied, simple thermal barriers were found to offer the best combination of operability, cycle flexibility, and performance. A separate nozzle material study examined several nonmetallics and coating schemes for evidence of passivating or catalytic tendencies. Two pilotless airblast nozzles were developed by employing finite-element modeling to optimize thermal barriers in the stem and tip. Operability of these prototypes was compared to a current state-of-the art piloted, prefilming airblast nozzle, both on the spray bench and through testing in a can-type combustor. The three nozzles were then equipped with internal thermocouples and operated at 1600°F air inlet temperature while injecting marine diesel fuel heated to 350°F. Measured and predicted internal temperatures as a function of fuel flow rate were compared. Results show that the thermal barrier systems dramatically reduced wetted-surface temperatures and the potential for coke fouling, even in an extreme environment.

I Introduction

To meet the U.S. Department of Defense IHPTET (integrated high-performance turbine engine technology) program goal of doubling current aircraft propulsion capability by year 2000, future military gas turbines must demonstrate both higher thrust-to-weight ratios and lower specific fuel consumption. Commercial aircraft operators, facing increased fuel costs and stiff competition, share this desire for reduced weight and higher efficiency. Military and commercial interests will also expect improved reliability and maintainability from their advanced engines. The reliability of these power plants will depend, in part, on fuel injection systems that resist coke fouling in spite of the higher combustor inlet temperatures and heat loadings required for increased performance. The provision of fuel flexibility for the military, and the option of lower-cost, heavy distillate commercial fuels further increases the potential for coking. Another complication is the trend toward use of the fuel as a heat sink for cooling the airframe, avionics, and the power plant itself, resulting in higher fuel temperatures at the nozzle inlet. The specific goals of the program, which are summarized in Table 1, drive the technical challenges outlined in Fig. 1.

Work was divided into four tasks over the course of the three-year effort. The concept identification/evaluation task employed a literature search to characterize the fuel thermal decomposition process and identify coke-resistant and coke-tolerant materials and technologies. A screening process and detailed evaluation of the most promising techniques then followed. Two candidates were selected for the detailed design task at the end of the first task. Fuel nozzles representing the

Table 1 Fuel nozzle design criteria

Parameter	Goal
Combustor Inlet Temperature	1600F
Fuel Temperature at Nozzle	350F
Fuel Types	JP-5, Marine Diesel (DFM)
Combustor Performance: Stability (LBO), Ignition, Combustion Efficiency, Exit Temperature Profile	Meet or Exceed Current Levels Throughout Flight Envelope
Applicable Engine Cycle	Turbojet, Turbofan, Turboprop, Turboshaft (All)

Contributed by the International Gas Turbine Institute and presented at the 36th International Gas Turbine and Aeroengine Congress and Exposition, Orlando, Florida, June 3-6, 1991. Manuscript received at ASME Headquarters February 6, 1991. Paper No. 91-GT-36. Associate Editor: L. A. Riekert.

Copyright © 1992 by ASME
Downloaded 02 Jun 2010 to 171.66.16.112. Redistribution subject to ASME license or copyright; see http://www.asme.org/terms/Terms_Use.cfm

two finalists were detailed and manufactured during the second task. The nozzle performance testing task compared both candidates to a current state-of-the art nozzle design. Spray quality measurements and nozzle performance tests in a high-pressure combustion rig were conducted. Finally, the internal temperature distribution for both candidates and the baseline nozzle were measured as a function of fuel flow rate by operating each nozzle at the conditions outlined in Table 1. Following is a detailed discussion of each task.

II Concept Identification/Evaluation

The purpose of this task was to gather information on the basics of the coke deposition process, as a foundation for gathering deposit-resistant and/or deposit-tolerant technology and materials. This information was summarized by assembling a number of nozzle concepts, each employing one or more of the techniques identified, for further analysis. A screening process then identified the two concepts most likely to satisfy all of the program goals.

The concept identification phase of the program also included an investigation of coking properties for several engineering materials. Although similar studies were identified in the literature (Smith, 1967; Johnston and Morita, 1968) few data were available for recently developed passivation techniques and coatings in general, and ceramics in particular. This study attempted to identify a material for use in the wetted portion of the nozzle that would inhibit thermal breakdown of the fuel and/or discourage adhesion of solids formed in the free stream. Ceramic materials, thought to be of some value for their low conductivity and emissivity, were also checked for evidence of either passivating or catalytic properties.

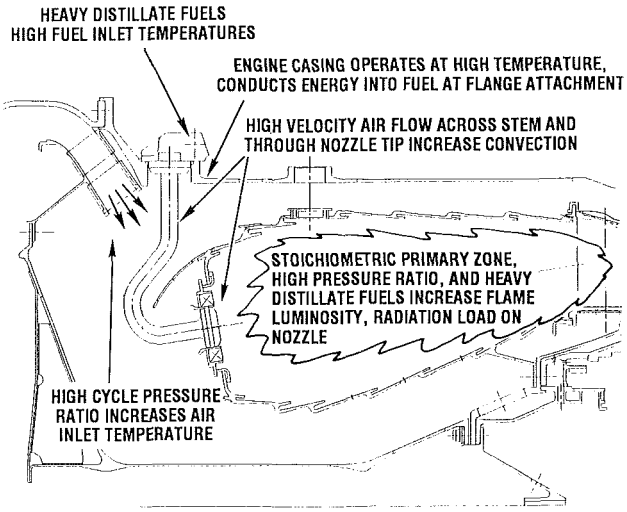


Fig. 1 Future propulsion engine fuel nozzles will encounter severe coking environment

Eight materials, including four metals (two of them treated) and four ceramics, were chosen: (1) SS316, a corrosion-resistant stainless steel often used in fuel systems, was a baseline. (2) SS416, a harder stainless steel, is used in portions of the nozzle that require erosion resistance. (3) A second SS416 coupon was passivated by exposure to hydrogen sulfide-doped helium at high temperature, a process developed for treating oil refinery components. (4) A third SS416 sample was coated with EYMYD, a fluorinated polyamide similar to Teflon. (5) PSZ (partially stabilized zirconia), a tough ceramic with low conductivity (1.3 Btu/ft-hr-F), and a thermal expansion rate similar to metals. (6) MACOR, a machinable silica-based ceramic. (7) LAS (lithium–aluminum–silicate), a crystallized glass with very low thermal conductivity. (8) Fused silica, a widely available amorphous glass, with good high-temperature strength and insulating properties.

Rectangular coupons approximately 5 in. long, 0.300 in. wide, and 0.125 in. thick, were fashioned out of each material. A groove 0.185 in. wide and 0.050 in. deep was machined down the center of each coupon to carry the hot fuel. Surface roughness in the groove, measured in the flow direction, was 22 μin./in. for the metal coupons, and ranged from 6 for the fused silica to 17 for the MACOR. All eight coupons were sandwiched between the halves of an SS307 block, equipped with fittings to conduct fuel through the groove in the coupons. A gasket prevented leakage from the block and communication between the coupons.

Marine diesel fuel (DFM) with a JFTOT breakpoint temperature of 400°F was used for the evaluation. Fuel was heated to 540°F by passage through a coil of aluminum tubing immersed in a barrel of thermal fluid maintained at 550°F by electric heating elements. The sample holder was maintained at 540°F by an electric heater, and heavily insulated to ensure uniform temperatures throughout. Fuel residence time in the aluminum heating coil was approximately 25 seconds; the Reynolds number for fuel inside the coil was above 10,000. Fuel residence time across the samples was 0.54 second. The local bulk velocity was 0.75 ft/sec, and the Reynolds number, based on the channel dimensions, was 1000. The fuel pressure was maintained at 75 psia to prevent boiling. The samples were exposed for 22 hours.

The coupons were dried and carefully weighed prior to the test, and the reflectance at one end and in the middle of each groove was measured using an optical densitometer. The coking ranged from hazy coffee-stain-like deposits on the SS316 and the ceramic materials to jet-black "sandbars" on the SS416. The quantitative results appear in Table 2. Based on the weight change of the SS416, site of the heaviest deposits, a coking rate of just over 20 μg/hr cm^2 was observed. This is consistent with measurements quoted by Marteney and Spadaccini (1986) for a wetted-surface temperature of 540°F.

The following conclusions were drawn from the evaluation. First, none of the materials tested outperformed SS316, a previously proven coke-resistant material. Second, coking rates

Table 2 Nozzle materials test results

Material	Weight Before, Grams	Weight After, Grams	Weight Change, mg	Reflect. Before	Reflect. After	Reflect. Delta, Mid	Sur. Fin.	Comments	Rank
SS316	19.6479	19.6487	0.08	14.8	7.6	-48.65%	22	Haze of Coke	1
SS316 EYMYD	19.5476	19.5495	1.9	8.9	4.5	-49.44%	22	Dark Streaks	6
SS416	18.9841	18.9877	3.6	9.5	3.5	-63.16%	23	Uniformly Black	8
SS416 Passiv	18.7625	18.7634	0.9		1.7		22	Patchy Black	7
LAS	6.0745	Broke	--	66.6	31.5	-52.70%	10	Stained	5
SIO	5.3728	Broke	--	6.9	6.1	-11.59%	6	Stained	3
MACOR	6.162	Broke	--	58.7	27.2	-53.66%	17	Stained	4
PSZ	14.7169	14.7179	1.0	48.4	28.5	-41.12%	15	Stained	2

Downloaded 02 Jun 2010 to 171.66.16.112. Redistribution subject to ASME license or copyright; see http://www.asme.org/terms/Terms_Use.cfm

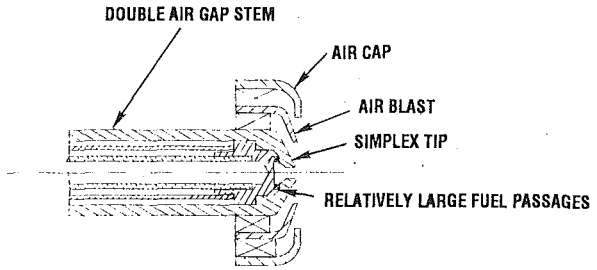


Fig. 2 The simplex-airblast prototype combines two proven forms of atomization, multiple air gap thermal protection

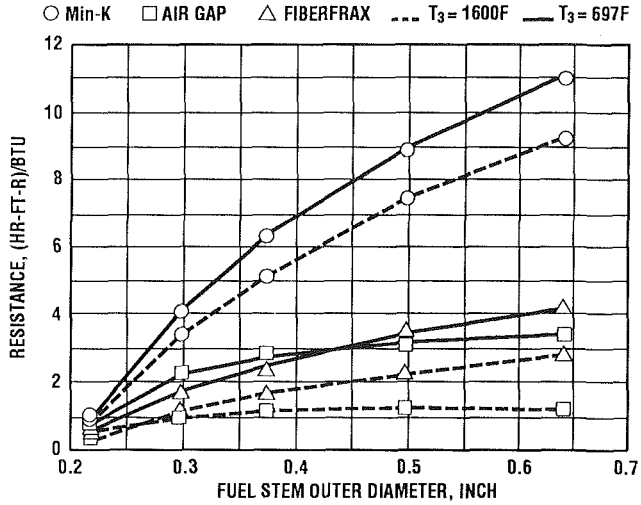


Fig. 3 Air gaps can be an effective thermal barrier to heat absorption in the injector stem

for the ceramics were nearly equivalent to those for SS316. With regard to coking alone, these materials can be used interchangeably. Similar results for both metals and nonmetals suggest that surface chemistry plays a limited role when no outright catalysts are present. This implies that coating or otherwise changing the surface of such materials will not be effective, at least in the temperature and flow range studied.

III Detailed Design

The Simplex-Airblast Prototype. A cross section of the simplex-airblast design is shown in Fig. 2. Atomization is accomplished by using a swirling flow of high-velocity air to shatter the conical fuel sheet emitted from a high-flow simplex tip, combining two widely used techniques in a single-circuit pilotless design. The airblast allows larger contamination-tolerant passages to be used in the simplex part of the nozzle, and improves patternation at high power settings. The thorough fuel/air mixing and other familiar benefits of airblast atomization are also realized. The smallest fuel passage dimension in this simplex-airblast is more than three times the minimum commonly found in piloted nozzles. Despite the large passages, the simplex portion of the nozzle is still capable of producing an "onion" or "tulip" structure at very low fuel pressure drops typical of ignition conditions. This is an advantage over purely prefilming nozzles.

A multiple air-gap thermal barrier insulates fuel-wetted surfaces in the simple-airblast prototype, both in the stem and tip regions. Use of the air gap, which allows a relatively simple all-metal construction, was suggested by an analysis of several approaches to fuel-stem insulation. GED's F125-GA-100 afterburning turbofan nozzle (baseline) was used for the stem geometry and length. This nozzle and the F125-GA-100 combustion system are described by Sanborn (1989). An eight-point engine cycle, consistent with the flight envelope of an

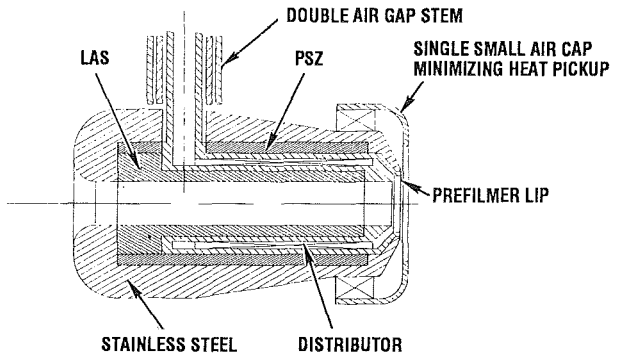


Fig. 4 The ceramoblast prototype is a prefilming, pure airblast design with monolithic ceramic insulation

advanced demonstrator engine, was derived for the analysis, with 350°F fuel and 1600°F air inlet temperatures at the design point. A cycle pressure ratio of more than 50:1 was required to obtain the desired combustor inlet temperature of 1600°F. This cycle is similar to those envisioned for future generations of the joint technology advanced gas generator (JTAGG) program. The conditions studied gave a fuel Reynolds number range from 1700 to 137,000, and an external air flow Reynolds number range from 34,000 to 324,000. Fuel properties were for JP-5.

One-dimensional radial heat flow, and steady-state, constant-property flow of both the fuel and air were assumed. In addition to the baseline case, the effect of increasing the gap between fuel-carrying tubes and the outer heat shield was investigated, both for the plain air-gap case, and with insulating materials inserted in that gap. Two excellent insulators, Carborundum's Fiberfrax ($k = 1.29$ Btu-in/hr-ft^2°F) and Manville's Min-K ($k = 0.37$ Btu-in/hr-ft^2°F at 1200°F) were selected for the analysis.

Figure 3 plots the total resistance of the fuel stem as a function of stem outer diameter for the three different barriers studied at two cycle points. The dashed lines are for a high-altitude, high-Mach number dash point, with combustor inlet temperature of 1600°F. The solid lines are for a subsonic cruise condition with inlet temperature of 700°F. The effectiveness of the air gap is comparable to that for the Fiberfrax insulation, but it deteriorates as the inlet temperature increases due to the increased radiative exchange between the outer heat shield and fuel tube through the air gap. Air gap conductivity is an effective value, based on both thermal conduction through the air and radiative exchange between the concentric cylinders. The Fiberfrax insulation is only marginally better than an air gap at the baseline stem dimensions, and the insulation is actually less effective for some stem diameters. Min-K, however, outperformed the air gap for the conditions studied. Generally speaking, insulator conductivity at or below 0.50 Btu-in/hr-ft^2°F is required to consistently better the effectiveness of a practical air gap. Another factor favoring air gaps is the dramatic reduction of effectiveness that both insulators suffer when contaminated with water, fuel, or other liquids.

The Ceramoblast Prototype. Figure 4 shows an annotated cross section of the second prototype. This nozzle is a single-circuit airblast design that uses both air gaps and monolithic-ceramic insulating materials to protect fuel-wetted parts. The well-established prefilming technique (Lefebvre, 1983) is used to produce a high-quality hollow cone spray. Recirculation zones and other stagnant spots in the fuel side of the nozzle that would contribute to deposit formation have been eliminated in the distributor by avoiding the sharp transitions, annular manifolds, and cross-drilling often found in these parts. Each passage is a continuous, smooth conduit from the stem exit to the prefilmer entrance, represented by the long crosses in the diagram.

Downloaded 02 Jun 2010 to 171.66.16.112. Redistribution subject to ASME license or copyright; see http://www.asme.org/terms/Terms_Use.cfm

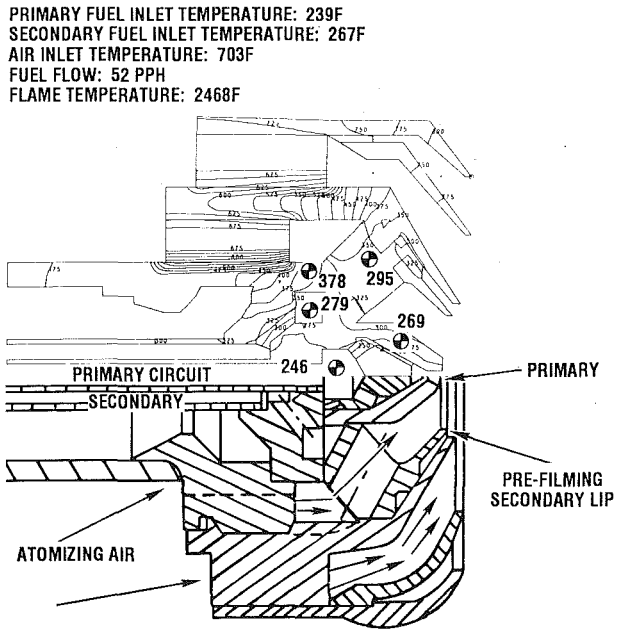


Fig. 5 Delavan piloted airblast design is state-of-the-art nozzle used in baseline afterburning turbofan

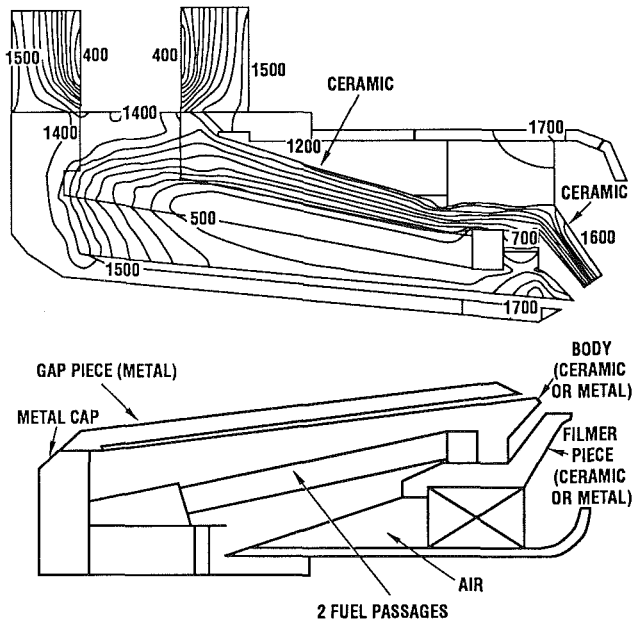


Fig. 6 Placement of thermal barriers and material choices are studied in model of pure airblast tip

The thermal protection scheme devised for the ceramoblast employs two of the monolithic ceramics studied in the materials experiment, PSZ and LAS. LAS is used for the inner heat shield because of its low coefficient of thermal expansion in comparison to the surrounding metal parts. PSZ is used for the outer heat shield because its coefficient of expansion is compatible with aerospace steels. Standoffs were machined into the metal parts, minimizing the contact between the insulation and fuel distributor, and providing air gaps on either side. An air gap was also placed between the prefilming lip and outer shell.

Location of insulation inside the nozzle was suggested by thermal studies of the baseline nozzle tip, and a generic prefilming pure-airblast tip similar to the ceramoblast design. A pseudo-three-dimensional model of both tips was generated, including all conduction paths, fuel and air convection, and the effect of flame radiation. The finite-element model of the nozzle tip was generated using an in-house quasi-three-dimensional thermal analyzer code. Axisymmetric elements allowed conduction in two directions and nonaxisymmetric elements were thermally linked in the tangential direction assuming a half-width conduction length. Additional convection faces were assigned to axisymmetric elements that bordered nonaxisymmetric elements. The boundary conditions were assumed to be convective everywhere except at the combustor-facing portion of the nozzle, where a flame radiation boundary condition was applied using a standard luminous flame correlation. The isotherms calculated are representative of the temperature midway circumferentially between the nonaxisymmetric elements. An instrumented baseline nozzle was operated in a combustion rig to verify the model predictions.

The baseline nozzle's excellent performance in rig and engine testing, and similar size and application to that envisioned for the two prototypes, made it a logical candidate for comparison throughout the program. The baseline nozzle employs a prefilming airblast secondary circuit (flow number = 18) for operation above idle throttle settings, and a pressure-swirl pilot (flow number = 2) for starting. (Flow number equals fuel flow [pph] divided by the square root of the pressure drop.) A cross section of the nozzle tip is shown in Fig. 5, beside a mirror-image contour plot of the predicted temperatures for an engine idle condition. Measured temperatures are also indicated in the figure, and compare favorably with the predicted values.

The contour plot provides a useful illustration of the distribution of heat energy and potential coking sites in the tip. Study of the baseline nozzle suggested that the two major sources of energy absorption in the nozzle were the air swirl vanes and any surface exposed to the flame. At an altitude cruise point, for example, the predicted heat flux entering the nozzle face from flame radiation is more than 20 times that absorbed by conduction and convection through the stem. The frontal area observing the flame is thus a key element in nozzle thermal loading. Although the fuel temperature rise amounted to less than 20 deg from inlet to exit for the worst case, surfaces in the secondary circuit rose significantly above the fuel temperature.

A second modeling effort was conducted using a generic prefilming, pure-airblast tip, very close to the configuration that eventually became the ceramoblast nozzle. Simplified two-dimensional axisymmetric geometry was employed to allow numerous combinations of materials to be studied. Figure 6 illustrates the major components of the concept and predicted temperature contours for the case where the fuel-carrying portion of the nozzle tip is a low-conductivity monolithic ceramic. The boundary conditions for the plot are from the altitude cruise point, with 1600°F combustor inlet temperature. Several conclusions that applied to the ceramoblast design were drawn from this study. In the generic stem/tip attachment scheme, the stem protection system, either an air gap or an insulating material, was terminated upstream of the stem/tip interface, for ease of manufacture. The modeling effort showed that the stem protection scheme must be brought down into the tip area to avoid conducting heat from the stem outer heat shield into the fuel-carrying stem-tip attachment. Both metal and ceramic prefilmers were studied. The ceramic prefilmer reduced the wetted-surface temperature several hundred degrees, and cut the fuel temperature rise in half. However, the severe thermal gradient across the part was beyond the mechanical capacity of the material.

Results of these thermal studies are reflected in the ceramoblast design. Although monolithic ceramics are used to avoid the possibility of fuel contamination associated with the Fiberfrax and Min-K materials, air gaps supplement both ceramic elements. A double air gap is employed in the stem and between the metallic prefilmer and outer case. The metallic distributor

Downloaded 02 Jun 2010 to 171.66.16.112. Redistribution subject to ASME license or copyright; see http://www.asme.org/terms/Terms_Use.cfm

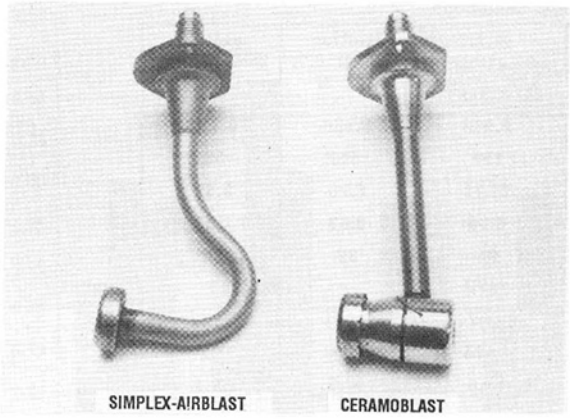


Fig. 7 Prototypes are similar to production baseline nozzle in size and weight

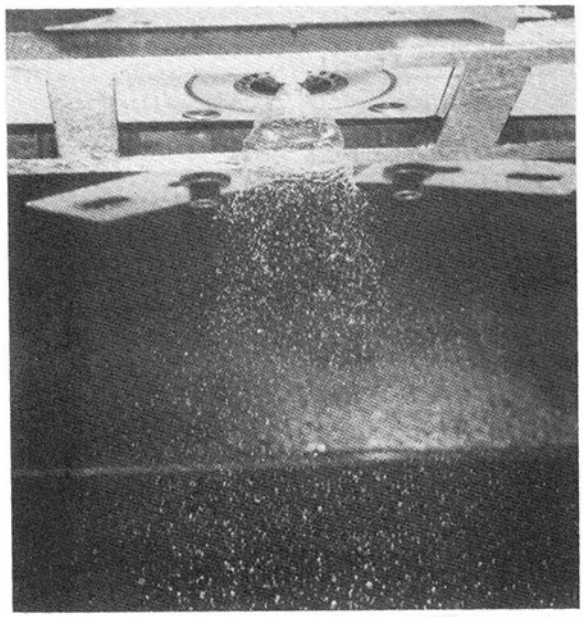


Fig. 8 Simplex-airblast prototype on spray bench flowing 20 pph with no airblast flow

is joined directly to the fuel-carrying inner tube; the stem inner heat shield continues into the tip. The outer heat shield is captured from the flange end of the stem and does not contact the tip. A single air swirler, made as small as possible, is placed at the extreme end of the tip. The vanes are undercut at the hub to reduce conduction from the air cap further. Frontal area of the fuel-carrying parts is minimized. The ceramoblast and simplex-airblast nozzles are compared in Fig. 7.

IV Nozzle Performance Testing

The purpose of this task was to determine the spray quality of the two prototypes over a significant operating range, and to determine the impact on operability of the single-circuit, coke-tolerant designs by operating both prototypes and the baseline nozzle in a high-pressure combustion rig. Flow number, spray cone angle, patternation, and mean drop size were measured over a significant range of air-pressure drops and fuel-flow rates. Spray measurements were performed using a Malvern Model 2600 instrument. Both standard MIL-C-7024 (1) and cold (12 centistoke viscosity) calibrating fluids were used. The flow number is 18 for the ceramoblast nozzle and 15 for the simplex-airblast. The atomizer is installed in a plenum box, which allows the pressure drop across the airside of the

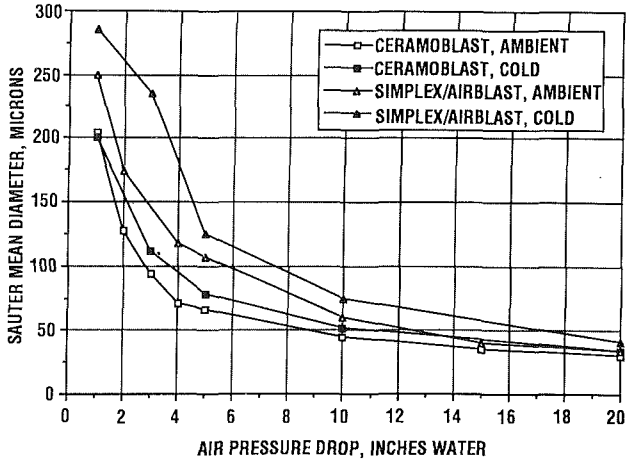


Fig. 9 Candidates demonstrate good spray quality in spite of single-circuit design

nozzle to be measured and varied. The nozzle is installed vertically, spraying downward into a vented drain. The simplex-airblast prototype is shown installed in the spray booth in Fig. 8.

Spray cone angle was consistently wider for the prefilming nozzle. The ceramoblast cone angle varied between 160 deg at ignition conditions (20 pph and 2 in. of water air pressure drop) and 110 deg at a high-power condition (250 pph and 60 in. of water). The simplex-airblast nozzle produced an angle of 75 deg at ignition, narrowed to 60 deg at the higher power condition. Air-cap dimensions can be adjusted to manipulate the spray angle for both nozzles, depending on the specific requirements of the system. Patternation tests showed a hollow cone spray for both nozzles. The ceramoblast showed the characteristic air-blast spray, with narrow inner cone angle and the mass flux evenly distributed across the base of the cone. The simplex nozzle showed a much more sharply peaked distribution, later reflected in the combustor exit temperature measurements. Sauter Mean Diameter of the spray at a 20 pph ignition fuel flow is plotted against the nozzle air pressure drop for the two prototypes for both standard and cold fluids in Fig. 9. The air/liquid ratio is the same for both nozzles at each pressure drop, since the air-flow area is identical. The 12-centistoke fluid does not have a significant impact on spray quality for either nozzle. As expected, the more complex prefilming technique produces the finest spray at all pressure drops. With no air flow, the simplex tip still produces an open spray cone; the ceramoblast does not.

Following the spray testing, each nozzle was evaluated for combustor performance. The scope of the program prevented tests in a full-scale, multiple-nozzle, high-pressure burner rig. Since only a single nozzle system could be tested, a can liner was modified to accept the prototypes and baseline nozzles. The dome has been modified to accept an axial swirler that co-rotates with both the dome louvres and the nozzle swirlers. A schematic of the rig is shown in Fig. 10. The fuel nozzle slip-fits through the dome swirler at the tip end and, using a metal compression gasket, bolts to an engine-plenum-style flange. Although the can had little in common with the full-annular system of an advanced demonstrator engine, the nozzle tested concurrently has a long history in both full-scale rig and engine tests. Comparison with this nozzle is thus a key link to the environment for which the prototypes were designed. The lean-stability, exit-temperature pattern factor and the combustion efficiency were measured for each of the cycle conditions summarized in Table 3 during the first sequence of tests, using both the JP-5 and DFM fuels. The reference velocity used in Table 3 is based on the can combustor flow area

Downloaded 02 Jun 2010 to 171.66.16.112. Redistribution subject to ASME license or copyright; see http://www.asme.org/terms/Terms_Use.cfm

Table 3 Combustion rig test conditions

Test Condition	Design, SLS	Cruise MCP, 10K, M=0.3	Idle, SLS	Alt. Decel. 20K, M=0.7	Ignition 16K, M=0.2, 10% N	Ignition 25K, M=0.2, 15% N
WA3, lb/sec	3.975	2.930	1.520	0.936	0.136	0.137
T3, F	500F	444	208	185	−55F	−52F
P3, psia	133.0	95	41.0	23.72	8.20	5.60
ΔP/P, percent	5	5.04	5.51	6.06	0.68	1.51
Wf, pph	250	171	50	25	20	20
EGT, F	1648	1525	866	727F	—	—
Far, total	0.0175	0.0162	0.0091	0.0074	0.041	0.041
Loading	0.131	0.192	0.675	1.125	1.64	3.2
VRef, ft/sec	81	78.4	69.8	71.6	18.9	28.1

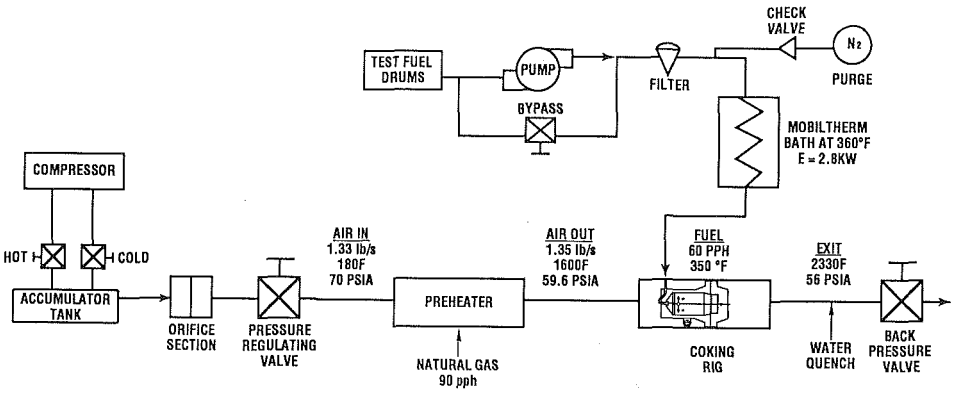


Fig. 10 High-temperature fuel nozzle test rig

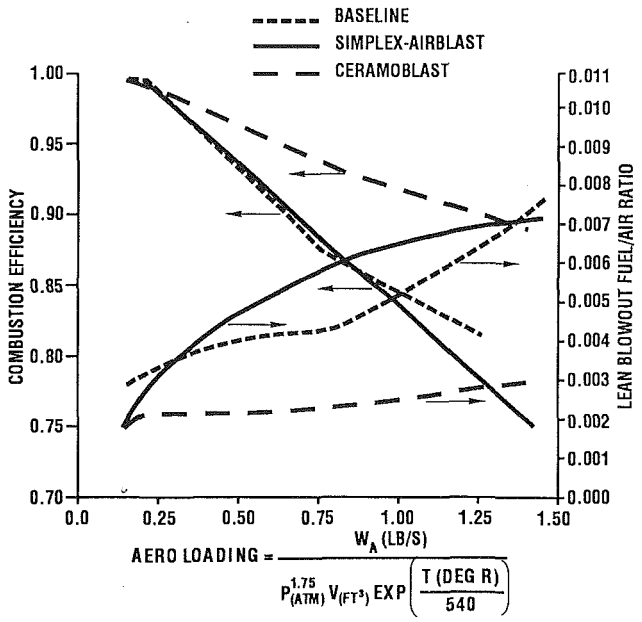


Fig. 11 Lean blowout and combustion efficiency measured for prototype nozzles compare favorably to baseline performance

and on the gas inlet temperature, pressure, and flow rate. The loading parameter is defined in Fig. 11.

The rig was equipped with multipoint thermocouples and kiel probes to measure inlet and exit pressures and temperatures. A propane-fired preheater set immediately upstream of the liquid-fueled can was used to achieve the 1600°F inlet temperatures. A water-cooled back-pressure valve was used to set rig pressure. Micro-Motion mass-flow sensors were used to measure fuel flow. Air flow was measured across standard ASME orifice sections. A methanol/dry-ice slurry was used to chill the fuels to the 12-centistoke point for cold-ignition tests. Combustion efficiency was calculated from a carbon balance by sampling the exhaust using industry standard nondispersive infrared analyzers for CO and CO_2, and a flame ionization detector for UHC. The gas sample was drawn through the rig exit pressure measuring ports.

Combustion efficiency and lean blowout fuel/air ratio are plotted against aerodynamic loading (Fig. 11) for both prototypes and the baseline nozzle. Lean stability and combustion efficiency for the prototypes are similar to those for the piloted nozzle, in spite of the much finer atomization available at low fuel flows with the baseline nozzle pilot. The highest stability and combustion efficiency were measured for the ceramoblast because it combines fine atomization with a very wide spray angle. The DFM's lower volatility is reflected in the generally higher fuel/air ratios required to keep the combustor alight, but neither prototype shows a particular sensitivity to the fuel type.

The pattern factor results (Fig. 12) show more distinct differences. Sharp peaks in the patternation measured during bench testing of the simplex-airblast nozzle are reflected in its high pattern factor. The ceramoblast nozzle also showed higher pattern factor than the baseline nozzle at low fuel/air ratios, but improved to a comparable value at the higher cruise throttle setting. The pattern factor for both nozzles could be adjusted, in practice, by varying both the spray angle and combustor aerodynamics.

Ignition tests were conducted by presetting the desired inlet conditions and fuel flow, then diverting fuel from a chilled circulating loop into the combustor as soon as the ignitor was switched on. Steady increase in the exit temperature within 5 seconds was considered a successful light. A single igniter plug is used, with a spark rate of three per second and four joules

Downloaded 02 Jun 2010 to 171.66.16.112. Redistribution subject to ASME license or copyright; see http://www.asme.org/terms/Terms_Use.cfm

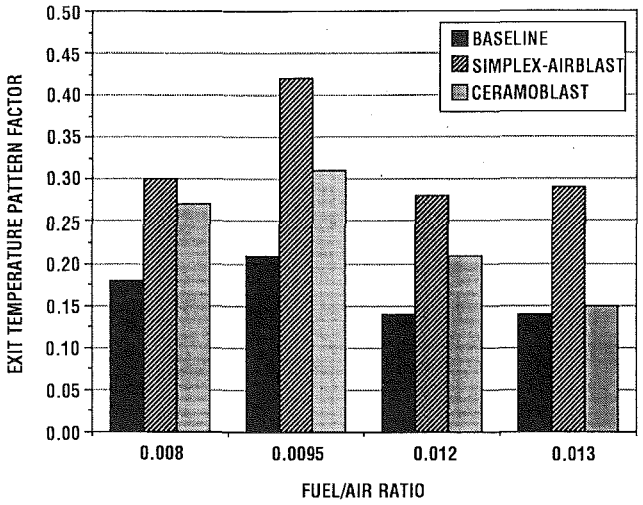


Fig. 12 Exit temperature profile for tested nozzles shows some patternation variation

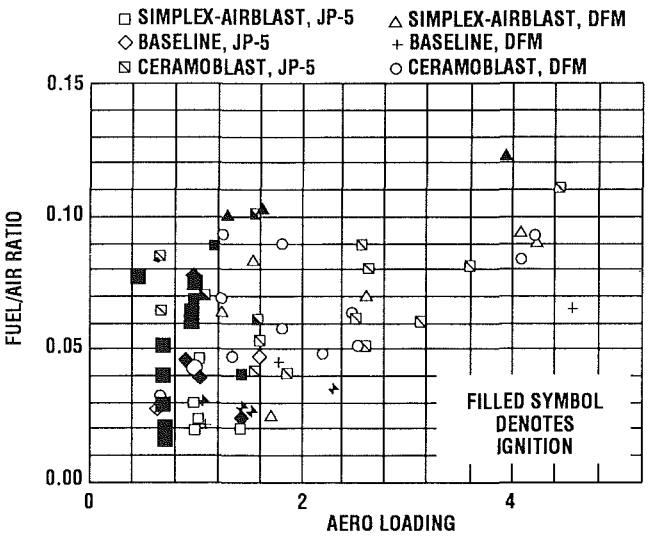


Fig. 13 Ignition results using cold fuel show that single-circuit, pure airblast designs require higher fuel/air ratio during start than does piloted nozzle

per pulse. Ignition fuel/air ratio versus aerodynamic loading is plotted for the three nozzles in Fig. 13. Although both prototypes required higher fuel/air ratios for ignition than did the piloted nozzle at the same loading, the range of operation for the simplex-airblast nozzle is roughly equivalent to the baseline design. Results for the ceramoblast were disappointing, given its excellent lean stability and finer spray quality. Similar experience (good stability, atomization quality, yet poor ignition) with other single-circuit, pure airblast prefilming nozzles in a variety of combustion systems suggests that some common characteristic of these nozzles may be at fault. The tendency of fine drops to be carried through the combustor primary zone and away from the igniter by the central atomizing air stream has been suggested as one explanation. Of the parameters checked, ignition characteristics are perhaps the most context-sensitive. Additional development would obviously be required to match the piloted ignition envelope with these single-circuit nozzles.

V High Temperature Testing

Each prototype was operated with hot JP-5 and DFM fuels at 1600°F air inlet temperature and 350°F fuel inlet temperature condition. Internal temperatures were measured for both

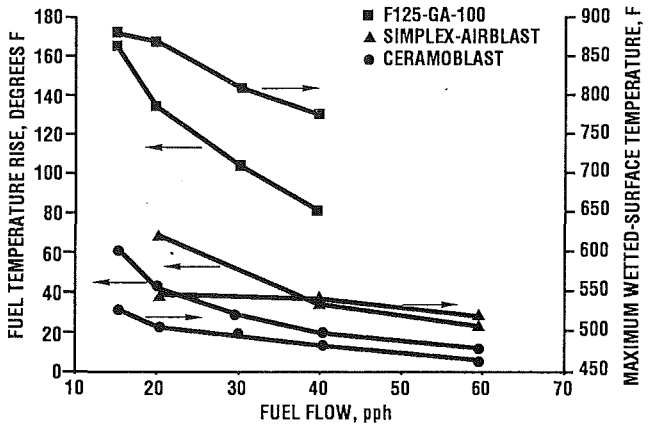


Fig. 14 Wetted-surface temperatures measured at severe test conditions show effectiveness of thermal barrier schemes

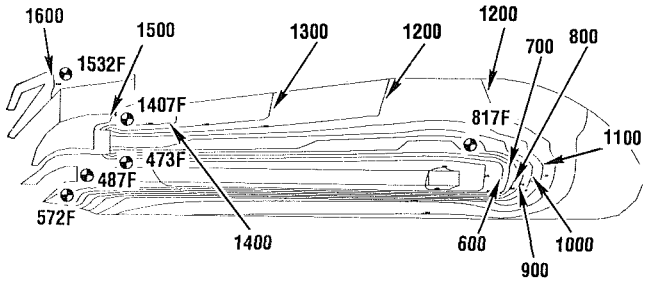


Fig. 15 Combination of monolithic ceramic insulation and air gap barriers keep fuel cool in ceramoblast tip

fuels over a range of flow rates. An in-line propane-fired preheater provided 1.6 lb/sec of vitiated air at 1600°F. Liquid fuel was supplied to the nozzle inlet at 350°F. The liquid-fueled combustor pressure drop was 5.4 percent at an inlet pressure of 60 psia. Fuel flow was varied between 20 and 60 pph. This test point combines a fuel flow consistent with an idle throttle setting with a takeoff inlet temperature and combustor pressure drop for the most severe thermal loading. The high pressure drop increases the air velocity and convection through the nozzle swirlers, while the low fuel flow minimizes the cooling effect of liquid. Primary zone equivalence ratio at this point is near 1.0, increasing the radiation loading on the nozzle face.

Both prototypes and a baseline nozzle were equipped with thermocouples for the test. These chromel-alumel junctions were installed at strategic locations in the stem and tip during assembly of the nozzles. In addition to wetted-part temperatures, fuel temperature at the nozzle flange and at the entrance to the tip was measured to gage the temperature rise through the stem. Fuel pressure, flow, and temperature at the nozzle, as well as rig pressure and inlet temperature, were continuously recorded on strip charts. The test nozzle was purged with nitrogen during lightoff of the preheater, and when shutdown was necessary.

Maximum wetted-wall temperatures and fuel temperature rise through the stem are plotted against fuel flow rate for all three nozzles in Fig. 14. Considering the severity of the inlet conditions, the wetted-surface temperatures measured indicate the effectiveness of the thermal barrier systems developed. Maximum wall temperatures were 518°F and 473°F for the simplex-airblast and ceramoblast nozzles, respectively. Figure 15 compares measured and predicted temperatures in the ceramoblast tip. The large gradients across the insulation and air gaps were accurately predicted. Good agreement between measured and predicted values on the air cap show that the vane convection and flame radiation terms are correctly modeled. However, the temperature rise in both stems was underestimated by some 25 percent. Although some variation can

Downloaded 02 Jun 2010 to 171.66.16.112. Redistribution subject to ASME license or copyright; see http://www.asme.org/terms/Terms_Use.cfm

be attributed to uncertainty in dimensions and other boundary conditions, consistent overprediction for both stems suggests that one or more of the assumptions in the analysis is flawed. Conduction through the flange into the fuel-carrying tube, which was left out of the original one-dimensional analysis, is the suspected heat source. A simple low-conductivity seal between the mounting flange and plenum, or an internal barrier between the flange and fuel-carrying tube, would effectively block this conduction path.

VI Conclusions

Substantial reduction in the stem temperature rise and fuel-carrying tip structure temperatures can be realized at extreme fuel and air inlet temperatures by using simple air gaps as thermal barriers. A threshold of approximately 0.5 Btu-in/hr-ft^2°F is required of an insulating material to improve on the effectiveness offered by practical air gaps.

Monolithic ceramic materials are compatible with the thermal stresses encountered in a high-temperature fuel nozzle, and have no measurable catalytic effects on coking.

Convection from air swirlers and flame radiation are the major sources of nozzle thermal loading in an advanced cycle. These sources can be moderated by the use of the barriers previously suggested, and by reducing frontal area, without substantially affecting nozzle function.

Common thermal modeling techniques can be successfully used to predict temperatures inside a fuel nozzle tip. Detailed analysis and simple thermal barriers, rather than exotic active cooling schemes, can produce dramatic improvements in thermal protection. Minimizing coking rates requires the limiting of fuel temperature rise and wetted-well temperatures inside the atomizer.

Acknowledgments

This research was funded by Contract No. N00140-87-C-0836 from the Naval Air Propulsion Center (NAPC), Trenton, New Jersey, USA. The authors are also indebted to the staff of the engineering laboratory at the Garrett Engine Division, Allied-Signal Aerospace, and the staff of the Delavan Spray Research Center.

References

Johnston, R. K., and Monita, C. M., 1968, "Jet Fuel Stability and Effect of Fuel System Materials," AFAPL-TR-68-20.

Lefebvre, A. H., 1983, *Gas Turbine Combustion*, McGraw-Hill, New York, pp. 413-448.

Marteney, P. J., and Spadaccini, L. J., 1986, "Thermal Decomposition of Aircraft Fuel," ASME JOURNAL OF ENGINEERING FOR GAS TURBINES AND POWER, Vol. 108, pp. 648-653.

Sanborn, J. W., 1989, "Advanced Turbofan Engine Combustion System Design and Test Verification," *AIAA Journal of Propulsion and Power*, Vol. 5, No. 4, pp. 502-509.

Smith, J. D., 1967, "The Effect of Metals and Alloys on the Thermal Stability of Avtur 50," *Aircraft Engineering*, Apr., pp. 22-27.

Downloaded 02 Jun 2010 to 171.66.16.112. Redistribution subject to ASME license or copyright; see http://www.asme.org/terms/Terms_Use.cfm

P. J. Vermeulen
Professor.
Assoc. Mem. ASME

P. Rainville
Graduate Student.

V. Ramesh
Research Associate.

The University of Calgary,
Department of Mechanical Engineering,
Calgary, Alberta T2N 1N4 Canada

Measurements of the Entrainment Coefficient of Acoustically Pulsed Axisymmetric Free Air Jets

Novel direct measurements of the entrainment coefficient in the initial zone of a pulsating air jet have been successfully accomplished. A series of pulsating air jets flowing from different nozzle orifice sizes into surrounding air were investigated for the effects of jet axial length, excitation power, and Strouhal number. The entrainment coefficient of the excited jet varied strongly with axial distance downstream of the orifice exit plane and with pulsation strength. The acoustic drive considerably increased the entrainment coefficient by up to 4.6 times at 10 diameters downstream of the nozzle. There was only a tendency for the entrainment coefficient to increase with the Strouhal number and hence an optimum Strouhal number for jet response was not found.

Introduction

The first direct measurements of the entrainment by steady fully developed turbulent axisymmetric free gaseous jets were made by Ricou and Spalding [1]. This work was later extended by Hill [2] by the first direct measurements of the local entrainment rate in the initial region of axisymmetric turbulent steady air jets. He found that the entrainment coefficient varied nonlinearly from 0.11 at one diameter downstream of the jet nozzle orifice, to the fully developed value of 0.32 at about 13 diameters.

Acoustic control of dilution-air mixing ina gas turbine combustor [3] provided indirect evidence suggesting that the jet entrainment rate was increased by acoustic pulsation. Also, by integrating velocity profiles, Crow and Champagne [4] showed that the entrained volume flow could be increased 32 percent by a low level of acoustic excitation of the jet. Using external excitation Binder and Favre-Marinet [5] indirectly established that the entrainment rate was increased by 90 percent by stronger pulsations. Vermeulen and Yu [6] acoustically excited air jets at strengths much greater than used by previous workers. They indirectly showed that the entrainment mass flow rate was more than doubled. Anderson [7] studied self-excited jet flows, and a more recent investigation by Hill and Greene [8] showed by integration of velocity profiles that the entrainment rate was increased.

Jet flow mixing is important in the performance of gas turbine combustors and jet entrainment is responsible for the mixing produced by a jet. The potential for improved jet mixing by pulsing the jet flows is therefore of important technical interest. To this end Vermeulen et al. [9] made the first direct measurements of entrainment by acoustically pulsed air jets, and found that the entrainment was increased by up to 6 times for distances greater than 15 diameters axially downstream of the orifice exit plane. Further work [10, 11] on the mixing of an acoustically excited air jet with a confined crossflow showed that penetration could be increased about 100 percent, and mixing by at least 34 percent three diameters downstream of the injection orifice. Since, for a typical combustor jet mixing is perhaps of most importance over the first 15 jet diameters, an extension of Hill's [2] work to include local entrainment rate measurements in the initial region of pulsed jets is desirable. Such a novel study will establish a more complete picture of pulsating jet mixing and is the purpose of the work to be reported here.

For small buoyancy effects in fully developed axisymmetric turbulent free jets, Ricou and Spalding established that the total jet mass flow rate $\dot{M}_t$ across a section normal to the jet axis, at an axial distance X from the orifice exit plane, is given by

$$\frac{\dot{M}_t}{\dot{M}_j} = 0.32 \frac{X}{D} \left(\frac{\rho_s}{\rho_j}\right)^{1/2} \tag{1}$$

where D = jet orifice diameter; $\dot{M}_j$ = jet mass flow rate at the orifice; ρ_j = jet density at the orifice; and ρ_s = density of surrounding atmosphere. If $\dot{M}_e$ is the entrained mass flow rate up to the position X then

$$\dot{M}_t = \dot{M}_e + \dot{M}_j \tag{2}$$

Differentiating Eq. (2) gives

$$\frac{d\dot{M}_t}{dX} = \frac{d\dot{M}_e}{dX}, \tag{3}$$

and differentiating Eq. (1) yields

$$\frac{d\dot{M}_t}{dX} = \frac{0.32\,\dot{M}_j}{D} \left(\frac{\rho_s}{\rho_j}\right)^{1/2} = \frac{d\dot{M}_e}{dX} \tag{4}$$

Contributed by the International Gas Turbine Institute and presented at the 36th International Gas Turbine and Aeroengine Congress and Exposition, Orlando, Florida, June 3-6, 1991. Manuscript received at ASME Headquarters March 4, 1991. Paper No. 91-GT-235. Associate Editor: L. A. Riekert.

Copyright © 1992 by ASME
Downloaded 02 Jun 2010 to 171.66.16.112. Redistribution subject to ASME license or copyright; see http://www.asme.org/terms/Terms_Use.cfm

$$\therefore\ 0.32 = \frac{D}{\dot{M}_j}\left(\frac{\rho_j}{\rho_s}\right)^{1/2}\frac{d\dot{M}_e}{dX} \tag{5}$$

Equation (5) defines the entrainment coefficient $C_e = 0.32$ for fully developed flow of a turbulent free jet.

Consider next a normal local slice ΔX between the orifice exit plane and the fully developed region ($X/D > 15$) defining $\Delta\dot{M}_e$ as the corresponding local entrainment mass flow rate. The entrainment coefficient can therefore be approximately expressed as

$$C_e \cong \frac{D}{\dot{M}_j}\left(\frac{\rho_j}{\rho_s}\right)^{1/2}\frac{\Delta\dot{M}_e}{\Delta X}, \tag{6}$$

and is not necessarily constant with X as was shown by Hill [2].

Equation (6) is the basis for the direct measurement of the entrainment coefficients of steady and pulsating jet flows. These novel experiments were designed to examine the influence on C_e of geometry, Reynolds number, acoustic driver power or pulsation strength, and Strouhal number, and to show the potential for improved combustor performance by application of acoustically excited jet flows.

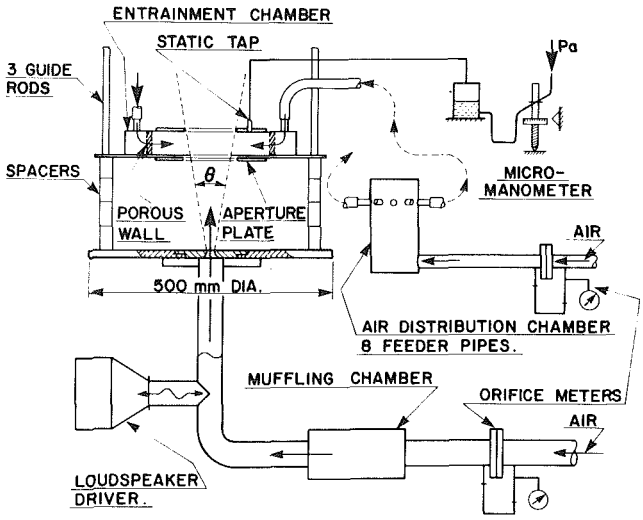


Fig. 1 Schema of apparatus for measurement of local entrainment mass flow rate

Experimental

Local Entrainment Rate Measurement Apparatus. Figure 1 shows the apparatus used, which follows that developed by Hill [2]. It consists of a movable porous walled entrainment chamber, mounted on three guide rods and spacers coaxially with the jet flow. A large base plate (500 mm diameter) positioned the rods together with a range of jet nozzles of orifice diameters 6.35, 9.53, 12.70, and 19.05 mm. The nozzles were supplied with air from a 20.1-mm-dia bore flow tube and were contoured according to International Standard ISO 5167. Compressed air for the nozzles was controlled by a regulator and needle valve and was metered by a standard sharp-edged orifice meter. The temperature and pressure upstream of the needle valve were kept constant, with the pressure sufficiently large to choke the valve, thereby assuring constant mass flow rate. Attached at right angles to the flow tube are the driver tube and loudspeaker driver of 250 W capacity. A muffling chamber was mounted in the flow tube, between the driver tube connection and orifice meter, in order to protect the flow meter from acoustic pulsations in the flow.

Care was taken in the design of the entrainment chamber to ensure uniform radial air flow to the entraining jet. The chamber consists of thin (1.6 mm thick) top and bottom aperture plates carefully sized to suit the jet flow at a particular axial location, and a concentric annulus formed by the 385 mm o.d. porous wall and 430 mm i.d. chamber outer wall. Two rings of 10-mm-thick, 365-mm-i.d. open cell foam were compressed together, for the porous wall, in order to provide sufficient pressure drop to ensure a uniform, radially inward entrainment flow, passed between the aperture plates. The pressure drop created was up to 200 mm of water. The entrainment flow was provided by the laboratory compressed air line via a pressure regulator and needle valve, to a standard sharp-edged orifice meter before delivery to a settling chamber, and then uniformly distributed to the entrainment chamber by eight flexible feeder tubes. A pressure tap in the top aperture plate, connected to an oil-filled micromanometer gage, allowed the static pressure inside the porous walled cylinder to be measured. The range of dimensionless axial distances X/D over which measurements with the chamber could be made was from 0.7 to 33 (depending on the jet orifice size). The separation between the aperture plates was adjustable, but because the plate boundary layers created an axial velocity profile, it was fixed at 19.05 mm to minimize this effect and to give an acceptable $\Delta X/D$ for the smallest jet diameter used. Hill [2] also used a separation of 19.05 mm, but had no $\Delta X/D$ problem since his smallest nozzle size was 19.05 mm diameter.

Acoustic excitation pulses the jet velocity U_j at the nozzle orifice exit plane, which in turn causes the jet flow to develop a train of toroidal vortices [6]. Jet velocity versus time data, on the centerline at the orifice exit plane, were measured by

Nomenclature

C_e = entrainment coefficient
D = jet nozzle orifice diameter
f = driving frequency
F, F_1 = functions
I = electric current to the loudspeaker driver
$\dot{M}_e$ = entrained mass flow rate up to position X
$\Delta\dot{M}_e$ = local entrainment mass flow rate through slice ΔX
$\dot{M}_j$ = constant average mass flow rate through jet nozzle orifice
$\dot{M}_t$ = jet total mass flow rate crossing a plane normal to jet axis
Re = Reynolds number of jet at nozzle orifice
St = jet Strouhal number at nozzle orifice = fD/U_j
U_e = jet velocity excitation pulsation amplitude, at nozzle orifice exit plane center (unsteady flow)
U_e/U_j = excitation or pulsation strength
U_j = steady mean jet velocity at the nozzle orifice exit plane
V = voltage across the loudspeaker driver
$\dot{W}$ = power at the loudspeaker driver
X = jet axial length from nozzle orifice exit plane; axial distance to point midway between aperture plates from nozzle orifice exit plane
ΔX = thickness of slice normal to jet axis at a particular X location
θ = top aperture plate included angle subtended at the nozzle exit plane orifice edges
ρ_j = density of jet flow at nozzle orifice exit plane
ρ_s = density of fluid surrounding jet

Downloaded 02 Jun 2010 to 171.66.16.112. Redistribution subject to ASME license or copyright; see http://www.asme.org/terms/Terms_Use.cfm

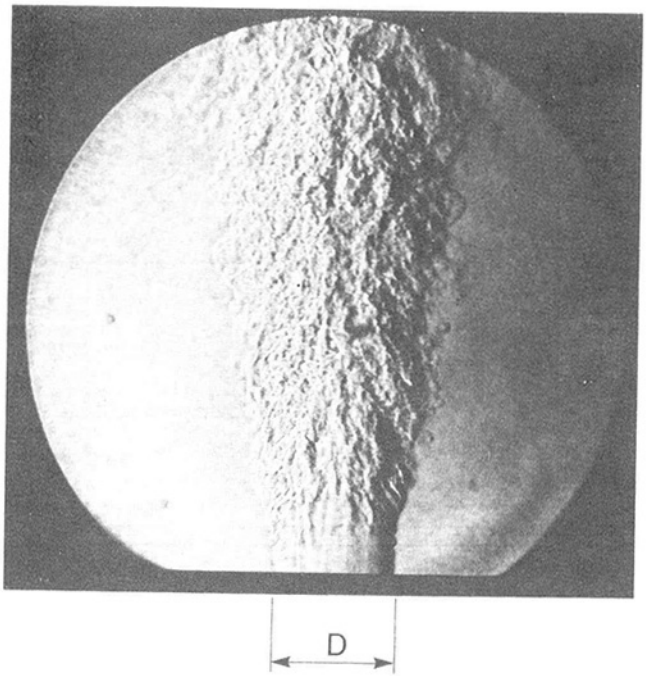


Fig. 2 Typical "no-drive" schlieren picture of jet flow, 19.05-mm-dia orifice, U_j = 18.0 m/s, Re = 27,750, $\dot{M}_j = 6.20 \times 10^{-3}$ kg/s, ρ_s = 1.04 kg/m^3

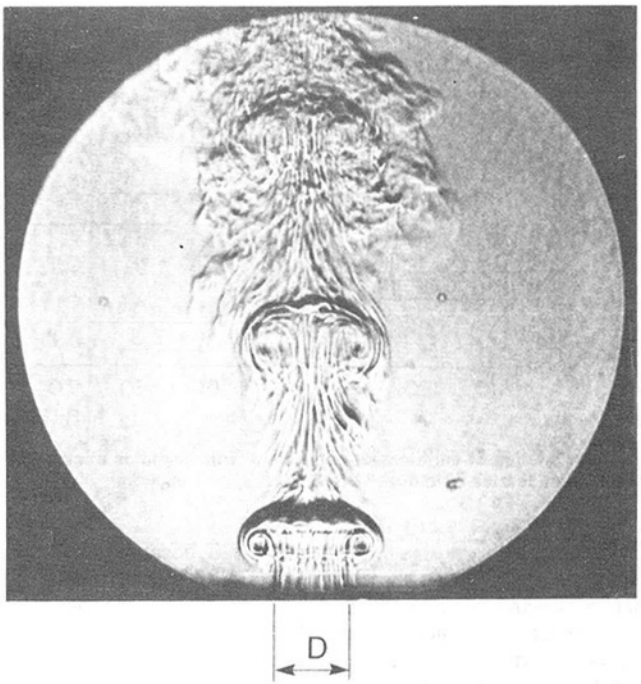


Fig. 3 Typical "with-drive" schlieren picture of jet flow, 12.70-mm-dia orifice, U_j = 10.9 m/s, Re = 10,410, f = 232 Hz, St = 0.270, U_e/U_j = 0.95, W = 58 W, $\dot{M}_j = 1.47 \times 10^{-3}$ kg/s, ρ_s = 1.04 kg/m^3

a linearized constant-temperature anemometer using a hot-film sensor of 0.05 mm diameter. The data were stored in a digitizing oscilloscope and retrieved by an X–Y plotter, from which the amplitude of the pulsation velocity U_e was obtained in a similar manner to that described in the previous work [6]. The excitation strength or pulsation strength may then be defined as U_e/U_j and is, of course, determined by the power at the loudspeaker driver. This power was measured by an a-c voltmeter and ammeter, and an investigation showed that the power factor correction was small, and small changes of frequency had negligible affects on the power measured. The power was therefore simply $W = VI$.

The response of the system consists of that of the mechanical system of tubes plus loudspeaker and that of the jet flow. The mechanical system response determines the frequencies for strongest excitation of the jet flow. By measuring the entrainment rate at $X/D = 9.3$ for a wide incremental range of frequencies, and keeping the driver power constant, the strongest driving frequencies were found to be 163 Hz and 244 Hz depending on the size of nozzle tested. The jet flow response depends on the Strouhal number St, and previous work [6], [9] showed this to be optimum for entrainment at about 0.25 for a free jet at $X/D = 1$ and $X/D = 25.1$, respectively. Thus the entrainment coefficient is expected to be affected in a similar manner.

The main variables having an expected influence on the local entrainment rate and therefore on the entrainment coefficient, and to be investigated, are the nozzle orifice diameter D, the jet axial length X measured from the orifice exit plane, the average steady (unexcited) jet velocity in the nozzle exit plane U_j, the jet pulsation velocity amplitude U_e, the driving frequency f, the Reynolds number Re, and Strouhal number St.

Measurement Method and Initial Proving Tests. Consider the air jet to be flowing "free," that is into a large air reservoir (or room). It is essentially at uniform pressure (atmospheric) with no axial pressure gradient outside of the jet boundary. The entrained air flows radially inward toward the jet axis. Now visualize the jet to be partially surrounded by the entrainment chamber as in Fig. 1, then for no air supply to the chamber, entrainment by the jet reduces the chamber pressure below atmospheric. If air is now supplied to the chamber such that the porous walled cylinder pressure is atmospheric with uniform radially inward flow and with no axial pressure gradient, then free-jet flow conditions are re-established. Under these conditions the supplied air mass flow rate to the chamber is equal to the entrainment mass flow rate of the jet. The measurement method, for a particular jet mass flow rate, at a given axial location, with or without acoustic drive, is then simply to adjust the air flow rate through the porous wall until the micromanometer can detect no pressure difference between the porous walled cylinder static pressure and the atmosphere. A smoke source was used to verify that the air flow in the porous walled cylinder was uniform and radially inward. Also a pattern of static pressure taps on the top and bottom aperture plates verified that pressure drops in the radial, azimuthal, and axial directions were negligible. From these measurements, the most sensitive position for the static pressure tap was determined to be at 25 mm radially from the hole edge in the top aperture plate, for all plates.

Following Hill [2] the holes in the top and bottom aperture plates were made the same diameter and the top aperture chosen so as not to interfere with the jet. The top aperture subtends an included angle θ at the nozzle exit plane orifice edges, which could be varied by using different sized aperture plates. Then for each aperture angle the entrainment mass flow rate $\Delta\dot{M}_e$ was measured for a particular $\dot{M}_j$ at a selected X/D value. This established that $\Delta\dot{M}_e/\dot{M}_j$ was a maximum for $\theta \cong 30$ deg for "no-drive" and "with-drive" conditions. Measurements were then made for the various nozzles, over a wide range of values of X/D, U_j and U_e/U_j, of C_e versus θ. This showed that C_e was a maximum when $\theta \cong 30$ deg and was therefore chosen as the aperture angle for all entrainment measurements, in agreement with that found in the previous works [1, 2, 9]. The maximum value of X/D, up to which measurements could be made, was limited by the maximum jet mass flow rate possible and the sensitivity of the micromanometer. Thus measurements were limited to $X/D = 32$ for the 6.35-mm-dia orifice and only $X/D = 12$ for the 19.05-mm-dia orifice. Furthermore the

Downloaded 02 Jun 2010 to 171.66.16.112. Redistribution subject to ASME license or copyright; see http://www.asme.org/terms/Terms_Use.cfm

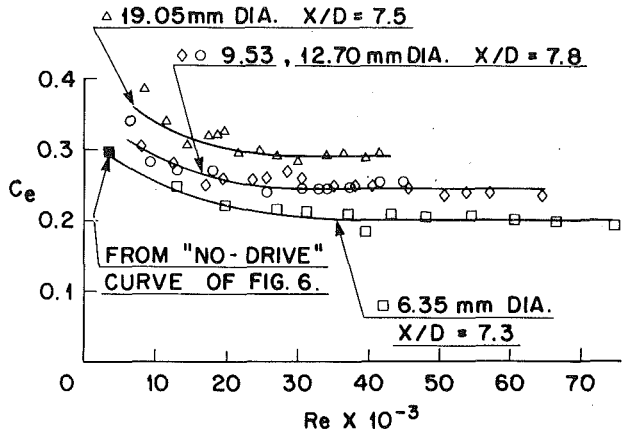


Fig. 4 Variation of entrainment coefficient with Reynolds number for the various nozzles. "No-drive" conditions, ρ_s = 1.03 kg/m^3.

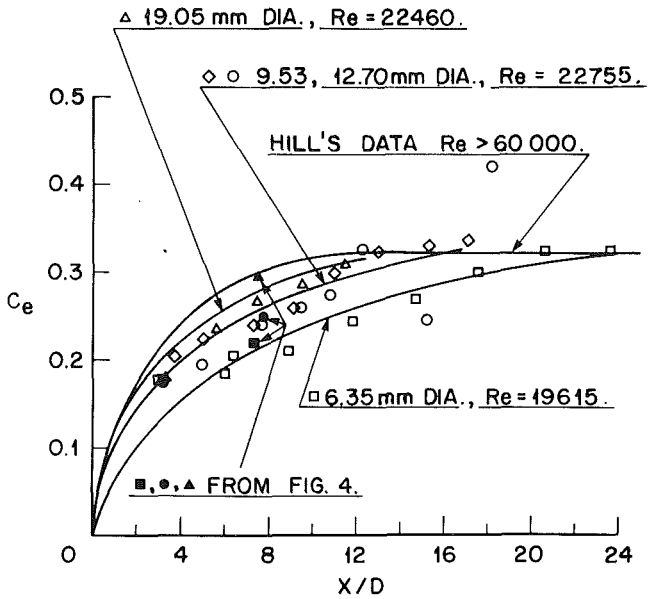


Fig. 5 Variation of entrainment coefficient with axial distance for the various nozzles; "No-drive" conditions, ρ_s = 1.04 kg/m^3

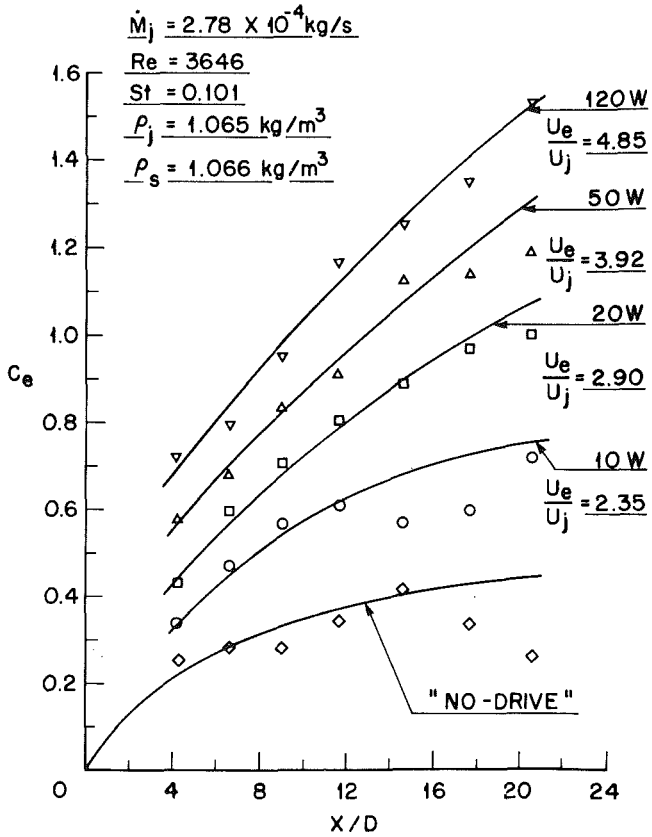


Fig. 6 Variation of entrainment coefficient with axial distance and pulsation strength, D = 6.35 mm diameter, U_j = 10.3 m/s, f = 163 Hz

measurements were also limited to $X/D > 3$, because the chosen aperture angle caused the aperture plates to interfere with the jet, producing erroneous values for C_e. This includes acoustic drive conditions where the problem was further complicated by the change in jet column shape ($0 < X/D < 3$) under the action of the shedding toroidal vortices, as may be seen by comparing the typical "no-drive" and "with-drive" schlieren pictures of Figs. 2 and 3. The choice of the same aperture in the top and bottom plates, with a fixed aperture angle of 30 deg, results in the bottom aperture being slightly too big for the jet. This was investigated by reducing the bottom aperture to better conform to the jet. The value of C_e increased by about 3–5 percent, which was considered to be too small an improvement in accuracy for the additional complication in technique required, particularly under "with-drive" conditions.

The choice of aperture angle θ ensured that the entrainment chamber had negligible interference with the natural development of the jet. However, the bottom aperture plate thickness blocks a small portion of the air flowing toward the jet. The area blockage varied from 8.7 percent (X/D = 3) to 1.4 percent (X/D = 32) for the 6.35-mm-dia orifice, and from 3.6 percent (X/D = 3) to 1.2 percent (X/D = 12) for the 19.05-mm-dia orifice. Thus, overall, the entrainment chamber had minimal interference with the natural jet flow development.

The influence of the jet Reynolds number on the entrainment coefficient was investigated for the various nozzles, over an X/D range including the initial jet zone and for "no-drive" conditions. Sample results are given in Fig. 4 showing that C_e was independent of Re above 30,000 for the flow tube and nozzles tested, which was also true for $3 < X/D < 32$. Such data can be used to correct for Re < 30,000, but this would become very complicated for "with-drive" conditions since pulsation strength and Strouhal number become additional factors. It was therefore decided to avoid this by making comparative measurements between "no-drive" and "with-drive" conditions at the same steady flow jet Reynolds number. However, in order to drive at high pulsation strength with the power available it was necessary to test at low jet mass flow rates (low Reynolds numbers), in which case it was sometimes impossible to obtain "no-drive" values of C_e versus X/D because of lack of measurement sensitivity.

In order to prove the apparatus and experimental technique, measurements of the entrainment coefficient for "no-drive" were made in the region of developing to fully developed flow. Figure 5 presents the results obtained for conditions of small Reynolds number effect with relevant extra data from Fig. 4. Immediately it will be observed that all nozzles tested converge to the same fully developed value of $C_e \cong 0.32$, at sufficiently large X/D, in agreement with Ricou and Spalding and Hill [2]. Hill's data have been shown for comparison, emphasizing that a size factor has appeared, since Hill's data are for nozzle orifice diameters $D \geq 19.05$ mm. The nozzles were geometrically similar, but Hill used a large contraction ratio (flow from a settling chamber) whereas this work was for much smaller ratios. Also, boundary layer development may be an important factor, particularly for the 6.35 mm diameter orifice nozzle. Whatever may be the explanation, it is not crucial to this work, since only comparisons between "no-drive" and "with-drive"

Downloaded 02 Jun 2010 to 171.66.16.112. Redistribution subject to ASME license or copyright; see http://www.asme.org/terms/Terms_Use.cfm

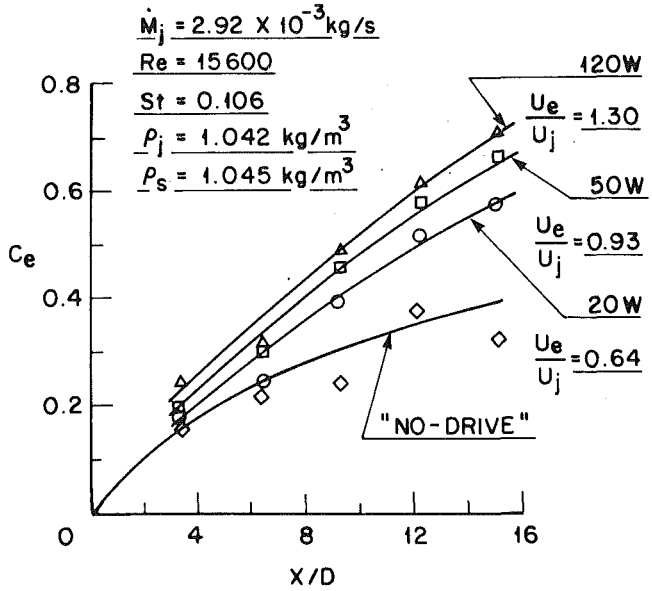


Fig. 7 Variation of entrainment coefficient with axial distance and pulsation strength, D = 12.70 mm diameter, U_j = 19.6 m/s, f = 163 Hz

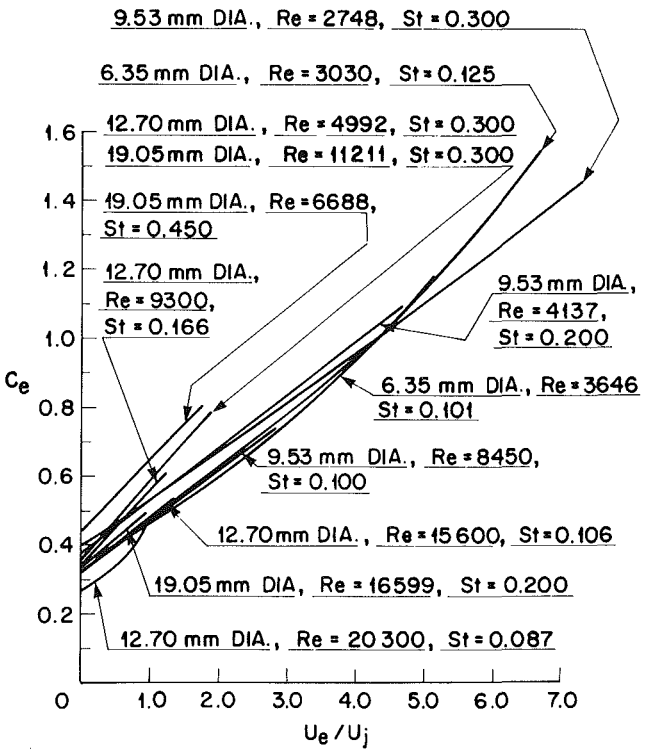


Fig. 8 Variation of entrainment coefficient with pulsation strength for the various nozzles, f = 163 Hz, X/D = 10, ρ_s = 1.04 kg/m^3

conditions are required. It was therefore assumed that the apparatus and experimental technique gave sufficiently reliable results.

Experimental Results. Figures 6 and 7 present typical experimental C_e versus X/D data for two nozzle sizes and for low and medium Reynolds numbers. The Strouhal numbers were almost identical, for a frequency of 163 Hz, and a good range of pulsation strength effect was exhibited. As can be observed, the entrainment coefficient varied strongly with X/D and pulsation strength, and the acoustic drive considerably increased the entrainment coefficient (3.4 times at X/D = 20.5, Fig. 6) as well as extending the developing zone. The

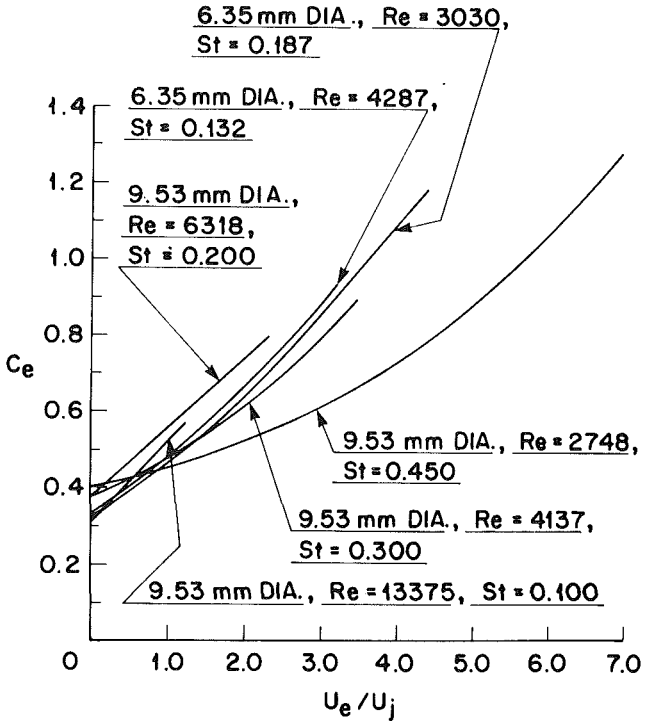


Fig. 9 Variation of entrainment coefficient with pulsation strength for the various nozzles, f = 244 Hz, X/D = 10, ρ_s = 1.04 kg/m^3

X/D range possible was insufficient to establish the fully developed value for C_e at a particular U_e/U_j magnitude, although for U_e/U_j = 2.35 (Fig. 6) it was approached at X/D = 20.5. It is reasonable to assume that C_e = 0 at X/D = 0 for "no-drive," but this is by no means certain for "with-drive" because of entraining action by the toroidal vortices at the nozzle exit plane. Therefore this has not been assumed when drawing the "with-drive" curves.

All the available data at X/D = 10 are summarized in Figs. 8 and 9, for the two frequencies, showing C_e versus U_e/U_j with Re and St as parameters. The best fit lines have been shown and experimental points omitted to avoid confusion. At U_e/U_j = 0 the range of Reynolds number effect is indicated, making it clear that the acoustic drive produces a significant change in the entrainment coefficient. Since these data are for X/D = 10 the maximum value of C_e measured is not shown. This is given in Fig. 10, but because of the low jet velocity "no-drive" values could not be reliably obtained, however, since Reynolds numbers are comparable the "no-drive" curve from Fig. 6 is the same within the experimental error and has been shown. Thus at X/D = 17.5 acoustic excitation has increased the value of C_e to 2.23, an increase of about 5.2 times for a driver power of 246 W at 163 Hz. Perhaps of more practical significance is the large increase in C_e obtained for $0 < X/D < 10$, i.e., an increase of 4.5 times at X/D = 10, $\dot{W}$ = 246 W, for the data of Fig. 10.

Discussion

Inspection of Figs. 6, 7, and 10 reveals that a much smaller range of pulsation strength was used for the 12.70-mm-dia nozzle than for the 6.35-mm-dia nozzle. This was a consequence of the almost linear dependence of $(U_e/U_j)^2$ on the power number $\dot{W}/(\rho_j D^2 U_j^3)$, at a particular frequency, as shown in [9, 10], i.e.,

$$\left(\frac{U_e}{U_j}\right)^2 = F\left[\frac{\dot{W}}{\rho_j D^2 U_j^3}\right] \tag{7}$$

or

Downloaded 02 Jun 2010 to 171.66.16.112. Redistribution subject to ASME license or copyright; see http://www.asme.org/terms/Terms_Use.cfm

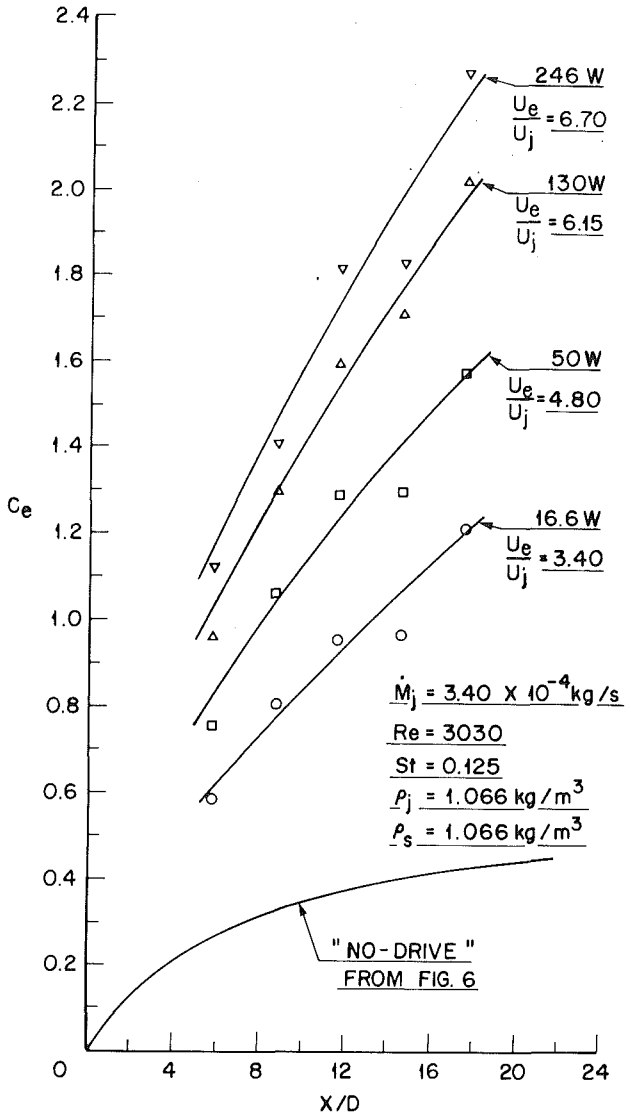


Fig. 10 Variation of entrainment coefficient with axial distance and pulsation strength, D = 6.35 mm diameter, U_j = 8.26 m/s, f = 163 Hz

$$\frac{U_e}{U_j} = F_1\left[\frac{\sqrt{\dot{W}}}{U_j\sqrt{\dot{M}_j}}\right] \tag{8}$$

Thus for limited power the pulsation strength rapidly decreases as D and U_j are increased. Apart from the considerable increase in the entrainment coefficient by pulsating the jet flow, there was a significant increase in the extent of the jet initial development zone. Unfortunately fully developed values of C_e could not be obtained because of measurement difficulties at the extended X/D values required. However, Fig. 10 suggests that $C_e > 3$ would be obtained were the measurements possible. This is consistent with the findings of [9], where a maximum fully developed value of C_e = 2.4 was obtained for a 6.35-mm-dia nozzle and for only 16 W at 250 Hz.

In the jet initial development zone the traveling toroidal vortices have a strength determined by the pulsation strength U_e/U_j, according to [6] which therefore means that the vortex core tangential velocity increases with U_e/U_j. Thus basing the Reynolds number on the steady jet velocity is simplistic. In reality perhaps the Reynolds number ought to be somehow based on the toroidal vortices, and therefore would have a decreasing effect on C_e as the pulsation strength is increased (rotating flow more turbulent). Hence, even though at the "no-drive" condition C_e may be appreciably affected by viscosity, this decreases toward the fully turbulent condition as the acoustic drive becomes stronger.

An examination of Figs. 8 and 9 shows comparable slopes for the various curves at the two different frequencies. It might be expected that C_e would change faster with U_e/U_j at 244 Hz than at 163 Hz, since the toroidal vortex spacing is less at the greater frequency. This is not the case, or perhaps a 50 percent increase in frequency is not sufficient to show an effect. There is no clear effect due to Strouhal number, although there is a tendency for slopes to be steeper at greater St values. Therefore an optimum value for the Strouhal number for jet response cannot be deduced, as would be expected from the previous works [6, 9]. It will be noticed that three curves have more curvature relative to the others. This is due to experimental error; there was a tendency to underestimate the value of C_e in these cases. This suggests perhaps that experimental error may be masking a possible Strouhal number effect. The decreasing Reynolds number effect, with U_e/U_j increase, may also play a part in masking possible Strouhal number effect.

Conclusions

Novel direct measurements of the entrainment coefficient in the initial zone of a pulsating air jet have been successfully accomplished. The entrainment coefficient of the excited jet varied strongly with axial distance downstream of the orifice exit plane and with pulsation strength. The acoustic drive considerably increased the entrainment coefficient, by up to 4.5 times greater than the "no-drive" case at X/D = 10.0, and by up to 5.2 times at X/D = 17.5, for a driver power of 246 W at 163 Hz. The acoustic excitation significantly increased the extent of the initial development zone of the jet, but because of measurement difficulties, fully developed values of C_e could not be obtained. Within the experimental range considered (163 Hz to 244 Hz) the effect of frequency change was negligible. There was only a tendency for the entrainment coefficient pulsation strength relationship to increase with the Strouhal number, and therefore an optimum value for the Strouhal number for jet response could not be discovered.

Acknowledgments

The authors are indebted to Mr. R. Bechtold, Chief Technical Supervisor; Mr. G. East, Technician, who diligently built the experimental apparatus; Mr. A. Moehrle, Research Technician, for expert assistance with the photographic schlieren system, and to Mr. R. W. Gustafson, Research Technician, for invaluable help with instrumentation requirements. The financial support of the Natural Sciences and Engineering Research Council of Canada, under Grant No. A7801 is also gratefully acknowledged.

References

1 Ricou, F. P., and Spalding, D. B., "Measurements of Entrainment by Axisymmetrical Turbulent Jets," *Journal of Fluid Mechanics*, Vol. 11, 1961, pp. 21-32.

2 Hill, B. J., "Measurement of Local Entrainment Rate in the Initial Region of Axisymmetric Turbulent Air Jets," *Journal of Fluid Mechanics*, Vol. 15, Part 4, 1972, pp. 773-779.

3 Vermeulen. P. J., Odgers, J., and Ramesh, V., "Acoustic Control of Dilution-Air Mixing in a Gas Turbine Combustor," ASME JOURNAL OF ENGINEERING FOR POWER, Vol. 104, 1982, pp. 844-852.

4 Crow, S. C., and Champagne, F. H., "Orderly Structure in Jet Turbulence," *Journal of Fluid Mechanics*, Vol. 48, 1971, pp. 547-591.

5 Binder, G., and Favre-Marinet, M., "Mixing Improvement in Pulsating Turbulent Jets," *ASME Symposium on Fluid Mechanics of Mixing*, Georgia Institute of Technology, Atlanta, GA, June 20-22, 1973, pp. 167-172.

Downloaded 02 Jun 2010 to 171.66.16.112. Redistribution subject to ASME license or copyright; see http://www.asme.org/terms/Terms_Use.cfm

6 Vermeulen, P. J., and Yu, Wai Keung, "An Experimental Study of the Mixing by an Acoustically Pulsed Axisymmetrical Air-Jet," *International Journal of Turbo & Jet-Engines*, Vol. 4, Nos. 3–4, 1987, pp. 225–237; ASME Paper No. 85-GT-49.

7 Anderson, A. B. C., "Structure and Velocity of the Periodic Vortex-Ring Flow Pattern of Primary Pfeifenton (Pipe Tone) Jet," *The Journal of the Acoustical Society of America*, Vol. 27, No. 6, 1955, pp. 1048–1053.

8 Hill, W. G., and Greene, P. R., "Increased Turbulent Jet Mixing Rates Obtained by Self-Excited Acoustic Oscillations," ASME *Journal of Fluids Engineering*, Vol. 99, No. 3, 1977, pp. 520–525.

9 Vermeulen, P. J., Ramesh, V., and Yu, Wai Keung, "Measurements of Entrainment by Acoustically Pulsed Axisymmetric Air Jets," ASME JOURNAL OF ENGINEERING FOR GAS TURBINES AND POWER, Vol. 108, No. 3, 1986, pp. 479–484.

10 Vermeulen, P. J., Chin, Ching-Fatt, and Yu, Wai Keung, "Mixing of an Acoustically Pulsed Air Jet With a Confined Crossflow," AIAA *Journal of Propulsion and Power*, Vol. 6, No. 6, 1990, pp. 777–783.

11 Vermeulen, P. J., Grabinski, P., and Ramesh, V., "Mixing of an Acoustically Excited Air Jet With a Confined Hot Crossflow," ASME JOURNAL OF ENGINEERING FOR GAS TURBINES AND POWER, Vol. 114, 1992, pp. 46–54.

Downloaded 02 Jun 2010 to 171.66.16.112. Redistribution subject to ASME license or copyright; see http://www.asme.org/terms/Terms_Use.cfm

CFD Analysis of Jet Mixing in Low NO_x Flametube Combustors

M. V. Talpallikar

C. E. Smith

CFD Research Corporation,
Huntsville, AL 35805

M. C. Lai

Wayne State University,
Detroit, MI 48202

J. D. Holdeman

NASA Lewis Reserch Center,
Cleveland, OH 44135

The Rich-burn/Quick-mix/Lean-burn (RQL) combustor has been identified as a potential gas turbine combustor concept to reduce NO_x emissions in High Speed Civil Transport (HSCT) aircraft. To demonstrate reduced NO_x levels, cylindrical flametube versions of RQL combustors are being tested at NASA Lewis Research Center. A critical technology needed for the RQL combustor is a method of quickly mixing bypass combustion air with rich-burn gases. In this study, jet mixing in a cylindrical quick-mix section was numerically analyzed. The quick-mix configuration was five inches in diameter and employed 12 radial-inflow slots. The numerical analyses were performed with an advanced, validated 3-D Computational Fluid Dynamics (CFD) code named REFLEQS. Parametric varation of jet-to-mainstream momentum flux ratio (J) and slot aspect ratio was investigated. Both nonreacting and reacting analyses were performed. Results showed mixing and NO_x emissions to be highly sensitive to J and slot aspect ratio. Lowest NO_x emissions occurred when the dilution jet penetrated to approximately midradius. The viability of using 3-D CFD analyses for optimizing jet mixing was demonstrated.

Introduction

In order to meet the growing need for faster transportation, High-Speed Civil Transport (HSCT) aircraft and associated propulsion systems have been under study in recent years. One major concern that has surfaced concerning HSCT engines is their impact on deteriorating the earth's ozone layer. Using current technology, a fleet of HSCT aircraft would produce large amounts of oxides of nitrogen (NO_x) while cruising in the stratosphere. Such high levels of NO_x, through a series of well-known reactions, would drastically reduce ozone levels. In order to reduce NO_x emissions, technology must be developed to design advanced, low emission combustors.

One combustor concept that has been identified as a leading candidate to reduce No_x emissions is the Rich-burn/Quick-mix/Lean-burn (RQL) combustor. Originally conceived and developed for industrial combustors (Mosier and Pierce, 1980; Pierce et al., 1980), the RQL concept utilizes staged burning, as shown in Fig. 1. Combustion is initiated in a fuel rich zone at equivalence ratios between 1.2 and 1.8, thereby reducing NO_x formation by depleting the available oxygen. Bypass combustion air is introduced in a quick-mix section and lean combustion occurs downstream at an overall equivalence ratio between 0.5 and 0.7. The quick-mix section usually has a smaller geometric cross-sectional area than the rich burn zone in order to prevent backflow and enhance mixing.

Perhaps the single most important issue of the RQL concept is the design of the quick-mix section. For previous laboratory combustors, Tacina (1990) has shown RQL No_x levels to be higher than lean, premixed combustor NO_x levels. The higher NO_x emissions for RQL was attributed to stoichiometric burning in the quick-mix section, thus emphasizing the need for optimized rapid mix concepts. Indeed, Nguyen et al. (1989) have shown that if instantaneous mixing is assumed in the quick-mix section, low NO_x emission index can be obtained at HSCT cruise flight conditions Hence, one challenge of the RQL concept is to identify quick-mix sections with rapid mixing.

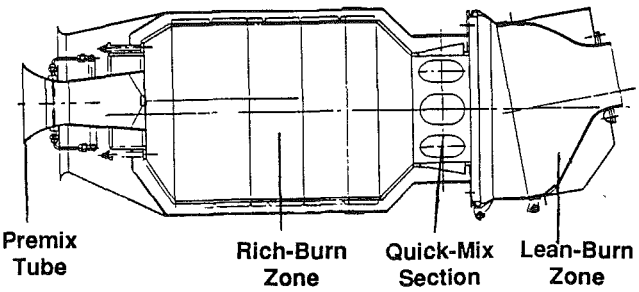


Fig. 1 Industrial Rich-burn/Quick-mix/Lean-burn (RQL) combustor (Pierce et al., 1980)

This study sought to investigate the influence of jet-to-mainstream momentum flux ratio (J) and slot aspect ratio (SAR) on mixing effectiveness in a RQL flametube combustor to be tested at NASA Lewis Research Center (LeRC). Conventionally, dilution air in can combustors has been introduced through radial inflow holes. According to Holdeman's correlation (Holdeman et al., 1987), optimum mixing occurs when the following expression is satisfied

$$n = \pi \frac{\sqrt{2J}}{C} \tag{1}$$

where

n = optimum number of holes
C = experimentally derived constant ~ 2.5
J = jet-to-mainstream momentum flux ratio ($\rho_j V_j^2 / \rho_\infty V_\infty^2$).

Contributed by the International Gas Turbine Institute and presented at the 36th International Gas Turbine and Aeroengine Congress and Exposition, Orlando, Florida, June 3-6, 1991. Manuscript received at ASME Headquarters March 4, 1991. Paper No. 91-GT-217. Associate Editor: L. A. Riekert.

Copyright © 1992 by ASME
Downloaded 02 Jun 2010 to 171.66.16.112. Redistribution subject to ASME license or copyright; see http://www.asme.org/terms/Terms_Use.cfm

Unfortunately, this correlation was developed for circular-holed dilution jet mixing and jet mass flow-to-mainstream mass flow ratios (m_j/m_∞) of approximately 0.5. The RQL combustor requires m_j/m_∞ of 2.0, thus necessitating slots instead of holes around the can's perimeter. The design of slots for optimum mixing needs further investigation, and was the focus of this study.

CFD Code

The approach in this study was to perform 3-D numerical computations on a cylindrical quick-mix section. The goal of the study was to provide improved understanding of slot injection and mixing. An advanced CFD code, REFLEQS, was used to perform the computations. REFLEQS was developed by CFD Research Corporation (Przekwas et al., 1990; Smith et al., 1988) to analyze turbulent, reacting flows. The basic capabilities/methodologies in REFLEQS include:

1 Solution of two and three-dimensional Navier-Stokes equations for incompressible and compressible flows;
2 Cartesian, polar, and nonorthogonal body-fitted coordinates,
3 Porosity-resistivity technique for flows with internal blockages;
4 Fully implicit and strongly conservative formulation;
5 Three differencing schemes: upwind, hybrid, and central differencing with damping terms;
6 Standard (Launder and Spalding, 1974) and extended (Chen and Kim, 1987) k–ϵ turbulence models, the two-scale turbulence model of Kim and Chen (1988), and the low-Reynolds number k–ϵ model of Chien (1985);
7 Instantaneous, one-step and two-step combustion models;
8 Modified form of Stone's Strongly Implicit Solver; and
9 Pressure-based solution algorithms including SIMPLE and a variant of SIMPLEC.

REFLEQS has undergone a considerable amount of systematic quantitative validation for both incompressible and compressible flows. Over 30 validation cases have been performed to date, and good-to-excellent agreement between benchmark data and predictions has been shown (Smith et al., 1989; Ratcliff and Smith, 1989; Avva et al., 1990). The good agreement gives confidence in the numerical results of this study.

Heat-Release Model

After reviewing the time scales for heat release at cruise-type conditions in RQL mixers, it was determined reaction rates were much faster than mixing rates. Hence, the combustion process was considered mixing controlled, and instantaneous reaction rates for heat release were assumed.

When rich burn gases (composed of equilibrium concentration of CO, CO_2, H_2O, and N_2) were mixed with air, they were assumed to react according to the equation

$$0.0570\ CO + 0.0197\ CO_2 + 0.03873\ H_2 + 0.0680\ H_2O + 0.1371\ N_2 + 0.1047\ O_2 + 0.3953\ N_2 \rightarrow 0.0767\ CO_2 + 0.1063 H_2O + 0.7123\ N_2 + 0.0565\ O_2 \quad (2)$$

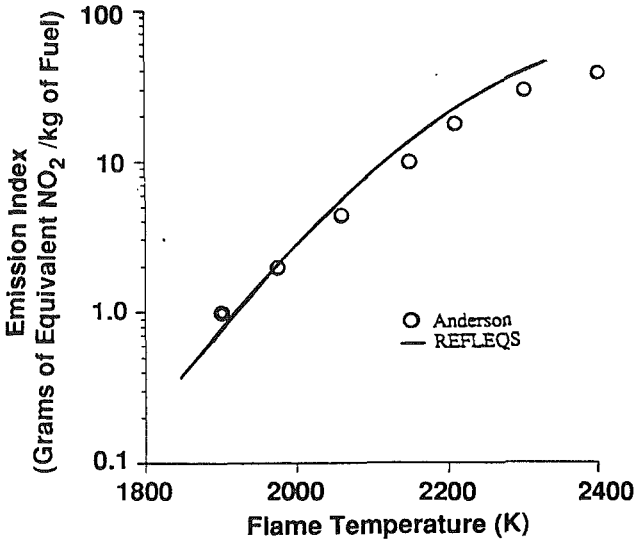


Fig. 2 Calibration of NO_x model in REFLEQS

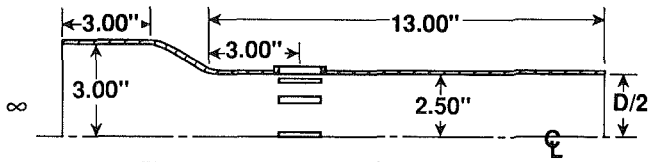


Fig. 3 Schematic of quick-mix geometry

Accordingly, any CO concentration that remained in the mixer exit was the result of unmixedness.

NO_x Model

It was assumed that the NO_x reactions did not contribute to the overall heat release in the combustor, thus allowing the NO_x reactions to be "decoupled" from the heat-release reactions. NO_x was calculated as a passive scalar after the computation of the reacting flowfield.

A simple Zeldovich reaction scheme was used to model the NO_x formation. According to the mechanism, NO formation can be described by

$$N_2 + O \leftrightarrow NO + N \quad (3)$$

and

$$O_2 + N \leftrightarrow NO + O. \quad (4)$$

The first reaction is much slower than the second one and hence controls the rate of NO formation. If the concentration of NO is much smaller than the corresponding equilibrium value, the rate equation for NO can be written as

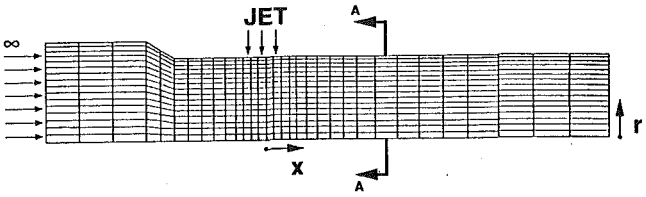
$$\frac{d(NO)}{dt} = K\,[N_2][O] \quad (5)$$

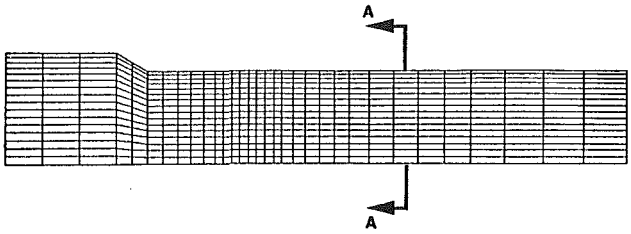
Approximating the concentrations of N_2 and O by the local equilibrium values, the rate equation is given by

Nomenclature

A = pre-exponential factor
D = diameter of quick-mix section
D_h = hydraulic diameter
EI = emission index
E/R = activation energy/gas constant
J = jet-to-mainstream momentum flux ratio
m_i = mass flow in each cell i
m_j = jet mass flow
m_∞ = mainstream mass flow
σ_T = mass-weighted standard deviation of temperature
n = optimum number of slots
NO_x = oxides of nitrogen
T_{avg} = mass-weighted average temperature
T_i = temperature in each cell i
u' = rms of U velocity
U = averaged axial velocity
v' = rms of V velocity
V = averaged radial velocity

Downloaded 02 Jun 2010 to 171.66.16.112. Redistribution subject to ASME license or copyright; see http://www.asme.org/terms/Terms_Use.cfm





GRID: x = 32
r = 16
θ = 18

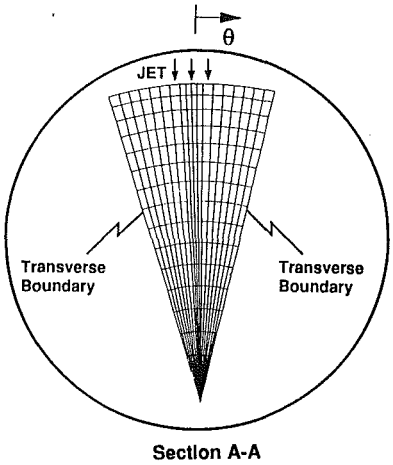


Fig. 4 Baseline grid

$$\frac{d(NO)}{dt} = A\, e^{-\left(\frac{E}{RT}\right)} [N_2][O_2]^{1/2} \tag{6}$$

From Quan et al. (1972), the rate constants were determined to be

$$A = 1.82 \times 10^{12} \frac{1}{\text{s}} \sqrt{\frac{\text{m}^3}{\text{Kmole}}} \tag{7}$$

$$\frac{E}{R} = 6.7 \times 10^4 \text{ K} \tag{8}$$

The NO_x model was calibrated against the experimental results of Anderson (1975), who used a premixed, prevaporized laboratory combustor. The REFLEQS test case consisted of premixed propane and air reacting in a straight channel and instantaneous heat release. The rate constants had to be modified to give good agreement with Anderson's data. The final constants used in this study were

$$A = 3.4 \times 10^{12} \frac{1}{\text{s}} \sqrt{\frac{\text{m}^3}{\text{Kmole}}} \tag{9}$$

$$\frac{E}{R} = 5.7 \times 10^4 \text{ K} \tag{10}$$

Figure 2 shows the computed results compared to Anderson's data of Emission Index (EI) as a function of adiabatic flame temperature.

Details of Numerical Model

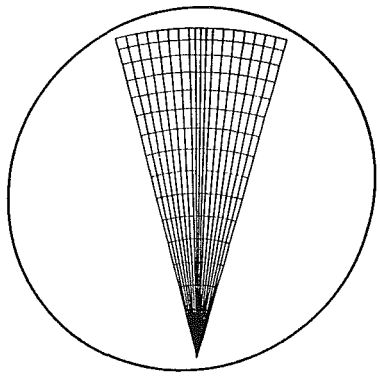
A geometry compatible with the NASA LeRC flametube combustor was selected for analysis. The geometry, numerical grid, numerical details, boundary conditions, grid independence, and convergence criteria are discussed next.

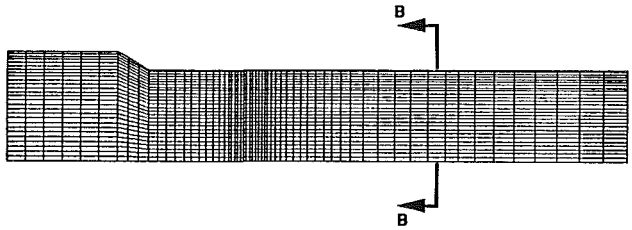
Geometry. The geometry of the numerical model consisted of three components: an inlet pipe, converging section and a quick-mix section (see Fig. 3). The inlet pipe was 0.152 m (6.0 in.) in diameter and 0.076 m (3.0 in.) in length. The inlet pipe converged into the quick-mix section which was 0.127 m (5.0 in.) in diameter (D). The length of the quick-mix section was

GRID: x = 32
r = 16
θ = 18

9216 CELLS

Section A-A





GRID: x = 60
r = 30
θ = 27

52,650 CELLS

Section B-B

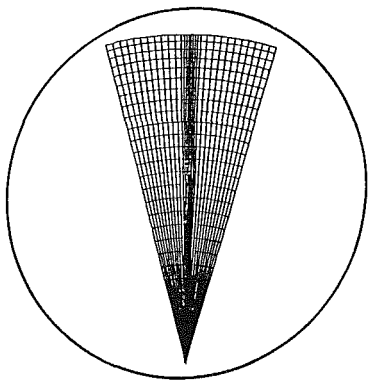


Fig. 5 Comparison of coarse and fine grids

Downloaded 02 Jun 2010 to 171.66.16.112. Redistribution subject to ASME license or copyright; see http://www.asme.org/terms/Terms_Use.cfm

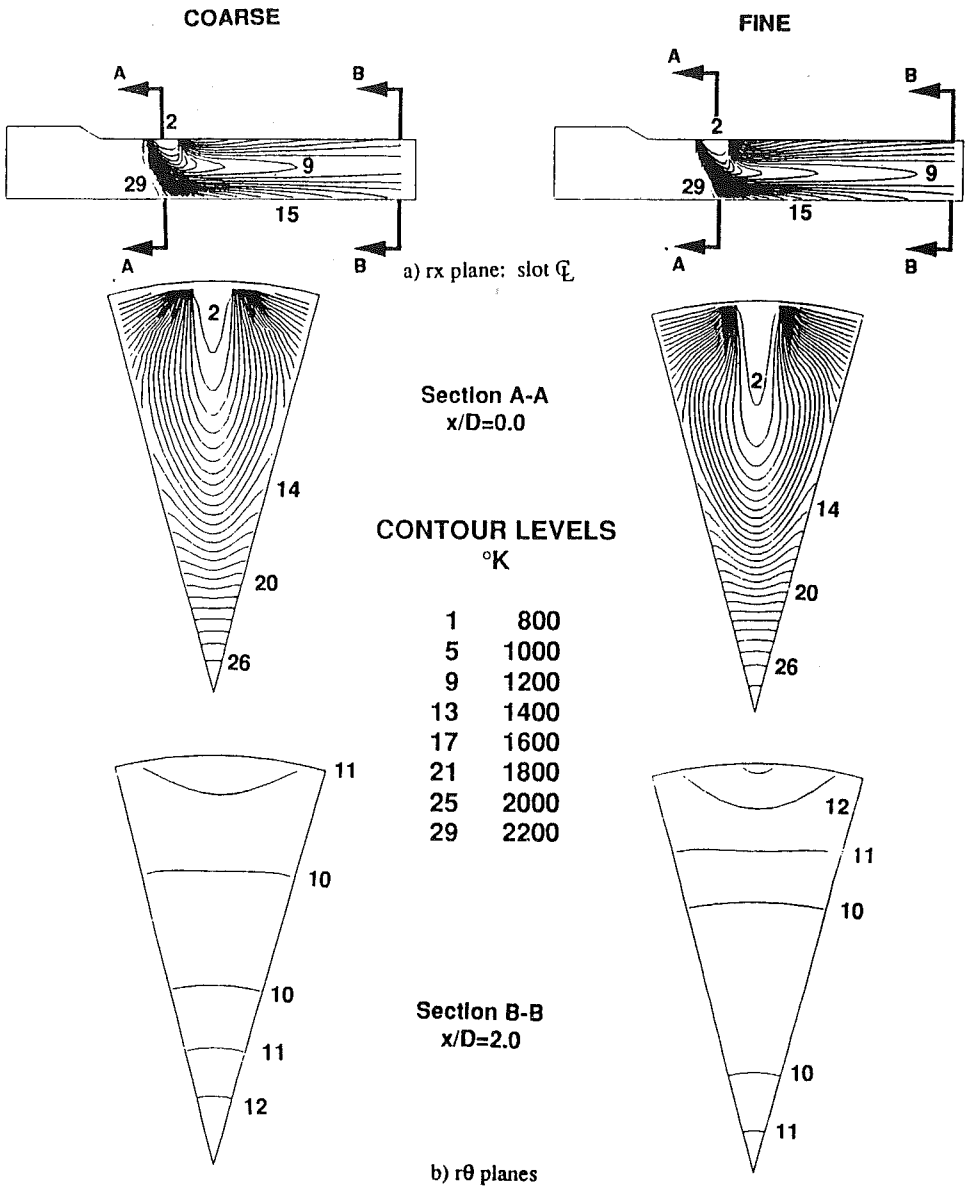


Fig. 6 Comparison of isotherms for coarse and fine grids: $J = 32$

0.333 m (13.0 in.). In reality, the length of actual quick-mix section hardware is approximately 6 in., but the computational domain is extended for better understanding of NO_x formation and to eliminate flowfield contamination by exit boundary conditions.

Twelve slots were located symmetrically around the perimeter of the quick-mix section. The axial location of the slot centerline was 0.076 m (3.0 in.) from the inlet of the quick-mix section. The baseline slots were rectangular in shape with an aspect ratio of four and aligned in the streamwise direction. Three variations in slot aspect ratio (SAR) were tested: 1, 4, and 16.

Due to geometric symmetry, only one slot was modeled with planes of symmetry set up halfway between adjacent slots. This allowed greater grid resolution and reduction of computer turn-around time. The $r\theta$ domain was reduced to a pie section with a central angle of 30 deg.

Grid. A baseline grid of 9216 cells ($32 \times 16 \times 18$ in x, r, θ directions) was selected and used for modeling the mixer. The grid is shown in Fig. 4. Note that the origin of the coordinate system is located at the center of the slot. The axial grid spacing is dense near the slot, and gets coarser upstream and downstream of the slot. The grid in the radial direction was non-

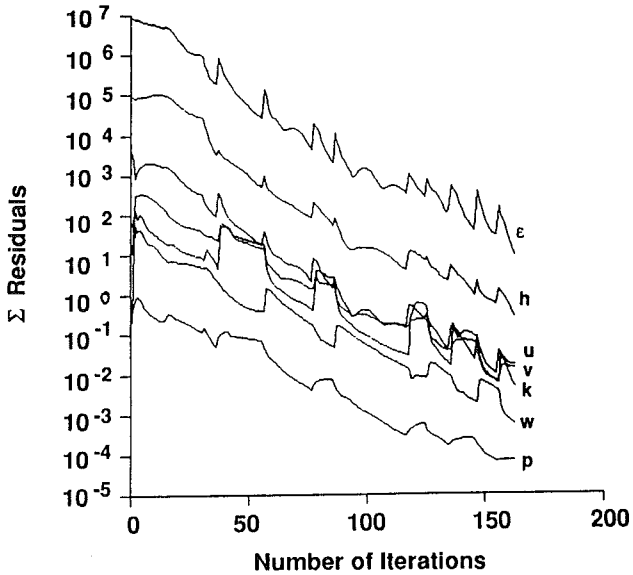


Fig. 7 Convergence history for a typical run

Downloaded 02 Jun 2010 to 171.66.16.112. Redistribution subject to ASME license or copyright; see http://www.asme.org/terms/Terms_Use.cfm

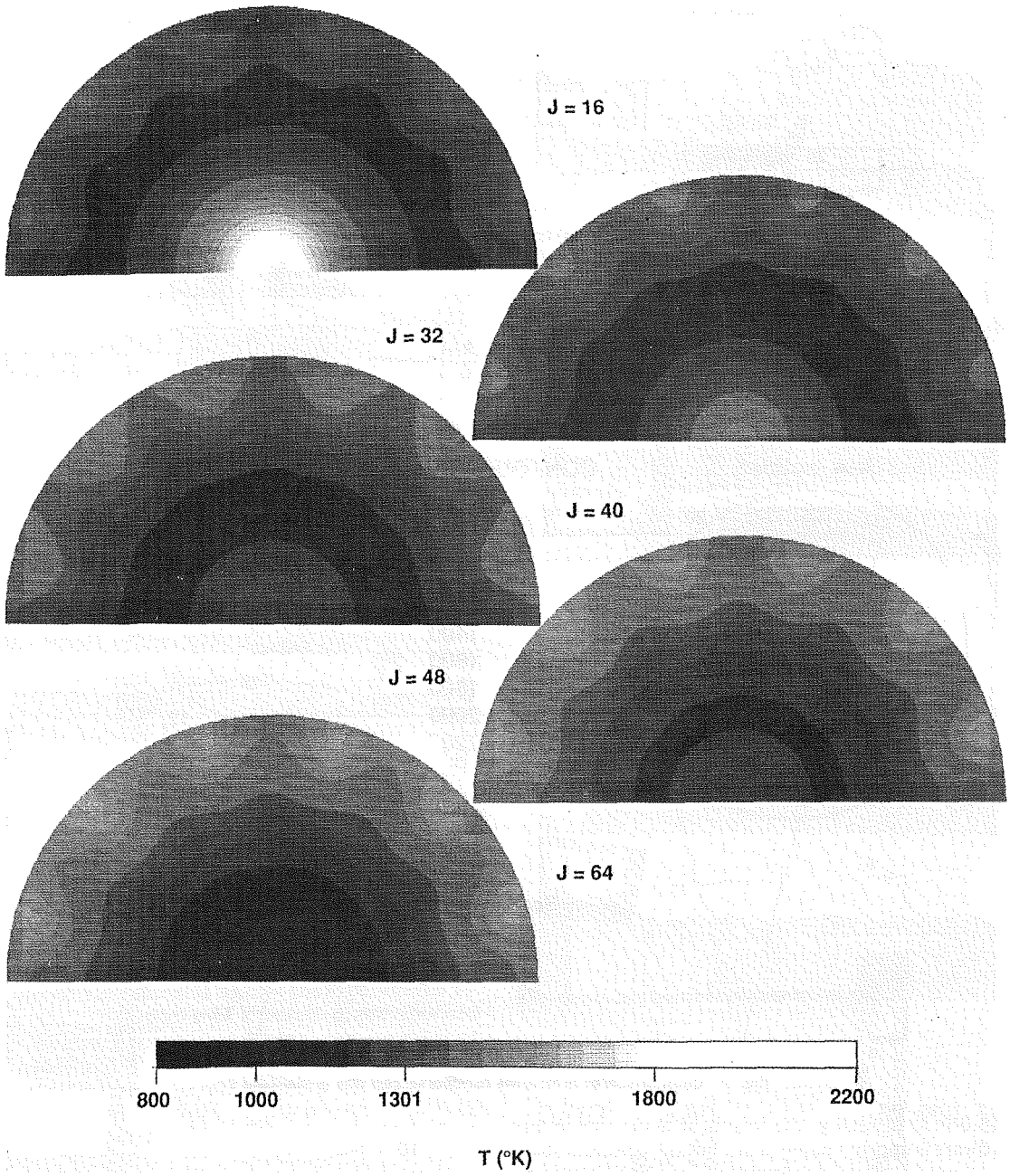


Fig. 8 Temperature contour maps for nonreacting conditions: $x/D = 1.0$

uniform with greater density near the combustor wall (power expansion of 1.2). The grid in the transverse direction was uniform in the slot, and slowly expanding away from the slot. The baseline slot was represented by a 6×6 mesh. As will be discussed in grid independence studies, this rather coarse grid is not grid-independent, but it does capture all of the relevant flow features. For comparative studies, it was felt sufficient.

Numerical Details. The numerical details of the calculations included:

1 Whole field solution of u momentum, v momentum, w momentum, pressure correction, turbulent kinetic energy k, dissipation rate ϵ, total enthalpy, and mixture fraction,
2 Upwind differencing for parametric studies of J and central differencing for parameteric studies of SAR;
3 Variable fluid properties (i.e., temperature dependency of specific heat, laminar viscosity, etc.)
4 Adiabatic walls;
5 Standard k–ϵ model with wall functions;
6 Turbulent Prandtl number of 0.9;
7 Instantaneous heat-release model; and
8 Six active chemical species.

Boundary Conditions. *Mainstream Boundary.* At the mainstream inlet boundary, propane and air are assumed to have completely reacted at an equivalence ratio (ϕ) of 1.6. The species and temperature of the reaction products were taken from the JANNAF-standard rocket code named One Dimensional Equilbrium (ODE) (Nickerson et al., 1989). Velocity and pressure were obtained from experimental test plans for the RQL flametube combustor. A uniform velocity profile was assumed with a turbulent intensity typical of primary zones in gas turbine combustors and a turbulent length scale corresponding to a turbulent viscosity 1000 times greater than laminar viscosity. The mainstream inlet conditions (at 6.0 in. dia) were:

Downloaded 02 Jun 2010 to 171.66.16.112. Redistribution subject to ASME license or copyright; see http://www.asme.org/terms/Terms_Use.cfm

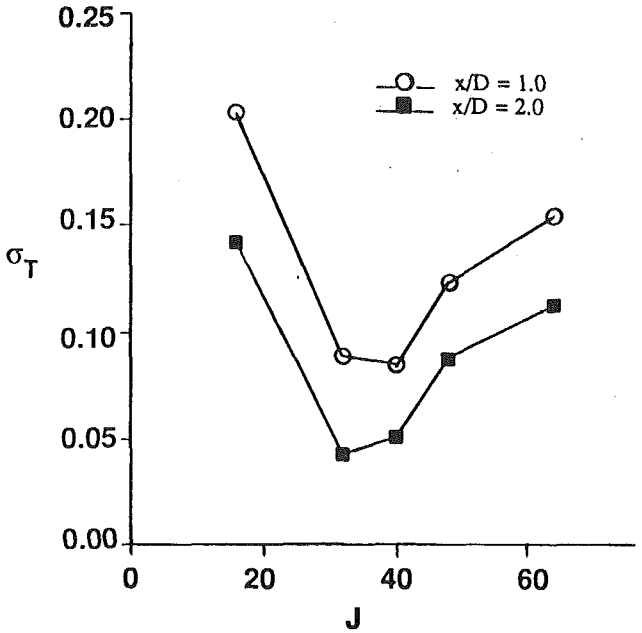


Fig. 9 Mixing effectiveness: nonreacting flow

Axial velocity	=	35.5 m/s
Temperature	=	2221 K
Density	=	2.32 kg/m^3
Composition (mass fraction)	=	0.134 CO, 0.068 CO_2, 0.006 H_2, 0.096 H_2O, 0.696 N_2
Turbulent intensity (u'/U)	=	50 percent
Turbulent length scale (l_t/D_∞)	=	0.02

Since equilibrium NO_x levels are very low for ϕ of 1.6 ($\approx$4 ppm), no NO_x was assumed in the mainstream inlet.

Jet Inlet. The composition at the dilution jet inlet was assumed to be air. A uniform velocity profile was assumed and turbulent properties were selected using the same logic as discussed for mainstream turbulence. The jet inlet flow conditions were:

Mass flux ratio (m_j/m_∞)	=	1.94
Jet temperature	=	811 K
Density	=	6.35 kg/m^3
Composition (mass fraction)	=	0.232 O_2, 0.768 N_2
Turbulent intensity (v'/V)	=	10 percent
Turbulent length scale (l_t/D_h)	=	0.13

The momentum flux ratio (J) was varied parametrically from 16–64 by variation of jet velocity from 120 m/s–240 m/s. The jet velocity variation corresponded to liner pressure drops ($\Delta P/P$) of 3–12 percent. For each jet velocity, the slot flow area was modified to maintain constant jet flow.

Exit Boundary. The exit boundary condition was a zero gradient boundary condition.

Transverse Boundaries. The transverse boundaries were assumed to be symmetry planes. These boundaries also were tested for possible outflow by setting them to be periodic boundaries. No discernible difference was seen between cases with symmetric and periodic transverse boundaries.

Combustor Wall. The combustor wall was treated as a no-slip adiabatic wall (zero enthalpy gradient). Wall functions were used for the calculations of wall shear stress and near-wall turbulent quantities (k and ϵ).

Centerline. The computational boundary at the centerline was assumed to be a symmetry plane.

Grid Independence. Two different sizes of grids were run to test grid independence: 9,216 and 52,650 cells. The finer grid was obtained by increasing the grid density by ~ 75 percent in all three directions. Comparison of the two grids is shown in Fig. 5.

Computational results from the two grids are presented in Fig. 6 for a momentum flux ratio (J) of 32.0. The isotherms in an rx-plane through the jet centerline are shown and compared. Qualitatively, they exhibit similar features, although the jet penetrated a little further in the case of the fine grid. Isotherms also are shown for two axial planes: x/D = 0.0 and 2.0. The isotherms at x/D = 2.0 show slightly higher temperatures (~ 22 K) for the fine grid. Also, the cold region in the fine grid solution is located closer to the centerline, indicating greater penetration. However, overall, the coarse grid solution is very similar to the fine grid solution.

Based on this grid-independence study, it appears the coarse grid captures the overall physics of the problem, and can be used to qualitatively compare quick-mix designs.

Convergence. The summations of all error residuals were reduced five orders of magnitude, and continuity was conserved in each axial plane. Typically, convergence required approximately 150 iterations as shown in Fig. 7. The relaxation on the velocity components (u and v only) was continuously varied during the run through a user specified input file. The repeated variation of relaxation allowed resolution of different scales of numerical error. This was found to speed up convergence by a factor of six compared to constant relaxation. Approximately 3 CPU hours were required on an Alliant FX/8 mini-supercomputer (operating on one computational element). Fine grid calculations took approximately 500 iterations and 40 CPU hours. For comparison, the ALLIANT computer speeds are ~ 20 times slower than a CRAY X-MP.

Results

Parametric numerical tests were performed for jet-to-mainstream momentum flux ratios (J), for both nonreacting and reacting gases. Parametric variation of slot aspect ratio (SAR) also was studied. Discussion of the findings are reported next.

Variation of J: NonReacting Flow. Five jet-to-mainstream momentum flux ratios were parametrically tested: 16, 32, 40, 48, and 64. All other flow conditions were held constant, including mass flow ratio (jet-to-mainstream) at 1.94. To maintain a constant mass flow, the slot size was changed for each J.

The slot aspect ratio was held constant at four, and was always centered at the same location. The same number of grid cells were used in all cases. However, since the slot size was changing, the grid density had to be slightly altered for each case. This variation is thought to have a minimal effect on the results discussed next.

Computed temperature contour maps are presented at x/D of 1.0, as shown in Fig. 8. The radial location of the lowest temperatures indicates the penetration location of the cold jet. As expected, increased jet penetration can be seen for larger values of J. Best mixing seems to occur when the jet penetrates to approximately midradius. J of 32 and J of 40 appear to be optimum mixers. For comparison, the optimum J is 45.6 using Eq. (1).

For a more quantitative comparison of mixing effectiveness, the mass-weighted standard deviation of temperature (σ_T) was calculated for each case. σ_T was defined as

$$\sigma_T = \frac{\sqrt{\sum_i m_i (T_i - T_{avg})^2}}{\sum_i m_i} \Big/ T_{avg} \qquad (11)$$

Downloaded 02 Jun 2010 to 171.66.16.112. Redistribution subject to ASME license or copyright; see http://www.asme.org/terms/Terms_Use.cfm

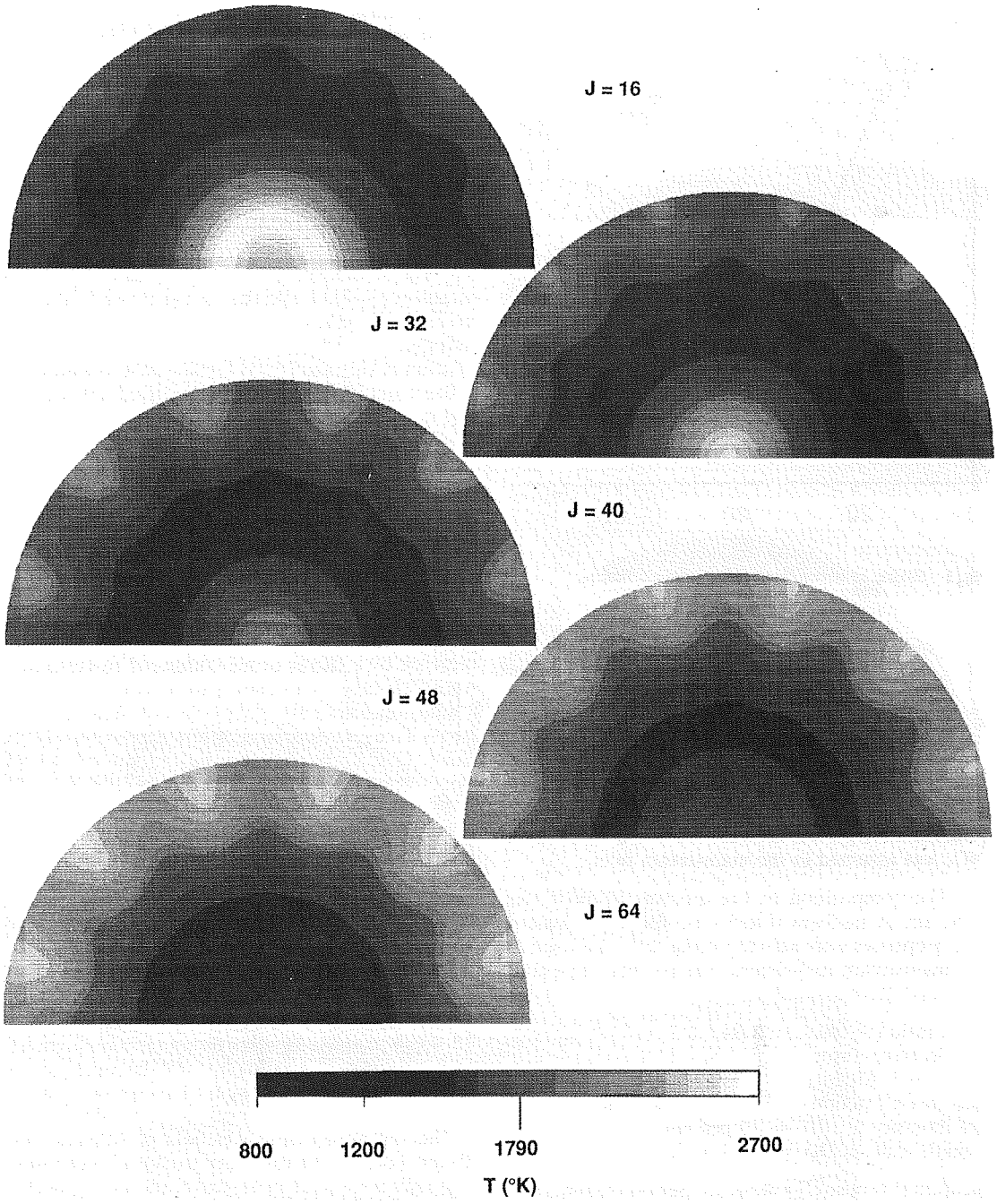


Fig. 10 Temperature contour maps for reacting conditions: $x/D = 1.0$

In Fig. 9, σ_T is presented versus J. It can be seen that J of 32 has the lowest σ_T at $x/D = 2.0$. Underpenetration is worse than overpenetration in terms of σ_T.

Variation of J: Reacting Flow. The same cases were analyzed previously, except chemical reaction was turned on. Due to reaction, the overall mass-averaged exit temperature increased from 1301 deg K for nonreacting flows to 1790 deg K for reacting flows. Figure 10 shows temperature contour maps for the reacting cases one diameter downstream of the jet center. From this figure, it appears that $J = 40$ is the best mixer. This can be further elucidated by looking at the mixing effectiveness (σ_T) shown in Fig. 11. Figure 11 shows $J = 40$ to be the best mixer at $x/D = 1.0$ and 2.0.

In addition to mixing effectiveness, another important criterion for evaluation of quick-mix sections is combustion efficiency. In particular, CO concentrations should be essentially eliminated from the combustor exit. The CO emission level in various axial planes downstream of the dilution jet is displayed in Fig. 12. For all cases except $J = 16$, it can be seen that the CO species has been oxidized (to CO_2) by $x/D = 0.25$. For $J = 16$, unreacted CO remains in the flowfield even at $x/D = 2.0$. This is due to jet underpentration, thus allowing rich burn gases (containing CO) on the centerline to pass through the quick-mix section without contact with dilution air.

The NO_x results are presented in terms of Emission Index (EI) in Fig. 13. For the optimum case ($J_{opt} = 40$), EI is 2.9 at $x/D = 2.0$. Significant increase in EI is predicted as J is increased or decreased from the optimum value. For J greater than J_{opt}, jet overpenetration causes jet backflow on the centerline, resulting in higher NO_x emissions. For J less than J_{opt}, underpenetration of the jet results in reaction (and high temperatures) on the combustor centerline.

Downloaded 02 Jun 2010 to 171.66.16.112. Redistribution subject to ASME license or copyright; see http://www.asme.org/terms/Terms_Use.cfm

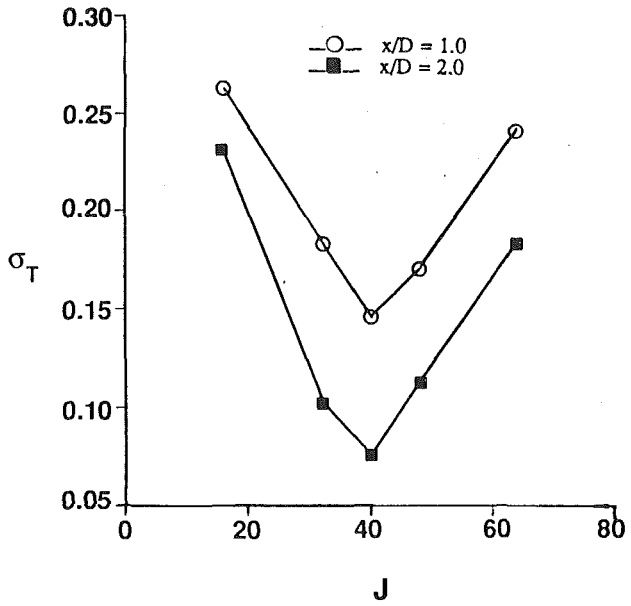


Fig. 11 Mixing effectiveness: reacting flow

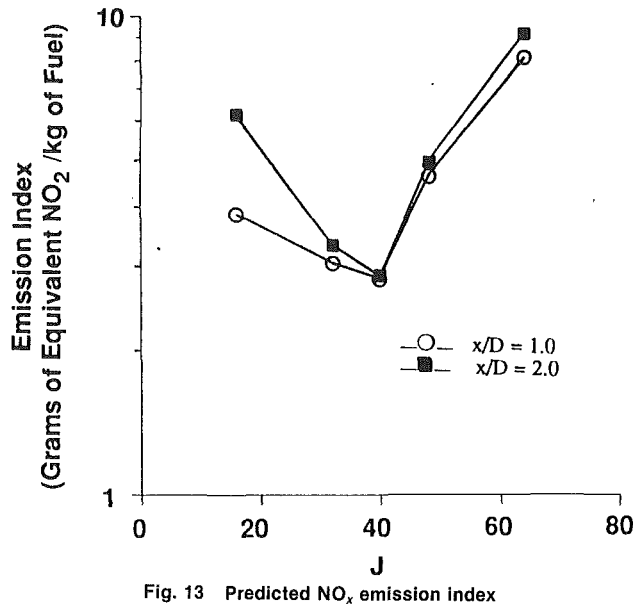


Fig. 13 Predicted NO_x emission index

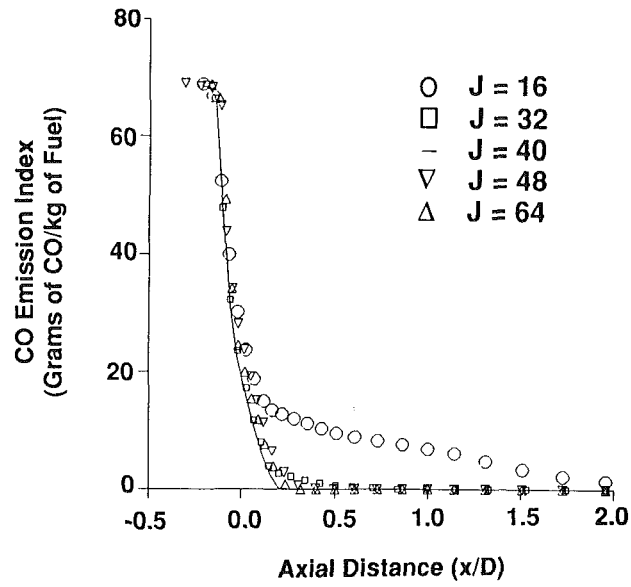


Fig. 12 Predicted CO emissions

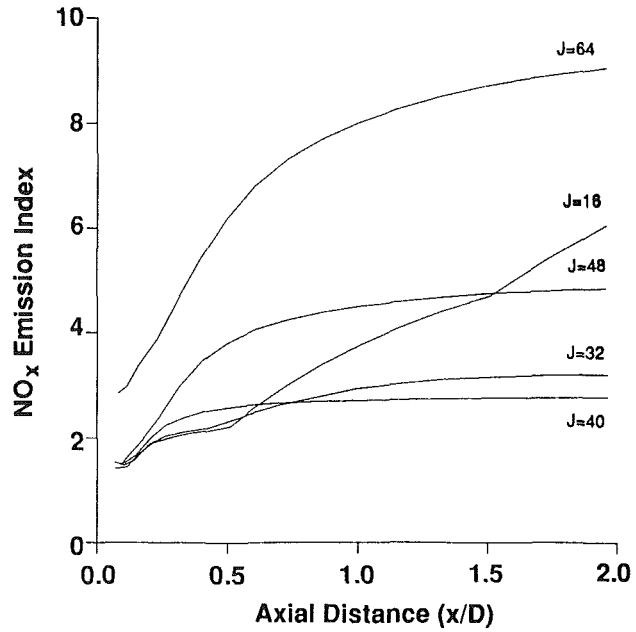


Fig. 14 History of NO_x formation in mixer

Fig. 14 shows NO_x concentrations convected out of each axial plane. Except for $J = 16$, all cases show very little NO_x formation downstream of $x/D = 1.0$. This indicates that high temperature zones are no longer existent. For the $J = 16$ case, NO_x formation is increasing significantly downstream of $x/D = 1.0$, indicating high temperature and chemical rection is still taking place.

Variation of Slot Aspect Ratio. Three slot aspect ratios (SAR) were numerically analyzed: 1, 4, and 16. The long dimension was aligned in the mainstream flow direction. The numerical grid was slightly modified for each slot, and central differencing was employed for increased accuracy. The jet-to-mainstream momentum flux ratio and mass flow ratio was maintained constant at 32 and 1.94, respectively.

Isotherms in the *rx*-plane through the jet centerline are shown in Fig. 15. As SAR increased, jet penetration increased (as seen in Fig. 15). This is due to reduced flow blockage as SAR is increased. Figure 16 shows the effect of SAR on NO_x emissions. For SAR of 1, predicted NO_x levels are less than those for SAR of 4, but chemical reaction and NO_x formation is still occurring at x/D of 1 due to jet underpenetration. This is evidenced by the steep slope of the NO_x curve at x/D of 1. A similar effect of delayed NO_x formation on the centerline caused by jet underpenetration was shown in Fig. 14 for J of 16 and SAR of 4. Hence, the best SAR is 4, with jet overpenetration for SAR of 16 (and corresponding higher NO_x levels).

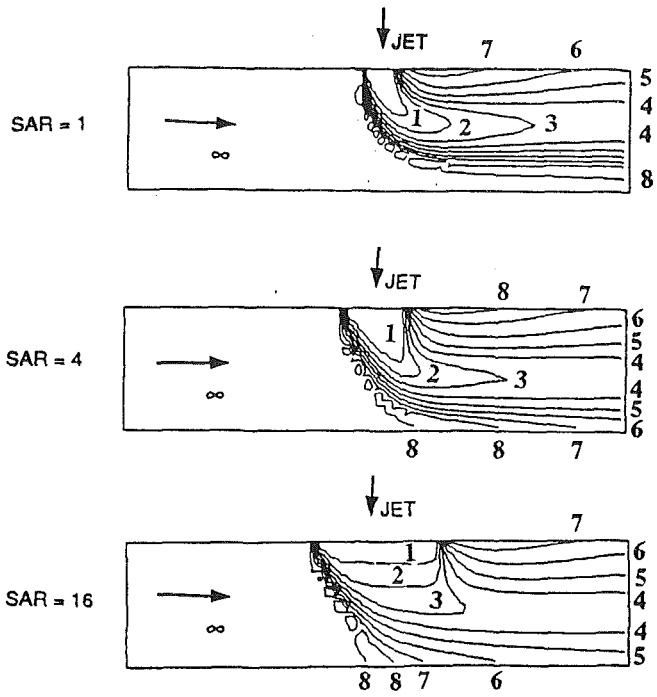
These results suggest the importance of SAR on NO_x emissions. As shown earlier for J variation, the jet must penetrate to approximately midradius of optimum mixing, and hence lowest NO_x.

Conclusions

The overall conclusions of this study were:

1 The viability of using 3-D CFD to model and screen quick-

Downloaded 02 Jun 2010 to 171.66.16.112. Redistribution subject to ASME license or copyright; see http://www.asme.org/terms/Terms_Use.cfm



CONTOUR LEVELS

	°K
1	1000
2	1200
3	1400
4	1600
5	1800
6	2000
7	2200
8	2400

Fig. 15 Isotherms in *rx* plane through jet centerline: effect of slot aspect ratio (SAR)

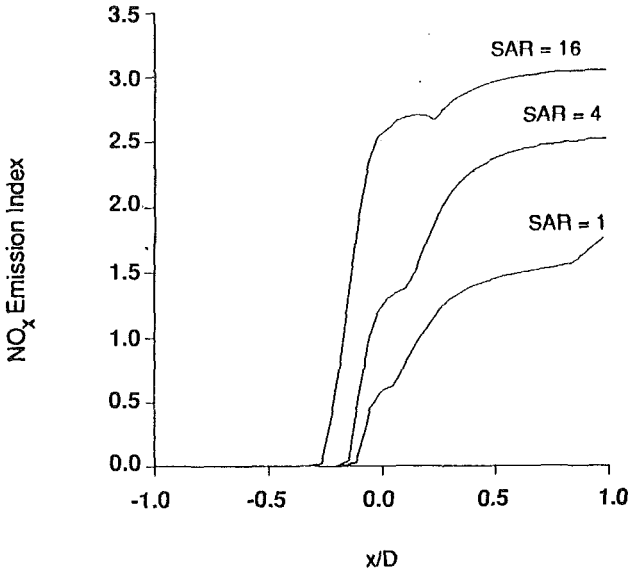


Fig. 16 Effect of slot aspect ratio (SAR) on NO_x emissions

mix concepts of low emission combustors was successfully demonstrated.

2 A 5-in-dia. quick-mix section compatible with the NASA LeRC Low Emission Combustor Program was numerically analyzed. The configuration consisted of 12 radial-inflow slots uniformly distributed around the perimeter of the quick-flow section. Optimum mixing for nonreacting flow occurred for a jet-to-mainstream momentum flux ratio (J) between 32 and 40. For reacting flow, the NO_x emission index was shown to be highly sensitive to J, with the lowest value of 2.9 calculated for J of 40 (at $x/D = 2.0$).

3 The numerical results suggest that slot aspect ratio has a pronounced effect on jet penetration and mixing effectiveness. Conventional correlations for optimum mixing effectiveness for holes may not be applicable for slots.

Acknowledgments

The authors wish to thank NASA Lewis Research Center for funding this work under NASA Contract NAS3-25834. Our thanks also are extended to Drs. Laurence Keeton, H. Q. Yang, Andrzej Przekwas, Anantha Krishnan and Mr. Sami Habchi of CFD Research Corporation.

References

Anderson, D., 1975, "Effect of Equivalence Ratios and Dwell Time on Exhaust Emissions From an Experimental Premixed Prevaporizing Burner," NASA TMX-71592.

Avva, R. K. Smith, C.E., and Singhal, A. K., 1990, "Comparative Study of High and Low Reynolds Number Versions of k- Models," Paper No. AIAA-90-0246, *28th Aerospace Sciences Meeting*.

Chen, Y. S., and Kim, S. W., 1987, "Computation of Turbulent Flows Using an Extended k-ϵ Turbulence Closure Model," NASA CR-179204.

Chien, K. Y., 1985, "Predictions of Channel and Boundary-Layer Flows With a Low-Reynolds-Turbulence Model," *AIAA Journal*, Vol. 23, No. 2.

Holdeman, J. D., Reynolds, R., and White, C., 1987, "A Numerical Study of the Effects of Curvature and Convergence on Dilution Jet Mixing," Paper No. AIAA-87-1953, AIAA/SAE/ASME/ASEE 23rd Joint Propulsion Conference.

Kim, S. W., and Chen, C. P., 1988, "A Multiple Time Scale Turbulence Model Based on Variable Partitioning of Turbulent Kinetic Energy Spectrum," Paper No. AIAA-88-1771.

Launder, B. E., and Spalding, D. B., 1974, "The Numerical Computation of Turbulent Flows," *Computer Methods in Applied Mechanics and Engineering*, Vol. 3, pp. 269–289.

Mosier, S. A., and Pierce, R. M., "Advanced Combustion Systems for Stationary Gas Turbine Engines," Vol. I, EPA Contract 68-02-2136.

Nguyen, H., Bittker, D., and Niedzwiecki, R., 1989, "Investigation of Low NO_x Staged Combustor Concept in High Speed Civil Transport Engines," Paper No. AIAA-89-2942, AIAA/ASME/SAE/ASEE 25th Joint Propulsion Conference.

Nickerson, G. R., Coats, D. E., Dang, A. L., Dunn, S. S., and Kehtarnavaz, H., 1989, "Two-Dimensional Kinetics TDK Nozzle Performance Computer Program; Vol. II: Programming Manual," NAS8-36863.

Pierce, R. M., Smith, C. E., and Hinton, B. S., 1990, "Advanced Combustion Systems for Stationary Gas Turbine Engines," Vol. III, EPA Contract 68-02-2136.

Przekwas, A. J., Habchi, S. D., Yang, H. Q., Avva, R. K., Talpallikar, M. V., and Krishnan, A., 1990, "REFLEQS-3D: A Computer Program for Turbulent Flows With and Without Chemical Reaction, Vol. 1: User's Manual," CFD Research Corp., Huntsville, AL, CFDRC Report GR-89-4.

Quan, V., Marble, F. E., and Kliegel, J. R., 1972, "Nitric Oxide Formation in Turbulent Diffusion Flames," *14th Symposium on Combustion*, pp. 851–860.

Ratcliff, M. L., and Smith, C. E., 1989, "REFLEQS-2D: A Computer Program for Turbulent Flow With and Without Chemical Reaction; Vol. 2: Validation Manual," CFD Research Corp., Huntsville, AL, CFDRC Report GR-88-4.

Smith, C. E., Ratcliff, M. L., Przekwas, A. J., Habchi, S. D., and Singhal, A. K., 1988, "Modeling of Turbulent Combustion in Liquid Rocket Engine Components," NASA MSFC Contract NAS8-37619, SBIR Phase I Final Report, CFDRC Report 4045/1.

Smith, C. E., Ratcliff, M. L. Przekwas, A J., and Habchi, S. D., 1989, "Validation of an Advanced Turbulent Combustion Code: REFLEQS," 7th SSME CFD Workshop, NASA MSFC.

Tacina, R. R., 1990, "Low NO_x Potential of Gas Turbine Engines," Paper No. AIAA-90-0550, 28th Aerospace Sciences Meeting.

Downloaded 02 Jun 2010 to 171.66.16.112. Redistribution subject to ASME license or copyright; see http://www.asme.org/terms/Terms_Use.cfm

Evaluation of NO_x Mechanisms for Lean, Premixed Combustion

R. A. Corr[1]

P. C. Malte

N. M. Marinov

Combustion Laboratories,
Department of Mechanical Engineering,
University of Washington,
Seattle, WA 98195

The formation of the oxides of nitrogen, NO_x, is examined through experiments and chemical kinetic modeling for lean, premixed combustion in a laboratory, atmospheric pressure, jet-stirred reactor. The experimental conditions are as follows: fuel-air equivalence ratio (ϕ) of 0.6, temperatures of 1460 to 1730 K, and reactor loadings of 20 to 150 kg/sec-m^3-atm^2, which correspond to reactor mean residence times of 11.4 to 1.8 milliseconds. Two fuels are examined: ethylene, because of its importance as a combustion intermediate, and methane, because of its importance as a component of natural gas. Besides the premixed operation, the reactor also is operated nonpremixed. For both modes, the NO_x increases with decreasing loading, from about 3–4 ppmv at the highest loading to about 11–21 ppmv at the lowest loading for the ethylene fuel. This increase in NO_x occurs because a hot spot develops on centerline when the reactor is lightly loaded. Also for the lowest loading, the nonpremixed mode produces about twice as much NO_x as the premixed mode, i.e., about 21 versus 11 ppmv. At the other reactor loadings, however, because of the intense mixing, the NO_x levels are only slightly elevated for the nonpremixed mode compared to the premixed mode. Upon switching to methane fuel, the NO_x decreases by about 25 percent. The major finding of this study is that prompt NO is the predominant mechanism for the NO_x formed. The other mechanisms considered are the Zeldovich and nitrous oxide mechanisms. Furthermore, the amount of NO_x measured and modeled agrees almost exactly with the extrapolation of Fenimore's (1971) original prompt NO data to the present conditions of $\phi = 0.6$. Although Fenimore conducted his experiments with porous plate and Meker-type burners for $0.8 \leq \phi \leq 1.7$, our findings show that his results apply well to high-intensity, lean combustion. In the gas turbine literature, e.g., see Shaw (1974) and Toof (1985), Fenimore's results are expressed as:

$$NO/(NO)_{equil} = P^{1/2}\text{func}\ (\phi) \quad (1)$$

It is func (ϕ) that extrapolates well to our conditions. This finding indicates that func (ϕ) applies to laboratory burners of widely different mixing intensity, i.e., from Fenimore's burners with structured flame fronts to our high-intensity burner with dispersed reaction. In our opinion, this finding strengthens the justification of using func (ϕ) for the prediction of NO_x formation in practical combustors, including lean, premixed combustors.

Introduction

Gas turbine engine manufacturers are focusing research and development on lean, premixed combustors. This includes heavy-duty engines, for which the dry NO_x goal has been about 25 ppmv (15 percent O_2 dry), though one also hears about lower goals, and engines for high-speed commercial aircraft, for which the NO_x must be reduced 80–90 percent in order to curtail stratospheric ozone depletion. For heavy-duty engines, recent combustor developments are discussed, for example, by Davis and Washam (1989), Sattelmayer et al. (1990), Jeffs (1989), and Maghon et al. (1988).

Lean, premixed gas turbine combustors operate in a regime for which the NO_x can in principle be contributed from three distinct chemical mechanisms; the Zeldovich mechanism leading to thermal NO, the prompt NO mechanism (Fenimore, 1971), and the nitrous oxide mechanism (Malte and Pratt, 1974).

The objective of our study has been to evaluate the relative importance of these mechanisms for lean, premixed, high-intensity combustion, through experiments conducted with a laboratory, atmospheric pressure, jet-stirred reactor, and through chemical kinetic modeling.

Please note that in this paper the formation mechanisms are expressed in terms of NO. However, exhaust emissions and general discussion of the problem are expressed in terms of NO_x, the sum of NO and NO_2, since some of the NO generally oxides to NO_2 within the combustor and sample probe.

[1]Present address: General Electric Company, Schenectady, NY.

Contributed by the International Gas Turbine Institute and presented at the 36th International Gas Turbine and Aeroengine Congress and Exposition, Orlando, Florida, June 3-6, 1991. Manuscript received at ASME Headquarters March 4, 1991. Paper No. 91-GT-257. Associate Editor: L. A. Riekert.

Copyright © 1992 by ASME
Downloaded 02 Jun 2010 to 171.66.16.112. Redistribution subject to ASME license or copyright; see http://www.asme.org/terms/Terms_Use.cfm

Mechanisms

The Zeldovich mechanism, through thermal NO modeling, is widely applied to conventional, diffusion flame, gas turbine combustors. The adiabatic, equilibrium, stoichiometric product gas temperature and composition are determined from chemical equilibrium modeling. Superimposed upon this field is the extended Zeldovich mechanism, listed as reactions in Eqs. (2)–(4). That is, the NO and N-atom are the only species determined kinetically. The effective residence time for the NO formation is very short. Shaw (1974) assumed 0.5 ms, and obtained good agreement with NO_x data for aircraft gas turbine engines. Toof (1985) evaluated the effective residence time by considering the combustor geometry and velocity. His residence time varied from about 0.4–0.8 ms.

$$N_2 + O \Leftrightarrow NO + N \quad (2)$$

$$N + O_2 \Leftrightarrow NO + O \quad (3)$$

$$N + OH \Leftrightarrow NO + H \quad (4)$$

The prompt NO mechanism was introduced by Fenimore (1971). By this mechanism, hydrocarbon radical fragments formed in the flame zone (or in multiple flame zones) react with N_2 to form cyano species and N-atom which oxidize to NO. The reaction that is now thought to be predominant in initiating this mechanism is as follows:

$$CH + N_2 \Leftrightarrow HCN + N \quad (5)$$

Toof (1985) compared the levels of thermal and prompt NO for conventional, diffusion flame, gas turbine combustors, and showed the significance of the prompt NO. The prompt NO concentration was computed by Eq. (1), assuming $\phi = 1.0$. Toof's modeling results for the case of a 14:1 pressure ratio gas turbine engine fired on nitrogen-free distillate oil gave about 240 ppmv (i.e., parts per million by volume) thermal NO and about 80 ppmv prompt NO. When water injection was added to the primary zone of the combustor, at a water-to-fuel ratio of 0.8 kg/kg, Toof's thermal NO prediction dropped to about 20 ppmv, and the prompt NO, which dropped to about 40 ppmv, became the predominant source of the NO_x exhaust emission.

The nitrous oxide mechanism for NO was developed by Malte and Pratt (1974) in order to explain relatively large amounts of NO_x measured from a CO-fired jet-stirred reactor. In this mechanism, the N_2 and O-atom undergo recombination reaction to form N_2O. The fate of the N_2O is fourfold as shown by reactions (6) and (9): dissociation back to N_2, attack by H-atom leading to N_2, and attack by O-atom leading to N_2 and NO. For CO combustion with reasonably dry air, the mechanism appears to be important because the H-atom attack pathway, i.e., reaction (7), is minimized. For hydrocarbon combustion, however, the role of the mechanism appears to be supporting, rather than predominant. Drake and Blint (1989), for the modeling of high-pressure, laminar, stoichiometric, methane-air flames find the mechanism to be responsible for about 10 percent of the total NO_x. For fuel-lean conditions, a greater percentage contribution is indicated by these authors. Glarborg et al. (1986), in a study of NO kinetic modeling for jet-stirred reactors, indicate that the mechanism contributes at lean conditions.

$$N_2 + O + M \Leftrightarrow N_2O + M \quad (6)$$

$$N_2O + H \Leftrightarrow N_2 + OH \quad (7)$$

$$N_2O + O \Leftrightarrow N_2 + O_2 \quad (8)$$

$$N_2O + O \Leftrightarrow NO + NO \quad (9)$$

As previously stated, all three mechanisms can contribute in the case of lean, premixed combustion. The predominance of the Zeldovich NO mechanism, which is experienced for conventional, undiluted, diffusion flame combustors, is curtailed for lean, premixed combustion because combustion temperatures are reduced and stoichiometric flame zones are eliminated. However, this mechanism cannot be discounted. Especially, pilot flames and nonuniformities in temperature and the active free radicals can contribute Zeldovich NO. The prompt NO mechanism, although associated mainly with rich combustion, contributes at lean conditions. Zones of oxidative pyrolysis contribute the hydrocarbon radical fragments which attack the N_2 and to the prompt NO. Results from this study, shown next, indicate the predominance of prompt NO. The nitrous oxide mechanism, as previously stated, also can contribute for lean, premixed combustion. However, there is uncertainty in its rate constants, and experiments of NO_x versus pressure do not support the mechanism. For example, Altemark and Knauber (1987) report a flat response of NO_x (10 ppmv) over the pressure range of 4–10 bar from a lean, premixed combustor, which is a laboratory simulation of a developmental gas turbine combustor. Because of the $N_2 + O$-atom recombination reaction of the nitrous oxide mechanism, a stronger pressure dependence than observed would be expected.

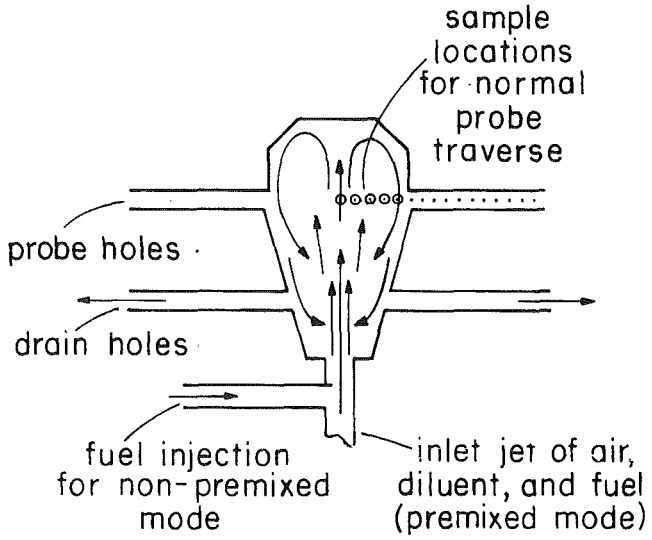


Fig. 1 Schematic of jet-stirred reactor cavity

Experimental

The jet-stirred reactor used in this study is shown in Fig. 1. The reactor, of cylindrically symmetric shape and 15.8 cm^3 volume, is fed at its base and stirred by a single jet. Reactor dimensions are as follows: jet inlet diameter is 4.4 mm, base diameter is 16 mm, maximum diameter of the reactor is 25 mm, and height of the reactor is 45 mm. The reactor has four 4-mm-dia drain holes equally spaced around its circumference and located 6 mm above the base, and three more holes of the same size located 25 mm above the base, which serve as probe ports. The reactor walls are made of castable fireclay, and the top piece and base are made of Inconel. The reactor is heavily insulated.

In this study, the reactor is operated in two modes, a premixed mode and a nonpremixed mode. These modes are defined later. First, however, it is helpful to discuss the history of the reactor. The reactor was developed by Thornton et al. (1987) for the detailed study of oxidation kinetics. The reactor was shown to be successful, and studies of the oxidation kinetics of several hydrocarbons were conducted. This objective required that the reactor be well-stirred, that is, the reactor had to exhibit uniformity in its time-mean temperature and composition. The rate of the chemistry had to be slow compared to the rate of the mixing. This was accomplished by maintaining the reactor temperature between 1000 and 1300 K, by injecting only a small amount of hydrocarbon fuel, and

Downloaded 02 Jun 2010 to 171.66.16.112. Redistribution subject to ASME license or copyright; see http://www.asme.org/terms/Terms_Use.cfm

Table 1 Experimental matrix

Fuel	ϕ	Mode	$\dot{m}/VP^2$ (kg/sec-m^3-atm^2)	Residence Time (msec)	Area-Average Uncorrected Temperature (K)	Area-Average Corrected Temperature (K)	Centerline Uncorrected Temperature (K)	Centerline Corrected Temperature (K)
Premixed:								
C_2H_4	0.60	Premix	21	11.4	1456	1562	1560	1753
C_2H_4	0.60	Premix	92	2.9	1449	1504	1431	1478
C_2H_4	0.60	Premix	151	1.8	1463	1459	1406	1382
Non-Premixed:								
C_2H_4	0.60	Non-Premix	21	11.4	1453	1555	1535	1704
C_2H_4	0.60	Non-Premix	87	3.0	1453	1509	1385	1412
C_2H_4	0.60	Non-Premix	143	1.8	1462	1458	1349	1308
Methane:								
CH_4	0.60	Premix	66	3.7	1431	1478	1470	1534
CH_4	0.60	Premix	100	2.4	1458	1518	1469	1533
Temperature Variation:								
C_2H_4	0.60	Premix	92	2.8	—	—	1466	1530
C_2H_4	0.60	Premix	85	2.8	—	—	1513	1595
C_2H_4	0.60	Premix	75	2.8	—	—	1589	1691
C_2H_4	0.60	Premix	71	3.0	—	—	1625	1730

by operating at short mean residence times of about 2 ms or less. In this setup, the inlet jet was sonic, had essentially the same temperature as the reactor, and had a nominal molar composition of 10 percent O_2, 15 percent H_2O, and 75 percent N_2. The inlet jet was created by a pressurized, lean, hydrogen-air burner located immediately below the jet-stirred reactor. The small amount of hydrocarbon fuel was seeded into the hot, sonic jet immediately upstream of the entry of the jet into the reactor.

Because of the uniformity of the well-stirred mode, it was desirable to attempt NO_x studies with it. However, as feared at the outset of these experiments, the temperature level of the well-stirred mode proved too low to reliably produce measurable NO_x (i.e., at least 1.0 ppmv). In these experiments, an argon-oxygen mixture was substituted for air in the hydrogen burner, and nitrogen was injected with the fuel just prior to the jet-stirred reactor. Although these experiments were not successful, the well-stirred mode is useful for studying the oxidation of NO to NO_2, and the reduction of NO_x. Results of this are listed in Appendix B.

For the present experiments, the jet was changed to cold reactants, and the hydrocarbon fuel-air ratio was increased to exceed the lean flammability limit. The minimum reactor mean temperature for sustainable combustion is about 1400 K. The two operating modes are now defined.

- *Premixed Mode:* The chamber below the jet-stirred reactor, which was previously the hydrogen-air burner, is now used simply as an unfired premixing chamber. The fuel and air, at a fuel-air equivalence ratio $\phi = 0.6$, and argon diluent used to modify the combustion temperature, are premixed in this chamber. The drawback of this configuration arises because of the higher minimum reactor temperature and hydrocarbon fuel input required compared to the well-stirred mode. Uniform reactor composition is no longer feasible. Oxidative pyrolysis of the hydrocarbons, including the formation and oxidation of secondary hydrocarbons and the formation of carbon monoxide, occurs predominantly in the jet before the reactants are dispersed throughout the reactor. Even for reactor mean residence times as short as 1–2 ms and temperatures as low as 1400 K, the rate of oxidative pyrolysis reaction, surrounded by a large, essentially uniform, recirculation zone of post-oxidative pyrolysis reactions, for example, reactions of CO oxidation and OH, H, O recombination. Nonetheless, the chemistry is much more dispersed than in low-turbulence laboratory burners with narrow, structured, continuous flame fronts.
- *Nonpremixed Mode:* The fuel is now added at the side injection tube of Fig. 1. This is the only change from the premixed mode. For high reactor loadings the fuel-air mixing in the jet is very rapid, and effectively, the reactor operates premixed. At low reactor loadings, fuel-air mixing continues into the reactor, and the reactor exhibits characteristics of well-aerated diffusion-flame combustion.

The experimental matrix is shown in Table 1. Four sets of experiments are listed, including the ethylene premixed experiments, the ethylene non-premixed experiments, the methane premixed experiments, and the ethylene temperature-variation experiments. During the first three sets of experiments, the area-average uncorrected temperature was held at a nominal value of 1450 K, and during the temperature-variation experiments, the reactor mean residence time was held at a nominal value of 2.8 ms. For the 12 experiments listed, the temperature and composition fields were measured. The species measured by probe sampling and gas analysis include NO, NO_2, O_2, N_2, CO, CO_2, and the C_1 to C_3 hydrocarbons. The locations measured in the reactor are indicated by the open circles along the path shown in Fig. 1. These include positions 0, 3, 5, 8, and 11 mm from the reactor centerline. The reactor wall is at 12.5 mm.

The temperature of the reactor is tuned to the desired level by using argon dilution. Temperature is measured with a type R thermocouple of 1 mm bead diameter, coated with BeO/YCI compound to prevent catalytic heat release. Temperature data are shown uncorrected, i.e., as measured, and also are shown corrected for thermocouple heat loss or gain. The corrected temperature represents the true gas temperature. The correction calculation is performed by balancing the three heat transfer processes which affect the measured, steady-state, thermocouple bead temperature. These are the convection exchange with the gases, the conduction loss through the thermocouple wires, and the radiation exchange with the reactor walls and radiation loss to cold spots seen by the thermocouple bead. Reactor wall brightness temperature is measured with a commercial red-line optical pyrometer. The temperatures listed in Table 1 are area-average data for the thermocouple probe path shown in Fig. 1, except for the fourth set of experiments, for which only the reactor centerline temperature is available. It also should be noted that the reactor mean residence time is based on the area-average corrected temperature. For the temperature-variation experiments, although area-average data were not obtained, the loading of the reactor is in the range for which spatial temperature differences are minimum. Thus the centerline temperatures for this case are assumed to be nearly equal to the area-average temperatures, and analysis is conducted using the centerline corrected temperatures.

The accurate measurement of small concentrations of NO and NO_2, of about 1–10 ppmv, from active flames is a difficult task. Free radical reactions affect the NO/NO_2 ratio and adsorption effects within the sampling system are possible. The sampling system and approach used is similar to that of Malte and Kramlich (1980). Sample gas at low pressure is drawn from the reactor through a cooled quartz sampling probe and tube

Downloaded 02 Jun 2010 to 171.66.16.112. Redistribution subject to ASME license or copyright; see http://www.asme.org/terms/Terms_Use.cfm

Table 2 Experimental results

			Area-Average, Corrected						Centerline, Corrected		
Fuel	Mode	$\dot{m}/VP^2$ (kg/sec-m^3-atm^2)	T (K)	NO (ppmv)	NO_2 (ppmv)	NO_x (ppmv)	CO (mole %)	Total HC (ppmvC)	T (K)	CO (mole %)	Total HC (ppmvC)
C_2H_4	Premix	21	1562	6.7	4.3	11.0	0.088	0	1753	0.261	13
C_2H_4	Premix	92	1504	0.0	5.0	5.0	0.451	94	1478	1.570	1500
C_2H_4	Premix	151	1459	0.0	3.9	3.9	0.913	32	1382	1.690	316
C_2H_4	Non-Premix	21	1555	15.8	5.6	21.4	0.099	6	1704	0.597	96
C_2H_4	Non-Premix	87	1509	0.1	5.8	5.9	0.535	251	1412	1.120	1800
C_2H_4	Non-Premix	143	1458	0.0	4.4	4.4	0.707	92	1308	1.360	725
CH_4	Premix	66	1478	0.0	4.4	4.4	0.395	1690	1534	0.656	7800
CH_4	Premix	100	1518	0.0	3.6	3.6	0.581	1230	1533	0.719	3790
				5 mm from CL, Corrected							
C_2H_4	T-Variation	92	—	0.0	6.7	6.7	—	—	1530	—	—
C_2H_4	T-Variation	85	—	0.0	7.5	7.5	0.358	10	1595	0.949	76
C_2H_4	T-Variation	75	—	0.9	9.2	10.1	0.303	0	1691	0.712	0
C_2H_4	T-Variation	71	—	2.1	8.6	10.7	—	—	1730	—	—

into an evacuated tank. The sampling at low pressure minimizes the conversion of NO to NO_2, and prevents condensation. Once the sample drawn into the tank reaches 0.13 atm, the tank is closed, the sample is compressed to 0.6 atm with nitrogen and allowed to stabilize. Analysis of the NO and NO_2 is then conducted with a NO/NO_x chemiluminescence analyzer. With this system, the uncertainty in the NO_x measurement is about ± 2.5 ppmv. The uncertainty is based on two effects: degree of repeatability in the experiments from day to day, and the accuracy of the NO/NO_x analyzer, including the influence of the agron quenching efficiency on the analyzer response. Lack of repeatability is the primary effect because of adsorption/desorption within the sampling system. For the other gases measured, GC analysis is conducted per the methods described by Thornton et al. (1987).

Results

The experimental results are listed in Table 2. Included in this table are the corrected data for temperature, NO, NO_2, and NO_x concentrations, CO concentrations, and total hydrocarbon (THC) concentrations. The THC concentrations are the sum of the CH_4, C_2H_2, C_2H_4, C_2H_6, and C_3H_8 concentrations, expressed on a C_1 basis, i.e., as ppmvC. Area-averaged data are listed for all experiments, except for the temperature, CO, and THC. Centerline data are not listed for the oxides of nitrogen, since these species always show nearly flat spatial profiles in the reactor (see below). For the temperature-variation experiments, the oxides of nitrogen are available for only one location, 5 mm from the centerline of the reactor.

Our definition of corrected temperature has been explained in the previous section. With respect to the concentration data, our correction involves normalization of the data to zero argon dilution. That is, the measured concentrations are multiplied by the ratio of the total moles with the argon present to the moles with the argon diluent subtracted from the total.

The temperature profiles for the premixed ethylene experiments and one nonpremixed experiment are plotted in Fig. 2. These are uncorrected data, except for one example of corrected data (92 kg/s-m^3-atm^3). These data show several features, which hold generally for the experiments, regardless of the fuel and degree of premixing. They are as follows:

- When operated at medium loading, e.g., the 92 kg/s-m^3 atm^3 case shown, the reactor exhibits nearly uniform temperature.
- With increased loading, e.g., the 151 kg/s-m^3-atm^2 case shown, because of the short amount of time available for chemical energy release, the centerline temperature is depressed somewhat compared to the temperature elsewhere in the reactor. Because of the short mean residence time, reactor heat loss is small, and the inside wall temperature is high.

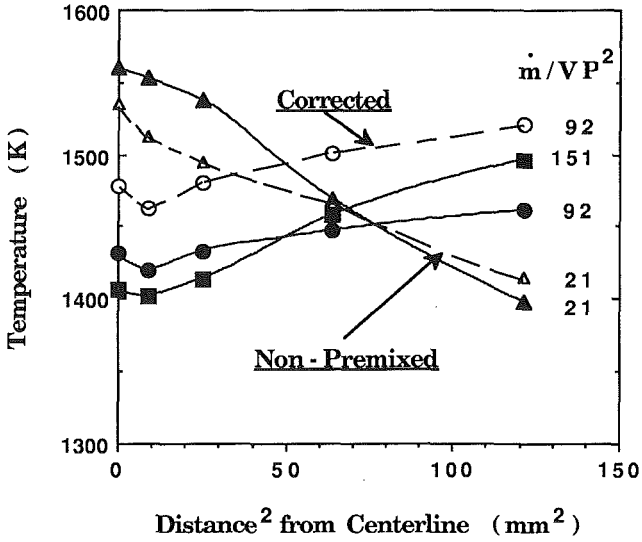


Fig. 2 Uncorrected thermocouple temperature profiles for the three ethylene premixed experiments. Also, the uncorrected temperature profile for the nonpremixed experiment at low reactor loading, and the corrected temperature profile for the premixed experiment at medium reactor loading. Parameter is reactor loading, $\dot{m}/VP^2$ as kg/s-m^3-atm^2.

- At light loading, e.g., the 21 kg/s-m^3-atm^2 case shown, because of the long residence time, heat loss from the reactor is significant. In order to maintain the overall temperature level of the reactor, the argon dilution is reduced or eliminated. This results in a hot spot on the centerline of the reactor.
- The correction for the medium loading case shown (92 kg/s-m^3-atm^2) added an increment of 50–60°C to the temperature. Although not shown, this increment increases as the reactor loading decreases, being about 100–200°C for the lowest loading and about 5–25°C for the highest loading. Also, the increment increases as the overall reactor temperature increases, being about 100°C for the medium loaded reactor when the corrected temperature is about 1700K.

The experimental results for NO_x are plotted in Figs. 3 and 4. In Fig. 3, profiles of NO_x are plotted and shown to be nearly flat. This is always the case in the jet-stirred reactor. The flat NO_x profiles imply one of two types of limiting behavior. Either (1) the NO_x forms very quickly in the jet of the reactor; or (2) the NO_x forms very slowly (compared to the mixing rate) throughout the reactor. Explanation (1) is thought to be the more likely of the two possibilities, as indicated in the next section.

In Fig. 4, the area-averaged NO_x is plotted versus reactor loading. The main features of this plot are described later. First, however, we wish to explain that the sharp upswing in

Downloaded 02 Jun 2010 to 171.66.16.112. Redistribution subject to ASME license or copyright; see http://www.asme.org/terms/Terms_Use.cfm

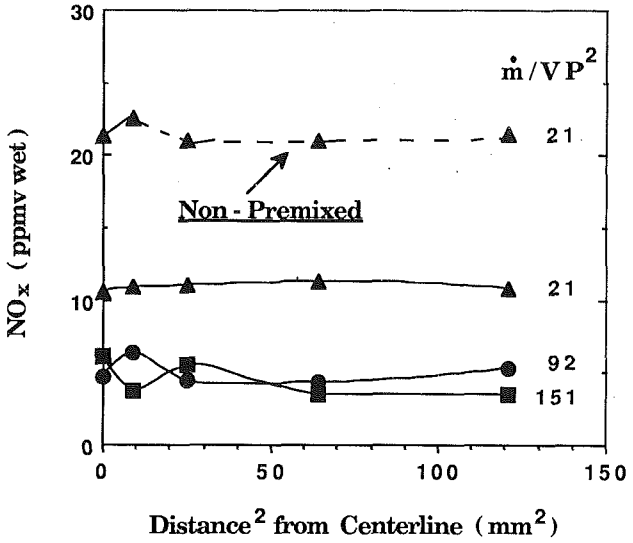


Fig. 3 NO_x profiles for the three ethylene premixed experiments, and for the nonpremixed experiment at low reactor loading. Parameter $\dot{m}/VP^2$ is defined in Fig. 1.

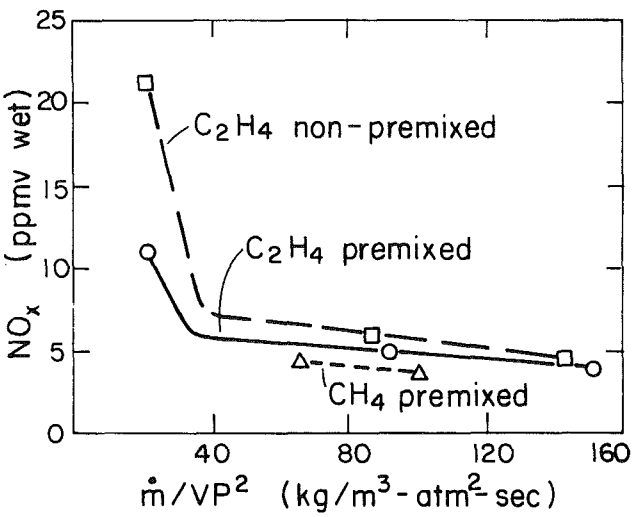


Fig. 4 Area-averaged NO_x versus reactor loading ($\dot{m}/VP^2$) for the ethylene premixed and nonpremixed experiments, and for the methane premixed experiments

NO_x at a loading of about 30 kg/s-m^3-atm^2 is not plotted arbitrarily. During preliminary experiments, data were obtained for a finer grid of loadings than used in the final experiments published here. These preliminary experiments did not use the low pressure sampling technique just described, and thus, the NO_x absolute values were subject to greater uncertainty than we wished. However, the trends with respect to loading were reliable. These measurements reliably demonstrated a sharp increase in NO_x as the reactor loading decreased into the 30 kg/s-m^3-atm^2 range, when the nominal, uncorrected, reactor temperature was between 1450 and 1650 K.

The features of Fig. 4 are now described:

- For the three cases plotted, the NO_x increases with decreasing loading. The gradual change observed for all but the lightly loaded reactor is due to two effects: (1) less residence time is available for NO_x formation and (2) the corrected, area-average temperature decreases slightly as loading increases (see Table 1 or 2).
- Except for lightly loaded reactor, the NO_x is measured as NO_2 (see Table 2). It is known that small concentrations of NO oxidize readily to NO_2 within jet-stirred reactors and sampling probes (Malte and Kramlich, 1980).
- Except for the lightly loaded reactor, the nonpremixed mode produces only slightly more NO_x than the premixed mode. This behavior is due to the strong mixing intensity within the reactor, which causes the nonpremixed mode to behave as if it were premixed.
- Methane combustion produces about 75 percent of the NO_x level observed when ethylene is burned at the same temperature. This difference is similar to that observed by Fenimore (1971), when he studied prompt NO from these two fuels.
- The lowest reactor loading has two distinct features. The NO_x levels increase significantly at this loading, and the nonpremixed mode produces about double the NO_x of the premixed mode. Only for this loading are significant amounts of NO measured, in addition to the 4–6 ppmv NO_2 generally observed in our experiments. The first feature, i.e., the sharp increase in NO_x, is thought to be associated with the hot centerline, which occurs when the reactor is lightly loaded. This hot region of the reactor is shown in Fig. 2; additional temperature data listed in Tables 1 and 2 support this temperature trend. The second feature, i.e., the factor two greater NO_x for the nonpremixed mode compared to the premixed mode, does not appear to be due to temperature differences between the modes. As plotted in Fig. 2, the nonpremixed mode shows a slightly less steep temperature gradient across the reactor than the premixed mode, which would tend to diminish NO_x. If the nonpremixed mode is leading to hot spots relative to the premixed mode, thereby increasing the NO_x, these hot spots have a length scale less than that of the thermocouple bead, which is 1 mm. A more likely explanation of the increased NO_x in the nonpremixed mode is an increase in the fuel-richness of the centerline region. As the nonpremixed mode loading decreases, the centerline jet of the reactor takes on an increasingly darker blue color with green color also noted. This indicates that ϕ is locally greater than the overall value of 0.6. Increasing ϕ at constant T is known to increase prompt NO, as discussed in the next section.

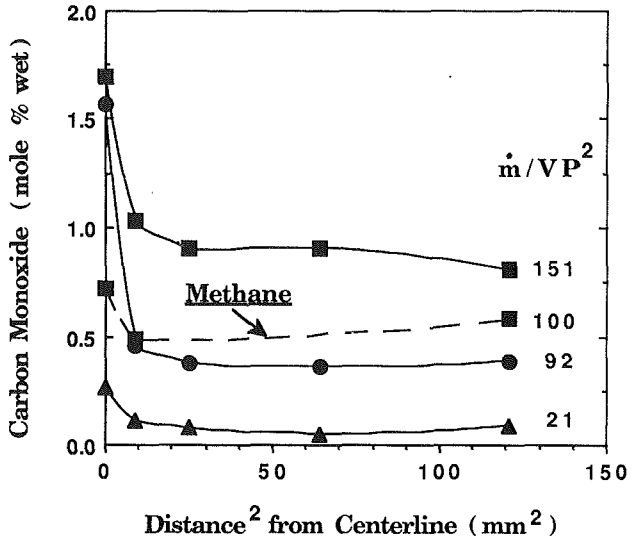


Fig. 5 Carbon monoxide profiles for the three ethylene premixed experiments, and one of the methane experiments at medium loading. The parameter $\dot{m}/VP^2$ is defined in Fig. 1.

Carbon monoxide and hydrocarbon profiles for the reactor are plotted in Figs. 5 and 6. Supporting data are listed in Table 2 and in Table C-1 of Appendix C. The figures verify that the oxidative pyrolysis chemistry is very fast, and not dispersed uniformly throughout the reactor. For the ethylene fuel, the hydrocarbon concentrations on centerline are an order of magnitude greater than the area-averaged concentrations, and the carbon monoxide concentrations are a factor 2–3 greater on

Downloaded 02 Jun 2010 to 171.66.16.112. Redistribution subject to ASME license or copyright; see http://www.asme.org/terms/Terms_Use.cfm

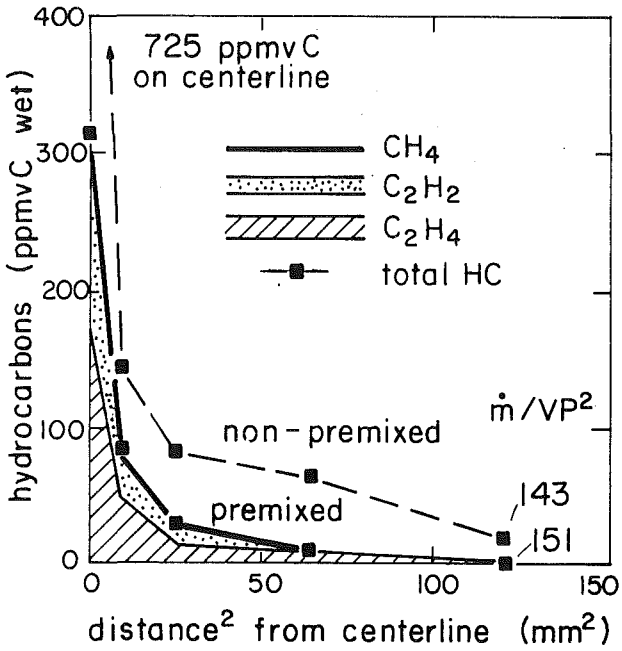


Fig. 6 Total hydrocarbon profiles for the ethylene premixed and nonpremixed experiments at high loading. Also, the contributions of methane, acetylene, and ethylene to the total hydrocarbon sum are shown for the premixed case. Parameter $\dot{m}/VP^2$ is defined in Fig. 1.

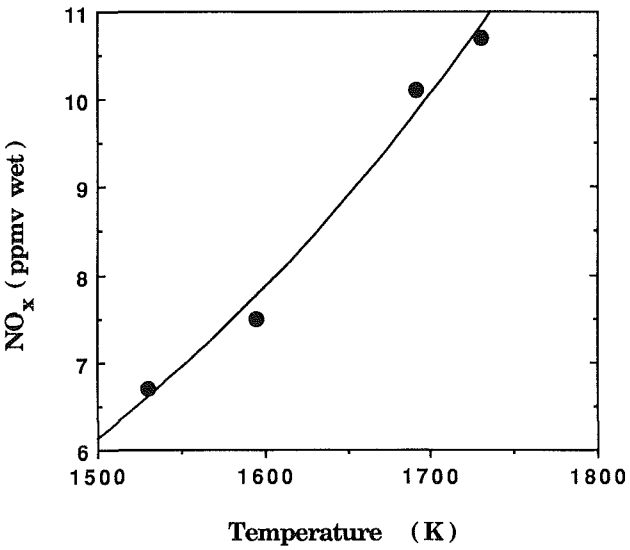


Fig. 7 NO_x at location 5 mm from centerline versus corrected centerline temperature for premixed ethylene experiments at normal mean residence time of 2.8 ms

centerline compared to the area-averaged data. The smallest area-averaged CO concentration is about 900 ppmv, for the lightly loaded, premixed case burning ethylene. The area-averaged THC concentration for this case is zero. Nonpremixed combustion shows a somewhat greater THC than premixed combustion, and a slightly greater CO except for a decrease in CO at the high reactor loadings.

The data on NO_x as a function of temperature, for constant mean residence time, are plotted in Fig. 7. The NO_x data vary from 6.7 ppmv at 1530 K to 10.7 ppmv at 1730.

Analysis

The NO_x data for the ethylene premixed experiment at medium loading (92 kg/s-m^3-atm^2) are given primary attention for analysis for the NO mechanisms. This is because this case

Table 3 Analysis of premixed ethylene case 92 kg/s·m^3-atm^2, 2.9 ms, 1521 K*, 5.0 ppmv NO_x

Mechanism	Free Radical Concentration Required to Give Measured NO_x	Predicted NO Based on Estimated Free Radical Concentration
Zeldovich	7.1 mole % O-atom	0.2mole % O-atom ⇒ 0.15 ppmv NO
Nitrous Oxide	11.1 mole % O-atom	0.2mole % O-atom ⇒ 0.75 ppmv NO
Prompt	0.13 ppmv CH	0.11 ppmv CH ⇒ 4.1 ppmv NO
Total		5.0 ppmv NO

*Peak corrected temperature of reactor profile.

exhibits a well-behaved temperature. The temperature profile shows only small variations, and the temperature correction is modest (50–60°C). Our analysis of this case is based on the highest corrected temperature found for the profile, which is 1521 K at the location 11 mm from the reactor centerline. The area-average value of 1504 K is not used, since we wish to be sure not to underestimate the Zeldovich NO.

The results of our analysis are listed in Table 3. Shown is the free radical concentration required to give the measured NO_x value of 5.0 ppmv, for a uniform reactor of measured residence time (2.9 ms), measured N_2 concentration (75.6 mole percent corrected), and 1521 K temperature. Unrealistic values of the free radical concentration either eliminate the mechanism or diminish its significance.

The extended Zeldovich mechanism applied to a uniform reactor of NO concentration very small compared to the equilibrium NO value gives the following equation:

$$X_{NO} = 2k_{2f}(P/RT)X_{N_2}X_o t \tag{10}$$

In this equation X denotes mole fraction, R is the universal gas constant, $k_{2f} = 2\times10^{14}\exp(-38500/T)$ is the forward rate constant of reaction (2) in cgs units, t is the mean residence time, and P is 1 atm.

Application of Eq. (10) shows that the O-atom concentration must be 7 mole percent, which is unrealistically high. Recalculation using the adiabatic equilibrium temperature (1554 K) also gives an unrealistic value, 4 mole percent.

Next, a reasonable value of O-atom concentration is estimated, and the Zeldovich NO production is calculated. Jet-stirred reactors of the type used, for the conditions used, exhibit O-atom concentrations in the approximate range of 0.05 to 0.2 mole percent. Singh et al. (1978) measured an O-atom concentration of 0.2 mole percent for a jet-stirred reactor fired on methane at $\phi = 0.7$, 1780 K temperature, and approximate 3 ms mean residence time. Since the present reactor is operated at ϕ and T lower than the experiments of Singh et al., the O-atom concentration for our experiments should be somewhat less than 0.2 mole percent. However, this value is representative, and is taken to be an upper limit for the present experiments.

As shown in Table 3, 0.2 mole percent O-atm yields a Zeldovich NO concentration of 0.15 ppmv. It is concluded that Zeldovich NO does not contribute significantly to the medium loaded reactor.

The nitrous oxide mechanism is analyzed next. As shown in Table 3, 11 mole percent O-atom is required to produce 5.0 ppmv NO. This value of O-atom is unrealistic. However, the nitrous oxide mechanism contributes weakly. That is, for an O-atom concentration of 0.2 mole percent, 0.75 ppmv NO is produced by the nitrous oxide mechanism. This is 15 percent of the measured amount.

The equation for the nitrous oxide mechanism is based on reactions Eqs. (6)–(9) previously discussed. Of the four pathways for destruction of the nitrous oxide, reaction Eq. (7) is

Downloaded 02 Jun 2010 to 171.66.16.112. Redistribution subject to ASME license or copyright; see http://www.asme.org/terms/Terms_Use.cfm

predominant for the present application. Also, the major hydrogen-oxygen free radicals are close to being in partial equilibrium. This is verified by our chemical kinetic modeling. Because of these points, a simplified equation may be written for the application of the nitrous oxide mechanism to a uniform reactor. This equation is as follows:

$$X_{NO} = 2(k_{6f} k_{9f} K^{1/2}/k_{7f})\,(P/RT)^2 (X_{N_2} X_{O_2}/X_{H_2O}^{1/2}) X_O^{1/2} t \quad (11)$$

where K is the equilibrium constant for $2H + 2O_2 = 3O + H_2O$. For the present application $K^{1/2} X_{O_2}/(X_{H_2O}^{1/2} \cong 0.08$. The rate constant data (k_{6f}, k_{9f}, k_{7f}) are from Miller and Bowman (1989). For further information on the derivation of Eq. (11), please see Malte and Pratt (1974).

The prompt NO mechanism is now analyzed, based on reaction Eq. (5). The rate constant of this reaction is taken from the study of Glarborg et al. (1986). However, our results are not significantly different when we use a rate constant taken from later research, i.e., Dean et al. (1990). In applying reaction Eq. (5), we assume that all of the HCN formed by it oxidizes to NO. The resultant equation is:

$$X_{NO} = k_{5f}(P/RT) X_{N_2} X_{CH} t \quad (12)$$

As shown in Table 3, 0.13 ppmv CH is required to produce 5.0 ppmv NO. This level of CH concentration is reasonable. It agrees with chemical kinetic modeling results discussed in the next section.

It is concluded from this analysis that prompt NO is the predominant mechanism for the reactor operated at medium loading, and that the nitrous oxide mechanism contributes a small additional amount of NO. This conclusion also should hold for the reactor operated at high loading, operated nonpremixed at medium and high loading, and operated on methane at medium loading, since as shown in Figs. 2, 3, and 4 and Tables 1 and 2, the reactor conditions which control the NO chemistry are not significantly different for these cases.

The lightly loaded reactor requires analysis different from that just used. And because of the temperature nonuniformity and relatively weak mixing of this case, the analysis is not as easily conducted as previously mentioned. The first feature analyzed is the increased NO_x of the premixed experiment at the lowest load. This is 11.0 ppmv. It is reasoned that this NO_x forms mainly in centerline region, because the elevated temperature of this region accelerates all of the mechanisms. Also, because of the relatively long mean residence time of 11.4 ms of this experiment, the fast prompt NO mechanism is expected to be concentrated in the centerline region; i.e., in the jet soon after it enters the reactor.

The average temperature of the centerline region is about 1725 K. The mean residence time of gas in the centerline region is estimated as 3 ms, based on the work of Thornton et al. (1987) for this reactor. The O-atom and CH concentrations are taken to be the same as previously shown, i.e., 0.2 mole percent and 0.11 ppmv, respectively. Application of Eqs. (10), (11), and (12) to these conditions gives the results shown in Table 4. As noted, the prompt NO again appears to be the major mechanism. However, the Zeldovich NO is significant. All of the mechanisms contribute.

The nonpremixed lightly loaded experiment is now analyzed. As discussed in the previous section, this experiment does not show an increase in centerline region temperature relative to the premixed case. Furthermore, because of the relatively slow mixing, less oxygen should be available on the centerline of the reactor compared to premixed case. Thus it is not thought likely that the Zeldovich and nitrous oxide mechanisms are responsible for the elevated NO_x. The explanation put forward for the increase in NO_x is enhanced prompt NO formation because of the increased ϕ of the centerline region. It it known from other studies on NO_x in premixed, constant temperature, jet-stirred reactors (Malte et al., 1981) that NO_x increases as

Table 4 Analysis of centerline region of premixed ethylene case at lowest loading 3.0 ms assumed, 1725 K, 11.0 ppmv NO_x

Mechanism	Estimated Free Radical Concentration	Predicted NO
Zeldovich	0.2 mole % O-atom	2.6 ppmv
Nitrous Oxide	0.2 mole % O-atom	1.7 ppmv
Prompt	0.11 ppmv CH	6.7 ppmv
Total .		11.0 ppmv

Table 5 Activation energy of NO formation NO (ppmv) ~ exp (– *E/RT*)

Present experiments	12 kcal/gmol
Flat flame "intercept" NO, for conditions as close as possible to the present, from Heberling (1976) and Eberius and Just (1973)	12 to 24 kcal/gmol
Present modeling, all three mechanisms	33 kcal/gmol
Prompt NO, alone, by present modeling	27 kcal/gmol
Nitrous oxide and Zeldovich NO mechanisms, by present modeling	57 kcal/gmol
Zeldovich NO mechanism, alone, by present modeling	90 kcal/gmol

ϕ increases, with the NO_x peaking at about $\phi = 1.3$, and that most of the NO_x is forced by the prompt NO mechanism. The results of this previous study are discussed in Appendix A, and plotted in Fig. A-1 of that Appendix.

The apparent activation energy of the NO_x formation is now analyzed. When the temperature-variation results of Fig. 7 are replotted as ln(NO_x, ppmv) versus $1/T$ a straightline is obtained. The slope of this line is E/R, where E is the apparent activation energy. The result obtained is $E = 12$ kcal/gmol. The apparent activation energy is quite sensitive to the measured values of NO_x and temperature and, consequently, the estimated uncertainty in the 12 kcal/gmol value is a factor 2.

The result for apparent activation energy is compared with other results in Table 5. Data from Heberling (1976) indicate an apparent activation energy of 24 kcal/gmol for experiments in which the NO concentration was extrapolated to zero time in a fuel-lean ($\phi = 0.6$) ethylene flat-flame at 1 atm. In flat-flame experiments, this "intercept" NO is the prompt NO. Data from Eberius and Just (1973), for propane-air flat-flames with ϕ varying from 0.9–1.4 and T varying from 1800–2100 K, show an apparent activation energy of the intercept NO of 12–16 kcal/gmol.

Also listed in Table 5 are results obtained by our perfectly stirred reactor/chemical kinetic modeling, described in the next section. The NO_x is computed for each condition of the temperature-variation experiments, and then the apparent activation energy is determined as shown previously from the slope of ln(NO_x, ppmv) versus $1/T$. The result for the prompt NO mechanism is 27 kcal/gmol, a value which is consistent with the literature just cited. The result for all three mechanisms operating jointly is 33 kcal/gmol.

It should be noted that the results listed in Table 5 reflect the activation energies not only of the NO forming reactions per se, but also of the formation of the free radical species necessary for the NO formation. Thus, for example, the apparent activation energy of the Zeldovich NO is greater than that of reaction (2), which is 76 kcal/gmol.

Chemical Kinetic Modeling

Chemical kinetic modeling is conducted using the perfectly

Downloaded 02 Jun 2010 to 171.66.16.112. Redistribution subject to ASME license or copyright; see http://www.asme.org/terms/Terms_Use.cfm

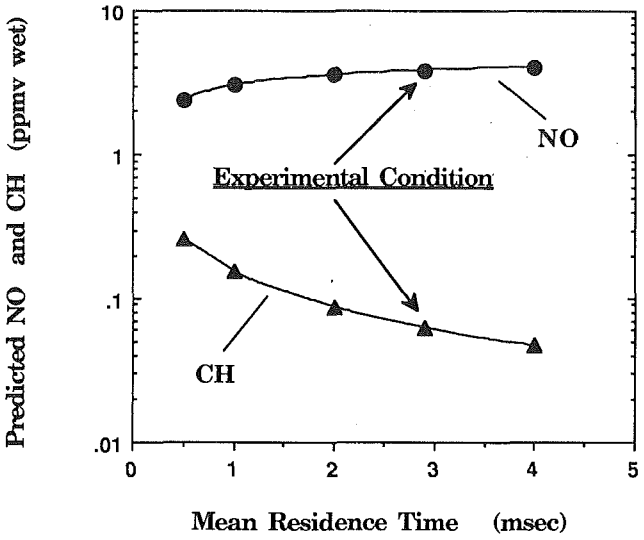


Fig. 8 NO and CH predicted by perfectly stirred reactor code with ethylene oxidation/three-mechanism NO kinetic model. Temperature (1504 K) and reactor inlet composition fixed at experimental values. Reactor mean residence time varied about experimental value (2.9 ms).

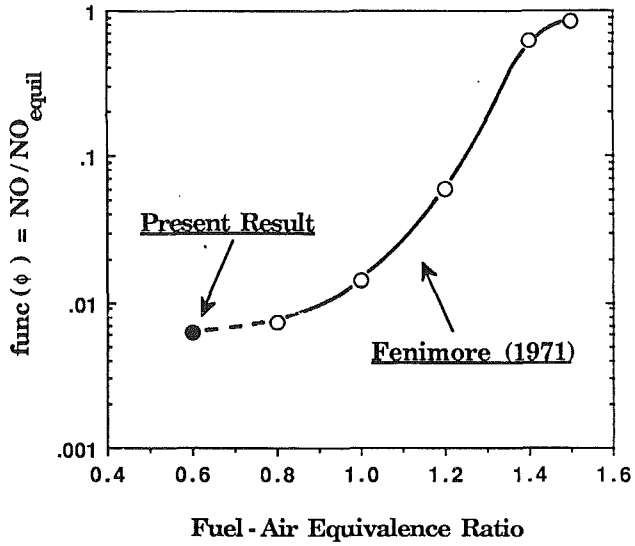


Fig. 9 Comparison of Fenimore's (1971) results (open circles) with present data (ϕ = 0.6). Ethylene combustion at one atmosphere. Conditions for our experiment: premixed, $\dot{m}/VP^2$ = 92 kg/s·m^3·atm^2, T = 1504 K, $NO_{expt'_1}$ = 5.0 ppmv, NO_{equil} = 811 ppmv.

stirred reactor code of Pratt and Wormeck (1976) with chemical kinetic mechanisms for ethylene oxidation and NO_x reaction. The ethylene oxidation mechanism is by Marinov and Malte (1991), and is based on previous ethylene oxidation experiments for the present reactor. The NO_x mechanisms are from Glarborg et al. (1986) and Miller and Bowman (1989). They include the extended Zeldovich NO mechanism, the nitrous oxide mechanism, and the prompt NO mechanism (abbreviated with only the essential reactions retained).

The model is applied to the premixed ethylene experiments conducted at medium loading. Measured conditions are used as input to the model. This includes the measured (corrected) temperature, pressure, mean residence time, and feed composition. The modeled reactor composition is corrected for argon dilution, in a manner analogous to that used for the experimental data. The model treats the reactor temperature and composition as uniform and time-steady. Mixing is assumed to occur instantaneously, and thus, all points of the modeled reactor have the same reaction and composition. The experimental reactor, on the other hand, is essentially uniform only in temperature (at medium loading) and NO_x concentration (though as just argued, the NO forming reactions are probably not uniformly dispersed).

In the previous section, modeling results for the determination of the apparent activation energy of NO formation were shown. The additional results given in this section pertain to the ethylene premixed experiment analyzed extensively in the foregoing text. This is the experiment with 1504 K area-average temperature and 2.9 ms mean residence time.

In Fig. 8, the predictions of the NO and CH are shown for this case. The NO is 4.0 ppmv and the CH is 0.06 ppmv, values which are close to those listed in Table 3. The NO is due to all three mechanisms, though the prompt NO contribution is predominant. Also shown in Fig. 8 are predictions for mean residence times shorter than the experimental value. This is done, since as explained in the previous section, the prompt NO mechanism is fast and thought to occur predominantly in the centerline region of the reactor. It is noted from Fig. 8 that as the mean residence time decreases, which is approximately equivalent to considering the earlier regions of the reactor, the CH increases and the NO essentially remains constant. The mean residence time and CH effects are offsetting.

This lack of sensitivity of prompt NO to mean residence time may explain why it is possible to analyze and model prompt NO with the assumption of a uniform reactor, even though the prompt NO chemistry is likely concentrated in the jet of the reactor. We appear to have benefitted from this behavior in preparing Table 3, and Glarborg et al. (1986) probably benefitted from it in their modeling of prompt NO chemistry for high-temperature jet-stirred reactors.

Comparison to the Results to Fenimore

In Fig. 9, the NO_x measured for the ethylene premixed experiment at medium loading is compared to the prompt NO data of Fenimore (1971). The experimental values of 1504 K area-average temperature, 2.9 msec mean residence time, and 5.0 ppmv NO_x, which is treated as NO for this analysis. The equilibrium NO corresponding to 1504 K is 811 ppmv. Our estimate of the weak contribution of the nitrous oxide mechanism is not subtracted from the 5.0 ppmv NO value, since this mechanism could have contributed weakly also to Fenimore's data. Also, no Zeldovich correction is made to our NO value, since this mechanism's estimated contribution is very small.

Fenimore's data for prompt NO from ethylene combustion in a 1 atm Meker-type burner are shown by the open circles in Fig. 9. Our result is shown by the darkened circle, and the dashed line shown is our extrapolation of Fenimore's data to ϕ = 0.6. Our result is func (0.6) = 0.0062, which agrees well with the extrapolation. Our curve fit of Fenimore's 1 atm data for $0.8 \leq \phi \leq 1.2$ is as follows:

$$\text{func}(\phi) = 0.0053 \exp(1.004\phi^{4.865}) \quad (13)$$

Extrapolation of this to ϕ = 0.6 gives func (0.6) = .0058.

Since Fenimore's burner was essentially adiabatic, and since his data are applied to combustors assumed to be adiabatic, it can be argued that the adiabatic equilibrium NO value should be used for our result. This gives func (0.6) = 0.0049, which does not agree as closely as to the extrapolation of Fenimore's data.

For methane combustion, based on our results, it is recommended that func (ϕ) by multiplied by 0.75. This is consistent with Fenimore's findings.

It is concluded that the prompt NO apparently formed in our reactor agrees well with the extrapolation of Fenimore's data to ϕ = 0.6. Although the underlying prompt NO chemistry is complex, our results strengthen the use of Fig. 8 and func (ϕ) for engineering estimates of prompt NO in combus-

Downloaded 02 Jun 2010 to 171.66.16.112. Redistribution subject to ASME license or copyright; see http://www.asme.org/terms/Terms_Use.cfm

tors. However, this statement applies strictly to atmospheric pressure combustion, since this evaluation does not address the issue of pressure-dependence. Fenimore indicated $P^{1/2}$, as shown by Eq. (1), but his results extended only to 3 atm.

Conclusions and Recommendations

In this study, it has been shown that prompt NO appears to be the predominant mechanism for the formation of NO_x in lean, premixed, highly loaded, turbulent combustion, and that engineering estimates of the prompt NO may be made with an equation based on Fenimore's (1971) original prompt NO data. A supporting role is indicated for the nitrous oxide mechanism; i.e., about 15 percent of the NO_x observed appears to be due to this mechanism. Our results also show that a reduction in loading increases the NO_x, and Zeldovich NO becomes contributory. A switch to nonpremixing at reduced loading further increases the NO_x, and appears to enhance the prompt NO formation.

Although the recirculation zone of the reactor, which represents the chemical composition of the exhaust of the reactor, contains CO and THC concentrations unacceptably high by gas turbine engine exhaust emission practices, it should be recognized that the reactor does not have attached to it a secondary zone for CO and THC burn-off. Furthermore, it should be recognized that since prompt NO is a phenomenon associated with the oxidative pyrolysis chemistry, it is necessary that detailed measurements of it for turbulent flames be conducted with bench combustors which emit significant unburned material.

The tasks required for additional evaluation of NO_x for lean, premixed combustion are as follows:

- The jet-stirred reactor needs to be modeled with a multizone model capable of predicting the nonuniform behavior. This is important since the prompt NO likely forms quickly in the centerline region of the reactor.
- The pressure dependence of NO_x needs to be studied experimentally and through modeling, since there is much uncertainty regarding this. There is some evidence for a weak-to-negligible pressure dependence of NO_x for lean, premixed combustors. Experiments on this effect need to be conducted with different types of well-understood flames and bench combustors. Modeling requires the use of multizone models which include recirculation between the zones. Perfectly stirred reactor models can give misleading information as the pressure increases, and are not recommended by us for studying pressure effects involving the oxidative pyrolysis chemistry, e.g., the prompt NO mechanism as a function of pressure. With the perfectly stirred reactor model, high pressure depresses the active species (OH, H, O) concentrations *throughout* the reactor, and thus, the rate of oxidation of the fuel can actually be *depressed* by the high pressure rather than enhanced, as is the usual experience.

Acknowledgments

This paper is drawn from the MSME thesis of Robert A. Corr. The research was supported by the Department of Mechanical Engineering of the University of Washington.

References

Altemark, L. B., and Knauber, R., 1987, "Ergebnisse von Untersuchungen an enimen Vormischbrenner unter Druck mit extrem niedriger NO_x Emission," *VDI Berichte 645*, pp. 299–311.

Davis, L. B., and Washam, R. M., 1989, "Development of a Dry Low NO_x Combustor," ASME Paper No. 89-GT-255.

Dean, A. J., and Hanson, R. K., and Bowman, C. T., 1990, "High Temperature Shock Tube Study of Reactions of CH and C-atoms With N_2," Paper Number 23-083, presented at 23rd Symposium (International) on Combustion, Orléans, France, July.

Drake, M. C., and Blint, R. J., 1989, "Calculation of NO_x Formation Pathways in Propagating Laminar, High Pressure Premixed CH_4/Air Flames," Report PC-556, General Motors Research Laboratories, Warren, MI.

Eberius, K. H., and Just, T., 1973, "Atmospheric Pollution by Jet Engines," AGARD Conf. Proc. No. 125, p. 16-1.

Fenimore, C. P., 1971, "Formation of Nitric Oxide in Premixed Hydrocarbon Flames," *Proceedings of 13th Symposium (International) on Combustion*, The Combustion Institute, Pittsburgh, PA, pp. 373–380.

Glarborg, P., Miller, J. A., and Kee, R. J., 1986, "Kinetic Modeling and Sensitivity Analysis of Nitrogen Oxide Formation in Well-Stirred Reactors," *Combustion and Flame*, Vol. 65, pp. 177–202.

Hayhurst, A. N., and Vince, I. M., 1983, "The Origin and Nature of 'Prompt' Nitric Oxide in Flames," *Combustion and Flame*, Vol. 50, pp. 41–57.

Heberling, P. V., 1976, "Prompt NO Measurements at High Pressures," *Proceedings of 16th Symposium (International) on Combustion*, The Combustion Institute, Pittsburgh, PA, pp. 159–168.

Jeffs, E., 1989, "Asea Brown Boveri Introducing a Dual Fuel Dry Low-NO_x Burner Design," *Gas Turbine World*, Vol. 19, No. 3, pp. 20–24.

Kramlich, J. C., and Malte, P. C., 1978, "Modeling and Measurement of Sample Probe Effects of Pollutant Gases Drawn From Flame Zones," *Combust. Science Tech.*, Vol. 18, pp. 91–104.

Maghon, H., Kreutzer, A., and Termuehlen, H., 1988, "The V84 Gas Turbine Designed for Base Load and Peaking Duty," presented at the American Power Conference, Chicago, IL, Apr.18–20.

Malte, P. C., and Kramlich, J. C., 1980, "Further Observation of the Effect of Sample Probes on Pollutant Gases Drawn from Flame Zones," *Combust. Science Tech.*, Vol. 22, pp. 263–269.

Malte, P. C., and Pratt, D. T., 1974, "The Role of Energy-Releasing Kinetics in NO_x Formation: Fuel-Lean, Jet Stirred CO-Air Combustion," *Combust. Science Tech.*, Vol. 9, pp. 221–231.

Malte, P. C., Schmidt, S. C., Kramlich, J. C., Spitzer, K. D., Yee, D., and Singh, S., 1981, "Behavior of OH and NO_x in a Mixing-Influenced Jet-Stirred Reactor," *AIAA Journal of Energy*, Vol. 5, pp. 193–200.

Marinov, N. M., and Malte, P. C., 1991, "Ethylene Oxidation Kinetic Model for a Well-Stirred Reactor," paper to be submitted.

Miller, J. A., and Bowman, C. T., 1989, "Mechanism and Modeling of Nitrogen Chemistry in Combustion," *Prog. in Energy and Combust. Science*, Vol. 15, pp. 287–338.

Pratt, D. T., and Wormeck, J., 1976, "CREK," Report No. TEL-76-1, Department of Mechanical Engineering, Washington State University, Pullman, WA.

Sattelmayer, T., Felchlin, M. P., Haumann, J., Hellat, J., and Styner, D., 1990, "Second-Generation Low-Emission Combustors for ABB Gas Turbines: Burner Development and Tests at Atmospheric Pressure," ASME JOURNAL OF ENGINEERING FOR GAS TURBINES AND POWER, Vol. 114, pp. 118–125.

Singh, S., Grosshandler, W. L., Malte, P. C., and Crain, R. W., 1978, "Oxides of Nitrogen Formed in High-Intensity Methanol Combustion," *Proceedings of 17th Symposium (International) on Combustion*, The Combustion Institute, Pittsburgh, PA, pp. 689–699.

Shaw, H., 1974, "The Effects of Water, Pressure, and Equivalence Ratio on Nitric Oxide Production in Gas Turbines," ASME JOURNAL OF ENGINEERING FOR POWER, July, pp. 240–246.

Thornton, M. M., Malte, P. C., and Crittenden, A. L., 1987, "A Well-Stirred Reactor for the Study of Pyrolysis and Oxidation Kinetics: Carbon Monoxide and *n*-Pentane Oxidation," *Combust. Science Tech.*, Vol. 54, pp. 275–297.

Toof, J. L., 1986, "A Model for the Prediction of Thermal, Prompt, and Fuel NO_x Emissions from Combustion Turbines," ASME JOURNAL OF ENGINEERING FOR GAS TURBINES AND POWER, Vol. 108, pp. 340–347.

APPENDIX A

Results are replotted in Fig. A-1, from one of our previous studies of NO_x formation in a jet-stirred reactor (Malte et al., 1981). This reactor had a 50 cm^3 volume; was fed with unheated, premixed, fuel, air, and diluent through a nozzle head containing seven jets; and had optical access for the spectroscopic determination of path-integrated temperature and O-atom and OH concentrations. The data plotted in Fig. A-1 were obtained for the reactor held at a constant nominal temperature of 1800 K (except for one case at 1580 K), using variable inert dilution. The data shown are normalized to zero dilution. O-atom concentrations were measured in all cases and found to depend weakly on the fuel type. Thus the results with the H_2 CO fuel mixture are taken to be representative of the NO_x formed by the Zeldovich and nitrous oxides routes for all of the cases. The additional NO_x with the hydrocarbon fuels is taken to be prompt NO.

The main features of the results in Fig. A-1 are the fuel-rich peaking of the NO_x and the significant sensitivity of the NO_x to fuel-type in the fuel-lean regime. For the hydrocarbon fuels, the NO_x peaks at about $\phi = 1.3$. This fuel-rich NO_x peaking is seen also in the jet-stirred reactor experiments of others. For those reactors, the fuel-rich NO_x has been modeled by Glarborg

Downloaded 02 Jun 2010 to 171.66.16.112. Redistribution subject to ASME license or copyright; see http://www.asme.org/terms/Terms_Use.cfm

et al. (1986), and shown to be caused mainly by the prompt NO mechanism. Regarding the sensitivity to fuel-type, the experiments of Hayhurst and Vince (1983), conducted using a premixed porous plate burner, showed features similar to those plotted in Fig. A-1; that is, increasing sensitivity to fuel-type with decreasing ϕ.

APPENDIX B

Results on the reduction and oxidation of NO_x are listed in Table B-1. These data are for the well-stirred mode. The NO_x entering the reactor is formed in the hydrogen-air burner used to create the hot, sonic jet. Into this jet, a small amount of ethylene is added. The oxidation of this fuel is responsible for a small reduction in the NO_x, and for a significant oxidation of the NO to NO_2. The chemical kinetic modeling of the NO to NO_2 oxidation in the reactor is conducted with NO to NO_2 oxidation reactions added to the kinetic mechanism previously outlined and using as input to the model the measured reactor temperature and measured feed jet composition. The NO_x reduction is not modeled. The main reaction for NO to NO_2 oxidation is $NO + HO_2 \rightarrow NO_2 + OH$. Results for the reactor modeled as a perfectly stirred reactor, and with the gases additionally reacted in a one-dimensional probe model, per Kramlich and Malte (1978), are listed. The probe pressure is the nominal experimental value. The modeled NO_2/NO_x ratio for the probe outlet agrees, though not exactly, with the measured data. The modeling indicates that NO to No_2 oxidation occurs within both the reactor and probe. Since these experiments are not the main focus of this research, only a limited discussion of the data and their analysis are presented.

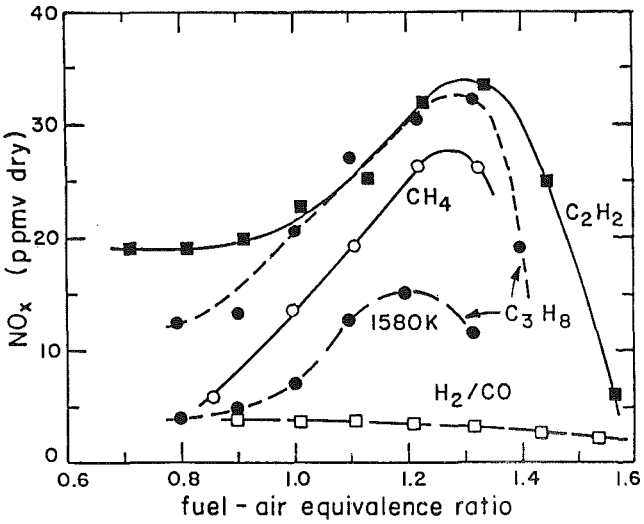


Fig. A-1 NO_x versus fuel-air equivalence ratio for jet-stirred reactor operated on 4 different fuels. Nominal, corrected temperature held constant at 1800 K, except for one experiment (C_3H_8) at 1580 K. Mean reactor residence time of 7 ms. From Malte et al. (1981).

APPENDIX C

Hydrocarbon speciation data for the reactor are listed in Table C-1. Trends also are shown in Fig. 6. For the ethylene fuel, the hydrocarbon species concentrations vary as follows:

$$C_2H_4 > \tilde{>} C_2H_2 > CH_4 \gg C_2H_6 \cong C_3H_8$$

For the methane fuel, the behavior is different:

$$CH_4 \gg C_2H_6 \tilde{>} C_2H_4 > C_2H_2 > \tilde{>} C_3H_8$$

These trends occur across the reactor.

These results are given without analysis and interpretation. They are available for comparison to future, more detailed modeling of the reactor.

Table B-1 NO_x reduction and oxidation well-stirred reactor mode (lean ethylene oxidation* at 2 ms)

REDUCTION of NO_x

T(K)**	Meas. Feed Jet NO_x (ppmv)	Meas. Reactor Output NO_x (ppmv)	$\Delta NO_x/(NO_x)_{in}$
1106	84	78	−0.071
1176	116	103	−0.112
1237	138	122	−0.116

NO_2/NO_x RATIO

T(K)**	Meas. Feed Jet	Meas. Reactor Output	Modeled Reactor	Modeled Probe Output
1106	0.16	0.60	0.36	0.56
1176	0.12	0.43	0.15	0.26
1237	0.06	0.26	0.06	0.16

* Nominal input by mole %: 10% O_2, 15% H_2O, 75 N_2, 0.37% C_2H_4.
**Uncorrected thermocouple temperature of jet-stirred reactor.

Table C-1 Hydrocarbon concentrations (corrected to zero argon dilution)

Fuel	Mode	$\dot{m}/VP^2$ (kg/sec-m^3-atm^2)	CL or Average	CH_4 (ppmvC)	C_2H_4 (ppmvC)	C_2H_6 (ppmvC)	C_2H_2 (ppmvC)	C_3H_8 (ppmvC)	THC (ppmvC)
C_2H_4	Premix	21	CL	5	6	0	2	0	13
			Avg	0	0	0	0	0	0
C_2H_4	Premix	92	CL	70	1234	8	188	9	1500
			Avg	6	78	0	12	0	94
C_2H_4	Premix	151	CL	26	174	0	116	0	316
			Avg	4	18	0	10	0	32
C_2H_4	Non-Premix	21	CL	6	70	0	20	0	96
			Avg	0	4	0	2	0	6
C_2H_4	Non-Premix	87	CL	64	1564	18	146	9	1800
			Avg	11	214	0	26	0	251
C_2H_4	Non-Premix	143	CL	45	516	0	164	0	725
			Avg	8	62	0	22	0	92
CH_4	Premix	66	CL	7288	190	276	30	12	7800
			Avg	1562	60	64	8	0	1690
CH_4	Premix	100	CL	3489	124	150	26	0	3790
			Avg	1128	46	50	10	0	1230
C_2H_4	T-Var. (1595K)	85	CL	8	38	0	30	0	76
			Avg	0	6	4	0	0	10
C_2H_4	T-Var. (1691K)	75	CL	0	0	0	0	0	0
			Avg	0	0	0	0	0	0

Downloaded 02 Jun 2010 to 171.66.16.112. Redistribution subject to ASME license or copyright; see http://www.asme.org/terms/Terms_Use.cfm

G. J. Sturgess
Pratt & Whitney,
East Hartford, CT 06106

S. P. Heneghan

M. D. Vangsness

D. R. Ballal

University of Dayton,
Dayton, OH 45469

A. L. Lesmerises
Wright-Patterson Air Force Base, OH 45433

Isothermal Flow Fields in a Research Combustor for Lean Blowout Studies

A propane-fueled research combustor has been designed and developed to investigate lean blowouts in a simulated primary zone of the combustors for aircraft gas turbine engines. To understand the flow development better and to ensure that the special provisions in the combustor for optical access did not introduce undue influence, measurements of the velocity fields inside the combustor were made using laser-Döppler anemometry. These measurements were made in isothermal, constant density flow to relate the combustor flow field development to known jet behavior and to backward-facing step experimental data in the literature. The major features of the flow field appear to be consistent with the expected behavior, and there is no evidence that the provision of optical access adversely affected the flows measured.

Introduction

A propane-fueled research combustor (Fig. 1) has been designed (Sturgess et al., 1992) and developed (Sturgess et al., 1992; Heneghan et al., 1990) to investigate lean blowouts in a simulated primary zone of combustors for aircraft gas turbine engines. The fundamental flow and heat release features of a gas turbine combustor primary zone, within which the flame is held, are generated by the geometrically simple design of the research combustor.

The research combustor consists of co-axial jets with a 29-mm-i.d. central fuel jet, surrounded by a 40-mm-dia annular air jet. The fuel is gaseous propane. Inserted inside the fuel tube 5 diameters from the discharge is a perforated conical baffle that serves to isolate the fuel supply acoustically from the combustor (Heneghan et al., 1990). The confluence of the jets is centrally located in a 150-mm nominal diameter duct. The duct is closed at its forward end to give a backward-facing step of 55 mm height. The sudden expansion of the jets caused by the step provides a recirculation region that can stabilize the flame. The duct is usually restricted at its discharge by a 45 percent blockage orifice plate, and has an overall length from step to discharge of 735 mm.

The duct forming the combustor is uncooled and is made in two sections, consisting of a window section of 475 mm overall length and an extension chimney of 260 mm length. Provision for optical access is made in the window section of the duct. The construction of the window section consists of thin, flat quartz windows mounted in a stainless steel frame. The frame establishes reference planes to ensure that the pairs of windows on opposite sides of the combustor remain flat and parallel to each other. The windows themselves are spring-

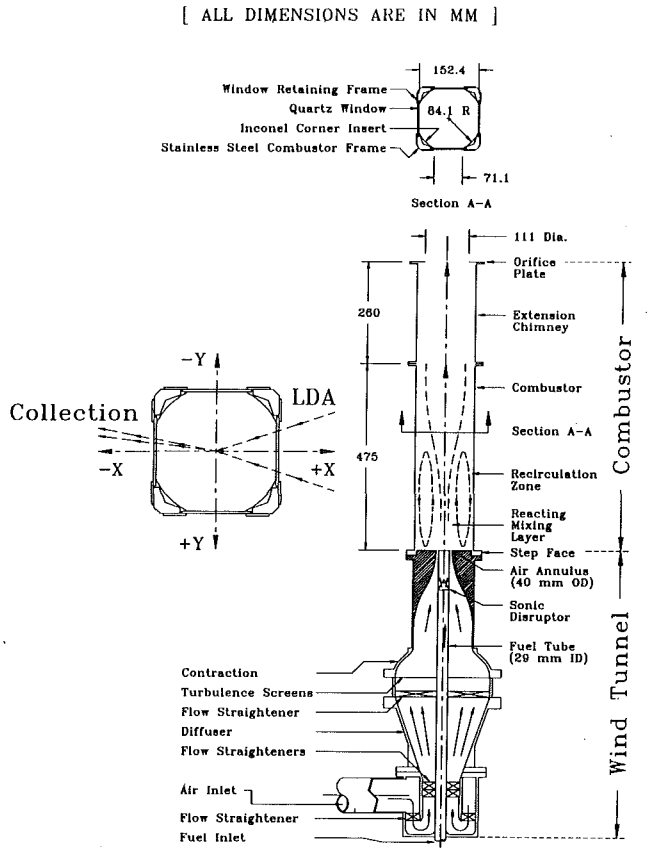


Fig. 1 Research combustor and axis convention

Contributed by the International Gas Turbine Institute and presented at the 36th International Gas Turbine and Aeroengine Congress and Exposition, Orlando, Florida, June 3–6, 1991. Manuscript received at ASME Headquarters February 6, 1991. Paper No. 91-GT-37. Associate Editor: L. A. Riekert.

Copyright © 1992 by ASME
Downloaded 02 Jun 2010 to 171.66.16.112. Redistribution subject to ASME license or copyright; see http://www.asme.org/terms/Terms_Use.cfm

loaded against the frames by means of 0.81-mm-thick Inconel corner inserts. The windows can float between the spring-loaded corner inserts and the rigid frames, thereby allowing differential thermal growth without stressing the windows.

The construction of the window section results in a duct cross section as shown in Fig. 1. The quartz windows are on a square of 152 mm inside dimension, within which the Inconel corner inserts form a circle of 84 mm. This results in a window width of 71 mm, and the length of the windows is 457 mm. The cross section of the window section is duplicated in the extension chimney, fabricated of Inconel.

The hybrid cross section of the combustor described above represents a hard-won compromise between the demands for geometric simplicity and flow two dimensionality, and the need for straightforward optical access to allow use of laser diagnostics. The flat windows avoid laser beam distortion, while the corner fillets distribute vorticity generation and reduce secondary flow developments due to interaction of the wall boundary layers on the flat windows. If unaddressed, corner-derived secondary flow vortices could influence combustion stability by providing spurious flame holding.

While the cross section of the combustor was designed to ameliorate the magnitude of secondary flow developments, it is not possible entirely to eliminate the local concentrations of vorticity where the circular-arc corner fillets run into the flat windows. However, the vorticity should be reduced in strength and distributed to a degree that secondary flow development does not substantially influence the bulk flow development in the combustor. While computational fluid dynamics (CFD) analyses showed that the introduction of the corner fillets resulted in the anticipated favorable modification of flow behavior, it was still necessary to demonstrate experimentally that such is the case. To this end, velocity field measurements were made in the combustor under isothermal, constant-density conditions. These measurements also serve to contribute to the understanding of the flow development in the combustor; in addition, they provide initial condition information and baseline data for testing subsequent CFD analyses employing blowout models being developed as part of this research.

LDA Arrangement

A custom-designed laser-Döppler anemometer (LDA) system was used for all the velocity measurements. The LDA uses the green (514.5 nm) and blue (488 nm) lines of a 15-W argon-ion laser as a source; two measurement channels of this system were separated by polarization, while the third uses the blue beam. The third channel optics were set up normal to the two-channel optics, and the scattered signal was collected in a forward direction at 10 deg off-axis. The effective probe volume was $50 \times 300 \times 750\ \mu$m. The instrument incorporates Bragg cells with a 5 MHz frequency shift for unambiguous measurements in recirculatory flows. A unique three-channel coincidence circuit with a 10 μs window for rapid validation of acquired data was also incorporated. This assists the integration of the LDA with CARS, Raman, or Rayleigh spectroscopic techniques to be used later with reacting flows.

A proprietary fluidized-bed seeder was used to inject submicron-sized Al_2O_3 or SiO_2 seed particles into the flowing streams. The primary source of error in the measurements is the statistical bias of the final measured velocity toward higher mass fluxes when number-weighted averages are used to calculate stationary statistics. Chen and Lightman (1985) and Glass and Bilger (1978) have discussed bias correction schemes. Seeding of the fuel and air stream separately and together was investigated. No differences of any significance were seen in the measured velocity profiles.

Scattered signals were detected by TSI Counter Processors, and were processed by custom-designed software to yield intensity, shear stresses, skewness and kurtosis, and pdf's. Typical sampling rates were up to 1 kHz. At each spatial location in the combustor, a total of 4096 realizations were acquired. A portion of these data (up to 2 percent), whose departure from the mean exceeded three standard deviations, was filtered to eliminate spurious signals due to seed agglomeration. Finally, a subroutine was used to correct for any particle and density biasing effect (nonreacting and reacting flows).

Error Analysis. Both the fuel stream and air stream flows were monitored and controlled by separate electronic flow control units to within 2 percent. Also, mass conservation balances in the exit plane of the fuel tube provided an additional cross-check against flow meter readings. After allowing for seeding bias, for single-stream seeding with the relatively high sampling rates used, the uncertainty in the measurement of mean velocity was 1 percent, for rms velocity 5 percent, and for skewness and flatness 7 percent. The long-term repeatability was found to be within 5 percent for the turbulence quantities.

Traverse Axes. The combustor is mounted vertically in the facility (Sturgess et al., 1992) and its centerline constitutes the z axis. Zero z is taken as the plane of the step. The x and y axes are diametral to the combustor cross section, with the x axis aligned with the LDA axis. The axis convention is shown

Nomenclature

a = upstream distance from step, defining effective origin of merged jets
D_L = combustor diameter
h = step height
i, j = Cartesian tensor coordinate directions
l_m = mixing length
L/D = length-to-diameter ratio
M_O/M_I = momentum ratio of outer jet to inner jet
n = exponent in definition of boundary layer velocity profile
R = radius
R_f = fuel tube interior radius
$R_{1/2}$ = radius at which $\bar{u}$ has fallen to 1/2 $\bar{u}_c$
$R_{u=0}$ = radius at which $\bar{u}=0$
U, U_{AVE} = mass-averaged axial velocity
U_L = mass-averaged axial velocity in combustor
U_I = initial mass-averaged axial velocity of center jet
$\bar{u}$ = time-mean axial velocity
u_{max} = maximum axial velocity in X, Y scan
$\bar{u}_c$ = time-mean axial velocity on combustor centerline
$\bar{u}_{c,min}$ = time-mean minimum centerline axial velocity
u_1, u_2 = maximum and minimum velocity in shear layer
u_f = fuel jet axial velocity
u' = fluctuating axial velocity
$\overline{u_i' u_j'}$ = Reynolds stresses
$\bar{v}$ = time-averaged radial velocity
v' = fluctuating radial velocity
X, Y = diametral coordinate directions
y = distance normal to wall
Z = downstream coordinate direction from combustor step plane
z_p = conditional potential core length
δ = shear layer width
η = dimensionless distance across shear layer
ξ_2 = dimensionless radius

Downloaded 02 Jun 2010 to 171.66.16.112. Redistribution subject to ASME license or copyright; see http://www.asme.org/terms/Terms_Use.cfm

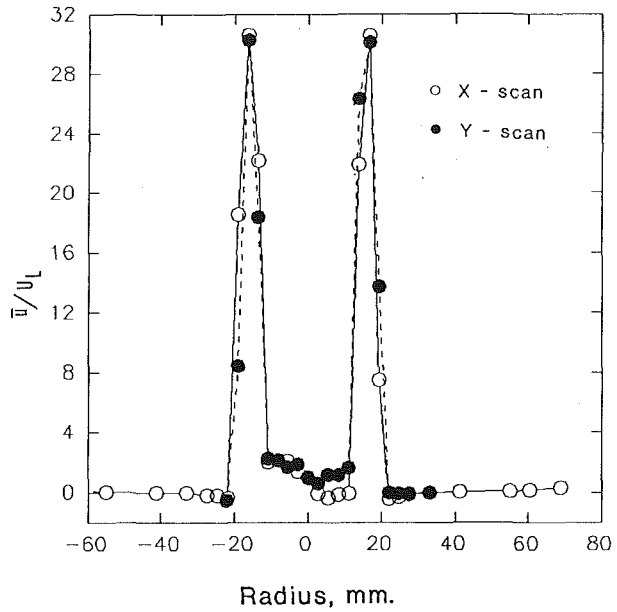


Fig. 2 *X* and *Y* scans of mean axial velocity at $z = 5$ mm with both jets flowing, showing induced asymmetry in central jet

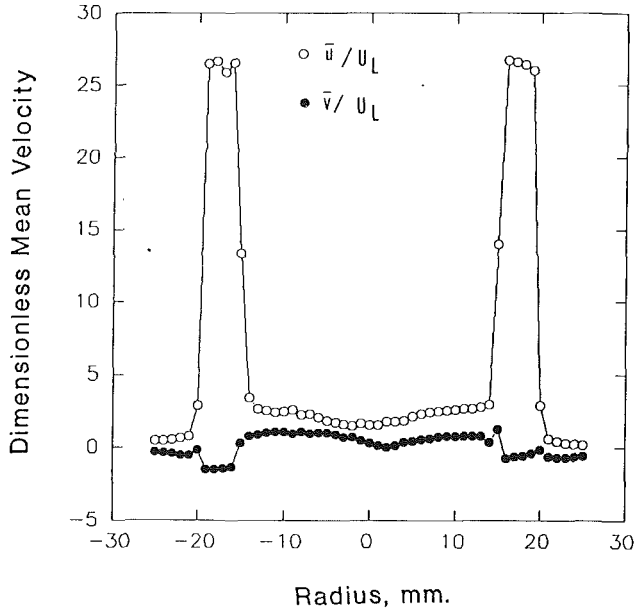


Fig. 3 Increased resolution *Y* scan of mean velocity profiles at $z = 5$ mm; combustor inlet condition

in Fig. 1. Velocities parallel to and increasing in the direction of the z axis, and velocities normal to and directed away from this axis, are also considered positive.

Windows. The geometric window sizes in the combustor, the LDA traverse mechanism (Sturgess et al., 1992), and the LDA beam focusing together define the effective windows within which data may be taken. This access window is given by $-68.7 \le x \le +68.7$ mm, and $-22 \le y \le +33$ mm; in the downstream direction it is $+2 \le z \le +358$ mm.

Test Conditions

Separate diametral traverses of the fuel jet and annular air jet were made by the LDA at the step with the combustor body removed, for a variety of inlet mass flow rates covering fuel jet Reynolds numbers from 1733 to 17,333, and air jet Reynolds numbers from 7233 to 72,322. Air was used for the fuel stream. This information was used to assess the uniformity of the inlet flows.

Detailed diametral traverses (both x and y scans) were made at a number of axial positions, together with a centerline axial traverse, with both jets flowing and the exit orifice plate removed. This information was to be used for comparison with round jet data from the literature. The jet inlet conditions resulted in an air jet Reynolds number of 56,413 and a fuel jet Reynolds number of 11,320 for this test. Some further centerline axial traverses were made at different inlet conditions as part of a study of the near-field jet development.

For reasons of safety and economy, the fuel stream was chosen to be air rather than gaseous propane. On a Reynolds number basis, the conditions at which the majority of the results to be presented were obtained correspond in this simulation to an actual lean blowout point for which the fuel jet is turbulent at inlet (Reynolds number > 9000) with an air jet Reynolds number appropriate to an equivalence ratio of about 0.5. The mass-averaged axial velocities for the fuel jet, air jet, and combustor at this condition are, respectively, 1.98, 20.6, and 3.06 m/s.

Results

Inlet Conditions. With the combustor removed, diametral LDA traverses (y scans) of the fuel jet alone at z of 2 mm from the step were made for several Reynolds numbers. The resulting diametral profiles of time-mean axial velocity were compared with Nikuradse's (Schlichting, 1960) turbulent profile for smooth pipes and Reynolds number around 100,000,

$$u/u_{\max} = (y/R_f)^{1/n} \tag{1}$$

where y is the distance from the fuel tube wall and n was taken as 7. The fluctuating axial and radial velocity profiles were compared with Laufer's (Hinze, 1975) data for smooth round pipes at a Reynolds number of 500,000.

The measured diametral profile of time-mean axial velocity was flatter than that for the familiar seventh power law. The flatness of the measured profile was increased for a Reynolds number of 8665, and reduced for one of 17,333. These changes are in accord with expected behavior (Schlichting, 1960) since the exponent $1/n$ is not constant, and n is a known function of Reynolds number. However, the excessive flatness results because the profile was generated by the acoustic isolator, and the jet does not represent true fully developed pipe flow. A slight asymmetry was observed in the measured data, and this was present over the range of Reynolds numbers.

The turbulence was reasonably isotropic, with higher values occurring toward the edges (wall) of the jet; levels were considerably above those measured by Laufer. For the lower Reynolds number of 8665, the turbulence was clearly anisotropic, but it was isotropic for the higher Reynolds number of 17,333. At the 17,333 Reynolds number, the trend of the fluctuating radial component of velocity with y appeared to be the reverse of Laufer's measurements, i.e., increasing values toward the jet center. Once again, the characteristics were strongly influenced by the presence of the acoustic isolator, which behaved similarly to a turbulence grid.

Velocity profile development in the annular air jet depends on the passage L/D, radius ratio, and weakly on Reynolds number. Although the convergent inlet to the annular jet is so short that the flow could not be fully developed (requiring an L/D of around 70), it was instructive to consider the measured radial profiles of mean axial velocity against the anticipated turbulent profiles.

The appropriate turbulent velocity profile for an annular jet was based on the experimental data of Rehme (1974), corrected to the radius ratio of 0.675 appropriate for the research combustor, and Nikuradse profiles with n appropriate to 60,000

Downloaded 02 Jun 2010 to 171.66.16.112. Redistribution subject to ASME license or copyright; see http://www.asme.org/terms/Terms_Use.cfm

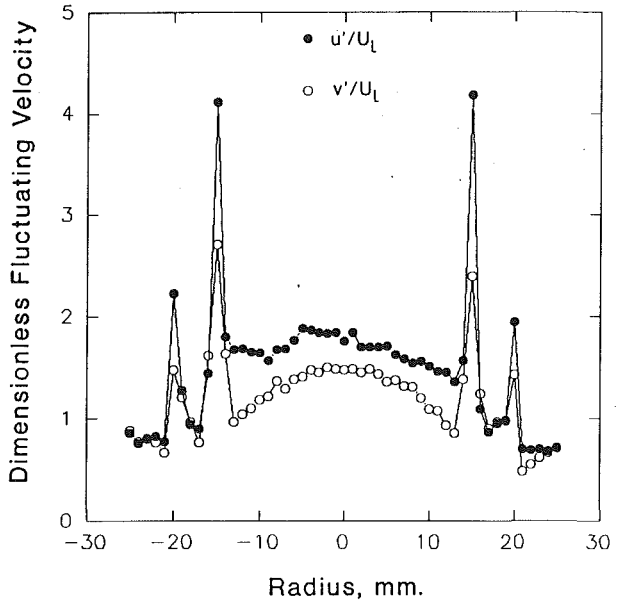


Fig. 4 High-resolution *Y* scan of fluctuating velocity profiles at $z = 5$ mm; combustor inlet condition

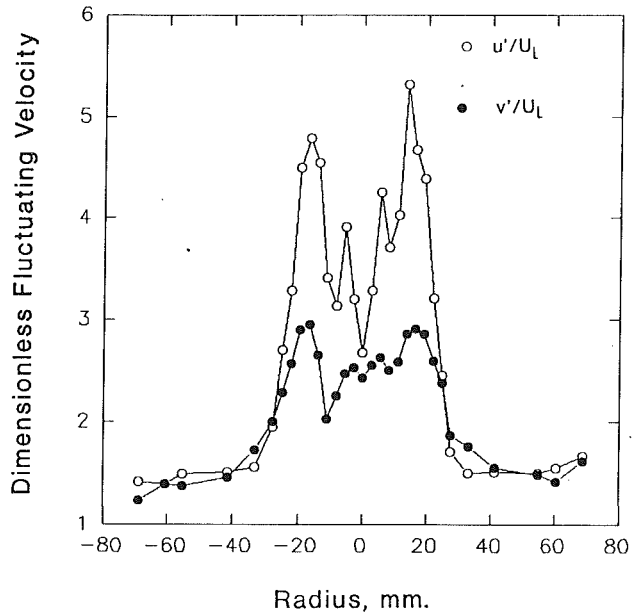


Fig. 6 *X*-scan diametral profiles of fluctuating velocities at $z = 55$ mm

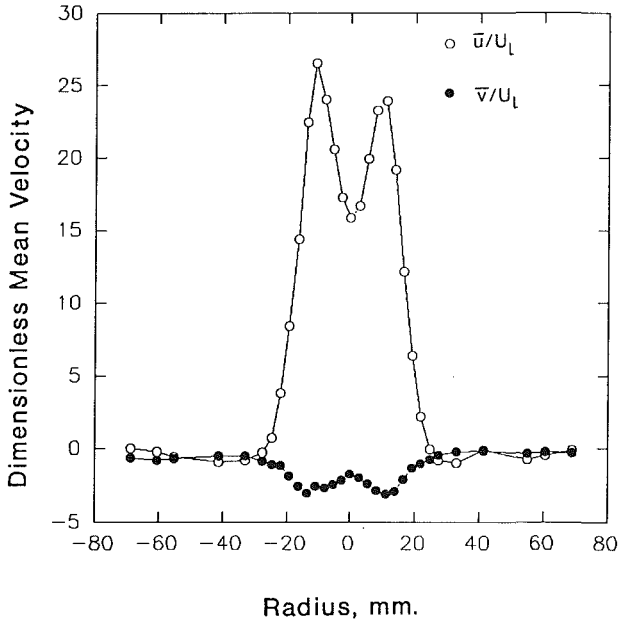


Fig. 5 *X*-scan diametral profiles of mean velocities at $z = 55$ mm

Reynolds number. This procedure resulted in a radius at which the profile exhibited its maximum of 16.537 mm, or 46.7 percent of the annular height from the jet inner radius.

The radial profile (y scan) of measured time-mean axial velocities, in the form of $\overline{u}/\overline{u}_{max}$, for a Reynolds number of 83,330, was much flatter than for fully developed flow, and the peak velocity occurred at about 15 mm radius, i.e., inward-peaked compared to anticipation. There was considerable asymmetry across the traverse, with the ratio of maximum time-mean axial velocity to mass-averaged axial velocity, $\overline{u}/U_{ave}$, being 1.214 for negative R and 1.186 for positive R. For an x-scan radial profile, the position of the maximum velocity was at a radius ± 14.6 mm, i.e., slightly more inward-peaked than the y-scan profile, while the values of $\overline{u}_{max}/U_{ave}$ were about 1.23, i.e., slightly more peaked.

The radial profile of local axial turbulence intensity $u'/\overline{u}$ from a y scan at 83,330 Reynolds number, was fairly flat at about 6 percent across the center section of the annular jet. Increases at the edges of the jet were due not only to the mean axial velocities decreasing, but also to an increase in the local fluctuating velocities due to the increased shear generated at the tube walls.

Despite the careful design of the inlet, it is apparent that the annular air jet is not being fed uniformly around its circumference, and that a radial velocity component is being developed that results in an inward flow toward the outer wall of the fuel tube.

With the combustor body mounted on the step, the closest axial station to the step at which LDA data can be taken is 5 mm. At this position with the combustor mounted and both jets flowing, the annular air jet takes control of the fuel jet. This can be seen in Fig. 2 for x- and y-scan diametral traverses, where the time-mean axial velocity divided by the mass-averaged axial velocity in the combustor, $\overline{u}/U_L$, is shown. This traverse is for a fuel jet Reynolds number of 11,320 and an air jet Reynolds number of 56,413. Comparison of the x- and y-scan data in the central region of the traverses reveals that fuel jet profiles have been distorted by the influence of the nonuniform air jet to produce a flow reduction in the $+X$, $+Y$ quadrant (see Fig. 1) that results in a small reverse flow region the x scan. Thus, the relatively minor nonuniformities in the isolated fuel and air jet flows have been magnified when both jets are flowing to result in significant distortion of the lower momentum fuel jet.

Figure 3 is a repeat of the y scan of Fig. 2 at an increased density of measurement; the $\overline{v}/U_L$ profile is also included. The improved resolution of the annular air jet can be seen. These profiles would represent adequate initial condition information for computational fluid dynamics calculations. The appropriate turbulence information is shown in Fig. 4.

General Flow Development. Selected diametral (x-scan) profiles of nondimensional time-average and fluctuating velocities at various axial positions in the combustor, Figs. 5–10, together with Figs. 3 and 4, present the general flow development in the combustor at the selected operating conditions.

The distinct high-velocity co-annular jet and the low velocity central jet (Figs. 3 and 4) quickly merge as the annular jet fills in the velocity defect represented by the central jet (Figs. 5

Downloaded 02 Jun 2010 to 171.66.16.112. Redistribution subject to ASME license or copyright; see http://www.asme.org/terms/Terms_Use.cfm

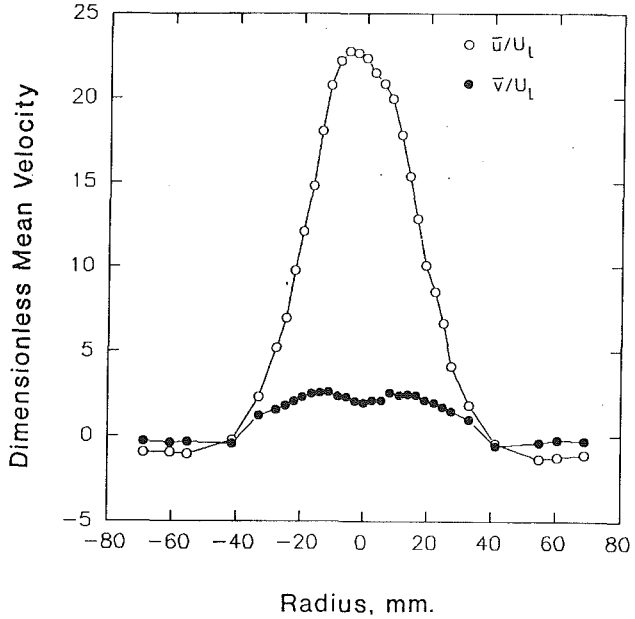


Fig. 7 *X*-scan diametral profiles of mean velocities at $z = 138$ mm

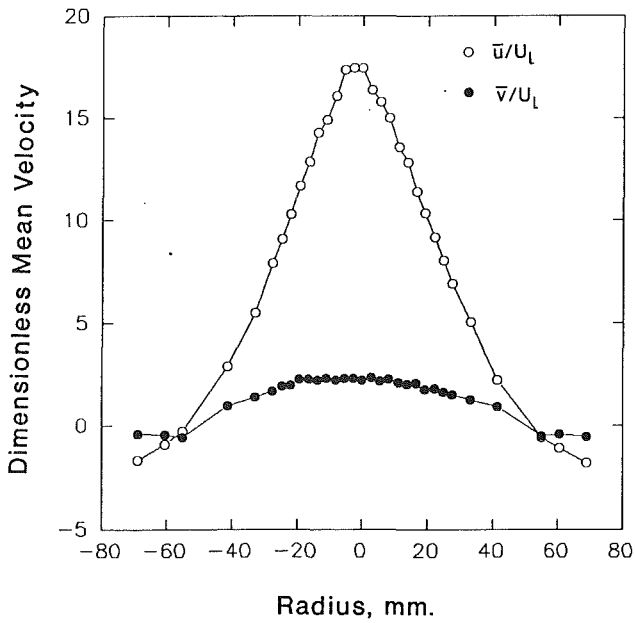


Fig. 9 *X*-scan diametral profiles of mean velocities at $z = 220$ mm

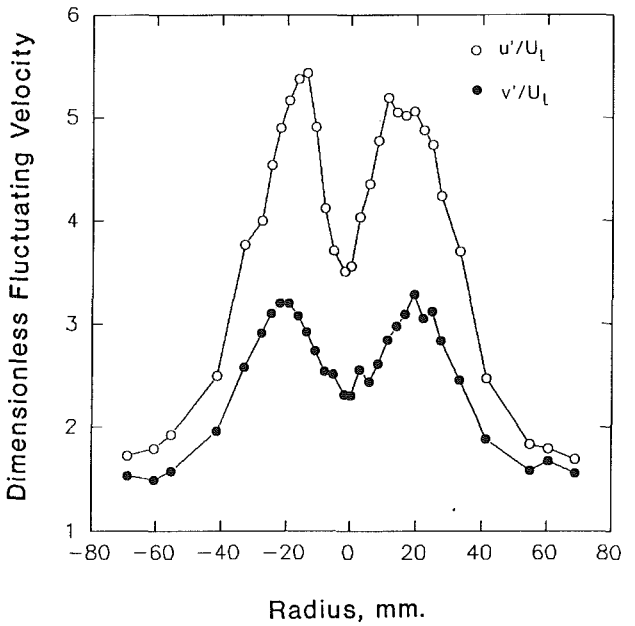


Fig. 8 *X*-scan diametral profiles of fluctuating velocities at $z = 138$ mm

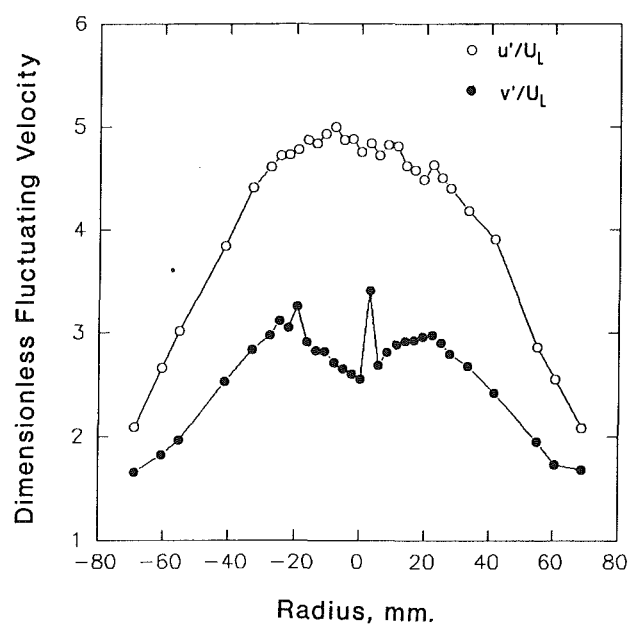


Fig. 10 *X*-scan diametral profiles of fluctuating velocities at $z = 220$ mm

and 6), and soon have the appearance of a single, central jet (Figs. 7–10). Note that the time-mean axial velocity profile reaches the single jet form (Fig. 7) before the fluctuating velocities do (Fig. 8). At all of the stations shown, the $\bar{u}$ profiles reveal the existence of the recirculation zone associated with the step; the window aperture does not permit full coverage of this region.

Figure 11 represents nondimensional time-averaged axial and radial velocity profiles from a y scan at an axial station of 138 mm. These plots should be compared with those in Fig. 7 (x scan) to obtain an assessment of the downstream asymmetry introduced into the flow by the upstream distortions due to the individual jet irregularities, Fig. 2.

The general characteristics are completed by Fig. 12, which gives centerline traverses of nondimensional time-averaged axial velocity. This shows that the initial momentum difference between the jets is so large that entrainment of the central jet by the annular jet results in the formation of a central recirculation bubble. Centerline axial velocity recovers and then overshoots as the annular jet expands to fill the central velocity deficit. Finally, the centerline axial velocity decays. High fluctuating axial velocities are associated with the fore and aft stagnation points of the central recirculation bubble.

Analysis of Results

Near-Field. The salient features of the near-field velocity development in the research combustor are displayed in Fig. 13, which is constructed from radial profile information.

Shown in Fig. 13 are data points and lines that represent the contours where the time-mean axial velocities are zero. These define the existence of the two recirculation zones noted above; one is associated with the step as expected, and the other on the centerline of the combustor is generated by jet

Downloaded 02 Jun 2010 to 171.66.16.112. Redistribution subject to ASME license or copyright; see http://www.asme.org/terms/Terms_Use.cfm

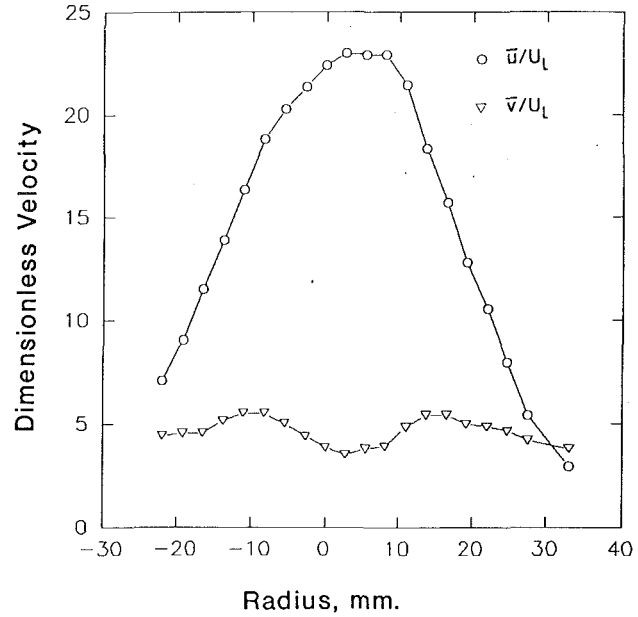


Fig. 11 Diametral profiles of mean velocities from a Y scan at $z = 138$ mm; for an assessment of flow distortion

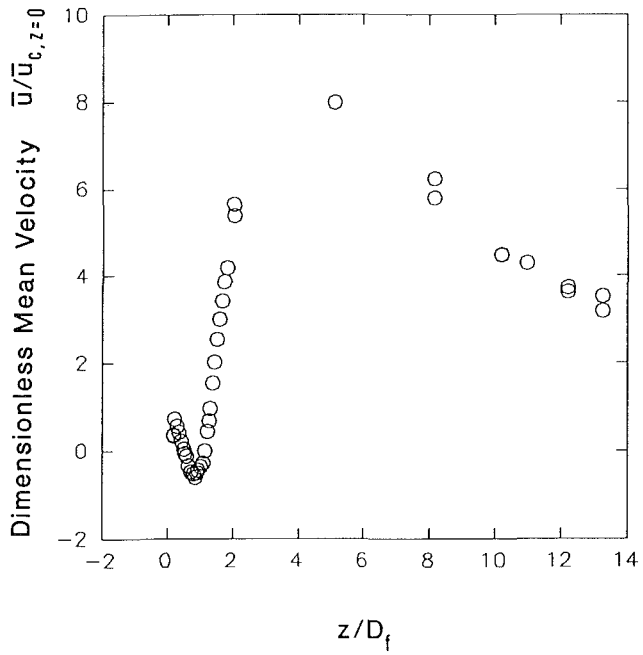


Fig. 12 Variation of axial mean velocity along combustor centerline, showing central recirculation zone

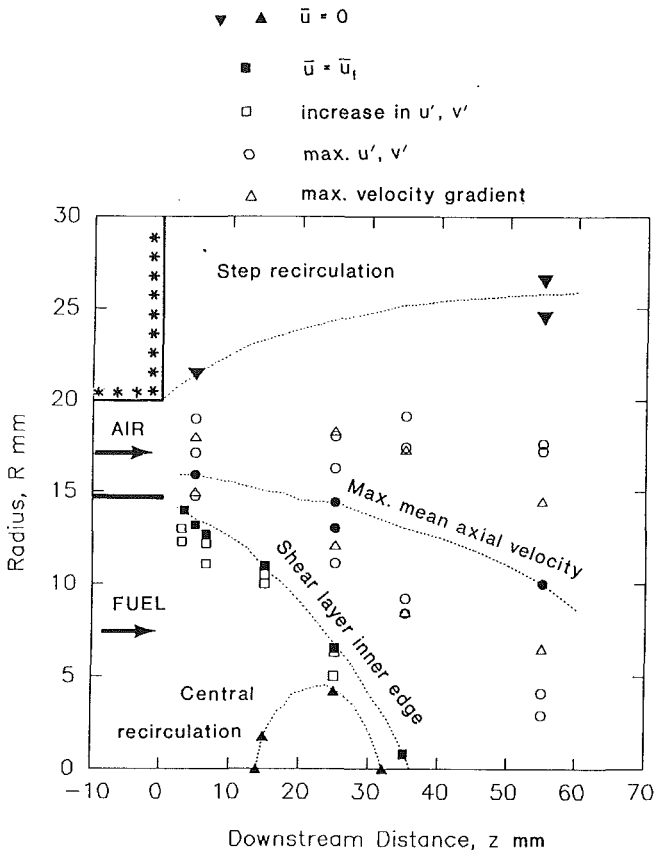


Fig. 13 Salient features of near-field development

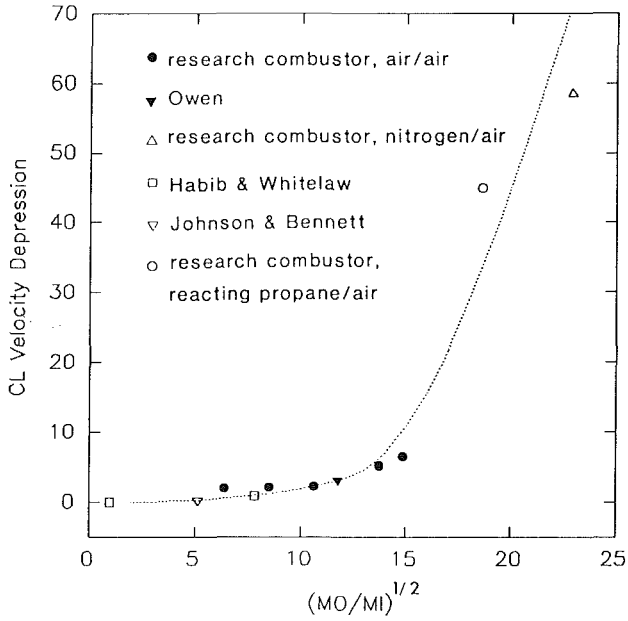


Fig. 14 Dependency of strength of centerline recirculation on jet momentum ratio, and comparison with data from the literature

interaction. These zero mean axial velocity lines delineate the beginnings and ends of the two separated flow regions, but not their radial extents. The central recirculation bubble is positioned on the combustor centerline at 14 mm downstream from the step, and extends downstream for another 18 mm.

Shear layers originate at the confluence of the central fuel jet and the concentric air jet. Shown are lines representing the locus of points where the local mean axial velocity is equal to the fuel mean axial velocity at the step, and also where it is equal to the maximum in the jet shear layer. The position of the inner edge of the jet shear layer can be checked by also plotting the locus of the radii where the fluctuating axial and radial velocity components exhibit a distinct increase from the fuel jet inlet values. This definition of the shear layer inner edge is at consistently reduced radii compared to the former definition.

The downstream distance where the inner edge of the jet shear layer intersects the combustor axis defines a conditional potential core length for the fuel jet. The fact that the fluctuating velocity definition of the shear layer inner edge is at smaller radii than the time-mean axial velocity definition is

Downloaded 02 Jun 2010 to 171.66.16.112. Redistribution subject to ASME license or copyright; see http://www.asme.org/terms/Terms_Use.cfm

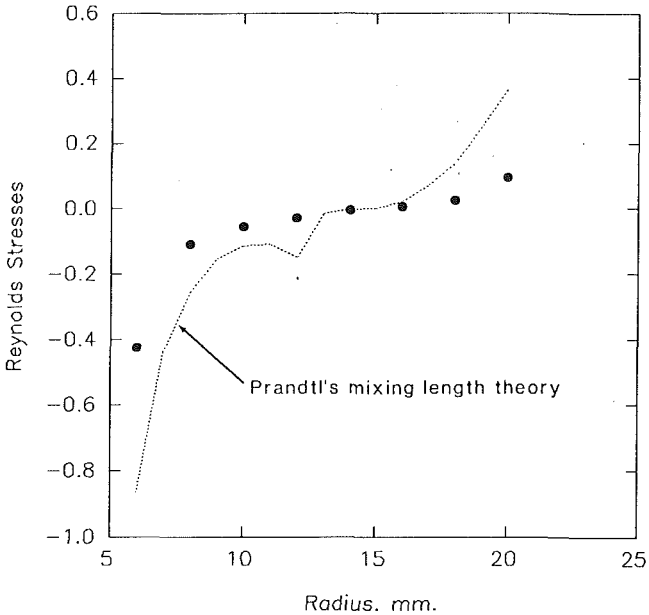


Fig. 15 Comparison of measured and calculated Reynolds stresses in jet shear layers at $z = 25$ mm

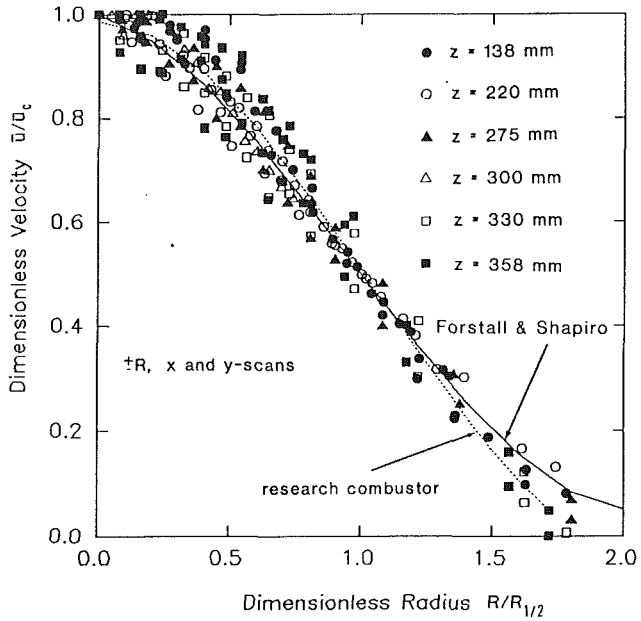


Fig. 17 Self-similarity of mean axial velocity profiles in far-field, and comparison with Shapiro's submerged round jet profile

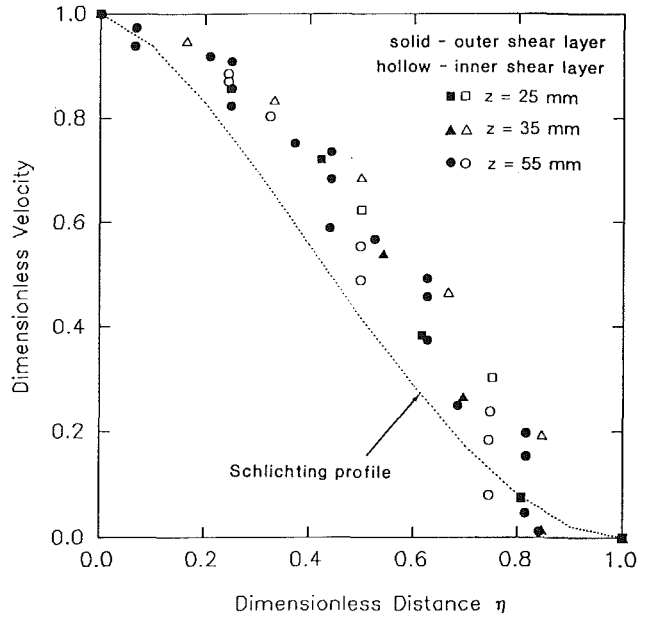


Fig. 16 Self-similarity of mean axial velocity profiles in jet shear layers, and comparison with Schlichting's profile

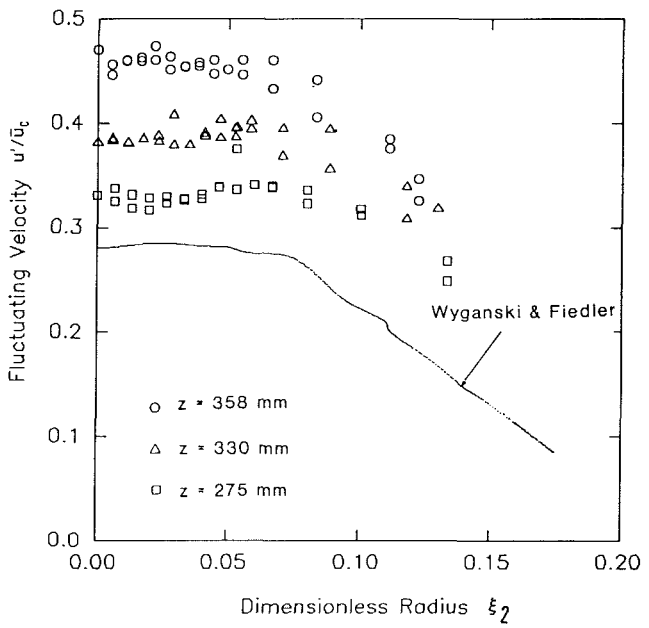


Fig. 18 Self-similarity of fluctuating velocity profiles in far-field, and comparison with Wyganski and Fiedler's free round jet profile

due to the existence of initial turbulence associated with boundary layer buildup on the interior surface of the fuel tube, upstream. Normal shear layer growth is linear, rather than the concave-downward curve seen in Fig. 13. This curvature is induced by the presence of the central recirculation bubble.

The dimensionless potential core length, z_p/R_f, is equal to 2.4. This value is in very good agreement with the theoretical calculations of Abramovich (1963) for coflowing jets with boundary layers.

The momentum difference that exists between the two jets initially results in entrainment of the low-momentum fuel jet by the high-momentum annular air jet surrounding it. The momentum difference is large enough to cause the centerline recirculation zone to form in the fuel jet. The strength of this effect can be characterized by the depression of the initial mean axial velocity on the combustor centerline, $(\overline{u}_{c,z=0} - \overline{u}_{c,\max})$. This velocity difference can be nondimensionalized by the maximum overall change, on a mass-average basis, that the center jet can undergo, i.e., $(U_I - U_L)$. Entrainment considerations would relate this ratio to the square root of the jet momentum ratio M_O/M_I.

Figure 14 is a plot of this relationship for the research combustor at a variety of operating conditions with air/air, air/nitrogen, and air/propane (reacting) flows, and for some similar geometries from the literature, e.g., Habib and Whitelaw (1979), Johnson and Bennett (1981), and Owen (1975). All of the present data points represent actual reverse flow conditions, while Habib and Whitelaw (1979) and Johnson and Bennett (1981) have points in which depression of the initial centerline velocity takes place, but no actual reverse flow occurs. This figure shows good agreement between the present data and those of other researchers.

Downloaded 02 Jun 2010 to 171.66.16.112. Redistribution subject to ASME license or copyright; see http://www.asme.org/terms/Terms_Use.cfm

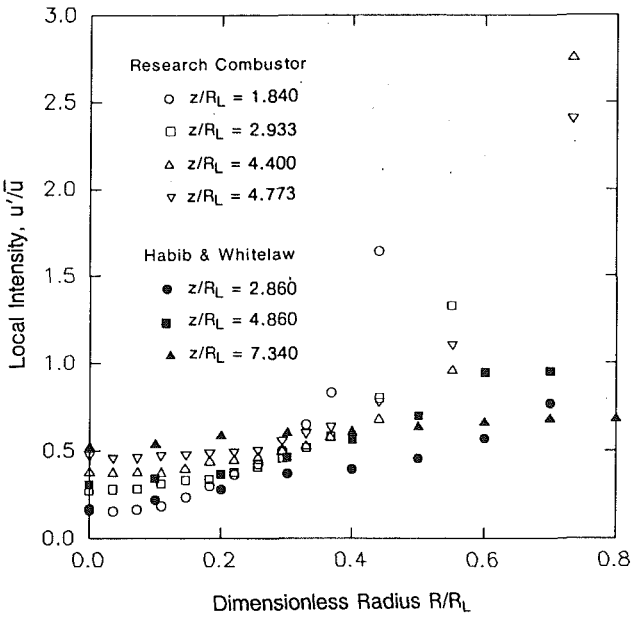


Fig. 19 Comparison of local turbulence intensities for Habib and Whitelaw with research combustor

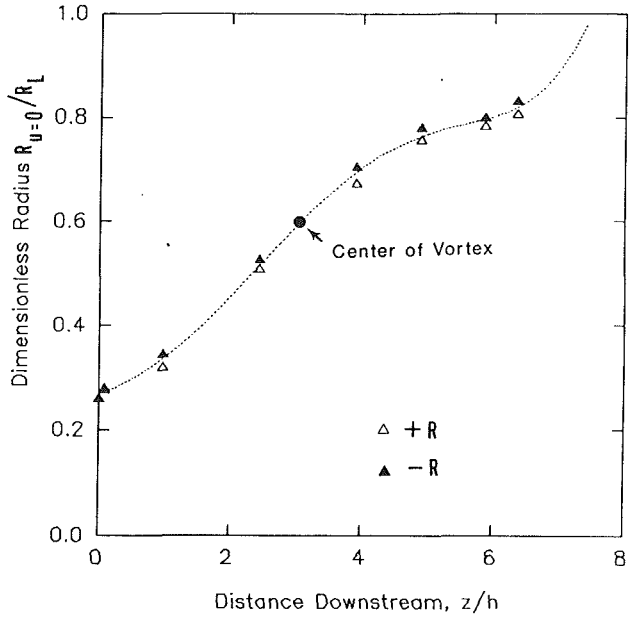


Fig. 20 Definition of step recirculation zone length

When considering Fig. 13, it was found that the locus of the radial positions in the jet shear layer where the fluctuating velocity components u' and v' reached a minimum coincided with the locus of the maximum mean axial velocity, and the maximum values of these components coincided with the loci of maximum velocity gradients in the mean velocity radial profiles. This is the case for a value of z equal to 35 mm, but only reasonably so at a station of z equal to 55 mm. For example, compare Figs. 5 and 6.

The implication of this behavior is that the local turbulence is generated by the local shear, through the local mean velocity profiles. This being so, the Reynolds stresses in the jet shear layer could be described by Prandtl's (1925) mixing length model (Abramovich, 1963),

$$\overline{u_i' u_j'} = l_m^2 \left|\frac{d\bar{u}_i}{dx_j}\right| \frac{d\bar{u}_i}{dx_j} \tag{2}$$

where for round jets the mixing length l_m is given by

$$l_m/\delta = 0.079 \tag{3}$$

and δ is the shear layer width.

Figure 15 compares a Reynolds stress radial profile calculated from Eqs. (2) and (3), and nondimensionalized by the square of measured local mean axial velocity, with the measured profile at z equal to 25 mm. The velocity gradients used in Eq. (2) were obtained from the measured mean velocity profiles.

By a z of 55 mm, the agreement between measured and calculated Reynolds stress profiles is only fair. This must be due to the upstream presence of the centerline recirculation zone, and the fuel jet high initial turbulence due to the presence of the acoustic isolator. By this axial station, the transport of turbulence is apparently becoming important in comparison with local shear generation.

The behavior of the shear layers with respect to Reynolds stresses suggests that the time-mean axial velocity profiles at different axial positions in these layers might be self-similar, that is, of the same shape but differing by a scale factor. To test this, several velocity profiles in both inner and outer layers were plotted in the dimensionless form,

$$\frac{u_1 - u}{u_1 - u_2} = F\left(\frac{y - y_2}{\delta}\right) \tag{4}$$

where u is the time-mean axial velocity in the shear layer at position y; u_1 and u_2, respectively, are the maximum and minimum velocities bounding the shear layer, and δ is its width. Inner and outer shear layer data were obtained from radial profiles at positive and negative radii for x scans and y scans at downstream positions of 25, 35, and 55 mm; the inner shear layer width at any axial position was defined from the positions of maximum jet velocity to that of the fuel jet (see Fig. 13), and the outer shear layer width from the position of maximum jet velocity to the zero velocity line in the step recirculation zone. The shear layer profiles are shown in Fig. 16.

Figure 16 demonstrates that the axial velocity profiles at the three positions downstream collapse onto a common relationship. There is no difference between the inner and outer layers. The flow asymmetries present in the flow should be recalled. The profiles, therefore, may be considered as being similar. Shown also on the figure is Schlichting's classical plane shear layer velocity profile (Schlichting, 1960)

$$\frac{u_1 - u}{u_1 - u_2} = (1 - \eta^{3/2})^2 \tag{5}$$

where

$$\eta = (y - y_2)/\delta \tag{6}$$

The correlated data have the same general form as Eq. (5), but differ from it in fullness. This difference is undoubtedly associated with the streamwise curvature of the jet shear layers in the research combustor.

Far-Field. In this region the individual jets interact vigorously with each other and have merged by 138 mm from their confluence (Figs. 7 and 8). Having lost their individuality, subsequent development takes place as though the two jets were a single round jet.

One of the major characteristics of the round jet is the development of self-similar profiles. The condition of similarity in the radial profiles of time-mean axial velocity is examined in Fig. 17 for axial stations of 138, 220, 275, 300, 330, and 358 mm by plotting the dimensionless radial profile of mean axial velocity $\bar{u}/\bar{u}_c$ against $R/R_{1/2}$ where R is radius and $R_{1/2}$ is the radius where the velocity $\bar{u}$ has fallen to one half of its centerline value $\bar{u}_c$. The data for $\pm R$ and x and y scans are included.

Downloaded 02 Jun 2010 to 171.66.16.112. Redistribution subject to ASME license or copyright; see http://www.asme.org/terms/Terms_Use.cfm

Figure 17 contains a line (with correlation coefficient 0.9998) representing Forstall and Shapiro's (Abramovich, 1963) data for submerged round jets with a variety of blowing ratios. A curve fit to the present data agrees excellently with the curve for Forstall and Shapiro's data out to a dimensionless radius of about 1.5, after which the two curves approach their own boundary conditions (i.e., submerging jet or step recirculation).

The effective origin (point source) of the apparent single jet can be found by extrapolating the locus of the radii $R_{1/2}$ for various axial stations backward until it intercepts the combustor axis. This yields an effective origin that is about 140 mm upstream of the step.

With the effective origin of the combined jet so determined, the turbulence profiles in the far-field region can be compared with the self-similar form of the turbulence profiles from Wyganski and Fiedler's round, free jet (Hinze, 1975). The similarity form used is the dimensionless radius ξ_2, where,

$$\xi_2 = R/(z+a) \tag{7}$$

and a is the distance upstream from the physical origin of the individual jets to the effective origin of the merged jets.

Figure 18 compares the dimensionless fluctuating velocity $u'/\overline{u}_c$ against ξ_2 for z of 275, 330, and 358 mm for $\pm R$ from an x scan. The line represents Wyganski and Fiedler's self-similar data to a correlation coefficient greater than 0.999. It can be seen that the turbulence profiles do not collapse onto a similar curve, but increase in intensity with increasing axial position. The behavior for the $v'/\overline{u}_c$ profiles is the same.

The behavior of the present turbulence profiles is in sharp contrast to that of Wyganski and Fiedler's round jet, and is in direct conflict with Fig. 17 where the time-mean axial velocity profiles are shown to be self-similar. The inevitable conclusion from this conflict is that the fluctuating velocity profiles in the far-field are not directly associated with, or derived from, the mean velocity profiles at the same axial station. Thus, for the turbulence field, flow history effects, i.e., convection of turbulence, dominates.

If the turbulence profiles are plotted in the form of a local turbulence intensity $u'/\overline{u}$ and $v'/\overline{u}$ against ξ_2, and compared with Corrsin's isothermal, free, round jet (Hinze, 1975) a similar finding is obtained. The present $u'/\overline{u}$ on the jet centerline is about twice that of Corrsin's jet, while $v'/\overline{u}$ is in better agreement; in both cases the present turbulence intensities increase much more rapidly with increasing dimensionless radius due to the presence of the combustor wall condition.

Despite the turbulence intensities being about twice the free round jet values, they are in accord with what is to be expected for the research combustor geometry. Radial profiles of local turbulence intensity $u'/\overline{u}$ at several axial stations are compared in Fig. 19 with those measured in a similar geometry by Habib and Whitelaw (1979). The increases in intensity at larger dimensionless radii represent falling values of $\overline{u}$ as the inner edges of the step recirculation zone are approached.

Step Recirculation. The downstream extent of the step recirculation zone may be found by tracing the locus of zero axial mean velocity ($R(u=0)$) from the individual radial profile measurements, such as Figs. 5, 7, and 9. This has been done for the x-scan profiles ($\pm R$), which cover a greater radial extent than the y-scan profiles; see Fig. 1. The results are plotted in Fig. 20 in the form of $R(u=0)/R_L$ versus z/h, where R_L is the combustor equivalent radius and h is the step height. The line representing the data is a fifth-order polynomial with a correlation coefficient of 0.9987. A portion of this curve appears in Fig. 13.

Although there are some small differences, the data show that the step recirculation zone development is fairly symmetric about the combustor centerline. The boundary marking the division between upstream and downstream flow exhibits at least one point of inflection. Along this line, the zero velocity point defines the center of the vortex, and this is shown on the figure at about three step heights downstream from the step. The approximate length of the recirculation zone is found by extrapolating the fitted curve to a dimensionless radius of unity. Such extrapolation results in a value of about 7.7 step heights, i.e., a z/D_L of about 3. When this value is compared with the collected step recirculation zone length experience (Morrison et al., 1987) for the test Reynolds number, the agreement is good.

Discussion

Optical access to the research combustor is acceptable and permits the behavior of the flow field to be mapped with reasonable coverage of the important features.

Efforts to condition the inlet flows result in individual jet flows that are reasonably uniform. The provision of a necessary acoustic isolator (Heneghan et al., 1990) in the fuel jet supply tube elevates the central jet fluctuating velocities over what would normally be associated with straight pipe flow and also affect the mean profiles. When the jets coflow and are enclosed, they interact extremely strongly, and the individual jet anomalies are amplified so that the symmetry downstream in the combustor is not especially good. This jet interaction effect is felt in the fuel jet upstream of the step, i.e., before the geometric confluence of the two jets, and it changes the inlet profiles of the central jet from the free-flow ones.

The step generates a large wall recirculation that extends a considerable distance down the combustor. It appears to be fairly symmetric. Jet momentum effects result in the creation of a small, central recirculation just downstream of the fuel jet discharge.

Outside the confines of the step recirculation and downstream of the central recirculation, the jet development takes place apparently largely unaffected by the presence of the recirculation zones. This time-mean development, in both near-field and far-field regions, is self-consistent, and is in good agreement with classical jet and shear layer behavior described through measurements in the literature. The initial turbulence generation in the jet shear layers is in accord with Prandtl's mixing length theory, but downstream of the central recirculation bubble and after the end of the fuel jet conditional potential core, the high initial level of turbulence and the transport of turbulence, i.e., flow history effects, start to dominate. Downstream, the individual jets merge into a single, central jet that has many of the time-mean characteristics of the classic free round jet and the submerged round jet. In this region the turbulence profiles are totally unassociated with the local velocity profiles.

There is no evidence that the special, nonaxisymmetric cross section of the research combustor influences the isothermal flow development to any serious degree. The influence of mass transfer, chemical reaction, and heat release on this flow field development will make an interesting future study.

Conclusions

1 The optical access in the research combustor is adequate to establish the major flow features.

2 Reliable LDA measurements of time-mean and fluctuating axial and radial velocity components have been made for the isothermal flow condition.

3 Three regions of flow development were observed: a near-field region, a far-field region, and a step recirculation region. In the near-field shear layer development leads to a potential core, within which is a recirculation bubble generated by the jet momentum ratio. In the far-field the individual jets have lost their identity and exhibit self-similarity. The step

Downloaded 02 Jun 2010 to 171.66.16.112. Redistribution subject to ASME license or copyright; see http://www.asme.org/terms/Terms_Use.cfm

recirculation bounds the near-field and part of the far-field regions.

4 The component flows that make up the overall flow development within the research combustor are in remarkable agreement with the descriptions provided by classical fluid dynamics.

5 There is no evidence that the presence of the flat optical windows and their interfacing with the corner fillets in the combustor cross section introduce any adverse effects on the flows measured. The cross section used provides a reasonable compromise between flow two dimensionality and optical access.

6 The major time-mean flow features of the research combustor could be calculated by the classical integral techniques of fluid dynamics. This is somewhat surprising. However, the fluctuating velocity fields, except for a very limited initial region, are uncoupled from the time-mean features. Realistic calculation of the complete flow characteristics therefore requires the solution of transport equations.

7 Initial conditions have been established that can be used as the basis for computational fluid dynamic calculations in this combustor.

Acknowledgments

This work was supported by the U. S. Air Force Wright Research and Development Center, Aero Propulsion and Power Laboratory, under Contract No. F33615-87-C-2822 to Pratt & Whitney, East Hartford, CT (Contract Monitor: Lt. A. L. Lesmerises) and Contract No. F33615-87-C-2767 to University of Dayton, Dayton, OH (Contract Monitor: Dr. W. M. Roquemore). The authors wish to thank Dr. Paul Hedman, Brigham Young University, and also staff members of Systems Research Laboratories, Inc., for access to some of their unpublished experimental data obtained in the research combustor, and used in Figs. 3, 4, and 14.

References

Abramovich, G. N., 1963, *The Theory of Turbulent Jets*, M. I. T. Press, Cambridge, MA.

Chen, T. H., and Lightman, A. J., 1985, "The Effects of Particle Arrival Statistics on Laser Anemometer Measurements," ASME FED-Vol. 33, pp. 172–176.

Glass, M., and Bilger, R. W., 1978, "The Turbulent Jet Diffusion Flame in Coflowing Stream—Some Velocity Measurements," *Combustion Science and Technology*, Vol. 18, pp. 165–177.

Habib, M. A., and Whitelaw, J. H., 1979, "Velocity Characteristics of a Confined Coaxial Jet," ASME Paper No. 79-WA/FE-9.

Heneghan, S. P., Vangsness, M. D., Ballal, D. R., Lesmerises, A. L., and Sturgess, G. J., 1990, "Acoustic Characteristics of a Research Step Combustor," AIAA Paper No. AIAA-90-1851, presented at AIAA/SAE/ASME/ASEE 26th Joint Propulsion Conference, Orlando, FL, July 16–18.

Hinze, J. O., 1975, Turbulence, 9th ed., McGraw-Hill, New York.

Johnson, B. V., and Bennett, J. C., 1981, "Mass and Momentum Turbulent Transport Experiment With Confined Coaxial Jets," NASA CR-165574.

Morrison, G. L., Tatterson, G. B., and Long, M. W., 1987, "A 3-D Laser Velocimeter Investigation of Turbulent, Incompressible Flow in an Axisymmetric Sudden Expansion," AIAA Paper No. AIAA-87-0119, AIAA 25th Aerospace Sciences Meeting, Reno, NV, Jan. 12–15.

Owen, F. K., 1975, "Laser Velocity Measurements on Confined Co-axial Jet With Recirculation," AIAA Paper No. 75-d120, 13th Aerospace Sciences Meeting, Pasadena, CA, Jan.

Rehme, K., 1974, "Turbulent Flow in Smooth Concentric Annuli With Small Radius Ratios," *J. Fluid Mech.*, Vol. 64, Pt. 2, pp. 263–287.

Schlichting, H., 1960, *Boundary Layer Theory*, 4th ed., McGraw-Hill, New York.

Sturgess, G. J., Sloan, D. J., Lesmerises, A. L., Heneghan, S. P., and Ballal, D. R., 1992, "Design and Development of a Research Combustor for Lean Blowout Studies," ASME JOURNAL OF ENGINEERING FOR GAS TURBINES AND POWER, Vol. 114, pp. 13–19.

Downloaded 02 Jun 2010 to 171.66.16.112. Redistribution subject to ASME license or copyright; see http://www.asme.org/terms/Terms_Use.cfm